Corrosion Mechanisms in Theory and Practice

Second Edition, Revised and Expanded

edited by

Philippe Marcus

Laboratoire de Physico-Chimie des Surfaces
Université Pierre et Marie Curie
Ecole Nationale Supérieure de Chimie de Paris
Paris, France



MARCEL DEKKER, INC. NEW YORK • BASEL

Copyright © 2002 Marcel Dekker, Inc.

First edition published as *Corrosion Mechanisms in Theory and Practice* edited by P. Marcus and J. Oudar.

ISBN: 0-8247-0666-8

This book is printed on acid-free paper.

Headquarters
Marcel Dekker, Inc.
270 Madison Avenue, New York, NY 10016
tel: 212-696-9000; fax: 212-685-4540

Eastern Hemisphere Distribution
Marcel Dekker AG
Hutgasse 4, Postfach 812, CH-4001 Basel, Switzerland
tel: 41-61-261-8482; fax: 41-61-261-8896

World Wide Web
http://www.dekker.com

The publisher offers discounts on this book when ordered in bulk quantities. For more information, write to Special Sales/Professional Marketing at the headquarters address above.

Copyright © 2002 by Marcel Dekker, Inc. All Rights Reserved.

Neither this book nor any part may be reproduced or transmitted in any form or by any means, electronic or mechanical, including photocopying, microfilming, and recording, or by any information storage and retrieval system, without permission in writing from the publisher.

Current printing (last digit):
10 9 8 7 6 5 4 3 2 1

PRINTED IN THE UNITED STATES OF AMERICA

Copyright © 2002 Marcel Dekker, Inc.

Preface

Corrosion is a major issue for the increase of service life and reliability of metallic materials. A detailed understanding of the mechanisms of corrosion helps us to solve existing corrosion problems and to prevent future problems.

The aim of this book is to review recent advances in the understanding of corrosion and protection mechanisms. A detailed view is provided of the chemical and electrochemical surface reactions that govern corrosion, and of the link between microscopic forces and macroscopic behavior, is provided.

In order to cover fundamental as well as practical aspects, the second edition, which has been revised and expanded (three new chapters have been added) contains in 19 chapters. Chapters 1 to 13 cover the basic phenomena in corrosion: adsorption, entry of hydrogen, anodic dissolution, passivation, passivity breakdown and localized corrosion (pitting and crevice corrosion), stress corrosion cracking, and corrosion fatigue. Chapters 14 to 19 provide the connection between the theoretical aspects of corrosion mechanisms and practical applications in industry: corrosion inhibition, atmospheric corrosion, microbially induced corrosion, corrosion in nuclear systems, corrosion of microelectronic and magnetic data-storage devices, and the technologically important area of corrosion protection by surface coatings.

This book is based on the results of intensive worldwide research efforts in materials science, surface science, and corrosion science over the past few years. The contributors, from leading academic and industrial research institutes, are highly recognized scientists in these disciplines.

Philippe Marcus

Copyright © 2002 Marcel Dekker, Inc.

Contents

Preface *iii*
Contributors *vii*

BASIC PHENOMENA

1. Introduction to Surface Reactions: Electrochemical Basis of Corrosion 1
Dieter Landolt

2. Introduction to Surface Reactions: Adsorption from Gas Phase 19
Jacques Oudar

3. Surface Effects on Hydrogen Entry into Metals 53
Elie Protopopoff and Philippe Marcus

4. Anodic Dissolution 97
Michel Keddam

5. Thin Oxide Film Formation on Metals 171
Francis P. Fehlner and Michael J. Graham

6. Growth and Stability of Passive Films 189
Barry MacDougall and Michael J. Graham

7. Passivity of Austenitic Stainless Steels 217
Clive R. Clayton and Ingemar Olefjord

8. Mechanisms of Pitting Corrosion 243
Hans-Henning Strehblow

Copyright © 2002 Marcel Dekker, Inc.

9. Sulfur-Assisted Corrosion Mechanisms and the Role of Alloyed Elements 287
Philippe Marcus

10. Further Insights on the Pitting Corrosion of Stainless Steels 311
Bernard Baroux

11. Crevice Corrosion of Metallic Materials 349
Pierre Combrade

12. Stress-Corrosion Cracking Mechanisms 399
Roger C. Newman

13. Corrosion Fatigue Mechanisms in Metallic Materials 451
T. Magnin

APPLICATIONS

14. Corrosion Prevention by Adsorbed Organic Monolayers and Ultrathin Plasma Polymer Films 479
Michael Rohwerder, Guido Grundmeier, and Martin Stratmann

15. Atmospheric Corrosion 529
Christofer Leygraf

16. Microbially Influenced Corrosion 563
Dominique Thierry and Wolfgang Sand

17. Corrossion in Nuclear Systems: Environmentally Assisted Cracking in Light Water Reactors 605
F. P. Ford and Peter L. Andresen

18. Corrosion of Microelectronic and Magnetic Data-Storage Devices 643
Gerald S. Frankel and Jeffrey W. Braithwaite

19. Organic Coatings 683
J. H. W. de Wit, D. H. der Weijde, and G. Ferrari

Index *731*

Copyright © 2002 Marcel Dekker, Inc.

Contributors

Peter L. Andresen Corrosion Coatings and Joining Research and Development Center, General Electric Company, Schenectady, New York

Bernard Baroux Ugine Research Center, Ugine-Savoie, Ugine, France

Jeffrey W. Braithwaite Sandia National Laboratories, Albuquerque, New Mexico

Clive R. Clayton Department of Materials Science and Engineering, State University of New York at Stony Brook, Stony Brook, New York

Pierre Combrade FRAMATOME, Centre Technique, Le Creusot, France

J. H. W. de Wit Netherlands Institute for Metals Science, Delft University of Technology, Delft, and Corus Research and Development, Ijmuiden, The Netherlands

Francis P. Fehlner Department of Advanced Materials, Corning Incorporated, Corning, New York

G. Ferrari TNO Industrie, Den Helder, The Netherlands

F. P. Ford Corrosion Coatings and Joining Research and Development Center, General Electric Company, Schenectady, New York

Gerald S. Frankel Department of Materials Science and Engineering, Fontana Corrosion Center, The Ohio State University, Columbus, Ohio

Michael J. Graham Institute for Microstructural Science, National Research Council of Canada, Ottawa, Ontario, Canada

Copyright © 2002 Marcel Dekker, Inc.

Guido Grundmeier Department for Interface Chemistry and Surface Technology, Max-Planck-Institut für Eisenforschung GmbH, Düsseldorf, Germany

Michel Keddam Laboratoire de Physique des Liquides et Electrochimie, Université Pierre et Marie Curie, Paris, France

Dieter Landolt Département des Matériaux, Laboratoire de Métallurgie Chimique, Ecole Polytechnique Fédérale de Lausanne, Lausanne, Switzerland

Christofer Leygraf Division of Corrosion Science, Department of Materials Science and Engineering, Royal Institute of Technology, Stockholm, Sweden

Barry MacDougall Institute for Environmental Chemistry, National Research Council of Canada, Ottawa, Ontario, Canada

T. Magnin Ecole Nationale Supérieure des Mines de Saint-Etienne, Saint-Etienne, France

Philippe Marcus Laboratoire de Physico-Chimie des Surfaces, Université Pierre et Marie Curie, Ecole Nationale Supérieure de Chimie de Paris, Paris, France

Roger C. Newman Corrosion Protection Center, University of Manchester Institute of Science and Technology, Manchester, England

Ingemar Olefjord Department of Engineering Metals, Chalmers University of Technology, Göteborg, Sweden

Jacques Oudar Laboratoire de Physico-Chimie des Surfaces, Université Pierre et Marie Curie, Ecole Nationale Supérieure de Chimie de Paris, Paris, France

Elie Protopopoff Laboratoire de Physico-Chimie des Surfaces, Université Pierre et Marie Curie, Ecole Nationale Supérieure de Chimie de Paris, Paris, France

Michael Rohwerder Department for Interface Chemistry and Surface Technology, Max-Planck-Institut für Eisenforschung GmbH, Düsseldorf, Germany

Wolfgang Sand Universität Hamburg, Hamburg, Germany

Hans-Henning Srehblow Institut für Physikalische Chemie und Elektrochemie, Heinrich-Heine-Universität Düsseldorf, Düsseldorf, Germany

Martin Stratmann Department for Interface Chemistry and Surface Technology, Max-Planck-Institut für Eisenforschung GmbH, Dusseldorf, Germany

Dominique Thierry Swedish Corrosion Institute, Stockholm, Sweden

D. H. van der Weijde Corrus Research and Development, Ijmuiden, The Netherlands

Copyright © 2002 Marcel Dekker, Inc.

1

Introduction to Surface Reactions: Electrochemical Basis of Corrosion

Dieter Landolt
Ecole Polytechnique Fédérale de Lausanne, Lausanne, Switzerland

INTRODUCTION

Most corrosion phenomena are of electrochemical nature. They imply two or more electrode reactions: the oxidation of a metal (anodic partial reaction) and the reduction of an oxidizing agent (cathodic partial reaction). To understand corrosion reactions one needs to study electrochemical thermodynamics and electrochemical kinetics of the partial reactions. For example, the corrosion of zinc in an acid environment proceeds according to the overall reaction:

$$Zn + 2H^+ \rightarrow Zn^{2+} + H_2 \tag{1}$$

This reaction includes the anodic partial reaction (2) and the cathodic partial reaction (3):

$$Zn \rightarrow Zn^{2+} + 2e \tag{2}$$

$$2H^+ + 2e \rightarrow H_2 \tag{3}$$

The corrosion rate depends on the electrode kinetics of both partial reactions. In principle, it can be predicted if all electrochemical parameters of the anodic and cathodic partial reactions are known. According to Faraday's law, there is a linear relationship between the metal dissolution rate at any potential, v_M, and the partial anodic current density for metal dissolution $i_{a,M}$:

$$v_M = \frac{i_{a,M}}{nF} \tag{4}$$

In this equation n is the charge number (dimensionless), which indicates the number of electrons exchanged in the dissolution reaction, and F is the Faraday constant, F = 96,485 C/mol. In the absence of an external polarization a metal in contact with an oxidizing electrolytic environment acquires spontaneously a certain potential, called the corrosion potential, E_{cor}. The partial anodic current density at the corrosion potential is equal to the corrosion current density i_{cor}. Equation (4) thus becomes:

$$v_{M(E=E_{cor})} = v_{cor} = \frac{i_{cor}}{nF} \tag{5}$$

Copyright © 2002 Marcel Dekker, Inc.

The corrosion potential always lies between the equilibrium potentials of the respective anodic and cathodic partial reactions. Its exact value is determined by the kinetics of the partial reactions.

ELECTROCHEMICAL THERMODYNAMICS

Electrochemical thermodynamics predicts the equilibrium potential of the partial reactions. The overall stoichiometry of any chemical reaction can be expressed by Eq. (6).

$$0 = \sum \nu_i B_i \tag{6}$$

Here the symbol B_i designates the reactants and products. The stoichiometric coefficients ν_i of the products are positive and of the reactants negative. The free enthalpy of reaction ΔG is

$$\Delta G = \sum \nu_i \mu_i \tag{7}$$

Here μ_i is the chemical potential of the participating species. If reaction (6) is carried out in an electrochemical cell, the corresponding equilibrium potential E_{rev} is given by

$$\Delta G = -nFE_{rev} \tag{8}$$

By analogy, under standard conditions (all activities equal to one) one gets

$$\Delta G^\circ = -nFE^\circ \tag{9}$$

where ΔG° represents the standard free enthalpy and E° represents the standard potential of the reaction.

It is common to write electrode reactions in the general form

$$\sum \nu_{ox,i} B_{ox,i} + ne = \sum \nu_{red,i} B_{red,i} \tag{10}$$

Here $\nu_{ox,i}$ represents the stoichiometric coefficient of the "oxidized" species, $B_{ox,i}$ appearing on the left side of the equality sign together with the free electrons, and $\nu_{red,i}$ indicates the stoichiometric coefficients of the reduced species, $B_{red,i}$, appearing on the right side of the equality sign, opposite to the electrons. Equation (10) corresponds to a partial reduction reaction and the stoichiometric coefficients $\upsilon_{ox,i}$ and $\nu_{red,i}$ are both positive.

By setting the standard chemical potential of the solvated proton and of molecular hydrogen equal to zero, $\mu^\circ_{H^+} = 0$, $\mu^\circ_{H_2} = 0$, one can define the standard potential of the partial reduction reaction (10) with respect to the standard hydrogen electrode. The standard potential of an electrode reaction thus corresponds to the overall reaction:

$$\sum \nu_{ox,i} B_{ox,i} + \frac{n}{2} H_{2(P_{H_2}=1\,bar)} = \sum \nu_{red,i} B_{red,i} + nH^+_{(aH^+=1)} \tag{11}$$

Table 1 indicates the standard potential of selected electrode reactions. Extensive compilations of data can be found in Refs. 1 and 2.

Copyright © 2002 Marcel Dekker, Inc.

TABLE 1 Standard Potentials of Electrode Reactions at 25°C

Electrode	$E^{\circ}N$
$Li^{+} + e = Li$	−3.045
$Mg^{2+} + 2e = Mg$	−2.34
$Al^{3+} + 3e = A$	−1.67
$Ti^{2+} + 2e = Ti$	−1.63
$Cr^{2+} + 2e = Cr$	−0.90
$Zn^{2+} + 2e = Zn$	−0.76
$Fe^{2+} + 2e = Fe$	−0.44
$Ni^{2+} + 2e = Ni$	−0.257
$2H^{+} + 2e = H2$	0
$Cu^{2+} + 2e = Cu$	0.340
$Ag^{+} + e = Ag$	0.799
$O_2 + 4H^{+} + 4e = 2H_2O$	1.229
$Au^{3+} + 3e = Au$	1.52

The chemical potential of a species B is defined by (12), where a_B represents its activity.

$$\mu_B = \mu_B^{\circ} + RT \ln a_B \tag{12}$$

Introducing (12) into (7) applied to reaction (11), one obtains for the free enthalpy of reaction

$$\Delta G = \Delta G^{\circ} + RT \ln \frac{a_{H^+}^{n} \prod a_{\text{red},i}^{\nu_{\text{red},i}}}{P_{H_2}^{n/2} \prod a_{\text{ox},i}^{\nu_{\text{ox},i}}} \tag{13}$$

With (8) and using $a_{H+} = 1$, $P_{H_2} = 1$ bar for the standard hydrogen electrode, one obtains the Nernst equation (14) of an electrode reaction. It expresses the variation of the equilibrium potential E_{rev} with respect to the standard hydrogen electrode as a function of the activities of the participating species $B_{ox,i}$ and $B_{red,i}$.

$$E_{rev} = E^{\circ} + \frac{RT}{nF} \ln \frac{\prod a_{\text{ox},i}^{\nu_{\text{ox},i}}}{\prod a_{\text{red},i}^{\nu_{\text{red},i}}} \tag{14}$$

In Eq. (14) the activity of pure substances is equal to one. The activity of dissolved ions cannot be determined unless nonthermodynamic assumptions are made. In corrosion one usually replaces the ionic activities by the respective concentrations. Thus for the electrode reaction (2) one obtains

$$E_{rev} = E_{Zn^{2+}/Zn}^{\circ} + \frac{RT}{2F} \ln c_{Zn^{2+}} \tag{15}$$

Using the data of Table 1 and replacing the natural logarithm by the logarithm base 10, this yields for 25°C

$$E_{rev} = -0.76 + \frac{0.059}{2} \log c_{Zn^{2+}} \tag{16}$$

Copyright © 2002 Marcel Dekker, Inc.

In a similar way, for the reaction

$$Zn(OH)_2 + 2H^+ + 2e = Zn + 2H_2O \tag{17}$$

the Nernst equation reads

$$E_{rev} = E^\circ_{Zn(OH)_2/Zn} + \frac{RT}{F} \ln a_{H^+} \tag{18}$$

At 25°C this becomes

$$E_{rev} = -0.439 - 0.059\ pH \tag{19}$$

In this equation $E^\circ_{Zn\,(OH)_2/Zn} = -0.439$ is the standard potential for the formation of a hydrated zinc oxide [2].

Pourbaix Diagrams

The graphical representation of the reversible potential as a function of pH is called the potential-pH diagram or Pourbaix diagram. In order to trace such diagrams one must fix the concentration of the dissolved species. Figure 1 shows a simplified Pourbaix diagram for zinc [2]. The numbers indicate different concentrations of

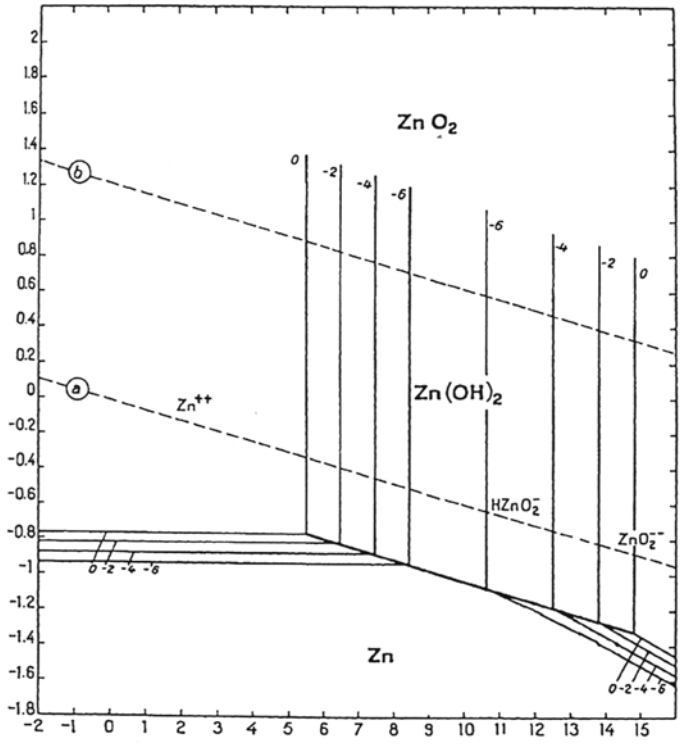


Figure 1 Potential-pH diagram of Zu (From Ref. 2).

Copyright © 2002 Marcel Dekker, Inc.

dissolved species, for example, 10^{-2}, 10^{-4} mol/L. The diagram shown takes into account the formation of zinc hydroxide, of Zn^{2+} and of the zincate ions $HZnO_2^-$ and ZnO_2^{2-}. At high potentials ZnO_2 may possibly be formed, but because the corresponding thermodynamic data are uncertain they are not presented in the diagram. The broken lines indicate the domain of thermodynamic stability of water. Pourbaix diagrams are widely used in corrosion because they easily permit one to identify the predominant species at equilibrium for a given potential and pH. On the other hand, being based on thermodynamic data, they give no information on the rate of possible corrosion reactions.

KINETICS OF CHARGE TRANSFER REACTIONS

At the electrode-electrolyte interface, a charge separation between the metal surface and the electrolyte occurs. The spatial region corresponding to the charge separation is called the electrical double layer. It is usually separated into two parts, the Helmholtz layer or compact double layer and Gouy-Chapman layer or diffuse double layer. The relative importance of the diffuse double layer increases with decreasing concentration. In very dilute solutions it may extend over a distance of several nanometers, whereas the compact layer never exceeds two to three tenths of a nanometer. The charges at the interface establish an electric field. Within the compact double layer the electric field reaches values of the order of 10^8 to 10^9 V/m. Charge transfer reactions occur across the compact double layer and the influence of the diffuse double layer is usually neglected.

Let us consider the transfer of n electrons between two species, B_{ox} and B_{red}.

$$B_{red} \underset{v_c}{\overset{v_a}{\rightleftharpoons}} B_{ox} + ne \tag{20}$$

According to Faraday's law, the current density across the interface corresponding to this reaction is equal to the difference of the anodic rate v_a and the cathodic rate v_c multiplied by nF.

$$i = nF(v_a - v_c) = k'_{a(E)} c_{red,s} - k'_{c(E)} c_{ox,s} \tag{21}$$

Here $k'_{a(E)}$ and $k'_{c(E)}$ are potential-dependent rate constants and $c_{red,s}$ and $c_{ox,s}$ represent the surface concentrations of B_{red} and $B_{ox,}$ respectively. The rate constants k'_a and k'_c obey the Arrhenius equation.

$$k'_{a(E)} = k'_{a,0} \exp\left(-\frac{\Delta G_a^{\#}}{RT}\right) \tag{22}$$

$$k'_{c(E)} = k'_{c,0} \exp\left(-\frac{\Delta G_c^{\#}}{RT}\right) \tag{23}$$

Here $\Delta G_a^{\#}$ and $\Delta G_c^{\#}$ represent the activation energies for the anodic and cathodic partial reactions, respectively, and $k'_{a,0}$ *and* $k'_{c,0}$ are preexponential factors. The presence of an electric field at the electrode-electrolyte interface modifies the activation energy of the partial oxidation and reduction reactions as shown

Copyright © 2002 Marcel Dekker, Inc.

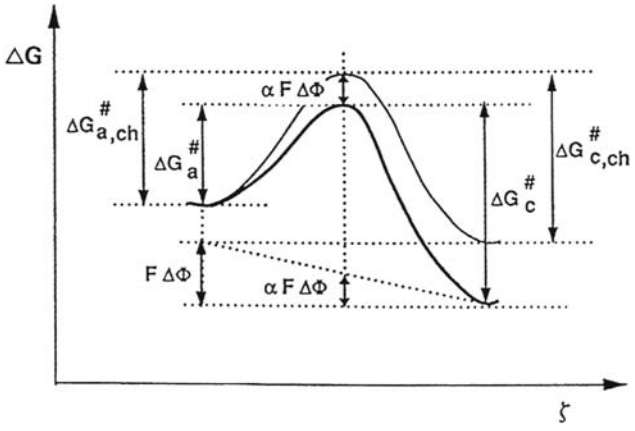


Figure 2 Free energy as a function of the reaction coordinate showing the influence of the electrical potential on the activation energy of a charge transfer process.

schematically in Figure 2. The electric field in this case diminishes the activation energy of the anodic partial reaction and increases that of the cathodic partial reaction.

$$\Delta G_{a}^{\#} = \Delta G_{a,ch}^{\#} - \alpha F \Delta\Phi \tag{24}$$

$$\Delta G_{c}^{\#} = \Delta G_{c,ch}^{\#} + (1-\alpha) F \Delta\Phi \tag{25}$$

Here $\Delta G_{a,ch}^{\#}$ and $\Delta G_{c,ch}^{\#}$ represent the potential-independent parts of the activation energies and $\Delta\Phi$ represents the potential difference across the interface. The proportionality factor α is called the charge transfer coefficient. Its value is usually close to 0.5 [3]. The absolute value of $\Delta\Phi$ is not measurable. It differs from the electrode potential E measured with respect to the standard hydrogen reference electrode by a constant.

$$E = \Delta\Phi + \text{constant} \tag{26}$$

Combining all potential-independent terms in the rate constants k_a and $k_{c,}$ one gets

$$\begin{aligned} k'_{a(E)} &= k_a \exp\left(\frac{\alpha n F}{RT} E\right) \\ k'_{c(E)} &= k_c \exp\left(-\frac{(1-\alpha) n F}{RT} E\right) \end{aligned} \tag{27}$$

With Eqs. (21) and (27) one obtains Eq. (28).

$$i = nFk_a c_{red,s} \exp\left(\frac{\alpha n F}{RT} E\right) - nFk_c c_{ox,s} \exp\left(-\frac{(1-\alpha) n F}{RT} E\right) \tag{28}$$

The current i corresponds to the sum of the partial anodic and cathodic current densities:

$$i = i_a + i_c \tag{29}$$

Copyright © 2002 Marcel Dekker, Inc.

The anodic and cathodic partial current densities, i_a and i_c, respectively, are given by

$$i_a = nFk_a c_{red,s} \exp\left(\frac{\alpha nF}{RT}E\right) \tag{30}$$

$$i_c = nFk_c c_{ox,s} \exp\left(-\frac{(1-\alpha)nF}{RT}E\right) \tag{31}$$

At the reversible potential, $E = E_{rev}$, the current density i is zero and the surface concentration of the reacting species is equal to the bulk concentration: $c_{red,s} = c_{red,b}$ and $c_{ox,s} = c_{ox,b}$. This allows one to define the exchange current density of a reaction by the relation:

$$i_{a(E=E_{rev})} = -i_{c(E=E_{rev})} = i_o \tag{32}$$

With (32) and (28) one gets

$$i_o = nFk_a c_{red,b} \exp\left(\frac{\alpha nF}{RT}E_{rev}\right) = nFk_c c_{ox,b} \exp\left(-\frac{(1-\alpha)nF}{RT}E_{rev}\right) \tag{33}$$

This expression shows that the value of the exchange current density depends on the concentration of the participating species. Defining the overvoltage $\eta = E - E_{rev}$, Eqs. (33) and (28) yield (34).

$$i = i_o \frac{c_{red,s}}{c_{red,b}} \exp\left(\frac{\alpha nF}{RT}\eta\right) - i_o \frac{c_{ox,s}}{c_{ox,b}} \exp\left(-\frac{(1-\alpha)nF}{RT}\eta\right) \tag{34}$$

If the rate of an electrode reaction is entirely controlled by charge transfer, the concentrations of reactants and products at the electrode surface are equal to the bulk concentrations. Equation (34) then reads

$$i = i_o \exp\left(\frac{\alpha nF}{RT}\eta\right) - i_o \exp\left(-\frac{(1-\alpha)nF}{RT}\eta\right) \tag{35}$$

This is the usual form of the Butler-Volmer equation, which describes the relationship between current density and potential for a simple electrode reaction controlled by charge transfer.

Normally, multielectron transfer reactions proceed in subsequent one-electron transfer reaction steps. For $n > 1$, Eq. (35), therefore, does not describe the physical mechanism. Indeed, depending on which reaction step is rate limiting, the value of the exponential terms may change. For example, the cathodic reduction of protons corresponding to the overall reaction

$$2H^+ + 2e \rightarrow H_2 \tag{36}$$

proceeds in two steps. The Volmer-Heyrovsky mechanism applies to most metal substrates:

$$H^+ + e \rightarrow H_{ads} \tag{37}$$

$$H^+ + H_{ads} + e \rightarrow H_2 \tag{38}$$

On certain noble metals of the platinum group, however, the so-called Volmer-Tafel mechanism applies:

Copyright © 2002 Marcel Dekker, Inc.

$$H^+ + e \rightarrow H_{ads} \quad |2\times \tag{39}$$

$$H_{ads} + H_{ads} \rightarrow H_2 \tag{40}$$

$$\overline{2H^+ + 2e \rightarrow H_2} \tag{41}$$

In this case the second step is a chemical recombination reaction of adsorbed hydrogen atoms produced in the first step, which according to the reaction stoichiometry must proceed twice. The two mechanisms presented here and the rate-determining steps can be distinguished by measuring Tafel slopes. For a more detailed discussion of this point the reader may refer to the literature [3–6].

In corroding systems the detailed mechanisms of the partial electrode reactions are frequently not known. Therefore, it has been found useful to introduce the empirical Tafel coefficients β_a and β_c defined by

$$\beta_a = \frac{dE}{d\ln i_a} \tag{42}$$

$$\beta_c = \frac{dE}{d\ln |i_c|} \tag{43}$$

Comparing these definitions with Eqs. (30) and (31), one finds $\beta_a = RT/\alpha nF$ and $\beta_c = RT/(1-\alpha)nF$. Equation (35) thus becomes:

$$i = i_o \exp\left(\frac{\eta}{\beta_a}\right) - i_o \exp\left(-\frac{\eta}{\beta_c}\right) \tag{44}$$

The Butler-Volmer equation written in the form (44) is frequently used in corrosion. It describes the relationship between current density and potential of an electrode reaction under charge transfer control in terms of three easily measurable quantities: i_o, β_a, and β_c. For large anodic overvoltages ($\eta/\beta_a \gg 1$) Eq. (44) reduces to (45).

$$i = i_a = i_o \exp\left(\frac{\eta}{\beta_a}\right) \tag{45}$$

Taking the logarithm and defining $a_a = -2.303\beta_a \ln i_o$ and $b_a = 2.303\beta_a$, this yields the Tafel equation for an anodic reaction:

$$\eta = a_a + b_a \log i \tag{46}$$

Analogously, for large cathodic overvoltages ($\eta/\beta_c \ll -1$):

$$i = i_c = -i_o \exp\left(-\frac{\eta}{\beta_c}\right) \tag{47}$$

Taking the logarithm and defining $a_c = -2.303\beta_c \ln i_o$ and $b_c = 2.303\beta_c$ yields the Tafel equation for an cathodic reaction:

$$\eta = a_c - b_c \log |i| \tag{48}$$

The Tafel equation applying to large overvoltages predicts a straight line for the variation of the logarithm of current density with potential.

Copyright © 2002 Marcel Dekker, Inc.

CHARGE TRANSFER REACTIONS AT MIXED ELECTRODES

If a metal is in contact with an electrolyte containing on oxidizing agent, two or more electrode reactions can take place simultaneously. Such a system is called a mixed electrode. Suppose a metal M dissolves while a species B_{ox} is reduced to B_{red}:

$$M + \nu_{ox} B_{ox} \rightarrow M^{n+} + \nu_{red} B_{red} \tag{49}$$

The two partial reactions are

$$M \rightarrow M^{n+} + ne \tag{50}$$

$$\nu_{ox} B_{ox} + ne \rightarrow \nu_{red} B_{red} \tag{51}$$

The total current density at the metal-solution interface is equal to the sum of the anodic and cathodic partial current densities of the two electrode reactions.

$$i = i_M + i_B = i_{a,M} + i_{c,M} + i_{a,B} + i_{c,B} \tag{52}$$

The subscripts M and B designate the partial reactions and the subscripts a and c stand for anodic and cathodic, respectively. Usually in a corroding system one can neglect the cathodic partial current of the metal and the anodic partial current of the oxidizing agent: $i_{c,M} \approx 0$, $i_{a,B} \approx 0$. Therefore (52) can be simplified:

$$i = i_{a,M} + i_{c,B} \tag{53}$$

At open circuit the mixed electrode is at its corrosion potential, $E = E_{cor,}$ and there is no net current. Hence:

$$i = i_{a,M_{(Ecor)}} + i_{c,B_{(Ecor)}} = 0 \tag{54}$$

This allows one to define the corrosion current density i_{cor}, which according to Eq. (4) is proportional to the corrosion rate.

$$i_{cor} = i_{a,M_{(E_{cor})}} = i_{c,B_{(E_{cor})}} \tag{55}$$

If charge transfer is rate limiting, the Butler-Volmer equation (35) described the current-potential relationship of each partial reaction. With the overvoltage of the metal dissolution reaction, $\eta_M = E - E_{rev,M}$, and for the reduction reaction, $\eta_B = E - E_{rev,B}$, one gets the following expression for the corrosion current density:

$$i_{cor} = i_{o,M} \exp\left(\frac{E_{cor} - E_{rev,M}}{\beta_{a,M}}\right) = i_{o,B} \exp\left(\frac{E_{cor} - E_{rev,B}}{\beta_{c,B}}\right) \tag{56}$$

Equation (56) shows that the corrosion current density for a charge transfer–controlled reaction is entirely determined by the kinetic parameters of the partial electrode reactions involved.

By definition, the polarization $\zeta = E - E_{cor}$ indicates the deviation of the electrode potential from the corrosion potential. The polarization ζ is related to the overvoltage of the partial electrode reactions by (57) and (58).

$$\zeta = \eta_M - (E_{cor} - E_{rev,M}) \tag{57}$$

$$\zeta = \eta_B - (E_{cor} - E_{rev,B}) \tag{58}$$

Copyright © 2002 Marcel Dekker, Inc.

With these expressions one can easily derive the Butler-Volmer equation of a mixed electrode corresponding to the corrosion reaction (49):

$$i = i_{a,M} + i_{c,B} = i_{cor} \exp\left(\frac{\zeta}{\beta_{a,M}}\right) - i_{cor} \exp\left(-\frac{\zeta}{\beta_{c,B}}\right) \tag{59}$$

At the corrosion potential the absolute values of the two partial current densities are equal. The reciprocal of the slope of the curve $i = f_{(E)}$ is called polarization resistance. A measurement of the polarization resistance at the corrosion potential, r_{cor}, allows one to determine the corrosion current density provided the anodic and cathodic Tafel coefficients are known. By definition:

$$r_{cor} = \left.\frac{dE}{di}\right|_{E_{cor}} = \left.\frac{d\zeta}{di}\right|_{\zeta=0} (\Omega\,m^2) \tag{60}$$

With Eq. (59) this yields

$$r_{cor} = \frac{1}{i_{cor}} \frac{\beta_{a,M}\beta_{c,B}}{\beta_{a,M} + \beta_{c,B}} \tag{61}$$

The value of the corrosion current density can also be obtained from a logarithmic plot (Fig. 3) by extrapolating the anodic or the cathodic partial current density to the corrosion potential. Indeed, for the anodic and cathodic Tafel regions, respectively, Eq. (59) yields

$$\ln i = \ln i_{a,M} = \ln i_{cor} + \zeta/\beta_{a,M} \tag{62}$$

$$\ln|i| = \ln|i_{c,B}| = \ln i_{cor} - \zeta/\beta_{c,B} \tag{63}$$

Semilogarithmic plots of the partial anodic and cathodic current densities of mixed electrodes as shown in Figure 3 are called Evans diagrams. The determination of the

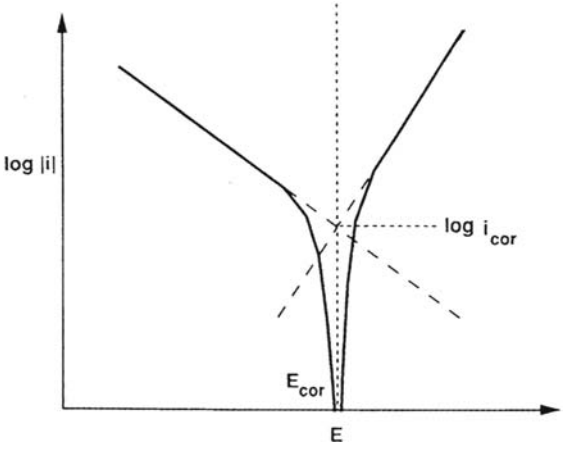


Figure 3 Logarithmic presentation of current-potential curve of a mixed electrode (Evans diagram) showing the corrosion potential E_{cor} and the corrosion current density i_{cor}. The broken lines indicate the partial current densities.

Copyright © 2002 Marcel Dekker, Inc.

corrosion rate from electrochemical polarization experiments was introduced by Stern and Geary [7], but the development of the theory of mixed electrodes, due to Wagner and Traud [8], dates much earlier.

MASS TRANSPORT-CONTROLLED ELECTRODE REACTIONS

For a corrosion reaction to take place, oxidizing agents must reach the electrode surface. Similarly, reaction products must be eliminated from the electrode surface by transport toward the bulk solution. If mass transport of reactants and products is slow compared to charge transfer, their concentration at the electrode surface differs from that in the bulk solution: the concentration of reactants diminishes, that of products increases. Figure 4 shows the concentration profile of a reactant. Three mechanisms contribute to mass transport: diffusion, convection, and migration. For neutral species such as dissolved oxygen and for ionic species present in small amounts in a supporting electrolyte, the contribution of migration is negligible. Transport then occurs by diffusion and convection only. To describe transport by diffusion and convection, one frequently uses the Nernst diffusion layer model, which postulates that the electrolyte volume can be divided into two regions. Near the electrode surface convection is negligible and transport occurs by diffusion only. In the bulk electrolyte, on the other hand, the concentration is uniform and no diffusion takes place. The thickness δ of the so-called Nernstdiffusion layer is obtained by extrapolating the gradient at the surface ($\upsilon = 0$) to the bulk concentrations (Fig. 4). Its value depends on convection conditions and is typically of the order of a few micrometers [4].

Let us assume that the reaction rate for the reduction of an oxidant B_{ox} is partly mass transfer controlled. If one neglects migration, the flux N_B at the electrode surface is given by Eq. (64).

$$N_B = -D_B \left.\frac{dc_B}{dy}\right|_{y=0} \tag{64}$$

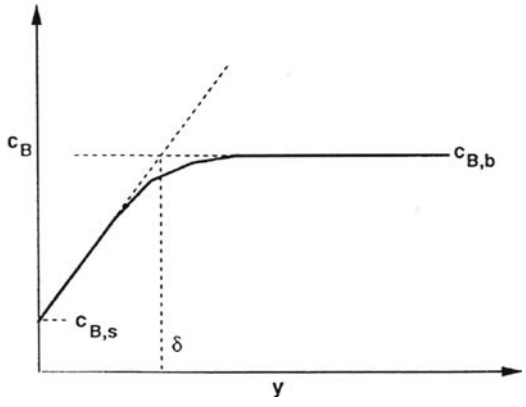


Figure 4 Concentration of a reacting species as a function of distance from the electrode.

Copyright © 2002 Marcel Dekker, Inc.

Integration over a constant diffusion layer thickness δ yields

$$N_B = -D_B \frac{c_{B,b} - c_{B,s}}{\delta} \tag{65}$$

In these equations D_B is the diffusion coefficient of B_{ox} and $c_{B,b}$ and $c_{B,s}$ indicate the bulk and surface concentrations of B_{ox}, respectively. With Faraday's law one obtains for the cathodic partial current density:

$$i_{c,B} = -nFD_B \frac{c_{B,b} - c_{B,s}}{\delta} \tag{66}$$

This expression is valid at all potentials. If the potential becomes increasingly cathodic the absolute value of the current density $i_{c,B}$ increases and, consequently, $c_{b,s}$ decreases. Eventually, a condition is reached where $c_{B,s}$ becomes zero. This situation corresponds to the maximum possible reaction rate, and the corresponding current density is called the limiting current density i_L.

$$i_{L,B} = -nFD_B \frac{c_{B,b}}{\delta} \tag{67}$$

Below the limiting current density, mass transport as well as charge transfer determines the overall reaction rate. For $\eta/\beta_{c,B} \ll -1$ the Butler-Volmer equation (34) reduces to (68), where $\beta_{c,B}$ is the cathodic Tafel coefficient for the reaction of species B.

$$i_{c,B} = -i_{o,B} \frac{c_{B,s}}{c_{B,b}} \exp\left(-\frac{\eta}{\beta_{c,B}}\right) \tag{68}$$

Combining this expression with (66) and (67), one obtains (69) and (70).

$$i_{c,B} = -i_{o,B}\left(1 - \frac{i_{c,B}}{i_{L,B}}\right) \exp\left(-\frac{\eta}{\beta_{c,B}}\right) \tag{69}$$

$$i_{c,B} = -\frac{i_{o,B} \exp(-\eta/\beta_{c,B})}{1 - (i_{o,B}/i_{L,B}) \exp(-\eta/\beta_{c,B})} \tag{70}$$

If $i_{o,B}/i_{L,B}\exp(-\eta/\beta_{c,B}) \ll 1$, Eq. (70) reduces to Eq. (47) describing a charge transport–controlled cathodic reaction obeying Tafel kinetics. On the other hand, if the absolute value of $i_{o,B}/i_{L,B}\exp(-\eta/\beta_{c,B})$ is large compared with 1 Eq. (70) becomes $i_{c,B} = i_{L,B}$. At the limiting current density the reaction rate is entirely controlled by the rate of mass transport and no longer depends on potential.

Figure 5 shows on a semilogarithmic plot a cathodic partial reaction corresponding to Eq. (69). At low current densities the reaction follows Tafel kinetics. As the current density increases, transport becomes more important and eventually a limiting current plateau is reached. The figure also shows a charge transfer–controlled anodic partial reaction. The corrosion potential is situated at the intersection of the two curves, which is located on the limiting current plateau of the cathodic partial reaction. The corrosion current density, therefore, is equal to the limiting current density of the cathodic partial reaction. The rate of corrosion in this case is mass transport controlled. Corrosion in neutral media in the presence of dissolved oxygen frequently follows this mechanism.

Copyright © 2002 Marcel Dekker, Inc.

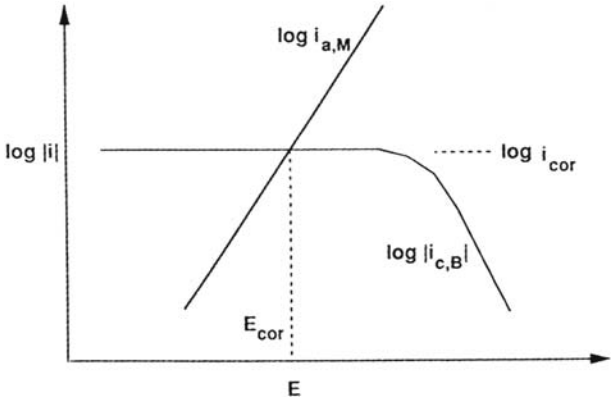


Figure 5 Evans diagram showing a cathodic partial reaction controlled by mass transport.

In the laboratory one frequently uses rotating-disk electrodes for the study of mass transport effects. According to the Levich equation [9], the limiting current density for a cathodic reaction at a rotating-disk electrode under laminar flow conditions varies linearly with the square root of the rotation rate.

$$i_{L,B} = -0.62nFc_{B,b}D_B^{2/3}\nu^{-1/6}\omega^{1/2} \tag{71}$$

In this equation ν represents the kinematic viscosity and ω the rotation rate in rad/s. The other symbols have their usual meaning. Combining (71) with (67) yields for the Nernst diffusion layer thickness:

$$\delta = 1.61D_B^{1/3}\nu^{1/6}\omega^{-1/2} \tag{72}$$

According to (72), the value of δ depends on the diffusion coefficient of the reacting species. This clearly shows that the Nernst diffusion layer is not a physical entity but a theoretical concept permitting us to treat separately the contributions of convection and diffusion to mass transport.

Under certain conditions the rate of transport of anodically formed dissolution products may become rate limiting. For example, the dissolution of iron in concentrated chloride media according to the reaction

$$Fe \rightarrow Fe^{2+} + 2e \tag{73}$$

leads to accumulation of ferrous ions in the diffusion layer. At sufficiently high dissolution rates the concentration at the electrode surface reaches the saturation concentration of ferrous chloride, causing the precipitation of a salt film on the surface. This condition manifests itself by the appearance of a transport-controlled current plateau on the current-potential curve. Neglecting migration, the limiting dissolution current density is given by Eq. (74) where $c_{Fe^{2+},sat}$ indicates the saturation concentration of ferrous ions at the electrode surface.

$$i = nFD_{Fe^{2+}}\frac{c_{Fe^{2+},sat} - c_{Fe^{2+},b}}{\delta} \tag{74}$$

Copyright © 2002 Marcel Dekker, Inc.

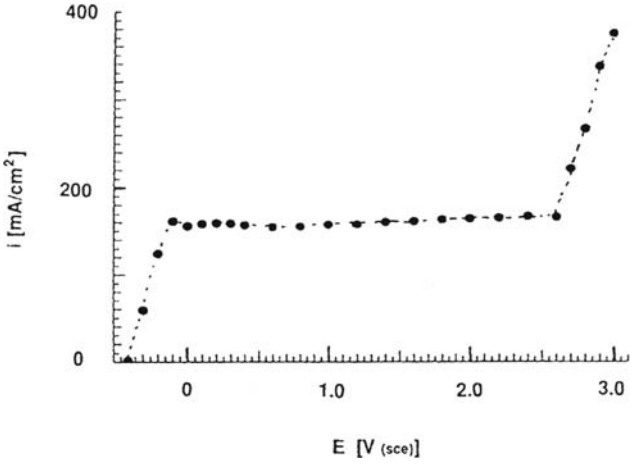


Figure 6 Anodic current-potential curve for iron dissolution in $FeCl_2$ showing a limiting current plateau due to a salt film. (From Ref. 10.)

In the absence of ferrous ions in the bulk solution this becomes:

$$i_{L,Fe^{2+}} = nFD_{Fe^{2+}} \frac{c_{Fe^{2+},sat}}{\delta} \tag{75}$$

Figure 6 shows an anodic current-voltage curve for iron dissolution in 4 M $FeCl_2$, measured with a rotating-disk electrode at 200 rpm. The limiting current plateau extends over more than 2 V. A thin salt film covers the electrode surface under these conditions [10]. At very high potentials the salt film is no longer stable, leading to dissolution of the metal at a high rate. The described transport mechanism involving salt film formation is of importance in pitting corrosion, where under certain conditions salt precipitation can occur at the bottom of a pit, leading to transport-controlled dissolution [5,6].

CORROSION CELLS

In the preceding sections the electrochemical theory of simple electrode reactions and of mixed electrodes relevant to uniform corrosion was developed. The described concepts are also applicable to corrosion cells, where anodic and cathodic areas are spatially separated. However, in the case of corrosion cells the rate of corrosion depends not only on charge transfer kinetics and on mass transport conditions at the anode and the cathode but also on the resistivity of the electrolyte and the geometry of the cell, which determine the internal resistance. This is illustrated by Figure 7, which shows schematically a corrosion cell formed between an anode and a cathode of equal surface area facing each other. Also shown is the electrical analogue of the corrosion cell. The voltage source corresponds to the difference in corrosion potentials of electrodes 1 and 2 when they are not connected to each other: $\Delta E_{cor} = E_{cor,2} - E_{cor,1}$. Once they are connected, a current flows whose magnitude depends on all elements present in the circuit. The nonohmic resistances $R_{p,1}$ and

Copyright © 2002 Marcel Dekker, Inc.

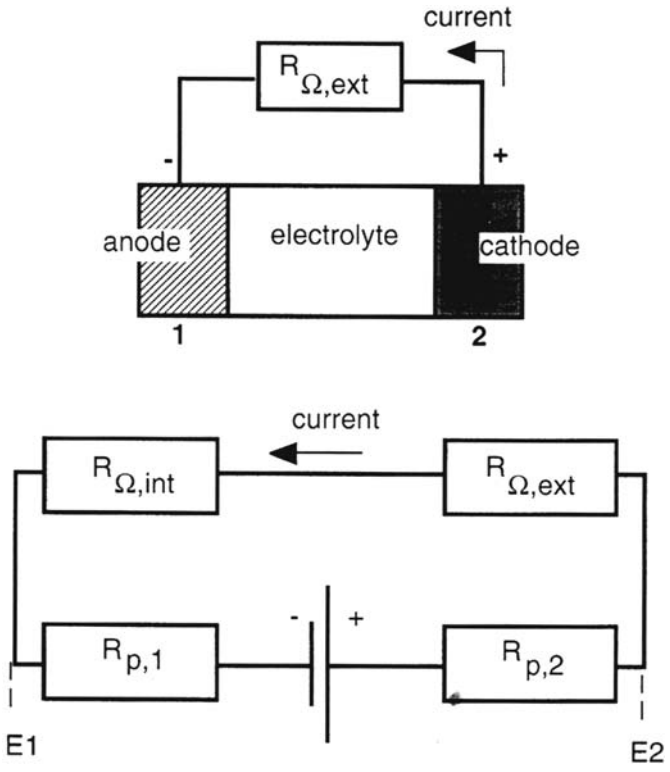


Figure 7 Schematic presentation of a corrosion cell consisting of an anode and a cathode immersed in the same electrolyte and in electrical contact through an external resistance. Also shown is the electrical analogue of the corrosion cell including the voltage source ΔE_{corr}, the polarization resistances $R_{p,1}$ and $R_{p,2}$ of the anode and the cathode, respectively, the internal resistance $R_{\Omega,int}$ due to the electrolyte, and the external resistance $R_{\Omega,ext}$.

$R_{p,2}$ represent the polarization resistance of the anode and the cathode, respectively. Because the electrode potential usually varies in a nonlinear way with current density (for example, following Butler-Volmer kinetics) the value of the polarization resistances $R_{p,1}$ and $R_{p,2}$ varies as a function of current density. The ohmic resistances $R_{\Omega,int}$ and $R_{\Omega,ext}$ represent the internal cell resistance and the resistance of the external circuit, respectively. The latter term is usually negligible.

It is easily seen from the figure that for a given potential difference ΔE_{cor} the current in the corrosion cell, and hence the corrosion rate at the anode, is the higher the smaller the value of the different resistances present. For example, if one increases the distances between the electrodes or the resistivity of the solution, the current between anode and cathode will become smaller. In practice, the anode and the cathode of a corrosion cell are usually not parallel and the current density therefore varies locally with distance. This is schematically illustrated by Figure 8, which shows an anode and a cathode in contact with each other in such a way that their surfaces exposed to an electrolyte are in the same plane. Such a situation could arise when two different metals are joined together. The figure shows schematically

Copyright © 2002 Marcel Dekker, Inc.

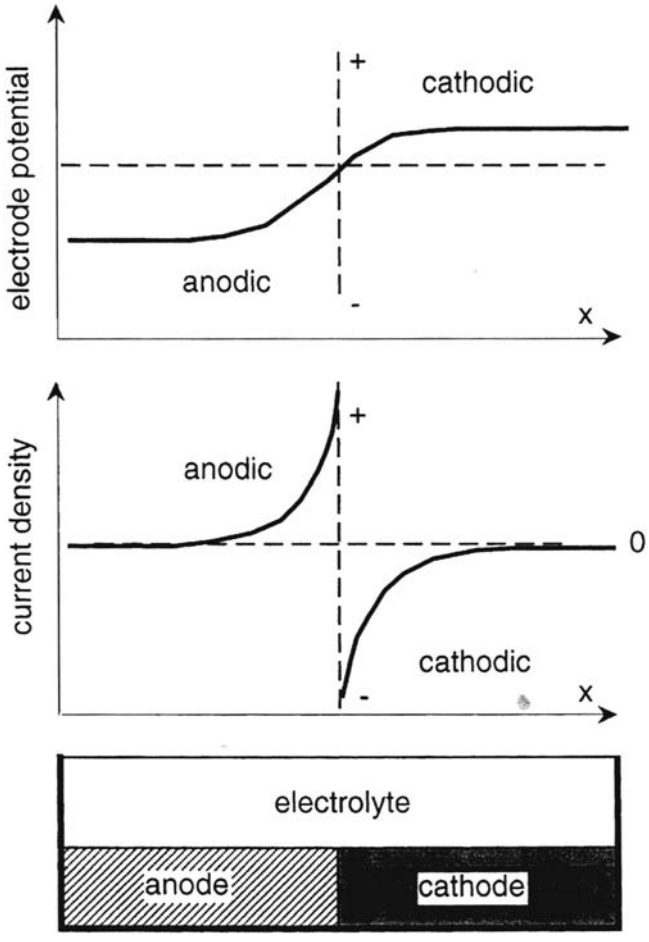


Figure 8 Schematic presentation of the variation of the current density and of the electrode potential as a function of the distance from the contact of two metals immersed in an electrolyte.

how the potential and the current density vary as a function of the distance from the electrical contact. At the contact, the potentials of the cathode and the anode are the same and where the local current density in principle should be infinitely high. In reality, the current density at the contact will always be finite because of limitations due to mass transport and reaction kinetics. Far from the contact the value of the potential approaches that corresponding to the corrosion potential of the metals in the absence of galvanic coupling. The current density in the metal far from the contact becomes zero. The distance where this occurs depends on geometric and electrochemical parameters and on the electrolyte conductivity.

The variation of current density and of potential as a function of distance can in principle be calculated using the theory of current and potential distribution in electrochemical systems [5,6,11]. In practical corrosion systems this is rarely done,

Copyright © 2002 Marcel Dekker, Inc.

however, because numerical simulations taking into account all meaningful parameters are rather onerous.

Corrosion cells not only are formed when two different metals are in contact with each other but also can be the result of differences in the corrosive environment. A typical example is differential aeration cells, which are due to differences in accessibility of oxygen to the surface of a metal. Because the value of the corrosion potential depends on the kinetics of the anodic as well as the cathodic partial reactions, a different accessibility of oxygen results in a difference in corrosion potential and hence in the establishment of a corrosion cell.

REFERENCES

1. A. J. Bard, R. Parsons, and J. Jordan, *Standard Potentials in Aqueous Solutions*, Marcel Dekker, New York, 1985.
2. M. Pourbaix, *Atlas of Electrochemical Equilibria in Aqueous Solutions*, 2nd ed, NACE, Houston, 1974.
3. K. J. Vetter, *Electrochemical Kinetics*, Academic Press, New York, 1967.
4. J. O'M. Bockris and A. K. N. Reddy, *Modern Electrochemistry*, Plenum, New York, 1970.
5. H. Kaesche, *Die Korrosion der Metalle 3*, Springer-Verlag, Berlin, 1990.
6. D. Landolt, *Corrosion et chimie des métaux,* Presses polytechniqes et universitaires romandes, Lausanne, 1993.
7. M. Stern and A. L. Geary, *J. Electrochem. Soc. 104*:56 (1957).
8. C. Wagner and W. Traud, *Z. Electrochem. 44*:391 (1938).
9. V. Levich, *Physicochemical Hydrodynamics*, Prentice Hall, Englewood Cliffs, NJ, 1962.
10. R. D. Grimm, A. C. West, and D. Landolt, *J. Electrochem. Soc. 139*:1622 (1992).
11. J. Newman, *Electrochemical Systems*, 2nd ed., Prentice Hall, Englewood Cliffs, NJ, 1991.

Copyright © 2002 Marcel Dekker, Inc.

2

Introduction to Surface Reactions: Adsorption from Gas Phase

Jacques Oudar
Laboratorie de Physico-Chimie des Surfaces, Université Pierre et Marie Curie, Ecole Nationale Supérieure de Chimie de Paris, Paris, France

INTRODUCTION

Atoms at a metal surface exhibit unsaturated bonds that are available for fixing reactive species, atoms or molecules, present in the gas or liquid surrounding the surface. Such a reaction, when limited to one monolayer or a fraction of a monolayer, is known as an adsorption phenomenon or chemisorption. Similarly, atoms present in the bulk metal may diffuse toward and enrich the surface by so-called thermal segregation. Segregation may also occur by selective evaporation of the metal in vacuum or in an inert gas or by selective dissolution of the metal in a liquid phase (anodic segregation). Whatever the mechanism of surface enrichment, there is strong experimental evidence that the same structural and chemical states can be achieved by adsorption or segregation.

The presence of adsorbed species at the metal-liquid interface may greatly influence electrochemical processes involved in corrosion, such as anodic dissolution, cathodic reaction, or passive film formation. Most of our understanding of adsorption has been acquired by studying gas-metal interactions at low pressure by means of ultrahigh-vacuum techniques. Low-pressure data cannot be directly related to electrochemical interfaces without some caution. On a polarized interface, the adsorption of charged species such as ions is potential dependent and requires the replacement of solvent molecules. Adsorbed ions may also retain part of their charge and interact with the solvent molecules. There is good evidence that small cations retain part of their solvated shell in the adsorbed state. It is expected that similarities between both kinds of adsorption will be more significant in systems characterized by strong interactions and nearly complete ion discharge.

In many systems, the reaction may proceed beyond the adsorption stage to the formation of a bulk compound; this transition may occur at gas-metal as well at metal-liquid interfaces.

In the following we will especially refer to adsorbates that play a direct role in electrochemical processes (hydrogen, oxygen, water) or that may influence the

Copyright © 2002 Marcel Dekker, Inc.

formation of the passive layer (carbon, nitrogen, sulfur, halogens). We will focus mainly on transition metals as substrates.

Finally, a short introduction to gas adsorption on oxides will be given. We will examine especially water adsorption, which is of special interest for understanding the behavior of passive films in aqueous solution.

MOLECULAR VERSUS DISSOCIATIVE ADSORPTION

Diatomic gases such as CO, NO, N_2, O_2, and H_2 can be molecularly or dissociatively adsorbed on metals. In the case of CO and NO, the borderline between both types of adsorption has been determined [1]. At room temperature N_2 is dissociatively adsorbed on W, Mo, and Fe, but not on Ni and Cu; O_2 on all metals but Au; and H_2 on transition metals but not on Al, Ag, and Au.

The transition from molecular adsorption to dissociative adsorption for a homopolar diatomic molecule is well represented by the classical Lennard Jones diagram. In this diagram, shown in Figure 1 for hydrogen, the potential energy of the system is plotted as a function of the distance of the molecule to the metal surface defined by the first plane of metal atoms. One curve corresponds to molecular hydrogen, the other to hydrogen atoms. In the first shallow minimum, hydrogen is molecularly adsorbed. As the metal-hydrogen distance decreases, dissociation may occur. The much deeper potential well close to the metal surface corresponds to chemisorbed hydrogen atoms. The energy path is represented in Figure 1 by the solid line. The dissociation takes place at the intersection between the two potential curves according to

$$H_2(g) + 2M \rightarrow 2M - H_{ad}$$

As shown in Figure 1, the intersection point may be located at positive or at negative potentials. When it is at a positive potential, the adsorption process is activated and the height of the activation barrier or activation energy is denoted by E^*_{ad}. When the intersection point is below $E = 0$, the dissociative adsorption of hydrogen is non-activated. This is the case for the chemisorption of hydrogen on most transition metals. The energy balance gives $E_{ad} + E_{diss} = 2E_b$ where E_{ad} is the adsorption

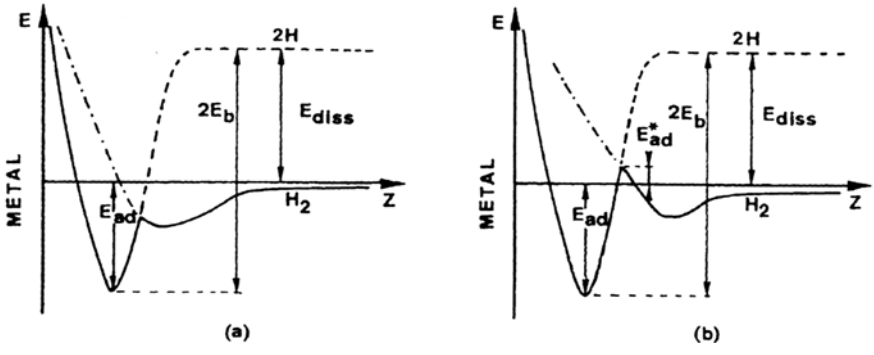


Figure 1 Schematic potential energy diagram for (a) nonactivated and (b) activated chemisorption of hydrogen on a metal surface.

Copyright © 2002 Marcel Dekker, Inc.

energy, E_{diss} is the energy required for the dissociation of the H_2 molecule (432 kJ/mol), and E_b is the hydrogen-metal bond energy.

ENERGETICS OF ADSORPTION

General Trends

Based on analyzing data for many gas-metal systems, some general remarks can be made:

1. The heat of adsorption is of the same order of magnitude as the heat of formation of the most stable bulk compound. A linear correlation between these two thermodynamic quantities has been experimentally established, as exemplified for O_2 and N_2 in Figure 2 [2,3] and for S_2 in Figure 3 [4].
2. The strength of the adsorbate bond follows the order C > N > O > S > H.
3. The heat of adsorption is not very sensitive to the surface structure. Variation from one plane to another does not exceed 10% of the total heat of adsorption. Stronger bonding usually occurs on rougher planes on an atomic scale.
4. The heat of adsorption and consequently the strength of the chemical adsorption bond usually decrease with increasing surface coverage due to adsorbate-adsorbate repulsive interactions.

Data mostly derived from studies performed on single crystals are summarized next for some selected systems.

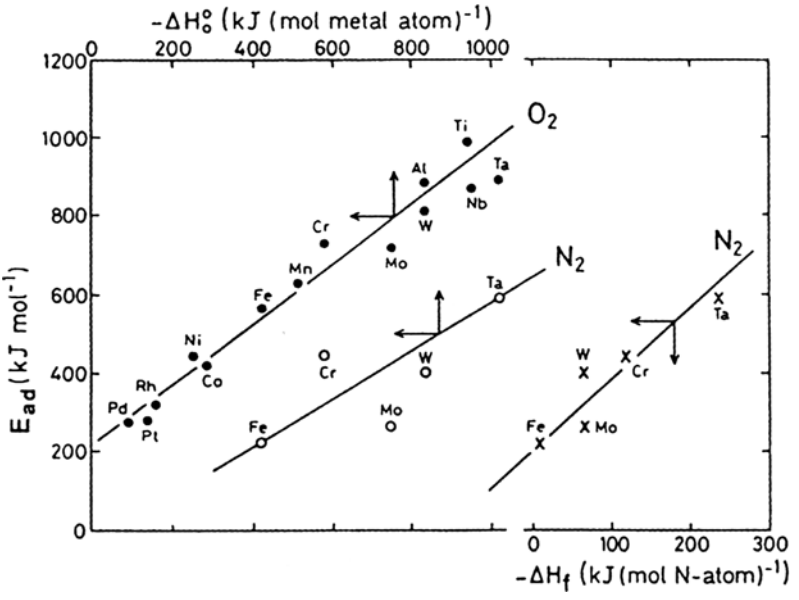


Figure 2 Correlation between the initial heat of chemisorption ($E_{ad,0}$) and the corresponding heat of oxide formation for O_2 (•) and N_2 (o) or nitride formation (for N_2 (x)). (From Refs. 2 and 3.)

Copyright © 2002 Marcel Dekker, Inc.

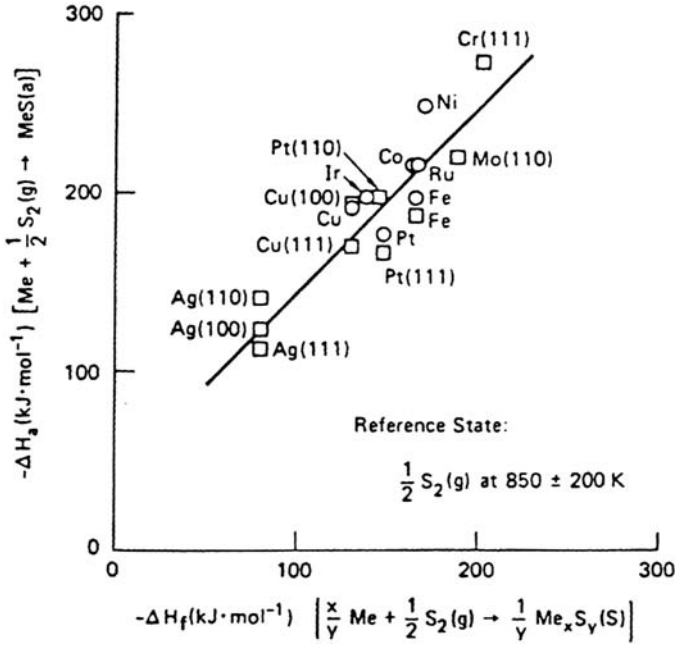


Figure 3 Correlation between the heat (enthalpy) of sulfur adsorption (ΔH_a) at half-saturation coverage and the corresponding heat (enthalpy) of sulflde formation (ΔH_f). (From Ref. 4.)

Hydrogen

Hydrogen adsorption on pure metals has been reviewed [5–7]. Fundamentals of hydrogen-metal interactions with special reference to the hydrogen degradation of materials in aqueous solution can be found in Ref. 8.

Experimental data obtained on single crystals (Table 1) show that the initial heat of adsorption does not depend much on the surface orientation. As seen on Ni,

Table 1 Some Selected Values for Initial Heats of Adsorption ($E_{ad,0}$), M–H Binding Energy (E_b), and Bond Strength, of Diatomic Hydride Molecules (E_{hy})

Metal surface	$E_{ad,0}$ (kJ mol^{-1})	E_b (kJ mol^{-1})	E_{hy} (kJ mol^{-1})	References
Fe(l10)	109	271		9
Fe(100)	100	265		9
Fe(111)	88	260		9
Ni(100)	95	264	251	10,11
Ni(111)	95	264		10,12
Ni(110)	90	261		10,13
W(100)	134	283		14
W(110)	138	285		14
W(111)	155	294		14

Copyright © 2002 Marcel Dekker, Inc.

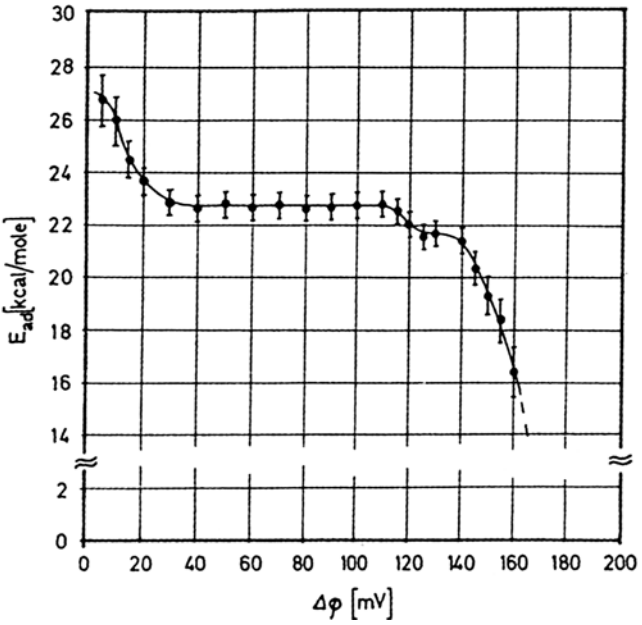


Figure 4 Isosteric heat of adsorption (kcal/mol) for hydrogen on Ni(100) surface as a function of hydrogen-induced work function change (which is a direct measure of the surface concentration of hydrogen). (From Ref. 10.)

the hydrogen-metal binding energy has the same order of magnitude as the bond energy in the corresponding hydride. Hydrogen adsorption is sensitive to surface defects. The preferential adsorption on monoatomic steps is reflected by the increase of the value of E_{ad} observed on Ni(100) at small coverages (Fig. 4). When the hydrogen coverage increases, the isosteric heat of adsorption decreases as far as repulsive lateral interactions between adsorbed atoms become significant. Most data in Table 1 concern H species adsorbed at low H_2 pressures ($<10^{-4}$ torr). The nature and binding energy of H adsorbed species formed at higher pressures can be different. Their possible role in heterogeneous catalysis as deduced from experiments made on dispersed metals is discussed in detail in Ref. 5.

A survey of the elements forming bulk hydrides is given in Ref. 6.

Carbon

Despite the fact that carbon is one of the most common elements in many metals, there are no precise data on its possible role in wet corrosion. The importance of carbon in metallurgy and heterogeneous catalysis (methanation) has motivated precise studies of metal single crystals. During exposure of Ni to CO, two kinds of surface carbon deposit have been identified by Auger electron spectroscopy (AES) [15]. The first one, limited to a fraction of a monolayer, is the "carbidic form," so named because of its similarity to the Auger spectrum of bulk nickel carbide. The second one is graphite. The carbidic form is an intermediary in the CO hydrogenation, whereas the graphitic carbon deactives the surface. The transformation of

Copyright © 2002 Marcel Dekker, Inc.

Table 2 Thermodynamic Properties of Carbon on Fe(100) [4]

C_b (wt ppm)	$-\Delta H_{seg}$ (kJ mol^{-1})	Surface coverage,[a] θ_c	Heat of formation of surface carbon relative to graphite[b] (kJ mol^{-1})
10	72.8	0.3	23
30	81.6	0.8	15
70	88.7	0.95	8
90	90.4	0.98	6
100	96.0	1.00	0

[a]At 923 K .

[b]Data from Ref. 8 based on heat of solution of 95 kJ mol^{-1}.

the carbidic form into graphite occurs beyond a critical carbon coverage. The two carbon states can be produced by exposure of nickel or iron to gases other than CO (C_2H_4 or C_2H_6) or by surface segregation.

Most data for determining the binding energy of adsorbed carbon in its carbidic form have been obtained by segregation studies of single crystals following a procedure given in Ref. 16. The thermodynamic properties of the different forms of surface carbon that can be present on Ni and Fe are described in Refs. 17 and 4. As an example, results obtained for Fe(100) are shown in Table 2. On this surface, carbon, irrespective of the coverage, is less strongly bonded in the adsorbed layer than in graphite. The average enthalpy of carbon segregation on Fe(100) (–85 kJ mol^{-1}) is significantly lower than that to grain boundaries (–57 kJ mol^{-1}). Surface site competition between Si and C has been reported on Fe-Si alloys [18,19].

As evidenced by its high reactivity in gaseous hydrogen [15], a "carbidic" adlayer is probably highly reactive in the presence of hydrogen cathodically formed in acid solution. The evolution of CH_4 during the cathodic hydrogen decarburation of steel at room temperature presumably originates from such a carbon deposit [20]. One may expect the formation of the passive film to be partially or totally inhibited on a surface partially or totally covered by graphite that is inert toward oxygen or H_2O at room temperature.

Nitrogen

Nitrogen adsorption has been especially studied on iron, which is the basis of the industrial catalyst for ammonia synthesis. This catalytic reaction is now relatively well understood [21]. The main function of iron is to activate the very stable N_2 molecule by dissociative adsorption. Results in Table 3 show that the Fe–N binding energy is approximately the same on the three main low-index planes. However, the rate of N_2 dissociation decreases by many orders of magnitude when going from Fe(111), the most active for ammonia synthesis, to the less active Fe(110).

On W the metal-nitrogen bond energy is estimated to be 640 kJ mol^{-1} irrespective of the surface orientation [24,25], about 60 kJ mol^{-1} higher than for the Fe–N. Nitrogen, like carbon, dissolves interstitially into cc iron in small

Copyright © 2002 Marcel Dekker, Inc.

Table 3 Initial Heat of Nitrogen Adsorption ($E_{ad,o}$), $E_{bM\text{-}M}$, and M-N Binding Energy on Iron [22,23]

Metal surface	$E_{ad,0}$ (kJ mol^{-1})	E_{bM-N} (kJ mol^{-1})
Fe(110)	212	578
Fe(100)	221	584
Fe(111)	213	579

concentrations. The bulk nitrogen concentration (N_b) expressed in wt %, in equilibrium with nitrogen at 1 atm is given by [26]

$$N_b = 0.098 \exp - (\Delta H_s/RT)$$

with ΔH_s = 30.2 kJ mol^{-1} (endothermic).

The heat of surface segregation ΔH_{seg} is the difference between the heat of chemisorption of $1/2N_2$ and the heat of segregation

$$\Delta H_{seg} = -108.5 - 30.2 = -138.7 \text{ kJ mol}^{-1} \text{ (exothermic)}$$

From direct segregation experiments with Fe-N alloys the value ΔH_{seg} = –110 kJ mole^{-1} has been found [19].

Oxygen

Data in Figure 2 refer to polycrystalline metals. As shown in Table 4, the heat of oxygen adsorption is approximately the same for the three metals Cr, Mo, and W. By contrast, the enthalpy of atomization is much lower for Cr than for Mo and reaches a very high value for W. This indicates that the Cr–Cr bond strength is much lower than the bond strength for the other metals. It is expected that phenomena involve disruption of the metal lattice in the presence of oxygen such that the transition from adsorption to oxidation will be much easier on Cr. This aspect is considered in more detail in a later section.

Sulfur

Most data on the thermodynamics of sulfur adsorption were derived from adsorption isotherms achieved in H_2S-H_2 gas mixtures [28,29]. At high temperature, sulfur is reversibly adsorbed on a metal surface in a range of H_2S partial pressures below that required for the formation of the most stable sulfide. At a fixed temperature the

Table 4 Thermodynamic Data for Cr, Mo, and W [27]

Metal	Enthalpy of atomization (kJ mol^{-1})	Heat of O_2 adsorption (kJ mol^{-1})
Cr	397	711
Mo	658	711
W	849	794

Copyright © 2002 Marcel Dekker, Inc.

adsorption isotherm reflects the surface coverage at equilibrium with the H_2S-H_2 gas composition that determines the chemical potential of sulfur in the gas phase.

The isosteric heat (enthalpy) of adsorption referred to H_2S can be determined from isotherms measured at different temperatures by means of the Van t'Hoff equation:

$$[\partial \ln(P\mathrm{H_2S}/P\mathrm{H_2})/\partial T]_\theta = -\Delta H_\theta / RT^2$$

where θ is the sulfur coverage.

From ΔH_θ the heat of adsorption with $S_2(g)$ as the reference state can be deduced, as well as the binding energy of adsorbed sulfur. Exchange between the bulk solid solution and the surface, namely segregation and dissolution, can also be taken into account. The various equilibria between the surface and either the bulk metal or the gas phase are interrelated according to:

$$\text{Sulfur dissolved in the metal} \underset{\text{dissolution}}{\overset{\text{segregation}}{\rightleftharpoons}} \text{Sulfur adsorbed on the Surface} \underset{\text{adsorption}}{\overset{\text{desorption}}{\rightleftharpoons}} H_2S/H_2$$

The heat of surface segregation is equal to the difference between the heat of adsorption and the heat of sulfur dissolution from the gas phase. Data obtained on nickel and iron are shown in Table 5. In this table ΔH_a corresponds to the reaction

$$M + \tfrac{1}{2}\, S_2 \rightarrow MS_{ad} \qquad \Delta H_a$$

ΔH_f is the heat of the bulk sulfide formation according to

$$x/y\ M + \tfrac{1}{2}\, S_2 \rightarrow 1/y M_x S_y \qquad \Delta H_f$$

All values refer to half-saturation coverage by sulfur.

The heat (enthalpy) of formation of chemisorbed sulfur on nickel with respect to ½ S_2 is –247 kJ mol^{-1}, i.e., –158 kJ mol^{-1} with H_2S as the reference state for sulfur (the heat of formation of gaseous H_2S is 89 kJ mol^{-1}). It is ~ 75 kJ mol^{-1} more exothermic than the enthalpy of formation of Ni_3S_2. This means that S adsorbed is energetically more stable than S in Ni_3S_2. A similar trend is observed for Fe. Indeed,

Table 5 Heat of Sulfur Adsorption ΔH_a (Referred to ½ S_2), Heat of Sulfide Formation ΔH_f (Referred to $1/y\ M_xS_y$), Heat of Dissolution from the Gas Phase (½ S_2), and Heats of Segregation

Metal	ΔH_a (kJ mol^{-1})	ΔH_f (kJ mol^{-1})	ΔH dissol. (kJ mol^{-1})	ΔH surface segr. (kJ mol^{-1})	ΔH grain bound. segr. (kJ mol^{-1})
Ni	−247 [29a]	−172 [30]	−54 [32]	−193	−98 [34]
Fe_α	−198 [29b]	−165 [31]	−77 [33]	−120[a]	−54 [35]

[a]In Ref. 29, a higher absolute value was derived by using wrongly for ΔH dissol. the value corresponding to Fe_γ instead of Fe_α.

Copyright © 2002 Marcel Dekker, Inc.

it was shown in Figure 3 that there is a correlation, for many metals, between the heat of chemisorption and the heat of formation of the bulk sulfide that fits approximately the relation $\Delta H_{ad} = 1.25\Delta H_f(1/y\ M_vS_v)$. The fact that chemisorbed sulfur is more stable than the three-dimensional sulfide has important consequences for corrosion processes. Indeed, sulfide on the surface may be dissolved while a monolayer or a fraction of it remains on the surface and changes, as described later in sulfur-assisted corrosion mechanisms (Chapter 9). The metal-sulfur bond strength is easily obtained from the heat of adsorption. The nickel-sulfur bond strength is –464 kJ mol^{-1}, based on –217 kJ mol^{-1} as the heat of formation of monoatomic gaseous sulfur. In the same way, the S–Fe bond strength is found to be –414 kJ mol^{-1}.

The heat of segregation of sulfur onto metal surfaces is generally markedly exothermic. Very low levels of sulfur dissolved in the bulk equilibrate with a very high surface coverage. Although segregation is an exothermic process, it takes place only at high enough temperatures to allow the diffusion of sulfur in the solid state. Usually temperatures above 600°C are required for sulfur to diffuse to the surface; at 800°C it takes a few minutes to obtain the saturation of the surface by sulfur adsorbed on a nickel sample containing ~ 10 ppm sulfur. The diffusion coefficient of sulfur in nickel is [36]

$$D(1073 - 1498\ \text{K}) = 1.4 \exp(-218.6/RT)$$

Similarly, sulfur may enrich grain boundaries even when present in the metal at very low concentration. Values of the heat of grain boundary segregation are shown in Table 5. One observes that the sulfur binding energy varies in the order free surface > grain boundaries > solid solution.

Grain boundary segregation of nonmetallic impurities influences many chemical and mechanical properties [37]. It increases the metal brittleness, favors hydrogen embrittlement, decreases the intergranular fatigue strength or the creep rupture life, and favors intergranular corrosion and stress corrosion cracking. In this respect, sulfur is one of the most detrimental elements. As shown on bicrystals of nickel, a close correlation exists between the intergranular sulfur segregation and the intergranular corrosion [38]. At 625°C, the intergranular segregation was observed for a sample with a sulfur content as low as 0.0005%. Thermodynamic data on sulfur dissolution in pure metals and alloys and on sulfur diffusion have been reviewed in Ref. 39.

Halogens

Halogen chemisorption on metals is of special importance in corrosion. This subject has been reviewed by various authors [40–42]. At room temperature, halogen molecules are dissociatively adsorbed on transition metals and, depending on the system and the halogen pressure, the reaction may proceed beyond the adsorption stage to give halogenide. For a given metal, the halogen binding energy decreases in the order F > Cl > Br > I. Data at low coverages deduced from desorption kinetics or from the heat of formation of halogenides are shown for Fe in Table 6.

For the refractory metals Nb, Mo, Ta, and W, the heat of adsorption of F and Cl at low coverage was observed to be nearly identical 450 ± 20 kJ mol^{-1} [45] whatever the metal or the surface orientation. For Br on Nb and Mo the same value

Copyright © 2002 Marcel Dekker, Inc.

Table 6 Metal-Halogen Binding Energy on Iron (kJ mol^{-1}) [43,44]

Cl	Br	I
386	256	251

of 350 ± 10 kJ mol^{-1} was measured [45]. On nickel, chlorine preadsorption totally inhibits the postadsorption of oxygen, whereas oxygen preadsorption has no influence on additional adsorption of chlorine [46].

WORK FUNCTION VARIATIONS

During adsorption a charge transfer takes place between the metal and the adsorbate and a dipole moment is established. The effective dipole moment μ of an individual adsorbate-metal complex can be derived from the measurable change of the work function $\Delta\phi$ at a coverage n_s (particles/cm^2) according to the relation $\Delta\phi = 4\,\Pi\, n_s \mu$. As a consequence of the existence of a dipole layer, pairwise repulsive interactions may develop.

For hydrogen, dipole-dipole interactions do not operate to a significant extent and only indirect interactions have to be considered. The indirect interactions, the forces that operate via the metal substrate, arise from a mutual coupling of the valence shells of the two adatoms through the substrate valence band. All other contributions to the interaction energy, essentially short range in nature, are completely negligible. In some cases such as H/Fe(110) the interactions can be reasonably treated by the simple lattice gas approximation [47], the calculated interaction energies being in agreement with the experimental values (4–8 kJ mol^{-1}). As stated before, the order of magnitude of the pairwise repulsive energy is generally about 10% of the chemisorption energy.

The variations of the work function on the three low-index faces of Fe with hydrogen adsorption at 140 K are shown in Figure 5. The main characteristics are (a) the small changes of $\Delta\phi$, indicating a low adsorbate dipole moment, a minor net charge transfer between adsorbate and substrate implying some covalent character of the hydrogen metal bond; (b) the nonlinear variation of ϕ with coverage, caused by interactions between adsorbed particles; and (c) the changes of opposite signs for $\Delta\phi$ on the various crystal faces, namely a decrease of the work function by 85 mV for Fe(110) in contrast to the increases by 75 and 240 mV for the (100) and (111) faces, respectively. The negative change of $\Delta\phi$ is somewhat unexpected because hydrogen is considered to be negatively charged on transition metal surfaces. A similar result has been reported for H/Pt. A possible explanation is related to the location of the H atom with respect to the metal surface plane, which affects both the sign and magnitude of $\Delta\phi$.

For electronegative species such as oxygen, sulfur, or halogen, the electron transfer takes place from the metal to the adsorbate, as indicated by the increase of the work function. Electronic transfer in the opposite direction does occur for less electronegative adsorbates, Se and Te. This trend is illustrated for Ni(100) covered

Copyright © 2002 Marcel Dekker, Inc.

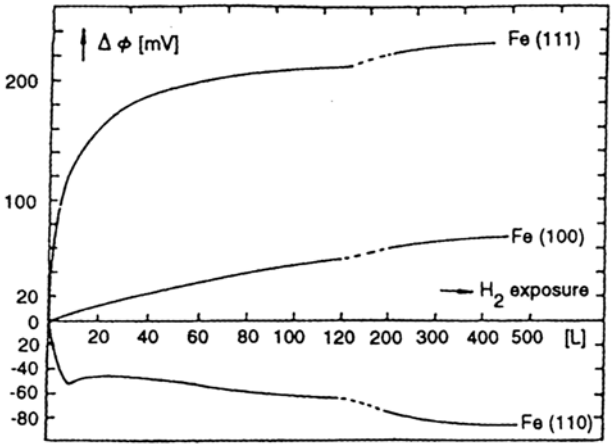


Figure 5 Changes in the work function with hydrogen adsorption on the low-index faces of iron. (From Ref. 9.)

by the same amount of adsorbate (0.5 adsorbed atom per surface metal atom) (Table 7).

Work function variations induced by sulfur at saturation on single crystals of copper are shown in Table 8. These variations are larger than on nickel and vary significantly from one orientation to another.

For S and O, the charge transfer never exceeds one tenth of one electron per adsorbate atom and the metal-adsorbate bond can be considered mainly covalent. Results for halogens on Fe (100) (Table 9) show that the charge transfer parallels the electronegativity of the adsorbate, decreasing in the order Cl > Br > I.

When the adsorption occurs in solution, the resulting charge transfer may significantly modify the metal-electrolyte potential and affect the electrochemical processes at the interface. It was shown that on silver the zero charge potential moves toward higher values with sulfur adsorption [51]. The variation exactly corresponds to the increase of work function induced by sulfur. The linear correlation between the zero charge potential and the work function is now well established both theoretically [52] and experimentally [53].

STRUCTURE OF ADSORBED LAYERS

During the last 20 years, considerable effort has been spent on solving the structure of adsorbed layers. Achievement in this matter is well illustrated by a handbook containing a catalog of these structures [54] and a database with a computer graphics

Table 7 Work Function Variation for Some Elements Adsorbed on Ni(100) [48]

Element	O	S	Se	Te
$\Delta\phi$ (eV)	0.36	0.38	−0.07	−0.43

Copyright © 2002 Marcel Dekker, Inc.

Table 8 Work Function Variations for S Adsorbed on Cu Single Crystals [49]

Face	(111)	(100)	(110)	(210)
Coverage	0.42	0.47	0.64	1.0
$\Delta\phi$ (eV)	0.435	0.703	0.670	0.705

program [55]. Only a few examples of structures will be given here. They have been selected in order to illustrate some of the more general features as well as the diversity of the overlayer crystallography.

In dilute phases (low coverage), chemisorbed atoms are usually not ordered. Ordering appears at intermediate coverages when interactions between adsorbed atoms become significant. On dense phases, atoms tend to be localized in the sites of highest coordination with the highest symmetry: threefold hollow sites on face-centered cubic (fcc) (111) surfaces, fourfold hollow sites on fee or body-centered cubic (bcc) (100) surfaces. For electronegative species, the bond distances between the chemisorbed atom and nearest-neighbor metal substrate atoms are in many cases nearly the sum of the covalent radius of the metal and the covalent radius of the adsorbed atom. This is the case for sulfur on nickel, whose crystallographic data are shown in Figure 6 [56]. These data refer to structures with a small coincidence mesh between the overlayer and the metal substrate: respectively c(2 × 2) on Ni(100) and Ni(110) (coverage one half) and (2 × 2) on Ni(111) (coverage one fourth).

Outward surface relaxation induced by adsorption is frequently observed. For S and O adsorbed on Ni(100) on which the same structures p(2 × 2) and c(2 × 2) are successively formed at respective coverages one fourth and one half, it was observed that the first layer distance increases linearly with increasing coverage and that oxygen is more effective than sulfur [57]. This increase of the metal-metal bond length certainly provokes a strong decrease of the metal-metal bond strength. A more complex surface rearrangement occurs when carbon is adsorbed on Ni(100) [58,59]. Half a monolayer of carbon induces a distortion of the outermost layer of nickel. On this distorted layer, carbon atoms occupy fourfold hollow sites. Similar surface rearrangement with possibly very little difference in the bond strength has been discussed for C/Co(100) [59,60], N/Ni(100) [61], and N/Cr(100) [62]. Surface stresses generated by carbon, oxygen, and sulfur adsorbed on Ni(100) have been determined [63]. Results support the concept that surface stress would be the driving force for the surface reconstruction induced by carbon.

During the surface reconstruction, new adsorption sites are created in order to optimize the surface chemical bond. In the cases of S on Fe(110) [64] and S on Ni(111) [65,66], sites with fourfold symmetry seem to prevail. The most drastic surface rearrangement concerns the S/Ni(111) system, in which the first layer of nickel reorganizes from a hexagonal plane into a nearly perfect (100) plane in order

Table 9 Work Function Variations at Saturation for Halogens on Fe(100) [50]

Element	I	Br	Cl
Coverage	0.58	0.73	0.75
$\Delta\phi$ (eV)	0.55 ± 0.05	1.06 ± 0.0	1.43 ± 0.03

Copyright © 2002 Marcel Dekker, Inc.

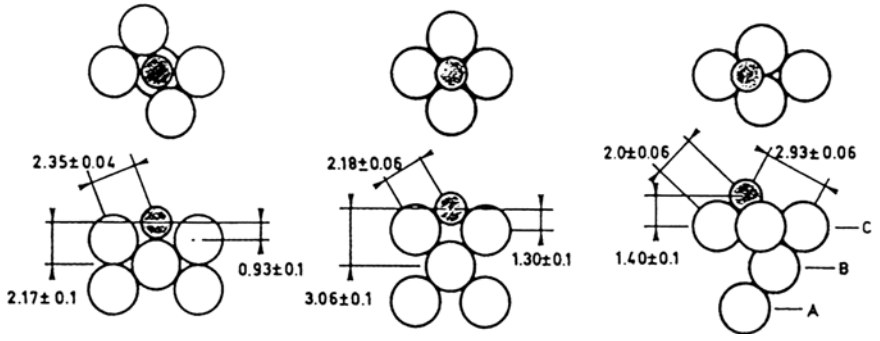


Figure 6 Schematic configurations of S/Ni(l10)–c(2×2), S/Ni(100)–c(2×2) and S/Ni(111)–p(2× 2) structures. (From Ref. 56.)

to accommodate the sulfur overlayer (Fig. 7). This overlayer strongly resembles that formed on Ni(100).

Another well-documented case of surface reconstruction is the H/Ni(110) system [67]. Above the critical concentration of one monolayer, the topmost nickel atoms are displaced by approximately 0.4 Å in one direction. This process may be considered as the prequisite for hydride formation. The importance of restructuring processes for the chemical reactivity of metals has been discussed [68]. When the strength of the adsorbate-substrate bond is lower than that of the substrate-substrate bond, the driving force is not sufficient to induce significant surface reconstruction. In this case complex structures frequently observed at high coverages can be described in terms of periodic antiphases or in terms of close-packed layers of atoms adsorbed on the undisturbed substrate. Halogens on the dense planes of transition metal seem to belong to this category [42].

Restructuring processes involving surface diffusion of metal atoms over distances larger than one atomic distance may also be induced by adsorption at coverages near saturation. In this case, the original surface becomes unstable and breaks into new crystallographic orientations selectively stabilized by the adsorbate. This phenomenon, usually called faceting, occurs by step coalescence. The reversible

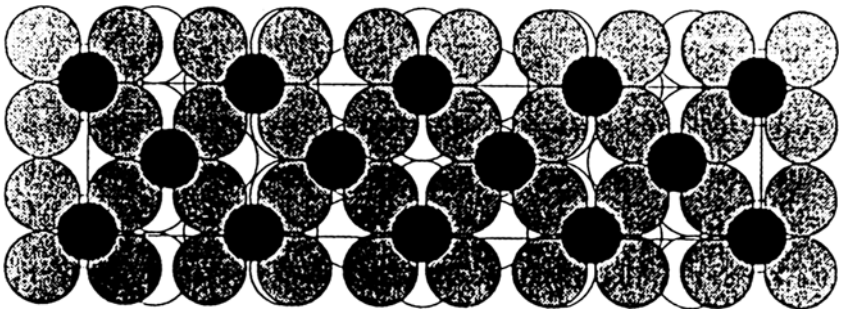


Figure 7 Surface reconstruction induced by adsorption of sulfur on Ni(111). (From Refs. 65 and 66.)

Copyright © 2002 Marcel Dekker, Inc.

character of the faceting process associated with the reversibility of adsorption was demonstrated first in the oxygen-silver system [69]. For iron-chromium alloys [70] and pure iron [71] the conditions for faceting induced by oxygen adsorption have been determined. In the case of iron, faceting inhibits the dissociation of nitrogen on the metal surface [72]. Presumably, the N_2 dissociation step is suppressed by the presence of adsorbed oxygen on the surface. A number of studies have established the close relationship between faceting and the thermodynamics of adsorption. Based on the analysis of Herring [73], conditions of faceting have been evaluated and experimentally demonstrated for oxygen adsorbed on silver [74]. The influence of carbon on the surface stability of nickel has been extensively studied [75].

TRANSITION FROM ADSORPTION TO OXIDATION

The transformation of the overlayer into a bulk compound is an important area of study. This aspect is discussed in detail for the oxidation of nickel and refractory metals Cr, Mo, and W [26]. Chapter 5 of this book is essentially focused on the oxide growth of thin oxide films. It is well accepted that relaxation or surface reconstruction plays an important role in this transformation by loosening the metal-metal bonds. When the reconstructed layer presents strong structural similarities to a dense plane of the bulk compound, it can be considered as a transition layer between the metal lattice and the bulk compound lattice. According to a theoretical model [76], the penetration of the nonmetal atoms into the metal and its conversion into bulk compound would be assisted by the electric field resulting from the charge transfer from the metal to the adsorbed atom. The magnitude of this field depends on the density of adsorbed atoms. As a consequence, the onset of the bulk compound formation occurs only beyond a critical concentration of adsorbed atoms in the overlayer.

The onset of oxidation has been accurately followed on Ni(100) by measuring simultaneously the absolute amount of oxygen fixed on the surface by Rutherford backscattering spectrometry and work function variations as a function of the exposure time. Results are shown in Figure 8 [77]. At first the work function increases, indicating a charge transfer from the metal to the adsorbed oxygen atoms. Well-ordered $p(2 \times 2)$ and $c(2 \times 2)$ structures successively appear. The onset of the oxide nuclei is indicated by the decrease of the work function. It occurs when about a half-monolayer of oxygen is adsorbed in the fourfold symmetry sites and 0.04 to 0.077 mL of oxygen is incorporated into subsurface sites.

From a comparison of the behavior of Cr, Mo, and W in the presence of oxygen, some general trends can be drawn [27]. These trends result directly from the characteristics of the metal and from the energetics of the metal-oxygen interactions as expressed in Table 4. The propensity for the surface to be reconstructed under the influence of oxygen and for the metal to be oxidized varies in the order Cr > Mo > W. It is the reverse of the order of metal-metal bond energies. For a given metal the ease of reconstructive oxidation varies in reverse order to the surface density of metal atoms (111) > (100) > (110). This emphasises the necessity of breaking the metal-metal bonds in order to form the oxide. This breaking is, as one would expect, favored by a low metal-metal bond strength and a high metal-oxygen bond strength. The best example is chromium. On this metal the energy dissipated by

Copyright © 2002 Marcel Dekker, Inc.

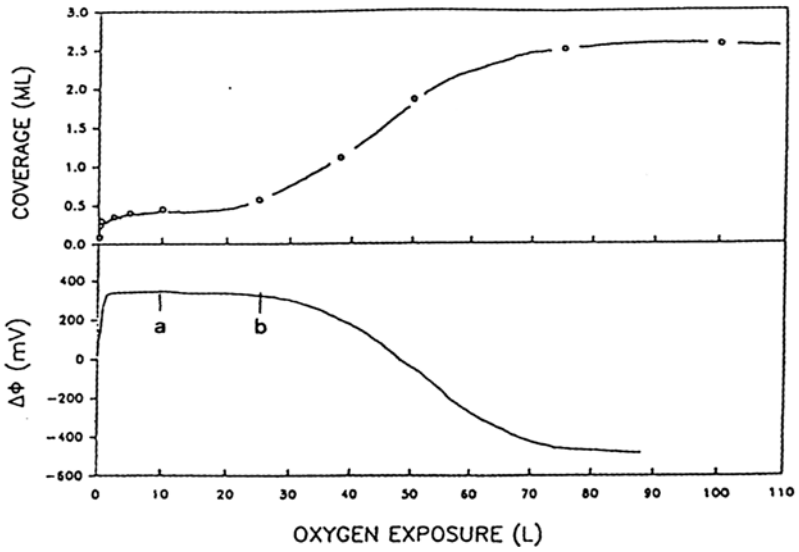


Figure 8 Adsorption of oxygen on Ni(100). (Top) Absolute coverage of oxygen in mono-layer (ML) as a function of oxygen exposure in Langmuir (L) at 329 K. (Bottom) Work function change corresponding to the data in the upper panel. (a) Onset of the filling of subsurface sites; (b) onset of the oxide nucleation. (From Ref. 77.)

the interaction of oxygen is sufficiently large to disrupt the metal-metal bond directly, without the formation of an oxygen adlayer. Zr and Ta behave similarly to Cr. By contrast, on W very stable adsorbed overlayers are formed before the appearance of the oxide. On Mo, which represents an intermediate case, open surfaces behave more like Cr and dense surfaces like W.

ADSORPTION AND SEGREGATION ON ALLOYS

The surface composition of an alloy at equilibrium is rarely the same as the bulk composition. In most cases, the surface tends to be enriched with the metal component having the lower surface energy. In addition, several mechanisms can affect the surface composition with respect to its equilibrium composition:

1. In vacuum or neural atmospheres, one component may be selectively evaporated.
2 In reactive gases, one component may be selectively combined with the gas to form two- or three-dimensional compounds.
3. In electrolyte, one component may be selectively dissolved and the surface or the region near the surface selectively enriched with the other component.

These surface modifications may significantly affect the resistance of the alloy to dry or wet corrosion. Alternatively, corrosion tests can be used as a probe for determining the surface composition of the alloy. Some of these aspects can be

Copyright © 2002 Marcel Dekker, Inc.

illustrated with reference to Fe-Cr alloys. When these alloys are treated at high temperature under pure flowing hydrogen or in vaccum, chromium is selectively evaporated. This phenomenon occurs at temperatures of ~ 1000°C, at which the chromium partial pressure becomes appreciable (~10^6 atm). Alloys superficially depleted in chromium have lower resistance to dry oxidation or corrosion in acid solutions. After treatment in pure hydrogen at 1200°C, the chromium content on the surface of Fe-18Cr or Fe-23Cr alloys can reach a value well below 13%. As a result, an alloy that is initially passive in acid solution becomes active and is dissolved until the layer depleted to below the critical value of 13% Cr is consumed. Chromium evaporation at high temperature can be suppressed by introducing traces of H_2S or H_2O into the hydrogen atmosphere [78]. At a critical partial pressure of H_2S or H_2O well below that corresponding to the formation of bulk compounds (sulfide or oxide), chromium combines selectively to give a two-dimensional sulfide or oxide. These very stable two-dimensional compounds, identified by AES [79], act as a barrier to chromium evaporation. The critical H_2S or H_2O partial pressure at which the chromium evaporation is suppressed can be accurately determined by measuring the corrosion potential of the alloy after the thermal treatment. This potential, which depends on the H_2S or H_2O content, reflects the surface coverage by sulfur or oxygen. Its variation with H_2S or H_2O partial pressure in the gas phase shown in Figure 9 is analogous to the respective adsorption isotherms for sulfur or oxygen at the temperature of the thermal treatment. In the case of sulfur, direct determination of surface concentration has confirmed that the transition from an active to a passive corrosion potential occurs at the transition from low to high sulfur coverage [80].

Surface segregation induced by adsorption is a general phenomenon. The metal element with the highest affinity to the reacting gas tends to be enrich surface provided that the reaction temperature is high enough to permit bulk diffusion [81,82].

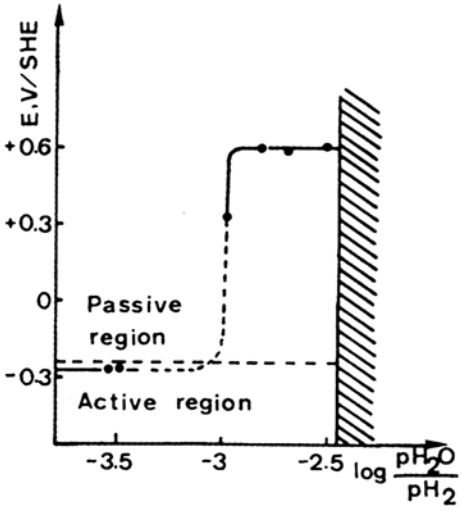


Figure 9 Variation of potential of Fe-23Cr alloy as a function of prior thermal treatment under different atmosphere compositions. (From Ref. 78.)

Copyright © 2002 Marcel Dekker, Inc.

As mentioned before is the case for Cr in Fe-Cr alloys in the presence of O or S in the gas phase. Cr behaves similarly in Ni-Cr alloys [83].

For $Ni_{75}Fe_{75}$, the composition of the sulfur-covered surface was observed to be identical to the bulk composition for both the (100) and (110) faces [84]. This is in agreement with the fact that the two metallic elements of the alloy have nearly the same affinity for sulfur. In contrast, the (111) face of the same alloy behaves differently. The sulfur-covered surface was shown to be enriched in Fe with a maximum Fe/Ni ratio of 1. Such an effect was explained by a competition between metal-metal and metal-sulfur interactions and an ordering of the adsorbed layer that maximizes the Ni– Fe bonds at the composition of the maximum.

When the difference in affinity for the gas of the two components of a binary alloy is large, only one element is preferentially incorporated into a two-dimensional (2D) compound. This is the case when oxygen interacts with $Pt_{80}Co_{20}$ to form a single layer of CoO [85]. Similarly, when an Ag-Ni alloy containing a low Ni concentration reacts with H_2S, a 2D Ni-S compound is formed as identified by radio-tracers for both S and Ni [86].

The nonmetal species that induces the surface enrichment of a metallic compound of an alloy may also originate from the bulk material. A thermodynamic treatment of the cosegregation process has been proposed [87,88], and various models of segregation have been critically discussed [89].

Equilibrium segregation of nonmetal species—C, N, O, Si, P, and S—on iron and iron-based alloy has been extensively studied [90]. Investigations of single crystals showed the formation of epitaxially arranged 2D surface compounds such as CrN on Fe-15%Cr-N(100) and VC on Fe-3% Si-0.04%V-C(100) [91–93]. Most concepts of segregation at free surfaces can be applied to grain boundaries [89].

WATER ADSORPTION

The main features of the interaction of water with solid surfaces have been reviewed with special emphasis on studies performed in ultrahigh-vacuum (UHV) systems on single crystals of metals [94]. Precise data on the binding energy, the orientation, the tendency for hydrogen bonding of H_2O molecules, and their ability to dissociate are now available. The effect of coadsorbed species has also been explored in some detail. The characterization by UHV spectroscopies of the interaction of water molecules with ionic species is a promising attempt for investigating the solid-electrolyte interface [95,96], The different steps of building an electrochemical double layer in the presence of specific adsorbed ions are shown in Figure 10. In UHV, the three first steps can be reached, allowing a study of the properties of the inner layer. Direct comparison between gas-phase experiments and electrochemical data is possible by measuring the work function change and the electrode potential, by properly referencing these two values. The potential drop across the interface can be measured and compared. It was shown by this method that the double layer can in some favorable cases be emersed essentially intact from solution [97].

Copyright © 2002 Marcel Dekker, Inc.

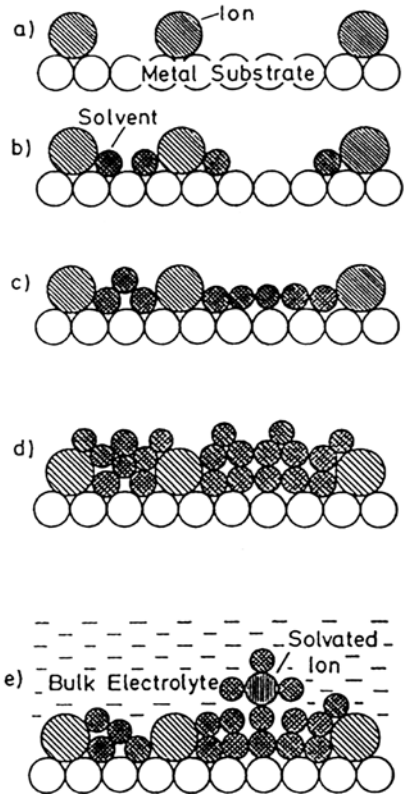


Figure 10 Schematic representation of the synthesis of the electrochemical double layer in UHV. (a) Adsorption of specifically adsorbed ions without solvent; (b) addition of hydration water; (c) completion of the inner layer; (d) addition of solvent multilayers; (e) model for the double layer at an electrode surface in solution. (From Ref. 95.)

Molecular Adsorption

The two lone pairs in the molecule enable the oxygen to interact with the substrate and with neighboring molecules. The general characteristics of the interaction of H_2O molecules with metals can be summarized as follows [94]:

1. Water bonds through the oxygen atom to the surface by overlap between the metal's orbitals and water's lone pair orbitals.
2. Water acts as an electron donor (Lewis base) to the substrate surface. As a consequence, the work function of the metal decreases during H_2O adsorption.
3. Preferred adsorption sites are the "on top" adsorption sites that are electron depleted.
4. Compared with the isolated molecule, the internal bond angle, bond lengths, and vibrational frequency are only slightly perturbed by the interaction with the surface.

Copyright © 2002 Marcel Dekker, Inc.

5. The chemical bond is typically of the order of 40 to 65 kJ mol^{-1} on the borderline of physisorption.
6. The adsorption of H_2O on metals is nonactivated—the probability of adsorption is close to unity.

Special attention has been devoted to the structure of the H_2O adsorbed layer. The strength of attractive interactions by hydrogen bonds in this layer is comparable to that with the substrate. As a result, H_2O molecules tend to form short- and long-range ordered structures. At fractional monolayer coverages, well-oriented dimers have been observed on Ni(110) [98].

At higher coverages the adsorbed layer is characterized on the densest plane of many fcc or hexagonal metals by an identical hexagonal low-energy electron diffraction (LEED) pattern for which a structural model similar to the ice lattice has been proposed [99,100] (Fig. 11). In this model, the first layer of water molecules is bound by direct chemisorption bond to the metal. Molecules in the second layer are linked by two or three hydrogen bonds to the first layer molecules. The stability of this bilayer is strongly dependent on the lattice matching between the metal and crystalline ice. The bilayer model may also be adapted with some distortions to nonhexagonal planes: fcc (100) or (110) [101].

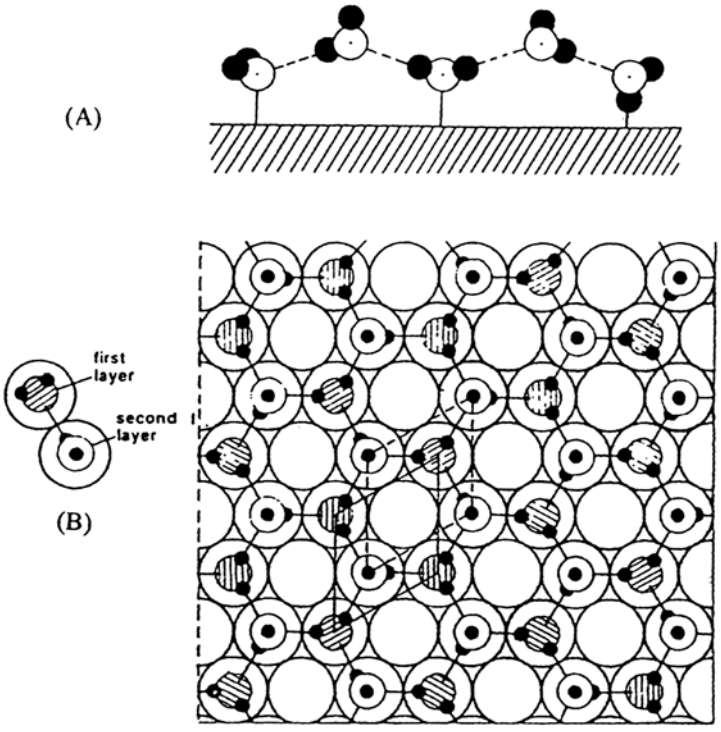


Figure 11 Schematic diagram of the water bilayer. (A) Side view; (B) top view. (From Ref. 99.)

Copyright © 2002 Marcel Dekker, Inc.

Water Dissociation

Water can be partially or totally dissociated on metals to form hydroxyl and hydrogen or atomic oxygen and hydrogen. The driving force for dissociation is provided by the heat of formation of the dissociation fragments (OH, H, O) relative to the chemisorption bond of molecular water.

Based on the enthalpy change that accompanies molecular or dissociative adsorption, metals for which dissociation is favored or not are listed in Figure 12. In this classification the most important factor is the metal-oxygen bond of atomic oxygen, which varies more strongly from metal to metal than it does from the metal-hydrogen bond strength. The same factor that stabilizes the electronegative oxygen atom also tends to stabilize the electronegative hydroxyl fragments. As a consequence, the same tendency is observed for total or partial water dissociation. Experimental results are also included in Figure 12 [94]. Better agreement is found between prediction for complete dissociation and experimental observations despite the fact that these results usually refer to partial dissociation.

The upper limit for dissociation is about 110 kJ mol^{-1}, far less than the barrier for breaking an OH bond in the free water molecule (500 kJ mol^{-1}). This illustrates the ability of the surface to stabilize the dissociation fragments during the OH bond breaking.

For borderline metals such as Co, Ni, Re, and Cu, water dissociation is favored by the roughness of the surface on an atomic scale, whereas the adsorption remains molecular on close-packed planes. A good example of a metal in this category is

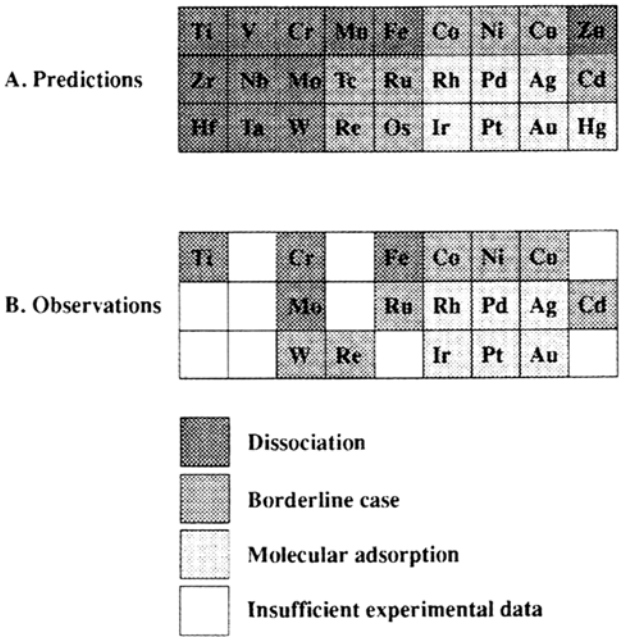


Figure 12 Comparison between predictions and experimental results for molecular versus dissociative H_2O adsorption on metals. Predictions refer to complete dissociation: $H_2O_a \rightarrow 2H_a + O_a$. (From Ref. 94.)

Copyright © 2002 Marcel Dekker, Inc.

nickel. There is no evidence of water dissociation on the clean, atomically smooth (100) and (111) planes. In contrast, on the atomically rough (110) face, water is dissociated at about 100 K into OH_a and H_a. On Ni(111), steps increase significantly the water binding energy and the tendency of water to dissociate [102]. This effect has been attributed to the presence at steps of acid $Ni^{\delta+}$ adsorption sites that enhance the electron transfer from water molecules to the substrate. The increase of the H_2O–Ni bond strength is correlated with a decrease in the intramolecular H_2O bond strength that favors the H_2O dissociation.

In addition to Ni(110), formation of a hydroxyl overlayer has been observed on Fe(100) [103] and Fe(110) [104], on Ag(100) [105,106], and on Ag(111) [107]. On Fe(100), mechanisms of water adsorption and dissociation have been studied by LEED, thermal desorption, and high-resolution electron spectroscopy [103]. At low temperature and low coverage, water is adsorbed by forming hydrogen-bonded molecular clusters. As the surface is warmed, the clusters break apart, wetting occurs, and water molecules begin to dissociate. Dissociation is complete at 250 K, forming a well-ordered OH overlayer with the OH bond tilted from the surface normal (Figure 13). Near 310 K the hydroxyl overlayer disproportionates or dissociates with water or hydrogen desorption, The remaining oxygen is bound in the fourfold hollow sites as for oxygen adsorbed from molecular oxygen.

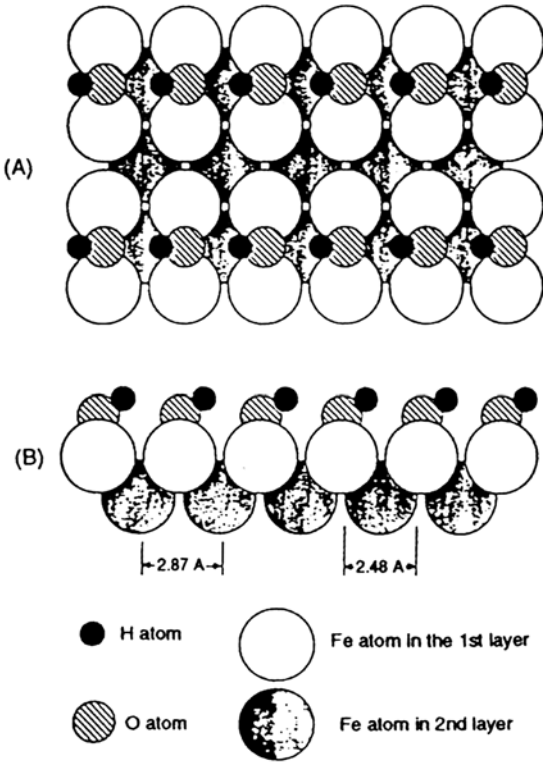


Figure 13 Hydroxyl species in p(1 × 2) structure of Fe(100) surface. (A) Top view; (B) side view. (From Ref. 103.)

Copyright © 2002 Marcel Dekker, Inc.

Effect of Additives

Preadsorbed additives significantly affect the binding energy of water molecules. Water molecules desorb at higher temperatures in the presence of an electronegative (Br), an electropositive (Cs), or a more covalent adsorbate (H) [108]. This has been attributed to the surface hydration of the ionic species, which creates stronger attractive interactions than the water interactions in the pure water adsorbed layer. On metals such as Ag, Cu, Ni, Pt, and Pd on which H_2O is molecularly adsorbed, a fractional monolayer of oxygen can significantly increase the H_2O-metal binding energy and eventually initiate the H_2O dissociation. The reaction proceeds via the hydrogen abstraction reaction with the formation of OH_a species:

$$H_2O_a + O_a \rightarrow 2OH_a \quad (1)$$

As shown on Cu(110) [109], this reaction occurs only for low oxygen coverage, the oxygen-saturated surface being totally inactive. A typical curve in Figure 14 shows that, for $\theta_o < 0.1$ the slope of the curve is 2, indicating that, as expected from reaction (1), $2OH_a$ are formed per adsorbed O_a.

Similarly, iron exposed to an equimolar gas mixture containing O_2 and H_2O reacts at room temperature according to [110]

$$2Fe + H_2O + \tfrac{1}{2}\,O_2 \rightarrow 2FeOH \quad (2)$$

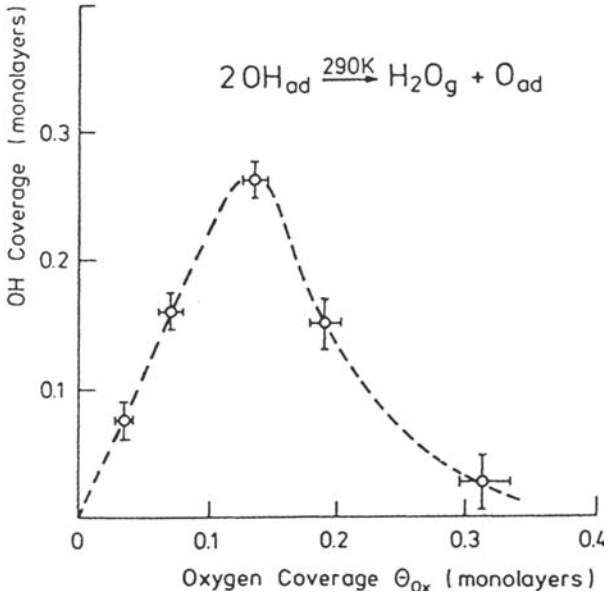


Figure 14 Hydroxyl coverage as a function of initial oxygen coverage, Θ_{Ox}, on Cu(110). Maximum hydroxyl formation occurs for $\Theta_{Ox} = 1/8$. (From Ref. 109.)

Copyright © 2002 Marcel Dekker, Inc.

ADSORPTION ON METAL OXIDES

Studies of chemisorption of gaseous molecules on oxides may provide new insights into the various processes involved in the formation, aging, and degradation of passive films. We will restrict ourselves to a brief description of the main features of the chemisorption behavior on oxides. We will focus on results obtained on well-defined surfaces of single crystals with O_2 and H_2O as adsorbates. In the past 10 years, precise data on the structure and the electronic properties of surfaces of single crystals of oxide have been obtained by LEED and surface-sensitive spectroscopies (UPS, XPS, HEELS). Excellent introductions to this subject can be found in Refs. 111 and 112. A large part of the data presented here is extracted from these reviews.

For many different bulk oxides in which metal cations are octahedrally coordinated, such as MgO, CoO, NiO, and TiO_2, the most stable surface is characterized by fivefold coordination of the surface cation. Such a surface, which is usually the cleavage plane, is shown in Figure 15 for the rock salt lattice. Linear defects such as step or point defects arising from anion or cation vacancies are also represented in this figure. To a first approximation the structure of the cleavage plane can be considered as the termination of the bulk lattice with minor relaxations (rumpling of only few percent of the interionic spacing has been detected by LEED). A good example showing the higher stability of the surface with fivefold coordination of surface cations concerns $TiO_2(001)$. This plane, which contains only fourfold-coordinated cations, decomposes spontaneously at moderate temperature into facets containing fivefold coordination cations.

On many oxides the reduction of the ligand coordination of the surface cations with respect to the bulk cations does not introduce specific band gap surface states and the surface oxide exhibits an electronic structure undistinguishable from that of

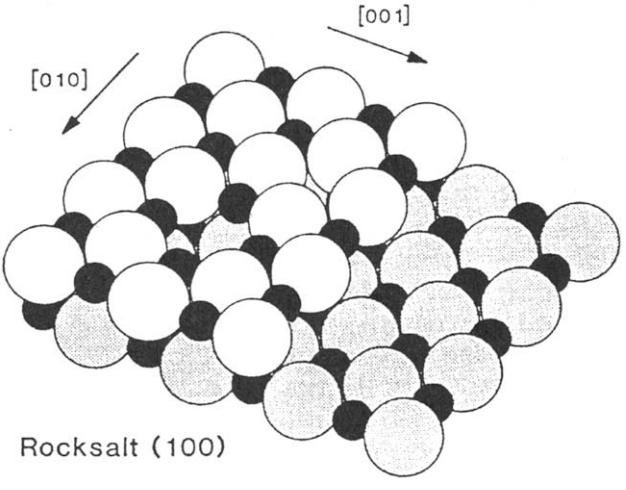


Figure 15 Model of the rock salt (100) surface. Large circles represent O anions; small circles represent metal cations. Surface defects: step, anion vacancy, and cation vacancy are also shown. (From Ref. 112.)

Copyright © 2002 Marcel Dekker, Inc.

the bulk. Further reduction of ligand coordination of cations due to their localization at steps does not change significantly the electronic structure of oxides.

Mechanisms of Chemisorption

Chemisorption [114] on an oxide surface differs significantly from that on metals. One of the main reasons for this difference is the ionic character of the solid, which favors acid-base or donor-acceptor reactions. Lewis sites are localized on the cations and basic sites on the anions. An example of this type of interaction is given by CO_2, which reacts with basic O^{2-} to give a surface carbonate CO_3^{2-}. Similarly, a donor molecule such as H_2O or NH_3 can be molecularly adsorbed via its lone-pair electrons, which react with an acidic (cation) site. An alternative to the molecular adsorption is that resulting from the heterolytic dissociation of the molecule. It may occur by abstraction of H atom transferred to a basic site, producing a hydroxyl group.

Chemisorption may also proceed by a mechanism involving an electron transfer between the adsorbate and the substrate (oxidation- reduction or redox interaction). It is the case for adsorbates such as O_2 or Cl_2 that are strong electron acceptors. O_2 can be molecularly or dissociatively adsorbed, Cl_2 is dissociatively adsorbed. The redox reactions that involve electronic carriers are expected to occur preferentially on semiconducting or metallic oxides. On wide-bang-gap insulators these reactions are promoted by surface defects such as ion vacancies, which may act as sources or sinks for electrons.

The role of coordinative unsaturation in determining the surface reactivity of metal oxides has been discussed with special references to the dissociation of Brönsted acids [115]. This reaction involves a metal-oxygen pair. The proton from the acid is bound to the surface oxygen anion, which acts as a base, and the conjugate base anion from the acid is bound to the surface metal cation, which acts as a Lewis acid. The very different chemistry exhibited by the two polar planes of wurtzite ZnO (Fig. 16) makes it possible to define the coordination requirement of the surface ions for acid dissociation. In bulk wurtzite each anion or cation is tetrahedrally coordinated to four cations or anions, respectively. At the oxygen polar (0001) surface, an oxygen anion is coordinated to three Zn cations in the plane immediately below. These cations are coordinatively saturated. At the Zn polar (0001) surface the reverse situation is found; a vacant coordination site is present on each surface cation, whereas oxygen anions in the layer below the surface are coordinatively saturated. The Zn polar plane was observed to dissociate various acids of the strength of carboxylic acid or less, whereas the O polar plane remained totally inert with respect to the dissociation of these acids. This result emphasizes the predominant role of coordination vacancy associated with the surface cation for the dissociation of Brönsted acids. It was also shown that doubly coordinatively unsaturated surface cations favor reactions involving the coupling of the ligands originating from the dissociation of two acid molecules.

As regards chemisorption involving redox interactions, it is useful to make a distinction between oxides whose cations are in their highest valence state (maximal valence oxide) and oxides whose cations are in a reduced valence state (suboxides). Among the most studied oxides, TiO_2, $SrTiO_3$, MgO, and Al_2O_3 belong to the first category and Ti_2O_3 V_2O_3, and MnO to the second one. Nearly perfect surfaces of

Copyright © 2002 Marcel Dekker, Inc.

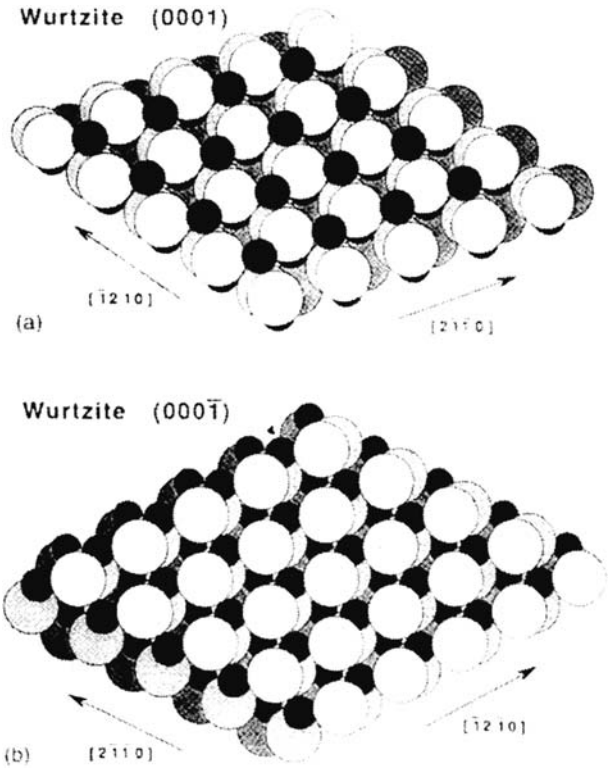


Figure 16 Models of wurtzite surfaces (a) (0001) and (b) (000–1) [From Ref. 113].

maximal valence oxide are quite inert in chemisorption involving an electron transfer from the oxide toward the adsorbed molecule because their surface cations are not able to supply electrons by oxidation. For example, NiO(100) is inert to O_2 to 10^3 L exposure (sticking coefficient lower than 10^{-9}). Conversely, CO, which is an electron donor, reduces NiO at low exposure by abstracting O^{2-} to form CO_2 and leaving a vacancy behind. Perfect suboxide surfaces react much more easily with a large number of molecules, particularly with O_2. This can be ascribed to the ability of surface cations to transfer their electron to adsorbed species. No general trends have been found to characterize the chemisorption behavior of suboxides, which varies significantly from one system to another.

Point defects are mainly involved in chemisorption on cleaved surfaces. On such surfaces the density of point defects is usually very small. They can be created by heating in vacuum and rapid quenching or by electron or ion bombardment. The predominant point defects are O vacancies (F centers) with two electrons at each vacancy in order to maintain the local electroneutrality. This localized charge partially overlaps with the adjacent cations, increasing the population of their lowest empty orbitals. The charge distribution does not affect significantly the O^{2-} anions near the vacancy defect because their already filled 2*p* shell cannot accept additional charge. The O vacancies affect predominantly the electronic structure in maximal

Copyright © 2002 Marcel Dekker, Inc.

valence oxides of transition metals. On most of these oxides, as observed for TiO_2 or $SrTiO_3$, new surface states appear in the band gap and usually increase the surface conductivity of the oxide. The only oxide that has been observed to become more insulating in the presence of O vacancies is CoO.

Oxygen vacancy defects on most oxide surfaces, maximal valence or suboxides, display a strong interaction with molecules such as O_2, H_2O, CO, or SO_2. O_2 molecules are dissociatively adsorbed to form O^{2-} ions. After saturation of the defect sites, a second species, tentatively identified as a doubly ionized molecular species, adsorbs much more weakly on the surface. O^{2-} ions adsorbed at the defect sites interact differently from lattice ions with H_2O or CO. A possible explanation is that these adsorbed O species, which are probably less ionic than oxygen ions, do not relieve completely the relaxation of the lattice around the defect site.

Water Adsorption

H_2O adsorption from water vapor has been extensively studied, first on powdered samples, more recently on single crystals. Most experiments on powders were carried out at high vapor pressures (> 1 torr). Experiments on single crystals are usually performed at low gas pressures (< 10^{-6} torr) because of the limitations of the modern surface science techniques. Powdered samples are highly defective and contain various crystalline orientations and structures. They are more representative of the behavior of passive films formed in aqueous solution. Studies on well-characterized surfaces of single crystals make it possible to investigate the role of surface defects and surface orientation on the mechanisms of chemisorption.

Results on powders can be summarized as follows:

1) H_2O is dissociatively adsorbed on metal oxides at room temperature at a pressure of a few torr to form hydroxyl groups. This reaction of acid-base type is schematically represented in Figure 17 for a surface oxide exposing both anions and cations. Two types of OH groups are shown. Those bound to two cations are strongly polarized, thus loosening the bond to hydrogen. These groups are acidic in character. The other OH groups bound to one cation are predominantly basic and easily exchangeable for other anions [116]. The high reactivity of defective oxides is confirmed by the external hydroxylation in aqueous solution of the films of NiO formed by Ni passivation [117] or by sputtering deposition [118].

2) Zurface OH may react with water molecules through hydrogen bonds. One may expect that the same type of interactions occurs at the passive film-aqueous solution interface and influence the structure of the double layer. The ratio H_2O/OH was found to be close to ½ on metal oxides such as MgO, TiO_2, Fe_2O_3, and Al_2O_3 [119]. Higher values close to one were observed on ZnO, SnO_2, and Cr_2O_3 [119]. The behavior of hydroxylated powder of Cr_2O_3 studied by infrared spectroscopy, adsorption isotherms from water vapor, and thermal adsorption [120] illustrates the complexity of the interactions between OH groups and H_2O molecules. Two kinds of adsorption were observed: (a) adsorption of H_2O molecules on localized OH groups with an adsorption energy of about 55 kJ mol^{-1} and (b) adsorption of H_2O on special OH groups leading to a phase transformation. This phase transformation is clearly seen on the adsorption isotherms at around 300 K (Fig. 18). It seems to be favored by the strong structural similarity between the hydroxylated (001) surface of Cr_2O_3 and the basal plane of ice. A large

Copyright © 2002 Marcel Dekker, Inc.

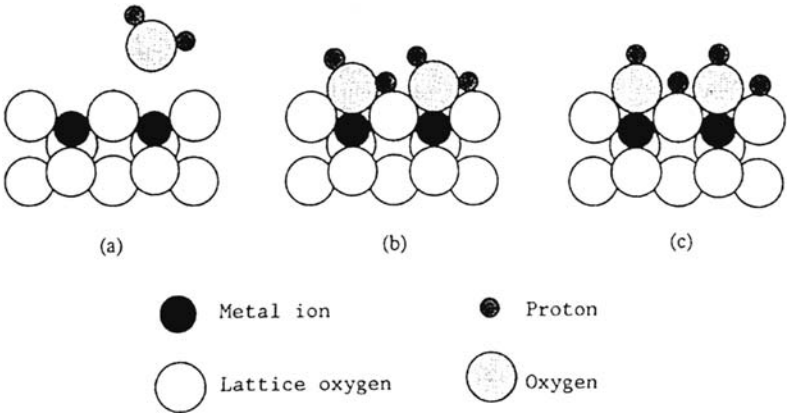


Figure 17 Schematic representation of oxyde hydroxylation. (a) hydroxyl-free surface; (b) physical adsorption of water; (c) dissociation of water giving rise to two distinct OH^- species.

proportion of OH on the Cr_2O_3 surface other than the foregoing two types was found inactive for H_2O adsorption. Differences in the polarization of the OH groups from one site to another may explain their more or less high ability to bind H_2O molecules. The existence of a 2D phase transformation has also been observed for H_2O on hydroxylated ZnO [119].

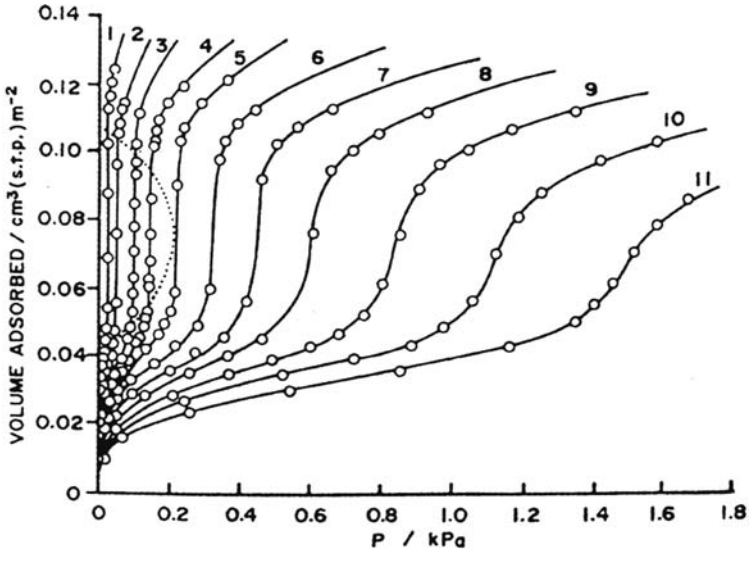


Figure 18 Adsorption isotherms of H_2O on hydroxylated Cr_2O_3. Adsorption temperature (K): (1) 275; (2) 284.9; (3) 294.6; (4) 299.2; (5) 303.6; (6) 307.8; (7) 312.4; (8) 317.1; (9) 321.4; (10) 325.7; (11) 330.8. The dotted line shows the range in which two phases coexist. (From Ref. 118.)

Copyright © 2002 Marcel Dekker, Inc.

3) Finally, on some oxides, hydration is not restricted to the surface but may lead to the formation of bulk hydroxide. That occurs on MgO at a vapor pressure of 4–6 torr [119].

Hydroxylation of well-characterized surfaces of single crystals has been investigated at a large range of vapor pressures. It was shown that up to a threshold pressure only defect sites are reactive. This threshold pressure is 10^{-4} torr on MgO(001) [121] and Fe_2O_3(0001) [122] and 1 torr on Al_2O_3(0001) [122]. At higher pressures the whole surface is hydroxylated. The threshold pressure, which seems to be thermodynamically controlled, provides a means of estimating the surface defect density. On MgO hydroxylation is throught to occur preferentially at both oxygen and magnesium defective sites [121].

The influence of crystalline orientation and surface structure on water reactivity was clearly shown in a study performed by ESCA, LEED, and STM on NiO thin films [123]. After oxidation at 300 K at low oxygen pressure of a single crystal of Ni(111), the thin film, three to four layers thick, consists mainly of NiO(111) grains in parallel epitaxy with the substrate. This film, otherwise unstable, is stabilized by a complete layer of OH^- formed by reaction with the residual water contained in oxygen gas. The hydroxyl groups are ionic (OH^-) and singly bonded to the surface metal atoms that terminate the polar NiO(111) plane [124]. The ionic character of the hydroxyl groups would compensate at least partially the repulsive interaction between Ni^{2+} cations in the outermost plane of NiO [124]. A further exposure (150 L) at room temperature to water leads to the formation of a nearly complete layer of nickel hydroxide with the terminal sequence OH–Ni–OH.

After oxidation at 500 K of Ni(111), about 93% of the surface is covered by NiO(100) areas and 7% NiO(111). As previously shown by other authors [125,126], H_2O does not react on the nonpolar NiO(100) plane at low water pressures. As a consequence, only the part of the surface made of NiO(111) grains and possibly defect sites on NiO(100) are covered by hydroxyl groups formed by the reaction with the residual water vapor. Exposing this film to 150 L of water at 300 K leads to the lateral extension of the hydroxylated NiO(111) grains that grow at the expense of the NiO(100) matrix. These results show the effect of the surface hydroxylation on oxide growth.

Hydrogen Sulfide

Similarly H_2O, H_2S may adsorb dissociatively on oxides by proton abstraction and formation of SH^- groups at room temperature. At higher temperature the replacement of O^{2-} leads to sulfur deposition of S^{2-} with water formation. On NiO(100) this last reaction occurs at 570 K and leads to the formation of a surface compound made of an Ni raft with sulfur atoms occupying fourfold hollow sites (Fig. 19) [127,128]. This Ni raft is expanded to fit the Ni(100) substrate. For larger exposure the growth of bulk sulfide Ni_3S_2 proceeds. Interaction of H_2S with CoO(100) leads to a surface compound similar to that observed on NiO(100) but the reaction starts at a lower temperature (373 K). Then the formation of Co_9S_8 was observed [129].

Copyright © 2002 Marcel Dekker, Inc.

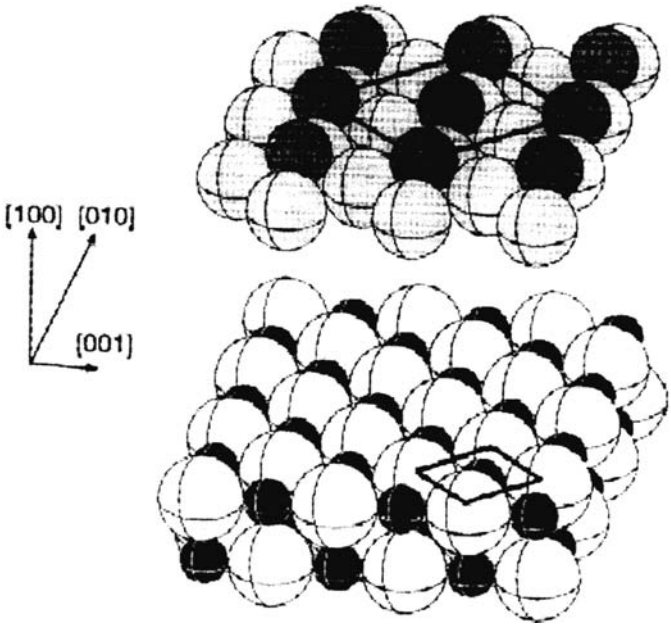


Figure 19 Model of the surface compound formed by reaction of sulfur with NiO(100). S is in fourfold symmetry on a raft of Ni atoms. For clarity, the surface compound is separated from its substrate [From Ref. 128].

CONCLUSIONS

Most corrosion processes, e.g., metal dissolution, hydrogen or oxygen evolution, and passive film formation, involve at least one adsorption step as a part of the overall reaction. This step can be significantly affected by the presence on the metal surface of a monolayer of nonmetal species. As evidenced by studies described in this chapter, adsorbed species may act by loosening the metal-metal bond or changing the electric field at the metal-electrolyte interface. They can also favor or inhibit the adsorption or the recombination of adsorbed atoms normally involved in the anodic or cathodic reactions.

As for the formation of bulk compounds, most thermodynamic data on adsorption have been acquired from gas-phase studies. These data are essential for determining in a potential-pH diagram the conditions under which a given species is present at a monolayer level on a metal surface in contact with an electrolyte. Some successful attempts in this direction have already been made [130].

Metal-water interactions are relatively well understood and there is no doubt that OH adsorbed groups originating from water dissociation are the precursors of the passive film formation on transition metals.

External hydration of oxide passive films found in many systems is in agreement with the high reactivity observed in water vapor for oxide surfaces that have a large number of defects. Further work remains to be done on the adsorption on

Copyright © 2002 Marcel Dekker, Inc.

oxides, which is the key for a better understanding of the initial stages of localized corrosion induced by species such as chloride or sulfur.

REFERENCES

1. G. Broden, T. N. Rhodin, C. Brucker, R. Benbow, and Z. Hurych, *Surf. Sci. 59*:593 (1976).
2. W. M. H. Sachtler and L. L. Van Reijen, *J. Res. Inst. Catal. Hokkaido Univ. 10*:87 (1962).
3. A. Ozaki and K. Aika, *Catalysis Science and Technology,* Vol. 1 (J. R. Anderson and M. Boudart, eds.), Springer-Verlag, New York, 1981, p. 94.
4. H. Wise, J. McCarthy, and J. Oudar, *Deactivation and Poisoning of Catalyst* (J. Oudar and H. Wise, eds.), Marcel Dekker, New York, 1985, p. 45.
5. K. R. Christmann, (a) *Hydrogen Effects in Catalysis* (Z. Paal and P. G. Menon, eds.), Marcel Dekker, New York, 1988, p. 3; (b) *Surf. Sci. Rep. 9*:1 (1988).
6. J. W. Geus, in Ref. 5, p. 45.
7. P. Nordlander, S. Holloway, and J. K. Norskov, *Surf. Sci. 136*:59 (1984).
8. R. A. Oriani, J. P. Hirth, and M. Smialowski, eds., *Hydrogen Degradation of Ferrous Alloys,* Noyes, Park Ridge, NJ, 1985.
9. F. Boszo, G. Ertl, M. Grunze, and M. Weiss, *Appl. Surf. Sci. 1*:103 (1977).
10. K. Christmann, O. Schober, G. Ertl, and M. Neumann, *J. Chem. Phys. 60*:4528 (1974).
11. K. Christmann, *Z. Naturforsch. A34*:22 (1979).
12. K. Christmann, R. J. Boehm, G. Ertl, M. A. Van Hove, and M. H. Weinberg, *J. Chem. Phys. 70*:4168 (1979).
13. K. Christmann, F. Chehab, V. Penka, and G. Ertl, *Surf. Sci. 152/153*:356 (1985).
14. P. W. Tamm and L. D. Schmidt, (a) *J. Chem. Phys. 51*:5352 (1969); (b) *52*:1150 (1970); (c) *54*:4775 (1971).
15. D. W. Goodman, R. D. Kelley, T. E. Madey, and J. T. Yates, Jr., *J. Catal. 63*:226 (1980).
16. J. M. Blakely, *Crit. Rev. Solid State Mater. Sci. 7*:333 (1978).
17. L. C. Isett and J. M. Blakely, *Surf. Sci. 55*:397 (1976).
18. H. J. Grabke, W. Paulitschke, G. Tauber, and H. Viefhaus, *Surf. Sci. 63*:377 (1977).
19. H. J. Grabke, *Chemistry and Physics of Fracture* (R. M. Latanision and R. H. Jones, eds.), NATO AS1 Series, 1987, p. 388.
20. H. Ishizuka, *J. Jpn. Soc. SAFEM Eng. 10*:326 (1971).
21. M. Grunze, *The Chemical Physics of Solid Surfaces and Heterogeneous Catalysis* (D. A. King and D. P. Woodruff, eds.), Vol. 4, Elsevier, Amsterdam, 1982, p. 143.
22. F. Boszo, G. Ertl, M. Grünze, and M. Weiss, *J. Catal. 49*:18 (1977).
23. F. Boszo, G. Ertl, and M. Weiss, *J. Catal. 50*:519 (1977).
24. T. A. Delchar and G. Ehrlich, *J. Chem. Phys. 42*:2686 (1965).
25. L. D. Schmidt, *Topics in Applied Physics,* Vol. 4 (R. Gomer, ed.), Springer-Verlag, New York, 1975, p. 77.
26. J. D. Fast and M. B. Verrij, *J. Iron Steel Inst. 180*:337 (1955).
27. C. R. Brundle and J. Q. Broughton, *The Chemical Physics of Solid Surfaces and Heterogeneous Catalysis* (D. A. King and D. P. Woodruff, eds.), Vol. 3, Elsevier, Amsterdam, 1982, p. 131.
28. J. Benard, J. Oudar, N. Barbouth, E. Margot, and Y. Berthier, *Surf. Sci. 88*:L35 (1979).
29. J. G. McCarty and H. Wise, (a) *J. Chem. Phys. 72*:6332 (1980); (b) *J. Chem. Phys. 76*:1162 (1982).
30. T. Rosenquist, *J. Iron Steel Inst. 176*:37 (1954).
31. C. B. Alcock and F. D. Richardson, *Nature 168*:661 (1952).
32. N. Barbouth and J. Oudar, *C. R. Acta. Sci. 269*:1618 (1969).

Copyright © 2002 Marcel Dekker, Inc.

33. W. H. Herrnstein, F. E. Beck, and M. G. Fontana, *Trans. AIME 242*:1049 (1968).
34. A. Larere, M. Guttmann, R. Dumoulin, and C. Roques-Carmes, *Acta Metall. 30*:685 (1982).
35. C. L. Briant, *Acta Metall. 33*:1241 (1985).
36. A. B. Vladimirov, V. N. Kaigorodov, S. M. Klotzmann, and I. S. Trakatenberg, *Fiz. Mater Met. 39*:319 (1975).
37. M. P. Seah, *Surf. Sci 80*:8 (1979).
38. L. Beaunier, M. Froment, and C. Vignaud, *Electrochim. Acta 25*:1239 (1980).
39. N. Barbouth and J. Oudar, *Mem. Sci. Rev. Metall. 86*:777 (1989).
40. M. Grunze and P. A. Dowben, *Appl. Surf. Sci. 10*:209 (1982).
41. P. A. Dowben, CRC Crit. Rev. *Solid State Mater. Sci. 13*:191 (1984).
42. G. Jones, *Prog. Surf. Sci. 27*:25 (1988).
43. S. Hino and R. M. Lambert, *Langmuir 2:*147 (1986).
44. P. A. Dowben, M. Grunze, and D. Tomanek, *Phys. Scr. T 4*:106 (1983).
45. G. Bolbach and J. C. Blais, *Surf. Sci. 137*:327 (1984).
46. W. Erley, *Surf. Sci. 114*:47 (1982).
47. W. Kinzel, W. Selke, and K. Binder, *Surf. Sci. 121*:13 (1982).
48. E. L. Muetterties, T. N. Rhodin, E. Band, C. F. Brucker, and N. R. Pretzer, *Chem. Rev. 79*:91 (1979).
49. L. Peralta, E. Margot, Y. Berthier, and J. Oudar, *J. Microsc. Spectrosc. Electron. 3*:151 (1978).
50. P. A. Dowben and R. G. Jones, *Surf. Sci. 88*:348 (1979).
51. C. Nguyen Van Huong, R. Parsons, P. Marcus, S. Montes, and J. Oudar, *J. Electroanal. Chem. 119*:137 (1981).
52. R. Parsons, *Modern Aspects of Electrochemistry* (J. O'M. Bockris, ed.), Butterworth, London, 1954, p. 170.
53. A. Hamelin and J. Lecoeur, *Surf. Sci. 57*:771 (1976).
54. J. M. McLaren, J. B. Pendry, P. J. Rous, D. K. Saldin, G. A. Somorjai, M. A. Van Hove, and D. D. Yvedensky, *Surface Crystallographic Information Service: A Handbook of Surface Structure,* Reidel, Dordrecht, 1987.
55. J. B. Pendry, *Surface Crystallographic Information Service: Data Base and Graphics Programs,* Riedel, Dordrecht, 1987.
56. J. E. Demuth, D. W. Jepsen, and P. M. Marcus, *Phys. Rev. Lett. 32*:1182 (1974).
57. W. Oed, U. Starke, K. Heinz, K. Müller, and J. B. Pendry, *Surf. Sci. 251/252*:488 (1991).
58. J. H. Onuferko, D. P. Woodruff, and B. W. Holland, *Surf. Sci. 87*:357 (1979).
59. Y. Gauthier, R. Beaudoing- Saudis, K. Heinz, and H. Landskron, *Surf. Sci. 251/252*:493 (1991).
60. M. Maglietta and G. Rovida, *Surf. Sci. 71*:495 (1978).
61. D. Arvanatis, K. Baberschke, and L. Wenzel, *Phys. Rev. B 37*:7143 (1988).
62. Y. Joly, Y. Gauthier, and R. Beaudoing, *Phys. Rev. B 40*:10119 (1989).
63. D. Sander, U. Linke, and H. Ibach, *Surf. Sci. 272*:318 (1992).
64. H. D. Shih, F. Jona, D. W. Jepsen, and P. Marcus, *Phys. Rev. Lett. 46*:731 (1981).
65. D. R. Warbuton, P. L. Wincott, G. Thornton, F. M. Quinn, and D. Norman, *Surf. Sci. 211/212*:71 (1989).
66. Y. Kitajima, T. Yokohama, T. Ohta, M. Funabashi, N. Kosugi, and H. Kuroda, *Surf. Sci. 214:*L261 (1989).
67. K. H. Rieder and W. Stocker, *Surf. Sci. 164*:55 (1985).
68. G. A. Somorjai and M. A. Van Hove, *Prog. Surf. Sci. 30*:201 (1989).
69. B. Chalmers, R. King, and R. Shuttleworth, *Proc. R. Soc. Lond. Ser. A 193*:465 (1948).
70. J. Moreau and J. Benard, *J. Chim. Phys. F 53*:787 (1956).
71. J. Moreau and J. Benard, *Acta Metall. 10*:247 (1962).
72. H. J. Grabke, *Arch. Eisen. Eisenhuettenwes. 44*:603 (1973).

Copyright © 2002 Marcel Dekker, Inc.

73. C. Herring, *Phys. Rev. 82*:87 (1951).
74. G. E. Rhead and M. McLean, *Acta Metall. 12*:401 (1964).
75. M. Eizenberg and J. M. Blakely, *J. Chem. Phys. 71*:3467 (1979).
76. F. P. Fehlner and N. F. Mott, *Oxid. Met. 2:*59 (1970).
77. T. D. Pope, S. J. Bushby, K. Griffiths, and P. R. Norton, *Surf. Sci. 258*:101 (1991).
78. J. Oudar, N. Barbouth, and J. Bénard, *Mem. Sci. Rev. Metall. 72:*649 (1975).
79. J. Oudar, N. Barbouth, and A. Trueba, *C. R. Acad. Sci. Paris 278*:545 (1974).
80. J. Oudar, N. Barbouth, and C. Jacques, C. *R. Acad. Sci. Paris 290C*:421 (1980).
81. R. Bouwman and W. M. H. Sachtler, *J. Catal. 25*:350 (1972).
82. C. Leygraf, G. Hultquist, S. Ekelund, and J. C. Eriksson, *Surf. Sci. 46:*157 (1974).
83. P. Humbert and A. Mosser, *J. Phys. 44:*L531 (1983).
84. P. Marcus, A. Teissier, and J. Oudar, *Surf. Sci. 129:*432 (1983).
85. U. Bardi, A. Atrei, G. Rovida, and P. N. Ross, *Surf. Sci. 251/252*:727 (1991).
86. B. Auffray, A. Rossand, and P. Gas, *Surf. Sci. 178*:872 (1986).
87. M. Guttmann, *Surf. Sci. 53:*213 (1975).
88. M. Guttmann, *Metall. Trans. 8A*:1383 (1977).
89. J. Cabané and F. Cabané, *Interface Segregation and Related Processes in Materials* (J. Novotny, ed.), Trans. Tech. Publ., 1991, p. 1.
90. C. Uebing, H. Viefhaus, and H. J. Grabke, *Surf. Interface Anal. 16*:4283 (1990).
91. C. Uebing and H. Viefhaus, *Surf. Sci. 236*:29 (1990).
92. C. Uebing, H. Viefhaus, and H. J. Grabke, *Appl. Surf. Sci. 32*:363 (1988).
93. C. Uebing, *Surf. Sci. 225*:97 (1990).
94. P. A. Thiel and T. E. Madey, *Surf. Sci. Rep. 7*:1 (1987) and references therein.
95. J. K. Sass and K. Bange, *ACS Symp. Ser. 378*:54 (1988).
96. F. T. Wagner and T. E. Moylan, *ACS Symp. Ser. 378*:65 (1988).
97. D. M. Kolb and W. N. Hansen, *Surf. Sci. 79*:205 (1979).
98. C. Nöbl, C. Benndorf, and T. E. Madey, *Surf. Sci. 157*:29 (1985).
99. D. Doering and T. E. Madey, *Surf. Sci. 123*:305 (1982).
100. P. A. Thiel, R. A. De Paola, and F. M. Hoffmann, *J. Chem. Phys. 80*:5329 (1984).
101. P. Brosseau, M. R. Brustein, and T. H. Ellis, *Surf. Sci. 280*:23 (1993) and references therein.
102. C. Benndorf and C. Mundt, *J. Vac. Sci. Technol. A10*:3026 (1992).
103. W. H. Hung, J. Schwartz, and S. L. Bernasek, *Surf. Sci. 248*:332 (1991).
104. A. M. Baro and W. Erley, *J. Vac. Sci. Technol. 20*:580 (1982).
105. J. Paul and F. M. Hoffmann, *J. Phys. Chem. 90*:5321 (1986).
106. F. J. Szalkowski, *J. Chem. Phys. 77*:5224 (1982).
107. J. E. Crowell, J. G. Chen, D. M. Hercules, and J. T. Yates, Jr., *J. Chem. Phys. 86*:5804 (1987).
108. J. K. Sass, D. Lackey, J. Shott, and B. Staehler, *Surf. Sci. 247*:239 (1991).
109. K. Bange, D. E. Grider, T. E. Madey, and J. K. Sass, *Surf. Sci. 137*:38 (1984).
110. G. Hultquist, M. Seo, Q. Lu, G. K. Chuah, and K. L. Tan, *Appl. Surf. Sci. 59*:135 (1992).
111. V. E. Henrich, *Rep. Prog. Phys. 48*:1481 (1985).
112. V. E. Henrich, *Surfaces and Interfaces of Ceramic Materials* (L. C. Dufour, C. Momky and G. Pekot-Eruas et al., eds.) Kluwer, Dordrecht 1989, p. 1, and references therein.
113. V. E. Henrich and C. A. Cox, *The Surface Science of Metal Oxides,* Cambridge University Press, Cambridge, 1994.
114. C. Noguera, *Physics and Chemistry of Oxide Surfaces,* Cambridge University Press, Cambridge, 1996.
115. M. A. Barteau, *J. Vac. Sci. Technol. A11*:2162 (1993).
116. H. P. Boehm, *Discuss. Faraday Soc. 52*:264 (1971).

Copyright © 2002 Marcel Dekker, Inc.

117. P. Marcus, J. Oudar, and I. Olefjord, *J. Microsc. Spectrosc. Electron. 4*:63 (1979).
118. D. A. Wruck and M. Rubin, *J. Electrochem. Soc. 140*:1097 (1993).
119. Y. Kuroda, E. Yasugi, H. Aoi, K. Miura, and T. Morimoto, *J. Chem. Soc. Faraday Trans. 1 84*:2421 (1988) and references therein.
120. S. Kittaka, T. Sasaki, N. Fukuhara, and H. Kato, *Surf. Sci. 282*:255 (1993).
121. P. Liu, T. Kendelewics, G. E. Brown, Jr., and J. A. Parks, *Surf. Sci. 412/413*:287 (1998).
122. P. Liu, T. Kendelewics, G. E. Brown, Jr., E. J. Nelson, and S. A. Chambers, *Surf. Sci. 417*:53 (1998).
123. N. Kitakatsu, V. Maurice, C. Hinnen, and P. Marcus, *Surf. Sci. 407*:36 (1998).
124. M. A. Langel and M. H. Nassir, *J. Chem. Phys. 99*:4162 (1995).
125. H. Kuhlenbeck, G. Odorfer, R. Jager, G. Illing, M. Menges, T. Mull, M. Polchen, V. Staemmler, S. Witzel, C. Scharfschwerdt, K. Wenneman, T. Liedke, and M. Neumann, *Phys. Rev. Condens. Matter 43*:1969 (1991).
126. D. Cappus, C. Xu, D. Ehrlich, B. Dillman, C. A. Ventrice, Jr., K. Al Shamery, H. Kuhlenbeck, and H.-J. Freund, *Chem. Phys. 177*:533 (1993).
127. A. Steinbrunn, P. Dumas, and J. C. Colson, *Surf. Sci. 74*:201 (1978).
128. A. P. Woodhead, S. P. Harte, S. A. Haycock, C. A. Muryn, P. L. Wincott, V. R. Dhanaka, and G. Thornton, *Surf. Sci. 420*:L138 (1999).
129. P. Dumas, A. Steinbrunn, and A. Colson, *Thin Solid Films 79*:267 (1981).
130. P. Marcus and E. Protopopoff, *J. Electrochem. Soc. 137*:2709 (1990).

Copyright © 2002 Marcel Dekker, Inc.

3

Surface Effects on Hydrogen Entry into Metals

Elie Protopopoff and Philippe Marcus
Laboratorie de Physico-Chimie des Surfaces, Université Pierre et Marie Curie, Ecole Nationale Supérieure de Chimie de Paris, Paris, France

INTRODUCTION

It is well known that H entry (absorption) into the bulk may lead to embrittlement of metals and alloys. This process, known as H embrittlement or H-induced cracking, often combined on non-noble metals with corrosion cracking, is particularly detrimental to the resistance of metallic materials [1]. High H concentrations may be produced in metals by thermal or electrochemical charging; H can accumulate and combine at internal defects such as microcracks or cavities present in most commercial metals or alloys; high H_2 pressures can build up within these cavities, which then grow and coalesce, forming microvoids leading to loss of ductility [1]. In aqueous medium, the reaction of H absorption (HAR) into an electrode proceeds in parallel to the reaction of H_2 gas evolution at the surface (HER), at cathodic overpotentials and, at the corrosion potential on non-noble metals, simultaneously with the anodic dissolution or oxidation reactions in the mixed process controlling the rate of corrosion. The H entry into transition metals increases drastically in the presence of dissolved compounds of some electronegative elements, which are known to be poisons of H adsorption. Although many explanations have been proposed to account for these effects, the detailed mechanisms of the action of these H entry promoters are not yet fully understood.

The HAR was usually studied from permeation experiments using the electrochemical permeation technique. The other way was by charging experiments. With the development of techniques of hydrogen storage in solid materials, there has been a renewal of interest in the H absorption reaction [2–6] and a need to monitor the conditions for obtaining high concentrations of H in the bulk (and establishing relations not restricted to low levels of H concentrations and to low overpotentials).

Surface reaction steps involving adsorbed hydrogen such as H adsorption, desorption, and surface-bulk transfer, play a determining role in the H cathodic reactions. The HAR and the HER most often share a common step of H electroadsorption from protons or water, and only a study of the overall mechanism of these reactions makes it possible to predict the conditions in which the H uptake under the surface is increased.

Copyright © 2002 Marcel Dekker, Inc.

The problem of analyzing all the data on H entry rate is that this rate, even in a pure metal, depends on many variables: the nature of the metal, its thermal-mechanical history, the surface conditions (especially on iron, surface states are not easily reproducible due to the difficulty of removing oxide films on the electrodes), composition of the electrolyte, cathodic current density or electrode potential, temperature, etc. The determining factors in the kinetics of the H cathodic reaction on bare metal surfaces are the cathodic overpotential and the surface variables, which are the density of sites for H adsorption and the binding energy of the adsorbed H atoms, both dependent on the structure and the chemical composition of the surface.

The aim of this chapter is to analyze how the surface factors control the surface adsorption (chemisorption) processes, i.e., H electroadsorption and coadsorption of other species, and hence the energetics and the mechanisms of HER and HAR at electrodes of transition metals in aqueous electrolyte. The metals of particular interest are Fe and Ni for their use as base metals for alloys. A prerequisite to a comprehensive understanding of these phenomena is to define precisely the characteristics of H adsorption and absorption common to the gas and liquid phases. First we present the elementary surface steps occurring in the two phases. We report the thermodynamic and structural data existing for the two phases and derive the kinetic relations for all the elementary surface reactions in aqueous solution, making clear the surface variables. This allows a unified treatment of the H reactions at the metal-gas interface and at the metal–liquid electrolyte interface. The role in H absorption inside the metals of the structure of H adsorption sites and of the adsorption energy in these sites is examined in detail. H absorption promoting effects by certain species are detailed; then a model of the effects of the species blocking the H adsorption sites on the rates and the mechanisms of the HER and HAR is presented that makes it possible to predict the surface conditions for H entry promotion.

THE HYDROGEN SURFACE REACTIONS

The H_2 Dissociative Adsorption and Absorption Reactions in the Gas Phase

Entry of H into the bulk of a transition metal from a gaseous dihydrogen phase is commonly considered to occur from atomic H adsorbed (more exactly chemisorbed) on the surface and thus involves the following steps [7,8]:

Transport of the H_2 molecules to the surface.
Molecular adsorption (physisorption).
Dissociation of H_2 and formation of a chemisorption bond between atomic hydrogen and a surface site consisting of a certain number of substrate atoms. H dissociative adsorption is quasi-nonactivated on most transition metals.
Surface-bulk transfer from adsorbed H to H dissolved beneath the surface (also called absorption step).
Diffusion into the bulk.
Possibly hydride formation near the surface when the H concentration reaches a critical value.

Copyright © 2002 Marcel Dekker, Inc.

H_2 Dissociative Adsorption

Dissociative adsorption of hydrogen from the gas phase has been described in Chapter 2 (see also Ref. 8). It proceeds as follows:

$$H_2(g) + 2(M) \rightleftarrows 2H_{ads}(M) \quad (1)$$

where (M) denotes one empty metal surface site and $H_{ads}(M)$ an H atom adsorbed at a surface site. The dissociative adsorption process may either occur directly (i.e., the rate is limited by the probability of finding two adjacent empty sites for dissociation) or involve a physisorbed H_2 precursor state mobile on the surface that may migrate H Surface-Bulk until it finds empty sites on which it may dissociate.

H Surface-Bulk Transfer

The surface-bulk transfer may be written:

$$H_{ads}(M) + [M] \rightleftarrows H_{diss}[M] + (M) \quad (2)$$

where [M] represents an empty H bulk interstitial site in the first planes beneath the surface, and $H_{diss}[M]$ is a dissolved (absorbed) H atom bonded to a bulk site.

Because both the coordination of the H atoms and the energy of the H state change drastically between surface and bulk, it is realistic to consider that the absorption step is not an elementary step but involves an H subsurface state (sorbed H), intermediate between the surface adsorbed state and the bulk absorbed state, located in the interstitial sites between the very first metal layers beneath the surface [9]. This state has been characterized by ultrahigh-vacuum (UHV) techniques on Pd, Ni, Pt, and Cu [8,10–17], and is believed to play a role in ordering of the H surface phases [14]. The subsurface sites become accessible by relaxation or reconstruction of the top layer of the metal substrate [8]. Figure 1 shows the different H sites at the vicinity of a metal surface.

Analysis of isotope effects on H thermal desorption spectra on Pd(111) has also evidenced a pathway of direct H entry into the bulk without equilibration with the chemisorption state [19]. However, this mechanism observed after H_2/D_2 exposure at 115 K is probably related to a quantum tunneling effect not operating at room temperature. Alternatively, it might be due to the presence of two types of surface entry sites on this particular face, one being more stable than the other for chemisorption (discussed later in the chapter).

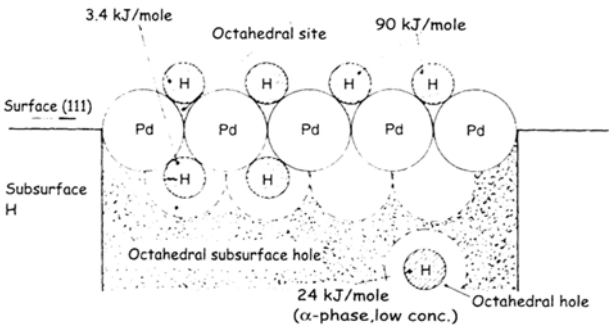


Figure 1 Structural model of a Pd(111) surface showing the surface, subsurface, and bulk sites. (From Fig. 9 in Ref. 18.)

Copyright © 2002 Marcel Dekker, Inc.

The Hydrogen Surface Reactions in Aqueous Electrolyte

The H entry into a metal from an aqueous electrolyte is believed to involve the same surface-bulk transfer step as in the gas phase, but the preliminary adsorption step is a more complex process because more H sources are involved in aqueous solution, allowing more possible H surface reactions, and also because of the specificity of the electrolyte-metal interface. Whereas H adsorption in the gas phase occurs by dissociative adsorption of gaseous H_2 on the free sites of a bare metallic surface, H adsorption in aqueous solution may occur either chemically by dissociation of dissolved H_2 or electrochemically from solvated (hydrated) protons or water molecules; it takes place on a hydrated surface and thus implies the displacement of adsorbed water molecules or specifically adsorbed ions and local reorganization of the double layer [20]; competition with the adsorption of oxygen species formed from the dissociation of water may also occur [21–23]. The adsorbed H layer is also in interaction with surrounding water molecules, i.e., it is hydrated [8c,24,25].

Elementary Surface Reactions

Chemical H_2 Dissociative Adsorption and H-H Combination (Tafel Reaction) Under conditions in which there is no specific adsorption of ions or adsorption of oxygen species, the reaction of adsorption from $H_{2(g)}$ in aqueous electrolyte occurs through the following steps:

Dissolution of H_2 gas into solution, in equilibrium: $H_{2(g)} \leftrightarrows H_{2(aq)}$

Transport of the dissolved H_2 molecules to the surface

Direct dissociative adsorption:

$$H_{2(aq)} + 2(M)_{(hyd)} \rightleftarrows 2H_{ads}(M)_{(hyd)} \tag{3}$$

where $H_{2(aq)}$ is a dissolved H_2 molecule, $2(M)_{(hyd)}$ represents a pair of adjacent hydrated sites available for adsorption of hydrogen, and $H_{ads}(M)_{(hyd)}$ represents an H atom adsorbed in a site (M) and hydrated.

The reverse reaction is the combinative desorption of H atoms, or chemical combination, also known as the Tafel reaction.

H Electroadsorption/Electrodesorption (Volmer Reaction) In aqueous electrolyte, because the metal substrate is an electrode with the electric potential as an additional variable, H adsorption may occur electrochemically (i.e., assisted by the potential) by reduction of hydrated protons or water molecules, depending upon the pH [26].

1. Proton discharge in acid medium: it involves:
   (a) Fast transport of hydrated protons from the bulk solution to the double layer between the electrolyte and the cathode surface
   (b) H electroadsorption by electron transfer from the electrode to the hydrated protons in the outer Helmotz plane [26]:

$$H^+_{(aq)} + e^-_{(M)} + (M)_{(hydr)} \rightleftarrows H_{ads}(M)_{hyd} \tag{4}$$

where $H^+_{(aq)}$ represents a hydrated proton, and $e^-_{(M)}$ an electron supplied by the metal M.

Copyright © 2002 Marcel Dekker, Inc.

2. Reduction of water in neutral or basic medium:

$$H_2O_{(l)} + e^-_{(M)} + (M)_{(hyd)} \rightleftarrows H_{ads}(M)_{(hyd)} + OH^-_{(aq)} \quad (5)$$

Although there is no limitation to the supply of water molecules in not too concentrated electrolytes (the water activity at the surface is equal to unity), this reaction has a lower rate constant than proton discharge for a given potential so that it is predominant only when the proton concentration is very low.

Electrodissociation/Electrocombination (Heyrovsky Reaction) The H atoms can be desorbed electrochemically by combination with hydrated protons or water molecules (Heyrovsky reaction or electrocombination). Again, depending upon the pH, two types of reaction occur:

1. Proton plus H atom reaction in acid medium:

$$H_{ads}(M)_{(hyd)} + H^+_{(aq)} + e^-_{(M)} \rightleftarrows H_{2(aq)} + (M)_{(hyd)} \quad (6)$$

2. Water plus H atom reaction in neutral or basic medium:

$$H_{ads}(M)_{(hyd)} + H_2O_{(l)} + e^-_{(M)} \rightleftarrows H_{2(aq)} + OH^-_{(aq)} \quad (7)$$

H Surface-Bulk Transfer The transfer step from the adsorbed to the absorbed state is equivalent to the reaction described for the gas phase [Eq. (2)] except that it occurs from adsorbed H atoms surrounded by water molecules or anions and it liberates surface sites for hydratation, as follows:

$$H_{ads}(M)_{(hydr)} + [M] = H_{diss}[M] + (M)_{(hydr)} \quad (8)$$

Overall Electrode Reactions

The H sources in solution, i.e., hydrated protons, and water molecules can be transformed through the preceding elementary adsorption and desorption steps into $H_{2(g)}$ (HER) or H_{abs} (HAR).

Hydrogen Evolution Reaction This overall reaction involves the following two-step pathways proceeding alone or in parallel:

1. Volmer-Tafel pathway: electroadsorption followed by chemical combination
2. Volmer-Heyrovsky pathway: electroadsorption followed by electrocombination

These steps are followed by transport of dissolved H_2 molecules away from the electrode via diffusion or gas evolution (formation of nuclei and phase separation).

On a noble metal, equilibrium of the HER (reversible H^+/H_2 electrode) may be attained provided that the partial H_2 pressure in solution is high enough because the kinetics are fast; from thermodynamic arguments, the HER occurs with a net rate if the potential is cathodic with respect to the equilibrium potential at the given H_2 pressure and pH. Conversely, if the overpotential is anodic, the reverse reaction, i.e., the H_2 oxidation reaction (HOR), prevails, involving H_2 dissociation into adsorbed H followed by H electrodesorption [27].

Copyright © 2002 Marcel Dekker, Inc.

On a corroding metal surface, a mixed process occurs because the main reverse reaction is dissolution or oxidation (passivation); consequently, the net current is a function of the overpotential with respect to the mixed (corrosion) potential (see Chap. 1). The anodic reaction and the H cathodic reaction proceed simultaneously close to the corrosion potential, which implies that the HER may occur on a surface covered by an oxide film (passivated) and that the detrimental effects of anodic dissolution and H entry may be combined in the embrittlement process.

The mechanisms of the HER on the metals currently studied in H entry experiments are relatively well known. At high overpotentials they all involve a coupled electroadsorption-electrocombination mechanism where the reverse steps are negligible.

On electrodes of noble metals of the Pt group, the mechanism of the HER involves at low overpotentials electroadsorption in quasi-equilibrium, followed by a rate-determining step (RDS) of chemical combination, then electrocombination at higher overpotentials [26,28].

On Ni, the reported mechanisms are electroadsorption in quasi-equilibrium followed by rate-determining electrocombination [26,29].

On Fe, early experiments indicated coupled mechanisms, with electroadsorption followed by chemical combination at low overpotential (low θ_H) or electrocombination at high overpotential (higher θ_H) [30–32]. However, more recent analyses reported a parallel pathways mechanism with the chemical and electrochemical combination steps occurring simultaneously, the former being predominant in 0.1 N H_2SO_4 up to high cathodic currents (current densities), whereas in 0.1 N NaOH or neutral solutions the latter (involving water molecules) already predominates at low cathodic currents [33,34]. The exact mechanism seems to depend on the structure and purity of the iron electrode and its surface composition.

Underpotential and Overpotential H Electroadsorption The process of reversible hydrogen electroadsorption occurs at the surface of metal electrodes of the platinum group at potentials anodic to the reversible hydrogen electrode at the given pH and at a pressure of 1 atm (half-standard reversible H^+/H_2 electrode at 1 atm, denoted RHE1 here): H is electroadsorbed at equilibrium at $E > 0V_{(RHE1)}$ up to a quasi-full monolayer. Because this process occurs, going cathodically, under the equilibrium potential of the RHE1, by analogy with underpotential metallic deposition, it is often called H underpotential deposition (UPD) and the adsorbed H UPD H [35]. Contrary to the HER, which is a steady faradic reaction consuming the H species electroadsorbed at overpotential, for which a stationary state is reached when the net rate of electroadsorption of reactants is equal to twice the net rate of H_2 formation, H UPD is a pseudocapacitive faradic process; i.e., at a given potential the adsorption current goes to zero once the equilibrium coverage is reached,corresponding to equality between the rate of adsorption and the rate of desorption of H atoms. It can be characterized only by transient techniques such as cyclic linear sweep voltammetry, giving for cathodic and anodic potential sweeps the well-known H adsorption/desorption pseudocapacitance peaks [35–39], symmetrical if the sweep rate is not too high [35]. By integration of a voltammogram, the electroadsorption/desorption charge flowing through the interface per unit area during a potential scan is obtained, which allows determination of the H surface density at a given potential. If the metal atomic

Copyright © 2002 Marcel Dekker, Inc.

density is known (e.g., on a well-ordered single crystal surface), the coverage θ_H (number of adsorbed H atoms per metal substrate atom) is obtained as a function of the potential, giving electroadsorption isotherms [24,37,38,40–42].

UPD H detection is limited cathodically by the onset of the HER, producing a steady current that is rapidly predominant; UPD is prevented on electrodes covered with electronegative adorbates (see under Influence of the Surface Modifiers on H Entry), and even on a clean electrode UP H adsorption may be hindered by competitive anodic processes such as UP adsorption of O or OH and electrode oxidation [23,29,43]. This explains why UPD H may be detected only on noble metals where the anodic preoxidation processes occur at relatively high anodic potentials so that there is a potential range where H atoms compete only with water molecules forming the metal hydration layer and the specifically adsorbed anions [23,35,39,59]. However, H UPD is not detected on Ag and Au, for which H adsorption from $H_{2(g)}$ is endothermic (see later). On Pd, significant H absorption occurs at underpotential in bulk samples [44,45], so equilibrium UP H adsorption may be characterized by cyclic voltammetry only on Pd thin films in which the low number of bulk H sites limits the absorption reaction [46,47]. On corroding or passivated metal electrodes, UPD H detection is impeded by the metal dissolution and oxidation processes and the voltammograms are not easily interpreted [43,48]; although some workers claimed that H electroadsorption occurs in aqueous electrolytes above 0 V (RHE1) on Ni [49], Fe [50], or W [51], at present there is no strong experimental evidence for this.

Conversely, the electroadsorption step involved in the HER at cathodic overpotentials on all electrodes is called H overpotential deposition (OPD) and the H_{ads} intermediate involved in the HER is called OPD H [35]. Because overpotential adsorption does not occur alone but is only a step in the steady HER process, it is much more difficult to characterize. A technique of measurements of potential relaxation transients (potential decay) could allow determining pseudocapacitance versus potential curves and obtaining the OPD H coverage by integration [29], but this is not straightforward. The OPD H fractional coverage is usually estimated from analysis of the kinetics of the HER and HAR. OPD H is also likely to be the intermediate of the HOR on Pt, in an anodic potential range overlapping that of UPD H [27]. In principle, the electroadsorption of OPD H can occur under true equilibrium only at the H^+/H_2 equilibrium potential, and the OPD H coverage versus potential variation depends upon the HER or the HOR mechanism (see later). It seems likely that the OPD H atoms reacting in the HER on Pt are adsorbed on top of Pt atoms, while the UPD H atoms are adsorbed in high coordination sites [52,53] (see later). There are no similar data for non-noble metals.

Hydrogen Electroabsorption Reaction (HEAR) In aqueous solution, the hydrogen absorption reaction occurs mainly by electrochemical reduction of protons or water molecules (electroabsorption). The overall H electroabsorption reaction from protons is:

It was demonstrated for iron, from the analysis of the relation between the

$$H^+_{(aq)} + e^-_{(M)} + [M] \rightleftarrows H_{diss}[M] \tag{9}$$

stationary cathodic and anodic currents measured on each side of a permeation membrane, that the HER and the HEAR share a common adsorbed H intermediate (H_{ads}) and a common first step of electroadsorption [see Eqs. (4) and (5)] [31]; then H

Copyright © 2002 Marcel Dekker, Inc.

enters the metal lattice by the surface-bulk transfer step [Eq. (8)], assumed to be in quasi-equilibrium because in most cases the permeation rate is found to be limited only by H diffusion through the bulk. This mechanism has been verified to be valid for permeation through iron and nickel and their alloys and it is the generally accepted one [28].

However, it has been suggested by Russian workers [54,55] for explaining the effects of adsorbed I^- ions on H permeation into Pd membranes that the process of H electroadsorption in the HER and the process of electroabsorption "should be regarded as occurring simultaneously and to a certain extent independently of each other" [55]. Thus, on Pd the HAR would not occur by the pathway described before, but by what has been interpreted since as direct H entry from protons [31,56]; this mechanism was invoked for explaining Pd membrane permeation data showing an anomalous relationship between steady-state cathodic and permeation currents [57]. Actually, because a direct entry would involve a quantum tunneling effect not likely at room temperature (see section on gas phase), a classical activation mechanism of H entry through a surface intermediate state different from the adsorbed state involved in the HER (OPD H) is more rational and has to be considered as a possible alternative to the preceding mechanism, at least on Pd. The observation that significant H electroabsorption into bulk Pd already occurs at positive potentials versus RHE1, before the HER takes place, and is likely to involve H UPD [44,58,59] could be consistent with the so-called direct entry mechanism as UPD H is an intermediate surface state different from the HER intermediate (see following section).

THERMODYNAMICS OF METAL-HYDROGEN SYSTEMS

Thermodynamics of H Adsorption and Absorption in the Gas Phase

Isotherms of the Metal-Hydrogen Equilibria

Isotherm of H_2 Dissociative Adsorption The equation of the isotherm of equilibrium adsorption from $H_{2(g)}$ [see Eq. (1)] is

$$\theta_H/(1-\theta_H) = f_{H2}^{1/2} \exp[-\Delta G_{Hads}(\theta_H)/RT] \tag{10}$$

where θ_H is the H surface fractional coverage in the sites (M), f_{H2} is the fugacity of hydrogen gas expressed in atm, and ΔG_{Hads} is the half-standard free energy of H adsorption referred to $\frac{1}{2}H_{2(g)}$ ($\Delta G_{Hads}(\theta_H) = \mu_{Hads}(\theta_H) - \frac{1}{2}\mu^\circ_{H2}$). ΔG_{Hads} is in the general case a function of the coverage θ_H [60]. θ_H is equal to the ratio Γ_H/Γ_{Hsat} of the H_{ads} surface density to the surface density at saturation. Γ_{Hsat} is not necessarily equal to the surface density of H sites on the given face because of H–H repulsive interactions [8].

Isotherm of H_2 Dissociative Absorption (Dissolution) The equation of the isotherm of equilibrium absorption (or dissolution) from $H_{2(g)}$ [see Eqs. (1) and (2)] is the following:

$$X_H/(1-X_H) = f_{H2}^{1/2} \exp[-\Delta G_{Hdiss}(X_H)/RT] \tag{11}$$

where X_H is the H bulk fractional solubility in the sites [M] and ΔG_{Hdiss} is the half-standard free energy of H dissolution from $\frac{1}{2}$ $H_{2(g)}$. ΔG_{Hdiss} is the general case a function of the fractional solubility X_H.

Copyright © 2002 Marcel Dekker, Inc.

X_H, the fractional solubility of H in the metal or fraction of the intersticial sites occupied by H, may be expressed as the ratio c_H/c_{Hsat} of the H volumic concentration to the concentration at saturation, or as r_H/r_{Hsat} where r_H is the hydrogen/metal (H/M) atomic ratio and r_{Hsat} is the ratio at saturation. In a particular lattice, only one kind of interstitial sites is populated by H at moderate pressures. In the ideal case where there were no H–H interactions, r_{Hsat} would be equal to the number of those interstitial sites per metal atom (= 1 for octahedral sites in face-centered cubic (fcc) metals, 2 for tetrahedral sites in hexagonal close-packed (hcp) metals, 6 for tetrahedral sites in body-centered cubic (bcc) metals) [5].

Isotherm of H Surface-Bulk Transfer The equation of the equilibrium isotherm for the surface-bulk transfer step [Eq. (2)] is [53,61,62]

$$X_H/(1 - X_H) = \theta_H/(1 - \theta_H)\ \exp[\Delta G_{Hads(\theta H)} - \Delta G_{Hdiss(XH)}]/RT \tag{12}$$

Thermochemical Data

H Adsorption All transition metals from column 3 to 10, plus Cu, are exothermic H adsorbers ($\Delta H_{Hads} < 0$; θ_H decreases when the temperature increases). For these metals, the values of the initial H adsorption heat on single crystal faces $[-\Delta H_{Hads}(\theta_H = 0) = \frac{1}{2}H^\circ_{H2} - H_{Hads}(\theta H = \theta)]$ fall in the range between 20 and 70 kJ mol^{-1} [8]. The M–H_{ads} bond energy at any coverage may be obtained from the relation:

$$E_{M-Hads}(\theta_H) = \tfrac{1}{2}E_{dH2} - \Delta H_{Hads(\theta H)} \tag{13}$$

where E_{dH2} is the dissociation energy of H_2, equal to 436 kJ mol^{-1} at 25°C. In consequence, the values of the M–H_{ads} bond energy at zero coverage fall in the range 240–290 kJ mol^{-1}, i.e., 2.5 to 3.0 eV [8c] (see Chapter 2).

Experimental heats of adsorption of H obtained on polycrystalline transition metal surfaces are shown in Figure 2a [63]. Calculated and experimental adsorption bond energies for H on the most close-packed surfaces of the transition metals are given in Figure 2b [64]. A diminution of the chemisorption bond strength is observed from center left to the right in each metal series (3d, 4d, and 5d).

Experimental data obtained on single crystals for the three low-index faces of Pd, Ni, and Fe are shown in Table 1 of Chapter 2. It is deduced that the initial heat of adsorption and adsorption bond energy depend slightly on the nature of the metal and the surface orientation.

H Absorption The solubility of H in metals varies over a great range, from 10^{-10} to 10^{-1} mol cm^{-3} [28]. According to the sign of the enthalpy of dissolution from $H_2(g)$, metals are exothermic H absorbers ($\Delta H_{Hdiss} < 0$; the H solubility decreases with increasing temperature) or endothermic absorbers ($\Delta H_{Hdiss} > 0$; the H solubility increases with temperature). Among the transition metals, the exothermic absorbers most often undergo a transition to a hydride phase when the bulk H/M ratio increases. These are metals of columns 3 to 5 [65]. Most other transition metals are endothermic absorbers and have very low H solubility at 25°C and 1 atm, especially Cu, Ag, and Au in column 11 [66]. The well-known exception is Pd, which is an exothermic absorber. When the H_2 pressure (or cathodic overpotential) increases, Pd forms with H an α solid solution up to the terminal solubility 0.03 H/Pd at 25°C, above which a β hydride phase with 0.55 H/Pd precipitates; then the H-saturated

Copyright © 2002 Marcel Dekker, Inc.

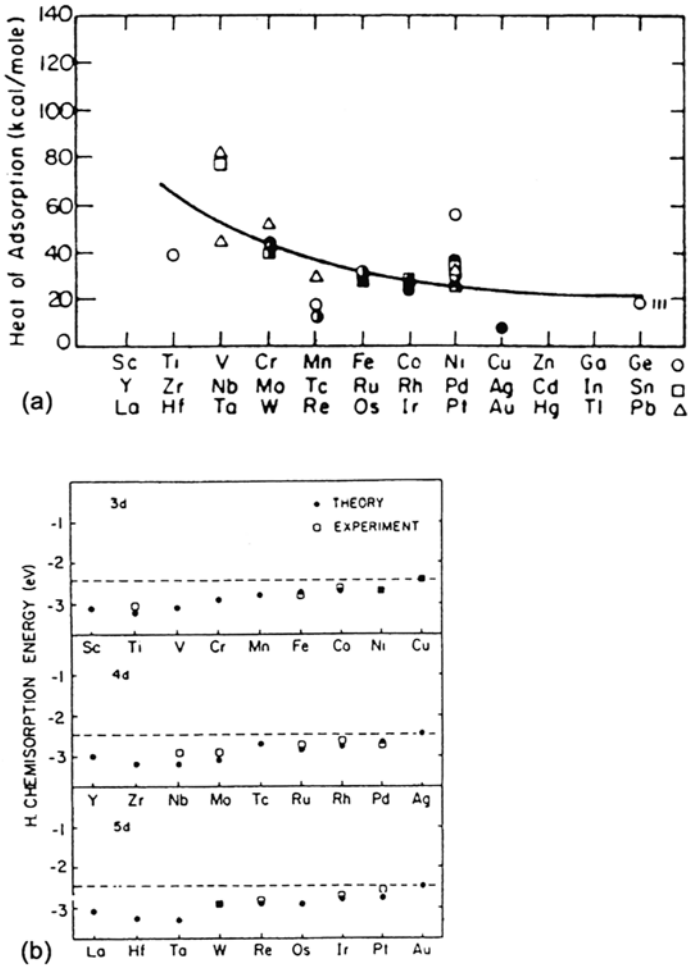


Figure 2 (a) Experimental heats of adsorption of hydrogen on polycnstalune transition metal surfaces. (From Fig. 2a in Ref. 63.) (b) Calculated and experimental chemisorption bond energies for H on the most close-packed surfaces of transitions metals (1 eV ≡ 96.5 kJ mol^{-1}). (From Fig. 2 in Ref. 64, with permission from Elsevier Science.)

metal and the H-deficient hydride coexist until the ratio H/Pd = 0.55 is passed; for very high pressures or overpotentials, the hydride may be enriched in H up to the stoichiometric compound PdH. Also a special case is Ni: (fcc), which exhibits the highest H absorption capacity of any purely endothermic absorber (solubility at 25°C and 1 atm: ~ 10^{-6} mol cm^{-3} [28], 1–5 × 10^{-5} H/Ni [67]; it may form a hydride out of equilibrium, i.e., under very high pressures or overpotentials, up to NiH [68]; Cr (bcc) also forms hydrides in these conditions. Both Mn and Cr exhibit a minimum in solubility as a function of temperature, which means that they change from exothermic absorbers at low temperatures to endothermic at high temperatures [68]. Fe (bcc) has low H solubility (about 3 × 10^{-9} mol cm^{-3}, 2–3 × 10^{-8} H/Fe [67] at 25°C and 1 atm).

Copyright © 2002 Marcel Dekker, Inc.

Table 1 Diagnostic Parameters for Various HER Mechanisms

Mechanism of HER	$-RT/F\partial\ln\theta_H/\partial E$		$\alpha = -RT/F\partial\ln i_c/\partial E$			$-RT/F\partial\ln X_H/dE = -RT/F\partial\ln i_p/dE$		$\partial\ln X_H/\partial\ln i_c = \partial\ln i_p/\partial\ln i_c$	
	$\theta_H \ll 1$	$\theta_H \approx 1/2$	$\theta_H \ll 1$	$\theta_H \approx 1/2$	$\theta_H \approx 1$	$\theta_H \ll 1$	$\theta_H \approx 1/2$	$\theta_H \ll 1$	$\theta_H \approx 1/2$
Volmer q.e. Heyrovsky r.d.s.	1	$\frac{2}{(4+g)}$	$1+\delta$	$\frac{2(1+2\delta+\delta g)}{(4+g)}$	δ	1	1	$\frac{1}{(1+\delta)}$	$\frac{(4+g)}{2(1+2\delta+\delta g)}$
Volmer q.e. Tafel r.d.s.	1	$\frac{2}{(4+g)}$	2	$\frac{2(2+\gamma g)}{(4+g)}$	0	1	1	1/2	$\frac{(4+g)}{2(2+\gamma g)}$
Volmer r.d.s. Heyrovsky q.e.	-1	$\frac{-2}{(4+g)}$	β	$\frac{2(1+2\beta+\beta g)}{(4+g)}$	$1+\beta$	-1	-1	$-\frac{1}{\beta}$	$\frac{-(4+g)}{2(1+2\beta+\beta g)}$
Volmer r.d.s Tafel q.e.	0	0	β	β	β	0	0	0	0
Coupled Volmer-Heyrovsky	$\beta-\delta$	$\frac{2(\beta-\delta)}{[4+(\beta+\delta)g]}$	β	$\frac{2(\beta+\delta+\beta\delta g)}{[4+(\beta+\delta)g]}$	δ	$\beta-\delta$	$\frac{(\beta-\delta)(4+g)}{[4+(\beta+\delta)g]}$	$\frac{(\beta-\delta)}{\beta}$	$\frac{(\beta-\delta)(4+g)}{2(\beta+\delta+\beta\delta g)}$
Coupled Volmer-Tafel	$\frac{\beta}{2}$	$\frac{2\beta}{[6+(\beta+2\gamma)g]}$	β	$\frac{2\beta(2+\gamma g)}{[6+(\beta+2\gamma)g]}$	0	$\frac{\beta}{2}$	$\frac{\beta(4+g)}{[6+(\beta+2\gamma)g]}$	1/2	$\frac{(4+g)}{2(2+\gamma g)}$

Derivatives expressing the dependency of the H coverage, the HER current and the H bulk fractional concentration beneath the surface/steady permeation current, on the potential and on the HER current, at given ΔG_{ads} (given surface conditions), for the main HER mechanisms, and different values of the surface coverage. The Tafel slope is related to the transfer coefficient α by the relation: $\partial E/\partial \log i_c = -RT \ln 10/\alpha F$. Rigorously, the last two derivatives are to the multiplied by the factor $(1 - X_H)/[1 + hX_H(1 - X_H)]$, which takes into account the limitation of bulk population due to possible interactions between dissolved H atoms and saturation of the bulk sites. This factor drops to zero when θ_H reaches unity. For endothermically absorbing metals, it can be considered as practically equal to unity for moderate coverages ($\theta_H \leq 1/2$).

Copyright © 2002 Marcel Dekker, Inc.

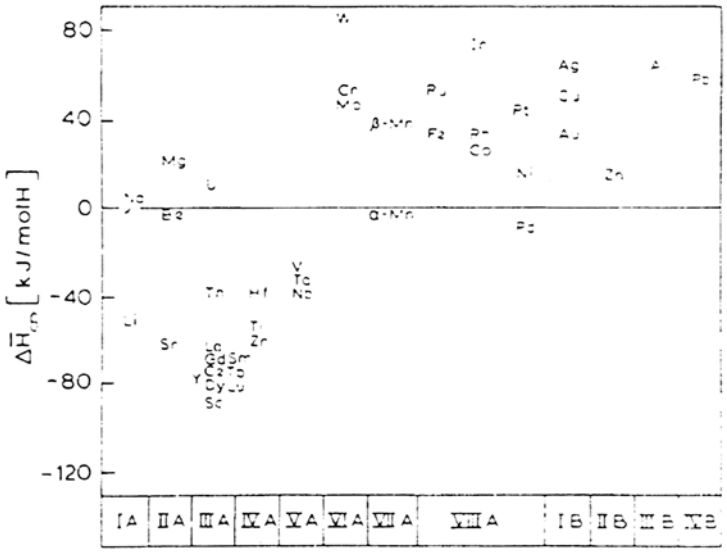


Figure 3 Enthalpies of solution of H at infinite dilution in metals; $\Delta H_{\infty} \equiv \Delta H_{Hdiss}$ in our conventions. (From Fig. 6.3 in Ref. 69.)

Figure 3 shows ΔH_{Hdiss} at infinite dilution plotted for most metals [69]. Figure 4 shows an approximately linear correlation between values of $-\Delta S_{Hdiss}$ (cal mol^{-1} K^{-1}) and ΔH_{Hdiss} for a given crystal structure [70], that is rather classic ($-\Delta S_{Hdiss}$ increases with $-\Delta H_{Hdiss}$): the larger the value of $-\Delta H_{Hdiss}$, the more tightly bound the interstitial H and the lower its vibration frequency, hence the greater the value of $-\Delta S_{Hdiss,}$ the reduction in entropy from the gaseous state to the dissolved state. The fcc and hcp metals give one correlation line and the bcc metals another one [70].

Thermodynamics of the M-H Equilibria in Aqueous Electrolyte

Isotherms of the Metal-Hydrogen Equilibria

Isotherm of H_2 Dissociative Adsorption/H-H Combination Under conditions in which there is no competitive specific adsorption of ions or adsorption of oxygen species in the H_{ads} potential range, the equilibrium of the dissociative adsorption from $H_{2(g)}$ in aqueous solution (or its reverse reaction, the chemical combination) [see Eq. (3)] leads to the same adsorption isotherm as Eq. (10):

$$\theta_H/(1-\theta_H) = f_{H2}^{1/2} \exp[-\Delta G_{Hads(aq)}/RT] \qquad (10b)$$

where θ_H, and f_{H2} have already been defined and $\Delta G_{Hads(aq)}$ is the half-standard free energy of adsorption in aqueous solution from $\frac{1}{2}H_{2(g)}$ [60] (which is a priori different from ΔG_{Hads} in the gas phase because adsorption in aqueous solution implies displacement of asorbed water molecules and reorganization of the double layer) [20,23].

Isotherm of H Electroadsorption/Electrodesorption The equation of the equilibrium H electroadsorption isotherm [see Eqs. (4) and (5)] is [53,58,61,71]:

$$\theta_H/(1-\theta_H) = a_{H^+} \exp[-FE_{(SHE)}/RT] \exp[-\Delta G_{Hads(aq)}/RT] \qquad (14)$$

Copyright © 2002 Marcel Dekker, Inc.

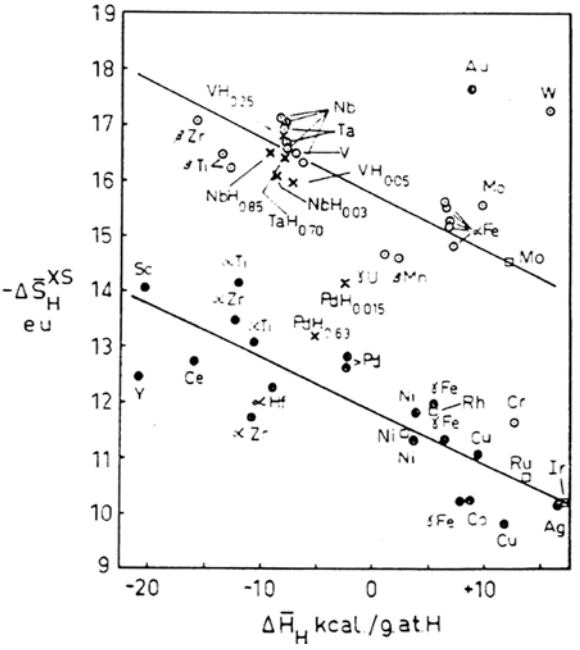


Figure 4 Correlation between excess entropy and enthalpy of solution of H in metals; $\Delta S_H^{XS} \equiv \Delta S_{Hdiss} = S_{Hdiss} + R \ln X_H/(1 - X_H) - \frac{1}{2}S°_{H2}$. (From Fig. 3 in Ref. 70, with permission from Elsevier Science.)

where $E_{(SHE)}$ is the electrode potential referred to the reversible standard hydrogen electrode; $\Delta G_{Hads(aq)}$ has been defined. If the equation is rearranged to involve the potential referred to the half-standard reversible hydrogen electrode in the same electrolyte (a_{H^+}, p_{H2} = 1 atm)(RHE1), $E_{(RHE1)} = E_{(SHE)} - RT/F \ln a_{H^+}$.

We obtain the simpler expression [41,53,58,71]:

$$\theta_H/(1 - \theta_H) = \exp[-FE_{(RHE1)}/RT] \exp[-\Delta G_{Hads(aq)}/RT] \tag{15}$$

Isotherm of Electrodissociation / Electrocombination Similarly, the isotherm of equilibrium electrodissociation of $H_{2(g)}$ [see Eqs. (6) and (7)] can be expressed as [61]

$$\theta_H/(1 - \theta_H) = f_{H2}/a_{H^+} \exp[FE_{(SHE)}/RT] \exp[-\Delta G_{Hads(aq)}/RT] \tag{16}$$

or

$$\theta_H/(1 - \theta_H) = f_{H2} \exp[FE_{(RHE1)}/RT] \exp[-\Delta G_{Hads(aq)}/RT] \tag{17}$$

Isotherm of H electroabsorption (HEAR) The equation of the equilibrium electroabsorption isotherm [Eq. (9)] is [53,61,62]:

$$X_H/(1 - X_H) = a_{H^+} \exp[-FE_{(SHE)}/RT] \exp[-\Delta G_{Hdiss}/RT] \tag{18}$$

or

$$X_H/(1 - X_H) = \exp[-FE_{(RHE1)}/RT] \exp[-\Delta G_{Hdiss}(X_H)/RT] \tag{19}$$

with ΔG_{Hdiss} as defined before for the gas-phase reaction [Eq. (11)].

Copyright © 2002 Marcel Dekker, Inc.

Isotherm of H Surface-Bulk Transfer The equation of the isotherm for the surface-bulk transfer step at equilibrium [Eq. 8] is identical to that in Eq. (2) except that ΔG_{Hads} is replaced by $\Delta G_{Hads(aq)}$.

H_2 Pressure / Potential Correspondence for Adsorption / Absorption Equilibria

Comparing Eqs. (10) and (11) with Eqs. (15) and (19) shows that the term $\exp[-FE_{(RHE1)}/RT]$ for isotherms in aqueous solution plays the role of the fugacity term $f_{H2}^{1/2}$ in chemical absorption from $\frac{1}{2}H_{2(g)}$. So in solution, at equilibrium, the fugacity of H_2 equivalent to a given potential versus RHE1 (reversible H electrode at 1 atm) is equal to:

$$(f_{H2})_{eqvt} = \exp[-2FE_{(RHE1)}/RT] \tag{20}$$

This equation provides the correspondence between adsorption / absorption equilibria in the gas phase and electroadsorption / electroabsorption equilibria in solution [28,73] (for example, the H coverage or bulk solubility at 0V / RHE1 is equal to the coverage or solubility at an H_2 pressure of 1 atm). However, this relation applies only to electrosorption processes in equilibrium or at least in quasi-equilibrium and is not valid not at large overpotentials where coupled mechanisms prevail.

Gibbs Free Energy of Adsorption for UPD H and OPD H

For gas-phase adsorption, from Eq. (10), it is deduced that the fugacity f_{H2} corresponding to $\theta_H = \frac{1}{2}$ is equal to $\exp[2\,\Delta G_{ads}(\frac{1}{2})/RT]$. Hence, adsorption sites with $\Delta G_{ads}(\frac{1}{2})$ negative, i.e., in which the Gibbs partial molar free energy (chemical potential) of the adsorbed H species at half-saturation is lower than $\frac{1}{2}G^{\circ}_{H2(g)}$, attain half-saturation for an H_2 pressure lower than 1 atm, whereas sites with $\Delta G_{ads}(\frac{1}{2})$ positive reach half-saturation only for a pressure higher than 1 atm. Similarly, analysis of Eq. (15) shows that H electroadsorption may occur significantly at $E > 0$V/(RHE1) (at underpotential) in sites with $\Delta G_{ads}(\frac{1}{2})$ negative [53,74], whereas the sites with $\Delta G_{ads}(\frac{1}{2})$ positive reach half-saturation only for $E_{RHE1} < 0$V (at cathodic overpotential). On Pt, the value of the Tafel slope at low cathodic overpotentials (~30 mV) indicates that the H intermediate of the HER is electroadsorpbed under quasi-equilibrium at very low coverages around 0V/RHE1 and reaches significant coverages only cathodically; i.e., it is overpotentially deposited (hence its name OPD H). So it is a weakly bonded H species that has a positive $\Delta G_{ads}(0.5)$ [53] and is adsorbed on or among a full monolayer of strongly bonded UPD H atoms with negative $\Delta G_{ads}(0.5)$ [29,35,51,53,75]. This simple a priori analysis shows that at least on Pt and neighboring metals, H UP electroadsorption can be correlated with low-pressure adsorption in the gas phase [37,40,76] and OP electroadsorption with high H_2 pressure adsorption in the gas phase [53].

Similarly, the fact that electroabsorption in Pd occurs at $E > 0$V / RHE1 [44,58,59] is correlated with the exothermic character of H absorption in Pd ($\Delta H_{diss} < 0$), giving a value of ΔG_{diss} close to zero at room temperature (see Figure 4).

Thermochemical Data for H Underpotential Electroadsorption on Pt in Aqueous Electrolyte

As mentioned earlier, thermodynamic measurements of H adsorption in aqueous electrolytes are possible only on the UPD H electroadsorbed reversibly above

Copyright © 2002 Marcel Dekker, Inc.

0V / RHE1 on some noble metals close to Pt [27,37,38,59,71] for which $\Delta G_{ads}(½)$ is negative. The analysis of the data obtained in aqueous electrolytes is complicated by the fact that the potential region of UPD H adsorption / desorption often overlaps the potential region of the specific adsorption / desorption of anions [39,59], in which case the two processes are competitive and the overall charge density obtained by integration of the voltammograms corresponds to a replacement reaction. The two processes do not occur in the same potential range on Pt(111) in $HClO_4$ or in diluted H_2SO_4 electrolytes [39,59]. Thermodynamic measurements on Pt(111) single-crystal electrodes show that the heat of adsorption of UPD H at zero H coverage and the Pt-UPD H bond energy at zero coverage [$\approx$ 260 kJ mol^{-1} for Pt(111)] [27,59] are close to those measured in low-pressure gas-phase experiments ($E_{M–Hads} \approx 255$ kJ mol^{-1}) [8].

Relation between the Energetic and Structural Aspects of H Adsorption

These thermodynamic measurements indicate that the M–H_{ads} bonds involved at the metal-electrolyte and the metal-gas interfaces at low pressure are of the same nature, hence that UPD H atoms probably occupy the same adsorption sites as those characterized by UHV techniques [24,40,53,59], i.e., the highly coordinated or hollow sites [8].

With the use of a ^{35}S radiotracer allowing accurate measurement of the sulfur coverage, the present authors studied quantitatively and compared on a Pt single-crystal surface the blocking by chemisorbed sulfur of the H underpotential (UP) adsorption and the HER. It was concluded that OPD H on Pt is not adsorbed in the same sites as UPD H [53,75]. More direct evidence was obtained by in situ infrared (IR) spectroscopy on a Pt(111) electrode at overpotential that the OPD H atoms reacting in the HER on Pt(111) are adsorbed on top of substrate atoms [52], while UPD H atoms are adsorbed in hollow sites.

Thus, a joint analysis of experiments in the gas phase and in aqueous electrolyte gives evidence of the existence of two main kinds of H adsorption sites on a Pt surface: high coordination sites (hollow sites) with a strong M–H_{ads} bond ($\Delta G_{Hads} < 0$) and low coordination / on-top sites with a weak M–H_{ads} bond ($\Delta G_{ads} > 0$); UPD H is adsorbed in the hollow sites as H adsorbed from H_2 in low-pressure gas-phase adsorption, whereas OPD H is probably adsorbed at the on-top sites, as the labile and highly reactive H involved at atmospheric or high pressure in the catalytic reactions [53,74].

On non-noble transition metals, the existence of two H_{ads} species with different bond energies and site coordinations is probable. H UPD is not detected by cyclic voltammetry on oxidable metals, although these metals readily adsorb H in the gas phase (ΔG_{Hads} for the hollow sites on these metals is more negative than on Pt), because the UPD oxygen species (O_{ads} or OH_{ads}) are even more strongly chemisorbed than H in the same sites. A thermodynamic calculation based on gas-phase data shows that on nickel and iron H electroadsorption is in direct competition with electroadsorption of oxygen species because O species are electroadsorbed near 0V / RHE1. So that H begins to electroadsorb in the hollow sites only at potentials where most of the oxygen layer is desorbed, i.e., slightly under or over 0V / RHE1, depending on the binding strength of the O species and their possible inhibiting effect on the M–H_{ads} bond [23]. It is likely that on non-noble transition metals, there is

Copyright © 2002 Marcel Dekker, Inc.

coexistence of a stable monolayer of H species electroadsorbed in the hollow sites around 0V / RHE1 by replacement of the O species and a mobile one adsorbed at overpotential at on-top sites and reacting in the HER [23].

MECHANISMS OF THE H SURFACE-BULK TRANSFER

Structural Aspects

H Bulk Interstitial Sites

Figure 5 shows the different kinds of bulk interstitial sites in perfect face-centered cubic (fcc), hexagonal close-packed (hcp), and body-centered cubic (bcc) lattice structures. The sites populated by H atoms in the concentration range of solid solution are known to be the octahedral sites for the fcc metals, whereas they are most probably the tetrahedral sites for the bcc and hcp metals [66]; In fcc and hcp metals, there are one octahedral site and two tetrahedral sites per metal atom, whereas in bcc metals there are three octahedral and six tetrahedral sites per metal atom.

For diffusion in fcc metals, because close-packed metal atoms row prevent the direct jumps from one octahedral site to another in the ⟨110⟩ directions, the H migration paths involve intermediate jumps in the ⟨111⟩ directions to nearest neighbor tetrahedral sites. If a is the cell parameter, an octahedral site is surrounded by 8 nearest neighbor tetrahedral sites at a distance of $a / \sqrt{3}$ in the ⟨111⟩ directions and 12 octahedral sites at $a / \sqrt{2}$ in the ⟨110⟩ directions (see Fig. 5). A tetrahedral site is surrounded by four octahedral sites.

For hcp metals, there exist possibilities of direct jumps from one tetrahedral site to another in the [0001] direction. For the bcc metals, the possibilities of jumps

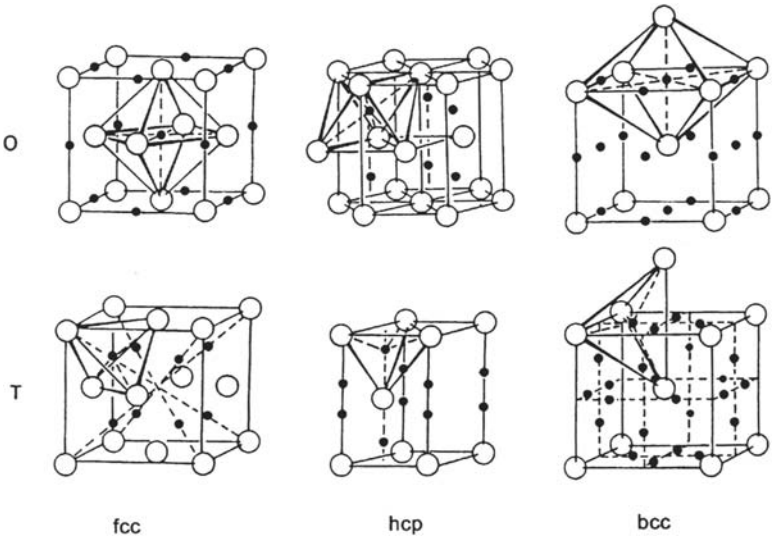


Figure 5 Interstitial sites: octahedral (O) and tetrahedral (T) sites in face-centered cubic (fcc), hexagonal close-packed (hcp), and body-centered cubic (bcc) lattices. (From Fig. 1.14 in Ref. 5.)

Copyright © 2002 Marcel Dekker, Inc.

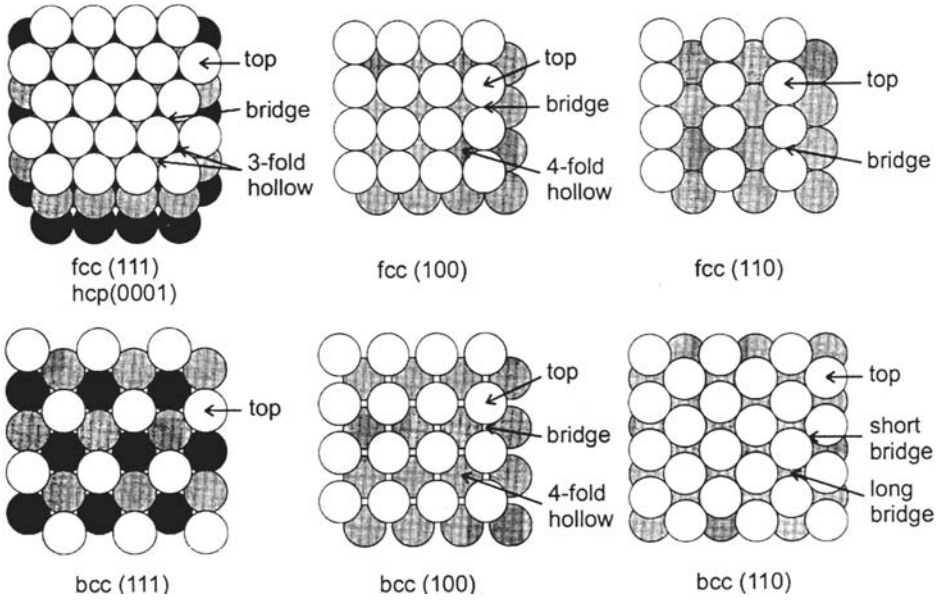


Figure 6 Top views of the atomic arrangement in the first two or three layers of the low-Miller-index faces of fcc, hcp, and bcc crystals. High-symmetry adsorption sites are indicated. (From Fig. 1 in Ref. 77.)

between tetrahedral sites are direct from one tetrahedral site to four nearest neighbor tetrahedral sites along the ⟨110⟩ directions or across the octahedrals sites to two next neighbors in the ⟨100⟩ directions. The distances between nearest neighbor tetrahedral sites in bcc metals are smaller by a factor of 2 than those between nearest neighbor octahedral sites in fcc metals [66], which leads to much lower activation energies for H diffusion than in fcc metals [78,79]. This explains the relatively high H diffusion coefficient in bcc iron (between 10^{-5} and 10^{-4} cm^2 s^{-1}), whereas in fcc metals it is about 10^{-6} cm^2 s^{-1} for Pd and between 10^{-10} and 10^{-9} cm^2 s^{-1} for Ni and Pt [66].

H Adsorption Sites

Figure 6 shows the atomic arrangement of the low-index faces of fcc, hcp, and bcc metals, with the high-symmetry sites of H adsorption. There is general agreement from UHV structural and vibrational measurements that the H adsorption sites under low hydrogen pressure are the sites of highest coordination, hollow or bridge sites [8,77]. On both the (111) face of fcc and the (0001) face of hcp, there are two kinds of threefold hollow sites: sites over a second-layer metal atom, called hcp type in surface science conventions, and sites over an interstice between three second-layer atoms, called fcc-type sites. It has been reported that H atoms adsorbed under low pressure tend to occupy the hcp sites on Pt(111) [80] and also that D atoms occupy preferentially the fcc sites on Ni(111) [81].

Role of the Surface Structure in H Entry: Entry Sites

For the low-index faces of fcc crystals, the possible directions of H jumps from the adsorption sites to the subsurface sites are represented in Figure 7.

Copyright © 2002 Marcel Dekker, Inc.

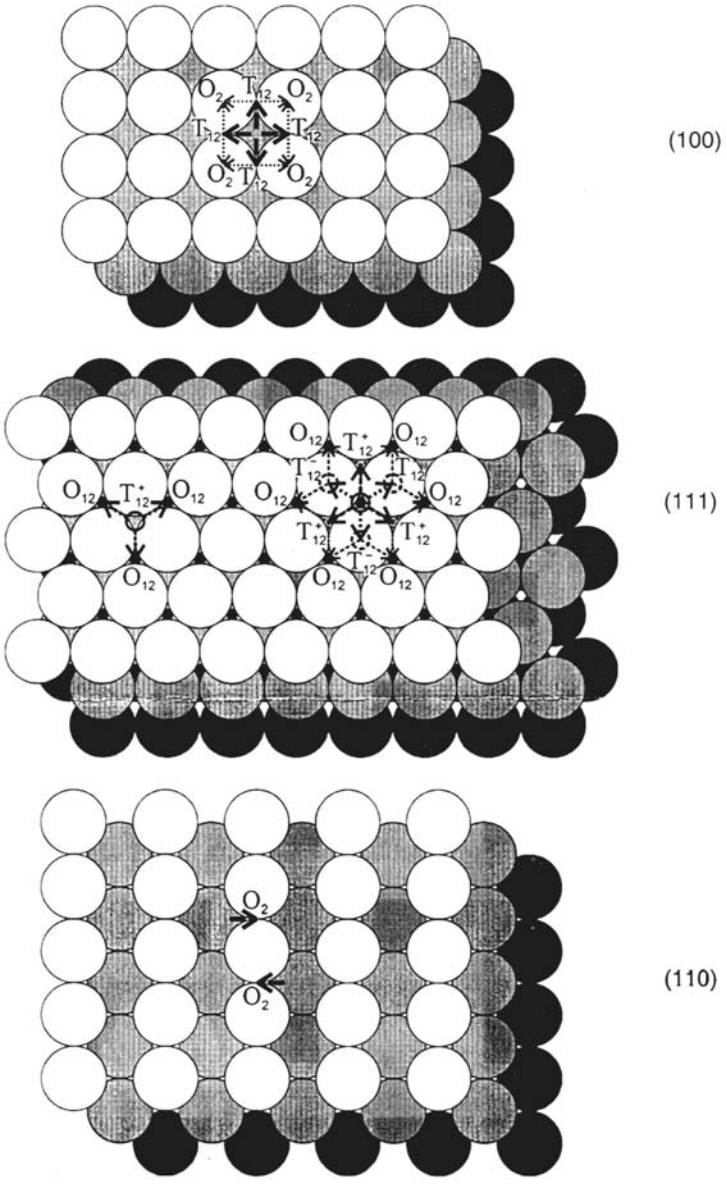


Figure 7 Possible paths of surface-bulk transfer on the low-index faces of fcc metals. The full line arrows indicate the directions of first H atom jumps from surface sites; the broken line arrows indicate second or third jumps from subsurface sites. On the (111) face, first jumps occur vertically, either from an hcp surface site to a tetrahedral site T_{12}^{+} (left) or from a fcc site to an octahedral site O_{12} (right).

Copyright © 2002 Marcel Dekker, Inc.

The lack of coordination above the surface leads to adsorbed H atoms closer to the underlying metal atoms than in the bulk, so distances of jumps from the adsorption sites to the nearest subsurface sites are shorter than the nearest neighbor distances in the bulk ($a / \sqrt{3}$).

On the (111) face, each hcp surface site is located just above a subsurface tetrahedral site T_{12}^{+} (located between the first and the second metal layer, below three surface atoms), from which three octahedral subsurface sites O_{12} may be reached. Each fcc surface site is just above such subsurface octahedral site O_{12}, from which, via three T_{12}^{+} or three T_{12}^{-} sites (below one surface atom), six O_{12} sites and three O_{23} sites (below the second layer) may be reached, which makes nine possibilities of jumps under the surface.

On the (100) face (if it is not reconstructed), an H atom adsorbed in a fourfold hollow site (at a position close to that of an octahedral site) may jump to four tetrahedral subsurface sites T_{12}, from each of which two octahedral sites O_2 (at the second layer level, below surface atoms)may be reached.

On the (110) face (the more open face of the three low-index faces on fcc metals) the adsorbed H atoms are alternatively adsorbed on each side of the close-packed [110] rows, in the pseudo-threefold fcc sites close to the bridge sites [82]. They may jump to one subsurface site O_2 at the second layer level, under the bridge sites. On the (110) faces of Ni and Pd, above a coverage of one, hydrogen induces reconstruction into a (110)-(1 × 2) structure, probably of the pairing-row type [8,15,82]. This opens the surface more and allows accommodation of H on the second metal layer, leading to a coverage of 1.5 H per first layer metal atom, and makes it easier to reach subsurface sites [8,83,84].

Energetic Aspects

Gas Phase

Energetic analysis using temperature-programmed desorption (TPD), also called thermal desorption spectroscopy (TDS), on a well-defined surface makes it possible to determine the structure sensitivity and the heights of the energy barriers of the surface processes. It was shown that the role of the substrate surface orientation in the population of subsurface sites is crucial. On the reconstructed (110) faces of Ni and Pd or on more open faces [8,83,84], subsurface sites are populated at temperatures as low as 100 K and low H_2 pressures (10^{-6} Pa), whereas higher temperatures and pressures are necessary with the more densely packed planes [8].

The overall energetics of the hydrogen-metal reactions are illustrated in the schematic drawing of Figure 8a showing the one-dimensional potential energy versus distance curves of the various H states at the metal-gas interface. Two H adsorbed states (corresponding to the hollow and on-top sites) are represented. Actually, the energy levels indicate the chemical potentials of these states, referred to the standard chemical potential of $\frac{1}{2}H_{2(g)}$. The standard free energy differences between the various states are indicated. The diagram show that at 1 atm nonactivated adsorption occurs spontaneously in the deep energy wells of the hollow sites, whereas adsorption is activated in the shallow wells of the on-top sites, which need a higher pressure to be filled. The diagram shows a case of endothermic H absorption, with a high activation energy barrier for the transition between strongly bonded H_{ads} and H_{diss}. The depths, of the wells and the height of the energy barrier,

Copyright © 2002 Marcel Dekker, Inc.

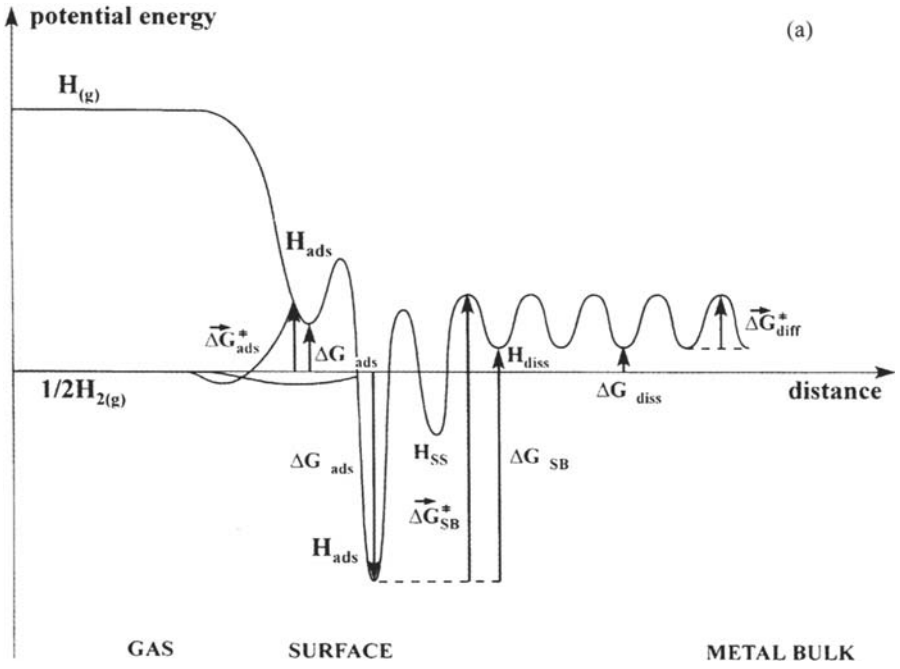


Figure 8 (a) Schematic diagram of the potential energy vs. distance curves for the various H states at the metal-gas interface, namely the two H adsorption states (weakly bonded, corresponding to on-top sites, strongly bonded, corresponding to hollow sites), the subsurface state (H_{ss}), and the bulk dissolved (absorbed) state (H_{diss}). The free energy changes and activation free energies for the different H processes are indicated (SB denotes surface-bulk transfer). (b) Same diagram as (a) for the metal–aqueous solution interface in an electrolyte where competition with adsorption of other species is negligible. The states are the same as for (a) except the specific state ($H^{+}_{(aq)} + e^{-}$), initial state of electroadsorption (EA), whose energy level with respect to the $H_{2(g)}$ level depends on the potential referred to RHE1. If E is positive (anodic), electroadsorption occurs in the strongly bonded state, hence denoted underpotential (UP) H_{ads}. If E is negative (cathodic), electroadsorption occurs in the weakly bonded state, hence denoted overpotential (OP) H_{ads}, and H_2 evolution (HER) occurs from this intermediate state.

which determines the rate of the H uptake, depend on the nature of the metal, the surface structure, and the H coverage. The barrier separating the chemisorbed and the subsurface H states may in addition be lowered by a surface reconstruction [8,13].

Aqueous Electrolyte

An equivalent energy diagram is shown in Figure 8b for the metal-aqueous solution interface [74]. It illustrates a case such as Pt(111) in $HClO_4$, where the free energy of adsorption of water from the liquid state can be neglected, and where specific adsorption of anions and electroadsorption of oxygen species occur at higher anodic potentials and do not perturb UP H adsorption [23]. The specificity of the metal-solution interface, apart from the competition of H adsorption with adsorption of water, anions, and oxygen species, is that the potential versus RHE1 is an external variable

Copyright © 2002 Marcel Dekker, Inc.

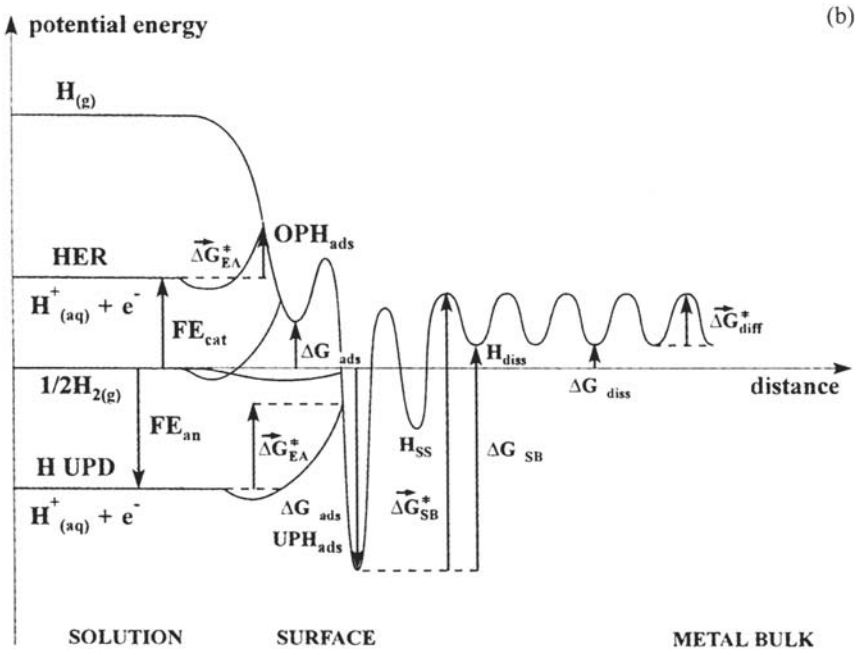


Figure 8b

that controls the energy level (more exactly the standard electrochemical potential) of the initial state ($H^+_{(aq)} + e^-$), with respect to the reference level of ½ $H_{2(g)}$, and hence the standard activation free energy of electroadsorption ($\Delta G^{\neq}_{ea}$) in the two kinds of sites. Thus two main situations occur, according to the potential versus RHE1:

1. The potential $E_{(RHE1)}$ is positive (anodic).

This is the range of underpotential (UP) H adsorption on metals of the Pt group. The energy levels of the initial state ($H^+_{(aq)} + e^-$) and the final state (strongly bonded H_{ads}, with $\Delta G_{ads} < 0$) are of the same order of magnitude and far below the energy levels of ½ $H_{2(g)}$ and the weakly bonded H_{ads}; this explains why at these potentials UP H electroadsorption is in equilibrium and there is negligible H electroadsorption in the weakly bonded state and H_2 evolution. In the case of an exothermic absorber, such as palladium, the energy level of H_{diss} is located near the level of ½ $H_{2(g)}$ ($\Delta G_{diss} \approx 0$), so H electroabsorption may occur at positive $E_{(RHE1)}$ [44,45,58,59] directly from UPD H, without H_2 evolution, according to the following path:

$$H^+_{(aq)} + e^-_{(M)} \rightarrow H_{ads}(\text{M-hollow}) \rightarrow H_{diss}[M] \qquad (21)$$

This possibility of absorption from UPD H on Pd electrodes is consistent with what was improperly called the "direct entry" mechanism, as explained earlier.

2. The potential $E_{(RHE1)}$ is negative (cathodic).

This is the range of overpotential (OP) H adsorption. The H electroadsorption occurs irreversibly in the sites with negative ΔG_{ads}, so the sites of UP H_{ads} are

Copyright © 2002 Marcel Dekker, Inc.

saturated, and OP H_{ads} is adsorbed in the sites with positive ΔG_{ads}. The energy level of OP H_{ads} is of the same order of magnitude or higher than the energy level of ½ $H_{2(g)}$ so H_2 evolution occurs. The energy level of the initial state ($H^+_{(aq)} + e^-$) is raised when the potential increases cathodically, so OP H electroadsorption may be in quasi-equilibrium only at low cathodic overpotentials and then becomes irreversible, giving rise to the coupled mechanisms. Only the chemical combination step is described in this simplified diagram, but the principle of the analysis may easily be extended to the electrocombination (Heyrovsky) step. In the represented case of endothermic absorption, cathodic overpotentials are needed to overcome the overall activation barrier for H penetration into the bulk.

Such mechanisms involving two adsorbed H species with different binding energies and sites probably apply to all transition metals. On oxidable metals, H electroadsorption in the hollow sites followed by absorption is possible only at potentials below the limit of desorption of the oxygen species, calculated for Ni and Fe to be close to $0V_{(RHE1)}$ [23]. As discussed earlier, it is likely that the sites for the HER adsorbed intermediate (OP H_{ads}) are the on-top sites on all transition metals. It is admitted that on iron and ferrous alloys the HER and the HAR share a common H_{ads} intermediate and that the surface-bulk transfer step is in quasi-equilibrium (see earlier) [31]. The mechanism of H absorption into the bulk of all transition metals at overpotential must then involve a sequence of two adsorption steps:

$$H^+_{(aq)} + e^-_{(M)} \rightarrow H_{ads}(\text{M-on top}) \rightleftarrows H_{ads}(\text{M-hollow}) \rightleftarrows H_{diss}[M] \qquad (22)$$

The weakly bonded OP H_{ads} in on-top sites simultaneously participates in the HER and the HAR. This mechanism distinguishes two adsorption steps instead of one in the surface-bulk transfer. Of course, this has no implications if the overall transfer step is in quasi-equilibrium, but if it is not—a situation occurring, for example, for H permeation in thin membranes [53,72]— the treatment of the kinetics of H absorption will become more complex.

KINETICS OF THE HER AND HAR

Expressions of the Absolute Rates of the Elementary Surface Steps

The absolute rates of all the H elementary surface reactions occurring during the HER and the HAR at the surface of an electrode M in aqueous solution may be expressed as functions of the potential and the Gibbs free energy of H adsorption, using the theory of absolute reaction rates [85] and the Brönsted-Polanyi relations [86,87]. As usual, a model of regular localized solution is assumed for adsorbed H (Frumkin-Fowler model) and dissolved H, i.e., random distribution of these atoms among their respective sites and pair interactions between nearest neighbor H atoms [88]. It is assumed that the activation free energies depend on θ_H or X_H only via their linear dependence on $\Delta G_{ads(aq)}$ [60]. $\Delta G_{ads(aq)}$ varies linearly with θ_H, according to

$$\Delta G_{ads(aq)} = \Delta G^\circ_{ads} + g_{HH} RT\theta_H \qquad (23)$$

where $\Delta G^\circ_{ads(aq)}$ is the initial adsorption free energy or free energy at zero H coverage and g_{HH} is a pair-energy parameter describing the lateral interactions between adsorbed H atoms [88]. Similarly,

Copyright © 2002 Marcel Dekker, Inc.

$$\Delta G_{\text{diss}} = \Delta G^{\circ}{}_{\text{diss}} + h_{\text{HH}} RTX_{\text{H}} \tag{24}$$

where $\Delta G^{\circ}_{\text{diss}}$ is the H dissolution free energy at infinite dilution and h_{HH} a parameter for interactions between dissolved H atoms [88].

Electroadsorption and Electrodesorption

Only adsorption by proton discharge in acid medium is considered here [Eq. (4)]; the expressions of the rates of adsorption from water are similar. The rates for the forward and reverse reactions are

$$\overrightarrow{v_{\text{ea}}} = k_{\text{ea}} \exp -\beta(\Delta G_{\text{ads(aq)}} + FE)/RT\, \gamma_{\text{H}^+}/\gamma^{\neq}_{\text{ea}}\, c_{\text{H}^+}(1-\theta_{\text{H}}) \tag{25}$$

$$\overleftarrow{v_{\text{ea}}} = k_{\text{ea}} \exp(1-\beta)(\Delta G_{\text{ads(aq)}} + FE)/RT\, 1/\gamma^{\neq}_{\text{ea}}\, \theta_{\text{H}} \tag{26}$$

with $k_{\text{ea}} = \kappa_{\text{ea}}\, kT/h\, \Gamma_{\text{s/2}} \exp -\Delta G^{\neq}_{\text{ea}}/RT$. (For definition of the terms used, see the following).

Chemical Combination and Dissociative Adsorption [Eq. (3)]

$$\overrightarrow{v_{\text{cc}}} = k_{\text{cc}} \exp 2\gamma\Delta G_{\text{ads(aq)}}/RT\, 1/\gamma^{\neq}_{\text{cc}}\, \theta^2_{\text{H}} \tag{27}$$

$$\overleftarrow{v_{\text{cc}}} = k_{\text{cc}} \exp -2(1-\gamma)\Delta G_{\text{ads(aq)}}/RT\, f_{\text{H2}}/\gamma^{\neq}_{\text{cc}}\, (1-\theta_{\text{H}})^2 \tag{28}$$

with $k_{\text{cc}} = \kappa_{\text{cc}} kT/h\; z_1 \Gamma_{\text{s/2}} \exp -(\Delta G_{\text{cc}}{}^{\neq} + \gamma\Delta G^{\circ}_{\text{sol}})/RT.$

Note: The reactions of chemical and electrochemical combination [Eqs. (3) and (6)/(7)] lead to $H_{2(aq)}$ dissolved in the electrolyte, so the rate equations for the reverse adsorption reactions involve the activity of H_2 dissolved in water, a_{H2}. However, as the reaction of dissolution of $H_{2(g)}$ is in equilibrium, $a_{H2} = f_{H2} \exp -\Delta G^{\circ}_{\text{sol}}/RT$, where $\Delta G^{\circ}_{\text{sol}} = \mu^{\circ}_{\text{H2(aq)}} - \mu^{\circ}_{\text{H2(g)}}$. So the expressions for the rates may be rearranged to involve the fugacity f_{H2} and $\Delta G_{\text{ads(aq)}}$, the free energy for adsorption from $H_{2(g)}$.

Electrocombination and Electrodissociation

[in Acid Medium—Eq. (6)]

$$\overrightarrow{v_{\text{ec}}} = k_{\text{ec}} \exp \delta(\Delta G_{\text{ads(aq)}} - FE)/RT\, \gamma_{\text{H}^+}/\gamma^{\neq}_{\text{ec}}\, c_{\text{H}^+}\, \theta_{\text{H}} \tag{29}$$

$$\overleftarrow{v_{\text{ec}}} = k_{\text{ec}} \exp \Delta G^{\circ}_{\text{sol}}/RT \exp(1-\delta)(-\Delta G_{\text{ads(aq)}} + FE)/RT\, f_{\text{H2}}/\gamma^{\neq}_{\text{ec}}\, (1-\theta_{\text{H}}) \tag{30}$$

with $k_{\text{ec}} = \kappa_{\text{ec}}\, kT/h\; \Gamma_{\text{s}} \exp -(\Delta G^{\neq}_{\text{ec}} + \delta\Delta G^{\circ}_{\text{sol}})/RT.$

Surface-Bulk Transfer

For simplicity, in the absence of detailed energetic characterization of the subsurface state and knowledge of the transition between the two adsorbed H states (see preceding section), the overall surface-bulk transfer reaction is considered here as an elementary step from one single adsorption state, as is usually done.

$$\overrightarrow{v_{\text{sb}}} = \overrightarrow{k_{\text{sb}}}\, \theta_{\text{H}}\, (1 - x_{\text{H}}) \tag{31}$$

$$\overleftarrow{v_{\text{sb}}} = \overleftarrow{k_{\text{sb}}}\, (1-\theta_{\text{H}})\, x_{\text{H}} \tag{32}$$

Copyright © 2002 Marcel Dekker, Inc.

with $\overrightarrow{k_{sb}} = k_{sb} \exp \nu(\Delta G_{ads(aq)} - \Delta G_{diss})/RT$

$$\overleftarrow{k_{sb}} = k_{sb} \exp(1 - \nu)(\Delta G_{diss} - \Delta G_{ads_{(aq)}})$$

$$k_{sb} = \kappa_{sb}\, kT/h\Gamma_s \exp -\Delta G^{\neq}_{sb}/RT$$

and κ_{ea}, κ_{cc}, κ_{ec}, κ_{sb} are the transmission factors for the different reactions; Γ_s is the surface density of H adsorption sites (number per unit area); z_1 [in k_{cc}, Eqs. (27) and (28)] is the number of adsorption sites adjacent to a given site (lateral or surface coordination), so that the surface density of dual sites is equal to $s/2z_1\Gamma_s$ [85]. The dimension of the rates is given by the product $kT/h\,\Gamma_s$ ($cm^{-2}\ s^{-1}$). Also, $\gamma^{\neq}_{ea}$, $\gamma^{\neq}_{cc}$, $\gamma^{\neq}_{ec}$, are the activity coefficients of the respective activated complexes, dependent on c_{H^+} and/or p_{H2}; $\Delta G^{\neq}_{ea}$, $\Delta G^{\neq}_{cc}$, $\Delta G^{\neq}_{ec}$, $\Delta G^{\neq}_{sb}$ are the intrinsic activation free energies (standard activation free energies of the respective reactions for $\Delta G = 0$) [86,87]; β, γ, δ, ν are energy-barrier symmetry factors or Brönsted coefficients ($0 < \beta, \gamma, \delta, \nu < 1$). The κ's, $\Delta G^{\neq}$'s and the symmetry factors are constant for a given reaction and independent of ΔG (i.e., of the potential and of the nature of the substrate) in a range of moderate variation of ΔG [87]. So k_{ea}, k_{cc}, k_{ec}, k_{sb} (intrinsic rate constants) are constant for a given reaction, provided that z_1 and Γ_s, i.e., the surface crystallography, are unchanged.

Steady-State Equations for the H Cathodic Reactions

The relation between the H atomic fraction in the bulk sites of the first planes beneath the surface and the surface variables depends on the mechanism of the global cathodic reaction, which is determined by the steady-state conditions. The following analysis is restricted to the current case of overpotential adsorption, with the simplifications stated earlier. In the steady state, the OP H_{ads} surface coverage is constant with time so the net rate of the electroadsorption step is equal to the sum of the net rates of the consecutive parallels steps consuming adsorbed H:

$$\Gamma_s d\theta_H/dt = (\overrightarrow{v_{ea}} - \overleftarrow{v_{ea}}) - (\overrightarrow{v_{ec}} - \overleftarrow{v_{ec}}) - 2(\overrightarrow{v_{cc}} - \overleftarrow{v_{cc}}) - (\overrightarrow{v_{sb}} - \overleftarrow{v_{sb}}) = 0 \tag{33}$$

The overall steady cathodic current density, i_{cat}, is given by

$$i/F = \overrightarrow{v_{ea}} - \overleftarrow{v_{ea}} + \overrightarrow{v_{ec}} - \overleftarrow{v_{ec}} = 2(\overrightarrow{v_{ec}} - \overleftarrow{v_{ec}} + \overrightarrow{v_{cc}} - \overleftarrow{v_{cc}}) + (\overrightarrow{v_{sb}} - \overleftarrow{v_{sb}})$$
$$= v_{HER} + v_{HAR} \tag{34}$$

According to the conditions at the surface of the sample, two main cases are distinguished in electrochemical experiments: charging or permeation experiments.

1. In charging experiments, the H concentration under the surface is imposed by galvanostatic or potentiostatic conditions. The steady state is reached when this concentration is reached in the whole sample; i.e., the rate of diffusion in the bulk is zero. This condition applied to Eqs. (33) and (34) leads to $i_c = Fv_{HER}$ and to the isotherm expressing the equilibrium of the surface-bulk transfer [Eq. (12)].
2. In permeation experiments, a concentration gradient in the bulk is imposed by different conditions at the two faces of a membrane, so H permeates through the sample and a steady diffusion (permeation) rate is established through the membrane (see Fig. 9). The H concentration under the entry surface is imposed by galvanostatic or potentiostatic conditions, and the

Copyright © 2002 Marcel Dekker, Inc.

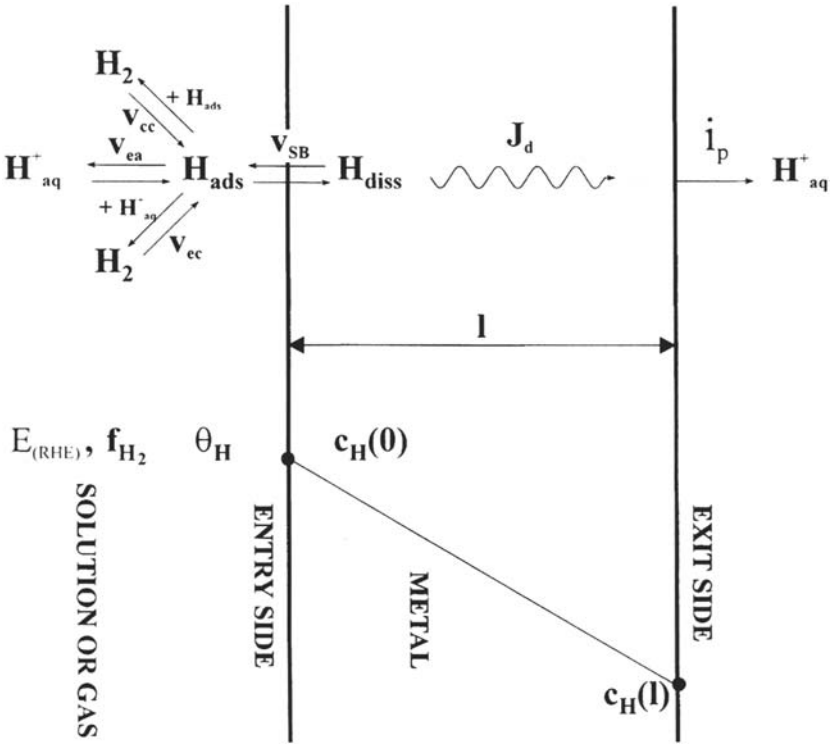


Figure 9 Balance of reactions during permeation of H through a metal membrane, in gas or aqueous solution, and concentration profile in the bulk.

concentration under the exit surface is usually fixed to zero by potentiostatic anodic conditions [28,89], such that H diffusing out of the exit face of the membrane is electrochemically oxidized. In this case, the anodic current density i_p provides a direct measure of the H permeation rate J_d. When the steady state is reached, the stationary H permeation rate, proportional to the concentration gradient through the membrane according to the first Fick law, is equal to the net absorption rate at the entry side. If the concentration under the exit face is zero, we obtain:

$$v_{HAR} = \overrightarrow{v_{sb}} - \overleftarrow{v_{sb}} = J_d = i_p/F = Dc_H/l = Dc_{Hsat}X_H/l \tag{35}$$

where D is the H diffusion coefficient in the bulk, L the thickness of the membrane, c_H the volumic concentration of H under the entry face, and c_{Hsat} is the same quantity at saturation.

From the steady-state Equations (33) and (35), the variations of the surface and bulk atomic fractions θ_H and X_H are interrelated and depend on the mechanism of the whole cathodic reaction, i.e., both the HER and HAR.

Equality (35), expressing $\overrightarrow{v_{sb}}$ and $\overleftarrow{v_{sb}}$ from Eqs. (31) and (32), yields the following expression for X_H versus θ_H:

$$X_H/(1 - X_H) = \overrightarrow{k_{sb}}\,\theta_H/[\overleftarrow{k_{sb}}\,(1 - \theta_H) + Dc_{Hsat}/l\,] \tag{36}$$

Copyright © 2002 Marcel Dekker, Inc.

In the limiting case where

$$Dc_{Hsat}/l \ll \overleftarrow{k_{sb}}(1 - \theta_H)$$

(this corresponds to conditions where D is low, the membrane is thick, θ_H is not close to unity, and $\overleftarrow{k_{sb}}$ is high), the permeation rate is limited by the bulk diffusion rate in the membrane, so the surface-bulk transfer step is quasi-equilibrium ($\overrightarrow{\upsilon_{sb}} \sim \overleftarrow{\upsilon_{sb}}$). It gives, as an approximation, the same expression for X_H versus θ_H as in the charging conditions [Eq. (12)] except that this equation applies only to the region of the bulk close to the entry surface:

$$X_H/(1 - X_H) \approx \exp[\Delta G_{ads}(\theta_H) - \Delta G_{diss}(X_H)]/RT\ \theta_H/(1 - \theta_H) \qquad (12b)$$

As the permeation rate is negligible with respect to the H_2 evolution rate (or the overall rate), as for charging, ($\overrightarrow{\upsilon_{sb}} - \overleftarrow{\upsilon_{sb}}$) may be neglected in Eq. (33) and then the variation of θ_H with the potential depends only on the HER mechanism and so does the variation of X_H. This is a good approximation for most experiments on permeation through iron, nickel, and their alloys, with relatively thick membranes, where $i_p / i_{cat} < 2/100$ (low permeation rates). In this case, X_H is thickness independent so, from the last equality of Eq. (35), i_p is proportional to $1/l$ [28]. It must be noted that this limiting case no longer applies when θ_H approaches unity. As θ_H increases, the complete Eq. (36) must be considered.

Dependence of the HER and HAR Rates on the Potential and the Adsorption Gibbs Free Energy

Only the current conditions, charging conditions, or permeation limiting case described before are considered here, so Eq. (12b) applies. Application of the steadystate Equations (33) and (12b), using the expressions (23)–(32), allows one to derive analytical expressions for θ_H and X_H versus the potential and ΔG_{ads} for each HER mechanism [61].

Analysis of the Dependence on the Potential

Differentiation of the preceding equations yields the (partial) derivatives of the logarithms of θ_H, X_H (proportional to the stationary permeation current i_p), and the HER current with respect to the potential for a given metal and surface composition, usually called diagnostic parameters, which may be compared with the experimental variations for the particular cases of low H coverage $\theta_H \ll 1$, midcoverage $\theta_H \approx ½$, or saturation coverage $\theta_H \approx 1$. The parameters calculated for six different HER mechanisms are reported in Table 1 and may be compared with previous calculations [28,56,90,91] made for particular values of the symmetry factors ($\beta = \delta = ½$), assuming Langmuir-type adsorption for low coverage and Temkin-type adsorption for medium coverage, with $\gamma = ½$ (activated molecular adsorption) or 1 (nonactivated), and $X_H \ll 1$. The simplified form of the Temkin adsorption model was used where the variations of θ_H, $1 - \theta_H$, $\theta_H / (1 - \theta_H)$ at $\theta_H \approx ½$ are neglected, whereas the Fowler-Frumkin adsorption model used here is more general. In Table 1 it can be checked that at $\theta \approx ½$, only for large positive values of g ($g \gg 4$), corresponding to strong repulsive interactions between adsorbed H atoms or high surface heterogeneity, the Tafel slopes are independent of the coverage and hence of the potential and the transfer coefficient α takes the values calculated previously [28,56,90,91] [$\alpha = -RT / F(\partial \ln i_c / \partial E)$ is related to the Tafel slope b for the HER by the relation

Copyright © 2002 Marcel Dekker, Inc.

$b = RT \ln 10 / \alpha F$]. The term $(1 - X_H)$ takes into account the fraction of available sites on the surface and in the bulk under the surface. It cannot be neglected a priori when θ_H (and X_H) approaches unity. The coefficient $(\partial \ln X_H) / (\partial \ln i_c)$, also reported in Table 1, gives the power of i_c to which X_H or the permeation current is proportional.

Analysis of the Dependence on the Gibbs Free Energy of Adsorption

Similarly, derivatives expressing the dependence of θ_H, i_c, and X_H on the Gibbs free energy of adsorption at fixed potential (potentiostatic control) are given in Table 2.

Table 2 shows that the variation of the logarithm of the rate of the HER i_c, at a given potential, with ΔG_{ads} gives a volcano curve for each mechanism, increasing for values of ΔG_{ads} such that $\theta_H \ll 1$, decreasing at values of ΔG_{ads} such that $\theta_H \approx 1$. In each case, the curve has a maximum for a value of θ_H depending on the values of β, δ, γ. This result is similar to a classic result obtained for the exchange current densities of the three HER steps [92–95]. For very high values of g (so-called Temkin case), the current is nearly independent of ΔG_{ads} in the midcoverage range [93,94]. This extreme situation does not apply to the adsorption of hydrogen on smooth metal substrates.

The steady-state equations for each HER mechanism where one step is quasi-equilibrium lead to the adsorption isotherms given in Eqs. (10b) and (14) to (17), hence to a quasi-equilibrium between H species in solution and H dissolved in the bulk [Eqs. (18) and (19)]. In this case, there is no dependence of the H bulk concentration on the Gibbs energy of adsorption at fixed potential, as seen in Table 2.

The steady-state conditions for the HER mechanisms where the electroadsorption step is coupled to one of the subsequent steps lead to pseudoequilibrium adsorption isotherms [26,28,61]. It is seen in Table 2 that for a coupled Volmer-Heyrovsky mechanism, the dependence of X_H on ΔG_{ads} is slight if $\beta + \delta \approx 1$. Only for the coupled Volmer-Tafel mechanism may X_H depend significantly on ΔG_{ads}, unless $\gamma + \beta/2 \approx 1$ for $\theta_H \ll 1$ or $\beta + 2\gamma \ll 3/2$ for $\theta_H \approx ½$. Figure 10a and b show the theoretical variations of log i_c, θ_H, and X_H versus $-\Delta G_{ads} / RT$ for an HER mechanism with the Volmer step in quasi-equilibrium and for the coupled Volmer-Tafel mechanism. From Table 2, the maximum of the HER current occurs at $\theta_H = ½$ if the symmetry factors are equal to ½ or for the two coupled mechanisms if $\beta = \delta$ or $\beta = \gamma$. For the coupled Volmer-Tafel mechanism, Figure 10b shows a case where X_H is minimum for $\theta_H \approx ½$ and maximum for extreme values of coverage ($\theta_H \ll 1$ or $\theta_H \approx 1$), i.e., of the adsorption free energy.

In order to analyze experiments in which instead of the potential, the cathodic current is the controlled variable (galvanostatic control), the partial derivatives of ln X_H with respect to ΔG_{ads} at fixed cathodic current density are also given in Table 2. At fixed current density i_c, X_H depends on ΔG_{ads} for most mechanisms, which may explain some surface effects reported for H permeation in galvanostatic conditions (see later).

INFLUENCE OF THE SURFACE MODIFIERS ON H ENTRY

Effects of Metal Oxide Films

Perfect oxide surfaces are essentially inert to H_2 dissociative adsorption, although atomic H may be adsorbed on and diffuse relatively fast in stoichiometric oxides [96]. Oxide layers on metal surfaces impede or prevent the H_2 adsorption and H

Copyright © 2002 Marcel Dekker, Inc.

Table 2 Dependence of θ_H, i_c, X_H on the Adsorption Free Energy for Various HER Mechanisms, at fixed Potential or Fixed Current

Mechanism of HER	$-RT\,(\partial \ln \theta_H/\partial \Delta G_{ads})_E$		$-RT\,(\partial \ln i_c/\partial \Delta G_{ads})_E$			$-RT\,(\partial \ln X_H/\partial DG_{ads})_E = -RT\,(d \ln i_p/d\Delta G_{ads})_E$		$-RT\,(\partial \ln X_H/\partial DG_{ads})_{ic} = -RT\,(\partial \ln i_p/\partial \Delta G_{ads})_{ic}$	
	$\theta_H \ll 1$	$\theta_H \approx 1/2$	$\theta_H \ll 1$	$\theta_H \approx 1/2$	$\theta_H \approx 1$	$\theta_H \ll 1$	$\theta_H \approx 1/2$	$\theta_H \ll 1$	$\theta_H \approx 1/2$
Volmer q.e. Heyrovsky r.d.s.	1	$\frac{2}{4+g}$	$1-\delta$	$\frac{2(1-2\delta)}{4+g}$	$-\delta$	0	0	$\frac{(\delta-1)}{(1+\delta)}$	$\frac{(2\delta-1)}{1+2\delta+\delta g}$
Volmer q.e. Tafel r.d.s.	1	$\frac{2}{4+g}$	$2(1-\gamma)$	$\frac{4(1-2\gamma)}{4+g}$	-2γ	0	0	$\gamma-1$	$\frac{2(2\gamma-1)}{2+\gamma g}$
Volmer r.d.s Heyrovsky q.e.	1	$\frac{2}{4+g}$	β	$\frac{2(2\beta-1)}{4+g}$	$-(1-\beta)$	0	0	1	$\frac{(1-2\beta)}{1+2\beta+\beta g}$
Volmer r.d.s Tafel q.e.	1	$\frac{2}{4+g}$	β	$\frac{2(2\beta-1)}{4+g}$	$-(1-\beta)$	0	0	0	0
Coupled Volmer-Heyrovsky	$\beta+\delta$	$\frac{2(\beta+\delta)}{[4+(\beta+\delta)g]}$	β	$\frac{2(\beta-\delta)}{[4+(\beta+\delta)g]}$	$-\delta$	$\beta+\delta-1$	$\frac{4(-1+\beta+\delta)}{[4+(\beta+\delta)g]}$	$2\delta-1$	$\frac{(4\beta\delta-\beta-\delta)}{\beta+\delta+\beta\delta g}$
Coupled Volmer-Tafel	$\frac{(\beta+2\gamma)}{2}$	$\frac{2(\beta+2\gamma)}{[6+(\beta+2\gamma)g]}$	β	$\frac{4(\beta-\gamma)}{6\left[+(\beta+2\gamma\right]\rangle g}$	-2γ	$\frac{\beta}{2}+\gamma-1$	$\frac{2[2(\beta+2\gamma)-3]}{[6+(\beta+2\gamma)/g]}$	$\gamma-1$	$\frac{2(2\gamma-1)}{2+\gamma g}$

Copyright © 2002 Marcel Dekker, Inc.

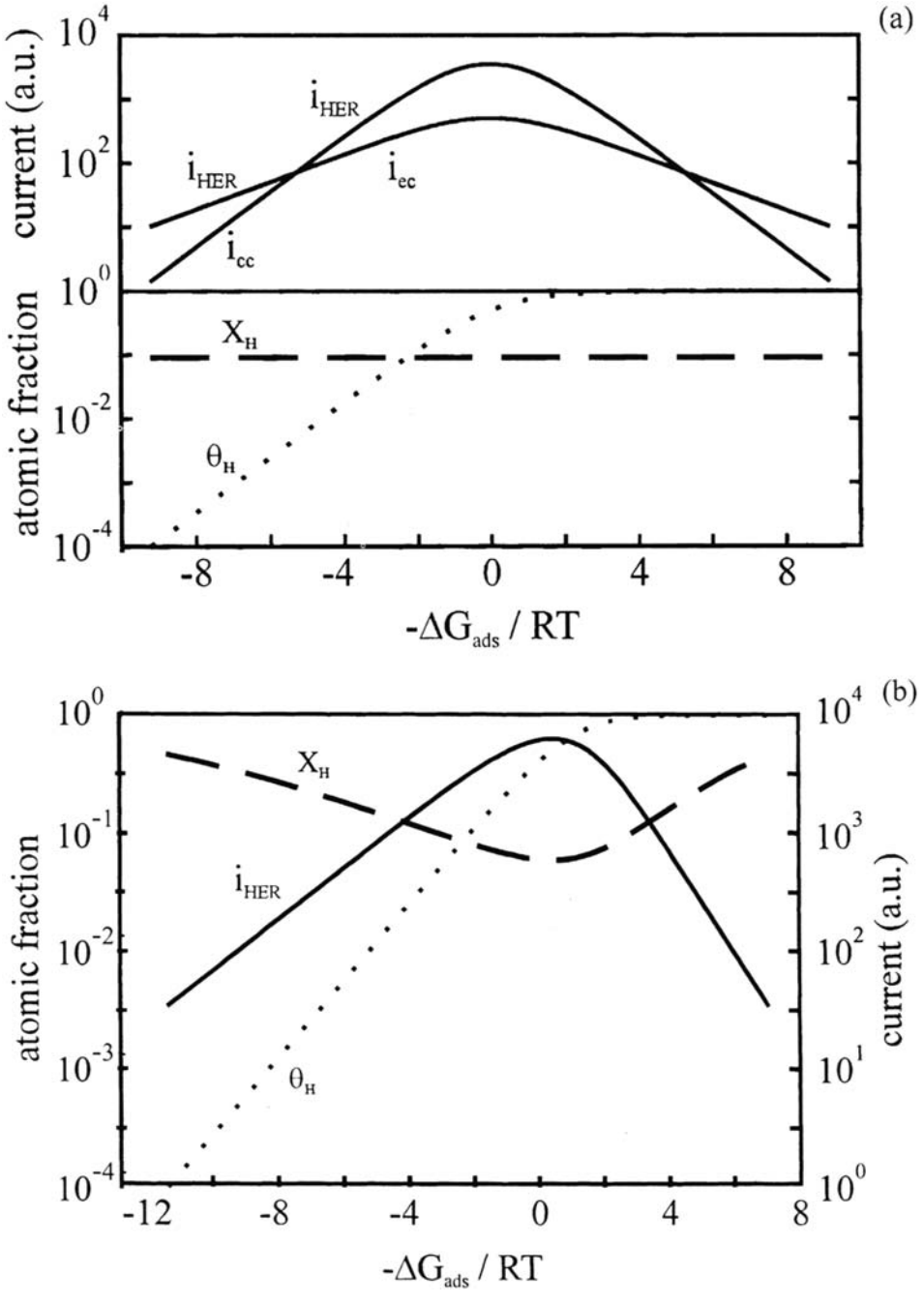


Figure 10 Theoretical variations at a fixed potential of the HER current, the surface coverage θ_H, and the bulk fractional concentration X_H with the H adsorption free energy ΔG_{ads} for two HER mechanisms: (a) electroadsorption step in quasi-equilibrium (a case where the rate-determining step changes from electrocombination to chemical combination); (b) electroadsorption coupled with chemical combination. The symmetry factors are all taken equal to 1/2. The represented case is for Langmuir type H adsorption.

Copyright © 2002 Marcel Dekker, Inc.

absorption reactions at temperatures below 400°C (97). Monolayer amounts of oxygen on transition metals reduce the H_2 adsorption and desorption rate by orders of magnitude [96,97]. The effect of oxygen precoverage on transition metals increases with the degree of oxide formation. Thin suboxide layers (in which cations are not in their highest valence state) formed during the initial stages of oxidation or by partial oxide reduction in H_2 impede the H absorption much less than layers of the maximal valence oxides. Transition metal overlayers on the oxide layer restore the original uptake rate of the substrate, which confirms that the effect of oxygen is essentially to impede the H_2 dissociation step [96,97]. Similarly, the effect of passive films formed anodically in solution is to impede H absorption [98,121].

Effects of Electronegative Species

As the H cathodic reactions are controlled by surface adsorption processes, they are drastically affected by electronegative species known to poison hydrogenation reactions on transition metals [99]. Electronegative elements are strongly chemisorbed (far more than H) on transition metal surfaces and, even at low concentrations, inhibit coadsorption of reactive species in the gaseous phase [100] as in aqueous medium [53,59,101,117,118]; they hinder H_2 dissociation in the gas phase [100,102] and the HER in electrolytes, increasing the cathodic overpotential [53,75,99,101,117,118], even if opposite effects have also been observed, particularly on Fe [103]. Compounds of elements of columns 15 and 16 of the periodic table, P, As, Sb, S, Se, and Te, added to the electrolyte, while being strong inhibitors of H underpotential adsorption, are known to promote H penetration into the bulk of transition metals in aqueous medium [99]: in iron, nickel, and steels [31,33,34,104–112]; palladium [73]; and platinum [113]. Additions of CN^-, I^-, and naphthalene to the electrolyte also increase the permeation rate into iron, although less efficiently, and additions of organic nitriles decrease it; however, all these additives increase the HER overpotential at fixed current density [31]. The surface step is clearly the determining step in these processes. The mechanisms of action of promoters are investigated in detail now.

MECHANISMS OF ACTION OF H ABSORPTION PROMOTERS

Conditions for H Absorption Promotion

It has been noted [104] that all the promoters of H entry into iron (and steel) formed from elements of columns 15 and 16 form gaseous hydrides of the type AsH_3, H_2Se, H_2Te, H_2S, PH_3, and SbH_3 and that the promotion is effective only in the cathodic overpotential region where the hydrides form [104,105,109], and in the range of pH in which they are stable [108]. For example, after addition of a compound of arsenic in the +III oxidation state, H entry inhibition is observed at low overpotentials, attributed to deposition by reduction of elemental arsenic, whereas at higher overpotentials, H uptake increases drastically [34,106,109] and AsH_3 gas is detected [106]. An additional proof is that a significant acceleration of H permeation results if PH_3, H_2S, or AsH_3 produced outside is bubbled into the electrolyte [110].

The paramount role of hydride in promoting H entry into iron and steel has been further confirmed by investigations conducted with a rotating-disk electrode, which

Copyright © 2002 Marcel Dekker, Inc.

also permitted a comparison of the effects of different compounds over a wide range of pH and electrode potential [56,110]. For a given compound, the critical cathodic overpotential at which the H entry efficiency begins to increase was related to the equilibrium potential of hydride formation from elements (for H_2S the latter is positive vs. NHE, which explains why the permeation efficiency increases from the free corrosion potential of steel while for AsH_3, where it is more negative, the permeation efficiency increases at higher overpotentials). Moreover, for S, Se, and Te compounds in moderately acid electrolyte, the permeation rate increases with the cathodic overpotential, reaches a maximum, and then decreases before attainment of the limiting cathodic current density for proton discharge; this was explained by the fact that at high current densities, due to limited proton transport, the activity of protons in the vicinity of the cathode falls to a value giving a local pH equal to the critical value from which the molecular hydrides begin to dissociate into anionic forms. For As and Sb, because the molecular hydrides AsH_3 and SbH_3 are stable in the whole pH range, the permeation rate may increase until the limiting cathodic current density for which the local pH is equal to 7 is reached, after which it decreases because the HER from water molecules is slower [56,110]. These results proved that only the molecular forms of the hydrides are active in promoting H entry [56,108,110].

The elements involved in the promoter species have been classified by various investigators according to their effectiveness in promoting H entry; it seems to depend upon the pH, the conditions of charging, and the method used for measuring the H concentration, which explains why the order varied according to the authors [28,56,107,108]. It has been suggested that the promoter efficiency is related to the strength of the M–H bond in the hydride [104].

Usually the H concentrations for a given polarization increases with the concentration of promoter up to a maximum, for relatively low concentrations, beyond which it eventually decreases [56,108,110]. Figure 11 shows the H permeation rate at a given cathodic current density as a function of the concentration of various compounds of the elements discussed here. All the curves show maxima, except the one for Na_2S,

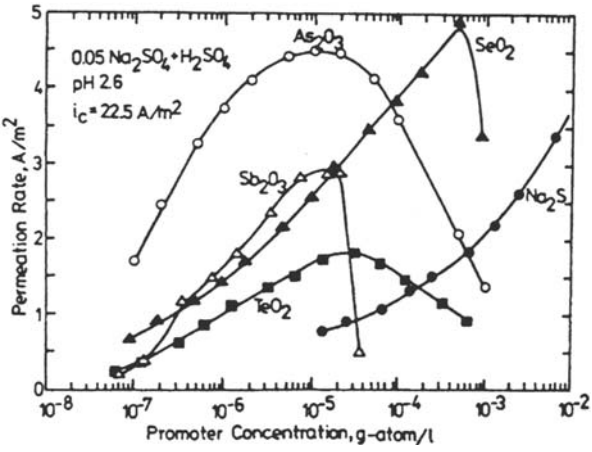


Figure 11 Effect of promoter concentration on hydrogen permeation rate through steel membranes. (From Fig. 11–11 in Ref. 56.)

Copyright © 2002 Marcel Dekker, Inc.

where a continuous increase is observed. It is believed that a decrease for concentrations higher than the optimal value is due to the formation of deposits of elemental As, Sb, Se, or Te that block the metal surface for H entry and that there is no such effect with Na_2S solutions, probably because the thermodynamic conditions for S formation are restrictive ad even deposited S does not form a protective film [56,110].

The embrittlement of steels (stress corrosion cracking) in H_2S-containing media is of great industrial importance, so the effect of dissolved H_2S deserves a special analysis here. According to most authors [56,111,112], H_2S enhances the HER on iron. This is to be compared with similar effects observed on Fe single crystals precovered by a fraction of a monolayer of adsorbed sulfur [53,103]. Classic explanations are that in acid medium H_2S molecules adsorbed on the cathode catalyze the proton discharge step by being proton transfer centers [56,112,114]. The HAR seems to be promoted only in the low pH region where H_2S is dissolved molecularly; the rate of H permeation through iron or steel increases with H_2S concentration, beginning from very low values [56].

The effects of surface oxides and dissolved H_2S on the HER and the HAR on/in steel have been investigated [111]. The effect of H_2S on the HER and hydrogen permeation on/in passivated and anodically depassivated surfaces of steel was analyzed, assuming that the HER occurs by the Volmer-Tafel path only. It was concluded that H_2S plays a multiple role: it increases the rates of iron dissolution and proton discharge, probably by roughening the metal and removing the passivation layer. It then poisons the chemical combination reaction on the depassivated surface, thereby permitting a large fraction of the H atoms to enter the metal [111].

Proposed Mechanisms of Action of Promoters

From the many suggestions made in the past to explain the mechanism of action of H entry promoters into ferrous metals, the more realistic ones are summarized here. It was often considered that the promoter is adsorbed on the surface, although for elements of columns 15 and 16 it was not clearly stated whether it is in elemental or hydride from [108,115].

1. The promoter increases the strength of the $M–H_{ads}$ bond, thus decreasing the rate of H–H combination and increasing the surface H coverage, which thereby increases the permeation rate [116].
2. The promoter lowers the $M–H_{ads}$ bond energy (weakens the $M–H_{ads}$ bond). This decreases the height of the energy barrier for H surface-bulk transfer [31,54,108].
3. The promoter inhibits the recombination step(s), so that it increases the H entry rate [33,73,107,111].
4. The promoter is adsorbed in the sites of H_{ads}, lowering the probability of finding a pair of H adsorbed at contiguous sites, necessary for H_2 formation; it thus poisons the H chemical combination step, so a high concentration of atomic H is built up on the surface, which increases the rate of H entry into the metal [112,115].

Explanation 1 is valid only for a Vomer-Tafel path with θ_H close to unity (see Fig. 10b). Furthermore, the promoters are known to be poisons for adsorption of H in the gas phase [100], adsorption of UPD H on Pt [41,42,101,117,118], and also

Copyright © 2002 Marcel Dekker, Inc.

adsorption of the HER intermediate (OPD H) [75,117,118]. They lower the H adsorption capacity and are likely to lower the $M–H_{ads}$ bond strength [41,42,101].

Explanation 2 was proposed in Ref. 31 for a coupled Volmer-Tafel path and is valid at constant current density, assumed to be due mainly to the combination rate (see Table 2). However, a lowering of the rate constant for surface-bulk transfer cannot by itself explain why H permeation is increased under potentiostatic conditions [113]. At fixed potential, the weakening of the $M–H_{ads}$ bond strength, associated with a strong reduction of the number of surface adsorption sites, should lead to a reduction of the H coverage, which would probably be the determining factor.

Explanation 3, rather phenomenological, is often given for an increase of permeation current under gavanostatic conditions, for an HER mechanism assumed to occur only by the Volmer-Tafel path. In this case, the constant cathodic current is related only to the electroadsorption rate, which is equal to the sum of the combination rate plus the permeation rate [see Eq. 34]. If the promoter inhibits the chemical combination step, the permeation rate is increased [33,111]. This trivial explanation fails to explain promoter effects occurring under potentiostatic conditions.

Explanation 4 is valid if the reaction of consumption of H_{ads} is solely the combination step: in addition to assuming the Volmer-Tafel path for the HER, the permeation rate must be negligible to allow an increase of the H coverage [see Eq. 33]. This classic explanation is apparently not self-consistent because it proposes that a high H coverage may appear whereas the H sites are occupied by poison, unless the sites for electroadsorption are supposed to be different from sites for combination, which would conflict with the present view [27,53,58,59]. However, a modeling of promoter effects shows that the relative coverage in the sites left active may well increase while, due to the blocking effect, the overall coverage decreases [53,61].

There are two recent significant contributions to the understanding of the mechanism of action of promoters on H permeation into iron:

1. Some authors, using the rather rough assumption that the mechanism of HER on iron in acid is only coupled Volmer-Tafel but taking the permeation current into account in the establishment of the steady-state equations (so-called IPZ model), analyzed their data on iron in acid solutions containing H_2S and concluded that H_2S increases the proton discharge rate constant and lowers the combination rate constant, leading to a coupled Volmer-Tafel mechanism at low overpotentials, a decreased overvoltage, an increased H coverage, and an increased permeation rate [112]. Their conclusions are essentially similar to explanation 4.
2. This explanation is contested in the latest permeation study [34], in which the promoting effects of dissolved species of As on iron are analyzed with accurate fitting of the experimental current-potential curves with the complete steady-state equations and taking into account the possibility of reduction of adsorbed As at cathodic potentials into the hydride AsH_3; yet a simplifying choice of parameters could not be avoided. It is concluded that the mechanism of HER cannot be or become the coupled Volmer-Tafel one. It is once again observed that the H entry is inhibited a low overpotentials, which is attributed to deposition of bulk As, and that promoting effects of As occur only at relatively high overpotentials, where As is likely to desorb into AsH_3. From the fit, the authors deduce that the

Copyright © 2002 Marcel Dekker, Inc.

H absorption promotion is associated with an increase of the H coverage. They suggest that the strongly adsorbed poison disturbs the bonding between substrate atoms so that the desorption of As into AsH_3 provides new active sites for H adsorption, leading to larger H coverage and hence enhanced H entry [34]. However, this explanation is speculative.

Description of the Adsorption Blocking Effect

The mechanisms of action of the promoters of H absorption may be rationalized in terms of their ability to poison adsorption reactions. In the phase, the use of ultrahigh-vacuum surface techniques, correlated with theoretical treatments, has allowed a detailed understanding of the mechanisms of poisoning of catalytic reactions by adsorbed electronegative elements of columns 14 to 17, called surface modifiers [100]. In aqueous solution, the effects of adsorbed sulfur on the HER on single-crystal surfaces of Ni, Fe, Ag, and Pt [53 and references therein] and the H underpotential adsorption on single-crystal Pt surfaces [41,42] were investigated, as well as the effects of the addition of compounds of S and As to the electrolyte [34,113,117,118]. Correlating the results of these studies with the knowledge gained in the gas phase, the following behavior of the surface modifiers in solution can be summarized [53,59,62,101]: these species are strongly chemisorbed in the atomic form on surfaces of transition metals in the domains of H UPD and HER at low overpotential (i.e., from 1.0 V to at least –0.1 V/RHE1 for S_{ads} on Pt); in this range their coverage is almost independent of potential, i.e., they are irreversibly adsorbed, as compared with H (for example, the M–S_{ads} bond energy is 464 and 414 kJ mol^{-1}, respectively, for Ni and Fe, whereas the M–H_{ads} bond energy is only 265 and 270 kJ mol^{-1} [Chap. 2]). At high cathodic overpotentials, they are reduced to molecular hydrides [23,34,117,118]. They have two main effects on H adsorption, arising from the electronic properties of the strong metal-modifier bond and the hydrogen-modifier lateral interactions [100]. (i) The first is a short-range blocking effect: an adsorbed poison atom induces a weakening of the M–H_{ads} bond into all nearest neighbor sites, so drastic that adsorption of H atoms in these sites is prevented; the range of this effect depends on the modifier and on the nature and surface orientation of the metal substrate; this effect diminishes the UP H adsorption capacity of a Pt surface, leading to total inhibition for a surface covered by a complete poison monolayer [41,42]. The second effect is a longer range effect on the energy of the M–H_{ads} bond in the sites left active (not blocked), corresponding to modifier-induced changes in the surface local density of states near the Fermi level, evidenced by a slight change of the Gibbs energy of adsorption [41,42]. It was demonstrated that for sulfur chemisorbed on Pt, the latter effect may be a weakening of the metal–UPD H bond and a strengthening of the metal–OPD H bond [53].

These data show that the electronegative elements and their derived compounds adsorbed on a surface are charaterized by irreversible chemisorption in a large domain of potential and a strong blocking effect on sites for H adsorption, while they may impede or promote the HER and the HAR. In consequence, because they may be poisons for one reaction and promoters for another, instead of calling such elements modifiers, poisons, or promoters, it is more logical to denominate these species reffering to their common property, i.e., they are adsorption site

Copyright © 2002 Marcel Dekker, Inc.

blockers (ASBs) (referred to elsewhere as site blocking elements [53,62,101b] or site blocking species [59].

Modeling of the Effects of Adsorption Site Blockers on the HER and HAR

Bases of the Model

The effects of adorption site blockers on the rates of the surface reactions involving adsorbed hydrogen may be modeled simply by taking into account simultaneously but separately the blocking effect that reduces the number of sites for H adsorption and the effect on the M–H_{ads} bond in the sites not blocked, without any a priori assumption on the direction of the latter effect.

On a surface irreversibly covered by an ASB, the H coverage at a given potential, θ_H, define as the ratio of the density of H sites occupied by adsorbed H atoms to the total density of H sites existing on the clean surface (Γ_S), can be expressed as

$$\theta_H(E) = \theta_{Hsat}\ \tau_H(E) \tag{37}$$

where θ_{Hsat} is the saturation coverage of H coadsorbed with ASB, equal to the fraction of H adsorption sites left active (not blocked by ASB), which depends only on the ASB coverage, and $\tau_H(E)$ is the "local" coverage in the active sites, equal to the fraction of the sites not blocked that are occupied by H atoms, which depends on the potential and on the energetics of H adsorption in the sites not blocked. The fraction of sites available for H adsorption, $(1–\theta_H)$ on a clean surface is replaced for a surface covered by coadsorbed ASB by $\theta_{Hsat}(1–\tau_H)$.

These terms replace the coverage terms in the expressions for the rates of the reactions requiring one H surface site, i.e., H electroadsorption, electrocombination, and surface-bulk transfer and the reverse reactions [Eqs. (25), (26), (29) to (32)]. So the separation of the global coverage θ_H into two variables allows clearly distinguishing the parameter that is sensitive to the ASB blocking effect on the nearest neighbor sites (θ_{Hsat}) from the parameter sensitive to the ASB effect on the energetics of H adsorption in the sites remaining active (τ_H).

The combination and dissociative adsorption steps require two H surface sites in nearest neighbor position, so the rates of these reactions are proportional to the density of pairs of nearest neighbor H sites occupied by H atoms, which is $\frac{1}{2}\Gamma_S\theta_H^2$, or unoccupied, $\frac{1}{2}\ ze\Gamma_S(1-\theta_H)^2$ [Eqs. (27) and (28)]. The fraction of pairs occupied by H atoms, equal to the probability of finding two nearest neighbour sites occupied by H atoms, θ_H^2 on a clean surface, is replaced for a surface covered by coadsorbed ASB by $p\tau_H^2$, where p is the fraction of pairs of nearest neighbor sites left active (not blocked by ASB). The fraction of pairs available for H_2 adsorption, equal to the probability of finding two nearest neighbor sites available for H, $(1–\theta_H)^2$ on a clean surface, is expressed for a surface covered by coadsorbed ASB as $p\ (1–\tau_H)^2$. The term p is the equivalent of θ_{Hsat} for a two-site reaction and depends only on the ASB coverage.

The variations of θ_{Hsat} and p ($p \le \theta_{Hsat}$) with the ASB coverage, which reflect the strength of the site blocking effect, are interrelated [53]. They depend on (a) the structure and the orientation of the substrate plane, (b) the nature of the adsorption sites for H and ASB, (c) the blocking range of the ASB, i.e., the number of H sites blocked by one isolated ASB adatom, and (d) the degree of order in the ASB overlayer. These variations have been modeled for low-index single-crystal faces of

Copyright © 2002 Marcel Dekker, Inc.

fcc metals [53]. In the particular case in which one ASB atom blocks one H site (geometric blocking effect), $\theta_{Hsat} = (1-\theta_{ASB})$ and p is equal to $(1-\theta_{ASB})^2$ for random adsorption of ASB or $(1-2\theta_{ASB})$ if the ASB layer is ordered [53].

The confusion between the overall coverage θ_H and the local coverage τ_H leads to frequent misunderstanding of blockers effects and to apparent discrepancies between authors, some explaining entry-promoting effects by an increase of the coverage of the HER intermediate OPD H [112], whereas others experimentally evidence a decrease of the coverage [101,117,118]. Whereas on the clean surface θ_H is equal to τ_H, when ASB is adsorbed these two quantities become different. Some techniques of characterization of the OPD H coverage yield $\theta_H = \theta_{Hsat}\ \tau_H$, which decreases when θ_{ASB} increases because of the preponderant effect of decrease of θ_{Hsat} [53,75,117,118]; other techniques yield the local coverage τ_{OPDH}, which may a priori decrease or increase [53,62]. Integration of H adsorption pseudocapacity versus potential curves for different ASB coverage measured at underpotential [41,42] or at overpotential with transient techniques [117–119], yields θ_H, which corresponds to the capacity of the surface to adsorb H for a given θ_{ASB} [62]. The local coverage τ_H can then be indirectly obtained by normalizing θ_H with respect to the saturation coverage θ_{Hsat} [41,42]. Analysis of the dependence of the HER and permeation currents on the potential for a cathode irreversibly covered by ASB (via the Tafel $\partial E/\partial \log i_c$ and permeation $\partial E/\partial \log i_p$ slopes) gives information only on the potential-dependent part of the OPD H coverage, which is τ_H [53]. In some cases, τ_H has been shown to increase [53], indicating a strengthening of the M–H_{ads} bond in the sites not blocked; then the ASB overall blocking effect and energetic effect in the sites left active were antagonistic. The blocking effect was dominant, so the resulting effect was a decrease of the coverage $\theta_H = \theta_{Hsat}\ \tau_H$ [42,53,62]. In consequence, the deduction made by some authors of an increase of the (in fact local) H coverage caused by so-called poisons [112,115] is not inconsistent with measurements of the diminution of the overall coverage, contrary to what was claimed elsewhere [101].

Predictions of the Effects of Adsorption Site Blockers on H Entry into Metals

On the basis of this model, it is possible to predict the effects of ASB on the bulk H concentration [53,61,62], assuming that H_{ads} is a reaction intermediate common to the HER and the HAR and that the surface-bulk transition is in quasi-equilibrium.

The rates of all the steps in the forward and reverse reactions may be expressed as functions of θ_{Hsat}, p, τ_H, ΔG_{ads}, and E. Applying the steady-state equations for H charging and H permeation [Eqs. (33)–(35)] to these modified rate equations, the H bulk fractional concentration beneath the surface is expressed by the following equilibrium equation, where τ_H the local coverage replaces the overall coverage θ_H in Eq. (12):

$$X_H/(1-X_H) = \tau_H/(1-\tau_H)\ \exp -\Delta G_{diss}/RT\ \exp \Delta G_{ads}/RT \tag{38}$$

This equation does not involve θ_{Hsat}, which means that the reduction of the number of active H adsorption sites has not direct influence on X_H and that the dependence of X_H on surface effects occurs only via the local coverage τ_H and the adsorption free energy in the sites not blocked. If the H_{ads} intermediate involved in the surface-bulk transfer step (and in the HAR) is the HER intermediate, i.e., OPD H (which is the case for most metals), the expression of the ratio $\tau_H/(1-\tau_H)$ and

Copyright © 2002 Marcel Dekker, Inc.

hence the ASB effects on the bulk H concentration depend upon the mechanism of the HER [53,61,62]. Let us consider the three main cases:

1. One of the steps of the HER is in quasi-equilibrium.

This situation is the aqueous solution analog of gas-phase charging from H_2. For example, let us consider the case where the Volmer step is in quasi-equilibrium, i.e., $\vec{v}_{ea} \approx \overleftarrow{v}_{ea}$ (this mechanism is operating on noble metals at low overpotentials). By combining Eqs. (25) and (26), the following expression is obtained:

$$\tau_H/(1-\tau_H) \approx \exp -\Delta G_{ads}/RT \ \exp -FE_{(RHE1)}/RT \tag{39}$$

Combining Eqs. (38) and (39) leads to the electroabsorption isotherm, in which of course there is no surface parameter:

$$X_H/(1-X_H) \approx \exp -\Delta G_{diss}/RT \exp -FE_{(RHE1)}/RT \tag{40}$$

Because both the H electroadsorption and surface-bulk transfer steps are in quasi-equilibrium, the HAR is also in quasi-equilibrium,and no surface effects may occur. X_H is dependent only on the overpotential and the free energy of H dissolution in the bulk from $\frac{1}{2}H_{2(g)}$. In this case, no promoting or inhibiting effects induced by ASB purely surface effects can exist in the steady state [53,61,62,113]. This conclusion can be extended to all the HER mechanisms where one step is in quasi-equilibrium. This analysis, which can also be performed by a thermodynamic treatment in expressing equalities of chemical potentials for hydrogen in the different phases, disagrees with the conclusions of a thermodynamic treatment of poison effects proposed by other authors, suggesting that a blocking effect may induce H absorption promotion in this case [101].

2. The Volmer and the Heyrovsky steps are coupled (coupled electroadsorption-electrocombination combination).

This mechanism is operating on most metals at high overpotentials. Here $\vec{v}_{ea} \approx \vec{v}_{ec}$, hence by equating Eqs. (25) and (29) a pseudoequilibrium adsorption isotherm is obtained where θ_{Hsat} is not involved.

$$\begin{aligned}\tau_H/(1-\tau_H)\exp(\beta+\delta)g\tau_H \\ \approx k_{ea}/k_{ec}\ \gamma_{ec}^{\neq}/\gamma_{ea}^{\neq}\ \exp -(\beta+\delta)\Delta G_{ads}/RT \exp -(\beta-\delta)FE_{(RHE1)}/RT\end{aligned} \tag{41}$$

combining Eqs. (38) and (41) leads to the following expression:

$$\begin{aligned}X_H/(1-X_H) \propto \exp -\Delta G_{diss}/RT\ \exp(1-\beta-\delta)\Delta G_{ads}/RT \\ \times \exp -(\beta-\delta)FE_{(RHE1)}/RT\end{aligned} \tag{42}$$

X_H is not dependent on θ_{Hsat} and unless β and δ take very different values, there is only a slight dependence of X_H on ΔG_{ads} and E. Only weak surface effects are expected.

3. The Volmer and the Tafel steps are coupled (coupled electroadsorptionchemical combination).

This mechanism has been reported for iron and ferrous alloys at low cathodic overpotentials [30–32].Here $\vec{v}_{ea} \approx \vec{v}_{cc}$, hence equating Eqs. (25) and (27) leads to a pseudoequilibrium adsorption isotherm:

Copyright © 2002 Marcel Dekker, Inc.

$$\tau_H^2/(1-\tau_H)\exp(\beta+2\gamma)g\tau_H = k_{ea}/k_{cc}\,a_{H^+}\gamma_{cc}^{\neq}/\gamma_{ea}^{\neq}\,\theta_{Hsat}/p\exp-(\beta+2\gamma)\Delta G_{ads}^{(0)}/RT\exp-\beta FE_{(RHE1)}/RT \quad (43)$$

Combining Eqs. (38) and (43) leads to the following expressions for $\tau_H \ll 1$:

$$X_H/(1-X_H) \propto (a_H^+)^{1/2}(\theta_{Hsat}/p)^{1/2}\exp-\Delta G_{diss}/RT \times \exp(1-\beta/2-\gamma)\Delta G_{ads}/RT\exp-\beta FE_{(RHE1)}/2RT \quad (44)$$

This equation shows that surface effects have an influence on X_H via ΔG_{ads} and θ_{Hsat}/p.

The curve in Fig. 10b where θ_H is to be replaced by τ_H shows that for this mechanism if $\beta = \gamma = ½$, X_H decreases or increases with the M–H_{ads} bond energy, according to the value of the local coverage τ_H in the sites not blocked. For low values of τ_H (at low overpotentials), an H entry increase may result from a weakening of the M–H_{ads} bond in the sites not blocked, as considered previously [31]. As mentioned earlier, the particular value of τ_{Hmax}, corresponding to the maximum of the current and the minimum of log X_H, is dependent on the values of β and γ. In the particular case of nonactivated adsorption from H_2 ($\gamma \approx 1$), $\tau_{Hmax} = 0$ and from Eq. (44) the H concentration can only increase if the M–H_{ads} bond is strengthened or decrease if the M–H_{ads} bond is weakened in the presence of the ASB.

The influence of the blocking effects on X_H via the parameter θ_{Hsat}/p is considered now. Modeling of the blocking effects shows that this ratio always increases with the ASB coverage [53], the magnitude of the increase depending on the ASB blocking range and the degree of order in the ASB overlayer. Figure 12 shows the variation of X_H with θ_{ASB} for the lowest increase of θ_{Hsat}/p, when one ASB atom blocks only one H site and the ASB overlayer is disordered, so $\theta_{Hsat}/p = (1-\theta_{ASB})^{-1}$ [53,62] (more drastic variations are expected in other conditions). It is remarkable that the ASB effect, which reduces the number of H adsorption sites and decreases the combination current, leads to an increase of the local coverage τ_H in the sites left active and according to Eq. (44) to an increase of the bulk H concentration X_H, although the overall coverage θ_H is decreased. In this case, H entry promotion is induced by the reduction of the number of active H adsorption sites, as postulated previously [53,61,62,112,113,115].

As a conclusion, the promoting effects of adsorption site blockers on H entry can be understood not by considering the effective diminution of θ_H the overall coverage of OPD H (determined by integration of adsorption pseudocapacitance vs. potential curves [117–119]), but by considering the variation of τ_H the local OPD H coverage in the sites not blocked [obtained by normalization of θ_H or from the Tafel and permeation slopes (see Tables 1 and 2)]. If the surface-bulk transfer step is in equilibrium, a significant increase of the bulk H concentration can be induced by ASB surface effects only for the HER mechanism where the steps of electroadsorption and chemical combination are coupled. This analysis provides a quantitative explanation of the effects of promotion of H absorption into iron and ferrous alloys.

Additional Suggestions for Explaining Promoting Effects

The preceding analysis provides no explanation for ASB promoting effects on H absorption observed in cases where the HER is not controlled by a coupled Volmer-Tafel mechanism, e.g., on noble metals such as Pt and Pd [73,74,101,113]. On

Copyright © 2002 Marcel Dekker, Inc.

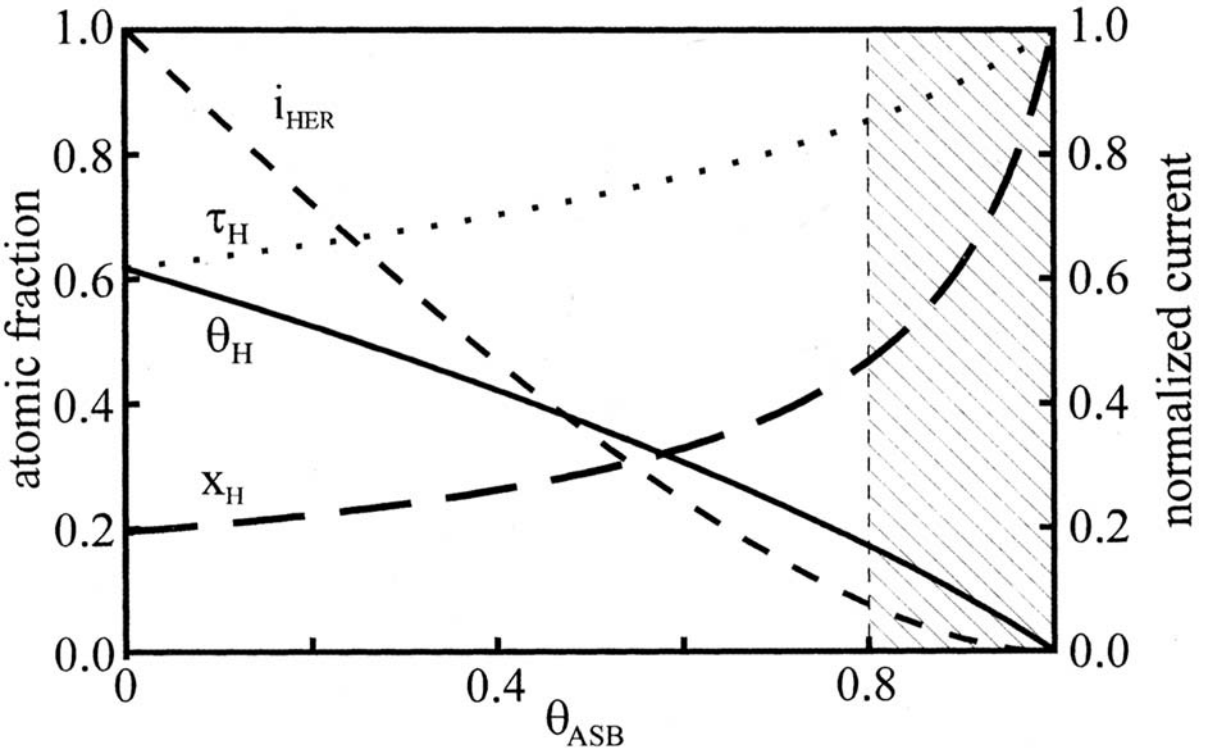


Figure 12 Theoretical variations, for a coupled electroadsorption–chemical combination HER mechanism, of the overall H coverage θ_H (full line), the local H coverage τ_H (dotted line), the HER current (dashed line), and the bulk H fraction for charging X_H (dashed line) with the coverage of adsorption site blocker (ASB). The represented case is for Langmuir type H adsorption and a "geometric" blocking effect, where one ASB atom blocks one H site, with random ASB adsorption: $\theta_H = (1 - \theta_{ASB})\tau_H$; $i_{HER} = k_{cc}\,(1- \theta_{ASB})^2\tau_H{}^2$. Above a certain value of θ_{ASB} (arbitrarily taken here), a three-dimensional metal-ASB compound forms (see Ch. 2).

Copyright © 2002 Marcel Dekker, Inc.

these metals, the electroadsorption step in the HER is in quasi-equilibrium at low cathodic overpotential (the chemical combination being the rate-determining step); when the overpotential increases, it becomes coupled to the electrocombination step [119]. So H absorption promotion by ASB on these metals can be explained only if the surface-bulk transfer step is not in equilibrium [i.e., Eq. (12), (38) does not apply], at least on the clean surface, and the ASB increases the kinetics of this step [53,62].

A suggestion made to explain sulfur promoting effects on Pt was the following: the H_{ads} state strongly bonded in the hollow sites (characterized by a deep energy well in Fig. 8b), responsible for underpotential adsorption, prevents the surface-bulk transfer through these sites on clean Pt ("UPD H blocks H absorption"); the adsorbed ASB drastically weakens the H adsorption bond in all the hollow sites in the vicinity of ASB atoms, i.e., raises the energy level of the corresponding H state in such a way that adsorption in those sites cannot occur at underpotential while the activation energy barrier for the surface-bulk transfer from these sites is lowered. So the ASB would block these H sites for UPD but unblock them for H entry [74]. This model describing the action of the ASBs as the lowering of the activation energy barrier for H entry provides an explanation for detecting H permeation through Pt membranes when the entry side is poisoned for UP H adsorption [74,113]. However, this explanation has not been demonstrated for metals apparently not showing H UPD, such as Fe or Ni.

Another explanation for the promoter effects could involve the subsurface sites. This explanation is that whereas surface adsorption is inhibited by adsorption site blockers, subsurface adsorption would still occur and could even be promoted [120a], but no direct experimental evidence exists.

An alternative explanation for the promoter effects exists for non-noble metals, such as Fe or Ni. Rarely does the HER occur on a bare surface of these metals because, except at high overpotentials, they are covered by corrosion products or passive oxide films [48,121]. Adsorption site blocking impurities such as sulfur block sites for O or OH adsorption and thus impede or inhibit surface oxidation. In the gas phase it has been shown that at low oxygen pressure and room temperature, Ni oxidation is inhibited when it covered by a complete sulfur monolayer [122]; in aqueous solution, sulfur inhibits the formation of the passive oxide film on Ni and alloys [123]. This may explain why on iron a fraction of a monolayer of sulfur may promote the HER in acid solution [103]. Similarly, by preventing the formation of a passivating oxide layer, which is a barrier to H penetration [98,121], sulfur adsorbed on the surface might promote hydrogen penetration into the metal compared with the oxide-covered metal [120b]. Another possibility consistent with the observations that promoting effects are related to promoter gaseous hydride formation could be that the hydride (H_2S) reduces the metal oxide film [21,22], allowing H entry into the depassivated metal [111].

There is still a lack of experiments on the cathodic reaction with well-controlled surface coverages by hydrogen, oxygen, and adsorption blockers. Such studies, as well as studies of the influence of the blockers on the occupancy of the subsurface sites, are necessary to understand fully the mechanisms of the hydrogen surface reactions involved in corrosion phenomena.

Copyright © 2002 Marcel Dekker, Inc.

REFERENCES

1. R. A. Oriani, J. P. Hirth, and M. Smialowski, eds., *Hydrogen Degradation of Ferrous Alloys*, Noyes Publications, Park Ridge, NJ, 1985.
2. W. M. Mueller, J. P. Blackledge, and G. Libowitz, eds., *Metal Hydrides*, Academic Press, New York, 1968.
3. G. Alefeld, and J. Volkl, eds., *Hydrogen in Metals*, Parts I and II, Springer-Verlag, New York, 1978.
4. L. Schlapbach, ed., *Hydrogen in Intermetallic Compounds*, (a) Part I, Springer-Verlag, New York, 1988; (b) Part II, Springer-Verlag, New York, 1992.
5. Y. Fukai, *The Metal-Hydrogen System*, Springer-Verlag, New York, 1993.
6. H. Wipf, ed., *Hydrogen in Metals*, Part III, Springer-Verlag, Berlin, 1997.
7. C. Wagner, *Z. Phys. 193*:386 (1944); *193*:407 (1944).
8. K. Christmann: (a) *Hydrogen Effects in Catalysis* (Z. Paal and P. G. Menon, eds.), Marcel Dekker, New York, 1988, Chapter 1, pp. 3–55, (b) *Surf. Sci. Rep. 9*: 1988; (c) *Electrocatalysis* (J. Lipkowski and P. N. Ross, eds.), Wiley-VCH, New York, 1998, chapter 4, pp. 1–41.
9. J. F. Lynch and T. B. Flanagan, *J. Phys. Chem. 77*:2628 (1973).
10. W. Eberhardt, F. Greuter, and E. W. Plummer, *Phys. Rev. Lett. 46*:1085 (1981).
11. G. Comsa and R. David, *Surf. Sci. 117*:77 (1982).
12. C. T. Chan and S. G. Louie, *Solid State Commun. 48*:417–420 (1983).
13. R. J. Behm, V. Penka, M. G. Cattania, K. Christmann, and G. Ertl, *J. Chem. Phys. 78*:7486–7490 (1983).
14. T. E. Felter, S. M. Foiles, M. S. Daw, and R. H. Stulen, *Surf. Sci. 171*:L379–386 (1986).
15. J. W. He, D. A. Harrington, K. Griffiths, and P. R. Norton, *Surf. Sci. 198*:413–430 (1988).
16. E. Kirsten, G. Parschau, W. Stocker, and K. H. Rieder, *Surf. Sci. Lett. 231*:L183–188 (1990).
17. D. Hennig, S. Wilke, R. Lober, and M. Methfessel, *Surf. Sci. 287/288*:89–93 (1993).
18. J. A. Konvalinka and J. J. F. Scholten, *J. Catal. 48*:374–385 (1977).
19. G. E. Gdowski, R. H. Stulen, and T. E. Felter, *J. Vac. Sci. Technol. A 5*:1103–1104 (1987).
20. E. Gileadi, *Electrosorption*, (E. Gileadi, ed.) Plenum, New York, 1967, Chapter 1.
21. P. Marcus and E. Protopopoff, *J. Electrochem. Soc. 137*:2710 (1990); *J. Electrochem. Soc. 140*:1571 (1993).
22. P. Marcus and E. Protopopoff, *J. Electrochem. Soc. 144*:1586 (1997); *Corros. Sci. 39*:1741 (1997).
23. P. Marcus and E. Protopopoff, *Electrochemical Surface Science of Hydrogen Adsorption and Absorption* (G. Jerkiewicz and P. Marcus, eds.), PV 97-16, The Electrochemical Society, Pennington, NJ, 1997, pp. 211–224.
24. P. N. Ross, Jr., *Chemistry and Physics of Solid Surfaces IV* (R. Vanselow and R. Howe, eds.), Springer Series in Chemical Physics, Vol. 20, Springer-Verlag, New York, 1982, Chap. 8.
25. F. Wagner, *Structure of Electrified Interfaces* (J. Lipkowski and P. N. Ross, eds.), VCH, New York, 1993, Chapter 9, pp. 309–400.
26. J. O'M. Bockris and A. K. N. Reddy, *Modern Electrochemistry*, Vol. 2, Plenum, New York, 1970.
27. N. M. Markovic, B. N. Grgur, and P. N. Ross, Jr., *J. Phys. Chem. B. 101*:5405 (1997); N. M. Markovic, S. T. Sarraf, H. A. Gasteiger, and P. N. Ross, Jr., *J. Chem. Soc. Faraday Trans. 92*:3719–3725 (1996).
28. P. K. Subramanyan, *Comprehensive Treatise on Electrochemistry*, (J. O'M. Bockris, B. E. Conway, E. Yeager, and R. E. White, eds.), Vol. 4, Plenum, New York, 1981, chapter 8, pp. 411–462.

Copyright © 2002 Marcel Dekker, Inc.

29. B. E. Conway and L. Bai, *J. Chem. Soc. Faraday Trans. I 81*:1841 (1985).
30. M. A. V. Devanathan and Z. Stachurski, *J. Electrochem. Soc. 111*:619 (1964).
31. J. O'M. Bockris, J. McBreen, and L. Nanis, *J. Electrochem. Soc. 112*:1025 (1965).
32. W. Beck and P. Fischer, *Corros. Sci. 15*:757 (1975).
33. E. G. Dafft, K. Bohnenkamp, and H. J. Engell, *Corros. Sci. 19*:591–612 (1979).
34. S. Y. Quian, B. E. Conway, and G. Jerkiewicz, *J. Chem. Soc. Faraday Trans. 94*:2945–2954 (1998).
35. B. E. Conway, H. Angerstein-Kozlowska, and F. Ho, *J. Vac. Sci. Technol. 14*:351 (1977); B. E. Conway, H. Angerstein-Kozlowska, and W. B. A. Sharp, *J. Chem. Soc. Faraday Trans. I 74*:1373 (1978).
36. A. Eucken and B. Weblus, *Z. Elektrochem. 55*:114 (1951).
37. M. Breiter, *Electrochim. Acta 7*:25 (1962); *Ann. N. Y. Acad. Sci. 101*:709 (1963).
38. F. Will, *J. Electrochem. Soc. 112*:451 (1965).
39. J. Clavilier, *J. Electroanal. Chem. 107*:211 (1980).
40. P. N. Ross, Jr., *Surf. Sci. 102*:463 (1981).
41. P. Marcus and E. Protopopoff, *Surf. Sci. 161*:533 (1985).
42. E. Protopopoff and P. Marcus, *Surf. Sci. 169*:L.237 (1986).
43. J. L. Weininger and M. W. Breiter, *J. Electrochem. Soc. 110*:484 (1963); *J. Electrochem. Soc. 111*:707 (1964).
44. J. McBreen, *J. Electroanal. Chem. 287*:279 (1990).
45. J. Horkans, *J. Electroanal. Chem. 209*:371 (1986).
46. G. A. Attard and A. Bannister, *J. Electroanal. Chem. 300*:467 (1991).
47. M. Baldauf and D. M. Kolb, *Electrochim. Acta 38*:2145–2153 (1993).
48. D. D. Macdonald, in Ref. 1, chapter 4, p. 97.
49. M. A. V. Devanathan and M. Selvaratnam, *Trans. Faraday Soc. 56*:1820 (1960).
50. A. Caprani and P. Morel, *J. Appl. Electrochem. 7*:65 (1977).
51. L. I. Krishtalik and B. B. Kuz'menko, *Elektrokhimiya 9*:664 (1973).
52. R. J. Nichols and A. Bewick, *J. Electroanal. Chem. 243*:445 (1988); *Adsorption of Molecules at Metal Electrodes* (P. N. Ross and J. Lipkowski, eds.), VCH, New York, 1992, chapter 7, pp. 347–389.
53. E. Protopopoff and P. Marcus, *J. Chim. Phys. 88*:1423 (1991).
54. I. A. Bagotskaya, *Zh. Fiz. Khim. 36*:2667 (1962).
55. A. N. Frumkin, *Advances in Electrochemistry and Electrochemical Engineering* (P. Delahay, ed.), Vol. 3, Interscience, New York, 1963, p. 379.
56. T. Zakroczymski, in Ref. 1, chapter 11, pp. 215–250.
57. G. Zheng, B. N. Popov, R. E. White, *J. Electrochem. Soc. 142*:154–156 (1995).
58. G. Jerkiewicz and A. Zolfaghari, *J. Electrochem. Soc. 143*:1240 (1996).
59. G. Jerkiewicz, *Prog. Surf. Sci. 57*:137–186 (1998).
60. E. Gileadi and B. E. Conway, *Modern Aspects of Electrochemistry* (J. O'M. Bockris and B. E. Conway, eds.), Vol. 3, Butterworths, London, 1964, chapter 5, p. 384.
61. E. Protopopoff and P. Marcus and *C.R. Acad. Sci. Paris 308 II*:1127–1133 (1989).
62. E. Protopopoff and P. Marcus, *Electrochemistry and Materials Science of Cathodic Hydrogen Absorption and Adsorption,* (B. E. Conway and G. Jerkiewicz, eds.), PV 94-21 The Electrochemical Society, Pennington, NJ, 1995, pp. 374–386.
63. I. Toyoshima and G. A. Somorjai, *Catal. Rev. Sci. Eng. 19*:105 (1979).
64. P. Nordlander, S. Holloway, and J. K. Norskov, *Surf. Sci. 136*:59 (1984).
65. F. E. Wagner and G. Wortmann, in Ref. 3, p. 131.
66. H. Wipf, in Ref. 6, pp. 51–91.
67. G. C. Smith, *Hydrogen in Metals*, American Society of Metals, 1963.
68. B. Siegels and G. G. Libowitz, in Ref. 2, p. 631, and reference therein.
69. R. Griessen and T. Riesterer, in Ref. 4a, p. 230.
70. R. B. McLellan and W. A. Oates, *Acta Metall. 21*:181 (1973).

Copyright © 2002 Marcel Dekker, Inc.

71. G. Jerkiewicz and A. Zolfaghari, *J. Phys. Chem. 100*:8454 (1996).
72. R. N. Iyer, H. W. Pickering, and M. Zamanzadeh, *J. Electrochem. Soc. 136*:2463–2470 (1989); *Scr. Metall. 22*:911–916 (1988).
73. M. Enyo, *Comprehensive Treatise of Electrochemistry* (B. E. Conway, J. O'M. Bockris, E. Yeager, S. U. M. Khan, and R. E. White, eds.), Vol. 7, Plenum, New York, 1983, pp. 241–300.
74. E. Protopopoff and P. Marcus, *Electrochemical Surface Science of Hydrogen Adsorption and Absorption* (G. Jerkiewicz and P. Marcus, eds.), PV 97-16, The Electrochemical Society, Pennington, NJ, 1997, pp. 159–179.
75. E. Protopopoff and P. Marcus, *J. Vac. Sci. Technol. A 5*:944 (1987); *J. Electrochem. Soc. 135*:3073 (1988).
76. P. Stonehart and P. N. Ross, Jr., *Catal. Rev. Sci. Eng. 12*:1 (1975); D. Ferrier, K. Kinoshita, J. McHardy, and P. Stonehart, *J. Electroanal. Chem. 61*:233 (1975).
77. C. M. Mate, B. E. Bent, and G. A. Somorjai, *Hydrogen Effects in Catalysis* (Z. Paal and P. G. Menon, eds.), Marcel Dekker, New York, 1988, chapter 2, pp. 57–81.
78. J. Volkl and G. Alefeld, in Ref. 3a, pp. 321–348.
79. M. I. Baskes, C. F. Melius, and W. D. Wilson, *Hydrogen Effects in Metals* (I. M. Bernstein and A. W. Thompson, eds.), The Metallurgical Society of AIME, Warrendale, (1981); R. P. Messmer and C. L. Briant, in Ref. 1, chapter 7, p. 162.
80. A. M. Baro, H. Ibach, and H. D. Bruchmann, *Surf. Sci. 88*:384 (1979).
81. K. Mortensen, F. Besenbacher, I. Stensgaard, and W. R. Wampler, *Surf. Sci. 205*:433–446 (1988).
82. T. Engel and K. H. Rieder, *Surf. Sci. 109*:140–166 (1981); K. H. Rieder and W. Stocker, *Surf. Sci. 164*:55–84 (1985).
83. M. G. Cattania, V. Penka, R. J. Behm, K. Christmann, and G. Ertl, *Surf. Sci. 126*:382–391 (1983).
84. M. Baumberger, K. H. Rieder, and W. Stocker, *Appl. Phys. A 41*:151 (1986).
85. S. Glasstone, K. J. Laidler, and H. Eyring, *Theory of Rate Processes*, McGraw-Hill, New York, 1941.
86. J. Horiuti and M. Polanyi, *Acta Phys. URSS 2*:505 (1935).
87. L. I. Krishtalik, *Comprehensive Treatise of Electrochemistry*, Vol. 7 (B. E. Conway, J. O'M. Bockris, E. Yeager, S. U. M. Khan, and R. E. White, eds.), Plenum, New York; 1983, pp. 87–172.
88. R. Fowler and E. A. Guggenheim, *Statistical Thermodynamics*, Cambridge University Press, Cambridge, 1952.
89. M. A. V. Devanathan and Z. Stachurski, *Proc. R. Soc. Lond. 270A*:90 (1962).
90. J. McBreen and M. A. Genshaw, *Proceedings of the First International Symposium on Corrosion*, Ohio State University, Columbus, 1967.
91. J. McBreen and M. A. Genshaw, *Proceedings of the First Conference on Fundamental Aspects of Stress Corrosion Cracking*, (R. W. Staehle, A. J. Forty, and D. van Rooyen eds.), NACE, Houston, 1969, p. 51.
92. H. Gerischer, *Z. Phys. Chem. N.F. 8*:137 (1956); *Bull. Soc. Chim. Belge 67*:506 (1958).
93. R. Parsons, *Trans. Faraday Soc. 54*:1053–1063 (1958).
94. L. I. Krishtalik, *Advances in Electrochemistry and Electrochemical Engineering*, Vol. 7 (P. Delahay, ed.), Interscience, New York, 1970, pp. 283–339.
95. A. J. Appleby, *Comprehensive Treatise of Electrochemistry*, Vol. 7 (B. E. Conway, J. O'M. Bockris, E. Yeager, S. U. M. Khan, and R. E. White, eds.), Plenum, New York, 1983, pp. 173–239.
96. L. Schlapbach, in Ref. 4b, pp. 14–95 and references therein.
97. E. Fromm, *Z. Phys. Chem. N. F. 147*:61–75 (1986).
98. A. M. Brass, J. Collet-Lacoste, M. Garet, and J. Gonzalez, in: *Rev. Metall. CIT Sci. Gen. Mater. 98*:197–207; A. M. Brass and J. Collet-Lacoste, *Hydrogen Transport*

Copyright © 2002 Marcel Dekker, Inc.

and Cracking in Metals, (A. Turnbull, ed.) J. Inst. Mater. 142 (1995); A. M. Brass, *Ann. Chim. Fr. 14*:273–300 (1989).
99. B. J. Berkowitz, J. J. Burton, C. R. Helms, and R. S. Polizzotti, *Scr. Metall. 10*:871–873 (1976).
100. M. P. Kiskinova, *Surf. Sci. Rep. 8* (1988).
101. (a) B. E. Conway and G. Jerkiewicz, *J. Electroanal. Chem. 357*:47–66 (1993); (b) G. Jerkiewicz, J. J. Borodzinski, W. Chrzanowski, and B. E. Conway, *J. Electrochem. Soc. 142*:3755–3763 (1995).
102. C. H. F. Peden, B. C. Kay, and D. W. Goodman, *Surf. Sci. 175*:215 (1986).
103. P. Marcus, S. Montes, and J. Oudar, *Atomistics of Fracture* (R. M. Latanision and J. Pickens, eds.), Plenum, New York, 1983, p. 909.
104. M. Smialowski, *Hydrogen in Steel*, Addison-Wesley, Reading, MA, 1962.
105. B. Baranowski and M. Smialowski, *Bull. Acad. Pol. Ser. Sci. Chim. 7*:663 (1959); B. Baranowski, *Bull. Acad. Pol. Ser. Sci. Chim. 7*: 887, 891, 897, 907 (1959); B. Baranowski and Z. Szklarska-Smialowska, *Electrochim. Acta 9*:1497 (1964); H. Jarmolowicz and M. Smialowski, *J. Catal. 1*:165 (1962).
106. H. Angerstein-Kozlowska, *Bull. Acad. Pol. Ser. Sci. Chim. 6*:739 (1958); *7*:881 (1959); *8*:49 (1960).
107. T. P. Radhakrishnan and L. L. Shreir, *Electrochim. Acta 11*:1007–1021 (1966).
108. J. F. Newman and L. L. Shreir, *Corros. Sci. 9*:631–641 (1969).
109. M. G. Fontana and R. W. Staehle, *Stress Corrosion Cracking of Metallic Materials*. Part III, *Hydrogen Entry and Embrittlement in Steel*, NTIS AD/A-010 265, National Technical Information Service, Springfield, VA, 1975, p. 5285.
110. T. Zackroczymski, Z. Szklarska-Smialowska, and M. Smialowski, *Werkst. Korros. 26*:617 (1975); E. Lunarska, Z. Szklarska-Smixalowska, and M. Smialowski, *Werkst. Korros. 26*:624 (1975); T. Zackroczymski, Z. Szklarska-Smialowska, and M. Smialowski, *Werkst. Korros. 27*:625 (1976).
111. B. J. Berkowitz and H. H. Horowitz, *J. Electrochem. Soc. 129*:468–474 (1982).
112. R. N. Iyer, I. Takeuchi, M. Zamanzadeh, and H. W. Pickering, *Corrosion 46*:460 (1990).
113. P. Marcus and F. Protopopoff, *Proceedings 4th International Conference on Hydrogen and Materials*, (P. Azou and N. Chen, eds.) Beijing, China, May 9–13, 1988, p. 168.
114. A. Kawashima, K. Hashimoto, and S. Shimodaira, *Corrosion 32*:321 (1976).
115. U. R. Evans, *The Corrosion and Oxidation of Metals*, Edward Arnold, London, 1961, p. 397.
116. K. E. Shuler and K. J. Laidler, *J. Chem. Phys. 17*:212 (1949).
117. L. Gao and B. E. Conway, *Electrochim. Acta 39*:1681–1693 (1994); L. Gao and B. E. Conway, *J. Electroanal. Chem.* 395:261–271 (1995).
118. J. H. Barber and B. E. Conway, *J. Chem. Soc. Faraday Trans. 92*:3709–3717 (1996).
119. B. E. Conway and L. Bai, *J. Electroanal. Chem. 198*:149–175 (1986); *Electrochim. Acta 31*:1013 (1986).
120. P. Marcus and J. Oudar, in Ref. 1, chapter 3, (a) p. 57; (b) p. 59.p. 59.
121. A. M. Brass and J. R. Collet-Lacoste, *Acta Mater. 46*:869–879 (1998).
122. I. Olefjord and P. Marcus, *Surf. Interface Anal. 4*:23–28 (1982).
123. J. Oudar and P. Marcus, *Appl. Surf. Sci. 3*:48 (1979).

Copyright © 2002 Marcel Dekker, Inc.

4

Anodic Dissolution

Michel Keddam
Université Pierre et Marie Curie, Paris, France

INTRODUCTION: ANODIC DISSOLUTION, GENERAL CONSIDERATIONS, SPECIFIC ASPECTS

The anodic dissolution of a metal is an electrochemical oxidation of its surface atoms resulting finally in the liberation of cations into the electrolyte. Anodic dissolution is of basic importance not only in corrosion but also in several technologies: negative electrodes of primary and secondary batteries, electromachining, electropolishing and electrowinning of metals, anodes for electrodeposition and cathodic protection and so forth.

Anodic Dissolution and Corrosion Phenomena

Anodic Dissolution as Part of Corrosion

As far as electrochemically assisted corrosion is concerned, anodic dissolution is only one half of the overall phenomenon because the oxidation current is being exactly counterbalanced by the cathodic component so as to maintain the condition of zero net current at the corroding specimen. In fact, the anodic dissolution of the material plays a central role in corrosion research. The kinetics and, to a greater extent, the mechanism of the cathodic process (oxygen or water or proton reduction in most cases) are taken into consideration far less. The outstanding importance given to the anodic dissolution is easily understood if one considers that it is the direct cause of the material decay. This explains why the potential dependence of the anodic dissolution, known from electrochemical experiments at controlled potential, is considered able to restitute the whole set of corrosion circumstances (rate and morphology) encountered by a material in a wide range of free corroding conditions.

Dissolution mechanisms of iron and iron group metals (Co, Ni) have been covered by some review articles [1–3]. This chapter is aimed primarily at introducing the reader to the present state of knowledge of the electrochemistry of corrosion [4–9]. Emphasis will be put on the decisive contribution of modern electrochemical techniques in the elucidation of these complex reaction paths. The examples are selected among the systems most relevant to the corrosion of widely used materials

Copyright © 2002 Marcel Dekker, Inc.

such as iron (mild steels), iron base alloys, and stainless steels. The anodic dissolution of some other nonferrous metals is also dealt with briefly.

Circumstances of Anodic Dissolution with Respect to Corrosion

It is usual to consider that various classes of anodic mechanisms exist depending on the range of potential with respect to the passivity domain. Active dissolution taking place at potentials preceding the passivation on a film-free surface is of major importance for the homogeneous corrosion in weakly oxidizing media such as acidic solutions of stable anions (e.g. sulfuric, perchloric, phosphoric, hydrochloric). Localized corrosion in pits, crevices, cracks, etc. is also assumed to proceed through active dissolution stabilized at passive potentials by ohmic drops and/or local chemistry.

The mechanism of active dissolution will be illustrated by the cases of iron, the metal most extensively investigated in this domain, and of iron-chromium alloys. The heterogeneous kinetics side of the mechanism of dissolution is first dealt with. Its coupling with mass transfer is then emphasized because it plays a determining role in the characteristic behavior of this metal during localized corrosion.

Mechanisms of dissolution in the full passive state are dealt with for introducing models currently invoked in passivity breakdown and localized corrosion phenomena. Dissolution at transpassive potentials apparently requires some solubilization of the passive layer often associated with higher oxidation states of the metal (Fe^{3+}, Cr^{6+}, Mo^{6+}, Ni^{3+}, etc.). Transpassive dissolution is essentially relevant to corrosion in strongly oxidizing media mainly for alloys such as austenitic stainless steels. This class of dissolution is also observed in the electrochemical processes initiated by the growth of an oxide layer at the metal surface, hence contributing to smooth dissolution (electropolishing, electromachining).

Energetics, Thermodynamics, and Kinetics of Anodic Dissolution

Energetics of Anodic Dissolution

Anodic dissolution is essentially a process of disintegration of a metal crystal lattice. As such, it can be dealt with in the framework of crystal-vapor equilibrium. According to this approach, the Gibbs free energy of dissolution would be equal to the sublimation energy W_k or to the energy of interaction W_i between first nearest neighbor atoms multiplied by the number of such atoms in a surface corresponding to a low-index plane of the lattice [e.g., 6 in a hexagonal compact plane of a face-centered cubic (fcc) crystal] [10]. However, this can be only a crude approximation because energy of ionization, energy of hydration, energy of complexation with various ligands, etc. must be taken into consideration. Of course, far from equilibrium, dissolution will give rise to additional irreversible polarizations to be accounted for by the classical theories of overvoltages (e.g., charge transfer, diffusion).

Thermodynamics of Anodic Dissolution

Actually, anodic dissolution has long been regarded as a reversible process in the framework of the so-called metal-metal ion interface [11,12]. Accordingly, the direct (metal oxidation and crystal dissolution) and the reverse (cation reduction and crystal growth) steps must proceed via the same routes even at the microscopic level [13,14]. This seems to be not always true even for systems mentioned as classical examples of equilibrium in textbooks [15]. The equilibrium point of view is a

Copyright © 2002 Marcel Dekker, Inc.

very attractive one because it allows applying to anodic dissolution the concepts previously elaborated in the theory of crystallization [16]. However, it was progressively recognized that, corrosion being an irreversible process, it makes little or no sense at all to use equilibrium principles for mechanistic purposes. The equilibrium approach must be restricted to predicting, on the basis of thermodynamic data (free enthalpy of the oxidation reaction), in which oxidation states and chemical compounds the metallic element may be found. Results are presented in the form of phase diagrams. The most popular ones are the well-known Pourbaix diagrams [17] from which the stability domains of dissolved cations (anodic dissolution) and of solid species supposed to be adherent and protective (passivity) can be inferred in a potential-pH coordinate system. Unfortunately, it is not possible to draw conclusions about whether corrosion or protection states actually settle and at which rate.

Kinetics of Anodic Dissolution

It was early intuited that anodic dissolution proceeds through the formation of chemical bonds between surface atoms and solution species (solvent molecules and ions) and cannot be described by the oversimplified view of vacuum ionization of surface atoms. Most of the works devoted to the mechanism of anodic dissolution are aimed at identifying the species formed at the lattice surface and their kinetic role in the reaction mechanism leading to stable cationic species in the solution as the final products. Advances in the field are largely due to the development and application in corrosion research of steadily improved electrochemical techniques and particularly AC techniques (electrochemical impedance spectroscopy and related techniques). Three review articles [5–7] give an updated view of the applications of these techniques in basic and applied corrosion science. Considering their wide-spread importance in research today, their background is further detailed in the following.

The Nature of the Intermediate Surface Species in Anodic Dissolution

It is now generally accepted that anodic dissolution involves the existence of intermediate surface bonds between the metallic state and the solution species. The nature and kinetic behavior of these entities are inferred from classical transient techniques relating the time or frequency response of the current, or of the potential, to the relaxation of their surface concentrations.

Activated State and Anodic Dissolution

Identification of the surface species taking part in anodic dissolution can be tentatively dealt with in the framework of the absolute reaction rate and activated complex theory [18]. A description of the activated state in metal dissolution is central to the understanding of corrosion and passivation. However, the identification of this activated state is difficult. For active metal dissolution the ionization is a very fast process (characteristic time estimated to be less than 10 μs). Following the chemical relaxation technique introduced by Eigen [19,20] for investigating fast homogeneous reactions, so-called scrape potential measurements were applied to the determination of the initial potential and of its relaxation time on fresh surfaces exposed to aqueous solution [21].

Copyright © 2002 Marcel Dekker, Inc.

This approach, referring to an initially film-free surface, is likely to be particularly relevant to the types of corrosion involving constant or sequential renewal of the corroding surface: stress corrosion cracking, abrasion and wear corrosion, etc.

Surface Species and Kinks: A Dual, Kinetic and Atomistic, Description of Anodic Dissolution

Mechanisms aimed at explaining the anodic dissolution of metals must account for the following features:

1. Transfer of one or several electrons to the electrode electron sea
2. Dependence of the kinetics on the electrode potential and solution composition
3. Role of the electrode structure, as reflected in the crystallographic orientation, and the nature and surface density of the active sites at the atomistic level

At first glance, a strikng similarity exists with heterogeneous kinetics in gas-phase and surface catalysis. But, in fact, the situation is much more intricate for the following reasons:

Adsorbable species and surface interactions are more numerous in the liquid condensed phase than in a simple gas.

The surface is continuously modified by the dissolution itself, exposing new atoms to the solution.

This last point must be emphasized. Because of atom removal from the lattice surface, chemical bonds of surface atoms with solution species can be thought either to be translated to a first nearest neighbor atom or maintained within the dissolving cation. In fact, each of these two processes is at the origin of one of the two principal mechanisms of Fe dissolution, the so-called catalyzed or catalytic mechanism [18,22] and the two consecutive charge transfer steps mechanism (noncatalyzed or consecutive mechanism) [23].

It is now generally agreed that the preceding condition 1 and 2 are fulfilled by the formation of surface compounds between the metallic element in various oxidation states and species, essentially anions and solvent molecules, present in the solution. The complex pH and anion dependence of the dissolution rate is assumed to reveal the competitive role of various types of mechanisms [24]. According to Sato [25]:

1. The aquo-ligand mechanism:

$$M \rightarrow M^{+}_{ads} + e^{-}$$

$$M^{+}_{ads} \rightarrow M^{2+}_{aq} + e^{-}$$

2. The hydroxo-ligand mechanism:

$$M + H_2O \rightarrow M\,OH_{ads} + H^{+} + e^{-}$$

$$M\,OH_{ads} \rightarrow M\,OH^{+}_{aq} + e^{-}$$

Copyright © 2002 Marcel Dekker, Inc.

3. The aniono-ligand mechanism:

$$M + A^- \rightarrow M A_{ads} + e^-$$

$$M A_{ads} \rightarrow M A^+_{aq} + e^-$$

It is also generally accepted that the hydroxo-ligand MOH_{ads} is the precursor in the competitive buildup of the prepassive and passive states. Branching mechanisms such as

$$M + H_2O \rightarrow M OH_{ads} + H^+ + e^-$$

$$M OH_{ads} \rightarrow M OH^+_{aq} + e^- \quad = \text{dissolution step}$$

$$M OH_{ads} + H_2O \rightarrow M(OH)_2 + H^+ + e^- \quad = \text{prepassivation step}$$

are most usually postulated. An exhaustive analysis of the active-passive transition of the iron group metals can be found in Ref. 26.

In fact, even though it is a very common experience that corrosion is deeply influenced by the metallurgical state of the material (e.g., cold working, annealing, grain size and boundaries, twinning), there are only few attempts to account for this in mechanistic studies. The cathodic process is merely dealt with from a crystal growth point of view as a part of the phase transition in the metal-vapor system [27]. In contrast, anodic dissolution is essentially considered in terms of electrochemical kinetics [10]. The contribution to this field is mainly due to Lorenz et al., who claimed in a series of papers [6,28] that the catalytic mechanism of iron dissolution is favored on highly active material, i.e., iron with a high density of crystal imperfections and dislocations produced by cold working. On the contrary, the consecutive mechanism would take place preferentially on relatively inactive, annealed, or single-crystal samples. However, at this time no clear atomistic view of the structure-mechanism relationship was reached.

An elaborated interpretation of the catalytic role played by FeOH in the catalytic mechanism was more recently proposed by Heusler et al. [1,2,29–31]. According to this model, FeOH is associated with a kink or half-crystal atom on a dissolving edge of terrace (or ledge). If one atom is removed from such a position, the active site for dissolution is simply transferred onto the next atom on the edge. In other words, FeOH is self-regenerated and can be regarded as a catalyst, a single entity being able to dissolve a very large numbers of atoms. Figure 1 displays, in a schematic way on a two-dimensional lattice, the shift of the active site for dissolution from one atom to the next one. Annihilation of kinks takes place by collision of two kinks of opposite sign, and generation of new kinks occurs at the corner position, intersection of steps.

In the case of alloy dissolution, where further complexity arises from selective dissolution, computer simulations seem to be a promising approach [32].

Electrochemical Techniques in The Study of Anodic Dissolution

The anodic dissolution of metal has long been and remains an important field of electrochemistry at solid electrodes. Advances were tightly conditioned by the introduction of new experimental techniques.

Copyright © 2002 Marcel Dekker, Inc.

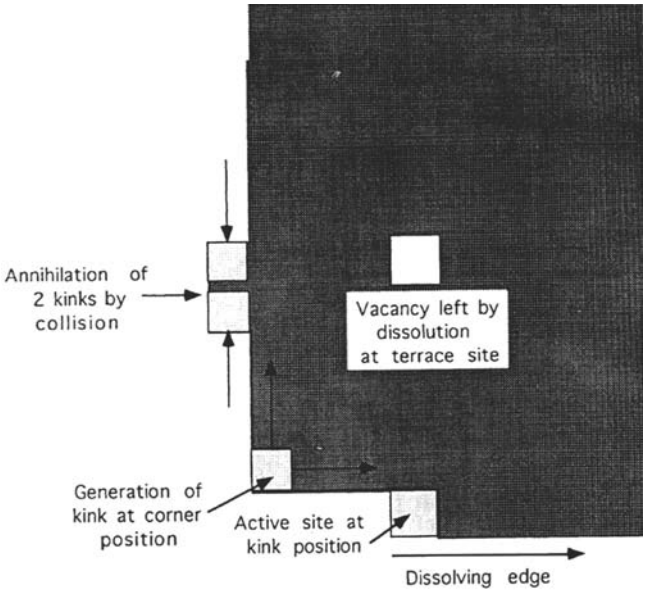


Figure 1. Definition of atomic crystallographic sites of significance in anodic dissolution. Schematic on a square 2-D lattice kinks at steps (edges or ledges), corners and terraces positions.

Classification of Electrochemical Techniques

They can be split into two main groups, each of them including steady-state and non-steady-state techniques.

Current-Voltage Techniques The electrochemical behavior of the electrode is defined by its current (potential) response to a potential (current) excitation under potentiostatic (galvanostatic) control of the polarization. Some rare kinetics may require specially designed regulating devices [33,34]. Steady-state or voltage sweep current-voltage curves and electrochemical impedance spectroscopy (EIS) are the main techniques. To this group also belong related techniques based on a more sophisticated processing of the same raw data (e.g., coulometry, determination of dissolution valencies). The application of Faraday's law to anodic dissolution is of primary significance. In principle, it yields the valence of dissolution, i.e., an integer number. However, there are a number of well-documented examples of metal exhibiting the so-called negative difference effect, i.e., a noninteger electrovalence lower than the oxidation state of the metal in the final cationic species in the solution [35]. Three possible causes can be considered:

1. Chunk effect
2. Dissolution with lower valence and subsequent chemical oxidation of the cation
3. Mixed potential effect where cathodic reduction of the solution coexists with the dissolution

Copyright © 2002 Marcel Dekker, Inc.

Non exclusively Current-Voltage Techniques In this class of techniques one handles an extraexperimental parameter (either excitation or response) in order to obtain additional information relevant to nonelectrical aspects of the dissolution phenomena.

To this group belong the techniques based on the rotating-disk electrode (RDE) [36]. They allow control of the rate of mass transport to and from the dissolving anode to determine the degree of diffusion control in the overall process. A closely related technique of primary interest for anodic dissolution is the rotating ring-disk electrode (RDE) in which the flux of soluble cations resulting from the dissolution of the RDE is collected through a proper redox reaction on a concentric outer ring electrode [37]. An AC extension is most usefully associated with simultaneous classical impedance measurements of the disk [38]. It is also worth pointing out the promising contribution to anodic dissolution studies of the electrochemical quartz crystal microbalance (EQCM), which yields in situ gravimetric information with a fair time or frequency resolution and a mass sensitivity far better than one monolayer of oxygen (50 ng cm^{-2}) [39].

Non-Steady-State versus Steady-State Techniques

Historical Trend The development of the electronic potentiostat from the early 1950s was at the origin of a new approach in the investigation of the anodic behavior of metals and alloys, particularly those exhibiting an active-passive transition not amenable to galvanostatic techniques [4]. It soon appeared that reliable mechanistic information cannot be drawn from steady-state techniques alone. Voltage sweep (potentiodynamic plots) was applied, but the sweeping rate was never introduced as a significant experimental parameter because the classical theories of cyclic voltammetry are not valid for multistep heterogeneous reactions with adsorbed intermediates. Even a single one-electron charge transfer adsorption requires a heavy numerical computation in order to obtain the voltammetric response [40].

In the case of iron dissolution, it was observed early that the time dependence of the faradic current following a potential step is more complex than that expected for simple charge transfer kinetics and may be, in some way, related to the mechanism of reaction [41]. Approximately at the time, similar kinetic situation in the hydrogen evolution reaction was being dealt with by Gerischer and Mehl [42] in terms of faradic impedance. For some time, both transient (time domain) and impedance (frequency domain) techniques have coexisted in anodic dissolution studies. At the end of the 1960s and during the 1970s, decisive advances were realized in the devices for complex impedance measurements down to the millihertz domain and in their interfacing with electrochemical cells. The technique became perfectly suitable for investigating in the frequency domain the long-range time responses of the dissolution-passivation kinetics [43–48].

Fundamentals of Non–Steady-State Techniques The basic idea behind these techniques is to extract information about the reaction mechanism and the rate constants from the time dependence of some measurable property of the electrochemical interface in response to a perturbation of its steady state.

Copyright © 2002 Marcel Dekker, Inc.

This relaxation is determined by the non-steady-state solutions of the kinetic equations. Each of the state-determining kinetic parameters is assumed to contribute by its own time of relaxation.

Mathematics of Non–Steady State The time dependence of the system is controlled by a set of nonlinear partial derivative equations, expressing the mass balance of chemical species under the influence of reaction and transport phenomena. The concentrations C_i of bulk species and $C_S i$ of surface species obey the kinetic equation

$$\frac{\partial C_i}{\partial t} = -\text{div}\,\psi_i + S_i(C_j) \tag{1}$$

where ψ_i is the local flux of species i under the influence of the gradient of electrochemical potential and S_i is a formal source term (positive or negative) due to homogeneous chemical reactions.

Similarly, mass balance due to heterogeneous reactions is given by an ordinary differential equation such as

$$\frac{dC_{S_i}}{dt} = S_{s_i}\ (E, C_j, C_{s_j}) \tag{2}$$

where S_{S_i} is also a formal source term due to heterogeneous reactions and E is the applied electrode potential.

Boundary conditions at the electrode surface are given by continuity equations between the flux ψ_i and the rate of reaction of species i expressed by surface kinetics laws.

The instantaneous intensity of the faradic current is given by

$$\frac{\mathrm{I}}{F} = \Phi(E,\ C_j,\ C_{S_j}) \tag{3}$$

where C_j, C_{S_j} are relative to those species reacting with electrons.

Integration of the set of equations (1) and (2), with the proper initial and boundary conditions and the $E(t)$ function selected as a perturbation, yields the relaxation behavior of the interface in terms of current response.

Most generally, this problem has no analytical solution and must be solved numerically unless the linearized form of these equations is used. A linearization procedure is allowed by using a small-amplitude perturbation $\Delta E(t)$ so as to neglect the nonlinear terms (degree higher than one) in the Taylor expansion of S_i, S_{S_i} and ψ_i around the mean steady state of the system. It is known from linear system theory that under these conditions the response $\Delta I(t)$ is proportional to the perturbation $\Delta E(t)$. The dynamic behavior of the electrode at this particular polarization point is completely described by its complex impedance $Z(j\omega) = \Delta E(j\omega) / \Delta I(j\omega)$ in the frequency domain where $\Delta E(j\omega)$ and $I(J\omega)$ are the Fourier transforms of $\Delta E(t)$ and $\Delta I(t)$.

The same approach can be generalized to any other pair of quantities for which equations such as (1), (2), and (3) can be established. It must be emphasized that all these transmittances are derived from the same model at only the expense of introducing a few specific parameters such as the density of surface compounds in the case of gravimetry. Therefore the confrontation of the model with experiments is much more meaningful than applying techniques restricted to the current-voltage relationship.

Copyright © 2002 Marcel Dekker, Inc.

A Fast Clue to the Origin and Interpretation of Impedance The background of impedance derivation is available in several monographs and review articles [7,8,49] and will not be detailed here. Only a shortcut to a qualitative understanding is given here, allowing one in principle to relate the main shapes of the impedance plots to basic features of the electrode processes.

This so-called faradic impedance Z_F basically displays the frequency response of the elementary phenomena participating in the electrochemical transfer of charges across the interface.

The general structure of the frequency dependence of Z_F stems readily from Eq. (3) in its differentiated form:

$$\frac{\Delta I_F}{F} = \frac{\partial \Phi}{\partial E}\Delta E + \frac{\partial \Phi}{\partial C_{sj}}\Delta C_{sj} + \frac{\partial \Phi}{\partial C_j}\Delta C_j \tag{4}$$

Each of these partial derivatives gives rise to a specific contribution to the faradic impedance. They can be split into two groups:

The partial derivative with respect to E (at constant C_j and C_{sj}) is assumed to represent the instantaneous (on our time scale) response of the charge transfer process. A pure resistance is therefore associated with this term: the charge transfer resistance denoted by R_t.

The partial derivative with respect to C_j and C_{s_j} that introduced, through the delayed resposes of C_j and C_{s_j} the frequency dependence of Z_F.

The simplest situation is found when the bulk concentrations are kept constant by an appropriate stirring device (usually RDE), hence $\Delta C_j = 0$. The ΔC_{s_j} are given by the solution of the set of ordinary linear first-order differential equations obtained by linearization of Eq. (2) under a sine wave potential perturbation $\Delta E = |\Delta E| \exp j\omega t$. Resolution by the Kramers method immediately shows that $\Delta C_j / \Delta E$ is expressed by a rational function of the imaginary angular frequency $j\omega$:

$$\frac{\Delta C_{s_j}}{\Delta E} = \frac{N_j(j\omega)}{D(j\omega)}$$

where the degree of D is equal to the number k of concentrations C_{s_j} involved in the kinetics; the degree of N is $k - 1$. More intricate situations are found when the bulk concentrations C_j also contributes to the relaxation. Integration of the linearized form of Eq. (1) with proper boundary conditions at the electrode surface, superscript (o), yields the complex ratio $\Delta C_j / \Delta \phi j$ as a function of the mass transfer parameters.

Diffusion across a Nernst boundary layer (thickness δ, diffusivity D) produces the well-known convective-diffusion term:

$$\frac{\Delta C^{\circ} j}{\Delta \phi_j} = -\frac{\delta}{D}\frac{\tanh\sqrt{(j\omega\delta^2/D)}}{\sqrt{(j\omega\delta^2/D)}} \tag{5}$$

Finally, Z_F is given by

$$\frac{1}{Z_F} = \frac{1}{R_t} + F\sum_j \frac{\partial \phi}{\partial C_{sj}}\frac{\Delta C_{sj}}{\Delta E} + F\sum_j \frac{\partial \phi}{\partial C^{\circ} j}\frac{\Delta C^{\circ} j}{\Delta \phi_j}\frac{\Delta \phi_j}{\Delta E} \tag{6}$$

where the charge transfer resistance R_t is the limit of Z_F for $\omega \Rightarrow \infty$.

Copyright © 2002 Marcel Dekker, Inc.

As illustrated in this chapter, Eq. (6), in parallel with the double-layer capacitance C_{dl}, generates identifiable shapes on the impedance curves in the Bode or Nyquist plane making possible to determine the number of chemical entities C_{s_j} and C_j participating in the reaction mechanism and thus providing information on the reaction pattern. In terms of dissolution-passivation processes, capacitive responses and negative resistances are related to inhibition or passivation whereas inductive behaviors arise from catalytic effects or activating intermediates [4–8]. Acquisition and processing of the transient response of electrochemical systems are easily performed by modern laboratory equipment [5,6,49] and do not deserve special attention in this chapter.

Local Electrochemical Measurements Practically any real-life solid electrode exhibits, for structural and/or geometric reasons, heterogeneities in surface properties and therefore in reactivity. The characteristic dimension may range between the nanometric scale and the macroscopic size of the electrode. The traditional electrochemical measurements provide surface average quantities, in both current and potential. The information can be extremely biased, in somes cases totally obscured, when sharp differences in reactivity are present. This is often the case for anodic dissolution under the influence of metallurgy and/or composition. In order to overcome the problem, techniques have been introduced for collecting local values of the potential and current densities at short distances above the electrode surface. Potential probes have long been known for attenuating the ohmic drop (Haber-Luggin capillaries). Current probes have been developped intensively in the last 15 years. They are based on the measurements of the ohmic drop along a short current path in the solution. Most of the studies used the so-called SVET technology (scanning vibrating electrode technique) or to a lesser extent twin electrodes. Current mapping thus obtained, with a spatial resolution at best about 15 μm, is essentially applied for imaging galvanic currents associated with local cells in corrosion. The techniques were extended to transient regimes, and spatially resolved impedance measurements (LEIS, local electrochemical impedance spectroscopy) [50–54] are now available with valuable performance. Undoubtedly, serious advances in the interpretation of the kinetics of anodic dissolution can be expected in the near future from the growing application of these techniques.

Complex transmittances relevant to corrosion phenomena have been introduced [36,38,39]. Examples are given in several parts of the chapter. Two of them deserve a particular interest. The case of techniques pertaining to the rotating ring disk electrode (RRDE) is dealt with here. Electrogravimetric transmittance, a frequency-resolved technique based on the electrochemical quartz crystal microbalance (EQCM), was presented in a paper in 1996 [55].

Background of Time/Frequency-Resolved Measurements with an Upstream (Emitter)–Downstream (Collector) Electrode Setup

These techniques are based on the discrimination between the dissolution and the surface film growth component of the working electrode current [56]. The following derivation makes used of the RRDE parameters indexed D (disk) and R (ring). The transposition to an upstream-downstream pair of electrodes in any kind of flow cell (e.g., channel flow double electrode, CFDE) is straightforward.

Copyright © 2002 Marcel Dekker, Inc.

Electrical Charge Balance In the non-steady-state regime the electrical charge balance equation at the disk surface is

$$I_D = n_d F \Phi_d + \frac{dQ_S}{dt} \tag{7}$$

with I_D = the electrical current supplied to the disk (at the exclusion of the double-layer charging)
n_d = the dissolution valence of the disk metal
Φ_d = the flux of n_d-valent cations released in the solution
Q_S = the faradic charge stored in surface layers

Equation (7) can be extended to the emission of more than one species with different oxidation states: n_d, m_d, …

$$I_D = F(n_d \Phi_d^n + m_d \Phi_d^m) \frac{dQ_S}{dt} \tag{8}$$

The Collection Efficiencies A fraction of the flux Φ_d is collected and converted into an electrochemical current I_R on a downstream electrode owing to the transfer of nR electrons in a convenient redox reaction. At steady state, the dimensionless ratio

$$N = \frac{I_R}{n_R \Phi_d} \tag{9}$$

called the *collection efficiency* is determined entirely by the electrode layout. At the non–steady state, Φ_d is obtained:

In the time domain, through a deconvolution because one has

$$I_R(t) = n_R \int \Phi_d(t) \mathcal{N}(t - \tau) d\tau \tag{10}$$

where $N(t)$ is the characteristic *transient collection efficiency* of the device experimentally defined for $\Phi_d(t)$ = Dirac function $\delta(t)$. Unlike N, it depends on both the electrode layout and the hydrodynamic parameters (fluid velocity, viscosity, diffusivity).

In the frequency domain, through a simple division by the *complex collection efficiency* $N(\omega)$, which yields

$$\Phi_d(\omega) = \frac{I_R(\omega)}{N(\omega) n_R} \tag{11}$$

The collection efficiencies are most easily determined by calibration experiments on redox systems. In practice, the deconvolution of (10) is carried out by FFT (fast Fourier transform) using the classical equation $N(\omega)$ = Fourier transform of $N(t)$ and

$$\mathcal{N}(0) = \int_{-\infty}^{+\infty} \mathcal{N}(t) dt = N \tag{12}$$

Copyright © 2002 Marcel Dekker, Inc.

Emission Efficiency and True Capacitance Exploitation in the time domain of the differential (7) or of the integrated form $Q_d = n_d F P_d + Q_s$, where P_d is the amount of species generated by the disk dissolution, yields as the main information the charge Q_s involved in the surface layer. In the frequency domain, if Δ stands for small-amplitude variables, (7) becomes

$$\Delta I_D = n_d F \Delta \Phi_d + j\omega \Delta Q_s \tag{13}$$

or

$$1 = \frac{n_d F \Delta \Phi_d}{\Delta I_D} + \frac{j\omega \Delta Q_s}{\Delta I_D} \tag{14}$$

where the ratio $N_D = (n_d F \Delta \Phi_d) / (\Delta I_D) = 1 - (j\omega \Delta Q_s) / (\Delta I_D)$ is the *emission efficiency* of the disk, a complex dimensionless quantity representing the fraction of the disk current actually consumed in dissolution. Graphs of N_d in the complex plane provide a direct criterion about the kinetic role of the surface charge Q_s. For instance $(\Delta Q_s) / (\Delta I_D) < 0$; i.e., charge buildup producing a decrease of the dissolution current (e.g., an electrochemically grown passivating layer) is displayed as a positive imaginary part.

In order to get the true electrode capacitance Γ_s, related exclusively to the film growth, Eq. (14) can be further coprocessed with the faradic impedance of the disk:

$$Z_{D,F} = \frac{\Delta E_D}{\Delta I_D} \quad \text{according to} \quad \Gamma_s = \frac{\Delta Q_s}{\Delta E_D} = \frac{\Delta Q_s}{\Delta I_D} \frac{1}{Z_{D,F}}$$

The application of the technique in the time and frequency domains is illustrated hereafter for the passivation of iron in acidic solutions.

Anodic Dissolution of Metals and Inductive Behaviors

It has long been recognized, originally in the time domain (transient measurements) and later in the frequency domain (impedance measurements), that the non-steady-state response of anodically dissolving metals displays in most cases an inductive-like behavior. With the galvanostatic step used in the early work, this behavior showed up as a voltage peak (overshoot), its counterpart in potentiostatic mode being a minimum of current density. In the frequency domain an inductive loop of the Nyquist plot was first identified by Keddam et al. [43–46] in the case of iron in acidic media and interpreted by the so-called consecutive dissolution mechanism (see later).

Classical Interpretation It was known from the previous work by Gerischer and Mehl [42] on hydrogen evolution that a reaction path involving two consecutive steps coupled by an adsorbed intermediate species can generate either an inductive or a capacitive reaction impedance depending on the kinetic parameters. The detailed derivation is given in the next section devoted to iron dissolution. It can be shown according to (6) that, for a Langmuir type of adsorption and single-electron transfers, Z_F is given by the equation

$$\frac{1}{Z_F} = \frac{1}{R_t} + \frac{1}{\rho} \frac{1}{[F_j \omega \beta / (J_1 + J_2)] + 1} \tag{15}$$

Copyright © 2002 Marcel Dekker, Inc.

where R_t and ρ are resistances depending on the kinetic parameters of the reaction steps, β is the maximum surface concentration of the adsorbed intermediate, J_1 and J_2 are the current densities of the first and second steps, and F is the Faraday constant. Z_F is inductive for parameter values such that ρ is positive; this is shown to occur for $J_1 < J_2$. In this case Z_F can be split immediately into two parallel branches by identification of (15) to (16):

$$\frac{1}{Z_F} = \frac{1}{R_t} + \frac{1}{jL\omega + \rho} \tag{16}$$

the self-inductance L being given by

$$L = \frac{F\beta\rho}{J_1 + J_2} \tag{17}$$

The characteristic frequencies associated are in the admittance plane

$$\omega_0^a = \frac{\rho + R_t}{L} = \frac{(J_1 + J_2)}{F\beta} \tag{18}$$

and in the impedance plane

$$\omega_0^z = \frac{\rho + R_t}{L} = \frac{[1 + (R_t/\rho)](J_1 + J_2)}{F\beta} \tag{19}$$

Both quantities are increasing functions of the DC current density:

$$J = 2\frac{J_1 J_2}{J_1 + J_2} \tag{20}$$

The ratio $F\beta$ is about one monolayer of elementary electrical charges per area unit of the interface. Many experiments were found to agree with this model even though several authors mentioned values definitely exceeding one monolayer and serious deviations from Eqs. (18)–(20). Inductive loops at lower frequencies with little or no current dependence are ignored in this discussion.

Weak Points and New Model: This problem was revisited in two papers [57,58]. The first one established from a thorough survey of the literature of metal and semiconductor dissolution that the frequency of the inductive impedance, in contradiction of Eq. (19), is remarkably proportional to the DC current over several orders of magnitude:

$$\omega_0^z = \frac{J}{F\beta} \tag{21}$$

The meaning of the deviation between (19) and (21) can be perceived by noting that according to (18) the frequency is determined by the faster of the two reaction steps wherever (21) relates it to the slower one. In the second paper, an original interpretation is proposed. It is based as well on a two-step process between the metal atom at the lattice surface and the cation in solution on the outer side of the double layer. A detailed presentation of this approach is far beyond the scope of this chapter. It will be only outlined briefly. Basically, the relaxation is ascribed to the time dependence of the surface concentration of an intermediate state of dissolution. In that sense, the model ingredients are quite similar to those of the consecutive mechanism, namely:

Copyright © 2002 Marcel Dekker, Inc.

The ionization proceeds through a two-step path involving an intermediate state (partially solvated).
The interface is (statistically) shared between the intermediate state (fractional coverage θ) and the ground metallic state (1 – θ).
The model is still compatible with monovalent dissolution (Ag ⇒ Ag^+, for instance).
The time dependence is due to the difference between the fluxes of metal species crossing the interface on the inner and outer sides of the intermediate state.

The new ideas lie essentially in the adjustement of the potential profiles in the metal side (jellium) and the electrolyte side of the double layer in order to comply with charge balance in conduction and electrostatic properties at the interface. This is sketched in Figure 2. According to Ref. [58], the impedance has a structure similar to (15). It can be cast in the form

$$\frac{1}{Z_F} = j\omega\left(\frac{C_1C_2}{C_1+C_2}\right) + \frac{1}{R_t} + \frac{j\omega[C_2/(C_1+C_2)] + (1/F\beta)(\partial J/\partial\theta)}{jL\omega + \rho} \tag{22}$$

where C_1 and C_2 are the capacitances of the inner and outer parts of the double layer, respectively. With this model, the linear dependence of frequency on DC current can be simulated for acceptable sets of parameters including values of C_1 and C_2 consistent with modern theories of the double layer. However, the ratio of one monolayer is hardly obtained.

Actually, the model introduces a strong coupling between charge transfer and double-layer structure, a feature generally discarded in spite of the high interfacial concentration of cations released by the dissolution. In some way it may be regarded as a ζ-potential approach to the problem. The topic of the kinetics content of the inductive impedance of anodically dissolving metals is still an open question. Obviously, it deserves further theoretical and experimental efforts.

ANODIC DISSOLUTION OF PURE METALS

Even though of little interest for practical corrosion problems, pure metals are extremely basic to any approach to the mechanism of anodic dissolution, which is believed to be much simpler than for alloys. However, the electrochemical behaviors of high-purity metals can be deeply influenced by vanishingly amounts of impurities able to segregate at the interface during anodic dissolution and also by metallurgical factors. This may explain misleading interpretations and serious discrepancies between materials from different sources with the same purity grade.

Mechanism of Heterogeneous Reaction: Dissolution in the Active State

The case of iron will be taken as an example of heterogeneous reaction in the active range of dissolution. Some other metals are also dealt with briefly.

Copyright © 2002 Marcel Dekker, Inc.

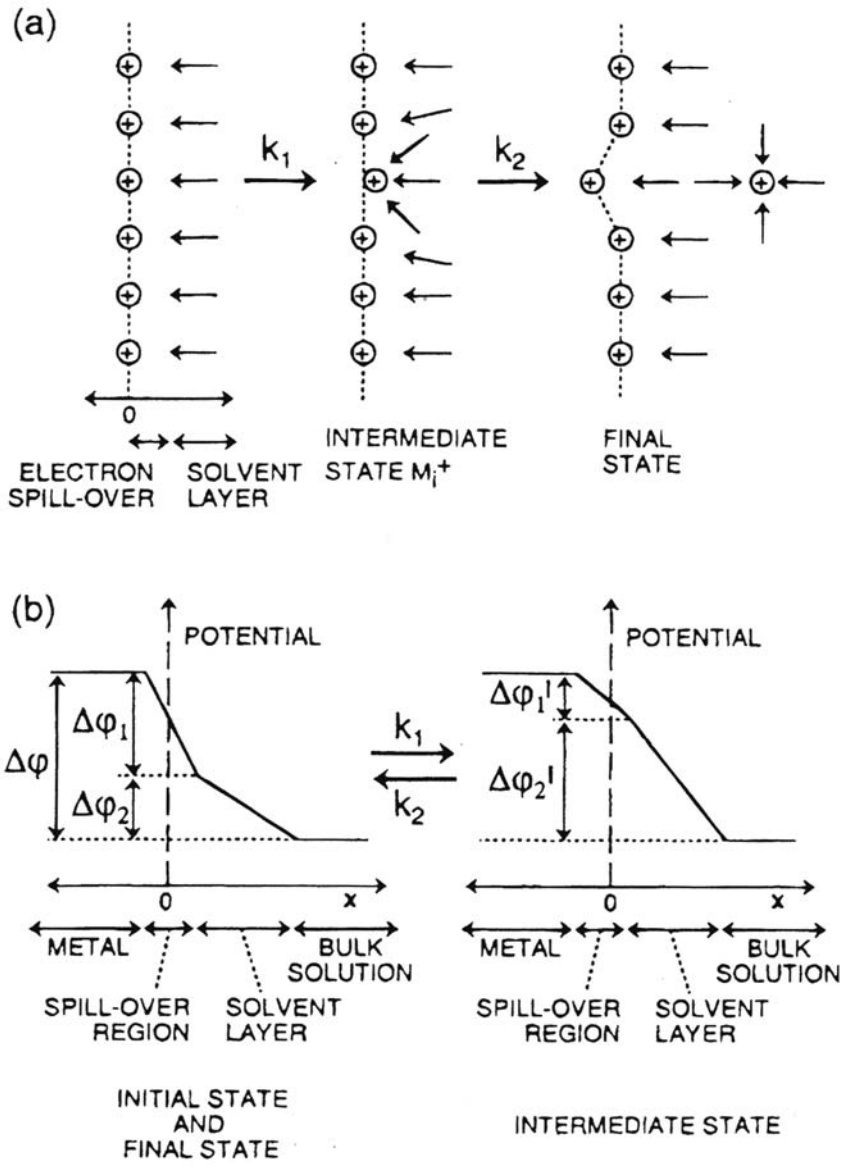


Figure 2. (a) Sketch of the two consecutive ion-tranfer steps in anodic dissolution (b) Sketch of the distribution of the interfacial potential drop $\Delta\varphi$ across the electrochemical double layer. From ref [58].

Active Dissolution of Iron in Acidic Solutions

The active dissolution of iron in acidic media has been the subject of a very large number of papers for the last 40 years. All the reaction mechanisms are based on the generally agreed upon experimental evidence that the dissolution rate increases with the solution pH at potentials well below the onset of passivity processes. The apparently unacceptable participation of hydroxyl ions in the reaction at these low pH

Copyright © 2002 Marcel Dekker, Inc.

values can be related to the strong dissociative power of transition metals with respect to water, an assumption supported for Fe by experimental evidence in ultra-high vacuum [59]. Both groups of mechanisms stem from a common initial hydrolysis step assumed to be at equilibrium:

$$Fe + H_2O \rightleftarrows (FeOH)_{ads} + H^+ + e^- \tag{23}$$

thus accounting for the pH dependence of the subsequent dissolution step. They diverge from each other by the nature of the dissolution steps leading to the soluble divalent species.

According to the catalytic mechanism [22], $(FeOH)_{ads}$ enters in a catalytic sequence of dissolution at the end of which $(FeOH)_{ads}$ is regenerated and Fe dissolved as ($FeOH^+$):

$$Fe + (FeOH)_{ads} \rightleftarrows Fe(FeOH)_{ads} \tag{24}$$

$$Fe(FeOH)_{ads} + OH^- \rightarrow FeOH^+ + (FeOH)_{ads} + 2e^- \tag{25}$$

A reluctant criticism of the catalytic mechanism is directed against the quantum mechanically unacceptable transfer of two electrons in a single step. It must be pointed out that on considering even a very crude atomistic content of this two-electron step it appears less definitely excluded. Interpretation in terms of kink Fe_k shifted to the next neighboring atom, denoted Fe′, in the dissolving edge:

$$Fe'(Fe_kOH)_{ads} + OH^- \rightarrow FeOH^+ + (Fe'_kOH) + 2e^- \tag{26}$$

clearly shows that the two electrons are not transferred from the same Fe species.

According to the consecutive mechanism [23], $(FeOH)_{ads}$ enters in a noncatalytic one-electron transfer step by which it is oxidized to ($FeOH^+$):

$$(FeOH)_{ads} \rightarrow FeOH^+ + e^- \tag{27}$$

Finally, $FeOH^+$ is assumed to react with solution protons:

$$FeOH^+ + H^+ \rightarrow Fe^{2+}_{aq} + H_2O \tag{28}$$

Mechanistic Criteria Based on Steady-State and Transient Polarization Data

For a long time, with the exception of the pioneering impedance approach of Epelboin and Keddam [60], the controversy about the validity of these mechanisms remained based on kinetic criteria drawn from true steady-state and fast polarization techniques. Tafel slopes and orders of reaction with respect to OH^- are the two main parameters taken into consideration.

In theory, the transient state is assumed to take place at times short enough to keep the concentration of $(FeOH)_{ads}$ "frozen" at its initial value. Therefore the initial transition is due only to the change of the reaction rate of step (26) or (27) under the effect of potential at constant $(FeOH)_{ads}$ concentration. The same discrimination between instantaneous and delayed contributions is at the origin of the frequency dependence of the faradic impedance. Table 1 shows the theoretical and experimental values of the steady-state and transient kinetic parameters for both mechanisms, according to Ref. 12.

According to Table 1, the delimitation between the two mechanisms relies on a quite clear-cut difference in the set of kinetics criteria and would not involve

Copyright © 2002 Marcel Dekker, Inc.

Table 1 Kinetic Data for Iron Dissolution at T = 298 K

	Catalytic mechanism		Consecutive mechanism	
	Calculated	Experimental	Calculated	Experimental
Tafel slope, mV	29.6	30 ± 2	39.4	40 ± 2
Reaction order/OH^-	2	2 ± 0.3	1	1 ± 0.1
		Steady-state		
Tafel slope, mV	59.2	60 ± 7	40	60 ± 7
Reaction order/OH^-	1	1 ± 0.1	0.5	00.5 ± 0.1
		Transient		

Source: Ref. 12.

controversy at all. In fact, a careful analysis of literature data putting the emphasis on experimental conditions leads to the following remarks [61,62]:

Tafel slope values are spread over a wide range from less than 30mV to more than 100 mV depending on ill-identified parameters. The role of metallurgical factors such as dislocations and subgrain boundaries was interpreted as favoring the catalytic mechanism (30 mV), whereas annealed iron with a low density of structural defects would obey the consecutive mechanism (40 mV) [61,62].

In many early studies iron dissolution was investigated as part of corrosion and inhibition at open-circuit potential under an H_2-saturated atmosphere, no account being taken of the interference of the H_2/H^+ reaction with the Tafel slopes [63,64]. Even under an inert atmosphere, the anodic parameters may be affected by slow hysteresis phenomena resulting in steeper Tafel lines [65–69].

Reaction order measurements are not always very reliable and are sometimes reported with fractional values [12].

Current transients are much too long to be consistent with the minimal exchange current density still compatible with reaction (23) being at pseudoequilibrium [70]. Alternative explanations based on local increase of pH have been proposed [65] and further elaborated [70].

From the impedance approach it was then established that the iron mechanism is far more complex than expected from early experiments and can hardly be investigated correctly by current-voltage plots in spite of continued efforts [71,72]. Thorough analysis over extended ranges of electrode potential, pH, and frequency is presented in the following.

Atomistic Interpretation of the Catalytic Mechanism Anodic dissolution of iron is probably the sole case for which an atomistic description was elaborated with a somehow successful issue. An early attempt to explain the transient regime of iron dissolution by relaxation of etched pits by a nucleation and growth model can be found in Ref. 65 and is analyzed in Ref. 60. Starting in the middle of the 1970s, Heusler et al. have developed in a series of papers [29–31] an experimental and modeling approach aimed at giving a crystallographic basis to the catalytic mechanism. Correlation of kinetic and morphological data was performed on a

Copyright © 2002 Marcel Dekker, Inc.

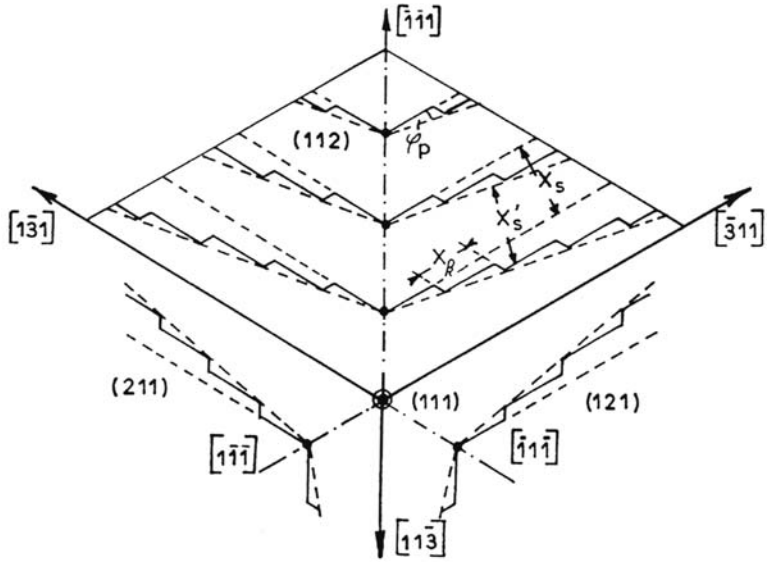


Figure 3. Schematic model of steps and kinks on crystallographic (211), (112) and (121) planes projected into a (111) plane. From ref [30].

surface vicinal to {211} (misorientation ≅ 1°) of iron single crystals in acidic solutions. These surfaces are found to develop a relatively simple steady-state morphology made of triangular pyramids limited by nearly perfect {211} planes and ⟨311⟩ edges. A schematic model of steps and kinks projected on a {111} plane is given in Figure 3.

Steps are generated at the pyramid apex and move away on the three {211} planes. The structure of the dissolving surface is determined by x_S, the mean distance of steps perpendicular to the ⟨311⟩ direction:

$x_s = bN_p / N_S$ with b = interatomic distance
N_P = probability of generation of six steps at the apex
N_S = probability of kink generation at the intersection of two monatomic steps

and x_k, the mean distance of kinks:

$$x_k = bN_k / N_P$$

where N_k is the probability of removing an atom from a kink.

The current density j is the product of the current on one kink ze_0N_k by the density of kinks: $j = ze_0N_k / x_sx_k$.

Scanning electron microscopy (SEM) examinations, [29] of the macroscopic morphology of dissolution were then substantiated by transmission electron microscopy (TEM) pictures of gold-decorated surfaces [30]. The better resolution, even though not truly atomic, allowed an estimate of x_s and x_k and of their dependence on the dissolution rate as shown in Figure 4. The surface concentration of kinks $(x_sx_k)^{-1}$ is an exponential function of the potential with an $\exp(FE/RT)$

Copyright © 2002 Marcel Dekker, Inc.

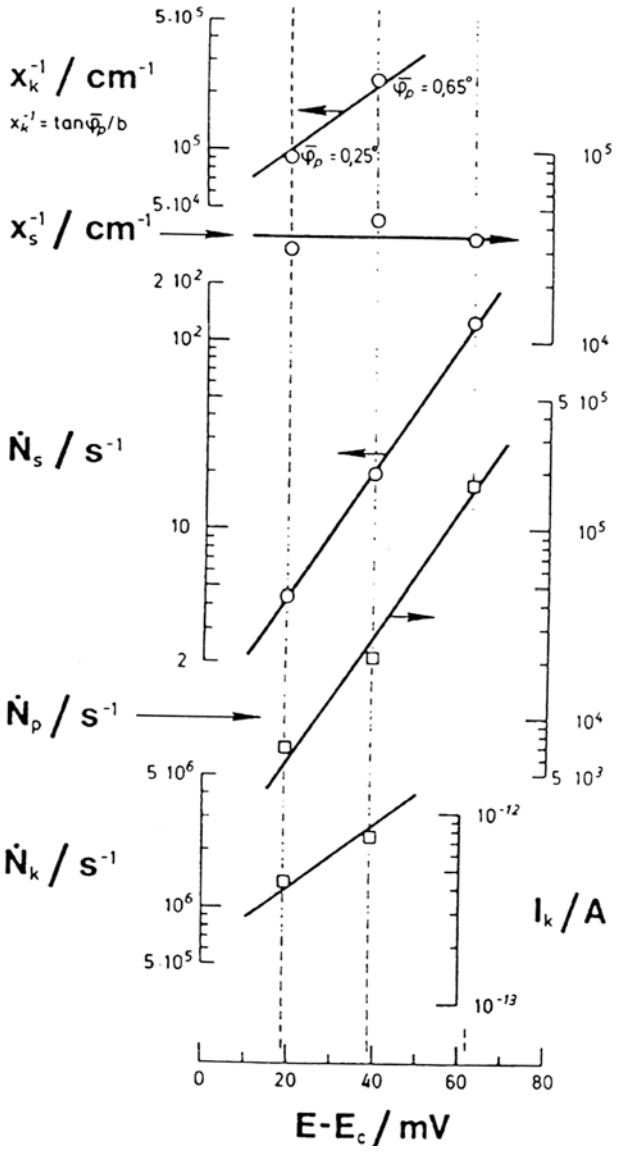


Figure 4. Potential dependence of structural parameters and mean rates of elementary processes for three different polarization conditions. TEM measurements on replica of gold-decorated surfaces after anodic dissolution. Johnson-Matthey iron. From ref [30].

dependence. The potential-dependent parameter is $x_k \cong \exp - (FE/RT)$ while the mean distance of steps, x_s, remains constant. Consistent with the catalytic mechanism, at steady state the dissolution rate of atoms at kinks obeys an $\exp(1 + 2\alpha)FE/RT$ Tafel law and, at constant kink density, the elementary rate of atom dissolution is proportional to $\exp(RE/RT)$, i.e., $\alpha = 0.5$ and transfer of $n = 2$ electrons in a single step.

Copyright © 2002 Marcel Dekker, Inc.

A rather convincing justification of the catalytic mechanism is reached in terms of atomistic events, at least on conveniently oriented crystal faces. Now, in turn, the problem remains of understanding the pH dependence of the step nucleation probability [31]. Further investigation of iron dissolution by impedance analysis has clearly proved that both catalytic and consecutive mechanisms are operative with a relative contribution depending upon electrode potential and solution pH.

Advanced Study of Iron Dissolution by Impedance Techniques Early application of impedance measurement to the anodic dissolution of iron in acidic media demonstrated the inductive character of the faradic impedances. The reaction scheme initially proposed [13,60] is modified according to:

$$\mathrm{Fe} + \mathrm{H_2O} \underset{K_0}{\overset{K_0}{\leftrightarrows}} \mathrm{FeOH^-} + \mathrm{H^+} \tag{29}$$

$$\mathrm{FeOH^-} \xrightarrow{K_1} (\mathrm{FeOH})_{\mathrm{ads}} + \mathrm{e^-} \tag{30}$$

$$(\mathrm{FeOH})_{\mathrm{ads}} \xrightarrow{K_2} \mathrm{FeOH^+} + \mathrm{e^-} \tag{31}$$

The initial fast chemical hydrolysis step is introduced to account for the order of the first reaction with respect to OH^- confirming the results of previous authors [13]. This modification, introduced later [71,72], implies clearly that the origin of chemisorbed hydroxyls is the dissociation of water.

Steady-state current-voltage characteristics and faradic impedance associated with the mechanism (24) to (31) were derived and numerically simulated with the following assumptions:

Step (29) in fast equilibrium, i.e., surface concentration of $FeOH^-$ proportional to $[OH^-]$ and time independent

Two-dimensional (2D) surface coverage θ by $(FeOH)_{ads}$ governed by a Langmuir adsorption isotherm

Rate constants K_1 and K_2 obeying Tafel kinetics with symmetry factors ($0 < \alpha_i < 1$) but not constrained to 0.5:

$$K_i = k_i \exp \frac{\alpha_i}{RT} FE$$

With this particular mechanism, Eqs. (2) and (3) are written as

$$\frac{\beta d\theta}{dt} = K_1(1-\theta)[\mathrm{OH^-}] - K_2\theta\beta \tag{32}$$

where β is the surface concentration of $(FeOH)_{ads}$ at full coverage ($\theta = 1$).

$$\frac{J}{F} = K_1(1-\theta)[\mathrm{OH^-}] + K_2\theta\beta \tag{33}$$

The steady-state coverage θ_S obtained by solving (32) for $d\theta/dt = 0$, introduced in (33), gives a current-voltage relationship:

$$J_S = \frac{2J_1J_2}{J_1 + J_2} \tag{34}$$

Copyright © 2002 Marcel Dekker, Inc.

where J_1 and J_2 are the partial current densities flowing through steps (1) and (2):

$$J_1 = FK_1[OH^-] \quad \text{and} \quad J_2 = FK_2\beta$$

Similarly to Eq. (6), the solution of the linearized form of (32) and (33) yields the impedance expression

$$\frac{1}{Z_F} = \frac{J_s F}{2RT}\left[\alpha_1 + \alpha_2 + \frac{(\alpha_1 - \alpha_2)\ (J_2 - J_1)}{Fj\omega\beta + (J_1 + J_2)}\right] \tag{35}$$

and an associated

$$R_t J_s = \frac{2RT}{F(\alpha_1 + \alpha_2)}$$

A fair model-experiment fit is obtained for both DC and AC responses with the same set of kinetic parameters and a value of β, 3×10^{-9} mol cm^{-2}, in good agreement with one monolayer of adsorbed OH^- ions on a low-index plane of the iron lattice (2×10^{-9} mol cm^{-2} on {100}).

The next advance was achieved owing to the extension of the frequency domain into the millihertz range by digital TFA [47]. The existence of a second inductive loop was then established at lower frequencies. A branching reaction mechanism was proposed by introducing in parallel with the consecutive mechanism a catalytic dissolution path [75]. This branching reaction path was already prefiguring the main features of the more recent models covering broader ranges of pH and current density.

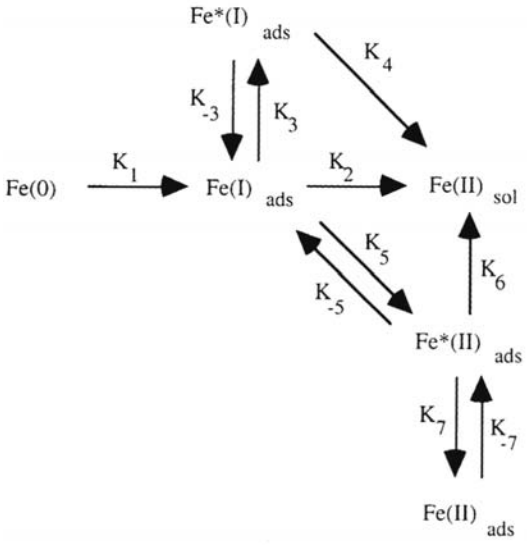
Later on, more accurate impedance measurements were reported by Lorenz et al. [76] and Keddam et al. [61,62] in 1 M sulfate solutions at $0 \le pH \le 5$ and $0 \le j \le 150$ mA cm^{-2}. Both groups agreed reasonably about the main impedance shapes and particularly the presence of three relaxation processes showing up at intermediate pH values (around 2). The models elaborated by these groups have in common the interpretation of the frequency dependence in terms of degrees of coverage by adsorbed species. However, very large differences lie in the basic assumptions regarding

- The actual nature of the surface species participating in the impedance response and the use of an adhoc "surface relaxation time constant" [68]
- The existence or not of a consecutive mechanism in one of the reaction routes
- The ability to interpret DC and AC data by a unique model in the active, transition, and prepassive range

A detailed discussion of the relative performances and flaws of these approaches can be found in Ref. 62.

A systematic analytic screening of all the possible 40 reaction schemes in which three Fe-containing surface species are involved completed by a numerical simulation finally led to selecting the reaction pattern [20] shown below. The three coverages determining the impedance properties in the active and transition domains are related to $Fe(I)_{ads}$, $Fe^*(I)_{ads}$, and $Fe^*(II)_{ads}$. The superscript (*) indicates species involved in catalytic dissolution paths. $Fe(II)_{ads}$ is a precursor of the passive film whose contribution is significant only near the second maxima and beyond.

Copyright © 2002 Marcel Dekker, Inc.



(36)

Numerical simulations showed that

The K_1, K_2 path is the consecutive mechanism early established by impedance measurements bounded to the hertz range and covering low pH and low current density [60].

The K_1, K_3, K_4 path is a catalytic route mainly operative in the transition range, the $Fe^*(I)_{ads}$ coverage being responsible for the decrease of dissolution rate past the first peak shown in Figure 5A in this range at higher pH.

The K_1, K_5, K_6 path is the main dissolution route at higher pH and current density ($j > 50$ mA cm^{-2} at pH 2 and $j > 10$ mA cm^{-2} at pH 5) controlling the second peak in Figure 5A.

Both catalytic paths introduced in this model were previously proposed by Lorenz et al. [78–81] for interpreting the prepassive dissolution range.

Comparison of Figure 5A and B at pH 5 illustrates the outstanding power of impedance measurements associated with modeling for mechanistic analysis.

The pH dependence of the rate constants proves that chemical bonds of Fe atoms with solution species contribute to a determining extent to the generation of active sites of dissolution, even in atomistic models where surface lattice features (kinks, steps, terraces, etc.) are generally put forward. Large similarities of glassy metals (amorphous) with crystalline ones [83,61] must also be regarded as arguing in favor of chemical bonds as predominant entities with respect to lattice related sites.

Further support for the existence of a branching reaction pattern was obtained from RRDE investigations [84]. It is found, as shown in Figure 6, that the collection efficiency N for the oxidation to the trivalent state of the divalent Fe species released by the dissolution of the iron disk decreases with pH and current density.

This is interpreted by paths K_4 and K_6 producing less reactive Fe(II) species than K_2 does. In agreement with this view, the lower the rotation speed, the larger the collection efficiency [84] because a homogeneous chemical reorganization of the

Copyright © 2002 Marcel Dekker, Inc.

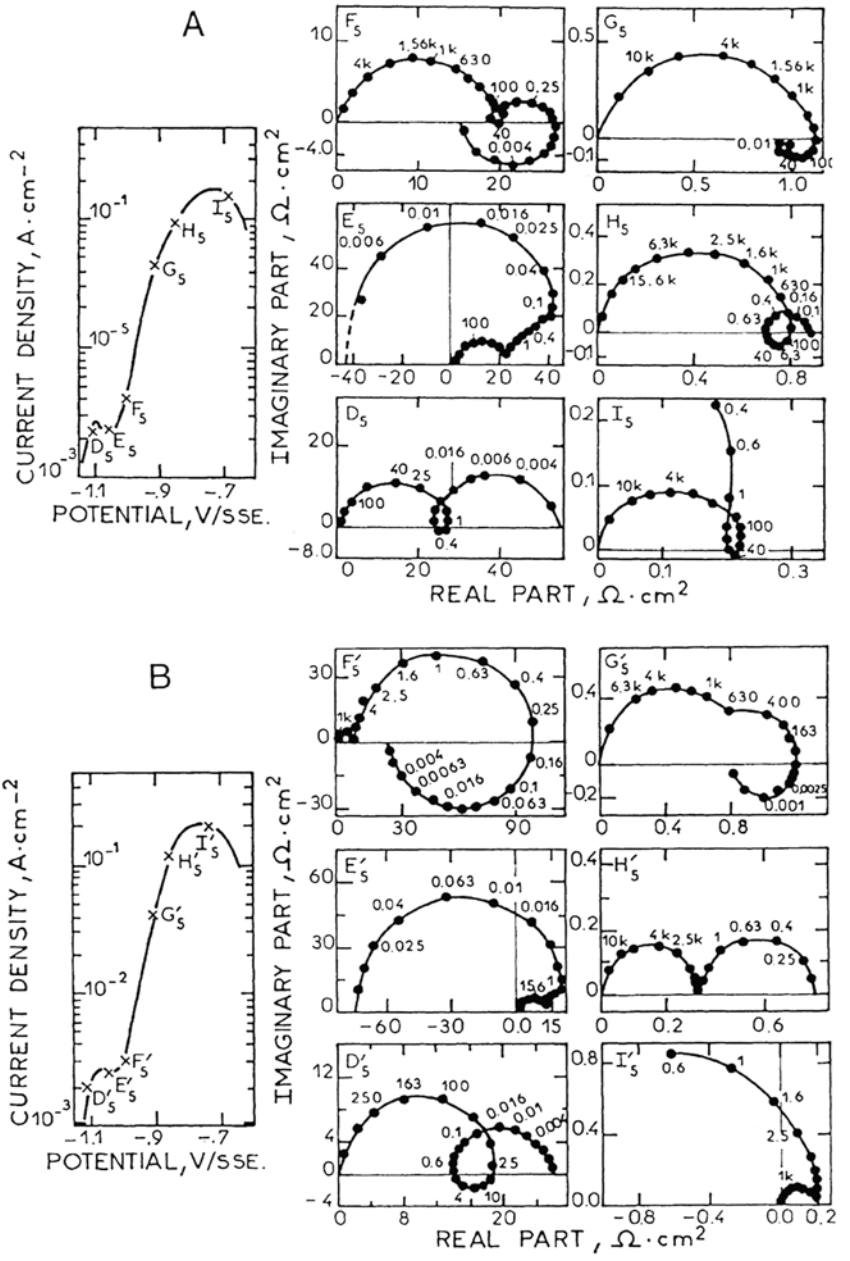


Figure 5. Experimental (A) and calculated (B) current-potential curves and complex impedance diagrams at the corresponding points labelled on I(E) curves (Frequency in Hz) (Johnson-Matthey iron, l M sulfate, pH = 5, 25°C). Numerical simulation (B) according to the reaction mechanism (36). From ref [61].

Copyright © 2002 Marcel Dekker, Inc.

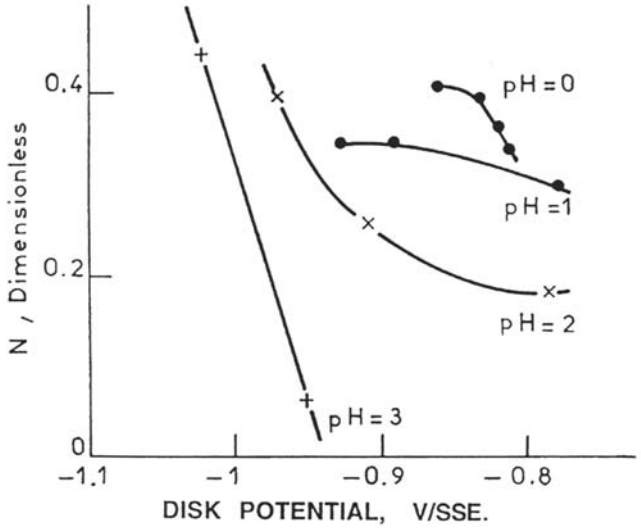


Figure 6. Potential dependence of the collection efficiency: influence of solution pH (ring reaction $Fe^{2+} \rightarrow Fe^{3+}$) for iron dissolution (Johnson-Matthey iron 1M sulfate). Theoretical collection efficiency [37]: 0.48. Shift to cathodic potentials at increasing pH is consistent with Figure 5. From ref [84].

cation into a more reactive one is taking place between disk and ring. Such a chemical step is formally accounted for in most reaction mechanisms by the following step:

$$FeOH^+ + H^+ \rightarrow Fe^{2+} + H_2O$$

Similar results are reported in Ref. 85 from channel flow double electrode (CFDE).

Role of Anions in the Anodic Dissolution of Iron

The specific role of the electrolyte composition at a given pH is an extremely common experience. The contribution of anions other than hydroxyl is expected through the acid-catalyzed or anion-ligand mechanism [24,25]. It must be emphasized that the role of pH in polyacids, such as H_2SO_4, may be obscured by the correlated changes of electrolyte composition depending on acidity constants [86].

Specific anion dependence is expected to occur in the passive and transpassive domains, and dissolution in the active range can be made to deviate from the hydroxo-ligand mechanism [87] only by anions able to replace OH^-, essentially SH^- [88] and the halide ions. In the case of iron, due to the well-known passivity breakdown and subsequent localized corrosion by halide ions and particularly Cl^-, chloride effects have been investigated extensively. Complexing anions such as acetate have also been considered to a lesser extent.

In the case of acetate, a series of papers [71,86,89] considered the participation of the anion from the initial reaction steps of dissolution and it was also claimed that this anion contributes only to the dissolution of aged solid phases [90]. Later studies [86,89] in acetate solutions at neutral and slightly acid pH reported a clear negative order with respect to A^- or HA. A model is derived on the basis of the participation of HA and OH^-, which are assumed to play a symmetric role with the formation of

Copyright © 2002 Marcel Dekker, Inc.

$(Fe(OH)_2)_{ads}$, $(Fe(OHA))_{ads}$, and $(FeA_2)_{ads}$. The kinetics of iron dissolution in the active range in the presence of halide ions X^- is largely dominated by the competitive adsorption of X^- [88] with the dissolution activating OH^-. A critical survey of the possible reaction paths in which Cl^- competes with other anion adsorption is given in Ref. 73. The mechanism is claimed to depend on the pH range. The catalytic step of dissolution in Cl^--free media [63] is considered to become at medium acidities (pH > 0.6):

$$FeCl^-_{ads} + FeOH^-_{ads} \rightarrow FeOH^+ + Fe + Cl^- + 2e^- \tag{37}$$

In strongly acidic solutions the formation of the surface complex $FeCl^-H^+$ and dissolution as $FeCl^-$ are proposed to interpret the accelerating effect of H^+ on the dissolution rate [73].

According to other authors [91,92], Cl^- and OH^- would play a symmetric role by forming $(FeClOH)^-_{ads}$ as an intermediate in a consecutive mechanism followed by the rate-determining step

$$(FeClOH)^-_{ads} \rightarrow FeClOH + e^- \tag{38}$$

and in highly acidic solutions [92] the contribution of Cl^- in the dissolution path is depicted by the formation of $(FeCl)_{ads}$ and $FeClH^+$ as intermediate species.

Impedance measurements have been applied to iron dissolution in Cl^--containing media [93–95]. Based on the mechanism for sulfate media and similarly to earlier work [61,62], a branching pattern was proposed in (HCl / NaCl) involving a consecutive and a catalytic dissolution path having $(FeOH)_{ads}$ as a common bifurcation species. A third reaction path of the consecutive type with $(FeClOH)^-$ as an intermediate is in agreement with Ref. 91. An interpretation of the role of Cl^- was advanced [94,95] in the framework of a progressive modification of the sulfate mechanism [61,62] as a function of the chloride concentration, up to the sulfate-free medium.

Mechanistic changes with pH are interpreted in a semiquantitative way as follows: a gradual increase of Cl^- content initially reduces the contribution of the (K_1, K_5, K_6) dissolution path in favor of a catalytic step similar to (K_4), the $Fe^*(I)_{ads}$ catalyst now being a Cl^--containing species.

Active Dissolution of Other Metals

The metals belonging to the so-called iron group (Co, Ni), which exhibit an active-passive transition, have been far less extensively investigated than iron itself. The state of the art can be found in Ref. 2. Little contribution is due to impedance measurements and the mechanisms must be regarded as much less solidly established than for iron.

Cobalt Cobalt seems to behave much similarly to iron and its dissolution is assumed to take place through the formation of $(CoOH)_{ads}$, a catalyst surface species produced in an initial step of dissociative adsorption of water analogous to Eq. (23). Regarding the structural description of the dissolution mechanism in term of kinks at the lattice surface, cobalt and iron apparently follow the same process in which atomic kinks are assimilated to catalytic sites $(CoOH)_{ads}$. Unfortunately, in the case of Co, microscopic evidence of the changes of surface morphology and consequently estimation of the kink-kink distance are lacking.

Copyright © 2002 Marcel Dekker, Inc.

Nickel The mechanism of active dissolution of nickel remains highly controversial. It seems that there is no agreement so far even on the actual shape of the current-voltage profiles. Two-peak or single-peak curves are reported, depending on the potential sweeping rate, the prepolarization conditions, the structural properties of the metal, etc. This erratic behavior is tentatively ascribed to either the remanence of stable natural oxides on the metal surface or strong interaction with hydrogen. It must be pointed out that experiments performed in situ on a surface continuously refreshed by mechanical abrasion never yielded more reproducible results.

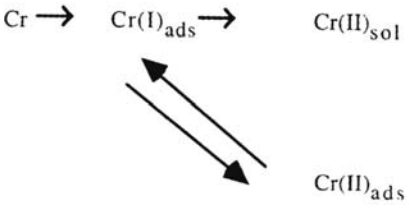
Chromium Due essentially to its role in the corrosion resistance of stainless steels, the anodic behavior of Cr has been far more extensively considered. An overview can be found in Ref. 96. Early studies were based on polarization curves [97] and potential transient experiments [98].

Most of the significant data are established by impedance [43,99,100] and RRDE [101,102] and reveal rather poor reproducibility, probably because of interference with hydrogen overvoltage and its metallurgical dependence. Simultaneous dissolution as Cr^{2+} and Cr^{3+} in the active and active-passive transition ranges [103] and no pH dependence of the dissolution rate led, in contrast to Fe group metals, to more direct dissolution mechanisms being proposed [104]. The following oversimplified model [105,106] was considered with the purpose of accounting for the Cr dissolution in the description of Fe-Cr alloys [107].

By means of CFDE the existence of adsorbed hydroxylated intermediates CrOH and $CrOH^+$ was proposed [101] in the active dissolution range. From impedance data on polycrystalline and (100) single crystal plane [96,99], simultaneous hydrogen evolution was introduced in the anodic behavior of Cr by assuming a strong dependence of the anodic reaction on the H–Cr bonding. Evidence of diffusion-controlled kinetics in the impedance was tentatively interpreted by surface diffusion of $Cr(I)_{ads}$, and Cr dissolution and H evolution were assumed to be competing on terraces. Figure 7 shows the main aspects of this approach, which attempted to elaborate a kinetic description on the basis of an atomistic picture of the metal surface.

One of the most innovative ingredients in this model is the coexistence of H evolution and Cr dissolution on the passive areas, but divalent state of Cr in the passive range appears quite contradictory to available data from X-ray photoelectron spectroscopy (XPS).

Other Metals Titanium [108–110] and copper [111] are among the more extensively investigated metals not pertaining to the iron group or being major constituents of stainless steels.



(39)

Copyright © 2002 Marcel Dekker, Inc.

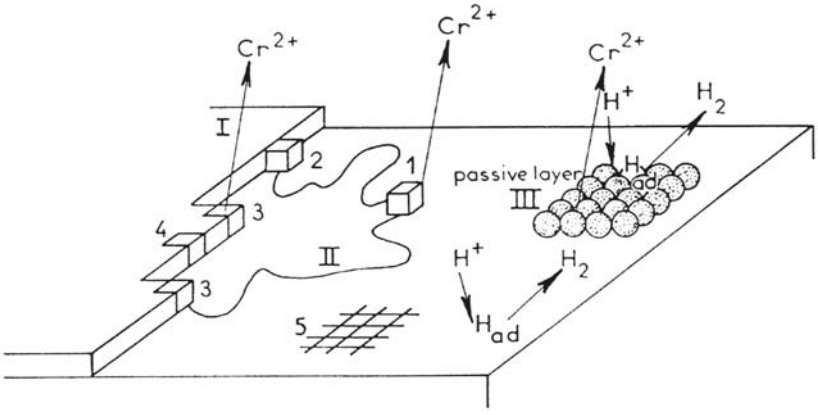


Figure 7. The corrosion processes occurring at a chromium-sulfuric acid solution interface. From ref [96].

Recent Advances in the Mechanism of Passivation by Downstream Collector Electrode Techniques

In spite of the very elaborate approaches based on current-voltage techniques, credible steady-state and transient mechanisms have hardly been derived for the transition from the active to the passive range. An accurate description of the whole set of elementary steps requires additional data on the relative contribution of the oxidation current to the formation and growth of 2D and 3D layers and on the release of cations in solution. Passivation mechanisms can be elaborated on the basis of the active-passive transition in two complementary ways:

Analysis of passivation transients on an initially active surface either by applying a steep potential jump into the passive range or by creating fresh surfaces at constant applied potential by nonelectrochemical depassivation (chemical: passivity breakdown; mechanical: scratching, ultrasonic waves, etc.; radiative: laser beam impact [112,113]). These techniques have proved to be of outstanding importance for the investigation of the mechanism of localized corrosion associated with passivity breakdown [114,115].

Analysis of tiny changes of the anode maintained potentiostatically between active and passive states in the negative slope of the dissolution peak. Electrochemical impedance and frequency-resolved RRDE data are used together.

Dissolution during Transient Passivation of Freshly Generated Iron Surfaces Pulse depassivation of the upstream iron anode and collection of the Fe(II) released into the solution on a downstream glassy carbon were performed in a CFDE [116]. Transient currents I_D on the Fe anode and collected currents I_R for Fe(II) oxidation are shown in Figure 8a and b. After processing for double-layer charging and collection efficiency, the charges involved in dissolution Q_d and Q_s were discriminated from the overall charge Q_D supplied to the disk. The results as a function of pH and disk potential E_D are shown in the Figure 8c and 8d. The

Copyright © 2002 Marcel Dekker, Inc.

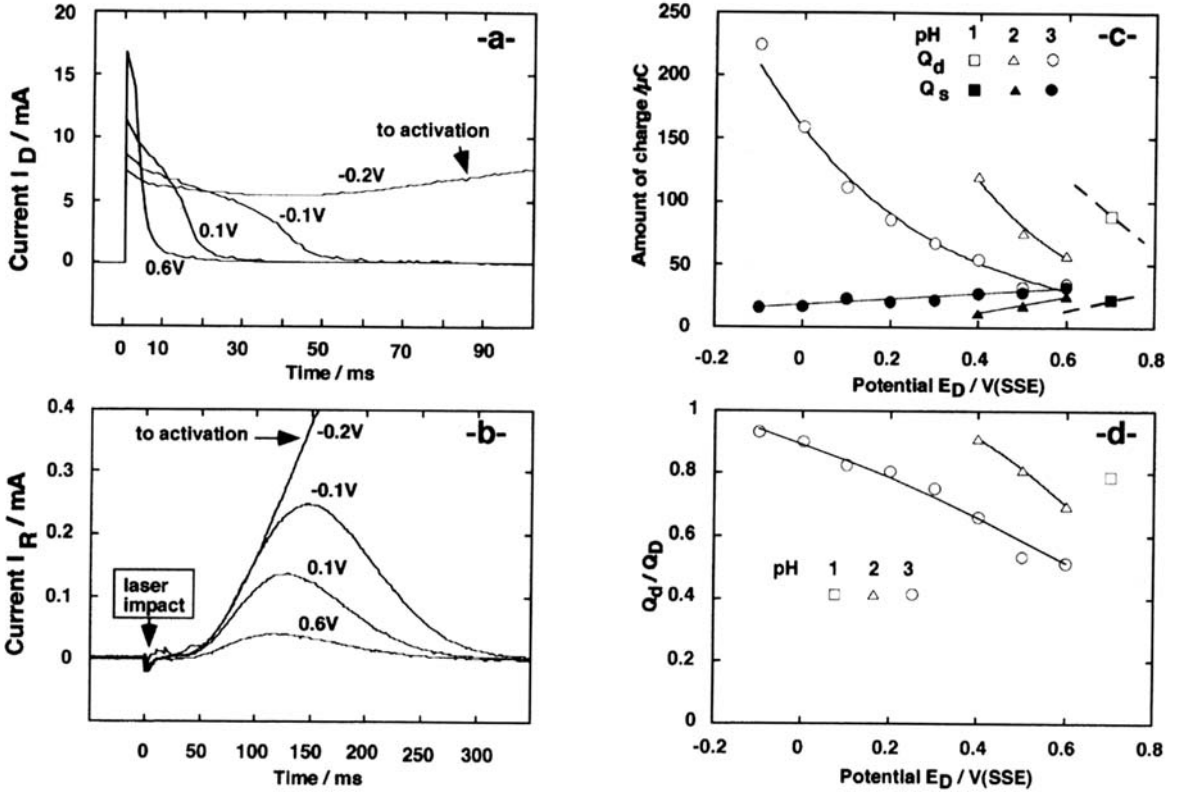
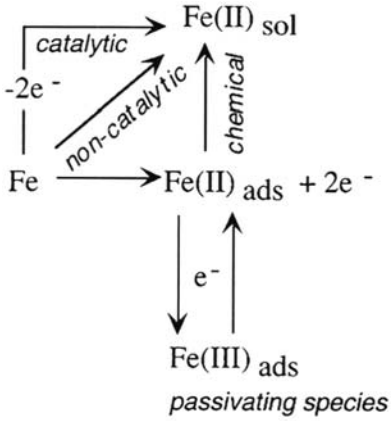


Figure 8. "a": transient currents on the Fe working (upstream) electrode. "b": detection currents on the glassy carbon collector (downstream) electrode 1M Na_2SO_4 acidified to pH 3. "c": potential dependence of the charge Q_d for dissolution of ferrous cations and Q_s for passive film formation at various pH. Depassivated surface area 0.08 cm^2. "d": potential dependence of the charge ratio Q_d/Q_D (integral emission efficiency) at various PH.

Copyright © 2002 Marcel Dekker, Inc.



(40)

whole set of data was interpreted by the reaction model (40), a simplified form of the one derived for the faradic impedance of active iron (36). The kinetic equations for the time dependence of the two coverages by Fe(II) and Fe(III) were integrated numerically. Considering the wide range of current densities covered by the transient, both noncatalytic and catalytic reactions paths were considered. Only Fe(II) species participate in the dissolution mechanism and passivation is ascribed to Fe(III). These assumptions are justified by the large degree of (super) saturation in ferrous species during short transients.

That is supported by the results of simulations indicating in the first milliseconds of the transient a fast buildup of the Fe(II) coverage to a maximum of about 0.5, which then falls off during the growth of the passive film. The higher the pH and the applied potential, the sooner and the steeper the transition from Fe(II) to Fe(III).

Impedance and AC RRDE Study of the Active-Passive Range of Iron
Impedance and the AC component of the ring current were simultaneously measured at a series of polarization points in the negative slope region of Fe in 1 M sulfuric acid [117]. This region immediately prior to the Flade potential is very meaningful for understanding the imbrication of dissolution and passivation steps. The ring potential E_R was settled at two different potentials for collecting Fe(II) by oxidation (0.80 V/SSE) and Fe(III) by reduction (–0.40 V/SSE).

Typical data obtained for one point of the polarization curve are shown in Figure 9. Impedance shows the well-known behavior of a passivation range characterized by the negative zero-frequency limit of the real part consistent with the slope of the steady-state current-voltage curve. The low-frequency capacitive arc displays the frequency response of the film growth. Emission efficiencies N_d relative to Fe(II) and Fe(III) going to the solution contain two frequency domains, i.e., a surface charge stored in two different species. For Fe(II) the largest changes take place in the same frequency range as for impedance. Its positive imaginary part establishes the passivating role of the faradic surface charge with respect to the active path of iron dissolution (see earlier). A small loop at higher frequencies is poorly visible. It reveals a feature not detected on the impedance spectrum and lies in the half-plane of negative imaginary parts reflecting a surface charge stored in a

Copyright © 2002 Marcel Dekker, Inc.

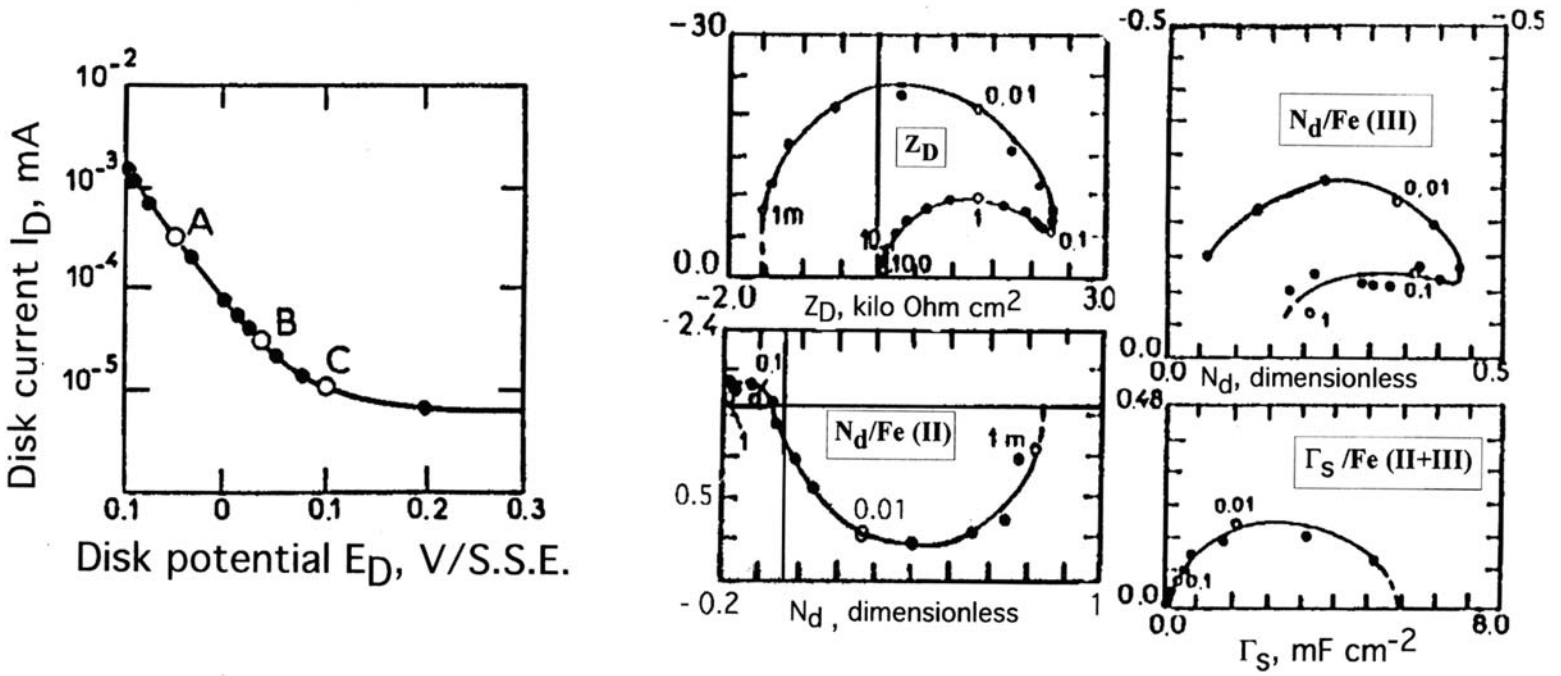


Figure 9. Impedance and AC-resolved RRDE of the active-passive transition of iron in 1 M H_2So_4. Rotation speed 900 rpm. Current-voltage curve of the iron disk. Data at polarization "B": Z_D: disk impedance, N_d/Fe(II) and N_d/Fe(III): emission efficiencies respectively for Fe(II) and Fe(III) species, ring potential respectively: 0.8 and –0.4 V/SSE, Γ_s/Fe(II+III) : faradaic capacitance of the passivating layer.

Copyright © 2002 Marcel Dekker, Inc.

dissolution intermediate. The emission efficiency for Fe(III) contains the same two domains of frequency but with quite different properties. Both are located in the negative real part region with modulus maximum around the transition frequency (0.1 Hz). Therefore both surface species participate as sources of dissolution of Fe(III). This is consistent with the generally accepted concept of a passivity current carried by the Fe(III) released by the film lattice. Finally, the capacitance Γ_s associated with the total charge as Fe(II) plus Fe(III) indicates that around 5.5 mC V^1 cm^{-2} are needed for passivation. Most of the current decay takes place within 0.2 V; therefore the charge content of the passive film at the Flade potential can be estimated as 1 mC cm^{-2}. This value is practically equal to the charge equivalent to one monolayer (one cell unit of a ferric oxide layer).

A kinetic model very close to that elaborated more recently for interpreting the transient dissolution of laser beam–depassivated iron was proposed. It made it possible to reproduce the main features of N_d and Γ_s shown in Figure 9.

Dissolution in the Passive State

Anodic dissolution in the active state generally results in equivalent corrosion rates unacceptable in practical applications (order of mA cm^2 or more). Self-limitation of the dissolution rate by the buildup of a thin surface layer under sufficiently oxidizing conditions, known as passivation, is the only relevant phenomenon in terms of corrosion control. The mechanism of dissolution in the passive state is dealt with in the following. A thorough survey of the field can be found in the proceedings volume of the last passivity symposia [118,122]

Film Relaxation and Dissolution in the Passive State

After completion of a full coverage through the initial stages of passivation, the subsequent behavior of a passivated metal is entirely determined by the bulk properties of the passive film and the reactions at its boundary interfaces with the metal and the electrolyte. In spite of the enormous amount of research carried out since Faraday's time, relations between the solid-state chemistry of the barrier layer and the electrochemistry of the passive metal remain largely unclear.

Concepts, Models, and Experimental Approaches Separation between film relaxation (growth or dissolution) and metal corrosion in the passive state is meaningless except at perfect steady state because both aspects of metal oxidation are intimately interrelated by the charge and mass balances at the metal-film-electrolyte interface.

$$I = I_G + I_C \tag{41}$$

The overall charge balance is expressed as

where I is the external current flowing to the electrode, I_G the component of I involve in the film growth, and I_C the corrosion current measuring the flux of metal cations released in the solution. Equation (41) must be considered algebraically; i.e., a negative (cathodic) value of I will produce film destruction by cathodic reduction and possibly a decrease of the corrosion current. Steady state is naturally defined for a constant film thickness, $I_G = 0$, and therefore an external current equal to the corrosion current.

Most of the concepts introduced for modeling film growth and dissolution have their origin in the theory of thermal (dry) oxidation initially adapted to thick (wet)

Copyright © 2002 Marcel Dekker, Inc.

oxides grown chemically or electrochemically on valve metals [123–125]. Much more intricate problems arise from electrochemical conditions. Dissolution processes in the passive state involve

Metal oxidation (ionization) at the metal-film interface
Transport of metal cation (and/or cation vacancies) across the film
Metal cation transfer into solution species (solvated, complexed) at the film-electrolyte interface.

Film growth can proceed at interfaces:

Metal-film by transport of oxygen anions to the metal-film interface or of oxygen vacancies toward the solutions
Film-electrolyte by transport of metal cations to the film-electrolyte interface or of cation vacancies toward the metal

Models differ essentially by the active participation of the lattice, via defects, to the transport properties and consequently to the growth and dissolution reactions at interfaces.

For simplicity, the dissolution behaviour of passive metals can be split into two groups:

Passive electrodes with a nearly constant corrosion current over an appreciable potential range. They are generally dealt with in terms of high field migration.
Passive electrodes with a potential-dependent current, most commonly exhibiting a minimum. Less advanced models are available; they involve the contribution of defects (e.g., point defect model).

Non-steady-state techniques played an outstanding role in reference papers in the field [4]. Galvanostatic and potentiostatic transients [126–129] are exploited either at short times, for plotting current-voltage characteristics at constant (frozen) film thickness, or at longer times as a function of increasing (or decreasing) film thickness estimated from the total charge $\int I\,dt$. Transient techniques were also extended to rapid changes of solution composition [130]. AC impedance in the very low frequency range (millihertz and submillihertz) proved quite successful for achieving finely resolved information on corrosion and film growth [4].

Passive Iron and the High-Field Migration The high-field migration model (also known as hopping mechanism) was applied to interpret the steady-state and non-steady-state behaviors of iron investigated by many different techniques during the last 40 years. Pioneering works by the German school [131,132] have been revisited in the past decade by more advanced experiments [133] and improved modeling [134].

Salient features accounted for by this model are

A steady-state corrosion current independent of the electrode potential over an appreciable range.
The existence of a specific potential, known as the Flade potential E_F, at the cathodic bound of passivity, to which all the film properties are referred in a simple form. It can be regarded as the zero thickness origin.

Copyright © 2002 Marcel Dekker, Inc.

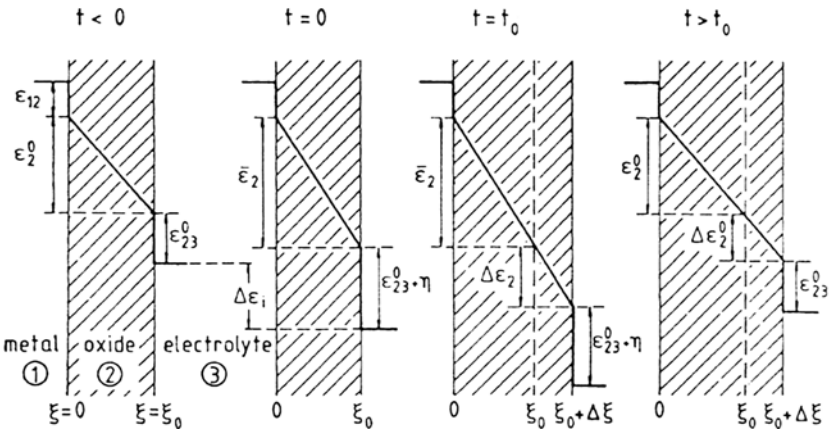


Figure 10. Positional changes of the potential from the metal (1) through the passive film (2) to the electrolyte (3) for different times of a galvanostatic square pulse. According to Vetter [131] and Wagner [123] at steady-state the film solution potential drop $\varepsilon_{2.3}$ is potential independent ($\eta = 0$).

A linear dependence of the film thickness (estimated coulometrically but also supported by surface-sensitive techniques such as ellipsometry) on the anodic overvoltage ($E - E_F$).

In its original form [125] the model was based on a multibarrier thermally activated cation transport giving rise to a current

$$I = I_0 \exp \frac{B(E - E_F)}{l} \tag{42}$$

where $B = zaF/RT$ with a the half-jump distance, z the number of elementary charges on the mobiles species, l the film thickness, and F, R, and T the usual physical constants. I_0 is a standard current assumed to depend on the density of charge carriers in the film.

At steady state, the potential-independent corrosion current is totally supported by a constant field strength in the film, i.e., a film thickness l proportional to $(E - E_F)$. The conservative flux of cations Fe(III) across the interface requires a potential-independent voltage drop at the film-electrolyte junction.

Most of the non-steady-state results were obtained by RRDE [135,136] and monitoring of Fe(III) in solution by analytical chemistry [131,132] or radiotracer techniques. Transfer of cations into the solution at the film-electrolyte interface was found to depend on the overvoltage according to redox kinetics and to be roughly proportional to the current forced in the electrode in excess of the steady-state value. Accordingly, as sketched in Figure 10, any change of the steady current, or potential, triggers a modification (positive or negative) of the film thickness that finally restitutes the initial electrical field strength and potential drop at the outer film surface, i.e., potential-independent DC current.

The overall problem of the non-steady-state passive iron has been reexamined with the purpose of reaching a consistent interpretation of the empirical equation

Copyright © 2002 Marcel Dekker, Inc.

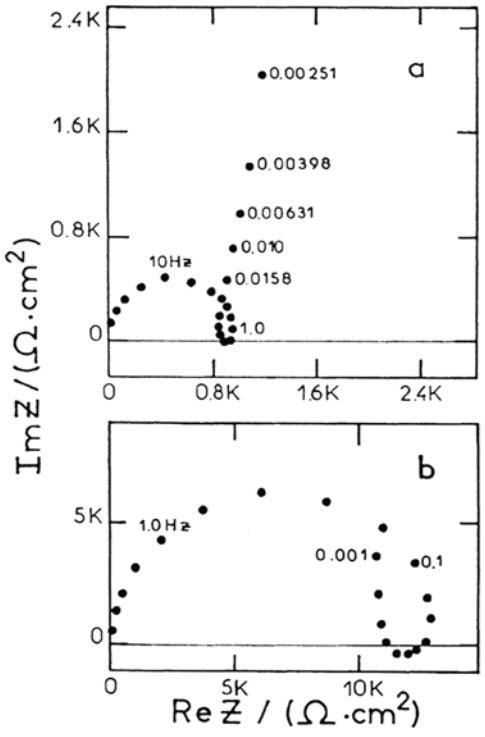


Figure 11. Impedance diagram of iron in the passive state. Johnson-Matthey iron. a. 1 M H_3PO_4, 37°C, E = –0.65 V/SSE b. 1M H_2SO_4, 25°C, E = –0.35 V/SSE Frequency in Hertz. From ref [133].

$$I = I_0 \exp(\beta E - Q/B)$$

firmly established in acidic [128] and neutral [126,127] media and also for nickel in acidic solutions [128] in classical papers. As stated earlier [134], this equation contradicts the high-field mechanism because it predicts a direct logarithmic $Q(t)$ relationship consistent with a place exchange mechanism, whereas the high field should generate an inverse logarithmic dependence [4].

It can be concluded that the key point lies in the potential distribution between the film bulk and the film-electrolyte interface in the transient regime. Subsequently, an attempt was made to incorporate the role of defects (cation vacancies) in the high-field mechanism [137].

AC Impedance of Passive Iron in Acidic Media Film resistance to cation migration and capacitance displaying the potential dependence of the charge stored by the film growth are expected. Figure 11 shows two complex impedance diagrams in the passive range in H_3PO_4 and H_2SO_4 solutions [133].

According to Eq. (42), the size of the HF loop is attributed to the derivative of the flux due to high-field migration, with respect to E at constant film thickness:

$$R_{HF} = \frac{l}{BI} \tag{43}$$

Copyright © 2002 Marcel Dekker, Inc.

The DC current I being potential independent, a linear dependence of $R_{HF}I$ on E is expected and fairly verified as shown in Figure 12 for various solution compositions and pH. The straight lines begin at the Flade potential E_F, where the film is restricted to its inner and outer boundaries and above which the 3D film starts growing.

From the slope, 0.06, of the straight line in Figure 12 and assuming $a = 0.5$ nm, a calculated field strength of 3×10^8 V m^{-1} and a potential dependence of the film thickness of 3.5 nm V^{-1} are calculated, in agreement with literature data. The inductive behavior at intermediate frequencies is physically equivalent to the overshooting transient considered in Ref. 137 and may be related to a relaxation of the carrier density. The low-frequency capacitive branch is perfectly consistent with the constant DC current. Its value is about one order of magnitude larger than estimated by Faraday's law applied to the thickness-potential dependence of the film. Little dependence is found with respect to the solution composition, supporting the interpretation of anion effect through the change of I_0 with the density of charge carriers.

According to the high-field migration model, iron dissolution across the film and film growth are only weakly coupled by the transient overvoltage η (see Fig. 10) at the film-electrolyte interface. In contrast, any model based on defect mobility necessarily implies a dynamic situation with two nonconservative reactions [138] (film growth at the inner interface and film dissolution at the outer one). The whole film is therefore translating outward with a velocity depending on the corrosion current.

Investigation of the Transient Dissolution of Passive Iron by Impedance and Electrogravimetric Transmittance One of the recurrent topics in passivity studies is the transient behavior of the passive state. That is, how is the current shared

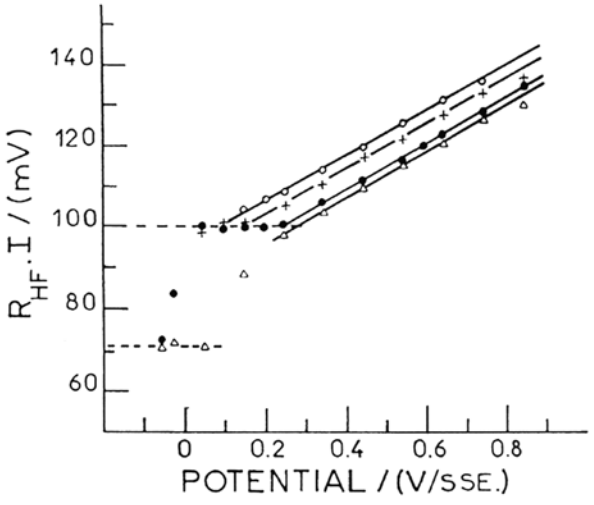


Figure 12. Potential dependence of the R_{HF}.I product for passive iron in various solutions (Johnson-Matthey iron. 25°C). Δ: 1M H_2SO_4, pH = 0.03. •: 1M H_3PO_4, pH = 1 +: 1M (H_3PO_4 + KH_2PO_4), pH = 2.2. o: 1M (H_3PO_4 + KH_2PO_4), pH = 2.8. From ref [133].

Copyright © 2002 Marcel Dekker, Inc.

between film growth and metal dissolution during the restoration of a new steady state after a change in the applied potential? As stated before, the predictions of the high-field model in the transient regime are extremely sensitive to the distribution of a potential increment between film bulk and interfaces. No ab initio answer is available and the efforts have been concentrated on the analysis of time or frequency domain experiments. Emphasis was put on the presence of an overshoot or inductive response, but the interpretation of the inductance remained quite ambiguous without no additional data. Quartz crystal microbalances are very well adapted to this problem because the low corrosion rate provokes no drift of the mean mass of the electrode while for the same reason the emitted flux of cation is below the detection limit of collector electrodes. Impedance when associated with frequency-resolved electrogravimetry is able to discriminate between the fraction of the overall charge Q taken up in film growth (mass gain) and consumed for dissolution (mass loss).

It was shown analytically that the high-field migration model is not able on its own to explain the inductive response shown in Figure 13a. Correlatively, the calculated mass transmittances $\Delta m/\Delta E$ and $\Delta m/\Delta Q$ simply reflect Faraday's law [55]. In particular, $\Delta m/\Delta Q$ is a real quantity determined by the antagonistic contributions of transitory film growth and metal dissolution. A new time constant besides that related to the relaxation of the film thickness was introduced [139,140] by deriving the impedance and AC mass response for the model proposed by Kirchheim [137]. It assumed that the density of cationic vacancies [or the density of mobile Fe(III) cations] in the film depends on the excess of current with respect to the corrosion current I_c. Consequently, the film resistance R_{HF} is lowered, producing an inductive-like transient of the migration current. Impedance is foreseen to contain, in addition to the series capacitance at low frequencies standing for the film growth, an inductance generated by the relaxation of the film conductance.

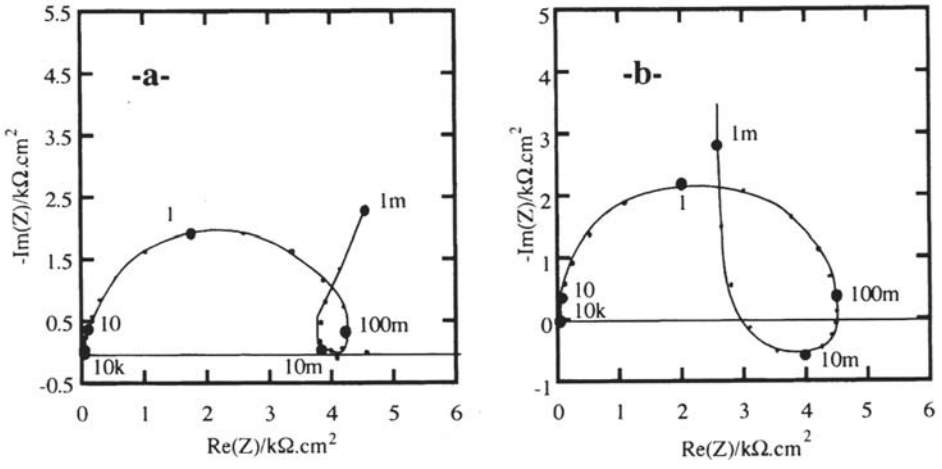


Figure 13. Impedance of iron in 1M H_2SO_4, potential 0.5 V/SSE. Experimental: "a" and numerically simulated : "b", with a model based on a relaxation of the charge carriers density in the passive film. From ref [139,140].

Copyright © 2002 Marcel Dekker, Inc.

Figure 13 displays experimental and computed Nyquist plots of the impedance. Similarly, the electrogravimetric transmittance was derived. It exhibits the mass counterpart of the relaxation of the film conductance. Again, consistent with Faraday's law, the low-frequency limit

$$\left(\frac{\Delta m}{\Delta Q}\right)_{\omega \Rightarrow 0} = \frac{1}{\Gamma}\left(\frac{\Delta m}{\Delta E}\right)_{\omega \Rightarrow 0}$$

is fixed by the mass equivalent to the film growth. Experimental and simulated complex electrogravimetric transmittances are shown in Figure 14.

The negative real limit at low frequencies reveals that the mass loss by the corrosion current I_c is much larger than the mass gain by the film growth. In agreement with values of the capacitance Γ, this limit, -12mg V^{-1} cm^{-2} is about 10-fold that of a 2.5 nm V^{-1} thick layer of Fe_2O_3. In contrast, the humped shape in the positive real part region at high frequencies visualizes the mass gain due to film growth. It is noteworthy that this takes place in the same frequency range as that covered by the inductive loop. With this set of parameters, which may be not optimal, both features are larger on simulated than on experimental curves. Paired contribution of these transmittances confirmed that

Transient is controlled by film interface with respect to bulk.
One intensive property of the film probably its ionic conductance, is at the origin of the inductive behavior.
The major part of the charge supplied to the film produces corrosion rather than film growth.

Passive Nickel and the Point Defect Model The passive state of nickel shows much more complicated behavior than for iron in the same solutions. A minimum of

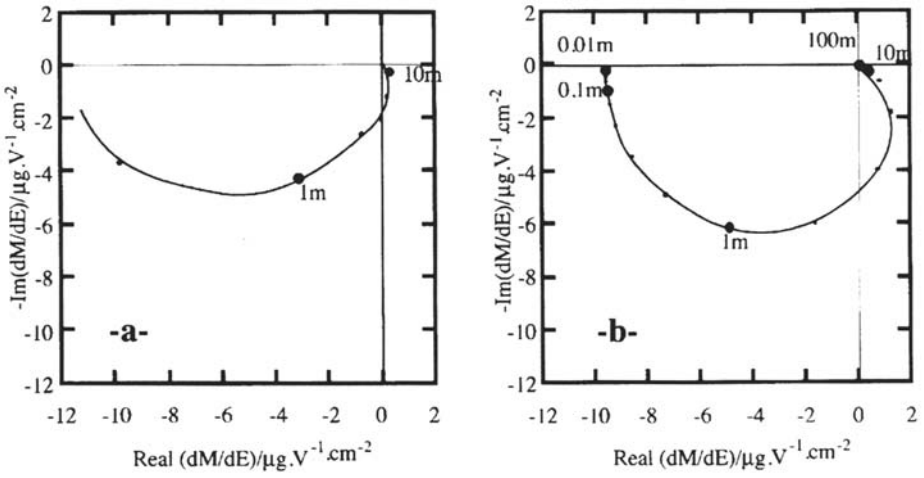


Figure 14. Electrogravimetric transfer function of iron in 1M H_2SO_4, potential 0.5 V/SSE. Experimental :"a" and numerically simulated : "b", with a model based on a relaxation of the charge carriers density in the passive film. Same set of parameters as for Figure 13a. From ref [139,140].

Copyright © 2002 Marcel Dekker, Inc.

dissolution current is most often observed in the middle of the passive range, and increasing dissolution takes place at higher potentials (transpassive range). It is now well established that passive and transpassive dissolutions are so tightly related that they cannot be dealt with separately. According to this behavior, the film is expected to undergo important modifications in its structure and thickness as a function of potential and solution composition.

An advanced form of the point defect model [123,124] has been applied to the passivation of Ni in neutral solutions in a series of papers [138,141,142]. Figure 15 shows the main features of the model and the five reactions considered; two of them, (2) and (5), are nonconservative and contribute directly to metal dissolution through translation of the film growing at the inner interface (reaction 2) and dissolving at the outer interface (reaction 5). The model involves many more assumptions and parameters than the high-field migration and is able to account for a broad spectrum of electrochemical responses to potential, pH, and cation concentration. Some aspects of the model were investigated by impedance in spite of the extremely low frequencies involved in the processes and control by cation vacancies was concluded [141,142].

Passive and Transpassive Dissolution of Nickel in Acidic Solutions The kinetics of nickel dissolution in the passive and transpassive ranges M remained totally unclear until the application of a very low frequency impedance technique. A general model was proposed on the basis of an extensive study of anion effects [143]. In the passive state, the frequency domain had to be extended far below 1 mHz and long-term stability was obtained only by using single-crystal electrodes [144].

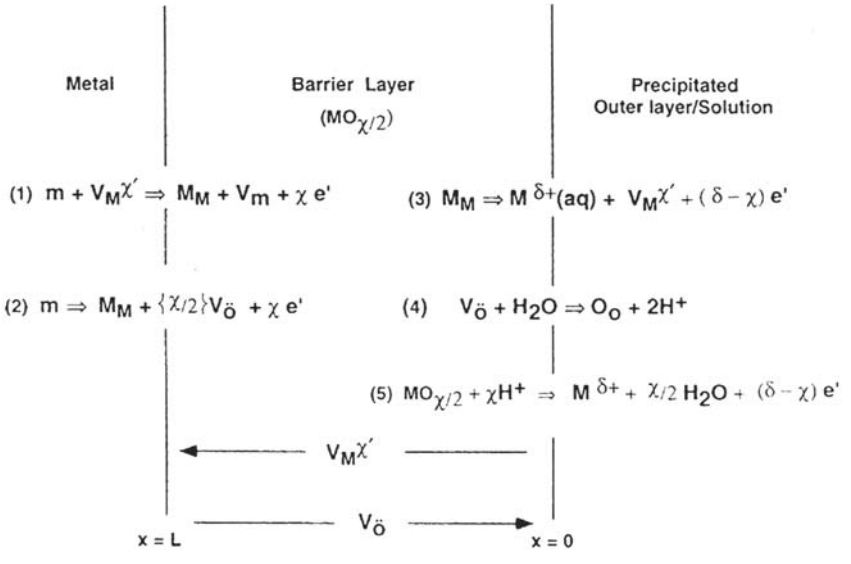


Figure 15. Schematic of the physicochemical processes that occur within a passive film according to the point defect model. From ref [138].

Copyright © 2002 Marcel Dekker, Inc.

Figure 16 shows two current-voltage profiles in molar sulfuric and phosphoric solutions. The behavior contrasts drastically with that of iron; a minimum is reached close to 5 μA cm^{-2}, thus suggesting the contribution of two antagonistic processes. This is substantiated by the impedance data of Figure 17 for the phosphoric medium (the lower frequency limit is less than 100 μHz). Diagram Ap has the characteristic shape associated with passivation kinetics (see earlier)

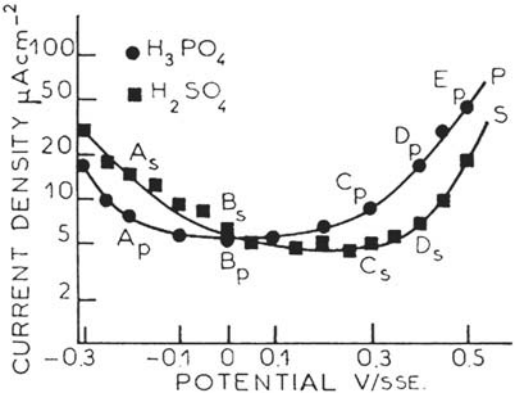


Figure 16. Steady-state polarization curves for nickel, (111) single crystal, in 1 M H_2SO_4 and 1 M H_3PO_4 solution. 25°C. From ref [144].

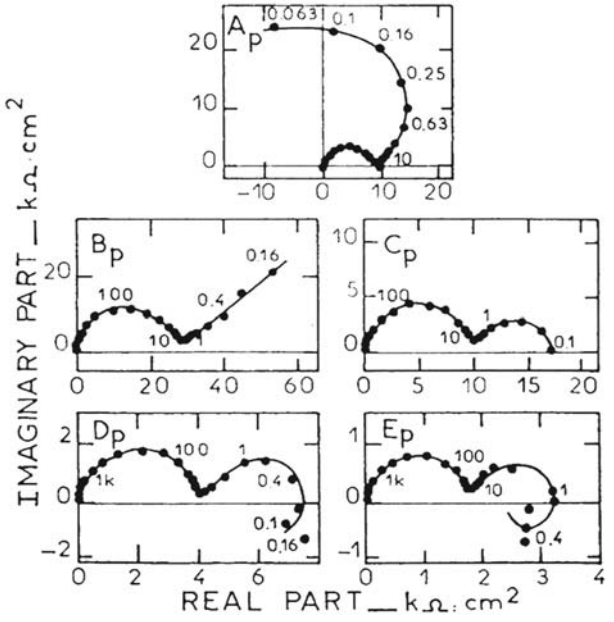


Figure 17. Impedance diagrams of passive Ni, (111) single crystal, in 1M H_3PO_4 solution. Potentials labelled in Figure 16. (Frequency in millihertz). From ref [144].

Copyright © 2002 Marcel Dekker, Inc.

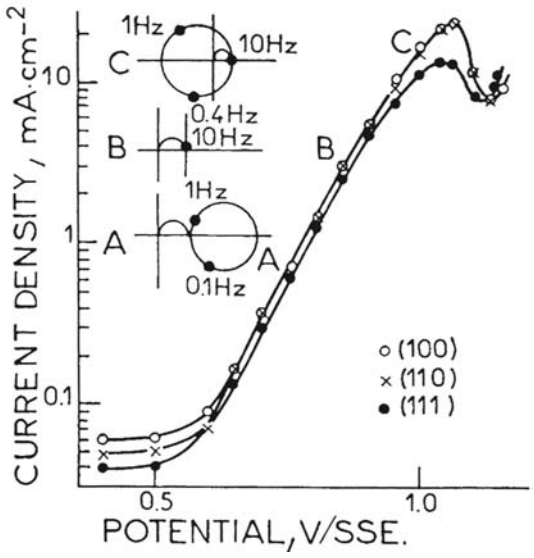


Figure 18. Current-potential curves and schematic impedance diagrams of transpassive Ni, 3 different single crystal orientations. 1 M H_2SO_4. From ref [148].

At the minimal c.d., Bp, typical diffusion control is observed consistent with the local plateau of the current-voltage curve. A diffusion term is associated with a transport limitation across the passive layer, whereas the inductive loop at the low-frequency end visualizes the contribution of a decaying film protection at increasing potentials. Application of a diffusion impedance equation to a finite-thickness layer (δ = 3 nm) given by

$$Z_D = R_D \frac{\tanh \sqrt{(j\omega \delta^2/D)}}{\sqrt{(j\omega \delta^2/D)}} \tag{44}$$

led to a diffusivity D of the order of 10^{-16} cm^2s^{-1}, This value is in agreement with solid-state diffusion at room temperature, and a decrease of the film thickness by a factor of 3 takes place between C_p and E_p.

An early paper [145] claimed on the basis of linear Tafel plots that the dissolution in the transpassive range is controlled by a single charge transfer reaction. It was then suggested that the electrochemical impedance behaves as a resonant circuit, i.e., at least two relaxation times [146]. This prediction was directly verified shortly after Ref. 147. Finally, a thorough investigation by impedance analysis at various pH values and anion concentrations was at the origin of a more elaborate model.

Figure 18 shows the current-voltage characteristics measured on three different crystal plan orientations. As reported in Ref. 145, a Tafel law is observed over more than two decades, but the impedance shapes display surprisingly intricate kinetics. A very characteristic impedance feature is observed at point B (but not on the polarization curves), where the impedance behaves like a perfect wave-trap circuit (the impedance becomes infinite at a resonant frequency ≅ 0.4 Hz). Above this transition

Copyright © 2002 Marcel Dekker, Inc.

point, e.g., C, the diagram is totally consistent with the electrochemical resonator described in Ref. 146.

Figure 19(1) shows a detailed evolution of the impedance. The impedance diagram turning counterclockwise when the frequency is decreased was related to the reaction pattern shown below elaborated and compared with experiments by numerical simulations [148].

Here Ni(II) stands for Ni cations pertaining to the lattice of the passive oxide film and Ni^*(II) is a cation in the film solubilized by chemical bonding with anions.

The likelihood of this species is also supported by the evidence of $Ni{=}SO_4$ band structures in the in situ Raman spectra of the $Ni\text{-}H_2SO_4$ interface in this particular potential region. At higher potentials all the film cations are converted into Ni(III) and Ni enters the secondary passivity region. Numerical simulations are presented in Figure 19(2) and reproduce with a fair accuracy the main features of experimental data, particularly the typical change of impedance trajectory between C′ and D′.

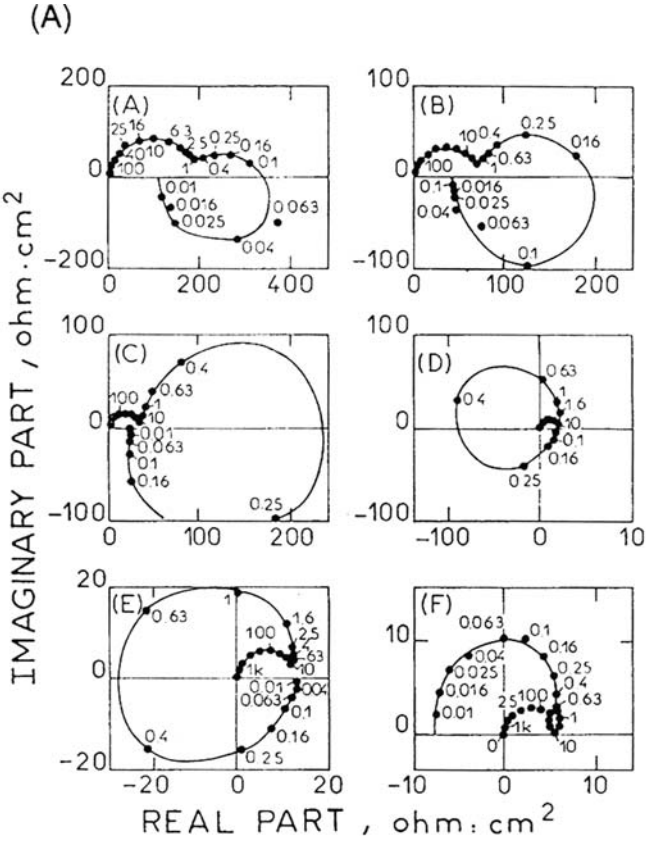


Figure 19. Experimental and calculated impedance diagrams of transpassive nickel (111) single crystal. 1M H_2SO_4, 25°C. (1) Detailed evolution, (2) numerical simulations. Measurement points are: A: 0.75 V/SSE; B: 0.8 V/SSE; C:0.8 V/SSE; D: 0.9 V/SSE; E: 0.95 V/SSE ; F: 1.1 V/SSE From ref [148].

Copyright © 2002 Marcel Dekker, Inc.

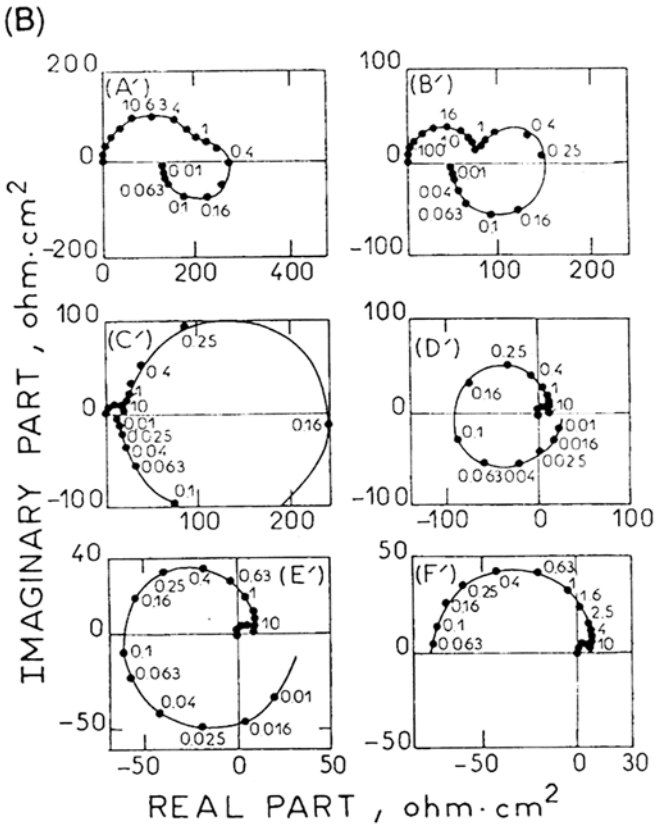
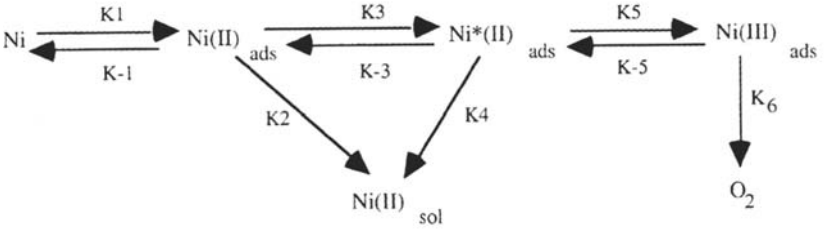


Figure 19 (*Continued*)

Anodic dissolution of chromium in the transpassive range as well shows a behavior generally attributed to the oxidation of the Cr(III) of the passive film to soluble Cr(Vl) oxyanions [43,149,150].

Transpassive dissolution of chromium, molybdenum, and alloys containing these elements has been extensively investigated by Bojinov et al. [151–153] using impedance analysis and steady-state RRDE. Additional in situ information concerning the conductance properties of the films is obtained by CER (contact electric resistance). Many-parameter models were proposed combining reaction steps



(45)

Copyright © 2002 Marcel Dekker, Inc.

coupled by adsorbed species and bulk conduction in 3D layers controlled by the mass balance of vacancies.

Anodic Dissolution Under Mass Transport Control

In corrosion practice, the rate of the heterogeneous anodic processes dealt with in the foregoing sections is ideally low enough that mass transfer is never a limiting factor. However, fast dissolution kinetics may occur in the following circumstances of obvious concern to corrosion:

Active dissolution as a transient regime in the initial stages of metal passivity
Dissolution of locally depassivated metals following passivity breakdown (e.g., pits, crevices, grain boundaries)

Because of the irreversibility of the dissolution reactions at high overvoltages, the coupling to mass transfer cannot be simply understood in the framework of classical transfer-diffusion theory:

A high concentration of dissolved cations in the Nernst boundary layer is incompatible with the supporting electrolyte approximation.
Limitation of the reaction rate by mass transfer must imply either back diffusion of an acceptor of metal cations (complexing or solvating species) toward the electrode surface or growth of a new phase on the surface with limitation of the reaction rate by ohmic drop or space charge overvoltage.

Little is understood at a mechanistic level because of an almost total lack of knowledge of the local chemistry within the boundary diffusion layer or solid films. The problem is essentially investigated in the framework of pitting, crevices, and stress corrosion cracking [154] by modeling and experiments on occluded cells (artificial pit designing).

Mass Transport Control and Corrosion

It is generally accepted that transport effects (diffusion and electromigration) are at the origin of a buildup of metal cation concentration concomitant with a depletion of H^+ and a overconcentration of anions (for electroneutrality reasons). Homogeneous chemical reaction can add their own contribution, e.g., hydrolysis of Cr(III) resulting in a local acidification of neutral media [155].

The most relevant consequence of the change of interfacial chemistry for corrosion is undoubtly the modification of the active-passive transition and the possible generation of self-sustained large-amplitude oscillations between active and passive states [156,157]. These phenomena were tightly associated with the manifestations of passivity from the earliest research, particularly in the case of iron in acid solutions. Theoretical investigations imply difficult nonlinear mathematics. A significant renewal of the field was observed in relation to the increasing interest in nonlinear phenomena and such concepts as bifurcation theory and chaos in chemistry [158–160].

In spite of this new sophistication, the basic model is still that due to Franck and FitzHugh [156] in which the following reactions are supposed to participate in a cyclic sequence.

An oversimplified form of dissolution and passivation reaction is considered:

$$Fe \rightarrow Fe^{2+} + 2e^- \tag{46}$$

Copyright © 2002 Marcel Dekker, Inc.

$$Fe + nH_2O \Leftrightarrow FeO_n + 2nH^+ + 2ne^- \quad (47)$$

Reaction (46) at high dissolution rates tends to decrease the pH by H^+ electromigration and to shift the passivation equilibrium reaction (47) to the right. At the same constant potential, the iron surface turns into the passive state, and back diffusion of H^+ takes place and restores the active dissolution by displacing the passivation equilibrium to the left. The same sequence restarts, generating a periodic regime. It should be observed that this model ignores the likely participation of salt layers ($FeSO_4,7H_2O$) and of ohmic drop and is unable to explain the coexistence at a same electrode potential of side-by-side active and passive areas, i.e., of stable localized corrosion coexisting with a passive sample. The latter self-stabilizing process of dissolution is very generally ascribed to the depassivating role of Cl^-, enriched by electromigration toward the active areas. However, similar behavior can be observed in chloride-free solutions [33,74].

Active Dissolution of Iron under Mass Tranport Control

The anodic dissolution of iron in sulfuric acid medium exhibits, with well-defined convection on a rotating disk electrode, a current plateau as shown in Figure 20, attributed to the limiting rate of transport between the dissolving surface and the solution bulk [161]. The curves shown in Figure 20 suggest that some critical phenomenon is associated with the common branching point from which all the curves merge toward their plateau region, whereas they overlap perfectly below. The nature of the process controlling the heterogeneous steps was investigated by a detailed analysis of the EHD impedance.

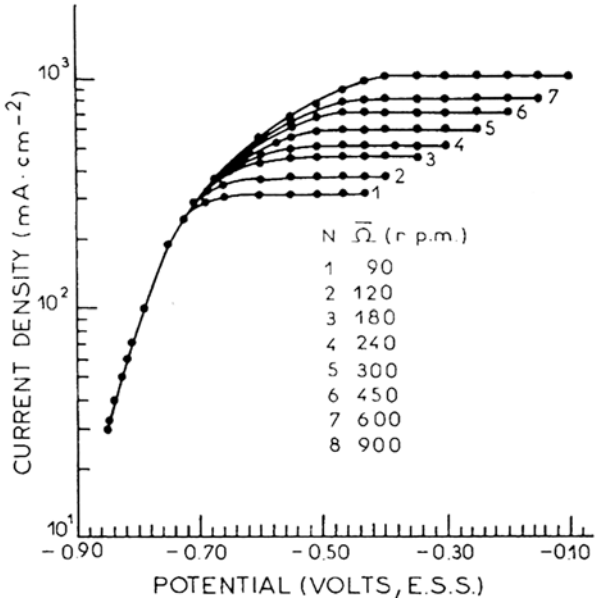


Figure 20. Current-potential curves for iron at different rotation speeds. Johnson-Matthey iron. 1.8 M H_2SO_4, pH = 0, 25°C. From ref [161].

Copyright © 2002 Marcel Dekker, Inc.

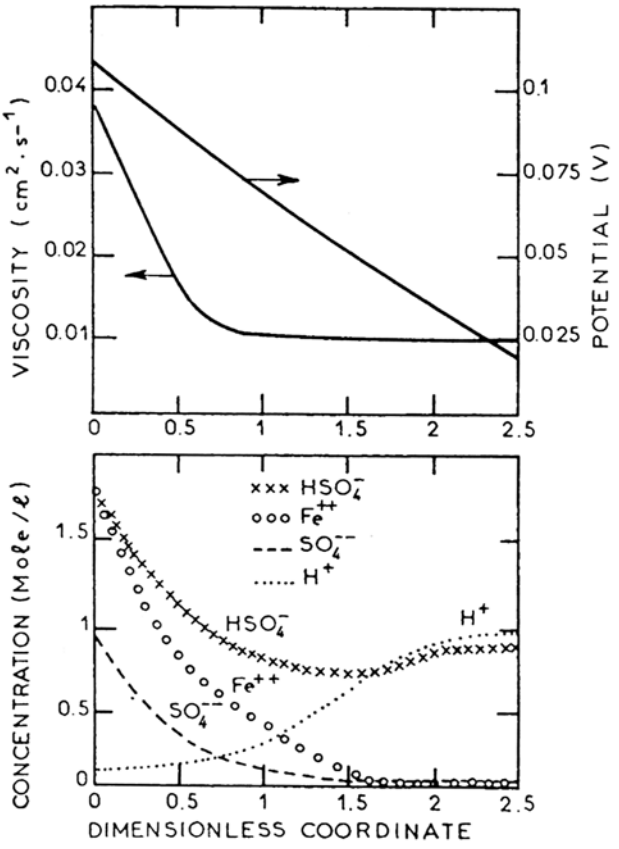


Figure 21. Concentration field calculated under the conditions of Figure 20. Top : viscosity and potential profiles. From ref [161].

EHD impedances are interpreted in terms of the existence of a viscosity gradient in the boundary layer estimated to be four- to fivefold between solution bulk and electrode surface. On this basis, the profiles of species participating in the mass and charge transport have been computed and are plotted in Figure 21.

The interfacial concentration of Fe^{2+} is in good agreement with solubility data. The increase of pH by H^+ migration is reflected in the profile of SO_4^{2-}. It is concluded that no barrier layer is involved in the mass transport control of iron dissolution. The heterogeneous reaction rate is reported as not dependent on the HSO_4^- concentration; therefore, the only acceptor species likely to limit the dissolution rate is water [74]. This is compatible with the modified form (29) of the initial step of dissolution in which one water molecule is dissociated and the depletion of free water at the electrode surface by Fe(II) hydration and electromigration of hydrated Fe(II) away from the surface.

Anodic Dissolution Controlled by Transport in the Presence of Solid Layers

In many practical cases of corrosion, the anodic dissolution takes place on a surface partially or totally covered by thick (order of micrometers) solid layers grown by

Copyright © 2002 Marcel Dekker, Inc.

several possible mechanisms (heterogeneous nucleation and growth, dissolution-reprecipitation) and usually regarded as porous. Until the past decade the mechanism by which this layer interferes, with the anodic dissolution, and particularly the transport phenomena, remained poorly understood. The last developments deal with iron and copper in HCl solutions and take advantage of steady-state RDE and RRDE associated with AC impedance (EIS and EHD) techniques. Mass transport and solution chemistry [162–163] let to a dissolution model [164] in which the electrochemical monoelectronic surface step:

$$Cu + Cl^- \Leftrightarrow CuCl_{ads} + e \tag{48}$$

is followed by a series of complexation reactions, the more likely being

$$CuCl^-_{ads} + Cl^- \Leftrightarrow CuCl_2^- \tag{49}$$

More advanced RDE studies were interpreted by the formation of a porous 3D layer of $CuCl_{ads}$ [156] in a step such as

$$CuCl_{ads} \rightarrow CuCl_{film} \tag{50}$$

Because of the reversibility of reactions (48) and (49), both Cl^- and $CuCl_2^-$ diffusing in opposite directions may control the dissolution rate. In the plateau region it was shown [164] by RRDE that compact coverage is attained. Therefore in the model elaborated in Ref. 165 the contribution of the layer to the rate of dissolution is twofold and constitutes the central ingredient of the model: the CuCl film is considered at the same time to dissolve at its outer boundary with the electrolyte:

$$CuCl_{film} + Cl^- \rightarrow CuCl_2^-$$

and to limit the rate of Cl^- diffusion to the Cu surface to form the film by reaction (48). This form of the model is sketched in Figure 22.

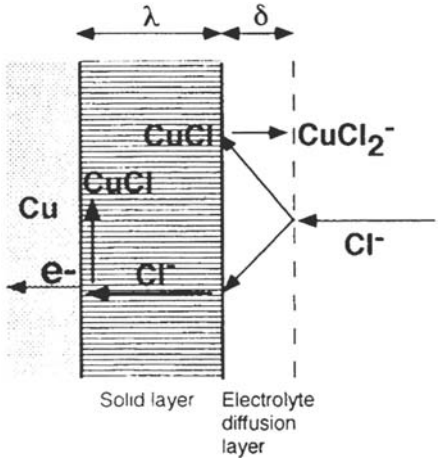


Figure 22. Model of dissolution of copper through a solid layer growing by a Tafel kinetics at the metal interface and dissolving by a chemical kinetics at the solution interface. Adapted from ref [165].

Copyright © 2002 Marcel Dekker, Inc.

It is noteworthy that this model is formally similar to the point defect model (transport of a metal acceptor toward the metal surface, film growth at its inner interface, dissolution at its outer one) shown in Figure 15. EIS and EHD responses associated with this model have been derived [165] taking into account the diffusion of both Cu^- and $CuCl_2^-$ in the solution (diffusion layer δ) and of Cl^- through the film (diffusion layer λ) and allowing for the modulation of the layer thickness by the AC potential, an effect discarded in Ref. 164. Comparison with the experiments substantiated the model. The mass transport by diffusion and migration and the potential drop at soluble anodes covered by salt films have been dealt with [166,167] by assuming compact (saturated) or porous (supersaturated) coverages (wet) on iron. Even more intricate situations on nickel have been tentatively approached [168].

ANODIC BEHAVIOR OF ALLOYS

A detailed understanding of the electrochemistry of alloys is still far from being achieved on the basis of the rather crude theory of pure metals. The complexity is expected to increase more rapidly than the number of components (cross-interactions) and it is doubful whether a unique mechanism can be at work in view of the extreme variety of compositions. As far as mechanistic information is concerned, only homogeneous (single phase) and binary alloys are considered in this section.

The Basic Concepts: A Survey

Thermodynamics and Rate Constant Approaches

It was thought very early that the change of rest potential and of dissolution rate with alloy composition cannot be understood without assuming surface modifications induced by the anodic processes themselves [169]. The nature of these modifications has been the aim of many electrochemical and surface analysis studies but is still not fully elucidated.

In an ideal case, in the absence of any free energy of mixing, the free energy of a metal in an alloy with respect to that of the pure metal is given by

$$\Delta G = RT \ln x$$

where x is the molar fraction of the metal in the alloy, and the corresponding shift of electrode potential is

$$\Delta E = -\frac{RT}{zF} \ln x$$

This equation is obeyed only by a few alloys and dilute amalgams [10]. The individual dissolution rates of Cu and Ni in Ni-Cu were investigated as a function of alloy composition [169,170]. In the framework of the activated state theory, a standard rate constant of the solution of the ith component of an alloy, $k°ia$, is calculated from the exchange current density at the standard potential:

$$(i_0)_i = Z_i F C_i \gamma i a_{iz^+} (1 - \alpha_{ia}) k^\circ_{iA} \tag{51}$$

where $\gamma_i C_i$ = activity of the element in the alloy

Copyright © 2002 Marcel Dekker, Inc.

a_{iz^+} = activity of the element cation in the solution
α_{ia} = transfer coefficient of the metal *i*–cation equilibrium

The $k°_{ia}$ is found independent of the alloy composition up to 60% Cu, above which a new phase is invoked.

This purely formal kinetic treatment is of very little utility because it is quite unable to dissociate the more elementary contributions to the alloy electrochemistry, namely from metal solid-state physics to surface physical chemistry:

1. Change of elementary rates of charge transfer by electronic interaction in alloy structure (alloying effect)
2. Change of the surface composition of alloy by selective dissolution of the less noble element
3. Growth of 2D or 3D layers resulting from chemical or electrochemical reactions of the alloy components with the solution

Following Rambert and Landolt [172], dissolution of single-phase alloys can be classified in two categories:

Simultaneous dissolution, where at steady state the alloy elements go into the solution at a rate proportional to their atomic concentration in the alloy. Well-known examples pertain to the iron-base stainless steels and especially ferritic Fe-Cr, on which this type of dissolution is repeatedly found [173,174].

Selective dissolution, where the less noble element dissolves selectively leaving behind a "porous" metal phase enriched in the more noble constituent, resulting in dealloying. The more common case is the selective dissolution of Zn (dezincification) from α-brass (Cu-Zn). Selective dissolution is in some instances associated with circumstances of stress corrosion cracking (SCC) [175].

Simultaneous Dissolution and Associated Formalism

The basic formulation was elaborated sometime ago [175,176]. A linear relationship of the form

$$I_{AB} = I_A\gamma_0 + I_B(1 - \gamma_0) \tag{52}$$

was suggested for representing the dissolution current of an alloy AB as a function of the elementary current densities of A and B, γ_0 and $(1 - \gamma_0)$ being the atomic proportions of A and B [commonly denoted $A - (1 - \gamma_0)B$].

It was simultaneously assumed [178] that, as a result of the alloy dissolution, its surface composition, $(\gamma, 1 - \gamma)$, can deviate from the bulk one. Consequently, the proportionality of the atomic fluxes of A and B going into the solution to their alloy content is expressed by

$$\frac{Z_B I_A \gamma 0}{Z_A I_B(1 - \gamma_0)} = \frac{\gamma}{1 - \gamma} \tag{53}$$

where Z_A and Z_B are the dissolution electrovalences.

In principle, Eq. (53) yields a γ_0 value matching simultaneous dissolution at any potential, I_A and I_B being known from the individual curves of A and B in the same electrolyte. In general, there is no particular reason why this γ_0 would restitute

Copyright © 2002 Marcel Dekker, Inc.

the correct value of I_{AB}. In the case of Fe-Cr alloys, the essential features of the current-voltage characteristics in the transition range (7 to 12%) are not satisfactorily reproduced [178] and nonlinear interactions must be introduced [105,106]. Application of EIS to this problem in the case of Fe-Cr alloys in the active and passivation ranges is illustrated in the following. In the full passive domain, compositional changes in the passive film, determined by XPS, play a role similar to the adjustement of the surface composition of the alloy phase to achieve the simultaneous dissolution [179]. According to Ref. 180, percolation phenomena, apparently relevant to selective dissolution, could also explain some features of the dissolution of Fe-Cr in the incompletely passivated state.

Selective Dissolution

Different mechanisms have been proposed to explain the selective dissolution of alloys and the formation of a porous dealloyed layer. A dissolution-redeposition mechanism [180] was proposed for α-brass dealloying. A larger group of models requires the description of atomistic processes of restructuring of the more noble atoms A in order to allow the dissolution of the more soluble element B to proceed across an A-enriched porous layer. A critical review of the mechanisms likely to participate in these surface phenomena can be found in Ref. 32. It was suggested [182] that the rate-determining step is a solid-state diffusion of the less noble atoms via divacancies. Surface diffusion can also be taken into account. Roughening by a mechanism of "negative" aggregation known to generate fractal interfaces [161] constitutes a fruitful approach. In the 1980s, a series of papers [175,180,184] underlined the existence of critical compositions and of a threshold concentration of the less noble constituent below which no dealloying appears. This sharp dealloying threshold is not consistent with any of the diffusion-based models of selective dissolution, which are supposed to produce essentially continuous behaviors. A model based on percolation phenomena was proposed and extensively worked out. Its main background and developments will be exposed.

Simultaneous Dissolution: Fe-Cr Alloys

In contrast to selective dissolution, evenly dissolving alloys can be dealt with, up to a sophisticated level including non-steady-state responses, by macroscopic, i.e., kinetic descriptions. As shown in Figure 23, Olivier [1851] pointed out that the steady polarization curves of Fe-Cr alloys in a 0.5 M sulfuric solution display the decay of active and passive currents with increasing Cr content and the emergence of the transpassive dissolution of Cr to the hexavalent state.

The studies have focused on two aspects of the behavior of Fe-Cr: the modifications brought about by the addition of chromium to iron in the active dissolution and prepassive ranges on the one hand and in the passive state on the other hand. Electronic interaction by filling up of the *d* level of Fe [186] was put forward. Most of the subsequent contributions concluded in some progressive change from an iron-to a chromium-like behavior without a further detailed mechanism in the absence of a satisfactory model for pure iron on its own. A particular ability of Cr to enhance the passive state of iron, even with low surface coverage, was repeatedly reported [187,188]. Regarding the passive state, advances of in situ surface analysis [Auger electron spectroscopy (AES) and XPS] associated with electrochemical

Copyright © 2002 Marcel Dekker, Inc.

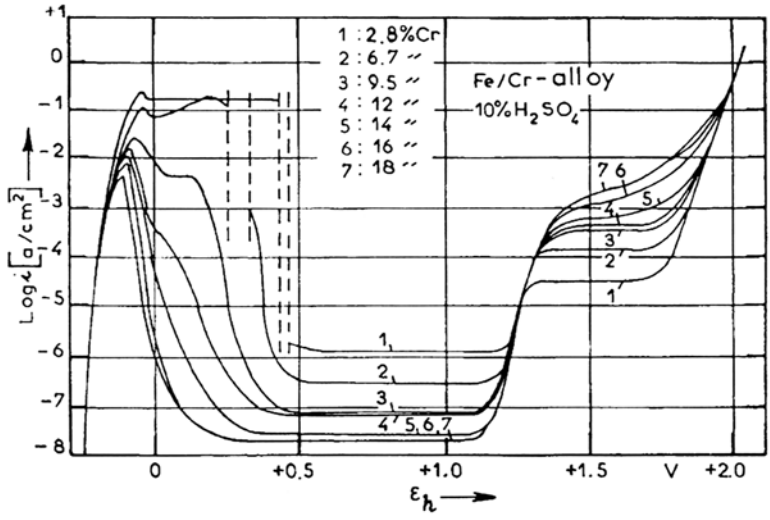


Figure 23. Current-potential curves of iron-chromium alloys as a function of Cr content. From ref [163].

measurements concluded in the formation of Cr-enriched passive films. Mechanistic aspects of the process have been investigated in detail by Kirchheim et al. [178,189,190] and several other groups [101,174,191].

Reaction Mechanism of the Anodic Dissolution of Fe-Cr

The anodic behavior of Fe-Cr alloys was investigated by using steady-state polarization curves and sampling by a large number of impedance measurements over the concentration domain (0–22% Cr) in H_2SO_4-Na_2SO_4 media ($0 < pH < 3$) [105,106]. The OH^- and Cr contents are found to play very similar roles in the reaction mechanism. The more salient characteristics of the role of Cr are visible at 7% Cr in pH 0 solution, as shown in Figure 24A, which exhibits a two-peak polarization curve and two perfectly separated passivation loops.

The passivating feature attributed to Cr at point D (capacitive loop of characteristic frequency 4 Hz) is therefore already visible at the beginning of the active domain (point A). Simulations of the current-voltage curves and of the impedance diagrams were performed on the basis of a mechanistic description derived from the reaction pattern previously elaborated for pure iron [61,62]. Therefore, coverages by five surface species were introduced in the derivation. The whole body of data led to taking into consideration, at the same time, the three types of interaction between Fe and Cr listed earlier namely

1. Alloying effects
2. Surface composition of the alloy distinct from the bulk one
3. Interaction of surface species with the neighbor atoms of either of the two alloy components

The last interaction was found to be the determining one for interpreting the impedance data and the steep onset of passivity. The mechanism is shown below. A

Copyright © 2002 Marcel Dekker, Inc.

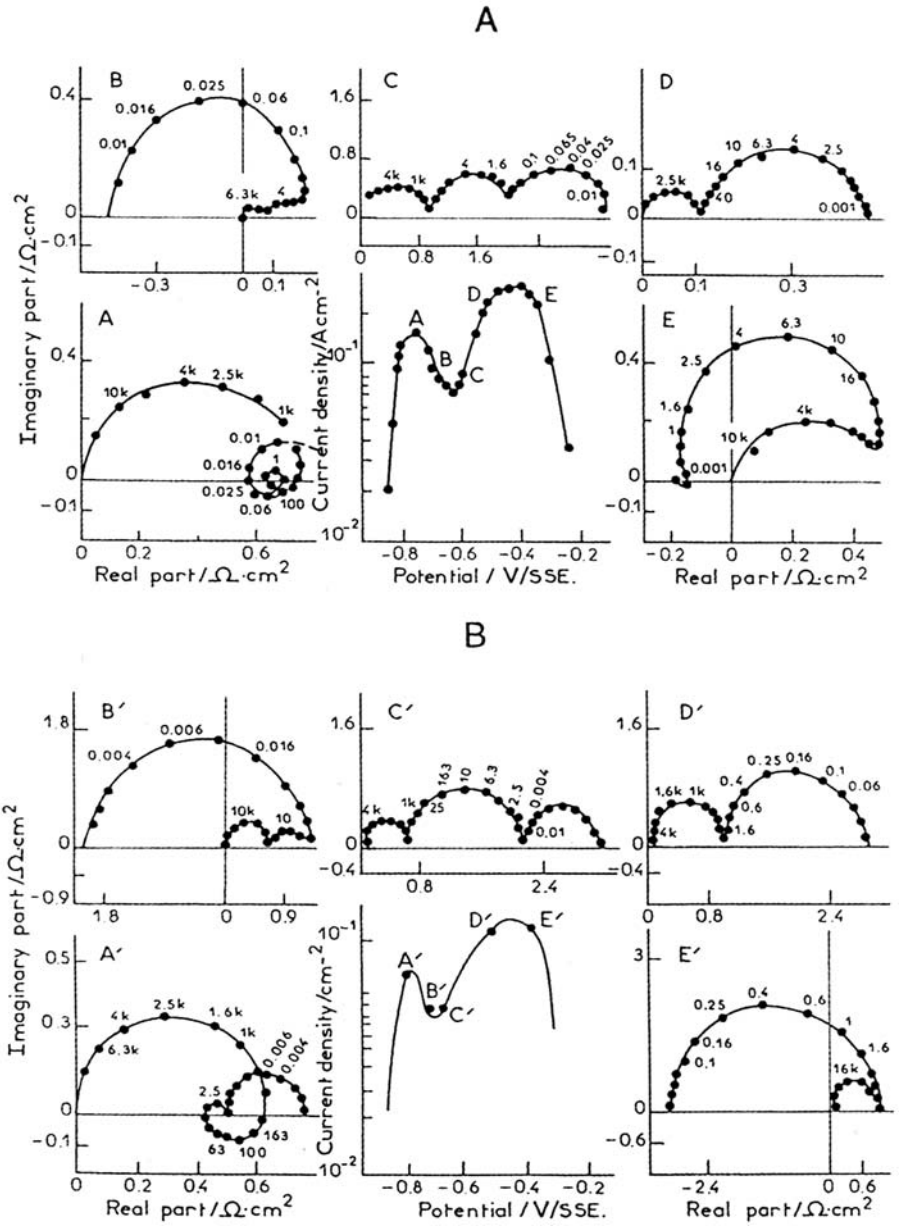
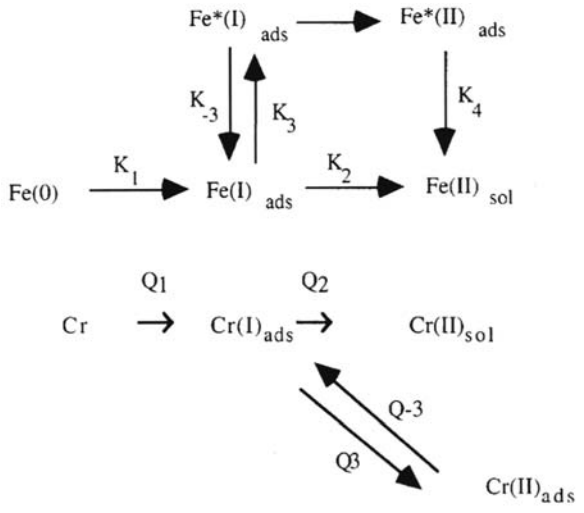


Figure 24. Experimental (A) and calculated (B) current-potential curves and impedance diagrams for a Fe-7Cr alloy (IRSID, France). 1M H_2SO_4, 25°C. Impedance diagrams at the corresponding polarization points on the I(E) curve. Frequency in Hertz. Simulations according to the reaction mechanism (54). From ref [105].

Copyright © 2002 Marcel Dekker, Inc.



(54)

specific nonlinear interaction with the chromium passivating species $Cr(II)_{ads}$ was supposed to affect the rate of iron dissolution. Figure 24B shows the result of simulations of the polarization curves and impedance diagrams. The sharp decay of the iron dissolution at increasing coverage $\theta_{Cr(III)}$ by $Cr(II)_{ads}$ was expressed by introducing the factor $(1 - \theta^{x}_{Cr(II)})$ with $x \cong 0.5$. A similar interaction function is adopted in the description of poisoning effects by foreign atoms in binary alloy catalysts. As emphasized for the first time in Ref. 106, this power law suggests that the threshold behavior arises from surface percolation of passivated chromium sites.

According to this interpretation, passivation would occur on an incompletely covered surface via long-range interactions between bare iron atoms and passive chromium connected in large clusters. A computer simulation later demonstrated the validity of this idea [184,192]. In the same paper [106], attention was also drawn to the atomistic description of the catalytic mechanism of dissolution (see earlier) in the case of a binary alloy. Therefore, purely macroscopic modeling of the kinetics of dissolution is no longer possible without consideration of the alloy microstructure, distribution of first and second nearest neighbors, and statistical composition at the atomic level. Concepts such as the size of clusters of atoms A and B and percolation phenomena [193] appear as determining and actually have been extensively worked out (see later).

Analytical and Mass Balance Approaches to Dissolution and Passivation of Fe-Cr Alloys

An important contribution is due to Japanese authors who developed rotating double-ring and split-ring disk electrode devices [191] and introduced channel flow arrangements [85] and data processing in the transient regime [101]. The respective behavior of Fe and Cr in the presence of Cl^- was investigated [191] for an Fe-30Cr alloy. It was concluded that chloride enters the soluble ferro-complex species while it behaves as an inhibiting species with respect to Cr. By employing time-resolved

Copyright © 2002 Marcel Dekker, Inc.

measurements on CFDE, previously introduced for iron studies [85], it was then shown [101] that in a sulfate medium the amounts of Fe and Cr dissolving at steady state are proportional to their concentrations in the alloy.

Active and Active-Passive Transition; Impedance and Frequency-Resolved RRDE Measurements The association of impedance and frequency-resolved RRDE techniques initially introduced for iron [38,117,197] has been extensively applied to the prepassive and passivation ranges of Fe-Cr alloys with and without chloride added [174,194,195]. Of course, the interpretation is more intricate than for pure metals (even with multiple dissolution valences). For kinetic reasons, Cr species are not detectable on the ring. In order to draw unambiguous conclusions, reasonable assumptions had to be made concerning simultaneous alloy dissolution at steady state (see thermodynamics and rate constant approach earlier) and dissolution valences of Cr.

Completely different behaviors were found depending on whether or not chloride is present. The salient features are

Emission efficiency for Fe(II) greater than 1 (for Fe-12Cr), an apparent paradox for a pure metal because that violates the principle of electrical charge conservation
A positive imaginary part of N_d (passivating charge) in the absence of Cl^-
A negative imaginary part of N_d (dissolution intermediate) in the presence of Cl^-

A model depicting the surface processes in terms of reaction paths and topographic interaction has been elaborated. It incorporates the key points previously introduced in the model based on impedances [37]. In particular:

Modification of the iron rate constants by chromium
Sharp passivation of the alloy represented by a nonlinear dependence of the blocking on the Cr species coverage

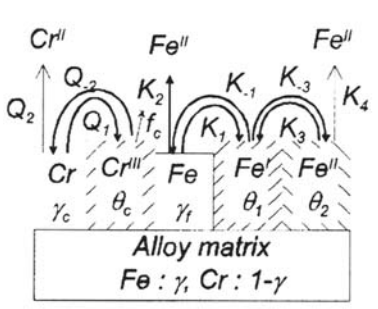
The reaction model and the corresponding surface picture are shown in Figure 25. It accounts for the nature and position of the first-order nearest neighbor for making explicit the interaction and mass balance of the surface species. This kind of approach was introduced in pioneering work [107] and then worked out in the framework of percolation models of passivation [180,192]. In view of the process complexity, an accurate fit is hopeless, but the main features could be semi-quantitatively simulated, including the amazing $N_d > 1$. A comparison of the experimental and computed N_d relative to Fe(II) is displayed in Figure 26.

According to the model, this extra emission of Fe(II) with respect to the electrical current across the electrode can be understood in terms of the contribution of chemical dissolution of an Fe(II) species by a step such as K_4.

Later on, the same model was considered for interpreting the results in chloride-containing media. The main modification was to enhance considerably the rate of dissolution (catalytic) via the $Fe(III)_{ads}$, whereas in Cl^--free media most of the iron dissolves from the $Fe(II)_{ads}$ (step K_2). The resulting change in the sign of N_d arises from the role of the dissolution intermediate of $Fe(II)_{ads}$. These results supported to some extent those of Ref. 191.

Dissolution in the Passive State In a series of papers by Kirchheim et al. [173,189,190], the dissolution rates of Fe and Cr in Fe-Cr alloys were investigated

Copyright © 2002 Marcel Dekker, Inc.



$$\underline{IRON}:$$

$$Fe \underset{K_{-1}}{\overset{K_1}{\rightleftharpoons}} Fe(I)_{ads} + e^-$$

$$Fe{\cdot}Fe(I)_{ads} \xrightarrow{K_2} Fe(I)_{ads} + Fe(II)_{sol} + e^-$$

$$Fe(I)_{ads} \underset{K_{-3}}{\overset{K_3}{\rightleftharpoons}} Fe(II)_{ads} + e^-$$

$$Fe(II)_{ads} \xrightarrow{K_4} Fe(II)_{sol}$$

$$\underline{CHROMIUM}:$$

$$Cr \xrightarrow{Q_1} Cr(II)_{sol} + 2e^-$$

$$Cr \underset{Q_{-2}}{\overset{Q_2}{\rightleftharpoons}} Cr(III)_{ads} + 3e^-$$

Figure 25. Schematic representation of the reaction mechanism and of the topographical interaction of reaction step and surface coverages. From ref [195].

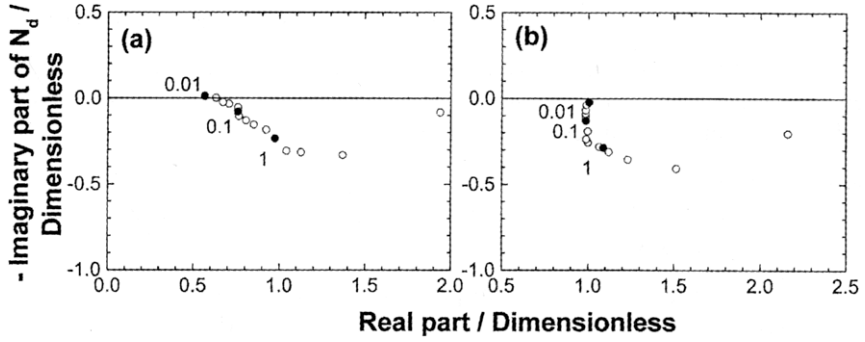


Figure 26. Emission efficiency of Fe(II) for Fe-l2Cr alloy in 0.5 M H_2SO_4. In the active dissolution ("a": E = 0.07V/SSE) and passivation ("b": E = 0.l8V/SSE) ranges. From [195].

within their passive range in H_2SO_4 solution. Time-resolved chemical analysis of the solution was performed by atomic absorption spectroscopy of samples of electrolyte. Selective dissolution of iron during the transient passivation stages was exploited in terms of Cr enrichment in the passive layer, and once the steady state was reached, simultaneous dissolution was accurately verified.

Figure 27 is an illustration of the time-resolved monitoring of the percentage of Cr in the dissolution products during a phase of film growth triggered by a galvanostatic square pulse [173]. In-depth concentration profiles of Fe and Cr in the film were concomitantly measured by XPS, and the significant enrichment in Cr for corrosion in the passive state was attributed to the outer first layer of the film. Equation (53) expressing simultaneous dissolution is applied to both the alloy phases (a) and the film outer layer (e):

$$i = i_{Fe} + i_{Cr}$$

Copyright © 2002 Marcel Dekker, Inc.

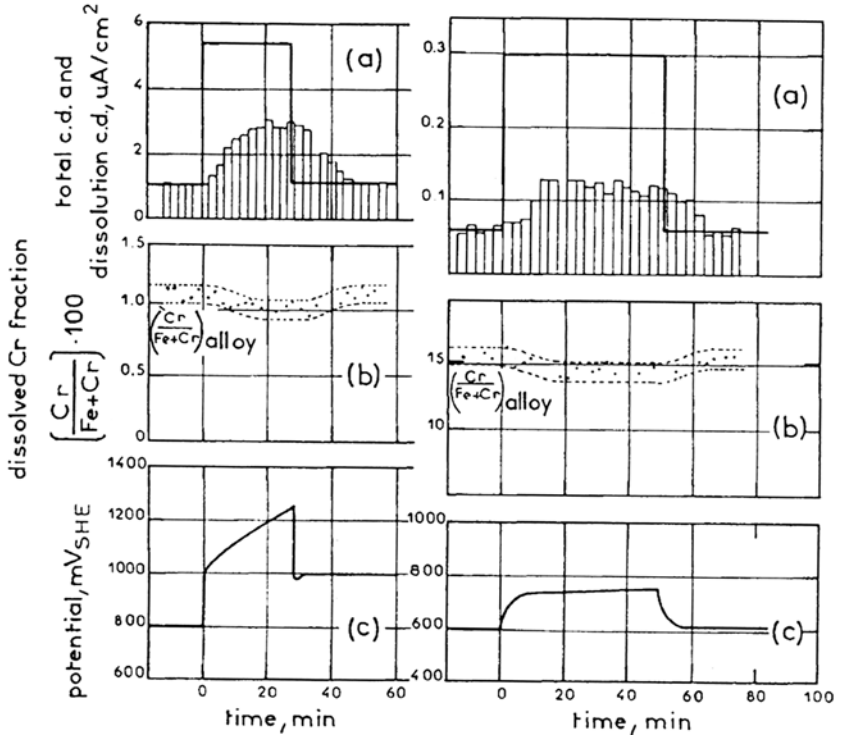


Figure 27. Galvanostatic transients for the dissolution (bars in a), the Cr fraction in the dissolution products (b) and the potential (c) for two different alloys (left: 1 at.%Cr, right: 14 at.%Cr) after attainment of steady-state. From ref [173].

and for the same dissolution valences of both components (3+).

$$i_{Fe} = ix_{Fe,a}$$

$$i_{Cr} = ix_{Cr,a}$$

where the x's refer to the molar fractions in the alloy. At the outer side of the film, the same partial currents are supported by the molar fractions of cations $x_{Fe,e}$ and $x_{Cr,e}$. The ratio of the individual dissolution rates of each of the elements from the metal (a) and the first layer of the passive film (e) is reflected in the dissolution currents of the pure metal components in the same passive conditions, $i_{co,Fe}$ and $i_{co,Cr}$, so that

$$\frac{x_{Cr,e}}{x_{Fe,e}} = \frac{i_{co,Fe}}{i_{co,Cr}} \frac{x_{Cr,a}}{x_{Fe,a}} \tag{55}$$

Chromium enrichment in the film, according to Eq. (53), is directly correlated with the lower dissolution rate of pure Cr with respect to pure iron. This is consistent with a lower diffusivity of this element in the film and tentatively explained by the high-field migration model. However, this is done at the expense of introducing, nonclassically, the diffusivity in the preexponential factor of Eq. (42) [188]. After

Copyright © 2002 Marcel Dekker, Inc.

simple transformation, Eq. (55) can be written as a reciprocal dependence of the passive current of the alloy with respect to its Cr content.

Figure 28 shows an example of the good agreement reported in Ref. 179 and considered as supporting the model. The model validity has been also discussed in the case of Fe-Mo and Fe-Al alloys [189]. Subsequently [190], precipitation from supersatured anolyte in the initial stage of active dissolution was proposed as a determining step of the passive film growth on alloys with a low Cr content at low pH. This hypothesis can be traced back to the 1930s [11].

Selective Dissolution

Conditions for simultaneous dissolution generally involve the formation of a 2D or 3D surface layer in which the relative dissolution rates of the elements are equal to their alloy fraction. Even in cases where simultaneous dissolution is obeyed, the process must begin by an initial period of selective dissolution at least at a 2D level [191]. As briefly mentioned earlier, many mechanisms have been invoked to explain how, for a nonpassive alloy, the dissolution of the more reactive element can continue across the dealloyed structure [32,1194]. Surface changes have been attributed to surface diffusion and recrystallization, redeposition, short-range atomic rearrangement, and a roughening transition by capillary effects.

Electrochemical measurements coupled with solution analysis were progressively backed up by analysis of the surface and in-depth profiling of the alloy composition in the dealloyed layer [198]. Current-voltage, current-time, and potential-time relationships, as a function of the alloy composition and of the degree of selective dissolution, are the techniques employed extensively. Contributions to the field using this kind of approach can be found in Ref. 173, 196, 199.

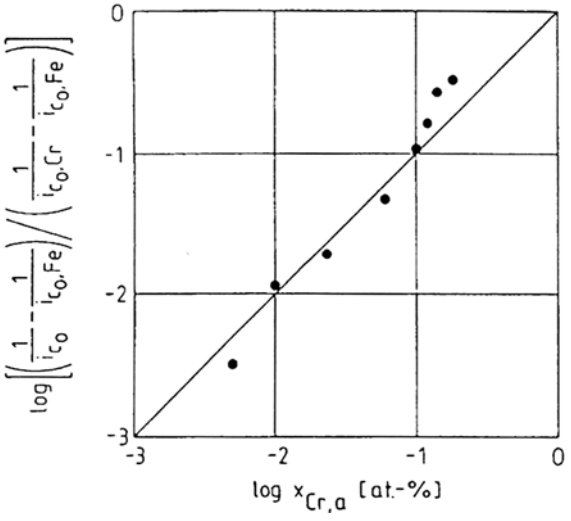


Figure 28. Relation between the passive current densities, i_{co}, and the concentration of chromium in Fe-Cr alloy, $x_{Cr.a}$ according to the model relating the dissolution of the alloy to the Cr/Fe proportion at the outer side of the film. From ref [179].

Copyright © 2002 Marcel Dekker, Inc.

Anodic Dissolution of Binary Alloys Studied by Electrochemistry, Solution, and Surface Analysis Techniques

These investigations have dealt with alloys such as AgPd, CuPd, NiPd, and AgAu under conditions of no passivation. Alloy-electrolyte (LiCl) combinations offer the possibility of observing both selective and simultaneous dissolution behaviors depending on the concentration of the noble metal. Two quantities are defined for describing the amount and in-depth property of the dealloyed surface:

e_B = surface excess of the more noble metal B:

$$e_B = \int_0^\infty (X_B(z) - X_{B,b})\, dz$$

where $X_B(z)$ is the mole fraction of B at distance z from the surface (z) and $X_{B,b}$ in the bulk alloy.

S_B = selectivity coefficient (dimensionless):

$$S_B = 1 - \frac{Q_B}{Q_{B,th}} \tag{56}$$

where Q_B is the charge corresponding to the amount of B dissolved (from solution analysis) and $Q_{B,th}$ its amount calculated for simultaneous dissolution by the same charge ($S_B = 1$ corresponds to complete selective dissolution of A, $S_B = 0$ to simultaneous dissolution).

The value of e_B can be estimated from potential-time transients or AES analysis, and the value of S_B is determined by weight loss and solution analysis. The potential increases with the dissolving charge passed at the interface in the selective dissolution stage, then reaches a critical value E_c and exhibits a plateau where either both components dissolve in stoichiometric proportion or only one keeps dissolving with formation of surface roughness. On Ag-Pd alloys the e_{Pd} values at the critical potential, estimated by electrochemistry and AES, are in reasonably good agreement; they show a steady decay when the Pd content in the alloy is increased and become negligible above 50%. Figure 29 shows an example of this dependence for three alloys [199]. A threshold of Pd concentration is observed around 0.2, beyond which no Pd enrichment takes place. This can be understood in the framework of percolation theory (see the next section).

Some mechanistic data on surface enrichment can be inferred. Surface enrichment is essentially constant after a minimal amount of dissolution (5 mC cm^{-2}), independent of the dissolution rate. Redeposition and surface diffusion are ruled out in favor of short-range rearrangements of surface atoms. A reciprocal shift of binding energy between Ag and Pd atoms is assumed to participate to some degree in simultaneous dissolution of Pd at potentials lower than from the pure metal [156]. Quite identical conclusions are reached for Cu-Pd, Ni-Pd, and Ag-Au alloys [180].

Investigation of the anodic dissolution below the critical potential is likely to provide more relevant information on the mechanism of selective dissolution [178]. The emphasis is generally put on the current-time relationships, which are supposed to reflect the mechanism of transport within the surface layer. Dynamic polarization curves and current-time decays have been investigated for Cu-Au and Ag-Pd in LiCl

Copyright © 2002 Marcel Dekker, Inc.

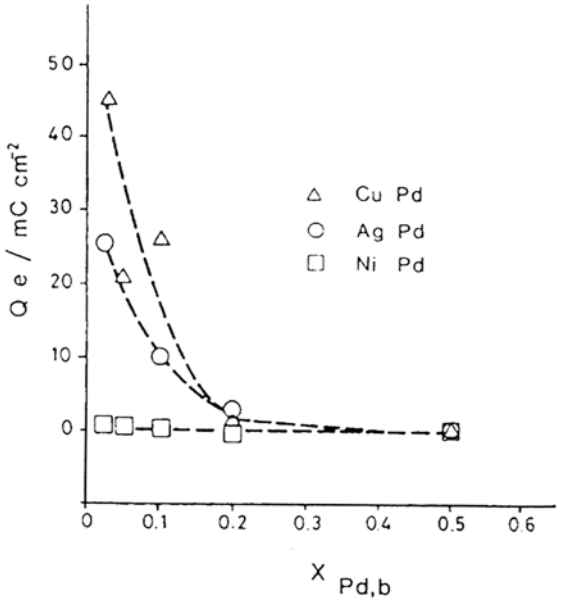


Figure 29. Measured charge corresponding to Pd enrichment as a function of Pd bulk mole fraction. From ref [199].

and acidic sulfate solutions. In all cases, current-voltage profiles display a plateau followed by a steep increase at the same critical potential E_c evidenced on the potential-time transient. The shape of these curve is shown schematically in Figure 30.

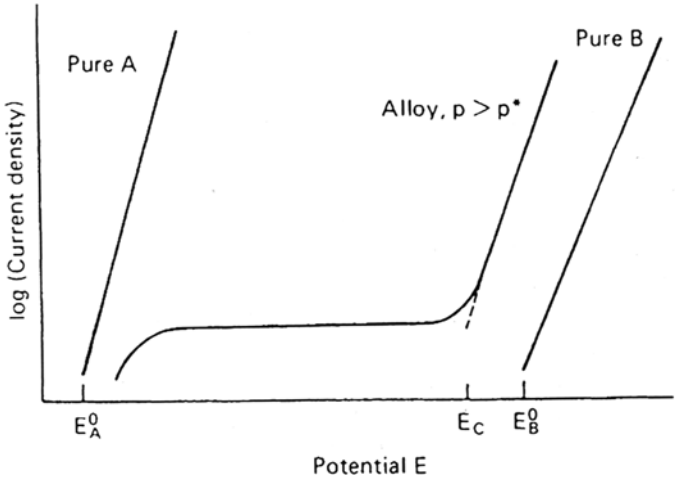


Figure 30. Schematic illustration of the anodic polarization curves for a binary A-B alloy with respect to the curves for the individual elements A and B. From ref [32].

Copyright © 2002 Marcel Dekker, Inc.

In agreement with previous work, the current-time transients recorded at various potentials below the critical potential are correctly represented by a reciprocal power law:

$$I \propto t^{-m} \quad \text{with } 0.8 \leq m \leq 1 \tag{57}$$

regardless of the alloy composition. The interpretation suggested in Ref. 196 is derived from the model of divacancy diffusion [182]. Diffusivity of the vacancies is supposed to depend on concentration and potential. The resulting nonlinear diffusion is most probably responsible for a t^{-m} current dependence, as indicated by numerical simulations.

Actually, even the sophisticated studies combining electrochemistry and surface analysis seem unable to yield any further decisive information on the detailed mechanism of selective dissolution. Atomic arrangements in which dissolution of atoms A can proceed throughout a rough electrode structure enriched in B type have been recognized as amenable to percolation theory [193]. The same theory was also applied to the passivation of binary Fe-Cr alloys in which, as suggested in Ref. 105, 106, passivation of the more soluble element, Fe, is enhanced by a connected surface lattice of passive Cr atoms. The main power of percolation theory is to provide diagnostic criteria for computer simulations in terms of concentration thresholds.

Atomistic Modeling of Selective Dissolution and Related Passivation by Percolation Theory

The now popular concept of percolation has proved quite successful in many fields in which a macroscopic property depends on the existence of a connected path within a two-phase discrete medium, most often a regular 2D or 3D arrangement of sites (site lattice percolation). Typical features related to percolation are the existence of a critical phenomenon, for instance, a threshold concentration of conducting sites when conduction is considered, and of a power law dependence with respect to the critical quantity in the close vicinity of the critical point. Both the site percolation thresholds and the power exponents have well-established theoretical values for any given lattice geometry and connection rules [193].

In spite of its extensive use in the description of heterogeneous systems, including electrolytic crystal growth, it seems that the percolation concept was considered relatively recently in the field of electrode processes for explaining sharply varying properties of alloys. The characteristic feature of a critical concentration of Zn in α-brass and Al in Al-Cu alloy was correlated with the percolation threshold on an fcc lattice [175].

Computer Simulations of Selective Dissolution An extensive contribution was reported [32] addressing the problems raised by experimental dealloying thresholds p^* at variance with theoretical site percolation thresholds p_c.

Possible interpretations are listed:

1. Dissolution from low-coordination sites (kinks and ledges) faster than from terraces
2. Not randomly distributed atoms in the alloy
3. Surface diffusion of B (noble atoms)

Copyright © 2002 Marcel Dekker, Inc.

4. Contribution of first-order and higher order nearest neighbors to the rate of dissolution of A (soluble atoms) leading to a high-density percolation problem

Computer simulations with a Monte Carlo algorithm of the selective dissolution of 2D square and 3D cubic lattices modeling binary alloys (A-B) are performed.

Dealloying Thresholds: Dealloying thresholds p^* are defined by the value of p, the fractional occupancy by A-type atoms, at which vacancy percolation occurs; i.e., continuous dissolution pathways start penetrating all the way through the lattice. Of course, in the absence of any surface diffusion, vacancy percolation maps closely the percolation of A atoms in the initial lattice. This is seen in Table 2, where no diffusion or diffusion restricted to atoms B with zero or one first nearest neighbor (lines 1 and 3) generates p^* close to the theoretical percolation threshold on 2D and 3D lattices (0.6 and 0.31, respectively). On the contrary, easy diffusion tends to produce smooth front and layer-by-layer dealloying on 3D lattices as indicated by p^* close to the 2D percolation threshold (lines 5 and 6). This likely explanation of p^* larger than p_c was questioned by in situ scanning tunneling microscopy (STM) demonstrating that Ag atoms dissolve from terraces well below the 3D percolation threshold [200].

Morphology of Dealloyed Structures on 2-D Lattices The roughness of the dissolution front is characterized by its fractal dimension, d (estimated from the mass theorem [190]). Variation of d as a function of p is shown in Figure 31, displaying the classical transition toward the dimension of the infinite cluster at the percolation threshold ($d \cong 1.60$).

Easier diffusion of B produces features such as a smoother dissolution front, internal vacancy clusters (polyatomic voids), and islands of A-type atoms hindered from dissolution. Qualitatively similar conclusions are drawn on 3D lattices except for the specific generation of pores with easier diffusion of B atoms as predicted [201] by a nonstochastic approach. This tendency to generate a tunneling attack at the cost of only surface diffusion could be considered as a likely explanation of pit nucleation at the atomic level, with no need for the concept of passive film breakdown.

Kinetics of Dealloying and Structure of the Dealloyed Layer The dealloying kinetics are represented by the time dependence of the flux of creation of vacancies, available from the computer data. The results are compared with the prediction by percolation theory, below and above the percolation threshold p^*. Below p^*, near-exponential decay of the current with time is predicted in agreement with experiments. Above p^*, experiments show a decay much steeper than expected, attributed to ohmic and mass transport effects in the porous interface. No mention is made of the negative power law decay reported in Ref. 196 [Eq. (56)].

The Critical Potential E_c The nature of the critical potential, (see Fig. 30) was addressed in the framework of this model. No definite conclusions are established. E_c may be the balance point between the smoothing action of surface diffusion and the roughening action of dissolution. Another explanation regards E_c as a threshold potential above which percolation becomes possible within a connected subset of A-type atoms with lowered reactivity due to their atomic surrounding (high-density percolation problem).

Copyright © 2002 Marcel Dekker, Inc.

Table 2 Summary of the Dissolution and Diffusion Rules Used in 2-D and 3-D Computer Simulations

Rule		Dimension	Dealloying threshold p^*	Percolation threshold p_c
Dissolution when nearest neighbors $\leq$ 3	Diffusion when nearest neighbors $\leq$ 1	2	0.595 ± 0.005	0.6
Dissolution when nearest neighbors $\leq$ 3	Dissolution when nearest neighbors $\leq$ 2	2	0.35 ± 0.05	0.6
Dissolution when nearest neighbors $\leq$ 5	No diffusion	3	0.310 ± 0.005	0.31
Dissolution when nearest neighbors $\leq$ 5	Dissolution when nearest neighbors $\leq$ 3	3	0.225 ± 0.025	0.31
Dissolution when nearest neighbors $\leq$ 4	Dissolution when nearest neighbors $\leq$ 2	3	0.60 ± 0.05	0.31
Dissolution when nearest neighbors $\leq$ 3	Dissolution when nearest neighbors $\leq$ 3	3	0.65 ± 0.05	0.31

Source: Ref. 32.

Copyright © 2002 Marcel Dekker, Inc.

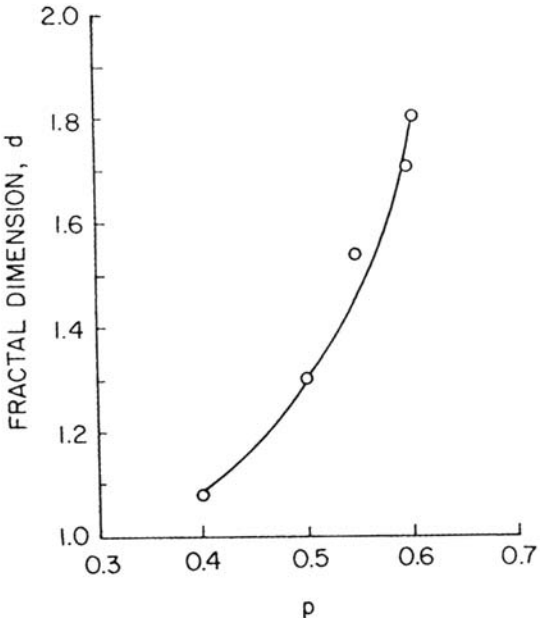
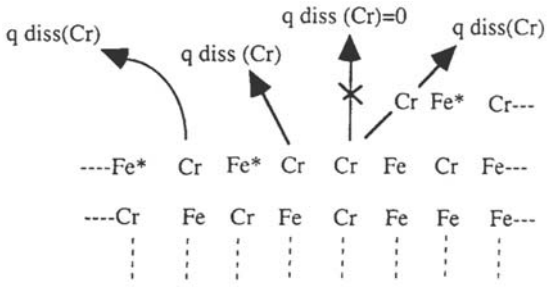


Figure 31. The fractal dimension *d* of the dissolution front as a function of p. For the 2-D rule (line 1 in Table 2). From ref [32].

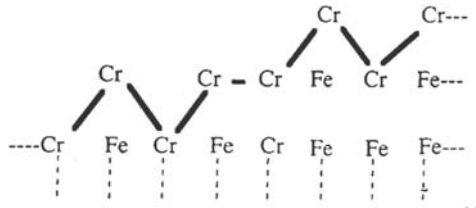
The use of a percolation approach clarifies substantially the selective dissolution of single-phase binary alloys. Computer simulations support the existence of a tight relationship between dealloying thresholds and site percolation thresholds. However, a careful survey of the literature over the last 10 years leads to the striking constatation that this important piece of work is totally ignored by other groups active in the field. It should be emphasized that a significant dissolution of the noble metal is repeatedly mentioned, e.g., Pd in Ag-Pd alloys [172], and is not allowed in the percolation model of selective dissolution. Dissolution of both alloy components at different rates is taken into account in the model of passivation of Fe-Cr alloys [184,192], presented in the following.

Curvature Effects, Roughening Transition, and Critical Potential Following the results of Monte Carlo simulations, the major contribution to the roughening process and macroscopic dealloying comes from a kinetically determined competition between dissolution and diffusion. The origin of roughening during the dissolution of single-phase binary alloys has been revisited [179]. The role of capillary phenomena, i.e., of surface curvature in the free surface energy, has been considered in a quantitative approach to this problem. Dynamic balance between dissolution and surface diffusion generates a modification of the surface profile and is shown to give rise to unstable modes (roughening transition). Equality between the wavelength of instabilities and the cluster size on the surface is thought to occur at the critical potential E_c. Reasonable consistency is claimed with literature data on Ag-Au alloys [176].

Copyright © 2002 Marcel Dekker, Inc.



Dissolution of Fe* atoms gives way to the Cr protection line shown below :



(58)

Percolation Model for Passivation of Binary Alloys, Case of Fe-Cr The Fe-Cr alloys are well known to display easier passivation above a critical Cr concentration close to 13 at % [180,186]. A computer approach was developed to demontrate the main atomistic features of a percolation model for passivation of binary alloys. In a way quite similar to that in Ref. 32, most aspects show up on 2D lattices. Computer simulations [191] were then extended to 3D [192]. Along the same lines as sketched earlier [105,106], the Monte Carlo simulations make use of dissolution probability rules of any atom that depend on its own atomic neighborhood. The Cr atoms having at least two Cr atoms as first or next nearest neighbors are considered as passivated. This allows Cr–O–Cr bridging bonds to block the Fe atoms of the underlying atomic row. Application of these rules and the resulting passivation at the surface of a random 2D lattice of Fe-Cr sites [184] is sketched in (58). A wide set of p and relative dissolution rates was explored. In all cases, larger Cr contents tend to passivate the alloy at the cost of an initial selective dissolution confined to only a few monatomic layers.

Current-voltage trends in the dissolution-passivation range are restituted by assuming Tafel kinetics for iron dissolution and a chemical rate-determining step for chromium. Extension to 3D lattices [192] leads to similar conclusions but highlights a critical concentration $p_c\{1, 2\}$ (the percolation threshold for interactions up to the second nearest neighbor) on a 3D lattice in better agreement with the transition of Fe-Cr to stainless steel behavior.

The atomistic approach to alloy dissolution shows a real possibility of achieving a unified description, incorporating at the same time the kinetic and geometric aspects of these intricate phenomena. Serious difficulties remain for estimating the probabilities of reaction of individual atoms and their dependence on local interaction. These models may involve as many parameters as in the

Copyright © 2002 Marcel Dekker, Inc.

macroscopic models of non-steady-state (impedance) responses of the anodic dissolution and passivation processes. In that sense, they are subject to the same kind of criticism. Estimation of the ability of the atomistic models at dealing with these non-steady-state behaviors is certainly one of the next challenges in the field.

REFERENCES

1. K. E. Heusler, *Encyclopedia of Electrochemistry of the Elements*, vol. 9A (A. J. Bard, ed.), Marcel Dekker, New York, Vol 9A, 1982, p. 230.
2. W. J. Lorenz and K. E. Heusler, Anodic dissolution of iron group metals, *Corrosion Mechanisms* (F. Mansfeld, ed.), Marcel Dekker, New York, 1987.
3. J. O'M. Bockris and S. U. M. Khan, *Surface Electrochemistry*. *A Molecular Level Approach*, Plenum, New York, 1993.
4. I. Epelboin and M. Keddam, Electrochemical techniques for studying passivity and its breakdown, *Passivity of Metals* (R. P. Frankenthal and J. Kruger, eds.), Electrochemical Society, Pennington, NJ, 1978, p. 184.
5. C. Gabrielli, M. Keddam, and H. Takenouti, The use of a.c. techniques in the study of corrosion and passivity, *Treatise on Materials Science and Technology*, Vol. 23, *Corrosion: Aqueous Processes and Passive Films* (J. C. Scully, ed.), Academic, Press, New York, 1983, p. 395.
6. F. Mansfeld and W. J. Lorenz, Electrochemical impedance spectroscopy (EIS): application in corrosion science and technology, *Techniques for Characterization of Electrodes and Electrochemical Processes* (R. Varma and J. R. Selman, eds.), Wiley, New York, I99l, p. 581.
7. D. D. Macdonald, Application of electrochemical impedance spectroscopy in electrochemistry and corrosion science, *Techniques for Characterization of Electrodes and Electrochemical Processes* (R. Varma and J. R. Selman, eds.), Wiley, New York, 1991, p. 515.
8. C. Gabrielli, M. Keddam, H. Perrot, H. Takenouti, and B. Tribollet, Generalized impedance spectroscopy applied to electrochemical systems, in preparation.
9. D. M. Drazic, *Modern Aspects of Electrochemistry*, Vol. 19 (J. O'M Bockris and B. E. Conway, eds.), Plenum, New York, 1989.
10. A. R. Despic, Deposition and dissolution of metals and alloys, *Comprehensive Treatise of Electrochemistry*, Vol. 7, Part B (B. E. Conway, J. O'M Bockris, E. Yeager, S. U. M. Khan, and R. E. White, eds.), Plenum, New York, 1983, p. 451.
11. K. J. Vetter, *Electrochemical Kinetics: Theoretical and Experimental Aspects*, Academic Press, New York, 1967.
12. F. Hilbert, Y. Miyoshi, G. Eichkorn, and W. J. Lorenz, Correlation between the kinetics of electrolytic dissolution and deposition of iron, *J. Electrochem. Soc. 118*:1919, 1927 (1971).
13. J. O'M. Bockris and D. Drazic, The kinetics of deposition and dissolution of iron: effect of alloying impurities, *Electrochim. Acta 7*:293 (1962).
14. T. Hurlen, Reaction models for dissolution and deposition of solid metals, *Electrochim. Acta 11*:1205 (1966).
15. F. Huet, Private communication, unpublished work.
16. J. N. Stranski, Zur Theorie des Kristallwachstums, *Z. Phys. Chem. 136*:259 (1928).
17. M. Pourbaix, Emploi de la thermodynamique et de la cinétique électrochimique pour l'étude des phénomènes de passivation, *Ber. Bunsenges. Z. Elektrochem. 62*:670 (1958).
18. K. J. Laidler, *Chemical Kinetics*, 2nd ed., McGraw-Hill, New York, 1965, p. 72.
19. M. Eigen, Ionic reactions in aqueous solutions with half-times as short as 10^{-9} second. Application to neutralization and hydrolysis reactions, *Discuss. Faraday Soc. 17*:194 (1954).

Copyright © 2002 Marcel Dekker, Inc.

20. M. Eigen, Determination of general and specific ionic interactions in solution, *Discuss. Faraday Soc. 24*:251 (1957).
21. R. T. Foley and P. P. Trzaskoma, The identification of the activated state in the dissolution and passivation of metals, *Passivity of Metals*, Corrosion Monographs series (R. P. Frankenthal and J. Kruger eds.), Electrochem. Society, Pennington, NJ, 1978, p. 337.
22. K. E. Heusler, Der Einflub der Wasserstoffionenkonzentration auf das electrochemische Verhalten des aktiven Eisen in säurer Lösungen. Der Mechanismus der Reaktion: $Fe = Fe^{2+} + 2e^{-}$, *Z. Elektrochem. 62*:582 (1958).
23. J. O'M. Bockris, D. Drazic, and A. Despic, The electrode kinetics of the deposition and dissolution of iron, *Electrochim. Acta 4*:325 (1961).
24. S. Haruyama, Accelerating factors of anodic dissolution, Proceedings Second Japan-USSR corrosion seminar: *Homogeneous and Heterogeneous Anodic Dissolution of Metals and Their Inhibition*, Japan Soc. Corros. Eng., Tokyo, 1980, p. 128.
25. N. Sato, Mechanism of homogeneous and heterogeneous anodic dissolution of metals, Proceedings Second Japan-USSR corrosion seminar: *Homogeneous and Heterogeneous Anodic Dissolution of Metals and Their Inhibition*, Japan Soc. Corros. Eng., Tokyo, 1980, p. 35.
26. J. R. Vilche and A. J. Arvía, Los modelos de reacción relacianados con la transición estado activo-estado pasivo en los metales de la familia del hierro, *An. Acad. Nac. Cien. Exactas Fis. Nat. Buenos Aires 33*:33 (1981).
27. E. B. Budevski, Deposition and dissolution of metals and alloys, *Comprehensive Treatise of Electrochemistry*, Vol. 7 (B. E. Conway, J. O'M. Bockris, E. Yeager, S. U. M. Khan, and R. E. White, eds.), Part A, Plenum, New York, 1983, p. 399.
28. G. Eichkorn, W. J. Lorenz, L. Alberg, and H. Fischer, Einflußder Oberflächenaktivität auf die anodischen Auflösungmechanismen von Eisen in sauren Lösungen, *Electrochim. Acta 13*:183 (1968).
29. W. Allgaier and K. E. Heusler, Morphology of (211) surfaces of iron during anodic dissolution, *Z. Phys. Chem. N.F. 98*:161 (1975).
30. W. Allgaier and K. E. Heusler, Steps and kinks on (211) iron surfaces and the kinetics of the iron electrodes, *J. Appl. Electrochem. 9*:155 (1979).
31. B. Folleher and K. E. Heusler, The mechanism of the iron electrode and the atomistic structure of iron surfaces, *J. Electroanal. Chem. 180*:77 (1984).
32. K. Sieradzki, R. R. Corderman, K. Shukla, and R. C. Newman, Computer simulations of corrosion: selective dissolution of binary alloys, *Philos. Mag. 59*:713 (1989).
33. I. Epelboin, C. Gabrielli, M. Keddam, J. C. Lestrade, and H. Takenouti, Passivation of iron in sulfuric acid medium, *J. Electrochem. Soc. 119*:1632 (1972).
34. I. Epelboin, C. Gabrielli, M. Keddam, and H. Takenouti, The study of the passivation process by electrode impedance analysis, *Comprehensive Treatise of Electrochemistry*, Vol. 4, *Electrochemical Materials Science* (J. O'M. Bockris, B. E. Conway, E. Yeager, and R. E. White, eds.), Plenum, New York, 1981, p. 151.
35. M. Garreau, Etude du mécanisme de la formation des ions métalliques à l'interface métal-électrolyte au cours de la dissolution anodique des métaux, *Met. Cor. Ind. 541*:3 (1970).
36. C. Deslouis and B. Tribollet, Flow modulated techniques in electrochemistry, *Advances in Electrochemical Science and Engineering*, Vol. 2 (H. Gerischer and C. W. Tobias, eds.), VCH Weiheim, New York, 1991, p. 205.
37. W. J. Albery and M. L. Hitchman, *Ring-Disc Electrodes*, Oxford Sci. Res. Pap., Clarendon Press, Oxford, 1971.
38. N. Benzekri, M. Keddam, and H. Takenouti, a.c. response of a rotating ring-disc electrode: application to 2-D and 3-D film formation in anodic processes, *Electrochim. Acta 34*:1159 (1989).

Copyright © 2002 Marcel Dekker, Inc.

39. S. Bourkane, C. Gabrielli, and M. Keddam, Investigation of gold oxidation in sulphuric medium. II. Electrogravimetric transfer function technique, *Electrochim. Acta 38*:l827 (1993).
40. H. Angerstein-Kozlowska, J. Klinger, and B. E. Conway, Computer simulation of the kinetic behavior of surface reactions driven by a linear potential sweep, *J. Electroanal. Chem. 75*:45 (1977).
41. K. F. Bonhoeffer and K. E. Heusler, Bemerkung über die anodische Auflösung von Eisen, *Ber. Bunsenges. Z. Elektrochem. 61*:122 (1957).
42. H. Gerischer and W. Mehl, Zum mechanismus der kathodischen Wasserstoffabscheidung am Quecksilber, Silber und Küpfer, *Z. Elektrochem. 59*:1049 (1955).
43. I. Epelboin, M. Keddam, and P. Morel, Evidence of multi-step reactions on iron, nickel and chromium electrodes immersed in a sulfuric acid solution, Proceedings 3rd Congress Metal Corrosion, Moscow, 1966, p. 110.
44. M. L. Boyer, I. Epelboin, and M. Keddam, Une nouvelle méthode potentiocinétique d'étude des processus électrochimiques rapides, *Electrochim. Acta 11*:221 (1966).
45. I. Epelboin, M. Keddam, and J. C. Lestrade, Variation de certaines impédances électrochimiques en fonction de la fréquence, *Rev. Gen. Electr. 76*:777 (1967).
46. I. Epelboin, M. Keddam, and J. C. Lestrade, Faradaic impedances and intermediates in electrochemical reactions, *Faraday Discuss. Chem. Soc. 56*:264 (1973).
47. C. Gabrielli and M. Keddam, Progrès récents dans la mesure des impédances électrochimiques en régime sinusoïdal, *Electrochim. Acta 19*:355 (1974).
48. R. D. Armstrong, Electrode impedance for the active-passive transition, *J. Electroanal. Chem. 34*:387 (1972).
49. I. Epelboin, C. Gabrielli, and M. Keddam, Non-steady state techniques, *Comprehensive Treatise of Electrochemistry*, Vol. 9, *Electrodics*: *Experimental Techniques* (E. Yeager, J. O'M. Bockris, B. E. Conway, and S. Sarangapani, eds.), Plenum, New York, 1984, p. 61.
50. E. Bayet, F. Huet, M. Keddam, K. Ogle, and H. Takenouti, A novel way of measuring local electrochemical impedance using a single vibrating probe, *J. Electrochem. Soc. 144*:L87 (1997).
51. E. Bayet, F. Huet, M. Keddam, K. Ogle, and H. Takenouti, Adaptation of the scanning vibrating electrode technique to ac mode: local electrochemical impedance measurement, *Mater. Sci. Forum 289–292*:57 (1998).
52. E. Bayet, F. Huet, M. Keddam, K. Ogle, and H. Takenouti, Local electrochemical impedance measurement: scanning vibrating electrode technique in ac mode, *Electrochim. Acta 44*:4117 (1999).
53. I. Annergren, F. Zou, and D. Thierry, Application of localized electrochemical techniques to study kinetics of initiation and propagation during pit growth, *Electrochim. Acta 44*:4383 (1999).
54. F. Zou and D. Thierry, Diffusion effects in localized electrochemical impedance measurements by probe methods, *J. Electrochem. Soc. 146*:2940 (1999).
55. C. Gabrielli and M. Keddam, Contribution of impedance spectroscopy to the investigation of the electrochemical kinetics, *Electrochim. Acta 4*:957 (1996).
56. C. Gabrielli, M. Keddam, and H. Takenouti, New Advances in the investigation of passivation mechanisms and passivity by combination of ac relaxation techniques: impedance, RRDE and quartz electrogravimetry, *Corros. Sci. 31*:129 (1990).
57. B. H. Erné and D. Vabmeakelbergh, The low-frequency impedance of anodically dissolving semiconductor and metal electrodes. A common origin? *J. Electrochem. Soc. 144*:3385 (1997).
58. D. Vanmaekelbergh and B. H. Erné, Coupled partial charge-transfer steps in the anodic dissolution of metals, *J. Electrochem. Soc. 1546*:2488 (1999).

Copyright © 2002 Marcel Dekker, Inc.

59. Y. Ishikawa, T. Yoshimura, and T. Ozaki, Adsorption of water on iron surfaces with reference to corrosion, *Corros. Eng. 40*:643 (1991).
60. I. Epelboin and M. Keddam, Faradaic impedances: diffusion impedance and reaction impedance, *J. Electrochem. Soc. 117*:1052 (1970).
61. M. Keddam, O. R. Mattos, and H. Takenouti, Reaction model for iron dissolution studied by electrode impedance. I. Experimental results and reaction model, *J. Electrochem. Soc. 128*:257 (1981).
62. M. Keddam, O. R. Mattos, and H. Takenouti, Reaction model for iron dissolution studied by electrode impedance. II. Determination of the reaction model, *J. Electrochem. Soc. 128*:266 (1981).
63. H. Fischer and H. Yamaoka, Zum Mechanismus der Inhibitionswirkung organischer Verbindungen in System Eisen/Säure, *Chem. Ber. 94*:1477 (1961).
64. W. J. Lorenz, H. Yamaoka, and H. Fischer, Zum electrochemishen Verhalten des Eisens in salzsauer Lösungen, *Ber. Bunsenges. Phys. Chem. 67*:932 (1963).
65. J. O'M. Bockris and H. Kita, Analysis of galvanostatic transients and application to the iron electrode reaction, *J. Electrochem. Soc. 108*:676 (1961).
66. E. J. Kelly, The active iron electrode. I. Iron dissolution and hydrogen evolution reaction in acidic sulfate solutions, *J. Electrochem. Soc. 112*:124 (1965).
67. W. J. Lorenz and G. Eichkorn, Discussion of "The active iron electrode. I. Iron dissolution and hydrogen evolution reactions in acidic sulfate solutions" by E. J. Kelly, *J. Electrochem. Soc. 112*:1255 (1965).
68. M. Keddam, O. R. Mattos, and H. Takenouti, Discussion of "Impedance measurements on the anodic iron dissolution", by H. Schweickert, W. J. Lorenz, and H. Friedburg, *J. Electrochem. Soc. 128*:1294 (1981).
69. I. Epelboin, P. Morel, and H. Takenouti, Corrosion inhibition and hydrogen adsorption in the case of iron in a sulfuric aqueous medium, *J. Electrochem. Soc. 118*:1283 (1971).
70. G. J. Bignold and M. Fleischmann, Identification of transient phenomena during the anodic polarisation of iron in dilute sulphuric acid, *Electrochim. Acta 19*:363 (1974).
71. G. Bech-Nielsen, The anodic dissolution of iron V. Some observations regarding the influence of cold working and of annealing on the two anodic reactions of the metal, *Electrochim. Acta 19*:821 (1974).
72. G. Bech-Nielsen, The anodic dissolution of iron. XI. A new method to discern between parallel and consecutive reactions *Electrochim. Acta 27*:1383 (1982).
73. E. McCafferty and N. Hackerman, Kinetics of iron corrosion in concentrated acidic chloride solutions, *J. Electrochem. Soc. 119*:999 (1972).
74. I. Epelboin, C. Gabrielli., M. Keddam, and H. Takenouti, A coupling between charge transfer and mass transport leading to multi-steady states. Application to localized corrosion, *Z. Phys. Chem. N.F. 98*:215 (1975).
75. B. Bechet, I. Epelboin, and M. Keddam, New data from impedance measurements concerning the anodic dissolution of iron in acidic sulphuric media, *J. Electroanal. Chem. 76*:129 (1977).
76. H. Schweickert, W. J. Lorenz, and H. Friedburg, Impedance measurements on the anodic iron dissolution, *J. Electrochem. Soc. 127*:1693 (1980).
77. J. A. Harrison and W. J. Lorenz, A comment on the transient dissolution of pure iron in acid solution, *Electrochim. Acta 22*:205 (1977).
78. D. Geana, A. A. El Miligy, and W. J. Lorenz, Zür anodischen Auflösung von Reineisen im Bereich zwischen aktiven und passiven Verhalten, *Corros. Sci. 13*:505 (1973).
79. D. Geana, A. A. El Miligy, and W. J. Lorenz, The kinetics of iron dissolution and passivation, *Passivity of Metals* (R. P. Frankenthal and J. Kruger, eds.), Electrochemical Society, Pennington, NJ, 1978, p. 607.

Copyright © 2002 Marcel Dekker, Inc.

80. D. Geana, A. A. El Miligy, and W. J. Lorenz, Galvanostatic and potentiostatic measurements on iron dissolution in the range between active and passive state, *Corros. Sci. 14*:657 (1974).
81. D. Geana, A. A. El Miligy, and W. J. Lorenz, A theoretical treatment of the kinetics of iron dissolution and passivation, *Electrochim. Acta 20*:273 (1975).
82. J. Bessone, L. Karakaya, P. Loorbeer, and W. J. Lorenz, The kinetics of iron dissolution and passivation, *Electrochim. Acta 22*:1147 (1977).
83. K. Juttner, W. J. Lorenz, and G. Kreysa, Dynamic system analysis on metallic glasses, *Corrosion, Eletrochemistry and Catalysis of Metallic Glasses* (B. B. Diegle and K. Hashimoto, eds.), Vol. 88-1, Electrochemical Society, Pennington, NJ, 1988, p. 14.
84. N. Benzekri, Contribution au développement de l'électrode disque-anneau en courant alternatif. Applications aux mécanismes de dissolution et passivation anodiques, Thesis, Université P.M. Curie, Paris, 1988.
85. T. Tsuru, T. Hishimura, and S. Haruyama, Anodic dissolution of iron as studied with channel-flow double electrode, Proceedings EMCR'2, Toulouse, France, *Mater. Sci. Forum 8*:429 (1986).
86. K. Takahashi, J. A. Bardwell, B. MacDougall and M. J. Graham, Mechanism of anodic dissolution of iron. I Behaviour in neutral acetate buffer solutions, *Electrochim. Acta 37*:477 (1992).
87. K. E. Heusler and G. H. Cartledge, The influence of iodide ions and carbon monoxide on the anodic dissolution of active iron, *J. Electrochem. Soc. 108*:732 (1961).
88. Z. A. lofa, V. V. Batrakov, and Cho-Ngok-Ba, Influence of anion adsorption on the action of inhibitors on the acid corrosion of iron and cobalt, *Electrochim. Acta 9*:1645 (1964).
89. K. Takahashi, J. A. Bardwell, B. MacDougall, and M. J. Graham, Mechanism of anodic dissolution of iron. II Comparison of the behaviour in neutral benzoate and acetate buffer solutions, *Electrochim. Acta 37*:498 (1992).
90. R. Schrebler, L. Basaez, I. Guardiazabal, H. Gomez, R. Cordova, and F. Queirolo, Electrodissolution and passivation of iron electrode in acetic/acetate solution, *Bol. Soc. Quim. 36*:65 (1991).
91. R. J. Chin and K. Nobe, Electrodissolution kinetics of iron in chloride solutions, *J. Electrochem. Soc. 119*:1457 (1972).
92. H. C. Kuo and K. Nobe, Electrodissolution kinetics of iron in chloride solutions. VI. Concentrated acidic solutions, *J. Electrochem. Soc. 125*:853 (1978).
93. D. R. MacFarlane and S. I. Smedley, The dissolution mechanism of iron in chloride solutions, *J. Electrochem. Soc. 133*:2240 (1986).
94. O. E. Barcia and O. R. Mattos, The role of chloride and sulphate anions in the iron dissolution mechanism studied by impedance measurements, *Electrochim. Acta 35*:1003, (1990).
95. O. E. Barcia and O. R. Mattos, Reaction model simulating the role of sulphate and chloride in anodic dissolution of iron, *Electrochim. Acta 35*:1601 (1990).
96. J. A. L. Dobbelaar, The use of impedance measurements in corrosion research. The corrosion behaviour of chromium and iron-chromium alloys, Thesis, Technical University of Delft, The Netherlands, 1990.
97. Y. M. Kolotyrkin, Electrochemical behaviour and anodic passivity mechanism of certain metals in electrolyte solution, *Z. Elektrochem. 62*:649 (1958).
98. T. Heumann and F. W. Diekötter, Untersuchugen über das electrochemische Verhalten des Chroms in Schwefelsäuren Lösungen in Hinblick auf die Passivitä, *Ber. Bunsenges. Phys. Chem. 67*:671 (1963).
99. J. A. L. Dobbelaar and J. H. W. de Wit, A detailed analysis of impedance measurements in the study of the passivation of chromium, *Corros. Sci. 31*:637 (1990).

Copyright © 2002 Marcel Dekker, Inc.

100. R. D. Armstrong, M. Henderson, and H. R. Thirsk, The impedance of chromium in the active-passive transition, *J. Electroanal. Chem. 35:*119 (1972).
101. T. Tsuru, Anodic dissolution mechanisms of metals and alloys, *Mater. Sci. Eng. A 146*:1 (1991).
102. S. Haupt and H. H. Strehblow, The analysis of dissolved Cr III with the rotating ring-disc technique and its application to the corrosion of Cr in the passive state, *J. Electroanal. Chem. 216*:229 (1987).
103. M. S. EI-Basiouny and S. Haruyama, The polarization behaviour of chromium in acidic sulphate solution, *Corros. Sci. 17*:405 (1977).
104. M. Okuyama, M. Kawakamal, and K. Ito, Anodic dissolution of chromium in acidic sulphate solutions, *Electrochem. Acta 30*:757 (1985).
105. M. Keddam, O. R. Mattos, and H. Takenouti, Mechanism of anodic dissoltion of iron-chromium alloys investigated by electrode impedances. I. Experimental results and reaction model, *Electrochim. Acta 31*:1147 (1986).
106. M. Keddam, O. R. Mattos, and H. Takenouti, Mechanism of anodic dissolution of iron-chromium alloys investigated by electrode impedances.II. Elaboration of the reaction model, *Electrochim. Acta 31*:1159 (1986).
107. I. Epelboin, M. Keddam, O. R. Mattos, and H. Takenouti, The dissolution and passivation of Fe and Fe-Cr alloys in acidified sulphate medium: influence of pH and Cr content, *Corros. Sci. 19*:1105 (1979).
108. R. D. Armstrong and R. E. Firman, Impedance of titanium in the active-passive transition, *J. Electroanal. Chem. 34*:391 (1972).
109. A. Caprani, I. Epelboin, and P. Morel, Valence de dissolution du titane en milieu sulfurique fluoré, *J. Electroanal. Chem. 43*:App2 (1973).
110. A. Caprani and J. P. Frayret, Behaviour of titanium in concentrated hydrochloric acid; dissolution-passivation mechanism, *Electrochim. Acta 24*:835 (1979).
111. A. Jardy, A. Legal Lasalle-Molin, M. Keddam, and H. Takenouti, Copper dissolution in acidic sulfate media studied by QCM and R.R.D.E. under a.c. signal, *Electrochim. Acta 37*:2195 (1992).
112. R. Oltra, G. M. Indrianjafy, M. Keddam, and H. Takenouti, Laser depassivation of a channel flow double-electrode: a new technique in repassivation studies, *Corros. Sci. 35*:827 (1993).
113. I. Efimov, M. Itagaki, M. Keddam, R. Oltra, H. Takenouti, and B. Vuillemin, Laser activation of passive electrodes, *Mater. Sci. Forum*, *185–188*:937 (1995).
114. F. Huet, M. Keddam, X. R. Novoa, and H. Takenouti, Frequency and time resolved measurements at rotating ring-disc electrodes for studying localized corrosion, *J. Electrochem. Soc. 140*:1955 (1993).
115. F. Huet, M. Keddam, X. R. Növoa, and H. Takenouti, Time resolved RRDE applied to pitting of Fe-Cr alloy and 304 stainless steel, *Corros. Sci. 38*:133 (1996).
116. M. Itagaki, R. Oltra, B. Vuillemin, M. Keddam, and H. Takenouti, Quantitative analysis of iron dissolution during repassivation of freshly generated metallic surfaces, *J. Electrochem. Soc. 144*:64 (1997).
117. N. Benzekri, R. Carranza, M. Keddam, and H. Takenouti, a.c. response of R.R.D.E. during the passivation of iron, *Corros. Sci. 31*:627 (1990).
118. R. P. Frankenthal and J. Kruger, eds., *Passivity of Metals*, Corrosion Monographs series, Electrochemical Society, Pennington, NJ, 1978.
119. M. Froment, ed., *Passivity of Metals and Semiconductors*, Elsevier, Amsterdam, 1983.
120. German-American Colloquium on Electrochemical Passivation, *Corros. Sci. 29* (2–3) (1989).
121. *Passivation of Metals and Semiconductors*. Proceedings of the 7th International Symposium on Passivity, Clausthal, Germany, 1994, Materials Science Forum (K. E. Heusler, ed.), Trans Tech publications, Vol. 185–188, 1995.

Copyright © 2002 Marcel Dekker, Inc.

122. *Passivity-8*, Proceedings of the 8th International Symposium on Passivity of Metals and Semiconductors, Jasper, Canada, 1999, Electrochemical Society, Pennington, NJ, in press.
123. C. Wagner, Beitrag Zur Theory des Anlaufvorgangs, *Z. Phys. Chem. B21*:25(1933).
124. C. Wagner, Models for lattice defects in oxide layers on passivated iron and nickel, *Ber. Bunsenges. Phys. Chem. 77*:1090 (1973).
125. M. J. Dignam, The kinetics of the growth of oxides, *Comprehensive Treatise of Electrochemistry*, Vol. 4, *Electrochemical Materials Science* (J. O'M Bockris, B. E. Conway, E. Yeager, and R. E. White, eds.), Plenum, New York, 1981, p. 247.
126. N. Sato and M. Cohen, The kinetics of anodic oxidation of iron in neutral solutions. I. Steady state growth region, *J. Electrochem. Soc. 111*:512 (1964).
127. N. Sato and M. Cohen, The kinetics of anodic oxidation of iron in neutral solutions. II. Initial stages, *J. Electrochem. Soc. 111*:519 (1964).
128. I. A. Ammar and S. Darwish, Growth of passive layers on iron and nickel, *Electrochim. Acta 12*:225 (1967).
129. M. Keddam and C. Pallotta, Galvanostatic response of the passive film on iron in acidic media, *Electrochim. Acta 30*:469, (1985).
130. M. Keddam and C. Pallotta, Electrochemical behavior of passive iron in acid medium. *J. Electrochem. Soc. 132*:781 (1984).
131. K. J. Vetter and F. Gorn, Kinetics of layer formation and corrosion processes of passive iron in acidic solutions, *Electrochim. Acta 18*:321 (1973).
132. K. J. Vetter and F. Gorn, Die instationäre Korrosion des passiven Eisens in säurer Lösung, *Werkst. Korros. 21*:703 (1970).
133. M. Keddam, J. F. Lizée, C. Pallotta, and H. Takenouti, Electrochemical behavior of passive iron in acid medium. I. Impedance approach, *J. Electrochem. Soc. 131*:2016 (1984).
134. R. Kirchheim, Growth Kinetics of passive films, *Electrochim. Acta 32*:1619 (1987).
135. K. E. Heusler, Untersuchung der Auflösung des passiven Eisen in Schwefelsäure mit der Rotierenden Scheiben-Ring Elektrode, *Ber. Bunsenges. Phys. Chem. 72*:1197 (1968).
136. T. Tsuru, E. Fujii, and S. Haruyama, Passivation of iron and its cathodic reduction studied with a rotating ring-disc electrode, *Corros. Sci. 31*:655 (1990).
137. R. Kirchheim, The growth kinetics of passive films and the role of defects, *Corros. Sci. 29*:183 (1989).
138. D. D. Macdonald, The point defect model for the passive state, *J. Electrochem. Soc. 139*:3434 (1992).
139. C. Gabrielli, M. Keddam, F. Minouflet, and H. Perrot, Investigation of the anodic behaviour of iron in, sufuric acid medium by the electrochemical quartz microbalance under ac regime, *Mater. Sci. Forum*, *185–188*:631 (1995).
140. C. Gabrielli, M. Keddam, F. Minouflet, and H. Perrot, ac electrogravimetry contribution to investigation of the anodic behaviour of iron in sulfuric medium, *Electrochim. Acta 41*:1217 (1996).
141. C. Y. Chao, L. F. Lin, and D. D. Macdonald, A point defect model for anodic passive film. III. Impedance response, *J. Electrochem. Soc. 129*:1874 (1982).
142. D. D. Macdonald and S. I. Smedley, An electrochemical impedance analysis of passive films on nickel (111) in phosphate buffer solutions, *Electrochim. Acta 35*:1949 (1990).
143. A. Jouanneau, M. Keddam, and M. C. Petit, A general model of the anodic behaviour of nickel in acidic media, *Electrochim. Acta 21*:287 (1976).
144. M. Keddam, H. Takenouti, and N. Yu, New data on the kinetics of passive nickel from very low frequency impedance measurements, *Corros. Sci. 27*:107 (1987).
145. K. J. Vetter and K. Arnold, Korrosion und Sauerstoffüberspannung des passiven Nickels in Schwefelsäure, *Z. Electrochem. 64*:244 (1960).

Copyright © 2002 Marcel Dekker, Inc.

146. J. Osterwald. Zum Stabilitätverhalten stationären Elektrodenzustand, *Electrochim. Acta 7*:523 (1962).
147. I. Epelboin and M. Keddam, Kinetics of formation of primary and secondary passivity in sulfuric aqueous media, *Electrochim. Acta 17*:171 (1972).
148. M. Keddam, H. Takenouti, and N. Yu, Transpassive dissolution of Ni in acidic sulfate media: a kinetic model, *J. Electrochem. Soc. 132*:2561 (1985).
149. R. D. Armstrong and M. Henderson, The impedance of transpassive chromium, *J. Electroanal. Chem. 40*:121 (1972).
150. R. D. Armstrong and M. Henderson, The transpassive dissolution of chromium, *J. Electroanal. Chem. 32*:1 (1971).
151. M. Bojinov, I. Betova, and R. Raicheff, A model for the transpassivity of molybdenum in acidic sulphate solutions based on ac impedance measurements, *Electrochim. Acta* 1173 (1996).
152. M. Bojinov, I. Betova, R. Raicheff, G. Fabricius, T. laitinen, and T. Saario, Mechanism of transpassive dissolution and secondary passivation of chromium in sulphuric acid solutions, *Mater. Sci. Forum*, *289–292*:1019 (1998).
153. M. Bojinov, G. Fabricius, T. Laitinen, and T. Saario, Transpassivity mechanism of iron-chromium-molybdenum alloys studied by AC impedance, DC resistance and RRDE measurements, *Electrochim. Acta 44*:4331 (1999).
154. A. Turnbull, ed., *Corrosion Chemistry within Pits, Crevices and Cracks*, National Physical Laboratory, London, 1987.
155. J. L. Crolet and J. M. Defranoux, Calcul du temps d'incubation de la corrosion caverneuse des aciers inoxydables, *Corros. Sci. 130*:575 (1973).
156. U. F. Franck and R. FitzHugh, Periodische elekroden Prozesse in ihre Beschreibung durch eine mathematisches Modell, *Z. Elektrochem. 65*:156 (1961).
157. U. F. Franck, Instabilität Erscheinungen an passivierbaren Metallen, *Z. Elektrochem. 62*:649 (1958).
158. D. Sazou and M. Pagitsas, Current oscillations associated with pitting corrosion processes induced by iodide ions on the partially passive cobalt surface polarized in sulfuric acid solutions, *Electrochim. Acta 38*:835 (1993).
159. M. pagitsas and D. Sazou, The improved Franck-FitzHugh model for the electrodissolution of iron in sulphuric acid solutions: linear stability and bifurcation analysis. Derivation of the kinetic equations for the forced Franck-FitzHugh model, *Electrochim. Acta 36*:1301 (1991).
160. P. Glansdorff and I. Prigogine, *Structures, stabilité et fluctuations*, Masson, Paris, 1971.
161. O. E. Barcia, O. R. Mattos, and B. Tribollet, Anodic dissolution of iron in acidic sulfate under mass transport control, *J. Electrochem. Soc. 139*:446 (1992).
162. A. Moreau, Etude du mécanisme d'oxydo-réduction du cuivre dans les solutions chlorurèes acides. II. Systèmes Cu-CuCl-$CuCl_2$ et Cu-$Cu_2(OH)_3Cl$-$CuCl^+$ Cu^{2+}, *Electrochim. Acta 26*:1609 (1981).
163. A. Moreau, J. P. Frayret, F. Del Rey, and R. Pointeau, Etude des Phénomènes électrochimiques et des transports de matières d'un système mètal-électrolyte: cas d'un disque tournant en cuivre dans des solutions aqueuses d'acide chlorhydrique, *Electrochim. Acta 27*:1281 (1982).
164. F. K. Crundwell, The anodic dissolution of copper in hydrochloric acid solutions, *Electrochim. Acta 37*:2707 (1992).
165. O. E. Barcia, O. R. Mattos, N. Pebere, and B. Tribollet, Mass-transport study for the electrodissolution of copper in 1M hydrochloric acid solution by impedance, *J. Electrochem. Soc. 140*:2825 (1993).
166. A. C. West, Comparison of modeling approaches for a porous salt film, *J. Electrochem. Soc. 140*:403 (1993).

Copyright © 2002 Marcel Dekker, Inc.

167. A. C. West, R. D. Grimm, D. Landolt, C. Deslouis, and B. Tribollet, Electrohydrodynamic impedance study of anodically formed salt films on iron in chloride solutions, *J. Electroanal. Chem. 330*:693 (1992).
168. C. Clerc and D. Landolt, a.c. impedance study of anodic films on nickel in LiCl, *Electrochim. Acta 33*:859 (1988).
169. R. P. Tischer and H. Gerischer, Electrolytische Auflösung von Gold-Silber Liegerungen und die Frage der Resistenzgrenzen, *Z. Elektrochem. 62*:50 (1958).
170. J. O'M Bockris, B. Rubin, A. R. Despic, and B. Lovrecek, The electrodissolution of copper-nickel alloys, *Electrochim. Acta 17*:973 (1972).
171. H. P. Lee and K. Nobe, Rotating ring-disk electrode studies of Cu-Ni alloy electrodissolution in acidic chloride solutions II.95/5, 90/10 and 70/30 Cu-Ni alloys, *J. Electrochem. Soc. 140*:2483 (1993).
172. S. Rambert and D. Landolt, Anodic dissolution of binary single phase alloys. I. Surface composition changes on Ag-Pd studied by Auger electron spectroscopy, *Electrochim. Acta 31*:1421 (1986).
173. B. Heine and R. Kirchheim. Dissolution rate of Fe and Cr in Fe-Cr alloys in the passive state, *Corros. Sci. 31*:533 (1990).
174. I. Annergren, M. Keddam, H. Takenouti, and D. Thierry, Application of electrochemical impedance spectroscopy and rotating ring-disc measurements on Fe-Cr alloys, *Electrochim. Acta 38*:763 (1993).
175. K. Sieradskl, J. S. Kim, A. T. Cole, and R. C. Newman, The relationship between dealloying and transgranular stress corrosion cracking, *J. Electrochem. Soc. 134*:1635 (1987).
176. M. Stern, Surface area relationships in polarisation and corrosion, *Corros. NACE, 14*:329t (1958).
177. W. A. Mueller, Derivation of anodic dissolution curves of alloys from those of metallic components, *Corros. NACE 18*:73t (1962).
178. R. F. Steigerwald and W. D. Greene, The anodic dissolution of binary alloys, *J. Electrochem. Soc. 11*:1026 (1962).
179. R. Kirchheim. B. Heine, H. Fischmeister, S. Hofman, H. Knote, and U. Stolz, The passivity of iron-chromium alloys, *Corros. Sci. 29*:899, (1989).
180. R. C. Newman, F. T. Meng, and K. Sieradski, Validation of a percolation model for passivation of Fe-Cr alloys. I. Current efficiency in the incompletely passivated state, *Corros. Sci. 28*:523 (1988).
181. H. Kaiser, *Corrosion Mechanisms*, Marcel Dekker, New York, 1987.
182. H. W. Pickering and C. Wagner, Electrolytic dissolution of binary alloys containing a noble metal, *J. Electrochem. Soc. 114*:698 (1967).
183. H. E. Stanley and N. Ostrowsky, eds., *On Growth and Form, Fractal and Non-fractal Patterns in Physics*, Martinus Nijhot, Dondrecht, The Netherlands, 1986.
184. Song Qian, R. C. Newman, R. A. Cottis, and K. Sieradski, Validation of a percolation model for passivation of Fe-Cr alloys: two-dimensional computer simulations, *J. Electrochem. Soc. 137*:435 (1990).
185. R. Olivier, Passiviteit van ljzer en ljzer-Chroom Legeringen, 6th International Commitee of Electrochemical Thermodynamics and Kinetics (C.I.T.C.E.) (Poitiers), Butterworths, London 1954, p. 314; Thesis, Leiden, The Netherlands, 1955.
186. H. H. Uhlig, Electron configuration in alloys and passivity, *Z. Elektrochem. 62*:700 (1958).
187. R. P. Frankenthal, On the passivity of iron-chromium alloys. I. Reversible primary passivation and secondary film formation, *J. Electrochem. Soc. 114*:542 (1967).
188. R. P. Frankenthal, On the passivity of iron-chromium alloys. II. The activation potential, *J. Electrochem. Soc. 116*:580 (1969).

Copyright © 2002 Marcel Dekker, Inc.

189. R. Kirchheim, B. Heine, S. Hofman, and H. Hofsass, Compositional changed of passive films due to different transport rates and preferential dissolution, *Corros. Sci. 37*:573 (1990).
190. R. Kirchheim, Kinetics of film formation on Fe-Cr Alloys, *Modification of Passive Films* (P. Marcus, B. Baroux, and M. Keddam, eds.), Institure of Materials, London, 1994.
191. M. Okuyama and S. Kambe, Dissolution of Fe-30 Cr alloy in active and passive states in acidic chloride solutions, Proceedings EMCR'3, Zürich, Switzerland, *Mater. Sci. Forum 44–45*:63 (1989).
192. Song Qian, R. C. Newman, R. A. Cottis, and K. Sieradski, Computer simulation of alloy passivation and activation, *Corros. Sci.31*:621 (1990).
193. J. W. Essam, Percolation theory, *Rep. Prog. Phys. 43*:833 (1980).
194. I. Annergren, M. Keddam, H. Takenouti, and D. Thierry, Modelling of the passivation mechanism of Fe-Cr binary alloys from ac impedance and frequency resolved RRDE. 2. Behaviour of Fe-Cr alloys in 0.5 M H_2SO_4 with an addition of chloride, *Electrochim. Acta 42*:1595 (1997).
195. I. Annergren. M. Keddam, H. Takenouti, and D. Thierry, Modelling of the passivation mechanism of Fe-Cr binary alloys from ac impedance and frequency resolved RRDE. 1. Behaviour of Fe-Cr aloys in 0.5 M H_2SO_4, *Electrochim. Acta 41*:1121 (1996).
196. J. Laurent and D. Landolt, Anodic dissolution of binary single phase alloys at subcritical potential, *Electrochim. Acta 36*:49 (1991).
197. N. Benzekri, M. Keddam, and H. Takenouti, a.c. measurements at a rotating ring-disk electrode for corrosion investigations, *Surfaces*, *Inhibition and Pasasivation*, Vol. 86-7, Electrochemical Society, Pennington, NJ, 1986, p. 507.
198. J.Gniewek, J. Pezy, B. G. Baker, and J. O'M. Bockris, The effect of noble metals additions upon the corrosion of copper: an Auger spectroscopy study, *J. Electrochem. Soc. 125*:17 (1978).
199. S. Rambert and D. Landolt, Anodic dissolution of binary single phase alloys. II. Behaviour of CuPd, NiPd and AgAu in LiCl, *Eletrochim. Acta 31*:1433 (1986).
200. I. C. Oppenheim, D. J. Trevor, C. E. D. Chidsey, P. L. Trevor, and K. Sieradski, In situ scanning tunneling microscopy of corrosion of silver-gold alloys, *Science 254*:687 (1991).
201. A. J. Forty and G. Rowlands, A possible model for corrosion pitting and tunneling in noble metal alloys, *Philos. Mag. A43*:171 (1981).
202. K. Sieradski, Curvature effects in alloys dissolution, *J.Electrochem. Soc. 140* 1993).

Copyright © 2002 Marcel Dekker, Inc.

5

Thin Oxide Film Formation on Metals

Francis P. Fehlner
Corning Incorporated, Corning, New York

Michael J. Graham
National Research Council of Canada, Ottawa, Ontario, Canada

INTRODUCTION

A thin oxide film on base metals provides the protective layer required to make metals useful. Without such a layer, they would adhere to and react with each other as well as with other materials. The film, invisible to the naked eye, forms at low temperatures. By low, we mean near room temperature. This contrasts with high-temperature oxidation, which occurs at several hundred degrees Celsius and above.

The formation of an oxide film at low temperatures may be illustrated by the machining of an aluminium block. The cutting tool removes the surface of the metal, exposing pristine metal. In less than a millisecond, atmospheric oxygen attacks the exposed metal atoms and a thin oxide layer begins to form. It attains a limiting thickness after a few days. The thickness is in the range of a few nanometers (nm).

The kinetic rate laws of low-temperature oxidation are logarithmic, either direct or inverse. At high temperatures, parabolic kinetics are usually observed. For intermediate temperatures, logarithmic kinetics transform with time into the parabolic type.

The mechanism by which a thin oxide film forms on a metal must explain the transition from a two-dimensional adsorbed oxygen layer to a three-dimensional oxide film. The process at one time appeared to be impossible at room temperature because growth of an oxide requires that ions overcome an energy barrier to move into and through the oxide. The thermal energy available at room temperature is insufficient to overcome this barrier, which is approximately 1 electron volt. Fortunately, the work of Cabrera and Mott [1] showed how tunneling electrons and an electrochemical mechanism could explain the phenomena.

The process of oxygen adsorption on metals has been discussed in Chapter 2 of this book. The transition to an oxide film is a gradual one in the sense that islands of oxide nucleate from the adsorbed oxygen and then grow laterally across the surface. Fehlner and Mott [2] proposed that islands of oxide grow on the metal by a process of place exchange. This requires cooperative movement of both cations and anions. The driving force is postulated to be the image force between an oxygen ion and the

Copyright © 2002 Marcel Dekker, Inc.

metal. Mitchell and Graham [3] suggested that activated processes are unnecessary for island growth when it occurs at a step edge on a metal surface. However, they subsequently reported [4] that misorientation of the (111) plane on a nickel surface did not affect the rate of low-temperature oxidation.

Island growth is the initial stage of three-dimensional oxide growth and has been emphasized for the low-temperature oxidation of Ba and Mg [5a]. During the transition from island growth to a three-dimensional oxide film, the kinetics of the process undergo a marked change from linear to logarithmic. This is readily observed only at low temperatures.

MECHANISM OF THIN OXIDE GROWTH

The model of Cabrera and Mott is discussed in the book on low-temperature oxidation by Fehlner [5b]. The basis of the model is the quantum mechanical concept of electron tunneling. An electron can penetrate an energy barrier without the requirement for thermal activation. As soon as a three-dimensional oxide forms on a metal, electrons tunneling through the oxide are captured by adsorbed oxygen on the oxide surface. The charge separation thus established between the oxide surface and the metal sets up an electric field across the oxide. The proposed mechanism is illustrated in Figure 1.

Ion movement into and through an oxide is required if an oxide film is to thicken. Such movement requires that an activation energy of approximately 1 electron volt be supplied. At high temperatures, thermal energy is sufficient to overcome the energy barrier and the ion can move from site to site within the oxide. This is no longer true at low temperatures. However, the electric field across the oxide lowers the activation energy for ion movement into the oxide, allowing the oxide to continue growing thicker.

The process is self-limiting. The amount of charge is fixed so that the voltage across the film is relatively constant. Thus, the field across the oxide decreases as the oxide thickens. At some critical thickness, the oxide essentially stops growing because the reduction of the activation energy by the field is insufficient to allow

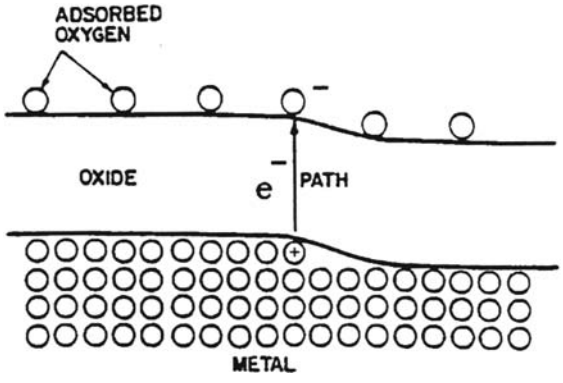


Figure 1 Proposed mechanism for low-temperature oxidation. (From Ref. 1.)

Copyright © 2002 Marcel Dekker, Inc.

continued ion movement. The overall process is quite analogous to anodic oxidation at constant voltage, which is discussed in Chapter 4 of this book. Thus, the rate of oxide growth is dependent on a preexponential factor and an activation term. The activation energy in the exponential is reduced by the electric field across the oxide. Corrosion, too, has been discussed in terms of an electrochemical mechanism [6,7]. See Chapter 1.

The rate of oxide growth according to the Cabrera-Mott expression can be written as

$$\frac{dx}{dt} = N\Omega\nu \exp\left(\frac{W - qaE}{kT}\right) \tag{1}$$

where x is the oxide thickness, t the time, N the number of potentially mobile ions, Ω the oxide volume per mobile ion, ν the atomic vibration frequency, W the energy barrier to ion movement into the oxide, q the ionic charge Ze, a half the ion jump distance, E the electric field V/x, k Boltzmann's constant, and T the temperature. Once the ion enters the oxide, it is assumed to pass easily to the other side, where reaction takes place.

Ghez [8] has integrated Eq. (1) to give the inverse logarithmic law:

$$\frac{x_1}{x} = -\ln\left(\frac{t + \tau}{x^2}\right) - \ln(x_1 u) \tag{2}$$

where

$$u = N\Omega\nu \exp(-W/kT) \tag{3}$$

and

$$x_1 = \left|\frac{ZeaV}{kT}\right| \tag{4}$$

The constant τ can be neglected if it is small compared with t. The value of u is expressed as nanometers per second and x_1 as nanometers. Fehlner [9] has utilized these equations to fit literature data on low-temperature oxidation. Some of these results will be included in this work.

Fehlner and Mott [2] pointed out that direct logarithmic kinetics could be derived from Eq. (1) if two conditions were met. First, the film must grow under constant field rather than constant voltage. This may happen when the growing field across the oxide causes ion movement to occur through the oxide before the maximum value of V is attained. Second, the oxide must rearrange with time so that the value of W increases by some factor, say ξx, where ξ is a constant and x is the oxide thickness. Thus, the activation term in Eq. (1) becomes

$$\exp[-(W + \xi x - qaE)/kT] \tag{5}$$

which integrates to a logarithmic expression.

The implication then is that the kinetics of low-temperature oxidation depend on the structure of the oxide. This can be considered in terms of network formers and modifiers. A network-forming oxide is one in which covalent bonds connect the atoms in a three-dimensional structure. There is short-range order on the atomic scale but no long-range order. For example, oxygen atoms form tetrahedra around

Copyright © 2002 Marcel Dekker, Inc.

ions such as silicon, triangles around aluminum. These continuous random networks can be broken up by the introduction of modifiers. Oxides such as sodium oxide have ionic bonding. When added to a network-forming oxide, they break the covalent bonds in the network, introducing ionic bonds, which change the properties of the mixed oxide.

It seems likely that direct logarithmic kinetics would be observed for modifying oxides rather than for network-forming oxides because the former have lower single oxide bond strengths and could rearrange more easily. See Table 1. The network formers would be expected to follow the inverse logarithmic kinetics of Eq. (2).

Kingery et al. [10a] have collected the experimental results for cation and anion self-diffusion coefficients in various oxides. For instance, the rate of diffusion of copper in Cu_2O, a modifier, is six orders of magnitude larger than that of aluminum in Al_2O_3, a network former when the aluminum is four coordinate. This result is for a temperature of approximately 1500°C, but the relative relationship is expected to hold at room temperature. This finding also supports the postulate that network modifiers can recrystallize more easily than network formers.

Table 1 Values of Single Oxide Bond Strengths[a]

M in MO_x	Valence	Bond strength (kcal mol^{-1})	Coordination number
B	3	119	3
Si	4	106	4
Ta	5	104	6
W	6	104	6
Al	3	101–79	4
P	5	111–88	4
Zr	4	81	6
Ti	4	73	6
Zn	2	72	2
Pb	2	73	2
Al	3	67–53	6
Zr	4	61	8
Cr	3	47	6
Sn	4	46	6
Cu	2	44	6
In	3	43	6
Mg	2	37	6
Li	1	36	4
Zn	2	36	4
Ba	2	33	8
Ca	2	32	8
Fe	2	32	6
Ni	2	28	6
Na	1	20	6
K	1	13	9

[a]Note: Glass formers have bond strengths > 75 kcal mol^{-1}, intermediates lie between 75 and ~50 kcal mol^{-1}, and modifiers lie below 50 kcal mol^{-1}.

Copyright © 2002 Marcel Dekker, Inc.

CONTROLLING FACTORS

Ion entry into a growing oxide occurs at the metal-oxide interface for cations and at the oxide-gas interface for anions. Davies et al. [11] have shown that one or both species can be mobile in an oxide undergoing anodization. The choice of mobile ion is related to the structure of the oxide, whether it is crystalline or noncrystalline, as discussed below. In the case of cation movement, the properties of the metal affect the rate of oxide growth. Such characteristics as crystal orientation, defects, and impurities are important. In the case of anion movement, gas pressure and the presence of moisture are most significant.

Metal Structure

The effect of crystallographic orientation on the rate of low-temperature oxidation is shown dramatically in the case of copper. Rhodin [12] published an early study of the copper-oxygen system at temperatures from –195° to 50°C. The (100) face oxidized approximately twice as fast as the (110) and (111) faces. Young et al. [13] showed that impurities could affect the rate of oxidation, especially on the (110) plane. Their results at 70°C are shown in Figure 2. Oxidation rates follow the order (100) > (111) > (110) > (311). Film thickness as a function of time appears to follow a linear relationship, but logarithmic kinetics have also been applied to the data.

The value of N in Eq. (1) is related to the number of sites where ion entry into the oxide can occur. However, in the case of cation movement, it has not been possible to predict the relative rates of oxidation according to the density of atomic packing on the various crystal faces. Cation loss from a surface occurs preferentially from steps and kink sites, so metal surface roughness and impurities play a major role. All these factors need to be considered when evaluating N.

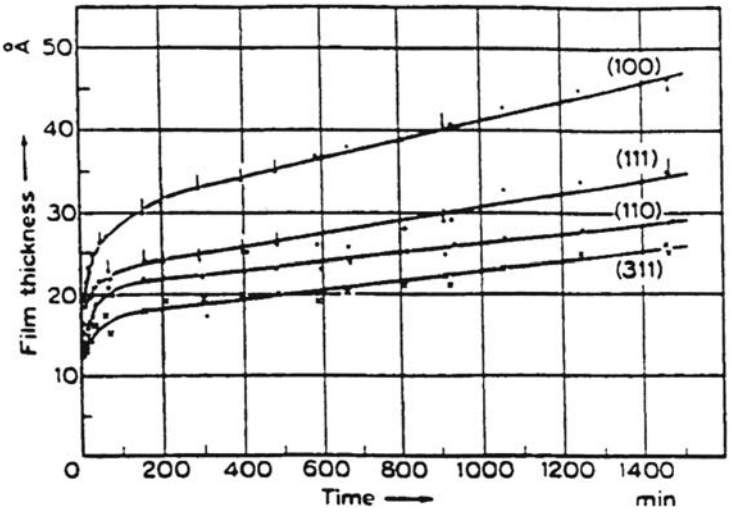


Figure 2 Copper oxidation. Oxidation of single-crystal copper surfaces in an atmosphere of oxygen at 70°C. (From Ref. 13.)

Copyright © 2002 Marcel Dekker, Inc.

Single-crystal studies as referenced above reveal the basic behavior of oxide growth on metals, but most metals are found as polycrystalline bodies. The gain boundaries that separate randomly oriented grains must accommodate the discontinuities between misoriented lattices. The resulting region of disorder serves as a sink for impurities and often a region of fast oxidation. As a result, a polycrystalline body can develop a very uneven, polycrystalline oxide layer. Metal grains with different crystallographic orientations oxidize at different rates. In addition, grain boundaries serve as points of weakness. The advent of glassy metal alloys has overcome some of these problems, at least at low temperatures [14, 15]. The lack of both a crystal lattice and grain boundaries eliminates orientation effects as well as impurity concentrations.

Oxide Structure

The book by Fehlner [5] emphasizes the role that vitreous (glassy or noncrystalline) oxide structure can play in oxide growth on metals. The structure of a vitreous oxide can have perfection equal to that of a single crystal. This fact is not well recongnized. At the atomic level, both structures are similar in that the short-range order is the same. For example, the local environments of silicon atoms in cristobalite and fused silica are very much alike. Each silicon atom is coordinated with four oxygen atoms in a tetrahedral arrangement. The difference in the structures is seen in the long-range order present in the crystal but absent in the fused silica glass. As a result, physical properties that depend on the local bonding are similar in the two structures but those dependent on long-range order differ. Both structures are expected to be more protective of a metal surface than a polycrystalline oxide would be. This is because the grain boundaries present in the polycrystalline oxide provide paths for easy ion movement and hence more rapid oxide growth.

The tetrahedral arrangement of atoms in silica lends itself to the formation of a three-dimensional network, which makes up the polymer-like structure of a glass. Glass can be formed from a single oxide or a mixture of oxides. Silicon dioxide is the permier glass-forming oxide either by itself or with other oxides. Additives to silica can either enter into the silica network or modify it. Modifiers such as sodium oxide break up the network, leading to l ower softening points (glasses have no sharp melting points), lower chemical durability, and higher ionic conductivity. Some oxides like zinc oxide can act as an intermediate oxide, i.e., either a network former, where it enters the silica tetrahedral network, or a modifer, where it breaks up the network. The choice depends on the other constituents in the glass. A basic review of the subject can be found in Kingery et al. [10b].

Several schemes are used to classify metal oxides as network formers, intermediates, or modifiers. A useful one is based on single oxide bond strengths. Values for the more common metals are collected in Table 1 from Sun [16] and Fehlner and Mott [2]. Glass formers tend to have single oxide bond strengths greater than 75 kcal mol^{-1}. The directional covalent bonds interfere with the crystallization of an oxide while it is being formed on the surface of a metal. Intermediates lie between 75 and approximately 50 kcal mol^{-1} and modifiers lie below this value. Their ionic bonds are not directional, so it is easier for the atoms to align in crystalline order.

This division can be related to thin oxide films on metals. The metals that fall into the network-forming or intermediate classes tend to grow protective oxides that

Copyright © 2002 Marcel Dekker, Inc.

support anion or mixed anion-cation movement. The network formers are non-crystalline, while the intermediates tend to be microcrystalline at low temperatures. The Cabrera-Mott inverse logarithmic expression [Eq. (2)] best fits the oxides that are noncrystalline, although a fine-grained oxide may be uniform enough to simulate a noncrystalline one. The metals that are in the modifier class have been observed to grow crystalline oxides by cation transport. These oxides are thicker and less protective. Their kinetics of growth fit direct logarithmic kinetics rather than the inverse type.

Impurities

Water is a major impurity that affects the rate of oxidation at low temperatures. It can, of course, be the sole source of oxygen at higher temperatures where dissociation of water can ocuur [17], but at low temperatures it serves to modify the structure of oxides. It has been found, for instance, that the rate of aluminum oxidation is increased [18] and that of copper is decreased [19] by the presence of water in oxygen. The details of the process as it affects low-temperature oxidation have yet to be elucidated. However, it may be postulated that water can act as a modifying oxide when added to network-forming oxides and thus weaken the structure. This would allow oxidation to proceed at a faster rate. On the other hand, water incorporation into modifiers may result in polymeric species [20] that are more stable than the polycrystalline oxides. They would form a stable protective gel layer.

The presence of other impurities such as sodium chloride, sulfur dioxide, or nitrogen oxides can also change the rate of thin-film formation. Examples of this are found in the literature of atmospheric corrosion, which is covered in Chapter 15 of this book.

TECHNIQUES FOR MEASURING THIN FILM GROWTH

A primary goal of the analytical work is to combine several methods so that a comprehensive picture of the metal-oxide system results. The features of particular interest include oxide structure and kinetics of the oxidation reaction.

Kinetics of Oxide Growth

Measurement of the rate of oxide growth on a metal surface is critical to sorting out the effects of time, temperature, oxygen pressure, metal structure, and impurities. The early use of manometric techniques has been supplemented by recording microbalances. Either method can give a continuous record of the weight gain or loss of a metal treated in a controlled-atmosphere furnace. Sensitivities in the submonolayer range are possible.

Resistivity measurements can supplement the information obtained from weight gain. Fehlner [5c] has pioneered a method that uses discontinuous metal films. The gaps between islands of metal accentuate the effect of surface oxidation.

Oxide Structure—Chemical

The initial stages of three-dimensional oxide growth can be studied using X-ray photoelectron spectroscopy (XPS) and Auger electron spectroscopy. The valence

Copyright © 2002 Marcel Dekker, Inc.

state of the atoms can be determined from energy shifts of the characteristic peaks. The escape depth of excited electrons from the oxide limits applications to the first 1–2 nm. This is, however, an important stage of growth where valence changes of impurities can be critical.

Examination of the composition of thicker films relies on depth profiles using XPS, Auger, or secondary ion mass spectrometry (SIMS), as well as Rutherford backscattering (RBS) and other nuclear techniques. In SIMS, an ion beam is used to bore a hole through the oxide. Simultaneously, a mass spectrometer records the ions that are generated during the boring. Thus, a continuous record in depth is obtained of the atomic composition. RBS also gives a depth profile of the oxide, but in a nondestructive manner. The energy distribution of backscattered ions such as helium is analyzed to reveal atomic mass as well as depth information. In both techniques, some interferences can be encountered for certain atomic masses.

Oxide Structure—Physical

Again, the methods can be divided into those best used for the initial stages of three-dimensional oxide growth and those useful in the latter stages. Low-energy electron diffraction (LEED) and reflection high-energy electron diffraction (RHEED) fall into the former class. They reveal the periodic structure and changes in that structure as an adsorbed oxygen layer evolves into the three-dimensional oxide. Thicker oxide is best examined using transmission electron microscopy (TEM) to look at both the plane of the film and the cross section. The physical features can be seen directly. The crystallography is studied using transmission electron diffraction. These techniques can be enhanced by applying selective etching to the samples.

Scanning tunneling microscopy (STM) and atomic force microscopy (AFM) are new developments that allow the atomic arrangement on a surface to be monitored. Changes in structure with oxidation time can be observed using these techniques.

EXAMPLES OF METAL OXIDATION AT LOW TEMPERATURES

The usefulness of a thin oxide film is often the reason for studying its growth rate and properties. For this reason, each of the examples below will be introduced by an application.

Silicon

Thin silica films of tunneling dimensions ($\leq$ 5 nm thick) are useful to the electronics industry. Formerly, such films interfered with good electrical contact at metal-to-metal junctions. Now, however, lateral dimensions on integrated circuits are reaching the submicrometer range and film thicknesses must scale accordingly. Metal oxide semiconductor (MOS) transistors with tunneling oxides as gate dielectrics are fabricated [21]. In the field of solar energy, the use of a thin oxide film between the silicon solar cell and the positive electrode has led to a conversion efficiency of 22% [22]. This equals the semi-empirical limit predicted by Bolton [23] and may be compared with the thermodynamic limit of 30%. We see then that thin silicon dioxide films are certainly useful.

Copyright © 2002 Marcel Dekker, Inc.

Logarithmic growth of oxide on silicon is found at temperatures up to approximately 500°C for pressures of 1 atmosphere. Higher temperatures over 1000°C can be used in reduced oxygen environments provided the total pressure is 1 atmosphere. Kamigaki and Itoh [24] worked with oxygen-nitrogen mixtures, and Ahn et al. [25] used nitrous oxide. In the latter case, some nitrogen was incorporated at the oxide-silicon interface. Other methods for forming thin oxides on silicon include rapid thermal oxidation [26], plasma oxidation [27], and moist oxygen in the presence of ultraviolet light [28]. The detailed mechanism of oxidation involving oxygen transport is still under discussion [42–44].

A noncrystalline oxide is formed on silicon. This is because the high oxide bond strength as given in Table 1 results in a very stable material. At the same time, it makes self-diffusion of oxygen or silicon difficult. It has been found that at high temperatures diffusion of oxygen molecules through the silica accounts for continued oxide growth. Oxygen atoms may be involved in the interfacial reaction with silicon. Under high electric fields, i.e., at low temperatures or during anodization, oxygen anions are postulated to be the mobile species. Fehlner [5d] discusses this point further.

The integrated form of the Cabrera-Mott expression [Eq. (2)] has been applied to the dry oxidation of silicon [29–31]. Values of N, W, and V have been calculated and are included in Table 2, which lists values for a number of elements. The values of W and V are reasonable but that of N is surprisingly low [9]. It may be related to the fact that anions are the mobile species in silica and the number of entry sites is limited.

Iron

This metal is used in many facets of industry, commerce, and home life. As such, the fact that it rusts away assumes vast economic importance. Scientists have labored to explain the mechanism of corrosion so that the destruction can be controlled. Both the nature of the corrosion film and the kinetics of the reaction have proved useful in understanding and avoiding the losses.

Table 2 Values of N, W, and $|V|$ Obtained from Kinetic Data by Fitting the Cabrera-Mott Expression [9][a]

Periodic Group	Element	N (cm^{-2})	W (eV)	$\lvert V\rvert$ (V)
IB	Cu	1×10^{21}	1.9	—
	Cu	2×10^{7}	0.5	86
IIIA	Al	6×10^{8}	1.6	~0.6
	Al	2×10^{3}	~0.9	~3.0
IVA	Si	1×10^{6}	1.5	2.6
	Ge	2×10^{6}	1.1	0.2
	Pb	7×10^{2}	0.4	1.5
VB	Ta	3×10^{12}	1.6	1.5
VIB	Cr	5×10^{13}	1.8	2.8
VIII	Fe	5×10^{8}	0.8	—
	Ni	3×10^{13}	1.6	2.3

[a]Note: Repeat runs for the same metal indicate two sources of experimental data.

Copyright © 2002 Marcel Dekker, Inc.

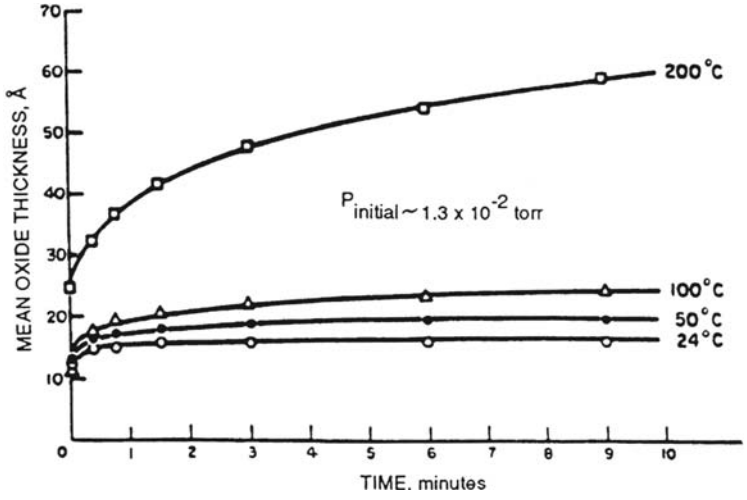


Figure 3 Iron oxidation. Oxide growth on polycrystalline iron as a function of temperature in an oxygen partial pressure of ~ 1.3×10^{-2} torr. (From Ref. 33.)

Iron can assume a valence of two or three in oxides. The former acts as a modifier as listed in Table 1, and the latter can be a network former, at least in mixed oxide glasses [32].

A logarithmic rate law is followed for the oxidation of polycrystalline iron in the temperature range 24 to 200°C. Results of Graham et al. [33] are shown in Figure 3. They were unable to distinguish between a direct and inverse logarithmic expression. Nevertheless, Eq. (2) has been applied to the data and values of the significant variables are included in Table 2. The number of active sites N on the metal surface, assuming cation transport through the oxide, may be related to the grain boundary population. The value of W is believable, but V was unreliable and is not included in the table.

Single-crystal studies show that the rate of oxidation varies with crystal face. The order was found to be polycrystalline > (110) > (112). Observations of the low-temperature oxide by electron diffraction were interpreted as epitaxial Fe_3O_4. Recently, XPS has been used to determine the composition of thin oxide films on iron [45–47].

A parabolic oxidation rate was found for temperatures above 200°C. It was controlled by oxide grain size as dictated by the grain size of the prior oxide. This was concluded from a study of the effect of surface pretreatment on the rate of oxidation [34]. Surface preparation is found to play an important role in the oxidation of many metals and alloys.

Nickel

This metal is less reactive with oxygen than iron. As such, it is used as a protective coating on base metals and as an additive in iron alloys to improve their corrosion resistance.

Copyright © 2002 Marcel Dekker, Inc.

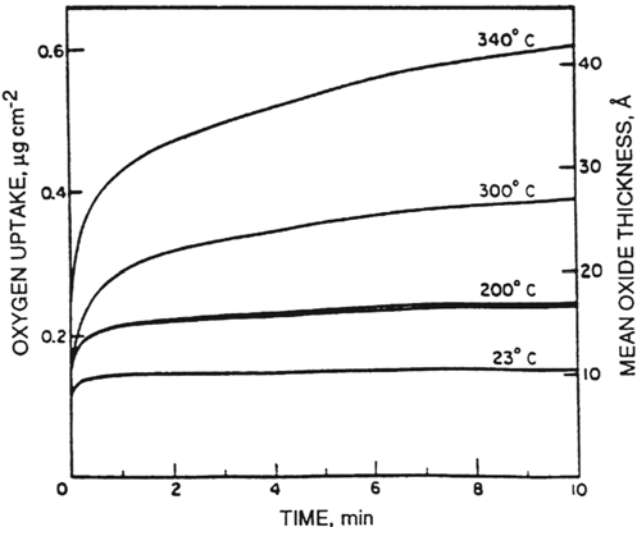


Figure 4 Nickel oxidation. Oxide growth on zone-refined, polycrystalline nickel sheet at 5×10^{-3} torr oxygen as a function of temperature. (From Ref. 35.)

Graham and Cohen [35] reported on the low-temperature oxidation of polycrystalline nickel. Their results for the temperature range 23 to 340°C are shown in Figure 4. A direct logarithmic law was followed for oxide thicknesses up to 3 nm. Parabolic kinetics were followed for thicker films. The crossover temperature was approximately 300°C.

The valence of nickel in the oxide is two. As a result, the oxide is a modifier (Table 1) and direct logarithmic kinetics are expected. The application of Eq. (2) to NiO as shown in Table 2 gave reasonable values but the applicability of the equation is in question. This may be a case where the factor ξx in Eq. (5) is insufficient to dominate the electric field so that inverse logarithmic kinetics still apply.

The nucleation and growth of oxide on nickel single crystals have been extensively studied. The results of Mitchell and Graham [3] are shown in Figure 5, which illustrates the transformation from oxygen chemisorption to three-dimensional oxide formation. At 40°C (Fig. 5a) the uptake of oxygen at low pressures shows two distinct plateaus, one corresponding to fractional monolayer adsorption and the other at longer exposures to the formation of an oxide film two or three atomic layers thick. A dramatically higher rate of oxidation has been reported for atomic oxygen-induced oxidation [48]. At 200°C (Fig. 5b) the second plateau is not observed. Instead, continuous uptake of oxygen occurs, indicative of continuing oxide growth. The kinetics of oxide formation can be explained in terms of oxide nucleation and growth, the density of nuclei depending on the particular crystallographic orientation, temperature, and oxygen pressure. Continuing oxide thickening, as on polycrystaline nickel, follows a logarithmic rate law.

Copyright © 2002 Marcel Dekker, Inc.

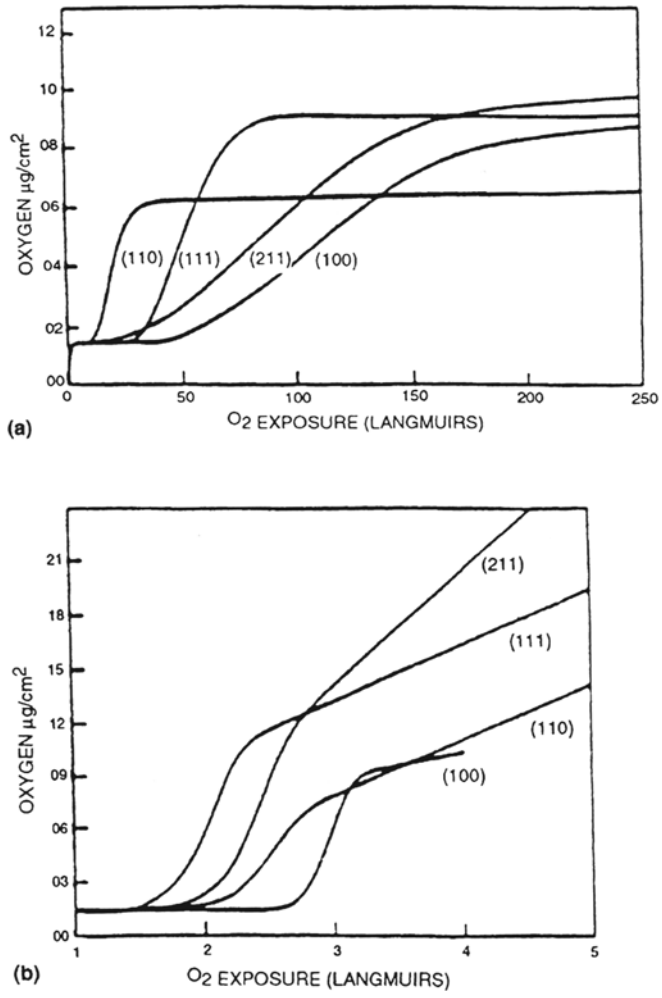


Figure 5 Nickel oxidation. Oxidation kinetics on various faces of nickel at (a) 40°C and (b) 200°C. One Langmuir equals 10^{-6} torr s. (From Ref. 3.)

Chromium

This metal by itself is very corrosion resistant. It is therefore used as a coating for base metals to maintain their integrity. An example is decorative trim forappliances. Of even greater importance is the use of chromium in alloys. It is the key component of stainless steel. McBee and Kruger [36] have shown that the addition of chromium to iron in an alloy causes the oxide film to go frompolycrystalline to noncrystalline as the amount of chromium increases. Ingeneral, oxidation of an alloy causes the more base component to segregate to the surface while the more noble component concentrates in the bulk of the alloy.

Low-temperature oxidation of polycrystalline chromium has been studied by Young and Cohen [37]. They found that a transition from inverse logarithmic to

Copyright © 2002 Marcel Dekker, Inc.

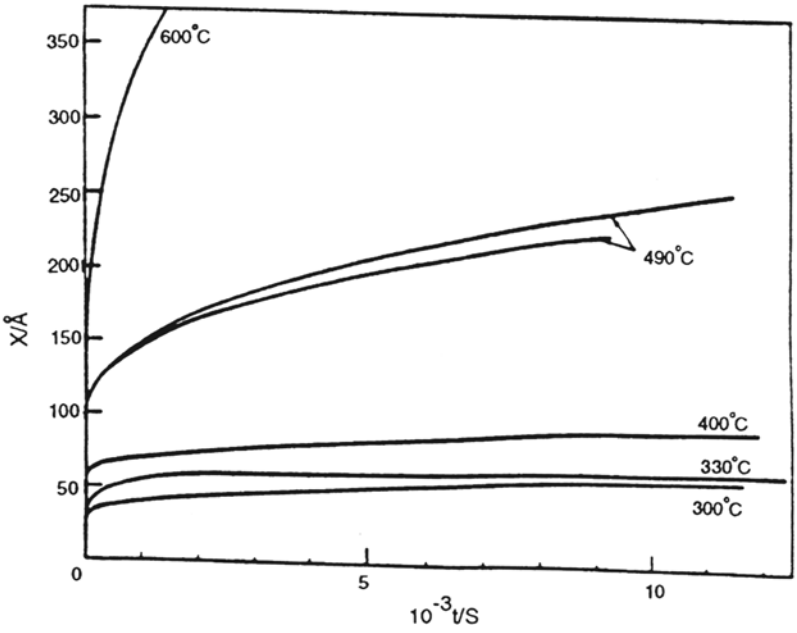


Figure 6 Chromium oxidation. Oxide growth on polycrystalline chromium at 4×10^{-3} torr oxygen as a function of temperature. (From Ref. 37.)

parabolic kinetics occurred at approximately 450°C for the data shown in Figure 6. However, the transition was a function of both time and temperature. It also correlated with a change in the oxide structure, from a fine-grained, almost vitreous oxide to a strongly preferred fiber texture. Ionic transport by cations was assumed and values for *N,W,* and *V* were calculated as shown in Table 2. However, Arlow et al. [38] present evidence that oxygen diffusion is the main mechanism for oxide film growth at temperatures below 300°C. Fortunately, Eq. (2) applies to both cation and anion movement. Only the value of *V* would change if the charge on the mobile ion was assumed to be different. At higher temperatures, mixed anion-cation movement takes place. These findings concerning ion motion agree with the fact that Cr_2O_3 can be an intermediate oxide, i.e., have properties between those of network-forming and modifying oxides, according to Table 1.

Arlow et al. [38] examined in detail the structure of thin oxides formed on a Cr(100) single-crystal surface. RHEED patterns distinguished the evolving atomic arrangements as shown in Figure 7. Two face-centered cubic (fcc) phases and a tetragonal phase were observed before the precipitation and growth of α-Cr_2O_3. There is also a transition from initial linear kinetics to a logarithmic reaction rate that approaches zero at some limiting thickness.

Recent work on Cr(110), under conditions where the kinetics of oxide growth are governed by chromium ion diffusion, shows that below 450°C Cr_2O_3 grows on a layer-by-layer basis whereas at higher temperatures the oxide surface roughens and cavities are formed at the metal-oxide interface [49–51]. In situ STM and Auger studies reveal that the oxidation of Cr(110) proceeds in three stages [52]. After an initially formed superlattice is saturated, it rearranges and characteristic oxide stripes

Copyright © 2002 Marcel Dekker, Inc.

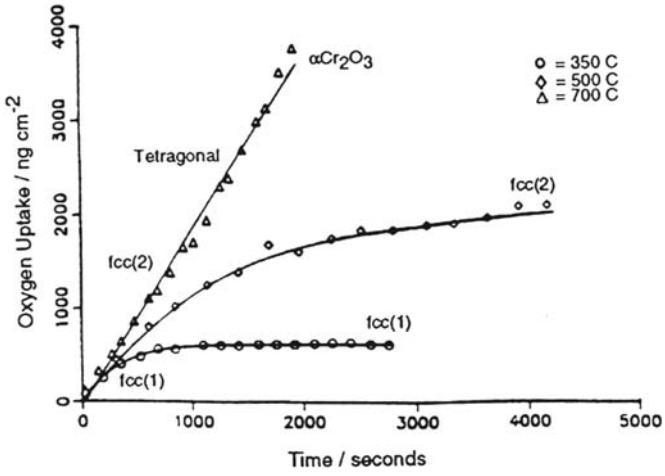


Figure 7 Chromium oxidation. Oxygen uptake by Cr(100) as a function of time at a pressure of 4.7×10^{-8} torr oxygen at 350, 500, and 700°C. Indicated on the kinetic curves are the temperature/mass regions over which the various oxide phases are observed. The two face-centered cubic phases are denoted as fcc(1) and fcc(2). At 700°C, the sticking factor is unity over the range shown. (From Ref. 38.)

form at terraces or above 700°C at steps on the surface. Subsequently, the stripes coalesce and bulk Cr_2O_3 growth continues.

Copper

Usefulness of the red metal is in the same class as that of iron. It is a mainstay of the modern industrial world. Electrical applications dominate, but it is also an important ingredient of alloys used for structural and decorative applications. The formation of a thin oxide on copper does not pose the electrical problem encountered with aluminum or silicon. Current passes quite easily through the oxide. Extensive corrosion of alloys, however, is a continuing problem.

Copper is not expected to follow Cabrera-Mott inverse logarithmic kinetics since its oxide is a modifier according to Table 1. In fact, copper follows direct logarithmic kinetics. This was emphasized by results (Table 2) from the analysis of experimental data [5e,9] including the results shown in Figure 2. No attempt is made here to apply the Fehlner-Mott direct logarithmic expression, Eq. (5) above. This is because the evidence for oxide recrystallization with time is very complex. Onay [39] reported on the formation of multiphase, multilayer scales on copper at 300°C. He found that they result from the dissociation of compact cuprous oxide scale that has lost contact with the copper substrate.

Recent in-situ transmission electron microscopy (TEM) studies by Yang et al. [53–56] present evidence that the "passive" oxide film on copper nucleates and grows as oxide islands, not as a uniform layer. Figure 8 from Ref. 53 shows the oxidation data of Young et al. [13] for (100) Cu (Fig. 2) together with a dark-field image from the Cu_2O reflection, where the bright specks are Cu_2O islands. These islands form at both atmospheric [53] and very low oxygen pressures [54,55] and in the latter case

Copyright © 2002 Marcel Dekker, Inc.

can be observed to grow and coalesce with time. Because the oxide island coverage is approximately 30%, the local oxide island thickness in Figure 8 is estimated to be ~ 400 Å, outside the range where an electron tunneling model would apply, and Yang et al. [53–55] consider that oxygen surface diffusion is the dominant mechanism for the transport, nucleation, and initial oxide growth on copper. In contrast to previous speculations, these authors [56] did not observe clear evidence that surface steps are preferential oxide nucleation sites.

Tantalum

This example illustrates the similarities between anodization and low-temperature oxidation. Tantalum has formed the basis for a solid-state capacitor that is extensively used in high-performance electronics. The dielectric is formed by anodization, a process studied by Vermilyea [40], The kinetics are expected to follow inverse logarithmic kinetics because the oxide is a network former, as seen in Table 1.

Ghez [8] used Eq. (2) to fit Vermilyea's results for the temperature range 150 to 300°C, and the resulting values of *N, W,* and given *V* are given in Table 2. All three are reasonable. The results of thermal oxidation of tantalum from 25 to 275°C [41] were also interpreted in terms of Cabrera-Mott theory.

CONCLUSION

The growth of thin oxide films on metals and semiconductors can be a useful as well as a destructive phenomenon. The study of the reactions involved leads to a measure of control. Specific oxide thickness and properties can be achieved for electronic

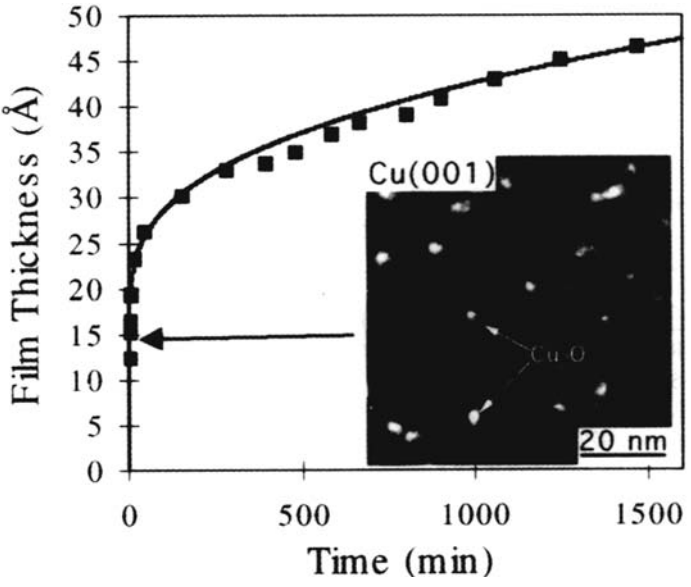


Figure 8 Copper oxidation. Oxidation of Cu (100) (Fig. 2 from Ref. 13) and dark-field TEM image from the Cu_2O reflection, where the bright specks are Cu_2O islands. (From Ref. 53.)

Copyright © 2002 Marcel Dekker, Inc.

applications. Materials that grow network-forming oxides are better for these purposes.

Metals that grow network-modifying oxides more easily undergo degradation by corrosion. The existence of grain boundaries or other paths of easy ion movement in the oxide allows continued film growth beyond the electron tunneling limit. A partial solution to this problem is to alloy the metal with one that forms a network oxide. The alloying metal tends to oxidize preferentially. It can segregate to the surface as a vitreous oxide film that protects the alloy from further attack.

The need for thin oxides on metals is increasing. Our ability to control the properties of the oxides will depend on our understanding at the atomic level of the processes involved.

REFERENCES

1. N. Cabrera and N. F. Mott, *Rep. Prog. Phys. 12*:163 (1948–49).
2. F. P. Fehlner and N. F. Mott, *Oxid. Metals 2*:59 (1970).
3. D. F. Mitchell and M. J. Graham, Intern. Corrosion Conf. Ser. *NACE-6,* p. 18 (1981).
4. D. F. Mitchell and M. J. Graham, *Surf. Sci. 114*:546 (1982).
5. F. P. Fehlner, *Low-Temperature Oxidation: the Role of Vitreous Oxides,* Wiley, New York, 1986, (a) p. 110, (b) pp. 148ff, (c) pp. 94ff, (d) pp. 228ff, (e) p. 199.
6. U. R. Evans, *An Introduction to Metallic Corrosion,* 2nd ed., Edward Arnold, London, 1963.
7. H. H. Uhlig, *Corrosion and Corrosion Control,* 2nd ed., Wiley, New York, 1971.
8. R. Ghez, *J. Chem. Phys. 58*:1838 (1973).
9. F. P. Fehlner, *J. Electrochem. Soc. 131*:1645 (1984).
10. W. D. Kingery, H. K. Bowen, and D. R. Uhlmann, *Introduction to Ceramics,* 2nd ed., Wiley, New York, 1976, (a) p. 240, (b) pp. 91ff.
11. J. A. Davies, B. Domeij, J. P. S. Pringle, and F. Brown, *J. Electrochem. Soc. 112*:675(1965).
12. T. N. Rhodin, Jr., *J. Am. Chem. Soc. 72*:5102 (1950); *73*:3143 (1951).
13. F. W. Young, Jr., J. V. Cathcart, and A. T. Gwathmey, *Acta Metall. 4*:145 (1956).
14. R. Ramesham, S. DiStefano, D. Fitzgerald, A. P. Thakoor, and S. K. Khanna, *J. Electrochem. Soc. 134*:2133 (1987).
15. D. J. Siconolfi and R. P. Frankenthal, *J. Electrochem. Soc. 136*:2475 (1989).
16. K.-H. Sun, *J. Am. Ceram. Soc. 30*:277 (1947).
17. O. Kubaschewski and B. E. Hopkins, *Oxidation of Metals and Alloys,* 2nd ed., Butter-worths, London, 1962, pp. 266ff.
18. J. Grimblot and J. M. Eldridge, *J. Electrochem. Soc. 128*:729 (1981).
19. W. E. Campbell and U. B. Thomas, *Trans. Electrochem. Soc. 91*:263 (1947).
20. C. S. G. Phillips and R. J. P. Williams, *Inorganic Chemistry,* Vol. I, Oxford University Press, New York, 1965, p. 533.
21. W. E. Dahlke and S. M. Sze, *Solid-State Electron. 10*:865 (1967).
22. *Solid State Tech.,* August 1992, p. 12.
23. J. R. Bolton, *Solar Energy 31*:483 (1983).
24. Y. Kamigaki and Y. Itoh, *J. Appl. Phys. 48:*2891 (1977).
25. J. Ahn, W. Ting, T. Chu, S. N. Lin, and D. L. Kwong, *J. Electrochem. Soc. 138*:L39 (1991).
26. C. A. Paz de Araujo, R. W. Gallegos, and Y. P. Huang, *J. Electrochem. Soc. 136*:2673 (1989).
27. T. Sugano, Thin Solid Films 92:19 (1982).

Copyright © 2002 Marcel Dekker, Inc.

28. Y. Ishikawa, T. Shibamoto, and I. Nakamichi, *Jpn. J. Appl. Phys 31*:L750 (1992).
29. A. M. Goodman and J. M. Breece, *J. Electrochem. Soc. 117*:982 (1970).
30. F. P. Fehlner, *J. Electrochem. Soc. 119*:1723 (1972).
31. R. J. Archer and G. W. Gobeli, *J. Phys.Chem. Solids 26*:343 (1965).
32. W. A. Weyl, *Coloured Glasses,* Dawson's of Pall Mall, London, 1959, pp. 108ff.
33. M. J. Graham, S. I. Ali, and M. Cohen *J. Electrochem. Soc. 117*:513 (1970).
34. M. J. Graham, *Int. Corrosion Conf. Ser. NACE-6,* p. 139 (1981).
35. M. J. Graham and M. Cohen, *J. Electrochem. Soc. 119*:879 (1972).
36. C. L. McBee and J. Kruger, *Electrochem. Acta 17*:1337 (1972).
37. D. J. Young and M. Cohen, *J. Electrochem. Soc. 124*:769, 775 (1977).
38. J. S. Arlow, D. F. Mitchell, and M. J. Graham. *J. Vac. Sci. Technol. A5*:572 (1987).
39. B. Onay, *J. Electrochem. Soc. 136*:1578 (1989).
40. D. A. Vermilyea, *Acta Metall 6*:166 (1958).
41. P. B. Sewell, D. F. Mitchell, and M. Cohen, *Surf. Sci. 29*:173 (1972).
42. G. F. Cerofolini, G. La Bruna, and L. Meda, *Appl. Surf. Sci. 89*:361 (1995).
43. H. C. Lu, T. Gustafsson, E. P. Gusev, and E. Garfunkel, *Appl. Phys. Lett. 67*:1742 (1995).
44. L. Verdi and A. Miotello, *Phys. Rev. B. 51*:5469 (1995).
45. P. C. J. Graat and M. A. J. Somers, *Appl. Surf. Sci. 100/101*:36 (1996).
46. T.-C. Lin, G. Seshadri, and J. A. Kelber, *Appl. Surf. Sci. 119*:83 (1997).
47. S. J. Roosendaal, B. van Asselen, J. W. Elsenaar, A. M. Vredenberg, and F. H. P. M. Habraken, *Surf. Sci. 442*:329 (1999).
48. J. A. Slezak, B. D. Zion, and S. J. Sibener, *Surf. Sci. 442*:L983 (1999).
49. A. Stierle, P. Bödeker, and H. Zabel, *Surf. Sci. 327*:9 (1995).
50. A. Stierle and H. Zabel, *Surf. Sci. 385*:167 (1997).
51. A. Stierle and H. Zabel, *Surf. Sci. 385*:310 (1997).
52. M. Müller and H. Oechsner, *Surf. Sci. 387*:269 (1997).
53. J. C. Yang, B. Kolasa, J. M. Gibson, and M. Yeadon, *Appl. Phys. Lett. 73*:2841 (1998).
54. J. C. Yang, M. Yeadon, B. Kolasa, and J. M. Gibson, *Appl. Phys. Lett. 70*:3522 (1997).
55. J. C. Yang, M. Yeadon, B. Kolasa, and J. M. Gibson, *Scr. Mater. 38*:1237 (1998).
56. J. C. Yang, M. Yeadon, B. Kolasa, and J. M. Gibson, *Proceedings of Spring ECS Meeting,* Seattle, Washington, May 1999.

Copyright © 2002 Marcel Dekker, Inc.

6

Growth and Stability of Passive Films

Barry MacDougall and Michael J. Graham
National Research Council of Canada, Ottawa, Ontario, Canada

INTRODUCTION

Interest in passivity started with the studies of Faraday [1] and Schönbein [2] over 150 years ago. The lack of metallic corrosion in the case of iron immersed in certain solutions was attributed to either the presence of an oxide film or an electronic change in the metal. This basic argument has persisted in various forms to this day, although the majority of scientific evidence suggests protection by a three-dimensional oxide film. Much has been published on passivity and its breakdown over the last 50 years. This chapter does not attempt to cover all the literature but concentrates on work over the past 10–15 years, emphasizing the passivity of iron, nickel, iron-chromium, and iron-nickel alloys in aqueous environments. Examples are given from the authors' and other selected laboratories.

Iron becomes passive in the absence of an applied current in a variety of solutions ranging all the way from concentrated nitric or sulfuric acids to basic solutions containing oxygen. In more recent years iron has been protected from corrosion in acid solutions by the addition of inhibitors usually containing nitrogen, sulfur, or hydroxyl groups. This complex subject is dealt with in Chapter 14. Here we concentrate on anodic passivity, dealing with the nature of passive films—their composition, thickness, growth, and stability—and their role and influence on pit initiation. Much of the information is obtained from surface analytical techniques like Auger electron spectroscopy (AES), X-ray photoelectron spectroscopy (XPS), and secondary ion mass spectrometry (SIMS).

ANODIC PASSIVITY

Although there is general agreement today that anodic passivity of metals such as iron and nickel is associated with the formation of a three-dimensional oxide film on the surface and that breakdown of passivity is due to the disappearance of this protective film either locally or generally, there is still considerable controversy concerning the nature, composition, and structure of the passive film. Here the most prominent models for passivity will be presented and the nature of the passive oxide film on common metals such as iron and nickel will be discussed.

Copyright © 2002 Marcel Dekker, Inc.

The use of Pourbaix diagrams in predicting the stability of metals in various environments will not be detailed in this chapter. The subject has been discussed on many occasions over the past 40 years (see, e.g., Refs. 3–5). It should, however, be pointed out that these equilibrium potential-pH diagrams can be extremely useful in establishing the regions of metal immunity as well as (possible) corrosion and passivation. Since the diagrams do not provide any direct kinetic information, the real rate of corrosion and extent of passivation are not evident from a simple examination of the diagrams. Some oxides (e.g., NiO) dissolve only very, very slowly in certain solutions (e.g., neutral borate buffer) for kinetic as opposed to thermodynamic reasons. It should also be pointed out that the oxide stoichiometries and thermodynamic information given in the Pourbaix diagrams are for thick, bulk oxides, which may be quite different from the very thin (often ≤ 1 nm) surface oxide films found on passivated metal surfaces. For this reason, it should not be surprising that the actual composition of passive oxide films is sometimes not identical to that found in the Pourbaix diagrams [e.g., the diagram for nickel does not show the presence of NiO but rather $Ni(OH)_2$; see below].

NATURE OF THE PASSIVE FILM ON IRON

Iron and nickel are examples of metals that display an active-passive transition when anodically polarized in many aqueous solutions. Passivity is generally ascribed to the presence of a thin oxide film 1–4 nm thick that isolates the metal surface from the corrosive aqueous environment. The resistance of this anodic oxide film to dissolution is related to its physical and chemical nature, which determines the corrosion resistance of the metal. The other major factor influencing the rate of metallic corrosion is the aggressiveness of the aqueous environment, i.e., the pH, temperature, and anion content of the solution.

Iron can be passivated in aqueous solutions by the application of either a constant potential or a constant current. In both cases a certain minimum potential or current is required before passivation occurs and a finite time is required to attain the passive (i.e., very slow dissolution) state. Early work dealing with the electrochemistry of iron was done in acid solution, but over the last 30 years studies have been carried out mainly in neutral buffered solution. The major impetus for work on neutral solutions came from the research of Nagayama and Cohen [6] using a pH 8.4 sodium borate–boric acid buffer solution. In Figure 1, a schematic of the passivation curve for iron in this solution is shown. Starting with an oxide-free surface, the current first increases as the potential is increased, reaches a maximum, and then decreases again. There is a region (of over a volt) in which iron does not dissolve, or is passive, and then the current rises again due to oxygen evolution and/or transpassive metal dissolution. In the passive region iron is covered by a thin film of cubic oxide of the γ-Fe_2O_3/Fe_3O_4 type, which is probably formed by reactions such as

$$3Fe + 4H_2O \rightarrow Fe_3O_4 + 8H^+ + 8e$$
$$2Fe + 3H_2O \rightarrow Fe_2O_3 + 6H^+ + 6e$$

The film thickness increases with anodic potential to a limiting value approaching 5 nm. This is the same type of film that is formed by the reaction of clean iron with oxygen or dry air. The dissolution of iron by corrosion processes usually takes place

Copyright © 2002 Marcel Dekker, Inc.

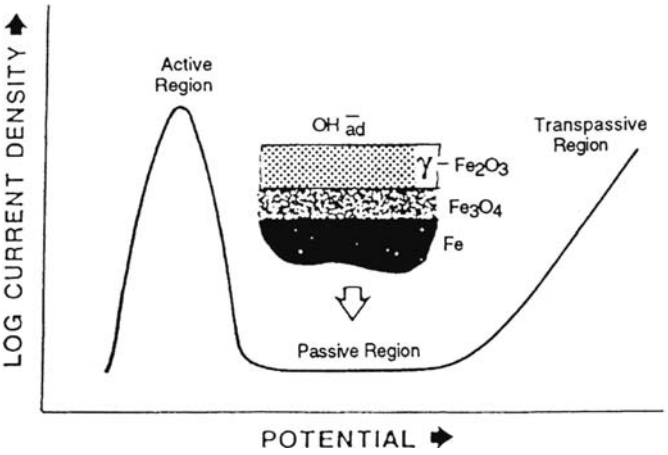


Figure 1 Anodic polarization curve (determine potentiostatically) for iron exhibiting passivity.

because of film breakdown and the rate of corrosion depends on the factors leading to film breakdown and repair.

The γ-Fe_2O_3/Fe_3O_4 structure for the passive film presupposes that the film is formed by a heterogeneous reaction between iron and the solution, probably, as in the case of inhibitors, involving adsorption (of H_2O or OH^- ions), reaction, and thickening steps. Other compositions and structures have been proposed for the passive film, some involving the inclusion of hydrogen [7,8] or the presence of water [9]. In fact, the composition of the passive film on iron depends on the type of electrochemical treatment for forming the film and the nature of the solution in which it is formed. If iron is anodized in either a neutral solution without good buffer capacity or an acid solution, e.g., Na_2SO_4 or H_2SO_4, respectively, the passivation process is very inefficient and most probably occurs with the participation of an $FeSO_4$-type salt film, which eventually precipitates on the iron surface. This surface oxide film cannot be described as a "good" passive film and may contain incorporated species from the passivating solution. Indeed, there are suggestions that true passivity (i.e., anodic currents in the range of 1 $\mu A\ cm^{-2}$) cannot be achieved in solutions such as sulfate unless a prior oxide film exists on the surface and is not removed before anodic polarization is applied [10,11]. There may even be problems with passivation of iron in pH 8.4 borate buffer if the anodic treatment allows the dissolution of substantial amounts of Fe^{2+} . In such a situation, the ferrous ion in solution may anodically deposit on the surface to give an outer γ-FeOOH layer. Sato and co-workers [12] suggest that such a film tends to arise in neutral solutions, and Seo et al. [13], using Auger spectroscopy, found incorporated boron in the oxide films formed in borate buffer solutions containing Fe^{2+} . If the passivation of iron is carried out in pH 8.4 borate buffer using a potential step to anodic values well into the passive region, the surface oxide film forms with a current efficiency of essentially 100% [14] and can be described as a "true" passive film.

One of the most important developments over the past 20 years in the study of passivity has been the use and application of surface analytical techniques.

Copyright © 2002 Marcel Dekker, Inc.

Techniques such as AES, XPS, and SIMS have been used with great advantage to obtain detailed information regarding the composition of thin passive oxide films on metals and alloys. However, these are ex situ techniques which involve removal of the sample from solution and installation into an ultrahigh-vacuum system. It has been suggested that the vacuum environment may cause dehydration of the passive film and remove bound water, which could play a vital role in conferring passivity. Because of this concern, many studies have been carried out using devices for transfer from solution to the vacuum system or have involved in situ measurements. Using a transfer device for Auger analysis, Bockris and co-workers [15] concluded that the passive film on iron is $Fe(OH)_2$ in a polymeric layered structure. In one of the earliest in situ structural investigations, O'Grady [16] used Mössbauer spectroscopy to examine both in situ and "dried" passive films at room and liquid helium temperatures. The in situ film was described as amorphous and polymeric, consisting of chains of iron atoms bonded together by dioxy and dihydroxy briding bonds further linked by water to form a continuous film. However, the film was reported to change character on removal from the passivating medium and long-term drying to more closely resemble γ-Fe_2O_3. Eldridge and co-workers [17] performed experiments similar to those of O'Grady but were unable to reproduce his parameters. They confirmed that the film was primarily Fe^{3+} but could not rule out the possibility that it was microcrystalline. Eldridge and Hoffman [18] also reported that with the exception of those formed at very low passivating potentials, passive films do not seem to undergo significant local structural changes upon drying in the air. Graham and co-workers [19] used the more surface-sensitive electron back-scattering Mössbauer spectroscopy to examine ex situ passive films. They found Mössbauer parameters somewhat different from those of O'Grady's in situ film but close to those of his dried film and within the error limits of data obtained by Eldridge et al. for in situ films. Although low-temperature Mössbauer data resembled those for amorphous iron oxides or hydroxides, interpretation in terms of a small particle size crystalline oxide, probably similar to γ-Fe_2O_3, appears more plausible. Complementary XPS data for films formed in Fe^{2+} -free solutions supported the model obtained from the Mössbauer measurements that the films resemble γ-Fe_2O_3. The lack of hydroxyl ions within passive films has been confirmed by Mitchell and Graham [20] using SIMS. Figure 2 shows experimental SIMS data for a passive film together with "dry" Fe_2O_3 and "wet" FeOOH standards. As seen in the figure, the profile for the passive film is very similar to that for the Fe_2O_3 standard until the oxide-metal interface is reached after ~7 min of sputtering (i.e., removal of the film by ion bombardment). The hydroxyl content within the film, calculated from the SIMS data, is zero (±0.1%); a fraction of a monolayer of OH^- is adsorbed on the oxide surface. From these Mössbauer, XPS, and SIMS data, and also from reflection high-energy electron diffraction (RHEED) measurements, it can be concluded that the passive film on iron is a small particle size γ-Fe_2O_3/Fe_3O_4-type film without any incorporated OH^-. These data from modern surface-analytical techniques therefore confirm the structure proposed by earlier workers. Hydrogen may be incorporated in the outer layer of the cation-deficient oxide. In films as thin as these there is probably no phase boundary between Fe_3O_4 and γ-Fe_2O_3 but a constant oxygen lattice with a varying ion concentration from the metal-oxide interface to the solution-oxide interface.

Although there may indeed be no sharp boundary between Fe_3O_4 and γ-Fe_2O_3, the sandwich model does underscore the fact that there are significant differences

Copyright © 2002 Marcel Dekker, Inc.

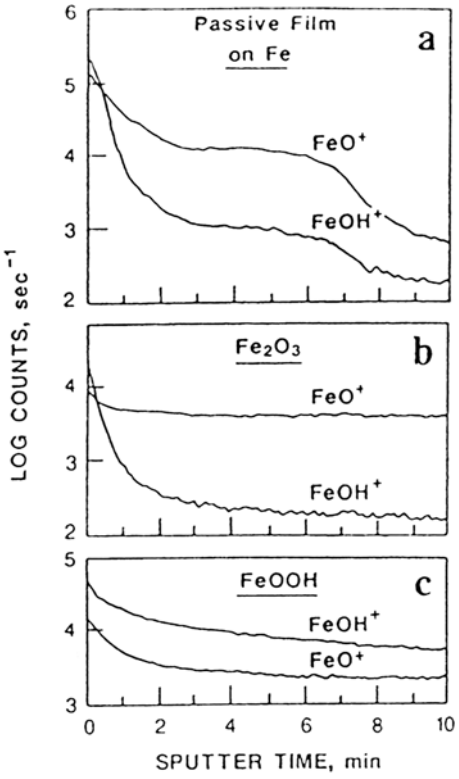


Figure 2 Passivity of iron. SIMS profiles from (a) a passive oxide film formed in pH 8.4 borate buffer solution at 0.14 V (vs. Hg/Hg_2SO_4) for 1 h; (b) a "dry" sputter-deposited Fe_2O_3 film; (c) a "wet" FeOOH film. Sputtering was by 1-keV xenon ions. (From Ref. 20.)

between the inner and outer layers. One of the important experimental results supporting the bilayer view is the two-stage cathodic reduction of the passive oxide film [6]. It has also been suggested [21] that the oxide film is a single-phase oxide and that the two cathodic reduction arrests discussed in the following are simply due to a two-stage reduction process, much like that seen with AgO or CuO. However, the experimental evidence in favor of the two-layer model is considerable, and the prevalent view at the present time favors the γ-Fe_2O_3/Fe_3O_4 structure.

SIMS can be used to study in detail the cathodic reduction (i.e., removal) of passive films formed on iron in borate solutions enriched with ^{18}O [14]. Figure 3a shows the typical cathodic reduction profile with two arrests, the first likely due to the reduction of γ-Fe_2O_3 and the second representing reduction of Fe_3O_4 [6]. Figure 3b shows the oxide thickness as determined by SIMS as a function of cathodic reduction. Experimentally, samples were anodized in 10% ^{18}O-enriched solution and, after rinsing, were reduced to various extents in nonenriched solution. The break point in Figure 3b corresponds to the sharp drop in potential in the reduction curve and provides direct evidence for two different reduction mechanisms corresponding to the two arrests in the cathodic reduction profile. Comparison of the slopes in Figure 3b with calculated charge efficiencies for various reactions indicates

Copyright © 2002 Marcel Dekker, Inc.

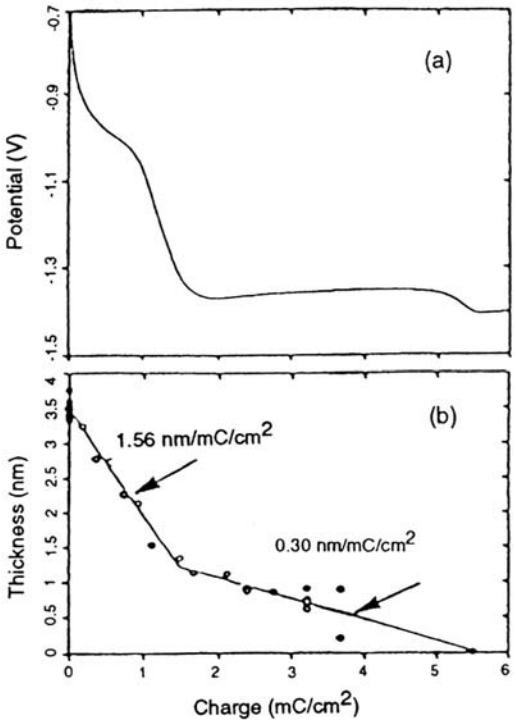


Figure 3 Passivity of iron. (a) Cathodic reduction profile (10 μA cm $^{-2}$) of a passive film formed in pH 8.4 borate buffer solution of 0.4 V (vs. Hg/Hg_2SO_4) for 1 h. (b) Oxide thickness as determined from ^{18}O/SIMS as a function of cathodic reduction; the slopes of the two lines are indicated. (From Ref. 14.)

that the first reduction represents γ-$Fe_2O_3 \rightarrow Fe^{2+}$ in solution (conversion rate, 1.56 nm/mC/cm^2). The observed efficiency is not in agreement with reductions of γ-FeOOH, supporting the SIMS data discussed earlier indicating that the film contains no bound OH^-. The second reduction is most probably associated with $Fe_3O_4 \rightarrow Fe$ (metal), with a current efficiency ~ 60%.

Additional support for the bilayer model comes from ring-disk experiments which indicate that reduction of the outer γ-Fe_2O_3 layer generates Fe^{2+} in solution [22] and the in situ ellipsometric work of Ord and DeSmet [23], which identifies an outer, electrically limiting layer of γ-Fe_2O_3 and an inner conducting layer of Fe_3O_4. An alternative model for the passive film is the chemiconductor model of Cahan and Chen [24], which suggests that the oxide is not a classical semiconductor but a highly doped film with Fe^{2+} and Fe^{4+} as defects; the stoichiometry of this film can vary over a wide, continuous range in response to changes in the electrode potential. It is evident that even with this model, the oxide film near the iron electrode contains Fe^{2+} and is therefore akin to Fe_3O_4. It is also interesting to note that the Fe^{4+} species discussed by Cahan and Chen is essentially equivalent to the Fe^{6+} defect species suggested by Nagayama and Cohen [6], each being a surface species which could influence film behavior such as breakdown. Schultze and co-workers [25,26]

Copyright © 2002 Marcel Dekker, Inc.

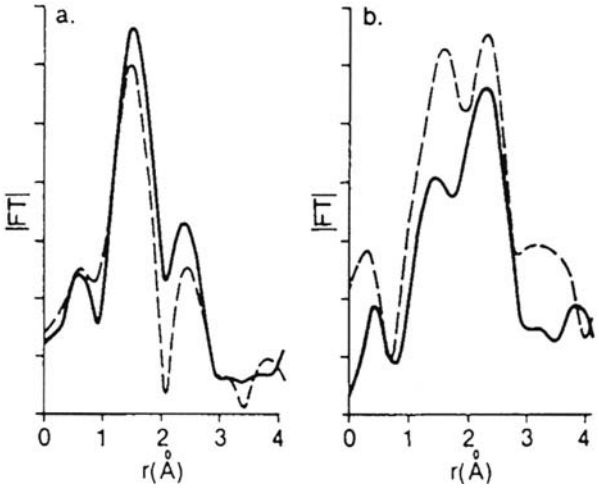


Figure 4 Passivity of iron. Magnitude of the Fourier transforms of EXAFS spectra for (a) ex situ and (b) in situ films. Nitrite-formed film results are given by the dashed lines and chromate formed film results by the solid lines. (From Ref. 30.)

have shown that the semiconductor model of the passive film can be used as a good approximation for the passive film in the steady state.

In a series of experiments designed to investigate directly the structure of oxide films on iron, Kruger et al. [27–31] employed the sophisticated technique known as EXAFS (extended X-ray absorption fine structure). The technique permitted spectra to be obtained for films in in situ conditions and for comparisons to be made with ex situ measurements (i.e., out of the electrolyte solution in the "dry" condition). It should be mentioned here that the majority of the films examined were not anodically formed but rather chemically prepared by exposure of iron to such passivating solutions as nitrite or chromate. Nevertheless, the results indicated very significant differences between the in situ and ex situ films, suggesting that "drying" of the films for ex situ examination does lead to major structural changes. Comparisons of ex situ and in situ films formed in nitrite and chromate are shown in Figure 4. The implication is that great care has to be taken when employing ex situ techniques, such as the ultrahigh-vacuum (UHV) spectroscopies or RHEED, because some films being studied may be structurally different from those present when the electrode is immersed in the electrolyte. In more recent research employing the spin-polarized neutron reflectivity technique, Krebs, Kruger, and co-workers [32,33] have studied in situ the passive film formed anodically on iron in the pH 8.4 borate buffer. The passive film was observed to be different from the air-formed film. If the passive film proves to be ferromagnetic, it would support an Fe_3O_4 or Fe_3O_4/γ-Fe_2O_3 bilayer model. However, as mentioned previously [19], there is some concern that what may appear as ferromagnetism in a bulk oxide would instead become superparamagnetism in a thin film. As pointed to by Krebs et al. [33], if this is the case for the passive film on iron, then it will be extremely difficult to apply a polarizing magnetic field strong enough to observe any changes in magnetic scattering density.

Copyright © 2002 Marcel Dekker, Inc.

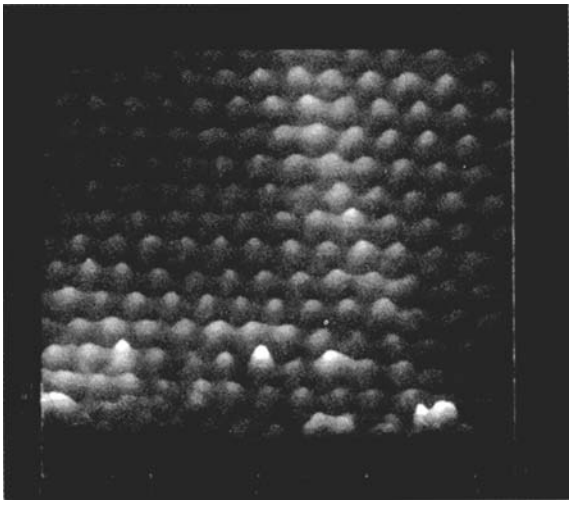


Figure 5 Atomically resolved STM image recorded in air of the passive film on iron in pH 8.4 borate buffer at 1040 mV (NHE) for 15 min. (From Ref. 119.)

More recent studies have used in situ and ex situ scanning tunneling microscopy (STM) [119] X-ray scattering [120,121] to study the passive film formed on iron in borate buffer solution. Ex situ STM examination in air (Fig. 5) showed long-range crystalline order on the film surface with the same triangular lattice of spacing 0.30 ± 0.01 nm appearing on all the crystallites studied. In situ STM at intermediate potentials after passivation at high potentials showed the same lattice on a large number of areas. The structure is consistent with a γ-Fe_2O_3/Fe_3O_4 structure of the passive film and the results refute the suggestion of a highly disordered or amorphous passive film. X-ray scattering data [120,121] of the passive film are consistent with a spinel oxide (γ-Fe_2O_3, Fe_3O_4, or related structure) and inconsistent with other crystalline bulk oxides, hydroxides, or oxyhydroxides. However, the data demonstrate that neither Fe_3O_4, γ-Fe_2O_3, nor any combination of these phases can adequately describe the experimental data. The model proposed [120,121] assumes a uniform distribution of vacancies and interstitials and the best-fit structure has a stoichiometry of $Fe_{1.9\pm0.2}O_3$, which indicates that most of the Fe cations are in the Fe^{3+} state. In the proposed structure, the octahedral vacancies are randomly distributed but occupy specific sites in γ-Fe_2O_3 and are absent in Fe_3O_4; in γ-Fe_2O_3 and Fe_3O_4 the tetrahedral sites are fully occupied and there are no octahedral interstitials.

NATURE OF THE PASSIVE FILM ON NICKEL

The situation with nickel is quite different from that for iron, passivity being readily achieved in a wide variety of solutions over a large range of pH [34]. In the case of nickel, there is not the necessity to have a highly buffered neutral solution in order to achieve good passivity, and this may be due to the fact that the potential for anodic deposition of an NiOOH film is fairly high [35]. For example, nickel passivates much more readily than iron in unbuffered pH 3.0 Na_2SO_4 [34]. Iron is much more

Copyright © 2002 Marcel Dekker, Inc.

sensitive to the conditions of passivation than nickel, and good passivity can be achieved with iron only under rather specific conditions. The fundamental reason for this difference is most probably associated with differences in the nature of the passive oxide film present on each metal.

As with iron, a considerable amount of works has been performed on nickel to investigate the nature of the passive oxide film. The exact composition of this film is still under discussion, but there is general agreement that its thickness is between 0.9 and 1.2 nm [35,36] and that anodic potential does not have a strong influence on thickness. In contrast, with iron and oxide film thickness varies from 1.5 to 4.5 nm depending on the electrode potential. The two most prevalent views of the passive film on nickel are that it is either entirely NiO with a small amount of nonstoichiometry giving rise to Ni^{3+} and cation vacancies [37] or that it consists of an inner layer of NiO and an outer hydrous layer of $Ni(OH)_2$ [38]. In the latter view, the film structure is similar to that observed when value metals (e.g., aluminum and tantalum) are anodized in acid solution. (A review of the subject is given in Ref. 39.) Evidence in support of the two-layer model comes mainly from XPS investigations [38,40,41]. Figure 6 shows XPS data of Marcus et al. [38]. The O 1s region for the passive film shows two fairly well-resolved peaks at 529.8 eV and 531.6 eV with a shoulder at higher binding energy. These two peaks correspond to the positions of oxygen in NiO and $Ni(OH)_2$. (The shoulder is assigned to sulfate.) There may, however, be other interpretations of these XPS data as suggested by Roberts and co-workers [42], who point out that Ni^{3+} defects can give rise to spectral features very similar to those of $Ni(OH)_2$. Another view is that the NiO film has some adsorbed hydroxyl ions on the

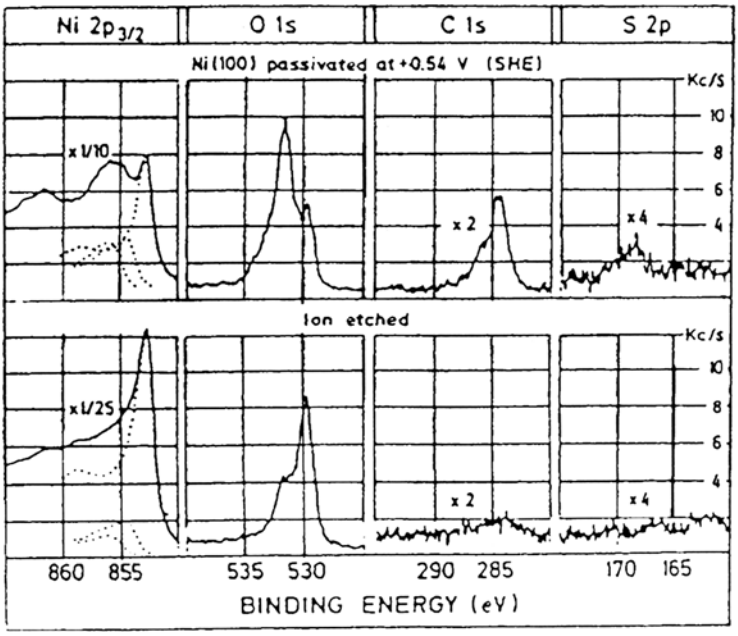


Figure 6 Passivity of nickel. XPS spectra of a nickel(100) electrode after passivation in 0.1 N H_2SO_4 at 0.54 V (vs. SHE) for 30 min. (row 1); row 2 shows spectra obtained after ion etching (0.5 keV, 1 min, $P_{Ar} = 4 \times 10^{-5}$ torr). (From Ref. 38.)

Copyright © 2002 Marcel Dekker, Inc.

surface and this gives rise to the observed spectral features [43]. Even the proponents of $Ni(OH)_2$ suggest that it is present not as the bulk hydroxide with a hexagonal lattice but rather as some modification to the NiO structure. The highly crystalline structure of the passive film formed on nickel in 0.05 M H_2SO_4 solution has been characterized by ex situ and in situ STM studies of Maurice, Talah and Marcus [44,122–124]. The crystalline lattice observed on an atomic scale is shown in Figure 7. The surface structure is characterized by the presence of steps and kinks (Fig. 7a) and point defects possibly related to vacancies (a divacancy is imaged in Fig. 7b). The lattice parameter is consistent with that of (111)NiO as the inner component of the passive film and the (0001) orientation of β-$Ni(OH)_2$ as the outer component of the passive film, which is ~ one monolayer thick. The formation of a stepped crystalline structure consistent with (111)NiO and (0001) β-$Ni(OH)_2$ has been confirmed in situ for Ni(111) passivated in pH 3 acid solutions [125,126]. It is clear that the passive film is composed almost entirely of Ni^{2+} cations, in contrast to the situation with iron, where one finds Fe^{2+}, Fe^{3+}, and possibly even Fe^{4+} and/or Fe^{6+}. The

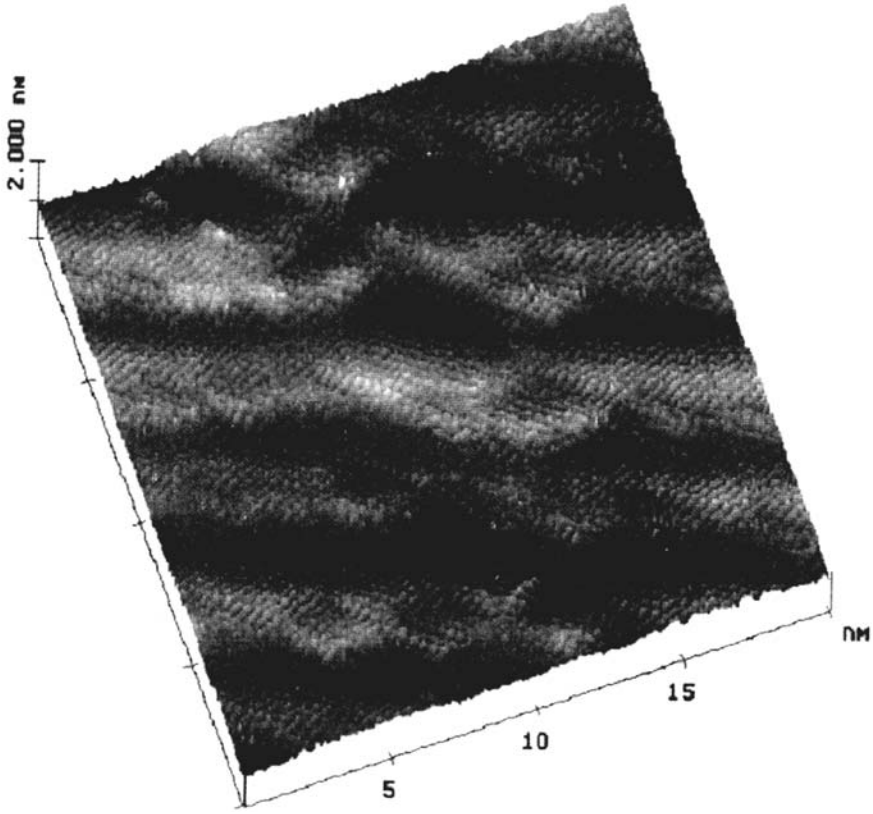


Figure 7 Ex situ STM topographic images of the passive film formed on Ni(111) in 0.05 M H_2SO_4 at +750 mV/SHE. The left image (a) above shows the stepped crystalline structure (V_t = +0.135 V, I_t = 0.8 nA, ΔZ = 0.6 nm). The right image (b) shows the lattice recorded on the terraces (V_t = +0.111 V, I_t = 0.5 nA, ΔZ = 0.6 nm). The hexagonal cell and two point defects are marked. (From Ref. 124.)

Copyright © 2002 Marcel Dekker, Inc.

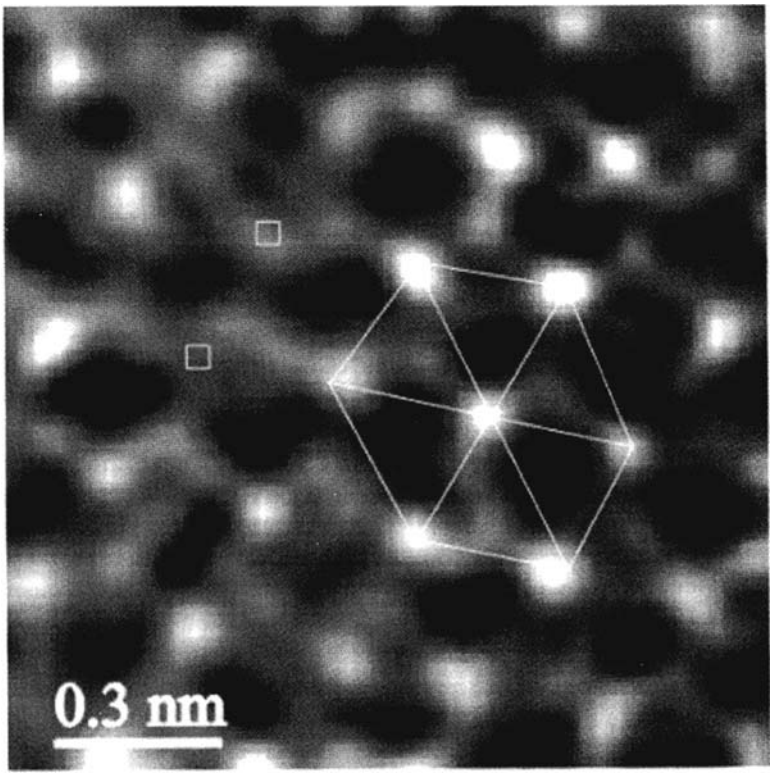


Figure 7b

passive oxide film on nickel, once formed, cannot easily be removed by either cathodic treatment or chemical dissolution; indeed, one usually has to revert to electropolishing to get back again to the bare nickel surface [45]. This is in sharp contrast to the situation with iron, where the passive film is readily removed, and again points to differences in oxide stoichiometry (and possibly structure) playing a major role.

KINETICS OF OXIDE FILM GROWTH

The growth of passive oxide films has been extensively studied on metals such as iron and nickel. Ideally, an electrolyte giving 100% current efficiency for oxide growth is used and the decay of current with time is monitored after the potential has been adjusted to a constant value (i.e., the electrode is under potentiostatic control). After some initial few milliseconds, the anodic current is usually observed to decrease in a manner which gives rise to a linear log i–log t plot (see, e.g., Fig. 11). The results can be understood in terms of a logarithmic growth of the oxide with time and a corresponding exponential decrease of the current with film thickness (d_{ox}), i.e.,

$$d_{ox} \propto \log t$$

$$i \propto \exp - d_{ox}$$

Copyright © 2002 Marcel Dekker, Inc.

or

$$d_{ox} \propto \log i$$

This means that each 10-fold increase in time results in the same increase in film thickness, say by an amount Δx, and that each increase by this amount Δx is capable of decreasing the rate of further growth by a factor of 10. As seen above, when oxide growth is governed by the direct logarithmic law, the slope of the log *i*–lot *t* plot will be –1. Another commonly observed growth law, the inverse logarithmic law, is based on the early work of Cabrera and Mott [46], which is considered in more detail in the chapter on thin oxide film formation. Cabrera and Mott suggested that growth occurs by a high-field conduction of metal ions through the oxide film and that the activation barrier is at the metal-oxide interface. This should be especially true when the film is very thin (nm thickness range) so that ion movement through the film is not the rate-determining step. Both the direct and inverse logarithmic laws give very similar kinetic results and it is extremely difficult to distinguish between them. Although the situation with oxide film growth in the early stages is a very complex topic, there seems to be more or less general agreement that the first-formed phase is a chemisorbed oxygen layer. At certain sites on the electrode surface this two-dimensional phase begins to convert to a three-dimensional phase oxide, which spreads across the entire surface. This is the so-called nucleation–lateral growth mechanism for oxide formation. The oxide continues to grow (i.e., thicken) as long as its rate of formation exceeds its rate of dissolution. It should be noted that not only the nature of the metal and the applied electrode potential but also the nature of the surrounding electrolyte are important in determining the kinetics of oxide growth.

PASSIVE FILM STABILITY

In the case of iron, as mentioned earlier, only films formed at very low passivating potentials thicken to ~ 1.7 nm upon air exposure. Oxide films on nickel are stable over the entire passive potential range and are not affected by air exposure, at least in terms of the amount of oxygen in the oxide film and its origin. This resistance to air exposure of passive films formed on iron and nickel makes their examination by ex situ techniques much more valid and the subsequent results more meaningful. Detailed work in the case of nickel, using the open-circuit potential decay technique, shows that the passive oxide film is most likely resistant to any transformation upon both air exposure and ultrahigh-vacuum pumping [47]. It needs to be emphasized, however, that the pH of the formation electrolyte can have a strong influence on ex situ analysis. This arises because upon breaking the electrical circuit prior to exposing the electrode to air, the oxide film is in contact with the electrolyte, which, if it is too aggressive, can dissolve at least some of the film. For this reason, it is not a simple matter to obtain reliable ex situ results when acid solutions (i.e., pH ≤ 2.0) are used. In this context, the safest solution when working with both iron and nickel is pH 8.4 borate buffer, in which the rate of oxide chemical dissolution is extremely low.

SIMS has also been used to study the air stability of oxide films formed on FeCr alloys in $H_2^{18}O$-enriched solutions [48,49]. At first glance, the results are somewhat surprising and suggest that the oxides are less stable to air exposure than those formed on nickel and iron. Indeed, the extent of this air instability increases

Copyright © 2002 Marcel Dekker, Inc.

significantly in going from Fe-6Cr to Fe-26Cr; i.e., more chromium in the alloy translates to more change upon air exposure. These results are discussed further in the sections on passive films on alloys.

BREAKDOWN OF PASSIVE FILMS ON IRON AND NICKEL

For iron, the consensus view is that the γ-Fe_2O_3 layer is responsible for passivity [14,23,50] while the Fe_3O_4 provides the basis for formation of the higher oxidation state but does not directly contribute toward the lowering of the anodic dissolution currents. The most probable reason that iron is more difficult to passivate (and is more sensitive to the passivating conditions) than nickel is that with iron it is not possible to go directly to the passivating species γ-Fe_2O_3. Instead, a lower oxidation state film of Fe_3O_4 is required, and this film is highly susceptible to chemical dissolution. Until the conditions are established whereby the Fe_3O_4 phase can exist on the surface for a reasonable period of time, the γ-Fe_2O_3 layer will not form and active-type iron dissolution will continue. Indeed, it is generally accepted that the active dissolution of iron occurs via an oxide intermediate [51], possibly $Fe(OH)_{ads}$ or $Fe(OH)_2$ as reviewed by Brusic [52], which is not a three-dimensional oxide phase. At a sufficiently high anodic potential (which depends on solution composition and pH), the conversion of this oxide intermediate into a true three-dimensional passive oxide is favored over its dissolution. A similar model for active dissolution applies to nickel, the oxide intermediate being $Ni(OH)_{ads}$ or $Ni(OH)_2$. Nickel, however, is different from iron in that the passivating species—an Ni^{2+} oxide considered to be NiO with possibly some $Ni(OH)_2$ at the outer surface—does not require any intervening oxidation state in order to exist. This means that passivity can be established, in a wide variety of solutions, without the need for large amounts of metal dissolution and subsequent salt film formation.

Although the passive oxide film on nickel is very thin (~ 1 nm), it can be highly resistant to breakdown by either chemical dissolution or cathodic reduction and can suppress the anodic dissolution current to very low values. In spite of the fact that there is little variation in the thickness of the oxide with film formation conditions, the resistance of the film to breakdown can vary over many orders of magnitude [53]. This can be explained in terms of the "defect" character of the film and the influence of conditions of film formation on the density of film defects. Indeed, the highly defective nature of the thin (< 1 nm) air-formed NiO film makes it possible to remove this particular film easily [54]. The nature of the defects is not really known but may well be related to Ni^{3+} and corresponding cation vacancies. The thickness of anodic oxides on nickel can be increased above 1.2 nm by galvanostatic polarization in borate buffer [55], with the thickness increasing with time and eventually reaching values in excess of 200 nm. The oxide film in this case consists of an inner compact layer of ~ 1 nm NiO with the thick outer porous part being β-NiOOH. The considerable increase in oxide film thickness does little or nothing to increase resistance to breakdown, as evidenced by the much faster film growth with increasing thickness [35]. Although there may be some exceptions, it is frequently found that the thicker the oxide, the less protective it is. In fact, it has been suggested that increasing the oxide film thickness beyond the normal passive film value is detrimental to its resistance to breakdown [56].

Copyright © 2002 Marcel Dekker, Inc.

The origin of passive currents has been the subject of considerable discussion, the obvious question being whether low passive currents always indicate a high degree of resistance to oxide film breakdown. Research on the passivation of nickel has resulted in considerable advances in our understanding of this area, especially with the use of ^{18}O/SIMS to identify changes which occur in the oxide film [57]. Figure 8 shows the results obtained when nickel previously passivated in a borate solution containing 23% ^{18}O is exposed to a pH 1.0 Na_2SO_4 solution containing no added ^{18}O. The percentage of ^{18}O decreases with time, suggesting that there are breakdown and repair events occurring within the oxide which lead to its eventual complete re-formation in the non-^{18}O electrolyte . In Figure 8, the rate of the current increase in the Na_2SO_4 electrolyte is a direct function of the conditions of prior anodization in the borate solution; the rate of current increase is lower at longer times and higher anodic potentials. The reorganization of the film to a new steady state in the more acid solution is therefore dependent on the defect character of the oxide. One important observation in this work [57] was the almost total absence of the influence of chloride ion (Cl^-) in the acid solution on the kinetics of film reorganization, suggesting that Cl^- in solution was not, at least in this particular case, facilitating chemical dissolution of the oxide film. The conclusion was that the defect character of the NiO film, in conjunction with the aggressiveness of the solution, established the current which flows in the passive region. Consequently, for constant solution aggressiveness, the passive current is a monitor of the defect character of the film. The situation with iron is somewhat different in that the current efficiency for passive film formation in pH 8.4 borate buffer is essentially 100%, meaning that all of the anodic charge is used to thicken the film [6]. In this case, the passive current is a measure of the rate of film formation, not iron dissolution. For nickel, even in pH 8.4 borate buffer, the current efficiency for film formation is ≤ 20%,indicating that a great deal of the anodic charge is associated with dissolution. Therefore, for nickel, the anodic current is a good measure of the resistance of the system to corrosion.

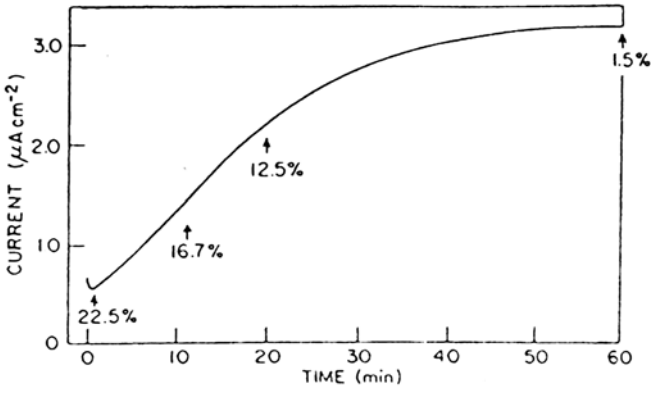


Figure 8 Passivity of nickel. Increase of anodic current with time for nickel prepassivated in pH 7.65 borate buffer solution (23% ^{18}O) at 0. 4 V (vs. Hg/Hg_2SO_4) for 5 min and then transferred to a pH 1.0 Na_2SO_4 (100% ^{16}O) solution for continued polarization at 0.4 V. Also shown is the percentage of ^{18}O detected in the oxide film by SIMS at various times of exposure to the pH 1.0 Na_2SO_4 solution. (From Ref. 57.)

Copyright © 2002 Marcel Dekker, Inc.

In discussions of passivity and its breakdown, the influence of solution anions is usually considered only with reference to aggressive species like chloride (Cl^-), bromide (Br^-), and fluoride (F^-). Some important papers, however, have concentrated on the influence of nonaggressive anions on metal passivity [11,58,59] and the importance of these species in the passivation process. For iron, while it is clear that solution pH plays a critical role in passivation, it is also apparent that the nature of the anion can determine the growth and development of the surface oxide film. For example, the anodic activity of iron is found to be much lower in borate than acetate solution at the same pH of 7.4. This suggests that the solution anion species in borate are highly beneficial for iron passivation, in agreement with a number of papers which have proposed the direct (inhibitive) participation of borate buffer anion species in iron oxidation [60,61]. The choice of borate as the "ideal" solution for passivating iron is therefore no mere accident but the selection of a solution with good inhibitive ability. The participation of solution anion species in the dissolution and passivation is clearly illustrated in experiments at constant pH (7.4) but with a widely varying acetate concentration [58,62]. The fact that the anodic activity depends on acetate concentration suggests the direct participation of acetate anions in the anodic processes. In this research area, a series of papers by Kolotyrkin and co-workers [63–65] has given considerable insight into the formation of charge transfer complexes at the iron surface and the involvement of these complexes in the passivation process. It is evident from the foregoing that solution anions can influence the current efficiency for passive oxide film formation on iron and can therefore dictate whether or not localized pitting corrosion will occur in halide-containing solutions (see, e.g., Refs. 66 and 67). These effects are much more subtle than the frequently encountered salt film development in nonbuffered solutions of sulfate or perchlorate but are certainly no less important. A major problem in this area of research is the inability to have a solution anion species with simultaneously good buffer capacity and absence of interaction with the iron anode surface; indeed, by their very definition, good buffers consist of anions with strong complexing ability. Because of this, the role of buffer capacity (through solution pH) and inhibiting absorption ability are next to impossible to separate. Such a separation becomes important in the area of pitting corrosion, since both large changes in local solution pH and competitive adsorption of aggressive anions such as Cl^- are occurring.

A great many papers have been written about the important role that solution anions play in corrosion and passivation, especially of iron. An excellent chapter was published some years ago by Hensler in *Encyclopedia of Electrochemistry of the Elements* [68]. Examples of other, more recent publications are articles by Sato [69] and Kuznetsov and Valuev [70]. The concept of solution anions interacting with the electrode surface and forming surface-ligand complexes, as well as influencing the potential distribution at the surface, is being developed. It is becoming apparent that in order to understand the mechanism of passivation and its breakdown, it is necessary to understand both the electrode and the electrolyte solution and the interaction between these two components of the corrosion process.

The strong influence of nonhalide anions on the passivation of iron is illustrated by experiments in which borate was added to sulfate solution. In pure sulfate, passivation occurs only after formation of a salt film, which requires the passage of considerable anodic charge. In borate solution, as mentioned earlier, the passive film forms with essentially 100% current efficiency, the addition of borate to sulfate

Copyright © 2002 Marcel Dekker, Inc.

results in a gradual decrease in the anodic passivation charge, and with a 20% borate addition the charge decreases to its minimum. The beneficial influence of borate is believed to be due to its ability to facilitate the nucleation of surface oxide [71] as well as controlling the surface pH during the potential step anodization. The fact that one does not require 100% borate in order to have a fairly efficient passive film growth has important implications for its use as a corrosion inhibitor.

In the case of nickel, the nature of the electrolyte does not play as major a role as it does with iron and slat films do not appear to play any role in the passivation process. Nevertheless, solution anions still exert some influence on nickel passivation [72]. Any discussion of the involvement of halide ions, such as Cl^-, in the passivation process must take into account the rather distinct differences in the passivation behavior of iron and nickel. It has been observed that Cl^- in solution has little or no influence on the anodic passivation of iron in pH 8.4 borate buffer [73], but the same is also true for nickel in borate solution. On the other hand, the passivation of nickel in pH 8.4 Na_2SO_4 is definitely influenced by the presence of Cl^- in solution [74], the anodic charge increasing with increasing [Cl^-]. The gradual addition of borate to a Cl^--containing sulfate solution is found to decrease the anodic passivation charge such that when ~ 10% borate is present, Cl^- no longer has much influence on passivation.

ROLE OF CHLORIDE ION IN PASSIVE FILM BREAKDOWN

Although it has been well known for many decades that Cl^- gives rise to local pitting corrosion of metals and alloys, the precise role of Cl^- in achieving pitting is not well understood. For example, it is still not clear whether Cl^- causes the initial local breakdown of the passive oxide film or simply interferes with the repassivation process after the film has broken down locally because of chemical dissolution [75–77]. In analyzing data on Cl^--induced pitting, it is important to determine whether the passive oxide film was formed in a Cl^--containing solution or the Cl^- was added only after passivity was established in the absence of Cl^-. The first type of experiment is much easier than the second in terms of reproducibility of results and the time needed for pitting to occur (usually called the induction time). One of the favored models to explain the initiation of pitting corrosion involves the incorporation of Cl^- into the oxide lattice and its possible diffusion to the metal-oxide interface to initiate local breakdown events [78–80]. To check this possibility, a considerable amount of research has been performed in an attempt to detect the presence of Cl^- in passive oxide films on iron and nickel. The best chance of getting Cl^- into the oxide lattice should be to form the film potentiostatically in a reasonably concentrated Cl^- solution (e.g., 0.25 M) under conditions where significant pitting has not begun so as not to simply detect a chloride-containing corrosion salt film which exists in well-developed pits [81]. In Cl^- -containing borate solution, there is no indication of any Cl^- in the anodic film on iron [82], perhaps in agreement with the fact that Cl^- has no influence on the passivation charge [73]. On the other hand, nickel passivated in a Cl^--containing sulfate solution is found to contain a considerable amount of incorporated Cl^-, the actual amount depending on the [Cl^-] in solution and the anodic potential [83]. This incorporated Cl^- makes the passive oxide film on nickel more defective, decreasing its resistance to open-circuit chemical dissolution [84]. It might

Copyright © 2002 Marcel Dekker, Inc.

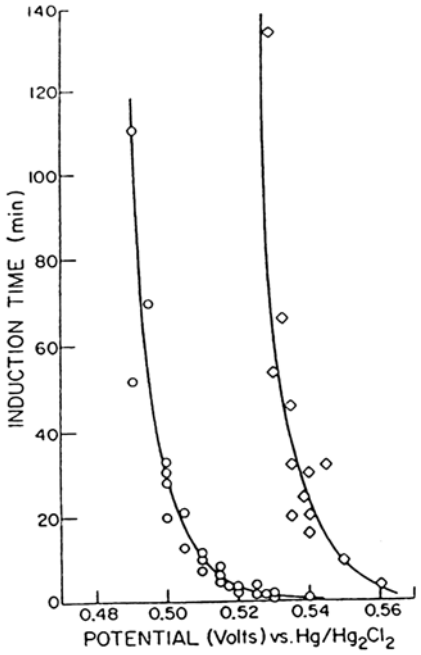


Figure 9 Passivity of nickel. Induction time for pitting vs. potential of anodization for nickel samples pretreated at 0.3 V in pH 4.0 Na_2SO_4 either with (◇) or without (○) 1 M Cl^- in solution, and pitted in a 0.08 M Cl^- solution. (From Ref. 84.)

be expected that this incorporated Cl^- would also increase the susceptibility of nickel to pitting, but this is not the case. In a series of carefully performed experiments, the resistance to pitting (based on the pitting potential) was actually much higher in the case in which the passive film on nickel contained Cl^- [84]. This is shown in Figure 9, which illustrates the results obtained when nickel prepassivated in either a Cl^--free or a Cl^--containing solution is exposed to a different Cl^--containing solution to measure the induction time to pitting. The sample prepassivated in the Cl^--containing solution (and with ≥ 5 at % Cl^- incorporated in the oxide lattice [83]) requires much higher anodic potentials for pitting to occur. Whatever the reason for this result, it certainly suggests that the Cl^- incorporation into the passive oxide film on nickel is not the reason for pit initiation.

Research by Heusler and Fischer on Cl^--induced pitting of prepassivated iron [85] and Fe-6Cr [86] in borate buffer solution suggested an interesting model for pit initiation. A rotating ring-disk electrode system was used to monitor the production of Fe^{2+} and Fe^{3+} after the addition of Cl^- to the borate solution. During the induction time before pitting began, the current associated with Fe^{3+} appeared to increase while that for Fe^{2+} production (as well as the total current) remained constant (the result is illustrated in Fig. 10). This was taken to indicate that Cl^- ions caused "local" currentless dissolution of the oxide, i.e., local film thinning, by adsorbing on the surface and interfering with film repair. When this had proceeded sufficiently, bare metal was locally exposed and pitting began, with a corresponding large increase in the current associated with Fe^{2+} production. It should be noted

Copyright © 2002 Marcel Dekker, Inc.

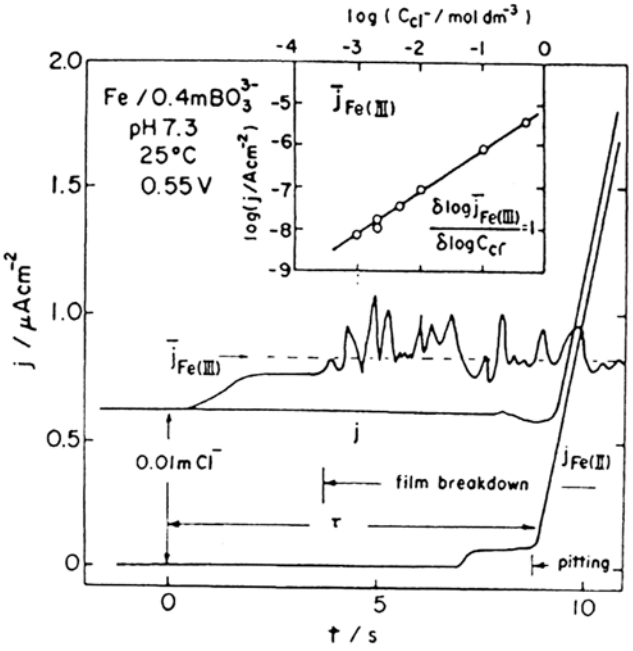


Figure 10 Passivity of iron. Charges in total anodic current j, iron(III) ion dissolution current j_{Fe}(III) (passive film dissolution current), and iron II $j_{Fe(II)}$ (pitting dissolution current) for passive iron in borate solution as function of time after introduction of chloride ions. (From Ref. 85.)

from Figure 10 that the induction time is very short (< 10 s) and the current associated with Fe^{3+} production (measured by applying a cathodic potential to the ring) is very noisy. These ideas have been further expanded by Heusler and colleagues (see, e.g., Refs. 87–89) by using electrochemical noise analysis to study the random pitting process. Although the ideas developed are intriguing, it should be noted that these important ring-disk experiments have not, to the best of our knowledge, been repeated by other researchers. Strehblow et al. [90] attempted to repeat the experiments but could not detect any Fe^{3+} . Independent confirmation of the result would be helpful in resolving important aspects of passivity.

There are strong suggestions from other experiments that Cl^- does not alter the passive film on iron during the induction time prior to pitting [91]. Indeed, it has been observed that once a "good" passive film on iron has been formed (e.g., in the pH 8.4 borate buffer solution), Cl^- will not cause pit initiation even at high potentials in the passive region [73,92]. In this situation pitting would have to await disruption of the film by mechanical, chemical (e.g., due to a change in solution pH), or electrochemical (e.g., due to transpassive dissolution at very high anodic potentials) means. In this latter work [73,92,93], an interesting model for pit initiation on iron was proposed. Pit initiation was found to be associated with a particular stage in the development of the passive film, corresponding to a specific film thickness, which was dependent on the halide concentration (Cl^- or Br^-) but not on the anodic

Copyright © 2002 Marcel Dekker, Inc.

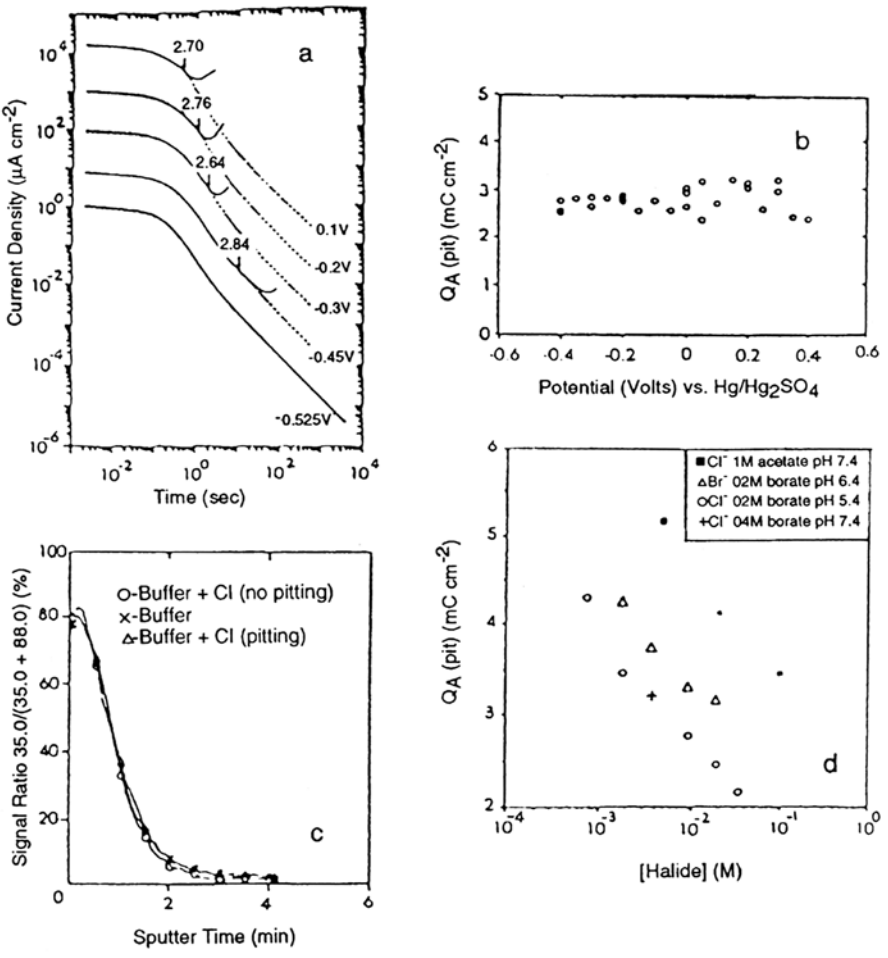


Figure 11 Breakdown of passive films on iron. (a) Current transients for various potentials in the passive region. The solid curves are for iron in solution containing 9.45×10^{-3} M NaCl in borate buffer and the dashed curves are for iron in pure borate buffer. The current density scale refers to the top curve, at 0.1 V. For clarity, at lower potentials the curves have been displaced by factors of 10. The arrows show the points at which the curves can be seen to diverge, with the number referring to the integrated anodic charge, in mC cm^{-2}, which has passed to this point. (b) This anodic charge passed [Q_A(pit)] before pitting occurred in 9.45×10^{-3} M NaCl as a function of anodizing potential, (c) SIMS [Cl^- /(Cl^- + $Fe^{16}O_2$)] signal depth profiles for films on iron in Cl^--free and Cl^--containing borate buffer solutions. The dta have been truncated at the oxide-metal interface. (d) Average values of Q_A(pit) as a function of halide concentration in various buffer solutions. (From Ref. 93.)

potential. This critical stage of development was characterized by the amount of anodic charge which had passed prior to pitting.

Figure 11a shows some potentiostatic current transients for iron in solutions with and without Cl^-. Below the pitting potential, the two curves are coincident. Above the pitting potential, after a certain anodization time, the two curves are seen to deviate.

Copyright © 2002 Marcel Dekker, Inc.

The charge passed to this point of deviation is defined as Q_A (pit). As seen Figure 11b, Q_A (pit) remains relatively constant with potential even though the induction time for pitting decreases as the potential increases. SIMS has been used to monitor the thickness and halide content of the film during growth [91]. During the induction time to pitting, the film was found to grow at the same rate in halide-containing and halide-free solutions. Figure 11c illustrates the Cl^- concentration in passive films formed in Cl^--containing and Cl^--free borate buffer under various conditions as determined by SIMS. Cl^- was present only on the surface of the samples, and its concentration did not depend on the presence of Cl^- in the solution and whether pitting had or had not occurred. These results suggest that pitting is associated with a particular combination of film thickness and halide concentration. This is illustrated in Figure 11d, which shows average values of Q_A (pit), obtained for a variety of buffer solutions and halide ion concentrations. Clearly, Q_A (pit) depends on the halide concentration, is independent of solution pH (between 7.4 and 8.4), and is strongly dependent on the identity of the solution species, both the nature of the halide ion (Cl^- or Br^-) and that of the supporting buffer (borate or acetate). A larger value of Q_A (pit) is associated with less aggressive solution, so Cl^- is seen to be more aggressive than Br^-, and 1 M acetate inhibits pitting compared with 0.4 M borate. While these experiments suggest that pit initiation is associated with the development of a particular thickness of oxide film, the exact reason for pitting susceptibility at a specific oxide film thickness is not clear but appears to be related to the formation of some sort of surface complex between the still developing oxide film and the halide ions in solution.

There are many different explanations for pit initiation, but there seems at least to be general agreement that locally high Cl^- concentrations and low solution pH values strongly favor the process [81,94,95]. One of the major problems over the years has been to distinguish between pit initiation and propagation, i.e., to determine if there is a difference between the factors which keep the pitting process going and those which started pitting in the first place. The electrolyte conditions inside well-developed pits have been investigated by a number of workers (see, e.g., Ref. 96), all of whom found a high [Cl^-] and low pH. On the other hand, the initiation process is much more difficult to study because the pits are extremely small [97] and the state is transitory. A technique known as noise analysis has been used by several groups to study pit initiation [98], but the results are still open to different interpretations. There are also suggestions that the pitting process is not determininstic (i.e., with a constant induction time for constant electrochemical conditions) but rather random and menable to stochastic (statistical) theory [99]. The ideas elaborated in Chapter 10 would explain the scatter of results and difficulty in achieving reproducibility when doing pitting experiments. The other point of view is that pitting is deterministic but at the same time very sensitive to many experimental parameters such that reproducibility is not easy to achieve. Although considerable effort and advances have been made in the stochastic approach to pitting, it has so far not made the mechanism of the pit initiation process much clearer.

PASSIVE FILMS ON IRON AND NICKEL ALLOYS

As indicated earlier, a clear understanding of the nature, role, and stability of the passive oxide film on pure iron and nickel is not easy to achieve. The difficulties are

Copyright © 2002 Marcel Dekker, Inc.

even more pronounced in the case of alloys, in which more than one metallic component is involved. The most important simple alloy is probably Fe-Cr, and this system has been investigated extensively for more than 50 years. The reason for the interest is straightforward: the addition of chromium to iron improves the corrosion resistance of the latter. This improvement is most probably due to changes in the nature of the passive oxide film because of the presence of chromium in the film. The resistance to corrosion tends to increase with chromium content in the alloy, with abrupt improvement occuring at ~ 12% chromium [100]. This result has been correlated with the increasing tendency of the oxide film to become more disordered (i.e., less crystalline) as the chromium content of the alloy increases [101], the suggestion being that an amorphous (or vitreous) oxide [102] is more resistant to breakdown than a crystalline one [103]. Besides these important changes in the oxide film structure, there are also changes in the composition and thickness of the film when chromium is present [104]. The oxide tends to be thinner and more chromium rich as the chromium content of the alloy increases [105]; the thickness of the passive oxide films is ~ 1.7 nm, in contrast to values of up to 5 nm for pure iron. With chromium in the alloy (especially ≥ 12%), the nature of the passivation solution is not nearly as important as it is in the case of iron. Indeed, it is more appropriate to work in aggressive (acid) solutions if one wants to remove the prior air-formed oxide film on, e.g., the electropolished alloy [106]. The explanation given above for the lack of corrosion resistance of iron was the nature of the passive oxide film and the necessity to form a prior Fe_3O_4-type oxide which is very susceptible to dissolution. With the addition of more than 12% chromium to the alloy, the mechanism and/or stages of passive oxide film formation change and the initially formed is stable even in very strong acid solution; i.e., there is no requirement for the formation of a salt layer to assist passivation.

Chromium is known to have a strong tendency to form oxyhydroxide compounds, and the presence of chromium in the passive film on Fe-Cr alloys is thought to ensure a somewhat hydrated structure for the oxide [107]. In fact, there have been suggestions that "bound water" is present in the film, and this helps to facilitate film repair after film breakdown [108] and thus helps Fe-Cr alloys to resist pitting corrosion. The bound water model is still, however, not generally accepted and remains the subject of some speculation.

The ^{18}O/SIMS work mentioned earlier on various Fe-Cr alloys [48,49] indicated that the more chromium in the alloy, the more likely it is that changes will occur on air exposure, with Fe-26Cr alloys being less resistant to change than Fe-6Cr alloys. This instability of the passive film on alloys with a high chromium content was taken to be an inherent property of the film, possibly associated with the presence of exchangeable hydroxyl species. This instability, however, gives the films the flexibility to respond to changing environmental conditions and may explain the increased resistance of the alloys to pitting Kruger [102], who suggested that the bond and structural flexibility of the oxide films on high chromium content alloys makes them more resistant to breakdown and therefore the system more resistant to corrosion. Fe-26Cr alloys tend to be very resistant to pitting corrosion, in fact so much so that special conditions are required to initiate pits [109]. Also, the oxide films are very resistant to removal and even the air-formed film on Fe-26Cr requires a strong etching treatment in an acid solution for its complete removal, as observed by Frankenthal [106] and others [49]. The oxide film on Fe-Cr alloys in the passive

Copyright © 2002 Marcel Dekker, Inc.

potential region consists mainly of Fe^{3+}, Cr^{3+}, and some Fe^{2+} [110], but at higher anodic potentials in the transpassive region- some of the Cr^{3+} is convered to Cr^{6+}, which is highly soluble [111]. For this reason, transpassive dissolution can lead to significant amounts of dissolution of the oxide film on Fe-Cr alloys and hence corrosion.

More recently, in situ XANES (X-ray absorption near edge spectroscopy) [127] and STM [128,129] have been used to study the composition and structure of oxides on Fe-Cr alloys. The XANES work [127] on a range of Fe-Cr alloys in pH 4.5 acetate buffer showed that at –1.2 V, the nonreducible oxide/hydroxide (remnants of the air-formed film) consists entirely of Cr^{3+} and resembles $Cr(OH)_3$ more than Cr_2O_3. Upon stepping the potential to –0.3 V, additional alloy is oxidized but significant amounts of the oxidized iron dissolve as Fe^{3+}. Upon stepping the potential from –1.2 to + 0.2 V, a significant amount of alloy oxidizes, in an Fe:Cr ratio identical to that of the alloy, accompanied by little dissolution of iron. This results in a passive film + 0.2 V with a composition less rich in chromium than at –0.3 V. The transpassive film formed at + 0.8 V is also enriched in chromium, primarily as Cr^{3+} but with a small amount of Cr^{6+}. Ex situ STM [128] of passive films formed on Fe-Cr alloys (15–25 at % Cr) in sulfuric acid solution shows more crystallinity in the oxide at lower chromium contents, but alloys with 18 and 21 at % Cr show time-dependent recrystallization. The films formed on 25 at % Cr alloys are normally disordered. The results are interpreted in terms of the structural stability of a Cr_2O_3 or CrOOH gel formed by oxygen bridging of chromium atoms as they are exposed by rapid selective dissolution of iron. When the gel is sufficiently mobile, it can crystallize on a low-index plane of the metal surface. The STM images of the crystalline surfaces are interpreted as [111] projections of the chromium oxide or hydroxide structure. Ex situ STM of passive films formed on Fe-22Cr(110) single-crystal surfaces [129] shows a coalescence of the oxide nuclei and a crystallization of the inner Cr_2O_3 layer in epitaxy with the substrate. The epitaxial relationship is α-Cr_2O_3 (0001)//Fe-22 Cr(110). Aging under polarization is beneficial to the stability of the passive film in air and prevents the dehydration reaction of the hydroxide coupled to an oxidation reaction of iron observed on freshly passivated surfaces. Comparison with a similar study of passivated Cr(110) surfaces [130] indicates that the presence of iron plays a role in the coalescence and crystallization process occurring during aging of the passivated alloy surface under polarization. The crystallization of oxide on (100)Fe-18Cr-13Ni single-crystal surfaces [131] proceeds faster than on Fe-22Cr(110) because the rate is modified by the presence of nickel in the alloy. Nickel is enriched in the metallic phase underneath the film and slows down the formation of Cr_2O_3 in the inner part of the film. This favors a more complete process of crystallization. Aging under polarization is again beneficial to the further stabilization of the passive film in air.

The electrochemical behavior of two Cr-containing alloys is compared with that of pure iron in Figure 12. In each case, the electropolished sample was cathodically reduced at –2.4 V prior to initiation of the anodic sweep. In the case of iron, the usual prepeak is observed at –1.2 V followed by an active dissolution peak at –1.06 V. The subsequent passive region extends up to the point at which oxygen evolution commences. The cathodic sweep displays two reduction waves, which, as described earlier, correspond to the two stages normally observed during galvanostatic reduction of the passive film. For the Fe-6Cr alloy, the active dissolution peak

Copyright © 2002 Marcel Dekker, Inc.

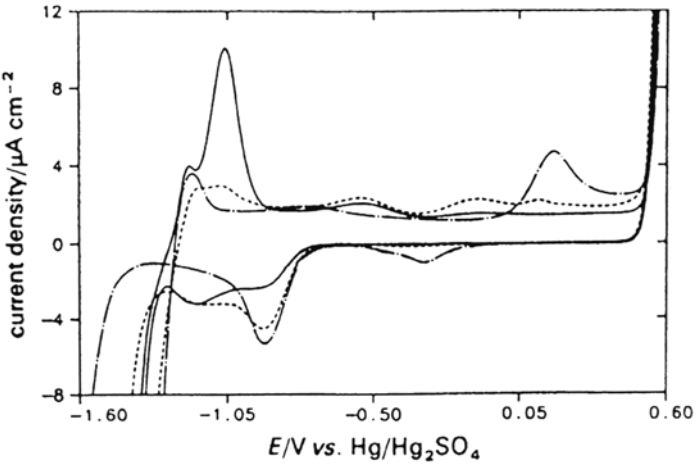


Figure 12 Cyclic voltammograms for iron, Fe-6Cr and Fe-26Cr at 0.5 mV s^{-1} in pH 8.4 borate buffer. (—) Fe; (- - -) Fe-6Cr; (– · –) Fe-26Cr. (From Ref. 49.)

is much smaller and there is some indication of transpassivity at 0.12 V. In the case of Fe-26Cr, there is no active dissolution peak, only the prepeak which is observed with pure iron. Also, a strong transpassive dissolution peak is present at 0.17 V; on the cathodic sweep, a corresponding reduction wave is observed at –0.31 V. Although this latter peak doubtless corresponds to the reduction of Cr^{6+} in the oxide film, the reaction is not quantitative because the anodic peak charge is substantially larger than the cathodic one. The most probable explanation for this is that during the scan of the anodic transpassive region, a significant amount of the generated Cr^{6+} dissolves into the electrolyte and is therefore not available in the oxide film for reduction during the next cathodic scan. The use of single anodic and cathodic scans, such as those shown in Figure 12, provides a great deal of information about the dissolution and passivation processes of metals and alloys. Considerable care, however, has to be taken in order to avoid artifacts and, even when these are avoided, interpretation of the results is not always simple. In comparison, current-time transients resulting from potential-step experiments do not reveal the same major differences between Fe, Fe-6Cr, and Fe-26Cr [49], except perhaps at longer times of passivation and then only in a rather subtle manner. Indeed, in those experiments in borate buffer the anodic currents at longer anodization times are actually higher with more chromium in the alloy. This initially unexpected result shows just how difficult it is to understand Fe-Cr passivation comprehensively. It also indicates that more than one electrochemical approach should be employed when studying these systems if one wishes to avoid the mistake of making sweeping general statements which are not necessarily correct. The subject of austenitic stainless steel passivation will be discussed in detail in a following chapter.

Although less work has been done on the passivation of other binary alloys, many interesting observations have been made and a few selected examples will be considered. In the case of Ni-Fe alloys of varying composition, alloy dissolution results in surface enrichment with nickel (as a consequence of the preferential dissolution of iron) and the formation of a passive film composed of an inner layer of

Copyright © 2002 Marcel Dekker, Inc.

NiO and an outer layer of nickel and iron hydroxides [112,113]. Because sulfur is frequently found in steel, Marcus and Olefjord [112] also investigated the role of sulfur in the passivation of Ni-Fe alloys. They found that sulfur is enriched on the surface during alloy dissolution and may concentrate to sufficiently high coverage to block passivation completely. An alloy addition which increases the pitting resistance of steels is molybdenum [114–116]; however, the role of molybdenum is still under discussion. Research has been carried out on the binary Ni-Mo system [117] in an attempt to better understand the role of molybdenum is suppressing corrosion. XPS work on Ni-6 at % molybdenum showed surface enrichment of molybdenum during alloy dissolution and enrichment of molybdenum in the passive film from 6% up to 10%. While nickel is still present as Ni^{2+}, molybdenum is present in the Mo^{6+} oxidation state [118]. It is interesting to note that the presence of molybdenum in the passive oxide film on the Ni-6% MO alloy was found to make the film more defective in comparison with NiO, with higher anodic currents in the passive potential region [118]. This might initially seem surprising considering that the presence of molybdenum in an alloy tends to increase the resistance to pitting corrosion. It should be remembered, however, that a similar trend was observed when Cl^- was incorporated in the passive film on nickel; i.e., the film is more defective so far as general dissolution is concerned but more resistant to localized pitting corrosion. The results again point to the observation that what is an oxide defect toward general chemical dissolution may not be a defect for Cl^--induced pitting. Indeed, as far as pitting is concerned, it may be better to have many oxide defects of a certain type rather than just a few of the ones which give rise to pitting corrosion. The surface enrichment of molybdenum is believed to facilitate the passivation process, e.g., by decreasing the active dissolution current; however, the passive oxide film thus formed is not as perfect as it would ordinarily be. Since there will be less active-type dissolution when the film breaks down, the current efficiency for repair will be higher. This will mean that less Cl^- migrates into the local breakdown area, and there is therefore a smaller probability of sustained breakdown, i.e., pitting corrosion. This research on alloys illustrates how important it is to distinguish between different types of defects in oxide films and their different susceptibilities to breakdown leading to pitting corrosion.

CONCLUSIONS

Very thin oxide films (1–4 nm) have been shown to have a profound influence on the corrosion rates of metals and alloys. Differences in the composition and stoichiometry of these films from metal to metal can lead to very large differences in their stability and efficiency of growth, as has been demonstrated for iron and nickel. Solution anions, even the nonhalide types, can play a major role in passive film growth and breakdown. The anions usually encountered in buffer solutions (e.g., borate) appear to have a beneficial (inhibitive) influence on oxide film growth over and above their ability to stabilize the solution pH. Consequently, when discussing oxide films on metals and alloys, it is necessary to consider the nature of both the oxide film and the solution in which the film is formed, as well as the electrochemical conditions of film formation. The precise role of halide ions such as Cl^- is still unclear, aside from the fact that they give rise to severe localized (i.e., pitting) corrosion. Their influence on oxide film growth, development, and breakdown is not a simple matter.

Copyright © 2002 Marcel Dekker, Inc.

The role of alloying elements in the passivation process has been briefly discussed. Alloying additions such as chromium and molybdenum can substantially influence the structure and composition of the passive oxide film and thereby the process of passivation. The alloys discussed have been of the fairly simple binary type, where it is easier to analyze the surface oxide films by surface analytical techniques and to understand the results. This treatise provides a basis for the following discussion of stainless steels, where the number of alloy additions is increased as is the complexity of the passivation process.

REFERENCES

1. M. Faraday, *Philos. Mag. 9*:*57* (1836).
2. C. T. Schönbein, *Philos. Mag. 9*:53 (1836).
3. E. Gileadi, in *Electrode Kinetics for Chemists, Chemical Engineers and Material Scientists,* VCH Publishers, New York, 1993, p. 502.
4. M. Pourbaix, *Atlas of Electrochemical Equilibrium in Aqueous Solutions,* Pergamon Press, Oxford, 1966.
5. M. G. Fontana, in *Corrosion Engineering,* McGraw-Hill, New York, 1986, p. 452.
6. M. Nagayama and M. Cohen, *J. Electrochem. Soc. 109*:781 (1962); *110*:670 (1963).
7. M. C. Bloom and M. Goldenberg, *Corros. Sci. 5*:623 (1965).
8. C. L. Foley, J. Kruger, and C. J. Bechtold, *J. Electrochem. Soc. 14*:994 (1967).
9. G. Okamoto, *Proceedings, 5th International Congress of Metal Corrosion,* 1972, National Association of Corrosion Engineers, Houston, 1974, p. 8.
10. D. Barry Gibbs and M. Cohen, *J. Electrochem. Soc. 119*:416 (1972).
11. S. Szklarska-Smialowska, *Passivity of Metals* (R. P. Frankenthal and J. Kruger, eds.) Electrochemical Society Corrosion Monograph Series, Princeton, NJ, 1978, p. 443.
12. N. Sato, K. Kudo, and T. Noda, *Electochim. Acta 16*:1909 (1971); T. Noda, K. Kudo, and N. Sato, *J. Jpn. Inst. Met. 37*:951, 1088 (1973).
13. M. Seo, J. B. Lumsden, and R. W. Staehle, *Surf. Sci. 42*:337 (1974).
14. J. A. Bardwell, B. MacDougall, and M. J. Graham, *J. Electrochem. Soc. 135*:413 (1988).
15. R. W. Revie, B. G. Baker, and J. O'M. Bockris, *J. Electrochem. Soc. 122*:1460 (1975).
16. W. E. O'Grady, *J. Electrochem. Soc. 127*:555 (1980).
17. J. Eldridge, M. E. Kordesch, and R. W. Hoffman, *J. Vac. Sci. Technol. 20*:934 (1982).
18. J. Eldridge and R. W. Hoffman, *J. Electrochem. Soc. 136*:955 (1989).
19. M. E. Brett, K. M. Parkin, and M. J. Graham, *J. Electrochem. Soc. 133*:2031 (1986).
20. D. F. Mitchell and M. J. Graham, *J. Electrochem. Soc. 133*:936 (1986).
21. C.-T. Chen and B. D. Cahan, *J. Electrochem. Soc. 129*:17 (1982).
22. A. Tsuru, E. Fujii, and S. Haruyama, *Corros. Sci. 31*:655 (1990).
23. J. L. Ord and D. J. DeSmet, *J. Electrochem. Soc. 113*:1258 (1966).
24. B. D. Cahan and C.-T. Chen, *J. Electrochem. Soc. 129*:927 (1982).
25. U. Stimming and J. W. Schultze, *Ber. Bungenses. Phys. Chem. 80*:1297 (1976).
26. U. König, M. M. Lohrengel, and J. W. Schultze, *Ber. Bungenses. Phys. Chem. 91*:426 (1987).
27. G. G. Long, J. Kruger, D. R. Black, and M. Kuriyama, *J. Electroanal. Chem. 150*:603 (1983).
28. G. G. Long, J. Kruger, D. R. Black, and M. Kuriyama, *J. Electrochem. Soc. 130*:240 (1983).
29. J. Kruger, G. G. Long, M. Kuriyama, and A. I. Goldman, *Proceedings, 5th International Symposium on Passivity,* Bombannes, France (M. Froment, ed.), Elsevier, Amsterdam, 1983, p. 163.

Copyright © 2002 Marcel Dekker, Inc.

30. G. G. Long, J. Kruger, and M. Kuriyama, *ibid.,* p. 139.
31. J. Kruger, *Int. Mater. Rev. 33*:113 (1988).
32. L. A. Krebs, J. Kruger, G. G. Long, J. F. Ankner, C. F. Majkrzak, S. K. Satija and D. G. Weisler, *Oxide Films on Metals and Alloys* (B. MacDougall, R. S. Alwitt, and J. A. Ramanrayanan, eds.), The Electrochemical Society, Princeton, NJ, Vol. 92–22,1992, p. 580.
33. L. A. Krebs, J. Kruger, G. C. Long, D. G. Wiesler, J. F. Ankner, C. F. Majkrazak, and S. K. Satija, *Proceedings 12th International Congress on Metal Corrosion,* Houston, Sept. 1993, National Association of Corrosion Engineers, 1993; Vol. 5B, p. 3863.
34. B. MacDougall, J. A. Bardwell, and M. J. Graham, *Surfaces, Inhibition and Passivation* (E. McCafferty and R. J. Brodd, eds.), The Electrochemical Society Inc., Princeton, NJ, 1986, p. 254.
35. B. MacDougall and M. J. Graham, *J. Electrochem. Soc. 128*:2321 (1981).
36. B. MacDougall, D. F. Mitchell, and M. J. Graham, *Corrosion 38*:85 (1982).
37. B. MacDougall, *Corros. Sci. 28*:211 (1988).
38. P. Marcus, J. Oudar, and I. Olefjord, *J. Microsc. Spectrosc. Electron. 4*:63 (1979).
39. T. Dickinson, A. F. Povey, and P. M. A. Sherwood, *J. Chem. Soc. Faraday Trans. I 73*:327 (1977).
40. J. W. Diggle, T. C. Downie, and G. W. Goulding, *Chem. Rev. 69*:365 (1969).
41. P. Marcus, J. Oudar, and I. Olefjord, *Mater. Sci. Eng. 42*:191 (1980).
42. A. F. Carley, R. P. Chalker, and M. W. Roberts, *Proc. R. Soc. Lond. Ser. A 399*: 167 (1985).
43. P. B. Sewell, B. MacDougall, D. Mitchell, and M. Cohen, *Proceedings 6th International Congress on Metal Corrosion,* Syndey, Australia, Australian Corrosion Association, 1975, p. 706.
44. V. Maurice and P. Marcus, *Proceedings, 2nd International Conference on Microscopy of Oxidation,* (S. B. Newcomb and M. J. Bennett, eds.), Cambridge, London, UK, March 1993, The Institute of Materials, p. 99.
45. B. MacDougall and M. Cohen, *J. Electrochem. Soc. 121*:1152 (1974).
46. N. Cabrera and N. F. Mott, *Rep. Prog. Phys. 12*:163 (1948–49).
47. B. MacDougall, J. A. Bardwell, D. F. Mitchell, G. I. Sproule, and M. J. Graham, *Proceedings, International Symposium on Application of Surface Science Methods to Environmental/Materials Interactions,* The Electrochemical Society, Princeton, NJ, 1991, Vol. 91–7, p. 454.
48. J. A. Bardwell, *Corros. Sci. 30*:1009 (1990).
49. J. A. Bardwell, G. I. Sproule, D. F. Mitchell, B. MacDougall, and M. J. Graham, *J. Chem. Soc. Faraday Trans. 87*:1011 (1991).
50. K. Takahashi, B. MacDougall, J. A. Bardwell, and M. J. Graham, *Proceedings, International Symposium on Materials Performance,* Ottawa, Ontario, 1991, p. 223.
51. J. O'M. Bockris, D. Drazic, and A. R. Despic, *Electrochim. Acta 4*:325 (1961); J. O'M. Bockris, M. A. Genshaw, V. Brusic, and H. Wroblowa, *Electrochim. Acta 16*:1859 (1971).
52. V. Brusic, *Oxides and Oxide Films,* Vol. 1 (J. W. Diggle, ed.), Marcel Dekker, New York, 1972, p. 1.
53. B. MacDougall and M. Cohen, *J. Electrochem. Soc. 124*:1185 (1977).
54. B. MacDougall, D. F. Mitchell, and M. J. Graham, *Isr. J. Chem. 18*:125 (1979).
55. B. MacDougall, D. F. Mitchell, and M. J. Graham, *J. Electrochem. Soc. 127*:1248 (1980).
56. S. Szklarska-Smialowska and G. Mrowczynski, *Br. Corros. J. 10*:187 (1975).
57. B. MacDougall, D. F. Mitchell, and M. J. Graham, *J. Electrochem. Soc. 132*:2895 (1985).
58. K. Takahashi, B. MacDougall, and M. J. Graham, *J. Electrochem. Soc. 137*:3023 (1990).
59. B. MacDougall and J. A. Bardwell, *J. Electrochem. Soc. 135*:2437 (1988).

Copyright © 2002 Marcel Dekker, Inc.

60. S. P. Tyfield, *Proceedings, 5th International Symposium on Passivity,* Bombannes, France (M. Froment, ed.), Elsevier, Amsterdam, 1983, p. 67.
61. Yu. I. Kuzentsov and M. E. Garmanov, *Elektrokhimiya 23*:381 (1987).
62. G. Bech-Nielsen, *Electrochim. Acta 19*:821 (1974); *20*:619 (1975).
63. Ya. M. Kolotyrkin, R. M. Lazorenko-Manevich, and L. A. Sokolova, *J. Electroanal. Chem. 228*:301 (1987).
64. Ya. M. Kolotyrkin, R. M. Lazorenko-Manevich, and L. A. Sokolva, *Dokl. Akad. Nauk. SSSR 295*:610 (1987).
65. Ya. M. Kolotyrkin, R. M. Lazorenko-Manevich, L. A. Sokolova, and V. G. Plotnidov, *Elektrokhimiya 14*:344 (1978).
66. A. D. Keitelman and J. R. Galvele, *Corros. Sci. 22*:739 (1982).
67. M. Janik-Czachor, *Werkstoffe Korros. 30*:225 (1979).
68. K. E. Hensler, *Encylopedia of Electrochemistry of the Elements* (A. J. Bard, ed.), Vol. IXA, Marcel Dekker, New York, 1982, p. 229.
69. N. Sato, *Corros. Sci. 27*:421 (1987).
70. Ju. I. Kuznetsov and I. A. Valuev, *Bull. Electrochem. 3*:393 (1987).
71. K. Ogura and K. Sato, *Passivity of Metals* (R. P. Frankenthal and J. Kruger, eds.), The Electrochemical Society Corrosion Monograph Series, Princeton, NJ 1978, p. 463; K. Ogura, *J. Electroanal. Chem. 79*:149 (1977).
72. B. MacDougall, J. A. Bardwell, and M. J. Graham, *J. Electrochem. Soc. 135*:340 (1988).
73. J. A. Bardwell and B. MacDougall, *J. Electrochem. Soc. 135*:2157 (1988).
74. B. MacDougall, *J. Electrochem. Soc. 126*:919 (1979).
75. T. P. Hoar, *Trans. Faraday Soc. 45*:683 (1949).
76. J. C. Scully, *Corros. Sci. 8*:513 (1968).
77. B. Kabanov, R. Burstein and A. Frumkin, *Discuss Faraday Soc. 1*:259 (1947).
78. C. L. McBee and J. Kruger, *Proceedings, U.R. Evans International Conference on Localized Corrosion,* 1971, National Association of Corrossion Engineers, Houston, 1974, p. 252.
79. J. R. Ambrose and J. Kruger, *Proceedings 4th International Congress on Metal Corrosion,* Amsterdam 1969, National Association of Corrosion Engineers, Houston, 1972, p. 698.
80. T. P. Hoar, D. C. Mears, and G. P. Rothwell, *Corros. Sci. 5*:279 (1965); L. F. Lin, C. Y. Chao, and D. D. MacDonald, *J. Electrochem. Soc. 128*:1194 (1981).
81. J. Mankowski and S. Szklarska-Smialowska, *Corros. Sci. 15*:493 (1975); *17*:725 (1977).
82. R. Goetz, B. MacDougall and M. J. Graham, *Electrochim. Acta 31*:1299 (1986).
83. B. MacDougall, D. F. Mitchell, G. I. Sproule, and M. J. Graham, *J. Electrochem. Soc. 130*:543 (1983).
84. B. MacDougall, and M. J. Graham, *J. Electrochem. Soc. 131*:727 (1984).
85. K. E. Heusler and L. Fischer, *Werkst. Korros. 27*:551 (1976).
86. K. E. Heusler and L. Fischer, *Werkst. Korros. 27*:788 (1976).
87. K. Nachstedt and K. E. Heusler, *Electrochim. Acta 33*:311 (1988).
88. R. Doelling and K. E. Heusler, *Z. Phys. Chem. 139*:39 (1984).
89. K. Nachstedt and K. E. Heusler, *Z. Phys. Chem. 160*:131 (1988).
90. W. Khalil, S. Haupt, and H.-H. Strehblow, *Werkst. Korros. 36*:16 (1985).
91. J. A. Bardwell, B. MacDougall, and G. I. Sproule, *J. Electrochem. Soc. 136*:1331 (1989).
92. J. A. Bardwell and B. MacDougall, *Electrochim. Acta 34*:229 (1989).
93. M. J. Graham, J. A. Bardwell, G. I. Sproule, D. F. Mitchell, and B. R. MacDougall, *Corros. Sci. 35*:13 (1993).
94. H.-H. Strehblow and B. Titze, *Corros. Sci. 17*:461 (1977).
95. H.-H. Strehblow and M. B. Ives, *Corros. Sci. 16*:317 (1976).
96. G. R. Wallwork and B. Harris, *Proceedings, U. R. Evans International Conference on Localized Corrosion,* 1971, National Association of Corrosion Engineers, Houston, 1974, p. 292.

Copyright © 2002 Marcel Dekker, Inc.

97. J. A. Bardwell, J. W. Fraser, B. MacDougall, and M. J. Graham, *J. Electrochem. Soc. 139*:366 (1992).
98. K. Nachstedt and K. E. Hensler, *Z. Phys. Chem. 160*:131 (1988); U. Bertocci and J. Kruger, *Surf. Sci. 101*:608 (1980).
99. M. Reuter and K. E. Heusler, *Electrochim. Acta 35*:1809 (1990).
100. G. Aronowitz and N. Hackerman, *J. Electrochem. Soc. 110*:633 (1963).
101. C. L. McBee and J. Kruger, *Electrochim. Acta 17*:1337 (1972).
102. A. G. Revesz and J. Kruger, *Passivity of Metals* (R. P. Frankenthal and J. Kruger, eds.), The Electrochemical Society Corrosion Monograph Series, Princeton, NJ 1978, p. 137.
103. T. P. Hoar, Palladium Medal Address, *J. Electrochem. Soc. 117*:17c (1970).
104. V. Mitrovic-Scepanovic, B. MacDougall, and M. J. Graham. *Corros. Sci. 24:*479 (1984).
105. J. E. Holliday and R. P. Frankenthal, *J. Electrochem. Soc. 119*:1190 (1972); K. Sugimoto and S. Matsuda, *Mater. Sci. Eng. 42*:181 (1980).
106. R. P. Frankenthal, *J. Electrochem. Soc. 114*:542 (1967).
107. G. Okamoto, *Corros. Sci. 13*:471 (1973).
108. B. Baroux, *Proceedings, 5th International Symposium on Passivity,* Bombannes, France (M. Froment, ed.), Elsevier, Amsterdam, 1983, p. 531.
109. V. Mitrovic-Scepanovic, B. MacDougall, and M. J. Graham, *Corros. Sci. 27*:239 (1987).
110. C. Calinski and H.-H. Strehblow, *J. Electrochem. Soc. 136*:1328 (1989).
111. J. A. Bardwell, A. J. Davenport, H. J. Isaacs, G. I. Sproule, B. MacDougall, and M. J. Graham, *J. Electrochem. Soc. 139*:371 (1992).
112. P. Marcus and I. Olefjord, *Corrosion 42*:91 (1986).
113. P. Marcus and I. Olefjord, *Surf. Interface Anal. 4*:29 (1982).
114. N. D. Tomashov, G. P. Chernova, and N. Markova, *Corrosion 20*:166t (1964).
115. Ya. M. Kolotyrkin and W. M. Khyazheva, *Passivity of Metals* (R. P. Frankenthal and J. Kruger, eds.), The Electrochemical Society Corrosion Monograph Series, Princeton, NJ, 1978, p. 678.
116. E. A. Lizlovs and A. P. Bond, *J. Electrochem. Soc. 116*:574 (1969).
117. V. Mitrovic-Scepanovic and M. B. Ives, *Corrosion 40*:655 (1984).
118. I. Olefjord and P. Marcus, *Proceedings, Eurocorr '87, European Corrosion Meeting,* Karlsruhe, Germany, 1987, p. 361.
119. M. P. Ryan, R. C. Newman, and G. E. Thompson, *J. Electrochem. Soc. 142*:L177 (1995).
120. M. F. Toney, A. J. Davenport, L. J. Oblonsky, M. P. Ryan, and C. M. Vitus, *Phys. Rev. Lett. 79*:4282 (1997).
121. M. F. Toney, M. P. Ryan, L. J. Oblonsky, and A. J. Davenport, *Synchrotron Radiat. News 11*:5 (1998).
122. V. Maurice, H. Talah, and P. Marcus, *Surf. Sci. 284*:L431 (1993).
123. V. Maurice, H. Talah, and P. Marcus, *Surf. Sci. 304*:98 (1994).
124. P. Marcus and V. Maurice, *Proceedings 8th International Symposium on Passivity of Metals and Semiconductors,* Jasper, Alberta, Canada, May 9–14, 1999 (p. 30).
125. T. Suzuki, T. Yamada, and K. Itaya, *J. Phys. Chem. 100*:8954 (1996).
126. D. Zuili, V. Maurice, and P. Marcus, *Passivity and Its Breakdown* (P. M. Natishan, H. S. Isaacs, M. Janik-Czachor, V. A. Macagno, P. Marcus, and M. Seo, eds.), Proc. Electrochem. Soc. PV97-26, Pennington, NJ, 1998, p. 1013.
127. L. J. Oblonsky, M. P. Ryan, and H. S. Isaacs, *J. Electrochem. Soc. 145*:1922 (1998).
128. M. P. Ryan, R. C. Newman, and G. E. Thompson, *Philos. Mag. B. 70*:241 (1994).
129. V. Maurice, W. P. Yang, and P. Marcus, *J. Electrochem. Soc. 143*:1182 (1996).
130. V. Maurice, W. P. Yang, and P. Marcus, *J. Electrochem. Soc. 141*:3016 (1994).
131. V. Maurice, W. P. Yang, and P. Marcus, *J. Electrochem. Soc. 145*:909 (1998).

Copyright © 2002 Marcel Dekker, Inc.

7

Passivity of Austenitic Stainless Steels

Clive R. Clayton
State University of New York at Stony Brook, Stony Brook, New York

Ingemar Olefjord
Chalmers University of Technology, Göteborg, Sweden

INTRODUCTION

Austenitic stainless steels appear to have significantly greater potential for aqueous corrosion resistance than their ferritic counterparts. This is because the three most commonly used austenite stabilizers, Ni, Mn, and N, all contribute to passivity. As in the case of ferritic stainless steel, Mo, one of the most potent alloying additions for improving corrosion resistance, can also be added to austenitic stainless steels in order to improve the stability of the passive film, especially in the presence of Cl ions. The passive film formed on austenitic stainless steels is often reported to be duplex, consisting of an inner barrier oxide film and outer deposit hydroxide or salt film.

Passivation is generally believed to take place by the rapid formation of surface-adsorbed hydrated complexes of metals, which are sufficiently stable on the alloy surface that further reaction with water enables the formation of a hydroxide phase that, in turn, rapidly deprotonates to form an insoluble surface oxide film. Failure in any of these stages would lead to continued active dissolution. The passivation potential is critical to this process, in part because it governs the oxidation state of the metal, which in turn governs its solubility. In addition, the electric field strength has to be sufficient to cause deprotonation of the surface hydroxide phase in order to enable the oxide barrier film to become estabilished. No evidence has been found by surface studies that passivity of austenitic stainless steels is possible by formation of a simple hydroxide film. It is perhaps surprising that the passive film formed on austenitic stainless steels does not always contain each of the alloying elements added to stabilize the austenitic phase, even when such additions appear to improve the chemical stability of the steel. Ni exemplifies this behavior.

To understand the influence of alloying elements on the passivity of stainless steels, researchers have combined electrochemical and surface analysis. Polarization diagrams provide the first indication of the overall influence of alloy additions on the active-passive transition, passivity, and pitting resistance. However, surface analysis by X-ray photoelectron spectroscopy (XPS) of prepassivated surfaces provides a direct observation of the location and the chemical state of an alloying element. Such

Copyright © 2002 Marcel Dekker, Inc.

information is invaluable for the development of a working model of the passivation process. The following surface layers have been attributed to the passivation process: barrier oxide layer, salt deposit layer, and alloy surface layer.

Alloying of transition elements, not surprisingly, often results in the formation of several different oxidation states. Some oxidation states are apparent at only a trace level and may be excluded from the general discussion. The main parameters that determine the oxidation state of an element in a passive film are:

The passivation potential or oxidizing power of the solution
The pH of the test electrolyte
Local pH within highly hydrated passive films
The age of the passive film
The location of the ion relative to the external surface

For the purpose of a general introduction to the nature of the passive films formed on stainless steels, we shall consider one of the media most corrosive to stainless steels, i.e., acidic chloride solutions. In this discussion we shall consider several studies that include a range of stainless steel compositions. Trends in the nature of the passive film formed on these alloys will be emphasized.

It is common to find that the passive film is duplex, consisting of an inner oxide barrier film that is considerably less hydrated than the often thinner, outer deposit film. The outer film often contains salts or hydroxides of the alloy consituent metals. Although the inner oxide is the primary diffusion barrier against egressing cations and ingressing anions such as Cl^-, there is some evidence that in some cases the deposit film may serve to control ion transport in the passive film by the influence of fixed charges. In other cases it has been considered to be a relatively insoluble film that serves to protect the metal surface from aggressive ions while a barrier film develops underneath.

It will also be shown that the thickness of the passive films, while varying with the potential of passivation, is commonly only a few nanometers. Finally, we shall see that in austenitic stainless steels the active stage of repassivation often results in considerable change in composition at the alloy surface. The possible role of this modified alloy layer in the overall passivation process will be discussed.

BARRIER AND DEPOSIT LAYERS

Surface analysis has provided the basis of our knowledge of the duplex nature of the passive film formed on austenitic stainless steels. Destructive depth profiling using inert gas ion sputter etching and nondestructive variable-angle electron spectroscopy are commonly used to probe the composition of these layers. Both types of analysis will be illustrated.

The first example involves the use of XPS with inert gas ion sputter depth profiling. This study [1] involved the active dissolution and passivation of the stainless steel, AVESTA 832SL (Table 1).

The test electrolyte was a deaerated solution of 0.1 M HCl + 0.4 M NaCl. The polarization behavior of the alloy is compared in Figure 1 with the alloy constituent metals. The corrosion potential is seen to be more noble than that of Cr and Fe but close to that of Ni and Mo. This is quite typical for the corrosion potential of

Copyright © 2002 Marcel Dekker, Inc.

Table 1 Composition of AVESTA 832L (wt %)

C	Mn	P	S	Si	Cr	Ni	Mo	Cu	N
0.040	1.64	0.020	0.003	2.62	16.7	15.0	4.28	0.10	0.27

austenitic alloys. It will be shown that Ni and Mo are enriched on the surface in the metallic state during anodic dissolution. As a consequence, the corrosion potential becomes close to the corrosion potential of these elements. From the polarization data it is suggested that both Cr and Mo are more likely to contribute to passivity, especially the barrier layer, than Fe or Ni and that Mo will contribute only in a narrow range of potential before it undergoes transpassive dissolution. These simple indications will be shown to be only partially correct. In Figure 2 are typical XPS spectra of the outer region of the surface films obtained in the same study for the alloy polarized at passive potentials (–100 and 500 mV vs. SCE).

The thicknesses of the films formed at the passive potentials –100 and 500 mV (SCE) were calculated to be 1.0 and 1.5 nm, respectively. It can be seen from Figure 2 that the Ni spectra contain almost no detectable oxidized Ni. Therefore, Ni does not contribute directly to the structure of the barrier or deposit films. This is surprising because Ni is well known to contribute to pitting resistance [2]. In addition, it can be seen that the film formed at 500 mV (SCE), which is several hundred millivolts above the transpassive potential of Mo, contains contributions from Mo^{4+} (as MoO_2), which has been shown to be the main cation in the passive film formed on Mo in 0.1 M HCl [3]. Therefore, it would appear that Mo contributes directly to the passive

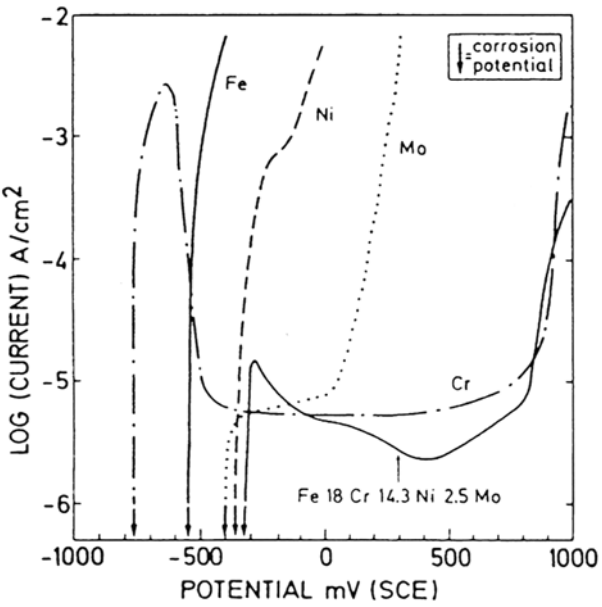


Figure 1 Anodic polarization curves of the pure metals Fe, Cr, Mo, and Ni and of an austenitic stainless steel, Fe18Cr14.3Ni2.5Mo (at %) (Fe16.7Cr15.0Ni4.28Mo wt%) exposed to 0.1 M HCl + 0.4 M NaCl at 25°C. Sweep rate, 3 mV/s. (From Ref. 1.)

Copyright © 2002 Marcel Dekker, Inc.

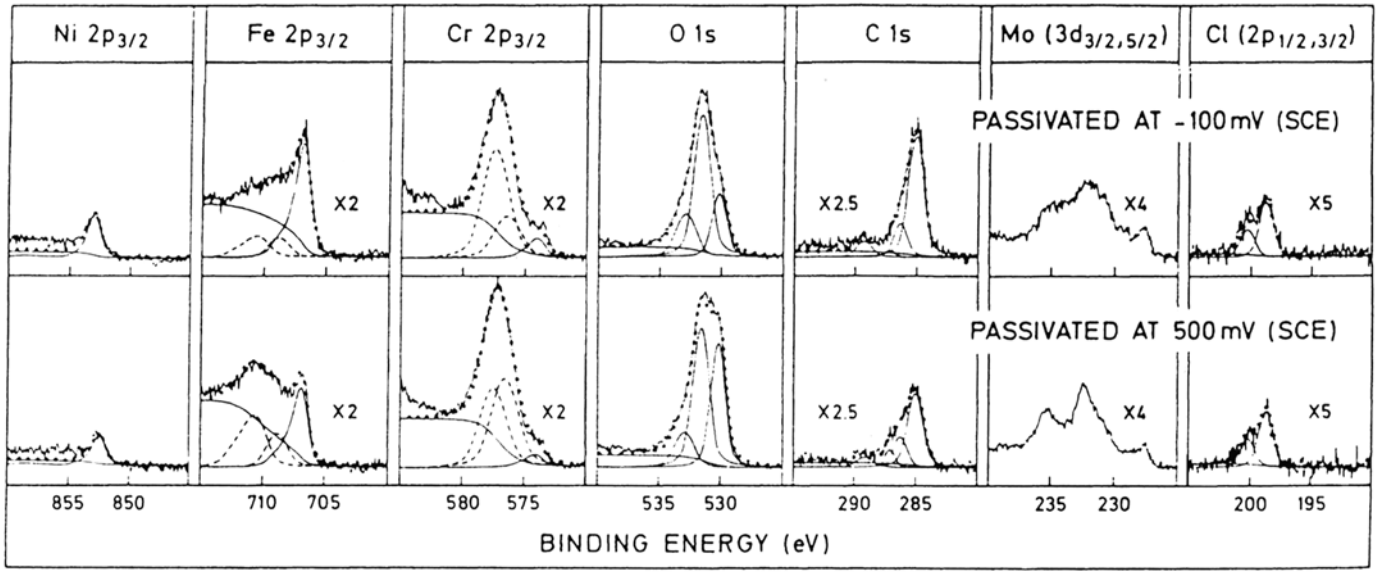


Figure 2 XPS spectra recorded from Fel8Crl4.3Ni2.5Mo (at %) after passivation at –100 mV (SCE) and 500 mV (SCE). (From Ref. 1.)

Copyright © 2002 Marcel Dekker, Inc.

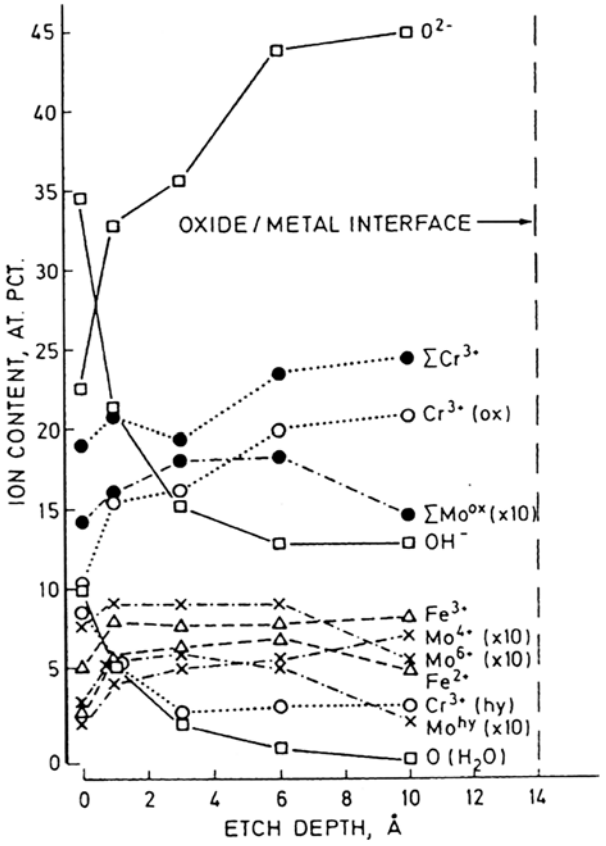


Figure 3 Ion content vs. etch depth for the austenitic stainless steel Fe18Cr14.3Ni2.5Mo polarized at 500 mV (SCE). (From Ref. 1.)

film formed on austenitic stainless steel. The general spectra of Figure 2 provide no direct information concerning the duplex nature of the passive film. However, in Figure 3 is a depth profile produced by argon ion sputter depth profiling of the passive film formed at 500 mV (SCE) for the same alloy. From this figure it can be seen that there exist two layers, an inner oxide-based layer (barrier layer) constituting the majority of the film and an outer hydrated layer (deposit layer), which is also richer in Mo^{6+} than Mo^{4+} . We shall discuss the role of Mo in the passivation process later. A further striking observtion is that Cr^{3+} is found in greater abundance in the passive film in both the inner and outer layers than Fe, despite the fact that Fe is the majority element in the alloy. Clearly, Cr is the main passivating species in stainless steels.

BOUND WATER IN PASSIVE FILMS

A series of reported studies provide some insights into the nature and the role of bound water in the passivity of austenitic stainless steels [4–6]. The studies primarily

Copyright © 2002 Marcel Dekker, Inc.

focused on the passivity of type 304 stainless steel, passivated in deaerated 0.5 M H_2SO_4. Radiotracer studies were conducted with tritiated water in order to determine the quantity of water bound into the lattice following the formation of the passive film. In addition, the rate of desorption of bound water from the film was determined by dioxane solvent extraction. Dynamic rupture and self-repair of the passive film were seen to be critically influenced by the nature of the bound water. Two classes of bound water were determined from XPS, radiotracer, Coulombic titration, pitting incubation, and noise analysis [4–6]. The two classes of bound water were of the following types: (a) M-H_2O and M-OH (aquo and olation groups) and (b) M-O or M-OOH with oxo and olation bridges.

In Figure 4 the proposed structure of the passive films is presented schematically [4]. The bound water was proposed to be associated largely with Cr but with its nature governed by the applied potential, temperature, and time at potential. It was established that the water content in the passive films formed on 304 stainless steel in deaerated 0.5 M H_2SO_4 changed abruptly at the critical potential of 400 mV (SCE) as shown in Figure 5 [5]. Later reflection high-energy electron diffraction (RHEED) studies based on the same alloy composition and test electrolyte [7] revealed that corresponding structural changes with potential and time at potential were associated with chromium and iron products composing the barrier and deposit layers, respectively. Passive films that were formed after 1 min were found to be amorphous. At longer times of passivation some crystallization was revealed. The inner barrier film, which was found by XPS to consist mostly of Cr_2O_3, was seen by RHEED to be amorphous at all potentials studied in the passive range, except at the transpassive potential, where it crystallized. Low-potential passive films (<400 mV) were seen to convert to the same structure as higher potential passive films (>400 mV), given sufficient time for field-induced deprotonation to take place. The chromium content of the deposit layer was observed to be $Cr(OH)_3$ in the presence of acidic SO_4^{2-}/Cl and CrOOH in the presence of 0.5 M H_2SO_4. Highly hydrated Fe compounds (including green rusts) were also observed, which rapidly deprotonated with corresponding charge-balancing oxidation of Fe^{2+} at the critical potential of 400 mV (vs. SCE).

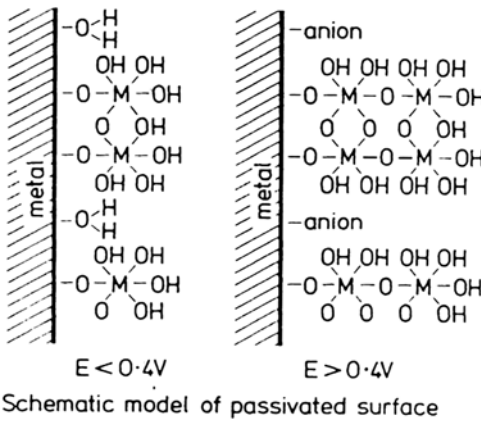


Figure 4 The Okamoto model of the structure of the passive film. (From Ref. 4.)

Copyright © 2002 Marcel Dekker, Inc.

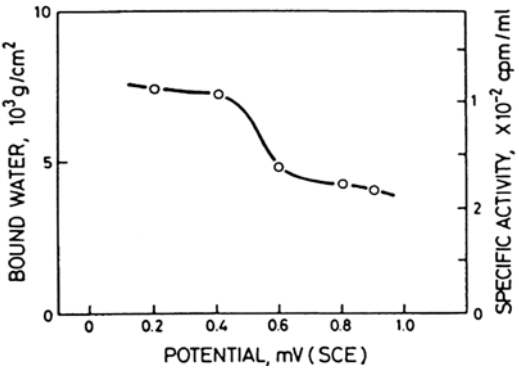


Figure 5 Amount of bound water in the passive film vs. the potential. (From Ref. 5.)

ROLES OF MOLYBDENUM IN THE PASSIVITY OF AUSTENITIC STAINLESS STEEL

One of the most effective elements added to austenitic stainless steel, and for that matter even ferritic stainless steel, in order to improve pitting resistance is Mo [8]. Molybdenum, however, is a highly versatile element, existing in the passive film in a number of oxidation states. In the case of the hexavalent state it has been observed in both the cationic and anionic states, namely as molybdenum trioxide and ferrous molybdate. It has most commonly been reported to exist in the quadrivalent state as molybdenum dioxide and oxyhydroxide.

The majority of the studies reported agree that Mo^{4+} is incorporated into the inner region of the passive film, whereas Mo^{6+} is present in the outer layer. However, the outer layer is variously defined as a salt layer or an extension of the barrier layer.

Numerous studies have attempted to elucidate the role of Mo in the passivity of stainless steel. It has been proposed from XPS studies that Mo^{6+} forms a solid solution with CrOOH with the result that Mo is inhibited from dissolving trans-passively [9]. Others have proposed that active sites are rapidly covered with molybdenum oxyhydroxide or molybdate salts, thereby inhibiting localized corrosion [10]. Yet another study proposed that molybdate is formed by oxidation of an Mo dissolution product [11]. The oxyanion is then precipitated preferentially at active sites, where repassivation follows. It has also been proposed that in an oxide lattice dominated by three-valent species of Cr and Fe, ferrous ions will be accompained by point defects. These defects are conjectured to be canceled by the presence of four- and six-valent Mo species [1]. Hence, the more defect-free film will be less able to be penetrated by aggressive anions. A theoretical study proposed a solute vacancy interaction model in which Mo^{6+} is assumed to interact electrostatically with oppositely charged cation vacancies [12]. As a consequence, the cation vacancy flux is gradually reduced in the passive film from the solution side to the metal-film interface, thus hindering vacancy condensation at the metal-oxide interface, which the authors postulate acts as a precursor for localized film breakdown [12].

The XPS spectra (Fig. 2) show that the passive film formed in Cl^--containing solutions contains Cl^-. It has been shown [13,14] that Cl^- is present in both the barrier layer and the hydroxide layer. It is believed that chloride ions substitute

Copyright © 2002 Marcel Dekker, Inc.

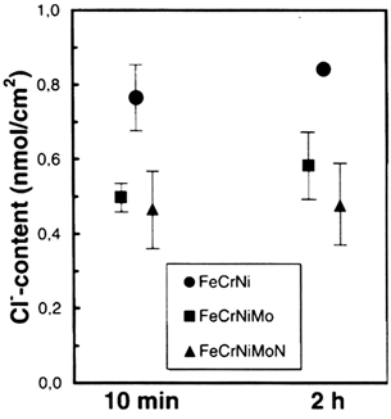


Figure 6 Total amount of Cl^- in the passive film formed at –75 mV (SCE) in 0.1 M HC1 + 0.4 M NaCl. (From Ref. 15.)

oxygen in the passive film. Thereby the stability of the film is reduced because the number of cation-oxygen bonds decreases and dissolution of the oxide is enhanced. In one study [14] high-alloyed steels, Fe20Cr20Ni, Fe20Cr20Ni6Mo, and Fe20Cr20Ni6Mo0.2N were exposed to 0.1 M HCl + 0.4 M NaCl at –75 mV (SCE) for 10 min and 2 h. It was found that the Cl^- content of the Mo-free alloy was considerably higher than the Cl^- content of the Mo-containing alloy. Figure 6 [15] shows the experimental result. It was suggested [14,15] that the mechanism for lowering the Cl^- content in the film is due to the ability of Mo to form soluble stable oxo-chloro complexes in diluted HCl solutions. Reference 16 gives details about the Mo complexes. Table 2 summarizes some of the possible soluble stable Mo-oxo-chloro complexes. Formation of these complexes, during the passivation process, lowers the Cl^- content in the passive film and thereby make the film more resistant for pitting corrosion.

It has been suggested that molybdate ions may act as cation-selective species in the deposit layer, thus producing a bipolar film with the anion- selective component represented by the barrier layer, which in acidic media is predicted to be anion selective [17]. The bipolar model of passivity is represented schematically in Figure 7.

Evidence in support of several of these models has been reported. XPS studies of the passive and transpassive films formed on Mo in deaerated 0.1 M HCl [3] established that molybdate was absent from both surface films. In a later study the same authors used a twin potentiostat arrangement, with a second working electrode

Table 2 Soluble Stable Mo-oxo-chloro Complexes in Aqueous HCl Solutions

Mo(II)	$[Mo_6Cl_8]^{4+}$
Mo(III)	$[Mo_2(OH)_2Cl_n]\ (H_2O)_{8-n}]^{(4-n)+}$, $n < 3$ $[MoCl_5(H_2O)]^{2-}$
Mo(IV)	$[Mo_3O_4Cl_n]\ (H_2O)_{9-n}]^{(4-n)+}$, $n < 4$
Mo(V)	$[Mo_2O_4Cl_4(H_2O)_2]^{2-}$ $[Mo_2O_3Cl_8]^{4-}$
Mo(VI)	$Mo(OH)_5Cl$

Copyright © 2002 Marcel Dekker, Inc.

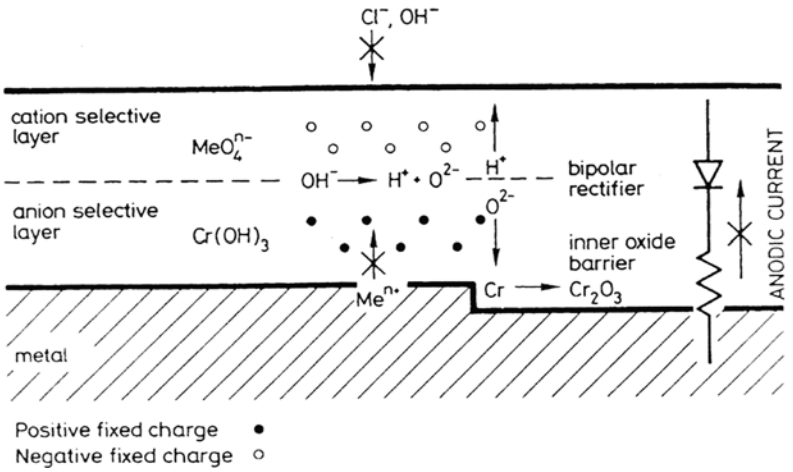


Figure 7 Schematically illustration of the bipolar model of the passive film. (From Ref. 3.)

of either Fe, Cr, or Ni that was polarized near an Mo electrode at the same potential (–180 mV vs. SCE) [18]. At this potential Mo and Cr are passive, while Ni and Fe are active. In this work it was shown that for the Fe-Mo and Ni-Mo electrode couples, iron or nickel molybdate was observed on the passive Mo surface. In the case of the Cr-Mo couple, molybdate was observed only on the passive film of Cr. This work was also able to show that transpassivity of Mo at 250 mV (SCE) was suppressed in the presence of Fe, which formed a molybdate salt on the surface of Mo. This indicated evidence of a possible mechanism by which Mo can remain passive in stainless steels at higher potentials than the transpassive potential of Mo. In addition, this work supported the idea that soluble molybdate anions can redeposit at active sites.

In other work, a major prediction of the bipolar model of passivity [19] was tested. This was that in the presence of a bipolar passive film with the cation-selective layer (molybdate anions, for example) in the outer layer or deposit film, there would be a tendency to increase O–H bond stretching and eventual deprotonation due to the conjoint effect of the electric field associated with the surface charge on the metal and the strong negative fixed charge on the oxyanion. As a result of this work it was shown by XPS analysis that when a passive film formed on an Fe-19Cr9Ni alloy was doped in solution with molybdate anions, there was a significant decline in the hydroxyl concentration in the film in favor of oxide anions. In addition, the concentration ratio of chromium oxide to hydroxide was increased. This work has several ramifications. First, it provides some support for the bipolar model of passivity, which would suggest that molybdate can rectify the transport of ions through the passive film in favor of inhibiting egress of cations other than protons as well as inhibiting the ingress of chloride ions that aid in the dissolution of the film. Second, the promotion of deprotonation of the passive film would favor oxidation of ferrous ions to ferric in order to establish charge neutrality. This would also have the effect of reducing the defect concentration in the trivalent-dominated oxide lattice in accordance with a previous suggestion [1].

Copyright © 2002 Marcel Dekker, Inc.

So far, the role of molybdenum in the passive film has been discussed. However, several workers have postulated that Mo may exclusively or additionally control the kinetics of the active dissolution process. These models can be separated into two kinds: (a) insoluble salt models and (b) surface alloy models. One of the earliest reports to indicate the importance of insoluble salts in the repassivation kinetics of ferrous alloys involved studies of Fe-Mo alloys [20]. It was shown that when the alloy content exceeded 5% a protective chloride salt film stabilized by ferrous molybdate precipitated from the test solution after the initial dissolution of molybdenum. This work suggests that a similar mechanism may occur in Mo-bearing austenitic stainless steels in chloride solutions. The stability of the molybdenum-bearing passive film in chloride solutions has also been attributed to the ability of Mo to form insoluble chloride complexes at the base of pits, thereby arresting chloride ions in the pit solution, which in turn enables subsequent repassivation to occur. This has been shown by Auger electron spectroscopy (AES) of pit surfaces [21]. XPS analysis has revealed [15,22] the Mo(II) valent compound β-$MoCl_2$ formed in the passive film on high-alloyed stainless steels passivated in hydrochloric acid. β-$MoCl_2$ is the only one of the nonsoluble chloride compounds that can easily be detected by XPS. Other insoluble high-Mo-valency chloride compounds such as α-$MoCl_3$, MoOCl, $MoOCl_2$ and MoO_2Cl[16] are not easily detected due to the overlap of their Mo signals with Mo-oxide peaks.

The activity of Cl ions in the pits of Mo-bearing stainless steels was also shown by AES to be significantly reduced by precipitation of an insoluble chloride complex containing Mo. This behavior is also reflected in the passivation of high-purity Moin a deaerated solution of 4 M HCl [23]. It has been shown that the passive range of potential for Mo in 4 M HCl is significantly greater than in 0.1 M HCl. XPS analysis of the surface of Mo polarized in the passive range for deaerated 4 M HCl solution provided evidence of a molybdenum oxyhydroxy chloride film. This product was not observed in the exclusively oxide-based passive film formed on Mo in 0.1 M HCl solution. The presence of such an insoluble film on Mo in 4 M HCl indicates that such a film may be formed on the bottom of pits formed onMo-bearing stainless steels.

It has been shown that the low pH value of pitting solutions is caused by high concentrations of metal chlorides [24]. Therefore the formation of insoluble chloride complexes in pit bottoms suggests that lowering the concentrations of soluble metal chlorides in the pitting solution would cause the pH to shift toward that of the bulk solutions. The conjoint effects of raising pH and deposition of salt films provide conditions more conducive to repassivation [25].

The effect of surface alloy modification by anodic dissolution on the passivation of Mo-bearing austenitic stainless steels is discussed later in a separate section.

ROLES OF NITROGEN IN THE PASSIVITY OF AUSTENITIC STAINLESS STEEL

Nitrogen may be added to austenitic stainless steel (commonly 0.2 to 0.7 wt %) in order to stabilize and strengthen the austenitic phase. However, in the presence of Mo additions very significant improvements in general and localized corrosion have

Copyright © 2002 Marcel Dekker, Inc.

been demonstrated by several workers [26–30]. This early work indicated a strong synergistic effect of Mo and N in the corrosion resistance of austenitic stainless steel.

More recently, it has been demonstrated [31] that N anodically segregates to the oxide-metal interface during passivation. The dots with the error bars in Figure 8 [15] show the measured intensity ratios, $N/(O^{2-} + OH^{-})$, recorded by XPS as a function of the take-off angle for an alloy (Fe20Cr20Ni6Mo0.2N) polarized in a 0.1 M HCl + 0.4 M NaCl solution at –75, 500 and 800 mV for 10 min. The distribution of N was estimated by utilizing quantitative analysis described in Ref. 32. The thick solid lines at the bottom of the three figures represent the expected intensity ratios one should obtain if the nitrogen atoms (concentration 0.2 wt %) are uniformly distributed in the phase below the passive film. However, the measured intensity ratios are significantly higher, which implies that N is enriched at the surface. By assuming a model shown in the upper right corner of the figure it was possible to find a distribution of N that satisfies the measured data. The thin solid lines in Figure 8 are theoretical intensity ratios calculated by assuming that N is enriched at the metal-oxide interface and that the bulk concentration is 0.2 w % N. The theoretical ratios are obtained for N coverage of 12, 17, and 20 at % at the interface.

It has been demonstrated [33] that a strong Mo-Ni-N interaction is likely to occur. In a series of papers on experimental N-bearing alloys #30 and #30c, which were compared with alloy AL6X, it was shown that nitrogen additions strongly improved corrosion resistance [29,30] (Table 3). In tests conducted in several acidic chloride solutions it was shown that nitrogen alloying was responsible for lowering the critical current density and passive current density at room temperature and at elevated temperature [29]. Alloy #30 was also tested at 80°C in a solution of 4% NaCl + 1% $Fe_2(SO_4)_3$ + 0.01 M HCl in which it showed no evidence of pitting. This result was all the more significant because it had previously been shown that for austenitic alloys a linear relationship existed between the critical pitting temperature and the compositional factor (wt % Cr + 2.4 wt % Mo) in the same solution [34]. The inference therefore remains that the N-bearing alloy may protect against pitting via an alternative overall mechanism.

In further studies of alloy #30 it was shown by Auger depth profiling [30] (see Fig. 9) that nitrogen segregated to the alloy surface at the metal-oxide interfacedur-ing passive dissolution at 500 mV (SCE) for 24 h in deaerated 0.5 M H_2SO_4. In later studies it was shown that N additions strongly influence the alloy composition at the metal-oxide interface [35]. Thus segregation of N was found to coincide with the enrichment of Ni and Cr in 304(N) stainless steel and Ni, Cr, and Mo inMo-bearing austenitic stainless steels such as 317LX(N), 904L(N), and AL6X(N) (Table 4).

It was determined from the N 1*s* photoelectron spectra that the form in which nitrogen was segregated is a surface nitride [33]. XPS studies of surface nitrides formed on Fe, Cr, Ni, Mo, and the stainless steels 304, 317LX, 904L, and AL6X show that the nitride anodically formed on nitrogen-bearing austenitic stainless steels was a mixed nitride. For this work and for the purpose of studying the interaction of anodically segregated N with the individual alloying constituents, a room temperature electrochemical nitriding process was developed [33]. The process involved the cathodic reduction of nitrate ions. The outcome of the treatment was that the same surface nitrides were formed on the stainless steels as formed by anodic

Copyright © 2002 Marcel Dekker, Inc.

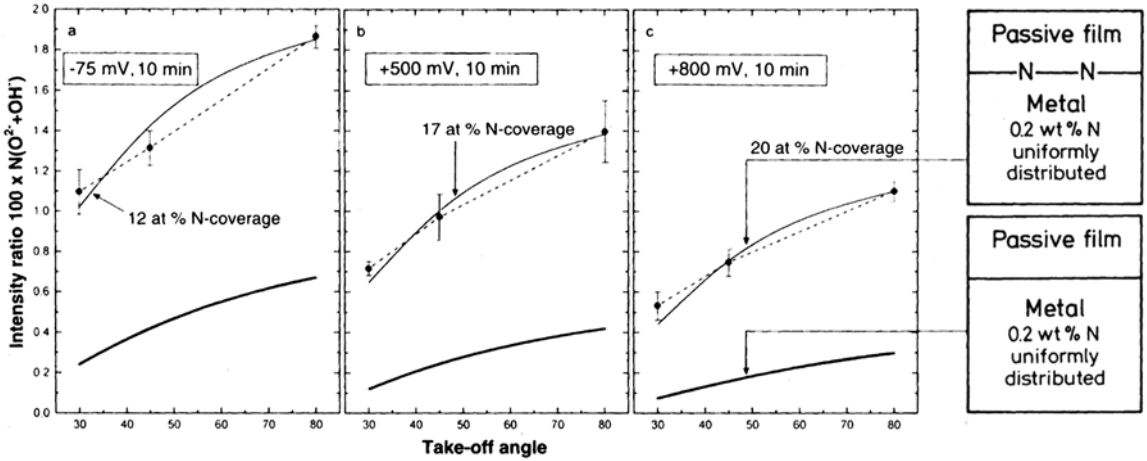


Figure 8 Measured intensity ratios, $100 \times N/(O^{2-} + OH^{-})$, at the take-off angles 30°, 45° and 80° after passivation of the Fe20Cr20Ni6Mo0.2N alloy at –75, 500 and 800 mV (SCE). The lower thick line and the upper thin line represent the estimated intensity ratios from the N-distributions shown in the models to the right of the figure. (From Ref. 15.)

Copyright © 2002 Marcel Dekker, Inc.

Table 3 Chemical Composition of Main Elements of Steels (wt%)

	Fe balance				
Steel	Cr	Ni	Mo	N	C
AL6X	20.5	24.7	6.7	0.04	0.02
#30	24.3	19.9	6.1	0.44	0.02
#30c	22.0	20.5	6.0	0.49	0.005

segregation. The benefit of the technique was that, unlike the case of ion implantation and plasma or thermal nitriding, a room temperature surface phase could be formed without expected surface damage or sensitization. The advantage of studying surface nitrides over the nitrogen-bearing alloys was reported to be that, whereas anodic segregation is a continuously regenerating process, surface alloying provides a finite quantity of nitrogen that can be monitored by surface analysis after anodic dissolution under active and passive conditions.

As seen in Figure 10, the potentiodynamic behavior in deaerated 0.1 M HCl of austenitic stainless steels is beneficially modified by the surface nitriding treatment, in agreement with previous studies of the same steels alloyed with nitrogen [33]. Each of the steels showed that the surface nitride stifles active dissolution and that this effect

Passivity of Austenitic Stainless Steels

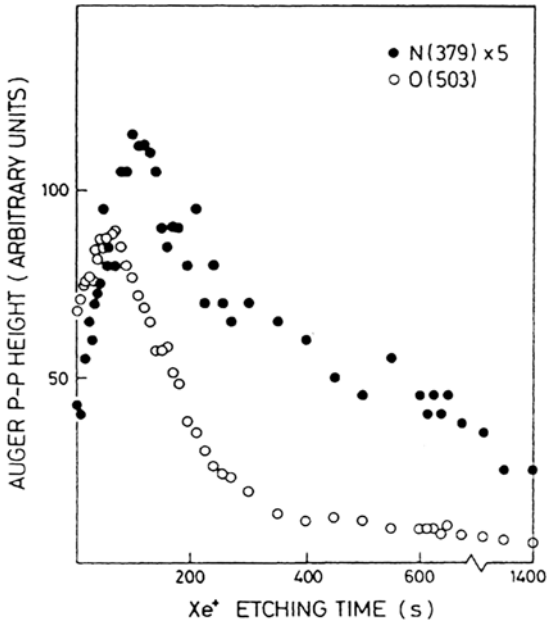


Figure 9 Auger depth profile for alloy 30 after passivation for 24 h in 0.5 M HCl + 2 M NaCl. Approximate etching rate was 0.01 nm/s. (From Ref. 30.)

Copyright © 2002 Marcel Dekker, Inc.

Table 4 Chemical Composition of Steels (wt%)

	Fe balance									
Steel	C	Mn	P	S	Si	Cr	Ni	Mo	Cu	N
304	0.053	1.77	0.031	0.008	0.41	19.27	8.49	0.36	0.16	0.040
317LX	0.022	1.52	0.018	0.015	0.41	18.43	13.13	3.34	0.01	0.050
AL6X	0.020	1.47	0.030	0.002	0.50	20.45	24.65	6.30	0.19	0.040
904L	0.019	1.50	0.023	0.002	0.44	20.46	24.40	4.51	1.48	0.050

is more pronounced as the addition of Mo is increased. In the lower alloyed steels, 304 and 317LX, the greatest influence of nitrogen was reported to be in raising the pitting potential. As shown by Figure 10, the pitting resistance of surface-nitrided 317LX steel is markedly better than that of type 304 due to the higher Mo content. It

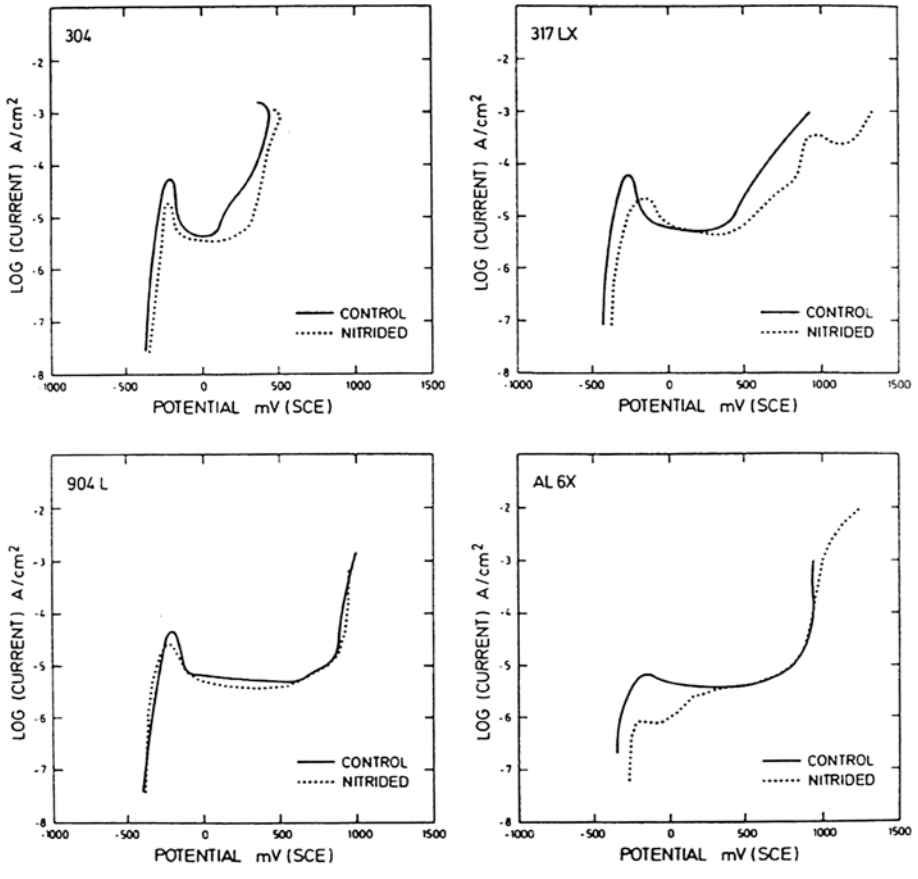


Figure 10 Polarization curves for surface-nitrided and untreated austenitic stainless steels in deaerated 0.1 M HCl where the specimens were permitted to float to the open-circuit potential before polarization. Sweep rate: 1 mV/s. (From Ref. 33.)

Copyright © 2002 Marcel Dekker, Inc.

is also apparent that the greatest anodic inhibition was achieved by the AL6X alloy, which has the highest Mo content of the alloys studied and in particular is very similar in composition to 904L except for an additional 1.8 wt % Mo. These observations imply that N and Mo support the same mechanism of corrosion inhibition.

The authors also noted that following potentiodynamic polarization from the corrosion potential to 0 mV at a scan rate of 1 mV/s, XPS analysis was still able to detect significant quantities of surface nitride. This is illustrated in Figure 11. The most active of the alloys studied, type 304, was determined to have dissolved approximately 20 monolayers. This suggested that the nitride may form a kinetic barrier that is protected by the oxide passive film from rapid protonation to ammonia and ammonium in the active range of potential. In the same study the nitride phase formed on Ni had little effect on anodic behavior in 0.1 M HCl,

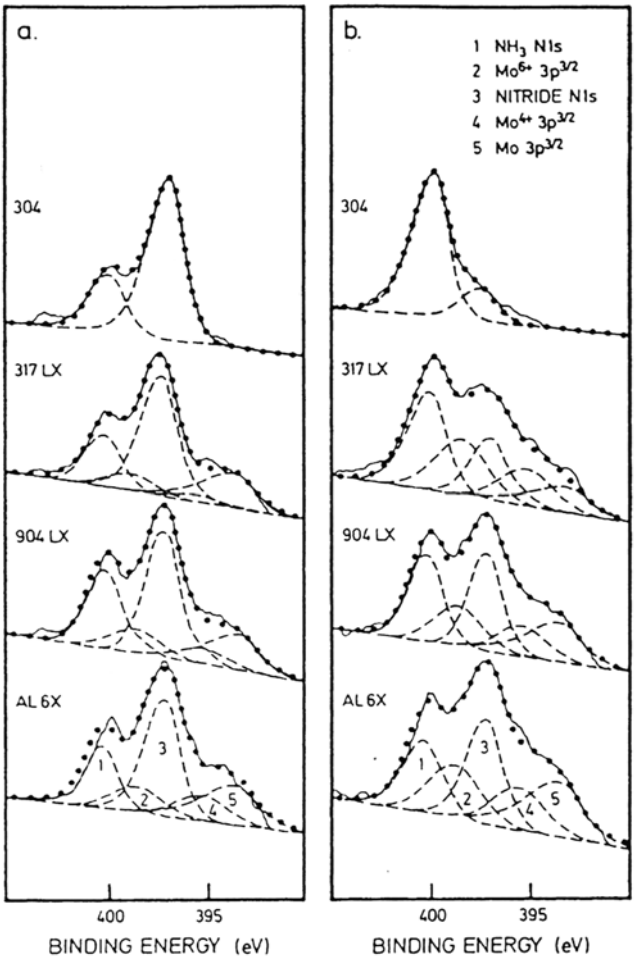


Figure 11 N Is spectra for austenitic stainless steels: (a) As nitrided; (b) follow polarization from open circuit to 0 mV. Sweep rate: 1 mV/s. (From Ref. 33.)

Copyright © 2002 Marcel Dekker, Inc.

whereas Fe became anodically activated by nitriding. Chromium exhibited complete removal of the active nose following nitriding. This was attributed to suppression of Cr^{2+} by direct chemical reaction of surface N and Cr forming a Cr^{3+} state as CrN, a precursor of Cr_2O_3, which was identified by XPS. Molybdenum, however, showed some ennoblement of the corrosion potential and transpassive potential. This effect on Mo was later found to be even more pronounced following thermal nitriding [36].

It has been reported that nitrogen alloying and surface nitriding result in a higher metal oxyanion content in the outer layers of the passive films of stainless steels formed in acidic solutions. By inspection of the *E*-pH diagrams of Mo and W, for instance, it is seen that MoO_4^{2-} and WO_4^{2-} are both more likely to form in the middle to high pH range [37]. The presence of the metal oxyanions in the outer region of passive films formed on stainless steels indicates that the products are developed during the active stage of repassivation, precipitating as salt films. The well-known pitting inhibition derived from metal oxyanions such as molybdate suggests that the presence of such anions in the outer layers of the passive films would tend to reduce the probability of pit initiation.

ALLOY SURFACE LAYERS

A stainless steel is normally used at potentials corresponding to the passive range. In this condition only a fraction of the oxidized atoms remain in the passive film; most are dissolved into the solution. The oxidation rate of the metal corresponds to the passive current density. As established earlier, the alloying elements Cr and Mo are enriched in the passive film. The other two main alloying elements, Fe and Ni, could in principle be found in the solution due to selective dissolution of these elements. XPS spectra [1,38–40] recorded from stainless steels after polarization to potentials in the active and passive regions show that the measured Fe content in the metal phase is lower than the composition of the bulk alloy. Fe must therefore be selectively dissolved and can thereby be found enriched in the solution. Ni and Mo, on the other hand, are enriched in the metal phase underneath the oxide. It has been proposed [1,38–40] that during active dissolution and passivation of stainless steel a thin layer of an intermetallic compound is formed in the outermost layers of the metal phase. Inhibition of the active dissolution of stainless steel by elemental Mo has been considered [41]. It was proposed that Mo serves to decrease active dissolution by binding to active surface sites such as kinks and thus increasing the coordination of more active species. More recently, it has been shown [42] by cyclic polarization and pit propagation rate tests on a series of Fe-Ni-Cr-Mo alloys having Mo contents of 3, 6, and 9 wt % for three Fe/Ni ratios that active dissolution was governed by an Ni-Mo surface complex. These observations led us to the conclusion that in describing the corrosion properties of stainless steel it is not enough to describe the reactions leading to formation of the barrier layer; it is also necessary to describe the reactions taking place in the outermost layers of the metallic phase.

The influence of the alloy composition on the polarization diagrams of austenitic stainless steels polarized in 0.1 M HCl + 0.4 M NaCl is shown in Figure 12. The curves represent the following steels: curve 1, 20Cr-18Ni-6.1Mo-0.2N (wt %); curve 2, AISI 316, 18Cr-13Ni-2.7Mo; curve 3, AISI 304, 18Cr-9Ni. The polarization curves show that the high-alloyed steel is passive within a broad potential range. The

Copyright © 2002 Marcel Dekker, Inc.

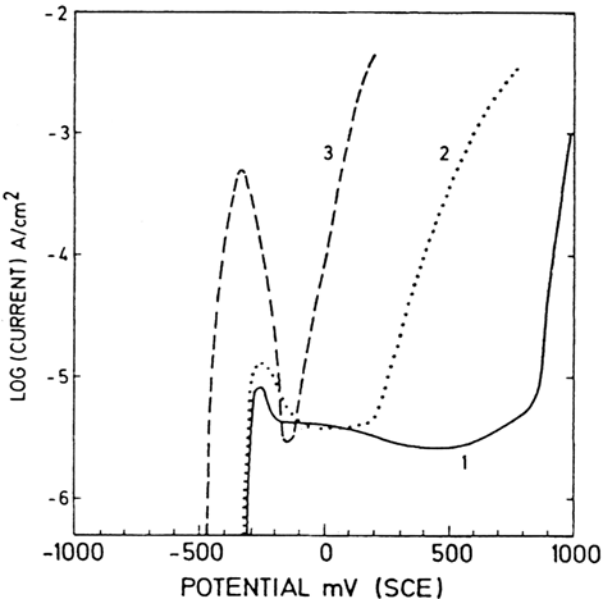


Figure 12 Polarization diagrams obtained during exposure to 0.1 M HC1 + 0.4 M NaCl of the following alloy steels: (1) Fe-200Cr-18Ni-6.1Mo-0.2N; (2) Fe-18Cr-13Ni-2.7Mo; (3) Fe-18Cr-9Ni. (From Ref. 32.)

other two alloys are sensitive to pitting corrosion in this solution. The critical current density is about the same for the two Mo-containing alloys, and it is an order of magnitude larger for the non-Mo-containing steel. The conclusion from the polarization diagrams is that the composition of the metal influences markedly the passivation and the pitting behavior of the steels. It will be shown in the following that synergistic effects exist between the alloying elements.

The spectra in Figure 13 were recorded from a high-alloyed austenitic stainless steel (16.7Cr-15Ni-4.3Mo) after polarization in 0.1 M HCl + 0.4 M NaCl at –320 mV (SCE). The potential represents the active dissolution potential slightly above the corrosion potential. The result is from the same study as Figure 2. It appears from the spectra of Figure 13 that the intensities of the metallic states are much higher after polarization to the active potential compared with the passive potentials of Figure 2. This is, of course, due to the fact that the oxide film formed on the sample polarized at the active potential is much thinner than on the passivated samples. One should in principle expect no oxide or at most a very small amount of oxidized species on the alloy polarized to the active region. However, during the rinsing and the transfer of the sample from the electrochemical cell to the XPS analyzer, the surface is slightly oxidized. The thickness of the oxide formed during handling of the sample polarized to the active region is about 0.5 nm.

The composition of the metal phase can be estimated from the recorded intensities. The dots in Figure 14a [1,40] show the apparent compositions of the metal phases of the alloy after polarization to the active potential. The composition is calculated from the measured peak intensities in Figure 13, taking into account the

Copyright © 2002 Marcel Dekker, Inc.

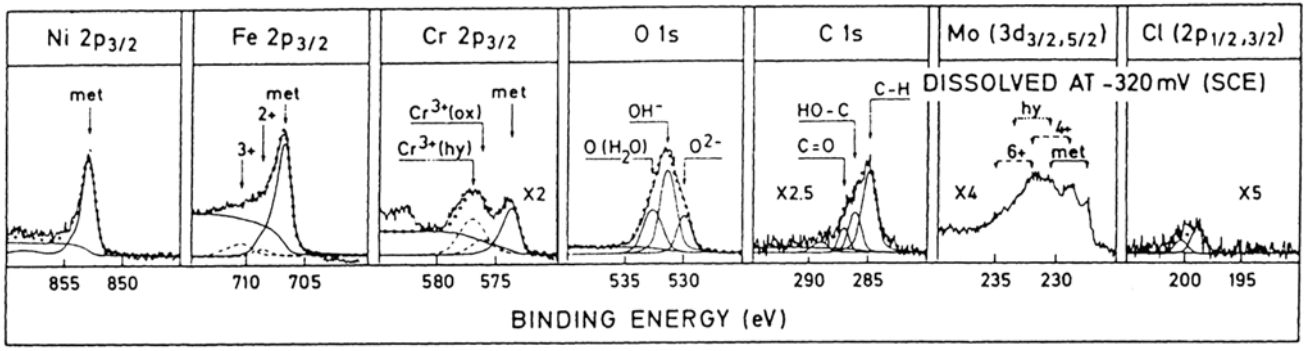


Figure 13 XPS spectra of an Fe-20Cr-18Ni-6.1Mo-0.2N (wt %) alloy recorded after polarization to the active potential –320 mV(SCR). (From Ref. 1.)

Copyright © 2002 Marcel Dekker, Inc.

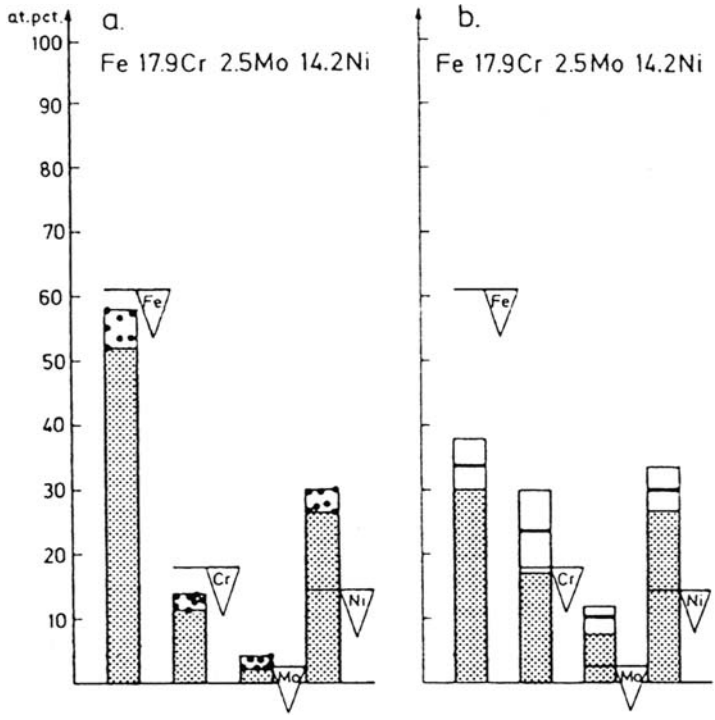


Figure 14 Composition of the metal phase during dissolution at an active potential. (a) Apparent metal content; (b) estimated metal content in the outermost atomic layer [1,40].

yields and the attenuation lengths of the photoelectrons. The horizontal lines in the up and down triangles in Figure 14 show the composition of the alloy. It appears from Figure 14a that Ni and Mo are enriched in the metal phase, while the elements Fe and Cr are depleted. The depth to which the composition changes from the bulk composition can be only a few atomic planes because of the very low diffusion rate at room temperature. The depth of analysis, which is about three times the attenuation length, is larger than the enriched zone. Hence, the bulk of the alloy contributes to the recorded spectral intensity. Thus, the composition in Figure 14a is an apparent composition. The actual surface composition can be found only if the distribution of the elements in the surface region is known. Unfortunately, this is not the case. It is therefore necessary to assume a realistic distribution function of the elements in order to be able to calculate the surface composition of the metal phase.

The simplest distribution function describes enrichment of the elements Ni and Mo in only one atomic plane. If this model is applied to the spectra shown in Figure 13, it becomes apparent that it is not possible to obtain mass balance. However, most of the oxide present on the surface during the analysis of the sample polarized to the active potential is formed during transfer of the sample from the cell. Therefore, to assess the composition of the surface during anodic dissolution, the cations detected have to be converted to their metallic states and added to the contribution from the metallic spectra. By assuming a model for the distribution of the elements, the surface composition can be calculated. The details of the procedure

Copyright © 2002 Marcel Dekker, Inc.

have been published [1,40]. Figure 14b shows the quantitative analysis of the metal composition during anodic dissolution. The distribution function used was an error function where the composition varies over three atomic planes. The composition of the second plane is 50% of the difference between the bulk composition and the composition of the surface. The values shown with the coarse solid line represent the composition of the outermost atomic layer during anodic dissolution. As already pointed out, it was assumed that most of the oxide observed on the surface was due to the transfer of the sample. It appears from Figure 14 that Ni and Mo are markedly enriched on the surface of the metal during anodic dissolution. Even the Cr concentration in the outermost layer is significantly higher than the bulk concentration. Because of the enrichment of Cr, it is easy to understand that the oxide formed during handling of the sample was mainly Cr oxide. Furthermore, Figure 14b shows that the Fe content in the outer surface layer is markedly lower than the alloy composition.

It was shown before that the Ni content of the passive film is low. One can therefore expect that the Ni content at the metal-oxide interface is still high after passivation. Figure 15 [1] illustrates the measured apparent metal content of the metal phase after polarization to the active potential, –320 mV (SCE), and the passive potentials, –100 mV and 500 mV (SCE). It appears from the figure that Ni largely remains in the alloy phase after passivation.

It has been pointed out that the passive currents for all three alloys whose polarization diagrams were shown in Figure 12 are about the same. Even the passive current for pure Cr (Fig. 1) is about the same as for the alloys. The noticeable difference in electrochemical behavior between the alloys is in the passivation current and the pitting potential. As shown earlier, the alloying elements are enriched on the

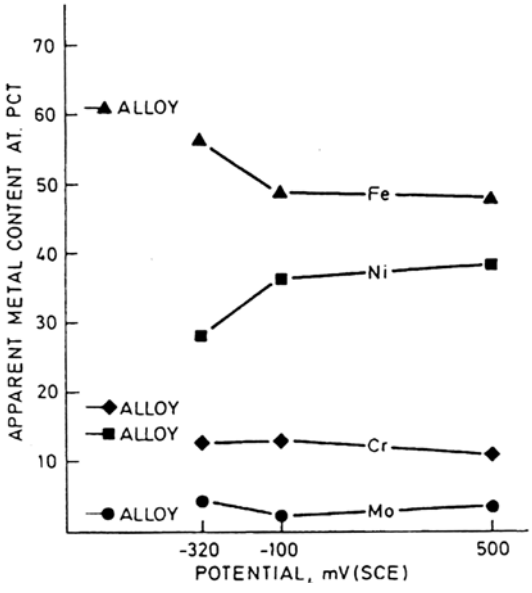


Figure 15 Apparent metal content of the alloy vs. the potentials (SCE). (From Ref. 1.)

Copyright © 2002 Marcel Dekker, Inc.

surface in their metallic states during active dissolution. It has been suggested [1,40] that an intermetallic surface phase is formed during dissolution.

The formation of an intermetallic surface phase can be understood from the Engel-Brewer [43] valence bond theory of metallic bonding by considering the ground state electronic configuration of the elements and the nature of the possible bonding processes. The model predicts intermetallic bonding between "hyper" and "hypo" *d*-electron transition metals, resulting in very strong bonding. Such bonding, in principle, should result in low dissolution rates due to a higher activation energy for anodic dissolution. Such systems are formed between transition metals from the left of the periodic table having more vacant *d* electrons and those to the right having fewer *d*-electron vacancies. The intermetallic bonding between elements suitablyseparated in the transition row may result from penetration of an electron pair from the hyper *d* electron into the *d* orbital of the hypo *d*-electron metal. XPS analysis [44] of thin Ni-Mo intermetallic layers has confirmed the charge transfer. Compared with those of pure metal lattices, the binding energies of Ni and Mo from the intermetallic layer are shifted higher and lower, respectively. It has been pointed out that the strength of the *d*-electron bonding increases from 3*d* to 4*d*, indicating that thestability of the intermetallic bond between Ni and Cr should be lower than that between Ni and Mo [33]. Therefore, it has been suggested that the overall latticeenergy increases during dissolution of Mo-alloyed austenitic stainless steel in the metal layers close to the passive film due to formation of intermetallic bonds between Ni and Mo atoms [45]. Consequently, the activation energy increases for anodicdissolution and the dissolution rate decreases. According to this model, bonding between Mo and Fe is predicted to be weaker than between Mo and Ni and Mo and Cr, and therefore Fe is selectively dissolved.

The Engel-Brewer model [43] of intermetallic bonding would explain how Ni can lower the critical current density and elevate the pitting potential of austenitic alloys, while playing no direct role in the construction of the passive film. It is evident that Mo not only plays several direct roles in the formation and stability of the passive film but also enhances Ni's role by further enhancing the anodic segregation of Ni. Therefore, it is proposed that through sluggish dissolution kinetics alone, Ni, when bonded with Cr and more strongly with Mo, will lower the rate of metal dissolution during the pitting process and thereby reduce the maximum metal chloride concentration in the pit solution [45].

In the N-bearing stainless steels, N has a pronounced influence on the pitting corrosion properties. It has already been pointed out [15,26,31] that the positive effect of N is obtained for the Mo-alloyed stainless steels. The lower dissolution rate of the Mo-containing alloys due to formation of intermetallic layer during active dissolution provides a model for the synergistic effect between Mo and N. Figure 16 shows the proposed mechanism. Three alloys with and without Mo and N are assumed to be exposed to an acid chloride–containing solution. Pits are initiated on all three alloys. The pits formed on the Mo-containing alloys become smaller than the pits on the Mo-free alloy because the Mo lowers the dissolution rate of the alloy by formation of an intermetallic surface layer. If the acidity and/or the chloride content of the solution is high enough, the pits formed on the Mo-free alloy will become critical and grow. The dissolved ions are hydrated and the hydrolysis causes increased acidity in the pits. The pH value in the small pits formed on the Mo-containing alloys becomes low due to the outlet diffusion of H^+ ions. The

Copyright © 2002 Marcel Dekker, Inc.

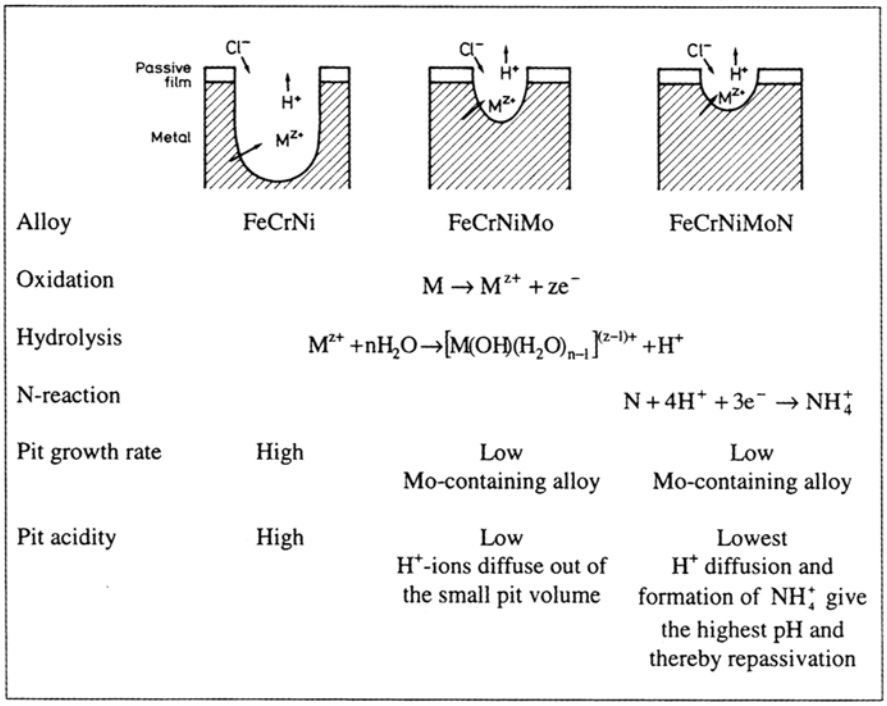


Figure 16 A model for the growth and repassivation of pits in Mo-free, Mo and Mo-N containing alloys. (From Ref. 15.)

environment in the large pits formed on the Mo-free alloy changes, on the other hand, noticeably because the production of the solvated H^+ ions is high, the drop in pH at the pit surface becomes more pronounced, and the ingress migration of Cl^- ions is more effective. For the N-bearing steels the lowering of pH due to hydrolysis is compensated by formation of NH_4^+, as suggested by Osozawa and Okato [26]. The pH value of the solution in the pits will be above a critical value and thereby repassivation will occur in an early stage of the pitting process. Hence, this model [31] concludes that the role of Mo is to lower the dissolution rate of the initiated pits and thereby limit the increase in acidity in the pitted volume.

It seems therefore that Mo plays a multifold role in corrosion protection of stainless steels: (a) it lower the chloride content in the passive film during passivation and repassivation and thereby makes the film more resistant to breakdown; (b) it lowers the dissolution rate of the alloy during initiation of pitting; (c) it forms insoluble salt at the bottom of pits, which is favorable to the formation of passive film; and (d) during the repassivation process it forms molybdate, which governs the deprotonation reaction of the poorly protective hydroxide and thereby a more protective barrier layer is formed. According to the thick-membrane studies [17], molybdate has been shown to promote ionic rectification, which retards chloride ingress and promotes deprotonation of the hydroxide. The synergistic effect of N, Ni, and Mo can be understood from the work of Jack [46], who reported that whereas single nitrides of Mo and Ni are thermodynamically relatively unstable, with

Copyright © 2002 Marcel Dekker, Inc.

Ni being the less stable of the two, a mixed Mo and Ni nitride of the form Ni_2Mo_3N exhibited very high thermodynamic stability. Although this suggests the likely involvement of Ni in such mixed surface nitrides formed during anodic segregation of N-bearing steels, it also suggests strong intermetallic bonding. This is not contrary to the nature of bonding in interstitial nitrides formed by transition elements. For example, although N is the electron acceptor in the mixed nitride phase, one would expect strong interaction between Mo and Ni and somewhat weaker interaction between Cr and Ni.

Finally, it is evident that less than one monolayer of surface nitride is capable of increasing the pitting resistance of 304 stainless steel [33] and therefore it is probable that this mixed nitride phase is situated at previously high-energy sites such as grain boundaries and surface dislocations, which are preferential sites for both pitting and surface nitride formation. In the case of Ni-bearing steels these sites would be initially the most active and therefore the sites where anodic segregation would tend to be first developed. Therefore, as a consequence of anodic segregation at high-energy sites during the active stage of repassivation, a more homogeneous passive film may be generated that would be less vulnerable to localized breakdown.

SUMMARY

The passivity of austenitic stainless steels is a field of study that will continue to develop as new service environments are found for this important class of steels. Many of the studies reviewed here provide a basis for new testing and analytical strategies that must be applied to these and similar materials to develop new stainless steels for such new markets as the bioprocessing industry and facilities for atmospheric scrubbing of industrial emmisions. In this chapter we have emphasized the importance of barrier oxide layers, salt deposit layers, and alloy surface layers in the overall process of passivity and breakdown of passivity. Finally, it has been shown that by combining electrochemical and surface analytical methodologies, both corrosion parameters and structure-property relationships can be combined to model passivation processes in a way that provides new insights into alloy performance and new alloy design concepts.

ACKNOWLEDGMENTS

This work has been supported by the National Swedish Board for Technical and Industrial Development (NUTEK), U.S.O.N.R. (A. J. Sedriks, Contract Officer) contract N0001485K0437, and the U.S.N.S.F. International Program Division (Christine Glenday, Contract Officer).

REFERENCES

1. I. Olefjord, B. Brox, and U. Jelvestam, *J. Electrochem. Soc. 132*:2854 (1985).
2. J. Horvath and H. H. Uhlig, *J. Electrochem. Soc. 115*:791 (1968).

Copyright © 2002 Marcel Dekker, Inc.

3. C. R. Clayton and Y. C. Lu. *J. Electrochem. Soc. 133*:2465 (1986).
4. G. Okamoto, *Corros. Sci. 13*:471 (1973).
5. H. Saito, T. Shibata, and G. Okamoto, *Corros. Sci. 19*:693 (1979).
6. K. Tachibana, K. Miya, K. Furuya, and G. Okamoto, *Corros. Sci. 31*:527 (1990).
7. A. R. Brooks, C. R. Clayton, K. Doss, and Y. C. Lu, *J. Electrochem. Soc. 133*:2459 (1986).
8. A. J. Sedriks, *Corrosion of Stainless Steels*, Wiley, New York, 1979.
9. K. Sugimoto and Y. Sawada, *Corros. Sci. 17*:425 (1979).
10. K. Hashimoto, K. Asami, and K. Teramoto, *Corros. Sci. 19*:3 (1970).
11. H. Ogawa, H. Omata, I. Itoh, and H. Okada, *Corrosion 34*:53 (1978).
12. M. Urquidi and D. D. MacDonald, *J. Electrochem. Soc. 132*:533 (1985).
13. L. Wegrelius and I. Olefjord, *Mater. Sci. Forum 185–188*:347 (1995).
14. L. Wegrelius, F. Falkenberg, and I. Olefjord, *J. Electrochem. Soc. 146*:1397 (1999).
15. F. Falkenberg and I. Olefjord, Proceedings, *International Symposium in Honor of Professor Norio Sato: Passivity and Localized Corrosion* (Eds. M. Seo, B. MacDougall, H. Takahashi and R. G. Kelly), Electrochemical Society Pennington New Jersey 404 (1999).
16. F. Falkenberg, Metastable pits on austenitic stainless steels, thesis for the degree Licentiate of Engineering, Chalmers University of Technology, Gothenburg, 1998.
17. M. Sakashita and N. Sato, *Corros. Sci. 17*:473 (1977).
18. C. R. Clayton and Y. C. Lu, *Corros. Sci. 29*:881 (1989).
19. Y. C. Lu, C. R. Clayton, and A. R. Brooks, *Corros. Sci. 29*:863 (1989).
20. J. R. Ambrose, *Passivity of Metals* (R. P. Frankenthal and J. Kruger, eds.), Electrochemical Society, Pennington, NJ, 1978, p. 740.
21. A. Schneider, D. Kuron, S. Hofmann, and R. Kircheim, Proceedings, Sixth International Symposium Passivity, PART I (N. Sato and K. Hashimoto, eds.), *Corros. Sci. 31*:191 (1990).
22. F. Falkenberg and I. Olefjord, Proceedings, Eight International Symposium on Passivity, Jasper, Alberta, Canada, 1999 (in press).
23. G. P. Halada, C. R. Clayton, H. Herman, S. Sampath, and R. Tiwari, *J. Electrochem. Soc. 142*:74 (1995).
24. Y. Hisamatsu, *Passivity and Its Breakdown on Iron Based Alloys*., USA–Japan Seminar (R. Staehle and H. Okada, eds.), National Association of Corrosion Engineers, Houston, 1976, p. 99.
25. Z. Szklaska-Smialowska, *Pitting Corrosion of Metals*, National Association of Corrosion Engineers, Houston, 1986, p. 358.
26. K. Osozawa and N. Okato, *Passivity and Its Breakdown on Iron and Iron Based Alloys*, USA–Japan Seminar, National Association of Corrosion Engineers, Houston, 1976, p. 135.
27. J. E. Truman, M. J. Coleman, and K. R. Pirt, *Br. Corros. J. 12*:236 (1977).
28. J. Eckenrod and C. W. Kovack, *ASTMSTP 679*, Philadelphia, 1977, p. 17.
29. R. Bandy and D. van Rooyen, *Corrosion 39*:227 (1983).
30. Y. C. Lu, and R. Bandy, C. R. Clayton, and R. C. Newman, *J. Electrochem. Soc. 130*:1774 (1983).
31. I. Olefjord and L. Wegrelius, *Corros. Sci. 38*:1203 (1996).
32. I. Olefjord, *Surface Characterization* (E. Brune, R. Hellborg, H. J. Whitlow, and O. Hunderi, eds.), Wiley-VCH, Weinheim, 1997, p. 291.
33. R. D. Willenbruch, C. R. Clayton, M. Oversluizen, D. Kim, and Y. C. Lu, Proceedings, Sixth International Symposium on Passivity, PART 1 (N. Sato and K. Hashimoto, eds.), *Corros. Sci. 31*:179 (1990).
34. J. Kolts, J. B. C. Wu, and A. I. Asphahani, Met. Prog. *September*:25 (1983).

Copyright © 2002 Marcel Dekker, Inc.

35. C. R. Clayton, G. P. Halada, and J. R. Kearns, Proceedings, US-Japan Seminar, Timberline Lodge, Mount Hood, OR, June 1994 (R. Latanision and K. Hashimoto, eds.), *Mater. Sci. Eng. A 198*:135 (1995).
36. Y. C. Lu, M. B. Ives, C. R. Clayton, and D. Kim, *Corros. Sci. 35*:89 (1993).
37. G. P. Halada and C. R. Clayton, *J. Vat. Sci. Technol. A11*:2342 (1993).
38. I. Olefjord, *Mater. Sci. Eng. 42*:161 (1980).
39. I. Olefjord and B.-O. Elfström, *Corrosion (Houston) 38*:46 (1982).
40. B. Brox and I. Olefjord, *Proceedings, Stainless Steel 84*, Institute of Metals, London, 1985, p. 134.
41. R. C. Newman, *Corros. Sci. 25*:331 (1985).
42. B. E. Clark, S. J. Thorpe, and K. T. Aust, *Corros. Sci. 31*:551 (1990).
43. L. Brewer, *Science 161*:115 (1968).
44. S. Börjesson and I. Olefjord, private communication.
45. I. Olefjord and C. R. Clayton, *ISIJ Int. 31(2)*:134 (1991).
46. K. H. Jack, *High Nitrogen Steels* (J. Fact and A. Henry, eds.), Institute of Metals, London, 1989, p. 117.

Copyright © 2002 Marcel Dekker, Inc.

8

Mechanisms of Pitting Corrosion

Hans-Henning Strehblow
Heinrich-Heine-Universität Düsseldorf, Düsseldorf, Germany

INTRODUCTION

Pitting corrosion occurs at passivated metal surfaces during the access of so-called aggressive anions. Halides very effectively attack passivating thin oxide layers, leading to an intense localized dissolution of the metal surface, which is otherwise protected by the passive layer against general dissolution. Chlorides cause the most serious problems due to their presence in many environments such as seawater and salt on roads, in food, and in the chemical industry. Many metals and their alloys are subject to this type of corrosion (e.g., iron, nickel, copper, aluminium, steels), whereas chromium is one of the few exceptions that resists pitting in aggressive environments. The restriction of the dissolution to pits within a large passivated metal surface, which may serve as a large cathode for the reduction of oxidants such as dissolved oxygen, leads to fast perforation of the metal, which weakens the construction and thus causes large economic losses and safety problems.

Pitting at passivated metal surfaces is a complex process with a sequence of steps. For each stage of the development and growth of a corrosion pit, one has to study the mechanistic details in order to understand the process as a whole. For a detailed mechanistic discussion the following stages are usually distinguished:

1. Processes leading to breakdown of passivity
2. Early stages of pit growth
3. Late stages of pit growth
4. Repassivation phenomena

The details of the mechanisms also depend on the metal or the composition of the alloys as well as on the electrolyte and other environmental conditions. Metallic and nonmetallic inclusions often play a decisive role in the start of a corrosion pit. In most cases the presence of aggressive anions is necessary for breakdown of passivity and stable pit growth. The discussion in this chapter explains the effect of these anions by their tendency to form complexes with metal ions. It concentrates on the behavior of some pure metals, such as pure Fe and Ni, in simple electrolyte solutions. Some basic concepts are the center of interest, although it is known from the technical applications of the different materials that the appearance and the

Copyright © 2002 Marcel Dekker, Inc.

details of the corrosion mechanisms may involve many complicating factors. Thus, this contribution intends to describe the main mechanistic aspects rather than the details of complicating factors.

Some Basic Details of Passivity

In order to get a better basis for the discussion and understanding of the corrosion mechanisms, a brief summary of the structure and the properties of passive layers is given. For more detailed information one should refer to the chapter on passivity in this book. Passive layers form on many reactive metals. If these films have semiconducting properties, as for Fe, Cr, Ni, and Cu, they will grow only up to a few nanometers in thickness to the potential for oxygen evolution. Valve metals such as Al, Nb, Ta, Ti, Zr, and Hf form insulating oxide films that may grow up to more than 100 V without oxygen evolution with thicknesses reaching several tens of nanometers. These films generally show a potential drop at the metal-oxide and the oxide-electrolyte interface as well as within the passive layer (see Fig. 2a in the section Breakdown of Passivity). The electrical field strength within the passive layer of some nanometers is in the order of some 10^6 V/cm, which enables the migration of ions through the film at room temperature at a measurable level in a region of corresponding current densities of some few $\mu A/cm^2$ or less. According to detailed studies using surface analytical methods such as X-ray photoelectron spectroscopy (XPS), the passive film has a complicated chemical structure that is described by a multilayer or at least by a bilayer model. Oxides and hydroxides are present, sometimes separated in different layers, sometimes as hydroxy-oxides. The size and structure of the related sublayers change with the electrode potential and with other factors such as the composition of the bulk metal and the electrolyte. At least one part of the passive layer acts as a barrier to corrosion, to which most of the details of the following discussion refer.

At appropriate pH the oxide films may be in equilibrium with the electrolyte according to the data of pH-potential diagrams of M. Pourbaix. In strongly acidic electrolytes the passive layer on metals such as Fe, Ni, Cr, and steels is far from its dissolution equilibrium, and passivity for these conditions is a consequence of the slow dissolution kinetics of the oxide. As this situation is not related to thermodynamics of layer formation, it is in contradiction to the results of Pourbaix diagrams. In other words, Pourbaix diagrams are not applicable to these situations. The phase diagram of Figure 2a shows the reactions occurring on a passive metal which are influenced by the potential drops $E_{1,2}$ at the metal-oxide and $E_{2,3}$ at the oxide- electrolyte interface and $\Delta\phi$ within the oxide layer. $E_{2,3}$ influences the kinetics of the dissolution reaction (1) of the metal ions and the related passive corrosion current density, as well as the kinetics of O^{2-} or OH^- formation of reaction (2) corresponding to the growth of the layer. Both reactions require in addition a field-assisted ion transport through the passive layer. Last but not least, electron transfer occurs as a third reaction (3) that is of interest for corrosion reactions under open-circuit conditions, where the reduction of oxidants as dissolved oxygen serves as a cathodic compensation for the anodic corrosion process. Redox reactions, of course, do not occur on insulating passive layers. For technically applied valve metals with insulating passive layers, inclusions with high electronic conductivity may provide sufficient electronic transfer from the passivated

Copyright © 2002 Marcel Dekker, Inc.

metal to a redox system within the electrolyte. They may serve as cathodic sites within the passivating oxide film on the metal, which enables a slow corrosion rate in the passive state or even the intense metal dissolution during localized corrosion. Copper inclusions in aluminum are a classical example. Here the differences in the electronic properties at the surface have been visualized with the scanning Kelvin probe, which tests the change of the work function with the material at the metal surface with lateral resolution [1].

A high electrical field is established at least in the part of a more complicated layer structure that serves as a barrier for metal dissolution. This in turn leads to logarithmic or inverse logarithmic growth of the film thickness and linear decay of the logarithm of the current density with time for potentiostatic passivation transients. The transfer of metal and O^{2-} ions through the passive layer increases exponentially with the electrical field strength. The transfer of aggressive anions through the film according to reaction (4) (Fig. 2a) is controlled similarly by the electrical field strength, which is important for the discussion of the penetration mechanism for breakdown of passivity. The potential drop $E_{2,3}$ influences the adsorption of anions including aggressive anions, the formation of O^{2-} and OH^- anions from the electrolyte, and the transfer of metal cations at the oxide-electrolyte interface. It thus rules layer formation and the passive corrosion current density. $E_{2,3}$ changes when the composition of the oxide changes at the surface in contact with the electrolyte, especially when approaching the transpassive potential range and intermediately for nonstationary conditions when the electrode potential is altered. It also changes with the pH via reaction 2 of Figure 2a. The electrochemical equilibrium for this reaction leads to a –0.059 V/pH dependence of the potential drop $E_{2,3}$ at the oxide-electrolyte interface and thus to a decrease of the passive current density with increasing pH. The transfer of metal ions into the electrolyte is also influenced by complexing anions, which will be discussed in detail in the chapter on the adsorption mechanism of pit nucleation.

Pitting Potentials and Inhibition Potentials

Pitting occurs when the potential exceeds a critical value E_p in the passive range of a polarization curve. E_p decreases with the logarithm of the concentration of the aggressive anions [A] according to Eq. (1). The presence of inhibiting anions I may shift it to more positive values. An interesting observation is the inhibition potential E_I for the additional presence of an inhibitor that causes an upper limit to pitting in the passive potential range. E_I increases with the logarithm of the concentration of the inhibitor [I] and decreases with that of the aggressive anion [A] according to Eq. (2) [2].

$$E_p = a - b \log[A] \tag{1}$$

$$E_I = a + b \log[A]/[I] \tag{2}$$

Nitrate and perchlorate may act as inhibitors. Figure 1 gives an example of the dependence of E_p and E_I on the electrolyte composition for Ni in chloride- and nitrate-containing solutions. The gap between the two lines is the potential range of pitting corrosion. Similar results have been obtained for ClO_4^- and Fe [2]. A very peculiar property is observed for Fe in ClO_4^--containing solutions. Although

Copyright © 2002 Marcel Dekker, Inc.

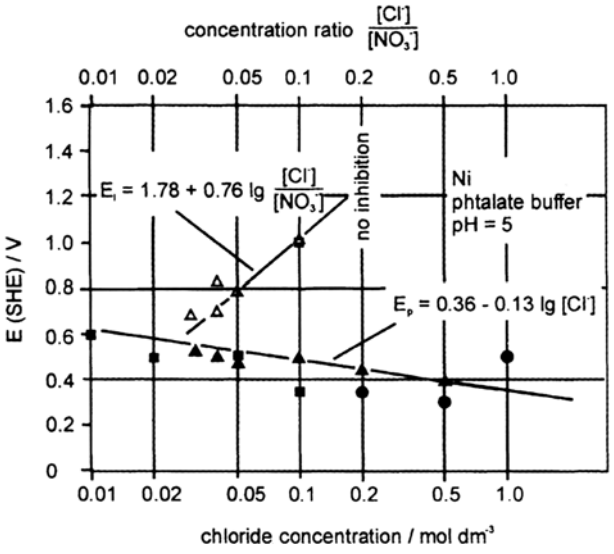


Figure 1 Pitting potential E_P and inhibition potential E_I as a function of the chloride concentration and the concentration ratio of chloride to nitrate in phthalate buffer, pH 5.0: (△) E_I, (▲) E_P, 1 M KNO_3; (□) E_I, (■) E_P, 0.1 M KNO_3; (●) galvanostatic experiments, 1 M KNO_3. (From Ref. 2.)

this anion is an inhibitor for chloride pitting at more negative potentials, it also causes pitting of Fe by itself with a very positive critical potential [2,3]. Its E_p follows Eq. (1), is pH independent, and may be measured with an accuracy of some few mV. Usually critical potentials may be measured with an uncertainty of several 10mV only. Surface analytical studies have shown that the aggressive properties of perchlorate are related to its decomposition close to the pitted surface, which yields aggressive chloride [3]. This is very special as one expects a ClO_4^- reduction at more negative potentials only where it is kinetically stable. As a possible explanation, the decomposition of ClO_4^- in the increased electrical field of the oxide-electrolyte interface has been proposed when approaching the transpassive potential range [3].

BREAKDOWN OF PASSIVITY

Three main mechanisms are discussed by most authors for the processes leading to breakdown of passivity: the penetration mechanism, the film breaking mechanism, and the adsorption mechanism [4]. Figure 2a to c presents diagrams for their explanation. The penetration mechanism (Fig. 2a), first discussed by Hoar et al. [5], involves the transfer of anions through the oxide film to the metal surface, where they start their specific action. The film breaking mechanism (Fig. 2b), proposed by Vetter and Strehblow [6] and Sato et al. [7,8], requires breaks within the film that give direct access of the anions to the unprotected metal surface. The adsorption mechanism, discussed first by Kolotyrkin [9] and Hoar and Jacob [10], starts with adsorption of aggressive anions at the oxide surface, which enhances catalytically the

Copyright © 2002 Marcel Dekker, Inc.

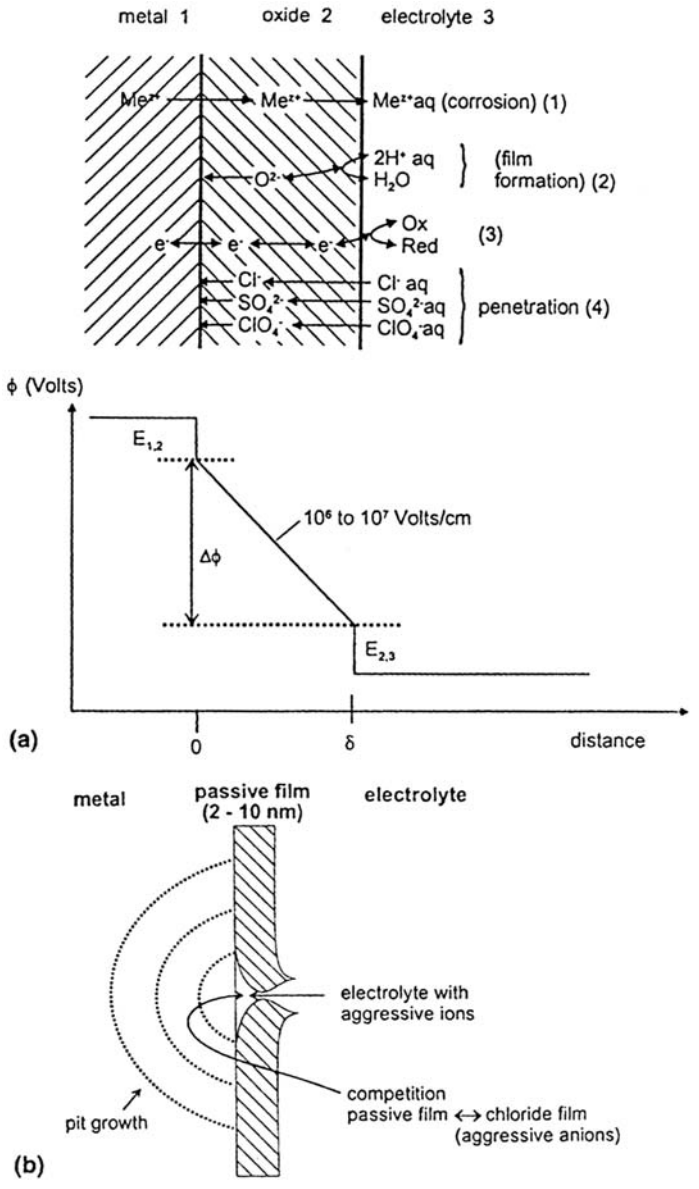


Figure 2 Phase diagram of a passive metal demonstrating the processes leading to pit nucleation. (a) Penetration mechanism and phase diagram of a passive layer with the related processes of ion and electron transfer within the oxide and at its phase boundaries including schematic potential diagram (ϕ). (b) Film breaking mechanism and related competing processes, (c) Adsorption mechanism with increased local transfer of metal ions and related corrosion current density i_c caused by complexing aggressive anions leading to thinning of the passive layer and increases in field strength and final free corrosion current density $i_{c,h}$ within the pit. (From Ref. 4.)

Copyright © 2002 Marcel Dekker, Inc.

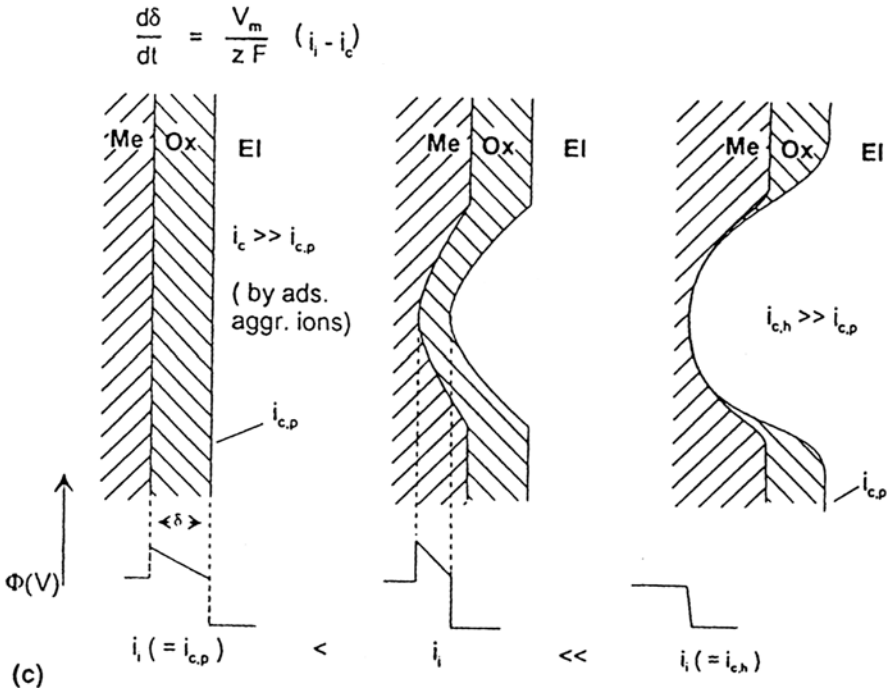


Figure 2 (Continued)

transfer of metal cations from the oxide to the electrolyte (Fig. 2c). This effect leads to thinning of the passive layer with possible final total removal and the start of intense localized dissolution. Strict separation of these mechanisms might not always be appropriate, as penetration of a passive layer via some very small defect is not necessarily very different from the occurrence of fissures in the film that permit easy access of the aggressive anions to the metal surface as in the film breaking mechanisms. In the following discussion of the mechanism of breakdown of passivity, a distinction is proposed between stationary and nonstationary conditions of the passive layer. These different experimental or environmental conditions may have a strong influence on the effective mechanism leading to breakdown of passivity.

Penetration Mechanism

The penetration mechanism (Fig. 2a) requires transfer of the aggressive anions through the passive layer to the metal-oxide interface, where they cause further specific action. The high electrical field strength and a high defect concentration within the presumably severely disordered structure of the passivating oxide layer may explain this transfer. Many authors even postulate an amorphous structure of the oxide layer [11]. Direct evidence is given by a few extended X-ray absorption fine structure (EXAFS) measurements [12]. Systematic studies with this method are, however, difficult and still missing. For a highly disordered structure it is not clear why the breakdown event occurs locally.

Copyright © 2002 Marcel Dekker, Inc.

On the basis of these ideas, Macdonald and co-workers [13,14] developed their model of passivity and its breakdown involving the action of vacancies within the passive layer. It is assumed that cation vacancies migrate from the oxide-electrolyte to the metal-oxide interface, which is equivalent to the transport of cations in the opposite direction. If these vacancies penetrate into the metal phase at a slower rate than their transport through the oxide, they accumulate at the metal-oxide interface and finally lead to a local concentration. The related voids lead to stresses within the passive film and its final breakdown. The inward diffusion or migration of cation vacancies is affected by the incorporation of Cl ions at the oxide-electrolyte interface according to the following mechanism: The concentration c of metal ion V_{M+}, and O^{2-} vacancies $V_{O^{2-}}$ are determined by the equilibrium of the Schottky pair formation at the oxide-electrolyte interface [Eq. (3)], which causes an inverse dependence of their concentrations [Eq. (4)].

$$\text{Null} = V_{M^+} + \frac{x}{2} V_O^{2-} \tag{3}$$

$$c_{v,M} = \text{const}\, c_{v,O}^{\frac{-x}{2}} \tag{4}$$

In the presence of Cl^-, its incorporation in O^{2-} vacancies occurs according to the equilibrium of Eq. (5), which is affected by the potential drop $E_{2,3}$ at the interface according to Eq. (6) with the concentration of oxygen vacancies $c_{v,O^{2-}}$ at the surface, the activity of chloride a_{Cl^-} within the solution, and the potential-independent part of the equilibrium constant K.

$$V_{O^{2-}} + Cl^-_{(aq)} = Cl_O \tag{5}$$

$$c_{v,O^{2-}} a_{Cl^-} = K \exp(\alpha F E_{2,3}/RT) \tag{6}$$

According to Eq. (6), $c_{O^{2-}}$ depends on a_{Cl^-} and the potential drop $E_{2,3}$; $c_{O^{2-}}$ in turn affects $c_{v,M}$, which is the driving force of the diffusion of the cation vacancies to the metal-oxide interface. Thus the interdependence of the concentrations of cation and anion vacancies within the oxide and the incorporation of Cl^- determine the concentration gradient of cation vacancies and their transport through the oxide layer that will cause a critical concentration for breakdown at the pitting potential. According to this outline, the further discussion yields a semilogarithmic dependence of the pitting potential E_p and the chloride activity a_{Cl^-} within the electrolyte similar to Eq. (1) [Eq. (7)]. The constant B contains the diffusivity constant of the cation vacancies within the oxide layer.

$$E_p = A - B \lg a_{Cl^-} \tag{7}$$

Objections to the point defect model are that in its original form it assumes linear transport equations with diffusion of the different species within the passive layer, whereas migration with an exponential dependence on the high electrical field strength of some 10^6 V/cm should be dominating as a driving force. It also concentrates the changes in electrode potential ΔE to the potential drop $E_{2,3}$ at the oxide-electrolyte interface, so that it fully enters the equilibrium of Cl^- incorporation of Eqs. (5) and (6). However, large parts of ΔE contribute to $\Delta\phi$, i.e., are located within the barrier part of the passive layer (Fig. 2), and $E_{2,3}$ changes only with the

Copyright © 2002 Marcel Dekker, Inc.

composition of the oxide surface, if at all, and the pH of the solution but not with the applied electrode potential, at least for stationary conditions. An overpotential $\eta_{2,3}$ for the potential drop $E_{2,3}$ is mainly expected for nonstationary conditions of the passive layer that will directly influence the adsorption equilibrium of Cl^-. The specific role of chloride and other halides in breakdown of passivity is still not sufficiently understood in light of this theory. Further refinements might improve this interesting view.

Surface analytical methods unfortunately do not always give a clear answer about the penetration of aggressive anions. Some authors found chloride within the film with XPS, Auger electron spectroscopy (AES) [15,16], and secondary ion mass spectroscopy (SIMS) [17]; others could not find it within the film [18–22]. The contradictory results may be explained in terms of sample preparation and the sensitivity of the methods. Very careful XPS studies with Fe-Cr alloys show incorporation within the outer hydroxide part of the duplex passivating film [23,24]. The inner oxide layer remains free of Cl^- if prepared within chloride-free electrolytes before exposure to the aggressive anions. Similarly, incorporation of Cl^- within the outer hydroxide layer was found for pure Ni [25]. It was found in the inner oxide part only when the passive layer was formed in solutions already containing Cl^-. If the electrode potential was above the critical value for breakdown, Cl^- penetrated into the preexisting oxide with possible lateral fluctuations of its concentration, leading finally to the formation of pits. According to these studies, the accumulation within the hydroxide overlayer serves as an accumulation of a sufficiently large amount to cause breakdown in the following step. Further discussions of the surface analytical investigations of passive layers that have been exposed to chloride-containing solutions may be found in the chapter on passivity in this book.

A detailed bilayer or even multilayer structure is observed for passive films on many metals and alloys [26,27]. The outer part is usually a hydroxide, whereas the main inner part is an oxide [23,25–27]. The hydroxide structure may well act as an ion exchanger or at least absorb anions, as has been proved for some systems. Although the access of aggressive anions leads to changes of the passive layer detected by ellipsometry [28] and reflection spectroscopy [29], it is still unclear what conclusion may be drawn from these observations. If the penetration of aggressive anions leads to weak channels where intense dissolution may start, it is unclear why the film does not re-form specifically at this site and why these defects do not repassivate. The self-healing mechanism of the passive layer is essential for its excellent protecting property. The specific role of the aggressive anions is missing in this mechanism of breakdown. Any explanation should involve the characteristic chemical properties of anions such as the halides.

Experiments with well-prepassivated specimens show that the formation of a corrosion pit may be an extremely fast process, in the time range of <1 s or even <1 ms [4,30]. Figure 3 depicts as an example the increase of the current density within less than 1 ms as a consequence of growing pits for an Ni specimen prepassivated for 1 s before a potential shift above the critical pitting potential. A simple comparison of the small stationary passive current densities in the range of $\mu A/cm^2$ with these short times leads to contradictions with the penetration mechanism [30,31]. If anions migrate inward as cations migrate outward during stationary dissolution, these fast nucleation times cannot be understood. Furthermore, it seems questionable that large anions such as SO_4^{2-} and ClO_4^- migrate sufficiently fast in the

Copyright © 2002 Marcel Dekker, Inc.

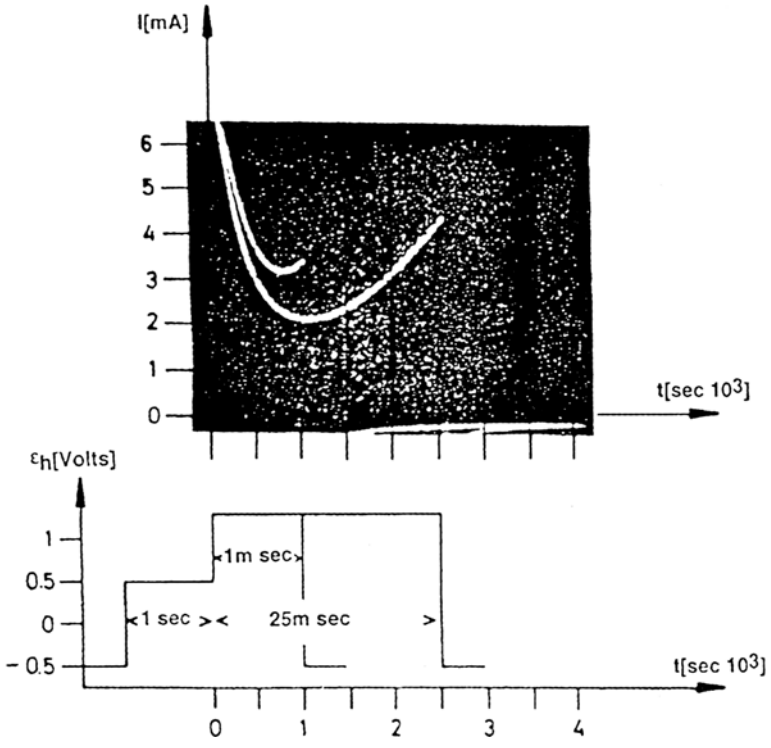


Figure 3 Pit nucleation of Ni ($A = 0.02\text{cm}^2$) at $E = 1.30$ V (SHE) in phthalate buffer, pH 5.0 + 0.1 M KCl after 1 s prepassivation at $E = 0.5$ V. (From Ref. 30.)

electrical field through the passive layer to cause nucleation in times $t < 1$ s [30,31]. These anions may also cause pitting of iron at the lower potential part of the passivity range and ClO_4 also at potentials close to the transpassive range [2,3]. However, the inward migration of aggressive anions and the outward migration of cations may be facilitated at local defects within the passive layer. Even for those situations, one needs the special chemical properties of the anions to understand why the defects do not repassivate but develop to a corrosion pit. Any mechanism of nucleation and growth of corrosion pits has to include the specific role of the aggressive anions that causes the formation of a pit instead of repassivating the defect site. These details will be discussed in one of the following sections.

In this regard, one experiment with well-passivated Fe electrodes should be mentioned [6]. If the penetration of aggressive anions through the passive layer was the rate-determining step, a high electrical field strength should favor their migration and accelerate pit nucleation. For nonstationary conditions, for passive Fe, exactly the contrary has been observed (Fig. 4). After passivation for 1 h at 1.18 V (SHE) in phthalate buffer pH 5.0 plus 0.1 M K_2SO_4, the nucleation rate was severely increased when the potential was stepped to 0.78 V immediately before Cl^- addition to 0.01 M. This pretreatment resulted in a much faster increase of the current density with time and a slope of 3 for a double logarithmic current-time plot was found, which is an indication of an increased nucleation rate that is constant with time. These

Copyright © 2002 Marcel Dekker, Inc.

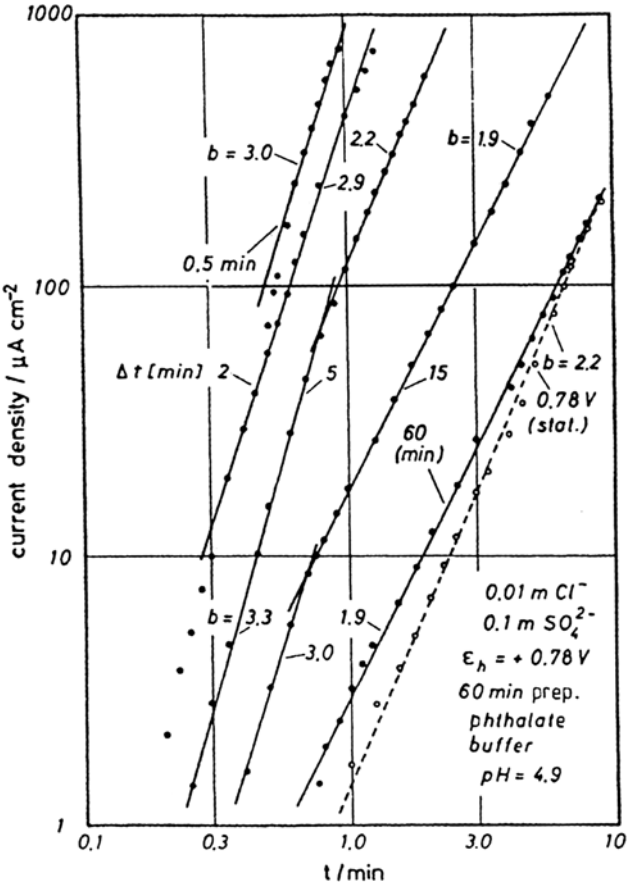


Figure 4 Double logarithmic plot of the increase of the geometric current density with time for electropolished iron during pitting corrosion, 1 h prepassivated at 1.18 V and potential drop to 0.78 V (solid line), Δt = time between potential change and chloride addition, 1 h prepassivated at 0.78 V (dashed line), phthalate buffer, pH 4.9, 0.1 M SO_4^{2-}, 0.01 M Cl^-. (From Ref. 6.)

observations were confirmed by direct microscopic examination of the specimen's surfaces. If one waits at the lower potential before chloride addition, the nucleation is reduced again with a related change of the current increase from a slope 3 to 2 for the double logarithmic plot, which indicates a variation from a constant nucleation rate to a constant number of pits, i.e., no further nucleation. Apparently the nucleation is severely increased for nonstationary conditions and is reduced again when approaching a new stationary state. An explanation of this effect with the penetration mechanism leads to contradictions. When the potential is stepped to lower values the electrical field strength is decreased and one expects reduced rather than increased migration of the aggressive anions through the passive layer (Fig. 2). Remaining at the lower potential before Cl^- addition should decrease the thickness of the passive layer because of an excess of film dissolution over its formation. The approach to the new stationary state with time at a lower potential

Copyright © 2002 Marcel Dekker, Inc.

should yield the original field strength with an increase of penetration. Again, the opposite effect was found [6]. Even the adsorption mechanism cannot explain these observations. If the potential is decreased, the voltage drop $E_{2,3}$ at the oxide-electrolyte interface will decrease intermediately with a negative overvoltage $\eta_{2,3}$ for O^{2-} formation from the water, i.e., the dissolution of the oxide, until a new stationary state with $E_{2,3} = E_{2,3,s}$ is achieved (Fig. 2). This situation should disfavor the adsorption of Cl^- at this interface, which again should slow down the penetration instead of increasing it.

Film Breaking Mechanism

The occurrence of fissures within the passive layer is a possible explanation for the observations mentioned last, especially for an nonstationary state of the passive layer. A sudden change of the electrode potential even in a negative direction will cause stresses within the film. Chemical changes [32] or electrostriction [7,8] is a reasonable explanation. Chemical changes, i.e., a reduction of Fe(III) to Fe(II), have been detected with XPS when negative potentials were applied to electrodes passivated at positive potentials well within the passive range [32]. There also exists direct evidence of film breaking events for these nonstationary conditions according to observations with a rotating Fe-disk-Pt-ring electrode [33]. Even in the absence of aggressive anions, a sudden potential decrease from 1.3 to 0.7 V causes release of Fe^{2+} ions after a few seconds into the electrolyte, as detected by a temporary peak of the analytical ring current detecting Fe^{2+} ions (Fig. 5). This is a consequence of film breaking and repair events. Any crack within the passive layer will lead to direct contact of small parts of the metal surface with the electrolyte and thus to dissolution of Fe as Fe^{2+} with current densities that refer to the relatively positive potentials, but without any protecting oxide at these defect sites. The self-healing mechanism of the passive layer causes only temporary Fe^{2+} formation of a few seconds duration. These potential changes should cause numerous defects of nanometer dimensions within the passive layer in order to get a sufficient amount of unprotected metal surface so that the temporary release of Fe^{2+} becomes measurable. In the presence of aggressive anions, their direct access to the metal surface will prevent repassivation and pits can form. The serious increase of the nucleation rate (Fig. 4) after these potential changes is further evidence for the suggested formation of a large number of defects in the nanometer range.

As already mentioned, pit nucleation is a very fast process. For well-passivated Fe specimens, the time for the occurrence of a first pit is less than a second for potentials well above the critical value E_p, as determined by the increase of the current density after the addition of chloride to the solution and direct microscopic observation with a camera [4]. Most of the time is used to get the aggressive anions to the specimen surface by convection. If chloride is already present in the electrolyte, a short passivation below the pitting potential for approximately 1 s and a subsequent potential increase cause pit formation within less than a millisecond [4]. Results obtained with these electrochemical pulse techniques suggest that nonstationary conditions of the passive layer favor the film breaking mechanism. The penetration of aggressive anions would require much longer times than observed during these pulse experiments. If the experimental conditions are not in favor of pitting, i.e., for

Copyright © 2002 Marcel Dekker, Inc.

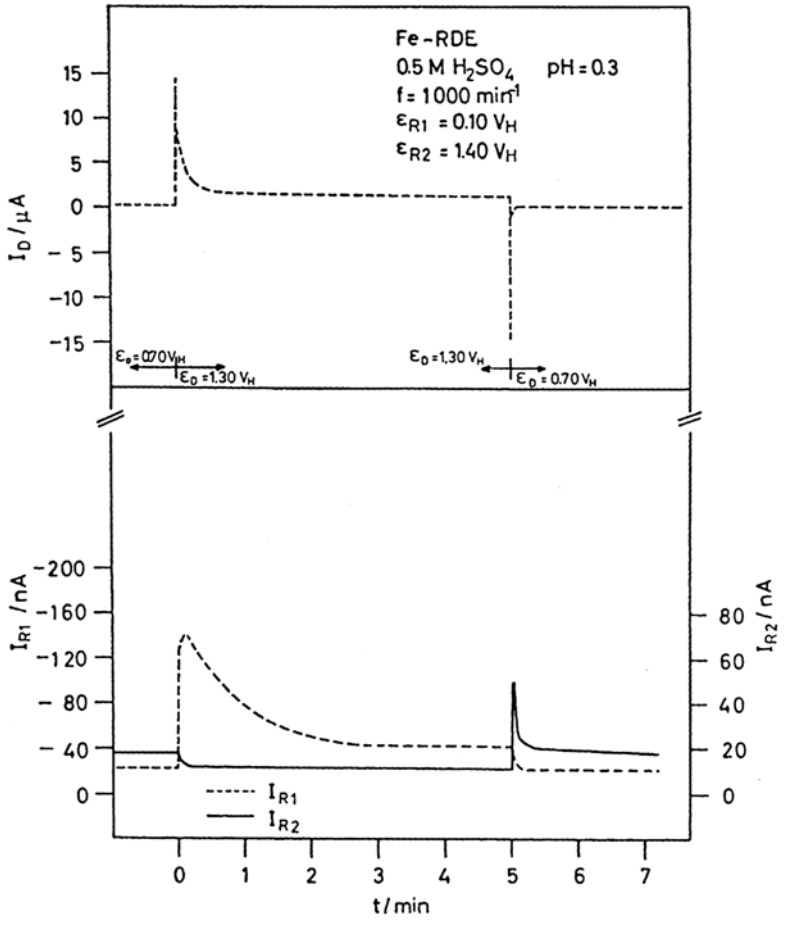


Figure 5 Disk current I_D and ring currents I_{R1} for Fe^{3+} analysis and I_{R2} for Fe^{2+} analysis for a potential variation from E_D = 0.7 V to 1.30 V and back. E_{R1} = 0.10 V, E_{R2} = 1.40 V, 0.5 M H_2SO_4, pH 0.3, f = 1000 min^{-1}, disk area A = 0.09cm^2. (From Ref. 33.)

small concentrations of aggressive anions (<10^{-3} M) or low potentials in the vicinity of E_p, pit nucleation requires times longer than these extremely short times.

Long passivation times suggest that film breaking is a good explanation for the pit nucleation for nonstationary conditions too. The current increase caused by pitting slows down when the passivation time is increased up to more than 10 h [6,31]. The passive layer is formed during the first seconds and does not grow much after that time. This is a direct consequence of the barrier character of these films, which leads to logarithmic or inverse logarithmic growth with time. Further decrease of the passive current density and especially of the pit nucleation after hours may easily be explained by constantly occurring film breaking and repair events. The related stresses will heal with passivation time so that these events become rare with time. Figure 6 shows an example of a decrease of pitting with passivation time and the related reduction of the current increase [31].

Copyright © 2002 Marcel Dekker, Inc.

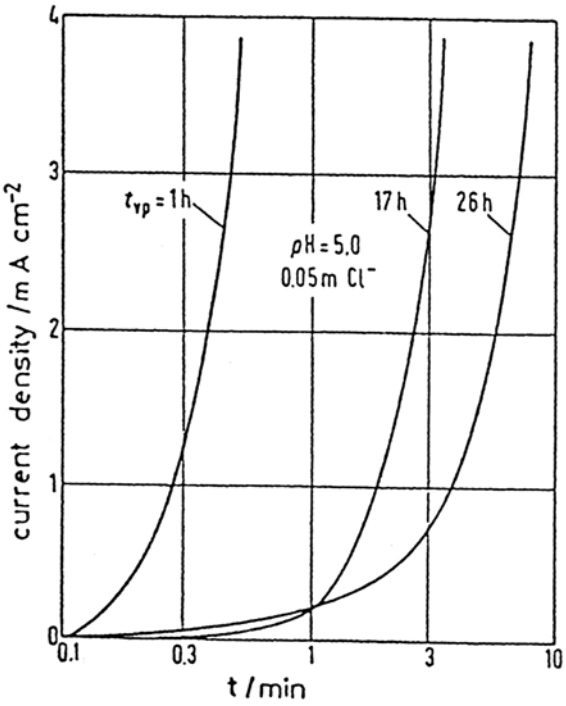


Figure 6 Increase of current density for passive Fe with pitting corrosion in phthalate buffer, pH 5.0 and 0.05 M Cl^- at E = 1.38 V for different prepassivation times t_{pp}. (From Ref. 31.)

Measurement of the electrochemical current noise has the aim of correlating the observed current fluctuations with breakdown and repair events that might lead to the formation of stably growing pits [34,35]. In the view of these theories, the application of statistical methods to the occurrence of current spikes and the observed probability of pit formation lead to a stochastic model for pit nucleation. The evaluation of current spikes in the time and frequency domains yields parameters such as the intensity of the stochastic process λ and the repassivation rate τ [34]. They depend on parameters such as the potential, state of the passive layer, and concentration of aggressive anions.

An interesting discussion of current measurements on microdimensional electrodes of stainless steel wires is given by Mattin and Burstein [36]. Their analysis of current transients at a very low level in chloride-containing 0.075 M $HClO_4$ leads to the distinction of metastable and stable pits. According to their discussion, the remaining passive layer protects the pit analyte from being diluted from the bulk solution. Only when the film breaks off too small pits will repassivate, whereas a few larger ones are deep enough to keep their local environment undiluted so that they survive.

Adsorption Mechanism

The passive current density is influenced by the action of anions even for conditions where pitting does not occur. Passive iron in 0.5 M H_2SO_4 shows stationary current

Copyright © 2002 Marcel Dekker, Inc.

densities (7 $\mu A/cm^2$) that are higher by approximately one order of magnitude than for 1 M $HClO_4$ (<1 $\mu A/cm^2$) [37]. This observation has been explained by a catalytic effect of SO_4^{2-} anions on the transfer of Fe^{3+} from the oxide to the electrolyte [38]. This cation transfer is the rate-determining step for the passive corrosion reaction. In the presence of SO_4^{2-} , an $FeSO_4^+$ complex forms. It is reasonable that this complex, with only one positive charge, requires less activation energy to be transferred from its O^{2-} ligands within the oxide matrix to the electrolyte than the highly charged Fe^{3+} ion. The complexation of cations by organic reagents cause a similarly enhanced dissolution in the passive state. The dissolution of Ni^{2+} from passive nickel and nickel base alloys is enhanced by organic acids such as formic acid, which may lead to the removal of NiO in the passive layer [39]. Similarly, additions of citrate to the electrolyte cause thinning of the passive layer on stainless steel and increase of the Cr content within the oxide layer. This is a consequence of accelerated transfer of Fe^{3+} from the film surface to the electrolyte [40]. Apparently the complexation and transfer of Cr^{3+} are not enhanced.

It is well established that metals that show passivity within strongly acidic electrolytes are far from the dissolution equilibrium of the oxide. The barrier character of the passive layers for these conditions requires slow dissolution kinetics at the oxide-electrolyte interface. Similarly to the catalytic effect of SO_4^{2-} and complexing organic agents, halides enhance the transfer of Fe^{3+} and Ni^{2+} from the oxide to the electrolyte. The adsorption mechanism for pit nucleation starts with the formation of surface complexes that are transferred to the electrolyte much faster than uncomplexed Fe^{2+} ions (Fig. 2c). These details have been studied for Fe in Cl^- - and F^- -containing solutions [21,41–43]. Similarly, Ni in solutions containing F^- has been studied [22,42–44]. Fe is a good metal with which to analyze the processes leading to passivity breakdown because of the characteristic changes of the valence of the dissolving ions, which may be measured with the rotating-ring-disk (RRD) technique. Fe^{3+} ions are dissolved if the metal surface is still covered completely with Fe(III) oxide, whereas Fe^{2+} is detected when bare metal comes into contact with the electrolyte at a pit surface or at a defect site, similar to Fe dissolution in the active state. The release of Fe^{3+} ions immediately after Cl^- has access to a prepassivated Fe electrode was taken as a measure of locally enhanced dissolution of the oxide film. This leads to a local thinning of the passive layer and finally to its complete breakdown and the formation of a pit. In the case of F^- in acidic electrolytes the attack is more general; i.e., the passive layer is subject to a general attack. As a consequence, the measured passive current density is increased by orders of magnitude (Fig. 7) [21,42,43]. Unfortunately, the strong $FeF_5H_2O^{2-}$ complex that finally forms in solution prevents its detection by its reduction to Fe^{2+} at the analytical ring. The current increases during the intermediate stage of attack with the first order of the HF concentration. Therefore a proposed mechanism should yield an electrochemical reaction order of one for HF. The following sequence of reactions has been proposed for the processes that lead to thinning of the passive layer and enhanced passive dissolution [21,42–44]:

$$Fe^{3+}(ox) + HF(aq) \leftrightarrow FeF^{2+}(ad) + H^+(aq) \tag{8}$$

$$FeF^{2+}(ad) \rightarrow FeF^{2+}(aq) \tag{9}$$

Copyright © 2002 Marcel Dekker, Inc.

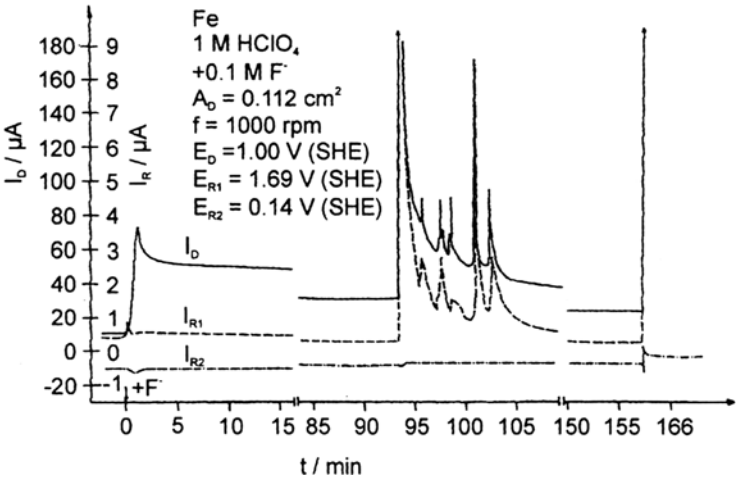


Figure 7 Current-time dependence of a rotating Pt-split-ring-Fe-disk electrode in 1 M $HClO_4$ after HF addition to 0.1 M, 2 h prepassivation at 0.1 V in 1 M $HClO_4$, Fe^{2+} detection at ring 1. (From Ref. 21.)

$$4HF + H_2O + FeF^{2+}(aq) \rightarrow FeF_5H_2O^{2-}(aq) + 4H^+(aq) \tag{10}$$

The adsorption (8) is assumed to be fast and in a quasi-equilibrium. Reaction (9) is the rate-determining step, and (10) is a fast following reaction step in solution leading to the stable fluoro-aquo complex. These assumptions lead to a first-order process for HF according to the rate equations (15) and (16). The Butler-Volmer equation (11) will hold for the rate-determining step (9) with a charge transfer coefficient α and with the potential drop $E_{2,3,s}$ at the oxide-electrolyte interface for stationary conditions. $E^0_{2,3,s}$ refers to a solution of pH 0. According to the equilibrium of O^{2-} formation of Figure 2a and Eq. (13), one obtains Eq. (14) for the pH dependence of the potential drop $E_{2,3,s}$ for stationary conditions of the passive layer:

$$i_{cs} = 3kF[FeF^{2+}_{ad}]\exp(2\alpha FE_{2,3,s}/RT) \tag{11}$$

Introducing equilibrium reaction (8) with its constant K according to Eq. (12):

$$[FeF^{2+}_{ad}] = K[HF_{aq}][Fe^{3+}_{ox}]/[H^+]\exp\{FE_{2,3,s}/RT\} \tag{12}$$

and the equilibrium of O^{2-} formation and the related pH dependence of the potential drop $E_{2,3,s}$

$$H_2O \leftrightarrow O^{2-} + 2H^+(aq) \tag{13}$$

$$E_{2,3,s} = E^0_{2,3,s} - 0.059\ \text{pH} \tag{14}$$

yields:

$$i_{c,s} = 3kKF[HF_{aq}][Fe^{3+}_{ox}]/[H^+_{aq}]\exp\{FE_{2,3,s}(2\alpha + 1)/RT\}$$

$$i_{cs} = i^0_{c,s}\exp\{FE^0_{2,3,s}(2\alpha + 1)/RT\} \tag{15}$$

Copyright © 2002 Marcel Dekker, Inc.

$$i^{0}_{c,s} = 3kKF[HF_{aq}][Fe^{3+}_{ox}][H^{+}]^{2\alpha} \quad (16)$$

The effect of HF is a model for pitting insofar as it involves the total passive surface so that the measured effects are much more pronounced and refer to a surface of known size instead of an unknown actual pit surface that even changes with time. The later stages of the attack of the passive layer lead to current peaks that go along with equivalent Fe^{2+} formation (Fig. 7). Finally, a general breakdown of the passive layer is observed with a steep increase of the dissolution current density and Fe^{2+} formation [21,42,43]. Apparently, one may observe the different steps of breakdown of passivity for fluoride directly, which are difficult to follow for the local events in the case of the other halides. The difference in the action of fluoride and the other halides may be explained by a comparison of the stability constants of their iron complexes as presented in Table 1 [30]. The stability constants K_1 with one anion are given, which refers to the reaction order one that has usually been found for the disssolution of passive layers under the influence of the aggressive anions. The reaction of Fe^{3+} with HF to FeF^{2+} and H^+ yields the more realistic value of $\log K_1 = 2.28$ due to the small dissociation constant of HF ($pK = -\log K_d = 2.98$). Table 1 also contains the constants K_1 for Ni^{2+}- and Cr^{3+}- halide complexes. Their falling values from fluoride to iodide and Fe^{2+} to Ni^{2+} support the decreasing tendency for enhanced dissolution of the passive layer and localized corrosion. These data can be referred to the situation at the oxide surface. The fluoro complexes are very stable and form with high concentrations at all surface sites. Therefore their much faster transfer to the electrolyte yields enhanced general dissolution, whereas the attack of the other halides is locally restricted and much less pronounced. Besides thethermodynamically based values, i.e., the stability constants, the kinetics of complex formation and of the complex transfer to the electrolyte are another decisive factor for the attack of the passive layer. In this sense, the situation of Cr^{3+} is very special and will be discussed separately.

XPS measurements of passivated Fe and Ni electrodes that have been exposed to aggressive anions (Ni and Fe to F^-; Fe to Cl^-, Br^-, and I^-) but have not already formed corrosion pits support this mechanism. The quantitative evaluation of the data clearly shows a decrease of the oxide thickness with time of exposure [22,48]. Not only F^- but also the other halides cause thinning of the passive layer (Fig. 8) [48]. The catalytically enhanced transfer of cations from the oxide to the electrolyte leads to a new stationary state of the passive layer. Its smaller thickness yields an increased electrical field strength for the same potentiostatically fixed potential drop, which in turn causes faster migration of the cations through the layer to compensate for the faster passive corrosion reaction (1) at the oxide-electrolyte interface (Fig. 2a). Statistical local changes

Table 1 p*K* Values of Stability Constants of Metal Ion Complexes with Halides for the Reactions $Me^{z+} + X^- \rightarrow MeX^{(z-1)+}$ including Constants Referring to HF (*) in Acidic Solutions [45–47]

Anion	Fe^{3+}	Ni^{2+}	Cr^{3+}
F^-/HF(*)	5.17/2.26(*)	0.66	4.36sol;1.42(*)
Cl^-	0.62	−0.25	−0.65
Br^-	−0.21	−0.12	−2.65
I^-	1.30	—	−5.0

Copyright © 2002 Marcel Dekker, Inc.

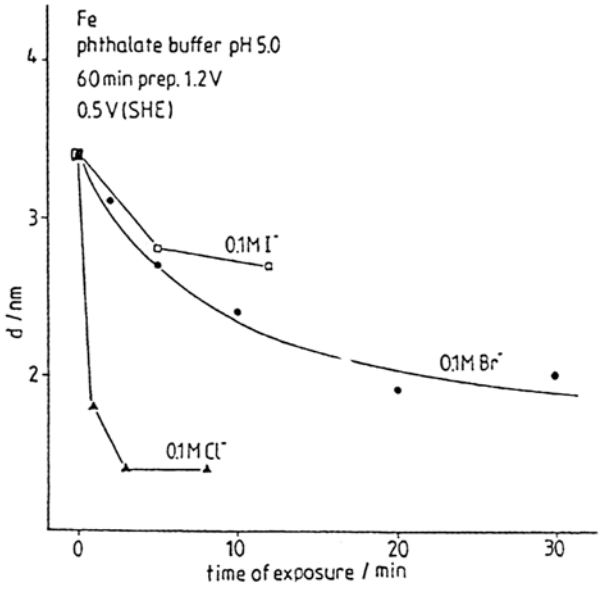


Figure 8 Decrease of oxide thickness with time of halide exposure at 0.5 V after 60 min prepassivation at 1.20 V for different halides, deduced from XPS measurements. (From Ref. 48.)

of this dissolution process will finally result in breakdown of the passive layer and exposure of bare metal surface to the electrolyte. For F^- this occurs after intermediate breakdown and repair events at the total surface. For the other halides, local effects and the formation of pits are found corresponding to their less pronounced complexing tendency. They will form complexes and cause their effect only at special active sites of the oxide surface. It should also be mentioned that fluoride causes a reduced local attack in more alkaline solutions such as phthalate buffer pH 5 [42], which finally leads to the formation of corrosion pits and not a general attack as observed in strongly acidic electrolytes, The thinning of the oxide layer is also much less pronounced or hardly detected for pH>5. For a higher pH the passive layer gets to or close to its dissolution equilibrium in the sense of the thermodynamically deduced potential-pH diagrams. In this situation, the tendency for the formation and transfer of soluble fluoride complexes will be reduced so that again only local effects are observed.

In this regard, the special situation of Cr should be discussed. This metal does not show pitting and the passive layer is not attacked in the presence of chloride. The stability constants of CrX^{2+} complexes are smaller than 1. Besides that, it is well known that the exchange of Cl^- ligands and H_2O between the inner and the outer sphere is an extremely slow process with a half-time of several hours [49]. This is a consequence of the large ligand field stabilization of the Cr(III) complexes with an octahedral coordination shell with three electrons in the lower t_{2g} and none in the e_g level. This situation causes "insolubility of $CrCl_3$ and Cr_2O_3 in cold water" as reported in literature [50]—however, it is rather the slow dissolution rate of the Cr^{3+} salt or oxide than their low solubility. The exchange of a ligand of the inner with one of the outer coordination shell requires a large activation energy, which makes the

Copyright © 2002 Marcel Dekker, Inc.

dissolution process even via complex formation extremely slow. Therefore one has to conclude that the presence of a $CrCl^{2+}$ complex at the surface will not increase the dissolution rate because it will form and dissolve very slowly by itself. In contrast to this situation, the exchange is rapid for Fe^{3+} complexes. Thus, a chemical change of Cr^{3+} ions from a part of the oxide matrix to a $CrCl^{2+}$ complex will not increase the dissolution rate. Besides these circumstances, the smaller stability constants of the Cr^{3+} complexes are also in favor of the stability of the passive layer. In consequence, the tendency for Cr^{3+} -halide complexes to form is negligibly small, and once they have formed their dissolution rate is not increased relative to Cr^{3+} within an oxide matrix. Therefore the halides will not attack the passive layer of chromium and pitting cannot occur, in agreement with the experimental findings.

For similar reasons, the dissolution rate of Cr(III) oxide is extremely slow in the passive state. Additions of Cr therefore stabilize the passive behavior of Fe-Cr alloys and stainless steel. Fe-Cr alloys are more resistant to pitting in chloride-containing electrolytes with more positive pitting potentials compared with pure Fe. The Cr concentration is increased within the passive layer relative to the composition of the bulk metal. Thus Fe-Cr alloys are more protected against the attack of aggressive anions and pitting by the beneficial effect of Cr.

Comparison of the Different Nucleation Mechanisms

The discussion of the different nucleation mechanisms on the basis of experimental results for iron and nickel leads to the conclusion that the film breaking and adsorption mechanisms are very effective. As usual in kinetics, the fastest reaction path is dominating. This, however, depends on the experimental or environmental conditions. For a stationary state of the passive layer the adsorption mechanism seems to be most effective, as demonstrated for Fe in weakly acidic electrolytes. If a nonstationary state is attained by a fast change of the potential, film breaking is most probable. Of course, other nucleation mechanisms may contribute as well, such as mechanical damage of the surface, dissolution of inclusions, and last but not least the penetration mechanism. Penetration is believed to be the leading mechanism for pitting of Ni in Cl^--containing electrolytes. A conclusive critical experiment to determine whether penetration of Cl^- is an initial step for breakdown of Ni passivity is still missing. The role of inclusions is the subject of another chapter in this book and will not be discussed in detail here. It was the aim of this chapter to discuss effects related to pure or at least single-phase metals. In the technical world, however, these other effects are very important. As chemistry plays a decisive role in the pitting process, one should discuss the tendency of the different cations to form complexes with halides. Thus, one has to include the properties of the aggressive anions and of the specific metals under study as well. This idea is often neglected but seems to be a key question for breakdown of passivity and the stable growth of corrosion pits, and it will be discussed again in the next section.

TRANSITION FROM PIT NUCLEATION TO PIT GROWTH, MICROSCOPIC OBSERVATIONS

In recent literature the transition of nucleation to a stable growth of corrosion pits is examined with the scanning tunneling microscope (STM) [51,52]. These studies

Copyright © 2002 Marcel Dekker, Inc.

try to follow the development of corrosion pits from a diameter of some few nanometers to several micrometers using besides the STM the scanning electron microscope (SEM). The results thus give an extension from previous investigations with the SEM and the light microscope [6] from the μm to the nm range. STM studies may trace corrosion pits down to a size of some few nm. In principle, these effects have been followed in two different ways. Maurice et al. [51] passivated Ni(111) single crystals in ~ 0.1 M sulfate solution of pH 3 for 30 min at $E = 0.85$ and exposed them finally to this solution after the addition of 0.05 V NaCl at the same potential (pitting potential 0.75 V). Numerous small pits ($5–9 \times 10^{10} cm^{-2}$) with a preferential round or some with a triangular shape aligned at steps of terraces of the (111) plane could be found (Fig. 9). They have an average lateral size of 20 nm and a depth of 2 nm, which is in the thickness range of the passive layer of ~ 1 nm. A comparison of the total area of these pits (number and size) leads to a charge of metal dissolution of ~ 0.7 mC cm^{-2}, which is about one order of magnitude less than the directly measured charge of 1.6 to 8 mC cm^{-2}. This result leads to the conclusion that increased metal dissolution in the passive state occurs, which is expected according to the adsorption mechanism for pit nucleation. These small pits are interepreted as pit nuclei that apparently did not grow further. About 1% of these pit nuclei grow larger (70 nm) but with the same depth and a triangular shape oriented still parallel to the step edges at the Ni surface.

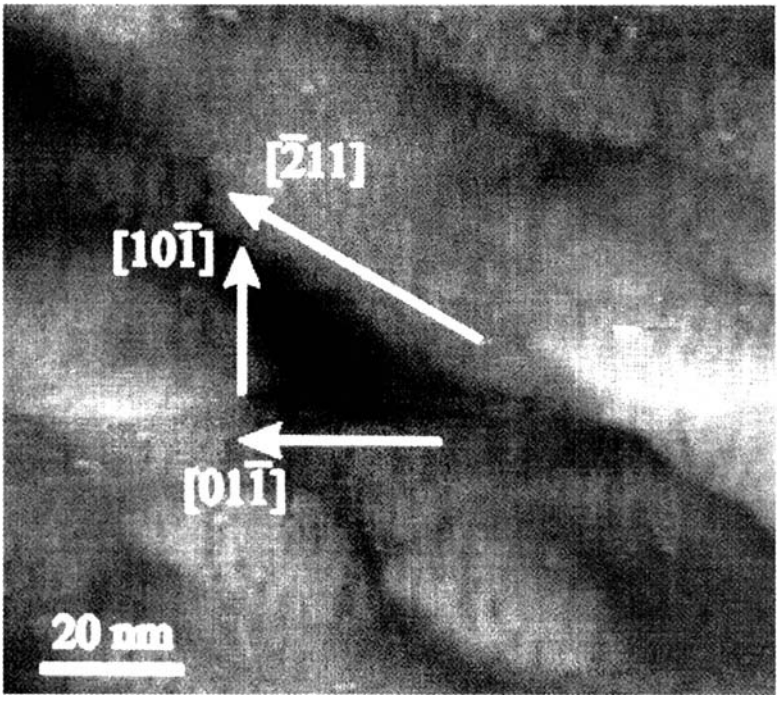


Figure 9 STM topographic image of a pit formed on Ni(111) passivated for 1800 s at 0.85 V (SHE) in 0.05 M Na_2SO_4, pH 3 and subjected to pitting in the same solution with additions of 0.05 M NaCl for 4500 s at the same potential. (From Ref. 51.)

Copyright © 2002 Marcel Dekker, Inc.

They presumably are repassivated pits. About 0.1% of the pits grow to a size of some few 100 nm with an elongated irregular shape parallel to the steps. These pits are seen as repassivated, i.e., metastable pits and grow when current transients are observed in the potentiostatic current-time curves.

Another approach is the growth of corrosion pits at potenials several hundred mV more positive than the pitting potential for short times in the ms range. Kunze and Strehblow prepassivated Ni(111) surfaces by changing the potential from –0.1 V to values below the pitting potential (E = 0.39 V) for a few seconds in a 0.2 M NaCl solution of pH 5.6 to prepassivate the surface [52]. Then the electrode was pulsed to potentials in the range 1.0 to 1.5 V for some few ms to grow pits and finally stepped back to –0.1 V to stop pit growth. These pulse measurements facilitated pit nucleation and thus caused a large density of very small corrosion pits [30,53] that could be studied in situ. The sulfate-free NaCl solution enhanced pit nucleation and hindered the early change of their shape from a polygon to a hemisphere [6]. Figure 10 presents a sequence of typical corrosion pits in different stages of development [52]. Small pits of less than 10 nm lateral size and 1.5 nm depth have an irregular slightly elongated shape. They change to triangular pits during further growth. This shape is easily explained by (111) crystal planes forming the pit surface and their intersection with the (111) Ni surface. They are the most densely packed crystal planes of face-centered cubic (fcc) Ni and thus have the largest resistance to metal dissolution. As a consequence, these planes remain during the dissolution of an actively corroding surface site and thus form the inner pit surface. They still grow further as shown on the SEM micrograph of

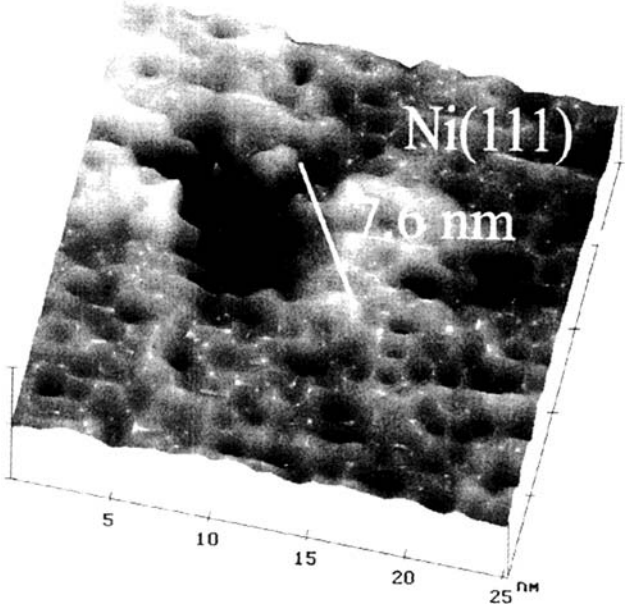
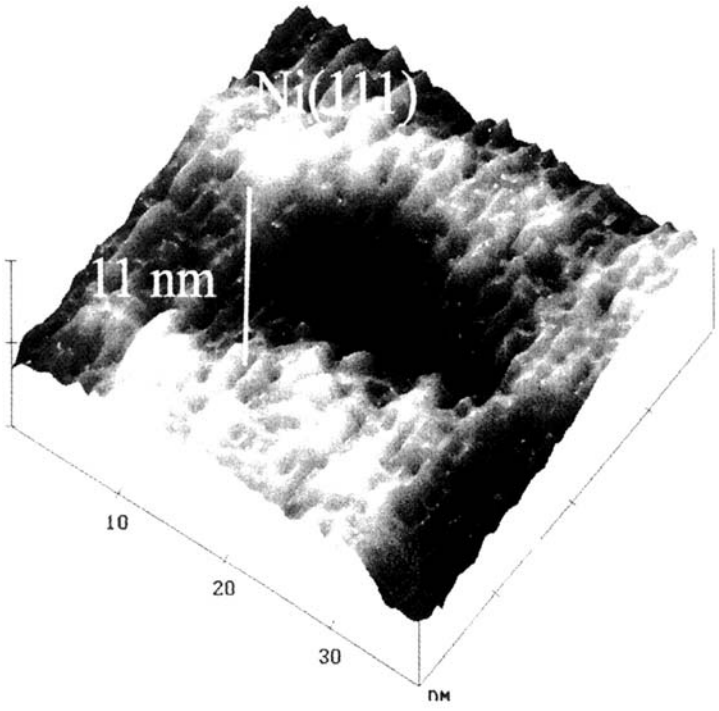
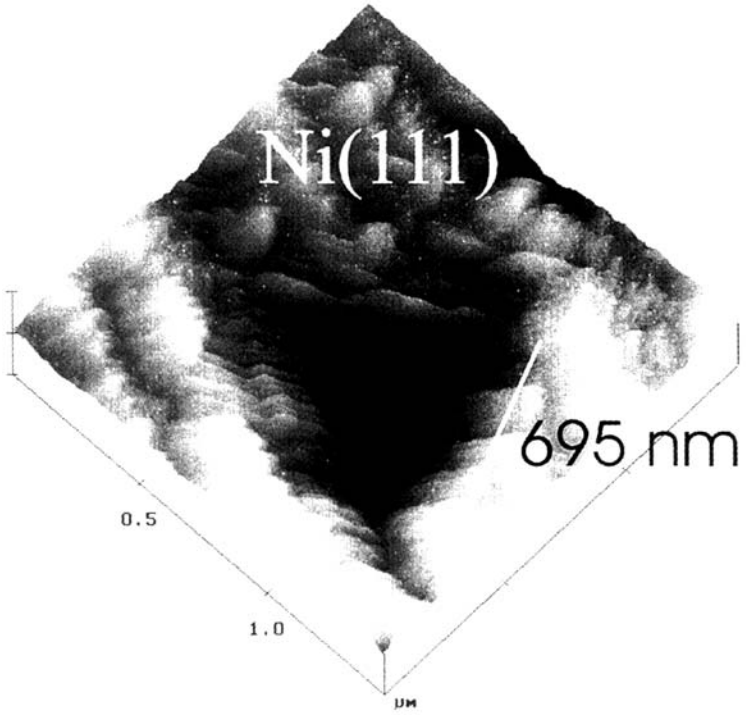


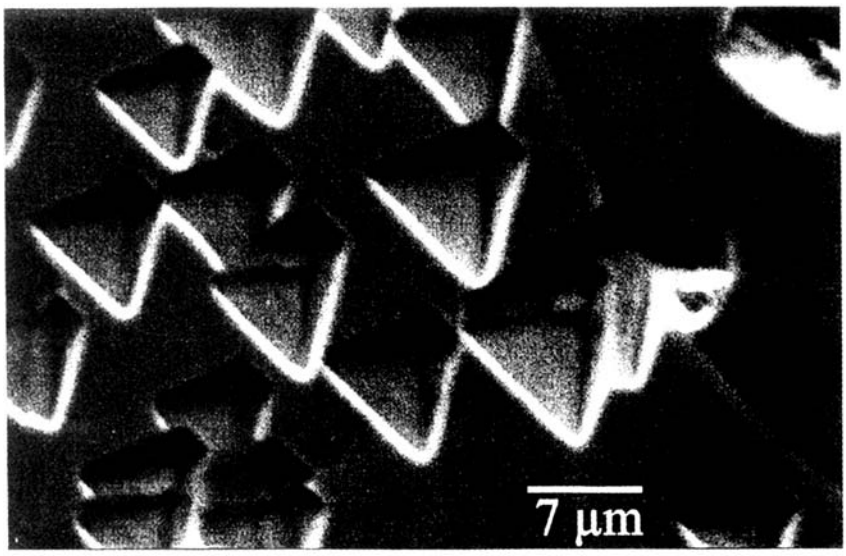
Figure 10 Sequence of in situ STM topographic images of growing pits formed on Ni(111) by potentiostatic pulses in 0.2 M NaCl. pH 5.6 during 50 ms at 1.1 V (SHE) after 3 s prepassivation at 0.39 V. (From Ref. 52.)

Copyright © 2002 Marcel Dekker, Inc.





Copyright © 2002 Marcel Dekker, Inc.



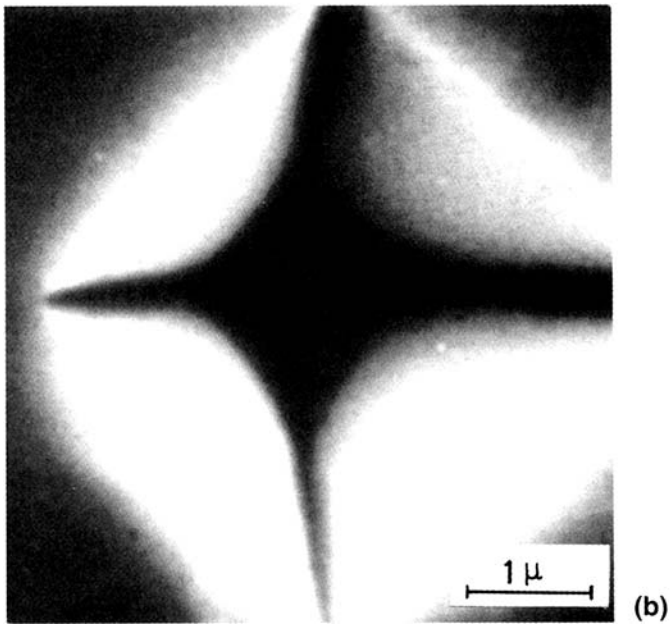


Figure 11 SEM images of pits formed on polycrystallinc Ni electrodes: (a) formed in 0.2 M NaCl, pH 5.6 for 5 ms at 1.5 V (SHE) after 10 s prepassivation at 0.5 V (from Ref. 52); (b) formed in 0.05 M phthalate buffer, pH 5.0 with addition of 0.1 M KCl for 200 ms at 1.00 V (SHE) after preactivation at –0.5 V and 1 s prepassivation at 0.50 V (from Ref. 58).

Copyright © 2002 Marcel Dekker, Inc.

Figure 11a for a similar experiment on polycrytalline Ni [52]. Depending on the orientation of the crystallite surfaces, other shapes of the pit orifice also appear such as squares (Fig. 11b) [58] or triangles with cut-off edges approaching a hexagon.

Figure 12 presents examples of the combination of (111) and (100) planes for pits on crystallites of body-centered cubic (bcc) Fe grown with the potentiostatic pulse technique described earlier [6]. These polygonal pits change their shape to hemispheres when the increasing concentration of corrosion products leads to the preciptation of a salt film. This situation causes electropolishing of the pit surface by diffusion-limited metal dissolution within the pit. It starts at the pit bottom, where the electrolyte is concentrated first, and finally includes the whole pit surface, changing the polygonal form to a hemisphere [55]. These electropolished hemispheres keep their form when crossing a grain boundary, whereas the polygons may change their shape because of the different orientation of the adjacent crytallite (Fig. 13a and b) [6]. The change of the pit surface from a polygon to a hemisphere will be discussed later in detail together with the calculation of the electrolyte composition for later stages of pit growth.

The change of the pit shape with its size and thus its age gives support to the film breaking mechanism. A rapid change of the electrode potential causes small cracks within the passive layer with a size similar to the thickness of the passive layer of 1 to 2 nm. This leads to small elongated pits of some few nm, which then change to polygonal forms during their growth to some 10 nm (Fig. 10a–c). If the potential is high and thus the local current density at the pit surface is large enough, the increasing concentration of corrosion products finally leads to a round and electropolished hemisphere. Low potentials with smaller pit current densities do not reach this stage at all or after a longer time so that large polygonal pits may be observed for these conditions. In the vicinity of the pitting potential, pit growth becomes instable. As a consequence, a metastable pit growth with a stop and go sequence will lead to the observed irregular shape.

The presence of large amounts of nonaggressive anions in the bulk electrolyte also causes their accumulation within the pits. This competition leads to smaller halide concentrations with a less stable condition for pit growth. The smaller dissolution current in the presence of these nonaggressive anions (see Fig. 15) further supports unstable growth and possible repassivation. As a consequence, discontinuous growth of pits with irregular shapes is observed. Figure 14 gives an example of a pit grown for 10 s on Ni in 0.05 M phthalate buffer, pH 5 with 0.1 M KCl and 0.1 M K_2SO_4. For these conditions pits grow into the metal leaving a metal cover that is perforated from their inner surface. Apparently, this irregular shape compensates for the lower current density. The covered pit keeps the accumulated halide inside and also causes a large ohmic drop that stabilizes its growth under less favorable conditions. At the inner surface of this larger pit a small triangular pit is observed, which supports the explanation of continuous passivation and nucleation for irregular growth. The formation of small corrosion tunnels with (100) surfaces during pitting of Al in the vicinity of its critical pitting potential further supports the dicontinuous irregular growth at microscopic and submicroscopic sites [54]. At more positive potentials, repassivation no longer occurs and pits with a hemispherical and electropolished surface are obtained.

Copyright © 2002 Marcel Dekker, Inc.

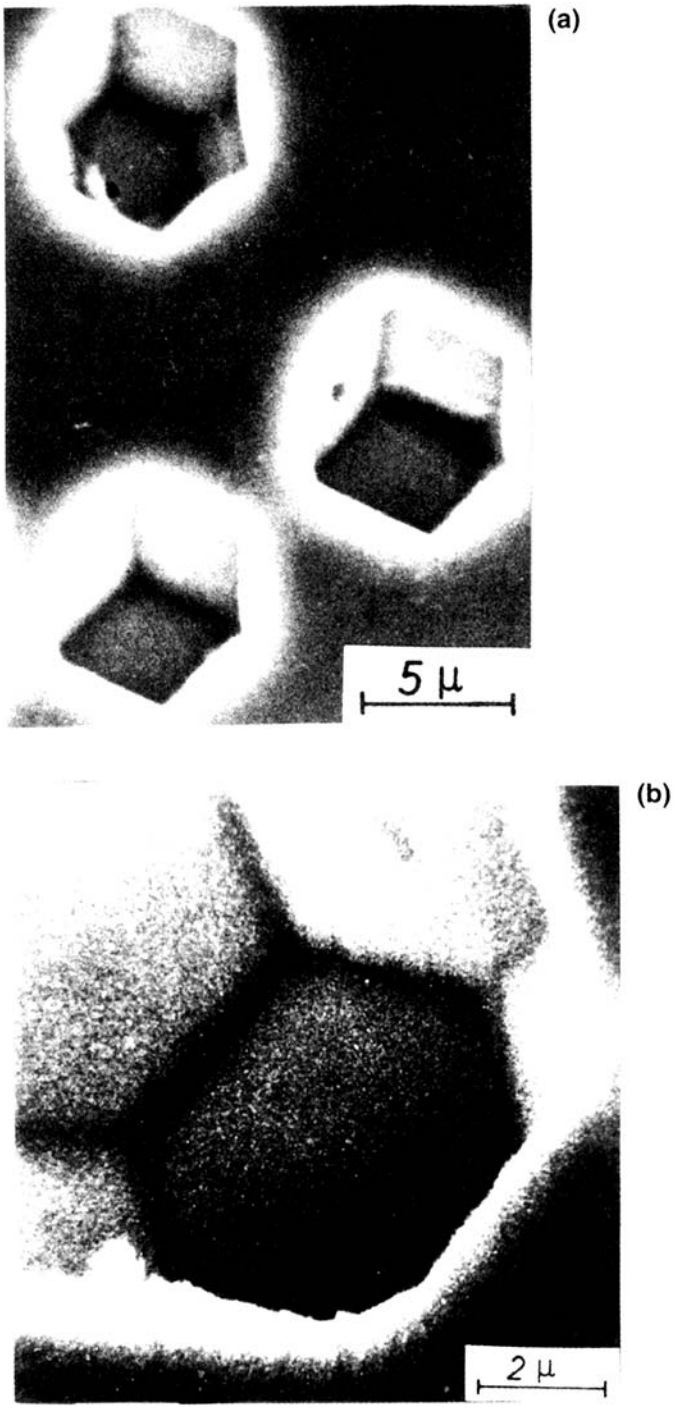


Figure 12 SEM images of pits on polycrystalline Fe formed in phthalate buffer, pH 5.0 with addition of 0.01 M KCl for 3 s at 1.10 V on crystallites with (111) orientation. (a) (110) planes at pit surface; (b) combination of (110) and (100) planes at pit surface. (From Ref. 6.)

Copyright © 2002 Marcel Dekker, Inc.

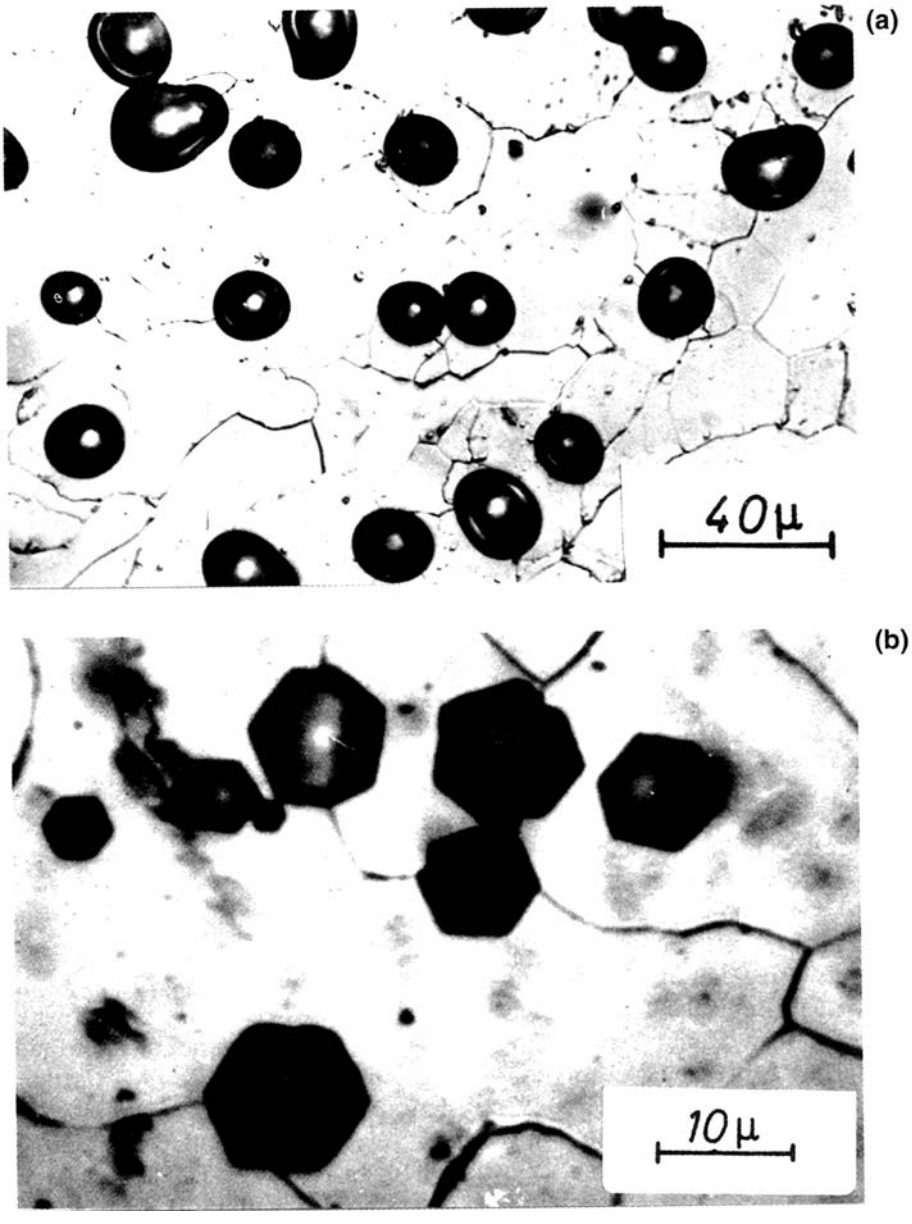


Figure 13 Microscopic images of pits on polycrystalline Fe formed in phthalate buffer pH 5.0. (a) With 0.01 M KCl and 0.1 M K_2SO_4 for 30s at 1.10 V (SHE). (b) with 0.01 M KCl only, for 3 s at 1.10 V. (From Ref. 6.)

PIT GROWTH

As visualized in the previous section, different stages of pit growth have to be distinguished, which are closely related to the question of the stability of localized corrosion. A pit will run through these different stages, each of which has its own

Copyright © 2002 Marcel Dekker, Inc.

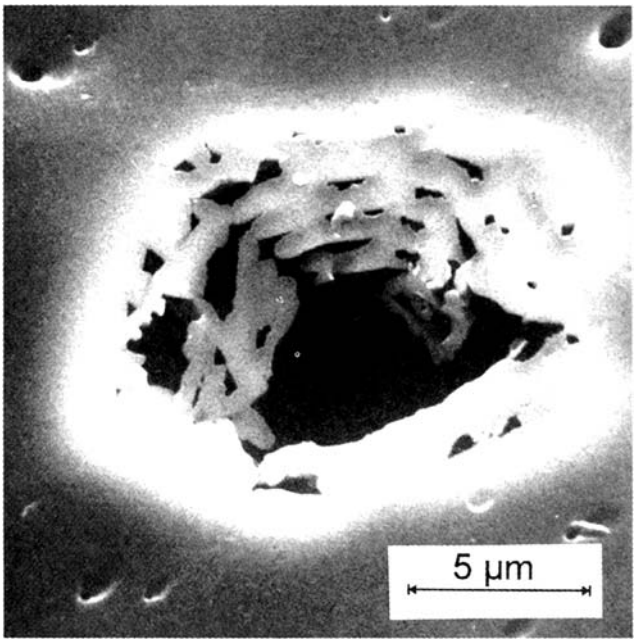


Figure 14 Microscopic image of a metal-covered pit with irregular shape on polycrystalline Ni formed in 0.05 M phthalate buffer, pH 5.0 with 0.1 M K_2SO_4 and 0.1 M KCl for 10 s at 0.90 V (SHE), Small triangular pit at inner pit surface. (From Ref. 58.)

characteristic conditions of stability. Once a pit has nucleated, its local current density refers to the applied electrode potential. For very positive potentials well within the passive range, extremely high dissolution current densities of several tens of A/cm^2 up to more than 100 A/cm^2 have been deduced from the growth of the corrosion pits using Faraday's law and taking into account their size and form (Fig. 15) [53,55]. Equivalent current densities are measured directly on small wire electrodes of <1 mm diameter embedded in resin when the passivation of the whole electrode surface is prevented in solutions of high chloride content (>1 M) starting with a preactivated oxide-free surface [53,56]. Extrapolating the dissolution kinetics of free metal corrosion to potentials in the passive range of the polarization curve leads to extremely high local current densities of 10^3 to 10^6 A/cm^2 [57]. These large current densities would cause precipitation of a salt film within 10^{-4} to 10^{-8} s. Current densities of more than 10^3 A/cm^2 are possible in principle but only up to 120 A/cm^2 has been observed for a free corroding metal surface [53,55].

The local current density increases with the chloride concentration, whereas the critical pitting potential decreases with increasing chloride concentration. If, however, $i_{c,p}$ is presented relative to E_p, the data fit a single curve. Apparently an increasing chloride concentration shifts the whole $i_{c,p}/(E - E_P)$ curve in the negative direction [58, p. 55]. The addition of nonaggressive anions such as sulfate or nitrate shifts the exponential current increase to positive potentials with a large potential-independent plateau at low potentials [53,58, p. 57]. These plateau values are in the range of a few A/cm^2, i.e., 5 A/cm^2 for Ni in 0.1 M KCl + 0.1 M K_2S0_4 and 2 A/cm^2

Copyright © 2002 Marcel Dekker, Inc.

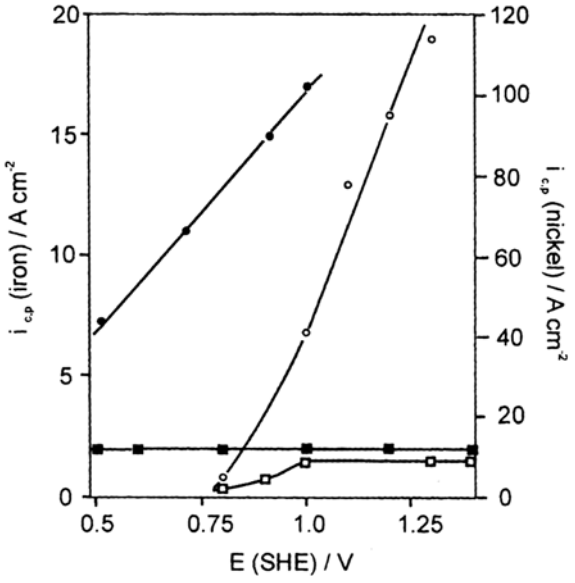


Figure 15 Local pit current density $i_{c,p}$, as a function of potential E deduced from pit growth on polycrystalline nickel and Fe electrodes in 0.05 M phthalate buffer, pH 5.0. Ni: (□) 0.1 M KCl + 0.1 M K_2SO_4, (○) 0.1 M KCl; Fe: (■) 0.01 M KCl + 0.1 M K_2SO_4, (●) 0.01 M KCl. (From Ref. 58.)

for Fe in 0.01 M KCl + 0.1 M KSO_4 (Fig. 15) [53]. Apparently the potential-independent plateau values of $i_{c,p}$ are related to the formation of a salt layer that provides electropolishing conditions at the pit surface (Fig. 13a). If, however, the current becomes still smaller such as for Ni below 1.0 V, the growth of the pit becomes unstable and irregular shapes are observed as shown in Figure 14.

A special geometry for localized corrosion studies has been applied by Frankel and co-workers [59,60]. They subjected vapor-deposited thin Ni-20% Fe and Al films on an inert substrate as working electrodes of a potentiostatic circuit to the local attack of chlorides, which causes fast perforation of the film and subsequent growth of two-dimensional pits with actively corroding cylindrical side walls. With this method the authors avoid the usual deepening of three-dimensional pits on bulk materials with the related increasing diffusion length for the transport of corrosion products and ohmic drops. Thus, the geometry for metal dissolution and transport of corrosion products was kept constant with time of growth of the two-dimensional pits. For this simpler and constant geometry, the local current density and the potential of repassivation of pits could be measured more accurately. The local current densities $i_{c,p}$ could be directly deduced from the growth of the radius of the two-dimensional pits applying Faraday's law without any assumptions for the geometry of the actively corroding surface. Usually, $i_{c,p}$ increases linearly with the electrode potential up to 100 A/cm^2, where it is controlled by mass transport and ohmic resistance. It finally gets to a diffusion-controlled potential-independent limiting value. There exist a critical local current density i_{cr} and a repassivation potential E_R that are closely related to each other. The accumulation of corrosion

Copyright © 2002 Marcel Dekker, Inc.

products is interpreted by the authors as a stabilizing factor for pit growth. If the local current density goes below a critical value i_{cr}, localized corrosion will stop due to a less aggressive environment corresponding to a smaller local concentration of the corrosion products that may be maintained. Apparently, a sufficiently high concentration of chloride is required to prevent repassivation. Estimates have shown that ~ 50% of the concentration of saturation is required to prevent repassivation [59]. As will be shown later for a hemispherical pit, the locally increased concentration of corrosion products and thus chlorides is proportional to the product of the local current density and the pit radius $i_{c,p}\ r$ [Eq. (18)]. For a two-dimensional circular pit this relation simplifies to a proportionality to $i_{c,p}$ which yields critical conditions that are independent of the radius of the two-dimensional pit [59]. In this sense, these studies may give valuable information on the stabilty of polygonal and hemispherical pits. With increasing metal film thickness and consequently larger side walls of the actively corroding cylinder surface, i_{cr} decreases due to a larger corroding surface and hence to an increased ohmic resistance and higher accumulation of corrosion products. For similar reasons, *di/dE* decreases with increasing film thickness.

As already discussed in relation to the adsorption mechanism of pit nucleation, the halides cause catalytically enhanced dissolution of the passivating oxide. Any attempt of the bare metal surface of a pit to passivate by oxide formation will fail in the presence of high concentrations of aggressive anions, similar to the galvanostatic transient behavior of preactivated specimens. Thus, there is a close correspondence of small iron and nickel electrodes in solutions of high Cl^- content (>1 M) and an intensively corroding pit surface that will be discussed in the next section. In both cases, the formation of a passive layer is suppressed. In the case of Al a sufficiently low pH by hydrolysis of the corrosion products will stabilize pitting additionally. Passivity of this metal requires a dissolution equilibrium of the anodic oxide with the electrolyte that requires weakly acidic to alkaline solutions. Localized acidification is therefore a good additional stabilizing factor for corrosion pits on Al. This special situation, however, does not contradict the necessary active chemical role of halides, i.e., their complexing properties.

Precipitation of Salt Films

After a sufficiently long time of high dissolution current densities, the accumulation of corrosion products will lead to the precipitation of a salt film. This precipitation is expected in an early stage of pit growth if sufficiently large potentials and as a consequence large current densities are applied. Galvanostatic transients of preactivated small electrodes in solutions of high chloride content are not subject to passivation, and the dissolution at potentials within the passive range leads to a related steep increase of the measured electrode potential after the transition time τ (Fig. 16). For the linear diffusion problem of the completely dissolving electrode surface it was found that Sand's equation is valid; this relates the current density $i_{c,p}$ and time t of corrosion to the difference $\Delta c = c_m - c_{m,b}$ of the metal ion concentration with c_m at the electrode surface and its bulk value $c_{m,b}$, their charge z_m, and diffusion constant D of the metal ions [56].

$$i\sqrt{t} = \frac{1}{2} z_m F \sqrt{\pi D \Delta c} \tag{17}$$

Copyright © 2002 Marcel Dekker, Inc.

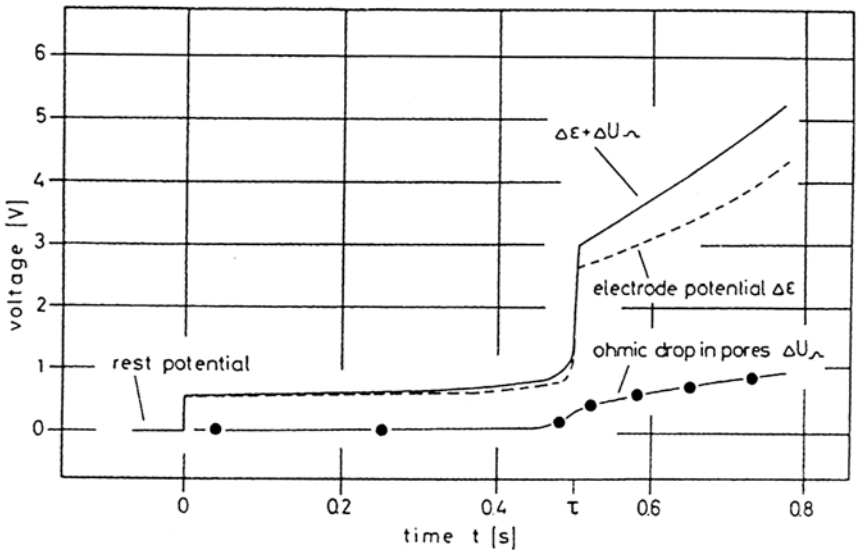


Figure 16 Galvanostatic transient of Ni in saturated $NiCl_2$ solution with $i = 1.5$ A/cm^2 and the related voltage drop $\Delta E + \Delta U_\Omega$ across the total salt layer and ohmic drop ΔU_Ω across the porous film. (From Ref. 56.)

In the absence of supporting electrolyte, i.e., in a solution containing the salt of the dissolving metal, a diffusion constant $D_{\text{eff}} = D(1 + z_m/|z_a|)$, which includes the contribution of migration to the transport, has to be used instead D. Here z_m and z_a are the valences of the metal ions and anions. Figure 17 presents the accumulation of metal ions Δc according to Eq. (17) during dissolution of a small nickel electrode in solutions of high chloride content as a function of $i\sqrt{t}$. When c_m reaches its value of saturation $c_{m,s}$ for $t = \tau$, precipitation of a salt film will occur. This salt film has been examined further with galvanostatic pulses superimposed on the main transient to determine ohmic drops (Fig. 16). The results lead to a model for the forming salt film with a spongy, porous outer part and a barrier-type inner part [56]. Besides experimental examinations [56], numerical calculations [61] have shown that Eq. (17) may also be applied for concentrated electrolytes. Different solutions with and without aggressive anions have been tested using galvanostatic transients with small Fe and Ni electrodes, such as 0.5 M H_2SO_4, 1 M $HClO_4$, 1 M $NaClO_4$, and 1M HNO_3. Figure 18 gives an example for Fe. In the absence of aggressive anions, no potential plateau but only a small shoulder was found for galvanostatic transients; i.e., only passivation with no large free metal dissolution was observed. The product $i\sqrt{\tau}$ starts at small values and decreases with increasing current density i. Only in the presence of > 1 M Cl^- (or possibly other halides) were much larger values independent of i found for $i\sqrt{\tau}$. These studies also prove that the presence of aggressive anions is necessary to prevent passivation of Fe and Ni surfaces.

For a hemispherical pit the diffusion-limited local current density $i_{c,p}$ changes according to Eq. (18), which is a simple combination of Fick's first diffusion law and

Copyright © 2002 Marcel Dekker, Inc.

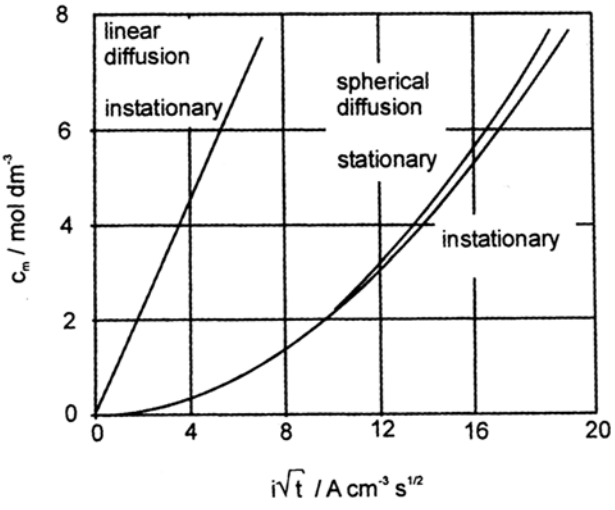


Figure 17 Concentration of $NiCl_2$ at a corroding Ni surface c_m as a function of the product $i\sqrt{t}$ for linear and spherical transport (including nonstationary conditions) calculated with Eqs. (17) and (20). (From Ref. 30.)

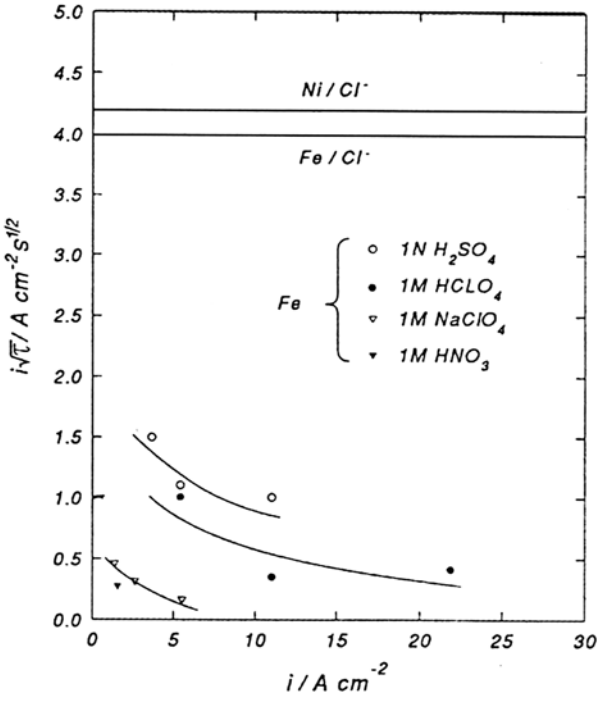


Figure 18 Plot of $i - i\sqrt{\tau}$, τ = transition time, for galvanostatic transients of small Fe electrodes in different solutions without and with 1 M Cl^- depending on the applied current density. (From Ref. 58.)

Copyright © 2002 Marcel Dekker, Inc.

Faraday's law for the hemispherical electrode geometry with the same varibles as used for Eq. (17):

$$i_{c,p} = z_m F D_{eff} \Delta c / ar \tag{18}$$

This equation contains a constant a that takes into account the change from the convex to the concave pit geometry. For the simple analytical solution of the convex hemispherical transport problem $a = 1$ will hold. For a concave hemispherical pit a has been estimated to be 3 [6,30,31]. Computer-assisted numerical calculations yield a result that is very close to this value for the pit bottom [62,63]. With the simple stoichiometric relation between the local current density $i_{c,p}$ of a hemispherical pit and its growth rate of the radius dr/dt and Faraday's law [Eq. (19)] one obtains Eq. (20), which is the equivalent relation for the transport from a hemispherical pit to the linear transport from a small electrode dissolving totally at its surface [Eq. (17)]. V_m is the molar volume of the metal under study. Figure 17 compares the calculated results for $NiCl_2$ for both electrode geometries. Precipitation of corrosion products is expected for the transition times $t = \tau$ when saturation is achieved at the pit surface with $c_{m,s}$ = 4.8 M and 4.2 M for $NiCl_2$ and $FeCl_2$, respectively. This condition is achieved first at the pit bottom for $a = 3$. The calculated data agree well with the experimentally observed precipitation within pits [30]. For Ni $i\sqrt{\tau}$ = 14.8 A cm^{-2} s$^{1/2}$ is obtained. With the assumption of nonstationary transport conditions one yields almost identical results (Fig. 17). Some deviation is obtained only for values $i\sqrt{t} > 12$ A cm^{-2} s$^{1/2}$ [30].

$$i_{c,p} = (z_m F / V_m)\, dr/dt \tag{19}$$

$$i_{c,p}\sqrt{t} = z_m F \sqrt{\frac{\Delta c D_{eff}}{V_m a}} \tag{20}$$

The precipitation of a salt film is closely related to a change in the growth of a corrosion pit. When the salt film is formed, the growth rate slows down and the pit morphology changes from a polygonal to a hemispherical structure. This change starts at the pit bottom, where it is expected first, and often is combined with an electropolishing effect [55]. Direct microscopic in situ and ex situ examinations of growing pits for potentiostatic conditions show a decrease of the growth of the radius when a salt film precipitates (Fig. 19) [58]. The time of change of the growth rate coincides with the electropolishing effect at the pit bottom [55]. Heimgartner and Böhni [64] discussed the growth of corrosion pits for longer times under diffusion-limited conditions in more detail. If the local current density $i_{c,p}$ in a pit is not constant and decreases inversely with the pit depth r according to Eq. (18a), one deduces with Eq. (19) a reciprocal relation of its growth rate dr/dt with its depth r [Eq. (21)]. Integration leads to a parabolic dependence of the pit radius on time t [Eq. (22)] and combination with Eq. (18a) to Eq. (23) with an inverse change of the local pit current density $i_{c,p}$ with $\sqrt{t}$. This discussion assumes a saturated solution with a change of the metal ion concentration $\Delta c = c_{m,s}$, i.e., a salt film at the actively corroding pit surface and a vanishing bulk concentration $c_{m,b}$. Therefore a later stage of pit growth is discussed and not the initial situation of free metal dissolution as for the beginning of pit growth of Figure 15. Equations (22) and (23) assume a minimum pit radius r_0 where a saturated solution at its surface is achieved. Equation (23) is simply the combination of Eqs. (18a) and (22).

Copyright © 2002 Marcel Dekker, Inc.

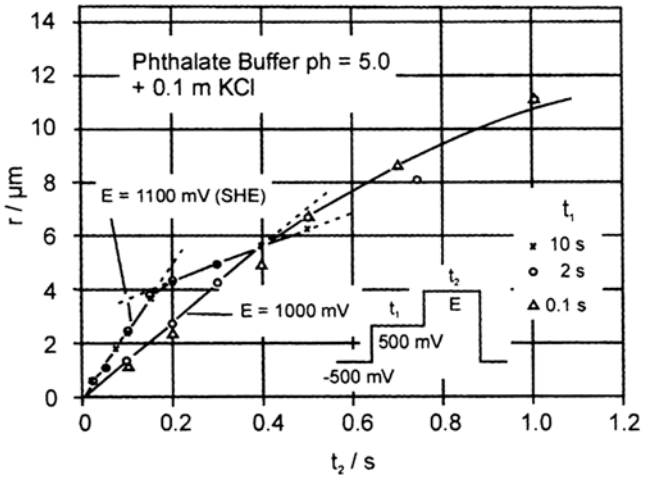


Figure 19 Deviation from linear pit growth with time when precipitation of a salt layer occurs, Ni, $E = 1.00$ and 1.30 V phthalate buffer, pH 5.0 + 0.1 M KCl with inserted diagram of applied potential pulses. (From Ref. 58.)

$$i_{c,p} = \frac{z_m F D c_{m,s}}{ar} \tag{18a}$$

$$\frac{dr}{dt} = \frac{i_{c,p} V_m}{z_m F} = \frac{D c_{m,s} V_m}{ar} \tag{21}$$

$$r - r_0 = \sqrt{\frac{D V_m t c_{m,s}}{a}} \tag{22}$$

$$i_{c,p} = \frac{z_m F D c_{m,s}}{a r_0 + \sqrt{2 D V_m c_{m,s} t/a}} \tag{23}$$

Enhanced convection may lead to a situation where ohmic resistance instead of diffusion is rate determining. Convection by an increasing flow rate of the electrolyte or the evolution of gas bubbles in corrosion pits will increase the local dissolution and finally cause ohmic current control. Like diffusion control, ohmic control will lead to a parabolic dependence of the pit radius or pit depth on time.

Potential Drops

There exist detailed studies for the potential drop ΔU, the composition of the pit electrolyte, and related changes of the pH. All these factors have been used to explain the stability of a corroding pit. The potential drop within the electrolyte for an open hemispherical pit can be estimated by the simple equation:

$$\Delta U = \frac{a i_{c,p} r}{\kappa} \tag{24}$$

Copyright © 2002 Marcel Dekker, Inc.

with specific conductivity κ, local current density $i_{c,p}$, radius r, and geometric factor $a = 3$ [6]. It depends on the specific situation whether ΔU is large enough to shift the potential below the Flade potential, i.e., in the active range of the polarization curve (Fig. 20). For 0.5 M H_2SO_4 with $\kappa = 0.22$ cm^1 and $i_{c,h} = 0.3$ A/cm^2, which is a reasonable value for moderately high pit current densities for Fe, one obtains $\Delta U > 1$ V for a pit radius $r > 2.4$ mm, but only $\Delta U = 0.41$ mV for $r = 1$ μm. This short calculation demonstrates that it is absolutely necessary to define well which state of the growth of a pit is discussed. Potential drops may stabilize localized corrosion for large pits but never for small ones, i.e., for initial stages. The conductivity of the electrolyte is, of course, another factor that has to be taken into account. The accumulation of ions within a corroding pit may increase κ and thereby reduce ΔU compared with the value obtained with the bulk conductivity. Evidence for potential control of pit growth is given for studies on Al by Hunkeler and Böhni [65]. They found a linear dependence of the product $i_{c,p}r$ on the voltage drop ΔU.

Composition of Pit Electrolyte

The accumulation of electrochemically nonactive electrolyte components is closely related to the potential drop ΔU within the electrolyte, similar to a Boltzmann dependence of the concentration c_j of these species on the electrical energy $\Delta U\, zF$ [6,30]. Together with the electroneutrality equation, one obtains a dependence of the concentration of the corroding metal ions c_m at the metal surface on ΔU with $c_m - c_{mb} = c_m$ for a vanishingly small bulk concentration c_{mb} [6,30]. The corresponding bulk values are $c_{j,b}$ and $c_{m,b}$

$$c_j = c_{j,b} \exp\left(\frac{-\Delta U z_j F}{RT}\right) \tag{25}$$

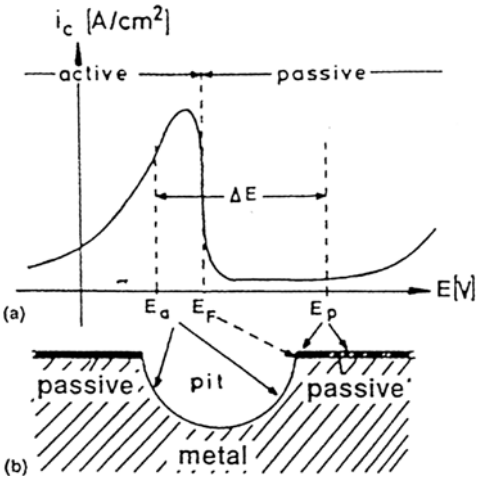


Figure 20 (a) Typical current density potential curve of a passive metal; (b) hemispherical pit with potentials E_a inside and E_p outside the pit according to the rejected theory frequently used for small pits. (From Ref. 31.)

Copyright © 2002 Marcel Dekker, Inc.

$$\Delta c = c_m - c_{m,b} = c_m = -\left(\frac{1}{z_m}\right)\sum c_{j,b} z_j \exp\left(\frac{-\Delta U z_j F}{RT}\right) \tag{26}$$

Equation (25) requires that only one electrochemical process occurs with no subsequent reactions within the bulk electrolyte. The concentration of the metal cations c_m may also be calculated from Eq. (18) or (18a). For vanishingly small bulk concentration of the cations, Δc equals the surface concentration c_m. The accumulation of cations is proportional to the local pit current density and the pit radius [Eq. (18)]. One may therefore take $i_{cp}r$ as a measure of the cation concentration at the pit surface, which depends on the age of the pit. Therefore this scale is included in Figures 21 and 22.

$$\Delta c = c_m = \frac{a i_{c,p} r}{z_m F D_{eff}} \tag{18}$$

The concentrations c_j at the pit surface of species that are not involved in the electrode process and the cation concentration have been calculated according to Eq. (25) for some bulk electrolytes frequently used for pitting studies (Fig. 21). Metal ion concentrations c_m go up to saturation of a few moles per liter when the potential drop increases to several tens of millivolts, which is usually the case for a pit radius of several micrometers. Equation (26) was applied for the calculation of the concentrations c_m at the pit surface as given in Figure 22.

pH shifts have often served to explain the stability of a corroding pit. Equation (25) permits the calculation for buffered solutions when the pH is not affected by hydrolysis of the corrosion products [30]. Buffer ions change in concentration in agreement with the pH shift as given for the phthalate buffer in Figure 21. An

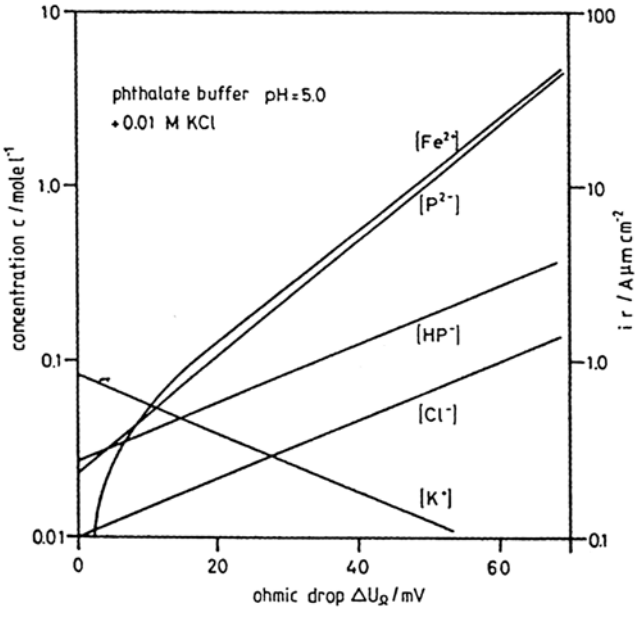


Figure 21 Ionic concentration at the metal surface depending on the ohmic drop ΔU_Ω within the electrolyte according to Eqs. (25) and (26). (From Ref. 30.)

Copyright © 2002 Marcel Dekker, Inc.

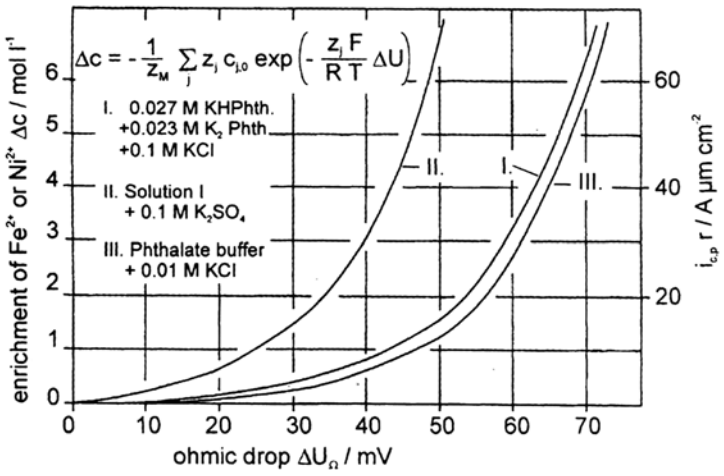


Figure 22 Concentration of metal ions at the dissolving metal surface depending on the ohmic drop ΔU_Ω and the parameter $i_{c,p}r$ according to Eq. (26). (From Ref. 30.)

accumulation of dissolving metal ions leads to accumulation of the (buffer) anions and to depletion of the other cations and consequently to a positive pH shift according to Eq. (27).

$$\mathrm{pH} - \mathrm{pH_b} = \Delta U/0.059 \tag{27}$$

In nonbuffered solutions the usual hydrolysis equilibrium of the metal ions leads to acidification according to

$$\mathrm{Me^{z+} + H_2O \leftrightarrow MeOH^{(z-1)+} + H^+}$$

With $[\mathrm{MeOH^{(z-1)+}}] = [\mathrm{H^+}]$ for nonbuffered electrolytes one obtains:

$$[\mathrm{H^+}] = \sqrt{K_h[\mathrm{M^{z+}}]} \tag{28}$$

With hydrolysis constants of $K_h = 10^{-10}$ and 10^{-7} one obtains for the saturation concentrations 4.8 and 4.2 M, pH values of 4.3 and 2.4 for saturated $NiCl_2$ and $FeCl_2$ solutions, respectively. These calculations show that the precipitation of hydroxide within a corrosion pit may be prevented for these metals by acidification. However, as discussed before, passivation should nevertheless be possible for many technically important metals. For Fe, Ni, and other metals, especially in acidic media, passivity cannot be explained on the basis of thermodynamic equilibria and Pourbaix diagrams. In these cases passivity is a kinetic phenomenon. Otherwise these metals should not show passivity in a strongly acidic environment. Thus, different explanations are required for the stability of a corrosion pit.

The pH shift of the passivation potential E_{pa} may not give an explanation either. Its change usually by –0.059 V/pH is much too small to cause a shift above the potentiostatically applied value E well within the passive range, so that the metal surface might reach the active range of the polarization curve. In 0.5 M H_2SO_4 the passivation potential for Fe or Ni is $E_{pa} = 0.58$ or 0.35 V, respectively, with a shift of –0.059 V per pH unit. If the potential is set in the passive range up to 1.5 V one has

Copyright © 2002 Marcel Dekker, Inc.

to explain a shift of the passivation potential by 0.9 to 1.15 V, which is absolutely out of range of any reasonable explanation. If, however, the potential E is set to values close to E_{pa}, as often realized in technical corrosion situations with open-circuit conditions, acidification may cause its shift above E with $E_{pa} > E$, which especially in weakly acidic and alkaline unbuffered solutions may fulfill these requirements. In addition, the much more negative passivation potential of Fe for neutral and alkaline solutions, such as $E_{pa} = -0.1\text{-}0.059$ pH for Fe, will not be effective as a consequence of acidification by hydrolysis. The passivation potential becomes more negative because of the insolubility of lower valent Fe oxides such as Fe_3O_4 or $Fe(OH)_2$ in neutral and alkaline solutions. However, these oxides dissolve very quickly in acidic electrolytes, so they do not provide passivity for these conditions. In conclusion, one may say that local negative pH shifts due to hydrolysis of corrosion products may support and stabilize pitting at negative electrode potentials for neutral and weakly acidic and alkaline bulk electrolytes. This will hold especially for metals that cannot be passivated at low pH, e.g., Cu and Al, because of their fast dissolution or high solubility in this environment. However, this interpretation does not hold for Fe, Ni, and steels in strongly acidic electrolytes at sufficiently positive electrode potentials. Thus, pitting needs another, more general explanation. Furthermore, anions of other strong acids such as perchlorates and sulfates should act as aggressive anions as well if hydrolysis and pH shifts are the essential causes of localized corrosion. However, ClO_4^- may even act as an inhibitor if the potenital is not too positive and most metals may be passivated in sulfuric and perchloric acid, which demonstrates that the specific chemical properties of the aggressive anions have to be taken into account in the explanation of pitting corrosion.

An attempt has been made to explain the requirement for a minimum concentration of aggressive anions to maintain stable pit growth [30,31]. With the assumption that a salt film of thickness δ has to be maintained at the growing pit surface, one obtains:

$$c_{min} = aV_m i_{c,p}\delta / DFV_s = 0.5 i_{cp}\delta \tag{29}$$

With this assumption the experimentally found value of $c_{min} = 3 \times 10^{-4}$ M has been confirmed with a local current density $i_{c,p} = 1$ A/cm^2, a salt layer thickness $\delta = 5$ nm, geometric factor $a = 3$, molar volume $V_m = 3.55$ cm^3/val for the equivalent volume for Fe metal and $V_s = 21.25$ cm^3/val for $FeCl_2$, and diffusion constant $D = 10^{-5}$cm^2/s for Cl^- ions.

The accumulation of aggressive anions has been found at the surface even of small polygnal pits of some few μm diameter when their change to a hemisphere by the precipitation of a salt film was not already achieved. A special preparation technique of pulling the electrode with actively corroding pits into a benzene layer above the electrolyte preserved the special situation at the corroding pit surface even after rinsing with acetone and dry storage in air [66]. These pits remained active and continued their growth immediately when reintroduced into the electrolyte at the same potential; however, they became inactive on rinsing with water or stepping the potential below the critical value. With electron microprobe analysis, chloride could be found that corresponded to layer of ~ 5 nm $FeCl_2$ when the pit remained active but was lost completely on rinsing with water or repassivation [66]. These studies show clearly that the formation of a thin layer of aggressive anions even in pits of some few μm is responsible for stable pit growth. The later precipitation

Copyright © 2002 Marcel Dekker, Inc.

of much thicker salt films in larger pits of several tens of μm provides further stabilization but is not a necessary condition for localized corrosion. The presence of nonaggressive anions in the bulk electrolyte also caused their accumulation but did not suppress the additional presence of aggressive anions that is absolutely necessary for a stable pit growth. The electropolishing conditions in sulfate-containing solution caused large amounts of these anions corresponding to several hundred nm of $FeSO_4$ within the hemispherical pits but did not avoid the additional and necessary accumulation of ~ 5 nm $FeCl_2$ [66].

Repassivation of Corrosion Pits

The kinetics of repassivation of small pits in an early stage of their development seem to be related to the transport of aggressive anions, such as the chloride accumulated locally during the intense dissolution process from the pit to the bulk [4,30]. If this transport is the rate-determining step, one expects the repassivation time to increase with the depth of a corrosion pit. If we simply apply the Einstein-Smoluchowski relation for the transport time t_r out of a pit of radius r [Eq. (30)] and if the radius r is given by the local current density i_{cp} and the lifetime t_p of the pit by Eq. (31), we obtain for the repassivation time t_r [Eq. (32)]

$$t_r = \frac{r^2}{2D} \tag{30}$$

$$r_r = \frac{i_{c,p} t_p V_m}{z_m F} \tag{31}$$

$$t_r = \frac{i_{c,p}^2 t_p^2 V_m^2}{2D z_m^2 F^2} = k t_p^2 \tag{32}$$

The t_r increases with the square of the lifetime t_p of a pit. The constants k_i have been estimated from $D = 5 \times 10^{-6}$cm^2/s, $zF/V_m = 2.72 \times 10^4$ A s/cm^3 for Fe and 2.93×10^4 A s/cm^3 for Ni to $k_{Fe} = 1.35 \times 10^{-4}\ i_{cp}^2$ and $k_{Ni} = 1.16 \times 10^{-4}\ i_{cp}^2$ for Fe and Ni, respectively. To check the i_{cp}^2 and t_p^2 dependence of t_r, potentiostatic pulse measurements have been performed. The potential was pulsed for some 10 ms up to 1 s to values above the pitting potential E_p and back to $E \le E_p$ for increasing time Δt. When the potential was finally pulsed back to the potential in the pitting region, the current density started to increase further at the same level reached at the end of the previous pitting period if Δt was short enough. When Δt was too long, at least some of the pits repassivated and the subsequent pitting period had to start again with the nucleation of new pits and a smaller value of the average current density of the electrode. The interval Δt of a fast deviation from a continuous increase of the current density for a set of pulse experiments is taken as the repassivation time t_r. A double logarithmic plot of t_r and t_p shows a slope of approximately 2 as required by Eq. (32). Also, t_r changes proportionally with i_{cp}^2. The estimated values agree sufficiently well with the experimental data of Figure 23.

One may therefore conclude that the rate-determining step for the repassivation is the transport of accumulated aggressive anions out of small pits. This result coincides well with the explanation that localized corrosion is stabilized at the initial stage by the accumulation of aggressive anions that prevent the formation of a passive layer at the active pit surface.

Copyright © 2002 Marcel Dekker, Inc.

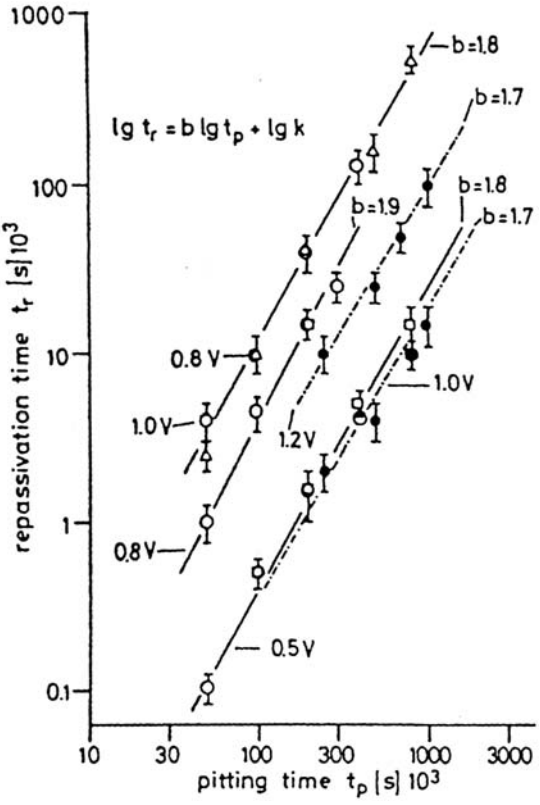


Figure 23 Repassivation time t_r vs. pitting time t_p for Fe ($A = 0.13$ cm^2) and Ni ($A = 0.2$ cm^2) at different potentials for pitting as indicated, t_r leading to deviations of continuous current increase for one potential sequence. (□) Fe 0.01 M Cl^-; (○) Fe 0.01 M Cl^-, (●) Ni 0.1 M Cl^- Δ Fe 0.01 M Cl^- t_r leading to continuous increase of current for many subsequent potential cycles, phathalate buffer, pH 5.0 (From Ref. 4.)

Factors Stabilizing Pit Growth

The factors that stabilize the growth of a pit depend on the stage of its development. Ohmic drops cannot serve as an explanation for small pits with micrometer dimensions. The ohmic drops are <1 mV for strongly acidic, well-conducting electrolytes such as 0.5 M H_2SO_4 and a pit radius of 1 μm. This is far too small to shift the potential from its potentiostatically fixed value below the passivation potential by more than 1 V (Fig. 20). However, in later stages for pits of several millimeters radius the ohmic drop might become high enough to satisfy this condition. The extremely high local current densities are a further proof of the absence of large ohmic drops. The local potential at the pit surface is in the vicinity of the potentiostatically fixed value in order to permit these high dissolution currents. Ohmic drops have already been corrected in Figure 15, presenting these high current densities for Ni.

Copyright © 2002 Marcel Dekker, Inc.

pH shifts also cannot explain the stable pit growth for metals such as Fe, Ni, and steels that are also passive in strongly acidic electrolytes. For these systems passivity is a kinetically determined phenomenon that is even in disagreement with the Pourbaix diagram. But there are metals with passivation potentials in close agreement with their Pourbaix diagrams that form passivating oxide layers which dissolve at a high rate in strongly acidic electrolytes, such as Al and Cu. For these systems, local destabilization of passivity may occur on acidification of the pit electrolyte with pitting in neutral or weakly acidic bulk electrolytes. However, even for these metals there still remains the question why halides are necessary for pit nucleation and pit growth. The pH dependence of the Flade potential of –0.059 V/pH as obtained for metals such as Fe and Ni cannot serve as a stabilizing factor. The pH shift required to obtain active conditions at the pit surface is much too large in comparison with the applied electrode potentials.

The requirement for aggressive anions and their influence on the repassivation kinetics demonstrate that their accumulation stabilizes localized corrosion in an early stage. The autocatalytically enhanced dissolution of the passive layer by these anions prevents any repassivation once a pit has formed. It should be mentioned again that pure Cr is one of the few metals that is not subject to pitting by chloride. In agreement with this finding, Cr(III) salts dissolve very slowly in water. Fast transfer of the complexed ions to the electrolyte is necessary for the attack on the passive layer, which provides a good explanation for the pitting resistance of this metal compared with Fe and Ni.

For sufficiently positive potentials the intense dissolution process leads to severe accumulation of corrosion products and finally, after a transition time, to the formation of a salt film, which is a further stabilizing factor for a pit. It may act as a reservoir to maintain a high concentration of the aggressive anions. These explanations are supported by the logarithmic dependence of the critical pitting and inhibition potential on the concentration of aggressive (A) or inhibiting (I) anions according to Eqs. (1) and (2).

These equations with large *b* factors have been found experimentally for Fe and Ni and various aggressive and inhibiting anions [2,67]. They have been deduced on the basis of a thermodynamic theory of adsorption of the anions at the metal surface of a pit in competition with each other and with the formation of the passive layer [37,67]. This explanation agrees well with the concept of repassivation prevented by accumulation of aggressive anions. According to this approach, a potential-assisted Langmuir type of adsorption isotherm for the aggressive anions is assumed at the parts of the bare metal surface where the passive layer has been removed by any of the mechanisms that have been discussed. For simplicity, homogeneous adsorption at the metal surface is assumed with no lateral interaction between the adsorbed ions. The accumulation of corrosion products andconsequently of the aggressive anions due to the extremely high dissolution rates supports their adsorption and increases their surface coverage Θ, which also increases with the electrode potential *E*. Stable pit growth will be achieved when Θ exceeds a critical value Θ_{crit}. It should be large enough to prevent the formation of a continuous oxide film, i.e., the repassivation of the pit surface. In the light of this concept, a given composition of the bulk electrolyte requires a minimum electrode potentials E_p to exceed Θ_{crit} and to achieve stable pit growth. Detailed evaluation of this adsorption equilibrium yields

Copyright © 2002 Marcel Dekker, Inc.

$$E_p = a - (RT2.303)/(\gamma F)\log\{[A]\} = a + b\log\{[A]\}$$
$$a = RT(2.303)/(\gamma F)\log\{\Theta_{A,crit}/(1-\Theta_{A,crit}\} + \Delta G^{\circ}_{ad,A}/(\gamma F) + \Delta\phi_h \quad (33)$$

where $\Delta G^{\circ}_{ad,A}$ is the standard Gibbs free energy (free enthalpy) of adsorption of the aggressive anions A, $\Delta\phi_h$ is the potential drop at the standard hydrogen electrode, and γ is the electrosorption valence, which takes into account the closest approach of the anions to the metal surface because of their own dimensions.

If inhibiting anions I are present as well, they compete with the aggressive anions A for the adsorption sites according to the same type of adsorption isotherm as given in Eq. (33) with their specific ΔG°_{ad} values and bulk concentrations. Combining the equations for the inhibiting and aggressive anions leads to the critical conditions of inhibition of localized corrosion. The detailed discussion [2] yields for the inhibition potential E_I

$$E_I = a + (RT2.303)/(\Delta\gamma F)\log\{[A]/[I]\} = a + b\log\{[A]/[I]\}$$
$$a = (RT2.303)/\Delta\gamma F\log\{\Theta_{A,cirt}/\Theta_{I,cirt}\} + \Delta G^{\circ}_{ad}/(\Delta\gamma F) + \Delta\phi_h \quad (34)$$

where ΔG°_{ad} is the difference in Gibbs free energies of species A and I, $\Theta_{A,ad}$ and $\Theta_{I,ad}$ are the surface coverages of both ions, and $\Delta\gamma$ is the difference in their adsorption valences. The negative $\Delta\gamma$ value causes a positive shift of E_I with increasing [A] and decreasing [I], which is an upper potential limit of the pitting range. The small values of $\Delta\gamma$ corresponding to small differences for the approach of ions A and I to the electrode surface cause large *b* factors for Eq. (34), which is found experimentally for nitrate and perchlorate [2,58].

Pits may also be stabilized by other complicating effects. In some cases the pit mouth is covered by precipitated corrosion products such as hydroxides or even a metal cover when the dissolution occurs irregularly (Fig. 14). In these situations an ohmic drop can lead to a potential shift of the pit surface below the passivation potential. The same will hold for large and especially deep and narrow pits. Crevice corrosion may be seen as a special case of localized corrosion. In these cases ohmic drops act as stabilizing factors for pitting. Last but not least, the presence a gas bubble within a pit will cause a situation similar to that of a crevice with related ohmic drops. Hydrogen bubbles have been observed by Pickering and Frankenthal [68] within pits and served as an explanation for stable pitting. In this situation it is still not understood how the potential becomes sufficiently negative within a small pit despite a potentiostatically fixed positive value to cause hydrogen evolution. Apparently gas bubbles may be an important stabilizing factor for some special systems and later stages of pit growth.

A further factor in the stability of a growing pit is alloy components that prevent or reduce pitting. They usually accumulate within the passive layer due to their slow dissolution kinetics. The special situation of Cr has already been discussed in detail. Fe-Si alloys with more than 20 at % Si are another example. A sufficiently large Si content causes the formation of a continuous SiO_2 layer especially in acidic electrolytes [69], which prevents localized corrosion. The dissolution of SiO_2 is not enhanced by halides, which apparently is a consequence of the missing complexation of Si(IV) so that the passive layer remains protective even in the presence of a large chloride concentration. If a pit starts, a large bulk concentration of Si will lead to Si

Copyright © 2002 Marcel Dekker, Inc.

accumulation at the pit surface, which then may form a protective Si(IV)-rich film. This situation will lead to repassivation of the corrosion pit in an early stage as observed experimentally [70].

CONCLUSION

The discussion of various experimental results has shown that different effects may serve as stabilizing factors for localized corrosion. It depends on the stage of development of a corrosion pit and the environmental conditions which one is the most effective. Therefore one has to refer to the special situation under discussion. Often the controversial points of view of authors depend on the different situations that are examined and discussed. It was in the aim of this contribution to sort out the different factors and to describe the conditions in which they are effective. In this sense, localized corrosion is a very complicated process involving different effects.

The same statement holds for the nucleation of corrosion pits. Here three main mechanisms have been discussed. Again, it depends on the experimental or environmental conditions which one is the most effective and dominates the nucleation step.

Although there are many common features in localized corrosion of the different systems, one should also take into account the specific chemistry of a system. In this sense the tendency of halides to complex with metal cations is very important and seems to be the key for an understanding of the stabilization of a corrosion pit by prevention of the repassivation of a defect site within the passive layer. Enhancement of the transfer of metal cations from the oxide to the electrolyte by halides, especially the strongly complexing fluoride, holds for many metals. The special situation of Cr, which is resistant to localized corrosion, may be understood in terms of the slow dissolution kinetics of the Cr(III) salts. One should also consider the different passivation mechanisms. Metals such as Al and Cu are not passive in strongly acidic electrolytes. In these cases localized acidification by the hydrolysis of corrosion products may well serve as a stabilizing factor for pitting. Other metals such as Fe, Ni, and steels are passive even in strongly acidic electrolytes, in disagreement with the predictions of the Pourbaix diagrams. Local acidification cannot be a stabilizing effect for pitting in these cases. In summary, all explanations of stable pit growth should include chemical arguments to explain why halides are so essential for localized corrosion. Their complexing and catalytic properties for the dissolution of the passive layers should not be ignored.

Besides the possible differences and the special influence of the chemical properties of the various systems, many common features are found for localized corrosion. Electrochemical and surface analytical methods for the study of passive layers and their breakdown have been very successful in the past, and closer insight into the effective mechanisms has been achieved. STM and SFM (Scanning Force Microscopy) will give valuable information about the nucleation and very early stages of growth of corrosion pits. The application of these methods for fundamental studies of pitting corrosion has just started. Further investigations using these methods and extension to other metals will broaden the experience and knowledge and will give better insight into the mechanisms of this technologically important type of corrosion.

Copyright © 2002 Marcel Dekker, Inc.

REFERENCES

1. P. Schmutz and G. S. Frankel, *J. Electrochem. Soc. 145*:2285 (1998).
2. H.-H. Strehblow and B. Titze, *Corros. Sci. 17*:461 (1977).
3. H. Prinz and H.-H. Strehblow, *Corros. Sci. 40*:1671 (1998).
4. H.-H. Strehblow, *Werkst. Koros. 27*:792 (1976).
5. T. P. Hoar, D. C. Mears, and G. P. Rothwell, *Corros. Sci. 5*:279 (1965).
6. K. J. Vetter and H.-H. Strehblow, *Ber. Bunsenges. phys. Chem. 74*:1024 (1970).
7. N. Sato, *Electrochim. Acta 16*:1683 (1971).
8. N. Sato, K. Kudo, and T. Noda, *Electrochim. Acta 16*:1909 (1971).
9. Ya. J. Kolotyrkin, *Corrosion 19*:261t (1964).
10. T. P. Hoar and W. R. Jacob, *Nature 216*:1299 (1967).
11. A. G. Revez and J. Kruger, *Passivity of Metals* (R.P. Frankenthal and J. Kruger, eds.), The Electrochemical Society, Princeton, NJ, 1978, p. 137.
12. J. Kruger, G. G. Long, M. Kuriyama, and A. J. Goldman, *Passivity of Metals and Semiconductors* (M. Froment, ed.), Elsevier Science Publishers, Amsterdam, 1983, p. 163.
13. C. Y. Chao, L. F. Lin, and D. D. Macdonald, *J. Electrochem. Soc. 128*:1191 (1981).
14. C. Y. Chao, L. F. Lin, and D. D. Macdonald, *J. Electrochem. Soc. 128*:1194 (1981).
15. J. Augustynski, in Ref. 11, p. 285.
16. S. Meitra and E. D. Verink, in Ref. 11, p. 309.
17. T. E. Pou, O. J. Murphy, J. O. M. Bockris, L. L. Tongson, and M. Monkowski, *Proceedings, 9th International Congress on Metallic Corrosion,* Toronto, 1984, Vol. 2, p. 141.
18. G. C. Wood, J. A. Richardson, M. F. Abd Rabbo, L. P. Mapa, and W. H. Sutton, in Ref. 11, p. 973.
19. S. Szlarska-Smialowska, H. Viefhaus, and M. Janik-Czachor, *Corros. Sci. 16*:644 (1976).
20. M. Janik-Czachor and K. Kaszczyszyn, *Werkst. Korros 33*:500 (1982).
21. B. P. Löchel and H.-H. Strehblow, *Electrochim. Acta 28*:565 (1983).
22. B. P. Löchel and H.-H. Strehblow, *J. Electrochem. Soc. 131*:713 (1984).
23. W. P. Yang, D. Costa, and P. Marcus, *Oxide Films on Metals and Alloys* (B. MacDougall, R. S. Alwitt, T. A. Ramanarayanan, eds.) Proceedings Vol. 92–22, The Electrochemical Society, Princeton, NJ, 1992, p. 516.
24. S. Mischler, A. Vogel, H. J. Mathieu, and D. Landolt, *Corros. Sci. 32*:925 (1991).
25. P. Marcus and J. M. Herbelin, *Corros. Sci. 34*:1123 (1993).
26. H.-H. Strehblow, *Proceedings Corrosion 91,* NACE, Houston, 1991, p. 76/1.
27. H.-H. Strehblow, *Proceedings Corrosion Prevention,* Australasian Corrosion Association, Brisbane, Australia, November 1997.
28. C. L. Me Bee and J. Kruger, *Localized Corrosion,* NACE, Houston, 1974, p. 252.
29. W. Paatsch, *Ber. Bunsenges. Phys. Chem. 77*:895 (1973).
30. H.-H. Strehblow, *Werkst. Korros. 35*:437 (1984).
31. K. J. Vetter and H.-H. Strehblow, in Ref. 28, p. 240.
32. S. Haupt and H.-H. Strehblow, *Langmuir 3*:873 (1987).
33. B. P. Löchel and H.-H. Strehblow, *Werkst. Korros. 31*:353 (1980).
34. U. Bertocci, *Advances in Localized Corrosion,* NACE Proceedings of 2nd International Conference on Localized Corrosion, Orlando, FL (H. S. Isaacs, U. Bertocci, J. Kruger, and S. Smialowska, eds.), NACE, Houston, 1987. p. 127.
35. J. Steward and D. E. Williams, in Ref. 34, p. 131.
36. S. P. Mattin and G. T. Burstein, *Progress in the Understanding and Prevention of Corrosion* (J. M. Costa and A. D. Mercer, eds.), Institute of Materials, 1993, p. 1109.

Copyright © 2002 Marcel Dekker, Inc.

37. H.-H. Strehblow, dissertation, Freie Universität, Berlin, 1971.
38. K. J. Vetter and F. Gorn, *Electrochim. Acta 18*:321 (1973).
39. S Benamar, thesis, Université Pierre et Marie Curie, Paris, 1998.
40. I. Milosev and H.-H. Strehblow, *Biomed. Mater. Res.,* submitted.
41. K. E. Heusler and L. Fischer, *Werkst. Korros. 27*:551 (1976).
42. H.-H. Strehblow, B. Titze, and B. P. Löchel, *Corros. Sci. 19*:1047 (1979).
43. H.-H. Strehblow and B. P. Löchel, *Passivity of Metals and Semiconductors* (M. Froment, ed.), Elsevier Science Publishers, New York, 1983, p. 379.
44. B. P. Löchel and H.-H. Strehblow, *J. Electrochem. Soc. 131*:522 (1984).
45. *Stability Constants of Metal Ion Complexes,* Suppl. 1, Special Publ. 25, The Chemical Society, London, 1971, p. 171.
46. Ref. 45, p. 167.
47. Ref. 45. p. 217.
48. W. Khalil, S. Haupt, and H.-H. Strehblow, *Werkst. Korros. 36*:16 (1985).
49. F. A. Cotton and G. Wilkinson, *Anorganische Chemie,* Verlag Chemie, Weinheim, 1980, p. 920.
50. *Handbook of Chemistry and Physics,* CRC Press, Boca Raton, FL, 1978, p. B105.
51. V. Maurice, V. Inard, and P. Marcus, Proceedings of the Symposium *Critical Factors in Localized Corrosion III,* 194th meeting of the Electrochemical Society, Boston, November 2–6, 1998 (R. G. Kelley, P. M. Natishan, G. S. Frankel, and R. C. Newman, eds.), The Electrochemical Society Proceedings Series, PV 98-17, Pennington, NJ (1998), pp. 552–562.
52. J. Kunze, diploma thesis, Heinrich-Heine-Universität, Düsseldorf, 1998, p. 64.
53. H.-H. Strehblow and J. Wenners, *Z. Phys. Chem NF, 98*:199 (1975).
54. H. Kaesche, *Die Korrosion der Metalle,* Springer, Berlin 1979, p. 268
55. H.-H. Strehblow and M. B. Ives, *Corros. Sci.l6*:317 (1976).
56. H.-H. Strehblow and J. Wenners, *Electrochim. Acta 22*:421 (1977).
57. Th. R. Beck and R. C. Alkire, *J. Electrochem. Soc. 126*:1662 (1979).
58. H.-H. Strehblow, *Habilitationsschrift,* Freie Universität, Berlin, 1977, p. 53.
59. G. S. Frankel, J. R. Scully, and V. Jahnes, *J. Electrochem. Soc. 143*:1834 (1996).
60. A. Seghal, D. Lu, and G. S. Frankel, *J. Electrochem. Soc. 145*:2834 (1998).
61. G. R. Engelhardt, A. D. Davydov, and T. B. Zhukova, *Sov. Electrochem. 26*:888 (1990).
62. J. Newman, D. N. Hansen, and K. J. Vetter, *Electrochim. Acta 22*:829 (1974).
63. G. Engelhardt and H.-H. Strehblow, *J. Electroanal. Chem. 365*:7 (1994).
64. P. Heimgartner and H. Böhni, *Corrosion 41*:715 (1985).
65. F. H. Hunkeler and H. Böhni, *Werkst. Korros. 34*:593 (1983).
66. H.-H. Strehblow, K. J. Vetter, and A. Willgallis, *Ber. Bunsen Ges. Phys. Chem. 75*:823 (1971).
67. K. J. Vetter and H.-H. Strehblow. *Ber. Bunsenges. Phys. Chem. 74*:449 (1970).
68. H. W. Pickering and R. P. Frankenthal, in Ref. 28, p. 261.
69. C. Schmidt and H.-H. Strehblow, *J. Electrochem. Soc. 145*:834 (1998).
70. U. Wolff, dissertation, Technische Universität Dresden, 1999.

Copyright © 2002 Marcel Dekker, Inc.

9

Sulfur-Assisted Corrosion Mechanisms and the Role of Alloyed Elements

Philippe Marcus
Laboratoire de Physico-Chimie des Surfaces, CNRS, Université Pierre et Marie Curie, Ecole Nationale Supérieure de Chimie de Paris, Paris, France

INTRODUCTION

Sulfur is an element which is found in the bulk of most materials (in saturated solid solution and often in inclusions) as well as in many environments (in the form of, e.g., HS^-, H_2S, SO_2, $S_2O_3^{2-}$).

The role of sulfide inclusions in corrosion has been recognized in early works. The fact that sulfur-containing species are detrimental to the resistance of metals and alloys to localized corrosion has been established for a long time but the mechanisms have remained unclear until recently. In the area of passivity breakdown, where substantial research effort has been expended for several years, the effects of chloride ions have been investigated much more than the effects of sulfur. The aim of this chapter is to review the fundamental aspects of the mechanisms of S-induced corrosion, with special emphasis on the role played by adsorbed (or chemisorbed) sulfur.

In the first sections of this chapter, the basic effects of adsorbed sulfur on anodic dissolution, on passivation, and on the breakdown of passive films are presented. In a subsequent section the effects of alloyed elements (essentially Cr and Mo) are presented and the way in which they can counteract the detrimental influence of sulfur is emphasized. In the next section, implications of the mechanisms of sulfur-induced corrosion for different areas of practical importance are given, with connections to the related chapters of this book. In the last section of this chapter, the thermodynamic predictions of the conditions of adsorption of sulfur on metal surfaces in water are given.

FUNDAMENTAL ASPECTS OF SULFUR-INDUCED CORROSION

The basic concepts and the associated mechanisms underlying the effects of adsorbed sulfur on the corrosion of metals and alloys are presented here. They have been derived to a large extent from studies performed on well-defined metal and alloy

Copyright © 2002 Marcel Dekker, Inc.

surfaces. In many cases, oriented single crystals have been used to control the structure of the surface on which the corrosion reactions were investigated. Controlled amounts of sulfur in the range of a monolayer were produced prior to the electrochemical measurements by dosing the surface with gaseous H_2S. Surface science techniques, including Auger electron spectroscopy (AES), electron spectro-scopy for chemical analysis (ESCA), also called X-ray photoelectron spectroscopy (XPS), low-energy electron diffraction (LEED), and a more specific radiochemical technique utilizing the ^{35}S radioisotope, were combined to analyze the surface prior to and after the electrochemical tests, in order to relate the electrochemical and corrosion behavior with the chemical composition and the structure of the surface. This approach has allowed us to determine the mechanisms of the sulfur-assisted corrosion reactions on an atomic scale.

Activation (or Acceleration) of Anodic Dissolution by Adsorbed Sulfur

The first studies were conducted on Ni [1–3] and Ni-Fe [4] single crystals with well-controlled coverages of radioactive sulfur. They clearly demonstrated that adsorbed sulfur accelerates the anodic dissolution of the metal and the alloys. This effect is seen in Figure 1, where the polarization diagrams for a nickel-iron single-crystal alloy [Ni-25Fe(100)(at %)] with and without adsorbed sulfur are shown. Two major findings are apparent from the measurements: (a) a significant increase

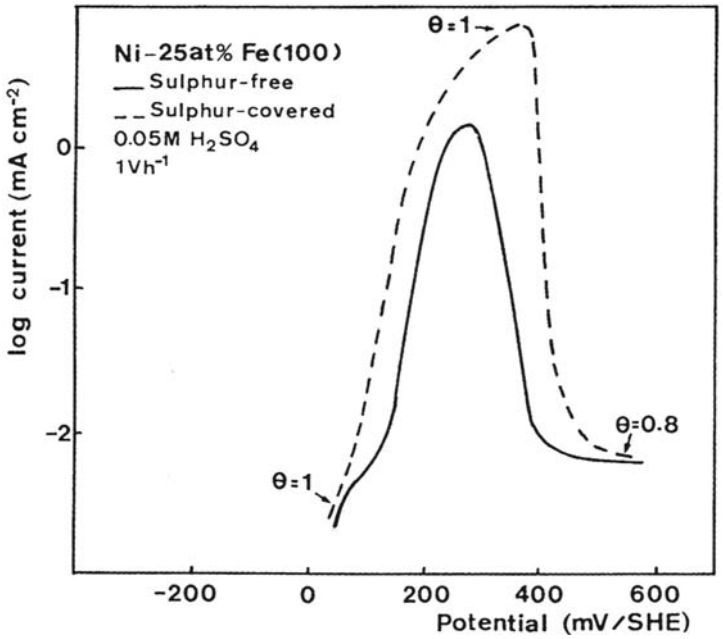


Figure 1 The influence of adsorbed sulfur on the *i-E* diagram for Ni-25Fe (at %) single crystal [(100) face] in 0.05 M H_2SO_4. θ is the coverage of the surface by adsorbed sulfur, measured with the radiochemical technique (^{35}S radiotracer).

Copyright © 2002 Marcel Dekker, Inc.

in anodic current density is observed when the surface is covered by a monolayer of adsorbed sulfur, showing that the dissolution is accelerated by the presence of sulfur, and (b) the surface sulfur is highly stable, since it remains adsorbed during dissolution of the metal. This result was established by the measurements of the coverage, denoted by θ in Figure 1. This gives evidence of the catalytic nature of the accelerating effect of adsorbed sulfur on the dissolution. In this way, a microscopic amount of adsorbed sulfur can stimulate the dissolution of a significant amount of material (about 1 μm of alloy is dissolved in the active region of Figure 1 under the catalytic action of a monoatomic layer of adsorbed sulfur). The catalytic effect of a monolayer of adsorbed sulfur on anodic dissolution of metals and alloys is summarized in the schematic *i-E* diagram of Figure 2 with, in the inset, potential shifts measured with adsorbed sulfur on different metals and alloys. Since the first direct demonstration of the accelerating effect of dissolution by adsorbed sulfur, which was for nickel and nickel-iron alloys, the more general nature of this effect has been revealed by similar experiments on nickel alloy 600 [5,6] and on austenitic stainless steels [7]. The acceleration factor *R* (ratio of the current densities at the maximum of the active peak with and without adsorbed sulfur) for nickel-base and iron-base alloys are reported in Table 1. Values in the range 5 to 12 have been observed. This striking effect has been attributed to a weakening of the metal-metal bonds induced by adsorbed sulfur, which leads to a lowering of the

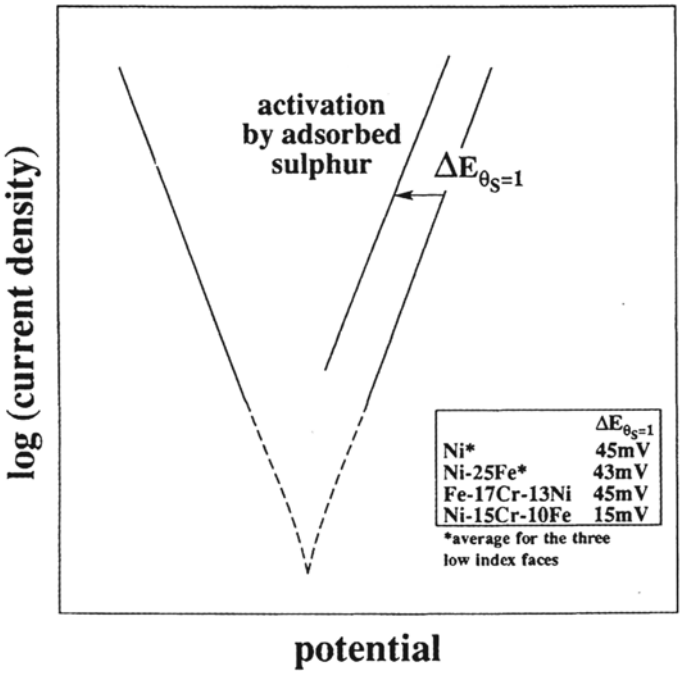


Figure 2 Schematic *i-E* plots showing the effect of adsorbed sulfur on anodic dissolution. Inset: Potential shift ($\Delta E_{\theta_s = 1}$) induced by a complete monolayer of adsorbed sulfur on different metals and alloys ($\Delta E_{\theta_s = 1}$ is measured at half-maximum of the active peak of the sulfur-free surface).

Copyright © 2002 Marcel Dekker, Inc.

Table 1 Ratio (R) of the Current Densities at the Maximum of the Active Peaks with and without Adsorbed Sulfur[a]

Metal or alloy	R	Reference
Ni-S_{ads}/Ni (average on the three low-index faces)	7.7	2
Ni-25Fe-S_{ads}/Ni-25Fe (average on the three low-index faces)	5.5	4
Fe-17Cr-13Ni-S_{ads}/Fe- 17Cr-13Ni [(100) face]	7	7
Ni-15Cr-10Fe-S_{ads}/Ni- 15Cr-10Fe	12	5

[a]Coverages of the surfaces by preadsorbed sulfur are (in 10^{-9} g/cm^2): 42 on Ni(100), 47 on Ni(111), 44 on Ni(110), 40 on Ni-25Fe (100), 42 on Ni-25Fe(111), 41 on Ni-25Fe (110), 40 on Fe-17Cr-13Ni(100), and 40 on Ni-15Cr-10Fe.

activation energy barrier for the passage of a metal atom from the surface to the solution. This mechanism is shown schematically in Figure 3 [8]. The existence of a dipole $M^{\delta+} - S^{\delta-}$ associated with the presence of sulfur can also promote the anodic dissolution.

The influence of sulfur can be strongly localized if the sulfur is not homogeneously distributed over the surface but adsorbed in specific sites, such as surface defects, where sulfur atoms are more tightly bonded.

Direct observation of the dissolution of sulfur-modified Ni(100) [9] using *in situ* scanning tunneling microscopy (STM) is in agreement with the previously shown effects of adsorbed S on dissolution (including the enhanced dissolution and the stability of the S layer). It also provides structural data at the atomic scale, indicating that the dissolution of nickel atoms is taking place at step edges, with a displacement of adsorbed S atoms from the edge of the upper terrace to the adjacent lower terrace, as shown in Figure 4.

On Cu, it was also shown that the anodic dissolution, in a mildly alkaline borate buffer solution, is catalyzed by a submonolayer of sulfur and that S remains adsorbed on the copper surface [10].

The anodic dissolution of iron in acidic medium is also accelerated by H_2S [11].

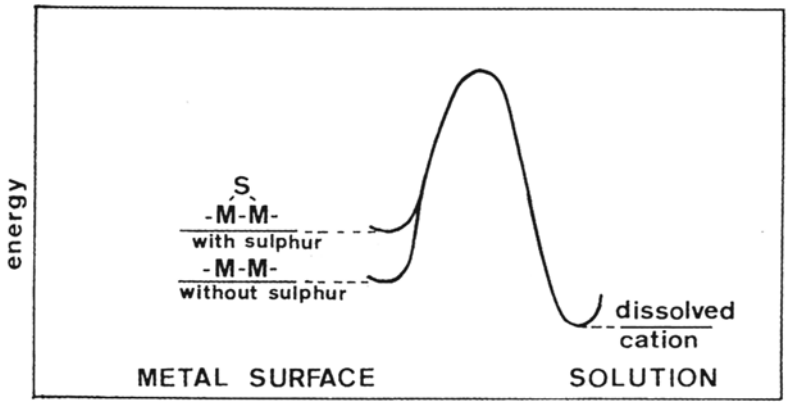


Figure 3 Weakening of the metal-metal bond by adsorbed sulfur and acceleration of the dissolution of the metal.

Copyright © 2002 Marcel Dekker, Inc.

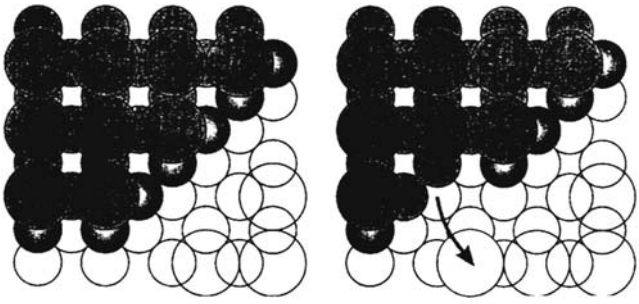


Figure 4 Model of the anodic dissolution process of sulfur-covered Ni(100) electrodes, showing dissolution of two Ni atoms from the step edge and displacement of an S atom from the upper terrace to a fourfold hollow site on the lower terrace (small circles denote Ni atoms, large circles denote S atoms, the gray color indicates atoms of the upper terrace). (Adapted from Ref. 9.)

The major conclusion of the results reviewed in this section is that a monoatomic layer of sulfur can promote the dissolution of macroscopic amounts of material. This gives evidence of a direct link between the atomic-level interactions of adsorbed sulfur atoms with metal surfaces and their macroscopic manifestations in corrosion.

Blocking or Retarding Effect of Adsorbed Sulfur on Passivation

Effect on the Growth of the Passive Film

Another important effect of adsorbed sulfur that was observed first on Ni [1–3] and later on Ni-Fe alloys [4] is the poisoning of passivation. This effect takes place above a critical coverage of the surface by sulfur that was found to be 0.7–0.8 monolayer. This effect of sulfur is observed in the *i-E* diagram shown previously in Figure 1, where the passivation potential of the surface covered by a complete monolayer of sulfur ($\theta = 1$) is shifted (by ~100mV) to a more anodic value with respect to the sulfur-free surface. In using the ^{35}S radiotracer, it was demonstrated that the desorption (or electro-oxidation) of ~20% of the full monolayer is necessary to allow the passive film to be formed. The retarding effect of sulfur on the growth of the passive film is caused by blocking the sites of adsorption of hydroxyl ions, which are the precursors in the formation of the passive layer. X-ray photoelectron spectroscopy (XPS) measurements have revealed that in the presence of adsorbed sulfur the adsorption of OH groups is not totally inhibited, but the OH groups on the surface are more diluted and thus the disproportionation reaction of adjacent OH groups is prevented. A schematic representation of this mechanism is given in Figure 5. In this way the oxide film, which would normally passivate the surface, is not formed.

Effect on the Passivation Kinetics

Measurements of the passivation kinetics by means of potential steps applied to surfaces without or with adsorbed sulfur have revealed that the time to complete passivation increases when the surface is covered by adsorbed sulfur. This effect is

Copyright © 2002 Marcel Dekker, Inc.

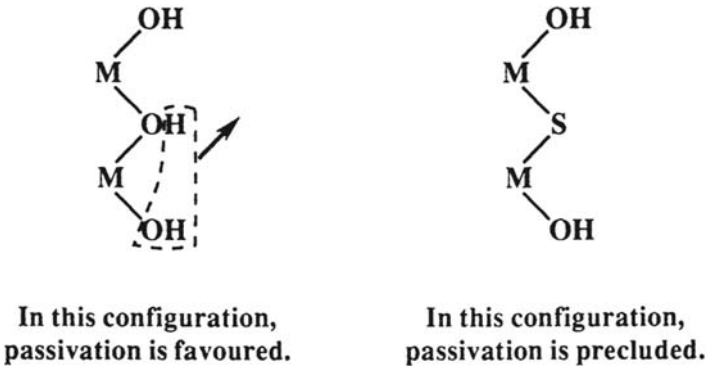


Figure 5 The mechanisms of the blocking effect of adsorbed sulfur on passivation.

represented in the *i-t* diagram of Figure 6. A rapid decrease of the current immediately after the potential step is observed for the clean surface, whereas for the sulfur-covered surface the current density decreases slowly, indicative of a slow process of lateral growth of the film on top of the remaining fraction of a monolayer of adsorbed sulfur. This is consistent with the view that a complete monolayer of sulfur inhibits the nucleation of the oxide, as observed on nickel, whereas a fraction of a monolayer does not inhibit the nucleation but may diminish the density of nucleation sites for the oxide and make the lateral growth of the film more difficult. These two effects can slow down the passivation kinetics.

Such kinetic effects have been observed on sulfur-contaminated nickel [8], on nickel alloy 600 [6], and on copper [12].

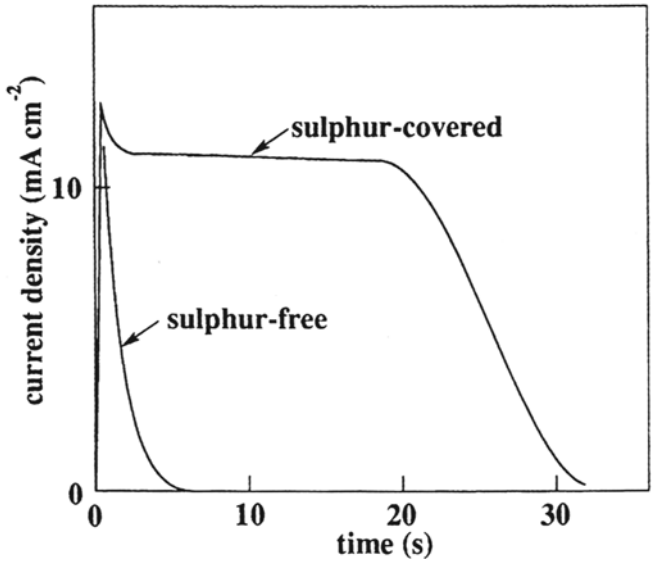


Figure 6 The effect of adsorbed sulfur on the passivation kinetics of nickel [Ni(111), 0.05 M H_2SO_4, 540 mV/SHE].

Copyright © 2002 Marcel Dekker, Inc.

Effect on the Structure and Properties of the Passive Film

Below the critical sulfur coverage of 0.7–0.8 monolayer on Ni, the passive film grows on top of the remaining adsorbed sulfur. However, the structure and the properties of the film formed on the sulfur-contaminated surface are modified. A study [2] by reflection high-energy electron diffraction (RHEED) of the structure of the passive films formed on nickel single crystals [Ni(111)] has shown that, in the absence of sulfur, a crystalline film epitaxial with the substrate is formed (a fact that has been confirmed by both ex situ and in situ atomic resolution imaging of the film by scanning tunneling microscopy [13–15]), whereas in the presence of sulfur the epitaxial growth is disrupted and a more defective polycrystalline film is obtained. Accordingly, the current density in the passive state is about four times larger for a film formed with sulfur at the metal-oxide interface. XPS measurements of the binding energy of sulfur (S 2*p*) provide evidence that it remains at the interface because the binding energy remains close to that of sulfur bonded to the metallic surface (~ 162 eV).

Anodic Segregation of Sulfur

The concept of anodic segregation was first proposed after the discovery that sulfur present as an impurity in the bulk of Ni and of Ni-25Fe alloys is enriched on the surface during anodic dissolution [2,4,16]. This phenomenon was also observed on Fe-50Ni [17] and on alloy 600 [5,18]. The experiments were performed on Ni and Ni-Fe alloys that had been doped with sulfur prior to the electrochemical treatments. The introduction of radioactive S into the bulk was performed by exposing the samples to an H_2S-H_2 gas mixture (with ^{35}S-labeled H_2S) at high temperature (1000 to 1200°C) under thermodynamic conditions in which sulfur is in solid solution in the metal or the alloy. Rapid quenching to room temperature after the high-temperature treatment avoids sulfide precipitation. The *i-E* curves recorded on a sulfur-free (i.e., annealed in pure hydrogen) Ni electrode and on Ni containing 50 ppm sulfur are shown in Figure 7a. The sulfur-free Ni sample exhibits the normal active-passive transition observed in 0.05 M H_2SO_4. The sample with bulk sulfur exhibits a completely different behavior: there is no active-passive transition, and the current density increases with increasing potential in the whole range of potentials corresponding to the passive state of sulfur-free Ni. The results of the measurements of the sulfur concentration on the surface, using radioactive sulfur, are shown in Figure 7a. They demonstrate that sulfur segregates on the surface during dissolution of the electrode with bulk sulfur (the measured values of the surface sulfur concentration are denoted $S_{segregated}$ in Fig. 7a). The values denoted $S_{exposed}$ in Figure 7a represent the integrated amount of sulfur that became available on the surface due to the dissolution of the metal matrix. Comparison of the data for $S_{segregated}$ and $S_{exposed}$ revealed that all the sulfur present in the bulk remains on the surface during dissolution, up to a surface concentration of 40×10^{-9} g/cm^2, which corresponds to a complete monolayer of sulfur on Ni(100). Above this surface coverage, nickel sulfide precipitates and then a thin layer of nickel sulfide is formed. The amount of sulfur in this layer is ~40×10^{-8}g/cm^2, which corresponds to ~25 Å of Ni_3S_2. Sulfur in excess of this amount is dissolved. The formation, before reaching the passivation potential, of a complete monolayer of sulfur and the subsequent

Copyright © 2002 Marcel Dekker, Inc.

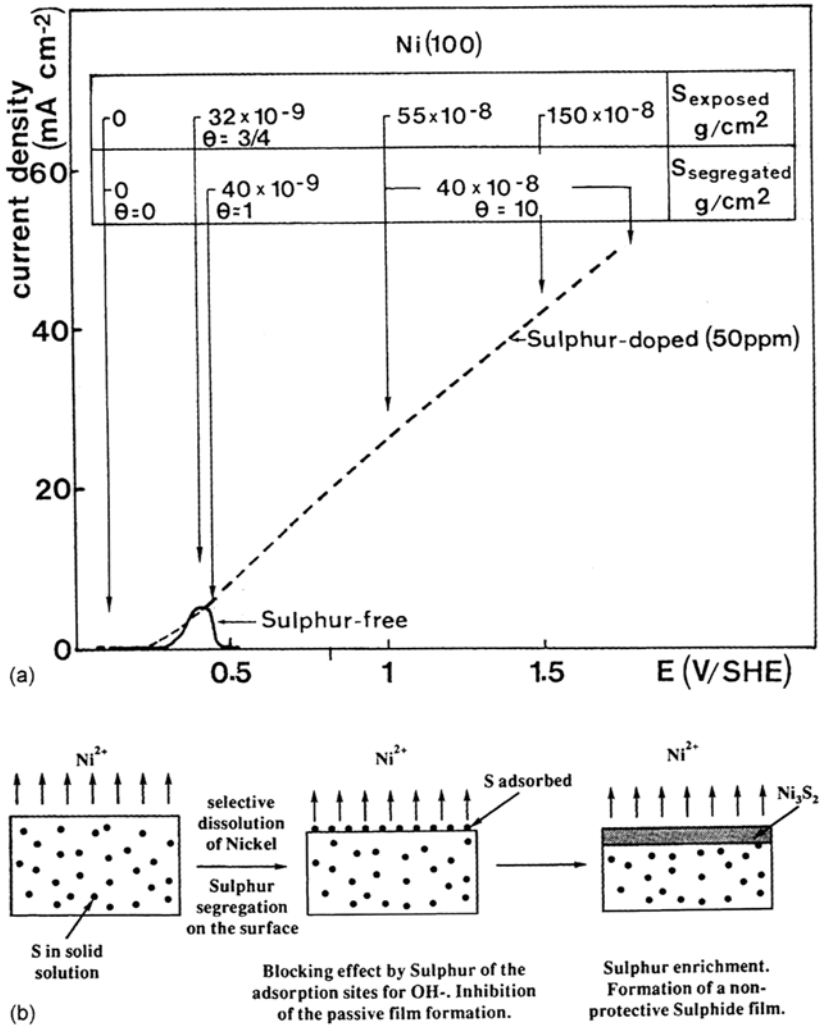


Figure 7 (a) Surface enrichment of sulfur during anodic dissolution: *i-E* curves and radiotracer measurements of the sulfur concentration on the surface of Ni(100) containing 50 ppm of sulfur (0.05 M H_2SO_4, 1 V h^{-1}). (b) The mechanism of anodic segregation.

growth of a sulfide layer preclude the formation of the passive oxide film. The sulfide layer is not protective and thus high corrosion rates are obtained in the range of potentials in which pure Ni is normally passivated. This phenomenon was called anodic segregation [3,4]. The anodic segregation rate depends on the sulfur content of the material and on the rate of anodic dissolution. Because of differences in dissolution rates for single-crystal surfaces of different crystallographic orientation, the sensitivity to sulfur increases in the order (111) ≤ (100) < (110), which is the order of increasing dissolution rates observed for Ni in 0.05 M H_2SO_4 [2]. The mechanism of anodic segregation is represented in Figure 7b.

Copyright © 2002 Marcel Dekker, Inc.

Passivity Breakdown Caused by Interfacial Sulfur

After the formation of the passive film on a bare metal surface, slow dissolution of the metal cations continues, involving dissolution at the passive film surface and transport of ions through the oxide (see Chap. 6). The question then arises as to where the bulk impurities, e.g., sulfur, go during this process. This question was addressed in a detailed investigation of Ni and Ni-Fe alloys that were doped with radioactive sulfur in order to trace the path taken by the sulfur atoms during the slow dissolution in the passive state [19]. The radiochemical results gave direct evidence that sulfur present in the bulk accumulates at the metal–passive film interface. The enrichment rate was shown to be proportional to the sulfur content in the metal and to the dissolution current density. Above a critical concentration of sulfur at the interface (metal-oxide), breakdown of the passive film was observed. This critical concentration of interfacial sulfur was measured with radioactive sulfur and found to be close to one monolayer of sulfur (i.e. $\sim 40 \times 10^{-9}$ g/cm^2). The loss of adherence (or the decohesion) at the interface for this critical coverage has been attributed to aweakening of the bonding of the oxide to the substrate caused by sulfur. The nucleation of the sulfide that is expected to take place when the sulfur concentration exceeds a complete monolayer may be responsible for the observed local breakdown of the film and pitting. The defects that are likely to exist at the interface could serve as specific sites for the nucleation of the sulfide, once a quasi-complete monolayer of sulfur has been accumulated at the interface. A schematic representation of the proposed mechanism of the sulfur-induced breakdown of the passive film is shown in Figure 8.

It is to be noted that the three following factors are in favor of sulfur remaining at the metal–passive film interface: (a) the sulfur-metal chemical bond is very strong (see Chap. 2), (b) the solubility of S in nickel oxide (which constitutes the inner part of the passive film on Ni and Ni-Fe alloys) is very low, and (c) the electric field across the passive film, which assists the passage of cations from the metal–passive film interface to the passive film–solution interface, should impede the transport of sulfur, which would be negatively charged.

The Joint Action of Sulfur and Chloride Ions

The passivity breakdown and pitting caused by Cl^- ions has been the subject of an enormous amount of work. This area has been reviewed in Chapter 8.

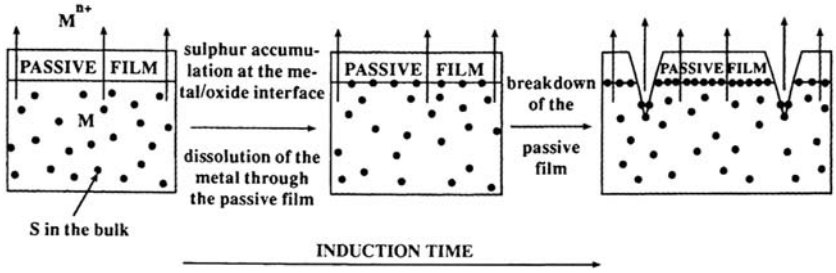


Figure 8 Mechanism of the breakdown of the passive film induced by enrichment of sulfur at the metal–passive film interface.

Copyright © 2002 Marcel Dekker, Inc.

In the preceding parts of this chapter we have seen that S alone can enhance the dissolution, block or retard the growth of the passive film, and cause passivity breakdown and pitting by enrichment at the metal-film interface. All these effects can evidently also take place in the presence of Cl^-. A major difference between the mechanisms of action of Cl^- and S is that S does not seem to interact directly with the oxide surface as strongly as Cl^-.

The effect of sulfur species and chloride ions has been studied in some detail in the case of corrosion of stainless steels in solutions containing thiosulfate ($S_2O_3^{2-}$) and chloride (Cl^-) ions [20–27].

It has been demonstrated [27] that $S_2O_3^{2-}$ is not reduced on the surface of the passive film formed in neutral solution on an Fe-17Cr alloy, whereas the reduction to adsorbed sulfur or sulfide does take place on the nonpassivated alloy surface. In this study, the combined action of chloride and sulfur was also investigated. The conclusion was that with 30 ppm thiosulfate added to the Cl^--containing solution (0.02 M) at pH 7, the initial breakdown of the passive film is caused by Cl^- and the thiosulfates do not play a major role in this step, whereas the presence of thiosulfate has a drastic effect on the subsequent step, the occurrence of stable pits. With Cl^-, and without $S_2O_3^{2-}$, unstable pits (i.e., pits that are repassivated) are formed over a wide range of potentials below the classical pitting potential corresponding to the formation of stable pits, whereas with the thiosulfates, the reaction on the bare metal surface produces reduced sulfur (adsorbed sulfur or sulfide), which precludes repassivation and causes a marked increase of stable pits at low potential. This effect is shown in Figure 9. The formation of adsorbed sulfur by reaction of $S_2O_3^{2-}$ with the bare metal surface was demonstrated by XPS measurements of the binding energy of the sulfur core level electrons (S2*p*), which was found to be 169eV for adsorbed thiosulfate on the passive film surface and 162eV after reduction of the thiosulfate on the Fe-17% Cr alloy surface. In previous works on the effects of addition of $S_2O_3^{2-}$ on corrosion of stainless steels [21,25], such a mechanism had been hypothesized, but direct experimental evidence was lacking. A synergistic effect of Cl^- and $S_2O_3^{2-}$ on pitting corrosion was also observed on 310 stainless steel [28]. Type 304L stainless steel suffers stress corrosion cracking in chloride solutions with 10^{-3} to 10^{-1} M $S_2O_3^{2-}$ (at 353 K). It was shown that the cracks initiated at pits [29] and the authors concluded that $S_2O_3^{2-}$ affects the initiation process of pitting and cracking.

To summarize, a likely mechanism for the combined action of chlorides and sulfur is the local breakdown of the film by Cl^-, which then permits all the effects of S shown above on metal and alloy surfaces to take place. A major consequence is the stabilization of otherwise unstable (or metastable) pits. This mechanism is consistent with the lower pitting potential and/or shorter incubation time observed experimentally.

Sulfur species in aqueous solution may also cause directly the breakdown of the film if the sulfide is thermodynamically more stable than the oxide, a case that would require a high concentration of the sulfur species in solution to provide a reaction of the type $M_xO_y + zH_2S \leftrightarrow M_xS_z + yH_2O + 2(z–y)H^+ + 2(z–y)e^-$.

Sulfide inclusions have been known for many years to be detrimental to the corrosion resistance of steels and extensive studies have been performed on stainless steels ([30–33] and references in Chapter 10). Preferential adsorption of Cl^- on sulfide inclusions has been suggested to be an important step in the corrosion mechanism. The precise mechanism of the joint action of Cl^- and the sulfide is not fully elucidated.

Copyright © 2002 Marcel Dekker, Inc.

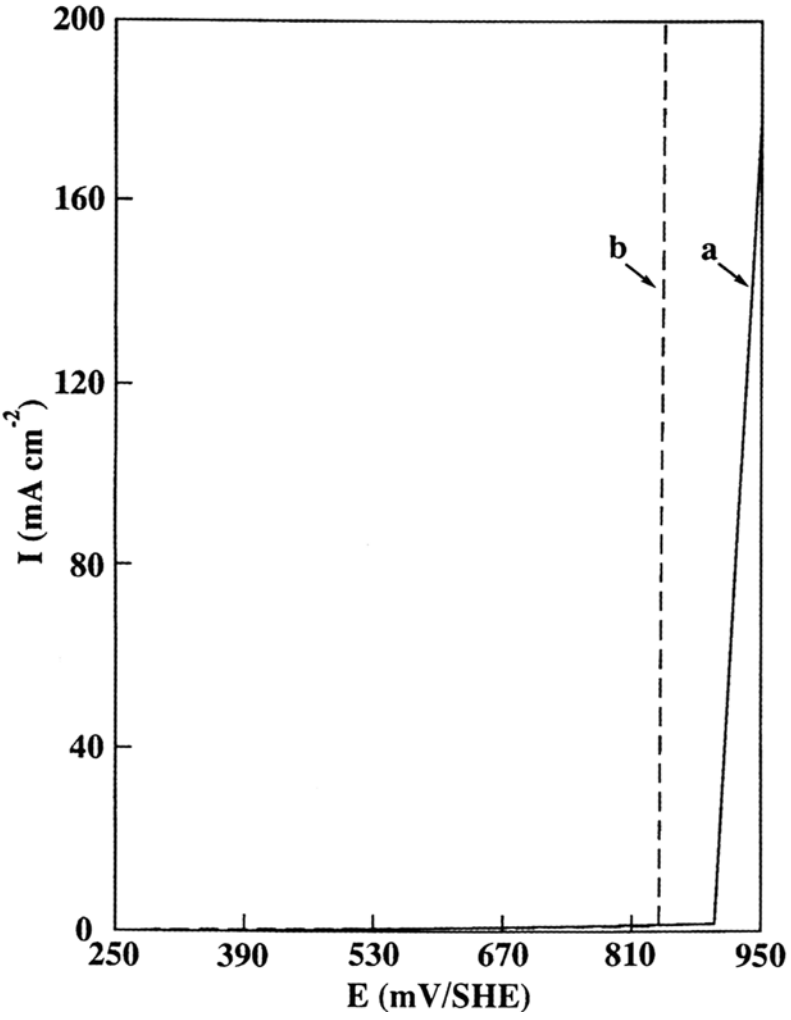


Figure 9 The joint action of $S_2O_3^{2-}$ and Cl^- on passivity breakdown and localized corrosion of an Fe-17Cr alloy. (a) 0.02 M Cl^-; (b) 0.02 M Cl^- + 30 ppm $S_2O_3^{2-}$. $S_2O_3^{2-}$ is reduced on the alloy surface, as evidenced by the difference in the binding energy of S 2*p* for $S_2O_3^{2-}$ (169 eV) and S_{ads} (162 eV).

COUNTERACTING THE SULFUR EFFECTS WITH ALLOYED ELEMENTS

The Role of Molybdenum

Numerous electrochemical and surface analytical studies have been performed to understand the effect of alloyed molybdenum on the corrosion resistance of stainless steels (see, e.g., the section on the role of Mo in Mo-containing austenitic stainless steels in Chapter 7).

Copyright © 2002 Marcel Dekker, Inc.

In order to reach a better understanding of the role of molybdenum in the presence of sulfur, studies were undertaken on simple systems, i.e., binary and ternary single-crystal alloys on which the surface concentrations of sulfur and of Mo could be precisely measured by radiochemical (^{35}S) and spectroscopic (XPS) techniques. The experiments performed on nickel-molybdenum alloys [Ni-2Mo and Ni-6Mo(at %)] provided the first direct evidence of a specific surface interaction between molybdenum and adsorbed sulfur leading to the removal of sulfur from the surface and thereby the attenuation or the disappearance of the detrimental effects of adsorbed sulfur [34,35].

The most conclusive experiments were done in (a) preadsorbing, in a gas mixture of H_2S and H_2, a known amount of sulfur on the well-defined surface of an Ni-2 at % Mo alloy [the (100) crystallographic orientation of this fee alloy was used] and (b) measuring the variation of the sulfur coverage during anodic dissolution in the active state (at 320mV/SHE) in 0.05 M H_2SO_4. The first and essential observation was that the sulfur coverage decreases, whereas it had been found to remainconstant on pure Ni (discussed earlier in this chapter). The precise measurement of the desorption kinetics is shown in Figure 10 in terms of sulfur coverage (weight per cm^2 and number of sulfur atoms per metal atom on the surface) versus the amount of dissolved material (expressed in number of dissolved atom layers). The initial coverage corresponds to saturation of the surface by adsorbed sulfur [42 ng/cm^2, one S atom for two M atoms on the surface of the (100) face]. Because sulfur was initially present only on the surface, the results demonstrate that a surface reaction between Mo and sulfur is the cause of the loss of the surface sulfur. This is a dynamic process in which the dissolution of the alloy brings Mo to the surface, which bonds to adsorbed sulfur and is then dissolved with it. A theoretical model was proposed for the mechanism of the effect of Mo. In this model, one S atom adsorbed on the surface reacts with k Mo atoms of the surface plane and the cluster that is formed (in which O or OH may participate) is dissolved. It was shown that the sulfur coverage on the surface after dissolution of (n+ 1) atom planes of the alloy, denoted $\theta_s(n + 1)$, has the following expression [34]:

$$\theta_s(n + 1) = \theta_s(n) - [(\theta_s(n))^2(C^s_{Mo})^k]$$

where C^s_{Mo} is the surface concentration of Mo, which was assumed to be identical to the bulk content of Mo, and k is the number, defined above, of Mo atoms required to form with sulfur a cluster that is dissolved. This equation was used to fit the experimental variation of the sulfur coverage. The results for $k = 1, 2, 3$ are computed in Figure 10. The curve with $k = 2$ provides a very good fit to the experimental curve. Similar findings were obtained with Ni-6% Mo (100). These results strongly support the proposed mechanism in which, on a (100) surface, two Mo atoms bond to and remove one adsorbed S atom. It is to be noted that in this mechanism the passive film is not directly involved, but of course the major consequence of the removal of sulfur by Mo is that the passive film may be formed on an otherwise blocked surface. The same model has been used successfully to interpret in a quantitative manner the fact that on other Ni-Mo alloys the surface enrichment of sulfur by anodic segregation of bulk sulfur was very limited [36] compared with what had been reported previously for Ni [2]. On Ni-6%Mo (100) with 32 ppm sulfur in the bulk, the coverage by sulfur measured after different times of anodic polarization in the active region (in 0.05 M H_2SO_4) was always less than a complete monolayer. The theoretical amount of sulfur, calculated using an equation similar to that given

Copyright © 2002 Marcel Dekker, Inc.

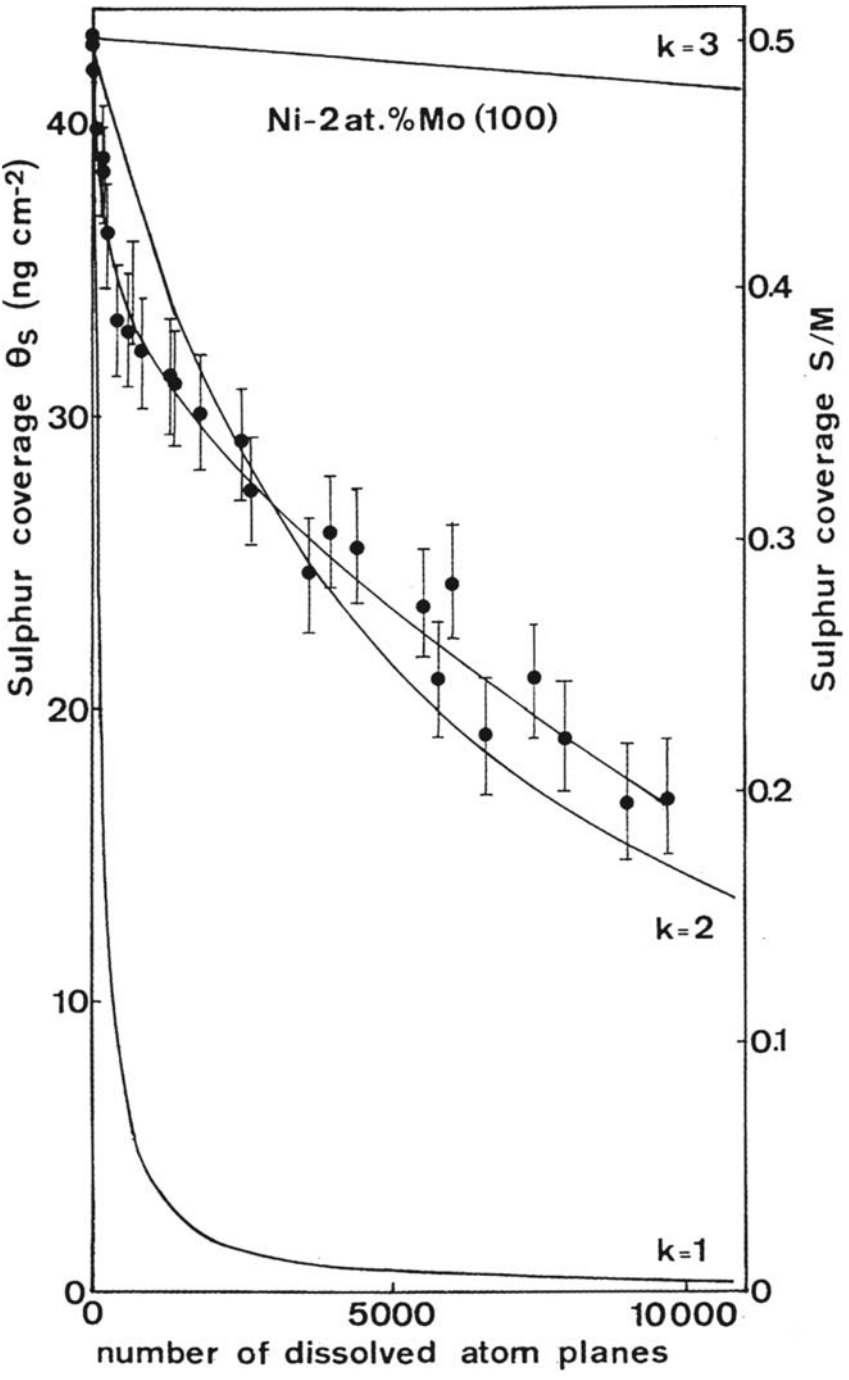


Figure 10 The loss of surface sulfur induced by molybdenum (experimental and theoretical curves).

above for the Mo-induced desorption of adsorbed S, but in which a term accounting for the supply of sulfur by the dissolution of the alloy was added, gave a good fit to the experimental values when the value of k was taken equal to 2. This confirmed the validity of the mechanism in which two Mo atoms bond to one sulfur atom and

Copyright © 2002 Marcel Dekker, Inc.

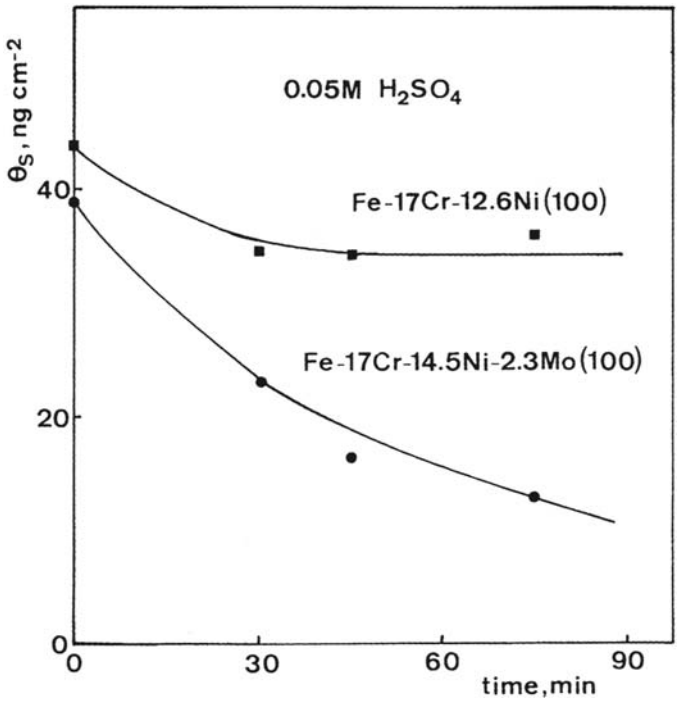


Figure 11 Mo-induced removal of sulfur adsorbed on a single-crystal alloy of composition close to 316 stainless steel. The measurements on an alloy of composition close to 304 stainless steel are shown for comparison. The coverage of sulfur was measured with radioactive sulfur (^{35}S).

remove it from the surface by dissolution of the cluster formed. More recently, the molybdenum-induced removal of adsorbed sulfur has been observed in measurements performed on single-crystal alloys with chemical compositions close to the compositions of type 304 and 316 stainless steels, i.e., without and with molybdenum, respectively [7]. After preadsorbing sulfur on the surfaces of the two alloys, the sulfur coverage was measured as a function of time of exposure of the alloys to 0.05 M H_2SO_4 at the corrosion potential. The results are shown in Figure 11. The monolayer of sulfur adsorbed on the 304-type stainless steel is stable in 0.05 M H_2SO_4 at the corrosion potential, whereas, owing to the presence of molybdenum, the desorption of sulfur is observed on the 316-type stainless steel. The model used above gives a fit of the experimental data for $k \sim 1$, instead of $k = 2$ for the Ni-Mo alloys. This suggests that chromium lowers the number of Mo atoms required to promote the dissolution of sulfur.

The Role of Chromium

The role played by alloyed Cr in the presence of sulfur has been investigated in detail on Ni-based alloys with various concentrations of Cr in the range 8 to 34% (a range of concentration within which alloys 600 and 690 are situated) [5,6,18]. The combined electrochemical, radiochemical (^{35}S), and spectroscopic (XPS) measurements

Copyright © 2002 Marcel Dekker, Inc.

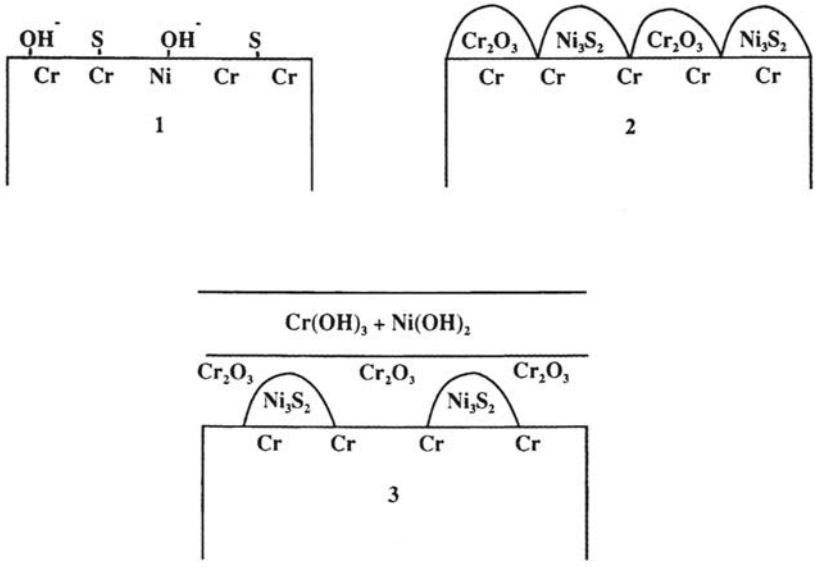


Figure 12 The mechanism of the antagonistic effects of chromium and sulfur on the corrosion resistance of Ni-Cr-Fe alloys.

performed with sulfur preadsorbed on the surface and with bulk sulfur (introduced in the alloy in controlled amounts by bulk diffusion of S at high temperature) revealed that Cr allows the surface to be passivated under conditions in which the passivation would be precluded by sulfur if there were no Cr. The surface analysis by XPS [18] revealed the coexistence of nickel sulfide and chromium oxide on the surface. The mechanism of this counteracting effect of Cr is totally different from the mechanism of the Mo effect discussed earlier. With Cr the desorption of sulfur is not the key factor. What Cr does is to react selectively with oxygen (i.e., with OH or H_2O) to give Cr oxide, whereas Ni reacts with sulfur. This leads to the coalescence of S in small nickel sulfide islands that can be covered by the lateral growth of the chromium oxide islands. In other words, the antagonistic effects of Cr and S are based on the fact that, on the considered alloys, Cr acts as an oxide former whereas Ni acts as a sulfide former. This competitive mechanism is represented schematically in Figure 12. In agreement with this mechanism, it has been observed that H_2S, which accelerates the anodic dissolution of chromium, has no influence on passivated chromium [37].

IMPLICATIONS IN AREAS OF PRACTICAL IMPORTANCE

There is much evidence for the damaging effect of sulfur species in a wide range of corrosion-related service failures. The relation between the sulfur-induced corrosion mechanisms presented in this chapter and the implications in areas of practical importance can be rationalized on the basis of (a) the source of sulfur, (b) the transport process to the metal surface, and (c) the conditions of the reduction (or

Copyright © 2002 Marcel Dekker, Inc.

oxidation) of the sulfur species into the harmful chemical state of sulfur, i.e., the adsorbed (chemisorbed) sulfur (or the sulfide if the concentration of the sulfur species is high). Table 2 summarizes some of these considerations and gives a few examples of practical areas in which detrimental effects of sulfur have been identified, e.g., oil and gas, pulp and paper industries, power plants (high-temperature water reactors), and atmospheric corrosion. Further details can be found in the other chapters of this book.

Two categories of sulfur species may be considered according to the origin of the species: (a) sulfur species (molecules or ions) in the environment, e.g., SO_2 (gaseous), H_2S (gaseous or aqueous), HS^-, $HS_2O_3^-$, $S_2O_3^{2-}$, $S_4O_6^{2-}$, HSO_4^-, SO_4^{2-}, and (b) sulfur in the material: sulfur in solid solution, sulfur segregated at the surface or in the grain boundaries, and sulfur in sulfide inclusions. After considering the source of sulfur, the process by which the sulfur species arrive at the surface (transport process) has to be identified. For environmental sulfur species it is generally diffusion in the liquid (e.g., aqueous solution). For sulfur present in the bulk metal or alloy, it may be surface segregation by solid-state diffusion at high temperature or anodic segregation (a process that has been defined in a preceding section). Higher anodic dissolution rates of grain boundaries, further accelerated by sulfur (according to the mechanism of sulfur-enhanced dissolution described earlier), result in rapid surface enrichment of sulfur at grain boundaries exposed to the electrolyte. In the case of sulfide inclusions, e.g., MnS, although their detrimental effect on corrosion of steels and stainless steels has been extensively studied [30– 33,38–41], the exact mechanism is not fully understood. The important case of sulfide inclusions in stainless steels is discussed in detail in Chapter 10. On the basis of the

Table 2 Sulfur Species that may be Present in the Environment or the Material, with the Process of Transport to the Surface, Nature of the Surface Reaction Producing Adsorbed Sulfur, and Examples of Areas of Practical Importance

Sulfur species	Transport process to the surface	Surface reaction producing adsorbed sulfur	Examples of areas of practical importance
Environmental			
H_2S	Diffusion in liquid	Oxidative reaction	Oil and gas
HS^-	Diffusion in liquid	Oxidative reaction	
$S_2O_3^{2-}$	Diffusion in liquid	Reductive reaction	Pulp and paper
SO_2	Diffusion in the atmosphere and in liquid	Reductive reaction	Atmospheric
HSO_4^-	Diffusion in liquid	Reductive reaction	
SO_4^{2-}	Diffusion in liquid	Reductive reaction	High-temperature water
Material			
Sulfur in solid solution	Solid-state diffusion (at high temperature) or anodic segregation		
Sulfur segregated at grain boundaries	Solid-state diffusion (at high temperature) or anodic segregation		All areas
Sulfide inclusions	Dissolution and readsorption		

Copyright © 2002 Marcel Dekker, Inc.

data reviewed here, other authors have invoked the role of adsorbed sulfur to explain the detrimental effects of sulfide inclusions in stainless steels [38–40]. It must be pointed out that early studies of the effects of H_2S addition on corrosion of stainless steels [41] have revealed the equivalence of the effects of sulfur added in the form of H_2S or present in sulfide inclusions. The effects of $S_2O_3^{2-}$ observed in the pulp and paper industry [23] and of sulfur species in the steam generators of pressurized water reactors [43] have also been interpreted on the basis of the data presented in this chapter. Attempts to investigate the transport of sulfur from the inclusions to the surrounding surface led to the conclusion that sulfur is cathodically deposited after dissolution of the sulfide, producing rings of sulfur around the sulfide inclusion [38]. In a study of the mechanisms of pitting corrosion of stainless steels using submicron resolution scanning electrochemical and photoelectrochemical microscopy [42] it was concluded that the electrodissolution of certain MnS inclusions in stainless steel is chloride catalyzed. The enchancement of the dissolution of sulfide inclusions by Cl^- had also been suggested in an earlier work [40].

After the process by which sulfur is transported to the surface, the nature of the surface reaction producing adsorbed sulfur must be considered. Sulfur may be adsorbed by electro-oxidation of sulfides [H_2S (aqueous) or HS^-] or by electro-eduction of sulfates (HSO_4^- or SO_4^{2-}) or thiosulfates ($HS_2O_3^-$, $S_2O_3^{2-}$).

The oxidative or reductive reactions and the conditions of potential and pH in which they may take place are detailed in the following. For SO_2, the surface reactions are presented in the chapter on atmospheric corrosion (chap. 15).

Once sulfur is present on the surface in the active chemical state (i.e., adsorbed), it has the same effects (which have already been described) irrespective of its origin.

The stage at which the surface reactions become localized is not exactly known. It is probably strongly related to the stage at which surface defects are crucial, which is the case for the surface reactions that produce adsorbed sulfur.

THERMODYNAMICS OF SULFUR ADSORPTION ON METAL SURFACES IN WATER

The principle of potential-pH (Pourbaix) diagrams has been extended to the case of bidimensional layers of elements adsorbed on metal surfaces [44,45]. It allows us to predict the conditions of stability of adsorbed sulfur on metals immersed in water containing dissolved sulfur species such as S, H_2S, HS^-, $HS_2O_3^-$, $S_2O_3^{2-}$, HSO_4^-, and SO_4^{2-}. The calculated *E*-pH diagrams show that the stability domain of adsorbed sulfur extends beyond the usually predicted range of stability of metal sulfides, and thus adsorbed sulfur layers can exist under conditions in which no bulk sulfide is stable. Potential-pH diagrams have been calculated for sulfur adsorbed on surfaces of iron, nickel, and chromium, in water containing sulfides or sulfates [44–46], and in water containing sulfides and thiosulfates [47]. They are now also available for copper [48].

Principle of *E*-pH Diagrams for Adsorbed Species

An element A (which may be O, S, N, or H) is adsorbed on a metal M in the form of a monoatomic layer, with a valence state equal to zero [denoted $A_{ads}(M)$]. The

Copyright © 2002 Marcel Dekker, Inc.

adsorption of A from a species dissolved in aqueous solution may be an electro-oxidation or an electro-eduction reaction, depending on the valence state of A in the dissolved species.

In contrast to adsorption in ultrahigh vacuum (UHV) and in gas phase, described in Chapter 2, the adsorption of an atom or a molecule on a metal surface in water involves replacement of adsorbed water molecules [$H_2O_{ads}(M)$] and competition with the adsorption of oxygen [$O_{ads}(M)$] or hydroxyl [$OH_{ads}(M)$] resulting from the dissociation of H_2O molecules on the metal surface.

In a Langmuir model for adsorption, it is assumed that the two-dimensional phase is an ideal solution, where water, oxygen or hydroxyl, and sulfur adsorb competitively on the same surface sites and there are no interactions between adsorbed species.

Under these conditions the chemical potential of each element A in the phase adsorbed on a metal M can be expressed as follows:

$$\mu_{Aads(M)} = \mu^{\circ}_{Aads(M)} + RT \ln \theta_A \tag{1}$$

where θ_A is the relative coverage of the surface of M by adsorbed A ($0 \le \theta_A \le 1$; $\theta_A = 1$ for the complete monolayer of A); $\mu^{\circ}_{Aads(M)}$ is the standard chemical potential of A, corresponding to saturation of the surface by A. The chemical potential of adsorbed water is also given by:

$$\mu_{H_2Oads(M)} = \mu^{\circ}_{H_2Oads(M)} + RT \ln \theta_{H_2O} \tag{2a}$$

with

$$\theta_{H_2O} = (1 - \sum_i \theta_{Ai}) \tag{2b}$$

As an example of the method of calculation of the *E*-pH relations, let us consider the adsorption on a metal of oxygen from water:

$$H_2O_{ads}(M) = O_{ads}(M) + 2H^+ + 2e^-$$

The equilibrium potential of this half-reaction is obtained by applying the Nernst law with the chemical potentials of adsorbed oxygen and water expressed as in Eqs. (1) and (2):

$$E = E^{\circ} + (RT \ln 10/2F) \log[\theta_O/(1 - \theta_S - \theta_O)] - (RT \ln 10/F)\ \text{pH} \tag{3a}$$

with the standard potential E° given on the standard hydrogen scale by

$$E^{\circ} = [\mu^{\circ}_{Oads(M)} + \mu^{\circ}_{H+} + \mu^{\circ}_{e-} - \mu^{\circ}_{H_2Oads(M)}]/2F \tag{3b}$$

with $\mu^{\circ}_{H+} + \mu^{\circ}_{e-} = \frac{1}{2}\mu^{\circ}_{H_2(g)}$.

Electrochemical experiments and surface analyses show that the adsorbed oxygen species in solution on most transition metals at 25°C are likely to be hydroxyls. Thermodynamic data obtained from electrochemical experiments are presently available only for OH_{ads} on copper [49]. Therefore O_{ads} is considered here on Fe, Ni, and Cr and OH_{ads} on Cu. The standard Gibbs energies of formation (chemical potentials) for sulfur and oxygen adsorbed on metal surfaces can be calculated [44–46] from literature thermodynamic data for reversible chemisorption at the metal-gas interface (see Chap. 2).

Copyright © 2002 Marcel Dekker, Inc.

E-pH Relations for the Equilibria between Dissolved and Adsorbed Species

In water containing thiosulfates, the sulfur species to be considered are the thermodynamically stable sulfide species $H_2S_{(aq)}$ and HS^-, and the metastable thiosulfate species $HS_2O_3^-$ and $S_2O_3^{2-}$. The *E*-pH relations associated with the various equilibria between water, the dissolved sulfur species and adsorbed sulfur, and oxygen or hydroxyl adsorbed on Fe, Ni, Cr, and Cu at 25°C are as follows:

$$S_{ads}(M) + H_2O_{(l)} = O_{ads}(M) + H_2S_{(aq)}$$
$$\log(\theta_O/\theta_S) = -pK - \log m_S \tag{4}$$
$$pK(Fe) = 18.8; \quad pK(Ni) = 27.4; \quad pK(Cr) = 13.6.$$

$$S_{ads}(M) + H_2O_{ads}(M) + H_2O_{(l)} = 2OH_{ads}(M) + H_2S_{(aq)}$$
$$\log[\theta_{OH}^2/\theta_S(1 - \theta_S - \theta_{OH})] = -pK - \log m_S \tag{5}$$
$$pK(Cu) = 19.7.$$

$$S_{ads}(M) + H_2O_{(l)} = O_{ads}(M) + HS^- + H^+$$
$$\log(\theta_O/\theta_S) = pH - pK - \log m_S \tag{6}$$
$$pK(Fe) = 25.8; \quad pK(Ni) = 34.4; \quad pK(Cr) = 20.6.$$

$$S_{ads}(M) + H_2O_{ads}(M) + H_2O_{(l)} = 2OH_{ads}(M) + HS^- + H^+$$
$$\log[\theta_{OH}^2/\theta_S(1 - \theta_S - \theta_{OH})] = pH - pK - \log m_S \tag{7}$$
$$pK(Cu) = 26.7.$$

$$H_2O_{ads}(M) = O_{ads}(M) + 2H^+ + 2e^-$$
$$E^{25} = E^{\circ 25} + 0.030 \log[\theta_O/(1 - \theta_S - \theta_O)] - 0.059\,pH \tag{8}$$
$$E^{\circ 25}(Fe) = -0.11\,V; \quad E^{\circ 25}(Ni) = 0.04\,V; \quad E^{\circ 25}(Cr) = -0.52\,V.$$

$$H_2O_{ads}(M) = OH_{ads}(M) + H^+ + e^-$$
$$E^{25} = E^{\circ 25} + 0.059 \log[\theta_{OH}/(1 - \theta_S - \theta_{OH})] - 0.059\,pH \tag{9}$$
$$E^{\circ 25}(Cu) = 0.095\,V.$$

$$H_2O_{ads}(M) + H_2S_{(aq)} = S_{ads}(M) + H_2O_{(l)} + 2H^+ + 2e^-$$
$$E^{25} = E^{\circ 25} - 0.030 \log m_S + 0.030 \log[\theta_S/\theta_{H_2O}] - 0.059\,pH \tag{10}$$
$$E^{\circ 25}(Fe) = -0.67\,V; \quad E^{\circ 25}(Ni) = -0.77\,V;$$
$$E^{\circ 25}(Cr) = -0.92\,V; \quad E^{\circ 25}(Cu) = -0.488\,V$$

$$H_2O_{ads}(M) + HS^- = S_{ads}(M) + H_2O_{(l)} + H^+ + 2e^-$$
$$E^{25} = E^{\circ 25} - 0.030 \log m_S + 0.030 \log[\theta_S/\theta_{H_2O}] - 0.030\,pH \tag{11}$$
$$E^{\circ 25}(Fe) = -0.88\,V; \quad E^{\circ 25}(Ni) = -0.97\,V; \quad E^{\circ 25}(Cr) = -1.12\,V;$$
$$E^{\circ 25}(Cu) = -0.695\,V.$$

Copyright © 2002 Marcel Dekker, Inc.

$$2S_{ads}(M) + 5H_2O_{(l)} = 2O_{ads}(M) + HS_2O_3^- + 9H^+ + 8e^-$$
$$E^{25} = E^{\circ 25} + 0.007\log(m_S/2) + 0.015\log(\theta_O/\theta_S) - 0.067\,pH \quad (12)$$
$$E^{\circ 25}(Fe) = 0.58\,V;\ E^{\circ 25}(Ni) = 0.71\,V;\ E^{\circ 25}(Cr) = 0.50\,V.$$

$$2S_{ads}(M) + 5H_2O_{(l)} = 2OH_{ads}(M) + HS_2O_3^- + 7H^+ + 6e^-$$
$$E^{25} = E^{\circ 25} + 0.010\log(m_S/2) + 0.020\log(\theta_{OH}/\theta_S) - 0.069\,pH \quad (13)$$
$$E^{\circ 25}(Cu) = 0.76\,V.$$

$$2S_{ads}(M) + 5H_2O_{(l)} = 2O_{ads}(M) + S_2O_3^{2-} + 10H^+ + 8e^-$$
$$E^{25} = E^{\circ 25} + 0.007\log(m_S/2) + 0.015\log(\theta_O/\theta_S) - 0.074\,pH \quad (14)$$
$$E^{\circ 25}(Fe) = 0.60\,V;\ E^{\circ 25}(Ni) = 0.72\,V;\ E^{\circ 25}(Cr) = 0.52\,V.$$

$$2S_{ads}(M) + 5H_2O_{(l)} = 2OH_{ads}(M) + S_2O_3^{2-} + 8H^+ + 6e^-$$
$$E^{25} = E^{\circ 25} + 0.010\log(m_S/2) + 0.020\log(\theta_{OH}/\theta_S) - 0.079\,pH \quad (15)$$
$$E^{\circ 25}(Cu) = 0.78\,V.$$

Potential-pH Diagrams

The preceding equations have been used to construct the potential-pH diagrams for sulfur and oxygen (hydroxyl) adsorbed in water containing sulfides (H_2S or H) or thiosulfates ($HS_2O_3^-$ or $S_2O_3^{2-}$) on Fe, Ni, Cr, and Cu [44–48]. The diagrams are shown in Figures 13 to 16 at 25°C for different sulfur coverages ($\theta_s = 0.01; 0.5; 0.99$) and a molality of dissolved sulfur $m_s = 10^{-4}$mol kg^{-1}. The diagrams are superimposed on the S-M-H_2O diagrams (M = Fe, Ni, Cr, Cu), calculated for a molality of dissolved metal $m_M = 10^{-6}$mol kg^{-1}.

These diagrams allow us to predict the *E*-pH conditions in which sulfur is adsorbed on a surface of Fe, Ni, Cr, or Cu in water by oxidation of sulfides or reduction of thiosulfates. In aqueous solution, when the potential is increased in the anodic direction, the adsorbed water molecules are replaced by sulfur atoms adsorbed from $H_2S_{(aq)}$ and HS^-. At higher potentials, sulfur is oxidized in $HS_2O_3^-$ or $S_2O_3^{2-}$ and replaced by adsorbed oxygen or hydroxyl. The replacement reaction is completed within a very narrow range of potential (~ 0.06 for O_{ads} and 0.08 V for OH_{ads}). The domains of stability of the adsorbed S monolayer (for $m_s = 10^{-4}$ mol kg^{-1} and $m_M = 10^{-6}$ mol kg^{-1}) overlap the domains of stability of the metals (Fe, Ni, Cr, Cu), the dissolved cations (Fe^{2+}, Ni^{2+}, Cr^{2+}, Cr^{3+}, Cu^+, and Cu^{2+}), and the oxides or hydroxides (Fe_3O_4, Fe_2O_3, $Ni(OH)_2$, NiO, Cr_2O_3, Cu_2O, CuO). The stability domains of S_{ads} are significantly wider than the stability domains of the bulk metal sulfides, and thus S_{ads} is stable in *E*-pH regions where there is no stable metal sulfide, which reflects the excess of stability of the chemisorbed state with respect to the corresponding 3D compound. On this basis, detrimental effects of sulfur on the corrosion resistance of metals are predicted even under potential and pH conditions where the metal sulfides are not thermodynamically stable. The comparison of the behaviors of the different metals in the presence of dissolved sulfur species shows that the

Copyright © 2002 Marcel Dekker, Inc.

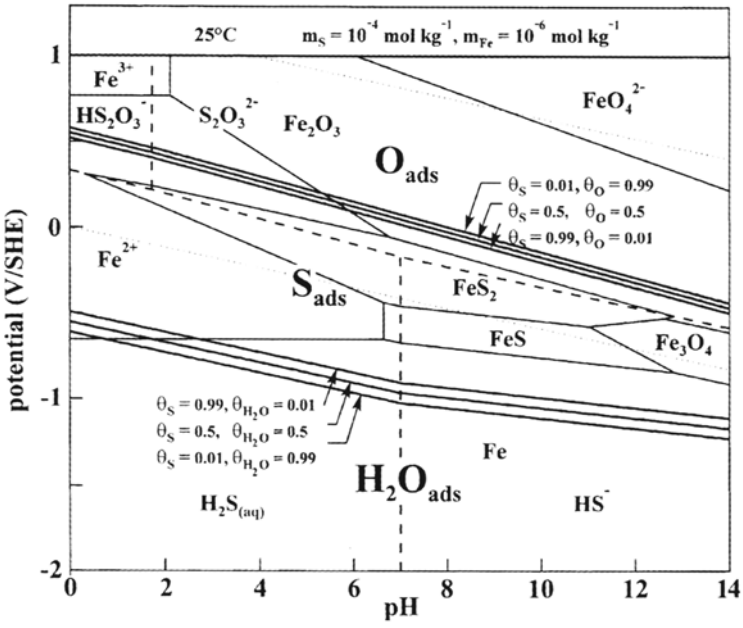


Figure 13 Potential-pH diagram for sulfur adsorbed on Fe (25°C, $m_s = 10^{-4}$ mol kg^{-1}).

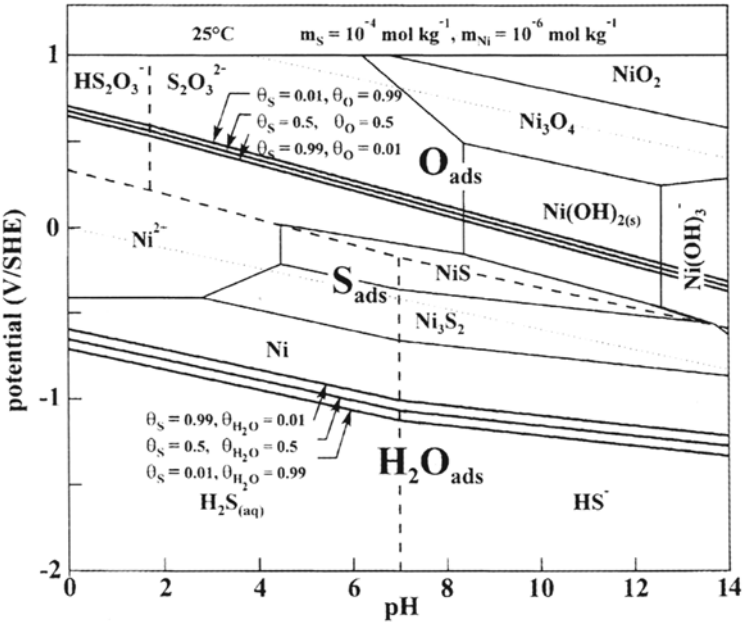


Figure 14 Potential-pH diagram for sulfur adsorbed on Ni (25°C, $m_s = 10^{-4}$ mol kg^{-1}).

Copyright © 2002 Marcel Dekker, Inc.

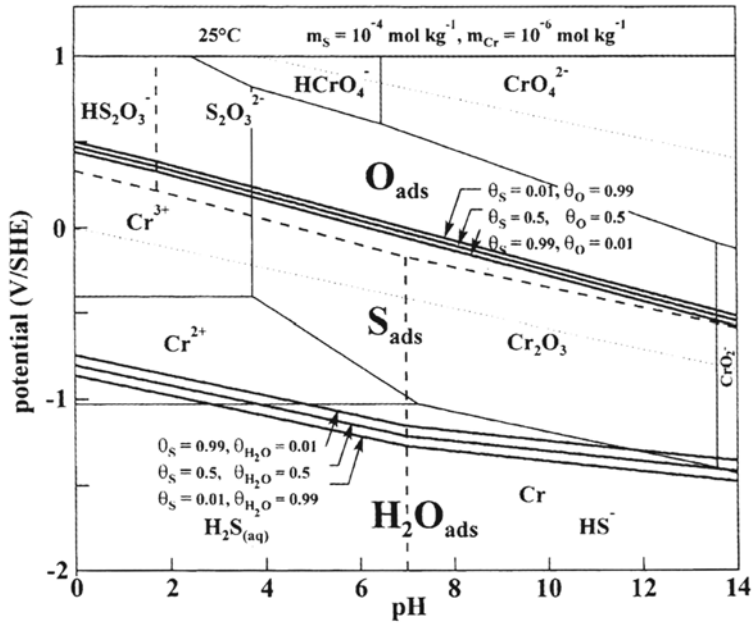


Figure 15 Potential-pH diagram for sulfur adsorbed on Cr (25°C, $m_s = 10^{-4}$ mol kg^{-1}).

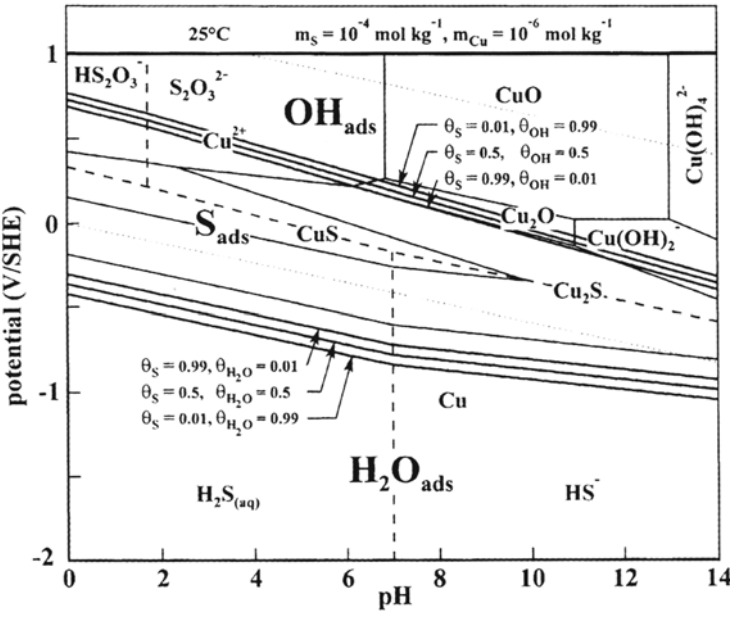


Figure 16 Potential-pH diagram for sulfur adsorbed on Cu (25°C, $m_s = 10^{-4}$ mol kg^{-1}).

Copyright © 2002 Marcel Dekker, Inc.

extent of the overlap of S_{ads} with the stable metals decreases in the sequence Ni, Fe, Cr, so the effect of thiosulfates on corrosion of these metals is expected to decrease in the same order Ni > Fe > Cr. Prediction of S adsorption in the active domains (i.e., during anodic dissolution) is also important because this is the condition in which S-enhanced dissolution is experimentally observed. Another effect of thiosulfates expected from the stability of S_{ads} in the passive domains is the blocking or retarding of passivation (or repassivation) of stainless steels. Such diagrams are useful to assess the risk of corrosion of metals and alloys induced by adsorbed sulfur produced by electro-oxidation of sulfides or electro-eduction of thiosulfates.

CONCLUSION

The fundamental aspects of sulfur-induced corrosion have been reviewed. The mechanisms have been derived from data obtained on chemically and structurally well-defined surfaces using electrochemical and surface analysis techniques (^{35}S radiotracer and surface spectroscopies).

The data obtained show the direct link that exists between atomic-scale surface reactions of sulfur and macroscopic manifestations (enhanced dissolution, blocking or retarding of passivation, and passivity breakdown). The data provide the fundamental basis required to rationalize the detrimental effects of sulfur species encountered in a large number of service conditions.

REFERENCES

1. P. Marcus, N. Barbouth, and J. Oudar, *C.R. Acad. Sci. Paris 280*:1183 (1975).
2. J.Oudar and P. Marcus, *Appl. Surf. Sci. 3*:48 (1979).
3. P. Marcus and J. Oudar, *Fundamental Aspects of Corrosion Protection by Surface Modification* (E. McCafferty C.R. Clayton, and J. Oudar, eds.), The Electrochemical Society, Pennington, NJ, 1984, p. 173.
4. P.Marcus, A. Teissier, and J. Oudar, *Corros. Sci. 24*:259 (1984).
5. P. Combrade, M. Foucault, D. Vançon, J. M. Grimal, and A. Gelpi, *Proceedings of the 4th International Symposium on Environmental Degradation of Materials in Nuclear Power Systems-Water Reactors* (D. Cubicciotti, ed.), NACE, Houston, 1990, p. 5.
6. D. Costa and P. Marcus, *Proceedings of the European Symposium on Modifications of Passive Films* (P. Marcus, B. Baroux, and M. Keddam, eds.), The Institute of Materials (EFC 12), 1994, p. 17.
7. A. Elbiache and P. Marcus, *Corros. Sci. 33*:261 (1992).
8. P. Marcus, *Advances in Localized Corrosion* (H. S. Isaacs, U. Bertocci, J. Kruger, and S. Smialowska, eds.), NACE, Houston, 1990, p. 289.
9. S. Ando, T. Suzuki, and K. Itaya, *J. Electroanal. Chem. 412*:139 (1996).
10. G. Seshadri, H.-C. Xu, and J.A. Kelber, *J. Electrochem. Soc. 146*:1762 (1999).
11. H. Ma, X. Cheng, G. Li, S. Chen, Z. Quan, S. Zhao, and L. Niu, *Corros. Sci. 42*:1669 (2000).
12. H.C. Xu, G. Seshadri, and J.A. Kelber, *J. Electrochem. Soc. 147*:558 (2000).
13. V. Maurice, H. Talah, and P. Marcus, *Surf. Sci. 284*:L431 (1993).
14. V. Maurice, H. Talah, and P. Marcus, *Surf Sci. 304*:98 (1994).
15. D. Zuili, V. Maurice, and P. Marcus, *J. Electrochem. Soc. 147*:1393 (2000).
16. P. Marcus, I. Olefjord, and J. Oudar, *Corros. Sci. 24*:269 (1984).

Copyright © 2002 Marcel Dekker, Inc.

17. P. Marcus and I. Olefjord, *Corrosion* (*NACE*) *42*:91 (1986).
18. P. Marcus and J.M. Grimal, *Corros. Sci. 31*:377 (1990).
19. P. Marcus and H. Talah, *Corros. Sci. 29*:455 (1989).
20. D. Tromans and L. Frederick, *Corrosion* (*NACE*) *40*:633 (1984).
21. R.C. Newman, H.S. Isaacs, and B. Alman, *Corrosion* (*NACE*) *38*:261 (1982).
22. A. Garner, *Corrosion* (*NACE*) *41*:587 (1985).
23. R.C. Newman, *Corrosion* (*NACE*) *41*:450 (1985).
24. R.C. Newman, K, Sieradski, and H.S. Isaacs, *Met. Trans. 13A*:2015 (1982).
25. R.C. Newman and K. Sieradski, *Corros. Sci. 23*:363 (1983).
26. S.E. Lott and R.C. Alkire, *J. Electrochem. Soc. 136:*973 and 3256 (1989).
27. C. Duret-Thual, D. Costa, W.P. Yang, and P. Marcus, *Corros. Sci. 39*:913 (1997).
28. H.-S. Kuo, H. Chang, and W.-T. Tsai, *Corros. Sci. 41*:669 (1999).
29. T. Haruna, T. Shibata, and R. Toyota, *Corros. Sci. 39*:1935 (1997).
30. Z. Szklarska-Smialowska, *Corrosion* (*NACE*) *28*:388 (1972).
31. G. Wranglen, *Corros. Sci. 14*:331 (1974).
32. G.S. Eklund, *J. Electrochem. Soc. 121*:467 (1974).
33. A. Szummer and M. Janick-Czachor, *Br. Corros. J. 9*:216 (1974).
34. P. Marcus, *C.R. Acad. Sci. Paris Ser. II 305*:675 (1987).
35. P. Marcus and M. Moscatelli, *J. Electrochem. Soc. 136*:1634 (1989).
36. P. Marcus and M. Moscatelli, *Mem. Et. Sci. Rev. Met. 85:561* (1988).
37. X. Cheng, H. Ma, S. Chen, L. Niu, S. Lei, R. Yu, and Z. Yao, *Corros. Sci. 41:112* (1999).
38. J.E. Castle and R. Ke, *Corros. Sci. 30*:409 (1990).
39. J. Stewart and D.E. Williams, *Corros. Sci. 33*:457 (1992).
40. M. Janik-Czachor, *Modifications of Passive Films* (P. Marcus, B. Baroux, and M. Keddam, eds.), The Institute of Materials (EFC 12), 1994, p. 280.
41. J.L. Crolet, L. Seraphin, and R. Tricot, *Met. Corros. Ind.*, no. 616 (1976).
42. D.E. Williams, T.F. Mohiuddin, and Ying Yang Zhu, *J. Electrochem. Soc. 145*:2664 (1998).
43. P. Combrade, O. Cayla, M. Foucault, D. Vançon, A. Gelpi, and G. Slama, *Proceedings of the 3rd International Symposium on Environmental Degradation of Materials in Nuclear Power Systems-Water Reactors,* Traverse City, (G.J. Theus and J.R. Weeks, eds.), The Metallurgical Society (1987) p. 525.
44. P. Marcus and E. Protopopoff, *J. Electrochem. Soc. 137*:2709 (1990).
45. P. Marcus and E. Protopopoff, *J. Electrochem. Soc. 140*:1571 (1993).
46. P. Marcus and E. Protopopoff, *J. Electrochem. Soc. 144*:1586 (1997).
47. P. Marcus and E. Protopopoff, *Corros. Sci. 39*:1741 (1997).
48. E. Protopopoff and P. Marcus, to be published.
49. V. Maurice, H.-H. Strehblow, and P. Marcus, *Surf. Sci. 458*:185 (2000).

Copyright © 2002 Marcel Dekker, Inc.

10

Further Insights on the Pitting Corrosion of Stainless Steels

Bernard Baroux
Ugine Research Center, Ugine-Savoie, Ugine, France

INTRODUCTION

Fundamentals of the pitting mechanisms have been discussed in Chapter 7 and the whole question of pitting corrosion was reviewed by Smialowska [1a] in 1986. It is intended here to shed light on some points of practical or theoretical importance which were recently investigated or revisited and to propose a comprehensive viewpoint on some rather scattered experimental evidence. The examples are restricted to stainless steels, in weakly acid chloride-containing aqueous media whose pH is larger than the depassivation pH, so that the passive film remains stable except in the pit itself.

The role of the chloride ions in pitting initiation can be related to local passive film destabilization, together with a counteracting effect vis-à-vis the passive film healing. However, it should be noted that the passive film breakdown and healing phenomena act on the microscopic scale (some nanometers), whereas the pits observed in the practical situations are on a macroscopic scale (some 100 micrometers). Between the microscopic and the macroscopic size scales, many phenomena can occur, such as pit growth, modifications of the local solution composition, and dissolution of the nonmetallic inclusions present in the steel, which act generally at the scale of some micrometers. In the same way, electrochemical assessment of the pitting corrosion resistance generally involves the measurement of anodic currents of the order of some microamperes (or some 10 μA). Measuring 1 μA during 1 s corresponds to a pit size of the order of some micrometers. This size scale will be referred to as the mesoscopic scale. It should be pointed out that the pit repassivation can occur in these mesoscopic stages as well as in the microscopic one, so that the passive film breakdown theories are often unable to predict the actual behavior of the alloy. Figure 1 shows a semideveloped pit observed at the scale of 10 μm on a 17% Cr stainless steel immersed in an NaCl-containing solution. The pit consists of an undermining hollow, covered by a thin metallic cap, leading to the formation of an occluded zone. Some secondary pits are visible all around the main hole. The possible collapse of the metallic cap can suppress the occlusion and provoke pit repassivation.

Copyright © 2002 Marcel Dekker, Inc.

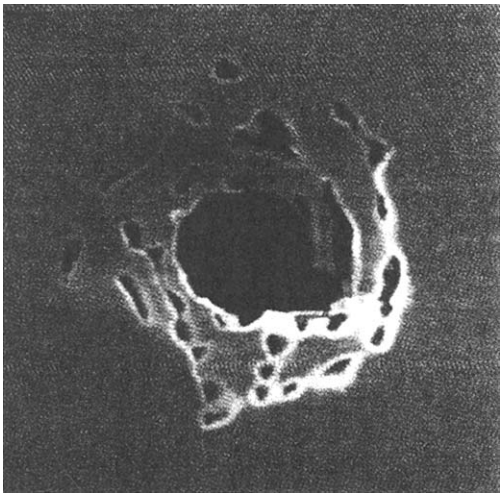


Figure 1 Scanning electron microscopy, × 1000. Typical view of a semideveloped pit at the end of the mesoscopic stage. A thin metallic film is still present and covers part of the pit. Secondary pits are visible all around the main hole. The pit may either go on or repassivate if the thin "top" film breaks down. (From Ref. 28.)

Furthermore, pit occurrence is often considered a random phenomenon. [2,3a,4a], which makes the probability of survival of the passive state difficult to predict and the measurement of pitting potentials uncertain. This random behavior can result either from the passive film breakdown and healing mechanisms (microscopic stage) or the phenomena occurring in the mesoscopic stages. Moreover, the pit occurrence probability varies with time, increasing to severe conditions but decreasing in milder ones so that the pitting sensitivity depends on the surface aging.

Last, pitting of industrial steels also depends on their metallurgical properties. It is obvious that the steel composition plays a major role, but the phenomena can be rather complex, depending on the pitting stage under consideration. The steel microstructure is a relevant factor as well, although scarcely taken into account by the current models. The unavoidable presence of some nonmetallic inclusions in industrial steels and the properties of these inclusions (which may act as pitting sites) are often more determining for the pitting resistance than the addition of expensive alloying elements.

In the following, some experimental results pertaining to these concerns are presented, making the relation between pitting theories and practical behavior more realistic and motivating future works to shed light on some poorly understood domains.

PITTING POTENTIAL MEASUREMENTS

The Experimental Procedure

Measuring the pitting potential provides some information on the pitting resistance in the test solution. However, the result of the measurement depends not only on the

Copyright © 2002 Marcel Dekker, Inc.

material itself but also on the passive film characteristics. On the other hand, the properties of the passive film depend on (a) its initial state before the test, then on the surface preparation procedure, and (b) the test procedure itself, since the film can be modified when immersed in the electrolyte. Moreover, a sample is considered to be pitted when the anodic current increases sharply and irreversibly. Then the question arises of when pitting becomes irreversible. In the most frequently used techniques, the anodic current increase associated with the onset of irreversible pitting is larger than some l0 μA; then pitting potential characterizes the occurrence of a macropit, or at least of a pit in the mesoscopic stage, but certainly not the nucleation of a micropit.

Two procedures are used for measuring the pitting potential. In the potentiostatic method, the sample is polarized at a potential V and the induction time $\tau(V)$ for pit occurrence is recorded. The pitting potential is the highest potential for which $\tau = \infty$. In practice, a large, but finite, value of τ is chosen. Note that when pit initiation is a purely deterministic process, τ can be considered as the "incubation time" necessary for the conditions for irreversible passive film breakdown to occur.

In the potentiokinetic method, the electrode potential is raised from the rest potential up to pitting. The measured pitting potential depends on the scanning rate s. Using a deterministic model, one finds [5a]

$$\frac{1}{s}\int_{V_{\text{rest}}}^{V_{\text{pit}}} \frac{dV}{\tau(V)} = 1$$

and then the pitting potential decreases when the scanning rate is lowered. However, it is believed that, at least for low scanning rates, the passive film is modified during the potentiokinetic scan, resulting in a pitting resistance improvement and in an increase of the incubation time $[(\frac{\partial \tau}{\partial t})_{v} > 0]$. Then, under such conditions, the measured pitting potential increases when the scanning rate is lowered, leading to the occurrence of a critical scanning rate, s_0 for which the pitting potential is minimum [3a,b].

Another characteristic potential is sometimes drawn from the potentiokinetic measurements, namely the so-called repassivation potential V_{rep}. The potential is first raised up to pitting; then, once the anodic current has reached a predetermined value i_1 corresponding to anodic dissolution into the pit, the scanning is reversed toward the cathodic potentials. The anodic current then decreases and the repassivation potential is obtained when the current measured during the backward scanning equals the one was found during the forward scanning. For potentials larger than V_{rep} the pit is active and for smaller values it repassivates. However, one should keep in mind (a) that the repassivation potential does not characterize the resistance to pitting initiation and (b) that it depends on the degree of pit development when the scanning is reversed, then on the arbitrary current density i_1.

Whatever the test procedure and the method chosen for analyzing the results, one must be aware of the fact that, even when the corrosive solution is well defined, associating an intrinsic pitting potential with a given material as a criterion of resistance to pitting should be definitely ruled out. The measured values are strongly dependent not only on the steel surface condition but also on the experimental procedure.

Copyright © 2002 Marcel Dekker, Inc.

In the following, some examples are given of various stainless steels tested at constant temperature in carefully deaerated NaCl aqueous solution (distillated water) whose pH was adjusted to the test value by adding either NaOH or HCl. The samples (S = 0.785 cm^2) were cut from thin cold-rolled sheets (thickness 0.5 to 1 mm), then mechanical polished (paper SiC grade 1200, under water) and aged 24 h in air (this aging procedure was shown to ensure better reproducibility of the results). Last, the specimens were immersed in the corrosive solution and left at rest potential for 15min before testing.

Probabilistic Behavior

Because pitting exhibits probabilistic behavior, the induction time τ (the time for the occurrence of the first pit) in potentiostatic conditions is a probabilistic value and here the model described above does not hold. In the same way, the pitting potential measured in potentiokinetic conditions is probabilistic.

For a set of N samples tested under strictly the same conditions (potentiostatic or potentiokinetic), the pitting probability at a time t (or at a potential V) is defined as n/N, and the survival probability P as $(N - n)/N$, where n is the number of pitted specimens. When N is large enough (which should be discussed), P also represents the survival probability (probability for no pit to occur) of a single specimen. Now, let us consider the pitting probability $\bar{\omega}.\ \delta S$ of an infinitesimal area δS of this single specimen (which implicitly assumes that ω is much smaller than the number of pitting sites per unit area). In the following, ω will be referred to as the elementary pitting probability [3a,b] (EPP). The survival probability of δS is $\delta P = 1 - \bar{\omega}\delta S$. The survival probability of the whole sample is then $P = (1 - \bar{\omega}\delta S)^{S/\delta S}$, which tends to exp-$\bar{\omega}S$ when δS tends to zero. Then the EPP is given by $\bar{\omega} = (-\mathrm{In}\ P)S$, where P is approximated by $P = (N - n)/N$. The elementary probability (for the occurrence of a single pit) is a probability per unit area. A more detailed statistical analysis shows that the smallest reliable value of ω which can be measured is of the order of $1/(NS)$. In the following examples, N is equal to 24 or 48.

The time derivative $g = d\bar{\omega}/dt$ of the elementary pitting probability ω is referred to as the pit generation rate. The intrinsic pitting potential (if it really exists) is given by $g = 0$ and can be deduced from the transition from $P = 1$ to $P = 0$ for infinite surface areas S. This condition is not easily fulfilled in laboratory experiments, and it is often more convenient to use small surface areas and to characterize the pitting resistance by the probabilistic function ω or g.

Let us note that this description of the probabilistic behavior for the appearance of observable pits does not imply, at this stage, any mechanistic assumption about the mechanisms responsible for this behavior. It is only a convenient way to describe the experimental results. Shibata and Takeyama suggested another way to analyze the probabilistic behavior. They proposed a stochastic model including a pit initiation $\lambda(V)$ frequency and a pit repassivation $\mu(V)$ frequency, leading to a conventional pitting potential V_{pit} defined by $\lambda(V_{Pit}) = \mu(V_{\mathrm{pit}})$.

Potentiostatic measurements on a sufficient number of samples, or simultaneous measurements using a multichannel device [2,3ab], given the survival probability P and then the elementary pitting probability $\bar{\omega}(V, t)$ as a function of the polarization time t (Fig. 2a). The probability density for the random function τ is $-dP/Pdt = Sg(V, t)$. Figure 2a and b show the pit generation rate time dependence

Copyright © 2002 Marcel Dekker, Inc.

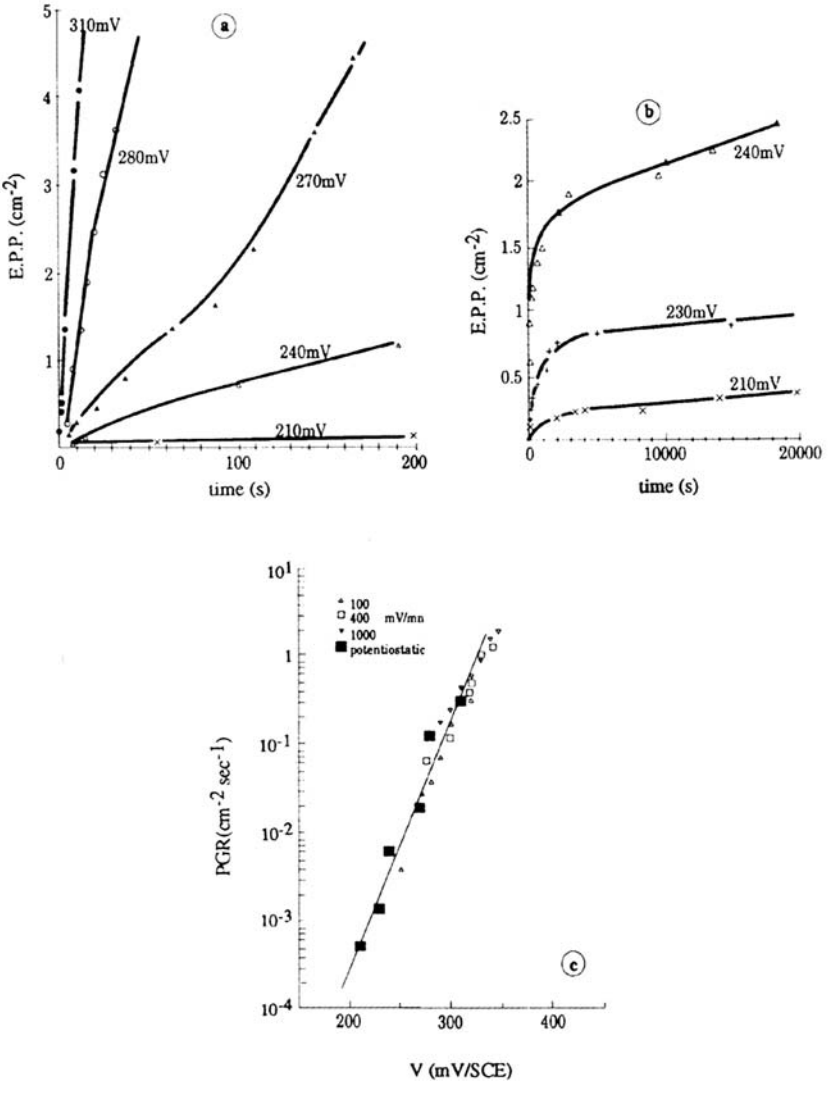


Figure 2 (a) Elementary pitting probability in NaCl (0.5 M) for an AISI 304 type stainless steel in potentiostatic conditions for different electrode potentials V; short holding times. (b) Same for long holding times. (c) Pit generation rate for $t = 0$ determined either in potentiostatic or potentiokinetic conditions. (From Ref. 3a.)

for several electrode potentials, which can be denoted $g = g_0(V)h(V, t)$, where $h(V, 0) = 1$. One sees (Fig. 2b) that for low enough potentials h is a decreasing function of time (which can be approximated by an exponential decay), showing that potentiostatic holding in the corrosive solution itself may improve the further pitting resistance. The initial pit generation rate $g_0(V)$ increases with V (Fig. 2c) and provides some information on the pitting resistance of the tested material before any polarization. A conventional pitting potential V_{pit} can be defined, for which $g_0(V_{pit})$

Copyright © 2002 Marcel Dekker, Inc.

has a small, but measurable, arbitrary value (for instance 0.1cm^{-2} s^{-1} in the following examples).

Potentiokinetic measurements give the elementary pitting probability $\bar{\omega}(V)$- for the potential V and the potentiokinetic pit generation rate $g(V) = d\bar{\omega}/dt = s\, d\bar{\omega}/dV$, both depending on the scanning rate s. For high enough scanning rates, the potentiokinetic scanning does not modify the pitting resistance. Therefore $g = g_0(V)$ and does not depend on the scanning rate. The elementary pitting probability is then $\bar{\omega}_0(V) = \int_{V_{rest}}^{V} g_0(V)dV$, which does not depend on V_{rest} since $g_0(V_{rest}) = 0$. For smaller scanning rates, $g < g_0(V)$ and then $\bar{\omega}(V) < \bar{\omega}_0(V)$.

It is convenient to define a conventional potentiokinetic pitting potential V_{pit} as $\bar{\omega}(V_{pit}) = \bar{\omega}_1$, where $\bar{\omega}_1$ is a conventional pitting probability ($\bar{\omega}_1 = 0.1$ cm^{-2} in the following examples). One sees that for large enough scanning rates, V_{pit} increases with s. For scanning rates smaller than a critical value, the pitting sensitivity of the surface decreases during the test and then V_{pit} increases when s decreases [3a]. For this reason, it can be better to choose a large enough scanning rate, which does not provide any change in the pitting sensitivity during the test and whose kinetic effect ($s = dV/dt$) on V_{pit} is readily taken into account. Following this idea, the effect of the passive film modifications can be studied either by using the potentiostatic mode or by prepolarizing the specimen at constant potential before a high scanning rate potentiokinetic test. Otherwise, the pitting potential obtained by the potentiokinetic method is a complex function of the scanning rate, including kinetic and surface modification effects. In the following examples, s = l00mV/min, which was shown to be larger than the critical scanning rate for all the studied steels, and the conventional pitting potential was defined as giving $\bar{\omega} = 0.1$ cm^{-2}.

METALLURGICAL ASPECTS

The Alloying Elements and the Metallurgical Processing

For stainless steels [3c], the chromium content is obviously one of the major parameters which controls the passive film properties and then the pitting resistance, at least for some conditions of passive film formation. This is illustrated in standard conditions by the results shown in Figure 3. Other oxidizable elements, such as silicon, which is present at the level of some tenths of a weight % in industrial AISI 430 or 304 type steels, can also enter the passive film and improve the pitting resistance.

The sulfur content is also a determining parameter for the pitting resistance, due to the formation of sulfides, which may act as pitting sites (see later). The free machining steels, such as AISI 303 type austenitic steels, containing 0.2% to 0.3% sulfur, which forms some numerous and large manganese sulfides. These inclusions are known to improve the steel machinability dramatically, but also to decrease the pitting resistance. AISI 430 or 304 contains less than 0.03% S, which leads to less numerous and smaller sulfides. Among them, the grades used for long products (bars and wires) often contain typically 0.02% S in order to ensure sufficient machinability. In contrast, the grades used for flat products (sheets and plates) generally contain less than 50 ppm S, which leads to improved pitting resistance. The precise role of Mn sulfides in pit initiation has been extensively studied [1b,6,7] and will be detailed later. It is known that sulfide dissolution provides some harmful sulfur species, but that

Copyright © 2002 Marcel Dekker, Inc.

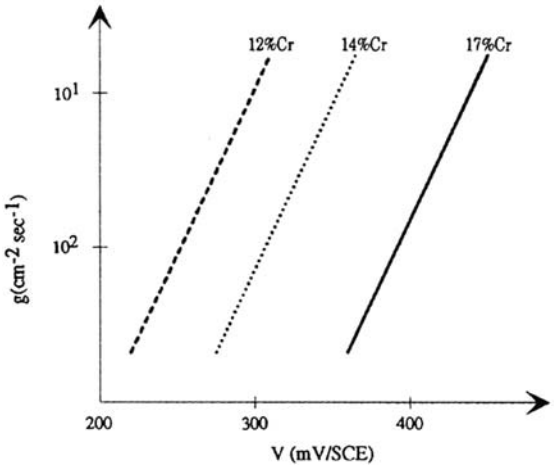


Figure 3 Effect of the Cr content on the pit generation rate in NaCl (0.02 M) for some Ti-bearing (Ti=0.4%) FeCr industrial alloys with different Cr contents. *V* is the electrode potential. (From Ref. 3c.)

alloying elements [8] such as Cu, Ni, and also Mo[5b] may combine in the aqueous solution with these sulfur species and then decrease their noxious effect.

The reason for the beneficial effect of some alloying elements which do not enter the passive film to a large extent (Ni in 304 or 316 steels, Mo in 434 or 316 steels) is not so clear for industrial steels, despite the numerous hypotheses which have been proposed on the basis of academic work. They might (a) lower the ionic current throughout the metal–passive film interface, (b) favor pit repassivation by changing the solution composition in an initiated pit (for instance, by preventing too large a pH decrease inside the pit), or (c) counteract the harmful effect of sulfur species as indicated above. The third mechanism accounts fairly for the Mo effects in 434 and 316 type stainless steels: accepting the idea that adsorbed sulfur plays a major role in pit initiation on such materials, Mo could act [9] by favoring the desorption of sulfur, possibly in a combined state with Mo, adsorbed uncharged S being unstable in the presence of Mo and then reducing finally to soluble H_2S.

The metallurgical processing of the steel (hot and cold rolling, heat treatments, welding, surface treatments) may dramatically modify the pitting resistance of a steel grade as well. The effect of heat treatments on the phase equilibria, recrystallization, and minor element segregation will not be discussed here, but some known or less known evidence must be recalled. First, the steel generally contains some nonmetallic phases such as precipitates (Cr carbides in ferritic steels, for instance) or inclusions (oxides, sulfides, etc.). The difference between precipitates and inclusions is that the former are produced in the metal solid state and the latter during (or at the end of) the melting process, in the metal liquid state. Then the inclusions do not generally produce any segregation at their interface with the metallic matrix, which is not the case for the precipitates (e.g., the chromium carbides). However, nonmetallic inclusions can be unstable inthe corrosive medium; that is the case for sulfides and even for oxides in some cases [10a]. Furthermore, because their ductility is generally not the same as that of the metallic matrix, hot and cold rolling may produce some

Copyright © 2002 Marcel Dekker, Inc.

microdecohesions at the metal-inclusion interface, which behave as micro-crevices and may be some preferential pitting sites, depending mainly on the cold rolling ratio. Anyway, it is now well established that, in industrial steels, inclusions may act as pitting sites [11]. On the other hand, chromium carbides may provoke some chromium depletion in the metal around the precipitate, after a welding treatment or even after the metal cooling at the end of a hot transformation process. Even when these local negative segregations are too weak to produce intergranular corrosion, they may lead to a decrease in the pitting resistance. For this reason, the final annealing must be carefully controlled, mainly for ferritic steels [due to the low carbon solubility in body-centered cubic (bcc) structures].

Last, the final phase for stainless sheet processing is generally annealing, or solution treatment in the case of austenitic steels, followed or not by pickling. When the annealing is performed in hydrogen-containing atmosphere (bright annealing), no pickling is needed but the composition of the annealing atmosphere (for instance, its residual water content) markedly influences the passive film properties [3d]. When annealing is performed in oxidant atmospheres, a pickling treatment should follow in order to remove the thick oxide film which was formed. The composition and the properties of the resulting passive film, together with a change in the metallic inclusion distribution at the metal surface, noticeably affect the pitting resistance. In the same way, so-called nitric acid decontamination treatments are sometimes performed after at the end of the process and also modify the surface properties. Last, the surface condition in the delivery state also depends on the surface roughness, which is itself controlled by the rolling conditions. One sees that the practical pitting resistance of an industrial material cannot be entirely predicted by the simple models developed on model systems!

The Sulfide Inclusions

Sulfide inclusions play a major role in pitting initiation on iron alloys, among them stainless steels. It is worth drawing attention to some of their physicochemical and metallurgical properties.

For AISI standards 430, 434, 304, 316, and more generally for all Ti-free stainless steels, sulfur is combined with Mn to form manganese sulfides, MnS, which act as pitting sites in current corrosive media (see later). Following the sulfur content of the steel and the metallurgical processing, MnS is found either isolated or stuck to other inclusions (generally oxides) or even combined in complex inclusions. Chromium may also substitute for Mn to form some (Mn,Cr) S sulfides, whose Cr content depends on the Mn content of the steel (currently 0.4% for ferritic steels and 1% or more for austenitic ones) as shown in Figure 4. The higher the chromium content in the sulfide, the higher the pitting resistance of the steel, resulting in a better pitting resistance for low-Mn steels [12a], at least when other metallurgical parameters are not modified by the Mn content lowering. In Ti-bearing steels (Ti > some 0.1% by weight or more), the MnS formation is prevented, since Ti sulfides (Ti_xS) are formed at higher temperature during the melting process. Ti sulfides are considered less harmful than MnS for pitting corrosion but are also able to act as pitting sites in some conditions [3e,12a,13].

Three basic characteristics of manganese sulfides are worthy of notice [5b] as far as they can influence the pitting initiation process: (a) They are electronic

Copyright © 2002 Marcel Dekker, Inc.

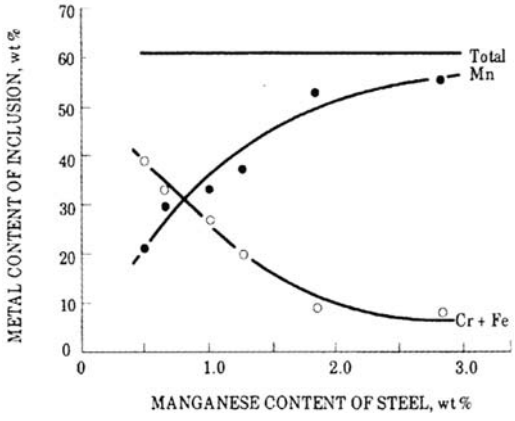


Figure 4 Composition of sulfide inclusions in type 416 (13%Cr 0.3%S) steel as a function of the steel Mn content. (From Ref. 8.)

conductors, but less than the surrounding metal, leading to pit initiation at the inclusion-matrix interface. Their conductivity should depend on their exact chemical composition. (b) They are polarized together with the surrounding metal, but should be unstable in the potential range where the metal is passive, and then readily dissolve, providing some local chemical and electrochemical conditions which differ from ones which prevail on other parts of the surface. (c) Their size morphology, together with their composition, plays an important role in their ability to promote pitting [14]. Rapid solidification or laser surface melting [15a] provides the removal or at least the redistribution of the Mn sulfides, resulting in a strong improvement in pitting resistance.

It should also be noticed that not all the sulfides present at the steel surface promote pit initiation, which some authors explained by differences in their composition and the morphology of the metal-sulfide interface. However, the question is not so clear, because the number of Mn sulfides acting as pitting sites is much smaller than the total number of Mn sulfides at the steel surface. In our opinion, the competition between sulfide dissolution and local modifications in the passive film properties could result in a low-probability stochastic initiation process, which might account for the small number of sulfides which are found to initiate pitting. Some authors underlined the importance of the pitting test procedure for the relation between the MnS dissolution kinetics and the pitting sensitivity [14], which shows once more the absence of any "intrinsic" pitting potential.

Last, the recognition that manganese sulfides are probably the least resistant pit initiation sites in standard industrial stainless steels motivated severe control of the steel microstructure, either by lowering the Mn content (which unfortunately also has some undesirable secondary effects) or, better, by adding small amounts of Ti as alloying elements, preventing the formation of Mn sulfides. However, this means of improving the pitting resistance is itself limited, because in the absence of MnS, pits can initiate on other inclusions—namely Ti sulfides, oxides, or silicates—or possibly on the passive surface itself, as the electrode potential or the chloride concentration increases.

Copyright © 2002 Marcel Dekker, Inc.

The first idea to be proposed to account for the effect of soluble sulfides on pitting initiation was that MnS dissolution provokes locally the formation of a virgin metal surface. This microarea is exposed to an acidified and sulfur species–enriched environment produced by the sulfide dissolution. When the solution near the microarea has reached a certain composition, the contacting metal can no longer repassivate and the metal starts to dissolve [6]. Following other workers [8], complete MnS dissolution is not needed, as the pits preferentially initiate at the metallic matrix-MnS interface. This model keeps open the questions of (a) the MnS dissolution mechanisms, (b) the nature and the effect of the dissolved sulfur species which form during this dissolution and (c) the role played by the passive film, either close to or possibly on the inclusion. From this last viewpoint, the surface condition of the steel is of major importance. The effect of MnS is probably not the same on freshly mechanically polished surfaces or after various surface treatments, including pickling, bright annealing, or electrochemical treatments.

There is some experimental evidence that Cl^- ions cluster either on the nonmetallic inclusions [10b] or at their boundaries with the metallic matrix [12b]. When the MnS is directly exposed to the electrolyte, Cl^- can preferentially adsorb on the inclusion due to its higher electronic conductivity, giving stronger electrostatic image forces than on the surrounding oxide film [8]. In our opinion, Cl^- adsorption is followed by the potential-assisted formation of the adsorbed complex $MnCl^+$, which then dissolves in the aqueous solution according to $(MnCl)^+_{ads} + Cl^- \rightarrow Mn^{2+} + 2Cl^-$. Because their is some evidence that pitting initiation on MnS-containing steels is strongly dependent on the solution pH (see below), it is suggested that Cl^- and OH^- adsorption compete on Mn sulfide surfaces, resulting in pH-dependent dissolution kinetics.

The MnS dissolution provokes the formation of an Mn^{2+}- and Cl^-- enriched local electrolyte [10c] (the Cl^- ions being attracted by the local excess in positive changes in the solution). As long as the concentration remains below a critical level, the pit walls can repassivate, but beyond this critical level an $MnCl_2$ salt layer is formed which may prevent the repassivation. The question of what happens at the metal–salt layer interface has been discussed [16a] and it was suggested that an FeCr oxychloride could form, whose properties, and also possible remnance once the salt layer has dissolved, could play a determining role in repassivation mechanisms. Following another idea, MnS would be covered with a defective passive film [lc] on which the chloride ions first adsorb and then penetrate, leading to the formation of a nonprotective salt chloride layer. The hydrolysis of this salt layer would then increase the local acidity, resulting in the dissolution of the defective passive film. Whatever the proposed mechanisms, chloride adsorption seems to be the first stage of the sulfide dissolution.

Several models have been proposed for the dissolution of sulfur from MnS inclusions. The first idea [6,8] is that, in acidified media, MnS dissolves according to

$$MnS + 2H^+ \rightarrow H_2S + Mn^{2+}$$

or [17]

$$MnS + 2H^+ \rightarrow S + Mn^{2+} + H_2$$

These reactions can be split into the anodic reaction [6,8,10b]

Copyright © 2002 Marcel Dekker, Inc.

$$MnS \rightarrow S + Mn^{2+} + 2e^{-},$$

whose potential is $V(\text{volts}) = -0.12 + .0.03 \log [Mn^{2+}]$, and the cathodic ones,

$$H^{+} + e^{-} \leftrightarrow 1/2H_2 \text{ or [6] } 2H^{+} + 2e^{-} + S \leftrightarrow H_2S$$

with $V = 0.14 - 0.06pH - 0.03 \log [H_2S]$, and possibly [5c]

$$H_2S \leftrightarrow H^{+} + HS^{-}, \text{ then } H^{+} + 2e^{-} + S \leftrightarrow HS^{-}$$

Direct action of water to form sulfates, sulfites or thiosulfates should also be considered [6,8,10b,15b,17].

$$MnS + 4H_2O \leftrightarrow Mn^{2+} + SO_4^{2-} + 8H^{+} + 8E^{-}$$

with $V = 0.23 - 0.06pH - .0074 \log[Mn^{2+}][SO_4^{2-}]$,

$$MnS + 3H_2O \leftrightarrow Mn^{2+} + HSO_3^{-} + 5H^{+} + 6e^{-}$$

then

$$HSO_3^{-} + 5H^{+} + 4e^{-} \rightarrow S + 3H_2O,$$

$$2MnS + 3H_2O \leftrightarrow 2Mn^{2+} + S_2O_3^{2-} + 6H^{+} + 8e^{-}$$

$$S_2O_3^{2-} + H_2O \rightarrow S_{ads} + SO_4^{2-} + 2H^{+} + 2e^{-}$$

All these reactions are potential and/or pH dependent, so they can occur or not according to the actual conditions in, or close to, the pit embryo. This makes rather complex the interpretation of the pitting potential pH dependence when sulfides act as pitting sites (see below). Furthermore, they do not explicitly take into account the effect of chloride ions for the dissolution of Mn^{2+}; they should then be slightly modified for this purpose, introducing the solution chloride content as the third critical parameter for the MnS dissolution kinetics.

It should be noted that photoelectrochemical investigations [15b] suggest that the last two reactions, involving the formation and then dismutation of $S_2O3_3^{2-}$ and resulting in the formation of adsorbed sulfur, are operating in some cases. Photoelectrochemical microscopy shows the deposition around the inclusions of a ring of material deduced to be sulfur, which is consistent with the results of several other studies [6,10b]. A detailed analysis of the fundamental aspects of the sulfur-assisted corrosion mechanisms is presented in Chapter 9.

AN EXAMPLE OF THE EFFECT OF NONMETALLIC INCLUSIONS

Studied Steels and Their Nonmetallic Inclusions

In the following, the steels under consideration are mainly some annealed AISI 430-type FeCr ferritic alloys containing also either Nb (steels A and A') or Ti (steels B and B') additions. Also, some solution-treated 304 and 321 AlSI-type steels were considered (C and D), in order to separate the matrix and inclusion effects. These two steels are austenitic and Ni bearing but the latter contains Ti and is MnS free, whereas the former contains MnS inclusions.

Copyright © 2002 Marcel Dekker, Inc.

Table 1 Steel Composition in wt % or (ppm)

	Cr	Ni	Si	Mn	Ti	Nb	(S)	(C)	(N)
A	16.4		.4	.45		.5	40	240	n.d.
A′	15.7		.4	.45		.7	50	340	340
B	16.8		.4	.45	.4		30	260	140
B′	17.4		.4	.45	.4		30	250	110
C	17.6	8.2	.4	1.4			20	530	470
D	17.8	9.3	.4	1.3	.4		30	310	170

Except for steel A, some Al additions are used as deoxidizing agents during the melting process, which leads to Al ~ 0.030% and induces the presence of some Al_2O_3 inclusions. Note the low sulfur content, which is easily attained with modern steelmaking techniques, and the presence of some stabilizing elements (Ti or Nb), which trap carbon and avoid the formation of chromium carbides. For steels A and A', sulfur is trapped under the form of manganese sulfide. The difference between steels B and B' is their Cr content; both contain Ti, which also traps nitrogen in the form of titanium nitrides and sulfur in the form of Ti sulfides; this trapping occurs during the steelmaking process before the steel solidification. Concerning steel A', some Mn sulfides are found around aluminum oxides (Fig. 5). Because these oxides have a poorer ductility than the metallic matrix, the cold-rolling process provokes some microdecohesions around the inclusion, where some manganese sulfides are often located, leading to the possible formation of noxious microcrevices. This phenomenon is not observed on Al-free steels, where oxides are mainly malleable silicates. However, the art of the steelmaker consists in avoiding the formation of Cr oxides, which could produce a similar but worse effect than Al oxides. In every case, some Mn sulfides are also found closely stuck to Nb carbonitrides (Fig. 6a). Because these carbonitrides precipitate at ~1200°C, this shows that (for the sulfur content considered), the high-temperature sulfur solubility is sufficient for MnS precipitation to occur in the solid steel (lower than 1200°C) while for higher sulfur contents MnS is generally considered to precipitate at the end of the steel solidification. Note that very few isolated MnS precipitates are found, probably because Nb(C,N) act as precipitation sites. This situation contrasts with the behavior of steel C (304), for which (a) no carbides may nucleate the MnS precipitate and (b) sulfides can precipitate in austenite at the delta→gamma transformation temperature.

Figures 5b and 6b show the location of Ti sulfides on steel B, i.e., around the titanium nitrides, embedded in a Ti carbide belt. Detailed examination suggests that al high temperature a homogeneous Ti carbosulfidc belt precipitates around the Ti nitrides (which formed in the liquid steel). Then, lowering the temperature, titanium sulfides and carbides separate at some points as shown in Figure 5b, producing the Ti carbide TiC and a Ti sulfide, identified in some cases (using electron diffraction) as the hexagonal phase Ti_2S. As another result, note that Al oxides have been identified in the core of the Ti nitrides (which is not known in the figures), playing the role of nuclei for TiN precipitation.

Copyright © 2002 Marcel Dekker, Inc.

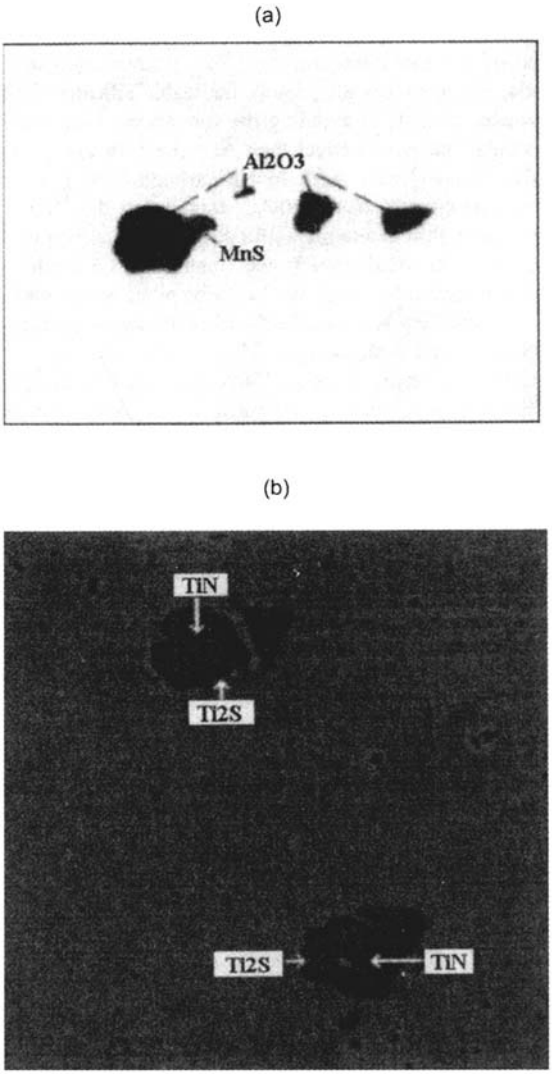
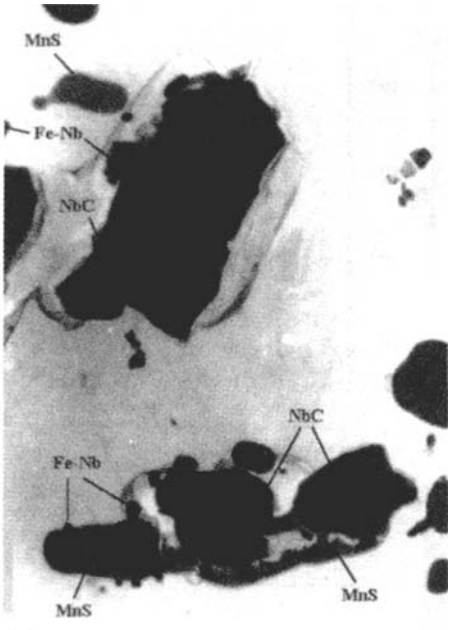


Figure 5 Nonmetallic inclusions (before pitting). Scanning electron microscopy, ×3000. (a) Steel A': MnS nucleated on an aluminum oxide. (b) Steel B: Ti nitride surrounded by sulfur compounds.

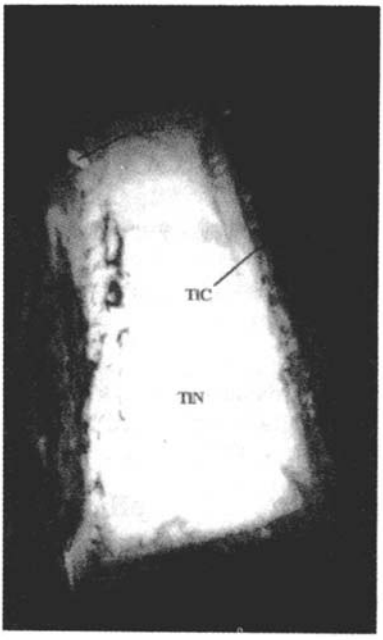
pH Effects and Pitting Sites

The pitting potentials were measured for all these steels using the potentiokinetic method in NaCl aqueous media whose pH was varied from 3 to 6.6. The results for steels A' and B in NaCl (0.02 M) are shown in Figure 7a. No pH dependence is observed for steel B. In contrast, for steel A', a sharp pitting potential decrease is evident when the pH is lowered below a critical value pH_c ranging between 4.5 and 5. Since the main difference between the two steels is the presence or absence of MnS, and Ti sulfides are known to have better stability in aqueous electrolytes than MnS,

Copyright © 2002 Marcel Dekker, Inc.



(a)



(b)

Figure 6 Nonmetallic inclusions (before pitting). STEM (×18,000) on thin foils. (a) Steel A': MnS nucleated on an Nb carbonitride. Intermetallic (Fe, Nb) phases are also observed, (b) Steel B: Ti nitride surrounded by a Ti carbide, in which some Ti sulfides are embedded.

Copyright © 2002 Marcel Dekker, Inc.

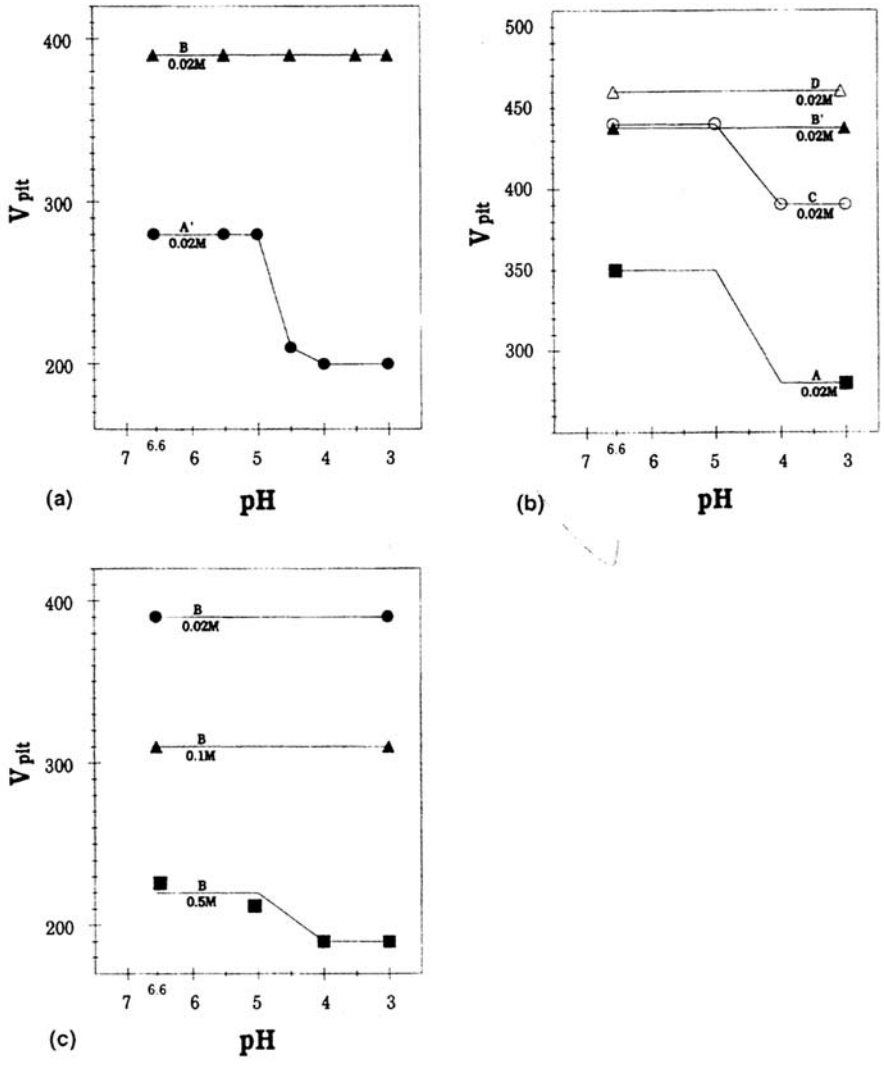


Figure 7 Effect of the solution pH on the pitting potentials. (a) Steels A' and B in NaCl (0.02 M). (b) Steels A, B' (FeCr steels) and C, D (FeCrNi steels) in NaCl (0.02 M). (c) Effect of the solution chloride content dependence for a Ti-containing steel. For low chloride contents (0.02 and 0.1M), there are no pH effects. For 0.5 M, lowering the pH decreases the pitting resistance.

one can assume that this decrease is due to the pH-assisted MnS dissolution. Note that the same phenomenon is observed (Fig. 7b) when comparing the two steels C and D, which are respectively MnS containing the MnS free, showing that the observed effect is related to the nature of sulfides present in the steel and not to other metallurgical factors. Figure 7b also shows the results obtained for steels, A and B', which confirm the above findings. The slight difference between steels B and B' may be attributed to the difference in Cr concentration. The strong difference between

Copyright © 2002 Marcel Dekker, Inc.

steels A and A' may be due to the difference in Cr concentration and sulfur contents but also to the Al oxides present in steel A' and around which MnS are found. The effect of the solution chloride content was also investigated between 0.02 and 0.5 M. Figure 7c shows that for high enough chloride concentrations, a pitting potential pH dependence is found even for Ti-containing steels, suggesting that Ti sulfides are not so stable in such electrolytes. The discontinuity of the pitting potential versus pH variations should then be related to the dissolution of sulfur species, which occurs easily for MnS-containing steels (whatever the steel matrix composition) but only for high enough chloride contents for Ti-bearing steels. Note that the critical pH which is found ($4.5<pH<5$) is the same for Ti-free and Ti-bearing steels and is close to the one deduced from the potential-pH equilibrium diagrams in some chloride-containing aqueous solutions [6,8]. This could support the idea that the critical pH can be deduced from the sulfur species-pH equilibria, regardless of the nature of the dissolved cation (manganese or titanium), once the conditions are reached for the sulfide to dissolve.

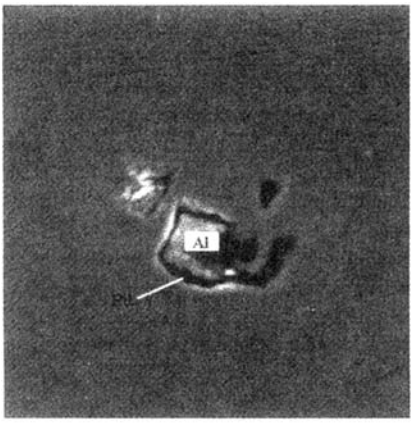
Figure 8 shows the typically observed pit initiation sites. For steel A', whatever the pH or the chloride content, pits initiate either around Al oxides (Fig. 8a), where some MnS is located, or on MnS inclusions (Fig. 8b) around Nb(C,N) or (seldom) isolated. This confirms the preceding hypothesis. For steel B in NaCl (0.5 M) solution, pitting generally occurs at the TiN boundary (Fig. 8c), where Ti sulfides are present. This shows clearly that for such chloride concentrations, Ti sulfides act as pitting sites and becomes unstable when the potential increases. For lower chloride concentration (0.2 M NaCl), the situation is not so clear and pits could initiate directly on the metallic matrix, with no direct relation to nonmetallic inclusions, or in some cases on titanium nitrides. In the two situations, however, Ti sulfides do not seem to act as pitting sites, which is consistent with the absence of any pitting potential pH dependence.

A practical consequence can be drawn from these results: Ti-stabilized steels exhibit better pitting resistance than Ti-free ones, provided that the corrosive medium is not too severe, i.e., the chloride content does not exceed a critical value, depending on the solution pH, which could cause the Ti sulfides destabilization. In the case of crevice corrosion, the situation is more complex. Inside a crevice, the pH decreases and the chloride concentration increases with time. It is an accepted idea that corrosion occurs when the pH becomes lower than a critical value, which is referred to as the depassivation pH. However, at least for the less resistant steels, pitting corrosion may occur in the crevice before this general depassivation. From these results, it is concluded that MnS-containing steels are much more sensitive to this pitting-induced crevice corrosion than Ti-bearing ones. For very severe crevices, however, the chloride content can drastically increase with time Ti-stabilized steels are no longer different from Ti-free ones.

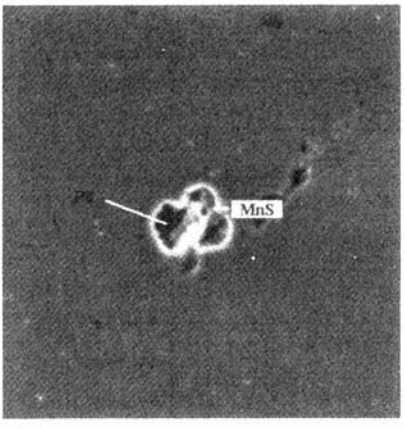
Inhibitive Effect of Sulfate Ions

Sulfate ions are known for inhibiting the pitting corrosion in chloride-containing media. Figure 9 presents the elementary pitting probability–potential variations obtained for steels A and B in 0.1 M NaCl. Three points are noticeable: (a) SO_4^{2-} additions decrease the pitting probability (for a given potential) and increase the conventional pitting potential (for a given chloride concentration). This effect is

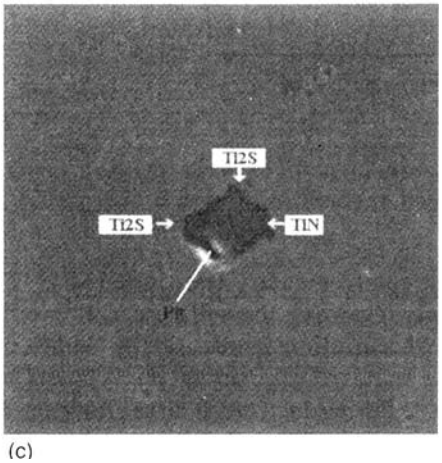
Copyright © 2002 Marcel Dekker, Inc.



(a)



(b)



(c)

Figure 8 Scanning electron microscopy (×3000) on pitted samples. (a) Steel A': pitting at the boundary of an alumina inclusion. (b) Steel A': pitting on a manganese sulfide. (c) Steel B: pitting at the boundary of a Ti nitride.

Copyright © 2002 Marcel Dekker, Inc.

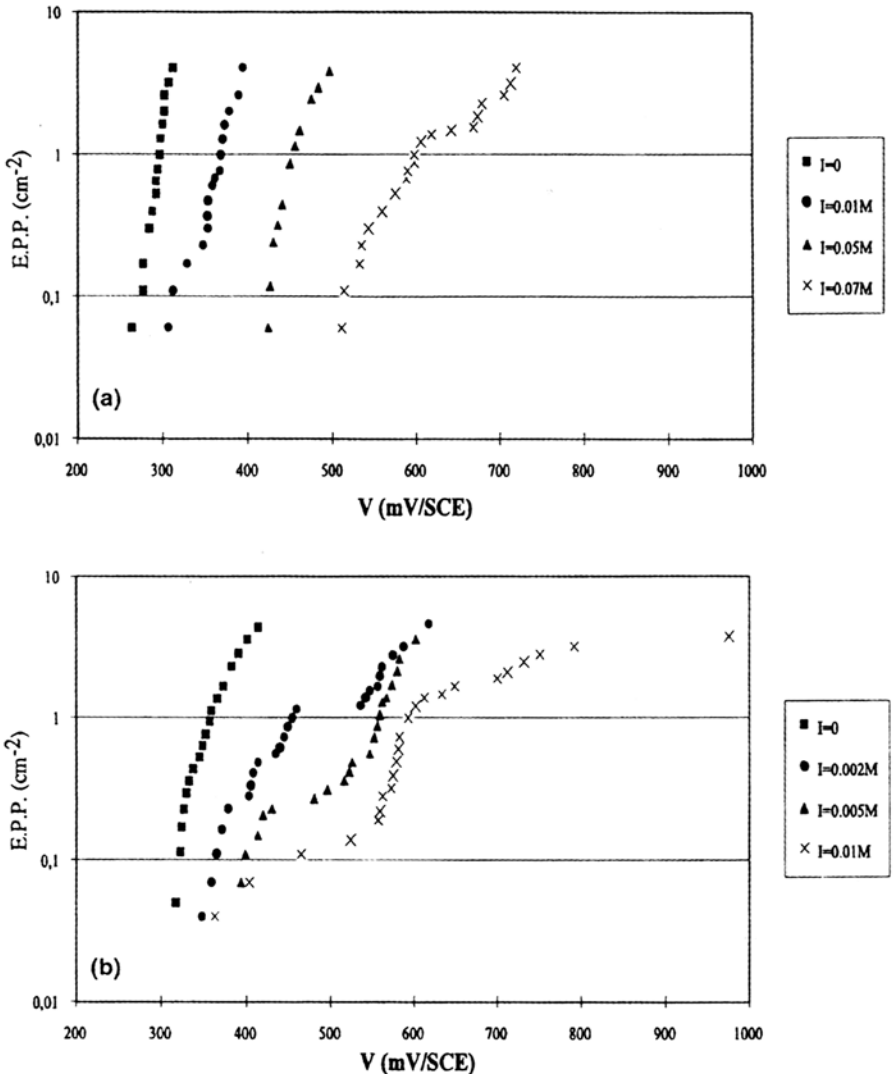


Figure 9 Effect of sulfate ions on the pitting probability in 0.1 M NaCl (pH 6.6). *I* is the sodium sulfate molarity and *V* the electrode potential. (a) Steel A; (b) steel B.

more marked for steel A than for steel B, but complementary tests in 0.5 M NaCl show that the difference between the two steels regarding the sulfate addition efficiency becomes smaller when the chloride concentration increases. (b) Sufficient sulfate additions result in a deviation from the standard exponential $\omega(V)$ law. The sulfate amount necessary to produce a noticeable deviation is much larger for steel A than for steel B. (c) For high enough sulfate amounts, steel B exhibits a bimodal behavior: exponential $\omega(V)$ laws are found both for high and for low electrode potentials. Between these two domains a transition behavior is noted. Further work is needed to interpret these results, but the difference between the MnS-containing and MnS-free steels is now well established.

Copyright © 2002 Marcel Dekker, Inc.

Prepitting Events

Recording the anodic current $i(t)$ during a polarization below the conventional pitting potential (Fig. 10a) provides two types of information. First, the average anodic current decreases with time, probably corresponding to the onset of improved passivity. Second, some oscillations of this anodic current are observed, which, through the same SEM observations as above, were shown to correspond to some initiated and then repassivated pits. The problem which arises for analyzing these oscillations is to separate them from the average anodic current decay (the "anodic current baseline"), which probably corresponds to some passive film modifications. The baseline is determined by associating to each point $[t, i(t)]$ the point $[t, i'(t) = \min \{i(t'), t' = t - \tau/2 \text{ to } t + \tau/2\}]$ where τ is an arbitrary time constant. The frequency $1/\tau$ should be smaller than the characteristic frequencies of the prepitting noise. Figure 10b shows the typical reduced signal obtained for steel A' using this method. For MnS-containing steels (A or A'), the prepitting events are numerous and produce what one may call a prepitting noise. In contrast, for MnS-free steels the anodic events are much less numerous and well seperated, as shown in Figure 10c. It is therefore logical to relate the so-called prepitting noise to the dissolution of manganese sulfides. For MnS-containing steels, the current time signature of the individual prepitting events is found to be a current increase varying approximately as t^2, followed by a sharp current decrease (Fig. 11a). The peak amplitude at 200mV/SCE is of the order of 0.1 to 1 μA. For the MnS-free steels, the form of the $i(t)$ transient is quite different (type II; see Fig. 11b) and the peak intensity is smaller (10 to 100nA at 200mV/SCE). In neutral NaCl (0.02M) solution, the transient is characterized by a sharp increase followed by a slow current decay, as expected for local passive film breakdown followed by passive film healing.

A simple way to analyze the reduced signal corresponding to the prepitting noise (Fig. 10b) is to build up a "distribution function" $N(I)$ which counts, for a given time period T(~ 8 min), the number of events for which the anodic intensity i is larger then I. This function N decreases with I (Fig. 12a). One sees that the prepitting noise increases with the electrode potential and the solution chloride content. Moreover, the solution pH acts in the same way as for the pitting potentials, since a discontinuity of N between pH 4 and 5 is once more evidenced (Fig. 12b). Last, the prepitting noise decreases with the polarization time (Fig. 12c).

Another way is to calculate the power spectral density (PSD) associated with the anodic current fluctuations. Let us consider a Poissonian series of birth and death events (birth frequency λ, death frequency μ), with a parabolic growth law between birth and death. This situation can be modeled as follows:

$$i(t) = \sum_n i_n(t) \text{ with } i_n(t) = \frac{\alpha}{2}(t - t_n)^2 H(t - t_n)[1 - H(t - t_n - \theta_n)]$$

where t_n and Θ_n are, respectively, the induction time and the lifetime of the event number n, H is the step function [$H(x) = 0$ when $x < 0$ and 1 when $x > 0$], and α is a constant. The average current $\langle i \rangle$ and the PSD $\Psi(f)$ are found [4a] to be $\langle i \rangle = \alpha\lambda/\mu^3$ and

$$\Psi(f) = \frac{\langle i \rangle^2}{\lambda} 8\mu^2 \frac{24\pi^4 f^4 + 18\pi^4 f^2 \mu^2 + 5\mu^4}{(4\pi^2 f^2 + \mu^2)^3}$$

Copyright © 2002 Marcel Dekker, Inc.

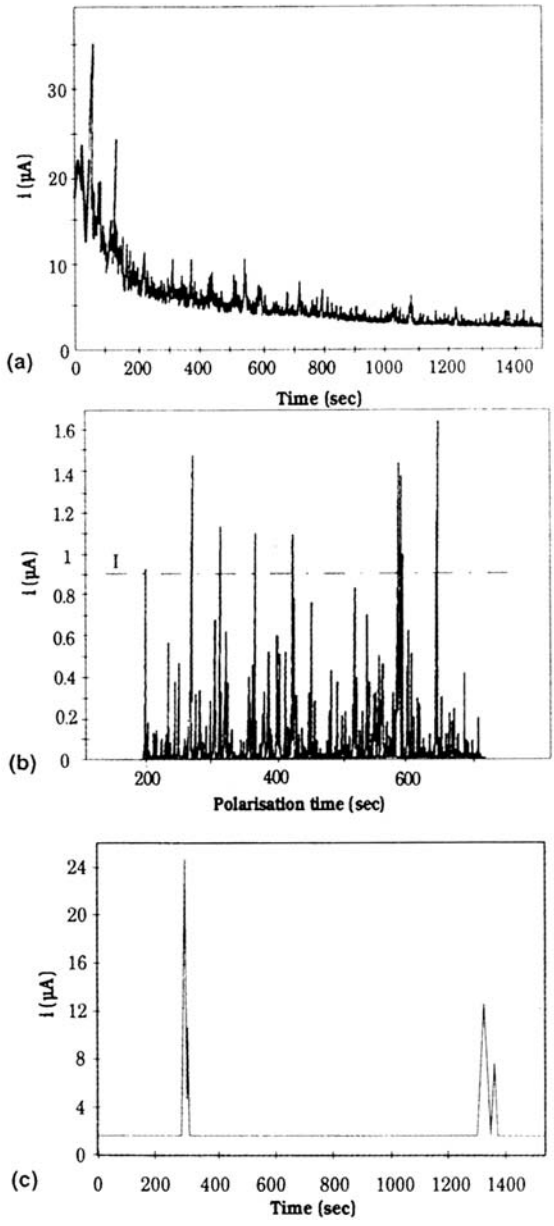


Figure 10 Prepitting events during a polarization at 200 mV/SCE in 0.02M NaCl, pH 6.6. (a) Typical anodic current variations for MnS-containing steels. (b) Typical prepitting noise for MnS-containing steels after substracting the anodic current baseline. (c) Typical anodic micro events for Ti-bearing steels.

Applying the fast Fourier transform (FFT) technique to the reduced signal $i(t)$ allows one to obtain the PSD and then the birth and death frequencies λ and μ by fitting these equations. The result evidences good agreement with the model (Fig. 13) but the values obtained for λ and μ should be considered with

Copyright © 2002 Marcel Dekker, Inc.

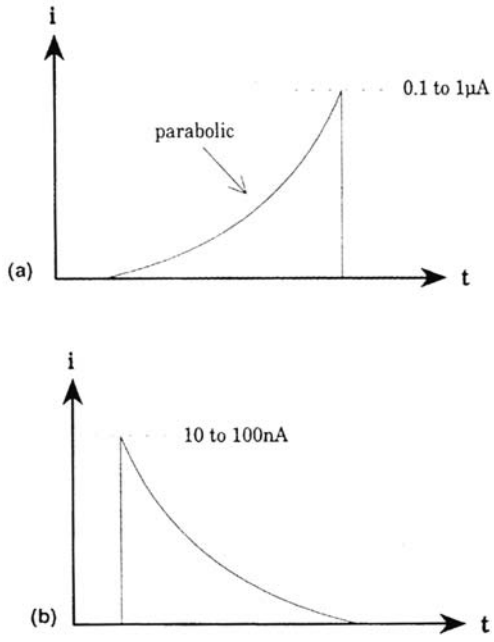


Figure 11 Forms of the individual anodic events. (a) MnS-containing steel; (b) MnS-free steel.

caution, since they may depend on the value of τ chosen for determining the $i(t)$ baseline.

Aging Effects

It has been shown above that the current fluctuations density for MnS-containing steels was a decreasing function of the polarization time. The first idea is that the pitting sites, having initiated an unstable pit. become inactive after pit repassivation, leading to a decrease of the available pitting sites and then of the further pits generation rate. However, it was observed that aging potentiostatically an MnS-free steel decreases the number of further prepitting events as well. Because in this case the prepitting events are very rare, the explanation above does not hold. It is believed that aging rather increases the resistance of the passive film. Figure 14 shows the effect of a prepolarization treatment (1 h at various potentials in the test solution itself) on the further pitting resistance. One can see that such a prepolarization increases the further pitting potential ($dV_{pit}/dV_{pol} \sim 0.5$ in any case, for $V_{pol} = -200$ to +200mV/SCE), regardless of the type of sulfide present in the steel. The main conclusion is that prepolarizing a sample in the corrosive solution under conditions in which pitting does not occur improves the further corrosion resistance, which is clearly related to passivity reinforcement. This shows that not only the nonmetallic inclusions but also the passive film play a role in the pitting initiation. However, increasing the prepolarization time from 1 to 16 h shows that the effect of the aging time is not the same for the two types of steels (Fig. 15). A 16-h potentiostatic aging is more beneficial for MnS-free steels than for MnS-containing ones. It is believed

Copyright © 2002 Marcel Dekker, Inc.

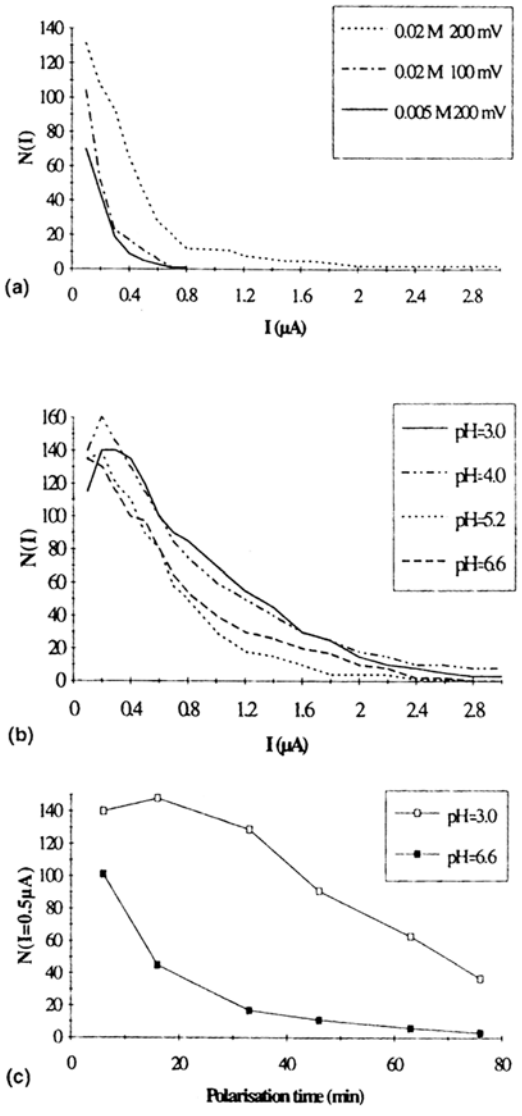


Figure 12 The distribution function $N(I)$ for an MnS-containing steel (A') polarized at various potentials (200 and l00mV/SCE) in some NaCl aqueous solutions. Measurements are made in the time period $[T_p, T_p + T]$ where $T \sim 8$ min. (a) Effect of electrode potential and of the solution chloride content, pH 6.6, $t_p = 16$ min. (b) Effect of the solution pH. NaCl 0.02 M, 200mV/ECS, $t_p = 8$min. Results at pH 6.6 and 5.2 are similar. The noise increases significantly for pH 4 or 3. (c) Effect of the polarization time t_p and of the solution pH on $N(I = 0.5\ \mu A)$, NaCl 0.02 M, 200 mV/SCE.

that the dissolution of sulfur-containing species counteracts in the latter case the beneficial effect of the passive film reinforcement. Furthermore, in the first case (MnS-free steel), the pitting probability law $\omega(V)$ exhibits a bimodal behavior, as already observed in the case of sulfate-containing medium.

Copyright © 2002 Marcel Dekker, Inc.

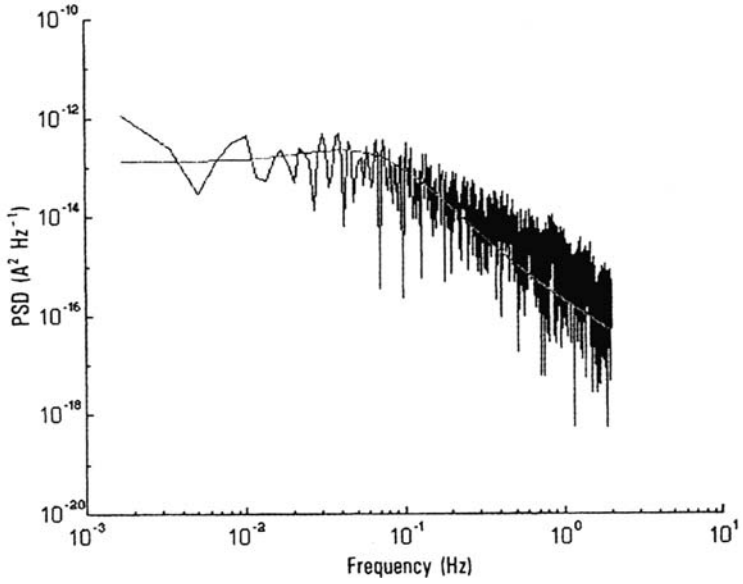


Figure 13 MnS-containing steel: typical PSD vs. frequency diagram for a unitary acquisition period (512s), $f < 2$ Hz. The high-frequency noise is due to the limited sampling (2048 points). Polarization at 200 mV/SCE in 0.02 M NaCl, pH 6.6. $\lambda = 0.023$ Hz, $\mu = 0.43$ Hz, PSD(0) = 1.33×10^{-13} A^2s.

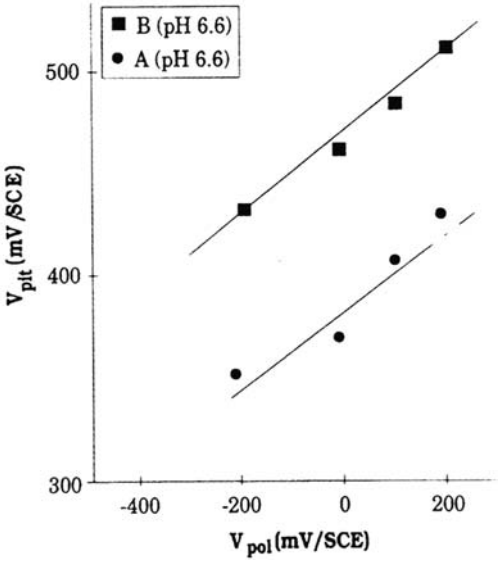


Figure 14 Effect of polarizing the samples 1 h at various potentials V_{pol} lower than the initial pitting potential on the further pitting potential V_{pit} (potentials vs. SCE). NaCl 0.02 M, pH 6.6.

Copyright © 2002 Marcel Dekker, Inc.

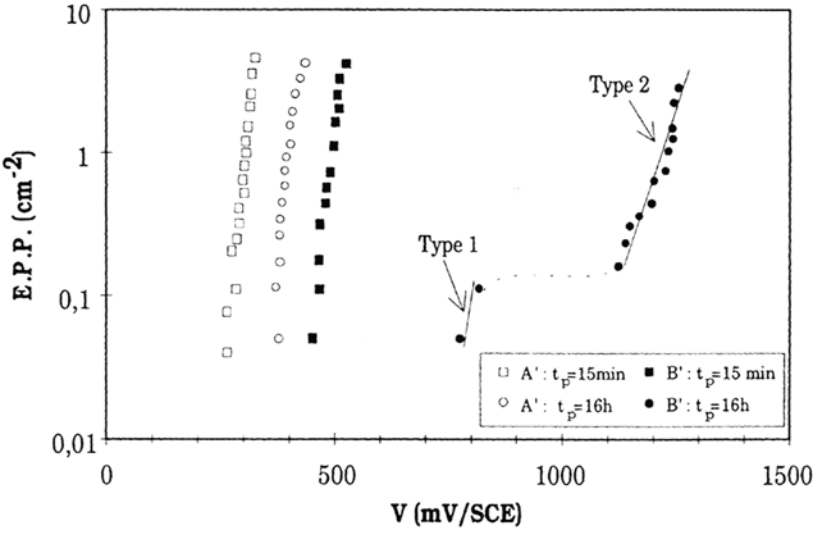


Figure 15 Effect of a 16-h aging at constant potential (steel A', 150 mV; steel B', 200 mV) on the elementary pitting probabilities $\bar{\omega}(V)$. NaCl 0.02 M, pH 6.6.

Figure 16 shows the effect of aging the samples for 24 h at rest potential before the pitting potential measurement in NaCl (0.02 M), pH 6.6, instead of for 15 min in the standard procedure. The rest potential evolution was recorded and found to be

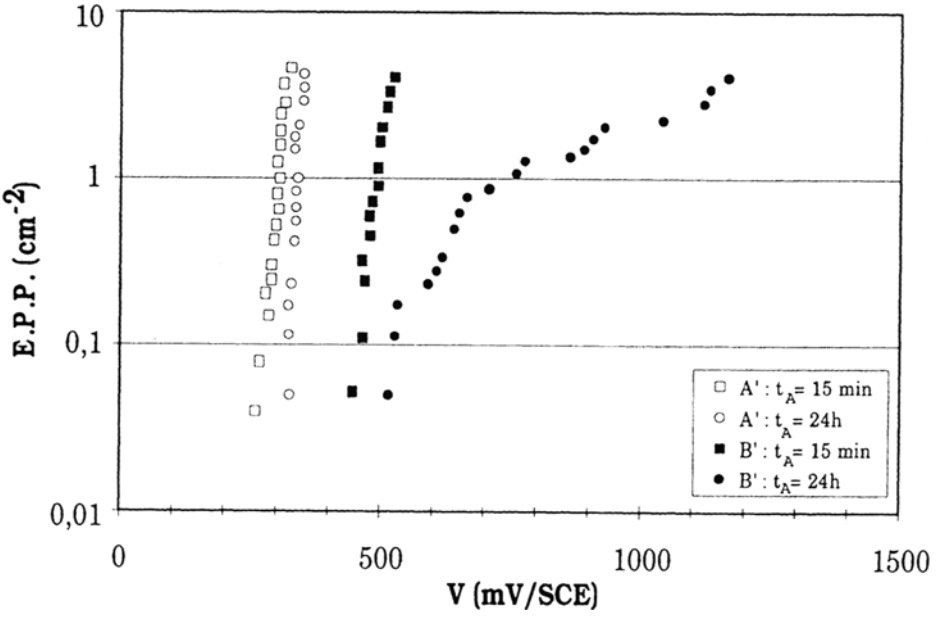


Figure 16 Effect of rest potentials aging on the elementary pitting probabilities $\bar{\omega}(V)$. NaCl 0.02 M, pH 6.6.

Copyright © 2002 Marcel Dekker, Inc.

the same for MnS-containing and MnS-free steels (from nearly –330 mV/SCE at time zero to nearly –150 mV after 24 h). Rest potential aging does not produce any measurable prepitting events (which would result in some rest potential fluctuations), at least in these experimental conditions. However, it slightly increases the further pitting potential, a little more for the MnS-free steels than for the MnS-containing ones. This rules out the first assumption, following which the pitting potential improvement could be the consequence of the decrease of active pitting sites.

The improvement of the pitting resistance by aging the passive surface in the corrosive medium itself but in conditions under which no pitting occurs is also a matter of practical evidence on a much larger time scale (of the order of some months). It is believed that this improvement is due to some passive film modifications. This question forms the subject of some current work [3d].

METASTABLE PITTING

Current Fluctuations Under Potentiostatic Control

The existence of some fluctuations in anodic current under potentiostatic control has been recognized for a long time [18] as resulting from the occurrence of metastable pits (prepitting events), and the role played by the inclusions acting as pitting sites was sometimes identified [5d]. In several works, however [4b,19], no particular attention was paid to the nature, number, or morphology of these inclusions, but it is likely that the presence of manganese sulfides was at the center of the problem. It is intended in this section to present a critical survey of these topics.

In the work by Bertocci et al. [19], the electrode potential is chosen close to the pitting potential and the anodic current is recorded in chloride-containing borate buffer solutions; the average current density is found to increase noticeably after an induction time corresponding to the setup of a stable pit. Some current fluctuations are observed within and beyond the induction period, but these two situations should be discussed separately. Before the pit "stabilization," the fluctuations are probably due to the occurrence of unstable pits (in the mesoscopic stage of pitting initiation) which then repassivate. The typical prepitting event consists of an anodic increase, followed by a sharp decrease sometimes up to negative values, and then a slow increase up to the stationary value (Fig. 17a). The number of events increases with the solution chloride content but decreases with the steel chromium content, becoming undetectable (smaller than the instrumental noise) for Fe-20%Cr alloys. After a stable pit has been initiated, the average anodic current increases (roughly linearly) but some fluctuations are also recorded, perhaps corresponding to some secondary pits or other phenomena. Note that (Fig. 17b) the first events to occur in this stage consist of a slow current increase (roughly parabolic) followed by a sharp decrease. Last, no fluctuations were found in chloride-free borate solutions.

The fluctuations of anodic current were investigated in a different way by Podesta et al. [20], who showed that in an H_2SO_4 (1 M) chloride-containing solution a high sulfur-bearing steel (AISI 303) exhibits some anodic current oscillations in a close potential range determined at the active-passive transition region. These oscillations are kept undamped for a particular value V_{osc} of the electrode potential at which their intensity (or the charge involved in a single oscillation) is also maximum.

Copyright © 2002 Marcel Dekker, Inc.

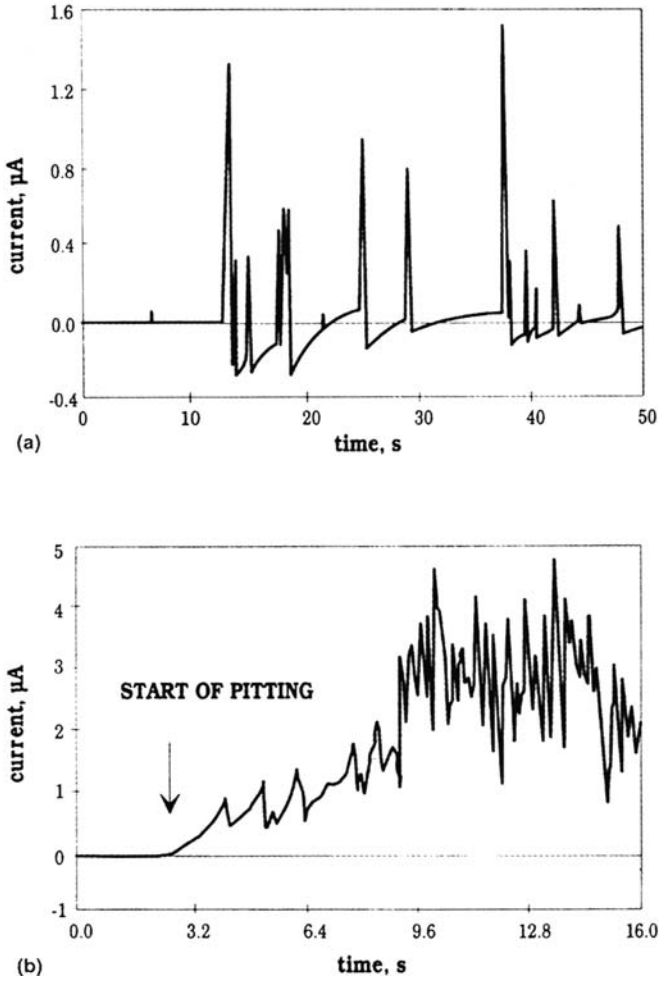


Figure 17 (a) Fe12% Cr alloy in buffered 0.1 M NaCl. Prepitting noise before the occurrence of a stable pit. (b) Fe20% Cr alloy, anodic transients in the course of a stable pit development. (From Ref. 19.)

The oscillation frequency, the maximum oscillation intensity, and the oscillation potential increase linearly with the chloride concentration, with V_{ocs} varying as 2.3 kT/q for large chloride concentrations (typically > 6000 ppm) and as 2.3 $kT/2q$ for smaller ones. The authors suggest the existence of a Lotka-Volterra oscillator acting between some active and passive regions at the steel surface, the nature of which is not clearly identified. This model could be slightly improved by considering three types of sites, active, passive, and blocked), being aware of the fact that further work is needed for applying this exciting idea to the actual pitting initiation mechanisms. Last, competitive adsorption between water molecules, chloride ions, and HSO_4^- ions, which possibly act as inhibiting species, should occur on some preferential sites, which are assumed to be some metallurgical defects, possibly including manganese sulfides (or their neighboring passive film).

Copyright © 2002 Marcel Dekker, Inc.

The work by Keddam and colleagues [4b] deals with the anodic current fluctuations during the potentiokinetic scan of an AISI 304-type stainless steel in NaCl (0.5 M) and NaCl (0.5 M) + Na_2SO_4 (0.5 M) aqueous solutions. It was found that the faster the potential is swept, the higher is the intensity of the fluctuations (in terms of their magnitude and frequency) but that the scan rate dependence is not consistent with the assumption of a nucleation frequency depending only on the electrode potential. The authors correlate the fluctuations of the passive current to the high-frequency dielectric behavior of the passive film and suggest a correlation between these fluctuations and the degree of nonstationarity of the passive film. This assumption is supported by the fact that stopping the potential sweep and recording the anodic current decay toward its steady state shows that the current fluctuations decline progressively and finally vanish. No reference is made to the possible role of MnS dissolution as the source of the prepitting events, but one should notice that the effect of the scan rate is not consistent with a determining effect of the MnS dissolution kinetics in the occurrence of prepitting events, showing that despite the major role played by the inclusions in pit initiation, the properties of the passive film cannot be disregarded. Last, no fluctuations are found in an equimolar sulfate + chloride aqueous solution, suggesting that competitive adsorption of water, chloride, and sulfate ions controls the first stage of pitting initiation, or its inhibition.

Cao et al. [21] analyzed the PSD for some AISI 304 (MnS-containing) and 321 (Ti-bearing, then MnS-free) steels. No reference is made to the difference in inclusions between the two steels. For 321 steel, the elementary prepitting event is found to consist of a linear increase in anodic current, up to some μA in the tested conditions, followed by an exponential decrease. The frequency dependence of the PSD depends on the time characteristics of these two processes (growth rate of the micropit and repassivation time constant), which are potential dependent. Following the values of these time characteristics, and then the electrode potential, the PSD varies as f^{-n} at the high-frequency limit, with $n = 2$ to 4. A white noise (no frequency dependence) is found at very low frequency (some 0.1 Hz). From this work, it is also inferred that the solution chloride content affects the nucleation frequency but not the growth or the repassivation kinetics of the micropit.

Tsuru and Saikiri [22] worked on a 304 steel and found that the elementary prepitting event consists of a progressive current increase (which seems to be linear or parabolic on the presented figures), followed by a sharp decrease. Moreover, the frequency of the fluctuations tends to decrease with polarization time, which is in accordance with the results presented in the preceding section.

Working on 304 steels in acidic media, Pistorius and Burstein [23a] found that the current increased as the square of time, up to some 100 nA. Using 50 μm-diameter electrodes, Burstein and Martin also observed [23b] some spikes with heights of the order of 10 to 100 pA. Two types of spikes were observed: a quick current increase followed by a relatively slow decay, and a slow increase followed by a sharp decrease (Fig. 18). Some additions of sulfate were shown [23c] to partially inhibit the pit nucleation but also to decrease the micropit growth rate, which is explained in terms of the change in solubility of the metal cations produced by the dissolution. No indication is given of the effect of sulfate on the repassivation rate, motivating some further investigations. The same authors also proposed a model for the transition of an unstable pit to stability. They established that the product of the

Copyright © 2002 Marcel Dekker, Inc.

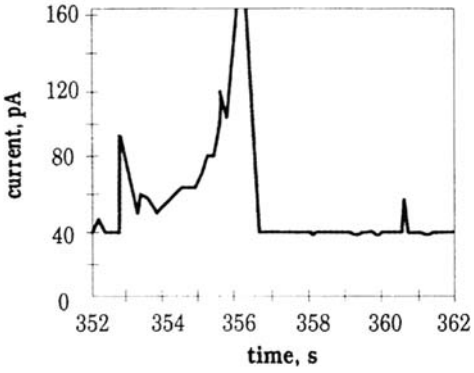


Figure 18 Detail of some prepitting events on AISI 304 steel (specimen size, 50 μm). (From Ref. 23b.)

pit depth and current density must exceed a minimum value for maintaining a sufficiently aggressive solution at the dissolving surface so that the pit does not repassivate. However, this minimum is generally not achieved in the first stages of pitting, and the pit growth requires the presence of a barrier to diffusion at the pit mouth, which is thought to be either a remnant of the passive film or a vestige of the outer surface of the metal itself. Rupture of this "pit cap" leads to repassivation of the metastable pit. The higher the current density inside a metastable pit, the larger the probability of the onset of stable pitting. However, this current density in *each* pit is independent of potential, since the growth is diffusion controlled. The effect of the potential on the distribution of the current densities of a *population* of pits, and then the potential dependence of the stable pit generation rate, is believed to be the result of a change in the type of activated pitting sites when the potential increases. As far as nonmetallic inclusions are concerned as pitting sites, their dissolution changes the local electrolyte composition, but this composition change is counteracted by the diffusion. The geometric conditions make the diffusion more restricted on some sites than on others; the former are therefore activated at a lower potential than the latter. Last, metastable pits formed at more positive potentials are more likely to grow into stable pits than those formed at lower potentials.

Working on some industrial steels with various Cr, Ni, and Mo contents, whose sulfur content is not specified but probably contains MnS inclusions, Schmucki and Bohni [24ab] correlated the pitting resistance and the number of prepitting transients to the electronic properties of the passive film. The number of transients was found to increase with the electrode potential, up to a critical potential V_{crit}, then to decrease, in the same way as the photoresponse of the passive layer. The number of transients is believed to increase with the concentration in deep localized electronic traps in the film. In this work, the existence of V_{crit} is explained by a Cr (III)/Cr(VI) transition in the passive film [24c], but it is likely that several other film modifications could be responsible for such behavior. Last, microscopic investigations revealed that sites which exhibit an enlarged photocurrent coincide with inclusions present in the bulk material.

From another point of view, Hunkeler et al. [24d] considered the potential-assisted formation of a salt film (instead of the protective oxide film) as responsible

Copyright © 2002 Marcel Dekker, Inc.

for the appearance of the current transients. This is not far from the idea proposed by Doelling and Heusler [25], then by Okada [26a], following which the prepitting noise is associated with halide island formation on the passive film. Another idea from Okada [26b] is that the noise is the result of a two-step initiation mechanism (Fig. 19), involving a competition between the OH^- and Cl^- adsorption and the formation of a transitional halide complex which promotes the dissolution. However, it is likely that such a mechanism does not act at the same scale as the one involving the pitting transients described above, since these transients clearly involve the dissolution of a significant part of the metallic substrate in the course of metastable pit development.

The Works by Williams and Colleagues

There are many papers on pitting initiation mechanisms by Williams and colleagues [15]. The authors proposed a model in which pits are randomly nucleated in space and time, with a probability per unit time and area λ, and then die with a probability per unit of time $\mu[1 - H(t - \tau_c)]$, where H is a step function (see above) and τ_c a critical age beyond which the pits becomes "stable" and always survive. The rate of nucleation of stable pits is then $\Lambda = \lambda \exp(-\mu\tau_c)$. Assuming that the current density at the pit nucleus rises linearly with time ($di/dt = C$), which is perhaps disputable, the authors give a detailed statistical analysis [15cd] of the anodic current distribution, deducing, for instance, the survival probability from the probability for the first passage of the anodic current beyond a critical level corresponding to the onset of stable pitting ($i_{crit} = C\tau_c$). The repassivation rate μ is found to be not dependent on the electrode potential and, more surprisingly, on the composition of the steel (one should however note that all the investigated steels were probably MnS containing, no attention being paid to the sulfur level). The nucleation rate for unstable pitting λ is said to be determined by the solution variables (conductivity and buffer capacity). Above a certain potential (depending on the steel) λ is approximately constant, independent of the steel or the electrode potential, and below another potential it vanishes. There is some confusion, however, between these two limiting potentials and no evidence is given that between the two, λ is not potential dependent (as other

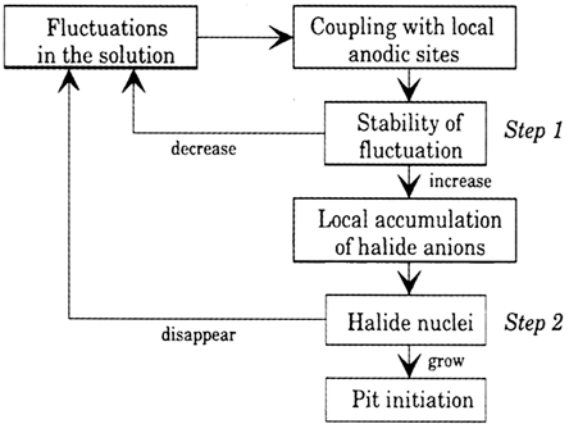


Figure 19 A two-step nucleation mechanism. (From Ref. 26c.)

Copyright © 2002 Marcel Dekker, Inc.

work suggested). In this model the rate C of current rise at the pit nucleus is the one parameter which would vary with the electrode potential. Note that, although the linear time dependence of the current makes this model different from that proposed by Gabrielli and colleagues [4b], the power spectral density frequency of the anodic current has the same asymptotic limit as Gabrielli's [i.e. $f^2\Psi(f)$ = constant when $f \to \infty$; see above]; however, in contrast with the Gabrielli model, no low-frequency plateau is found.

Going further, the authors proposed that pitting initiation is controlled by the onset and the maintenance of a sufficient gradient of acidity (provided by the hydrolysis of the dissolved metal cations) and electrode potential on the scale of the surface roughness of the specimen. Fluctuations in these gradients, leading to the birth and death of events, could arise because of fluctuations in the boundary layer thickness in the liquid at the metal surface; a pit would become stable when its depth, including the surface roughness, significantly exceeds the thickness of the solution boundary layer. Let us note that such ideas are not far from those proposed by Okada [26], which additionally involve the definition of a critical wavelength for the potential fluctuations parallel to the surface, which would be of the order of magnitude of the average distance between some "efficient" metallurgical flaws. However, the idea that local acidification is the cause of pit nucleation does not seem to be supported by experimental evidence, particularly in unbuffered acidic media, at least for the initial stages of pit initiation. In our opinion, the electric field at the filmsolution interface (the electrical potential gradient) and the chloride ion enrichment are probably responsible for pit nucleation (see later) and their fluctuations should therefore be at the origin of the prepitting events.

Furthermore [15e], the stable pit generation rate Λ was shown to be proportional to the microscopic pit generation rate λ, at least for some given alloy and corrosive medium. However, the proportionality factor $\lambda/\Lambda = \exp(-\mu\tau_c)$ is much smaller than 1, so that unstable pits can appear (even at very low chloride concentrations, such as 10 ppm) at much lower potentials than stable ones (for the definition of which a critical current of the order of 10 μA was chosen, to be compared to some 100 nA for the detection of unstable pits). Prepitting a specimen does not lead to increased sensitivity to further pitting, probably due to reinforcement of the passive film resistance during the prepitting experiment, which the authors attribute to an increase in passive film thickness. Although the observed effect is not questionable, one should not consider as implicit evidence that the pitting resistance improvement is caused by an increase in passive film thickness, since other beneficial modifications of passive film (Cr enrichment, film dehydration) may occur during aging.

In another paper, Stewart and Williams [15a] investigated the pitting sensitivity of some AISI 304 steels with various sulfur contents (in fact, the modern 304 low-sulfur industrial steels probably have a lower, or at least equivalent, sulfur content as the high-purity steel considered in the study, in which S is some 30 ppm). Some sensitive techniques were used to detect unstable pits at the level of some nA. It is clearly demonstrated that sulfur-rich inclusions dominate as pitting nucleation sites and that the lifetime of unstable pits is related to the sulfide particle size. It is proposed that the sulfur derived from the inclusion helps to stabilize the pit growth, which we reformulate by saying that it helps to stabilize the micropit in its mesoscopic stage by preventing the repassivation, possibly leading to a growing macroscopic pit. Last, laser melting treatments considerably reduce the nucleation frequency and the

Copyright © 2002 Marcel Dekker, Inc.

lifetime of micropits, which is consistent with the inclusion size effect, since this process dramatically reduces the inclusion size at the specimen surface.

Studies using microelectrodes [15f] reveal some events whose amplitude is of the order of 10 to 100 pA, the coulombic charge being of the order of 100 nC, and the frequency of some 10 mHz, which the authors associate possibly with the microscopic stage of pitting initiation (i.e., the breakdown and healing of passive films). An important point is that most of the events are characterized by a sharp rise of the anodic current followed by a slow decay, in contrast to the current transients associated with pit nucleation on macroelectrodes for the same MnS-containing steels. Anyway, these events could not be detected on macroelectrodes because they could not be distinguished above the background current. This is an important point of the paper, to be compared with the different forms of current transients shown in the preceding section for steels containing different types of sulfides. Last, the authors discussed the form of the observed current decay during the repassivation process and showed that it is consistent with the cluster percolation theory that they proposed [15g] for binary alloy dissolution and passivation. The important point is that some arguments are put forward for the observed prepitting events to occur at the microscopic (atomistic) scale and not at the mesoscopic one, as for the results generally obtained on macroelectrodes.

Remarks

It is worth noting that, in whatever way a pit nucleus was born, its further development to form a pit embryo (growing metastable pit) depends on the electrolyte concentration which locally sets up in the electrolyte when the metal dissolves. The development of the pit embryo implies the local stabilization of an acidic corrosive medium, differing from the surrounding one. This local acidification induces a local dissolution of the metal in the active state, which is compensated only by the diffusion of the corrosion products. This dissolution in turn provokes an acidification due to the hydrolysis reactions and the process is self-sustained, provided that the diffusion or the electromigration is slow enough in the electrolyte. Formally [3h,5d], if J is the anodic current and X represents the concentration in corrosion products, one has $dX/dt = KJ(V, X) - DX$, where the metal-electrolyte potential difference V is a control parameter (J increases with V) and parameters K and D represent respectively the production in corrosion products by the anodic dissolution and their dilution into the electrolyte by a diffusion process. The steady state conditions write $dX/dt = 0$. The system is locally stable when

$$\frac{\partial}{\partial X}\left(\frac{dX}{dt}\right) < 0 \Leftrightarrow \frac{\partial}{\partial X} J(V, X) < \frac{D}{K}$$

This condition is fulfilled when V is smaller that a critical potential V_{crit} (the "protection potential") which depends on the bulk electrolyte concentration and on the nature of the pitting site. The critical potential acts as a bifurcation parameter beyond which a metastable pit can grow and below which it repassivates (as far as the diffusion parameter D does not decrease). When a pit nucleus repassivates ($V < V_{crit}$), the current transient is expected to show the form presented in Figure 11a. This situation occurs generally when no efficient diffusion barrier takes place (D/K large) but this is of course dependent on the presence or not of some nonmetallic inclusions (e.g., MnS) whose dissolution can provide harmful chemical

Copyright © 2002 Marcel Dekker, Inc.

species. In contrast, when a pit embryo grows ($V > V_0$), the current transient is expected to show the form presented in Figure 11b, with a slow current increase corresponding to the pit growth, followed by a sharp decrease corresponding to the breakdown of the diffusion barrier (D drastically increases), for instance, the breakdown of the pit cap formed by a vestige of the outer metallic surface at the pit mouth (see Fig. 1). The growth rate of the metastable pit and the conditions for the diffusion barrier to vanish depend of course on the electrolyte composition inside the pit and then on the presence or not of dissolving nonmetallic inclusions.

Now considering = $\{X_i\}$ as a set of concentrations for chemical species i, the master equations of the system evolution are written as $dX_i/dt = K_iJ(V, X_j) - D_iX_i$, which is a set of ordinary differential equations. Since $J(V, X_i)$ is nonlinear in X_i, the system may produce in some cases (close to V_{crit}) some complex oscillations, explaining qualitatively the existence of a prepitting noise.

Rest Potential Fluctuations

In open-circuit conditions, the prepitting events result in some rest potential fluctuations as well, although this question is less well documented in the literature than the anodic current transients. In a general discussion of the phenomena occurring in the early stages of pitting [16b], Isaacs cited some work on Ni-base alloys, from which it appears that rest potential prepitting transients consist of some sharp potential falls followed by slower return to the stationary value. On the other hand, Magaino [27] analyzed the power spectral density of the rest potential fluctuations on a 304 type steel and evidenced two results of great metallurgical importance: (a) The potential fluctuations are more pronounced for cold-rolled specimens than for solution-annealed ones, and (b) in the 0.05–2-Hz frequency range, the PSD amplitude increases with the steel sulfur content.

Hashimoto and colleagues [28] published a stochastic analysis of potential fluctuation during passive film breakdown and repair on iron, later criticized by Isaacs [16c]. The typical form of the prepitting transient is shown in Figure 20, leading to the consideration of several stages in pit initiation: (a) nucleation (onset of the rest potential decrease), (b) micropit growth (quick potential decay), (c) termination of this growth and (d) pit repassivation. The authors state that:

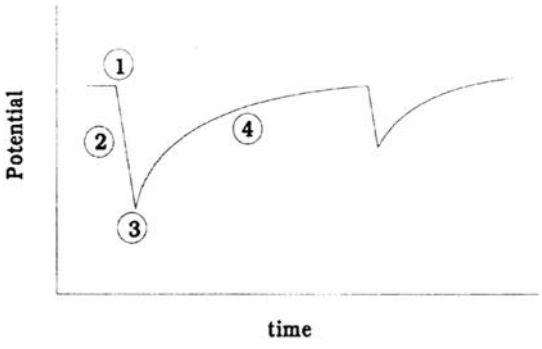


Figure 20 Schematic representation of rest potential fluctuations due to prepitting events. (From Ref. 16c.)

Copyright © 2002 Marcel Dekker, Inc.

1. Pit nucleation can be approximated to a Poissonian process, the nucleation rate λ decreasing exponentially with time as shown in an earlier section and Ref. 3g.
2. In the micropit growth, the pit area A_{pit} is proportional to the square of the time and the potential fall ΔV (measured from the average rest potential V_0 corresponding to the passive state, so that $V = V_0 - \Delta V$) is given by $\Delta V = b \ln(1 + A_{pit} i_{pit}/A i_p)$, where A is the specimen area, b a constant, i_p the current density in the passive state, and i_{pit} the current density into the dissolving pit (assumed to be a constant).
3. The maximum potential fall ΔV_m (stage 3) follows a Gaussian distribution law. The average value $V_m = V_0 - \Delta V_m$ of the lowest reached potential appears to be independent of the immersion time. At the opposite, the average rest potential V_0 increases with time due to the reinforcement of the passivity during rest potential aging (which is briefly said in this paper to be the consequence of the film thickening). Thus, ΔV_m increases with the immersion time. V_m is assumed to be a critical potential and $(V - V_m)$ the driving force for pitting initiation. The pit initiates when a critical driving force is reached but, in the following stages, the potential and then the driving force decrease, leading finally to termination of growth when $\Delta V = \Delta V_m$.
4. The potential decay reflects the repassivation kinetics. For the authors, this stage is controlled by the passive film growth inside the pit after the potential has decreased below V_m, which progressively reduces the anodic current i_{pit}. Using a direct logarithmic law for the passive film growth and reformulating slightly the authors' discussion, one finds $\exp \Delta V = b \ln(t/\tau + \exp \Delta V_m/b)/(t/\tau + 1)$ where τ is a time characteristic of the transition from the high dissolution rate situation to the situation where $i \sim 1/t$, as expected when the current is controlled by the passive film growth.

This last point (the repassivation mechanism) is debated by Isaacs [16c], particularly as the formation and growth of a passive layer should not be sufficient to provide the anodic current for the potential difference ΔV to nullify, considering the balance with cathodic reactions which occur inside an active pit. For this author, the role of the capacitance of the passive surface is crucial to the interpretation of the transient potential changes during pitting. Following this review, cathodic current is drawn from the interfacial capacitance of the passive surface during the micropit growth (stage 2) and repassivation (stage 4) is the reverse process (a slow recharging of the capacitance). Then the slow potential decay in stage 4 is not controlled by film growth but by the progressive polarization of the cathodic reaction. It is worth noting that the capacitance model also has some implications in stage 2, since the potential changes should be related to the charge of the pit [16d].

Oltra and colleagues [29] analyzed the role of the capacitance during a "birth and death" pitting event, with reference to some 304 stainless steels. The time constant for repassivation is found to depend on the impedance of the passive surface in open-circuit conditions. From these results it can be inferred that the micropit growth is under the control of the electrode area, which not only has some practical

Copyright © 2002 Marcel Dekker, Inc.

consequences but also sheds light on the applicability of some current laboratory techniques (such as noise analysis), since the cell geometry may be a determining factor and the actual pit current may be distorted before reaching the measurement setup.

CONCLUDING REMARKS

The results presented in this chapter show that pitting initiation on industrial stainless steels exhibits a combination of metallurgical influences, such as nonmetallic inclusion effects, and stochastic behavior, as evidenced by both the scattering of the measured pitting potentials and the prepitting noise. A third essential factor is the influence of the passive film properties on the establishment of a stable pit. However, many problems come in mind when considering the relative or combined effects of these three factors. First, the proper effect of the passive film is not clear when pitting initiates on nonmetallic inclusions. The current models for pit initiation generally refer to the passive film breakdown, while the investigated steels contain many nonmetallic inclusions, which probably act as pitting sites. Second, since many stages are involved in the formation of a metastable pit, at the onset of stable pitting, the question remains open which stage is deterministic and which stage is probabilistic. Third, the size effects are often disregarded, and microscopic models are frequently proposed to account for macroscopic effects. However, the recent findings of several workers make the situation clearer, and we feel that the route is now open for a better understanding and then better modeling in this rather complex field.

For simplicity, the elementary pitting process can be divided into three phases (Fig. 21).

1. Pit nucleation, which leads to the formation of a small area of bare, unfilmed, metal (pit "nucleus"). Pit nucleation as a whole is likely to be a probabilistic process but can itself be the result of several elementary steps at the atomic scale, involving possibly deterministic and probabilistic mechanisms. The nucleation rate ($cm^{-2}\ s^{-1}$) is denoted G.
2. The development of a metastable pit, which leads to local dissolution of a significant part of the underlying metal. The dissolving metal area is referred to as a pit "embryo." The result is either the formation of a stable pit (pit stabilization) or the repassivation of the embryo. The development and the repassivation of a metastable pit are probably deterministic processes for *each* embryo but may be probabilistic for a *population* of embryos, growing on different pitting sites. The formation of a stable pit (stages 1 and then 2) will be referred to as the initiation stage. The rate of formation ($cm^{-2}\ s^{-1}$) of a stable pit is the pit generation rate and is de noted g. In some experimental conditions (for instance, high scanning rate potentiokinetic tests) the repassivation rate of the metastable pits is expected to be constant and then g is proportional to the nucleation rate G. In this case, the measurement of g provides some information on the nucleation stage. In other experimental conditions (for instance, potentiostatic tests at suitable potentials), some information is obtained on the repassivation processes involved in stage 2. Last, it is believed that

Copyright © 2002 Marcel Dekker, Inc.

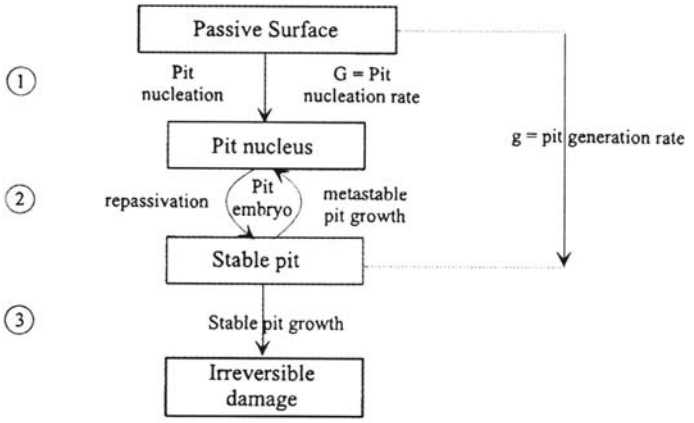


Figure 21 Multistep mechanism for the onset of a stable pit.

prepitting noise results from nonlinear feedback phenomena [15h] occurring in phase (2).

3. The growth of a stable pit, which is deterministic. This third step is outside the present concern but it is itself a complex stage of pitting, involving possible repassivations at a macroscopic scale.

As far as nucleation is concerned, three situations may occur. First, pit can nucleate directly on the passive film, far from any nonmetallic inclusion. This is the case generally considered in most theoretical models, but there is no evidence that it is the prevailing situation for industrial stainless steels and more work is needed to clarify this point. It is a point for future work to study in more detail both the effect of the electronic properties of the passive film and the reactions occurring at its outer interface (adsorption, complex formation, etc.), seeking a better understanding of the distribution of potentials throughout the interface. Second, pitting can arise from the dissolution of unstable inclusions (such as MnS), leading to a small area of bare metal when the inclusion is entirely dissolved. The point to be clarified is then the proper role of the passive film properties in the pit nucleation process. Last, passive film and inclusions can interact together. Referring to the results presented earlier, a simple model can be proposed in the case of the MnS inclusions. It has been pointed out that MnS dissolution is pH and chloride assisted, producing some Mn^{2+} ions and some sulfur-containing species, followed by a pH decrease and a local increase in chloride concentration. This increase in chloride concentration is provoked by the electromigration of chloride ions from the solution bulk to the pit embryo (due to a local excess of positive charges close to the dissolving sulfur), resulting in an increase in the $[Mn^{2+}][Cl^{-}]$ product, then the precipitation of a nonprotective salt layer. However, only a small number of MnS sulfides produce a pit embryo, which is generally explained by differences between the sulfide properties (or the properties of the metal-inclusion interface). Another idea is that at the beginning of MnS dissolution, the local excess of positive charges is not sufficient to increase significantly the local chloride concentration and that this process should be assisted by passive film breakdown

Copyright © 2002 Marcel Dekker, Inc.

in the inclusion neighborhood, which produces a large amount of metal cations, leading to local Cl^- enrichment due to electromigration. One suggests that beyond a critical electrode potential a large number of microscopic passive film breakdown events are randomly produced, generally followed by passive film healing, except close to the MnS sulfides, where some dissolved sulfur species can prevent the repassivation. This phenomenon is a low-probability event, explaining the small number of the inclusions acting as pitting sites. From this situation, the stable sulfide dissolution may arise, as proposed above. The question remains open whether the sulfur species act only as inhibitors of the passive film healing or also increase the film breakdown probability at the atomistic scale. Anyway, such a model shows that the pitting rate is influenced by the passive film properties at the early stages of pit nucleation and accounts for the fact that pits initiate close to the inclusions. In a further step the inclusion may dissolve, producing a bare metal area (pit nucleus).

More generally, it should be pointed out that, whatever the pit nucleation mechanism, the survival probability of a pit nucleus (or even of a pit embryo) depends on the state of the surrounding passive film, since different passive films formed on the same alloy do not exhibit the same pitting resistance. The distribution of potentials and electric charges around the pit nucleus should likely provide a better assessment of the intensity of the anodic reactions than the average potential difference V and are probably a function of both the pitting site characteristics and the surrounding passive film properties [3i].

REFERENCES

1. (a) Z. Szlarska-Smialowska, *Pitting Corrosion of Metals,* Nace, Houston, 1986; (b) Z. Szlarska-Smialowska, *Corrosion (Nace) 28*: 389 (1972); (c) Z. Szklarska-Smialowska and E. Lunarska, *Werk. Korr. 32*: 478 (1981), cited in Ref. 8.
2. T. Shibata and T. Takeyama, *Corrosion (Nace) 33*: 243 (1977).
3. (a) B. Baroux, *Corros. Sci. 27*: 969 (1988); (b) B. Baroux, *Mem. Sci. Rev.* Met. December 683 (1988) (in French); (c) B. Baroux, F. Dabosi, and C. Lemaitre, *Stainless Steels* (P. Lacombe, B. Baroux, and G. Béranger, eds.), Les Editions de Physique Les Ulis (France), 1993, p. 314; (d) D. Gorse, J. C. Joud, and B. Baroux, *Corros. Sci.* 33: 1455 (1992); (e) B. Baroux and D. Gorse, Proceedings of the European Symposium on Modification of Passive Film (P. Marus, B. Baroux, and M. Keddam, eds.). The Institute of Metals, 1994, p. 300.; (f) B. Baroux, 11th international Congress of Corrosion, Florence, Italy April 1990, 5, 469; (g) B. Baroux and D. Gorse, NATO Workshop on Aqueous Corrosion modeling. Plymouth, 1993, in press.; (h) B. Baroux, *Passivity of Metals and Semiconductors* (M. Froment, ed.), Elsevier, Amsterdam, 1983; (i) D. Gorse and B. Baroux, to be published.
4. (a) G. Gabrielli, F. Huet, M. Keddam, and R. Oltra, *Corrosion (Nace) 46*: 266 (1990); (b) M. Keddam, M. Krarti, and C. Pallotta, *Corrosion (Nace) 43*: 454 (1987).
5. J. L. Crolet, L. Seraphin, and R. Tricot, (a) *C.R. Acad. Sci. Paris 280C*: 333 (1975) (in French); (b) *Mem. Sci. Rev. Met. 73*: 703 (1976) (in French); (c) *Mem. Sci. Rev. Met. 74*: 281 (1977) (in French); (d) *Mem. Sci. Rev. Met. 74*: 647 (1977) (in French).
6. G. S. Eklund, *J. Electrochem. Soc. 121*: 467 (1974).
7. A. J. Sedriks, *Int. Met Rev. 28*: 295 (1983).
8. G. Wranglen, *Corros. Sci. 14*: 331(1974).

Copyright © 2002 Marcel Dekker, Inc.

9. A. J. Betts and R. C. Newman, *Corros. Sci. 34*: 1551 (1993).
10. (a) M. A. Baker and J. E. Castle, *Corros. Sci. 33*: 1295 (1992); (b) Ruoru Ke and J. E. Castle, *Corros. Sci. 30*: 409 (1990); (c) M. A. Baker and J. E. Castle, *Corros. Sci. 34*: 667 (1993).
11. P. Poyet, A. Desestret, H. Coriou, and L. Grall, *Mem. Sci. Rev. Met.* February 133 (1975) (in French).
12. (a) A. Szummer, K. Lublinska, and M. Janik-Czachor, *Werk. Korr. 41*: 618 (1990). (b) A. Szummer and M. Janik-Czachor, *Br. Corros. J. 9*: 216 (1974).
13. B. R. T. Anderson and B. Solly, *Scand. J. Metall. 4*: 85 (1975).
14. P. E. Manning, D. J. Duquette and W. F. Savage, *Corrosion, (Nace), 36*: 313 (1980).
15. J. Steward and D. E. Williams, *Corros. Sci. 33*: 457 (1992); (b) A. R. J. Kucernak, R. Peat, and D. E. Williams, *J Electrochem. Soc. 139*: 2337 (1992); (c) D. E. Williams, C. Westcott, and M. Fleismann, *J. Electroanal. Chem. 180*: 549 (1884); (d) D. E. Williams, C. Westcott, and M. Fleismann, *J. Electrochem. Soc. 132*: 1796 and 1804 (1985); (e) J. Steward and D. E. Williams, *Advances in Localized Corrosion*, Nace 9, Orlando, FL, 1987, p. 131; (f) A. M. Riley, D. B. Wells, and D. E. Williams, *Corros. Sci. 32*: 1307 (1991); (g) D. E. Williams, R. C. Newman, Q. Song, and R. G. Kelly, *Nature 350*: 216 (1991); (h) D. E. Williams, J. Steward, and P. H. Balkwill, *Critical Factors in Localized Corrosion* (G. S. Frankel and R. C. Newman, eds.), The Electrochemical Society, Corrosion Division, Proceedings volume 92-2, p. 36.
16. (a) U. Steinsmo and H. S. Isaacs, *J. Electrochem. Soc. 140*: 643 (1993); (b) H. S. Isaacs, *Corros. Sci. 29*: 313 (1989); (c) H. S. Isaacs, *Corros. Sci. 34*: 525 (1993); (d) H. S. Isaacs and Y. Ishikawa, *J. Electrochem. Soc. 132*: 1288 (1985).
17. S. E. Lott and R. C. Alkire, *J Electrochem. Soc. 136*: 973 (1989).
18. J. M. Defranoux, *Corros. Sci. 3*: 75 (1963).
19. U. Bertocci and Y. Yang-Xiang, *J. Electrochem. Soc. 131*: 1011 (1984).
20. J. J. Podesta, R. C. V. Piatti, and A. J. Arvia, *Corros. Sci. 22*: 193 (1982).
21. C. Cao, Q. Shi, and H. Lin, *Bull. Electrochem. 6*: 710 (1990).
22. T. Tsuru and M. Saikiri, *Corros. Eng. 39*: 401 (1990).
23. (a) P. C. Pistorius and G. T. Burstein, *Mater. Sci. Forum 111–112*: 429 (1992); (b) G. T. Burstein and S. P. Martin, *Philos. Mag. Lett. 66*: 127 (1992); (c) P. C. Pistorius and G. T. Burstein, *Corros. Sci. 33*: 1885 (1992).
24. (a) P. Schmucki and H. Bohni, *Werkst Korr. 42*: 203 (1991); (b) P. Schmucki and H. Bohni. *J. Electrochem. Soc. 139*: 1908 (1992); (c) P. Schmucki and H. Bohni, *Oxide Films on Metals and Alloys*, The Electrochemical Society, Toronto, 1992, p. 326; (d) F. Hunkeler, G. S. Frankel, and H. Bohni, *Corrosion (Nace) 43*: 189 (1987).
25. R. Doelling and K. E. Heusler, *Z. Phys. Chem. 139*: 39 (1984).
26. T. Okada, (a) *J. Electrochem. Soc. 132*: 537 (1985); (b) *Corros. Sci. 26*: 839 (1986); (c) *Critical Factors in Localized Corrosion* (G. S. Frankel and R. C. Newman eds.), The Electrochemical Society, Corrosion Division, Proceedings volume 92–2, p. 65.
27. S. Magaino, *J. Electroanal. Chem. 258*: 227 (1989).
28. M. Hashimoto, S. Miyajima, and T. Murata, *Corros. Sci. 33*: 885 (1992).
29. R. Oltra, G. M. Indrianjafy, and R. Roberge, *J. Electrochem. Soc. 140*: 343 (1993).

Copyright © 2002 Marcel Dekker, Inc.

11

Crevice Corrosion of Metallic Materials

Pierre Combrade
FRAMATOME, Centre Technique, Le Creusot, France

INTRODUCTION

Crevice corrosion is a form of localized corrosion that occurs in zones of restricted flow where a metallic material surface is in contact with a small volume of confined, stagnant liquid whereas most of the material surface is exposed to the bulk environment.

Crevice zones may result from the design of the component (see Fig.1) or from the formation of deposits during service, shutdown, or even fabrication. These deposits may come from suspended solids in the environment, corrosion products, or biological activity. Low-flow areas are prone to the formation of such deposits.

Crevice corrosion occurs mainly (but not exclusively) on passive materials. The most important problem is the crevice corrosion of stainless steels, nickel-base alloys, aluminum alloys, and titanium alloys in aerated chloride environments, particularly in sea or brackish water, but also in environments found in chemical, food, and oil industries. Other cases of crevice corrosion are also known such as the so-called *corrosion by differential aeration* of carbon steels, which does not require the presence of chloride in the environment. Also mentioned in the literature is the crevice corrosion of steels in concentrated nitric acid and inhibited cooling water and of titanium alloys in hot sulfuric environments.

In this chapter, the basic mechanisms of crevice corrosion are briefly presented but most of the text is devoted to the crevice corrosion of passive alloys, particularly Fe-Ni-Cr- … alloys in aerated chloride environments. Phenomenological aspects, the mechanisms of initiation, the conditions of propagation, the modeling, the experimental techniques, and the possibility of prevention are successively described.

BASIC MECHANISMS OF CREVICE CORROSION

The specificity of the crevice zones arises (Fig. 2) from (a) the limited mass transport by diffusion and convection between the inside of the crevice and the bulk environment, (b) the high (metal surface area)/(solution volume) ratio inside the

Copyright © 2002 Marcel Dekker, Inc.

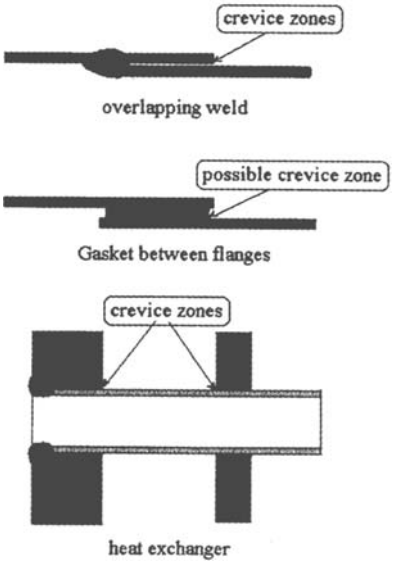


Figure 1 Examples of crevice zones due to design.

crevice, (c) the presence of large external surfaces exposed to the bulk environment, and, in many cases, (d) the significant solution resistance between the inside and the outside of the crevice.

Crevice corrosion is caused by a change of the local environment inside the crevice zone into more aggressive conditions. On passive materials, the local conditions must become severe enough to cause passivity breakdown and the onset of active dissolution.

Usually the local change of environment occurs in two steps. The *first step* is due to the local exhaustion of reactants, usually the dissolved oxygen, and/or the local accumulation of corrosion products as a consequence of the restricted transport kinetics between the crevice and the bulk environment. This leads to the buildup

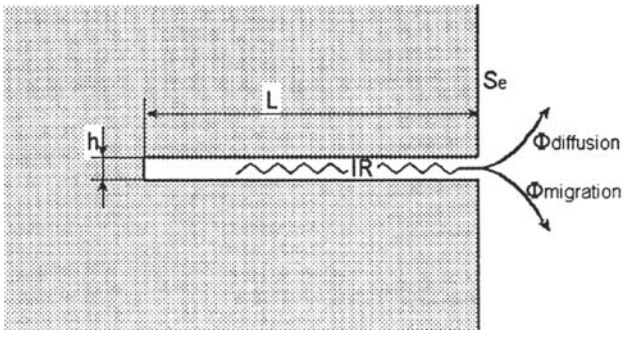


Figure 2 Characteristics of a crevice zone: reduced diffusional exchanges with the bulk solution, low $\Phi_{diffusion}$; small solution volume in contact with large surface area, L/h large; large external surfaces S_e; solution resistance between crevice gap and bulk solution, IR drop.

Copyright © 2002 Marcel Dekker, Inc.

of a galvanic cell between crevice and external surfaces with two consequences: (a) a difference in the corrosion potential inside and outside the crevice due to the solution resistivity* and (b) an additional source of environment modification caused by the electrolytic migration between the crevice and the bulk solution. This *second step* is self-accelerated if the local environment becomes more severe and tends to increase the galvanic current and the electrolytic migration.

Crevice Corrosion Due to *IR* Drop

In some instances, the increase of the corrosion rate in the crevice may be due only to the *IR* drop. The more classical case where the *IR* drop is responsible for crevice corrosion is the corrosion by differential aeration of unalloyed steels in near-neutral water.

Unalloyed steels exhibit an active-passive transition in near-neutral water (Fig. 3). In aerated environments, the availability of a cathodic current from oxygen reduction allows steel passivity to be stable, whereas active dissolution prevails in deaerated conditions (Fig. 3a). Inside a crevice, the local change of environment is due to the rapid consumption of the dissolved oxygen. However, a cathodic current from oxygen reduction may be still provided by the external surfaces. If the *IR* drop is low enough, the surface may remain passive inside the crevice (curve 1 in Fig. 3b). If the *IR* drop is too large (more efficient crevice effect), however, the corrosion potential inside the crevice is too low for the passivity to be stable (curve 2 in Fig. 3b) and the surfaces inside the crevice gap become active. In this case, the corrosion rate in the crevice is usually much higher than the corrosion rate of the free surfaces in a deaerated environment because of the supply of cathodic current by the external surfaces.

Crevice Corrosion Due to Local Changes of Anodic Behavior of the Material

In most cases, crevice corrosion also requires a local change of the environment that results in a change of the material anodic behavior. For example, crevice corrosion of stainless steels in aerated chloride environments requires a local depletion of the oxidizing species, but it is triggered by a second step of environment modification that causes a pH drop and an increase of chloride concentration in the crevice (see later).

Local pH drop is not the single cause of crevice corrosion. For example, local depletion of passivating species may be the origin of crevice corrosion as is the case for steels in cooling water with anodic inhibitors such as nitrite or chromate ions.†

Initiation and Propagation

Because of the general mechanisms described previously, crevice corrosion always includes two steps: (a) an *initiation or incubation period* required for the local environment to undergo a critical change during which no significant dissolution damage occurs in the crevice and (b) a *propagation period* during which the corrosion

* This potential difference is usually referred to as *IR* drop.

†Note that cathodic inhibitors do not cause such severe crevice corrosion because their local depletion does not significantly increase the cathodic current available in a deaerated crevice.

Copyright © 2002 Marcel Dekker, Inc.

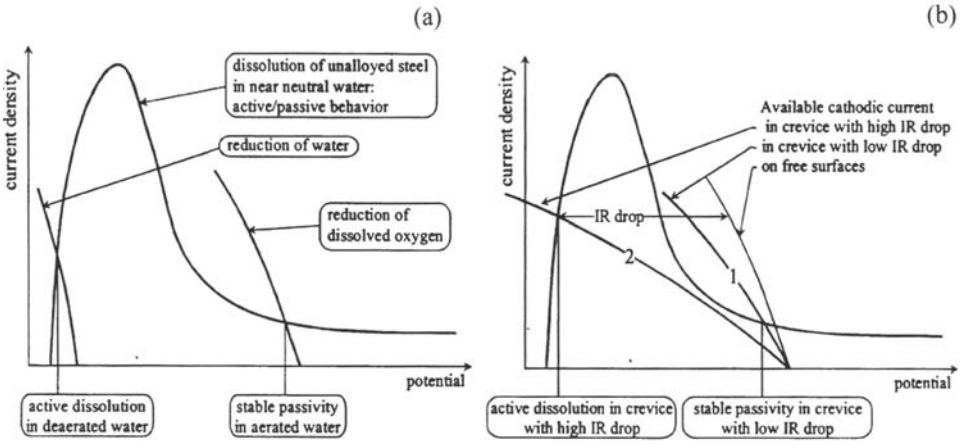


Figure 3 Crevice corrosion of unalloyed steel in near-neutral water. (a) Behavior of "uncreviced" steel surface in aerated and deaertated water. (b) Behavior in presence of crevice—role of *IR* drop.

damages occur. Depending on the cause of the localized corrosion, the initiation time may or may not be a significant part of the lifetime of a structure suffering crevice corrosion.

Parametric Effects

Crevice Geometry

The severity of the crevice regarding the initiation stage strongly depends on its geometry, i.e., the crevice gap (h) and the crevice depth (L).

The crevice gap h (Fig. 2) controls the volume/surface ratio of the crevice: the smaller this ratio, the faster the environment changes due to surface reactions. However, the crevice gap must be wide enough for the environment to enter but it becomes inefficient if it is too wide. Figure 4 [1] shows the extent of crevice corrosion of unalloyed steel in nitric acid as a function of the gap. For stainless steels in chloride environments, short incubation times are obtained for crevice gaps of the order of a micrometer or less [2,3] and the incubation time increases rapidly with the crevice width. As a consequence, surface roughness is of major importance, and, for example, crevice corrosion can be avoided by polishing the surfaces in contact with seals to a smooth finish.

The crevice depth L (Fig. 2) controls the transport processes: the deeper the crevice, the slower the transport kinetics between the crevice tip and the bulk environment. A minimum crevice depth is often required for corrosion to occur [2].

Bernhardsson et al. [4] introduced the parameter L^2/h as a geometric criterion of crevice severity. A similar r_0^2/h ratio is included in one of the nondimensional parameters introduced by Alkire et al. [5].

External Surfaces

The free surfaces outside the crevice gap constitute the cathode, which provides cathodic current to balance the anodic dissolution in the crevice gap. Thus, the larger

Copyright © 2002 Marcel Dekker, Inc.

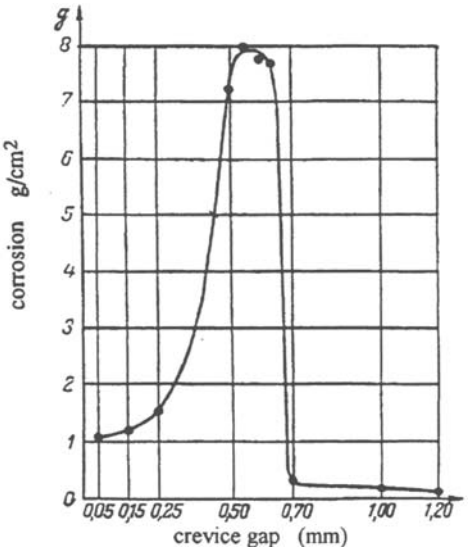


Figure 4 Effect of crevice gap on the amount of corrosion of unalloyed steel in nitric acid [1].

the free surfaces and the higher the bulk solution conductivity, the higher the available cathodic current and the higher the corrosion potential in the crevice. Except in the cases where the *IR* drop is the driving factor for crevice corrosion (see earlier), this usually shortens the incubation period and increases the corrosion rate in the propagation stage.

IR drop

The *IR* drop depends on both the crevice geometry and the solution conductivity. Most of the *IR* drop usually occurs inside the crevice gap, but the *IR* drop in the bulk solution may be of major importance in dilute solutions and limit the effective area of the cathode.

It is worth noticing that the *IR* drop and the diffusion fluxes between the crevice and the bulk solution are controlled by the same restricted transport path. Thus, the more limited the diffusion transport, the larger the *IR* drop.

The *IR* drop is responsible not only for the buildup of a potential difference between the crevice and the free surfaces but also for potential gradients inside the crevice. If large enough, the *IR* drop could make possible water reduction near the crevice tip and this may create a more complex situation, the crevice tip becoming an additional source of cathodic current and reversing the environmental evolution [6].

PHENOMENOLOGY OF CREVICE CORROSION OF PASSIVE ALLOYS IN AERATED CHLORIDE ENVIRONMENTS

The first point to emphasize is that *crevice corrosion of passive alloys does not occur in environments deprived of oxidizing species other than water.* Generally, it does not occur in deaerated solutions. On the contrary, oxidizing agents such as many biocides (hypochlorite, chlorine, chlorine dioxide, etc.) may cause crevice corrosion.

Copyright © 2002 Marcel Dekker, Inc.

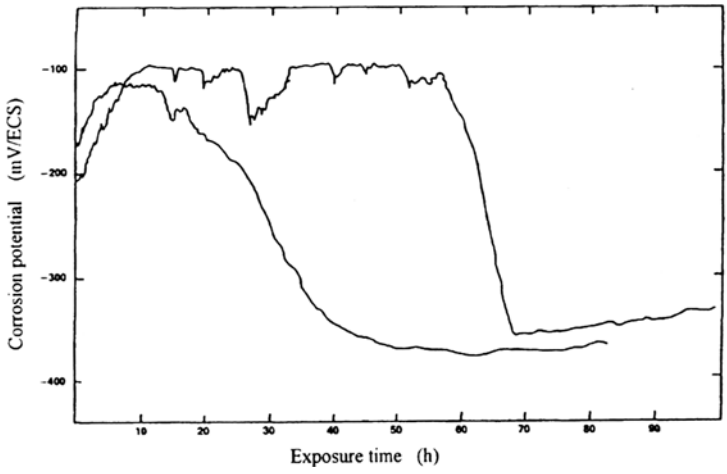


Figure 5 Potential drop due to initiation and propagation of crevice corrosion (crevice area ratio 1:1) in two different tests on a 316 stainless steel in 1 M NaCl, pH 6 solution at room temperature. (From Ref. 3.)

As the other crevice corrosion phenomena, the development of crevice corrosion on passive alloys in aerated (and more generally in oxidizing) chloride environments involves two steps:

First, there is an *incubation period*, which may be very long for the more resistant materials. During this period, short corrosion potential transients can possibly be observed (Fig. 5), but, when examining the surface inside the crevice, no significant traces of corrosion are observed.

Then, *initiation* of rapid corrosion occurs inside the crevice and the *propagation period* begins during which the corrosion proceeds quite rapidly. The formation of deposits outside the crevice allows visual detection of the corrosion. Initiation of corrosion in the crevice is also marked by a significant drop in the corrosion potential of the material [3] (Fig. 5). Thus, monitoring of the corrosion potential can be an efficient way to detect crevice corrosion (as well as other types of localized corrosion) in its early stages or even during the incubation period.

Figure 6 shows an example of severe crevice corrosion of stainless steel bolts in seawater.

Effect of Potential: Critical Potentials for Initiation and Repassivation

For a given bulk environment, crevice initiation appears to be dependent on the corrosion potential of the free surfaces: initiation occurs when this potential exceeds a critical value E_{crev}. The propagation may occur at potentials significantly lower than the potential that caused the initiation to occur, and indeed, the potential of a freely corroding material is generally lower during the propagation compared with the incubation period (Fig. 5). However, propagation stops below a critical potential for the crevice repassivation E_{rp}.

Copyright © 2002 Marcel Dekker, Inc.

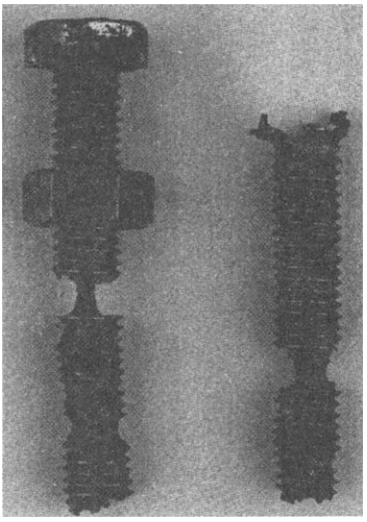


Figure 6 Severe crevice corrosion of stainless steel bolts in seawater (after A. Désestret).

As a consequence, the polarization curves drawn on a specimen equipped with a crevice former device exhibit (Fig. 7) features very similar to those typical of pitting corrosion. During the upward potential scan, crevice corrosion initiates quite abruptly at a critical potential E'_{crev} that is generally lower than the pitting potential. Then, during a subsequent backward potential scan, corrosion stops at a critical potential E'_{rp} significantly lower than E'_{crev}.

However, both crevice and repassivation potentials are dependent on the experimental conditions and particularly on the scan rate when determined by using potentiokinetic techniques. Nevertheless, long-term experiments tend to show that there is a minimum value of E_{crev} above which the incubation time decreases as the

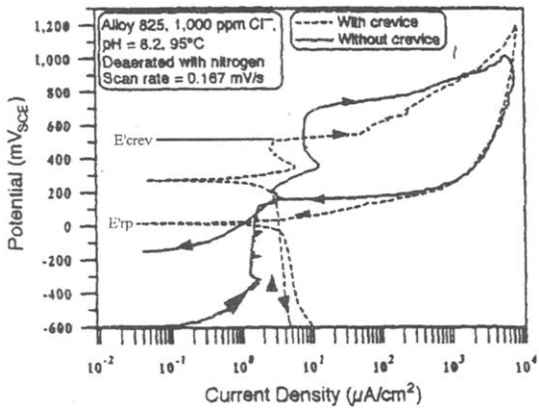


Figure 7 Polarization curves of alloy 825 in chloride solution: comparison of curves for pitting and crevice corrosion. (From Ref. 8.)

Copyright © 2002 Marcel Dekker, Inc.

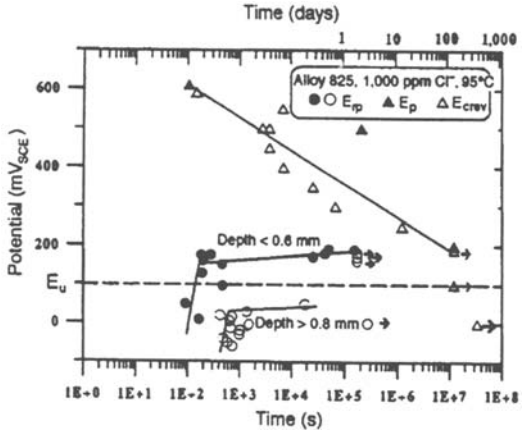


Figure 8 Effect of time on the crevice and repassivation potentials of alloy 825 in chloride solutions. (From Ref. 8.)

potential increases (Fig. 8 [8] and 9 [7]). Thus, adding an oxidizing agent (for example, biocides) in a chloride environment strongly enhances the crevice initiation (as well as the pitting probability).

Conversely, there is some agreement that a critical value E_{pr} (usually referred to as protection potential) exists that is the maximum possible value of E_{rp} below which no crevice corrosion may propagate significantly. This is consistent with the fact that crevice corrosion of passive alloys in chloride environments does not occur in deaerated environments.

Figure 8 suggests that long-term crevice and pitting potentials tend to the same value [8], but this still needs confirmation. In particular, it remains to be established whether this common value is intrinsic to the alloy-environment system or whether it depends on the crevice geometry.

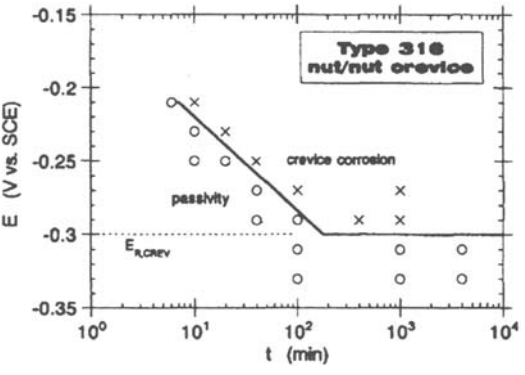


Figure 9 Effect of potential on the initiation time of crevice corrosion on 316 stainless steel (SS) in 3% NaCl solution. (From Ref. 7.)

Copyright © 2002 Marcel Dekker, Inc.

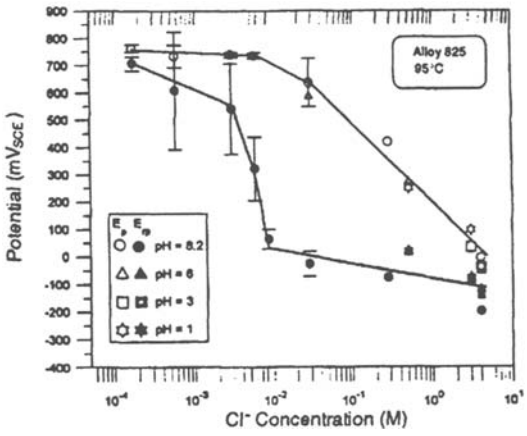


Figure 10 Effect of chloride concentration on the crevice and repassivation potential of alloy 825 at 95°C [11].

Effect of the Environment

For a given crevice geometry, the critical potentials for crevice initiation and repassivation decrease with increasing chloride content (Fig. 10) and increasing temperature (Fig. 11) of the bulk solution. This means that the susceptibility to crevice corrosion of passivated alloys increases with the chloride content and the temperature. For example, titanium alloys become sensitive to crevice corrosion only in hot concentrated chloride solutions around 100/150°C [9,10]. Propagation rates also increase with temperature.

The presence of sulfate ions or buffering species may retard crevice initiation, at least in dilute chloride solutions [13].

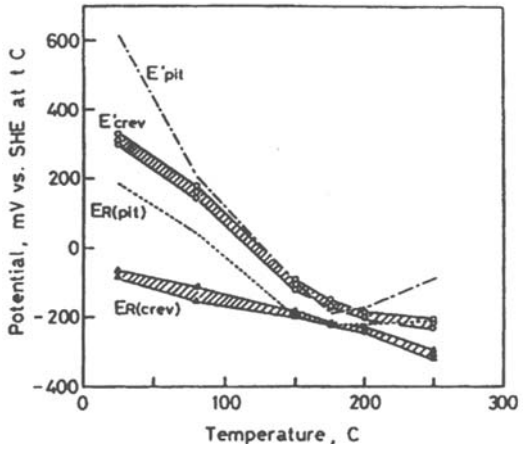


Figure 11 Effect of the temperature on the critical potentials for crevice and pitting corrosion on 304 SS in 0.5 M NaCl solution [12].

Copyright © 2002 Marcel Dekker, Inc.

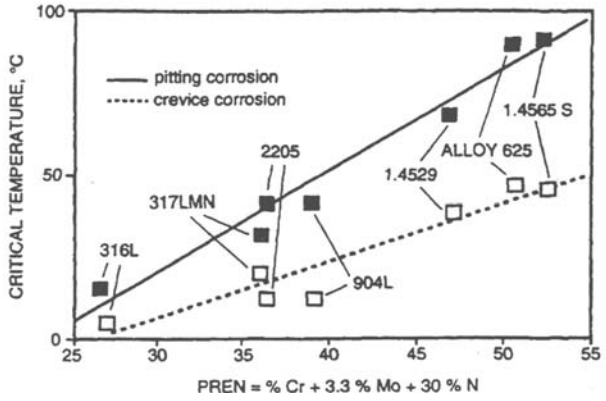


Figure 12 Effect of composition on the resistance to crevice and pitting corrosion of stainless alloys in chloride environments—the PREN index. (From Ref. 15.)

Geometric Factors

The incubation time is strongly dependent on the crevice geometry (see also Parametric Effects earlier). The initiation time decreases with decreasing crevice gap. By changing the crevice gap from about 0.2 to 5 μm, Oldfield [3] raised the initiation time from 6.5 to 350 h on AISI 430 stainless steel.

The crevice gaps that exhibit the greater efficiency in crevice initiation are of the order of tenth of micrometers to a few micrometers. At this scale, surface roughness is of major importance.

The area of the free surface surrounding the crevice zone is also of importance: a large free surface area causes shorter crevice initiation time, faster propagation rate, and smaller potential drop at the crevice initiation.

Alloy Composition

Chromium, molybdenum, and nitrogen are the most efficient alloying elements for increasing the resistance to crevice (and to pitting) corrosion initiation of stainless alloys (Fe-Ni-Cr-Mo-N- … alloys). A pitting index has been derived that characterizes the resistance of stainless alloys to these forms of corrosion [14] (Fig. 12 [15]):

$$\text{PREN} = (\text{wt \%Cr}) + 3.3(\text{wt \%Mo}) + 16 \text{ to } 30(\text{wt \%N})$$

As an example, PREN values of about 40 to 45 are requested for a stainless alloy to resist crevice corrosion in natural seawater. This leads to the use of sophisticated alloys containing usually about 23 to 25% Cr, up to 7% Mo, up to 0.45% N, and very often Cu and W additions.

The harmful effect of sulfur [16] as an alloy impurity has been mainly attributed to the presence of reactive sulfide inclusions (usually MnS), which constitute very efficient sites for initiation of localized corrosion (see later). Low sulfur or Ti alloying* improves the alloy resistance to crevice corrosion [16].

* The beneficial effect of Ti alloying is probably due to the formation of sulfide compounds more stable than mangnese sulfide.

Copyright © 2002 Marcel Dekker, Inc.

The propagation rate also depends on the composition of the alloy, but Oldfield [3] observed that the ranking of alloys may be different because the effects of elements are different for initiation and propagation. For example, he claimed that Cr, which is very efficient in retarding the initiation, favors fast propagation rates Mo definitely has a positive effect on both stages [17,18], but Ni seems to have a positive effect only on the propagation rate [16,18].

Propagation of Crevice Corrosion

Crevice corrosion occurs at very high rates, which make this form of corrosion very difficult to manage as the lifetime of a corroding structure may be determined by the initiation period.

Laboratory studies showed that for most alloys, the corrosion rate is higher near the mouth of the crevice [19,20]. However, alloys such as ferritic stainless steels may corrode faster near the dead end of the crevice [20].

An interesting observation on long-term crevice tests of Fe-Ni-Cr-Mo-N alloys [21] is that well-developed crevice corrosion may stop spontaneously even though the environmental conditions do not change. If confirmed, such behavior could be of major importance because it would mean that crevice corrosion may not necessarily cause the failure of structures, particularly in applications involving thick materials such as the containers for long-term storage and disposal of radioactive wastes.

PROCESSES INVOLVED IN CREVICE CORROSION OF PASSIVE ALLOYS IN AERATED CHLORIDE ENVIRONMNENTS

The generally accepted scenario is that the environment in the crevice suffers a progressive evolution that leads to the breakdown of passivity and to a propagation stage during which the metal inside the crevice undergoes active dissolution. The following paragraphs briefly describe the current understanding of the different processes, i.e., environment evolution, passivity breakdown, and active dissolution in the crevice gap.

Environment Evolution in the Crevice Gap

The following mechanism is generally accepted to describe the evolution of the crevice environment on passivated alloys exposed to aerated chloride environments.

Step 1: Deaeration of the Crevice Environment

On the free surfaces, the cathodic reaction is the reduction of oxygen. However, the environment in the crevices becomes deaerated after periods of time that can be very short, at least compared with the lifetime of an industrial apparatus. As an example, a passive current of 10 nA/cm^2 will cause the deaeration of a crevice with a surface/volume ratio of 10^3 cm^{-1} (i.e., a crevice gap of 20 μm between two metal surfaces) in about 3 h.

The lack of oxygen causes the inhibition of the cathodic reaction inside the crevice. Thus, the local anodic reactions must be balanced by cathodic reactions occurring on the surfaces exposed to the bulk solution. This builds up a galvanic cell

Copyright © 2002 Marcel Dekker, Inc.

between the inside and the outside of the crevice. As a consequence, the *IR* drop between the crevice and the bulk is responsible for the buildup of a corrosion potential difference between the inside and outside surfaces, the former becoming more anodic. However, the contrary to what happens on unalloyed steels (see earlier), the stainless alloys exposed to neutral chloride solutions are passive in both aerated and deaerated solutions and the local oxygen consumption has no significant effect of the dissolution kinetics. Thus, this step does not induce any corrosion damage but it is essential to trigger the following process.

Step 2: pH Evolution and Concentration of Dissolved Species

The anodic dissolution of the metal inside the crevice produces metallic cations (and/or oxides that contribute to thickening the passive layer, at least before initiation of the propagation stage).

Production of solid oxides or oxyhydroxides

$$xM + (y+z)H_2O \rightarrow M_xO_y(OH)_z + (2y+z)H^+ \quad (1)$$

Production of solvated metallic cations

$$M \rightarrow [M(H_2O)_n]^{z+} + ze^-, \quad \text{where } n \text{ is usually 6} \quad (2)$$

These metallic cations cannot concentrate indefinitely and they undergo hydrolysis.

The earlier theories assumed the formation of simple hydroxides:

$$[M(H_2O)_n]^{z+} \rightarrow [M(H_2O)_n]^{(z-h)+} + hH^+ \quad (3)$$

It is now recognized that metallic cations may also form metallic chlorides and/or complex oxy-hydroxy-chlorides according to reactions such as

$$M(H_2O)_n^{z+} + mCl^- \rightarrow [M(H_2O)_{(n-m)}Cl_m]^{(z-m)+} + mH_2O \quad (4)$$

$$[M(H_2O)_{(n-m)}Cl_m]^{(z-m)+} + hH_2O \rightarrow [M(H_2O)_{(n-m-h)}(OH)_hCl_m]^{(z-m-h)+} + hH_3O^+ \quad (5)$$

The formation of metallic polycations should also be considered [4].

These anodic processes result in a local excess of cations inside the crevice. Because there is no cathodic reaction inside the crevice, the restoration of electrical neutrality requires the onset of a galvanic current in the base metal and a migration flux in the liquid. At least in the early stages of crevice evolution, most of the ions conveyed by this migration are chloride ions that are transported from the bulk solution into the crevice [22].

All these processes are summarized in Figure 13, where hydrolysis reaction (3) is assumed. As a consequence, *the crevice environment becomes more and more acidic and more and more concentrated in metallic ions (including metal chloride complexes) and free chloride ions.* We will see later that, in some instances, this pH evolution, combined with an *IR* drop, can make possible the reduction of water in the crevice.

Copyright © 2002 Marcel Dekker, Inc.

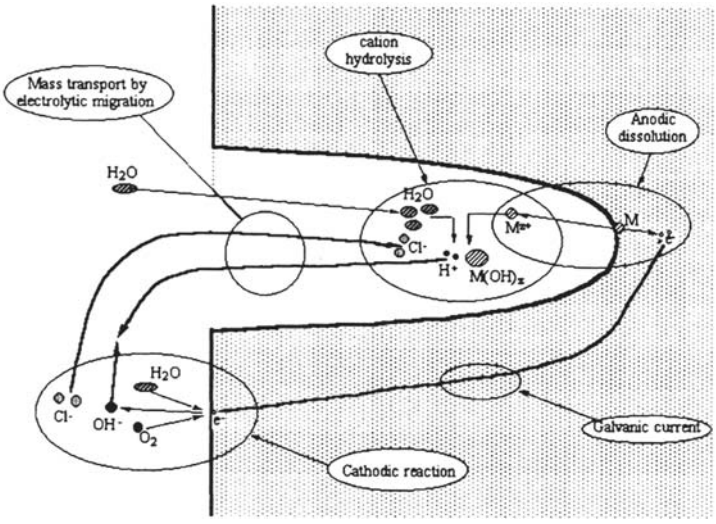


Figure 13 Sketch of the main processes leading to environment evolution in a crevice.

Indeed, numerous experimental studies have been performed to study the evolution of the environment in a crevice. Most data were obtained in actively corroding artificial crevices or pits, either by sampling the solution or by direct pH and Cl^- concentration measurements. Table 1 summarizes significant results that confirm the foregoing trends. In crevice solutions, the drop of pH depends on the hydrolysis constants of the metal cations. On stainless alloys, chromium and molybdenum are considered to be the cause of the very low, sometimes negative, pH observed. Iron, nickel, and aluminum exhibit much less acidic hydrolysis reactions and the pH values in the crevices are higher: values of 3 to 5 are reported for iron, values of 3 to 4 for the aluminum alloys.

It must be noted that the pH drop is due to the dissolution of the base material: thus, the more resistant the material, the lower is the pH required for dissolution to occur. Thus, the more acidic crevice pH values are observed on the more resistant materials. This is shown, for example, in the studies of Bogar and Fujii (Fig. 14 [24]) on Fe-Cr ferritic stainless steels and Suzuki et al. [28] on 304L, 316L, and 18Cr-16Ni-5Mo austenitic stainless steels (Table 1).

The concentration of the ions in the crevices can reach very high values of the order of several mol/L [28,33], and the solution may eventually become saturated, which possibly limits the dissolution rate. In such concentrated solutions, salt films may form on the dissolving metal surfaces: $NiCl_2$ has been identified in nickel [34] and $FeCl_2$ in iron [35] and stainless steel [35] pits or crevices.

Several studies also outline the strong effect of the potential of the free surfaces on the pH drop inside an actively corroding crevice: in particular, early work of Pourbaix [36] on unalloyed steel showed (Fig. 15) that the higher the potential of the external surfaces, the higher the potential and pH drops in the crevice. Similar results were obtained by Zuo et al. [37] for stainless steel actively corroding in an artificial crevice. Conversely, Pourbaix [36] and Turnbull and Gardner [38] on unalloyed

Copyright © 2002 Marcel Dekker, Inc.

Table 1 Some Experimental Measurements of Local pH and Composition in Crevices[a]

Material	Bulk solution	pH	Local composition	References and notes
Unalloyed steel	0.06 to 0.6 M NaCl	3 to 4.7		Data collected in Ref. 23
	Seawater	3.3		
Mild steel	0.5 N NaCl[b]	~4.3	Up to 2.5 N Fe, 5.5 N Cl	22
Fe–10% Cr	0.6 M NaCl	3.2	0.36 M Fe, 0.06 M Cr	24
Fe–15% Cr	0.6 M NaCl	3.0	0.21 M Fe, 0.17 M Cr	24
Fe–20% Cr	0.6 M NaCl	2.4	0.14 M Fe, 0.33 M Cr	24
Fe–25% Cr	0.6 M NaCl	1.8	0.11 M Fe, ?? M Cr	24
Fe–12% Cr	0.1 M NaCl + 0.01 M $NaHCO_3$	2.5		25
304 SS	Seawater	2.3		Data collected in 23
		1.5 to 2.2		
304 SS	0.6 M NaCl	1.7–2.7		26
304 SS	1 M NaCl[b]	0		27
304 SS	0.5 N NaCl[b]	1.6	Up to 0.5 N Cr, 6 N Cl	22
Fe	0.5 N NaCl, 70°C[b]	4.7		28, Artificial pit
Cr	0.5 N NaCl, 70°C[b]	0.09		28, Artificial pit
Ni	0.5 N NaCl, 70°C[b]	2.93		28, Artificial pit
304 L SS	0.5 N NaCl, 70°C[b]	0.6–0.8	2.3 N Fe, 1.06 N Cr, 0.34 N Ni, 3.87 N Cl^-	28, Artificial pit
316 L SS	0.5 N NaCl, 70°C[b]	0.06–0.17	4.3 N Fe, 1.5 N Cr, 0.68 N Ni, 0.14 N Mo, 6.47 N Cl^-	28, Artificial pit
18Cr-16Ni-5Mo	0.5 N NaCl, 70°C[b]	0.13–0.08	3.26 N Fe, 1.79 N Cr, 0.95 N Ni, 0.31 N Mo, 6.2 N Cl^-	28, Artificial pit
7075 Al alloy	3.5% NaCl	3.45	1600 ppm Al + Zn + Mg + Cu	29
7474	3% NaCl	3.6–4.2		30
Pure Al	1 M NaCl—pH 11	3–4		31 Natural pit

[a]For more details see Turnbull [32].
[b]Anodic polarization.

Copyright © 2002 Marcel Dekker, Inc.

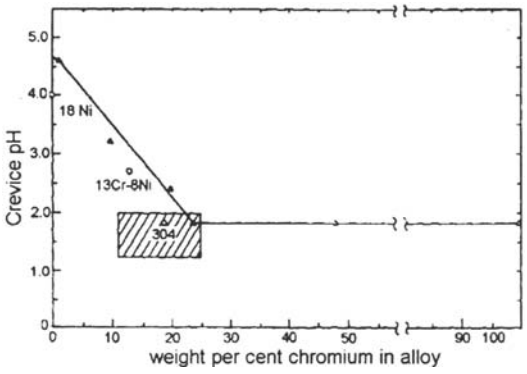


Figure 14 Effect of chromium content of the alloy on the pH in the crevice. (From Ref. 24.)

steels and Peterson and Lennox [39] on 304 stainless steel showed that cathodic polarization of the free surfaces induced an increase of pH and a cathodic polarization of the surfaces inside the crevice (Figs. 15 and 16).

In the artificial crevice experiments, several other features are interesting. As an example, for the same 304 stainless steel:

The relationship between the total amount of anodic charge passed in an artificial crevice and the pH is not unique (Fig. 17),

The relationship between the chromium content (and more generally the composition) of the crevice solution and the pH is not unique and does not agree with any simple hydrolysis reaction (Fig. 18),

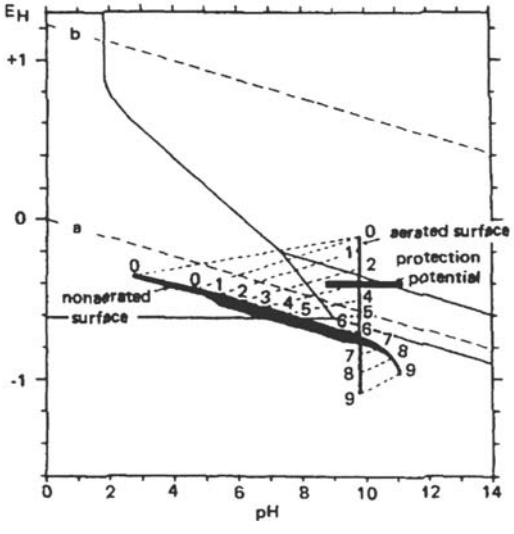


Figure 15 Effect of the potential of the external surfaces on the pH and potential inside an artificial C-steel crevice [36]. Same numbers refer to the corresponding conditions on the free surface and inside the crevice.

Copyright © 2002 Marcel Dekker, Inc.

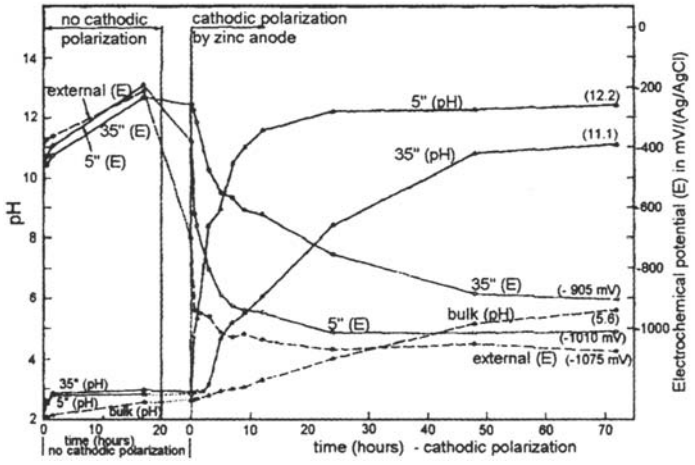


Figure 16 Effect of cathodic polarization by zinc anode on the pH and potential inside a 304 SS crevice [37].

The pH of a synthetic solution made of reagent grade transition metals and sodium chlorides does not have the same pH as the crevice solution of the same composition (Fig. 19). In addition, this pH spontaneously decreases with time [33,40] (Figs. 18 and 20) for periods of time of several weeks which should not be neglected when modeling the crevice evolution. Indeed, Zhen [41] showed, by ultraviolet (UV) spectroscopy, the presence of at least two different Cr compounds in stainless steel crevice solutions and observed a spontaneous evolution with time toward one of these species.

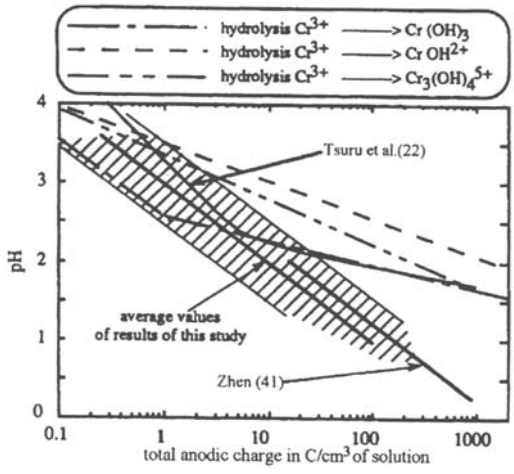


Figure 17 Experimental relationships obtained by different authors between pH and dissolution current 304 SS artificial crevice and comparison with simple hydrolysis equilibria [40].

Copyright © 2002 Marcel Dekker, Inc.

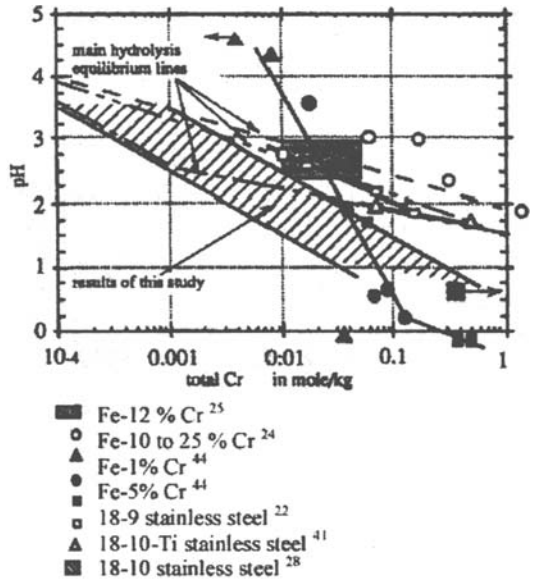


Figure 18 Experimental relationship obtained by different authors between pH and Cr content of artificial crevice solutions [40].

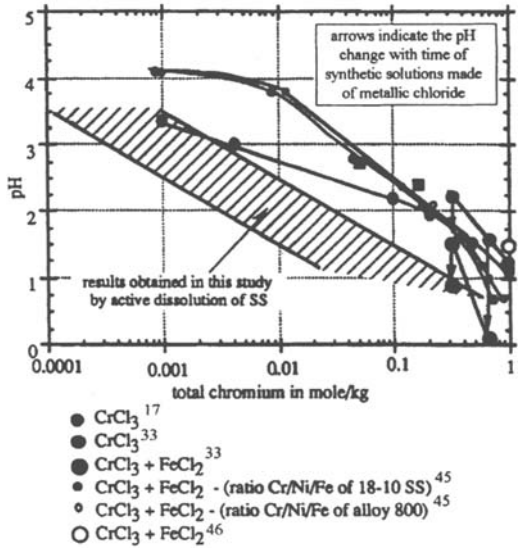


Figure 19 Comparison of artificial crevice solution with synthetic solution of the same composition [40].

Copyright © 2002 Marcel Dekker, Inc.

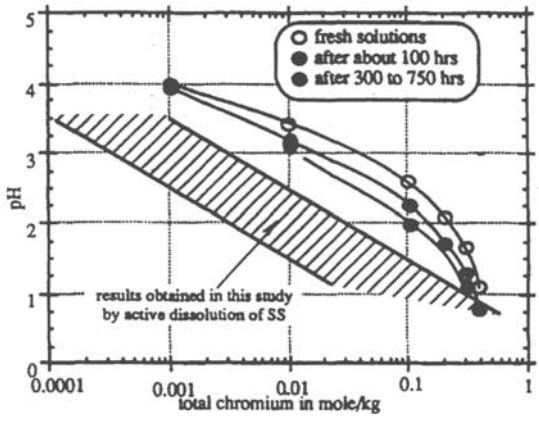


Figure 20 Evolution with time of the pH of synthetic solution made of metallic chloride salts [40].

Thermodynamics of the Crevice Environments for Fe-Ni-Cr Alloys

Thus it appears that the detailed chemistry of the crevice environments is not very well known for the following reasons:

The ions and solid species formed may be more complex than the simple metal hydroxides assumed in most models. For example, Tsuru et al. [22] and Ogawa [42] have shown, in the case of stainless steel, the formation of chloro-hydroxy complexes involving up to 20 chloride ions, although the coordination number of chromium ions should not exceed 6. Tsuru et al. [22] also showed that in iron and stainless steel crevices, iron is likely to be complexed to chloride as $[FeCl(H_2O)_5]^+$ (i.e., $FeCl^+$), but Brossia et al. [35] found that $CrCl^{2+}$ is the most likely metallic chloride in stainless steel crevices.

In concentrated solutions, the presence of large amounts of chloride has been shown to decrease the pH [22,33,42] by increasing the activity coefficient of the hydrogen ions.

Some reactions of hydrolysis and complexation are not as fast as usually assumed (see earlier).

This may suggest that the nature of the cationic species produced by the anodic dissolution may depend on the surface conditions of the alloy and on the local environment. In particular, the analyses of passive films on stainless steels showed [43] that the external layers are very hydrated and contain chloride. On the other hand, the number of hydroxyl groups and chloride ions adsorbed on active surfaces is likely to be dependent on the local pH, chloride content, and surface potential. Thus, dissolution from a passive surface may produce metallic hydroxy-chlorides different from those resulting from active dissolution, and active dissolution may produce cations depending on the local conditions.

Copyright © 2002 Marcel Dekker, Inc.

Other Environmental Evolutions in the Crevice Gap

In the case of stainless steels, Lott and Alkire [47] consider that the dissolution of sulfide inclusions (MnS) inside a crevice is the main environment change before passivity breakdown. They showed by direct analysis of the local environment in an artificial crevice that manganese sulfides were oxidized to thiosulfates, which are known to promote pitting in aerated chloride environments [48–50] and, more generally, to inhibit film repair on stainless alloys. More recent work of Brossia and Kelly [51,52] showed that the dissolution of manganese sulfides actually produced sulfide rather than thiosulfate ions. Whatever the nature of the reactive sulfur species produced by the degradation of MnS inclusions, they can be deleterious for the passive layer, particularly because they may form on the bare metal surfaces an adsorbed layer of sulfur that enhances the anodic dissolution and inhibits (or retards) the formation of the passive film [53]. Indeed Crolet et al. [54] showed that in acidic environments representing crevice solutions an increase in the sulfur content of the stainless steels favored the onset of active dissolution.

In the case of dissimilar crevices where one of the crevice walls is made of a nonmetallic material, such as a gasket, the possibility of dissolution of foreign elements must also be considered.

Breakdown of Passivity inside the Crevice

The detailed mechanism of passivity breakdown inside a crevice is not clearly established and different possibilities are still discussed. Indeed, it is quite possible that different mechanisms may be involved depending on the material, bulk environment, crevice geometry, and, possibly, surface condition of the metal.

"Classical" Mechanism": General Breakdown of Passivity in Low pH, High Chloride Solutions

The more "classical" mechanism involves general film breakdown in a *critical environment* characterized by a low pH and a high chloride content. Low pH and high chloride concentrations are known to be deleterious for the passivity of most alloys. Thus, the progressive evolution of the crevice environment causes a degradation of the passive film that may result in the following successive situations (Fig. 21a):

1. An increase of the passive current
2. The onset of an active dissolution domain with a peak current that increases with decreasing pH and increasing chloride content (and, thus, increasing with time)
3. A complete inhibition of passivity

Passivity breakdown is thought to occur either when the corrosion potential of the crevice surfaces is located in the active peak due to ohmic drop (Fig. 21b) or when there is no more active-passive transition on the anodic curve.

This mechanism of initiation gave rise to the notion of critical pH for film breakdow [55], which was extensively used as a criterion to rank the resistance of stainless alloys to crevice corrosion. For Crolet et al. [55] the critical pH is the pH corresponding to the onset of an active peak in the polarization curves, while Ogawa [42] considered the pH of spontaneous film breakdown under free corrosion conditions. These differences changed somewhat the critical pH values but usually not

Copyright © 2002 Marcel Dekker, Inc.

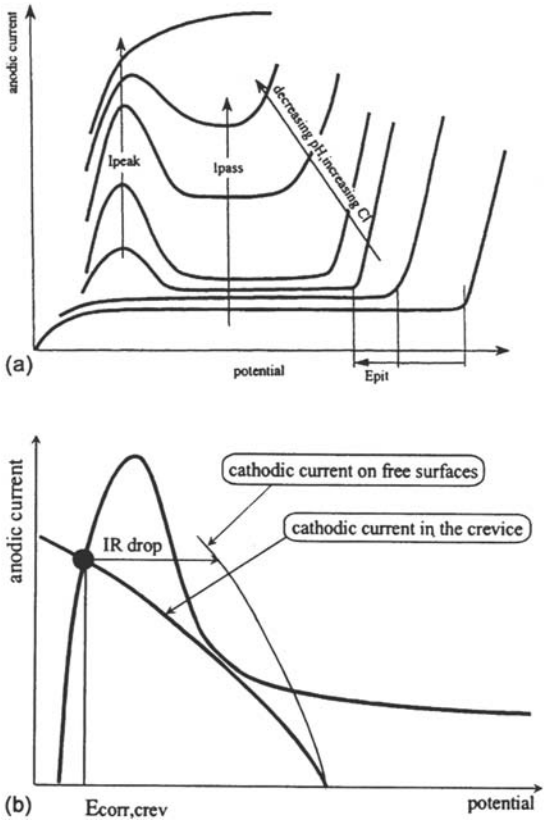


Figure 21 (a) Evolution of the anodic characteristic of passivated alloy when decreasing the pH and increasing the chloride content. (b) Activation inside a crevice when the corrosion potential is located in the activity peak due to ohmic drop in the crevice.

the alloy ranking. Table 2 gives some results of critical pH evaluated on stainless alloys. Okayama et al. [56] performed measurements of the depassivation pH of over 50 stainless steels and nickel-base alloys and found that the effect of alloying elements of austenitic materials was given by

$$pH_D = 4.09 - 0.248\,\text{wt \% Cr} - 0.219\,\text{wt \% Mo} + 1.29\log(\text{wt \% Ni}) + 75\,\text{wt \% S} + 2.66\,\text{wt \% C} \quad (6)$$

Table 2 Examples of Depassivation pH Measured according to Crolet et al. [47] and Oldfield and Sutton [54] Criteria

Stainless alloy	PH of depassivation	Reference
AISI 430 SS	2.9	Crolet et al.
304 L	19.5–2.25	Crolet et al.
316 L	1.7	Crolet et al.
904 L	1.4	Crolet et al.
	1.25	Oldfield and Sutton
Alloy 625	0	Oldfield and Sutton

Copyright © 2002 Marcel Dekker, Inc.

This relation showed the well-known beneficial effect of Cr and Mo and confirmed the very deleterious effect of sulfur (see previous section).

On very resistant stainless alloys, the criterion of depassivation pH tends to be replaced by a criterion of critical crevice solution (CCS) [19,57] and Gartland assumes that crevice corrosion occurs when the solution is so aggressive that passivity is no longer possible over the whole potential range.

However, this classical mechanism appears not to be consistent with different observations, at least on less resistant materials:

Several experiments [58–60] with in situ local measurement of pH and/or chloride concentration with microelectrodes showed that the large changes in crevice pH and chloride content mentioned in the former paragraph occurred not before but after passivity breakdown. In these experiments [58,61], the potential difference between crevice and free surfaces (i.e., the ohmic drop) is often very low before initiation (few mV) and becomes larger only after crevice initiation.

This mechanism does not explain clearly why the initiation time is so dependent on the potential of the external surfaces [60,62], particularly if the passive current is not significantly dependent on the potential as is assumed in most crevice models. This strong dependence on the applied potential would support the idea that the pH drop rate in the crevice is controlled by the migration process and/or by the available cathodic current. This is hardly understandable at the very low current densities involved during the initiation stage, when considering that dissolution rates several order of magnitude higher can be sustained during the propagation stage.

The following points have been raised to account for these observations:

The corrosion initiates by local passivity breakdown in the crevice as a result of (a) microcontacts due to wall asperity or (b) pitting inside the crevice.

The critical environment involves the buildup of deleterious species such as (c) sulfur or (d) chloride species rather than low pH.

"Microcrevices" inside the "Macrocrevice" Gap

Several authors [1,14,60] raised the point that at the scale of the crevice gap, the surface roughness may play a major role in the environment evolution. Local contact between the opposite surfaces may constitute very tight local "microcrevices" inside the "macrocrevice" (Fig. 22).

Due to their very narrow gap, these microcrevices could be very efficient in promoting a very local pH change (see Modeling Crevice Corrosion later) and a local

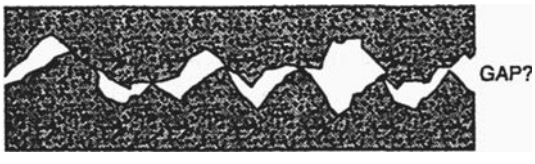


Figure 22 Crevice formed by asperity contact [14].

Copyright © 2002 Marcel Dekker, Inc.

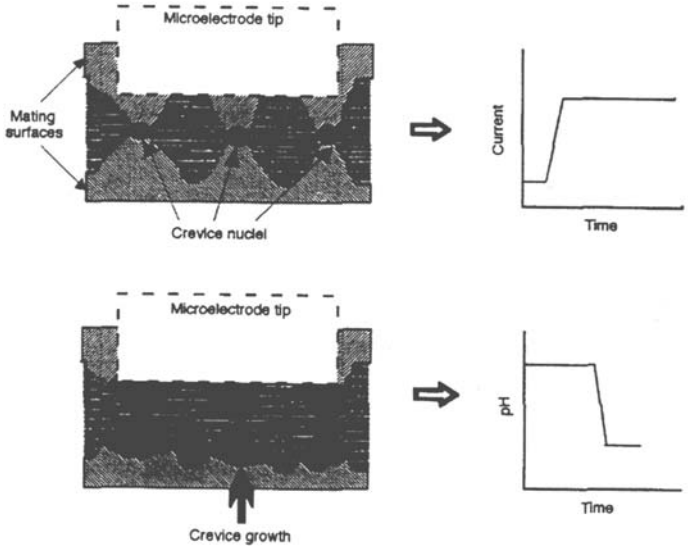


Figure 23 Development of localized corrosion inside a crevice gap formed by asperities and corresponding response of current [60].

passivity breakdown by the mechanism presented in the former paragraph. As soon as active dissolution occurs somewhere inside the macrocrevice, the breakdown of passivity spreads out progressively to the whole crevice provided the potential inside the crevice is high enough.

Thus, according to this view, the classical mechanism could operate at the scale of the microcrevices because of asperity contacts rather than at the scale of the whole crevice. Most of the "apparent" incubation period would be a period of very local corrosion extending progressively into the whole crevice zone, and thus, it would be sensitive to the potential because of the locally active dissolution.

This interpretation is also consistent with the observation that pH and chloride microelectrodes detect only a significant environment evolution after a time tag following the current increase because the size of the sensitive area of these electrode is much larger than the size of the crevice nuclei inside the crevice. Thus, these microelectrodes detect only the spreading of the corrosion through the whole crevice (Fig. 23).

Pitting in the Crevice Gap

The initiation of crevice corrosion by pitting inside the crevice gap is mainly invoked for stainless steels. Indeed, several investigators [23, 46, 63, 64] have observed pitting and further coalescence of the pits inside stainless steel crevices. Eklund [64] showed that pitting on MnS inclusions near the mouth of the crevice may be the initial stage of crevice corrosion of stainless steels. Oldfield and Sutton [46] have given a detailed description of the sequence of micropitting, pit coalescence, and crystallographic etching that results in a rapid dissolution stage in a stainless steel crevice in 1 M NaCl solution (Fig. 24). In this case, early corrosion damages progressively spread through the crevice, suggesting an effect of the environment evolution in the crevice. By using

Copyright © 2002 Marcel Dekker, Inc.

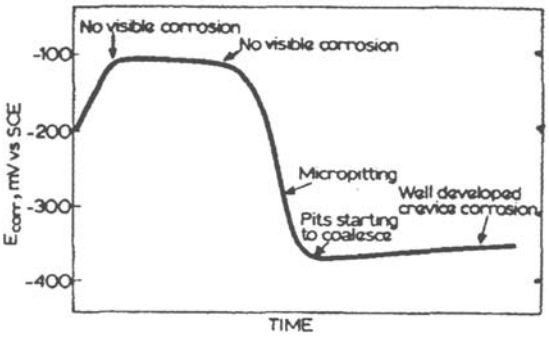


Figure 24 Crevice initiation by micropitting observed by Oldfield and Sutton [46] on 316 SS in 1 M NaCl, pH 6 solution.

a moiré fringe technique to observe directly the metal dissolution in a crevice, Shinohara et al. [65] confirmed the localized character of the early dissolution events and their lateral extension and coalescence.

It is worth noting that the crevice may favor pit initiation in two ways: (a) the pitting potential of a stainless alloys decreases with increasing chloride content (Fig. 21a); (b) the restricted transport conditions may contribute to stabilize pit embryos at potentials lower than on the free surfaces [66]. This last point is supported by the experimental and modeling work of Laycock et al. [62]. Indeed, the deleterious effect of anodic polarization on the initiation time is obviously consistent with a pitting process.

Role of Sulfide Inclusions on Stainless Steel

Besides their possible role in pit initiation (see earlier), the dissolution of the MnS inclusions can generate thiosulfates [47, 67] or more likely sulfide [51, 52] ions, which are known to favor passivity breakdown. Indeed, Crolet et al. [54] observed higher depassivation pH on stainless steels with high sulfur content. According to Brossia and Kelly, the initiation involves a critical $[Cl^-]/[HS^-]$ ratio. This effect of MnS is unlikely in modern stainless alloys with very low sulfur contents.

Passivity Breakdown Due to High (Metal) Chloride Concentration

On pure aluminum, Hebert and Alkire [68] proposed that passivity breakdown occurred when a critical concentration of aluminum chloride is attained in the crevice environment. Indeed, they showed convincingly (Fig. 25) that the presence of aluminum cations in the solution caused passivity breakdown for a pH and chloride concentration at which solutions containing only sodium cations did not.

Based on an experimental work on alloy 7475 crevices and propagating cracks, Holroyd et al. [30] agree with this assumption. The critical aluminum concentration required decreases as chloride content increases [68] but low pH and high chloride content are not a prerequisite for passivity breakdown.

The possibility of the existence of a critical concentration of chloride rather than a critical pH has been proposed for stainless steels, for example, by Zakipour and Leygraf [69] in relation to a critical composition of the passive film (chromium content of about 48%).

Copyright © 2002 Marcel Dekker, Inc.

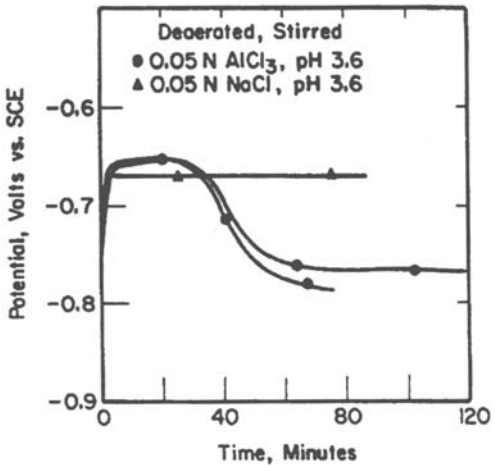


Figure 25 Effect of dissolved Al on the activation of pure Al in pH 3.6 solution [68]. Test under galvanostatic conditions.

On stainless steels, several authors [70–73] showed that a minimum concentration of metallic chloride is required for stable propagation to occur. As mentioned previously, the external layer of the passive films on stainless steels contains hydroxyl groups and chloride. Thus, it may be possible that the presence in the solution of metal complexes modifies the external layers of the passive films and contributes to lowering their stability.

The Role of IR Drop in the Initiation of the Crevice Corrosion

The role of *IR* drop in crevice initiation is not clear. Different authors [58,60,61] observed crevice initiation on stainless steels at a very low *IR* drop level. It is clear that initiation processes can be separated into two classes: (a) those that operate at relatively high potentials (pitting in the crevice gap), which cannot be enhanced by large ohmic drops, and (b) those that occur at low potential (general passivity breakdown), which are favored by large *IR* drops. However, on stainless steels and nickel-base alloys, there is at present no direct evidence to support the last type of process, mainly because high free surface potential always enhances crevice initiation of passive alloys.

On titanium alloys, however, the metal still has an active-passive transition in the crevice environment and the surface potential must be low enough for the active corrosion to occur. Thus, *IR* drop is required to stabilize the active dissolution [9,74], particularly when large cathodic currents are available.

Propagation of Crevice Corrosion

Propagation of crevice corrosion occurs by active dissolution in an occluded cell and it is generally considered analogous to the propagation stage of pitting corrosion.

Copyright © 2002 Marcel Dekker, Inc.

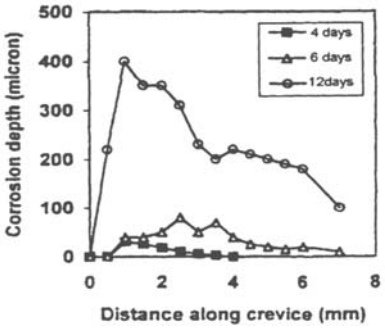


Figure 26 Preferential propagation near the crevice mouth [75].

At least in a first stage, corrosion may not affect the whole crevice gap: it has been shown that on austenitic stainless steels, dissolution is mainly located near the mouth of the crevice [3,19] (Fig. 26), whereas on ferritic stainless steels the maximum of dissolution rate is located deeper in the crevice [3].

As a consequence of rapid corrosion inside the crevice, the rate of evolution of the environment toward more acidic and more concentrated solutions increases, and indeed several experiments confirmed this point. However, the dissolution rate and the environment evolution may be limited by the following factors:

Immediately after passivity breakdown, the dramatic increase of the dissolution current has two consequences that contribute to limit the dissolution rate by decreasing the corrosion potential of the active surfaces in the crevice:

1. The cathodic reaction kinetics increase on the free surfaces to balance the increased anodic dissolution and this induces a drop of their corrosion potential. Potential drops of several hundreds of mV can be observed on the free surfaces due to the initiation of crevice corrosion (see Fig. 5) Large cathodic areas, high solution conductivity, and cathodic reaction depolarizers (such as carbon deposits) can increase significantly the amount of available cathodic current and thus the crevice propagation rate.
2. The migration current from the crevice gap increases dramatically and this also increases the ohmic drop: a role of the ohmic drop in the control of the propagation rate is consistent with a maximum of corrosion rate located near the crevice mouth as observed by several author [3,19]. One must notice that ohmic drop is not limited to the solution inside the crevice. Significant ohmic drops may also occur in the bulk solution near the crevice mouth, particularly in dilute environments.

Later, several other events may also occur to limit the environment evolution and the dissolution rate:

The solution inside the crevice reaches saturation and a salt film is formed on the active surface. The corrosion rate is then limited by mass transport trough the salt layer. Recent results [34,35,73,76–78] confirm this possibility, which was not as clearly established as it is for pit propagation.

Copyright © 2002 Marcel Dekker, Inc.

The pH and the potential in the crevice may become low enough for local water reduction to be possible. This stifles further pH decrease as the local cathodic reaction is able to balance the production of cations by anodic dissolution.

Balance between production and outward transport of cations and dilution due to geometric changes of the crevice [79] are also invoked as possible limiting processes. However, on the simple basis of the difference of density between the dissolved metal and the saturated crevice solution, Hakkarainen [80] pointed out that at least 97% of the dissolved cations must be evacuated out of the active crevice. This weakens the preceding point. But, on the contrary, the possible limitation by the diffusion of water through a saturated salt layer has not been considered.

Thus, even though the corrosion occurs by active dissolution, its rate is not controlled by an activation process and, generally, it remains limited to current densities of the order of tens of mA/cm^2 in the saturated solutions, which prevail on well-developed crevices [19,33,57,70,71]. Figure 27 shows how the dissolution rate decreases when saturation of the solution is approached.

When discussing the propagation of crevice corrosion, it is worth noting that the analogy with the propagation of pits may have limitations. Most of the experimental work and many simplified calculations refer to a geometry of the corroding crevice with an aspect ratio *L/h* close to 1. This may have consequences for conclusions regarding the distribution of the dissolution current inside the crevice gap and the rate-controlling processes because an almost uniform corrosion potential on the corroding surface and an almost uniform transport path for the diffusion and migration processes can be assumed in pits. In very deep crevices, the potential and the transport path vary along the crevice profile; thus, the evolution of the local environment may vary. Consequently, the saturation and the formation of salt films leading to a dissolution process controlled by diffusion may not occur simultaneously on the whole crevice surfaces. In addition, the increasing *IR* drop near the tip of the crevice gap may allow the reduction of water to occur, changing the local pH evolution before any saturation has been reached.

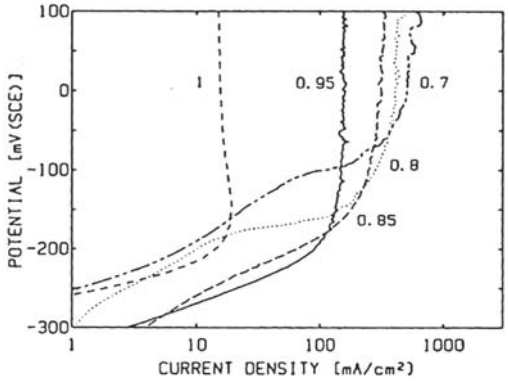


Figure 27 Anodic dissolution of 304 SS in simulated crevice solutions [71]. The numbers indicate the degree of saturation of the solution.

Copyright © 2002 Marcel Dekker, Inc.

Crevice Repassivation

Spontaneous Crevice Arrest

Observations (see Propagation of Crevice Corrosion earlier) suggest that, under constant bulk environment conditions, crevice corrosion may spontaneously cease. This has been taken into account in a model developed by Gartland [19]. Gartland attributed this behavior to an environment dilution caused by the geometric change of the crevice, but we have seen that this argument is not always likely. It also seems appropriate to invoke salt precipitation and/or local dryout due to the slow diffusion of water through a salt film of increasing thickness. This suggests that mass transport could not be efficient enough to eliminate such a large amount of corrosion products and this could lead to the precipitation of solid products that would fill the crevice gap. Another cause of self-arrest, or at least of kinetic limitation, could be lack of sufficient water in the crevice gap. Further studies are required to establish the conditions and the mechanisms involved in this spontaneous arrest, in order to take advantage of it in practical situations.

Repassivation Potential

The propagation of crevice corrosion can also be arrested by decreasing the potential of the outside surfaces below a critical value (see earlier). The existence of a "repassivation" or "protection" potential was recognized very early, in particular by Pourbaix et al. [81] for pitting corrosion. From a practical point of view, the existence of a protection potential below which no crevice corrosion is possible is of major importance because it guarantees the immunity of passivated alloys in near-neutral chloride solutions in the absence of oxidizing species and because it makes possible the cathodic protection of structures.

However, the significance and the intrinsic nature of this potential are still under discussion. There are at least two possible causes for active corrosion inside crevices to stop below a critical potential:

First, the critical potential may be a "deactivation potential", i.e., a potential that corresponds to a cancellation of the overpotential required for dissolution in the crevice. According to Starr et al. [82], if active corrosion stops by deactivation with decreasing potential, a further increase of the corrosion potential would cause an immediate reactivation of the crevice. Indeed, Starr et al. [82] and Dunn and Sridhar [83] observed such a reactivation on low-grade stainless steels in acidic environments.

Second, the critical potential may be a repassivation potential. It has been shown in artificial active crevices that lowering the potential of the free surfaces causes the local environment to become less aggressive (see, for example, Pourbaix [36]). Thus, at some point, the environment becomes not aggressive enough for active dissolution to be sustained and the metal surface in the crevice becomes passive. In this case, a subsequent increase of the corrosion potential does not produce immediate reactivation inside the crevice. Starr et al. [82] observed this situation on 12% Cr stainless steels in near-neutral environments; Dunn and Sridhar [83] observed the same behavior on alloy 825. However, the repassivation may be attributed to different environment changes: an increase of local pH in the crevice [82,84], a destabilization of the salt film that controls the

Copyright © 2002 Marcel Dekker, Inc.

dissolution kinetic in the crevice [77,85,86], or a decrease of the chloride concentration below a critical value [34,35,71–73,77,78,83]. Recent experimental observations [34,35,78] show that corrosion may be stable even after dissolution of the salt film.

In fact, studies of Cragnolino et al. [8,11] suggest that, depending on the conditions of the experimental determination, the "arrest" potential measured by backscan polarization may be close to either potential: using a relatively high scan rate, which does not allow time for the local environment to be significantly modified, the measured arrest potentials are close to the deactivation potentials and they are significantly lower than those measured under a low potential scan rate. The latter are more likely to be due to a modification of the local environment toward less aggressive conditions. We have already seen that the maximum repassivation potential seems to be almost identical to the minimum initiation potential (Fig. 8). This observation has been reported for a relatively resistant stainless alloy (alloy 825) and it would support the idea of Gartland [19,57] (see earlier) that there is a critical environment for passivity breakdown and that the local environment required for repassivation is not very different. This could be an argument against the mechanism of initiation by pitting in the crevice and in favor of a mechanism involving a critical environment.

A pending question is still to know whether this repassivation potential has a unique value or depends on corrosion damages and crevice geometry. The following arguments are in favor of such a unique value:

1. For a given bulk environment and a given crevice configuration, the repassivation potential becomes independent of the corrosion extent as soon as some critical damage size is exceeded [8] (Fig. 28).
2. At least for high chloride concentrations, the repassivation potential exhibits low values which are poorly dependent on the chloride content of the environment [87] (Fig. 29). Dunn et al. expressed the average values of the repassivation potential as follows:

$$E_{rp} = E^0_{rp}(T) + B(T)\log[Cl^-] \tag{7}$$

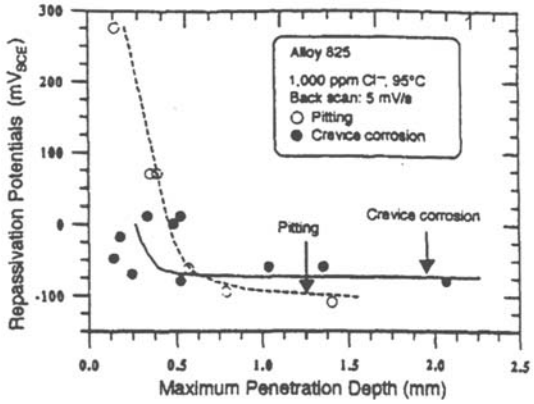


Figure 28 Influence of the corrosion damage on the repassivation potential of an alloy 825 in a 1000 ppm Cl^- solution at 95°C [8].

Copyright © 2002 Marcel Dekker, Inc.

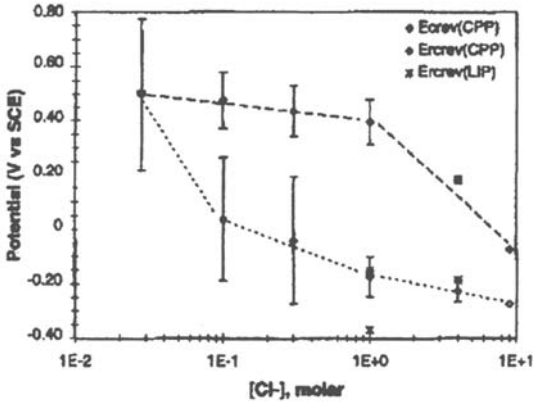


Figure 29 Influence of the chloride content on the repassivation potential of an alloy 625 at 95°C [87].

with

$$E^0_{rp}(T) = 181.8 - 481(T) \quad \text{and} \quad B(T) = -64 - 0.8(T) \text{ for alloy 825} \qquad (8)$$

However, the Fig. 29 shows that the effect of chloride content is low on the repassivation potential, particularly when looking at the lower bound of the scatter b and of the measured value which is almost constant for chloride contents in excess of 10^{-1} M. This is consistent with the presence of a nearly saturated solution and/or precipitated salt film in well developed crevice corrosion, and indeed such environments should be almost independent on the bulk solution chemistry. Thus, a repassivation potential which, according Pourbaix [36], is close to the local potential of an actively corroding crevice should be poorly or no dependent on the bulk environment and crevice geometry.

Nevertheless, this point still requires more work, particularly regarding the exact meaning of the high values of the repassivation potentials measured in low chloride and/or low temperature environments (left side of the Fig. 10, 11 and 29). In this case, the local environment inside the crevice is likely to be controlled by mass transport and thus the repassivation potential could be dependent on the crevice geometry.

MODELING CREVICE CORROSION

In order to try to predict the behavior of passive materials in chloride environments and particularly stainless alloys in seawater, many attempts have been made to model the environment in a crevice, mostly for stainless Fe-Ni-Cr-Mo alloys. Two kinds of model have been developed:

Steady state model [2,89–92], which try to calculate the environment in a propagating crevice or, more frequently, a pit, and

Transient models [2,4,19,57,79,93–99], which intend to describe the environment evolution in a crevice and, in most instances, to predict the passivity breakdown by using a criterion usually based on a critical environment resulting from experimental data.

Copyright © 2002 Marcel Dekker, Inc.

Modeling the environment or the environment in a crevice requires solving a set of equations including:

- The kinetics of surface reactions in the crevice, mainly the metal dissolution because the cathodic reaction is generally assumed to occur only on the outside surfaces
- The kinetics of the reactions within the crevice solution, mainly the formation of metal chlorides and the hydrolysis of cations, which is the fundamental cause of pH drop within the crevice
- The transport processes including electrolytic migration and chemical diffusion, as most of the models assume no convection inside the crevice gap
- The mass and electrical charges balance in the crevice solution, across the metal-solution interfaces, and at the mouth of the crevice

Surface Reactions

With few exceptions [19], the passive anodic current of metal dissolution is usually taken as a constant and potential independent during the initiation stage and/or it is a parameter of the calculations.

During the propagation stage, different models are used, from the Tafel law [100] to experimentally fitted laws [19]. To take into account the strong current limitation due to the formation of a saturated salt layer on the dissolving surface, Gartland [19] introduced a damping coefficient that increases exponentially as the local concentration approaches saturation.

The possibility of water reduction inside the crevice gap is taken into account by Gartland [19] as a possible situation when the local pH and potential become low enough. Only one model [99] includes the cathodic reaction outside the crevice gap. It is more or less implicitly assumed in most models that this reaction is not a controlling process for the environment evolution inside the gap.

Solution Chemistry

The description of the crevice solution chemistry is probably the most difficult step (at least from the corrosion or chemistry standpoint if not the computer programming) as a result of the lack of reliable data. The main problems are:

- The thermodynamic description of the solution inside the crevice, which cannot be done by the dilute solution models, at least during the propagation stage
- The nature of the complex ions formed in the crevice and their thermodynamic properties, which are required to calculate the hydrolysis reactions governing the environment evolution

Solution Models—Activity Coefficients

Most models use dilute solution assumptions and former models [93] assumed unit values [2,19,93,94] of all activity coefficients (except in some cases for H^+ ions). Bernhardsson et al. [4] reached a compromise by using two sets of equilibrium constants, one for dilute solutions and the other for concentrated solutions.

Copyright © 2002 Marcel Dekker, Inc.

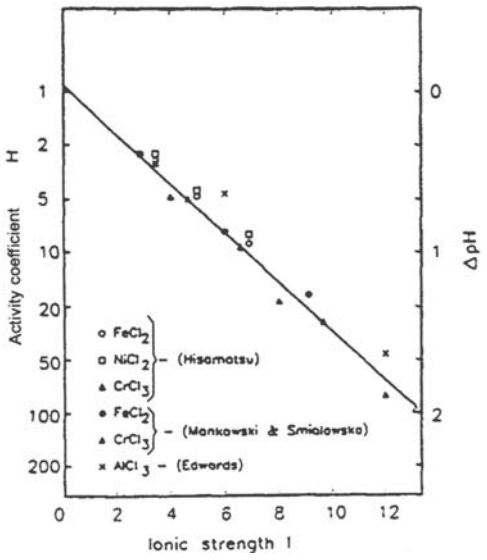


Figure 30 Influence of the ionic strength on the H^+ activity in chloride solutions [19].

Other authors used Debye-Hückel, the truncated Davies model [96,98], or the B-dot Debye-Hückel model [98] to derive the activity coefficients in concentrated solutions.

A particular case is the activity coefficient of H^+ ions. It has been shown experimentally (Fig. 30) that the presence of metal ions strongly decreases the pH of a chloride solution. Many models [2,19,94,97] include a pH correction derived from the results of Mankowski and Smialowska [33].

More recently, Brossia et al. [35] introduced an approach based on new correlations for activity coefficients in concentrated solutions. This approach [101] is based on the Helgeson-Kirkham-Flowers equation for standard-state properties with a nonideal solution model based on the activity coefficient expression developed by Bromley and Pitzer. Using specific software, Brossia et al. were able to predict the dominant ionic species and the salt precipitation in Ni, Fe, Cr, and 308 stainless steels crevice solutions. Fair agreement was observed with the in situ analyses of these crevice solutions by Raman spectroscopy.

Hydrolysis and Complexation Products and Reactions

These species and reactions include the products of the metal cation hydrolysis and the formation of metallic chlorides.

In one of the first models [93], the formation of metal chlorides was not taken into account and the cation hydrolysis was assumed to produce solid hydroxides. In the case of stainless steels, the pH drop was assumed to be driven by the hydrolysis of chromium cations according to the following reaction:

$$Cr^{3+} + 3H_2O \rightarrow Cr(OH)_3 \tag{9}$$

Copyright © 2002 Marcel Dekker, Inc.

Table 3 Solubility and Hydrolysis equilibria in the Model of Gartland [19]

$Cr^3 + H_2O \rightleftharpoons Cr(OH)^{2+} + H^+$	pK = 4.84
$2Cr^3 + 2H_2O \rightleftharpoons Cr_2(OH)_2^{4+} + 2H^+$	pK = 4.64
$Cr^{3+} + Cl^- \rightleftharpoons CrCl^{2+}$	pK = 0.65
$Ni^{2+} + Cl^- \rightleftharpoons NiCl^+$	pK = 0.25
$Ni^{2+} + 2Cl^- \rightleftharpoons NiCl_2$	pK = 0.05
$Fe^{2+} + Cl^- \rightleftharpoons FeCl^+$	pK = −0.36
$Fe^{2+} + 2Cl^- \rightleftharpoons FeCl_2$	pK = −0.40
$Mo^{3+} + 2H_2O \rightleftharpoons MoO_2 + 4H^+ + 2e$	E_0 = 0.061 V SCE

In the case of aluminum alloys, the hydrolysis reaction was assumed to be

$$Al^{3+} + 3H_2O \rightarrow Al(OH)_3 \tag{10}$$

Actually, the drop of pH is related to more complex reactions and species. Thus, in more sophisticated models, several hydrolysis reactions and metal chloride formation are taken into account but the selection of species and reactions is somewhat different from model to model. Oldfield and Sutton [94] and Watson and Postlethwaite [2] considered only hydroxides as the product of cation hydrolysis. Sharland [96] introduced simple metallic chlorides. The most complete set of species and reactions has been used by Bernhardsson et al. [4], which made available the thermodynamic data of a large number of species, including several iron, nickel, chromium, and molybdenum polycations as well as metal chlorides and hydroxychlorides. Gartland [19] used a more limited set of species (Table 3) selected among the Bernhardsson data. According to their experimental results, Hebert and Alkire [95] included $Al(OH)_n^{3-n}$ as the hydrolysis product in their model of the crevice corrosion of aluminum alloys.

A common feature of all the models is that all the chemical reactions of complex formation and cation hydrolysis are fast enough for thermodynamic equilibrium to be assumed. This may also be an incorrect assumption because we have already mentioned that the pH of synthetic crevice solutions can evolve for significant periods of time (up to several weeks) before reaching a stable value [33,40].

Transport Processes

Most models use transport equations for dilute solutions including diffusion, electrolytic migration, and convection such as:

$$\mathbf{J}_i = -D_i \nabla C_i - z_i F u_i \nabla \varphi + \mathbf{v} C_i \tag{11}$$

with

$$D_i = RTu_i \quad \text{(Nernst-Einstein relation)} \tag{12}$$

Copyright © 2002 Marcel Dekker, Inc.

However, different attempts have been made to take into account the deviation from ideality of the crevice solutions:

Walton et al. [98] wrote the transport equation (11) in a form using the activity instead of the concentrations.

$$N_n = \frac{-D_n C_n}{RT} \nabla \tilde{\mu}_n = \frac{-D_n C_n}{RT} \nabla (\mu_n + z_n F \Phi_s) \tag{13}$$

However, this formulation assumes the validity of the Nernst-Einstein equation for any ionic strength.

Gartland [19] made an attempt to use corrected ionic mobility coefficients: he used the diffusion coefficients collected by Bernhardsson [4] regardless of the solution concentrations but, to calculate the ion mobility coefficient, he introduced in the Nernst-Einstein equation an ionic strength–dependent correction factor based on a limited set of experimental data.

Walton [102] also included a porosity tortuosity factor in the diffusion coefficient to take into account the presence of porous solids and/or gas bubbles in the crevice gap.

The ionic fluxes are generally used to derive the current flowing in the crevice:

$$\mathbf{i} = \sum_i z_i \mathbf{J}_i \tag{14}$$

One common assumption of most, if not all, the available models is that the transport is purely unidimensional; i.e., the crevice is assumed to be narrow enough for the transverse concentration and potential gradients to be negligible. In fact, this assumption is required in order to simplify the numerical solutions.

Mass Balance

The mass balance equation:

$$\frac{\partial C_i}{\partial t} = -\nabla \mathbf{J}_i + R_i \quad (= 0 \text{ in steady-state propagation models}) \tag{15}$$

includes the production of species by chemical reactions in the liquid phase R_i. These reactions are the complexation and hydrolysis reactions as well as dissolution reactions on the crevice walls because models assume unidimensional transport fluxes.

Electrical Charge Balance

The electrical charge balance inside (and in one instance outside) the crevice is modeled in two ways:

Many models assume the electrical neutrality in any point [4,93,95,96]:

$$\sum_i z_i C_i = 0 \tag{16}$$

The potential distribution is obtained by using the Ohm law applied to the currents calculated in Eq. (14) and solution resistivity calculated from mobility coefficients.

Copyright © 2002 Marcel Dekker, Inc.

Others [2,79,97,99] solve the Poisson equation, which also gives the potential distribution along the crevice gap:

$$\nabla^2\Phi = \frac{F}{\epsilon}\sum_i z_i C_i = 0 \tag{17}$$

The solution of the Poisson equation dramatically increases the complexity and duration of the numerical simulations and requires numerical shortcuts. In addition, Watson and Postlethwaite [2] mentioned that the time required for electrical neutrality to be reached appears to be less than 10^{-10} s. This is very short compared with the time required for chemical equilibrium, and it is not clear whether the simple assumption of electrical neutrality could significantly change the results of such models.

Crevice Initiation Criteria

All criteria rely on a critical environment for passivity breakdown:

Critical pH [93]
Critical crevice solution [2,19,46,94] taking into account the pH and the chloride content but not the effect of metal cations
Critical dissolved Al content [95]

Despite the experimental observations, no attempt has been made to model crevice initiation by local pitting.

Results of the Models

As expected, the models predict the drop of local pH and the increase of chloride and metal ion content in the crevice gap. The predictions of several models were compared, with variable success, with the environment modifications observed in artificial crevices. Figure 31 shows a typical example of results indicating that the transport process is probably well enough modeled as indicated by the fair prediction of the chloride content but that the pH calculations are far less accurate. In Figs. 32 and 33, the set of data of Alavi and Cottis [26] has been compared with several models: the pH drops are generally underestimated (Fig. 32a–e), the potential gradient inside the crevice is not well described (Fig. 32f), and no model is able to predict the pH increase observed near the crevice tip (Fig. 3a–c).

Gartland [19] showed (Fig. 33) that the use of a correction factor to evaluate the H^+ activity is necessary to approach the actual pH, regardless of the fact that the equilibria involving solubility and hydrolysis of metal cations are taken into account. This may be one of the major causes of the underestimation of pH drop observed in the preceeding models.

Beside the quantitative results, which are impaired by the lack of basic knowledge of the crevice chemistry, the models provide interesting parametric results:

All models confirm that the crevice geometry is of major importance. As previously mentioned, Bernhardsson [4] introduced an L^2/h geometric

Copyright © 2002 Marcel Dekker, Inc.

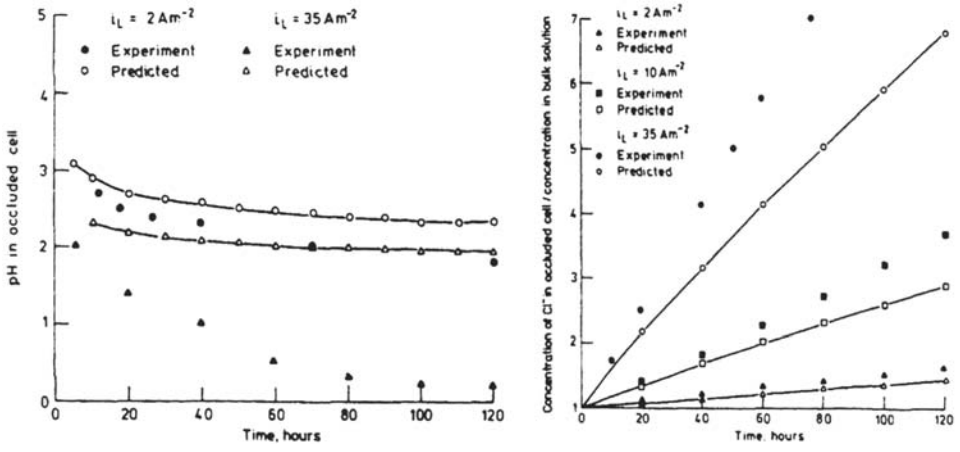


Figure 31 Comparison of the results of Zuo et al. [37] with the predictions of the model of Sharland [96]: note that the chloride content is fairly well predicted, whereas the pH drop is underestimated.

factor (in fact, a severity factor $S = i_a L^2/h$, Fig. 34) that appears to control the environment evolution. The trends shown in Figure 34 are one of the main reasons to study in more detail the effect of crevice depth/width ratio on the crevice repassivation (see Crevice Repassivation earlier).

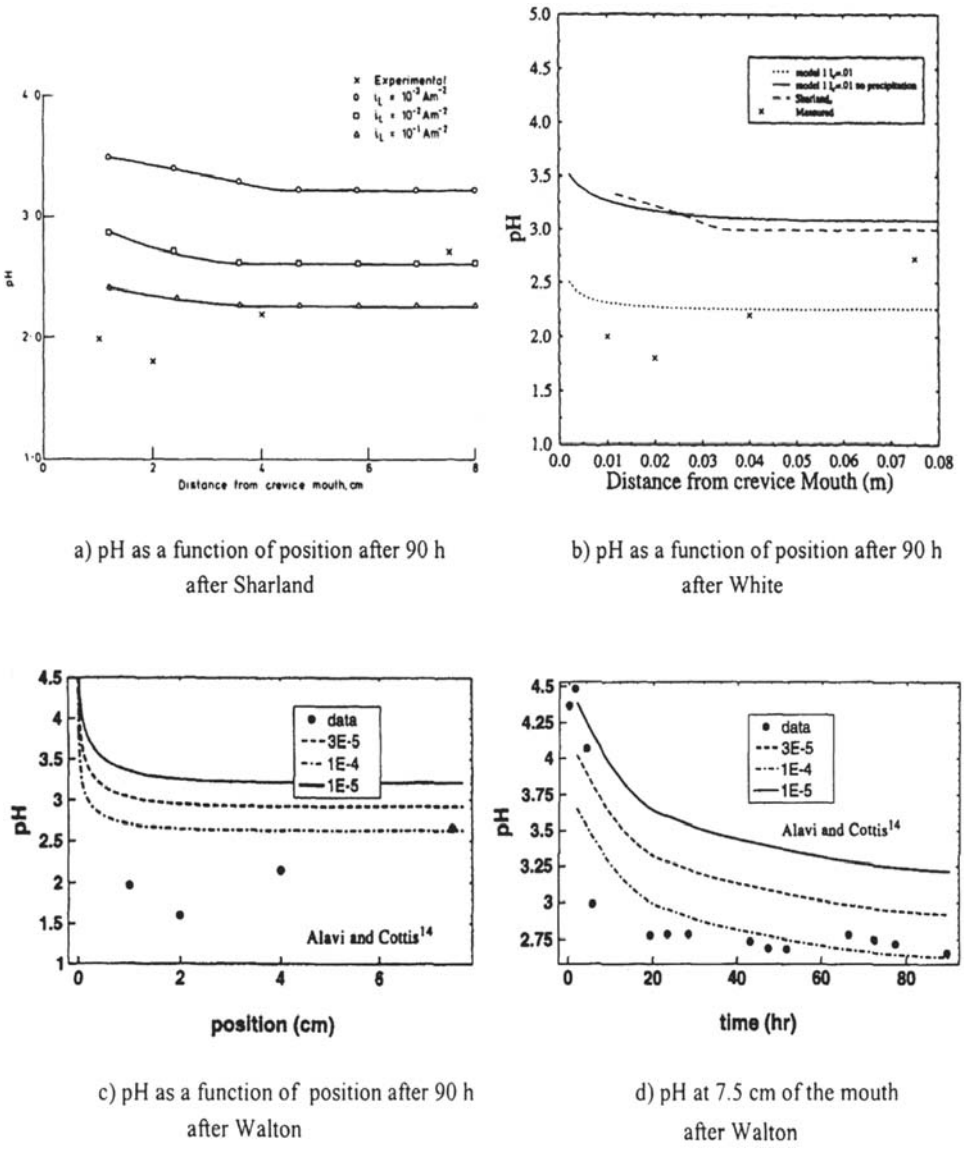
More precisely, the results of the Watson model clearly indicate (Fig. 35) that corrosion can start only if the crevice is tight and deep enough and support the fact that a critical crevice size may exist. This is consistent with one conclusion of White et al. [99] which indicates that their model is not able to predict pH low enough for crevice initiation in gaps of the order of several tens of micrometers. These results, as well as results of Gartland [19], also show that efficient crevice gaps are of the order of micrometers or less, in accordance with experimental results of Oldfield [3]. This supports the assumption that microcrevices due to asperity may play a major role in crevice initiation, as suggested by Sridhar and Dunn [60].

Gartland [19] also predicted, in agreement with observation (Fig. 26), that initial crevice damages are mainly located near the crevice mouth (Fig. 36), where the *IR* drop is low, which makes possible higher dissolution rates.

Finally, these models also show that the initial pH drop may be fast but that, rapidly, the rate of evolution becomes very slow (Figs. 34 and 37).

In summary, these models supply interesting information but still rely on experimental fitting to predict the initiation times correctly. Among their weaknesses, there is lack of precise data on the local chemistry of concentrated solutions and lack of prediction of the effect of the potential of the free surfaces. The use of a unidimensional transport equation and the assumption of instantaneous equilibrium of the hydrolysis and solubility reactions are also questionable.

Copyright © 2002 Marcel Dekker, Inc.



a) pH as a function of position after 90 h after Sharland

b) pH as a function of position after 90 h after White

c) pH as a function of position after 90 h after Walton

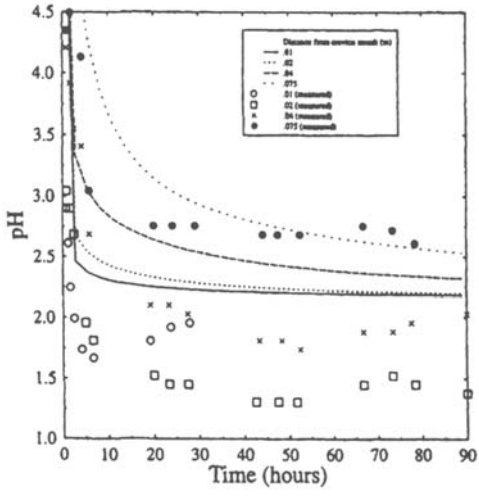
d) pH at 7.5 cm of the mouth after Walton

Figure 32 Comparison of the experimental results of Alavi and Cottis [26] with the predictions of the models of White et al. [99], Sharland [96], and Walton et al. [98] assuming various current densities.

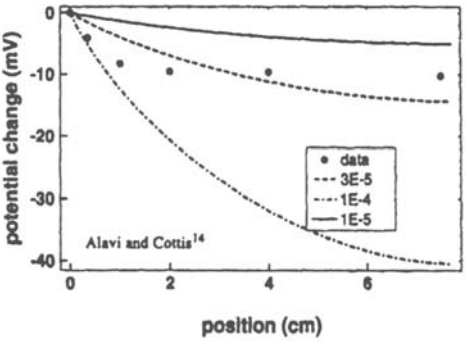
Finally, whatever their accuracy, the use of crevice initiation models will always meet with some limitation because of the uncertainty in the actual crevice geometry.

However, a very useful model to be developed would be a propagation model, particularly in an attempt to obtain theoretical support to describe the repassivation potentials and, if possible, to predict self-arrest of crevice corrosion.

Copyright © 2002 Marcel Dekker, Inc.



e) pH after 90 h after White



f) Potential drop as a function of the position after 90 h, after Walton

Figure 32

EXPERIMENTAL CHARACTERIZATION OF THE ALLOYS VERSUS CREVICE CORROSION

In order to select alloys for safe use in aerated chloride environments, a series of tests and criteria has been designed. They can be divided in several classes:

Exposure tests in environments representative of the service environment
Exposure tests in conventional environments
Electrochemical tests, which can be divided into two classes: (a) those intended to measure critical potentials for crevice initiation or protection and (b) those used to derive initiation criteria from the behavior of materials in conventional solutions supposed to simulate the crevice environment

For a more detailed description of crevice testing, the reader may consult the papers of Oldfield [103] and Ijsseling [104]

Crevice Former Devices

All the exposure and electrochemical tests that involve the use of crevice former devices encounter the problem of the geometry of the crevice. Many different designs of crevice former have been used, some examples of which are given in Figure 38a. The ASTM standard G78 defines a crevice former (Fig. 38b) that involves 20 crevice zones and gives a series of recommendations, for example, for the setup of the specimens in the test vessels. This device allows more reproducible results because of the statistical effect of the large number of crevice zones. However, the standard does not specify important points such as the condition of the contact surface of the crevice former.

Copyright © 2002 Marcel Dekker, Inc.

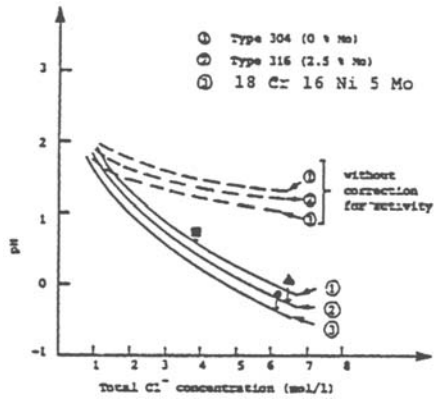


Figure 33 Effect of H^+ activity correction on the pH calculated by the Gartland model.

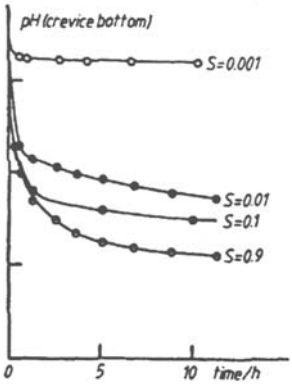


Figure 34 Effect of severity factor on pH drop calculated by the Bernhardsson model.

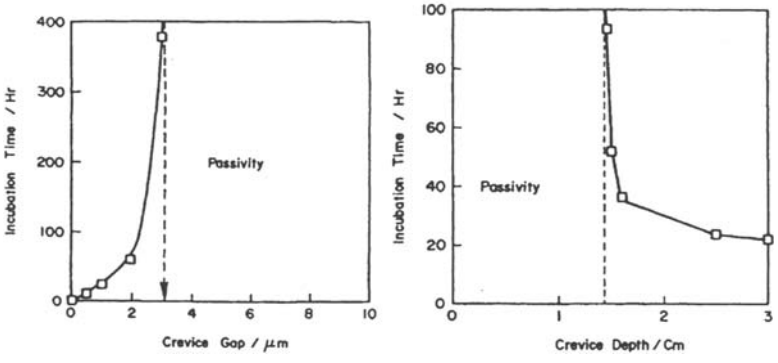


Figure 35 Effect of crevice geometry on crevice initiation time calculated by the Watson model.

Copyright © 2002 Marcel Dekker, Inc.

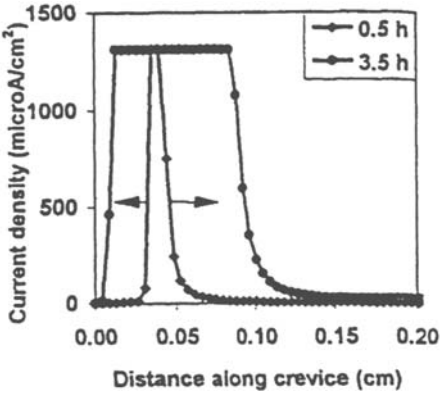


Figure 36 Prediction of the initial corrosion damage near the crevice mouth by the Gartland model (see Fig. 26 to compare with experimental data).

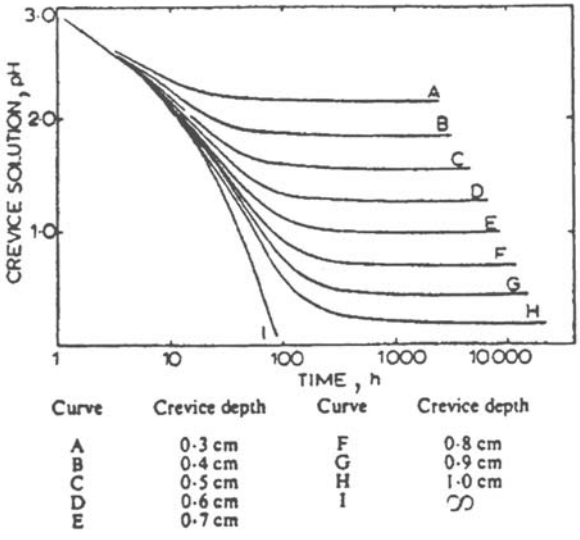


Figure 37 Drop of pH versus time as predicted by the Oldfield model.

Exposure Tests in Representative Environments

These tests are designed to rank the behavior of different alloys, to get orders of magnitude of initiation times in service, and/or to select alloys that should guarantee long-term resistance to crevice initiation. Thus, they can be very long (months or even years) with carefully selected crevice former devices, materials, and surface conditions. A problem is the test monitoring to detect crevice initiation without any perturbation of the local processes.

Apart from the selection of the crevice former device, it is important to have in mind that the severity of the test may depend on the availability of cathodic current.

Copyright © 2002 Marcel Dekker, Inc.

Thus, it is important to use specimens with large free surface area, particularly if the environment has high electric conductivity that allows long-distance galvanic coupling (seawater, for example).

There are different monitoring possibilities for exposure tests:

Periodic examination of the specimens is the simplest technique but it may dramatically modify the incubation period if the crevice zone becomes more or less dried during the examination. In particular, opening the crevice former to observe the inner surfaces may modify completely the local environment and cause the effective test time to go back to almost zero.

Monitoring of the corrosion potential allows one to detect any increase of the corrosion rate due to the polarization of the cathodic reaction on the free surfaces. Thus, the initiation of active corrosion in the crevice may be detected. In addition, electrochemical noise (i.e., potential fluctuations) indicating some dissolution transient may be interpreted as precursor events of passivity breakdown or at least of a low degree of passivity. The analysis of potential noise in terms of stochastic versus chaotic features has been shown [106] to allow early detection of pit initiation. This type of analysis should be checked for crevice corrosion.

Periodic measurements of polarization resistance may also be used to detect the onset of active corrosion.

Exposure Tests in Conventional Environments: The Ferric Chloride Test

This test is defined by the ASTM standard G48 and it is used for stainless steels and nickel-base alloys. Coupons with a crevice former device are exposed to a 6% $FeCl_3$ solution. Two criteria are used to characterize the tested materials:

The weight loss after a given time of exposure at a given temperature.

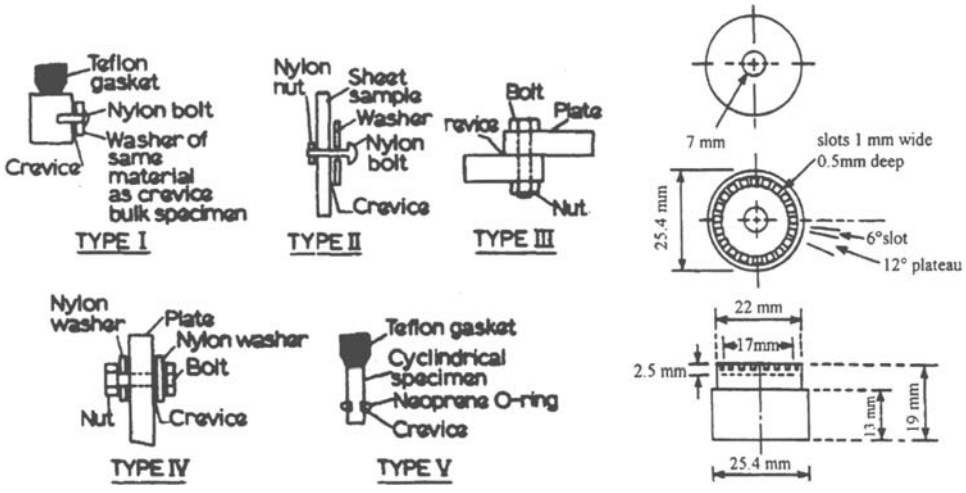


Figure 38 Crevice former devices for crevice corrosion testing. (a) Different types of crevice former (From Ref. 105). (b) ASTM G 78 crevice former device.

Copyright © 2002 Marcel Dekker, Inc.

A critical crevice temperature obtained by periodically increasing the temperature by steps of 2.5 or 5°C until passivity breakdown occurs in the crevice. However, because the passive film becomes more stable with increasing exposure time, the critical temperature may depend to some extent on the temperature selected to start the test.

An experimental correlation shows that this test can be used to rank the behavior of stainless alloys in seawater. In practice, it is also used as a control test to guarantee the constant quality of a product or to check the effect of fabrication parameters such as thermal treatment, welding, and surface condition.

Electrochemical Tests

Determination of Critical Potentials for Initiation and Protection

These tests are the same as those used to determine the pitting resistance except that a crevice former device is present on the test coupons. The measured parameters are:

The crevice potential and the repassivation potential obtained on polarization curves (potentiokinetic technique) or, in some instances, by using potential steps or potentiostatic tests

The critical temperature for the crevice at a given potential

Potentiokinetic Techniques Figure 7 of this chapter represents typical polarization curves of a passivated alloy in a near-neutral chloride solution with and without a crevice former device. The shapes of the two curves are identical except that the crevice potential is definitely lower than the pitting potential. In addition, it may depend on the crevice geometry if not properly measured.

As already discussed, the main difficulty of this technique, beside the problem of the crevice former geometry and reproducibility, is that the results are strongly dependent on the potential scan rate both because of the time-dependent stability of the passive films and because of the time-dependent evolution of the environment inside a crevice. In particular, the repassivation potential may be overestimated if corrosion is not well developed in the crevice and it can be underestimated if the potential backscan is too fast to allow the evolution of the local environment to be in "quasi-steady" conditions. It is generally admitted that the scan rate has to be very low, which causes the two critical potentials to become closer. But the appropriate scan rate must be determined on each system because it may depend on the alloy and on the environment.

Potentiostatic Techniques To determine the critical potential of crevice initiation, coupons in a crevice former device are exposed for a fixed period of time under potentiostatic control and monitoring of the anodic current is used to detect the onset of active corrosion. Several experiments are performed at different potentials and the crevice potential is the threshold potential that corresponds to an infinite initiation time (see Fig. 8 and 9 at the beginning of this chapter).

To measure the repassivation potential, severe crevice corrosion must be initiated on a "creviced" specimen and allowed to propagate for a fixed period of time or, more usually, to a definite amount of anodic charge. Then the potential is

Copyright © 2002 Marcel Dekker, Inc.

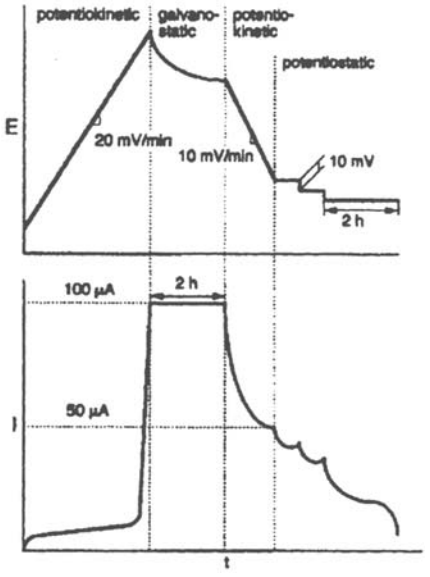


Figure 39 Stepwise potential backscan and current response to determine the repassivation potential [12].

stepped to a lower value and current monitoring is used to check the propagation or repassivation. As shown in Figure 8, the repassivation time increases with increasing applied potential and the repassivation potential is the potential corresponding to an infinite repassivation time. Apparently, the repassivation potential may depend on the development of corrosion before the potential is stepped down only if the amount of accumulated charge is lower than a critical value.

The potentiostatic techniques should be preferred to the potentiokinetic ones, but they require more specimens and longer experiments.

A more sophisticated repassivation test has been designed [7,12] to minimize the number of specimens by using a stepwise backscan potential (Fig. 39). During each step, the evolution of the current is analyzed and time is allowed to determine the trend. If, after decreasing, the anodic current increases again, indicating that propagation is not inhibited, the potential is stepped down again until repassivation occurs.

Determination of the Material Behavior in Simulated Crevice Environments

The tests that have been widely used in the past years are intended to determine the conditions of passivity breakdown in the crevice. Alloy coupons with no crevice area are tested in solutions that are supposed to simulate the local conditions in crevices. This is usually done by using acidic solutions with an increased chloride content compared with the bulk environment. For example, to perform tests to characterize the behavior in seawater, solutions containing 30 to 150 g/L of NaCl were used, the pH being lowered by HCl additions. Different measurements can be performed.

Copyright © 2002 Marcel Dekker, Inc.

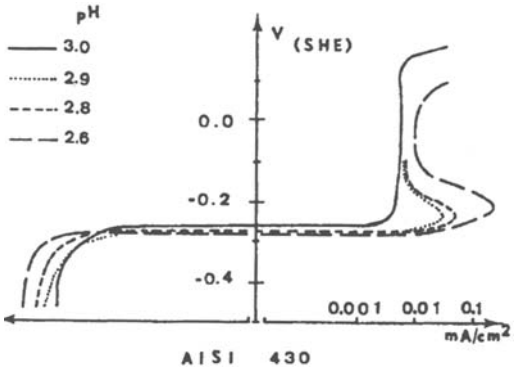


Figure 40 Measurement of activation pH on 430 SS [107] (2 M NaCl, 23°C).

Activation pH This pH is the pH below which an active peak is present on the polarization curves, (Fig. 40). This criterion was mainly developed by Crolet et al. [55]. The lower the activation pH, the more resistant the alloy to crevice corrosion.

pH of Spontaneous Film Breakdown It is measured by continuously lowering the pH of the solution until a freely corroding test coupon suffers a sudden potential drop due to passivity breakdown (Fig. 41). This criterion, which leads to a critical pH somewhat lower than the former, was used by Ogawa [42].

Active Peak Current as a Function of pH Several authors [3,103,108] use the measurement of the active peak current below the activation pH to compare the propagation kinetics of crevice corrosion on different materials. Figure 42 shows an example of this kind of measurement. Notice that the peak current of the duplex stainless steels (UR 47, 31803, 31603) is much higher at low pH values than that of austenitic grades (304 and 904L). This is consistent with the beneficial effect of nickel on the crevice propagation rate mentioned earlier.

All these electrochemical criteria suffer from several drawbacks:

1. It is assumed that passivity breakdown in a crevice is due to pH drop but, as discussed, the actual mechanisms may be different.

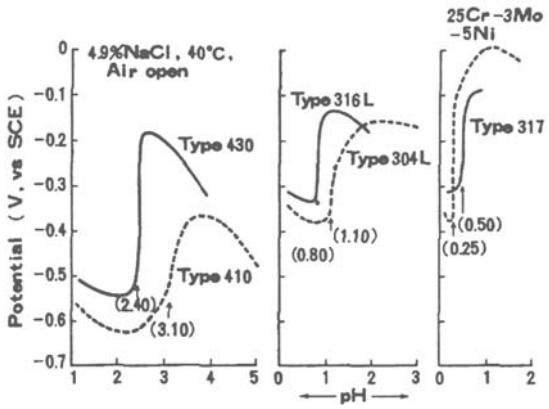


Figure 41 Measurement of spontaneous film breakdown pH [42].

Copyright © 2002 Marcel Dekker, Inc.

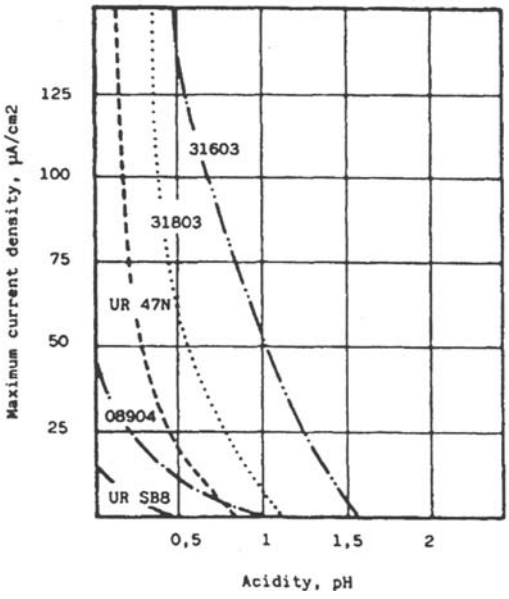


Figure 42 Evolution of peak current as a function of pH on different stainless steels [107].

2. Conventional solutions that are not representative of crevice environment are used. In particular, the presence of metal cations in the crevice solution is not considered.

However, these criteria probably allowed a correct ranking of the stainless alloys because the various methods are sensitive to the alloying elements that improve passivity (mainly Cr and Mo)

PREVENTION OF CREVICE CORROSION

Prevention of crevice corrosion must be taken into account at different stages of the life of an industrial apparatus:

–*Material selection*: the more resistant the materials to crevice corrosion (and more generally to localized corrosion) in chloride environments, the more expensive they are. Thus, the selection of a material exhibiting a very high resistance to crevice corrosion should not be the only way considered to prevent crevice corrosion: improved design, construction procedures, surface finish, maintenance procedures, and process management can be of a major importance.

–*Cathodic protection*: because crevice corrosion occurs above a critical potential, cathodic protection is an efficient way to prevent crevice corrosion by maintaining the potential of the free surfaces below the protection potential. This is the case of 17-4-PH stainless steel, which is not resistant to crevice corrosion in seawater but is commonly used because it performs

Copyright © 2002 Marcel Dekker, Inc.

very well under cathodic protection (this protection is often due to galvanic coupling to unalloyed steel).

–*Design*: an improved design should minimize the crevice areas, for example, by avoiding overlapping welded parts and by polishing seals bearing. However, crevice zones can be created by the formation of deposits during service and/or shutdown periods. Deposits can be minimized, for example, by avoiding low flow rate areas and by allowing complete draining of tanks,

–*Fabrication procedure and surface finish*: the intrinsic resistance of a material to crevice corrosion may be dramatically hampered by inappropriate fabrication procedures. The most sensitive points are *welding procedures*, which must be optimized by an appropriate energy input and, if necessary, by the use of more alloyed filler metal; *thermal treatments*, particularly if stress relief has to be performed; and *surface conditions*, which may suffer from fabrication events (scratches with iron incrustation, drops of welding filler metal, etc.) and which should be restored at the end of the fabrication process, for example, by a passivation treatment in the case of stainless alloys.

–*In service, transient, and shutdown conditions—maintenance procedures*: care has to be taken of the possible change of conditions during shutdown and/or transient Periods, which are not necessarily less prone to the development of crevice corrosion. An example is the case of desalination plants where concentrated chloride solutions may become very dangerous during shutdown if strict deaeration is not maintained. The possibility of formation of deposits during transient and shutdown periods and the occurrence of surface damage during maintenance operations are among the risks that have to be considered. Generally speaking, the best possible cleanliness of the apparatus must be maintained during all the apparatus lifetime.

CONCLUSION

Crevice corrosion occurs in restricted transport zones where the access of reactants and the elimination of corrosion products can be very slow. The detrimental effect of a crevice is related to a very small volume of solution in contact with very large metal surfaces. The restricted transport path between crevice and bulk solution is responsible not only for low diffusion exchanges but also for the buildup of a potential difference between the free surfaces and the crevice that becomes more anodic (ohmic drop effect).

These conditions trigger an evolution of the local environment in the crevice. Crevice corrosion may occur when the environment becomes more aggressive in the crevice than in the bulk environment.

On passivated alloys, and particularly on stainless alloys (Fe-Ni-Cr-Mo-…alloys), crevice corrosion occurs when the local conditions in the crevice cause passivity breakdown and the onset of active dissolution. As a consequence, crevice corrosion exhibits two different stages: an incubation period during which the local environment in the crevice evolves toward critical conditions and

Copyright © 2002 Marcel Dekker, Inc.

a propagation period that starts at the initiation time corresponding to the passivity breakdown.

The most widespread cases of crevice corrosion of passivated alloys are caused by aerated (or more generally oxidizing) chloride solutions such as sea or brackish water. In these chloride solutions, the environment in the crevice becomes progressively more acidic and more concentrated in chloride anions and metal cations. There are several possible causes of passivity breakdown, including low pH, high chloride content, presence of metallic chloride complexes, and pitting inside the crevice gap. Passivity breakdown occurs only if the corrosion potential of the free surface exceeds a critical value, but the relationship between the potential of the external surfaces and the evolution of the environment in the crevice is not completely understood.

Whatever the initiation mechanism, propagation causes further evolution of the local environment, which eventually becomes saturated (with concentrations estimated to be several mol/L of chloride and metal cations). At this point, a salt layer may form on the corroding surfaces. Thus, active corrosion in the crevice is rarely controlled by an activation process but rather by the ohmic drop and, for well-developed crevices, by cation transport through the salt layer, the thickness of which determines the corrosion rate.

An interesting feature that can be used to avoid crevice corrosion is that propagation stops if the potential of the free surfaces becomes lower than a critical value, referred to as repassivation potential. At least for alloys exhibiting a significant resistance to crevice corrosion, it is believed that this corrosion arrest is due to a repassivation of the metal surface inside the crevice. It is quite possible that, after long exposure periods, the critical potential for crevice initiation and the protection potential have a common value, but this point must be confirmed. The "protection" or "repassivation" potential can be a safe design criterion to avoid localized corrosion in long-term service. In particular, it provides a criterion independent of the surface condition because it guarantees against propagation of corrosion of the bulk material.

As the basic mechanisms of crevice corrosion have been understood to some extent, many models have been developed either to describe the steady state of an actively corroding crevice or to calculate the environment evolution and predict the passivity breakdown. These models are able to reproduce some major features of crevice corrosion, particularly geometric effects, but they all suffer from the lack of knowledge of the complex concentrated solutions that are formed in the crevice.

Crevice corrosion is a typical example of a corrosion problem in which the solution involves more than just the selection of fully resistant alloys. Design, fabrication procedure, and surface finish must be optimized and attention paid to the management of service conditions, as well as transient and shutdown periods. Optimization of maintenance procedures to maintain the best cleanliness of the surfaces may also contribute to prevent crevice corrosion.

REFERENCES

1. I. L. Rosenfeld, 5th International Congress on Metallic Corrosion, Tokyo, 1972, p. 53.
2. M. K. Watson and J. Postlethwaite, *Corrosion 46*:522–530 (1990).

Copyright © 2002 Marcel Dekker, Inc.

3. J. W. Oldfield, 19th Journées des Aciers Spéciaux—International Symposium on Stainless Steels, Saint Etienne, France, 1980.
4. S. Bernhardsson, L. Eriksson, J. Oppelstrup, I. Puigdomenech, and T. L. Wallin, 8th International Congress on Metallic Corrosion, Mainz, Germany, 1981, pp. 193–198.
5. R. C. Alkire, T. Tomasson, and K. Hebert, *J. Electrochem. Soc. 132*:1027–1031 (1985).
6. D. F. Taylor and C. A. Caramihas *J. Electrochem. Soc. 129*:2458–2464 (1982).
7. M. Akashi, G. Nakayama and T. Fukuda, CORROSION/98, paper 158, 1998.
8. D. S. Dunn, G. A. Cragnolino, and N. Sridhar, *Corrosion 52*:115–124 (1996).
9. P. Mckay and D. B. Mitton, *Corrosion 41*:52–62 (1985).
10. A. Takamura, *Corrosion* 306–313 (1967).
11. N. Sridhar and G. A. Cragnolino, *Corrosion 49*:885–894 (1993).
12. H. Yashiro, K. Tanno, H. Hanayama and A. Miura, *Corrosion 46*:727–733 (1990).
13. J. W. Oldfield and R. N. Kain, 12th International Congress, 1993, p. 1876.
14. A. J. Sedriks, CORROSION'96—Research Topical Symposia. Part 2. Crevice Corrosion: The Science and Its Control in Engineering Practice, 1996, pp. 279–310.
15. Remanit 4565S-Nitrogen Alloyed Austenitic Stainless Steels with Maximum Corrosion Resistance and High Strength, Thyssen Stahl AG, Krefeld, Germany, 1995.
16. T. Sydberger, *Werkst. Korros. 32*:119–128 (1981).
17. W. Yang, R. Ni, H. Hua, and A. Pourbaix, *Corros. Sci. 24*:691–707 (1984).
18. F. Hunkeler, and H. Boehni, *Passivity of Metals and Semiconductors* (M. Froment, ed.), Elsevier: Amsterdam, 1983.
19. P. O. Gartland, CORROSION'96—Research Topical Symposia. Part II. Crevice Corrosion: The Science and Its Control in Engineering Practice, 1996, pp. 311–339.
20. J. W. Oldfield, T. S. Lee, and R. N. Kain, *Corrosion Chemistry in Pits, Crevices and Cracks*: (A. Turnbull ed.), Her Majesty Stationery Office, London, 1987.
21. S. Valen, P. O. Gartland, and U. Steinsmo, CORROSION/93, paper 496, New Orleans, 1993.
22. T. Tsuru, K. Hashimoto, A. Nishikata, and S. Haruyama, *Materials Science Forum*, Vols. 44 and 45, Trans Tech Publications, Switzerland, 1989.
23. W. B. A. Sharp and L. H. Laliberté, CORROSION/78, paper 16, Houston, TX, 1978.
24. F. D. Bogar and C. T. Fujii, NRL report 7690, AD 778 002, 1974.
25. E. D. Verink, K. K. Starr, and J. M. Bowers, *Corrosion 32*:60–64 (1976).
26. A. Alavi and R. A. Cottis, *Corros. Sci. 27*:443–451 (1987).
27. B. E. Wilde and D. E. Williams, *Electrochim. Acta 16*:1971–1985 (1971).
28. T. Suzuki, M. Yamabe, and Y. Kitamura, *Corrosion 29*:18–22 (1973).
29. M. Marek, J. G. Rinker, and R. F. Hochman, 6th International Congress on Metallic Corrosion, Sydney, 1975, p. 502.
30. N. J. H. Holroyd, G. M. Scamans, and R. Hermann, *Corrosion Chemistry in Pits, Crevices and Cracks*, (A. Turnbull, ed.), Her Majesty's Stationery Office, London, 1987.
31. K. P. Wong and R. C. Alkire, *J. Electrochem. Soc., 137*:3010–3015 (1990).
32. A. Turnbull, *Corros. Sci. 23*: 833–870 (1983).
33. J. Mankowski and Z. Szklarska-Smialowska, *Corros. Sci. 15*:493–501 (1975).
34. N. Sridhar, and D. S. Dunn, *J. Electrochem. Soc. 144*:4243 (1997).
35. C. S. Brossia, D. S. Dunn, N. Sridhar, *Critical Factors in Localized Corrosion III* (R. G. Kelly, G. S. Frankel, P. M. Natishan, and R. C. Newman, eds.), The Electrochemical Society Proceedings Vol. 98-17, 1998, p. 485.
36. M. Pourbaix, *Corrosion 26*:431–438 (1970).
37. J. Y. Zuo, Z. Jin, S. Zhang, Y. Xu, and G. Wang, 9th International Congress on Metallic Corrosion, Toronto, 1984; p. 336.
38. A. Turnbull and M. K. Gardner, *Br. Corros. J. 16*:140 (1981).
39. M. H. Peterson and T. J. Lennox, Jr, *Corrosion 29*:406–410 (1973).

Copyright © 2002 Marcel Dekker, Inc.

40. P. Combrade, M. C. Bonnet, and H. Pagés, Innovation Stainless Steels, Florence, Italy, 1993, p. 215.
41. L. Y. Zhen, 9th International Congress on Metallic Corrosion, Toronto, 1984, p. 350.
42. H. Ogawa, A Mechanistic Analysis of Crevice Corrosion on Stainless Steels and the Calculation of the Incubation Time of the Crevice Corrosion Nucleation, Nippon Steel Corporation, 1987.
43. P. Marcus and V. Maurice, *Corrosion and Environmental Degradation* (M. Schütze, ed.), Wiley, New York, 2000.
44. N. Lukomski and K. Bohnenkampf, *Werkst. Korros. 30*:482 (1979).
45. W. Battista, A. M. T. Louvisse, O. R. Mattos, and L. Sathler, *Corros. Sci. 28*:759–768 (1988).
46. J. W. Oldfield and W. H. Sutton, *Bri. Corros. J. 13*:104–111 (1978).
47. S. E. Lott and R. C. Alkire, *J. Electrochem. Soc. 136*:973–979 (1989).
48. A. Garner, *Corrosion 41*:587–591 (1985).
49. R. C. Newman, *Corrosion 45*:282–287 (1989).
50. A. Garner and R. C. Newman, CORROSION/91, paper 186, 1991.
51. C. S. Brossia and R. G. Kelly, *Critical Factors in Localized Corrosion II*, The Electrochemical Society Proceedings Volume, 1995, pp. 201–217.
52. C. S. Brossia, R. G. Kelly, *Corros. Sci. 40*:1851–1871 (1998).
53. P. Marcus, this book, Chapter 9.
54. J. L. Crolet, L. Séraphin, and R. Tricot, *Rev. Metall.* 937–947 (1975).
55. J. L. Crolet, J. M. Defranoux, L. Séraphin, and R. Tricot, *Mem. Sci. Rev. Metall. 71*:797–805 (1974).
56. S. Okayama, S. Tsujikawa, and K. Kikuchi, *Corros. Eng. 36*:631–638 (1987).
57. P. O. Gartland and S. Valen, CORROSION/91, paper 511, Cincinnati, OH, 1991.
58. S. E. Lott and R. C. Alkire, *Corros. Sci. 28*:479–484 (1988).
59. K. Sugimoto and K. Asano, *Advances in Localized Corrosion—NACE 9* (H.S. Isaacs, U. Bertocci, J. Kruger, and S. Smialowska, eds.), NACE, Houston, 1990.
60. N. Sridhar and D. S. Dunn, *Corrosion 50*:857–872 (1994).
61. G. Karlberg and G. Wranglen, *Corros. Sci. 11*:499–510 (1971).
62. N. J. Laycock, J. Stewart, and R. C. Newman, *Corros. Sci. 39*:1791–1809 (1997).
63. Z. Szklarska-Smialowska, and J. Mankowski, *Corros. Sci. 18*:953–960 (1978).
64. G. S. Eklund, *J. Electrochem. Soc. 123*:170–173 (1976).
65. T. Shinohara, N. Masuko, and S. Tsujikawa, *Corros. Sci. 35*:785–789 (1993).
66. L. Stockert and H. Boehni, *Mater. Sci. Forum. 44/45*:313 (1989).
67. S. E. Lott and R. C. Alkire, *J. Electrochem. Soc. 136*:3256–3262 (1989).
68. K. Hebert, R. C. Alkire, *J. Electrochem. Soc.130*:1001–1007 (1983).
69. S. Zakipour and C. Leygraf, *Corrosion 37*:363–368 (1981).
70. T. Hakkarainen, *Electrochemical Methods in Corrosion Research—Materials Science Forum* (M. Duprat, ed.), Vol. 8, Trans Tech Publications, Switzerland, 1986.
71. T. Hakkarainen, *Corrosion Chemistry in Pits, Crevices and Cracks* (A. Turnbull, ed.), Her Majesty's Stationery Office, London, 1987.
72. G. T. Gaudet, W. T. Mo, T. A. Hatton, J. W. Tester, J. Tilly, and H. S. Isaacs, *AIChEJ. 32*:949–958 (1986).
73. U. Steinsmo and H. S. Isaacs, *J. Electrochem. Soc. 140*:643–653 (1993).
74. J. C. Griess, *Corrosion 24*:96–109 (1968).
75. S. Valen, thesis, Norwegian Institute of Technology, Department of Materials and Processes, 1991.
76. H. S. Isaacs, J.-H. Ho, M. L. Rivers, and S. R. Sutton, *J. Electrocherm. Soc. 142*:1111–1118 (1995).
77. N. J. Laycock and R. C. Newman, *Corros. Sci. 39*:1771–1790 (1997).

Copyright © 2002 Marcel Dekker, Inc.

78. N. Sridhar, D. S. Dunn, C. S. Brossia, and G. A. Cragnolino, CORROSION 2001—Research Topical Symposium on Localized Corrosion, 2001.
79. R. W. Evitts, J. Postlethwaite, and M. K. Watson, CORROSION/92, paper 75, Nashville, 1992.
80. T. Hakkarainen, CORROSION 96—Research Topical Symposia. Part II. Crevice Corrosion: The Science and Its Control in Engineering Practice, 1996, pp. 355–366.
81. M. Pourbaix, L. Klimzack-Mathieu, C. Martens, J. Maunier, C. Vanlengenhaghe, L. D. Munch, J. Laureys, L. Nellmans, and M. Warzee, *Corros. Sci. 3*:239 (1963).
82. K. K. Starr, E. D. Verink, and M. Pourbaix, *Corrosion 32*:47–51 (1976).
83. D. S. Dunn and N. Sridhar, *Critical Factors in Localized Corrosion*, Pennington, NJ, 1995, pp. 79–92.
84. J. R. Galvele, *Corros. Sci. 21*:551 (1981).
85. H. Boehni and F. Hunkeler, *Advances in Localized Corrosion—NACE 9* (H. S. Isaacs, U. Bertocci, J. Kruger, and S. Smialowska, eds.), NACE, Houston, 1990.
86. T. R. Beck, *Advances in Localized Corrosion—NACE 9* (H. S. Isaacs, U. Bertocci, J. Kruger, and S. Smialowska, eds.), NACE, Houston, 1990.
87. K. A. Gruss, G. A. Cragnolino, D. S. Dunn, and N. Sridhar, CORROSION/98 paper 149, 1998.
88. D. S. Dunn, G. A. Cragnolino and N. Sridhar, *Corrosion 56*:90–104 (2000).
89. A. Turnbull and J. G. N. Thomas, *J. Electrochem. Soc. 129*:1412–1422 (1982).
90. S. M. Gravano and J. R. Galvele, *Corros. Sci. 24*:517–534 (1984).
91. S. M. Sharland and P. W. Tasker, *Corros. Sci. 28*:603–620 (1988).
92. S. M. Sharland, *Corros. Sci. 28*:621–630 (1988).
93. J. L. Crolet and J. M. Defranoux, *Corros. Sci. 13*:575–585 (1973).
94. J. W. Oldfield and W. H. Sutton, *Br. Corros. J. 13*:14–22 (1978).
95. K. Heber and R. C. Alkire, *J. Electrochem. Soc. 130*:1007–1014 (1983).
96. S. Sharland, *Corros. Sci. 33*:183–201 (1992).
97. N. Sridhar, G. A. Cragnolino, H. Pennick, and T. Y. Torng, *Life prediction of Corrodible Structure* (R. N. Parkins, ed.), Vol. 1, NACE, Houston, 1994.
98. J. C. Walton, G. A. Cragnolino, and S. K. Kalandros, *Corros. Sci. 38*:1–18 (1996).
99. S. P. White, G. J. Weir, and N. J. Laycock, *Corros. Sci. 42*:605–629 (2000).
100. S. Tsujikawa, Y. Soné, and Y. Hisamatsu, *Corrosion Chemistry within Pits, Crevices and Cracks* (A. Turnbull, ed.), Her Majesty's Stationery Office, London, 1987.
101. A. Anderko, J., S. S. and R. D. Young, *Corrosion 53*:43–53 (1997).
102. J. C. Walton, *Corros. Sci. 30*:915–928 (1990).
103. J. W. Oldfield, *Int. Met. Rev. 32*:153–170 (1987).
104. F. P. Ijsseling, *Br. Corros. J. 15*:51–69 (1980).
105. B. E. Wilde, *Corrosion 28*:283 (1972).
106. B. Baroux and H. Mayet, ECS Meeting, Proceedings, Vol. 95-15, Chicago, 1995.
107. J. L. Crolet, L. Séraphin, and R. Tricot, *Mater. Tech.* 355–359 (1978).
108. J. P. Audouard, A. Désestret, D. Catelin, and P. Soulignac CORROSION/88, paper 413, St. Louis, 1998.

Copyright © 2002 Marcel Dekker, Inc.

12

Stress-Corrosion Cracking Mechanisms

Roger C. Newman
University of Manchester Institute of Science and Technology, Manchester, England

Several testable models for stress-corrosion cracking (SCC) of metals are discussed in terms of the main experimental variables: stress, metallurgy, and environment. Slip-dissolution, film-induced cleavage, and hydrogen embrittlement models are all shown to be consistent with experimental data in particular systems. Other models that cite effects of corrosion (without a film) or adsorption on crack tip deformation, leading to microcleavage or plastic microfracture, are less easy to test. No model can be "universal" in view of the demonstrable multiplicity of mechanisms. In many cases the atomistic mechanism is unknown, yet cracking can be controlled or predicted via the localized corrosion process that precedes SCC.

DEFINITION AND SCOPE OF STRESS-CORROSION CRACKING

SCC is defined as the growth of cracks due to the simultaneous action of a stress (nominally static and tensile) and a reactive environment. For metals, "reactive" excludes gaseous hydrogen, cathodic polarization, and liquid metals but includes aqueous and nonaqueous electrolytes and reactive atmospheres (H_2O, I_2, Cl_2). Related phenomena occur in inorganic glasses and ceramics, especially in water, and are thought to be involved in major geological processes including earthquakes and midocean vulcanism. Static stress does not exclude slow monotonic straining or low-amplitude cycling ("ripple loading"), which accelerate SCC in many metallic systems—for example, by promoting oxide film rupture at the crack tip. Stresses arise in practice from applied loads or from residual stress due to welding or inhomogeneous plastic deformation.

This review deals mainly with metals. The literature on their SCC is immense, and there are many useful texts and conference proceedings [1–12]. A brief history was published by Newman and Procter [13] and should be consulted for further historical details, especially the metal-environment combinations known to exhibit SCC. Plasticity plays a key role in SCC of metals, in contrast to inorganic glasses and ceramics, which are brittle solids and crack via reaction of the corrodent with highly stressed bonds at an atomically sharp crack tip [14]. Metal-induced fracture [15], formerly called liquid-metal embrittlement, remains a tantalizing phenomenon and

Copyright © 2002 Marcel Dekker, Inc.

there is no agreement on the mechanism or the relationship to SCC. Several authors have proposed universal models of SCC and corrosion fatigue [16–18] or even universal models of environment-assisted fracture, encompassing aqueous, gaseous, and liquid-metal environments [19,20]. We shall conclude that although these models may apply to particular systems, they are *not* universal, and there remain several valid mechanisms of SCC. Finally, hydrogen effects play an important part in SCC but are also the subject of a large separate literature [21,22]. The atomistic action of hydrogen will be covered quite briefly here but can be investigated further by referring to Refs. 1–12, 21, and 22.

CANDIDATE MODELS FOR SCC

We have selected three testable cracking models that may account for most known cases of SCC in metals: slip-dissolution, film-induced cleavage, and hydrogen embrittlement. Other important models involve microcleavage [16,17] or plastic microfracture [19] induced by dissolution or adsorption, respectively. A sixth model, surface mobility [20], will be discussed only briefly, as there appear to be serious problems with the basic physics of this model [23], although not necessarily with the general concept. A model based on vacancy injection during dissolution, even of pure metals, was proposed by Jones [18]; this deserves attention but has not yet made any successful new predictions, and it relies on processes that might be discounted in the future using modern techniques such as scanning tunneling microscopy.

Slip-Dissolution Model

According to this model [24–33], crack growth occurs by extremely localized anodic dissolution. The sides of the crack are protected by a film, ususally an oxide, which is fractured as a result of plastic strain in the metal at the crack tip. Crack growth proceeds by a cyclic process of film rupture, dissolution, and film repair (Fig. 1). This model was once favored for both intergranular and transgranular SCC in a wide variety of systems [25] but is now applied mainly to the intergranular cracking of ferritic steels in passivating environments such as carbonate-bicarbonate solutions [26,27] and to sensitized stainless steels [28–32].

Film-Induced Cleavage Model

Film-induced cleavage originated with the suggestion by Edeleanu and Forty [34] that superficial dezincification of α-brass in ammonia solution could trigger a brittle fracture through several micrometers of the unattacked substrate; they believed that the material through which this crack was propagating (between slip bands) was embrittled by short-range ordering. Their optical microscopy was elegant and came near to proving the reality of the crack-jumping phenomenon, which was later confirmed by Pugh and others using the scanning electron microsope (SEM) [35–39]. In the modern theory of film-induced cleavage [40–45] there is no special property of the face-centered cubic (fcc) substrate through which the crack jumps; the special properties lie in the film itself, which must be able to trigger a crack with a velocity of hundreds of meters per second within less than 100 nm (Fig. 2). Nanoporous

Copyright © 2002 Marcel Dekker, Inc.

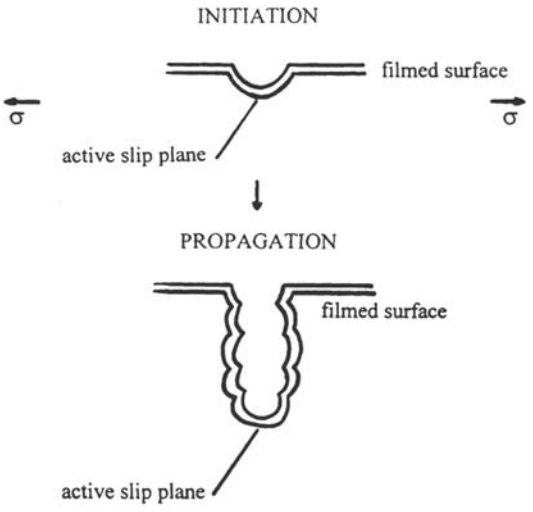


Figure 1 Schematic drawing of crack initiation and growth by slip-dissolution. (Adapted from Ref. 25.)

metallic layers produced by dealloying seem to be very effective, as they can be both brittle and epitaxial, or at least strongly bonded to the substrate. Tests of the film-induced cleavage model [33,46–51] have relied on producing single-shot brittle events through thin alloy foils and have shown that *intergranular* fracture can also be triggered by dealloyed layers in gold alloys. It may turn out that film-induced fracture involves a slower and more plastic process than originally envisaged by Sieradzki and Newman [40], but the reality of the phenomenon is now well established.

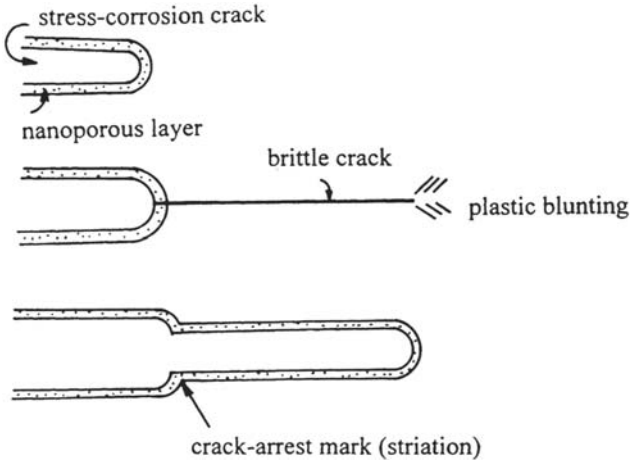


Figure 2 Schematic drawing of crack growth by film-induced cleavage in an fcc metal or alloy. (Adapted from Ref. 36.)

Copyright © 2002 Marcel Dekker, Inc.

Hydrogen Embrittlement Model

Hydrogen absorption is clearly responsible for SCC of high-strength steels in aqueous environments [52], notably in the presence of H_2S, where the fraction of discharged hydrogen that is absorbed by the metal can approach 100% owing to poisoning of the recombination reaction ($H + H = H_2$) by sulfur adsorption [53]. The role of hydrogen in fcc systems remains controversial, with positive indications in Al-Zn-Mg-Cu alloys [54,55] but waning evidence in austenitic stainless steels and Ni alloys [56]. Transgranular SCC of stable austenitic steels at high temperatures such as 300°C does not correlate with their susceptibility to hydrogen embrittlement. Hydrogen discharge and absorption are favored when there is acidification of the local environment by cation hydrolysis [54], especially if this acidification damages or destroys a passive film in the crack. Once absorbed in the metal, hydrogen can promote cleavage, intergranular separation, or a highly localized plastic fracture. In hydride-forming metals such as titanium, formation of brittle hydrides can be part of the fracture mechanism.

THE RATE OF SCC: EFFECTS OF STRESS INTENSITY FACTOR

"Classical" SCC phenomena, such as the cracking of brass in aqueous ammonia, are classical because they occur at low stresses and at high rates: 10^{-9} to 10^{-6} m/s or 0.1 to 100 mm/day. The crack velocity varies with the mode I stress intensity factor (K_I) as shown in Figure 3 [$K_I \simeq \sigma(\pi a)^{1/2}$, where σ is the stress and a is the crack length] [57]. The plateau at intermediate K_I values indicates that something chemical rather than something mechanical is controlling the crack velocity; this might be dissolution, diffusion, or adsorption. SCC has been detected growing with very low velocities such as 10^{-12}m/s (0.1 μm/day, or 1mm every 30 years) [58]. Such processes, occuring in piping or steam generator tubes, threaten the long-term integrity of nuclear power plants [59]. At these low rates and relatively high temperatures (300°C), solid-state transport of substitutional elements becomes a feasible part of the SCC mechanism, hence the aqueous SCC phenomenon starts to blend with high-temperature oxidation and might be controlled by processes such as grain boundary diffusion of atomic oxygen [60,61].

The important quantities in Figure 3 are the *threshold stress intensity,* K_{th} or K_{ISCC}, and the *region II crack velocity,* υ_{II}. In strong materials that can suffer fast fracture, the *critical stress intensity* or fracture toughness, K_{IC}, terminates the life of a component catastrophically, whereas ductile alloys fail by leakage or loss of cross section. The classical SCC systems have low K_{ISCC} values, especially austenitic stainless steel in hot chloride, where values as low as 1 Mpa $m^{1/2}$ have been reported [62,63]; there is a wide range of values in the literature, up to 12 Mpa $m^{1/2}$. The superior performance of duplex (austenoferritic) stainless steels in these environments is associated with a much higher (3–10 times) K_{ISCC} value [62]; thus duplex components must be highly stressed or defective in order to fail by SCC in hot chloride solutions. Incidentally, all the K_{ISCC} values mentioned, even the lowest, are high enough to cause yielding at the crack tip.

THE APPEARANCE OF SCC

SCC failures are macroscopically brittle in the sense that the ductility and load-bearing capacity of the material are impaired. Microscopically, the cracks are either

Copyright © 2002 Marcel Dekker, Inc.

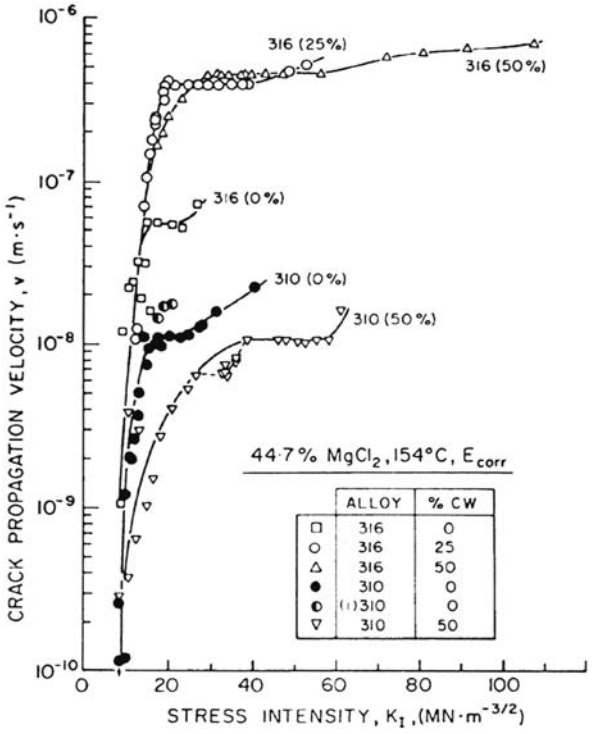


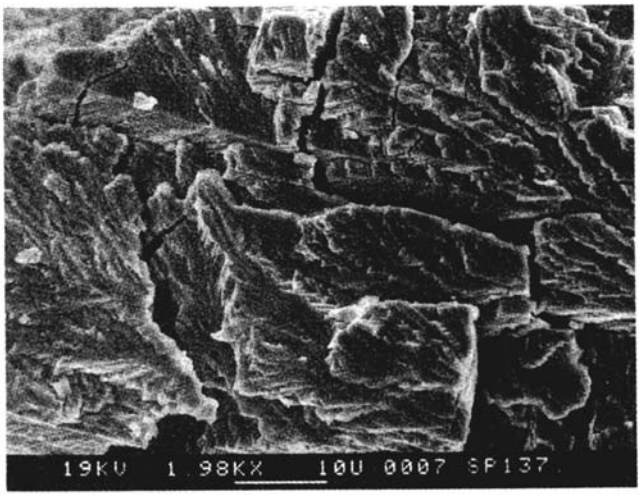
Figure 3 Examples of crack velocity–stress intensity curves for SCC, showing the effects of alloy composition and cold work on SCC of austenitic stainless steels in a hot chloride solution. (From Ref. 57. Courtesy of Pergamon Press.)

intergranular (sometimes along old boundaries such as those of prior austenite in martensitic steels) or transgranular and cleavage-like (Fig. 4a and b). In duplex microstructures, one phase often cracks more easily than the other, leading to characteristic cracking patterns (Fig. 4c). Plastic deformation always accompanies crack growth and plays a key role in most cracking mechanisms. Sometimes the fracture surfaces show evidence for stepwise (discontinuous) crack advance, especially in transgranular SCC [35–39] (Fig. 5). It is possible to produce similar crack front markings by periodic over- or underloading [37,38,64,65] and to show that the natural crack arrest marks do indeed correspond to positions of the crack front. The average orientations of transgranular cracks are specific, e.g., {110} in α-brass [35], but such surfaces are sometimes composed of very fine, alternating {111} microfacets [66]. Fracture of the ligaments between the {110} crack facets, which produces the river lines on the fracture surface, is usually a ductile process such as necking (in pure Cu) or crystallographic shear (in α-brass). The latter favors crack propagation at low stresses owing to the small displacement involved [39]. The presence of intact ligaments behind the crack tip shields the tip from some of the applied stress intensity and explains why cracks are often much sharper [34] than one would calculate using elastic-plastic fracture mechanics. Ligament fracture, or its absence, can play a role in the formation of the crack arrest markings shown in Figure 5.

Copyright © 2002 Marcel Dekker, Inc.



(a)



(b)

Figure 4 Examples of SCC fracture surfaces, all obtained with the slow strain rate test. (a) Intergranular SCC of α-brass in Mattsson's [109] solution, pH 7.2. (b) Transgranular SCC of α-brass in 15 M cuprous ammonia solution equilibrated with Cu and Cu_2O (courtesy of T. Shahrabi). (c) SCC of 25Cr duplex stainless steel plate (50% ferrite) in NaCl-H_2S solution at 80°C, showing flat, cleavage-like cracking of ferrite and mainly ductile fracture of austenite (courtesy of V. M. Salinas Bravo). (d) High-contrast schematic of (c), showing necked austenite grains as light (high) areas.

Copyright © 2002 Marcel Dekker, Inc.



(c)

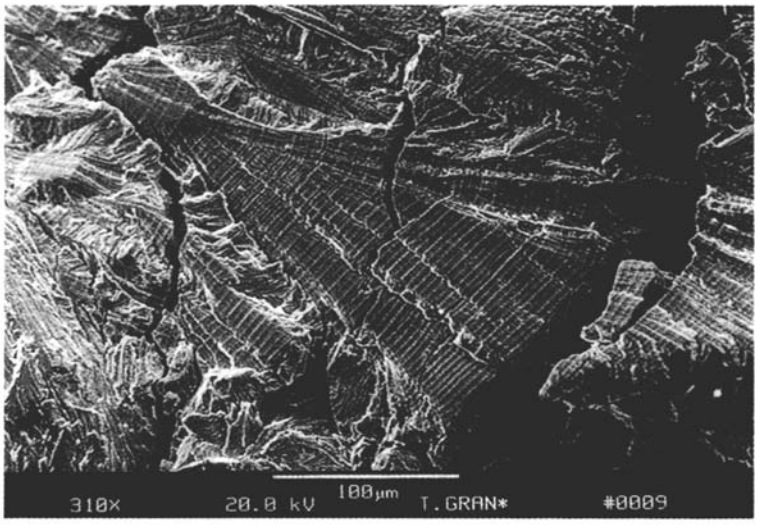


(d)

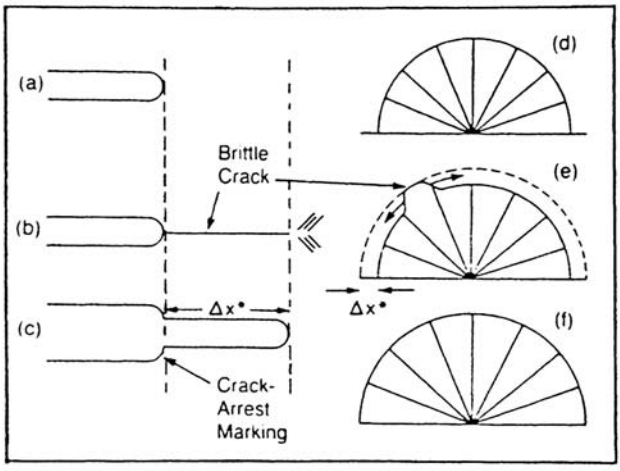
INITIATION OF SCC: THRESHOLD STRESSES AND ROLE OF LOCALIZED CORROSION

SCC initiation at smooth surfaces shows a threshold stress (σ_{th}) that varies from 20% to more than 100% of the yield stress (σ_y), depending on the metal and the environment. Thermal stress relief of welded or cold-worked components can prevent SCC if σ_{th}/σ_y is fairly high, e.g., 0.7. In some systems, σ_{th} can be lowered by low-amplitude dynamic loading (Fig. 6), which is very important in practice [67].

Copyright © 2002 Marcel Dekker, Inc.



(a)

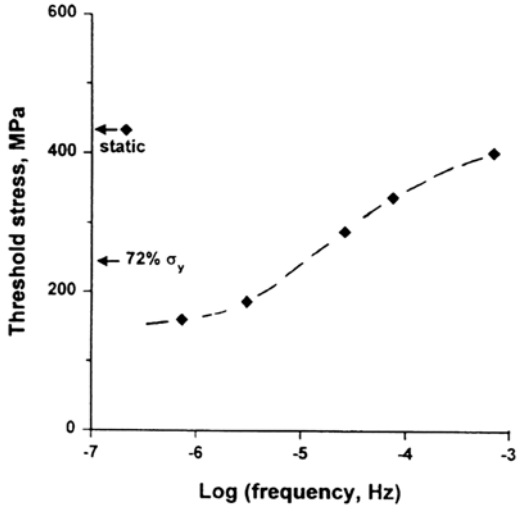


(b)

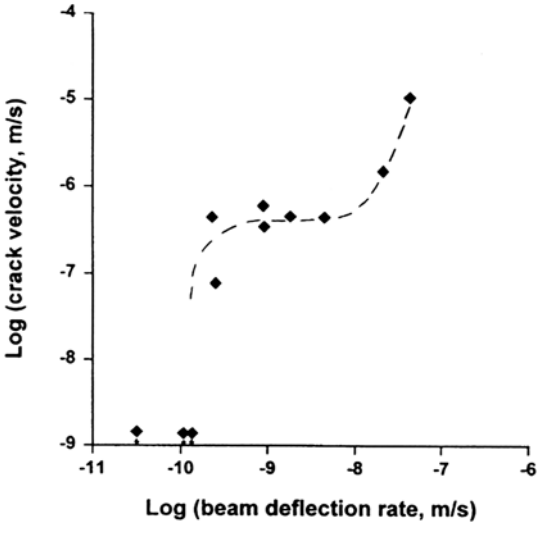
Figure 5 (a) Crack arrest marks on a transgranular SCC surface, observed near the overload region on a slow strain rate specimen ($\dot{\epsilon} = 10^{-5}$ s^{-1}) of 70–30 brass tested in pH 7.2 Mattsson's [109] solution with 0.05M NaCl; (b) schematic drawing of the transgranular SCC process and the mechanism of striation formation. (After Refs. 35–39. Courtesy of NACE.)

SCC is usually nucleated by some form of localized corrosion; in chloride-SCC of stainless steels [68] or aluminum alloys [54], cracks start from areas of pitting, intergranular corrosion, or crevice corrosion that create the stress concentration and the acidity required for cracking (Fig. 7). In SCC of C-Mn or low-alloy steels, intergranular corrosion occurs along segregated zones rich in carbon, nitrogen, or phosphorous and provides a stress concentration (helps to achieve K_{ISCC}) [27]

Copyright © 2002 Marcel Dekker, Inc.



(a)



(b)

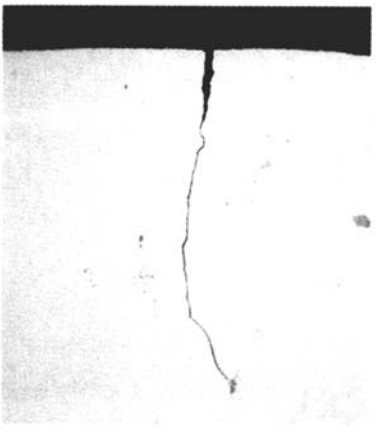
Figure 6 (a) The effect of low-amplitude cyclic loading on the threshold mean stress for SCC of C-Mn steel in carbonate-bicarbonate solution. (b) The corresponding data for growth of single cracks [67]. (Redrawn from Ref. 164.)

(Fig. 8). Pure iron shows no intergranular corrosion or SCC in this kind of solution. In mechanistic studies, one often comes across references to rupture of passive films, but in fact SCC rarely occurs in a true (local) passive state. There is usually some form of intergranular corrosion, pitting, crevice corrosion, or dealloying, or else SCC occurs in a conventional active state via a hydrogen embrittlement mechanism (as in high-strength, low-alloy steels). There are surface films in cracks, and these need to

Copyright © 2002 Marcel Dekker, Inc.



(a)



(b)

Figure 7 Aspects of the nucleation of SCC by localized corrosion. (a) Peak aged Al-Li-Cu-Mg alloy 8090 after unstressed preexposure in aerated 3.5% NaCl for 7 days. (b) SCC initiated from one of the fissures shown in (a), following removal of the solution and continued exposure to laboratory air under a short transverse tensile stress (courtesy of J. G. Craig, unpublished data). (c) Creviced region of 316L stainless steel after a slow strain rate test in 0.6M NaCl + 0.03M $Na_2S_2O_3$ at 80°C and an applied anodic current of 25μA, showing unstable pitting leading to crevice corrosion and SCC initiation (courtesy of M. I. Suleiman).

be ruptured to expose bare metal, but in many cases (such as carbon steel in sodium hydroxide), the film has a precipitated or gel-like nature rather than conforming to the conventional idea of a compact passive film a few nanometers in thickness.

Copyright © 2002 Marcel Dekker, Inc.

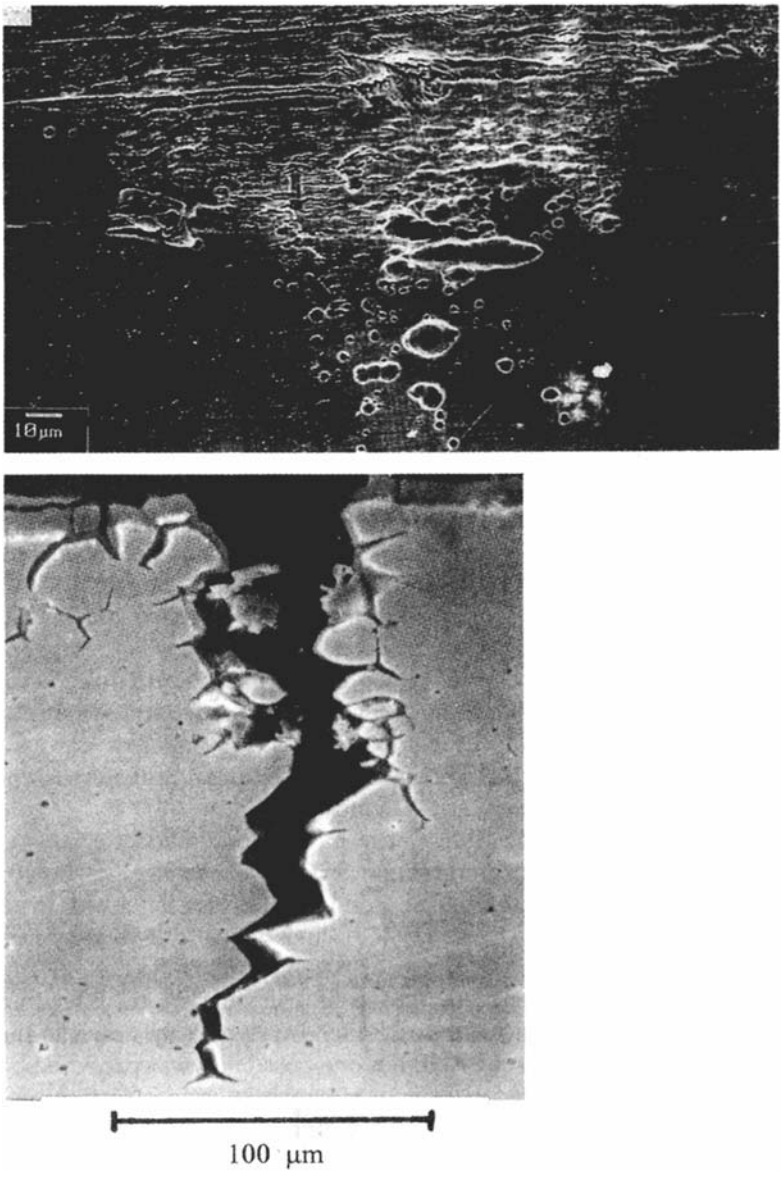


Figure 8 Caustic SCC of an Fe-3Ni-1Mo pure alloy at –400 mV (Hg-HgO) in a slow strain rate test in 9 M NaOH at 98°C [85], showing the intergranular corrosion that initiated SCC.

METALLURGY OF SCC

The main metallurgical variables in SCC are

Solid solution composition
Grain boundary segregation
Phase transformations and associated solute-depleted zones

Copyright © 2002 Marcel Dekker, Inc.

Duplex structures
Cold work

In the case of hydrogen-induced SCC of high-strength steels, one could add strength, no matter how this is achieved. Environmental criteria for SCC are necessary but not sufficient: SCC will not occur without a susceptible metallurgy. The only exceptions to this rule are transgranular cracking processes in pure metals, e.g., iron in anhydrous ammonia [69] or copper in sodium nitrite solution [65,70].

"Advanced" materials such as metal-matrix composites also show SCC phenomena, but these are not distinctive and research has been quite qualitative in this area.

Solid solution composition classically controls the SCC of brasses [71,72], austenitic stainless steels in hot chloride solutions [73,74], and noble-metal alloys [75]. In all these systems there is evidence that *dealloying* dominates the SCC mechanism, although this remains controversial for stainless steels. Transgranular SCC ceases above a critical content (parting limit or dealloying threshold) of the most noble alloying element, either 80–85% in Cu-Zn or Cu-Al or 40% in Ni-Cr-Fe or Au-X alloys (Figs. 9 and 10). These values have been interpreted using percolation theory [72,76,77]. In all these systems the crack walls are either oxide free or else have thick porous oxides that allow contact of metal and electrolyte [78,79]. Flangan and co-workers [80,81] have shown that SCC of Au-Cu alloys occurs below the critical potential for macrodealloying (E_c) and consequently reject film-induced cleavage for this system. However, because dealloying in Au-Cu occurs in a localized mode resembling pitting [82,83], this conclusion may be premature. The concentration of Cl^- that occurs in the pit lowers E_c locally by complexing Cu(II), and any transient electrochemistry should be done in a $CuCl_2$-rich solution, simulating the crack environment, if it is to reproduce the behavior of a crack tip.

Minor alloying elements (C, P, N, As, …) can have several distinct effects on the electrochemistry of SCC. In caustic intergranular SCC of carbon steel, carbon or nitrogen segregation (and/or precipitation) at grain boundaries interferes with passive film formation and may affect plasticity [27], and phosphorus segregation introduces SCC in a new, more oxidizing range of potentials [84,85] (Fig. 11). In chloride-SCC of austenitic stainless steels, the group 5B elements are so influential on *transgranular* cracking that it is difficult to crack high-purity ternary alloys in the laboratory [86]. This is not understood in detail, but one possibility was proposed by the author [87,88]: adsorption of group 5B elements is known to reduce surface self-diffusivity in electrolytes, and dealloyed layers need extremely fine porosity to cause SCC by film-induced cleavage, so if the 5B elements are absent there is a rapid coarsening of the porosity and a reduced susceptibility to SCC (Fig. 12). This idea unifies the well-known effect of arsenic in brass with that of N or P (or even As) in stainless steel.

Phase transformations are used in strong alloys to provide dispersion (precipitation) strengthening and also occur in ductile alloys during welding or simply as a by-product of the traditional metallurgy of the system. In strong alloys, there is a different sequence of nucleation and growth at grain boundaries compared with the matrix [54]. Depending on the phase(s) formed at the grain boundary, enhanced reactivity may result, either of the phase itself or of an associated solute-depleted zone [89]. The most important of these systems are the Al-Zn-Mg (7000 series) aerospace alloys, which become especially susceptible to SCC when further alloyed

Copyright © 2002 Marcel Dekker, Inc.

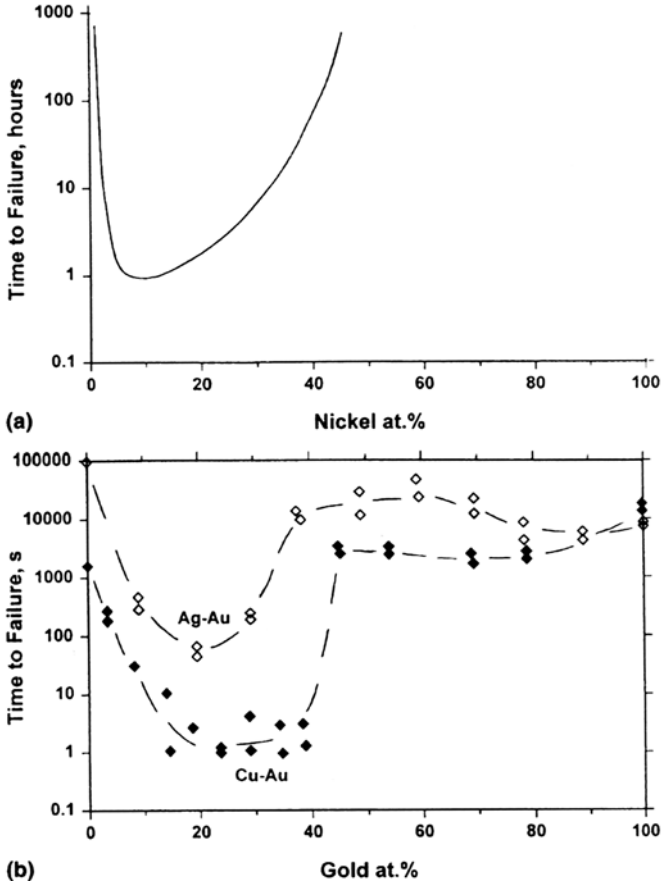


Figure 9 Direct and indirect evidence for a role of dealloying in SCC. (a) The Copson curve showing the dependence of SCC in austenitic stainless steels on their nickel content [73]. (b) Similar behavior for gold alloys in aqua regia, where dealloying is known to control SCC [75].

with Cu. Grain boundary segregation of Cu has been detected in susceptible conditions using analytical electron microscopy [90]. Hydrogen plays a role in this cracking [54], and it is difficult to seperate the roles of hydrogen and dissolution, let alone the contributions of the reactive $MgZn_2$ phase, the segregated Cu, the solutedepleted zone, and the grain boundary strength. Precipitation of grain boundary phases containing Cu-depleted (less noble) regions; this is easily demonstrated in Al-Cu (2000 series) systems, but the narrow and deep Cu depletion occurs only in underaged, noncommercial heat treatments, so practical problems are relatively rare, especially as these alloys are normally used in sheet rather than extrusion form (the arrangement of grain boundaries in unrecrystallized sheet inhibits transverse SCC). In the 7000-series alloys the high SCC susceptibility is shifted to the peak strength condititon—a major inconvenience to users, as it denies them the use of the strongest condition of the alloy (it must be overaged for most applications). Progress is being made in complex thermomechanical treatments to improve the toughness and SCC resistance at peak strength [54].

Copyright © 2002 Marcel Dekker, Inc.

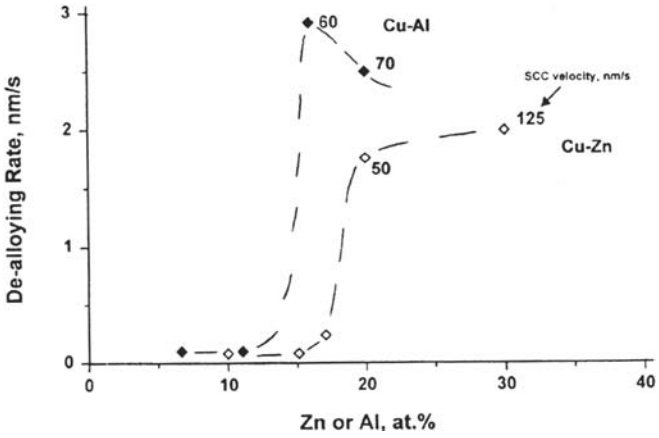


Figure 10 Direct and indirect evidence for a role of dealloying in SCC: SCC and dealloying of Cu-Zn and Cu-Al monocrystals in cuprous ammonia solution as a function of solute content [72].

Intergranular corrosion does not necessarily correlate with SCC in aluminum alloys. The 6000-series (Al-Mg-Si) alloys such as 6061 can suffer intergranular corrosion but never fail by SCC. Examination of fractured specimens following intergranular corrosion shows crystallographic tunneling attack on either side of the grain boundary.

Precipitation strengthening of steels, such as the PH grades of ferritic stainless steel containing Cu, affects SCC when the operative mechanism is hydrogen embrittlement [91]. *Precipitation*, without strengthening, can occur at grain boundaries and is responsible for the most expensive form of SCC: the cracking of

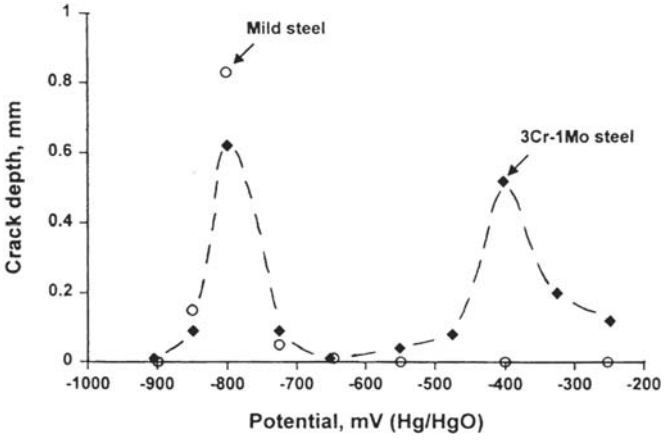


Figure 11 SCC penetration as a function of potential for carbon steel and low-alloy Cr-Mo steel tested in hot NaOH solution, showing a cracking regime at higher potential induced by P segregation to grain boundaries [66]. See also Figure 22.

Copyright © 2002 Marcel Dekker, Inc.

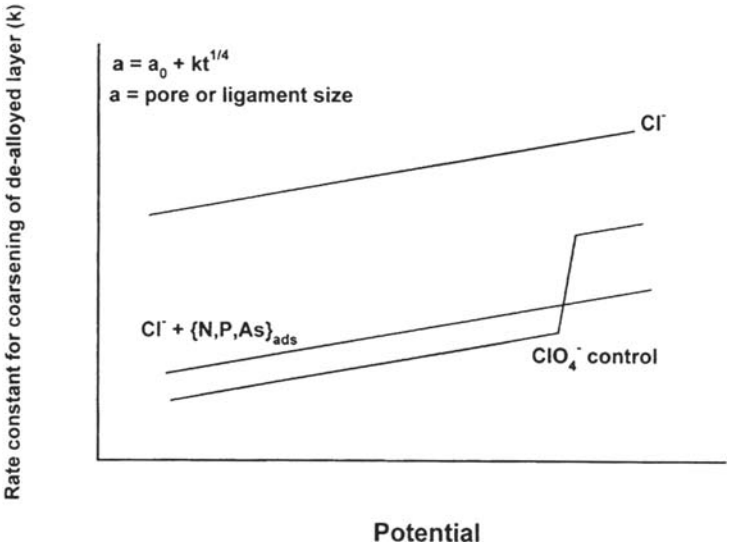


Figure 12 Schematic drawing of the proposed mechanism of action of group 5B elements on chloride-SCC of austenitic stainless steels [88].

weldsensitized austenitic stainless steel in oxygenated high-temperature water (boiling-water reactor pipe cracking) [59]. The sensitization process in AISI type 304 stainless steel consists of the precipitation of chromium carbides at the grain boundaries in the zone either side of a weld where the temperature has reached about 600–800°C. This leaves narrow Cr-depleted zones that repassivate more slowly than the matrix and therefore provide an active crack path. Effective remedies are the reduction of carbon content to about 0.03% (the 304L grade) or the addition of alternative carbide formers (Ti, Nb, e.g., the 321 grade). The fraction of sensitized grain boundaries required to provide a continuous crack path in slow strain rate tests has been shown to conform to a percolation model with a percolation threshold of about 23% [92] (Fig. 13). Under static loads the required fraction of sensitized boundaries may be higher.

Other phase transformations occuring in austenitic and duplex stainless steels (σ phase, α′ phase) generally produce *discontinuous* Cr-depleted zones around these Cr-rich phases, so crack growth is not necessarily enhanced, although pitting resistance is greatly degraded by σ phase, so SCC is initiated much more easily [91]. The austenite-ferrite transformation will be considered later.

Martensite is very susceptible to hydrogen embrittlement, and strong low-alloy steels based on tempered martensite have an inescapable tendency for hydrogen-induced SCC in saltwater or other neutral environments [93]. *Bainite* can be the basis of strong steels (although not as strong as lightly tempered martensites) that are slightly less susceptible. Depending on the flux of hydrogen into the steel (highest in acidic H_2S, lower in NaCl or fresh water, lower still in moist air), curves of K_{ISCC} versus yield strength can be drawn for martensitic steels as shown in Figure 14. A current challenge is to improve the hydrogen embrittlement resistance of quenched and tempered steels in the 700–850Mpa range of yield strengths so that they can be used in wet H_2S environments; one strategy is to exploit the greater resistance of

Copyright © 2002 Marcel Dekker, Inc.

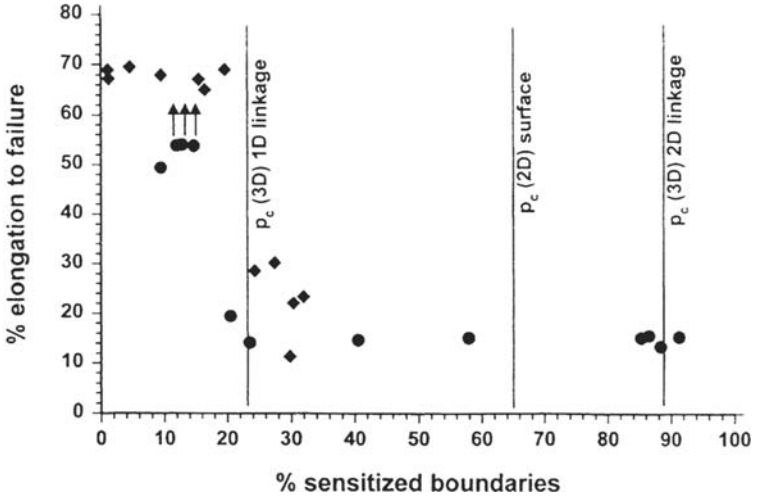


Figure 13 Dependence of SCC on the fraction of sensitized grain boundaries for slow strain rate tests of type 304 stainless steel in sodium thiosulfate solution, showing behavior in accordance with a 3D percolation model for linkage of sensitized grain boundary facets with a sharp cracking threshold at 23% [92]. The thresholds at 65% and 89%, representing growth of the crack as a continuous rumpled sheet, may be relevant in constant-load tests where ductile ligaments can arrest the cracks.

recrystallized ferrite that forms in some of these steels. Some specialized high-strength steels can show superior performance, such as cold-drawn pearlite [94] (prestressing wire or tire cord) and especially work-hardened, high-nitrogen austenite [58], which is virtually immune to hydrogen embrittlement. Neither of these materials is suitable as a general-purpose structural steel. Cold-drawn steel wire derives its

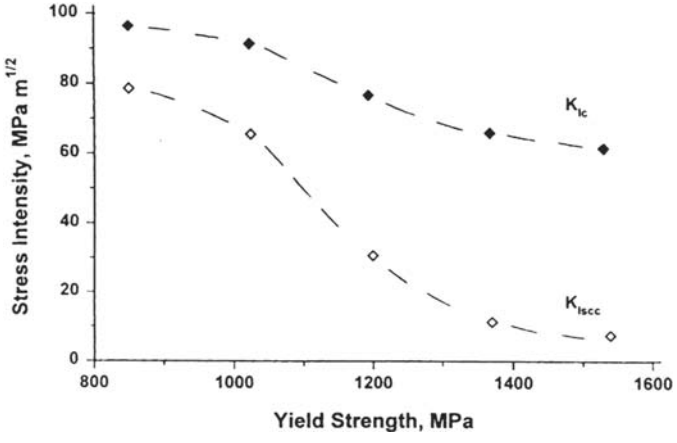
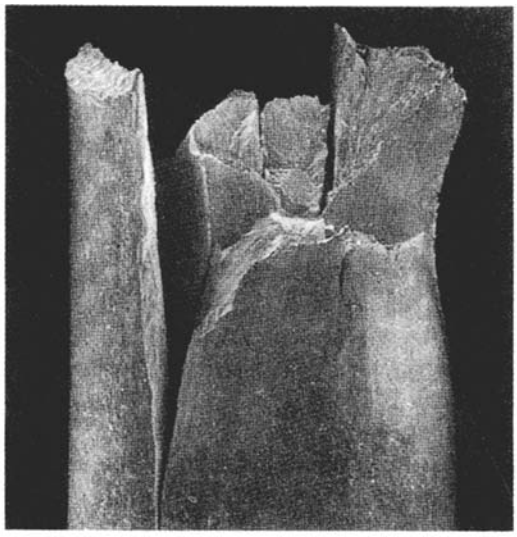


Figure 14 Dependence of K_{ISCC} and K_{IC} on yield strength for AISI 4340 high-strength steel tested in flowing seawater. (Redrawn from Refs. 93 and 152.)

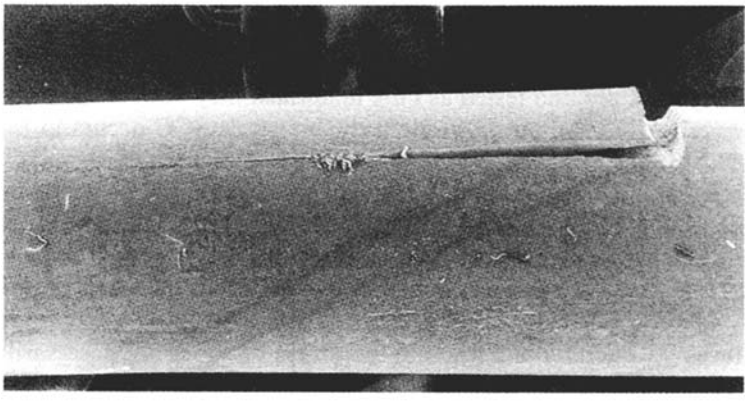
Copyright © 2002 Marcel Dekker, Inc.

SCC resistance from its highly directional microstructure; the resistance of such microstructures to transverse, intergranular SCC is well known in many systems including aluminum alloys and steels (Fig. 15).

Duplex structures are defined as alloy microstructures in which two phases are present in comparable proportions. Duplex (austenoferritic) stainless steels have become very popular materials because they combine strength and SCC resistance and can be welded with good microstructural control [91,95]. Their pitting and crevice corrosion resistance compare favorably with those of austenitic steels of similar Mo content.



(a)



(b)

Figure 15 Example of transverse SCC resistance in a highly directional microstructure: 5-mm-thick wires of martensitic prestressing steel, notched and tested at a constant load [higher in (a) than in (b)] in 0.6 M NaCl solution. (Courtesy of A.S. Doughty, unpublished data.)

Copyright © 2002 Marcel Dekker, Inc.

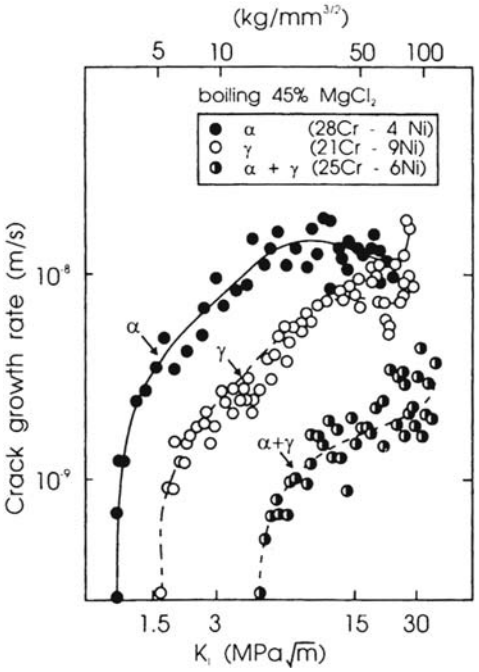


Figure 16 υ-K curves for a duplex stainless steel and its individually synthesized phases in hot chloride solution [62].

The SCC resistance of duplex stainless steels is manifested as a high value of the threshold stress intensity, K_{ISCC}, compared with austenitic steels [62] (Fig. 16). This arises from the different chemistry of the individual phases, which gives them, *individually*, different optimal ranges of potential for SCC (higher for γ, lower for α). Because there can only be one electrode potential at the tip of the crack, at least one of the phases must be below or above its best cracking potential (Fig. 17). If the individual phases are synthesized and tested as bulk materials, they both crack easily with very low K_{ISCC} values [62,95], but in modern duplex steels SCC occurs in the ferrite and is arrested by the austenite (Figs. 18a and 4c). However, if there is a strong oxidant present, or if oxygen is supplied through a thin boiling layer (as in evaporating seawater, which leaves behind a layer of saturated $MgCl_2$ solution), then the austenite is no longer protected by the ferrite (Fig. 18b) and K_{ISCC} drops significantly. Such results are consistent with the reported effect of anodic polarization in deaerated $MgCl_2$ solution [91].

Cold work reduces the ductility and fracture toughness but does not necessarily increase the SCC velocity or reduce K_{ISCC}. In austenitic stainless steels that transform partially to martensite, the region II crack velocity in hot chloride solution is increased by cold work, and the crack path becomes partly intergranular [57,96,97]. This may be associated with a change of mechanism. In alloy 600 exposed to reducing high-temperature water, the velocity of intergranular SCC increases dramatically with increasing cold work [59,60,98]; according to Scott and Le Calvar [60],

Copyright © 2002 Marcel Dekker, Inc.

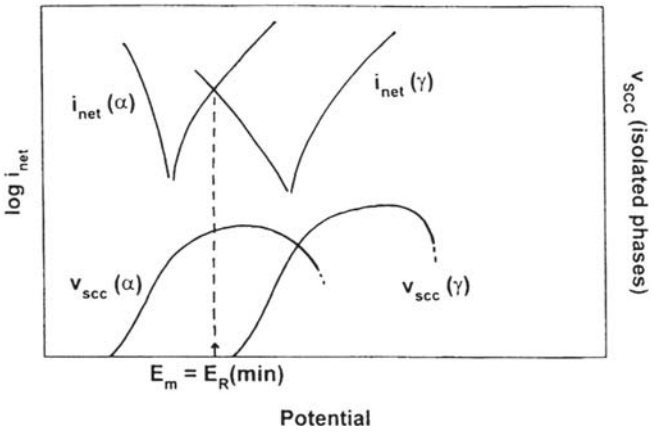


Figure 17 Schematic electrochemistry of chloride-SCC of duplex stainless steel.

this may be related to enhanced intergranular oxidation, a familiar effect in high-temperature gaseous environments.

THE ELECTROCHEMISTRY AND MECHANISMS OF SCC

There are at least five electrochemical conditions that can lead to SCC in electrolytes, given that the material has a susceptible metallurgy; these are shown schematically in Figure 19:

A: A state of imperfect passivity near an active-passive transition, e.g., carbon steel in aqueous hydroxide, nitrate, or carbonate-bicarbonate solutions [26,27].

B: A state of slow, chloride-induced localized corrosion in stainless steels, aluminum alloys, or titanium alloys [54,68].

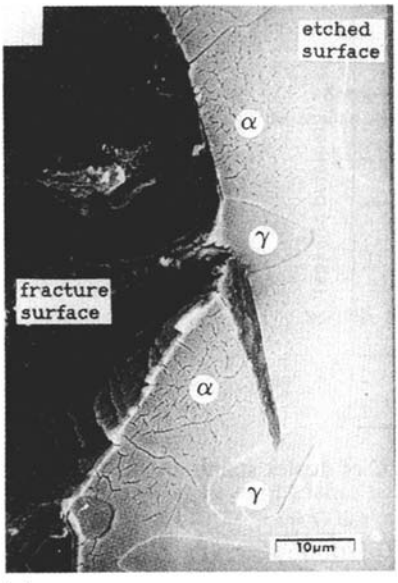
C: A state of surface dealloying with no continuous oxide, e.g., gold alloys in many aqueous solutions [75,99]. Dealloying may also occur within localized corrosion sites in passive alloys such as austenitic stainless steels.

D: Formation of unusual surface films that may play a casual role in SCC, e.g., nitrides formed on steel in anhydrous ammonia [69,100]. There are a number of related, room-temperature gaseous systems such as Zr/I_2 [101] and high-strength steel/Cl_2 [102,103]. Where such films cause only intergranular cracking and this occurs only at elevated temperatures, it is almost certainly due to penetration of atoms of the gaseous species along grain boundaries [60] and not to surface mobility as proposed by Bianchi and Galvele [104].

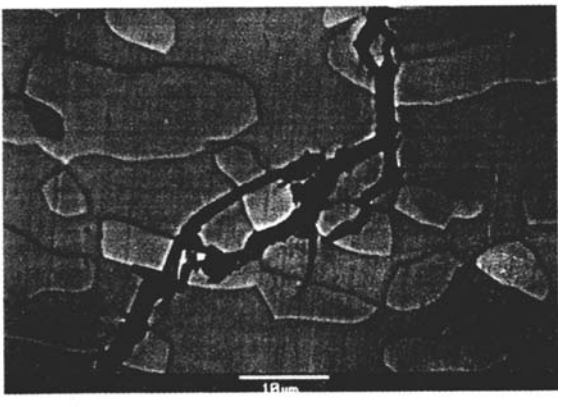
E: An active state leading to hydrogen-induced SCC, usually in high-strength steel [52,93,105,106] or medium-strength steels in H_2S media [53,107].

The most extensive mechanistic investigations have been carried out on passive systems showing cracking of type A or type B. All SCC mechanisms rely on the exposure of bare metal to the environment, and if this is too brief (owing to

Copyright © 2002 Marcel Dekker, Inc.



(a)



(b)

Figure 18 (a) Typical cracking pattern of chloride-SCC in a duplex stainless steel, showing cracking of ferrite and partial arrest by austenite (courtesy of W. J. R. Nisbet). (b) Cracking of a similar steel in evaporating seawater, showing little or no restraint of the crack by the austenite under this more oxidizing condition (courtesy of H. Ezuber).

immediate repassivation), none of the likely cracking agents, such as dissolution or hydrogen, can operate. This explains the importance of a slow *repassivation rate* [26] (Fig. 20). The kinetics of repassivation on bare metal surfaces have been measured by numerous potentiostatic techniques such as scratching, rapid straining, and laser illumination [108]. As well as active-passive transitions with potential, similar transitions occur with *pH* under free-corrosion conditions and may lead to critical pH requirements for SCC, notably for α-brass in near-neutral ammoniacal solutions [109,110].

Copyright © 2002 Marcel Dekker, Inc.

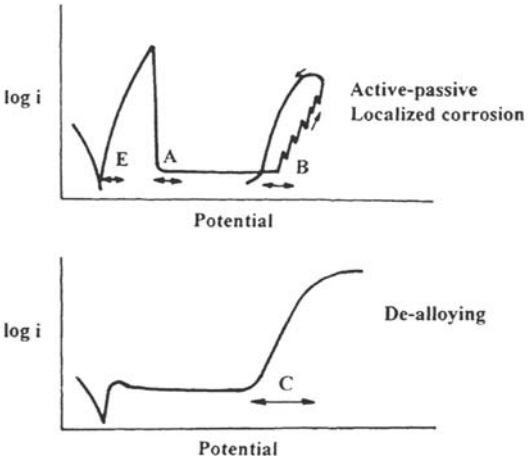


Figure 19 Correlation between SCC and various types of electrochemical behavior. The letters A, B, C and E refer to the types of SCC defined in the text. The arrows indicate possible potential ranges of SCC.

This classification of SCC is useful in practice, as it can lead to remedial measures or material developments without necessitating a complete understanding of the atomistic mechanism. For example, in type B SCC it is sufficient to prevent the

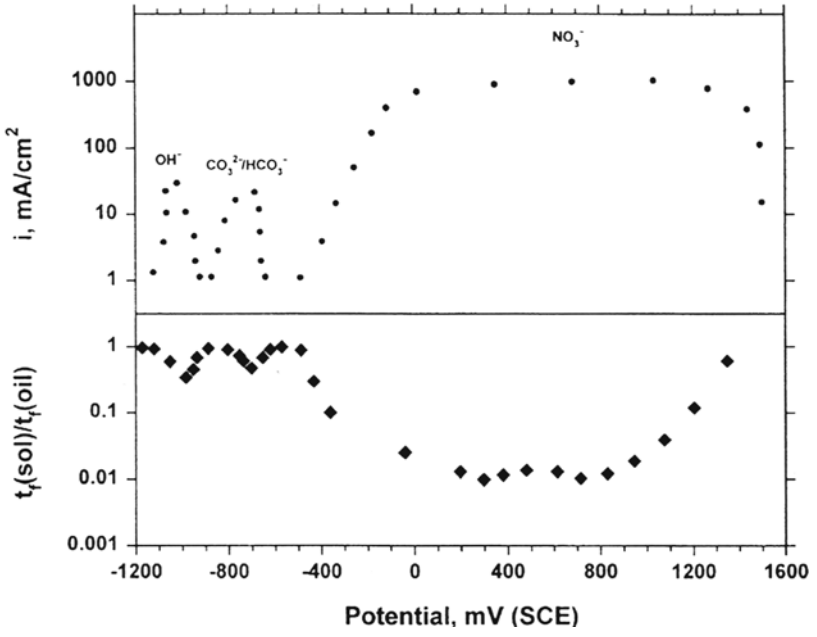


Figure 20 Correlation between inverse passivation rate (difference between current densities in fast and slow polarization scans) and slow strain rate SCC behavior for carbon steel in three SCC environments [26].

Copyright © 2002 Marcel Dekker, Inc.

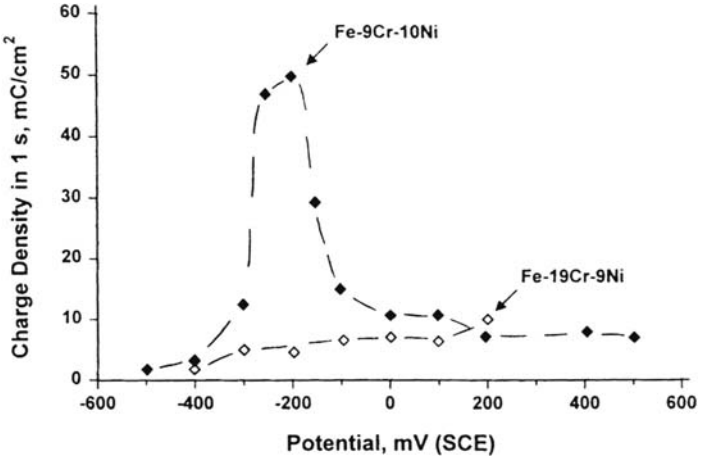


Figure 21 Delayed repassivation of material simulating the chromium-depleted grain boundary zone in sensitized stainless steel, measured in sodium thiosulfate solution using a scratch method [32].

localized corrosion process or to ensure that it occurs too rapidly to allow crack nucleation [68,111,112]. This topic will be discussed in detail later.

Type A SCC normally occurs by intergranular slip-dissolution and is related to grain boundary segregation or precipitation. Most of our present understanding has been developed by studying the passivation characteristics of bulk material [26,27], but alloys or compounds simulating the grain boundary composition can be useful for assessing the effect of segregation or precipitation on the repassivation kinetics [25,84,85] (Fig. 21). Rapid solidification can be used to incorporate large concentrations of segregants such as phosphorus [85] (Fig. 22). In a number of systems it has been shown that the region II SCC velocity (υ_{II}) correlates with the maximum (reasonably sustained) anodic current density on a bare surface (i_{max}), via

$$\upsilon_{II} = \frac{i_{max} A}{nFs} \tag{1}$$

where A is the atomic weight (relative atomic mass) of the metal and s is its density—that is, crack growth occurs by strain-enhanced intergranular corrosion [26]. The role of stress is to produce plastic strain in the metal, which fractures a brittle oxide layer.

SCC data are presented as velocity versus *static* stress parameter such as K_I, yet it is the *dynamic* plasticity at the crack tip that actually features the newly formed oxide film [67,113]. This problem was considered by Vermilyea [24], who showed that under a static stress the corrosion process could advance the crack tip into a region that had reached an equilibrium distribution of plastic strain (ε_p), and produce a *strain transient* ($\Delta\varepsilon_p$) that could fracture a newly formed oxide (Fig. 23). Later Sieradzki [44] showed that the depth of transient corrosion required in Vermilyea's original model was unreasonably large (~ μm), confirming that static slip-dissolution models can apply only to *intergranular* SCC, where there is a directional active path with a very low repassivation rate [33]. It is not clear how the shielding of the crack

Copyright © 2002 Marcel Dekker, Inc.

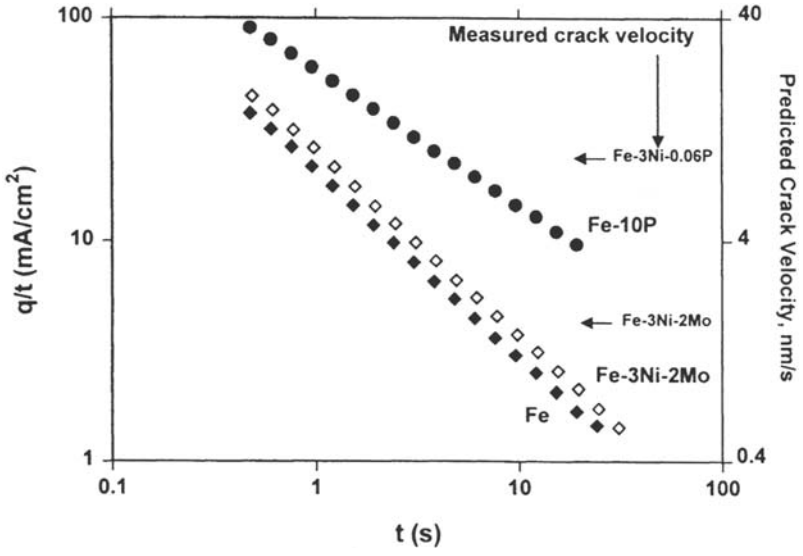


Figure 22 Anodic current decays for Fe, Fe-3Ni-2Mo, and an Fe-10P amorphous alloy (simulating a grain boundary) in 9 M NaOH solution at 98°C and –400 mV (Hg-HgO) [85]. The original $i(t)$ decays have been converted into $q(t)$ (charge density versus time) and then into $q(t)/t$ for comparison with a slip-dissolution model of SCC where the crack velocity is proportional to $q(\tau)/\tau$ with τ being the interval between film rupture events at the crack tip. The indicated crack velocities measured for Fe-Ni-Mo and Fe-Ni-P alloys are consistent with a single value of $\tau(6 \pm 3$ s), giving some validity to the use of a simulated grain boundary alloy.

tip stress intensity by intact metal ligaments [39] enters into this argument—it certainly makes real cracks much sharper than one would expect from fracture mechanics.

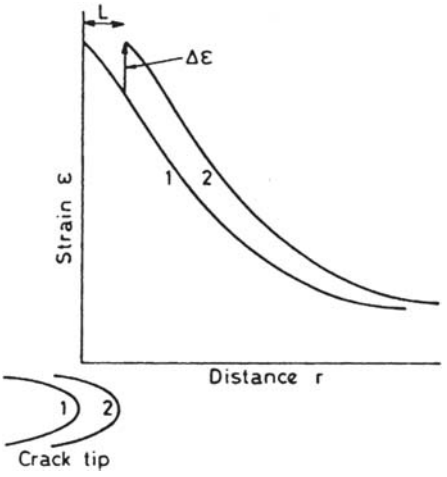


Figure 23 Plastic strain distribution ahead of a stress-corrosion crack tip and the effect of corrosion, according to Vermilyea [24].

Copyright © 2002 Marcel Dekker, Inc.

The introduction of a *crack tip strain rate* ($\dot{\epsilon}_c$) enables a wide range of SCC information to be rationalized [30]. For example, Eq. (1) can be generalized to

$$v = \frac{\bar{i}A}{nFs} \tag{2}$$

where i is the time-averaged anodic current density at the crack tip. For a cyclical process in which the bare surface is exposed by film rupture, partially repassivated, and then exposed again, the interval t^* between the film rupture events is given by

$$t^* = \frac{\epsilon_f}{\dot{\epsilon}_c} \tag{3}$$

where ϵ_f is the fracture strain of the newly formed oxide film; thus i is given by

$$\bar{i} = \frac{\int_0^{t^*} i(t)dt}{t^*} \tag{4}$$

Writing the integral as q_t, this gives

$$v = \frac{q_{t^*} A\dot{\epsilon}_c}{nFs\epsilon_f} \tag{5}$$

The film rupture interval t^* decreases with increasing strain rate until eventually $i = i_{max}$ and v approaches the maximum or region II velocity v_{II}. For cyclic loads or slow strain rate tests, $\dot{\epsilon}_c$ is relatively easy to estimate, and one can *test* the slip-dissolution model as a function of strain rate and potential [30–33]. More generally, one can include a continuum version of Vermilyea's concept [114]:

$$\dot{\epsilon}_c = \frac{A\dot{\epsilon}}{N} + \left[B\ln\left(\frac{C}{N}\right)\right]v \tag{6}$$

where $\dot{\epsilon}$ is the bulk strain rate, N is the number of identical circumferential cracks per unit length, and A, B, and C are constants.

The disappearance of SCC above a critical applied strain rate (mechanical blunting) is rationalized by recognizing that, to maintain a sharp crack.

$$v(\dot{\delta}) \geq \dot{\delta} \tag{7}$$

where $\dot{\delta}$ is the rate of increase of the crack tip opening displacement (δ) due to the applied strain rate [33]. Sometimes SCC also vanishes *below* a particular strain rate, especially in systems that show extremely slow repassivation (chemical blunting); now a possible condition for crack stability is

$$u(\dot{\delta}) \leq \frac{\delta_{max}}{2} \tag{8}$$

where $u(= t^*v)$ is the depth of material dissolved between film rupture events and δ_{max} is the maximum value of the crack tip opening displacement consistent with continued crack growth. This might correspond to the transition from small-scale to general yielding, given $\delta_{max} \simeq 2$–$3\mu m$ for carbon steel in typical test geometries [see Eq. (9) below]. That is, the amount of corrosion between film rupture events must not enlarge the mechanical crack opening to such an extent that the crack degenerates into a blunt slot. Because t^* is a function of $\dot{\delta}$ this leads to another equation

Copyright © 2002 Marcel Dekker, Inc.

similar to Eq. (7); the regions of SCC, chemical blunting, and mechanical blunting can then be mapped for various functions $i(t)$ (Fig. 24). The main uncertainties in such a procedure are the composition of the material that is reaching at the crack tip [this obviously affects $i(t)$] and the restricted crack geometry, which alters the environment and increases both the solution resistance and the effective diffusion length. However, the wedge-shaped geometry of a real crack [33,115,116] significantly reduces the solution resistance and dissolved cation concentration compared with a one-dimensional slot. The crack tip opening displacement w_0 ($\equiv \delta$, see Fig. 25) is given by

$$w_0 \equiv \delta = \frac{\alpha K_I^2}{E\sigma_0} \tag{9}$$

where E is Young's modulus and σ_0 is the flow stress (roughly the average of the yield and ultimate stresses); α is a constant that varies with the stress state and strain hardening coefficient and is about 0.3 for carbon steel under plane strain [117].

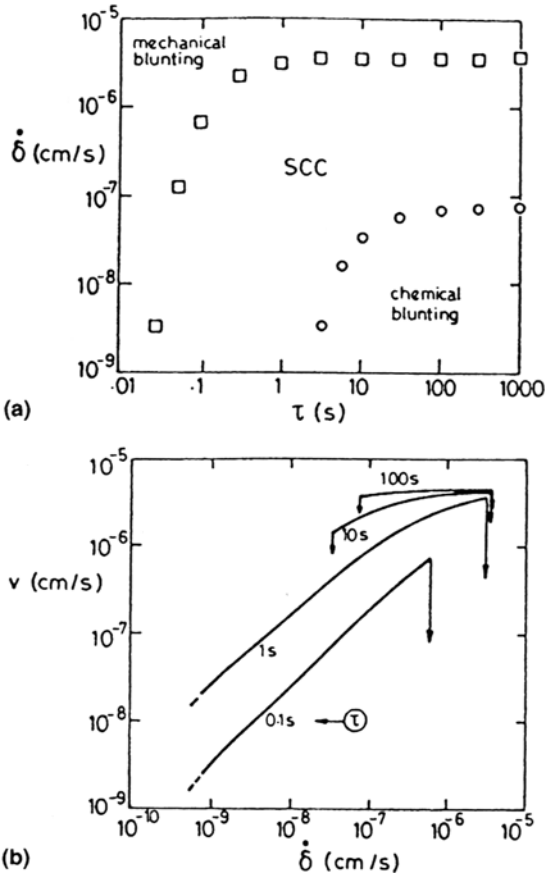


Figure 24 The effect of strain rate on SCC velocity by slip-dissolution for a system showing a t^{-1} current decay on a fresh surface, for various values of the decay time constant [33].

Copyright © 2002 Marcel Dekker, Inc.

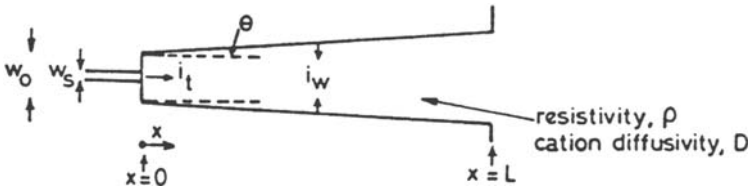


Figure 25 Crack geometry for calculation of the potential drop and metal ion concentration in a crack [33].

For small-scale yielding, the crack half-angle θ is given by the elastic solution:

$$\theta = \frac{2(1-v^2)\sigma}{E} \tag{10}$$

where υ is Poisson's ration, about 0.33. The *IR* potential drop or dissolved metal cation concentration in a growing crack (with small-scale yielding, passive walls, and an active path of width w_s embedded in w_0) was shown to depend on the stress and the crack velocity but not on the crack length [115]:

$$\Delta\phi = \frac{\rho E w_s i_t}{4\sigma} \ln\left(1 + \frac{4\sigma_0}{\sigma}\right) \tag{11}$$

where ρ is the electrolyte resistivity and i_t is the anodic current density on the width w_s of active material at the crack tip [i.e., $i_t \equiv i$ in Eq. (2)]. This provides an interesting similitude argument for constant-load SCC tests of for practical SCC failures: no decrease in crack velocity with increasing crack length should be expected under constant load. The preceding argument is only slightly affected by the observation that real stress-corrosion cracks are sharper than would be expected from fracture mechanics [16,34,38,66,116], owing to the existence of uncracked ligaments that shield the crack tip from some of the applied stress intensity—the region over which this occurs (about one grain) is small compared with the crack length as a whole.

One can also analyze the strain-rate dependence of SCC for a slow strain rate test with general rather than small-scale yielding, assuming that plastic stretching at the crack sites dominates the specimen extension from shortly after crack initiation [33,115]. The crack half-angle θ is now given by

$$\theta = \frac{\dot{\epsilon}}{2N\nu} \tag{12}$$

and the crack electrolyte resistance by

$$R = \frac{\rho N\nu}{\dot{\epsilon}} \ln\left(1 + \frac{L\dot{\epsilon}}{N\nu w_0}\right) \tag{13}$$

Values of θ at least 10 times those obtained in static tests are readily achieved in a slow strain rate test, with a large corresponding decrease in the *IR* potential drop or crack tip metal cation concentration for a given value of i_t. Such arguments show that concerns about the saturation of metal ions or very high *IR* potential drops within cracks are unfounded for slow strain rate tests, even if there is no active path

Copyright © 2002 Marcel Dekker, Inc.

w_s. Historically, this is an important issue, as these concerns were partly responsible for the abandonment of the slip-dissolution model by Galvele [20,118].

For a resistive system, the crack-tip anodic current density i_t can be written

$$i_t = \frac{E - E_m}{w_s R} \tag{14}$$

where E is the potential at the external surface, E_m is the mixed (corrosion) potential of the straining crack tip, and R is the electrolyte resistance in the crack. The crack velocity can be derived on this basis as

$$v = \left[\frac{\dot{\epsilon}(E - E_m)A}{nFsw_s\rho N}\right]^{0.5}\left[\ln\left(1 + \frac{\dot{\epsilon}L}{Nvw_0}\right)\right]^{-0.5} \tag{15}$$

As the log term is nearly a constant, this equation explains the commonly observed relationship [29]

$$v \sim \dot{\epsilon}^{0.5} \tag{16}$$

without considering any of the details of the $i(t)$ transient. It would be valuable to incorporate some of these crack geometry considerations into more rigorous electrochemical crack models [119].

Type B SCC includes a large number of passive systems in which cracking is induced by chloride ions. All these systems share an acid crack environment and an active or semiactive state at the crack tip. For a while it was thought that Al-Li-Cu-Mg alloys might be an exception to this rule because alkaline crack chemistries are possible under special conditions (little or no cathode area outside the crack), but it soon became clear that rapid cracking in this system is associated with acidification in the crack [120,121].

A fundamental requirement in type B SCC is that the crack velocity must be able to exceed the localized corrosion velocity; otherwise the crack will degenerate into a blunt fissure [68] (Figs. 26 and 27). This leads us to expect SCC over a *range* of potentials between the repassivation potential of the localized corrosion process (E_R) and a higher potential (E_u) at which the localized corrosion velocity equals the crack velocity at the prevailing stress intensity value. By manipulating the composition of a susceptible austenitic stainless steel (Ni, P, Mo, Cu, Al), these potentials can be made to coincide, guaranteeing immunity to SCC [111,112]. An increase in temperature is then required to increase E_u sufficiently for SCC to occur; i.e., the manipulation of alloy composition increases the *critical temperature* for SCC initiation from a crevice. All the applicable alloying elements alter both the SCC velocity and the crevice corrosion kinetics, so a complete analysis would be quite complicated.

It is evident that type B SCC rarely occurs by the slip-dissolution mechanism. The metal in the crack is already in an essentially active state, although there may be a porous oxyhydroxide layer and possibly a dealloyed metallic layer [78,79]. If SCC does occur by anodic dissolution in such a system, it is of the trivial kind seen in sensitized stainless steel or underaged Al-Cu alloys [122] in chloride solutions: the kinetics of an intergranular pitting process are simply enhanced by the opening of the crack, reducing the ohmic resistance according to Eq. (13).

All type B systems generate hydrogen within cracks, and in some strong alloys, such as martensitic stainless steels [91], the cracking is obviously due to hydrogen

Copyright © 2002 Marcel Dekker, Inc.

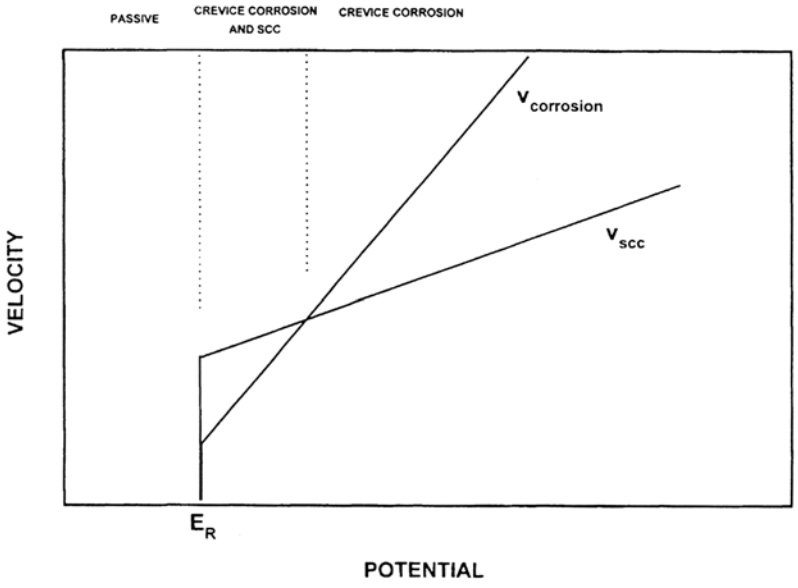


Figure 26 Rationale for occurrence of type B (localized corrosion-related) SCC over a range of potentials [68,111,112].

embrittlement. High-strength Al-Zn-Mg-Cu (7000 series) alloys also have a proven role of hydrogen in SCC [54,55] (Fig. 28). Both the formation and the entry of hydrogen are favored by the active state in the crack, but the *presence* of hydrogen does not guarantee a *role*, especially in fcc systems. A further complication is that in some Al alloys, slow crack growth occurs in the absence of an environment, due to creep-like processes or solid-metal embrittlement by lead particles in the alloy [54,123].

The mechanism of chloride-SCC of austenitic stainless steels is still debatable. We may discount the slip-dissolution model for crack growth at 80°C [68]: the required anodic current density of some 50mA/cm^2 (a velocity of about 2×10^{-8}m/s) is not available in the crevice environment, except during the first milliseconds of exposure of a fresh surface, and t^* [Eq. (3)] could never be this low. Hydrogen may play a role, especially in unstable austenites at relatively low temperatures, but it is difficult to rationalize a hydrogen effect in stable austenitic steels at very high temperatures such as 300°C [56]. The film-induced cleavage model [40,41] has indirect support: dealloying (Ni enrichment) has been demonstrated in simulated crack solutions [78] and observed on the sides of cracks [79], and the dependence of SCC on Ni content [73,74] is very similar to that seen in Au-Cu alloys as a function of Au content [75] (Fig. 9). However, there is no direct evidence for film-induced substrate cleavage of the kind found in Cu-Zn, Au-Ag, and Au-Cu alloys [46–51]. The austenitic steel cracks only from sites of localized corrosion, so "single-shot" cleavage experiments are much more complicated than in systems that show uniform dealloying.

The electrochemistry of Cl-SCC in duplex (α-γ) stainless steels was discussed earlier and displayed in Figure 17. The ferrite phase has a higher E_R value, due to its higher Cr content, but dissolves more rapidly (due to its lower Ni content) when both phases are in the active state [124]. The crack approaches (from above, due to *IR*

Copyright © 2002 Marcel Dekker, Inc.

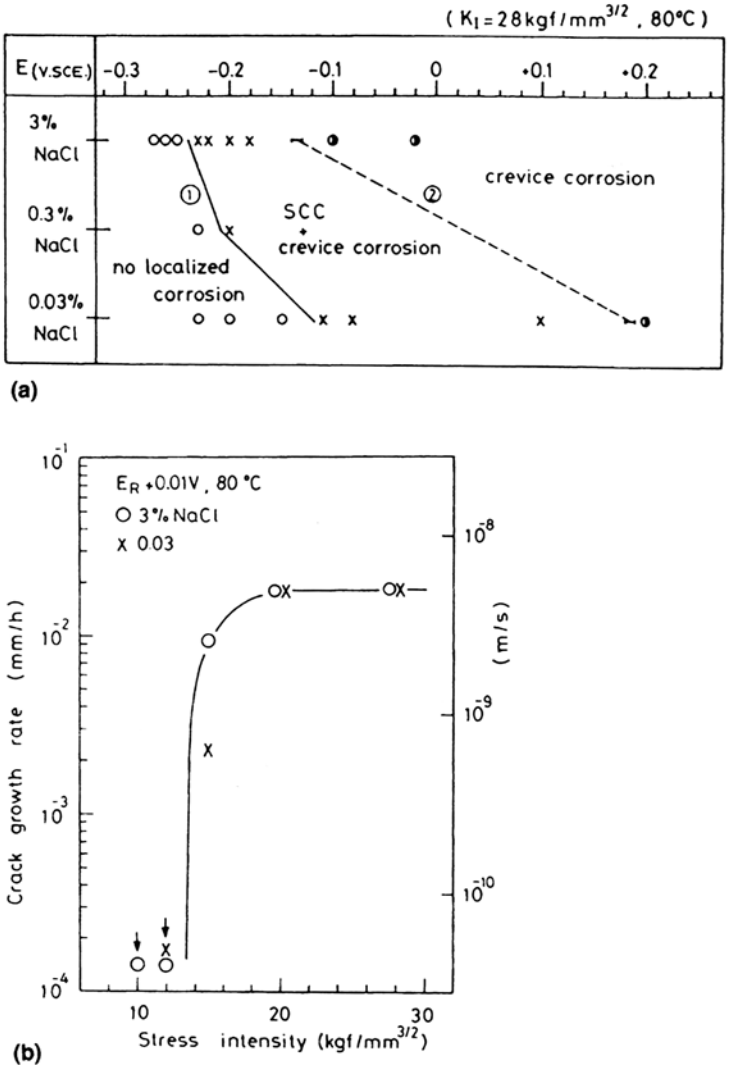


Figure 27 (a) Localized corrosion and SCC regimes from Tamaki et al. [68] using potentiostatic tests on creviced samples of 316L stainless steel in NaCl solution at 80°C. (b) υ-K curves measured in two different concentrations of NaCl just above the respective repassivation potentials (E_R), showing that SCC is controlled by local chemistry. (Courtesy of NACE.)

limitations) a mixed potential where the austenite is a net cathode and the ferrite a net anode. The ferrite is thus polarized above its normal (isolated) cracking potential and cracks rapidly, while the austenite is below its isolated cracking potential and cracks slowly or not at all. Cracks propagate in the ferrite and tend to be arrested by the austenite. Another situation is possible if the ferrite can remain passive in the crack while the austenite corrodes; now cracking occurs in the austenite and is hindered by the ferrite.

Copyright © 2002 Marcel Dekker, Inc.

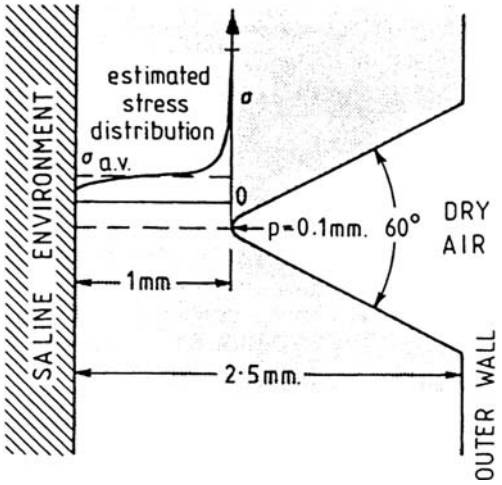


Figure 28 Notched hollow tube experiment of Ratke and Gruhl [55], used to show that SCC of high-strength Al-Zn-Mg alloys could involve internal crack initiation by hydrogen. (From Ref. 54. Courtesy of NACE.)

Addition of H_2S or its oxidation product $S_2O_3^{2-}$ (thiosulfate) greatly enhances localized corrosion and Cl-SCC of austenitic and duplex stainless steels [91,125,126]. The effect of H_2S is slight up to a critical concentration around 0.01 M because below this concentration it is depleted in deep pits and cracks [127]. "Nonpropagating" cracks found around this H_2S concentration have run out of H_2S at the crack tip (Fig. 29). Enhancement of SCC by H_2S is often ascribed to a hydrogen effect, by analogy with low-alloy steels, but for stable austenites such as 310SS this argument is not tenable. Adsorption of sulfur on the active surface in the pit or crack changes the dissolution and passivation kinetics of the material, specifically by catalyzing Fe and Ni dissolution, and possibly by hindering passivation (but the passivation potential is not necessarily altered because no interaction between Cr and S is expected in aqueous systems) [128–130]. Austenite, with its lower Cr and Mo content, will tend to show more sulfur-induced activation than ferrite [130,131]; thus the kinetic difference between the phases will be reduced when adsorbed sulfur is presnet provided that both phases are in the active state. This may be one aspect of the increased susceptibility of duplex steels in Cl^-/H_2S systems, but obviously there is also an effect of S_{ads} on the atomistics of SCC.

SCC of austenitic or duplex stainless steels in Cl^-/H_2S environments usually occurs from pits, even at moderate temperatures such as 80°C, whereas crevice or underdeposit corrosion is normally needed to nucleate Cl^--SCC at such temperatures. This may be understood from Figure 26: pits in Cl^- solutions at 80°C are normally growing faster than cracks (so no SCC occurs), whereas in Cl^-H_2S solutions the crack velocity is increased *and* the pitting velocity can be lower without repassivation, owing to the stabilization of pit dissolution by adsorbed sulfur and possibly also the resistive effect of the black corrosion product that forms in the pits.

In Cl^-H_2S systems, the effect of Ni content is basically the same as in Cl-SCC, except that there is easier cracking around 20–30% Ni, and a new form of mainly

Copyright © 2002 Marcel Dekker, Inc.

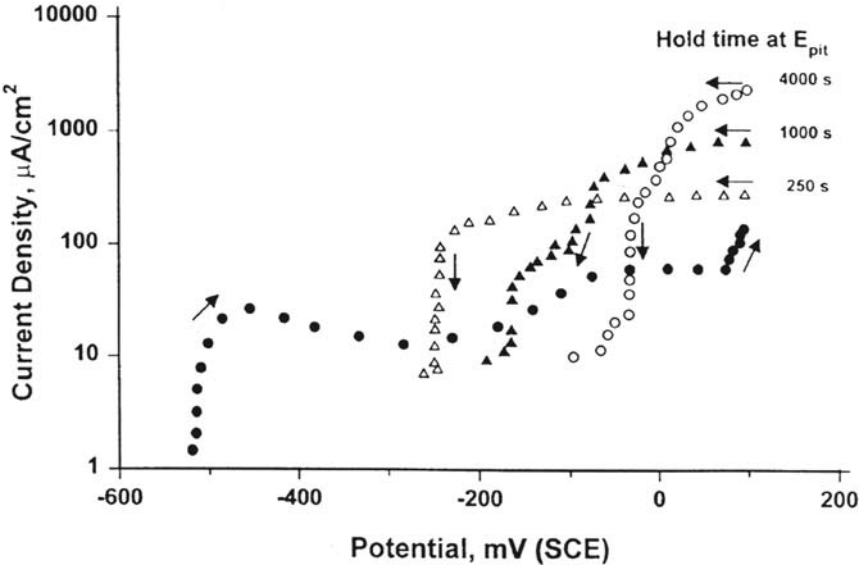


Figure 29 Potentiodynamic pittin g scans for 25Cr duplex stainless steel in 20% NaCl + 0.03 M H_2S, pH 3.4 (acetate-buffered) at 80°C, with different hold times just above the pitting potential, showing the paradoxical raising of the repassivation potential (E_R) with increasing pit (crack) depth, due to depletion of H_2S at the dissolving surface. (Courtesy of S. B. Mat.)

intergranular cracking appears at high T and [H_2S]; this latter cracking does not respect the Ni content [132].

Molybdenum alloying is not particularly beneficial for SCC resistance of austenitic stainless steels; nickel is the most important beneficial element. Referring to Figure 26, Mo increases E_R and E_u by about the sme amount, through its effect on the localized corrosion velocity, while Ni (above 10%) decreases the crack velocity, thus lowering E_u [68,111,112].

Type C (dealloying-related) SCC has been mentioned in the context of austenitic stainless steels, but direct analytical evidence of dealloying is lacking in that case. However, a number of systems definitely show dealloying and can crack in an oxide-free state or with a loose, precipitated tarnish film, such as Cu-Zn, Cu-Al, Au-Cu, and Au-Ag. The original SCC system (brass in ammonia) clearly comes into this category [133], and the ease of dealloying in brass explains why it cracks in so many different environments, especially in slow strain rate tests [134,135]. In brass the dealloying is quite superficial (less than 100nm) but correlates with SCC and can trigger foil fractures in cuprous [$Cu(NH_3)_2^+$] solutions that simulate the crack environment [46,72,87,136,137] (Figs. 10 and 30). In gold alloys, the correlation can be demonstrated more easily, as the electrochemistry is much simpler without any competing anodic reaction on the gold [47–51]. The attempt of Flanagan, Lichter, and others [80,81] to account for SCC of Au-Cu alloys without dealloying is premature, as rapid dealloying may well occur in the chloride-rich environment of a crack.

In several systems, including Au and Cu alloys, gross macrodealloying in chloride solutions has been shown *not* to favor SCC or microcleavage [33,47,48,87,135,136]. One view is that this represents a kind of crack blunting (in a

Copyright © 2002 Marcel Dekker, Inc.

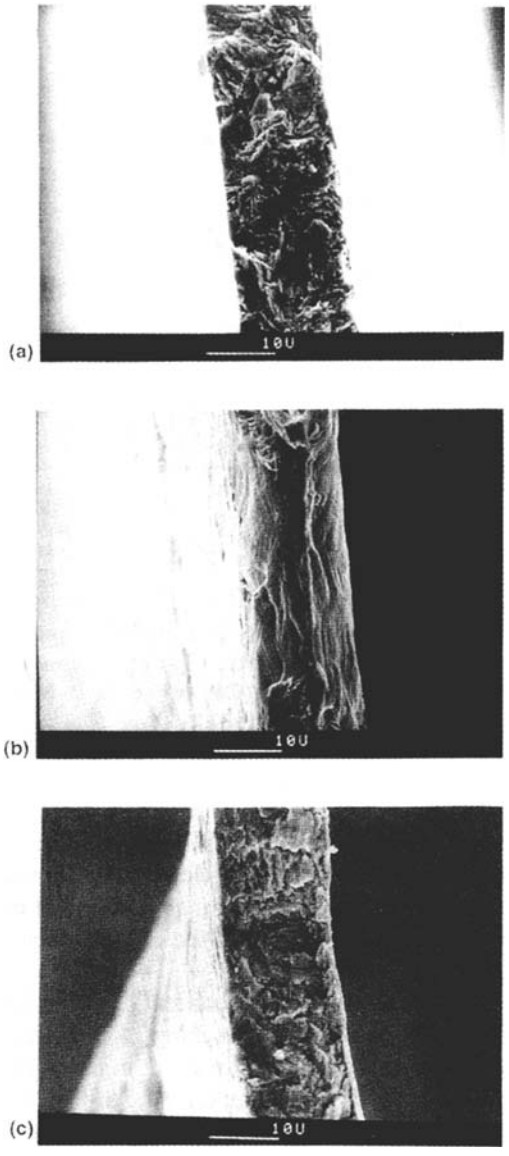
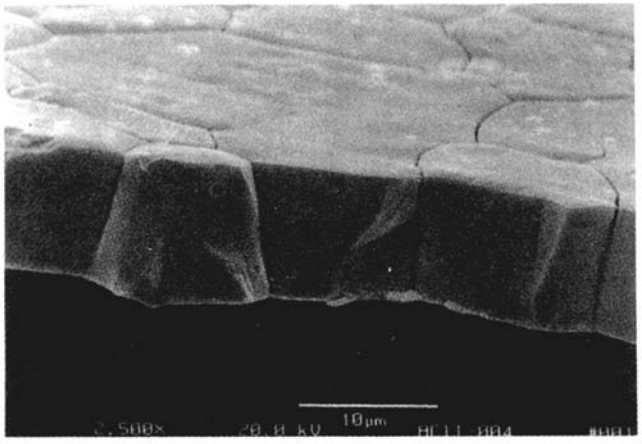


Figure 30 (a) Single-shot cleavage failure of α-brass rapidly strained in a cuprous ammonia solution after 100 min immersion. (b) Identical specimen rinsed in deionized water and dried with cool air before fracturing, showing aging of the dealloyed layer to a harmless form. (c) Identical specimen quenched in liquid nitrogen without rinsing, then fractured near 77 K, confirming that cleavage can occur with no liquid environment present [46].

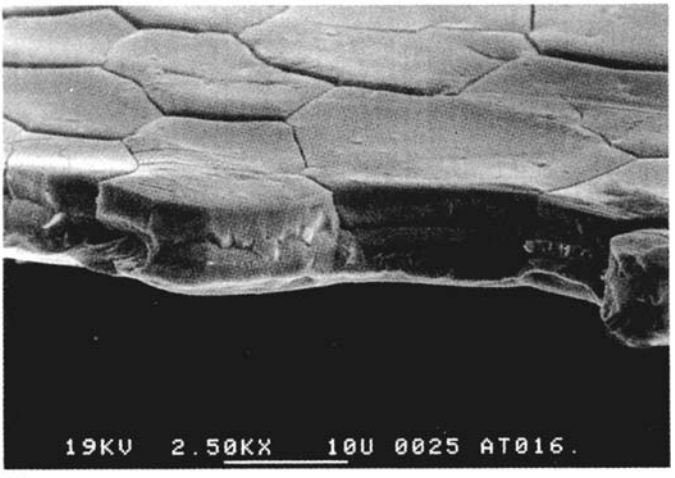
slip-dissolution context) [135], but we have proposed a more detailed interpretation based on the film-induced cleavage model [47–49,87,88]. Essentially, gross dealloying is indicative of coarsening of the pores within the dealloyed material (by surface self-diffusion), to the point that the pores are too coarse to nucleate a brittle crack in the unattacked substrate. This aging phenomenon has been demonstrated directly in

Copyright © 2002 Marcel Dekker, Inc.

gold alloys (Figs. 31 and 32) and in brass it has been shown that alloyed arsenic causes a transition from macro (μm) to micro (nm) dealloymg [87,136], favoring SCC in chloride environments but having no effect in ammonia, where microdealloying occurs irrespective of the presence of arsenic; ammonia and arsenic are both believed to hinder surface mobility of Cu, by specific adsorption in cationic or uncharged form [87,88,136–138]. The dealloyed layers formed on brass in ammoniacal solutions



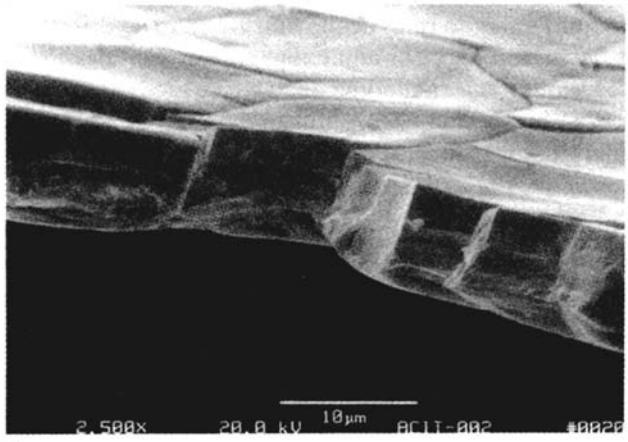
(a)



(b)

Figure 31 (a) Ag-20 at % Au foil specimen, dealloyed to a depth of 3μm in perchloric acid without stress, then fractured after stepping the potential to 0 V (SCE) for 5 min (brittle intergranular failure). (b) Dealloyed and stepped to 700 mV for 30 min (ductile failure—the coarsening of the porosity in the dealloyed layer is more rapid at higher potentials). (c) As in (a) but with 10 mM NaCl added after stepping the potential to 0 V (ductile failure due to rapid pore coarsening). (d) As in (c) but with a further addition of 10 mM pyridine (brittle failure due to counteraction of chloride effect by pyridine) [33,49].

Copyright © 2002 Marcel Dekker, Inc.



(c)



(d)

Figure 31 Continued

age very rapidly when out of contact with the solution, losing the ability to trigger cleavage in thin foils (Fig. 30).

Cracking of silver alloys has been reported by Galvele and others in a series of papers [139–141]. Interesting SCC phenomena were reported in both aqueous and gaseous environments, including halogen vapor. Clearly, all these systems involve selective reaction of the silver in the alloy, which in halide solutions or atmospheres generates a composite of silver halide and nearly pure noble metal (Au or Pd); this layer should behave mechanically much like a dealloyed layer formed under conditions of free silver dissolution, so the mere occurrence of SCC does not help to distinguish between SCC mechanisms. Foil-breaking experiments [33,46–51] should be performed in some of these environments to test the generality of the film-induced intergranular fracture mechanism.

Type D SCC involves surface films that are neither oxides nor dealloyed layers. The cracking of high-strength 4340 steel in dry Cl_2 [102,103] or dissociated N_2 [142]

Copyright © 2002 Marcel Dekker, Inc.

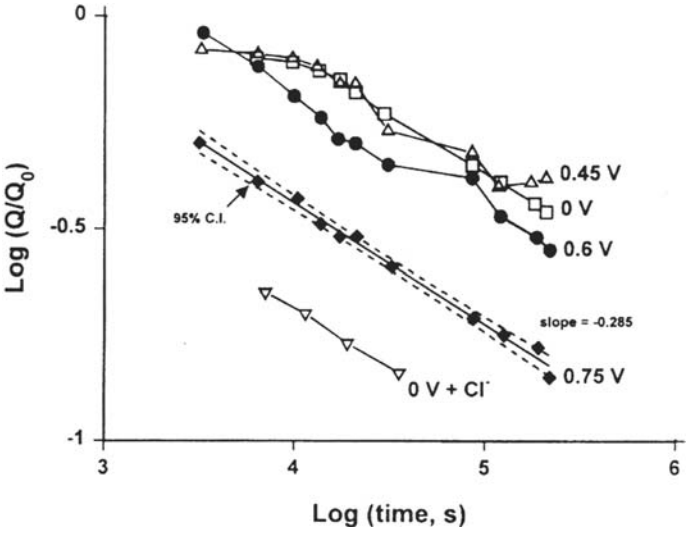


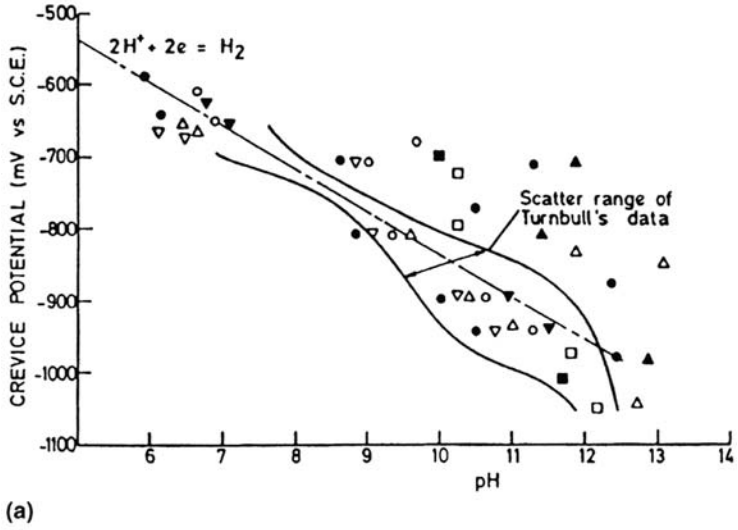
Figure 32 Measurements of double-layer capacitance (proportional to pore surface area; inversely proportional to pore radius) as a function of time during potentiostatic aging of dealloyed layers on Au-Ag, showing the effects of potential and chloride ions [48].

appears to be a film-induced process; Sieradzki [103] proposed that $FeCl_2$ acted as a stiff layer, causing a ductile-to-brittle transition due to the modulus mismatch with the substrate. Later the lattice parameter was emphasized as a casual factor [143]. A detailed rationalization of SCC was made for iron exposed to anhydrous ammonia-methanol, where anodic oxidation of ammonia leads to interstitial penetration of nitrogen [69,100]. According to the film-induced cleavage model, such very thin, brittle layers are sufficient to allow cleavage through several μm of a body-centered cubic (bcc) material, whereas in fcc systems a nanoporous metallic layer 10–100 nm thick is a specific requirement as it is the only way of epitaxially coupling a brittle reaction product of sufficient thickness to the fcc substrate. A special case may be the SCC of pure copper or silver, where a micropitted or tunneled zone is a possible brittle layer that could nucleate cracking [144,145].

There are several other film-induced SCC processes, such as cracking of Zr alloys in gaseous iodine [101]. In no case has monolayer *adsorption* been validated as the cause of SCC—every known case involves a 3D film. However, liquid metal embrittlement often occurs, even in fcc systems, without alloy or compound formation [15]. Possibly there is a regime of very rapid adsorption-induced cracking that is rarely accessed in aqueous systems as it requires the adsorption process to be faster than plastic relaxation processes at the crack tip; hence in aqueous environments this is likely to occur only in very reactive metals (Al, Ti, Mg).

Type E SCC (embrittlement of steels by cathodic hydrogen in the active state) is quite well understood except for the atomistic action of the hydrogen, which is still debatable. Briefly, hydrogen atoms are produced by water reduction during corrosion in neutral solutions, and some of them enter the steel, especially if their recombination to H_2 is poisoned by adsorption of S, As, P, or Sb. Once in the steel, the

Copyright © 2002 Marcel Dekker, Inc.



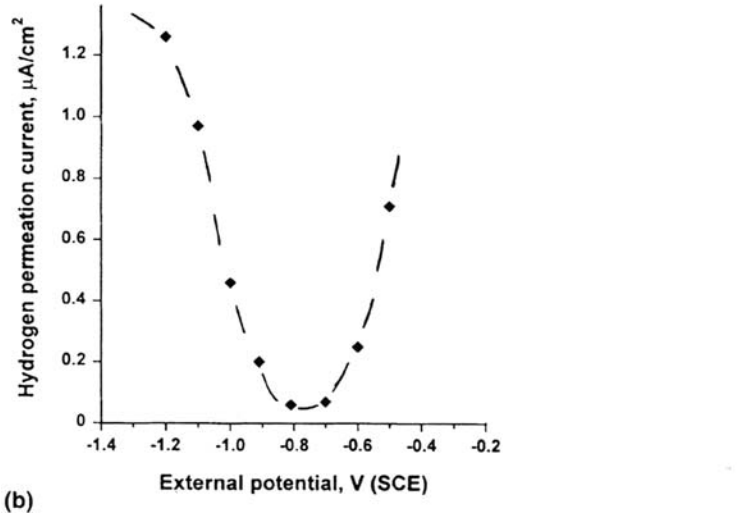


Figure 33 (a) Crevice potential and pH and (b) hydrogen permeation rate, as a function of potential for carbon steel crevices in NaCl solution. (From Ref. 154. Courtesy of HMSO.)

hydrogen can move with an effective diffusivity (D_{eff}) of 10^{-8} to 10^{-4}cm^2/s, depending on the microstructure as well as temperature [21] (e.g., small carbides in tempered martensite act as traps and greatly reduce (D_{eff}). The lattice (interstitial) hydrogen solubility is elevated ahead of stressed cracks or notches, and these sites accumulate higher hydrogen concentrations. The same hydrostatic tension that increases the H solubility in the lattice also enhances hydride phase precipitation in

Copyright © 2002 Marcel Dekker, Inc.

metals such as Ti and Nb [101]. Hydrogen segregrates to interfaces, including grain boundaries, and may weaken these in combination with other segregants such as P and Sb [146]. Once it reaches its site of action, and provided it is in a strong microstructure, the hydrogen causes local fracture by cleavage [147], intergranular separation [146], or enhanced microplasticity [148], or some combination of these processes. In low-strength steels, dynamic loading is required for cracking. If the input fugacity of hydrogen is high enough (hundreds of atmospheres in media such as acidic H_2S), recombination at internal sites such as nonmetallic inclusions may cause blistering or cracking (hydrogen-induced cracking, or HIC). This is minimized in pipeline steels by careful microstructural control.

The altered solution chemistry within cracks is an important aspect of SCC and corrosion fatigue in structural and high-strength steels. Turnbull [149–151] has shown that crack acidification, as proposed by Brown [152], is not the norm for steels corroding freely in NaCl solutions or seawater. Only in Cr-containing steels with very short cracks could any acidification be predicted [153]. Possibly some of Brown's historic measurements were flawed by oxidation of Fe^{2+} by atmospheric oxygen; more recent work shows that deep cracks normally become net cathodes and reach a pH of about 9 [154] (Fig. 33). Nevertheless, with assistance from the *IR*-induced isolation of the crack enclave, the potential can remain below that of a reversible hydrogen electrode, and in sufficiently strong steels embrittlement will occur above some K_{ISCC} value. An excellent correlation exists between hydrogen uptake on the walls of simulated cracks and SCC of high-strength steels in the same solution [154] (Fig. 34). Cathodic protection, within limits, can reduce the hydrogen uptake from cracks by increasing the local pH [149–151]; however, this is rarely used for high-strength steels that are sensitive to hydrogen, even though major benefits can be demonstrated in the laboratory. The problem in practice is that most cathodic protection systems locally reduce the potential to values that are dangerously low for high-strength steels.

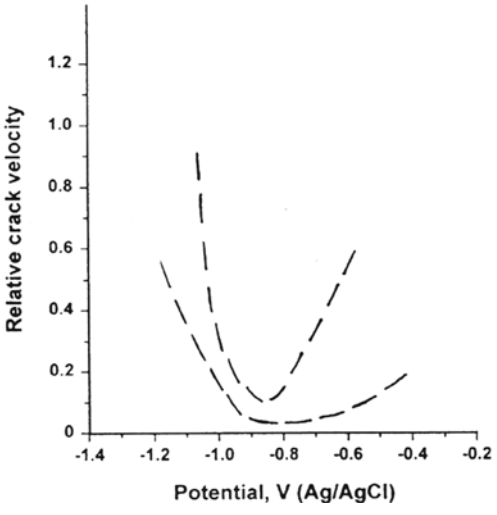


Figure 34 Band of results showing the effect of potential on the rate of SCC, for a range of high-strength steels in seawater [152]; compare with Figure 33b.

Copyright © 2002 Marcel Dekker, Inc.

Hydrogen effects often show the same kind of strain rate sensitivity as slip-dissolution processes. Low-strength steels are immune to SCC under static loads in salt water, but steels of all strengths can suffer hydrogen-assisted fatigue crack growth [105,155]. High strength continues to be detrimental, but relatively less so than under static loading.

STRESS-CORROSION TESTING IN RELATION TO MECHANISMS OF CRACKING

Because standard methods of SCC testing have been excellently reviewed by Sedriks [156], we focus on the implications of mechanisms for testing and vice versa.

To rationalize or predict service performance, and to test models of SCC, the slow strain rate test [26,27,113,157] is convenient as it enables a large number of tests to be conducted at a large number of potentials within a defined time; the maximum duration is simply the failure time in air (Fig. 35). The maximum load, elongation to failure, and percent reduction in area at fracture are measured in the test environment and normalized to values measured in an inert environment. The disadvantages are that the mechanical condition is relatively undefined when there are multiple cracks, the crack velocity cannot be measured continuously, and failures occur in materials that would never fail by SCC in service. An elastic slow strain rate or ultraslow cyclic test [67] is a useful compromise that maintains the dynamic loading without gross plastic straining (Fig. 36), but these tests are difficult to carry out in large numbers. It has been suggested that slow strain rate and cyclic-loading tests are part of a continuum [28–30,113,158] and that in some systems SCC and corrosion fatigue are also a continuum with a single mechanism (Fig. 37); certainly the fractography of slow strain rate SCC and low-frequency fatigue crack growth can be very similar, e.g., in low-strength steels. The most notorious cases in which the slow strain rate test overestimates the susceptibility of a material are the hydrogen-induced cracking of low-strength steels under cathodic protection [159], the SCC of commercial-purity titanium in salt water [160], and the hydrogen-induced cracking of duplex stainless steels [161]. In every case the K_{ISCC} value, if it exists, is extremely high, at least 50 MPa $m^{1/2}$. Sometimes this hydrogen-induced cracking, which would not occur in practice, overshadows a "genuine"-SCC phenomenon that occurs at a lower velocity but has a much lower K_{ISCC} value, e.g., SCC of carbon steel in CO-CO_2-H_2O solutions [162,163]. One approach to this kind of problem (without changing the test) is to study the distribution of secondary cracks on the failed tensile specimen. Cathodic hydrogen embrittlement is confined to the necked region [159,164], but the genuine SCC is distributed as secondary cracks along the whole length of the tensile specimen [162] (Figs. 38 and 39).

Having classified CO_2-induced cracking as possibly an artifact, we note that this is a favored mechanism for a transgranular cracking phenomenon seen in high-pressure gas transmission pipelines. Clearly, the hydrogen uptake in CO_2 or $NaHCO_3$ solution must be high compared with cathodic protection in salt water, where similar steels do not crack, or else the coexistence of localized corrosion and hydrogen entry helps to maintain the crack tip strain rate. Dynamic service stresses are also an important factor.

Copyright © 2002 Marcel Dekker, Inc.



(a)



(b)

Figure 35 Typical fractures of C-Mn steel obtained in slow strain rate tests: (a) in air; (b) in anhydrous ammonia-methanol. (Courtesy of I. M. Hannah and W. Zheng.)

Having reviewed some of the flaws of slow strain rate testing, we must stress that this is an outstanding useful test. It is always desirable to have the slow strain rate information, even if it is not used for direct prediction of service performance. Neither the pipe cracking in boiling water reactors [59] nor the SCC of high-pressure gas transmission lines [27,67] (both type A systems) could have been predicted by static-load tests on smooth specimens.

Loading rate, or dK_I/dt, affects SCC initiation and growth in precracked specimens [113] (Fig. 37) and a good appreciation of the cracking mechanism is

Copyright © 2002 Marcel Dekker, Inc.

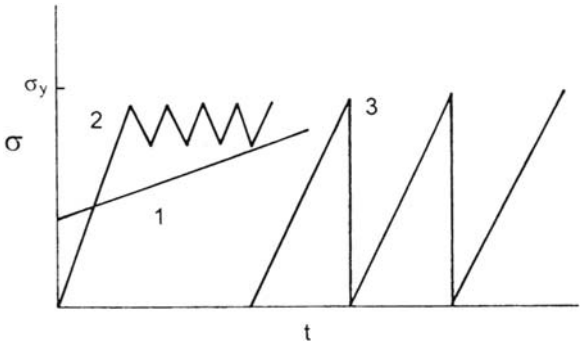


Figure 36 Various types of elastic slow strain rate test.

essential to avoid surprises in service, as not all variants of $K_I(t)$ can be tested in the laboratory. Attempts to rationalize all such data with the slip-dissolution model (for high-temperature aqueous environments) have been more in the nature of a sophisticated fitting exercise than a first-principles approach [29], and there is a great divergence of views on the cracking mechanisms, especially in pressurized water reactor (PWR) pressure vessel steels, where everything from slip dissolution [28–30] to hydrogen embrittlement [165] to film-induced cleavage [42] to surface mobility [166] has been suggested.

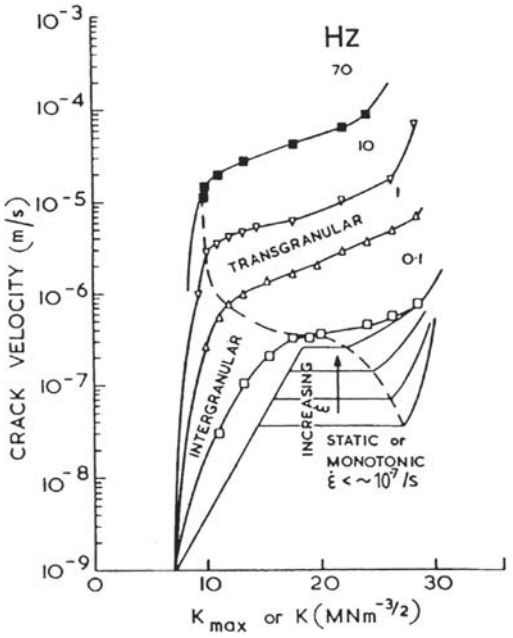


Figure 37 The effect of crack tip strain rate, via loading rate, on crack growth in a high-strength aluminum alloy [54,158]. (Courtesy of NACE.)

Copyright © 2002 Marcel Dekker, Inc.

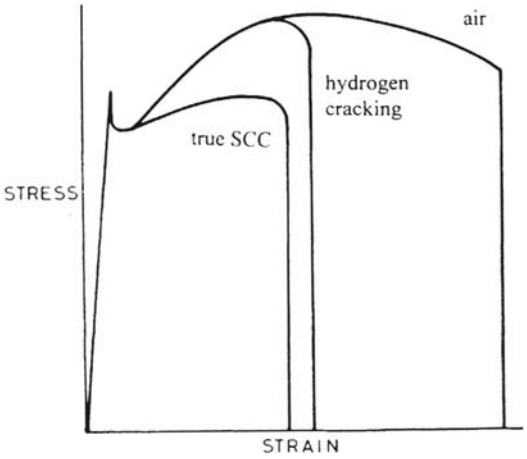


Figure 38 Stress-strain curves for "real" SCC (cracks initiated soon after yield) and cathodic hydrogen embrittlement (where cracking is confined to the necked region), for low-strength steels.

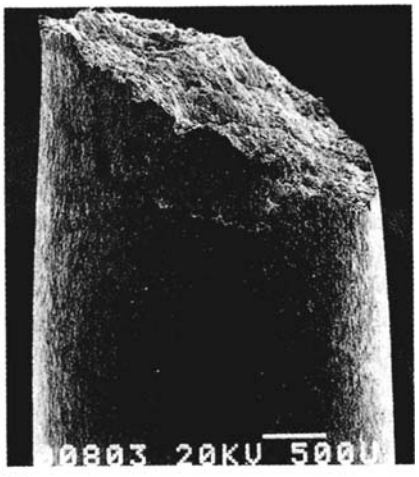
In some systems, SCC is initiated at a very large number of sites, and the crack tip strain rate is greatly reduced at each individual site, leading to near arrest of the cracks (another reason for crack arrest might be discontinuous segregation or precipitation; recall Fig. 13). Coalescence of two or more cracks is then required to produce a dominant crack that causes final failure [27,167] (Fig. 40). Statistical physicists are very interested in similar problems [168], ranging from mud cracking to fracture of random composite media. *Multiple crack interactions* are a major growth area in fracture mechanics. Such phenomena are peculiar to smooth specimens and provide a strong argument for carrying out several kinds of laboratory test.

A major area of development in SCC testing is the role of crevices in crack initiation. We have discussed the essential role of localized corrosion in Cl-SCC of austenitic stainless steels [68,111,112], and topical problems with duplex stainless steels necessitate extension of the same approach to these more resistant materials. The incorporation of crevices into slow strain rate specimens is not at all trivial, as we discovered during 2 years' work by Suleiman at UMIST [169]. Tamaki et al. [68] showed that a fine notch or precrack could be used to establish a reproducible condition in a fracture mechanics specimen, but this too is difficult work, especially if one attempts to carry out the work potentiostatically. Tamaki et al. found that, for 316L stainless steel at 80°C, SCC sometimes occurred only within a few tens of mV above the repassivation potential of the crevice (E_R) (Figs. 25 and 26). Without accurate prior knowledge of E_R, or in a complex service environment, such work can be very time consuming, so we have proposed a galvanostatic variant in which a low anodic current is applied that automatically establishes a steady potential just above the lowest possible value of E_R before starting the tensile machine (see Fig. 7c). This galvanostatic technique is also applicable to the rapid screening test used by Shinohara and colleagues [112], in which two sheets of austenitic steel are spot

Copyright © 2002 Marcel Dekker, Inc.



(a)



(b)

Figure 39 Fractography corresponding to Figure 38 [162], for C-Mn steel in CO-CO_2-H_2O solution: (a) genuine SCC; (b) cathodic hydrogen embrittlement. (Courtesy of I. M. Hannah.)

welded together and polarized in a chloride solution. All these procedures are recommended for further development except perhaps the use of the creviced slow strain rate test.

NOTES ON OTHER PROPOSED SCC MECHANISMS

Magnin's model of SCC and corrosion fatigue [16,17] proposes that the motion of crack-tip dislocations is impeded by an obstacle ahead of the crack tip, which in

Copyright © 2002 Marcel Dekker, Inc.

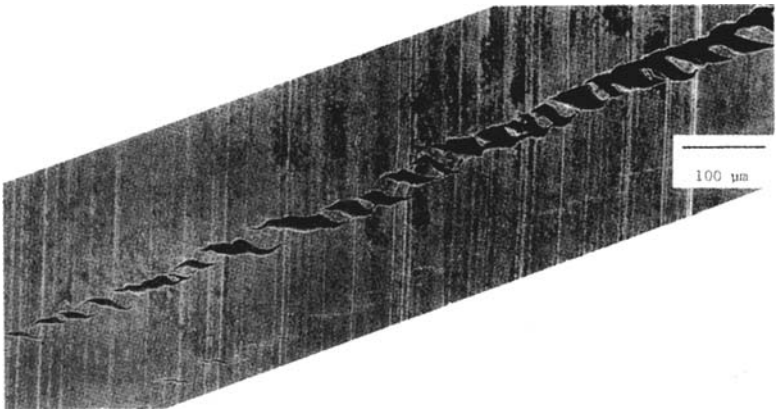


Figure 40 Crack coalescence of {110} microcracks leading to a dominant slip-band crack for a Cu monocrystal dynamically strained in $NaNO_2$ solution [65].

the purest case might be a Lomer-Cottrell lock. Dissolution down a slip band toward the obstacle leads to the achievement of K_{Ic} at the obstacle and the propagation of a cleavage crack on the slip plane back toward the crack tip; in addition (or alternatively), this decohesion of the microfacet can be facilitated by hydrogen adsorption on the fracture plane (Fig. 41). Such a model is consistent with certain observations in corrosion fatigue cracking, and with fractographic studies of Dickson and others [66,170] on transgranular SCC surfaces, but is not yet adapted to explain the multitude of special environmental factors in SCC. Application of this model to alloy 600 in hydrogenated high-temperature water [17] might be considered arbitrary in comparison with Scott and Le Calvar's [60] highly focused investigations of intergranular oxidation. Magnin's model is elegant and plausible but can be tested only by fractography, which is bound to be inconclusive.

The model of environmental cracking proposed by Lynch [19] will be considered only briefly as it accounts for none of the special environmental effects in SCC. This does not mean that the model is wrong, only that it is untestable except by microscopic means. The concept of enhanced local plasticity leading to plastic microfracture is an important aspect of hydrogen embrittlement [148] and has interesting implications in liquid metal embrittlement. Most authorities reject Lynch's adsorption-based approach to hydrogen effects preferring to appeal to effects of *internal* hydrogen on plasticity, yet Lynch has a powerful argument based on the similarity between liquid metal–induced and hydrogen-induced fractures in certain systems. There is no doubt that plastic microfracture will form part of the complete SCC spectrum, should this ever be elucidated, but we must reject the notion that all SCC can be explained by such mechanisms.

"Universal" models of environmental fracture rarely survive for long, and SCC specialists such as Parkins [27,171] have devoted much effort to promoting a spectrum of mechanisms from mainly chemical (intergranular slip-dissolution) to mainly mechanical (hydrogen-induced SCC of high-strength steel). Nevertheless,

Copyright © 2002 Marcel Dekker, Inc.

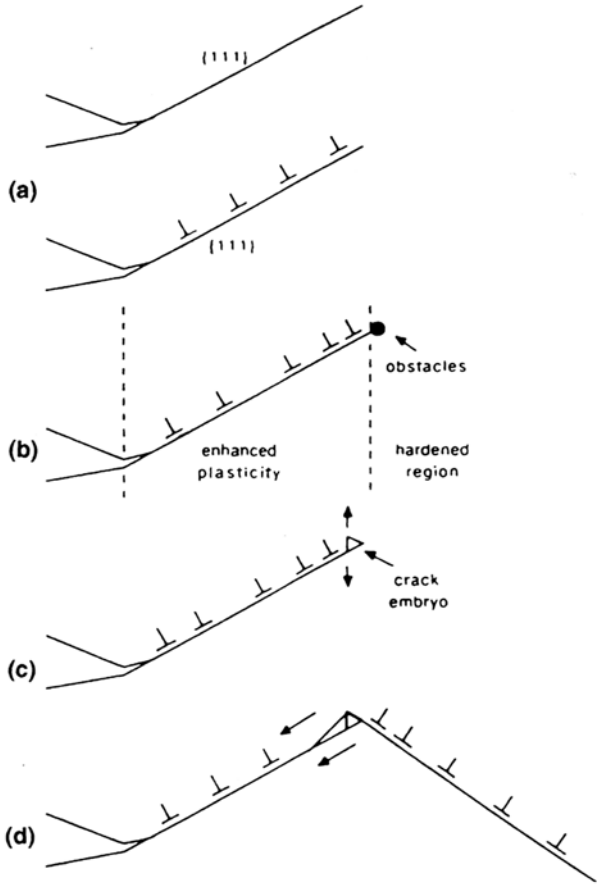


Figure 41 Magnin's model of SCC [16,17].

universal models continue to appear from time to time and must be tested seriously. Galvele's surface mobility model [20,166] proposes that cracks grow by surface diffusion of metal atoms (possibly combined with ions or molecules from the environment) from a very sharp crack tip to the crack walls, i.e., capture of vacancies by the crack tip (Fig. 42). Formation of surface compounds with low melting points promotes SCC by increasing the surface self-diffusivity of the metal, D_s. The details of the crack tip and its interaction with the environment (i.e., electrochemistry) are considered to be secondary factors that contribute by maintaining the critical surface compound. The model is applied to liquid metal embrittlement as well as SCC and seems to have considerable predictive power. One of the key factors in Galvele's conversion to surface mobility was his conviction that slip-dissolution could not work in the restricted geometry of the crack, but, as explained earlier, the crack is not a one-dimensional slot and the crack opening angle permits very high anodic current densities in cracks without saturation of metal salts or very high *IR* potential drops.

Copyright © 2002 Marcel Dekker, Inc.

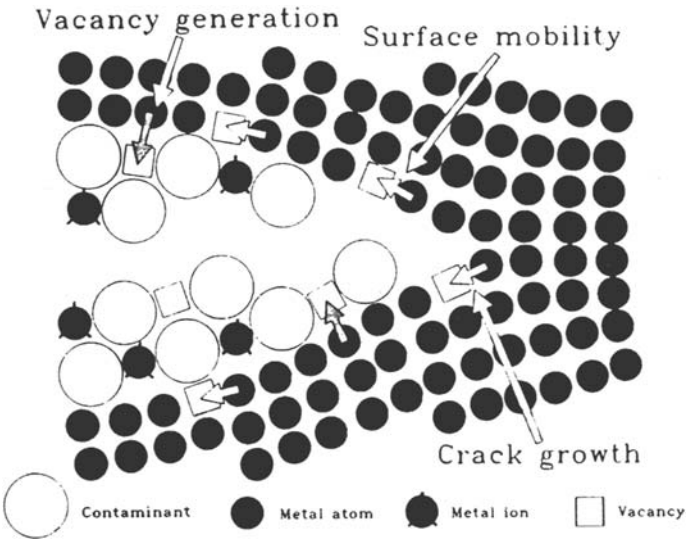


Figure 42 Galvele's surface mobility model for SCC [20].

According to Galvele's model, the crack velocity (υ) is given by

$$v = \frac{D_s}{L}(e^{\sigma a^3/kT} - 1) \tag{17}$$

where D_s is the surface self-diffusion coefficient, L is a characteristic diffusion length, σ is the elastic surface stress at the crack tip, and a^3 is the volume of a vacancy. The treatment of the diffusion process is greatly simplified, but this is not one of the main flaws in the analysis. These are, according to Sieradzki and Friedersdorf [23]:

1. The equilibrium vacancy concentration in a plane can be increased by a *normal* tensile stress [172], but Galvele applied the relevant equation to the crack tip where this stress is zero. Lacking this effect, one must appeal to small, second-order effects.
2. Proper accounting of the chemical potential of the vacancies must include a capillary term of the form $+\gamma a^3/r$ (γ = surface energy, r = crack-tip radius) [173]. This prevents the crack from attaining very low r values, yet the surface mobility mechanism assumes an atomically sharp crack.

Sieradzki and Friedersdorf end their analysis by concluding that the crack velocities attainable by surface mobility (with the blunt crack tip just mentioned) are 10^8 to 10^{14} times lower than those calculated by Galvele. Their expression for the crack velocity is

$$v = \frac{D_s N_s \Omega^2}{kT}\frac{2}{\pi}\frac{1}{r^2}\left(\frac{\sigma_{yy}^2}{2E} - \gamma\kappa\right) \tag{18}$$

where N_s is the number of lattice sites per unit area, Ω is the atomic volume (a^3), and κ is the curvature, which is just $1/r$ for the crack tip.

Copyright © 2002 Marcel Dekker, Inc.

SUMMARY AND RECOMMENDATIONS FOR THE FUTURE

Several models of SCC have been tested successfully in particular systems. It would be premature to regard these tests as definitive (there is a particular need for direct studies of crack dynamics in Au-Cu or similar alloys showing film-induced cleavage), but they encourage us to look to other, unsolved systems for a more complete picture of the range of SCC phenomena. Some of these systems are:

1. Creep-like phenomena that may involve cavity formation induced by *internal oxidation* [60,61]. These will normally occur at elevated temperatures, and the outstanding example is the SCC of alloy 600 in PWR primary water or steam-hydrogen mixtures. The species being internally oxidized may include both Cr and C [174]; hence Ni-C alloys may also crack under some conditions. Some progress has been made by preexposing thin foils to the SCC environment, then allowing hydrogen to escape and straining the foils to failure at room temperature [61]; significant irreversible embrittlement has been observed and is confined to the surface, suggesting an internal oxidation effect rather than an irreversible hydrogen effect such as methane bubble formation.
2. Gaseous embrittlement by species other than H_2 [101–103,141,142], where a thorough test of the applicable models, using filmed thin foils would be valuable.
3. SCC of iron or carbon steel under controlled potential conditions in conducting, high-temperature aqueous environments [29], where more than one mechanism may be operating, but the slip-dissolution and film-induced cleavage models are eminently testable using established methods with modern refinements.
4. Brittle SCC in iron exposed to $CO\text{-}CO_2\text{-}H_2O$ [162,163] or anhydrous NH_3 [69]; indirect evidence for film-induced cleavage has been presented, but this is too indirect at present, and the special surface layers that form in these environments need to be studied.
5. Liquid metal embrittlement (LME) [15] (properly called metal-induced fracture, as the metal need not be liquid so long as it is at a high T/T_m) remains an outstanding problem for SCC specialists. Lynch [19] has stated that transgranular LME, in particular, involves only a surface interaction with the environment and hence must be classed as an adsorption-induced process even in the fcc materials; in situ electron microscopy, to observe the cracking process directly, seems to be one way forward (although not with such a crude environment as liquid mercury). The softening or local plastic fracture claimed by Lynch may be demonstrated or may resolve into a hardening or cleavage process at high enough resolution. Not enough is known about the total crack tip system in liquid metal embrittlement, and a proper accounting of all the forces and chemical potential gradients has not been made.
6. Systems of interacting cracks should be studied using techniques developed by statistical physicists [168].

Finally, there is room for more careful surface chemistry studies in SCC, utilizing recent advances in the characterization of the crack solution (pH, etc.) and the

Copyright © 2002 Marcel Dekker, Inc.

crack path (segregation, etc.). Although these studies may not reveal anything radically new, they are essential for a rigorous development of the subject, for example:

1. Interactions of anhydrous liquid ammonia with iron surfaces, to test the proposed role of nitride layers [69,100]. An experimental problem is that extremely low H_2O levels are required to produce the pure Fe-N interaction on a free surface, whereas in a crack the gettering action of the crack walls maintains a very low water content at the crack tip.
2. Surface analysis of films formed transiently on bare, e.g., laser-irradiated surfaces [175], should be undertaken. Such studies should include rapidly solidified alloys that incorporate segregant elements and should be integrated with mechanical studies on the same films.
3. The status of dealloying and film-induced cleavage in chloride-SCC of austenitic stainless steels is still unclear. Further studies should be undertaken in solutions that simulate the acid crack environment. The role of alloyed P [88] should be examined using these or simpler (Fe-Ni) alloys.
4. High-resolution Auger or secondary ion mass spectrometry (SIMS) analyses of SCC fracture surfaces, especially around crack-arrest features, have not kept pace with instrument development, and there is great scope for well-designed experiments of this type supported by cross-sectional transmission electron microscopy.
5. The scanning tunneling and atomic force microscopes (STM and AFM) have considerable potential for mapping fracture surface topography at very high resolution [176], provided one chooses an appropriate system with minimal corrosion and large flat areas on the fracture surface—this is illustrated every time one tests an STM or AFM on cleaved graphite or mica. Such studies may resolve some of the micromechanics of film-induced cleavage—for example, by showing that crack-arrest markings are present everywhere on transgranular fracture surfaces but are simply too fine to be resolved in the SEM. One may also be able to use the new generation of these instruments, with their improved position control and microscope facilities, to carry out high-resolution side-surface studies *during* SCC.

Finally, while SCC of metals is important in our industrial society, SCC of other inorganic solids can be said to have shaped our whole world. It is now widely accepted that time-dependent fracture (stress corrosion) of rocks in contact with water is responsible for such phenomena as premature fault movement leading to earthquakes [177] and fracture of newly formed crustal rocks emerging on the ocean floor [178].

REFERENCES

1. *Physical Metallurgy of Stress Corrosion Fracture* (T. N. Rhodin, ed.), Interscience, New York, 1959.
2. *Fundamental Aspects of Stress-Corrosion Cracking* (R. W. Staehle, A. J. Forty, and D. van Rooyen, eds.), NACE, Houston, 1969.
3. *Theory of Stress Corrosion Cracking* (J. C. Scully, ed.), NATO, Brussels, 1971.
4. *Stress-Corrosion Cracking and Hydrogen Embrittlement of Iron-Base Alloys* (R. W. Staehle, J. Hockmann, R. D. McCright, and J. E. Slater, eds.), NACE, Houston, 1977.

Copyright © 2002 Marcel Dekker, Inc.

5. *Mechanisms of Environment Sensitive Cracking of Materials* (P. R. Swann, F. P. Ford, and A. R. C. Westwood, eds.), The Metals Society, London, 1977.
6. *Corrosion Chemistry Within Pits, Crevices and Cracks* (A. Turnbull, ed.), HMSO, London, 1987.
7. *Chemistry and Physics of Fracture* (R. M. 'Latanision and R. H. Jones, eds.), Martinus Nijhoff, Dordrecht, 1987.
8. *Embrittlement by the Localized Crack Environment* (R. P. Gangloff, ed.), TMS-AIME, Warrendale, PA, 1984.
9. *Environmental-Induced Cracking of Metals* (R. P. Gangloff and M. B. Ives, eds.), NACE, Houston, 1990.
10. *Corrosion sous Contrainte* (D. Desjardins and R. Oltra, eds.), Les Editions de Physique, Les Ulis, 1992.
11. *Parkins Symposium on Fundamental Aspects of Stress-Corrosion Cracking* (S. M. Bruemmer, E. I. Meletis, R. H. Jones, W. W. Gerberich, F. P. Ford, and R. W. Staehle, eds.), TMS, Warrendale, PA, 1992.
12. *Corrosion-Deformation Interactions* (T. Magnin and J.-M. Gras, eds.), Les Editions de Physique, Les Ulis, 1993.
13. R. C. Newman and R. P. M. Procter, *Br. Corros. J. 25*:259 (1990).
14. D. R. Clarke and K. T. Faber, *J. Phys. Chem. Solids. 48*:1115 (1987).
15. N. S. Stoloff, in Ref. 9, p. 31.
16. T. Magnin and J. Lepinoux, Metallurgical aspects of the brittle SCC in austenitic stainless steels, in Ref. 11, p. 323.
17. T. Magnin, in Ref. 12, p. 27.
18. D. A. Jones, *Metall. Trans. A 16A*:1133 (1985).
19. S. P. Lynch, *Acta Metall. 36*:2639 (1988).
20. J. R. Galvele, *Corros. Sci. 27*:1 (1987).
21. *Hydrogen Degradation of Ferrous Alloys* (R. A. Oriani, J. P. Hirth, and M. Smialowski, eds.), Noyes, Park Ridge, NJ, 1985.
22. *Hydrogen Effects on Material Behavior* (N. R. Moody and A. W. Thompson, eds.), TMS, Warrendale, PA, 1990.
23. K. Sieradzki and F. J. Friedersdorf, *Corros. Sci. 36*:669 (1994).
24. D. A. Vermilyea, in Ref. 4, p. 208.
25. R. W. Staehle, in Ref. 4, p. 180.
26. R. N. Parkins, *Corros. Sci. 20*:147 (1980).
27. R. N. Parkins, in Ref. 9, p. 1.
28. F. P. Ford, *Corrosion Processes* (R. N. Parkins, ed.), Applied Science Publishers, London, 1982.
29. F. P. Ford, in Ref. 9, p. 139.
30. F. P. Ford, in Ref. 10.
31. P. L. Andresen, *Corrosion 47*:9–17 (1991).
32. R. C. Newman, K. Sieradzki, and H. S. Isaacs, *Metall. Trans. A 13A*:2015 (1982).
33. R. C. Newman and M. Saito, Anodic stress-corrosion cracking: Slip-dissolution and film-induced cleavage, in Ref. 12, p. 3.
34. C. Edeleanu and A. J. Forty, *Philos. Mag. 46*:521 (1960).
35. J. A. Beavers, and E. N. Pugh, *Metall. Trans. A 11A*:809 (1980).
36. E. N. Pugh, *Atomistic of Fracture* (R. M. Latanision and J. R. Pickens, eds.), Plenum, New York, 1983, p. 997.
37. M. T. Hahn and E. N. Pugh, *Corrosion 36*:380 (1980).
38. D. V. Beggs, M. T. Hahn and E. N. Pugh, *Proceedings of the A. R. Troiano Honorary Symposium on Hydrogen Embrittlement and Stress-Corrosion Cracking* (R.Gibala and R. F. Hehemann, eds.), ASM, Metals Park, OH, 1984.
39. E. N. Pugh, *Corrosion 41*:517 (1985).

Copyright © 2002 Marcel Dekker, Inc.

40. K. Sieradzki and R. C. Newman, *Philos. Mag. A 51*:95 (1985).
41. K. Sieradzki and R. C. Newman, *J. Phys. Chem. Solids 48*:1101 (1987).
42. R. C. Newman and K. Sieradzki, in Ref. 7, p. 597.
43. K. Sieradzki, in Ref. 7, p. 219.
44. K. Sieradzki, in Ref. 9, p. 125.
45. T. B. Cassagne, in Ref. 10.
46. R. C. Newman, T. Shahrabi, and K. Sieradzki, *Scr. Metall. 23*:71 (1989).
47. R. G. Kelly, T. Shahrabi, A. J. Frost and R. C. Newman, *Metall. Trans. A 22A*:191 (1991).
48. R. G. Kelly, A. J. Young and R. C. Newman, *Electrochemical Impedance Spectroscopy*, ASTM STP 1188 (J. R. Scully, D. C. Silverman, and M. W. Kendig, eds.), ASTM, Philadelphia, 1991, p. 94.
49. M. Saito, G. S. Smith, and R. C. Newman, *Corros. Sci. 35*:411 (1993).
50. J. S. Chen, M. Salmeron, and T. M. Devine, *Scr. Metall. 26*:739 (1992).
51. J. S. Chen, M. Salmeron, and T. M. Devine, *J. Electrochem. Soc. 139*:L55 (1992).
52. G. E. Kerns, M. T. Wang, and R. W. Staehle, in Ref. 4, p. 700.
53. C. S. Carter and M. V. Hyatt, in Ref. 4, p. 524.
54. N. J. H. Holroyd, in Ref. 9, p. 311.
55. L. Ratke and W. Gruhl, *Werkst. Korros. 31*:768 (1980).
56. R. C. Newman and A. Mehta, in Ref. 9, p. 489.
57. J. I. Dickson, A. J. Russell, and D. Tromans, *Can. Met. Q. 19*:161 (1980).
58. M. O. Speidel, Proceedings of *Stainless Steels '91*, ISIJ, Tokyo, 1991, Vol. 1, p. 25.
59. R. W. Staehle, in Ref. 9, p. 561.
60. P. M. Scott and M. Le Calvar, Some possible mechanisms of intergranular stress corrosion cracking of alloy 600 in PWR primary water, Proceedings of *6th International Symposium on Environmental Degradation of Materials in Nuclear Power Systems—Water Reactors*, San Diego, 1993.
61. T. S. Gendron and R. C. Newman, Irreversible Embrittlement of Alloy 600 in Hydrogenated Steam at 400°C, *Corrosion/94*, paper 227, NACE, Houston, 1994.
62. H. Nagano, T. Kudo, Y. Inaba, and M. Harada, *Met. Corros. Ind. 56*:81 (1981); also *Boshoku Gijutsu* (Corrosion Engineering) *30*:218 (1981).
63. M. O. Speidel, *Corrosion 33*:199 (1977).
64. H. Stenzel, H. Vehoff, and P. Neumann, in Ref. 7, p. 652.
65. K. Sieradzki, R. L. Sabatini, and R. C. Newman, *Metall. Trans. A 15A*:1941 (1984).
66. Li Shiqiong, J. I. Dickson, J.-P. Bailon, and D. Tromans, *Mater. Sci. Eng. A119*:59 (1989).
67. R. N. Parkins, and R. R. Fessler, *Mater. Eng. Appl. 1*:80 (1978).
68. K. Tamaki, S. Tsujikawa, and Y. Hisamatsu, *Advances in Localized Corrosion* (H. S. Isaacs, U. Bertocci, J. Kruger, and S. Smialowska, eds.), NACE, Houston, 1991, p. 207).
69. R. C. Newman, W. Zheng, and R. P. M. Procter, *Corros. Sci. 33*:1033 and 1009 (1992).
70. S. P. Pednekar, A. K. Agrawal, H. E. Chaung, and R. W. Staehle, *J. Electrochem. Soc. 126*:701 (1979).
71. E. N. Pugh, J. V. Craig and A. J. Sedriks, in Ref. 2, p. 118.
72. K. Sieradzki, J. S. Kim, A. T. Cole, and R. C. Newman, *J. Electrochem. Soc. 134*:1635 (1987).
73. H. R. Copson, in Ref. 1, p. 247.
74. M. O. Speidel, *Metall. Trans. A 12A*:779 (1981).
75. L. Graf, in Ref. 2, p. 187.
76. K. Sieradzki, R. R. Corderman, K. Shukla, and R. C. Newman, *Philos. Mag. A 59*:713 (1989).
77. K. Sieradzki, R. C. Newman, and T. Shahrabi, in Ref. 68, p. 161.
78. R. C. Newman, R. R. Corderman, and K. Sieradzki, *Br. Corros. J. 24*:143 (1989).

Copyright © 2002 Marcel Dekker, Inc.

79. W. J. R. Nisbet, G. W. Lorimer, and R. C. Newman, *Corros. Sci. 35*:457 (1993).
80. R. M. Bhatkal, W. F. Flanagan, and B. D. Lichter, in Ref. 12, p. 43.
81. L. Zhong, W. F. Flanagan, and B. D. Lichter, in Ref. 12, p. 309.
82. M. Saito, M.Sc. thesis, UMIST, 1993.
83. F. J. Friedersdorf, Ph. D. thesis, Johns Hopkins University, 1993.
84. R. P. Harrison, D. de G. Jones, and J. F. Newman, in Ref. 4, p. 659.
85. N. Bandyopadhyay, R. C. Newman, and K. Sieradzki, *Proceedings, of the 9th International Congress on Metallic Corrosion*, NRC, Ottawa, 1984, Vol. 2, p. 210.
86. V. Cihal, *Corros. Sci. 25*:815 (1985).
87. T. Shahrabi and R. C. Newman, *Mater. Sci. Forum, 44–45*:169, Trans Tech, Zurich (1989) (Proceedings of *Electrochemical Methods in Corrosion Research III*, Zurich, 1988).
88. R. C. Newman, *Corros. Sci. 33*:1653 (1992).
89. J. R. Galvele and S. de Micheli, *Corros. Sci. 10*:795 (1970).
90. W. Hepples, M. R. Jarrett, J. S. Crompton, and N. J. H. Holroyd, in Ref. 9, p. 383.
91. H. Spaehn, in Ref. 9, p. 449.
92. D. B. Wells, J. Stewart, A. W. Herbert, P. M. Scott, and D. E. Williams, *Corrosion 45*:649 (1989).
93. B. F. Brown, in Ref. 3, p. 186.
94. R. N. Parkins, M. Elices, V. Sanchez-Galvez, and L. Caballero, *Corros. Sci. 22*:379 (1982).
95. J. Hochmann, A. Desestret, P. Jolly, and R. Mayoud, in Ref. 4, p. 956.
96. A. J. Russell and D. Tromans, *Metall. Trans. A 10A*:1229 (1979).
97. A. J. Russell and D. Tromans, *Metall. Trans. A 12A*:613 (1981).
98. M. O. Speidel and R. Magdowski, in Ref. 12, p. 107.
99. T. B. Cassagne, W. F. Flanagan, and B. D. Lichter, *Metall. Trans. A 17A*:703 (1986).
100. M. Ahrens and K. E. Heusler, *Werkst. Korros. 32*:197 (1981).
101. D. Hardie, in Ref. 9, p. 347.
102. G. E. Kerns, and R. W. Staehle, *Scr. Metall. 6*:1189 (1972).
103. K. Sieradzki, *Acta Metall. 30*:913 (1982).
104. G. L. Bianchi and J. R. Galvele, *Corros. Sci. 34*:1411 (1993).
105. R. P. Ganglofff, in Ref. 9, p. 55.
106. R. P. Wei and M. Gao, in Ref. 22, p. 789.
107. M. Kimura, N. Totsuka, and T. Kurisu, *Corrosion 45*:340 (1989).
108. R. C. Newman, *Corrosion Chemistry Within Pits, Crevices and Cracks* (A. Turnbull, ed.), HMSO, London, 1987, p. 317.
109. E. Mattsson, *Electrochim. Acta 3*:279 (1961).
110. T. P. Hoar and G. P. Rothwell, *Electrochim. Acta 15*:1037 (1970).
111. T. Adachi, in Ref. 58, p. 189.
112. S. Tsujikawa, T. Shinohara, and Chenghao Liang, in Ref. 58, p. 196.
113. R. N. Parkins, *Environment-Sensitive Fracture: Evaluation and Comparison of Test Methods* (S. W. Dean, E. N. Pugh, and G. M. Ugiansky, eds.), ASTM STP 821, ASTM, Philadelphia, 1984, p. 5.
114. J. Congleton, T. Shoji, and R. N. Parkins, *Corros. Sci. 25*:663 (1985).
115. R. C. Newman, *Corrosion 50*:682 (1994).
116. M. J. Danielson, C. A. Oster, and R. H. Jones, in Ref. 108, p. 213.
117. J. R. Rice and R. Sorensen, *J. Mech. Phys. Solids 26*: 163 (1978).
118. J. R. Galvele, *J. Electrochem. Soc. 133*:953 (1986).
119. D. D. Macdonald and M. Urquidi-Macdonald, *Corros. Sci. 32*:51 (1991).
120. N. J. H. Holroyd, A. Gray, G. M. Scamans, and R. Herrmann, Proceedings of *Aluminium-Lithium III*, Institute of Metals, London, 1986, p. 310.
121. J. G. Craig, R. C. Newman, M. R. Jarrett, and H. J. H. Holroyd, *J. Phys. (Orsay) 48*:825 (colloq. C3) (1987) [Proceedings of *Aluminium-Lithium IV*, Paris, 1987].

Copyright © 2002 Marcel Dekker, Inc.

122. A. Rota and H. Boehni, in Ref. 87, p. 177.
123. Y. S. Kim, N. J. H. Holroyd, and J. J. Lewandowski, in Ref. 9, p. 371.
124. C. Edeleanu, *J. Iron Steel Inst. 173*:140 (1953).
125. T. Kudo, H. Tsuge, and T. Moroishi, *Corrosion 45*:831 (1989).
126. M. Barteri, F. Mancia, A. Tamba, and G. Montagna, *Corros. Sci. 27*:1239 (1987).
127. S. B. Mat and R. C. Newman, Local chemistry aspects of hydrogen sulfide–assisted SCC of stainless steels, *Corrosion/94*, paper 228, NACE, Houston, 1994.
128. J. Oudar and P. Marcus, *Appl. Surf. Sci. 3*:48 (1979).
129. P. Marcus and J. Oudar, in Ref. 7, p. 670.
130. R. C. Newman, *Corros. Sci. 25*:341 (1985).
131. P. Marcus, *C. R. Acad. Sci. Paris 305*:675 (1987).
132. R. H. Jones and S. M. Bruemmer, in Ref. 9, p. 287.
133. R. P. M. Procter and G. N. Stevens, *Corros. Sci. 15*:349 (1975).
134. A. Kawashima, A. K. Agrawal, and R. W. Staehle, *Stress-Corrosion Cracking—The Slow Strain Rate Technique* (G. M. Ugiansky and J. H. Payer, eds.), ASTM STP 665, ASTM, Philadelphia, 1977, p. 266.
135. R. N. Parkins, C. M. Rangel, and J. Yu, *Metall. Trans. A 16A*:1671 (1985).
136. T. Shahrabi, Ph. D. thesis, University of Manchester, 1989.
137. T. Shahrabi, R. C. Newman, and K. Sieradzki, *J. Electrochem. Soc. 140*:348 (1993).
138. R. C. Newman, T. Shahrabi, and K. Sieradzki, *Corros. Sci. 28*:873 (1988).
139. G. S. Duffo and J. R. Galvele, *Corros. Sci. '34*:79 (1993).
140. G. S. Duffo and J. R. Galvele, *Metall. Trans. A 24A*:425 (1993).
141. G. L. Bianchi and J. R. Galvele, *Corros. Sci. 36*:611 (1994).
142. K. Sieradzki and P. Ficalora, *Scr. Metall. 13*:535 (1979).
143. A. Paskin, K. Sieradzki, D. K. Som, and G. J. Dienes, *Acta Metall. 31*:1258 (1983).
144. K. Sieradzki and J. S. Kim, *Acta Metal. Mater. 40*:625 (1992).
145. S. G. Corcoran and K. Sieradzki, *Scr. Metall. 26*:633 (1992).
146. J. Kameda and C. J. McMahon, *Metall. Trans. A 14A*:903 (1983).
147. W. W. Gerberich and S. Chen, in Ref. 9, p. 167.
148. H. K. Birnbaum, in Ref. 9, p. 21.
149. A. Turnbull, *Corros. Sci. 23*:833 (1983).
150. A. Turnbull, *Corros. Sci. 27*:1323 (1987).
151. A. Turnbull, in Ref. 68, p. 359.
152. B. F. Brown, in Ref. 4, p. 747.
153. A. Turnbull and R. C. Newman, *Small Fatigue Cracks* (R. O. Ritchie and J. Lankford, eds.), TMS-AIME, Warrendale, PA, 1986, p. 269.
154. R. A. Cottis and E. A. Taqi, in Ref. 88, p. 483.
155. S. Suresh, G. F. Zaminski, and R. O. Ritchie, *Metall. Trans. A 12A*:1435 (1981).
156. A. J. Sedriks, *Stress Corrosion Testing Made Easy*, NACE, Houston, 1991.
157. See various references in Ref. 134.
158. N. J. H. Holroyd and D. Hardie, *Corros. Sci. 23*:527 (1983).
159. B. R. W. Hinton and R. P. M. Procter, *Corros. Sci. 23*:101 (1983).
160. J. C. Scully and T. A. Adepoju, *Corros. Sci. 17*:789 (1977).
161. J. R. Valdez-Vallejo, R. C. Newman, and R. P. M. Procter, in Ref. 22, p. 1003.
162. I. M. Hannah, R. C. Newman, and R. P. M. Procter, in Ref. 22, p. 965.
163. A. Brown, J. T. Harrison, and R. Wilkins, in Ref. 4, p. 686.
164. R. P. M. Procter, *Cathodic Protection* (V. Ashworth and C. J. L. Booker, eds.), Ellis Horwood, Chichester, UK, 1986.
165. H. Hanninen, H. Illi and M. Kemppainen, in Ref. 6, p. 646.
166. J. R. Galvele, in Ref. 11, p. 85.
167. R. N. Parkins, *Corrosion 46*:178 (1990).
168. P. Meakin, *Statistical Models for the Fracture of Disordered Media* (H. J. Herrmann and S. Roux, eds.), Elsevier, Amsterdam, 1990, p. 291.

Copyright © 2002 Marcel Dekker, Inc.

169. M. Suleiman, Ph.D. thesis, University of Manchester, 1993.
170. J. I. Dickson, D. Tromans, S. Li, S. El Omari, and X. Z. Wu, in Ref. 12, p. 643.
171. R. N. Parkins, *Corrosion* (L. L. Shreir, ed.), 2nd ed., Newnes-Butterworths, London, 1976, ch. 8.1.
172. F. C. Larche and J. W. Cahn, *Acta Metall*. *33*:331 (1985).
173. R. J. Asaro and W. A. Tiller, *Metall. Trans*. *3*:1789 (1972).
174. A. Pineau, in Ref. 9, p. 111.
175. R. Oltra and M. Keddam, in Ref. 68, p. 17.
176. J. Lankford and M. Longmire, *J. Mater*. *Sci*. *26*:1131 (1991).
177. S. Das and C. H. Scholz, *J. Geophys*. *Res*. *86*:6039 (1981).
178. P. G. Meredith (University College, London), private communication.

Copyright © 2002 Marcel Dekker, Inc.

13

Corrosion Fatigue Mechanisms in Metallic Materials

T. Magnin
Ecole Nationale Supérieure des Mines de Saint-Etienne, Saint Etienne, France

INTRODUCTION

The deleterious effect of an aqueous environment on fatigue crack initiation and propagation in metals and alloys has been observed for a long time [1–5]. The applied electrochemical potential has a large influence on localized corrosion reactions and, consequently, on corrosion fatigue (CF) damage. These complex effects are used for cathodic protection in offshore structures. Nevertheless, CF is influenced by various mechanical, chemical, and microstructural parameters that interact locally. Even if anodic dissolution versus hydrogen effects are known to occur during CF, the damage mechanisms are still controversial and fatigue lifetime predictions are still empirical.

The application of linear elastic fracture mechanics (LEFM) led to the determination of threshold stress intensity factors for long crack growth, which are quite useful for engineering material–environment systems. Nevertheless, it is now well established [6,7] that short cracks can develop and grow from smooth surfaces, due to localized corrosion-deformation interactions, at crack tip stress intensities below the previous threshold. CF damage models of short crack growth are then necessary to improve the fatigue damage predictions in aqueous solutions.

In the first part of this chapter, crack initiation mechanisms are reviewed and quantitative approaches are discussed, bearing in mind the limitations related to the evaluation of localized corrosion-deformation interactions. A particularly interesting example of electrochemical and mechanical coupling effects during CF in duplex stainless steels will illustrate the complexity of the interactions that lead to crack initiation.

Crack propagation models are then presented for both short and long cracks. Anodic dissolution and hydrogen effects at the crack tip are analyzed. Finally, the possible relation between stress corrosion cracking and CF is shown for crack initiation and crack propagation processes.

CORROSION FATIGUE CRACK INITIATION

It is well known that slip bands, twins, interphases, grain boundaries, and constituent particles are classical sites for crack initiation. Moreover, persistent slip band

Copyright © 2002 Marcel Dekker, Inc.

(PSB)–grain boundary interactions are often observed to be preferential crack initiation sites during CF, as well as localized pits around metallurgical heterogeneities.

The main need in fatigue crack initiation modeling is related to the quantitative approach to local synergistic effects between environment and cyclic plasticity. In this section, quantitative approaches to corrosion fatigue crack initiation from different electrochemical conditions are presented. Then improvement of such models is given through corrosion-deformation interaction effects. Finally, an interesting example is given of the coupling effects between cyclic plasticity and corrosion that must be taken into account to improve the crack initiation resistance of duplex stainless steels in chloride solutions.

Classical Approaches to Corrosion Fatigue Damage

Electrochemical corrosion can be schematized as an "electronic pump or an electronic circuit" related to oxidation and reduction reaction:

$$M \rightarrow M^{n+} + ne^- \quad \text{anodic dissolution}$$

$$\left.\begin{array}{l} 2H_2O + O_2 + 4e^- \rightarrow 4OH^- \\ 2H^+ + 2e^- \rightarrow H_2 \end{array}\right\} \quad \text{cathodic reactions}$$

together with a cation hydrolysis reaction: $M^{n+} + nH_2O \rightarrow M(OH)_n + nH^+$.

Here M^{n+} is a solvated ion, e^- is an electrorn, and n represents the ion state of charge. The electrons, liberated by the oxidation, must flow through the material M to be consumed in an appropriate cathodic reaction. Beyond a solubility limit, precipitates of hydroxide or hydrated oxide are formed, and this surface film can provide a barrier to further dissolution. In fact, there are two film formation mechanisms: the dissolution-precipitation mechanism addressed before and also the solid-state oxidation process $M + H_2O \rightarrow MO + 2H^+ + 2e^-$. Some films are termed "passive," for stainless steels or aluminum alloys, for instance. These films can play an important role in environment-sensitive crack initiation and fracture. Under thermodynamic equilibrium conditions, the film stability may be inferred from $E = f(\text{pH})$ diagrams, where E is the electrical potential related to the chemical free energy G by $G = -nEF$, and F is Faraday's number. At equilibrium, one can define the electrode potential (related to ΔG) and the current density I ($I \sim e^{-\Delta G^*/RT}$ where ΔG^* is the activation energy of dissolution).

Thus, the relation $E = f(I)$ gives different corrosion rates for a given metal in a given solution. Figure 1 shows such a relation (polarization curve) in the case of an austenitic stainless steel in an acidic Cl^- solution. Five domains can be considered for corrosion and corrosion fatigue damage:

(1) In zone 1, $E > E_r$, pitting occurs by destabilization of the passive film. Pits act as stress concentrators during fatigue. During CF under pitting conditions, pits grow into the material. If such a pit reaches a critical depth d_{CL}, a fatigue crack can develop. The critical depth is then a function of the applied stress range [8].

Let us suppose the following conditions:

Constant corrosion conditions (pH, concentration of bulk solution)
Constant alternating load, $d\Delta P/dt = 0$
Constant loading frequency $dv/dt = 0$

Copyright © 2002 Marcel Dekker, Inc.

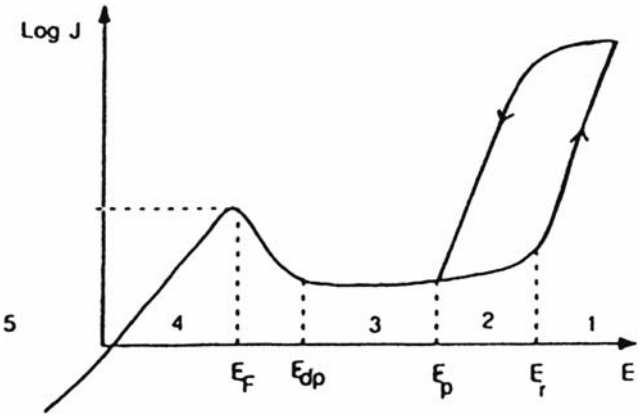


Figure 1 General polarization curve for an austenitic stainless steel in acidic Cl^- solutions.

It is well established that growth kinetics of corrosion pits are determined by a simple power law such as

$$d_L(t) = C(t - t_0)^{\beta}, \qquad t > t_0 \tag{1}$$

where t_0 is the incubation time for pit nucleation. If the pit depth reaches the critical value:

$$d_L(t) = d_{CL} \tag{2}$$

corrosion fatigue crack initiation occurs. The critical pit depth d_{CL} depends on the applied stress range $\Delta\sigma_0$, the cyclic yield strength σ_{FC} (which can be different from the tensile yield strength), the fatigue crack growth threshold ΔK_0, and the geometry of the specimen, expressed in terms of a geometric factor G. It can be calculated by elastic-plastic fracture mechanisms based on the Dugdale model [7]. Then d_{CL} is, given by the following equation:

$$d_{CL} = \frac{\cos(\pi\Delta\sigma_0/4\sigma_{FC})\ \pi\Delta K_0^2}{32G^2\sigma_{FC}^2[1 - \cos(\pi\Delta\sigma_0/4\sigma_{FC})]} \tag{3}$$

The number of cycles to initiate a corrosion fatigue crack under pitting conditions is, by combining the previous equations with $N = tv$,

$$N_i = \nu[t_0 + (d_{CL}/C_2)^{1/\beta}] \tag{4}$$

The dependence of N_i on the applied stress range $\Delta\sigma_0$, calculated according to the previous equation, is schematically represented in Figure 2a. Also, under pitting conditions no corrosion fatigue limit exists. For $N_i \le \nu t_0$, the influence of corrosion on the fatigue crack initiation life disappears (only if pitting is the necessary effect). Then, the lifetime is determined by the air fatigue behavior. Figure 2b shows an example for which the proposed calculation of N_i seems quite appropriate. Nevertheless, the main problem is related to the fact that the coefficients C and β of the pit kinetics are often not constant during cycling; it is a clear example of a cooperative effect between plasticity and electrochemistry that needs finer analyses.

Copyright © 2002 Marcel Dekker, Inc.

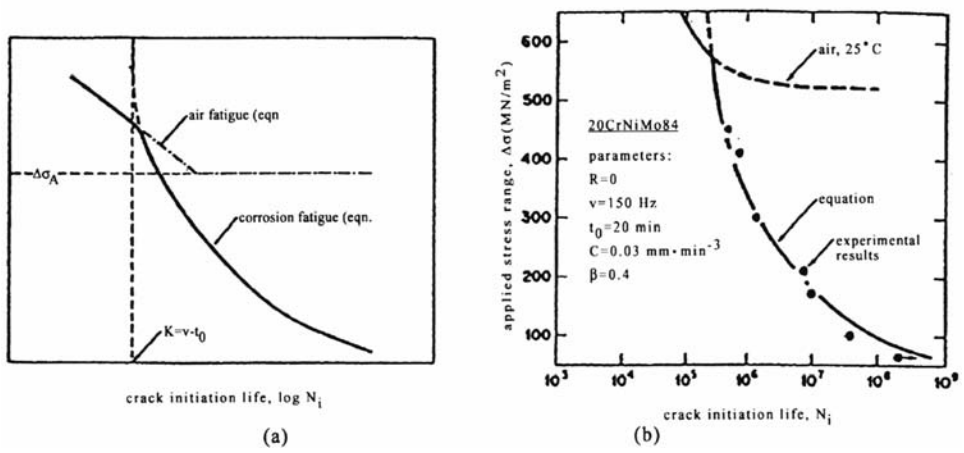


Figure 2 Corrosion fatigue crack initiation by pitting corrosion: (a) Schematic representation of a σ-*N* curve. (b) Comparison of experimentally and theoretically derived fatigue lives for the 20Cr-Ni-Mo alloy in 30 g/L NaCl solutions [8].

Figure 3 illustrates the fatigue crack initiation from a pit in a face-centered cubic (fcc) Fe-Mn-Cr alloy cyclically deformed at low strain rate in a Cl^- solution. In many multiphase engineering materials, the presence of constituent particles favors pitting and crack initiation.

(2) In zone 2, $E_p < E < E_r$, pits are repassivated. If the plastic strain amplitude is too small for localized depassivation (by slip band emergence), pits will



Figure 3 Crack initiation from a pit for a Fe-17Mn-13Cr alloy during CF in a 110°C Cl^- solution at a plastic strain amplitude $\Delta\varepsilon_p/2 = 4 \times 10^{-3}$ and a strain rate $\dot{\varepsilon} = 10^{-5}$ s^{-1}.

Copyright © 2002 Marcel Dekker, Inc.

not grow and the CF behavior is then close to that in air. On the other hand, pits can grow if mechanical depassivation occurs and the CF behavior is then close to that of zone 1.

(3) In the passive region 3, a competition between the kinetics of depassivation by slip and that of repassivation takes place. Thus the influence of the plastic strain amplitude and strain rate is quite obvious. In the same mechanical conditions as in (1), the quantity of matter dissolved per cycle (related to a distance) in the depassivated slip bands can be expressed, using Faraday's law:

$$dN = \frac{M}{nF\rho}\, 2\int_0^{1/v} i(\text{repassivation})\, dt \tag{5}$$

where i (repassivation) is generally of the form $i_{max} \exp(-\gamma t)$ with γ taken as a constant. Then $N_i = N$ (for $dN = d_c$). If d_c is taken as the grain size ϕ, for instance, then

$$N_i = \frac{\phi}{dN} = \phi \frac{nF\rho}{M} \frac{\gamma}{2i_{max}} [1 - \exp(\gamma/v)]^{-1} \tag{6}$$

A schematic representation of the equation is given in Figure 4a and corresponding experimental results are shown in Figure 4b.

Neverthless, one of the main problems is that the repassivation law evolves during cycling as shown in Figure 5. This result also emphasizes the synergy in CF that leads to a complex predictive approach.

(4) In zone 4, generalized dissolution occurs, which is generally quite dangerous for materials even without stress! In some cases, general corrosion can, however, blunt the cracks, which improves the fatigue life.

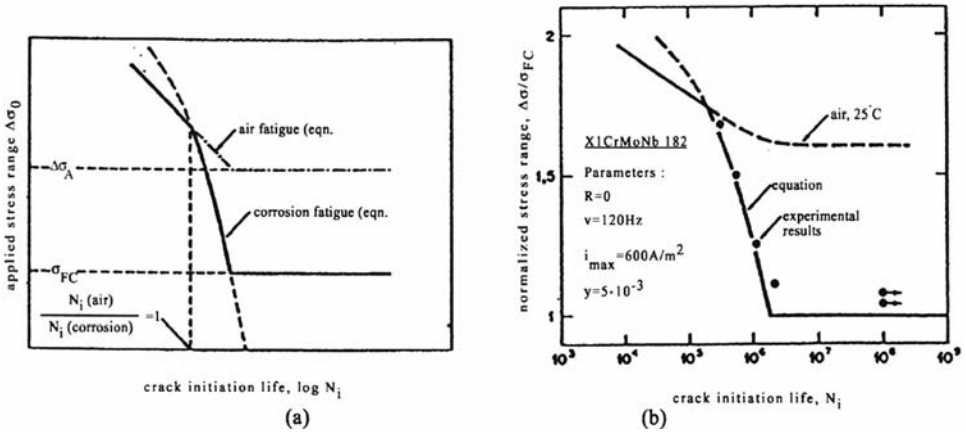


Figure 4 (a) Schematic representation of a σ-*N* curve for CF crack initiation under passive conditions. (b) Comparison of experimentally and theoretically derived fatigue lives for the X1 Cr MoNb 182 alloy in 30 g/L NaCl at 80°C [8].

Copyright © 2002 Marcel Dekker, Inc.

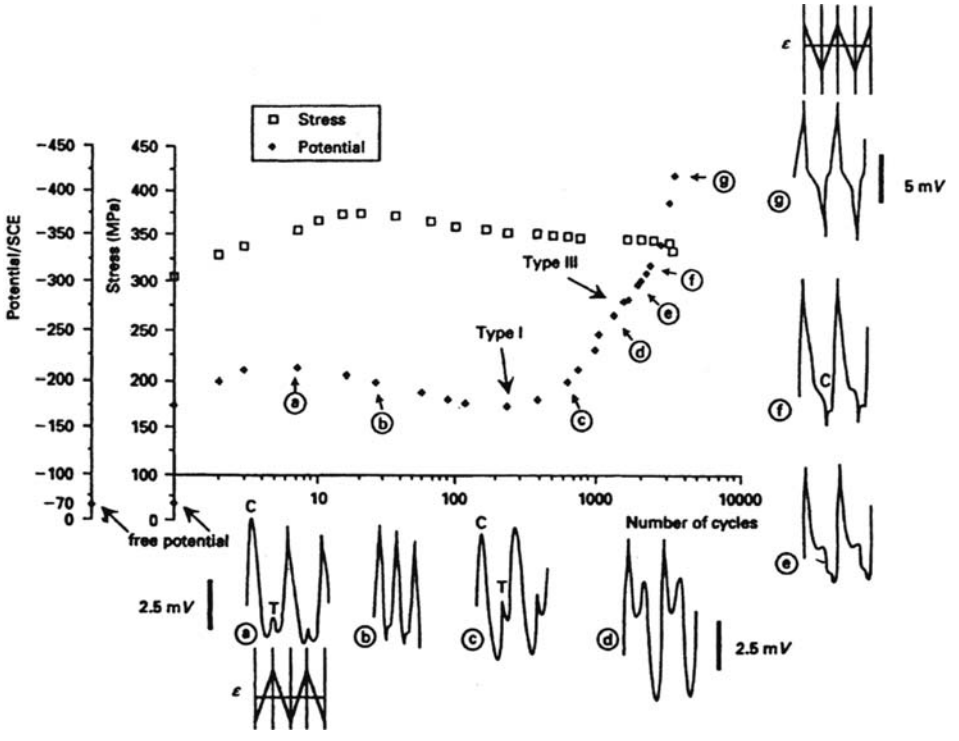


Figure 5 Simultaneous evolution of the cyclic stress σ, the average potential, and the shape of the cyclic potential transients for a 316L alloy in 30 g/L Na Cl ($\Delta\varepsilon_p/2 = 10^{-3}$, $\dot{\varepsilon} = 10^{-2}\ s^{-1}$).

(5) In zone 5, cathodic reactions are favored. If reduction of hydrogen occurs, we can have

$$2H^+ + 2e^- \rightarrow H_2$$

$$\rightarrow 2H_{adsorbed} \rightarrow H_2$$

$$H_{ads} \rightarrow H_{absorded}$$

which can induce hydrogen diffusion and/or transport by dislocations, often leading to macroscopic brittle fracture under stress.

The electrochemical approach presented here has many limitations. First of all, the kinetics of the electrochemical reactions are closely dependent on the cyclic plasticity and the number of cycles [9,10]. Thus, predictive laws are very complex. Moreover, these laws use the local current densities, which are very difficult to model. Finally, this approach does not really take into account the local corrosion-deformation interactions (CDIs) and the effects of the corrosive solution on the deformation mode. Indeed, such synergetic effects between corrosion and deformation can be of prime importance; the following examples emphasize the role of CDI in crack initiation processes.

Copyright © 2002 Marcel Dekker, Inc.

Influence of Cyclic Plasticity on Electrochemical Reactions

The evolution of dissolution current density transients during cycling of ferritic and austenitic stainless steels in NaCl solutions is shown in Figure 6, where curves $J_T = f(N)$ are plotted. Here J_T is the peak current density related to the depassivation process due to cyclic plasticity, and N is the number of cycles. During the first cycles the amount of dissolution increases, particularly at a high strain rate. One of the ferritic steels exhibits twinning, which induces a more marked depassivation during cycling, compared with the behavior of the second ferritic steel, which deforms by pencil glide [11].

Figure 6 clearly illustrates the influence of the deformation mode on the electrochemical reactions and the evolution of such electrochemical transients as a function of N (i.e., the localization of the plastic deformation with a decrease of J_T after the first cycles and then the formation of microcracks with a new increase of J_T until fracture due to a more difficult repassivation process).

PSBs and intense slip bands are very prone to specific dissolution, not only for passivated alloys but also in conditions of generalized dissolution as shown in Figure 7 for copper single crystals in $NaClO_4$ solution [9].

As soon as the PSBs form, the anodic current increases even though the applied plastic strain remains constant. This effect is related not only to the localization of the cyclic plasticity but also to the influence of the dislocation microstructure of PSBs on the free energy of dissolution ($-\Delta G$) and the energy of activation (ΔG^*) [10].

Moreover, cyclic plasticity has also been shown to promote localized pitting well below the pitting potential without stress [10]. Thus, for the ferritic Fe-26Cr-1 Mo stainless steel in 3.5% NaCl solution, a high strain rate $\dot{\varepsilon}$ promotes strain localization at grain boundaries, which induces intergranular pitting for an applied potential of about 400 mV below the pitting potential without stress effect.

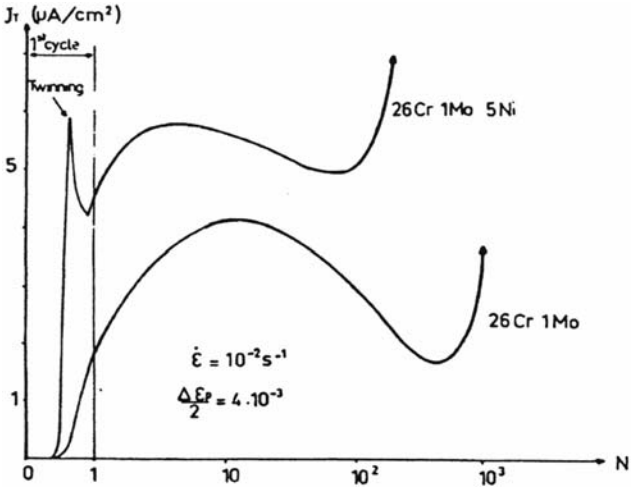


Figure 6 $J_T = f(N)$ curves for stainless steels during CF in a 3.5% NaCl solution.

Copyright © 2002 Marcel Dekker, Inc.

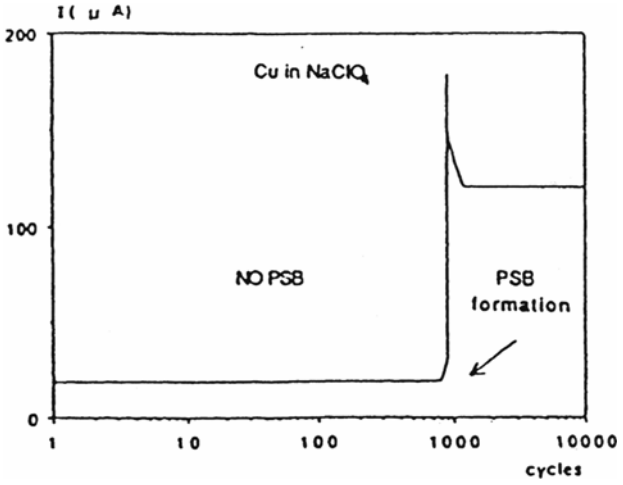


Figure 7 Influence of the PSB formation on the dissolution current for Cu single cyrstals in $NaClO_4$ [9].

The applied strain rate (or frequency) is a very sensitive parameter for CF damage. Figure 8 gives an interesting example for an Al-Li 8090 alloy in NaCl solutions. N_i is defined as the number of cycles to obtain a rapid 3% decrease of the saturation stress [10]. At high strain rate ($\dot{\varepsilon} > 5 \times 10^{-3}$ s^{-1}), the anodic dissolution occurs at slip band emergence and induces an enhancement of the transgranular mechanical microcracking. At medium strain rate (5×10^{-5} $s^{-1} < \dot{\varepsilon} < 5 \times 10^{-3} s^{-1}$), pitting is favored and responsible for crack initiation. So when the plastic strain decreases, pitting is more profuse (because of time) and the reduction in the fatigue life to crack initiation is more pronounced in comparison with air.

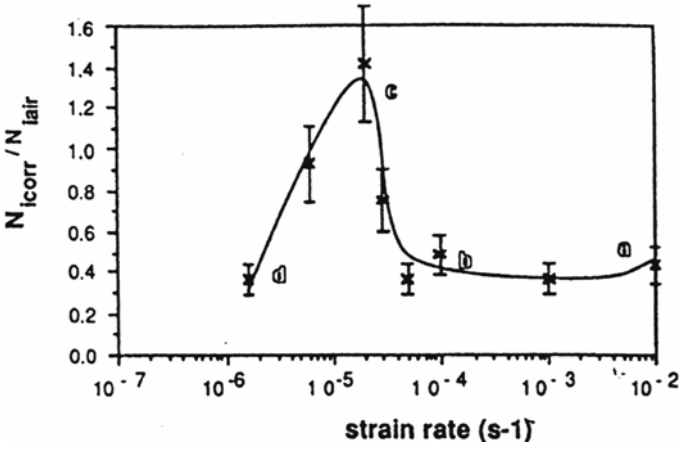


Figure 8 Influence of strain rate on 8090 Al-Li alloy fatigue life to crack initiation in a 3.5% NaCl solution for $\Delta\varepsilon_p/2 = 4 \times 10^{-3}$ at free potential.

Copyright © 2002 Marcel Dekker, Inc.

At low strain rate ($5 \times 10^{-6}\ s^{-1} < \dot{\varepsilon} < 5 \times 10^{-5}\ s^{-1}$), the fatigue time to initiation increased by blunting of the mechanically formed microcracks because of generalized pitting that acts as general corrosion. At very low strain rate ($\dot{\varepsilon} < 5 \times 10^{-6}\ s^{-1}$), CF crack initiation occurs by intergranular stress corrosion due to localized dissolution at grain boundaries. The rapid occurrence of stress corrosion cracking (SCC) induces a marked decrease of N_i.

Softening Effect due to Anodic Dissolution

CF tests on smooth specimens were performed at room temperature on a 316 L austenitic stainless steel in a 0.5 N H_2SO_4 solution at different electrochemical potentials and for a prescribed plastic strain amplitude of 4×10^{-3} ($\dot{\varepsilon} = 10^{-2}\ s^{-1}$). The depassivation-repassivation process occurs in a very regular way, well before any microcracks can form [11]. It is of particular interest to follow the evolution of the maximum flow stress in the corrosive solution at free potential and at imposed cathodic potential and to compare this evolution with that observed in air (Figure 9). It clearly appears that (a) a cyclic softening effect occurs at the free potential in comparison with the behavior in air; (b) this softening effect disappears when the cathodic potential is applied (and the anodic dissolution is markedly reduced), after about 150 cycles; (c) the softening effect then occurs in the same way when the free potential is reestablished; and (d) a delay in the evolution of the flow stress with regard to the number of cycles for which a potential change is imposed can be observed for the free potential to the cathodic potential change (and vice versa).

This effect has also been observed during creep in corrosive solutions for copper [1]. It corresponds to the time during which vacancies due to dissolution are still acting on the dislocation mobility.

The macroscopic cycling softening effect observed in H_2SO_4 solution at room temperature (which is not due to microcracking) is very relevant to take into account

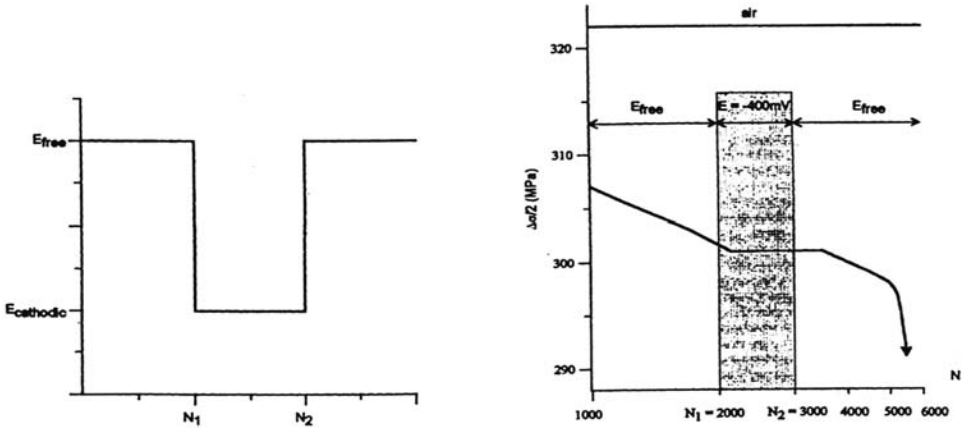


Figure 9 Evolution of the peak stress $\Delta\sigma/2$ during cycling in a 0.5 N H_2SO_4 solution at free potential for $\Delta\varepsilon_p/2 = 4 \times 10^{-3}$ and $\dot{\varepsilon} = 10^{-2}\ s^{-1}$ compared with the air behavior.

Copyright © 2002 Marcel Dekker, Inc.

quantitatively the local dissolution-deformation interactions that will lead to the fatigue crack initiation process.

Influence of Corrosion on PSB Configurations

Electrochemical control of corrosion has been shown to affect significantly the morphology of surface deformation. A modification of the number of persistent slip bands (PSBs) and of the slip offset height in PSB has been observed for Ni single crystals [4] in 0.5 N H_2SO_4 and in copper single crystals [4,9] according to the applied potential, in comparison with air. It is easy to understand that such influences on PSB distribution will affect the crack initiation conditions. Figure 10 shows histograms of the PSB distribution produced on monocrystalline nickel in 0.5 N H_2SO_4 at a constant strain amplitude.

Experiments conducted at the corrosion potential and at +160 mV/SCE result in a reduction of the inter-PSB distance and a reduction of slip offset height.

An Example of Mechanical and Electrochemical Coupling Effects: The CF Crack Initiation Mechanisms of a Two-Phase Stainless Steel in NaCl Solutions

Mechanical and electrochemical coupling effects are generally the key for understanding the crack initiation mechanisms in multiphase alloys. This is

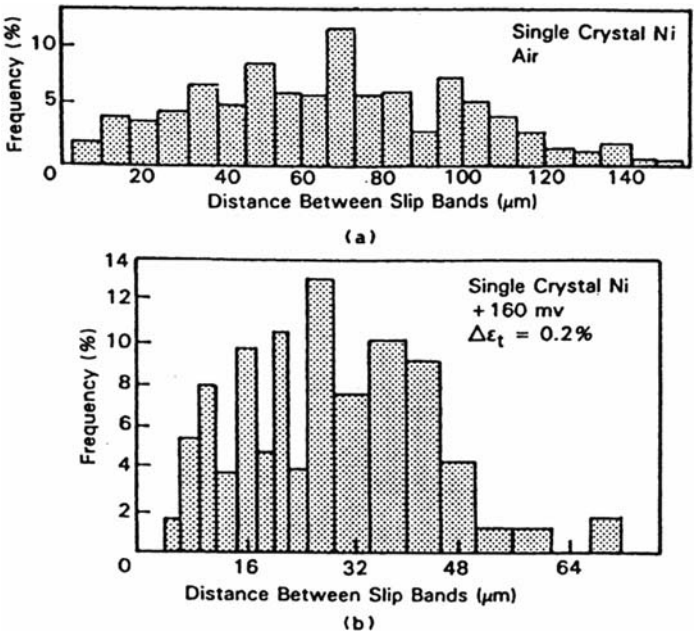


Figure 10 Histograms of distance between PSB clusters, from the replicate Ni single-crystal specimens fatigued for 1000 cycles under total strain control $\Delta\varepsilon_t$. Shear strain = 0.12%, (a) air and (b) +160 mV/SCE in 0.5 N H_2SO_4 [4].

Copyright © 2002 Marcel Dekker, Inc.

clearly illustrated for a duplex α/γ stainless steel (without nitrogen) in a 3.5% NaCl solution at pH 2 and free potential [11]. At low plastic strain amplitude, the softer γ phase is depassivated but this phase is cathodically protected by the non–plastically deformed α phase [11]. This coupling effect reduces the dissolution of the γ phase and delays CF damage, which is not the case at higher strain amplitude when the α phase is also depassivated by slip band emergence.

Observations of the crack initiation sites by scanning electron microscopy showed that at low plastic strain amplitudes ($\Delta\varepsilon_p/2 < 10^{-3}$) for which the fatigue resistance of the α-γ alloy is close to that of the γ alloy, cracks nucleate only in the austenitic phase (Fig. 11a), but at higher strain amplitudes ($\Delta\varepsilon_p/2 < 10^{-3}$), the first cracks nucleate principally in the ferritic phase (Fig. 11b). The excellent CF resistance of duplex stainless steels (for $\Delta\varepsilon_p/2 < 10^{-3}$) can then be understood through the electrochemical and mechanical coupling effects on crack initiation processes.

CORROSION FATIGUE PROPAGATION MECHANISMS

Phenomenology

One can find an enormous amount of mechanistic work about corrosion fatigue crack growth in the literature (see, for instance, Refs. 4,6,7,12). The aim of this section is not to review such studies but to analyze the possible mechanisms at the crack tip leading to crack advance. The question is, "What is the crack tip driving force that controls the corrosion fatigue crack growth?" among the different mechanical (stress, strain, strain rate) and chemical (dissolution, film formation, hydrogen production) effects.

Figure 12 shows the influence of different environments on the crack growth rate of a classical industrial steel [4]. Moist air is shown to have a marked influence on the crack growth rate in comparison with vacuum. Crack tip velocity is very sensitive to sodium chloride solution.

In fact, one must distinguish between long crack growth and short crack growth. For long crack growth, using linear elastic fracture mechanics (LEFM),

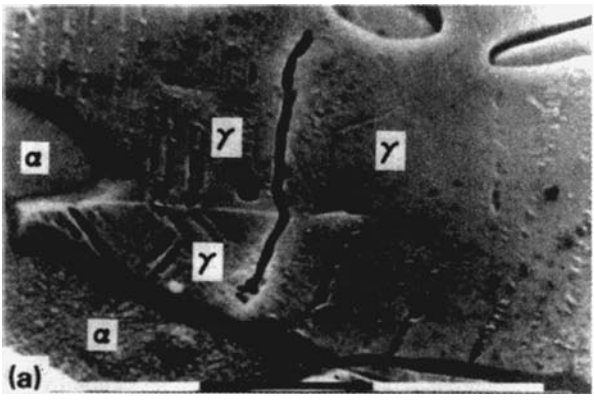


Figure 11 Crack initiation in a duplex stainless steel at $\dot{\varepsilon} = 2 \times 10^{-3}\ s^{-1}$. (a) In the γ phase at $\Delta\varepsilon_p/2 = 3 \times 10^{-4}$. (b) In the α phase at $\Delta\varepsilon_p/2 = 4 \times 10^{-3}$.

Copyright © 2002 Marcel Dekker, Inc.

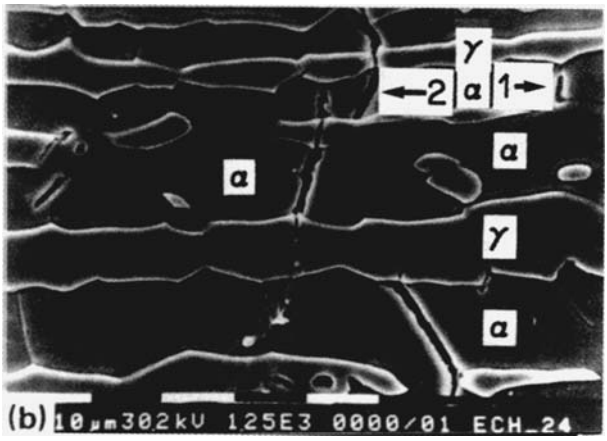


Figure 11. (Continued).

typical characteristics of the corrosion fatigue behavior are given in Figure 13 as a function of the stress intensity factor ΔK. Interactions with SCC are emphasized.

The models then propose that the rate of crack growth corresponds either to the sum of pure mechanical fatigue and the rate of stress corrosion cracking or to the

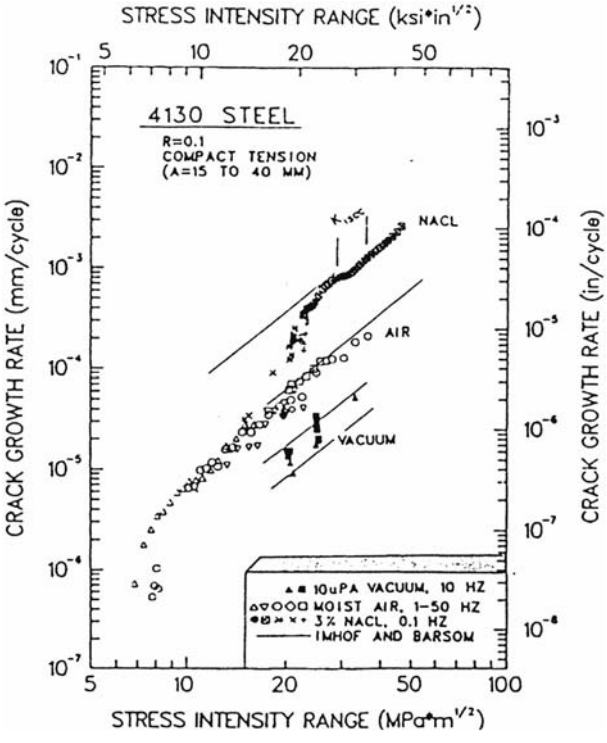


Figure 12 Influence of environment on the crack propagation velocity for a 4130 steel [4].

Copyright © 2002 Marcel Dekker, Inc.

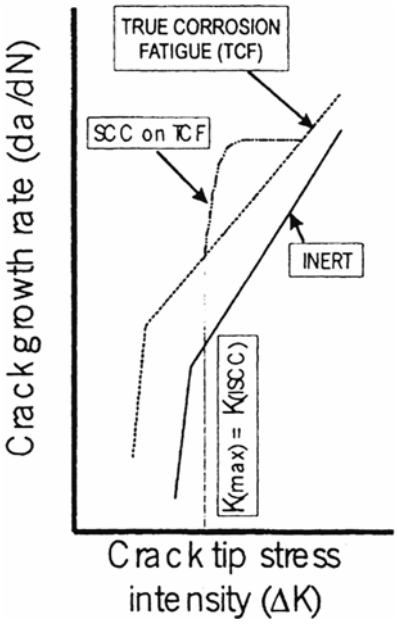


Figure 13 Schematic of fatigue and corrosion fatigue crack growth rate as a function of crack tip stress intensity.

fastest available mechanisms among those described in the following. Figure 14 summarizes the influence of corrosion on the fatigue crack growth characteristics [13–15]. To the purely mechanistic mode I crack propagation behavior under vacuum (curve 1) must be added (a) the effect of closure [4,6] and mode II on the near-threshold (curve 2), (b) the hydrogen-assisted crack propagation behavior (curve 3), and (c) the influence of absorption and diffusion of hydrogen at low loading R ratio (curve 4) and at higher R ratio (curve 5). One must also take into account dissolution and film effects.

However, it has been shown that short cracks propagate at stress intensity factors well below the long crack threshold, as shown in Figure 15 for carbon steel in seawater.

The application of microstructural fracture mechanisms (MFMs) has been successfully used to predict the growth of short cracks during fatigue in air [16]. These models have been adapted to characterize and predict the uniaxial and multiaxial corrosion fatigue loading [17].

The two following equations provide the basis of the Brown-Hobson model [18], in which the fatigue crack growth rate is expressed as a function of an equivalent strain term γ_{eq} for stage I and stage II cracks, respectively.

$$\frac{da}{dN} = B_{\mathrm{I}}\, \gamma_{eq}^{\beta_{\mathrm{I}}}(d_i - a) \quad \text{(stage I, shear crack growth)} \tag{7}$$

$$\frac{da}{dN} = B_{\mathrm{II}}\, \gamma_{eq}^{\beta_{\mathrm{II}}}\, a - D \quad \text{(stage II, tensile crack growth)} \tag{8}$$

Copyright © 2002 Marcel Dekker, Inc.

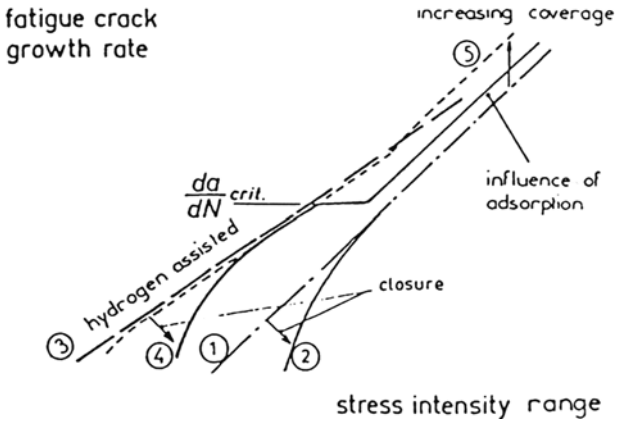


Figure 14 Schematization of the different CF crack growth mechanisms [13].

where a is the crack length; d a microstructural parameter such as grain size; i the number of grains through which the crack has traversed; B_I, B_{II} and β_I, β_{II} are constant depending upon the material-environment system; and D is the long crack threshold.

The determination of the crack tip environment is not easy because of the numerous electrochemical reactions and the associated mass transport and thermodynamic criteria that govern this environment. The nature of the solution (composition, pH, species, corrosion products that can induce roughness, etc.) can

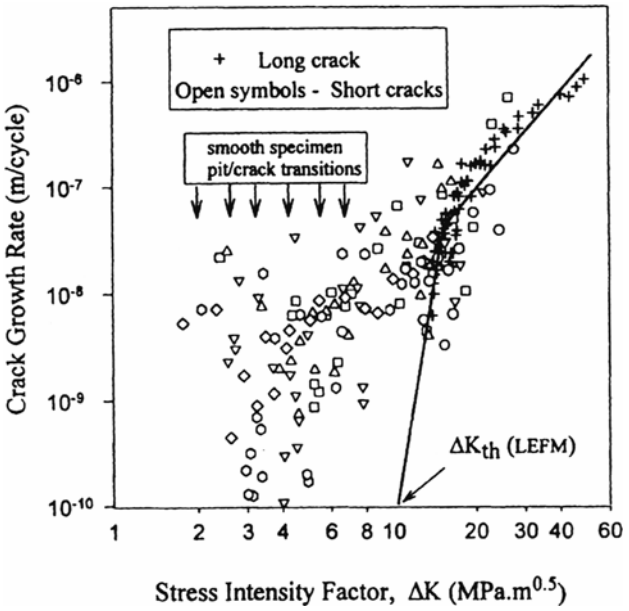


Figure 15 Comparison of long and short CF crack growth rates for carbon steels (σ_y = 500 MPa) in artificial water, 0.2 Hz, R = 0.1 [15].

Copyright © 2002 Marcel Dekker, Inc.

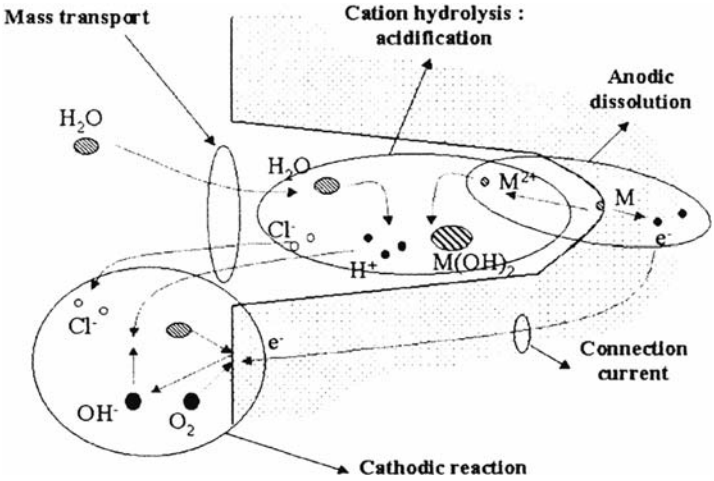


Figure 16 Possible electrochemical reactions at a corrosion fatigue crack tip.

be very different at the crack tip and in the bulk solution. Figure 16 shows the possible electrochemical reactions at the crack tip. Both anodic dissolution effects and a coupled hydrogen reaction must often be taken into account. The mathematical modeling of the localized crack tip chemistry is therefore possible [19].

One can find in Ref. 20 a very significant effect of the transport properties of the crack solution on the CF crack growth rates of steel in seawater.

Anodic Dissolution Effects

Anodic dissolution has been shown to occur preferentially in slip bands [11] very near the crack tip, which leads to many effects on the CF behavior as shown in Figure 17. A restricted slip reversibility model for stage I fatigue crack propagation has been proposed. The average crack growth increment per cycle, Δ_{χ}, is determined by factors controlling slip reversibility on the forward slip planes (i.e., S1 and S4). For fcc materials, it involves alternating slip on (111) planes near the crack tip. The slip reversibility is controlled by the degree of work hardening and recovery on a slip plane and the presence of corrosion products (oxides) on the slip steps. The rate of hydrated oxide nucleation plays a critical role in this model and therefore is expected to control stage I fatigue crack growth of an austenitic stainless steel in Cl^- solutions.

This localized dissolution process is not easy to take into account in numerical modeling of crack propagation. The slip dissolution model for CF is based on the fact that for many alloys in different solutions the crack propagation rate is proportional to the oxidation kinetics. Thus, by invoking Faraday's law, the average environmentally controlled crack propagation rate $\bar{V}_t$ for passive alloys is related to oxidation charge density passed between film rupture events, Q_f:

$$\bar{V}_t = \frac{M}{n\rho F} Q_f \frac{1}{t_f} \tag{9}$$

Copyright © 2002 Marcel Dekker, Inc.

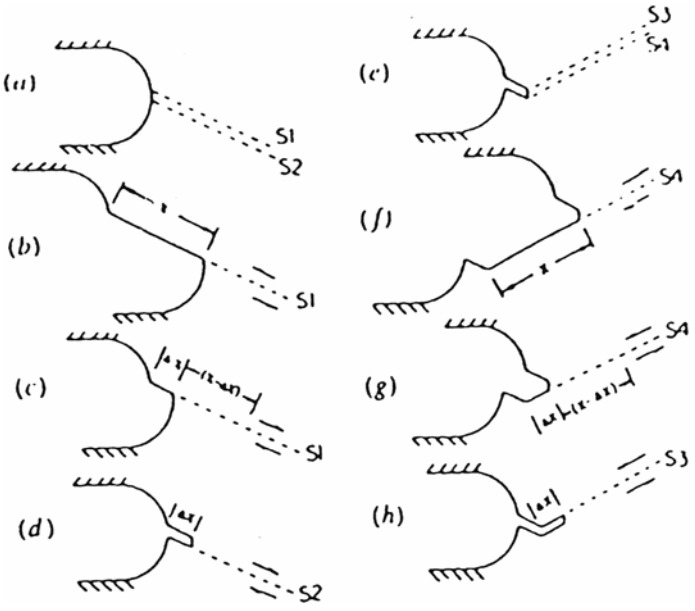


Figure 17 Schematic diagram of stage I corrosion fatigue crack propagation mechanism [21].

where t_f is the film rupture period. Thus:

$$\bar{V}_t = \frac{M}{n\rho F} Q_f \frac{\dot{\varepsilon}}{\varepsilon_f} \tag{10}$$

where $\dot{\varepsilon}$ is the strain rate and ε_f the strain for film rupture (about 10^{-3}).

If we take a classical law for current transients at the crack tip,

$$Q_f = i_0 t_0 + \int_{t_0}^{t_f} i_0 \left(\frac{t}{t_0}\right)^{-\beta} dt \tag{11}$$

Then, for $t_f > t_0$, $\beta > 0$,

$$\bar{V}_t = \frac{M i_0 t_0 \dot{\varepsilon}}{n\rho F(\beta - 1)\varepsilon_f} \left[\beta - \left(\frac{\dot{\varepsilon} t_0}{\dot{\varepsilon}_f}\right)^{\beta - 1}\right] \tag{12}$$

Even if mechanical analyses give good approximations for $\dot{\varepsilon}$ at the crack tip, some problems still remain with the previous equation. In particular, the value of β evolves all along cycling. But the main effect is related to the localized corrosion-deformation described previously. It has been shown that vacancy generation at the crack tip due to localized dissolution can induce cyclic softening effects and that hydrogen absorption, which can also be coupled to localized dissolution, can also enhance the local cyclic plasticity. This is why improvement of CF predictive laws is needed even if V_t can be adjusted in the equation, which is still very useful. New models based on the description of Figure 17 but taking into account the localized corrosion deformation processes are under study.

Copyright © 2002 Marcel Dekker, Inc.

Moreover, films related to solid-state oxidation ($M + H_2O \rightarrow MO + 2H^+ + 2e^-$) can also play a role in the crack advance. This needs further studies to be quantitatively more relevant [22].

Hydrogen Effects

Hydrogen-assisted cracking is often invoked, particularly for body-centered cubic (bcc) materials but also together with anodic dissolution for fcc alloys. Figure 18 shows schematically a hydrogen-assisted cracking event. Interactions between a discretized dislocation array and the crack tip under an applied stress produce a maximum stress field from behind the tip. When the hydrogen concentration reaches a critical value, a microcrack is nucleated because either the local cohesive strength is reduced or dislocation motion is blocked in the hydrogen-enriched zone, or both. The microcrack arrests about 1 μm ahead of the original location of the tip and these processes then repeat, leading to discontinuous microcracking.

Other mechanisms have been proposed, particularly the hydrogen-induced plasticity model for precipitates containing materials such as Al-Zn-Mg alloys. This model is shown in Figure 19 [5].

Absorbed hydrogen atoms weaken interactomic bonds at the crack tip and thereby facilitate the injection of dislocations (alternate slip) from the crack tip. Crack growth occurs by alternate slip at crack tips, which promotes the coalescence of cracks with small voids nucleated just ahead of the cracks. In comparison with the behavior in neutral environments, the CF crack growth resistance decreases as the

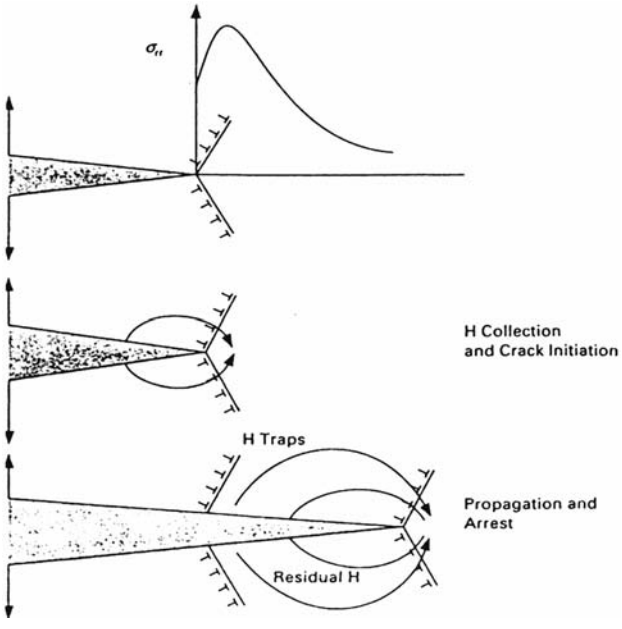


Figure 18 Schematic illustration of hydrogen-assisted cracking mechanism [22].

Copyright © 2002 Marcel Dekker, Inc.

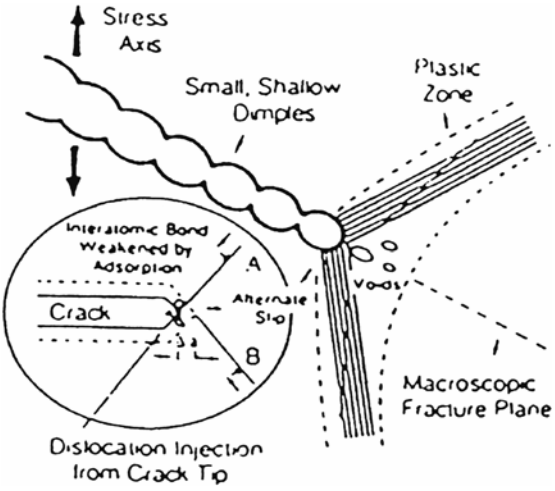


Figure 19 Schematization of the hydrogen-induced plasticity model for CF cleavage like cracking [5].

proportion of dislocation injection to dislocation egress increases. More closely spaced void nuclei and lower void nucleation strains should also decrease the resistance to crack growth in CF. This mechanism is proposed for Al-Zn-Mg alloys and is highly supported by observations that environmentally assisted cracking can occur at high crack velocities in materials with low hydrogen diffusivities and that the characteristics of cracking at high and low velocities are similar.

Other hydrogen-dislocation interactions at the corrosion fatigue crack tip must be taken into account. One can show, for instance, that hydrogen promotes planar slip in fcc materials. Cross-slip ability can be discussed for the peculiar situation of the dissociation of a perfect screw dislocation into two mixed partials separated by a stacking fault ribbon (Fig. 20). The cross-slip probability depends on the work necessary for recombination.

Each partial is subjected to two forces: the repulsion due to the other partial and the attraction due to the stacking fault ($\Gamma \simeq 100$ mJ/m^2 in nickel, for instance). In the absence of an external stress, the partials are in equilibrium at a distance where the two forces annihilate.

Hydrogen interacts only with the edge parts of the partials (hydrostatic stresses). It migrates to the tensile zone of the edge parts, as shown in Figure 20 from an initial concentration C_0 (for calculations, see Ref. 23).

The dilatation strains due to the antisymmetric hydrogen distribution induce a net shear component along the dislocation line, whose sign is opposed to that of the edge dislocation. Because the Burger's vectors of the two edge parts of the partials have opposite sign, hydrogen segregation will induce a supplementary effect, which is to reduce their normal attraction. From the viewpoint of the mixed partials, the repulsion between the screw parts is the leading term, and hydrogen induces a supplementary repulsion by "screening" the attraction between the edge components.

This screening of the pair interactions between coplanar edge dislocations was shown to be independent to the first order on the distance between dislocations [23], provided that diffusion time and temperature allowed the hydrogen distribution to

Copyright © 2002 Marcel Dekker, Inc.

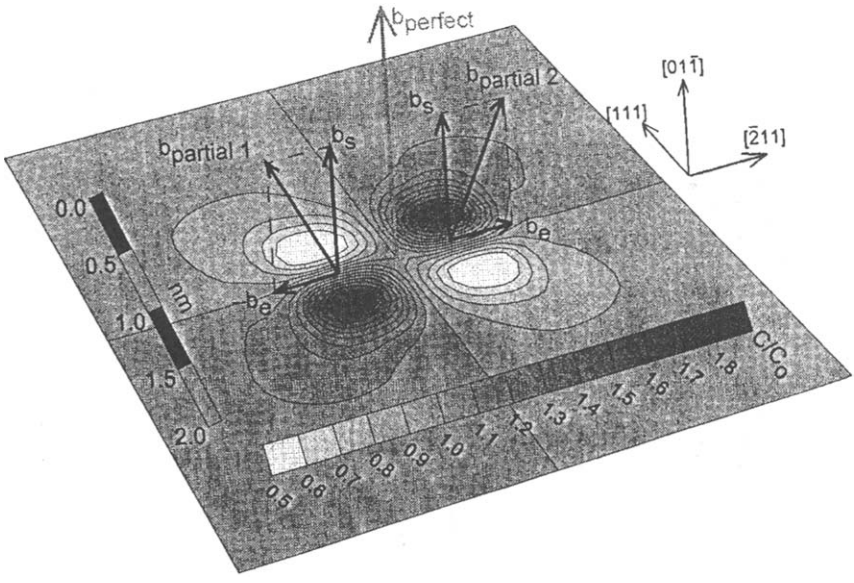


Figure 20 Equilibrium hydrogen distribution around a dissociated screw dislocation in nickel (C_0 is the initial concentration of hydrogen).

reach a configuration "in equilibrium with the local stress." Under these conditions, the relative screening of the pair interactions (i.e., the "hydrogen component" of the resolved shear stress normalized by that of the dislocation itself) was shown by numerical simulations to be given with excellent accuracy by the following simple expression [23]:

$$A(C_0, T) = \frac{75\%}{1 + \beta(T/C_0)} \quad \text{with} \quad \beta = \frac{9(1-\nu)RV_M}{2EV^{*2}} \tag{13}$$

where C_0 is the remote hydrogen concentration (in atom fraction); T is the absolute temperature; R is the gas constant; E, ν, and V_M are Young's modulus, Poisson's ratio, and the molar volume of the host metal; and V^* is the hydrogen partial molar volume. The coefficient β contains all the material parameters that influence the hydrogen screening effect as a function of temperature and concentration. In nickel, $\beta = 2.34 \times 10^{-4}\ K^{-1}$. Using this expression for the dissociated configuration of Figure 20, Figure 21 shows the forces on one partial versus the width of the stacking fault ribbon in nickel for an initial amount of hydrogen $n_H/n_{Ni} = 0.05$ at room temperature. The d_0 and d_H are respectively, the equilibrium distances in the absence and in the presence of hydrogen, neglecting a possible decrease of Γ. The recombination work is represented by the hatched areas between the curves. In the presence of hydrogen at concentration $C = 0.05$, calculations show that the recombination work is increased by 50%. The elastic effect of hydrogen is to increase the recombination work and then to decrease the cross-slip ability. This confirms experimental studies that show that hydrogen promotes planar glide [24].

Finally, it must be said that very often anodic dissolution and hydrogen effects must both be taken into account.

Copyright © 2002 Marcel Dekker, Inc.

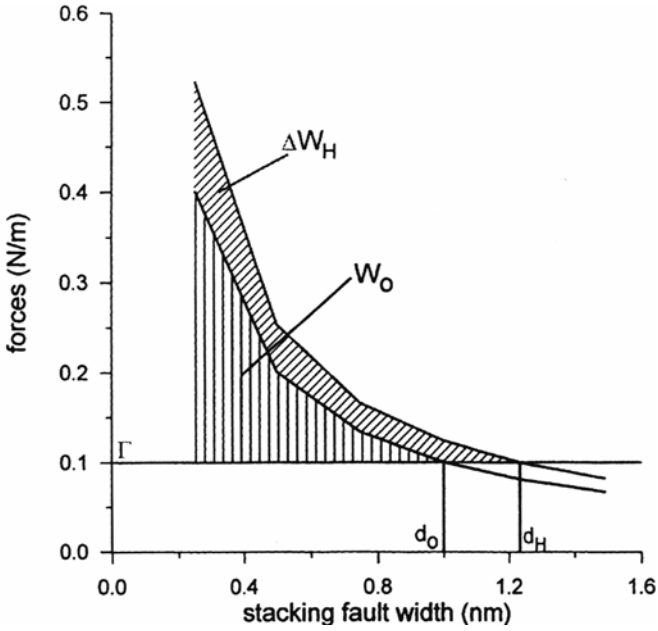


Figure 21 Effect of hydrogen on the work of recombination of partials in nickel at 300 K.

MONTE CARLO-TYPE SIMULATIONS OF CORROSION FATIGUE LIFETIMES FROM THE EVOLUTION OF SHORT SURFACE CRACKS

Introduction

The modeling of fatigue and corrosion fatigue damage is still not completely solved. Its definition is controversial, and it depends on the scale of interest in the study. The high-cycle fatigue regime was first investigated, and it has been summed up as due to the propagation from scratch of a single crack leading eventually to fracture [25,26]. Hence, an equivalence between the level of damage and the fatigue crack depth was considered [27]. In this case, fatigue damage accumulation corresponds to the bulk growth rate of one crack. Those speculations have proved to be both successful and satisfactory.

The next step aimed at extending the latter definitions from high- to low-cycle fatigue. However, as multiple cracks nucleate and propagate simultaneously in low-cycle fatigue, the previous definitions of both fatigue damage and fatigue damage accumulation are ambiguous. The majority of cracks are comparable to each other from a surface length viewpoint. Moreover, all crack lengths are comparable to grain size throughout all the fatigue lives.

On the one hand, the mechanical approach describes the behavior of long through-cracks in a macroscopically elastic field [7,25]. It has given interesting empirical laws but is unable to take into account the physical processes of fatigue damage. On the other hand, the microscopic approach was developed with the analysis of the dislocation behavior, the corresponding strain hardening or softening effects, and the formation of persistent and intense slip bands [28,29]. Nevertheless,

Copyright © 2002 Marcel Dekker, Inc.

this approach is generally limited to the formation of the first microcracks: the corresponding physical and numerical models concern only the first 10% of the fatigue lifetime for polycrystalline materials. Moreover, when applied to crack propagation, the microscopic approach does not take into account the influences of other formed cracks. Thus, the classical mechanical and microscopic approaches cannot be used to model the evolution of a population of surface cracks and the corresponding low-cycle fatigue damage.

In this section an investigation of the fatigue damage process at an intermediate scale (i.e., a mesoscopic scale corresponding to the grain size) is addressed. The importance of the latter scale to modeling low-cycle fatigue lifetimes is pointed out through the physical analysis of fatigue damage and of fatigue damage accumulation. Particular attention is paid to the evolution of populations of surface short cracks. Experimental results mainly correspond to push-pull low-cycle fatigue tests of 316L stainless steel in air and in 3% NaCl solutions. From these results and from assumptions concerning surface short crack behavior, a numerical model is developed. Monte Carlo principles are used to deal with random crack nucleation and crack interactions. It is finally shown that such an analysis is very relevant to prediction of corrosion fatigue lifetimes of austenitic stainless steels in chloride solutions.

Physical Description of the Fatigue Damage

The experimental results on the low-cycle fatigue damage of 316L stainless steel have been fully discussed elsewhere [30,31]. Transgranular cracking is generally observed in the 316L polycrystalline stainless steel for fully reversed push-pull tests at intermediate plastic deformation amplitudes ($\Delta\varepsilon_p/2$ in the range [5×10^{-5}, 5×10^{-3}], the plastic deformation rate being 10^{-3} s^{-1}).

Multiple short cracks are observed at the specimen surface. Different surface short crack types are introduced according to both cracking behavior and surface lengths. Surface short cracks, the lengths of which are less than one grain size (i.e., less than 50 μm, which is the average grain size in the case of classical 316 alloy), are the more numerous ones. Every crack propagates first crystallographically, i.e., within the intense slip bands. The first main obstacles to their propagation are the grain boundaries. The closer to the grain boundary, the lower the crack growth rate [30,32]. Once the grain boundary is crossed, the propagation speeds up to the next grain boundary. It has been observed experimentally that two to three grain boundaries need to be crossed for the change of cracking behavior to take place. Surface crack propagation evolves from crystallographic to "mechanical" growth. The surface cracks are then observed to grow perpendicular to the specimen axis (likely to be related to the onset of the so-called stage II cracking). The preceding cracking process leads to distinction of three main categories of surface short cracks.

Type I cracks have a surface length less than one grain size. Type II cracks are longer than one grain size at the surface but smaller than three (two to three grain boundaries have been overcome by the surface short crack). Type III crack surface length goes from 3 up to 10 grain sizes. A fourth type concerns cracks longer than 10 grain sizes at the surface. The latter cracks are numbered in the range 1 to 3 per specimen and form during the last 10% of the fatigue lifetime, following completion of N_i cycles. N_i corresponds to the number of cycles to form the type IV short crack. It is about 90% of the fatigue lifetime [30,31].

Copyright © 2002 Marcel Dekker, Inc.

The type I crack population evolves in three steps following a first hardening of samples, which needs 5 to 10% of the reduced lifetime (N/N_i). The first step consists of numerous nucleations of new cracks and leads to a surface density of approximately 50 type I cracks per mm^2 in less than 25% of the reduced lifetime. Crossing of the grain boundary corresponds to a second step during which the new crack nucleation rate decreases by two thirds. A few type II cracks form. This step extends up to 60 to 70% of the reduced lifetime N/N_i. The type I crack density reaches about 70 cracks per mm^2. This is the highest type I crack density during the test. Stage III of the damage process corresponds to the remaining lifetime. There is a speeding up of damage accumulation. Numerous type II cracks form while the type I crack population decreases by a half (final density is about 40 cracks per mm^2). Their interactions and their surface propagation lead to generation of type III cracks. Two to three type IV cracks are eventually formed for the total specimen surface and propagate into the bulk, leading to rupture.

High short crack density and competitive growth of the multiple surface short cracks during more than 90% of lifetimes suggest a random process to form a fatal crack. High surface crack densities have been reported on other materials submitted to fatigue tests [33–35]. Randomness must occur during both surface crack nucleation and propagation. Consequently, crack interactions are likely to be unpredictable one by one. As fatigue damage results from a combination of these mechanisms (i.e., nucleation, propagation, and interactions), the usual approach of fatigue through a single crack growth relation is unsatisfactory. As a matter of fact, this approach does not take into account the effect of crack densities and hence the statistical aspect of fatal crack formation.

A result [33,34] has been achieved emphasizing both the importance of the statistical aspect of the fatigue damage accumulation and the role of type I surface short cracks. An accumulation of elementary damage events, the cracking of a single grain, was assumed and was shown to be successful in deducing the Coffin-Manson relationship using the statistical physics of disordered systems.

A few numerical models have been developed to take into account the developments and the interactions of surface short crack populations [34,36]. The next paragraph briefly presents results of such modeling.

Numerical Modeling

The simulation has been developed according to the statistical aspect of the physical damage accumulation process. Surface short cracks nucleate at random. Their subsequent propagation is not continuous from a time viewpoint. Hence, a random treatment was chosen to deal with both nucleation and propagation mechanisms. Moreover, only surface data are taken into account because surface fatigue damage dominates over 80% of the fatigue lifetime in low-cycle fatigue. The modeling therefore belongs to a 2D Monte Carlo type [36].

Figure 22 shows predictions of crack density evolutions with statistical scatter. Moreover, the simulations help to plot major crack developments. Figure 23a illustrates the fatal crack evolutions. Interestingly, for $\Delta\varepsilon_p/2 = \pm 4 \times 10^{-3}$, the curve clearly exhibits multiple coalescence even for crack length of the order of two grain sizes (i.e.. 100 μm). The coalescences lead to significant increases of surface lengths. Note the absence of those sharp increases in Figure 23b for $\Delta\varepsilon_p/2 = \pm 4 \times 10^{-4}$.

Copyright © 2002 Marcel Dekker, Inc.

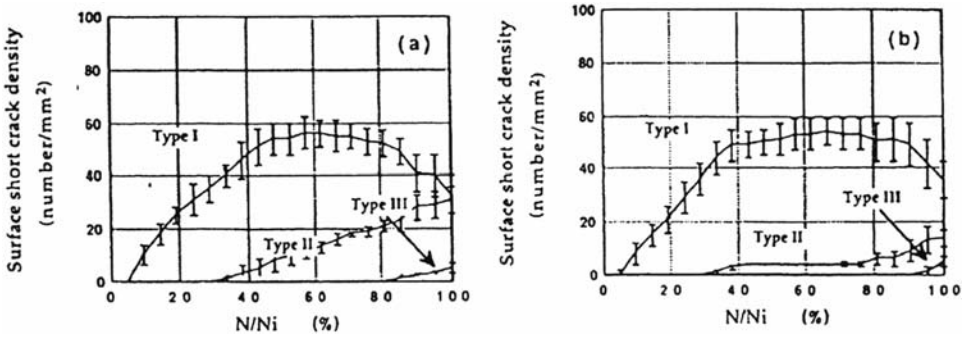


Figure 22 In-air test simulations. Surface short crack density vs. N/N_i at (a) a plastic strain amplitude of 4×10^{-3}, $N_i = 6800 \pm 800$ cycles and (b) a plastic strain amplitude of 4×10^{-4}, $N_i = 250{,}000 \pm 35{,}000$ cycles. Scatter is calculated from several computations.

More results are detailed elsewhere [36]. For example, Table 1 compares a few experimental lifetimes with the corresponding simulation results.

Furthermore, the three short crack type densities correlate well. Also, the screen display of the simulated specimen surface shows similar patterns of crack spatial distribution (Figs. 23 and 24).

Finally, the relevance of the mesoscopic scale considered in the present study (i.e., the grain size) can be emphazised when predicting the corrosion fatigue behavior of 316L alloys in a 3.5% NaCl solution under free potential. In the corrosive solution the fatigue lifetime decreases by a factor of 2 for an applied plastic strain $\Delta\varepsilon_p/2 = \pm 4 \times 10^{-3}$ [11]. In this case the localized anodic dissolution at the slip band emergence increases mainly the number of nucleation sites, the surface micro-propagation threshold (particularly to cross the grain boundaries), the kinetics of surface propagation, and then the formation of the fatal crack. The experimental evolution of the short crack densities is shown in Figure 25a. It must be noted that the evolution of type I, II, and III crack populations is homologous to its evolution

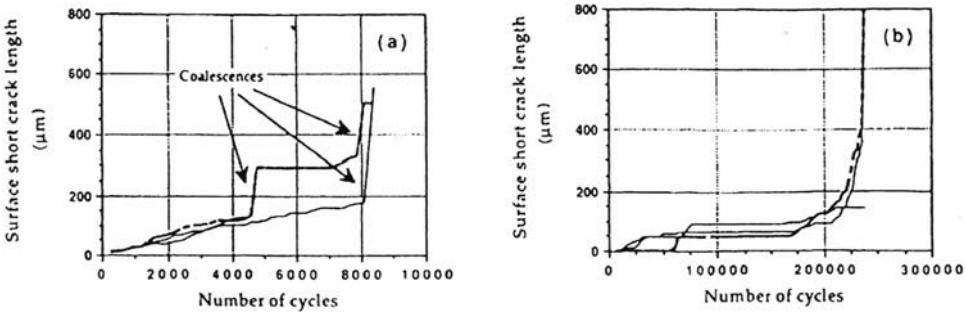


Figure 23 In-air test simulations. Major crack development vs. the number of cycles. (a) $\Delta\varepsilon_p/2 = \pm 4 \times 10^{-3}$ and (b) $\Delta\varepsilon_p/2 = \pm 4 \times 10^{-4}$. Coalescence mechanisms participate strongly in formation of a fatal crack at $\Delta\varepsilon_p/2 = \pm 4 \times 10^{-3}$.

Copyright © 2002 Marcel Dekker, Inc.

Table 1 Comparison of Experimental and Fatigue Lifetimes (316L Alloy at $\dot{\varepsilon} = 10^{-3}$ s^{-1})

	$\Delta\varepsilon_p/2 = \pm 4 \times 10^{-4}$		$\Delta\varepsilon_p/2 = \pm 2 \times 10^{-3}$		$\Delta\varepsilon_p/2 = \pm 4 \times 10^{-3}$	
Experimental lifetime (cycles)	268,000		19,250		7,500	
Modeling prediction (cycles)	250,000	38,000	16,440	1,800	6,800	950
		Standard scatter		Standard scatter		Standard scatter

for in-air tests when referring to N/N_i. The simulation (Fig. 25b) shows satisfactory agreement with experiments. A very interesting tool for corrosion fatigue prediction, based on the effect of the corrosive solution at the mesoscopic scale, is then available. This is new in this field. Other effects of a corrosive solution (such as pitting) can now be introduced in the software to simulate other possible corrosion fatigue mechanisms in metal and alloys.

Finally, such Monte Carlo treatment has been successfully applied to other fcc single-phase materials [37].

INTERACTIONS WITH STRESS CORROSION CRACKING (SCC)

It is well known that SCC can interfere with corrosion fatigue during crack propagation (Fig. 13). But this interaction also occurs for crack initiation and crack propagation near the threshold, as illustrated in Figure 3 for an fcc Fe-Mn-Cr alloy cyclically deformed at low strain rate in a Cl^- solution and in Figure 8 for Al-Li alloys in 30 g/L NaCl. On the fracture surface of the Fe-Cr-Mn alloy, a crack initiates from a pit (which is favored by fatigue processes) by SCC with a cleavage-like process that has been described in detail elsewhere [22]. Then fatigue and corrosion fatigue take place with classical striations. Finally, it must be noted that the distinction between stress corrosion cracking and fatigue cracking is not always easy to make because SCC can also be discontinuous (see the mechanisms in Ref. 22) with crack arrest markings very similar to fatigue ones. Thus, combination of pure SCC and fatigue mechanisms is often possible during corrosion fatigue damage.

CF can sometimes be more dangerous than SCC because it occurs whatever the strain rate is. This is illustrated in the case of a 7020 Al-Zn-Mg alloy for two different heat treatments, T4 (underaged) and T6DR (peak aged). Figure 26 compares the SCC behavior through the ratio between the elongation to fracture in 30 g/L NaCl and the elongation in air for tensile tests at an imposed strain rate with the CF behavior at a given applied plastic strain $\Delta\varepsilon_p/2 = 10^{-3}$, for different strain rates. One can see that, whatever the strain rate, CF always occurs, unlike SCC, which takes place only below a critical strain rate dependent on the heat treatment. Moreover, CF is affected by SCC below the critical SCC strain rate, as shown by the fact that crack initiation is intergranular only when SCC occurs.

Copyright © 2002 Marcel Dekker, Inc.

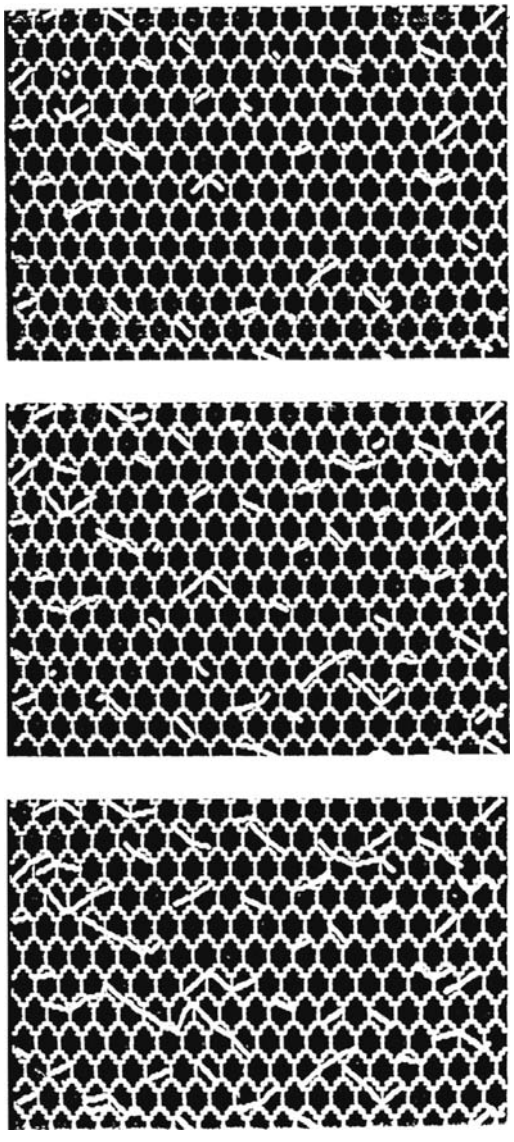


Figure 24 Screen display of modeling surface. $\Delta\varepsilon_p/2 = \pm 4 \times 10^{-3}$.

Nevertheless, cyclic loading is not always deleterious in regard to SCC. The example of cracking in alloy 600 for a pressurized water reactor (PWR) illustrates such behavior. Intergranular SCC is known to occur in the alloy 600/PWR system [38] when tests are performed on CT specimens for constant loading conditions with a stress intensity factor $K_I = 30$ MPa$\sqrt{m}$. The effect of cycling loading at a load ratio $R = 0.7$ with a triangular wave form at $K_{max} = 30$ MPav$\sqrt{m}$ is shown in Figure 27 according to the imposed frequency.

An increase in frequency induces a decrease of the crack growth rate and a transition from intergranular to transgranular cracking mode until air cyclic behavior becomes predominant.

Copyright © 2002 Marcel Dekker, Inc.

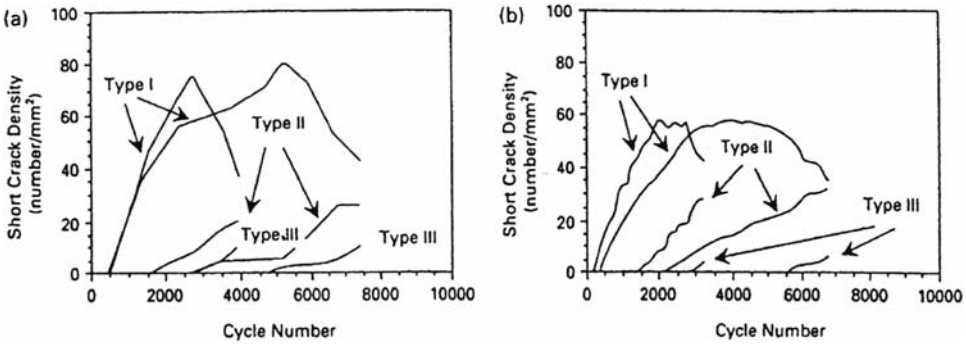


Figure 25 Influence of the environment on the evolution of type I, II, and III surface crack densities vs. the number of cycles (thick lines are for in-air test, thin ones for a 3.5% NaCl solution test). (a) Experimental data and (b) simulation results.

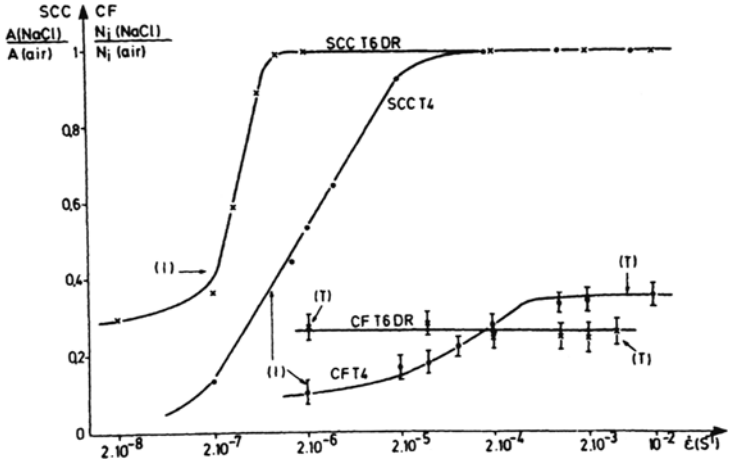


Figure 26 Comparison of SCC and CF (at $\Delta\varepsilon_p/2 = 10^{-3}$) behavior of a 7020 T4 and T6DR alloy at free potential in a 30 g/L NaCl solution. Crack initiation can be transgranular (T) or intergranular (I) according to the strain rate $\dot{\varepsilon}$.

This last example clearly shows that cycling can completely change the crack propagation mode when stress corrosion crack propagation is intergranular.

CONCLUDING REMARKS

The analysis of CF micromechanisms related to anodic dissolution and hydrogen effects is in progress but needs to be more quantitative through the localized corrosion-deformation interactions. The trends for future research are mainly related to:

Copyright © 2002 Marcel Dekker, Inc.

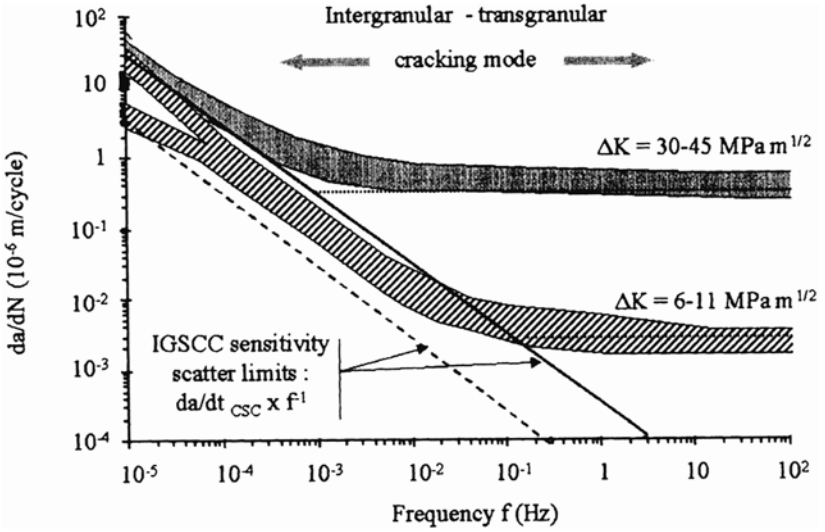


Figure 27 Crack growth rates versus frequency during CF and SCC on CT alloy 600 specimens in a PWR environment [38].

1. The modeling of crack tip chemistry
2. The quantitative analysis of corrosion-deformation interactions at the CF crack tip (scale of 1 μm) according to the electrochemical conditions
3. A comparison between CF and SCC based on a detailed analysis of micro-mechanisms near the fatigue threshold
4. Development of numerical simulations at mesoscopic scales.

These studies are needed to propose predictive laws for CF damage increasingly based on physicochemical controlling factors.

REFERENCES

1. C. Laird and D. J. Duquette, *Corrosion Fatigue,* NACE, New York, 1972, p. 82.
2. C. Patel, *Corros. Sci. 21*:145 (1977).
3. (a) R. P. Wei and G. W. Simmons, *Int. J. Fract. 17*:235 (1981); (b) J. Congleton, J. H. Craig, R. A. Olich, and R. N. Parkins, *Corrosion Fatigue, Mechanics, Metallurgy, Electrochemistry and Engineering*, ASTM 801 (T. W. Crooker and B. W. Leis, eds., ASTM, Philadelphia, 1983, p. 367.
4. R. P. Gangloff and D. J. Duquette, *Chemistry and Physics of Fracture* (R. Latanision, ed.), Nijhoff, Dordrecht, 1987, p. 612.
5. S. P. Lynch, *Acta Metall. 36,* L10:2639 (1988).
6. R. O. Ritchie and J. Lankford, *Small Fatigue Cracks,* TMS-ASME, 1986, p. 33.
7. K. J. Miller and E. R. de Los Rios, *The Behaviour of Short Fatigue Cracks,* EGF1, Mech. Eng. Pub., London, 1986.
8. M. Mueller, *Metall. Trans. 13A*:649 (1982).
9. B. D. Yan, G. C. Farrington, and C. Laird, *Acta Metall. 33*:1593 (1985).
10. T. Magnin and L. Coudreuse, *Acta Metall. 35*:2105 (1987).
11. T. Magnin and J. M. Lardon, *Mater. Sci. Eng. A 104*:21 (1988).

Copyright © 2002 Marcel Dekker, Inc.

12. P. Scott and R. A. Cottis, *Environment Assisted Fatigue,* EGF/MEP, London, 1990.
13. G. Henaff and J. Petit, *Corrosion Deformation Interactions CDI'92* (T. Magnin ed.), Les Editions de Physique, Paris, 1993, p. 599.
14. L. Hagn, *Mater. Sci. Eng. A 103*:193 (1988).
15. R. Akid, *Env. Degradation of Eng. Materials,* Vol. I, Technical Univ. Gdansk and Univ. Bordeaux 1, 1999, p. 112.
16. A. Navarro and E. R. de Los Rios, *Fat. Fract. Eng. Mater. Struct. 11*:383 (1988).
17. W. Zhang and R. Akid, *Fat. Fract. Eng. Mater. Struct. 20*:167 (1997).
18. P. D. Hobson, M. W. Brown, and E. R. de Los Rios. *The Behaviour of Short Fatigue Cracks* (K. J. Miller and E. R. de Los Rios, eds.), EGF1, London, 1986, p. 441.
19. A. Turnbull, *Corrosion sous contrainte* (D. Desjardins and R. Oltra, ed., Les Editions de Physique, Paris, 1990, p. 79.
20. C. J. Van der Wekken, *Corrosion Deformation Interactions CDI'96* (T. Magnin, ed.), Institute of Materials, London, 1997, p. 76.
21. C. Fong and D. Tromans, *Metall. Trans. 19A*:2765 (1988).
22. T. Magnin, *Advances in Corrosion Deformation Interactions,* Trans Tech, Zurich, 1996 (see p. 126, with reference to Gerberich et al., Parkins Symposium, TSM, 191, 1992).
23. D. Delafosse, J. P. Chateau, and T. Magnin, *J. Phys. IV 9*:251 (1999).
24. J. P. Hirth and J. Lothe, *Theory of Dislocations, Krieger Publications, Miami, Florida,* 1992.
25. P. C. Paris and F. Erdogan, *J. Basic Eng. Trans. AIME D 85*:528, (1963).
26. B. Tomkins, *Philos. Mag. 18*:104 (1968).
27. K. J. Miller, *Fatigue Eng. Mater. Struct. 5*:223 (1982).
28. T. Magnin, J. Driver, J. Lepinoux, and L. P. Kubin, *Rev. Phys. Appl. 19*:467 (1984).
29. H. Mughrabi, F. Ackermann, and K. Herz, *Fatigue Mechanisms,* ASTM STP 675 (J. T. Fong, ed.), ASTM, Philadelphia, 1979, p. 69.
30. T. Magnin, L. Coudreuse, and J. M. Lardon, *Scr. Met. 19*:1487 (1985).
31. C. Ramade, thesis, St Etienne, 1990.
32. K. J. Miller, H. J. Mohammed, and E. R. de Los Rios, *The Behaviour of Short Fatigue cracks* (K. J. Miller and E. R. de Los Rios, eds.), Mech. Eng. Pub., Sheffield, 1986, p. 491.
33. Y. Brechet, T. Magnin, and D. Sornette, *Acta Metall. Mater. 40*:2281 (1992).
34. A. Bataille, T. Magnin and K. J. Miller, *Short Fatigue Cracks* (K. J. Miller, ed.), Sheffield, Esis 13, Mech. Eng. Pub., 1997.
35. J. Weiss and A. Pineau, *Low-Cycle Fatigue and Elasto-Plastic Behaviour of Metals* (K. T. Rie, ed.), Elsevier Applied Science, Amsterdam, 1993, p. 82.
36. A. Bataille and T. Magnin, *Acta Metall. Mater. 42*:3817 (1995).
37. A. Bataille, thesis, University of Lille, 1992.
38. C. Bosch, M. Puiggalli, and J. M. Olive, *Corrosion Science,* to be published.

Copyright © 2002 Marcel Dekker, Inc.

14

Corrosion Prevention by Adsorbed Organic Monolayers and Ultrathin Plasma Polymer Films

Michael Rohwerder, Guido Grundmeier, and Martin Stratmann
Max-Planck-Institut für Eisenforschung GmbH, Düsseldorf, Germany

INTRODUCTION

Traditionally, corrosion protection of many reactive materials is associated with organic coatings, which are applied as thick multilayer films with thicknesses ranging from some 10 μm to some 100 μm. However, increasing interest exists in thin and ultrathin corrosion protecting films. This is particular true for modern areas of materials research such as microelectronic devices or micromechanics. In both cases, any corrosion protecting film must be much less than 0.1 μm in thickness and frequently even monolayer films are wanted. However, even for conventional materials such as steel, galvanized steel, or Al-based alloys, thin film coatings are of considerable interest as frequently such films are generated with unusual properties by modern surface technology. For such applications the time scale for film preparation must be in the seconds range and many techniques allow only the preparation of thin films under those restrictions. Then the thin layer coating may serve as an inner film only with top coats prepared by conventional techniques. The possible role for the thin film then lies in corrosion protection as well as in adhesion promotion of the additional polymeric layers. This chapter will focus on two surface modification techniques: molecular self-assembly and plasma polymerization.

The corrosion rate of reactive metals can be reduced significantly by a modification of the metal surface by organic molecules or polymers. A well-known example is the corrosion protection by lacquers and other organic coatings [1–3], which is used in most practical applications to protect, e.g., cars against atmospheric corrosion, pipelines against corrosion in humid soil, and ships against corrosion in seawater. It has long been believed that the corrosion protection is due to the barrier properties of the coating, which impedes the penetration of water and oxygen [4] to the metal/polymer interface. However, many coatings are highly permeable for water and oxygen, and therefore it is not the barrier effect on the diffusion process that gives rise to the corrosion stability but the specific electrochemical properties of the metal/polymer interface, in particular the formation of an extended diffuse double

Copyright © 2002 Marcel Dekker, Inc.

layer [5–7]. In the presence of defects (pores, pinholes, etc.), which may penetrate through the coating, the diffusion barrier is lowered, and the delamination rate of the polymer at the defect is determined by the formation of galvanic elements [8–12]. In many circumstances, the local anode of this elements is the defect and the local cathode, at which predominantly oxygen is reduced, is given by the delamination frontier. In other cases—in particular for Al-based alloys—the galvanic element is just opposite and the delamination frontier is characterized by the local anode. In the first case the stability of the metal/polymer interface is determined by inhibition of the oxygen reduction at this interface, as during the electrochemical reduction of oxygen very aggressive species are liberated ($OH^{\cdot}$, OH^{-}), which will immediately attack and destroy chemical bonds within the polymer [13–16]. The corrosion inhibition of the coating therefore depends more on the composition, structure, and chemical bonds of the metal/polymer interface than on the thickness of the coating.

It is therefore desirable to improve the chemical interaction between the first monolayer of the coating and the substrate such that electrochemical reactions such as the reduction of oxygen are inhibited and the bonds may withstand the attack of water and other aggressive species such as $OH^{\cdot}$. Modern concepts are aimed at the development of "molecular adhesion promoters" (Fig. 1) [17–19], which will provide a link between the substrate and the organic coating. This model requires, however,

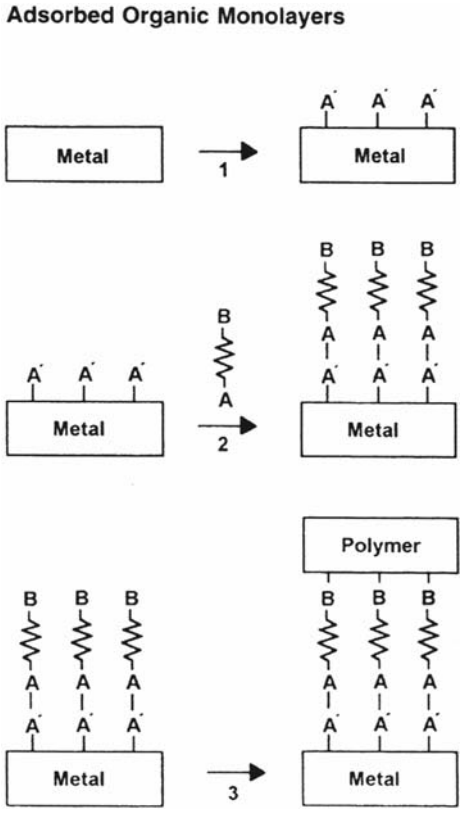


Figure 1 Principal scheme of the chemical modification of metal surfaces.

Copyright © 2002 Marcel Dekker, Inc.

that reactive centers are prepared on top of the metal substrate, which may serve as anchor sites for suitable functional groups of the organic molecules, as shown in Figure 1. The question is how to select reactive centers, organic molecules, and reaction conditions [20–25].

In order to do so, it is useful to study the relevant literature, which is concerned with organic molecules being used as corrosion inhibitors [26–29]. It is well known that many organic compounds are able to reduce the corrosion rate of metals significantly [30–34]. Inhibitors reduce the rate of either or both of the partial reactions of the corrosion process, the anodic metal dissolution and the cathodic oxygen reduction. Various inhibition mechanisms must be considered, taking into account the different situations created by changing, on the one hand, the chemical properties of the inhibitor and, on the other hand, the medium. The organic compounds may either be dissolved in the electrolyte (conventional inhibitors) or adsorbed onto the metal surface by condensation from the vapor phase (volatile corrosion inhibitors). From a mechanistic point of view [35], the inhibitors may change the composition of the medium (e.g., hydrazinium reduces the oxygen activity) or they may be enriched at the metal-medium interface. In the latter case they may enhance the formation of passive films on top of the substrate, such as benzotriazole on Cu [30,31] or benzoates on Fe (passivators), or they may form monomolecular adsorption layers and prevent the dissolution of the substrate and the reduction of oxygen by changing the potential drop across the interface and/or the reaction mechanism (interface inhibitors) [36]. The interaction between organic ions or dipoles and electrically charged metal surfaces may be purely electrostatic, due to the electric field at the outer Helmholtz plane of the electric double layer. A competitive adsorption between water dipoles and the monomer has to be considered, and water adsorption always takes over the adsorption of nonpolar monomers if the electrode potential is shifted far from the potential of zero charge (PZC), as then the surface is highly charged [37]. The adsorption of the monomer prevails in the vicinity of the PZC. Cations are adsorbed at potentials negative to PZC, anions at potentials positive to the PZC. Because of the dependence on the charge of the metal surface, the adsorption is not specific for certain metals.

The charge of the anions or cations may be constant but also may charge during adsorption. The number of electrons exchanged per adsorbed molecule is called the adsorption valence (typically less than 1) [38–40]. Because of the low activation energy, the adsorption based on pure electrostatic interaction is fast and reversible. If no electron transfer occurs, this kind of adsorption is frequently called physisorption. However, during adsorption an electron transfer between the substrate and the adsorbed molecule may occur with orbital overlap between a single pair of electrons of the adsorbed molecule (N, S, P) and empty bands of the solid. Strong interaction is then observed (chemisorption) and the adsorption itself is highly irreversible [41–43]. Chemisorption is slower than physisorption, and it requires a higher activation energy. In contrast to physisorption, it is specific for certain metals. Electron transfer is typical for transition metals having vacant low-energy *d*-electron orbitals. On the other hand, the inhibitor should have free single electron pairs, or π electrons. The higher the polarizability of the involved heteroatom, the stronger is the adsorption (Lewis acid-base concept). The inhibitor is then the electron donor and the metal is the electron acceptor. This is in agreement with the principle of soft and hard acids and bases (SHAB).

Copyright © 2002 Marcel Dekker, Inc.

It is clear from the situation just described that the latter situation is ideal for a stable chemical modification of the metal substrate and that molecules should be chosen that are able to interact strongly with the metallic substrate. However, there are some characteristic differences between corrosion inhibitors and molecular adhesion promoters: whereas for corrosion inhibition the composition and structure of the metal surface are defined by the corrosive medium, the surface properties can be changed and adjusted to the structure of the adhesion promoter. Inhibitors must be soluble in the electrolyte (e.g., water) and can be applied only for well-defined reaction conditions. Adhesion promoters, however, may be applied from aqueous or nonaqueous solvents or even from the gas phase and the reaction conditions can be optimized for the given substrate. Therefore, some characteristic molecular features of inhibitors such as heteroatoms S, P, and O should be incorporated into the structure of the adhesion promoter; however, the molecule itself should show minimum solubility in water and the possibility to bind a polymer onto the adhesion promoter.

In this chapter, only very simple molecules will be discussed. They are composed of one reactive center such as —SH, —$Si(OCH_3)_3$, or $PO(OH)_2$, which should be able to bind to the metal surface [20,21], and a long aliphatic chain (e.g., —$C_{18}H_{37}$), which allows ordering of the individual molecules and the formation of a dense packing on top of the substrate (self-organization) (see Fig. 2). We will discuss

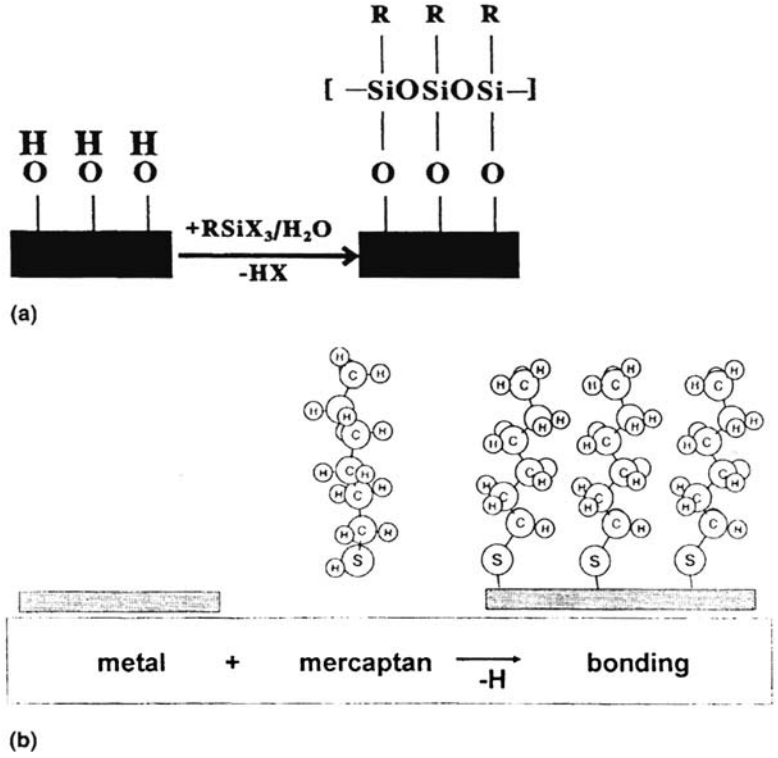


Figure 2 (a) Reaction of silanes with hydroxylated surface in humid atmospheres. (b) Reaction of mercaptans with metal surfaces.

Copyright © 2002 Marcel Dekker, Inc.

how these modified surfaces may be prepared, what kind of structure is observed, and how stable the modification is in aggressive electrolytes.

The preparation technique must fulfill certain requirements: the surface properties of the substrate, e.g., the density of chemisorbed OH groups, must be well defined and the organic monomer must be allowed to bind to the reactive centers of the surface without destroying the defined surface structure; the monomer itself should form a dense structure with a high degree of ordering so that the substrate surface is not accessible to water molecules.

Another method for the modification of metal surfaces by ultrathin organic films is plasma polymerization. Plasma polymerization, as a process technology for corrosion-resistant thin-film deposition, has been explored during the last 20 years. Plasma polymers can be deposited from an electric discharge containing organic or metal-organic molecules [44,45]. A glow discharge is formed by exposing a gaseous monomer at reduced pressure to an electric field. The monomer is fragmented in the discharge and the reactive intermediates generated polymerize on a substrate according to a special reaction mechanism [46,47]. The resulting films can be highly cross-linked and, depending on process parameters, show more inorganic or more organic properties; moreover, adhesion is excellent to most metal surfaces, i.e., the process is less specific to certain metals than is the case with molecular self-assembly, and deposition of ultrathin films is fast. The main disadvantage is that up to recently the process required a very low residual pressure; i.e., vacuum equipment was needed. Lately, plasma polymers have also been prepared under atmospheric pressure conditions.

ORGANIC MONOLAYER FILMS

Corrosion Protection by Self-Assembled Films

As outlined above, in order to improve the stability of the polymer/metal interface it is of utmost importance to find ways to prepare interfaces that have better ability to inhibit oxygen reduction and are less vulnerable to the products of oxygen reduction. One way is to use monolayers of bifunctional molecules as adhesion promoters. Ideally, such a molecule should form a tight chemical bond to the metal or metal oxide surface with its head group and to the polymer with its tails groups. The monolayer should be as dense as possible with as few defects as possible, for optimum stability and inhibition capability. Also, for technical application the formation of such monolayers should be quick, i.e., be finished within a few seconds.

The following paragraph will focus on electrochemical aspects of the self-organization and the resulting effect on the final defect structure. The discussion will distinguish between oxide-covered and oxide-free surfaces. The protective impact of the films will also be discussed.

In recent years the process of molecular self-assembly on solid surfaces, i.e., the adsorption and self-organized formation of highly ordered monolayers from monomers in solution, has received increasing interest, especially the self-assembly of thiols on gold [48]. As could be shown, thiol monolayers proved to be excellent inhibitors of oxygen reduction and moreover are not easily destroyed by the radicals set free during the oxygen reduction [49]. First tests on iron also gave promising results [50,51] although the preparation is not easy on this substrate.

Copyright © 2002 Marcel Dekker, Inc.

Because thiol molecules do not adsorb on iron oxide, the iron has to be electrochemically polarized to cathodic potentials in order to get rid of the oxide layer and then to keep it free of oxide during self-organization. The SA of BTA on copper was investigated by Magnussen and Behm [52]. Now, even though self-organization is the subject of hundreds of publications, up to very recently nothing has been known about the influence of the electrode potential and surface charge on the self-assembly process. For bare metal surfaces the surface charge is controlled by the electrode potential, for oxide-covered samples by the pH of the solution.

Self-Assembly on Oxide-Free Metal Surfaces

Thiol Self-Assembly on Gold The well-studied system thiol/Au is ideal for investigating the effect of the electrode potential on the kinetics of self-assembly and on the resulting defect structure.

A direct way to monitor the self-assembly in situ is to measure the decrease in capacitance of the immersed sample (see Fig. 3). The double layer at the metal/electrolyte interface is pushed apart by the growing monolayer, which causes a decrease of capacitance. Because an electrode's capacitance depends on the electrode potential, it is useful to normalize curves obtained for adsorption at different potentials, e.g., by referring the change in capacitance ΔC at the time t to the final capacity change ΔC_{max}. Such normalized curves for the adsorption at –400 and –800 mV versus a special Ag/AgCl reference electrode [19,53] in ethanol and typical nanoscopic structures of the films at different stages of the thiol self-assembly are shown in Figure 4. A detailed analysis of the curves yields the distinction of three characteristic potential ranges for thiol self-assembly [19,53].

An intermediate potential range from –400 to + 200 mV versus the Ag/AgCl reference electrode where the rate of self-assembly shows only a comparatively weak dependence on the electrode potential; scanning tunneling microscopy (STM) images of the completed films show basically the same features already known from the literature [54–62].

A cathodic potential range where the rate of self-assembly decreases significantly with increasingly cathodic potentials; STM images of the completed films show that the average domain size also increases, so that for adsorption at –800 or –900 mV the thiol domains fill whole terraces, even if the lateral size of these exceeds 100 or even 200 nm (Fig. 4).

An anodic potential range where there is a slight decrease in the rate of self-assembly with increasingly anodic potentials.

Whereas the film is finished to 95% within 10 s at potentials of –400 to +200 mV, yielding a film composed of domains with a lateral size of 10–20 nm, it takes thousands of seconds at very cathodic potentials for the domains to cover the surface, but the domains are much larger. A detailed analysis shows that the thiol adsorption is at least a two-step process: physisorption followed by chemisorption [53a]:

$$R{-}SH_{sol} \xrightarrow{phys.} R{-}SH_{ad}$$

$$R{-}SH_{ad} \xrightarrow{chem.} R{-}S{-}Au + H^+ + e^- \text{ (oxidation)}$$

Copyright © 2002 Marcel Dekker, Inc.

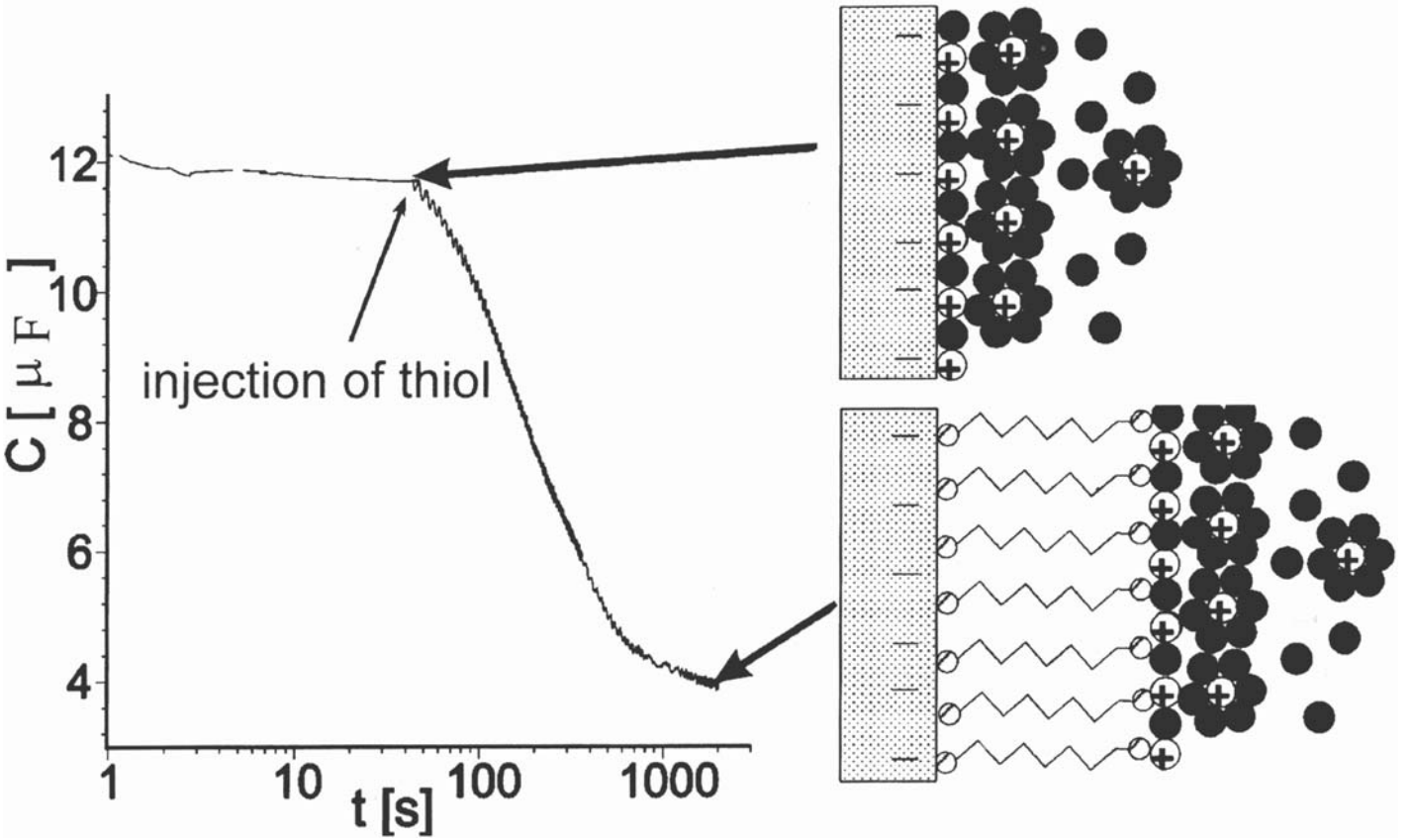


Figure 3 If the capacity of the gold surface is measured during thiol adsorption, a decrease in capacitance can be observed due to the pushing apart of the double layer by the adsorbing thiol.

Copyright © 2002 Marcel Dekker, Inc.

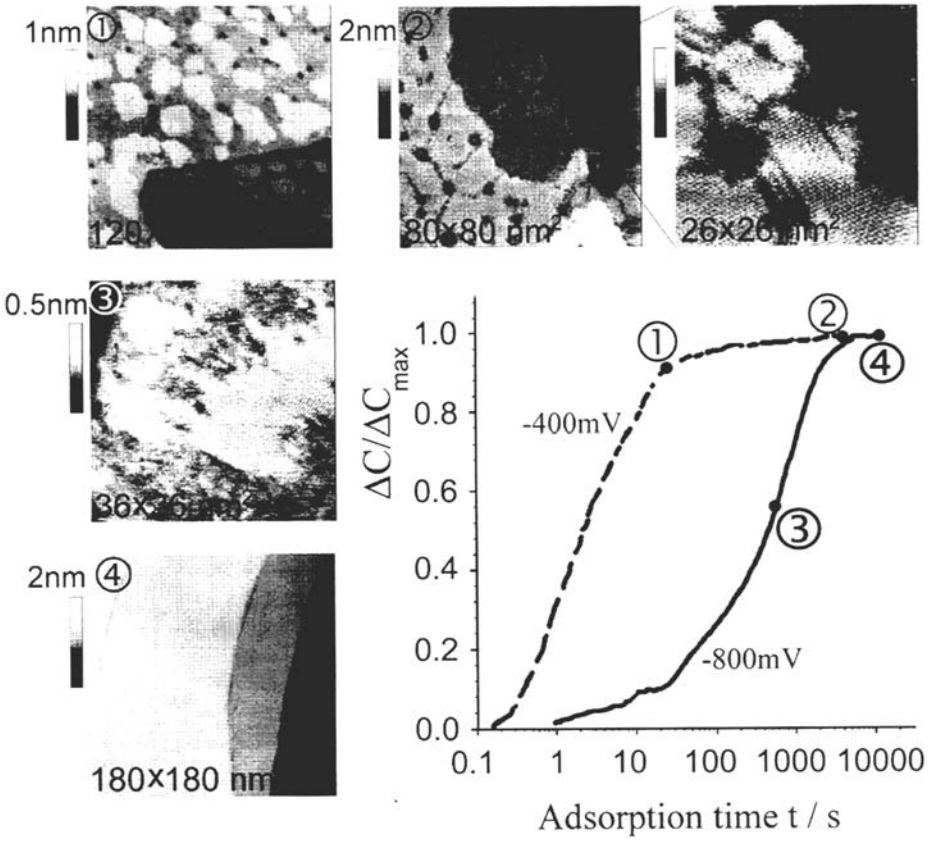


Figure 4 The normalized capacity curves clearly show that thiol (here decanethiol) self-assembly is much faster at intermediate potentials (here –400 mV) than at cathodic potentials (–800 mV). Typical STM images of the film structure are shown for different stages of self-assembly at the two potentials. At –400 mV, thiol self-assembly is fast and occurs via small individual domains (1), which sets the foundation for the final domain structure (2). At –800 mV, self-assembly is very slow and occurs via domains that are interconnected by molecular rows of chemisorbed thiol (3), and thus very large domains result in the final film (4).

It is the electrode potential dependence of the latter step that is responsible for the extreme slow-down in adsorption velocity at cathodic potentials.

Assuming a symmetry factor $\beta = 0.5$ (because of the symmetry of the system) and a complete charge transfer, it can be shown from the measured capacity curves that about 36% of the overall potential difference between the electrode and the solution occurs over the alkane chains; i.e., the longer the alkane chain, the smaller the slowdown effect at cathodic potentials. This could be shown for the adsorption of octadecylthiol as compared with decylthiol [53b].

Thiol on Iron For technical application this proves to be a problem, because adsorption times on the order of thousands of seconds are out of the question. In order to circumvent this problem, another coating technique has to be applied: the sample (the working electrode in the figure) is polarized to cathodic potentials to

Copyright © 2002 Marcel Dekker, Inc.

reduce the oxide layer and to prevent oxide formation during the coating process and then pulled through a thiol film, floating on top of the aqueous electrolyte [50,51]. In this way about 10-nm-thick multilayer films can be prepared, which show excellent blocking of oxygen reduction (see Fig. 5). It is quite obvious that the oxygen reduction is drastically limited on the modified surface and a much higher cathodic overpotential is necessary to reduce oxygen at significant rates. If oxygen is reduced, however, the film is destroyed by the radicals formed during oxygen reduction.

For adhesion promotion only the first monolayer will be effective. Because it proved not to be possible to prevent iron surface reoxidation completely while pulling the sample through the floating thiol film, and thus parts of the sample are not covered by chemisorbed thiols but by oxide, it is necessary to get rid of such defects in a second preparation step in order to improve the quality of the chemisorbed monolayer beneath the multilayer film. Immersing the as-prepared sample in aqueous solution and cycling the potential from the cathodic limit, where hydrogen evolution is beginning, through the potential range where iron is oxidized (peak in curves 1 and 2), and back for several times results in a healing of the disordered film (see Fig. 6), as can be seen from the decrease of the oxidation peak with increasing number of cycles. With each sweep into the potential range where iron oxide is reduced, bare iron is exposed at the defect sites to the thiol in the multilayer, and in the subsequent anodic sweep the thiol can at least partly be chemisorbed before reoxidation of the remaining bare iron surface sets in. Finally, all the surface is covered by chemisorbed thiol molecules. Then the modified sample is pulled out of the solution and the polymer coating is applied. Alternatively, the sample may be polarized at negative –800 mV. But then the healing process takes much longer (see Fig. 7a) because the thiol chemisorption at cathodic potentials is very slow (see earlier). Most of the multilayer thiol is dissolved into the polymer so that the first chemisorbed monolayer should perform its function as an adhesion-promoting layer.

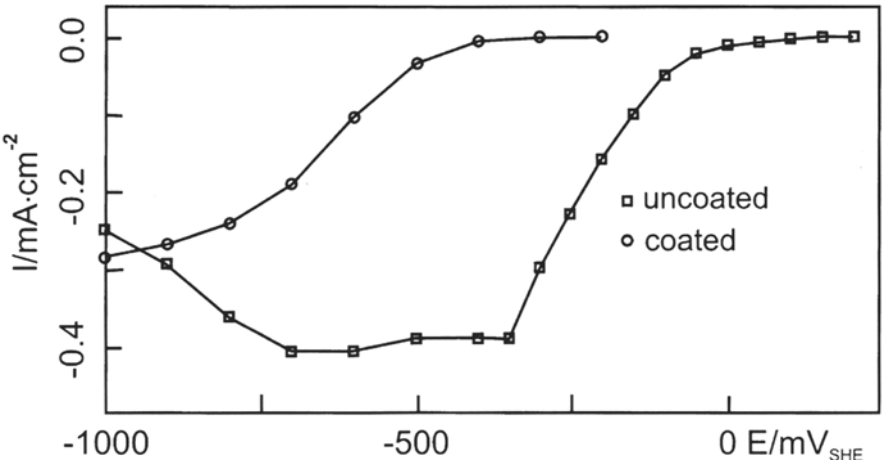


Figure 5 Rate of oxygen reduction on iron (○) and iron modified by one monolayer of *n*-decylmercaptan (□).

Copyright © 2002 Marcel Dekker, Inc.

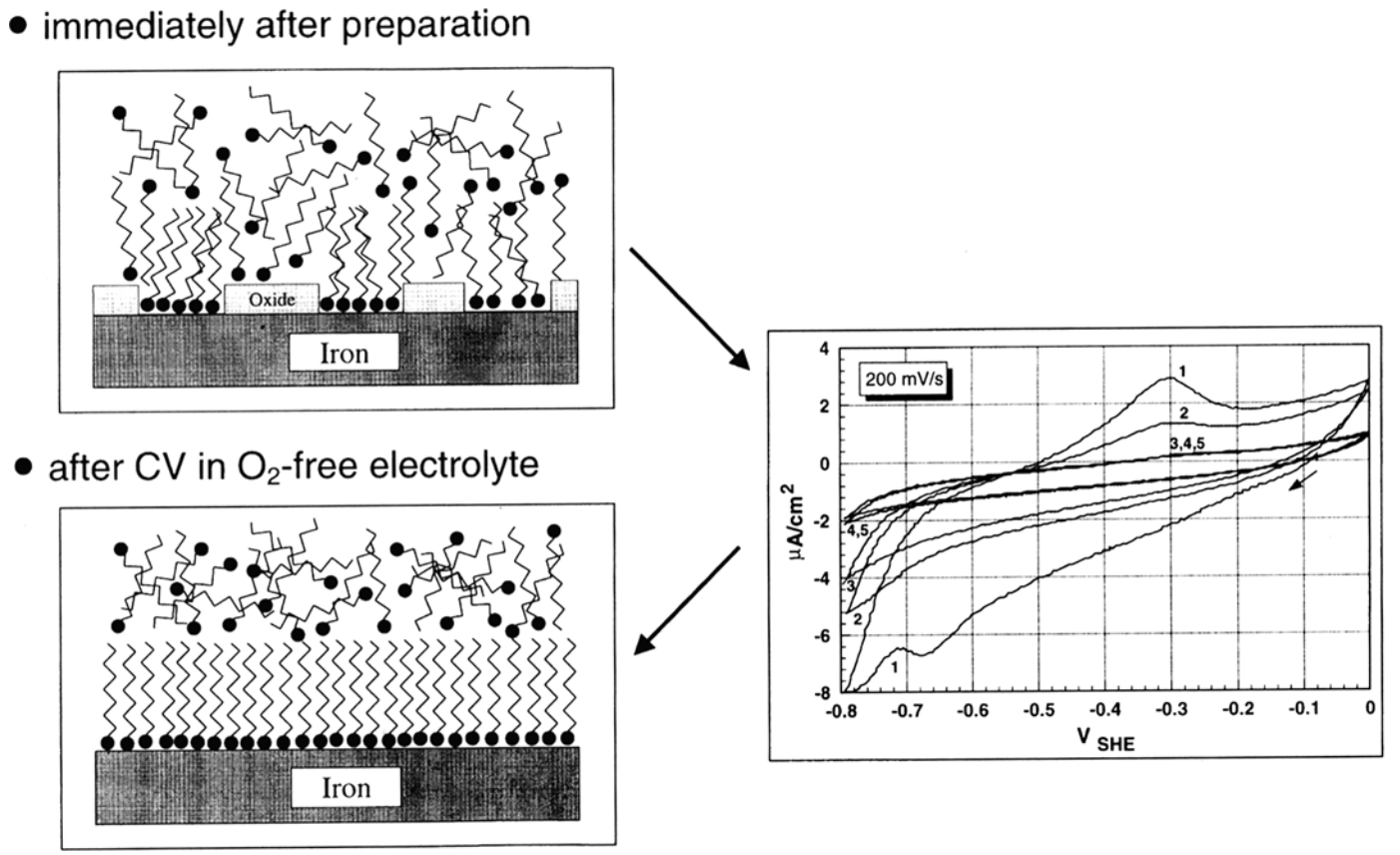


Figure 6 (Upper left) Model of a thiol multilayer on iron with remnants of oxide. After several cycles of the electrode potential (CV) in O_2-free electrolyte (right), the interface between thiol and iron is healed (lower left).

Copyright © 2002 Marcel Dekker, Inc.

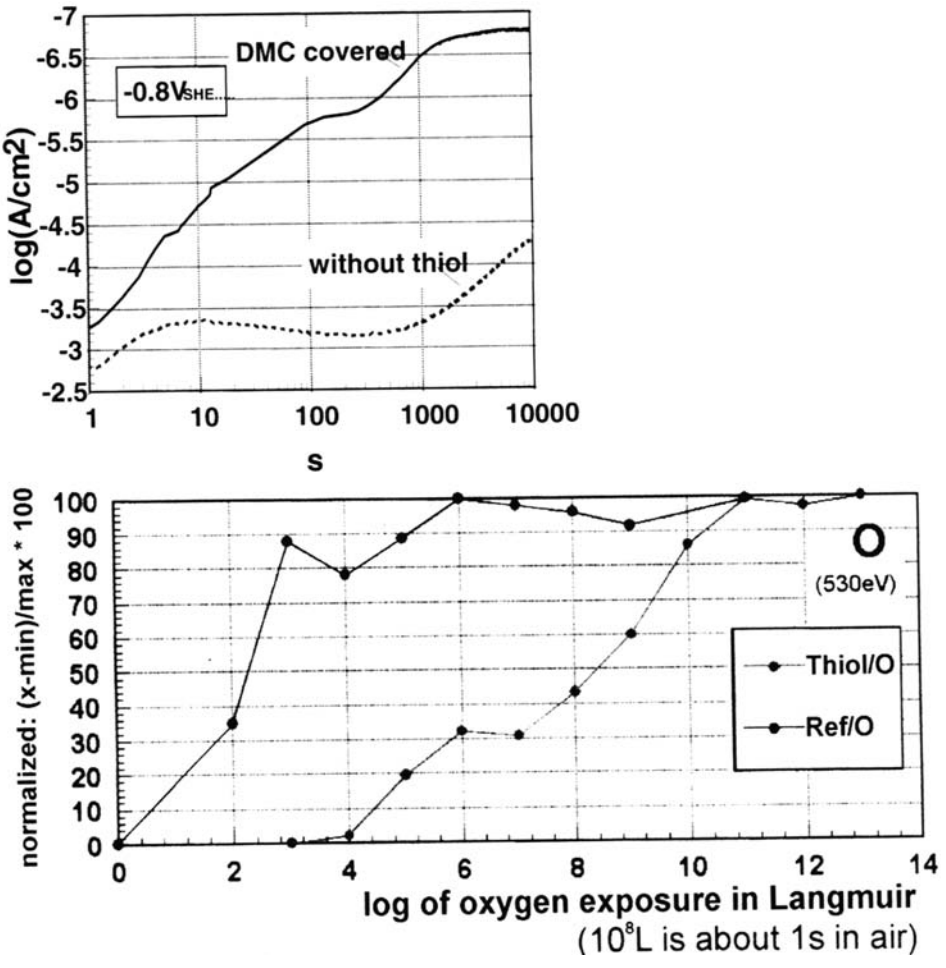


Figure 7 (a) Current observed during healing at –800 mV of a decanethiol monolayer compared with bare iron. (b) Normalized oxygen peak vs. oxygen exposure for thiol-covered iron in comparison with bare iron.

Scanning Kelvin probe mappings of a thus modified iron sample coated with a polymer show more than three times slower delamination kinetics. Still, a more pronounced effect is desirable for future applications.

Closer investigation shows that the bond between the first thiol monolayer and the metal surface is destroyed by reoxidation of the iron surface beneath the multilayer film within tens of seconds. Of course, this results in diminished ability of the layers to promote adhesion compared with what would be expected from an intact monolayer. This reoxidation is faster the thinner the multilayer film. For a monolayer film the reoxidation takes about 10s. That is an impressive factor of 10^6 to 10^7 slower than for bare iron, achieved by an only 1-nm-thick monolayer film, as can be seen from Figure 7b.

Copyright © 2002 Marcel Dekker, Inc.

A first step to find ways to improve this technique is a understanding of the reoxidation process, which is at the center of current research. Important parameters are chain length and functional groups of the thiol molecules. If the choice of more suitable thiols together with a more refined modification technique resulted in a thiol layer that survives even one order of magnitude longer in air, this could be an important breakthrough, because then the polymer coating could be applied before most of the thiol film is destroyed.

Self-Assembly on Stable Oxide Surface

Self-Assembly of Phosphonate Films Whereas in the case of iron the adhesion layers have to be adsorbed directly on the metal because the oxides are unstable, the situation is different for metals that form stable oxides. Here it is better to have the films formed on the stable oxide. On aluminum oxides, for example, phosphonates, X—R—PO_3^{2-}, form stable and well-ordered monolayers. In X—R—PO_3^{2-}, X designates the functional end group, R the alkane chain, and PO_3^{2-} the head group.

With technical samples, high-resolution STM is not applicable to obtain information about the molecular order. Other methods such as Fourier transform infrared (FTIR) spectroscopy and X-ray photoelectron spectroscopy (XPS) have to be applied.

The adsorption of phosphonates on aluminum surfaces is an acid-base reaction. The driving force is the formation of a surface salt [63]. Figure 8 shows FTIR spectra supporting this theory. The similarity in the spectra of a Zn-biphosphonate multilayer on gold and of an self-assembly (SA) film of biphosphonic acid on aluminum oxide clearly supports this theory. The peaks at wave numbers 1100 and 950 cm^{-1} are attributed to vibrational modes of the RPO_3^{2-} anion.

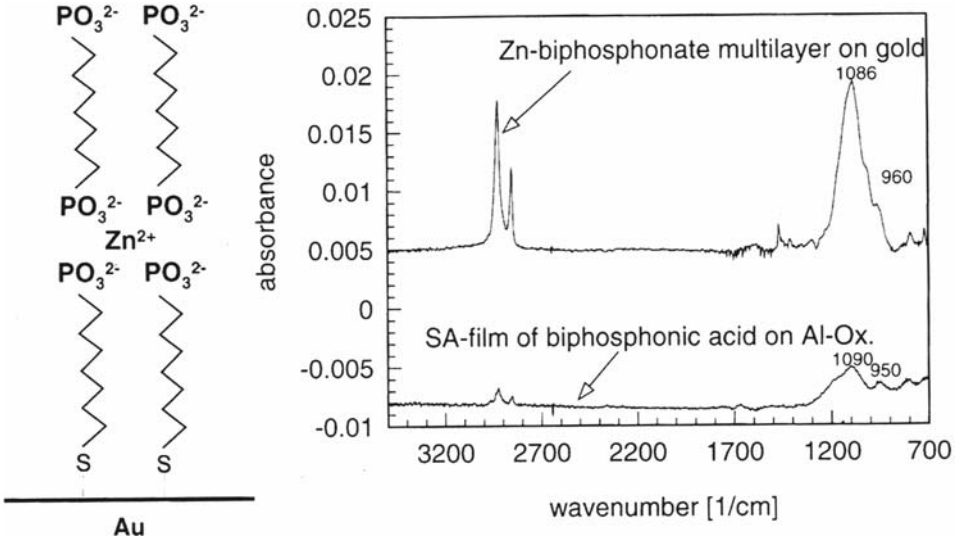
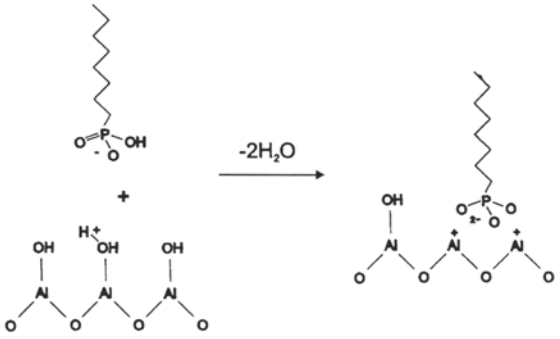


Figure 8 Infrared adsorbance spectra of a phosphonate film on an aluminum oxide surface and of Zn-biphosphonate multilayer on gold (see figure on the left).

Copyright © 2002 Marcel Dekker, Inc.

The following adsorption scheme is supposed:



This requires the presence of OH groups on the aluminum oxide surface. Different levels of OH on the oxide surface can be adjusted by gas-phase adsorption of different amounts of oxygen and water on aluminum in a special ultrahigh vacuum (UHV) chamber, which also allows electrochemical experiments and adsorption from solution without exposing the samples to air. After the OH ratio in the oxide layer was determined with XPS, the sample was exposed to the phosphonate solution and then the amount of adsorbed phosphonates was determined with XPS. Figure 9 shows that for low OH content in the oxide surface no phosphonate adsorption occurs.

Because aluminum is only rarely used as the pure material, it is of crucial importance for a successful application of the protecting and adhesion-promoting monolayer films that not only the aluminum surface is covered by the molecules but also the inclusions, such as Al_2Fe, as they are typical of most aluminum alloys. Even

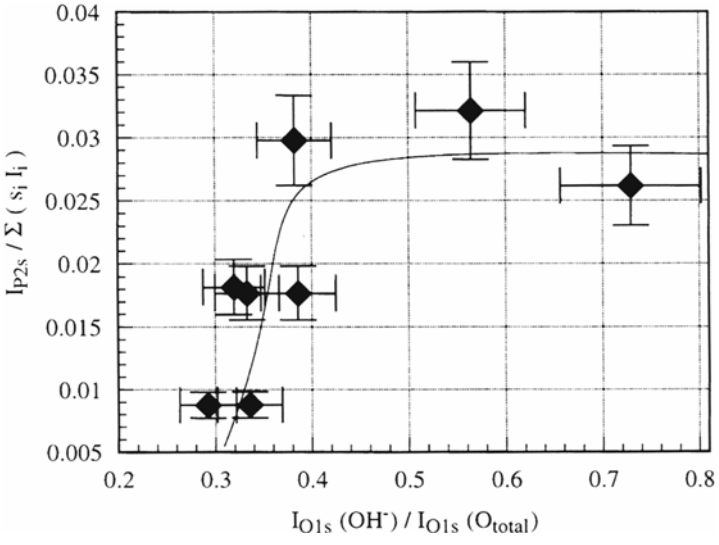


Figure 9 Intensity of the phosphorus 2*s* photoelectron signal as a function of the OH^- content in the oxide surface.

Copyright © 2002 Marcel Dekker, Inc.

though these inclusions of submicron to few microns size usually cover less than a few percent of the surface, they play the key role in the delamination of polymer films from aluminum alloys because they are not covered by an insulating passive oxide and thus reactions such as oxygen reduction can easily occur on their surface.

Cathodic water decomposition and especially oxygen reduction require considerable overvoltages on Al and Al alloys. Usually, potentials below –400 mV_{SHE} are required to activate a cathodic current. Thus, both water decomposition and oxygen reduction occur together and both contribute to the overall current density. The effect of the inclusions on the current/potential curves can be seen in Figure 10, where the curves for aluminum, Al_2Fe, and AlMgl in an oxygen-purged 0.1 M $NaSO_4$ electrolyte are shown. The scans start at the OCP with a velocity of 1mV/s, while the samples are rotated at 200 rpm. Obviously, the inclusions in the AlMgl act as active sites for the cathodic reactions.

Investigation of the inclusions in an AlMgl surface that has been polarized to cathodic potentials for a short time typically shows a corrosive attack of the Al matrix around the inclusion. Obviously, the inclusions act as local cathodes and the matrix in their vicinity will dissolve anodically in the alkaline electrolyte around the inclusion. The extent of the attack on the Al matrix surrounding the inclusion, i.e., the trenches around the inclusions, varies considerably. This means the oxygen reduction occurs to a different extent on the different inclusions, which can easily be explained by the concept of a microelectrode array: at low rotation velocities the oxygen transport to the inclusions is limited and diffusion cones issuing from the inclusions will evolve and overlap at a certain distance from the surface, from which a planar diffusion zone is effective. Thus, the situation occurs that diffusion conesof inclusions active earlier than others use up all the oxygen available and thus shield the other inclusions from the oxygen. Figure 11 shows a scanning electron microscope (SEM) and an Scanning Auger microscope (SAM) image of such an inclusion. Clearly visible is the corrosion trench in the matrix surrounding the inclusion; also interesting is the ringlike deposit of oxides around the trench. The surface of the inclusion is mostly Fe_3O_4, whereas before its activation it showed a high content of

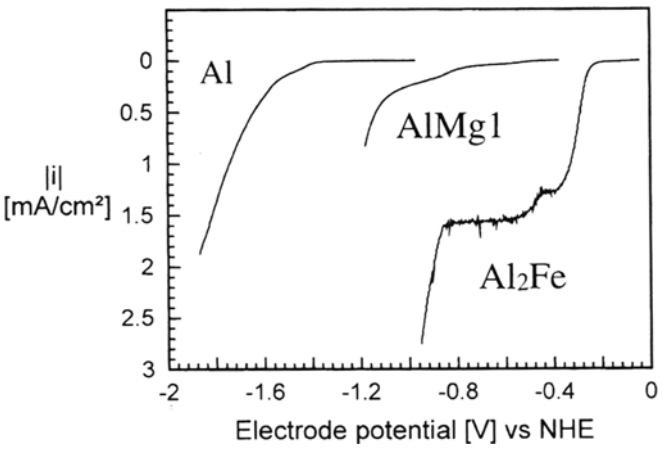


Figure 10 Current/potential curves for Al, AlMgl, and Al_2Fe in oxygen-purged 0.1 M Na_2SO_4 electrolyte.

Copyright © 2002 Marcel Dekker, Inc.

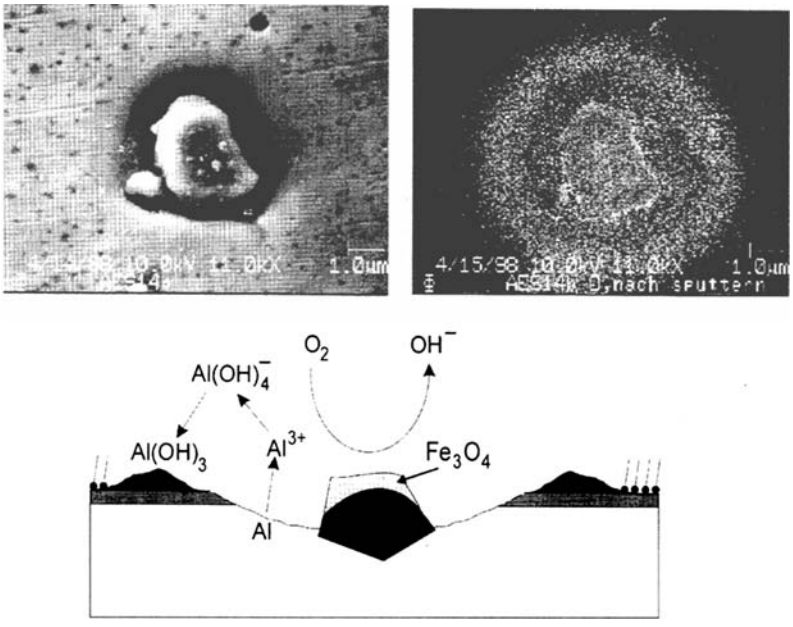


Figure 11 (Top) SEM image and oxygen SAM mapping of an Al_2Fe inclusion in AlMgl. (Bottom) Reaction scheme for corrosion at the inclusions.

Al oxide. The lower part of Figure 11 depicts a schematic drawing of the processes going on at the inclusions. Activation of the surface, i.e., the dissolution of the Al oxides from the surface of the inclusion as it is induced by an increase in pH caused by oxygen reduction, results in an iron oxide–rich surface, oxygen reduction can take place with high reaction rates, Al is dissolved from the matrix surrounding the inclusion, and Al hydroxides precipitate in the vicinity of the trenches.

A good test of the protective properties of self-assembled monolayer films is to investigate to what extent these layers can inhibit the activation of the inclusions. This can be done by cathodic potential jumps and monitoring the current transients. Figure 12 shows such transients for an ummodified surface at different rotation velocities.

Three stages of the $i(t)$ curves can be distinguished. For the first seconds an onset of the cathodic currents can be seen. Here the activation of the inclusions occurs. The decrease in the cathodic current in stage II is most likely due to the onset of the anodic aluminum corrosion in the surrounding matrix. The behavior in stage III is more complicated to explain; it is assumed that deposition of corrosion products plays an important role here.

Figure 13 shows the transients for AlMgl samples modified with biphosphonic or aminophosphonic acid; samples modified with octadecylphosphonic acid do not show much difference from the unmodified samples. Especially the aminophosphonic acids show a significant improvement in the corrosion behavior. Sputter profiles on the matrix and inclusions show that similar films are formed on the Al matrix but that the aminophosphonic acid forms several nanometer thick multilayer films on the inclusions, much thicker films than the biphosphonic acid. In this way the inclusions are better passivated in the case of modification with aminophosphonic acids.

Copyright © 2002 Marcel Dekker, Inc.

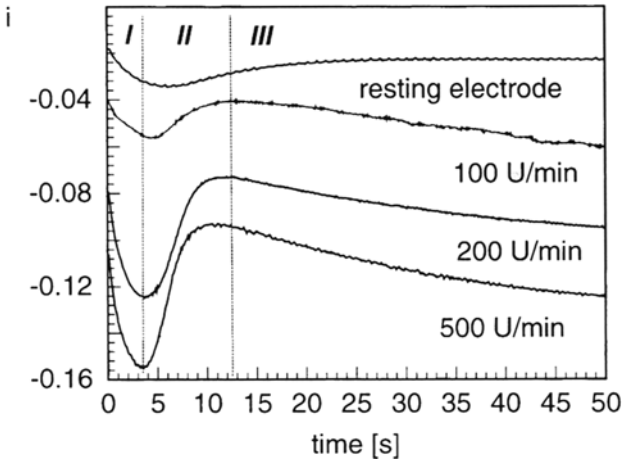


Figure 12 Current transients for AlMgl samples after potential jumps from the OCP to –800 mV for different rotation velocities.

At a first look the decrease of the peak current by a factor of 4–5 and the delay of the activation peak by a factor of 20–40, from 3–4 s to 60–120 s, does not seem to be sufficient for an effective improvement. In the case of an additional polymer coating, a factor of 20 increase in activation time might extend the lifetime of a product by several years. For this reason, aminophosphonate monolayers may prove suitable as adhesion promoters.

Figure 14 shows the effect of the phosphonate monolayer (self-assembled *N*-ethylaminophosphonate, NEAP) on the delamination of an amine-modified

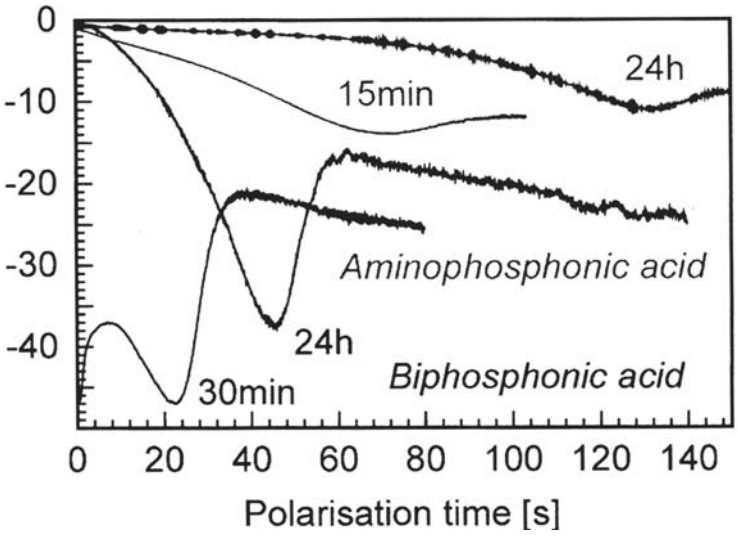


Figure 13 Current transients for the resting samples after modification with aminophosphonic or biphosphonic acid, respectively.

Copyright © 2002 Marcel Dekker, Inc.

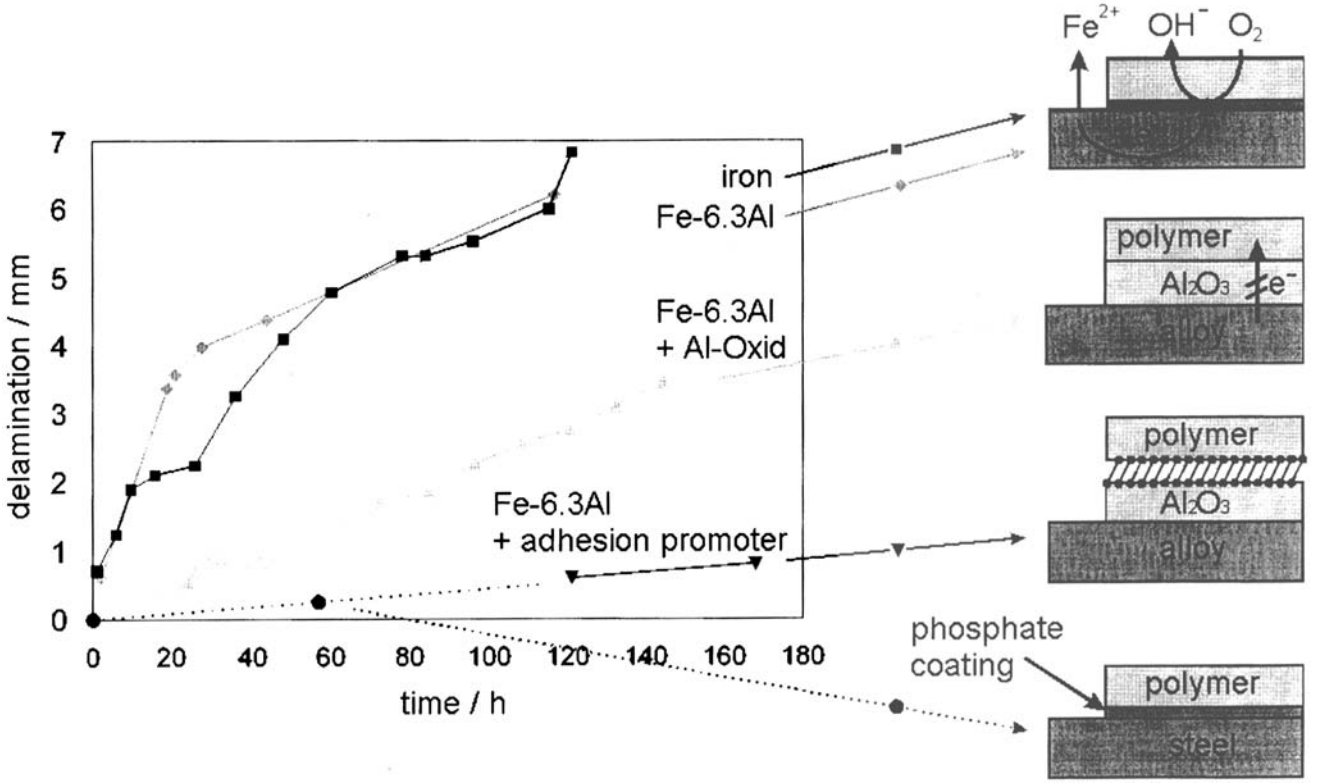


Figure 14 Delamination of an amino-modified epoxide ester from differently pretreated Fe-6.3Al-alloy surfaces and phosphated steel as a reference.

Copyright © 2002 Marcel Dekker, Inc.

epoxide ester from Fe-6.3Al-alloy surfaces. This ester is a basis for a number of industrial primers. As can be seen, the just polymer-coated alloy is delaminated quite rapidly. Delamination is much slower if the alloy is thermally treated in such a way that a thin insulating layer is formed by selective oxidation, and thus oxygen reduction is inhibited. If an additional phosphonate layer is built into the interface, the delamination is again significantly slowed down [64].

Adhesion Promotion by Phosphonate Films Besides inhibiting oxygen reduction, the role of the self-assembled monolayer is to improve the adhesion of the polymer film to the surface under mechanical strain. Usually, it is assumed that it is the covalent bond of the head group of the molecules to the surface and the tail group to the polymer that is responsible for the improved mechanical stability. To protect microelectronic devices, especially microchips, from harmful environmental influences, more than 90% of all semiconductor devices are encapsulated with polymeric compounds. Often the polymers have to be briefly heated up to temperatures around 200–250°C to improve their protective properties. In this case, the explosive evaporation of adsorbed moisture can cause considerable mechanical strain at the polymer/substrate interface, which in turn might result in breakage of the polymer/substrate composite at the interface. More precisely, the failure occurs mostly not directly at the interface but near the interface [65–72]. For this kind of adhesive breakage near the interface, several nanometers of polymer coating are usually still covering the substrate. It seems that the molecular forces between substrate and polymer are not crucial for the failure behavior, but the transition zone from the substrate into the polymer bulk plays the key role.

In order to investigate the effects of an aminophosphonate monolayer on the adhesive properties, aluminum samples were modified with NEAP and then coated with a polycyanurate film [a prepolymer of the dicyanate of bisphenol A (DCBA), which consisted mostly of monomers and trimers of DCBA, and was dissolved in tetrahydrofuran (THF) (25 mg/mL) and then the prepolymer solution spin coated on the samples and exposed for 2h at 220°C in laboratory air to complete the polymerization]. The triazine rings in the DCBA monomer are IR inactive when parallel to the substrate surface and increasingly IR active with increasing normal component. Figure 15 shows the normalized intensity of the corresponding IR signal (at wave number 1380 cm^{-1}) as a function of the thickness of the polymer film for NEAP-modified and unmodified samples. The normalization of the signal was to divide the signal obtained from thicker polymer films (> 40 nm) by their thickness as obtained by ellipsometry and set this to one. It can be seen from Figure 15 that for the unmodified samples the orientation of the triazine rings in the monomers near the interface has, in comparison with the statistically oriented molecules in the polymer bulk, a distinct preferred component parallel to the surface. This preferred orientation extends up to about 10nm from the interface. For the modified sample this transition zone extents only over the first 2 nm from the surface. The reason for this is that the NEAP molecules are adsorbed on the surface as a oriented monolayer with the secondary amino group of the NEAP molecules at the surface. This amino group can react with the cyanate group of the polycyanurate prepolymer to an isourea bond, forcing it to a more or less upright orientation. Thus the transition zone at the interface is reduced by a factor of 5. This is shown schematically in Figure 16.

Copyright © 2002 Marcel Dekker, Inc.

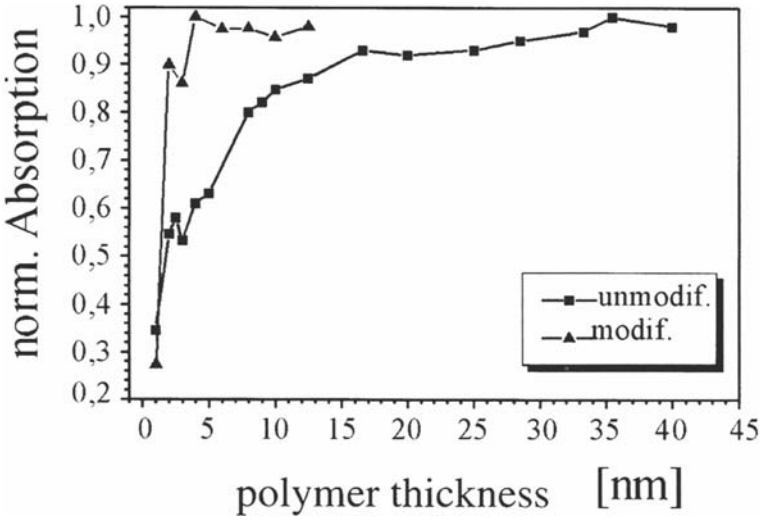


Figure 15 Normalized infrared adsorbance at the wave number 1380 cm^{-1} for polycyanurate films of different thickness for the unmodified and the NEAP-modified sample.

Technical butt joint tests on samples coated with 400-nm polycyanurate polymer result for the samples not modified with NEAP in failures of the polymer/aluminum bond for stresses between 2 and 6 MPa, depending on the relative humidity. Interestingly, the failure occurred not directly at the interface but about 6–10 nm away from it, as could be derived from SEM and XPS measurements. This clearly shows that failure occurs within the transition zone. For samples modified with NEAP no failure of the polycyanurate-polymer/NEAP/aluminum composite could be measured because of cohesive breakage in the coupling glue (XD4600) used for the test at about 7 MPa, independent of humidity; i.e., much higher stability is to be expected.

Stability of Defective Monolayer Films

Defects at the interface most likely play an important role in the delamination process. Unfortunately, the defects in self-assembled films are mostly nanoscopic and can be studied only with atomic force microscopy (AFM) and STM, which require very time-consuming preparation and limit the flexibility of the experiments. Other operation modes such as scanning Kelvin probe force microscopy (SKPFM) [73] will play an important role in future work [74].

Another way to study the role of defects is to prepare films with larger defects with the Langmuir-Blodgett (LB) technique, which allows deposition of ordered monolayers of suitable (amphipilic) organic molecules on a solid substrate.

Thiol LB Films

Thiols are classic SA molecules but it is possible to transfer thiol LB films onto gold [75]. Lösch et al. [75] studied the LB transfer of thiol molecules onto gold under electrochemical potential control. Because the gold electrode is charged as a consequence of the polarization, there is an excess of counterions (Na^+ for a negatively

Copyright © 2002 Marcel Dekker, Inc.

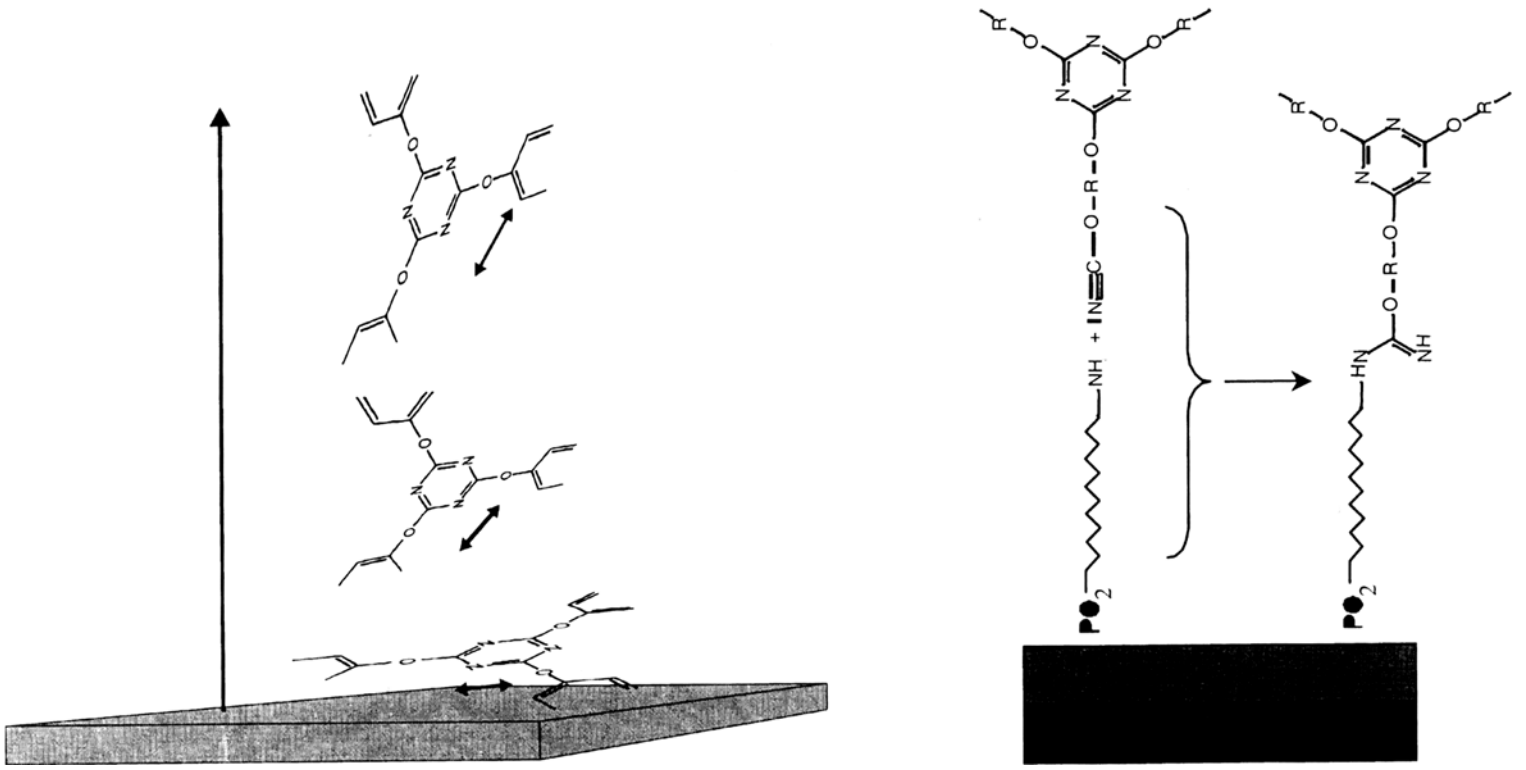


Figure 16 (Left) Supposed molecular structure within the polymer near the unmodified surface. The orientation of the molecules is parallel to the surface. (Right) Molecular structure at the interface in the case of NEAP modification.

Copyright © 2002 Marcel Dekker, Inc.

charged surface and ClO^-_4 for a positively charged surface) in the electrolyte as part of the electrochemical double layer. For any chemical interaction it is essential that these counterions are replaced by the LB molecules. Figure 17 shows the amounts of Na and Cl as detected by an XPS analysis of a gold electrode modified by octadecylmercaptan (ODM) at different electrode potentials. For potentials cathodic to the potential of zero charge (PZC) Na^+ can be detected, but for potentials anodic to the PZC no counterions are observed at all. Obviously, the sulfur of the ODM molecule, which is partly negatively charged, is for electrostatic reasons not able to replace Na^+ at negative potentials. Indeed, the area of the sodium XPS signal is in the range expected for the amount of Na^+, which balances the charge of the metal surface. This is in excellent agreement with the observed slowdown of the chemisorption during self-assembly at cathodic potentials (as reported earlier). But whereas in this latter case chemisorption finally occurs, the molecules transferred at negative potentials via the LB technique are only physisorbed (see Fig. 18).

At potentials anodic of the PZC, the negatively charged sulfur atoms in the ODM molecules balance the charge of the positively charged surface; no perchlorate can be detected. This is also confirmed by Figure 18. Between –0.88 and +0.62 V the binding energy is continuously shifted toward smaller values. This is direct evidence for continous negative charge on the sulfur atom. At all potentials the binding energy is smaller than the binding energy of S(2*p*) measured for bulk ODM. This is attributed to the interaction with the metal surface. At +0.62 V the binding energy (162 eV) is close to that of mercaptan molecules chemically attached to iron substrates. Figure 18 shows that a chemical anchoring of the mercaptan is strongly dependent on the electrode potential. A dramatic change in the high-resolution spectra of sulfur is observed at high anodic potentials (+1120 mV and + 1500 mV). A new peak shows up in the range 167 eV–169 eV. This band can be referred to sulfur in the oxidation state + VI ($R—SO_3^-$). Apparently, it is possible to oxidize the sulfur at the mercaptan/substrate interface during the transfer process of the LB film, while the ordering within the film remains intact.

The effect of the electrode potential during transfer on the film stability is shown in Figure 19. Here cyclovoltammograms (CVs) of gold covered by one monolayer of *n*-octadecylmercaptan are depicted. The CV of unmodified gold shows

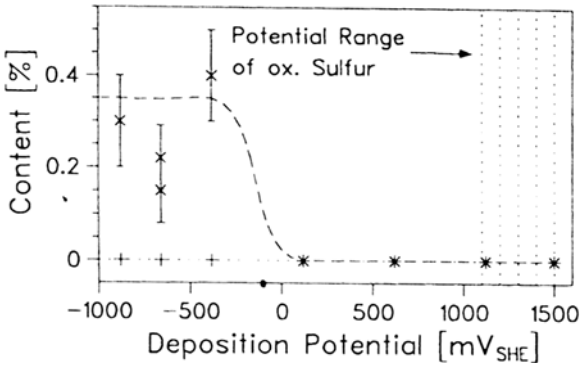


Figure 17 The amount of Na^+ (×) and ClO_4^- (+) detected by XPS on gold surfaces modified by one monolayer of octadecylmercaptan at various deposition potentials [75].

Copyright © 2002 Marcel Dekker, Inc.

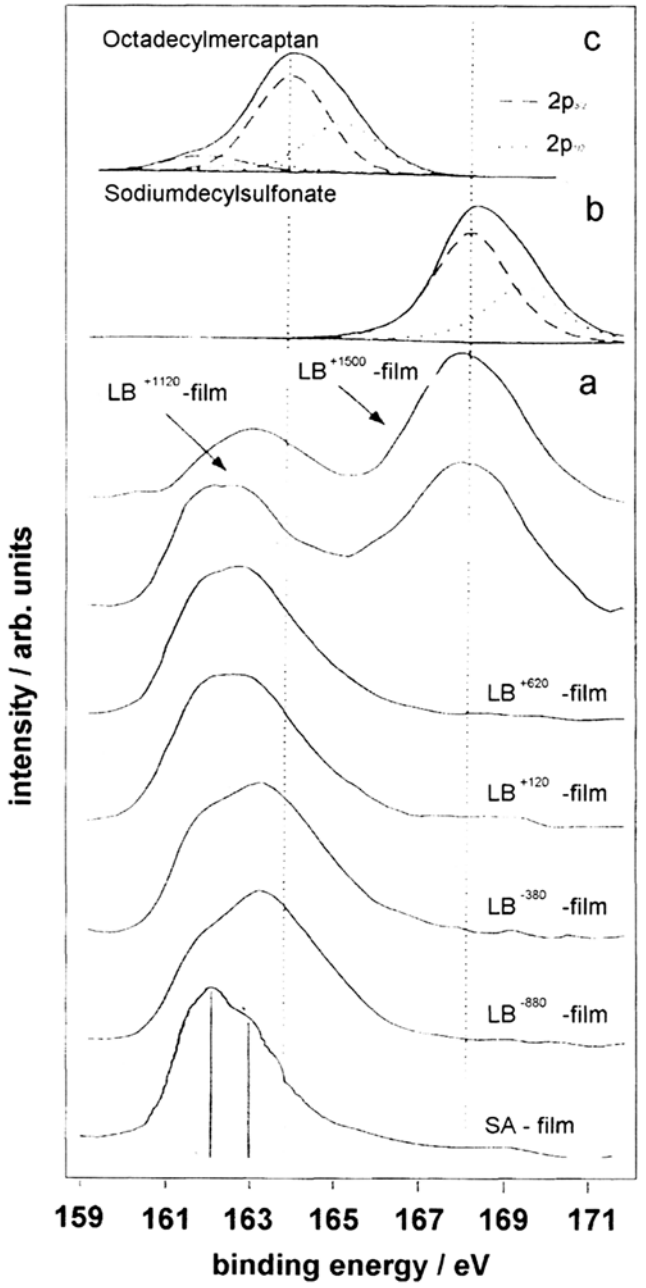


Figure 18 S(2*p*) XPS spectra of a gold surface modified by one monolayer of octadecylmercaptan (ODM) at various electrode potentials (c). Reference spectra of sodium decylsulfonate (b) and nonchemisorbed ODM (a) are included, as well as that of a self-assembled film.

Copyright © 2002 Marcel Dekker, Inc.

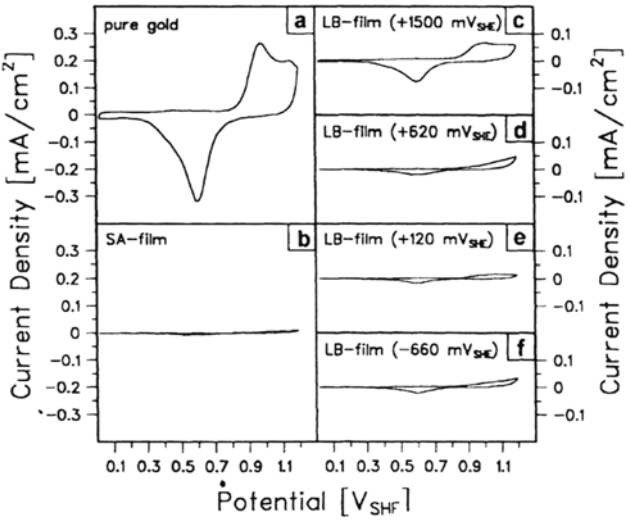


Figure 19 Cyclovoltammograms in deaerated borate buffer (pH 8.3; scan speed 100 mV/s) for a solvent-cleaned gold surface (a), gold modified by one monolayer of SA film (b), and gold modified by one monolayer of LB films prepared at +1500 mV_{SHE} (c), +620 mV_{SHE} (d), +120 mV_{SHE} (e), and –660 MV_{SHE} (f) [75].

the typical peaks of gold oxidation and gold reduction, whereas these peaks are diminished in size for the coated gold electrodes. The residual peaks are determined by the part of the gold surface that is not blocked by chemisorbed thiol, and the effect of the electrode potential on the stability is clearly visible.

Silanol LB Films

The LB technique can also be successfully used for transferring a monolayer of silanol molecules onto a metal surface. Silanols are widely used for corrosion protection [76]. Now, in contrast to mercaptan, a dissociation of the head group takes place on the water surface [77] followed by the formation of silanols and a polymerization. So a two-dimensional polymer results. The existence of the Si—O—Si bonding is proved by infrared spectroscopy. Figure 20 shows the IR spectrum measured in external reflection (RRAS) of an LB film prepared at +500 mV in comparison with the KBr spectrum of an octadecyltrichlorosilane (ODTCS) bulk polymer. In both cases the fingerprint region of the Si—O—Si double peak (1112 and 21018 cm^{-1}) is obvious. The weaker signals of the CH_2 stretching signals for the LB film are due to the selection rule of the IRRAS.

It should be noted that the two-dimensional polymer film formed on the water aqueous subphase is rather stiff and viscous, so that during the transfer a cleavage of the film occurs and an island structure of the monomolecular LB film results on the substrate. This gives ideal samples for investigation of the role of defects in delamination. An ideal tool for such investigations is the scanning Kelvin probe (SKP).

Until recently it was impossible to analyze locally the integrity of the metal/polymer bond under in situ reaction conditions. This is now possible using a scanning Kelvin probe. This technique allows the measurement of localized

Copyright © 2002 Marcel Dekker, Inc.

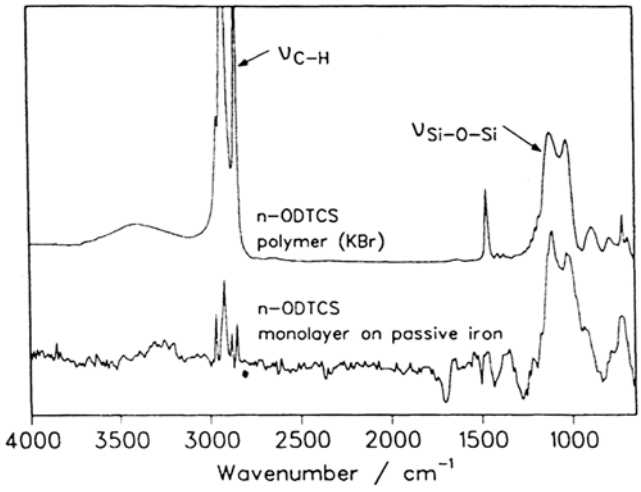


Figure 20 KBr spectrum of octadecyltrichlorosilane (ODTCS) after full polymerization in H_2O (top) and one monolayer of octadecyltrichlorosilane on iron after chemisorption at +0.5 V in an LB balance (bottom).

corrosion potentials without touching the surface under investigation [78–85]. The Kelvin probe has a sharp vibrating needle that scans above the surface, the distance between probe and substrate being approximately 10 μm. A capacitor is formed between substrate and needle, and the capacitor is charged by a potential difference, which is called the Volta potential difference, if both metals are connected by a conducting wire. As the capacity of the capacitor is changed sinusoidally with the vibration, an alternating current results between both metals. If an additional voltage difference is imposed between the two metals, then the capacitor may be discharged and the AC signal vanishes when the external voltage is equal to the Volta potential difference.

In principle, therefore, the Volta potential of the metallic substrate is measured with the Kelvin probe. For dry atmospheres, the Volta potential difference ($\Delta\Psi^{Ref}_{sample}$) is given by the difference between the work functions of the substrate and the probe [86]. The work function of the sample, however, includes the dipole potential of the metal:

$$\Delta\Psi^{Ref}_{Sample} = (W^{Sample} - W^{Ref})/F = (\mu_e^{Sample}/F - \chi) - W^{Ref}/F$$

where

W = work function of sample or reference metal
F = Faraday constant
μ_e = electrochemical potential of the electrons in the sample (constant)
χ = dipole potential of the sample surface

The dipole potential of the surface will change in the presence of polar organic molecules at the metal/air interface. This can be seen in Figure 21a, which shows an SEM picture of an iron surface partly coated by one monolayer of octadecylsilanol. In this situation, the individual molecules are ordered, as they have been deposited by the Langmuir-Blodgett-Kuhn method. Laterally resolved Auger analysis shows

Copyright © 2002 Marcel Dekker, Inc.

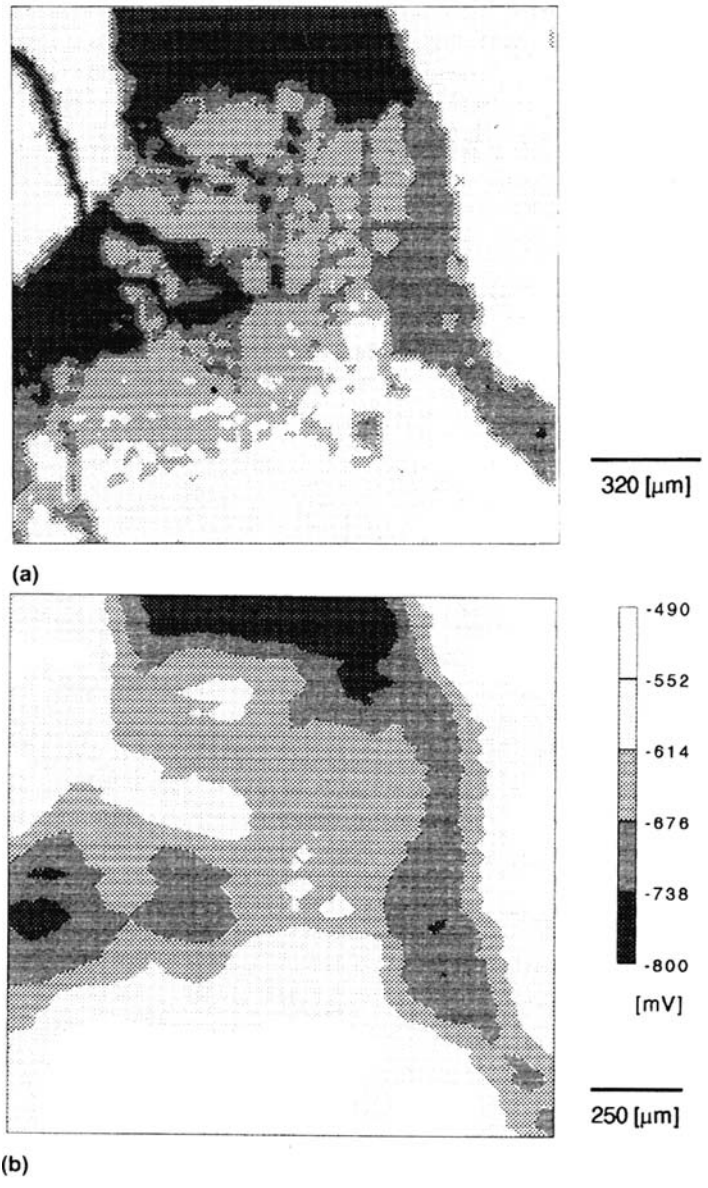


Figure 21 (a) SEM map of iron modified by approximately 0.7 monolayer of octadecylsilanol (ODS). Bright areas: surface covered by ODS; dark areas: surface not covered. (b) Map of the Volta potential of the same surface as in (a) [79].

that the dark areas correspond to the noncoated substrate, whereas the bright areas are coated by one monolayer of the organic molecule. It is interesting that the same contract is obtained with a scanning Kelvin probe (Fig. 21b). This is due to the fact that the covered part of the substrate has a different dipole potential in comparison with the noncovered areas and this also results in a different Volta potential [77].

Copyright © 2002 Marcel Dekker, Inc.

In humid atmospheres, a thin electrolyte layer is formed on top of the substrate surface. Under those circumstances the Volta potential of the surface of the electrolyte layer is measured. It has been shown that this Volta potential is mainly determined by the Galvani potential difference of the metal/electrolyte interface and therefore by the electrode or corrosion potential [79,80,86]:

$$\Delta\Psi^{\mathrm{Ref}}_{\mathrm{sample}} = E_{\mathrm{corr}} - (W^{\mathrm{Ref}}/F - \chi^{\mathrm{Gas}}_{\mathrm{El}} - \varepsilon_{\mathrm{ref}})$$

where

E_{corr} =corrosion potential of the corroding surface
$\chi^{\mathrm{Gas}}_{\mathrm{El}}$ =dipole potential of the electrolyte/gas interface
$\varepsilon_{\mathrm{ref}}$ =half-cell potential of a standard reference electrode (e.g., SHE) needed to relate the absolute potential scale to the electrochemical potential scale

Again, the Kelvin probe can be used to monitor the local corrosion potential of a partly coated metal surface in a humid atmosphere. If, for example, the presence of the organic molecule changes the kinetics of the metal dissolution reaction, then this is reflected in a change of the corrosion potential: an acceleration of the metal dissolution will shift the corrosion potential cathodically, a retardation will shift the corrosion potential anodically. As an example, Figure 22 shows a map of the corrosion potential of an iron surface that is partly coated by one monolayer of octadecylsilanol as measured with the Kelvin probe in a humid atmosphere [87]. The corrosion potential changes locally by several 100 mV due to the presence or absence of the film and it has been proved that the anodic potentials correspond to the areas that are coated by the polymer [53]. The potential plot of Figure 22 is therefore a representation of the inhibition of the anodic metal dissolution in a humid atmosphere.

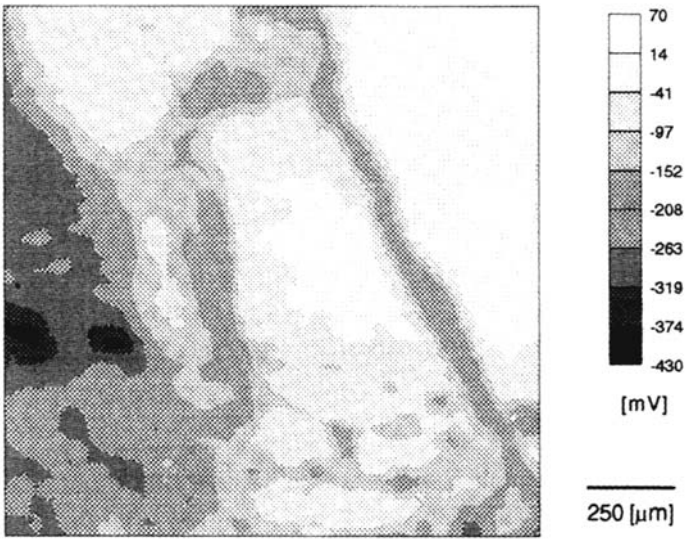


Figure 22 Map of the Volta potential of one monolayer of octadecylsilanol on iron after exposure to 100% relative humidity for 343h. Area: 5 × 5mm [87].

Copyright © 2002 Marcel Dekker, Inc.

If the same specimen is exposed to a water-saturated atmosphere for longer corrosion times, no significant change is observed in comparison with Figure 22: the uncoated areas of the iron surface start to corrode (negative corrosion potentials), whereas the areas that are covered by one monolayer of octadecylsilanol stay at very anodic potentials. The scanning Kelvin probe is therefore an ideal tool for the investigation of inhibiting properties of organic molecules and it also allows analysis of the expansion of corrosion on partly inhibited surfaces.

A second example of the analysis of inhibitor-covered surface is shown in Figure 23. Iron substrates have been immersed in a solution containing the inhibitor ammonium benzoate at a concentration of 0.025 M [88]. After exposure, the samples are removed from the electrolyte and the corrosion potential map is recorded with the Kelvin probe. Large potential differences result for the surface immersed in the solution with a low concentration of inhibitor. Again, anodic potentials correspond to the inhibited area whereas negative potentials close to the free corrosion potential of the active iron electrode are representative of the noninhibited surface. Obviously, at a concentration of 0.025 M the inhibitor is not able to protect the iron surface completely. If the inhibitor concentration is increased to 0.05 M, no active corrosion is observed and the potential stays at very anodic values. Similar results have been obtained by Schultze et al. [89,90] for the inhibitor toloylanaline on iron.

The scanning Kelvin probe is therefore an ideal tool for in situ analysis of the delamination of ultrathin organic coatings on reactive metal substrates. Until now, only the detection of intrinsic defects has been discussed. It is possible, however, to prepare monolayer coatings nearly free of such defects. Suitable techniques are self-assembly chemisorption and the Langmuir-Blodgett-Kuhn method, if the monomers and preparation parameters are optimized. Then the Kelvin probe will detect a homogeneous corrosion potential and the delamination may be studied only in the presence of artificial defects. As an example, Figure 24 shows a map

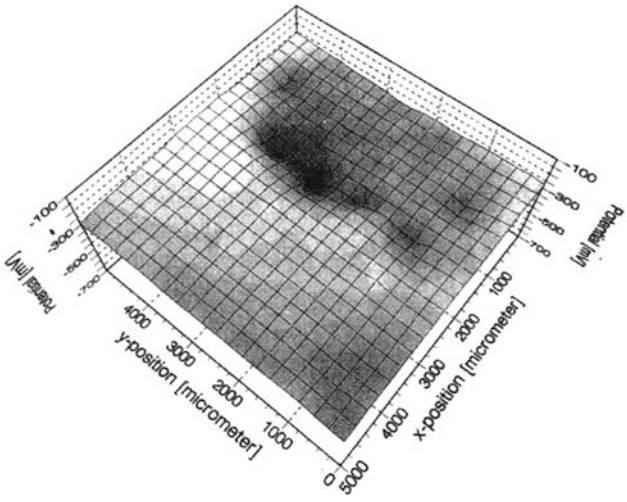


Figure 23 Map of the Volta potential of iron after immersion in a 0.025 M solution of ammonium benzoate in 0.01 M Na_2SO_4 for 24 h. Area: 5 × 5mm. Potential excess: 200 mV (bright area) to –500 mV (dark area) [88].

Copyright © 2002 Marcel Dekker, Inc.

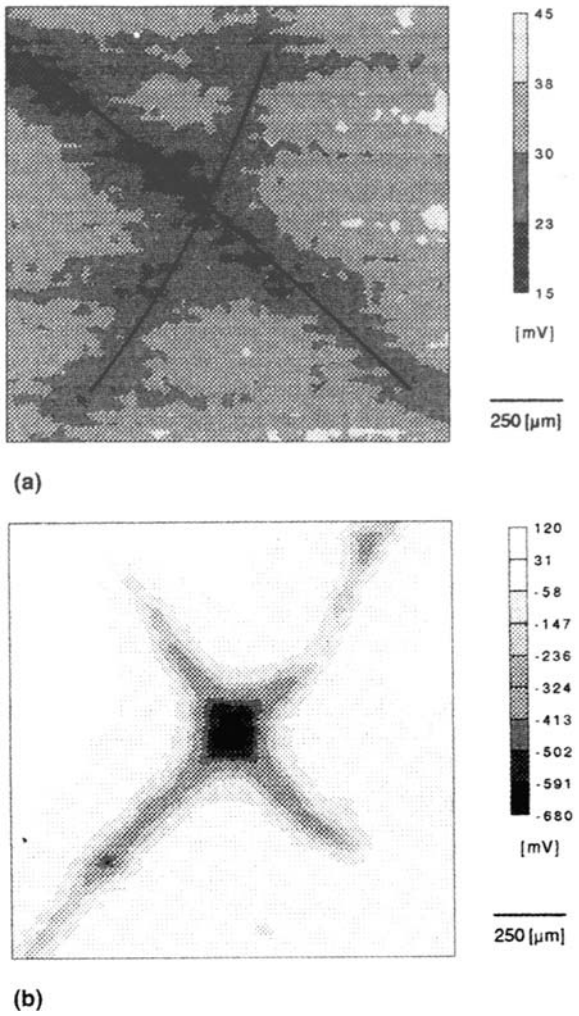
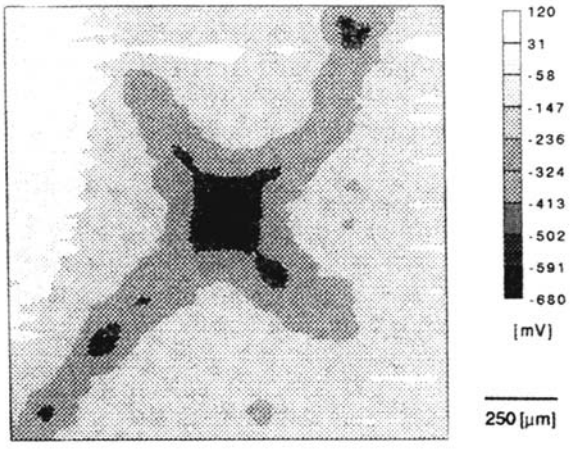


Figure 24 (a) Map of the Volta potential of iron modified by one monolayer of dimethylhexadecylsilanol. Surface has been scratched in the form of a cross. Area: 1 × 1 mm. (b) map of the Volta potential of the same surface as (a) after adsorption of 0.5g/m^2 SO_2 and exposure to 100% relative humidity for 7 h. Area: 5 × 5 mm. (c) Same surface as in (b) after exposure for 20h. at 100% relative humidity. Area: 5 × 5 mm [87].

of the corrosion potential of an iron surface covered by one monolayer of dimethylhexadecylsilanol [77,79]. The film has been destroyed by an artificial defect in the form of a cross, which is clearly seen even in dry air (Fig. 24) because of the change of the local dipole potential. The potential difference is small in comparison with Figure 21, as the dipolar moment of dimethylhexadecylsilanol is smaller than that of the monomer used in Figure 21. If such a surface is exposed to humid air highly contaminated with SO_2, the metal surface is activated at the parts where the monolayer has been destroyed. This is seen in rather negative local corrosion potentials (Fig. 24b). Even after prolonged exposure, the active corrosion is limited to the same area and the width of the

Copyright © 2002 Marcel Dekker, Inc.



(c)

Figure 24 (Continued).

defect increase very slowly (Fig. 24c). The undermining of the monolayer close to the defect is, however, much faster than the delamination of the intact film far from the defect; in this respect the results are similar to those obtained with lacquers and paints.

For the first time, the delamination of the monolayer coating can be evaluated quantitatively and directly compared with the delamination of industrial paints. Such a comparison is shown in Figure 25, and it is quite obvious that the delamination rate is determined not by the thickness of the coating but by the bonds that prevail at the interface. Using the scanning Kelvin probe in the future, the stability of other

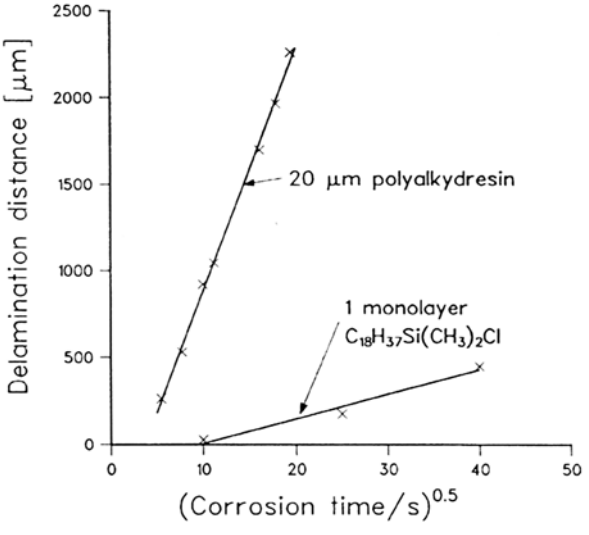


Figure 25 Comparison of the delamination rate of iron coated by 20-µm polyalkyd resin with iron coated by one monolayer of dimethylhexadecylsilanol. (Data from Ref. 32.)

Copyright © 2002 Marcel Dekker, Inc.

suitable metal/polymer bonds may be analyzed under corrosive conditions, and it is very likely that coatings will be developed that are considerably superior to the ones used up to now. It is essential, however, to understand the chemical or electrochemical reactions that take place at the metal/polymer interface and that give rise to the undermining of the defect as shown in Figure 24. Such studies are performed preferentially on homogeneous electrode surfaces, as most spectroscopic and electrochemical techniques do not provide spatially resolved information. Exceptions are the scanning probe microscopy techniques such as scanning tunneling microscopy (STM) or atomic force microscopy (AFM). However, as already stated the application of these techniques for investigation of the corrosion properties of chemically modified surfaces has only begun and few results have been obtained so far.

PLASMA POLYMERS AS CORROSION-RESISTANT THIN FILMS ON METALS

A typical reactor for plasma polymerization under reduced pressure is shown in Figure 26 [47]. However, modern developments in plasma polymerization enable a stable plasma even at atmospheric pressures. Details of the mechanisms of plasma polymerization can be found in Ref. 45. Organic precursors.

Plasma polymers are generally characterized by an extremely tight and three-dimensional network. In Figure 27 a typical structure of an organosilicon plasma polymer network is shown [47]. It has been shown that the water permeability of a thin plasma polymer (thickness around 20 nm) can be two or three orders of magnitudes lower than that of polyethylene [91]. Moreover, Yasuda et al. showed that under special conditions of plasma polymerization even "atomic interfacial mixing" (AIM) occurs providing a water-resistant interface [46].

Studies in the 1990s revealed the good corrosion protection properties of silicon-based plasma polymers on steel substrates and the crucial influence of the pretreatment process on the stability of the resulting interface [92–101]. The pretreatments for trimethylsilane-based films may consist of an oxidative step (O_2-plasma) to remove organic contaminations from the substrate and a second reductive step (Ar/H_2-plasma) to remove the metal oxide layer. Although the successive application of both steps provides the best corrosion protection of various plasma treatments for steel in combination with a cathodic electrocoat, little is known about the chemical structure of the interface. Yasuda et al. [101] and van Ooij and Conners [97] in particular have shown that the deposition of plasma polymers on steel and galvanized steel might even substitute the chromatation process.

Yasuda et al. [100,101] showed that the formation of carbides on the iron surface prior to plasma polymer deposition led to excellent corrosion protection properties in combination with a cathodic E-coat. In this work a special cathodic plasma polymerization with magnetic enhancement was used. With this experimental setup they were able to remove the oxide layer on steel almost completely in an Ar/H_2 plasma and to form Fe—C groups. The formation of Fe—C is the result of intensive ion bombardment of the surface.

In the following, plasma polymers are discussed as corrosion-resistant thin layer with the focus on their morphology, chemical structure, and resistance to corrosion.

Copyright © 2002 Marcel Dekker, Inc.

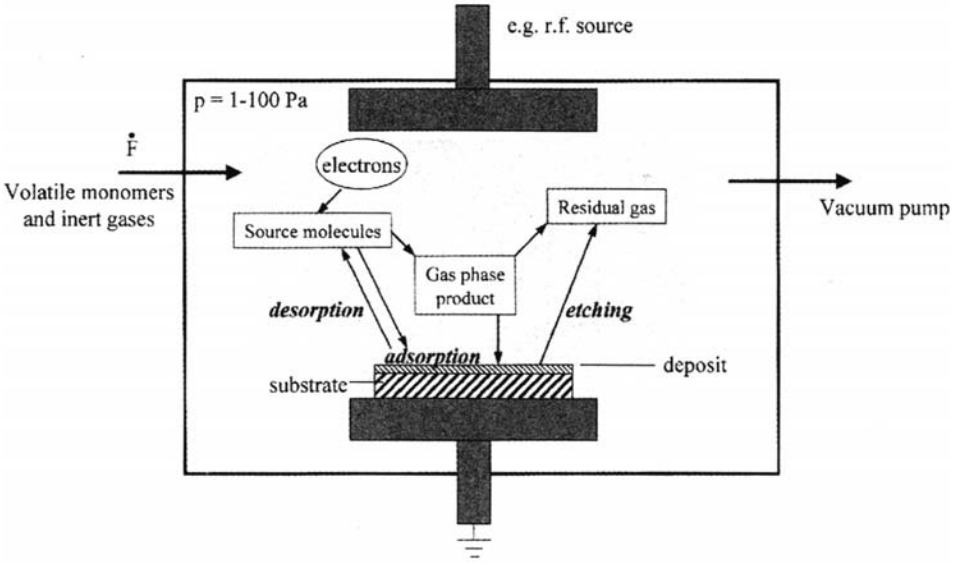


Figure 26 Schematic of a plasma deposition reactor and the important plasma processes.

Plasma Cleaning of Metal Surfaces

Under atmospheric conditions, freshly prepared surfaces of reactive metals such as iron or zinc are covered by an oxide with a thickness of about 2 to 3nm [102,103]. Moreover, organic molecules tend to adsorb strongly to the oxide surface, leading to a lower surface energy compared with the uncovered oxide. For intimate adhesion between the plasma polymer and the oxide, these residual organic contaminations have to be removed. An oxygen plasma leads to oxidative etching of organic molecules. It was also observed by ex situ XPS and AES sputter profiles [92,94] that the thickness of the iron oxide increased during the oxygen plasma treatment. Besides the oxygen plasma cleaning, argon and hydrogen plasmas can be effectively used to clean metal surfaces and even partially reduce the oxide layer [100,101,104].

As an example, Figure 28 shows the in situ infrared reflection absorption spectrum (IRRAS) of the iron surface after the oxygen plasma treatment. The spectrum measured right before the plasma treatment served as the reference spectrum. The spectra were measured while the sample was still in the plasma chamber at a pressure of 10^{-4} mbar [105]. The negative peaks at 2900 and 1450 cm^{-1} indicate the loss of amorphous organic contaminations, whereas the positive peaks at about 1316, 1130 and 690 cm^{-1} are assigned to the formation of iron oxyhydroxide and iron oxide [106–108]. The peak at 690 cm^{-1} can be assigned to γ-Fe_2O_3, while the broad peaks between 900 and 1400 cm^{-1} are in the region of oxyhydroxides and vary in position and relative intensity as a function of the iron surface pretreatment. The FeOOH peak cannot be assigned to any specific crystalline form of FeOOH. Plasma oxidation of electrogalvanized steel also leads to the removal of organic contaminations and the formation of an oxyhydroxide on the surface (see Fig. 29). The latter shows a strong and broad absorption at 1150 cm^{-1} [109]. Moreover, strong

Copyright © 2002 Marcel Dekker, Inc.

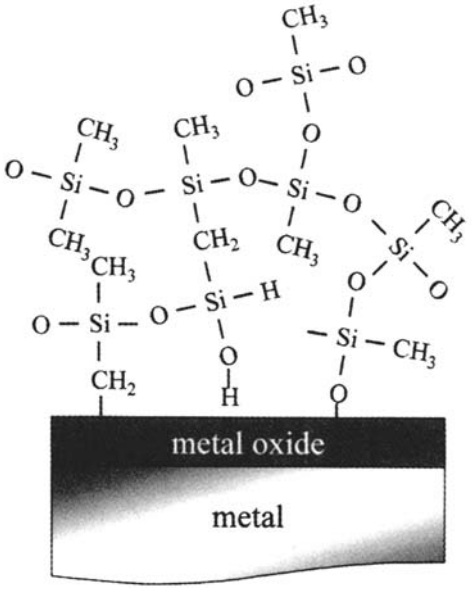


Figure 27 Simplified schematic of an Si-organic plasma polymer (precursor: hexamethyldisiloxane) as a surface layer on a metal substrate.

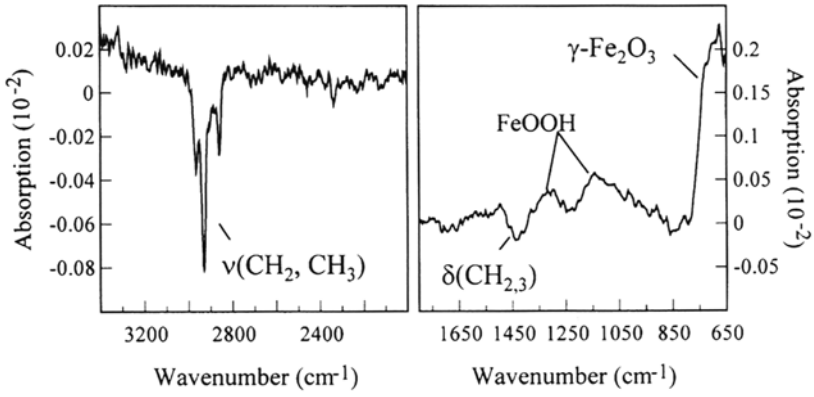


Figure 28 IRRA spectrum of an iron surface (Fe-coated quartz) that was exposed to an oxygen plasma for 300s [110].

negative peaks at 3250 and 1620 cm^{-1} indicate the removal of associated H_2O molecules. It is likely that the electrolytic deposition of zinc leads to a surface with adsorbed residual water layers. These water molecules could then take part in the plasma oxidation process as electron acceptors at the oxide surface according to

$$O^* + H_2O_{ads} + e^- \rightarrow OH^-_{ads} + OH_{ads}$$
$$OH_{ads} + e^- \rightarrow OH^-_{ads}$$
$$2OH^- + Zn^{2+} \rightarrow Zn(OH)_2$$

and would thereby lead to a highly protonated zinc oxyhydroxide.

Copyright © 2002 Marcel Dekker, Inc.

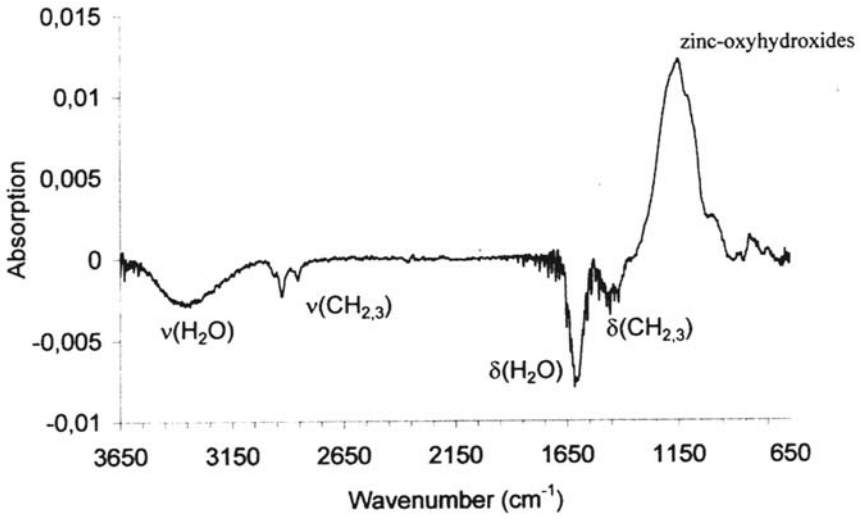


Figure 29 IRRA spectrum of a zinc surface (zinc-coated quartz) that was exposed to an oxygen plasma for 600s [105].

XPS sputter profiles, calibrated by sputtering of an SiO_2 layer of defined thickness, confirmed the thickening of the oxide for both metals. For Fe, the sputter profile shows 3nm for the native oxide in accordance with literature values and 6.5 nm after the plasma oxidation process [105,110]. For Zn, approximately 1.2 and 2.7-nm oxides were observed for the native oxide and plasma-oxidized surface [105]. It is assumed that the thickness of the additional oxide produced during the oxygen plasma treatment results from the high-field mechanism of oxide growth initiated by the adsorption of oxide ions and hydroxides on top of the metal oxide. The validity of the high-field growth mechanism for plasma oxidation of metals was shown by Fromhold [111] for the oxidation of lead. Thus, in the case of iron and zinc it can be assumed that Fe^{2+} and Zn^{2+} ions migrate from the metal/oxide to the oxide/plasma interface.

Plasma Polymerization of Organosilanes

Chemical Structure of Organosilane Plasma Polymers

Organosilanes are the precursor molecules most often used for the deposition of corrosion-resistant films. Details of organosilane plasma polymerization can be found in Refs. 112–114. Figure 30 shows a comparison of the spectrum of the hexamethyldisilane (HMDS) monomer in the gas phase and the IRRA spectrum of a 13-nm-thick HMDS plasma polymer on an iron substrate [115]. The characteristic features of the polymer spectrum revealing the cross-linking and termination are assigned. The assignments of all bands are given in Table 1.

As indicated in the spectrum of the plasma polymer, siloxane (≡ Si—O—Si ≡), dimethylsilyl(—$Si(CH_3)_2$—), and methylene (—CH_2—) groups give rise to the polymer cross-linking. In addition to this, hydrogen atoms bound to silicon (≡ Si—H) are observed. The oxygen-containing residual gas in the vacuum

Copyright © 2002 Marcel Dekker, Inc.

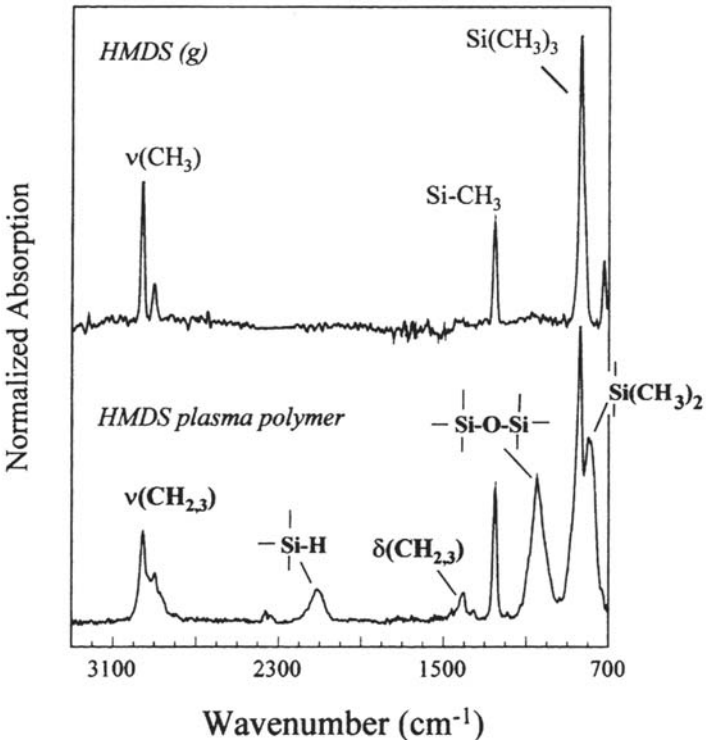


Figure 30 IRRA spectrum of an about 13-nm-thick plasma polymer deposited from a mixture of argon and hexamethyldisilane (p_{Ar} = 25 Pa, p_{HMDS} = 10 Pa). For comparison, the gas-phase spectrum of hexamethyldisilane is also shown. Indicated are the peaks that are specific for the polymer. All peaks are assigned in Table 3 [115].

chamber is incorporated as part of the siloxane network. There is a significant amount of dimethylsilyl groups in the polymer, which can be formed only by cleavage of the Si—C bond. Thus, it can be concluded that the polymerization mechanism is dominated mainly by the formation and recombination of silyl radicals. The abstraction of methyl groups is confirmed by the atomic concentrations measured by XPS. The measured concentrations correspond to $Si_2C_{4.1}O_{0.9}H_x$ compared with $Si_2C_6H_{18}$ in the case of the monomer [117]. The oxygen in the polymer is almost exclusively bound to silicon, as measured by IR spectroscopy and XPS.

Morphology of Ultrathin Plasma Polymer Films

Despite the fact that plasma polymerization leads to rigid and laterally homogeneous films, a varying number of pinholes is observed in most cases [118]. Pinholes are crucial defects when the plasma polymer serves as a coating for reactive metals. In this case, electrolyte can penetrate through these channels to the uncovered metal surface and give rise to localized forms of corrosion. Not surprisingly, the ultrathin plasma polymers contain several pinholes or intrinsic channels that can be located by immersion of the coated sample in a copper sulfate solution

Copyright © 2002 Marcel Dekker, Inc.

Table 1 Assignment of the IR Peaks of Gaseous HMDS and the HMDS Plasma Polymer

Group	Wave number (cm^{-1}) HMDS (g) (transmission)	HMDS-PP (80° IRRAS on Fe)	Assignment [116]
$Si-CH_3$	2957	2955	$\nu_{as}(CH_3)$
$Si-CH_3$	2901	2899	$\nu_s(CH_3)$
$Si-CH_2-$	—	2928	$\nu_{as}(CH_2)$
$Si-CH_2-$	—	2860	$\nu_s(CH_2)$
Si–H	—	2108	ν(Si–H)
$Si-CH_x (x = 2, 3)$	1428	1408	$\delta_S(CH_x)$
$Si-CH_x (x = 2, 3)$	1254	1250	$\delta_s(CH_x)$
Si–O–Si	—	1047	ν_{as}(Si–O–Si)
$-Si(CH_3)_3$	835	839	r($Si-CH_3$)
$—Si(CH_3)_2—$	—	795	r($Si-CH_3$)

[$c(CuSO_4) = 10^{-3}$mol/e] [115]. Copper was deposited in the pinholes while the rest of the surface was effectively isolated from the electrolyte even by films of a few nanometers thickness. Van Ooij et al. [104] studied the topology of plasma polymers deposited on stainless steel substrates from a DC plasma by means of STM. The topology was dependent on the plasma parameters. Films deposited at low pressure (6 Pa) were significantly smoother than those deposited at higher pressures (66 Pa).

The lateral homogeneity of ultrathin plasma polymers was confirmed by atomic force microscopy measurements on flame-annealed gold substrates [117]. Flame annealed Au was chosen because of its large (about 200 × 200 nm) monoatomic flat terraces. The measurement was done in the tapping mode to protect the plasma polymer surface from damage. Figure 31b shows, as an example, the structure of an about 3-nm-thick hexamethyldisilazane (HMDSZ) plasma polymer. The film structure can be revealed by a comparison with the bare flame-annealed Au surface (Fig. 31a). The shallow features of the plasma polymer show an average diameter of about 20 nm and a height of about 0.5 nm. The structure of the HMDS-PP resembles that of HMDSZ-PP and is published elsewhere [117]. By calculating the roughness (RMS value) of the plasma polymers on monoatomic flat terraces, the microstructure of the plasma polymers can be revealed as a function of the nature of the monomer and the film thickness (see Table 2). For comparison, a self-assembling monolayer of octadecylmercaptan (ODM) on flame-annealed gold was prepared (adsorption from ethanolic solution at open circuit potential, Δt_{ads} = 12 h) and measured in the same way.

The plasma polymer–coated surface shows increased roughness in comparison with the bare gold surface, whereas the ODM monolayer leads only to a slight increase in roughness. The lower RMS value of the 1-nm-thick HMDSZ-plasma polymer in comparison with the thicker films might be due to incomplete coverage of the measured area so that the bare gold surface contributes to the overall value. However, it appears that a constant roughness value is measured for a thickness above 3 nm.

Copyright © 2002 Marcel Dekker, Inc.

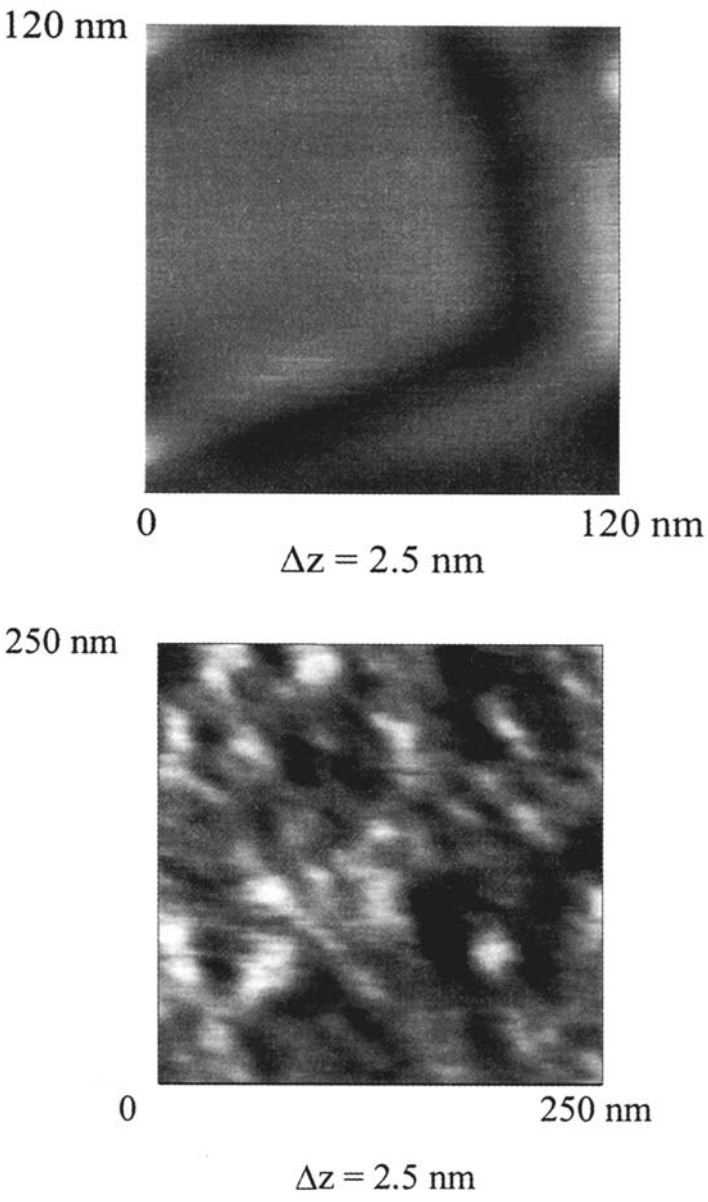


Figure 31 (a)AFM picture of a flame-annealed Au surface. The measurement was done in the tapping mode. The brightness increases with the height. (b) AFM picture of a flame-annealed Au surface coated with an about 3-nm-thick hexamethyldisilazane [$(CH_3)_3Si—NH—Si(CH_3)_3$, HMDSZ] plasma polymer that was deposited at p_{HMDSZ} = 5 Pa. The brightness increases with the height [105].

Copyright © 2002 Marcel Dekker, Inc.

Table 2 Calculated RMS Values for Different Plasma Polymer Layers and a Self-Assembled octadecylmercaptan (ODM) Film of Flame-Annealed Gold [105]

Adsorbate	Thickness (nm) (±20%)	Substrate	RMS on monoatomic terrace (± 10%) (nm)
—	—	Au(111)	0.03
HMDSZ-PP	1	Au(111)	0.22
HMDSZ-PP	2.5	Au(111)	0.29
HMDSZ-PP	22	Au(111)	0.32
HMDS-PP	5	Au(111)	0.30
ODM	1 monolayer	Au(111)	0.08

Interaction between the Polymerizing Plasma and the Oxide Surface

By using an in situ FTIR cell, Grundmeier and Stratmann [117] could reveal interactions at the *iron oxide/plasma polymer* interface. Prior to the plasma polymer deposition, the iron surface was plasma oxidized. The in situ IRRA spectrum of the plasma-oxidized surface now served as reference spectrum for the subsequent measurements. A very short (1–2s) plasma polymer deposition was then performed and the in situ IRRA spectra were measured again. This procedure was repeated twice on the same sample, resulting in three layers. The first absorption spectrum was subtracted from the second one and the second from the third. This procedure leads to three spectra that represent the structure of each of the three plasma polymer layers (see Fig. 32). All spectra were normalized by the thickness of the respective layer, *d*, as measured by the QCM. The IRRA spectrum of the first layer (thickness ~ 0.7 nm) shows two peaks at 1200 and 955 cm^{-1}, which are not found in the spectrum of the third layer. The spectrum of the second layer (thickness ~ 1nm) contains the same two peaks but the intensities are much lower than in the first layer. In addition, the Si—O—Si peak occurs at 1065 cm^{-1} in the first layer and shifts to 1056 cm^{-1} in the second and to 1042 cm^{-1} in the third layer. The higher frequency of the Si—O—Si peak at the interface might be a consequence of the change in the angle of the siloxane group induced by polar interactions between the oxygen of the polymer and hydrogen on the oxide surface. Any change in the bonding angle means that a higher energy of the system leads to an increase in the vibration frequency of the Si—O—Si asymmetric stretching, as observed for an SiO_2 layer on silicon [119].

A comparison of the thickness of the layers with the results concerning the microstructure of the films leads to the conclusion that almost complete coverage of the surface by the plasma polymer is reached when the film thickness is about 2 nm. Thus, the special peaks in the first and second layers might be assigned to the interaction of the deposited layer with the oxidized iron surface. The third layer is deposited onto a surface that is almost completely covered by the HMDS-plasma polymer film and therefore cannot interact with the oxide. According to the literature, the peak at about 955cm^{-1} can be assigned to a metal-oxygen-silicon bond and the peak at 1200 cm^{-1} is most probably due to a Si—O—CH_3 or a metal—O—CH_3 group [116]. Silanol groups would also lead to absorption in this wavelength region. The IR peak of silanols, however, was observed at 920 cm^{-1} for the chemisorption of polysiloxanes on iron using the

Copyright © 2002 Marcel Dekker, Inc.

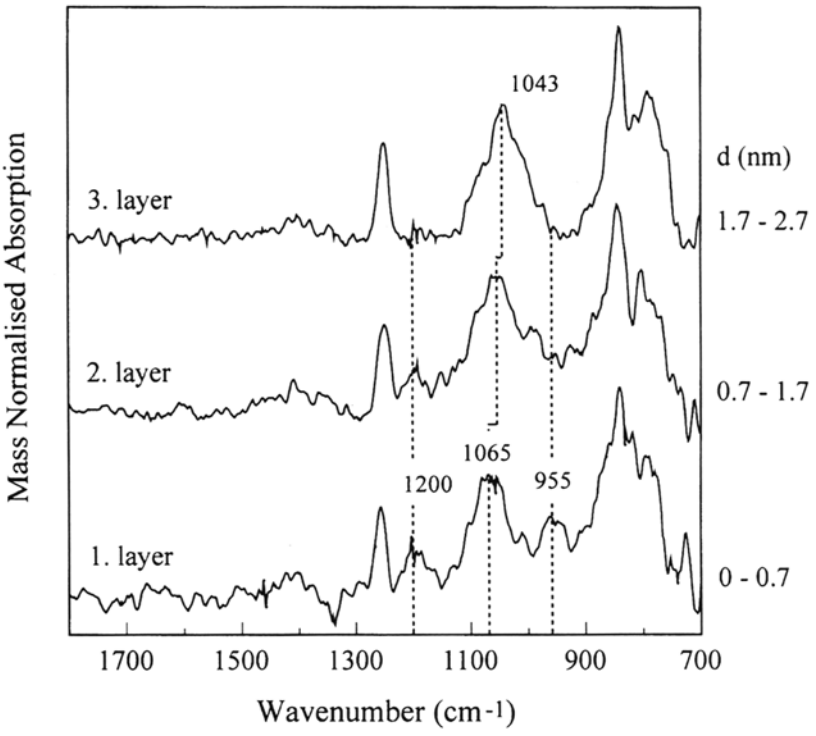


Figure 32 In situ IRRA difference spectra revealing the structure of the subsequently deposited three layers of HMDS plasma polymer on plasma-oxidized iron. The polymer was deposited at a partial pressure of p_{HMDS} = 5Pa. The value *d* means the thickness of each deposited plasma polymer layer [117].

same reflection assembly [120]. This value is about 35 cm^{-1} lower in wave number than the peak observed in Figure 32. Van Ooij et al. [104] studied the influence of the substrate on the plasma polymer formation using stainless steel as substrate. Films were deposited from a DC plasma. The authors observed especially for films deposited at high pressures a dependence of the film structure on the film thickness and thus proposed a two-stage mechanism. While the film adjacent to the substrate resembles polydimethylsiloxane, it becomes more random for higher film thickness.

Applications of Plasma Polymers as Corrosion-Resistant Layers on Reactive Metals

Delamination of Ultrathin Plasma Polymers

Plasma polymers may be applied without subsequent painting. In this case, corrosion may start in local defects in the plasma polymer and spreading of these defects is a critical degradation process. Moreover, plasma polymers may be used as model ultrathin polymers coatings. Grundmeier et al. [121] studied the delamination of ultrathin plasma polymers by using a scanning Kelvin probe and surface analytical methods.

Copyright © 2002 Marcel Dekker, Inc.

The delamination rate was determined with a scanning Kelvin probe. A small amount of fine sodium chloride was introduced into a circular deepening in the middle of the polished and ethanol-cleaned iron sample. After the sample was introduced into the plasma reactor, it was cleaned and activated in one step by an oxygen plasma, leading to a carbon-free and highly oxidized iron surface. In the next step an ultrathin plasma polymer of hexamethyldisilane was deposited on the cleaned substrate, leading to a well-defined metal-polymer interface. The thickness of the deposited polymer was controlled by the in situ measurement of the resonance frequency of the quartz crystal and was about 5 nm, so that the film thickness is in the range of the escape depth of the photoelectrons.

This special kind of defect preparation has the advantage that water condenses slowly after the insertion of the sample into the scanning Kelvin probe at 93% relative humidity. The growing droplet is fixed in the deepening due to the hydrophobic nature of the plasma film (water contact angle 92 ± 2°). Thus, the electrolyte does not spread over the delamination zone. Because a saturated sodium chloride solution is formed within the deepening, no drying of the defect is observed. A Cr/Ni wire was used as the vibrating reference electrode and provided a local resolution of about 100 μm. X-ray photoelectron spectra were obtained using a Physical Electronics ESCA 5600 XP spectrometer.

In Figure 33 the potential distribution over the circular defect and the surrounding intact plasma polymer–coated area as measured with the scanning Kelvin probe is shown with increasing corrosion time. Obviously, negative potentials are measured within the defect and very positive potentials are observed in the intact region. With increasing corrosion time the delamination front marked by the sharp decrease of the corrosion potential shifts into the former intact area and reveals that undermining occurs. Line scans shown in Figure 34 reveal the activation of the defect and the progress of the delamination front.

An interesting question refers to the comparability of the delamination of ultrathin polymers to that of macroscopic thick coatings. Therefore the sample was inserted into the XP spectrometer and the delaminated area was analyzed locally with high-energy resolution (0.6 eV). Figure 35 presents the line scans of the Na 1*s* and the Cl 2*p* peaks starting at the border of the defect and moving toward the intact area. The local resolution was 400 μm and the total length of the line scan was 2000 μm. The line scan reveals that no chloride is found in the delaminated area and that the concentration of sodium ions decreases toward the delamination frontier. The final length of the undermined region measured by the scanning Kelvin probe and the distribution of sodium ions as measured by means of electron spectroscopy for chemical analysis (ESCA) are in good accordance.

It can be concluded from the former results that the delamination of the ultrathin polymers behaves similarly to that of the model coating. It is now an advantage of the very small thickness that the metal-polymer interface can be characterized by XP spectroscopy without the separation between polymer and metal substrate, which otherwise leads to significant distortions caused by organic contamination, water absorption, and oxidation at ambient atmosphere. It was found that the ultrathin solid films are oxidized and transformed to a gel-like structure due to the osmotic swelling of the film in the delaminated region [121].

Copyright © 2002 Marcel Dekker, Inc.

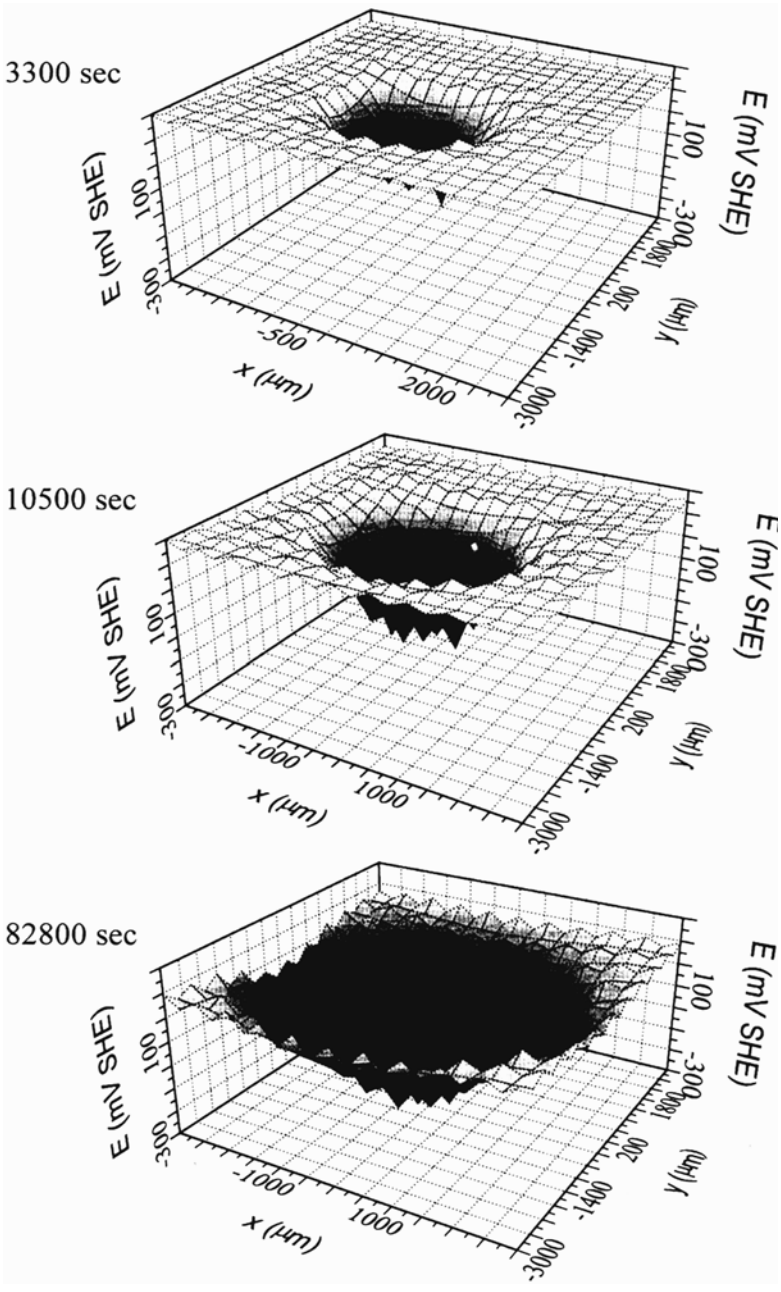


Figure 33 Potential distribution over the circular defect and the surrounding intact plasma polymer–coated area as measured with the scanning Kelvin probe is shown with increasing corrosion time [121].

Copyright © 2002 Marcel Dekker, Inc.

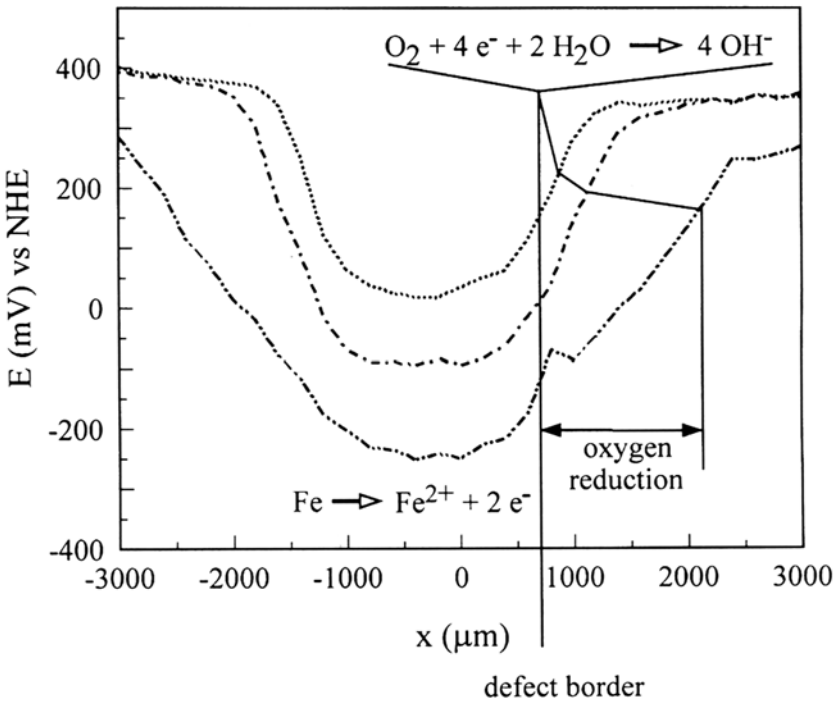


Figure 34 Scanning Kelvin probe line scans shown across the circular defect in Figure 33, revealing the activation of the defect and the progress of the delamination front [121].

Influence of Ultrathin Plasma Polymers on Delamination Kinetics of Polymer-Coated Steel and Galvanized Steel

As stated before, an ultrathin plasma polymer usually requires a stabilizing top coat. Iron substrates were plasma modified by an oxygen plasma treatment and by the deposition of an ultrathin plasma polymer as described before. Grundmeier and Stratmann [115] investigated the influence of an interfacial plasma polymer on the delamination kinetics of a clear coat on iron. The sample was coated with a water-based, one-component, polyurethane acrylate primer. An artificial defect with a reservoir for the electrolyte (0.5 M NaCl) and a linear defect border was prepared within the coated substrate. To reveal the influence of the plasma deposition on the delamination kinetics the sample was prepared with one half of the substrate not modified and the other half plasma modified. Masking of the unmodified region was achieved using a thin aluminum foil placed on the desired area. This technique guarantees that both areas have the same properties before the plasma treatment and are coated with the primer in the same way. Any observed differences should, therefore, be due only to the plasma deposition.

Figure 36 shows a 3D plot of a scanning Kelvin probe measurement of an iron sample that was coated with a 5-nm-thick HMDS plasma polymer on one half of the sample surface prior to the deposition of the primer [115]. The water contact angle

Copyright © 2002 Marcel Dekker, Inc.

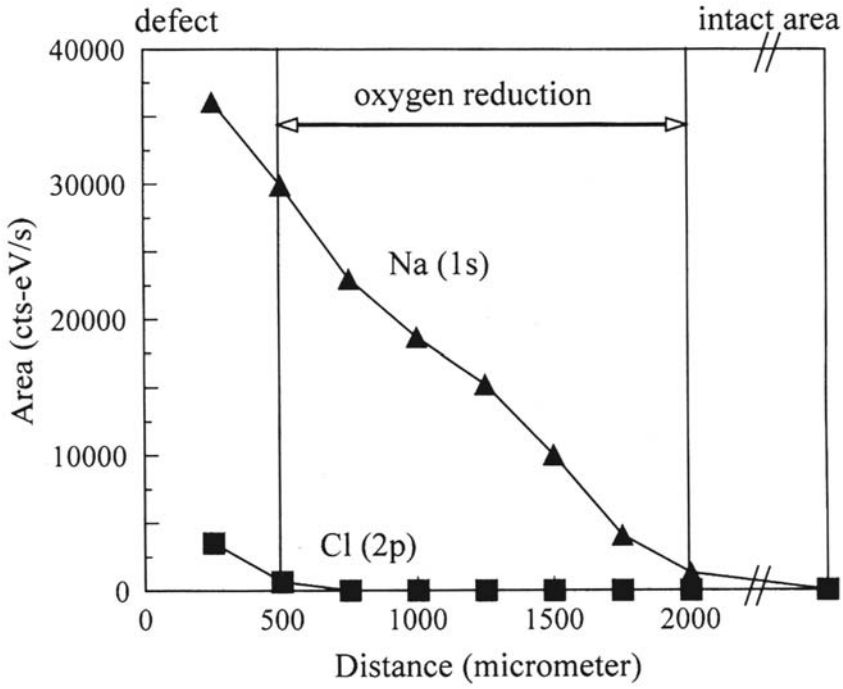


Figure 35 Small spot ESCA line scans of the Na_{1s} and the Cl_{2p} peaks starting at the border of the defect (see Figs. 33 and 34) and moving toward the intact area (spatial resolution 400 μm, total length of the line scan 2000 μm) [121].

on the HMDS plasma polymer was 92 ± 2°. This means that the surface energy decreased with respect to a plasma-oxidized surface, which shows a water contact angle of less than 10°. Nevertheless, wetting of the plasma polymer surface by the primer was sufficient to lead to homogeneous spreading and adhesion of the primer. The area modified by the plasma polymer shows little undermining even after 1265 min, whereas the area coated only by the primer shows fast delamination. A comparison of the delamination kinetics is shown in Figure 37. The progress of the steepest slope of the potential profile is plotted versus the time after the activation of the defect. Comparison of the corresponding kinetics leads to the conclusion that the ultrathin plasma polymer gives rise to a significant decrease in the delamination rate.

Plasma polymers with a special surface structure suitable to bond to an epoxy amine primer were used as interfacial coupling layers on iron and galvanized steel and led to even better results [122]. However, in all cases the system always showed cathodic delamination at the polymer/metal oxide interface, indicating the importance of oxygen reduction on the oxide surface. For verification, after the delamination of the sample, the delaminated polymer was pulled off and the underside of the polymer and the iron surface were investigated by XPS to reveal whether the system delaminated at the plasma polymer/metal interface or at the

Copyright © 2002 Marcel Dekker, Inc.

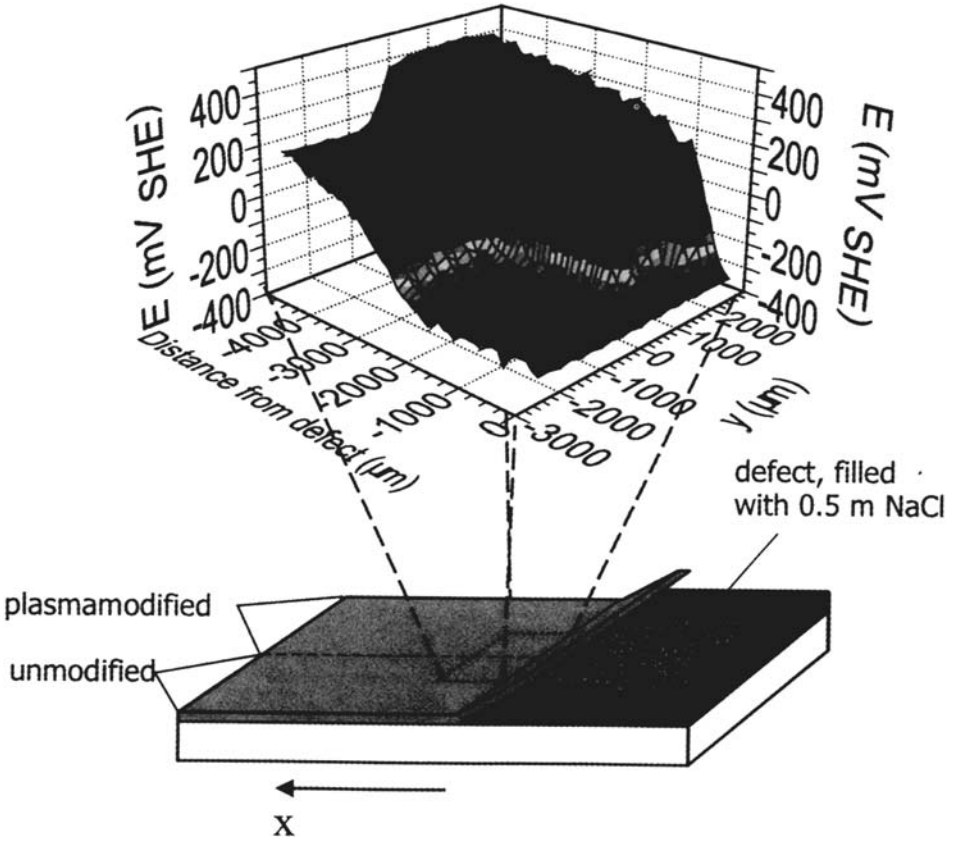


Figure 36 Potential profile of a delaminated primer-coated iron specimen that was half side plasma polymerized and afterward coated by a 100-μm-thick primer ($x = 0$: defect border, $y < 0$: not plasma modified, $y > 0$: plasma plasma polymerized). The thickness of the HMDS plasma polymer was 5 nm [105].

Copyright © 2002 Marcel Dekker, Inc.

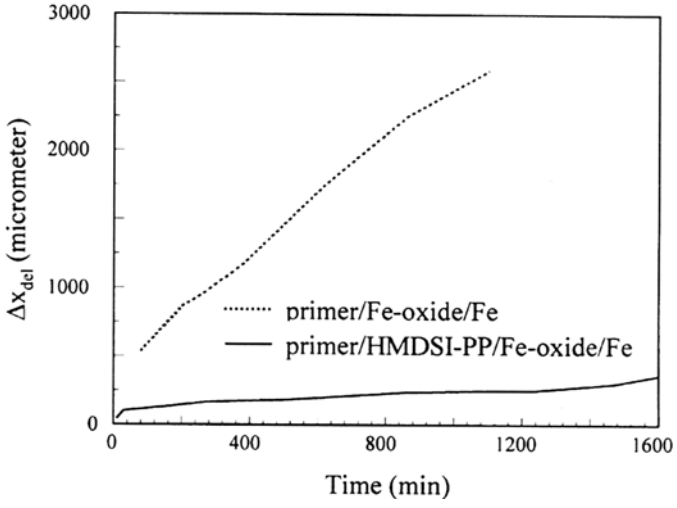


Figure 37 Progress of the delamination front as a function of time after the defect activation for the different surface pretreatments presented in Figure 31 [105].

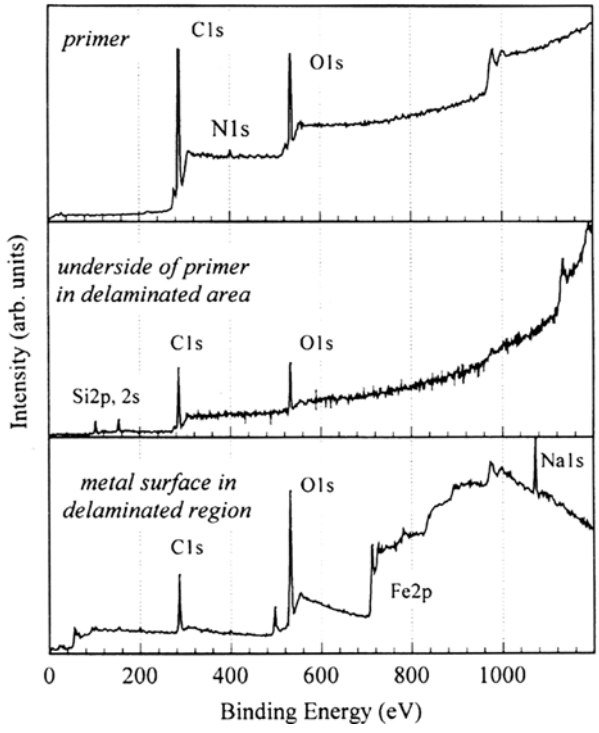


Figure 38 XP survey spectra of the interface of the delaminated region in comparison with the primer composition [105].

Copyright © 2002 Marcel Dekker, Inc.

primer/plasma polymer interface. Figure 38 shows the survey spectra of the underside of the polymer and the metal surface in the delaminated area. The underside of the polymer clearly shows the presence of HMDS plasma polymer, indicated by the Si2*p* and Si2*s* peaks. The metal surface, on the other hand, exhibits only negligible amounts of silicon but a significant amount of sodium. Thus, the XP spectra in Figure 38 confirm that the interface failure takes place between the plasma polymer and the oxide.

Corrosion Protection of Aluminum and Copper Surfaces

For passive metals such as aluminum and copper, plasma polymers have been used as thin corrosion-protecting layers without an additional top coat [123–125]. Oehr and Schindler [124] deposited plasma polymer barrier layers on aluminum and gold. Vinyltrimethylsilane showed good adhesion to gold and a sufficient degree of stability against sulfuric acid. Iriyama et al. [123] studied plasma polymerization of tetraethoxysilane as a corrosion-protecting layer for aluminum granules. Corrosion resistance was tested in an alkaline medium. The dissolved aluminum was compared for unmodified and plasma polymer–covered granules. Effective corrosion protection could be achieved at pH 11.

Lin and Yasuda [125] considered the effect of plasma polymer deposition methods on the corrosion protection of copper. The properties of trimethylsilane plasma polymers were investigated in DC cathodic polymerization, with and without anode magnetron enhancement, af magnetron glow discharge polymerization, and rf glow discharge polymerization. The corrosion test consisted of wet/dry cycles using 0.1 M NaCl. DC magnetron cathodic polymerization offered the best corrosion protection based on enhanced deposition uniformity and adhesion. The application of plasma polymers with permeation resistance and surface dynamic stability greatly reduced the pitting densities.

REFERENCES

1. H. Leidheiser, Jr., ed., *Corrosion Control by Organic Coatings*, NACE, Houston, 1981.
2. R. A. Dickie and F. L. Floyd, eds., *Polymeric Materials for Corrosion Control*, American Chemical Society, Washington, DC, 1986.
3. H. Leidheiser, Jr., *Corrosion Mechanisms* (F. Mansfeld, ed.), Marcel Dekker, New York, 1987.
4. A. J. Kinloch, *Adhesion 3* (K. W. Allen, ed.), Applied Science, London, 1979.
5. R. Feser, Ph.D. thesis, University of Clausthal-Zellerfeld, 1990.
6. R. Feser and M. Stratmann, *Werkst. Korros. 42*:187 (1991).
7. M. Stratmann, R. Feser, and A. Leng, *Electrochim. Acta 39*:1207 (1994).
8. H. Leidheiser, Jr., W. Wang, and L. Igetoft, *Prog. Org. Coat. 11*:19 (1983).
9. H. Leidheiser, Jr. and W. Wang, in Ref. 1, p. 70.
10. H. Leidheiser, Jr., in Ref. 2, p. 124.
11. E. L. Koehler, Proceedings 4th International Congress on Metallic Corrosion, 1972, p. 736.
12. E. L. Koehler, in Ref. 1, p. 87.
13. J. J. Ritter and J. Kruger, in Ref. 1, p. 28.

Copyright © 2002 Marcel Dekker, Inc.

14. H. Leidheiser, Jr., L. Igetoft, W. Wang, and K. Weber, Proceedings 7th International Conference on Organic Coatings, Athens, 1981.
15. J. S. Hammond, J. W. Holubka, and R. A. Dickie, *J. Coat. Technol. 51*:45 (1979).
16. J. E. Castle and J. F. Watts, in Ref. 1, p. 78.
17. M. Stratmann, *Adv. Mater. 2*:191 (1990).
18. M. Stratmann, B. Reynders, and M. Wolpers, *Haftung bei Verbundwerkstoffen und Werkstoffverbunden* (W. Brockmann, ed.), Deutsche Gesellschaft für Materialkunde, Oberursel, 1991.
19. M. Rohwerder and M. Stratmann, *MRS Bull. 24*:43 (1999).
20. E. P. Plueddemann, *Silane Coupling Agents,* Plenum Press, New York, 1982.
21. K. L. Mittal, ed., *Silanes and Other Coupling Agents,* VSP, Utrecht 1992.
22. K. L. Mittal, ed., *Adhesion Aspects of Polymeric Coatings*, Plenum Press, New York, 1983.
23. D. E. Leyden, ed., *Silanes*, *Surfaces and Interfaces*, Gordon & Breach Science Publishers, New York, 1985.
24. P. E. Cassidy and B. J. Yager, *J. Macromol. Sci. Rev. Polym. Technol. D1(1)*:1 (1971).
25. H. Ishida, *Polym. Compos. 5*:101 (1984).
26. G. Trabanelli, *Corrosion Mechanisms* (F. Mansfeld, ed.), Marcel Dekker, New York, 1987.
27. H. Kaesche, *Die Korrosion der Metalle,* Springer, Berlin, 1990.
28. Proceedings of the (a) 1st, (b) 2nd, (c) 3rd, (d) 4th, (e) 5th, (f) 6th, (g) 7th European Symposium on Corrosion Inhibitors, Ferrara (a) 1961, (b) 1966, (c) 1971, (d) 1976, (e) 1980, (f) 1985, (g) 1990, Annali dell'universita di Ferrara, Sezione V.
29. J. Lipkowski and P. Ross, eds., *Adsorption of Molecules at Metal Electrodes,* Verlag Chemie, Weinheim, 1992.
30. M. E. Tarvin and B. A. Miksic, Corrosion, New Orleans, 1989, paper no. 344.
31. B. A. Miksic, M. Tarvin, and G. R. Sparrov, Corrosion, New Orleans, 1989, no. 607.
32. D. M. Brasher and A. D. Mercer, *Br. Corros, J. 95*:122 (1967).
33. G. Schmitt, *Br. Corros. J. 9*:165 (1984).
34. A. Leng, Diploma thesis, University of Düsseldorf, 1991.
35. H. Fisher, *Werkst. Korros. 23*:445 (1972).
36. W. J. Lorentz and F. Mansfeld, *International Conference on Corrosion Inhibition,* NACE, Houston, 1987.
37. J. O. M. Bockris and R. A. J. Swinkels, *J. Electrochem. Soc. 111*:736 (1964).
38. K. J. Vetter and J. W. Schultze, *J. Electroanal. Chem. 53*:67 (1974).
39. J. W. Schultze and K. D. Koppitz, *Electrochim. Acta 21*:327 (1976).
40. K. J. Vetter and J. W. Schultze, *Ber. Bunsenges. Phys. Chem. 76*:920 (1972).
41. N. Hackermann and R. M. Hard, *1 International Congress Metal Corrosion,* Butterworth, London, 1962.
42. R. G. Pearson, *Science 151*:172 (1966).
43. L. Horner, *Chem. Ztg, 100*:247 (1976).
44. H. K. Yasuda, *J. Polym. Sci. Macromol. Rev. 16*:199 (1981).
45. R. d'Agostino, ed., *Plasma Deposition, Treatment, and Etching of Polymers,* Academic Press, New York, 1990.
46. H. Yasuda, *Plasma Polymerization,* Academic Press, New York, 1985.
47. N. Morosoff, *Plasma Deposition, Treatment, and Etching of Polymers* (R. d'Agostino, ed.), Academic Press, New York, 1990, pp. 1–95.
48. See Refs. 54–62 and references within.
49. E. Vago, K. de Weldige, M. Rohwerder, and M. Stratmann, *Fresen. J. Anal. Chem. 335*:316 (1995).
50. M. Volmer, M. Stratmann, and H. Viefhaus, *Surf. Interface Anal. 16*:278 (1990).

Copyright © 2002 Marcel Dekker, Inc.

51. M. Volmer-Uebing, and M. Stratmann, *Appl. Surf. Sci. 55*:19 (1992).
52. O. M. Magnussen and R. J. Behm, *MRS Bull. 24*:16 (1999).
53. (a) M. Rohwerder, K. de Weldige, and M. Stratmann, *J. Solid State Electrochem. 2*:88 (1998); (b) M. Rohwerder, dissertation, Shaker Verlag, 1997.
54. C. A. Widrig, C. A. Alves, and M. D. Porter, *J. Phys. Chem. 113*:2805 (1991).
55. C. A. Alves, E. L. Smith, C. A. Widrig, and M. D. Porter, SPIE, *Appl. Spectrosc. Mater. Sci. II 1636*:125 (1992).
56. Li Sun and R. M. Crooks, *J. Electrochem. Soc. 138*:L23 (1991).
57. Y.-T. Kim and A. J. Bard, *Langmuir 8*:1096 (1992).
58. K. Edinger, A. Gölzhäuser, K. Demota, Ch. Wöll, and M. Grunze, *Langmuir 9*:4 (1993).
59. G. E. Poirier and M. J. Tarlov, *Langmuir 10*:2853 (1994).
60. E. Delamarche, B. Michel, Ch. Gerber, D. Anselmetti, H. -J. Güntherodt, H. Wolf, and H. Ringsdorf, *Langmuir 10*:2869 (1994).
61. J. A. M. Sondag-Huethorst, C. Schönenberger, and L. G. Fokkink, *J. Phys. Chem. 98*:6826 (1994).
62. C. Schönenberger, J. Jorritsma, J. A. M. Sondag-Huethorst, and L. G. J. Fokkink, *J. Phys. Chem. 99*:3259 (1995).
63. I. Maege, E. Jaehne, A. Henke, H.-J. P. Adler, C. Bram, C. Jung, and M. Stratmann, *Macromol. Symp. 126*:7 (1997).
64. M. Dannenfeldt, dissertation, Erlangen, 2000.
65. J. Marsh, L. Minel, M. G. Barthes-Labrousse, and D. Gorse, *Appl. Surf. Sci. 133*:270 (1998).
66. A. M. Taylor, C. H. McLean, M. Charlton, and J. F. Watts, *Surf. Interface Anal. 23*:342 (1995).
67. A. M. Taylor, J. F. Watts, J. Bromley-Barrat, and G. Beamson, *Surf. Interface Anal. 21*:697 (1992).
68. J. F. Watts, R. A. Blunden, and T. J. Hall, *Surf. Interface Anal. 16*:227 (1990).
69. G. M. Chritchlow and A. Madison, *Surf. Interface Anal. 17*:539 (1990).
70. D. M. Brewis, *J. Int. Adhesion Adhesives 13*:251 (1993).
71. B. De. Neve, M. Delamar, T. T. Nguyen, and M. E. R. Shanahan, *Appl. Surf. Sci. 134*:202 (1998).
72. C. L. Olsson-Jaques, A. R. Wilson, A. N. Rider, and D. R. Arnott, *Surf. Interface Anal. 24*:569 (1996).
73. H. Jacobs, H. Knapp, and A. Stemmer, *Rev. Sci. Instrum. 70*:1756 (1999).
74. E. Hornung, M. Rohwerder, and M. Stratmann, Elektrochemische Reaktionen an verborgenen Metall/Polymer-Grenzflächen Elektrochemische Verfahren für neue Technologien, GDCh Monographic Bd. 21 (2000) 22–30.
75. R. Lösch, M. Stratmann, and H. Viefhaus, *Electrochim. Acta 39*:1215 (1994).
76. K. L. Mittal, ed., *Silanes and Other Coupling Agents,* Vol. 2, VSP, 2000.
77. A. P. Nazarov, M. A. Petrunin, and Y. N. Mikhailovsky, Proceedings of the 11th International Corrosion Congress, Florence, 1990.
78. M. Stratmann, R. Feser, and A. Leng, *Electrochim. Acta 39*:1207 (1994).
79. M. Stratmann, M. Wolpers, H. Streckel, and R. Feser, *Ber. Bunsenges. Phys. Chem. 95*:1365 (1991).
80. M. Stratmann and H. Streckel, *Corros. Sci. 30*:681 (1990).
81. M. Stratmann and H. Streckel, *Corros. Sci. 30*:697 (1990).
82. M. Stratmann, R. Streckel, K. T. Kim, and S. Crockett, *Corros. Sci. 30*:715 (1990).
83. M. Stratmann, H. Streckel, and R. Feser, *Farbe Lack 97*:9 (1991).
84. M. Stratmann, H. Streckel, and R. Feser, *Corros. Sci. 32*:467 (1991).
85. M. Stratmann, R. Feser, and A. Leng, *Farbe Lack 100*:93 (1994).

Copyright © 2002 Marcel Dekker, Inc.

86. M. Rohwerder and M. Stratmann, *Localized In Situ Methods for Investigating Electrochemical Interfaces* (A. C. Hillier, M. Seo, and S. R. Taylor., eds.), PV 99-28, The Electrochemical Society, Pennington, NJ, 1999, p. 302.
87. M. Wolpers, M. Stratmann, H. Viefhaus, and H. Streckel, *Thin Solid Films 210/211*:592 (1992).
88. A. Leng and M. Stratmann, *Corros. Sci. 34*:1657 (1993).
89. K. Saurbier, V. Mendorf, J. W. Schultze, J. Geke, and H. Roßmaier, *Corros. Sci. 33*:1351 (1992).
90. K. Saurbier, J. W. Schultze, and J. Geke, *Electrochim. Acta 39*:1171 (1994).
91. Y. Lin, Ph.D. thesis, University of Missouri-Columbia, 1995.
92. K. D. Conners, W. J. van Ooij, S. J. Clarson, and A. Sabata, *J. Appl. Polym. Sci. 54*:167 (1994).
93. A. Sabata, W. J. van Ooij, and H. K. Yasuda, *Surf. Interface Anal. 20*:845 (1993).
94. W. J. van Ooij, D. Surmann, and H. K. Yasuda, *Prog. Org. Coat. 25*:319 (1995).
95. W. J. van Ooij, A. Sabata, D. B. Zeik, C. E. Taylor, F. J. Boerio, and S. J. Clarson, *J. Test. Eval. 23*:33 (1995).
96. W. J. van Ooij and N. Tang, *Polym. Mater. Sci. Eng. 74*:155 (1996).
97. W. J. van Ooij and K. D. Conners, *Proc. Electrochem. Soc. 95–13*:229 (1995).
98. M. Miyama and H. K. Yasuda, *J. Appl. Polym. Sci. 70*:237 (1998).
99. S. Lucas, P. Vanden Brande, and A. Weymeersch, *Surf. Coat. Technol. 101*:251 (1998).
100. T. F. Wang, T. J. Lin, D. J. Yang, J. A. Antonelli, and H. K. Yasuda, *Prog. Org. Coat. 28*:291 (1996).
101. H. K. Yasuda, T. F. Wang, D. L. Cho, T. J. Lin, and J. A. Antonelli, *Prog. Org. Coat. 30*:31 (1997).
102. N. Sato, K. Kudo, and T. Noda, *Electrochim. Acta 16*:1909 (1971).
103. H. Mishimada, B. A. L. Dmishima, E. Santos, C. P. Depauli, K. Azumi, and N. Sato, *Electrochim. Acta 36*:1491 (1991).
104. S. Eufinger, W. J. van Ooij, and K. D. Conners, *Surf. Interface Anal. 24*:841 (1996).
105. G. Grundmeier and M. Stratmann, Interfacial and corrosion studies of plasma polymer coated steel and galvanised steel, *Silanes and Other Coupling Agents* (K. L. Mittal, ed.), Vol. 2, VSP, 2000.
106. U. Schwertmann and R. M. Cornell, *Iron Oxides in the Laboratory*, VCH, Weinheim, 1991.
107. A. Raman, B. Kuban, and A. Razvan, Corrosion Sci. 32 (1991) p. 1295 (1991).
108. R. Jasinski and A. Iob, J. Electrochem. Soc. 135 (1988) p. 551 (1988).
109. M. G. Bernard et. al., Corrosion Sci. *35*, No. 5–8, 1339 (1993).
110. G. Grundmeier and M. Stratmann, *Appl. Surf. Sci. 141*:43 (1999).
111. A. T. Fromhold, *Thin Solid Films 95*:297 (1982).
112. A. M. Wróbel, M. Kryszewski, and M. Gazicki, *J. Macromol. Sci. Chem. 20*:583 (1983).
113. A. M. Wróbel and M. R. Wertheimer, *Plasma Deposition, Treatment, and Etching of Polymers* (R. d'Agostino, ed.), Academic Press, New York, 1990.
114. A. M. Wróbel, J. Kowalski, J. Grebowicz, and M. Kryszewski, *J. Marcromol. Sci. Chem. A17*:433 (1982).
115. G. Grundmeier and M. Stratmann, *Mater. Corros. 49(3)*:150 (1998).
116. M. W. Urban, *Vibrational Spectroscopy of Molecules and Macromolecules on Surfaces,* John Wiley & Sons, New York, 1993, pp 214–222.
117. G. Grundmeier and M. Stratmann, *Thin Solid Films 352*:119 (1999).
118. K. Doblhofer, *Makromol. Chem. 8*:323 (1987).
119. M. K. Weldon, Y. J. Chabal, D. R. Hamann, S. B. Christman, and E. E. Chaban, *Surf. Sci. 368*:163 (1996).
120. G. Grundmeier, E. Matheisen, and M. Stratmann, *J. Adhes. Sci. Technol. 10*:573 (1996).

Copyright © 2002 Marcel Dekker, Inc.

121. G. Grundmeier, C. Reinartz, M. Rohwerder, and M. Stratmann, *Electrochim. Acta 43*:165 (1996).
122. M. Brettmann and G. Grundmeier, Publication in progress.
123. Y. Iriyama, T. Ihara, and M. Kiboku, *Thin Solid Films 287*:169 (1996).
124. C. Oehr and B. Schindler, *Surf. Coat. Technol. 98*:848 (1998).
125. Y. Lin and H. Yasuda, *J. Appl. Polym. Sci. 60*:543 (1996).

Copyright © 2002 Marcel Dekker, Inc.

15

Atmospheric Corrosion

Christofer Leygraf
Royal Institute of Technology, Stockholm, Sweden

INTRODUCTION

Atmospheric corrosion is the oldest type of corrosion recognized, and the atmosphere is the environment to which metals are most frequently exposed [1]. The impact on high-technology societies has been exemplified by the assumption that the cost of protection against atmospheric corrosion is about 50% of the total costs of all corrosion protection measures [2].

Atomospheric corrosion is the result of interaction between a material—mostly a metal—and its atmospheric environment. When exposed to atmospheres at room temperature with virtually no humidity present, most metals spontaneously form a solid oxide film. If the oxide is stable, the growth rate ceases and the oxide reaches a maximum thickness of 1 to 5 nm (1 nm = 10^{-9} m). Atmospheric corrosion frequently occurs in the presence of a thin aqueous layer that forms on the oxidized metal under ambient exposure conditions; the layer may vary from monomolecular thickness to clearly visible water films. Hence, atmospheric corrosion can be said to fall into two categories: "damp" atmospheric corrosion, which requires the presence of water vapor and traces of pollutants, and "wet" atmospheric corrosion, which requires rain or other forms of bulk water together with pollutants [3].

It was the pioneering work of Vernon [4] that developed the field of atmospheric corrosion to a scientific level. He discovered that corrosion rates increase rapidly above a "critical humidity" level, and he was also the first scientist to demonstrate the combined accelerating effects of SO_2 and relative humidity on atmospheric corrosion rates. Later, Evans [3], Rozenfeld [5], Barton [2], and others demonstrated that electrochemical processes play important parts, and it became evident that atmospheric corrosion of metals involves a broad range of electrochemical, chemical, and physical processes. The progress in the understanding of atmospheric corrosion has been reviewed in several books and review chapters [2, 5–7] and updated in various conference proceedings [8–10].

There are obvious reasons why scientists' interest in atmospheric corrosion has become even more widespread during the past decades and why atmospheric corrosion has become a truly interdisciplinary field of science. Environmental effects on outdoor constructions—not least those that are part of our cultural and historical

Copyright © 2002 Marcel Dekker, Inc.

heritage—and on vehicles have triggered national and international exposure programs with comprehensive characterization of acidifying pollutant levels. Today the environmental effects not only concern what the environment does to metals but also what the metal does to the environment after running off any outdoor construction and reaching the biosphere. Frequently observed failures of highly miniaturized electronic components and equipment—even at low levels of pollutants—have focused technicians' and scientists' interest on indoor conditions too. Furthermore recent progress in the development of new analytical techniques has resulted in a more detailed understanding of surface and interface phenomena as well as a better characterization of the corrosion products formed.

The purpose of this chapter is to outline briefly some of the new insights that have emerged as a result of basic studies of the atmospheric corrosion of metals. The chapter is entirely devoted to metallic materials, which means that the reader will have to turn to other sources for reviews of atmospheric corrosion of, for example, calcareous stones, glasses, plastics, painted materials, and textiles.

The complex interaction between the metal and the environment ranges from the atmospheric region over the thin aqueous layer to the solid surface region. Hence, the next three sections are devoted to various reactions and other phenomena in each of the regions involved. They are followed by two sections that deal with selected aspects of atmospheric corrosion outdoors and indoors, respectively.

THE ATMOSPHERIC REGION

The main constituents of the troposphere—the atmospheric region closest to the earth—are N_2, O_2, and rare gases (Ne, Kr, He, and Xe). They comprise more than 99.9% by weight of all molecules involved [11, p. 9]. Among these, N_2 and the rare gases are of no significant importance to atmospheric corrosion because of their inability to react with metal surfaces. O_2, on the other hand, is of paramount importance due to its participation as an electron acceptor in cathodic reactions and its involvement in chemical transformations of the atmosphere. Other tropospheric constituents conducive to atmospheric corrosion are H_2O and CO_2. H_2O is of critical importance in several respects (its role is discussed in more detail in the following sections). Its concentration in the troposphere varies over several orders of magnitude—from around 100 volume parts per million (ppm) to 10,000 ppm. The role of CO_2 has been strikingly overlooked in studies of atmospheric corrosion. This naturally occurring molecule, which has a concentration of about 330 ppm and high solubility in water, contributes to the acidification of the aqueous layer.

The remaining constituents of importance in atmospheric corrosion are present only as trace gases with a total concentration of less than 10 ppm. Numerous investigations based on both laboratory and field exposures have proved at least the following gaseous constituents to be of significant importance [12]: O_3, H_2O_2, SO_2, H_2S, COS, NO_2, HNO_3, NH_3, HC1, Cl_2, HCHO, and HCOOH. Typical ranges for most of these constituents are given in Table 1 for outdoor and indoor conditions. Their presence may be the result of either natural or anthropogenic processes, and they may undergo a variety of chemical transformations during transport in the troposphere. Because all species are reactive, they have a certain average lifetime, which is often limited by the ability to react with important atmospheric oxidizers,

Copyright © 2002 Marcel Dekker, Inc.

Species	Outdoor	Reference	Indoor	Reference
O_3	4–42	17	3–30	17
H_2O_2	10–30	18	5	19
SO_2	1–65	17	0.3–14	17
H_2S	0.7–24	17	0.1–0.7	17
NO_2	9–78	17	1–29	17
HNO_3	1–10	18	3	19
NH_3	7–16	17	13–259	17
HCl	0.18–3	17	0.05–0.18	17
Cl_2	< 0.005–0.08[a]	17	0.001–0.005	17
HCHO	4–15	18	10	19
HCOOH	4–20	18	20	19

[a]Corresponding to 5wt % HCl according to Ref. 17.

primarily the hydroxyl radical, OH·, and O_3. OH· is generated by photoinduced dissociation of O_3 and the subsequent reaction of the electronically excited, energy-rich, oxygen atom $O(^1D)$ and water vapor:

$$O_3 + h\nu \rightarrow O(^1D) + O_2 \quad (\lambda < 310\,\text{nm}) \tag{1}$$

$$O(^1D) + H_2O \rightarrow 2OH\cdot \tag{2}$$

Although OH. molecules can oxidize several of the corrosion-stimulating species, such as SO_2, H_2S, and NO_2, a large fraction of OH· molecules are consumed through reactions with hydrocarbon molecules, whereby one of the end products is the hydroperoxyl radical, $HO_2\cdot$. This is another important component in gas-phase chemistry because it disproportionates into hydrogen peroxide, H_2O_2, and O_2 according to:

$$HO_2\cdot + HO_2\cdot \rightarrow H_2O_2 + O_2 \tag{3}$$

H_2O_2, being highly soluble in aqueous environments, is another powerful oxidizer. The importance of oxidizing species in atmospheric chemistry and the multitude of reaction paths can be exemplified by considering different sulfur- , nitrogen- , and chlorine-containing compounds of significance in atmospheric corrosion.

Sulfur-Containing Compounds

SO_2 has long been recognized as the most important gaseous stimulant in atmospheric corrosion. It has many anthropogenic sources, such as combustion of sulfur-containing coal and oil, and emission from metal, petrochemical, and pulp and paper industries. Depending on the environment, there are several possible ways for SO_2 to oxidize, some of which are summarized below. In the gas phase, SO_2 can oxidize according to [13]:

$$SO_2 + OH\cdot \rightarrow HSO_3\cdot \tag{4}$$

Copyright © 2002 Marcel Dekker, Inc.

$$HSO_3 \cdot + O_2 \xrightarrow{M} SO_3 + HO_2 \cdot \quad (5)$$

$$SO_3 + H_2O \rightarrow H_2SO_4 \quad (6)$$

where M designates another gaseous molecule (e.g., N_2 or O_2) that collides with a generated $HSO_3 \cdot$ molecule and removes some of the excess energy released. In the aqueous phase [14]:

$$SO_2 + xH_2O = SO_2 \cdot xH_2O \quad (7)$$

$$SO_2 \cdot xH_2O = HSO_3^- + H_3O^+ + (x-2)H_2O \quad (8)$$

$$HSO_3^- \xrightarrow{H_2O_2} SO_4^{2-} \quad (9)$$

The oxidation of S(IV) to S(VI) in the aqueous phase may also slowly proceed through:

$$SO_2 + H_2O + \tfrac{1}{2}O_2 \rightarrow H_2SO_4 \quad (10)$$

or be promoted by O_3, Fe(III)- or Mn(II)-containing catalysts, or an increased pH [14].

H_2S, together with COS, is another principal atmospheric corrosion stimulant. It is emitted both from natural biological sources (e.g., volcanoes, moss, or swamp areas) and from anthropogenic sources (e.g., pulp and paper industries, catalyst converters in motor vehicles, sewage plants, garbage dumps, animal shelters, and geothermal power plants). H_2S can react with $OH \cdot$ to form SO_2 according to [15]:

$$H_2S + OH \cdot \rightarrow HS \cdot + H_2O \quad (11)$$

$$HS \cdot + 2O_2 \rightarrow HO_2 \cdot + SO_2 \quad (12)$$

Nitrogen-Containing Compounds

NO and NO_2 are mainly formed through high-temperature combustion processes in power plants, vehicles, etc. The fraction of NO in the combustion gas is much higher than that of NO_2 but it is rapidly converted to NO_2 according to:

$$2NO + O_2 \rightarrow 2NO_2 \quad (13)$$

Farther away from the emission source NO may also form NO_2 through:

$$NO + O_3 \rightarrow NO_2 + O_2 \quad (14)$$

NO_2 plays a most important part in atmospheric chemistry by absorption of solar light and the subsequent formation of O_3 through:

$$NO_2 + h\nu \rightarrow NO + O \qquad (\lambda < 420\,\text{nm}) \quad (15)$$

$$O + O_2 \xrightarrow{M} O_3$$

NO_2 can also be oxidized to nitric acid according to:

$$NO_2 + OH \cdot \xrightarrow{M} HNO_3 \quad (16)$$

Copyright © 2002 Marcel Dekker, Inc.

Several of the reactions described have been identified in so-called photochemical smog formation [16]. This complex set of reactions involves an initial mixture of nonmethane organic compounds, NO, and NO_2, which is photochemically transformed into a final mixture including HNO_3 and O_3, aldehydes, and peroxyacetylnitrate.

Principal sources of emission of NH_3 are animal shelters, fertilizer production, and cleaning detergents. In the aqueous phase, NH_3 establishes equilibrium with NH_4^+, which results in increased pH. An important role of NH_3 in atmospheric corrosion chemistry is to partly neutralize acidifying pollutants by forming particulate $(NH_4)_2SO_4$ and acid ammonium sulfates, such as NH_4HSO_4 and $(NH_4)_3H(SO_4)_2$. By increasing the pH of the aqueous phase, NH_3 also increases the oxidation rate of S(IV) to S(VI), as discussed earlier.

Chlorine-Containing Compounds

Chlorides participate in atmospheric corrosion reactions mainly as aerosols through transport from marine atmospheres. Other important sources are road deicers and dust binders on roads, coal burning, municipal incinerators, and fingerprints. Burning of high-chlorine coals may also result in emission of HCl, which is highly soluble in water and strongly acidifies the aqueous phase. Cl_2 is emitted from industrial processes, such as bleaching plants in pulp and paper industries and certain metal production industries, and from cleaning detergents. Cl_2 can also photodissociate into chlorine radicals, which react with organic compounds (RH) and form HC1 according to:

$$Cl_2 + h\nu \rightarrow Cl\cdot + Cl\cdot \qquad (\lambda < 430\,\text{nm}) \tag{17}$$

$$RH + Cl\cdot \rightarrow R\cdot + HCl \tag{18}$$

Other Atmospheric Compounds

In addition to the gaseous species already commented on, Table 1 includes HCHO and HCOOH, which are important indoor corrosion stimulants (as discussed later) and which can originate from adhesives, tobacco smoke, combustion of biomass, and plastics, for example. A comparison between typical outdoor and indoor concentrations of the most important gaseous corrosion stimulants (Table 1) reveals, in general, lower levels indoors than outdoors. This is mostly due to enhanced indoor absorption of gases and particulates and also to the retardation and damping of outdoor variations by ventilating systems and air filtration. Exceptions are NH_3 and the organic species, which, as a rule, show higher levels indoors than outdoors as a result of anthropogenic activity.

Of utmost importance in atmospheric corrosion is the presence of particles and aerosols (an ensemble of particles suspended in the air) of mostly chlorides, sulfates, and nitrates. The size, shape, and chemical and physical properties of these particles and aerosols can vary widely. A more detailed description of particles and their role in (indoor) atmospheric corrosion is given elsewhere [20].

Copyright © 2002 Marcel Dekker, Inc.

THE AQUEOUS LAYER

Formation of the Aqueous Layer

The reaction of water vapor with a metal surface is of paramount importance to atmospheric corrosion. A large number of studies of initial water–metal interaction have been made on well-defined single-crystal surfaces of pure or oxidized metals (for a review, see Ref. 21). Water may bond in molecular form to most clean and well-characterized metal surfaces. Through the oxygen atom it bonds to the metal surface or to metal clusters and acts as a Lewis base, as bonding is connected with a net charge transfer from the water molecule to the surface. Simple models of preferred adsorption sites are based on Lewis acid-base chemistry, in which water adsorbs on electron-deficient adsorption sites [22]. Water may also bond in dissociated form, in which case the driving force is the formation of metal-oxygen or metal-hydroxyl bonds. The end products resulting from water adsorption are then adsorbed hydroxyl, atomic oxygen, and atomic hydrogen [21]. On metal oxides, water may also adsorb in either molecular or dissociative form. The tendency to dissociate seems to be facilitated by lattice defect sites, as observed, for instance, on monocrystalline TiO_2 [23], NiO [24], and a-Fe_2O_3 [25]. The monomolecular thick film of surface hydroxyl groups formed from dissociation of water is relatively protective and reduces the subsequent reaction rate of water [26]. The first monolayer of water adsorbed to the hydroxylated oxide substrate appears to be highly immobile, whereas the second and third monolayers are more randomly oriented and less immobile [27]. The water layer adjacent to the gas phase appears to have an icelike structure [28]. The adsorption characteristics of water are strikingly similar for many different metals, and the exact nature of the metal oxyhydroxide seems to have only a minor influence on water adsorption phenomena. The quantity of reversibly adsorbed water increases with the relative humidity and with time. Table 2 presents the approximate number of water monolayers at 25°C and steady-state conditions, which have been experimentally determined by the quartz crystal microbalance method on a variety of metals [28,29].

The bond strength between water and the hydroxylated metal surface is similar to the bond strength between neighboring, hydrogen-bonded, water molecules [21]. From this follows the possibility of water clusters on relatively homogeneous surfaces, which is further promoted on less well-defined surfaces with highly reactive sites, such as kinks or steps, thereby increasing the probability of anode-cathode area formation.

The aqueous phase formed acts as a solvent for gaseous constituents of the atmosphere. Preferred sites for corrosion attack may be related to sites where water

Table 2 Approximate Number of Water Monolayers on Different Metals Versus Relative Humidity

Relative humidity (%)	Number of water monolayers
20	1
40	1.5–2
60	2–5
80	5–10

Copyright © 2002 Marcel Dekker, Inc.

adsorption is favored and gaseous molecules, such as SO_2 and NO_2, are easily dissolved. At aqueous films thicker than about three monolayers, the properties approach those of bulk water [30]. The relative humidity when this occurs is close to the "critical relative humidity" [31,32], above which atmospheric corrosion rates increase substantially and below which atmospheric corrosion is insignificant. The critical relative humidity for different metals in the presence of SO_2 has been reported to be between 50 and 90% [28].

Electrochemical Reactions

The aqueous phase also acts as a conductive medium for electrochemical reactions. Although atmospheric corrosion is largely dependent on electrochemical reactions, relatively few electrochemical studies have been focused on the elucidation of these basic mechanisms. The reason seems to be obvious if one considers the difficulties in reproducing a thin aqueous film in an electrochemical experiment. The thickness of such a film may vary with different outdoor exposure conditions, involving the complex chemistry and photochemistry produced by atmospheric pollutants together with solar light and resulting in the precipitation of representative corrosion products and changed transport properties. Nevertheless, systematic electrochemical experiments have been conducted with special emphasis on atmospheric corrosion (see, e.g., Refs. 5,33–37). In the absence of pollutants, the most common anodic and cathodic processes in corrosion of metals exposed to a thin, neutral, aqueous phase are:

$$\mathrm{Me} \rightarrow \mathrm{Me}^{n+} + n\mathrm{e}^- \qquad \text{(anode reaction)} \tag{19}$$

$$\mathrm{O_2} + 2\mathrm{H_2O} + 4\mathrm{e}^- \rightarrow 4\mathrm{OH}^- \qquad \text{(cathode reaction)} \tag{20}$$

Under most atmospheric corrosion conditions, the anode reaction rather than the cathode reaction is observed to be the rate-limiting step [2]. Upon evaporation of the aqueous layer, a film of corrosion products—consisting of metal hydroxides or metal oxyhydroxides—may precipitate. With repeated condensation–evaporation cycles, this film usually hinders the transport of ions through the corrosion product or the transport of Me^{n+} from the anodic site. Hence, the anodic reaction rate is lowered and, thereby, the atmospheric corrosion rate.

Acidifying Pollutants

In the presence of atmospheric acidifying pollutants, such as SO_2, the anode reaction is facilitated and, consequently, the total corrosion rate as well. Upon deposition of SO_2, interaction with the aqueous phase proceeds with the following reactions:

$$\mathrm{SO_2} + x\mathrm{H_2O} = \mathrm{SO_2} \cdot x\mathrm{H_2O} \tag{7}$$

$$\mathrm{SO_2} \cdot x\mathrm{H_2O} = \mathrm{HSO_3^-} + \mathrm{H_3O^+} + (x-2)\mathrm{H_2O} \tag{8}$$

$$\mathrm{HSO_3^-} = \mathrm{H^+} + \mathrm{SO_3^{2-}} \tag{21}$$

Despite numerous studies of the important influence and role of SO_2, there is as yet no complete description of the interaction, on a molecular level, of SO_2 with an

Copyright © 2002 Marcel Dekker, Inc.

oxidized metal substrate in the presence of an aqueous phase. Recent in situ studies by means of infrared reflection-absorption spectroscopy have provided evidence that HSO_3^- is coordinated with the hydroxylated metal oxide surface through a fast ligand exchange mechanism, in which the surface OH^- group is replaced by SO_3^{2-} [38]; see Figure 1. Surface-bound H^+ released according to, e.g., reactions (8) and (21), may easily move from one functional group to another or from one surface site to another. In accordance with earlier proposed mechanisms for mineral dissolution in aquatic environments [39], the SO_3^{2-}-coordinated metal surface center may be detached from the oxide lattice when surrounded by two or more H^+-bonded functional groups. This results in the release of H^+ ions, which can participate in the detachment of another SO_3^{2-} -coordinated metal surface center. The net effects represent an acid-dependent dissolution rate (R_{diss}) of the oxide that has been written as:

$$R_{diss} = C[a_{H^+}]^n \tag{22}$$

where $[a_{H^+}]$ is the activity of the protons, and C and n are constants [40]. When further elaborated, Eq. (22) should include the influence of surface coordinated ligands.

If S(IV) is oxidized to S(VI), this will result in the formation of H_2SO_4 and the release of considerably more H^+ than if H_2SO_3 is involved. It follows that possible reaction paths for the oxidation of S(IV) to S(VI) are of crucial importance to atmospheric corrosion rates, and this has also been the subject of many investigations. Examples of reaction paths have been summarized in the preceding section.

The acid-dependent dissolution rate of the initially formed oxide or oxyhydroxide requires that all of the most important acidifying atmospheric pollutants be considered. Besides SO_2, these pollutants include CO_2, NO_2, and carbonyl compounds, such as HCHO and CH_3CHO, which can contribute to the total acidity in the aqueous film by forming H_2CO_3, HNO_3, HCOOH, and CH_3COOH.

At equilibrium between the water film and the atmosphere, the concentration of dissolved atmospheric gases in the film is expressed according to Henry's law:

$$[X] = H(X)p(X) \tag{23}$$

where

[X] = concentration in aqueous phase
H(X) = Henry's law constant for species X
p(X) = partial pressure of X in atmosphere

For many gases, reversible ionization reactions occur and the ordinary Henry's law constant, H, is replaced by an effective Henry's law constant, H_e. In the case of SO_2 this can be written as:

$$[H_2SO_3] + [HSO_3^-] + [SO_3^{2-}] = H_e(SO_2) \times p(SO_2) \tag{24}$$

Less dissociation takes place if the pH is decreased, which also results in a decrease of the effective Henry's law constant and a further slowdown of the dissolution of SO_2 in the aqueous layer [41].

The pH of the aqueous layer can be determined by formulating the general requirement equation that electrical neutrality must be maintained within the layer.

Copyright © 2002 Marcel Dekker, Inc.

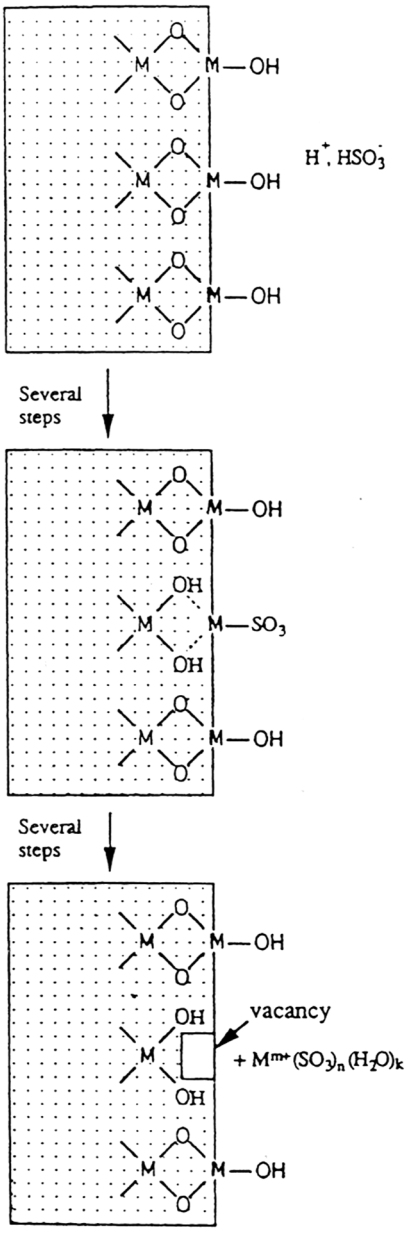


Figure 1 Fundamental processes in the initial stages of SO_2-induced atmospheric corrosion, including coordination of HSO_3^- with the hydroxylated metal oxide surface, replacement of surface OH^- group by SO_3^{2-} and detachment of the SO_3^{2-}-coordinated metal surface center when surrounded by two or more H^+-bonded functional groups.

Copyright © 2002 Marcel Dekker, Inc.

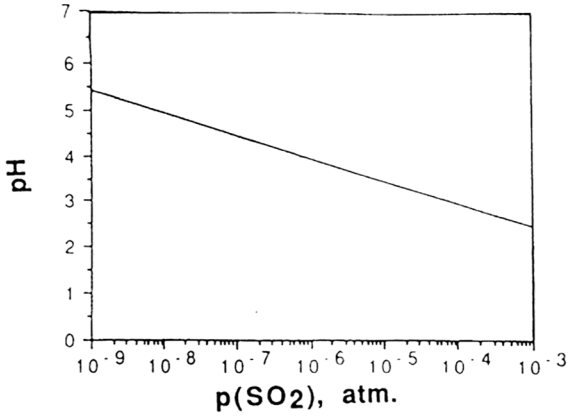


Figure 2 Variation of pH of the aqueous layer as a function of $p(SO_2)$.

This means that the sum of products of molar concentration and charge of cationic species must equal the sum of products of molar concentration and charge of anionic species. If we consider only the interaction of SO_2 with the aqueous layer, the pH is determined by

$$[H^+] = [HSO_3^-] + 2[SO_3^{2-}] + [OH^-] \tag{25}$$

The calculated pH of the aqueous layer as a function of $p(SO_2)$, according to (24) and (25), is shown in Figure 2. A more exact estimate of the aqueous layer pH must involve the contribution of other acidifying pollutants, such as CO_2, NO_2, and HCHO, as well as the properties of the solid surface film, such as its coordination properties and dissociation product. A complicating factor is the high ionic strength of many species involved, especially if the aqueous film undergoes wetting and drying cycles. If so, the concentrations of species are replaced by their activities. Henry's law constants for different gases are given in Table 3. It should be noted that Henry's law applies only if equilibrium is maintained between the gas in the atmosphere and that in the aqueous phase. Consequently, it does not apply under nonequilibrium conditions, caused by mass transport restrictions in the atmosphere, in the aqueous layer, or across the gas–liquid interface.

Deposition of Pollutants

The incorporation of atmospheric species into the aqueous layer may occur through either dry or wet deposition. In dry deposition there is no involvement of any precipitation, whereas wet deposition requires, e.g., rain, dew, fog, or snow for atmospheric pollutants to deposit. Indoors or in highly polluted areas close to emission sources, dry deposition is considered to be dominating but the relative importance of wet deposition may be difficult to establish because of the incidental nature of precipitation. Controlled field studies combined with extensive laboratory exposures have been undertaken within the National Acid Precipitation Assessment Program (NAPAP) to explore the relative contribution of wet and dry deposition to increased corrosion rates of a number of metals [45].

Copyright © 2002 Marcel Dekker, Inc.

Table 3 Characteristics of Selected Gaseous Air Constituents[a]

	A	B	Eq. Conc. (μM)		Deposition velocity (cm/s)		Deposition rate (ng/cm^2 s)	
Species	H	(M/atm)[b]	Outdoor	Indoor	Outdoor	Indoor[d]	Outdoor	Indoor
O_3	1.8	(−2)	2.3 (−4)	1.7 (−4)	0.05–1[c]	0.036	5.8 (−3)	6.8 (−4)
H_2O_2	2.4	(5)	4.2 (3)	1.2 (3)	—	0.07	—	5.0 (−4)
SO_2	1.4		1.1 (−2)	2.9 (−3)	0.01–1.2[c]	0.05	7.5 (−3)	2.7 (−4)
H_2S	1.5	(−1)	6.1 (−4)	4.0 (−5)	0.38[e]	0.03	2.2 (−3)	1.1 (−5)
NO_2	7.0	(−3)	1.9 (−4)	3.8 (−5)	0.02–0.8[c]	0.006	2.0 (−2)	6.2 (−5)
HNO_3	9.1	(4)	2.9 (2)	2.7 (2)	0.1–30[c]	0.07	1.4 (−2)	5.5 (−4)
NH_3	1.0	(1)	1.1 (−1)	5.8 (−1)	0.3–2.6[f]	0.05	6.6 (−3)	2.1 (−3)
HCl	2.0	(1)	1.5 (−2)	1.9 (−3)	—	0.04	—	5.8 (−6)
Cl_2	6.2	(−2)	1.2 (−6)	1.4 (−7)	1.8–2.1[e]	—	1.1 (−4)	—
HCHO	1.4	(4)	1.1 (2)	1.4 (2)	—	0.005	—	6.3 (−5)
HCOOH	3.7	(3)	3.3 (1)	7.4 (1)	—	0.006	—	2.3 (−4)

[a]The equilibrium solution concentration and deposition rate values were based on concentrations from Table 1 and using geometric mean values for the intervals. 1.8 (–2) means 1.8 ˘ 10^{-2}.
[b]Henry's law constant, from Ref. 19.
[c]Ref. 42.
[d]Ref. 19.
[e]Ref. 43.
[f]Ref. 44.

A useful parameter is the dry deposition velocity, which is defined as the ratio of deposition rate or surface flux per time unit of any gaseous compound and the concentration of the same compound in the atmosphere [46]. The concept of dry deposition velocity of SO_2 and its relevance to atmospheric corrosion rates is well established [47]. By examining data based on both field and laboratory exposures. it can be concluded that the factors controlling dry deposition fall into aerodynamic processes and surface processes. Aerodynamic processes are connected with the actual depletion of the gaseous constituent (e.g., SO_2) in the atmospheric region next to the aqueous phase and the ability of the system to mix new SO_2 into this region. This ability depends on, for instance, the actual wind speed, type of wind flow, and shape of sample. Surface processes, on the other hand, are connected with the ability of the aqueous layer to accommodate SO_2. This ability increases with the thickness of the aqueous layer and, hence, with the relative humidity, the pH of the solution (as discussed earlier), and the alkalinity of the solid surface.

The dry deposition velocity (V_d) can be expressed as the inverse of the sum of two resistances, namely the aerodynamic resistance (R_a) and the surface resistance (R_s):

$$V_d = 1/(R_a + R_s) \tag{26}$$

Under most exposure conditions the dry deposition velocity will be the combined effect of both resistances [46]. At well-stirred and highly turbulent airflow conditions, however, R_d » 0 and the dry deposition velocity solely depends on surface

Copyright © 2002 Marcel Dekker, Inc.

processes. Ideal absorbers of SO_2 are alkaline surfaces such as lead peroxide or triethanolamine, for which R_s » 0. The dry deposition velocity in this case is determined mainly by aerodynamic processes. Typical ranges for dry deposition velocities onto various materials under outdoor and indoor conditions are summarized in Table 3.

A combined experimental and theoretical approach to mass transport limitations in atmospheric corrosion has been performed by Volpe [48,49] to obtain dry deposition velocities and probabilities of H_2S, NO_2, and O_3 reacting with Ag. This approach clearly shows the effect of airflow velocity on the corrosion rate and the significance of hydrodynamic and concentration boundary layers next to the metal surface, characterized by deviating tangential airflow velocity and concentration of air constituents; see Figure 3. An application of boundary layer theory to buildings and other objects has been reported aimed at postulating the economic assessment of corrosion damage [50].

An immediate consequence of dry deposition velocities is the kinetic constraints to obtain equilibrium between a gas in the atmosphere and the same gas in the aqueous layer. Especially in outdoor exposure conditions, characterized by wet-dry cycles, it is anticipated that the actual concentration of most corrosion-stimulating gases under many conditions may be far from equilibrium. Nevertheless, thermodynamic considerations have been most useful for predicting the formation of different corrosion end products and their stability domains [51,52]. A general and useful observation made by Graedel is the similarity between corrosion products found after prolonged exposure of metals and minerals formed by natural processes and containing the same metals (see, e.g., Ref. 53).

Figure 4 is a schematic illustration of important processes occurring in or at the aqueous layer.

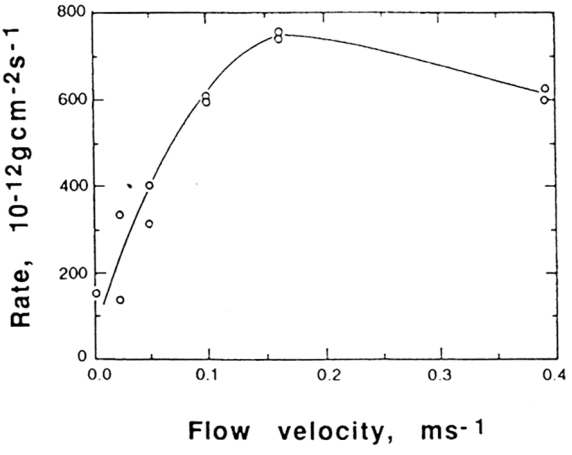


Figure 3 Influence of airflow velocity on atmospheric corrosion rate of Cu in a laboratory mixed-gas environment. (From Ref. 49. Courtesy of The Electrochemical Society.)

Copyright © 2002 Marcel Dekker, Inc.

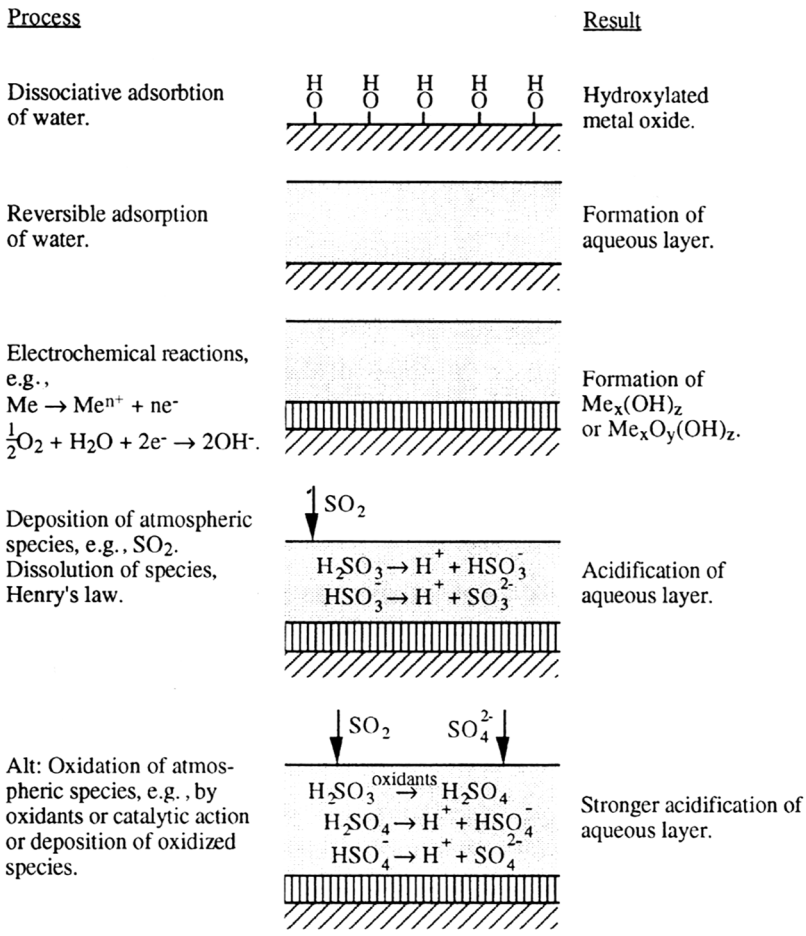


Figure 4 Schematic illustration of processes occurring in or at the aqueous layer.

THE SOLID PHASE

Acid-Dependent Dissolution

As discussed earlier, initial electrochemical reactions and repeated wet-dry cycles may result in precipitation of thin films of metal hydroxide, oxyhydroxide, or oxide. The precipitation processes of these compounds are complex and pass through the colloid state before solid films are formed [54]. These films form on the metal surface normally by fast nucleation and spreading and by slower thickening, once the film has completely covered the surface. If the film is stable, it thickens through a high-field ion conduction mechanism; otherwise the film may thicken through a dissolution-reprecipitation mechanism [55]. One approach to predicting the ability to form a protective oxygen-containing film is by considering the heat of the adsorption of oxygen on the metal. Compilations of such data [56] suggest strong metal-oxygen bond formation and highly protective layers in various atmospheres in the case of, e.g., Ti, Al, or Cr, but only weak metal-oxygen bonds

Copyright © 2002 Marcel Dekker, Inc.

and practically nonexistent protective oxygen-containing films in the case of, e.g., Ag or Zn.

As a consequence of exposure to the aqueous layer, the oxygen-containing film can dissolve—the corrosion rate being normally controlled by the rate of dissolution of the film formed [55]. As mentioned in the preceding section, the dissolution rate of many oxides and other minerals is acid dependent and can be written in the form:

$$R_{\text{diss}} = C[a_{H^+}]^n \tag{22}$$

Metal-Anion Coordination Based on the Lewis Acid–Base Concept

During prolonged exposure a variety of different corrosion products may form, the exact nature of which largely depends on the ability of the dissolving metal ion to coordinate with other ions in the aqueous layer. A general treatment of classification of participating ions in coordination processes can be based on the Lewis acid–base concept. So far this theory has found only few applications in corrosion science [57]. It turns out to be most useful in rationalizing the specific behavior of different metals during atmospheric corrosion and therefore merits a short introduction.

Upon interaction of two species, a pair of electrons from one species can be used to form a covalent bond to the other one. The species that donates the electron pair is called a *Lewis base*, and the species that accepts the electron pair is called a *Lewis acid*. Acids or bases with valence electrons that are tightly held and not easily distorted are *hard* acids or bases. Acids or bases with valence electrons that are easily polarized or removed are *soft*. According to the hard and soft acid-base (HSAB) principle, hard acids are preferably coordinated with hard bases and soft acids are preferably coordinated with soft bases [58]. The hardness of an element usually increases with its oxidation state. Selected Lewis acids and bases and their classification into hard, intermediate, and soft acids and bases are listed in Table 4 [59].

In full agreement with experience from atmospheric corrosion, Table 4 suggests that hard acids such as Cr^{3+} and Ti^{4+} form oxygen-containing films, whereas soft acids such as Cu^+ and Ag^+ coordinate with reduced sulfur compounds. Intermediate acids, such as Fe^{2+}, Cu^{2+}, and Zn^{2+}, are expected to coordinate with a broader range of bases.

Table 4 Classificaiton of Selected Lewis Acids and Bases

Hard	Intermediate	Soft
	Acids	
H^+, Na^+, Mn^{2+}, Al^{3+} Cr^{3+}, Fe^{3+}, Ti^{4+}	Fe^{2+}, Ni^{2+}, Cu^{2+} Zn^{2+}, Pb^{2+}	Cu^+, Ag^+
	Bases	
H_2O, OH^-, O^{2-} SO_4^{2-}, NO_3^-, CO_3^{2-}	SO_3^{2-}, NO_2^-	R_2S, RSH RS^-

Source: From Ref. 59.

Copyright © 2002 Marcel Dekker, Inc.

Formation of Corrosion Products

The atmospheric corrosion rate is influenced by many parameters, one of the most important being the formation and protective ability of the corrosion products formed. The composition of the corrosion products depends on the participating dissolved metal ions and the access to anions dissolved in the aqueous layer. The eventual thickening of the film of corrosion products can be described in a sequence of consecutive steps—dissolution–coordination–reprecipitation—where the dissolution step is acid dependent, coordination is based on the HSAB principle, and reprecipitation depends on the activities of the species involved.

Depending on the rate of crystallization and the rate of formation, the corrosion products may be amorphous or crystalline. If the former is rate determining, one expects amorphous phases to form. From colloid chemistry it is known that aging or slow growth of amorphous phases may result in a transition from the amorphous to the crystalline state, a process that may occur through slow transformation in the solid state or through dissolution–reprecipitation processes [60]. This seems to be in agreement with findings of a transition from amorphous to crystalline basic nickel sulfates, the former being less corrosion resistant than the latter [61a].

Figure 5 is a schematic illustration of important processes occurring in or at the solid phase.

Atmospheric Corrosion of Selected Metals

Access to new and more sensitive analytical techniques has resulted in substantial progress in the characterization of corrosion products formed under both laboratory and field exposure conditions. These techniques permit the determination of, e.g., thickness, chemical composition, and atomic structure of corrosion products formed at both early and later stages of exposure. When combined with environmental data, such as deposition rates of corrosion-stimulating atmospheric constituents, relative humidity, temperature, and sunshine hours, the new techniques have resulted in a more comprehensive understanding of the complex processes that govern atmospheric corrosion. In a series of papers, Graedel has summarized the corrosion mechanisms of zinc [62], aluminum [63], copper [18], iron and low-alloy steel [64], and silver [19]. It is beyond the scope of this chapter to provide a detailed description of the specific atmospheric corrosion behavior of each individual metal. Nevertheless, a summary of atmospheric corrosion behavior of selected metals will be given in light of the general processes that have been discussed. The summary is based on the papers by Graedel, unless otherwise stated.

The atmospheric corrosion of zinc starts with the instant formation of a thin film of zinc hydroxide, which seems to occur in different crystal structures, and the subsequent formation of a protective layer of basic zinc carbonate, $Zn_5(CO_3)_2(OH)_6$. The pH of the aqueous layer controls the stability of initial corrosion products and results in the dissolution of Zn^{2+}. From the HSAB principle one expects Zn^{2+}, classified as an intermediate acid, to coordinate with a number of different bases. In accordance with this, the prolonged exposure of zinc can proceed along a variety of different paths of reaction sequences depending on the actual deposition rates of atmospheric constituents. Among these Cl^- and SO_2 seem to be the most important.

Copyright © 2002 Marcel Dekker, Inc.

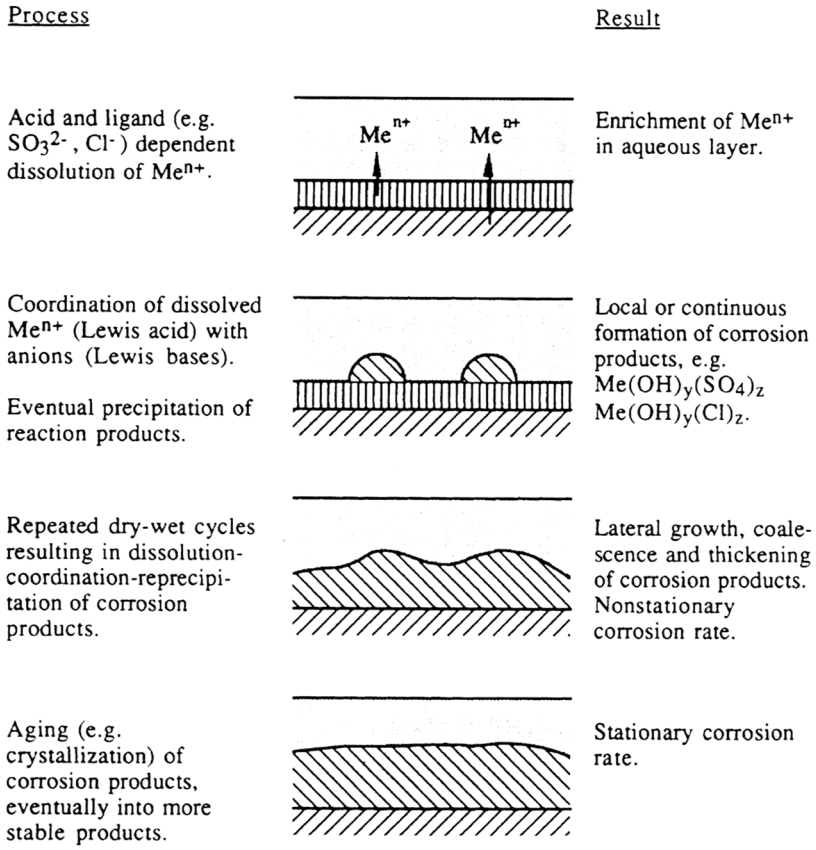


Figure 5 Schematic illustration of processes occurring in or at the solid phase.

In a relatively benign rural atmosphere, the basic zinc carbonate may continue to grow slowly or may be followed by the formation of a protective basic zinc sulfate, e.g., $Zn_4SO_4(OH)_6 \cdot 4H_2O$. In a typical marine atmosphere, characterized by higher amounts of deposited Cl^- than of SO_2, islands of a less protective basic zinc chloride, $Zn_5Cl_2(OH)_8 \cdot H_2O$, are formed within days of exposure. These islands grow laterally and coalesce. Within weeks of exposure, a more protective basic zinc chlorosulfate, $NaZn_4Cl(OH)_6SO_4 \cdot 6H_2O$, may be observed [65]. In a typical urban environment, characterized by higher amounts of deposited SO_2 than of Cl^-, the basic zinc sulfate, $Zn_4SO_4(OH)_6 \cdot 4H_2O$, is observed within, typically, weeks of exposure. In highly polluted industrial environments, it is eventually followed by another basic zinc chlorosulfate, $Zn_4Cl_2(OH)_4SO_4 \cdot 5H_2O$. A feature common to most zinc-containing corrosion products observed is their strong structural resemblance, with sheets of Zn^{2+} in octahedral and tetrahedral coordination and with the main difference between the structures being the content and bonding between the sheets [66]. A generalized reaction sequence has been proposed that considers the evolution of corrosion products on sheltered zinc in a variety of atmospheric environments, including rural, marine, urban, and industrial [66]. Figure 6 displays schematically the

Copyright © 2002 Marcel Dekker, Inc.

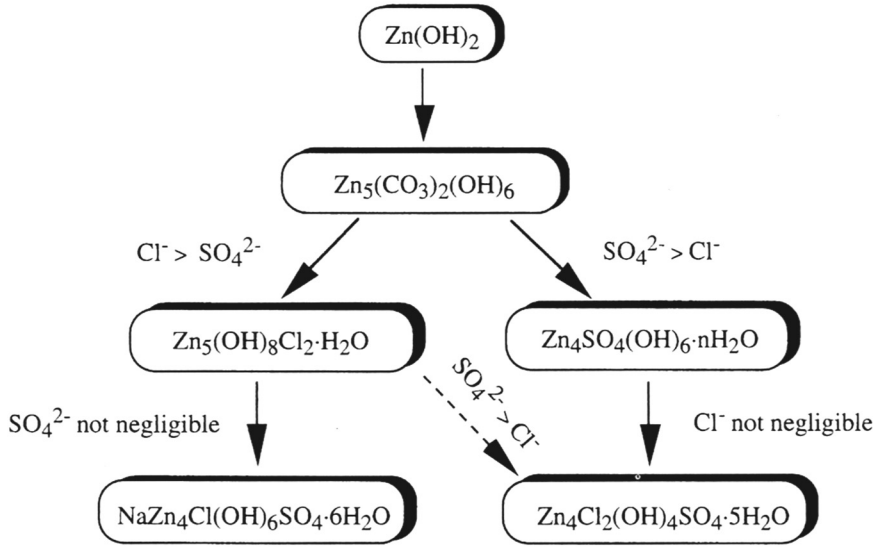


Figure 6 Formation sequences for compounds in zinc corrosion products formed under sheltered conditions dominated by chloride deposition (left sequence) and sulfate deposition (right sequence). (From Ref. 66. Courtesy of the American Society for Testing and Materials.)

reaction sequence in which sulfate deposition dominates over chloride deposition (right part) and the reaction sequence in which chloride deposition dominates over sulfate deposition (left part). Reported corrosion rates (in μm/year) of zinc in outdoor atmospheres range from 0.2 to 0.3 (rural), from 0.5 to 8 (marine), and from 2 to 16 (urban, industrial).

Aluminum forms initially a few-nm-thick layer of aluminum oxide, γ-Al_2O_3, which after prolonged exposure in humidified air is covered by aluminum oxyhydroxide, γ-AlOOH, and subsequently by various hydrated aluminum oxides and aluminum hydroxides. The stability of the compounds decreases with acidity and results in the dissolution of Al^{3+}. The ability of aluminum to form various oxygen-containing corrosion products is in agreement with the HSAB principle; this is also the case with the general observation of frequent formation of basic or hydrated aluminum sulfates and no detection of aluminum sulfides. The sulfates most frequently found on aluminum are poorly soluble, amorphous, and highly protective. As with other passivating metals, atmospheric corrosion rates of aluminum increase readily in the presence of Cl^-, resulting in local rather than uniform corrosion. Rates of uniform corrosion (in μm/year) of aluminum outdoors are substantially lower than for most other structural metals and are from 0.0 to 0.1 (rural), from 0.4 to 0.6 (marine), and ≈1 (urban).

In ambient air copper initially forms a film with a total thickness of around 3 nm. It seems to contain at least two layers, both of which contain copper as Cu^+. The inner layer close to the metal consists of Cu_2O and the outer layer of bound hydroxyl, water, and adventitious hydrocarbon [67]. Cu dissolves into the aqueous layer as Cu^+, which readily oxidizes to Cu^{2+}. From the presence of both Cu^+ (soft acid) and Cu^{2+} (intermediate acid) a variety of corrosion products are expected.

Copyright © 2002 Marcel Dekker, Inc.

With reduced sulfur compounds present in significant concentrations, copper mainly forms Cu_2S. Without reduced sulfur compounds, the corrosion products are frequently complex mixtures of basic copper sulfates, chlorides, nitrates, and carbonates, with a composition that depends on the actual deposition rates of the corresponding air constituents. Abundant phases are $Cu_4SO_4(OH)_6$ and $Cu_3SO_4(OH)_4$ in urban areas and $Cu_2Cl(OH)_3$ and possibly basic sulfates in marine atmospheres. Other phases observed are $Cu_4SO_4(OH)_6 \cdot H_2O$, $Cu_2NO_3(OH)_3$, and $Cu_2CO_3(OH)_2$. Similar to that for zinc, a generalized reaction sequence has been proposed for sheltered copper, which integrates all existing knowledge of phases formed in copper patina during exposure in atmospheric environments with varying degree of sulfur and chloride pollution [67]. The phases observed bear structural resemblance and are mostly layered, a common observation in basic salts of divalent cations such as Cu^{2+} and Zn^{2+}. Representative corrosion rates (in μm/year) of copper exposed outdoors are ≈ 0.5 (rural), ≈ 1 (marine), 1–2 (urban), and ≤ 2.5 (industrial).

Initial stages of atmospheric corrosion of iron involve the incorporation of oxygen and water into a rich variety of different iron oxides or iron oxyhydroxides as rust layers. These processes are preceded by initial dissolution of Fe^{2+}, which only slowly oxidizes to Fe^{3+}. From this follows that corrosion products formed at earlier stages of exposure contain iron in both valence states but only as Fe^{3+} at later stages. A complex chemistry is anticipated with the participation of an intermediate acid slowly transforming into a hard acid. The oxidation of Fe^{2+} in the aqueous layer may involve several possible oxidants, such as the hydroxyl radical ($OH\cdot$), the hydroperoxyl radical ($HO_2\cdot$), and hydrogen peroxide (H_2O_2). Detailed discussions of the interaction between SO_2 and iron have been presented elsewhere [68]. It results in the formation of iron(II) sulfates, subsequent oxidation of Fe^{2+}, and concomitant formation of iron(III) oxyhydroxide, the release of SO_4^{2-}, the dissolution of more Fe^{2+} formation of new iron(II) sulfate, etc. [69]. This acid regeneration cycle continues until basic iron(III) sulfate is formed as an end product. The complex interaction of SO_2 and iron is believed to take place in locally distributed sulfate "nests,"

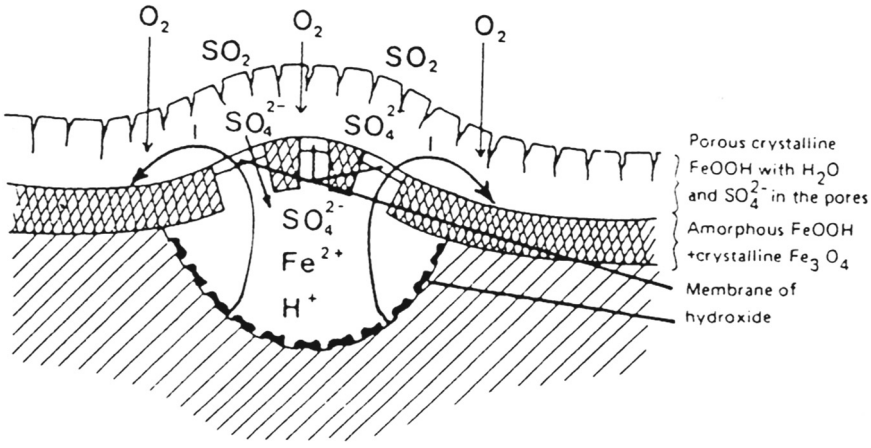


Figure 7 Sketch of sulfate "nest" on steel. (From Ref. 6.)

Copyright © 2002 Marcel Dekker, Inc.

which involve the assumed existence of semipermeable membranes of iron(III) oxyhydroxide maintaining a high activity of species involved at localized parts of the electrolyte (Fig. 7). Evidence of nitrate- or carbonate-containing corrosion products is sparse, although coordination of these anions with Fe^{3+} is expected according to the HSAB principle. There is abundant evidence of accelerated atmospheric corrosion rates for iron caused by chlorides, which may result in the formation of basic iron(II,III) chlorides and b-FeOOH. Atmospheric corrosion rates for iron are relatively high and exceed those of other structural metals. They range (in μm/year) from 4 to 65 (rural), from 26 to 104 (marine), from 23 to 71 (urban), and from 26 to 175 (industrial).

In addition to the structural metals already discussed, results have been reported from studies of the atmospheric corrosion behavior of other metals, many of which are used as materials in electronic or electric equipment.

The atmospheric corrosion of nickel is similar to that of zinc. Nickel exists solely as Ni^{2+} and instantaneously forms nickel hydroxide and, subsequently, $NiSO_4 \cdot 6H_2O$, has been observed [61b]. After prolonged exposure, an amorphous basic nickel sulfate is formed, frequently mixed with small amounts of carbonate, with less protective ability. This phase can crystallize and form another basic nickel sulfate, with higher stability and protective ability [61a]. No evidence of other anions in the corrosion products has been found so far. The corrosion rates of nickel are comparable to those of copper [70].

Silver exhibits a corrosion behavior which hardly resembles that of any of the other metals described. Its unique behavior is to a large extent governed by the existence of Ag^+ upon dissolution of silver into the aqueous layer. Ag_2S is the most abundant component of the corrosion products formed. AgCl can form in environments with high chloride content, whereas no oxides, nitrates, sulfates, or carbonates have been reported in connection with atmospheric exposure. Silver exhibits corrosion rates comparable to those of aluminum, lower than those of zinc, and much lower than those of iron.

Tin forms both SnO_2 and SnO as dominating corrosion products in a variety of environments, resulting in a relatively high protective ability. Laboratory exposures involving mixtures of SO_2, NO_2, and H_2S suggest that tin is relatively unaffected by these pollutants [71]. Accordingly, efforts to correlate corrosion effects of tin in natural atmospheric environments with concentrations of SO_2 and NO_2 have so far been unsuccessful [72]. Tin exhibits corrosion rates comparable to those of silver [72].

ATMOSPHERIC CORROSION OUTDOORS

Early field exposure programs with selected metals were implemented in the United States and the United Kingdom in the beginning of the 20th century. The environments were classified as "rural," "urban," "marine," and "industrial," and it was soon recognized that corrosion rates vary considerably between different types of environment. Over the decades a large number of outdoor corrosion test programs have been implemented with the general aim of identifying and, possibly, quantifying the most important environmental parameters involved in atmospheric corrosion processes. The large body of data available has provided evidence that corrosion rates under outdoor exposure conditions are strongly influenced by SO_2

Copyright © 2002 Marcel Dekker, Inc.

and Cl^- as well as by climatic factors (humidity and temperature). Despite this, the general goal of predicting the performance of a given metal in a given environment is far from being attained [73]. The reason is that many other factors influence corrosion rates: initial exposure conditions, sample mass and orientation, extent of sheltering, wind velocity, the nature of corrosion products formed, and pollutants that are not measured. The difficulties in making accurate predictions of corrosivity can be exemplified by the variations in corrosion rates between steel and zinc in a world-wide ASTM Site Calibration at 45 outdoor locations [74]. The mass loss between different sites for both steel and zinc after 2 years of exposure varied two orders of magnitude or more. Moreover, the ranking of test sites with respect to mass loss of zinc was considerably different from that of iron. The ratio of steel to zinc mass loss varied from around 10 to more than 350. Significant variations in mass loss between different exposure periods were also observed for both metals. Similar experience has been gained from several other exposure programs [75,76].

According to Barton [2], a generalized description of corrosion rate versus time includes an induction period, a period for establishing stationary conditions, and a stationary period; see Figure 8. These periods can be associated with the present description of the aqueous layer and formation of corrosion products. During the induction period, the metal is covered with a spontaneously formed oxide and the aqueous layer, which affords a certain protection depending on the metal and the aggressiveness of the atmosphere. The transition period involves the transformation from the oxide layer into a fully developed layer of corrosion products via local formation and coalescence of corrosion products. The stationary period, finally, is characterized by full coverage of the surface by corrosion products, eventually reaching constant properties with respect to chemical composition and atomic structure, and stationary corrosion rates. The two initial periods are shorter the more aggressive the exposure conditions are. For steel they typically last for years in very benign (indoor) atmospheres but only a few months in highly polluted industrial areas [2].

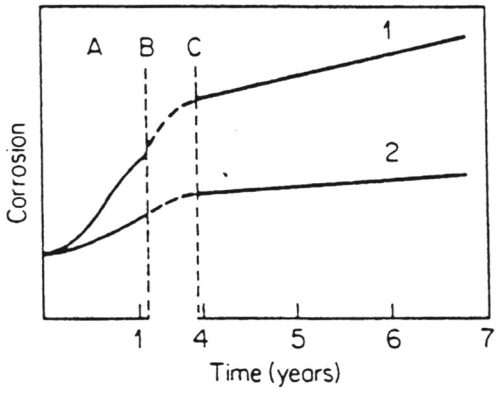


Figure 8 Schematic division of atmospheric corrosion into different periods, namely an induction period (A), a period for establishing stationary conditions (B to C), and a stationary period (from C). (From Ref. 2. Courtesy of John Wiley & Sons.)

Copyright © 2002 Marcel Dekker, Inc.

A frequent observation during the two initial periods is the marked influence of initial exposure conditions on the subsequent corrosion rate [77,78]. Wet conditions—caused by rainfall or high relative humidity—are more severe than dry conditions during the first days of exposure; they result in higher corrosion rates when the exposure time extends to several months. In this respect zinc seems to be more sensitive than steel. These observations are, at least partly, explained by the formation of corrosion products possessing different protective abilities. Especially on zinc, a diversity of structurally related corrosion products can be formed, the nature of which depends on initial exposure conditions [66]. An additional cause may be the seasonal dependence of the concentrations of H_2O_2 and O_3 [62].

During the third period of exposure, characterized by stationary corrosion rates, the interpretation of corrosion rates in terms of environmental data is more easily accomplished than during the two initial periods with varying corrosion rates. In reality, atmospheric corrosion is only quasi-stationary and regarded as a series of processes, when the surface is wet enough to allow rapid corrosion rates, and interrupted by periods of dryer conditions with negligible corrosion rates. An important concept here is the so-called time of wetness based on devices that monitor the actual time during which the surface is wet or the critical relative humidity exceeded [79]. In many cases, time of wetness estimates have been based on measurements of temperature and relative humidity. A common definition of time of wetness is the time during which, simultaneously, the temperature is above 0°C and the relative humidity ≥80%. However, this definition should not be taken too literally because the actual time when the surface is wet enough for rapid corrosion to occur depends on many other parameters, such as type, mass, orientation, and degree of sheltering of the metal; hygroscopic properties of corrosion products and of surface contaminants; type and level of pollutants; air velocity; and solar flux. An alternative way to estimate the time of wetness is by means of electrochemical cells (Fig. 9), which consist of thin electrically separated metal electrodes and involve the detection of a current or an electromotive force when the thickness of the aqueous layer is sufficient to accelerate atmospheric corrosion [79–82]. In this case, too, the result will depend on many parameters, such as cell design, formation of corrosion products on metal electrodes, and criteria for defining time of wetness based on current or electromotive force responses.

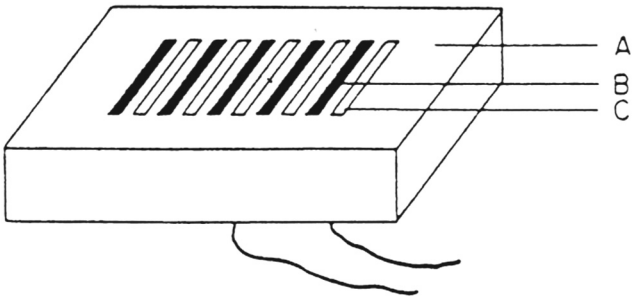


Figure 9 An electrochemical cell for determining time of wetness. (A) Material containing the embedded electrodes. (B) Noble metal electrodes (e.g., Pt or Cu). (C) Base metal electrodes (e.g., Fe or Zn). (From Ref. 2. Courtesy of John Wiley & Sons.)

Copyright © 2002 Marcel Dekker, Inc.

It is also possible to measure quantitatively the amount of water on metal surfaces under in situ conditions by means of the quartz crystal microbalance [83]. This is illustrated in Figure 10, where the water content quotient on a gold surface, given as the mass of water in the aqueous adlayer divided by the mass of other deposited species on gold, is plotted as a function of relative humidity during consecutive 24-h cycles in an outdoor environment. Each cycle is represented by one increase (during nighttime) and one decrease (during daytime) in water mass and relative humidity, respectively. From the figure it is evident that significant amounts of water are present at relative humidity far below 80%. Analysis of the data shows that the actual time when the surface is wetted is significantly longer than the time when the temperature is above 0°C and the relative humidity ≥ 80%. Hence, this definition of time of wetness may be erroneous [83]. Despite these uncertainties in definition and experimental accuracy, the time of wetness exhibits a surprisingly good correlation with outdoor corrosion rates of steel in many types of environment [84].

Because of the many parameters capable of influencing atmospheric corrosion rates, exposure programs have placed increased emphasis on standardized test procedures. The International Organization for Standardization (ISO) has formulated several corrosion testing standards [85–88] and also implemented a

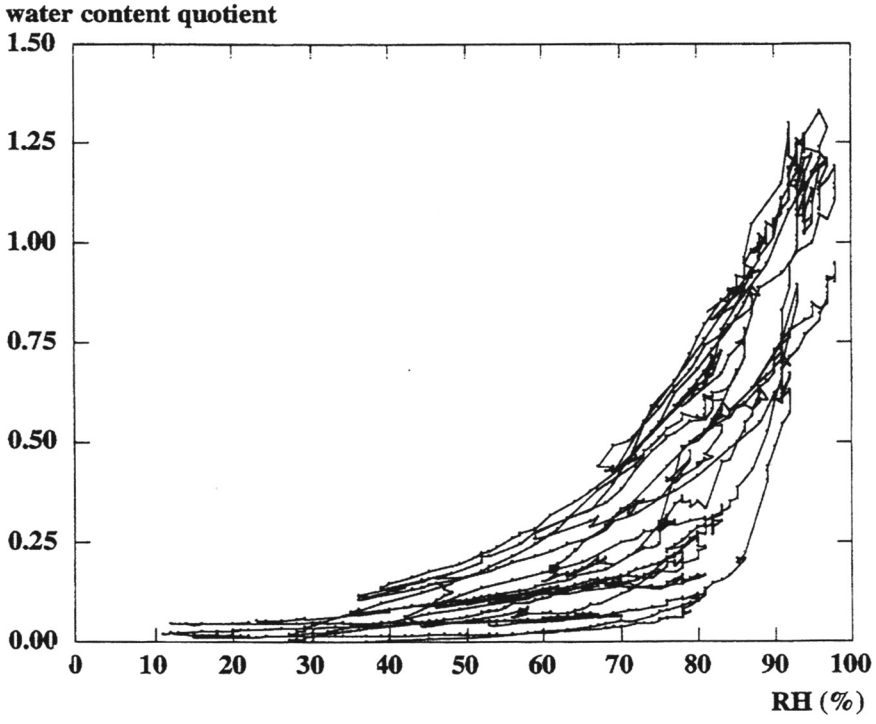


Figure 10 The water content quotient on gold, given as the mass of water in the aqueous adlayer divided by the mass of other deposits, as a function of relative humidity (RH) during 14 consecutive days of outdoor exposure in an urban environment. (From Ref. 83. Courtesy of The Electrochemical Society.)

Copyright © 2002 Marcel Dekker, Inc.

worldwide atmospheric exposure program known as ISOCORRAG [89]. This program aims at generating a basis for the procedures used in the ISO classification system. The ISO classification system presents two different approaches to assessing the corrosivity of any environment. One approach is based on the exposure of standard specimens of aluminum, steel, copper, and zinc for 1 year and determining a *measured corrosivity class* from mass loss data. The other approach is based on SO_2 concentration, deposition of Cl^-, and time of wetness at the site, which results in an *estimated corrosivity class*. Having determined a corrosivity class with one of these methods, it is possible to estimate the extent of corrosion damage to aluminum, steel, copper, and zinc for either short-term or long-term exposures. The ISO classification system provides adequate data for many practical purposes, including prediction of long-term corrosion behavior in different environments and the need for protective coatings. However, experience has shown that certain observations need further clarification. These observations include the frequent difference in corrosion rate between the top side and bottom side of flat standard specimens and between flat standard specimens and open helix standard specimens [90]. They also include the possible role of pollutants other than those measured. Future work within ISOCORRAG and other exposure programs should shed more light on these and other not yet fully elucidated issues.

With the increasing concern about acidifying pollutants and their influence on atmospheric corrosion rates, scientists' interest has been focused on NO_2 as an additional gaseous corrosion stimulant. Whereas the SO_2 concentration has shown a significant decline over the past decades in many urban and industrial areas, estimated emission of NO_2 has shown a continuous increase in the same type of environment [91]. Studies in laboratories using synthetic air have provided unambiguous evidence of increased corrosion rates when NO_2 is added to air containing SO_2 (Fig. 11).

The synergistic effects of SO_2 and NO_2 interactions are based on observations of several metals: copper [92], nickel [93], steel [94], and zinc [95]. With the general aim of performing a quantitative evaluation of the effect of sulfur pollutants in combination with NO_x, other pollutants, and climatic parameters, an international exposure program within the UN Economic Commission for Europe (UN/ECE) was implemented in 1987, including 39 test sites in 12 European countries, the United States, and Canada [96]. The program is based on exposure of structural metals, stone materials, paint coatings, and electric contact materials at test sites where measurements of environmental parameters are already in progress. Judging from analysis of results after 8 years of exposure, the influence of SO_2 on the corrosion rate of, e.g., carbon steel, weathering steel, zinc, cast bronze, and nickel is significant. No influence of NO_2 has so far been observed on any of the materials investigated [97]. Hence, the important role of NO_2 in laboratory exposures is not visible in the present field exposures—most likeky as a result of catalysts or oxidizers (e.g., O_3) in field exposures that aid in promoting the oxidation of S(IV) to S(VI) and hide the effect of NO_2. Future work should explore more precisely the reason for this discrepancy.

The conclusions from the UN/ECE program can be compared with those from another exposure program performed at three test sites in Southern California and characterized by very low levels (< l0 ppb) of SO_2. Under these conditions, SO_2 is

Copyright © 2002 Marcel Dekker, Inc.

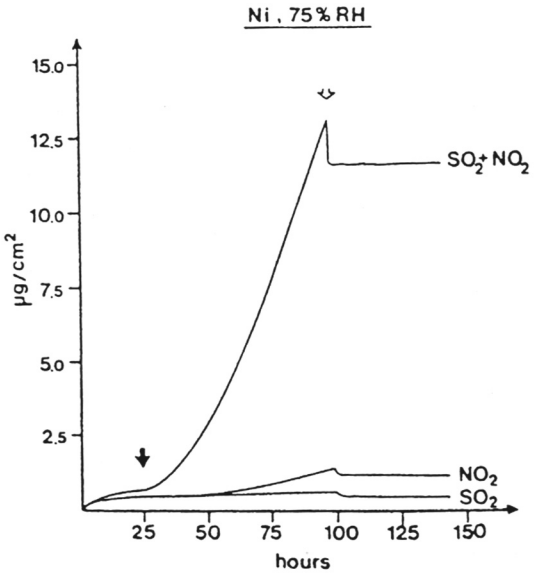


Figure 11 Mass changes of nickel as a function of exposure time in humid (75% relative humidity) flowing air. The filled arrow indicates introduction of 250 ppb SO_2 and/or 300 ppb NO_2, and the open arrow indicates termination of the supply of gaseous pollutants and of high humidity in the flowing air. (From Ref. 93. Courtesy of The Electrochemical Society.)

shown to be of little consequence, whereas NO_2, which is photochemically converted to HNO_3, is of significant importance [98].

There is ample evidence that synergistic effects caused by interacting atmospheric constituents are significant in laboratory exposures. It remains to be proved to what extent they contribute during field exposures. In addition to SO_2 and NO_2, the interaction between SO_2 and O_3 [95] and between H_2S and Cl_2 [99] is expected to be important.

ATMOSPHERIC CORROSION INDOORS

Whereas the accumulated knowledge of outdoor exposures has extended over many decades of corrosion tests, the history of indoor corrosion tests is short and mainly goes back to the growing interest in corrosion effects on electronic materials during the last two decades or so [100,101]. There are obvious differences in outdoor and indoor exposure conditions and, consequently, expected differences between outdoor and indoor corrosion behavior, some of which are summarized here.

The aqueous layer formed under outdoor exposure conditions is strongly influenced by seasonal and diurnal variations in humidity and by precipitation, dew, snow, or fog. Indoors, on the other hand, the aqueous layer is often governed by relatively constant humidity conditions. This means that there are practically no wet-dry cycles indoors and that the influence of indoor humidity can hardly be described by introducing a time of wetness factor.

Copyright © 2002 Marcel Dekker, Inc.

Mostly due to enhanced indoor absorption of gases and particulates and also due to retardation and damping of outdoor variations by ventilating systems and air filtration, comparisons between outdoor and indoor concentrations of the most important gaseous corrosion stimulants in general reveal lower levels indoors than outdoors (Table 1). Exceptions are NH_3 and HCHO, which usually exhibit higher levels indoors than outdoors as the result of anthropogenic activity [17]. Another important difference is the decreased levels of indoor atmospheric oxidants, many of them photochemically produced as described earlier, and of Fe(III)- and Mn(II)-containing catalysts for promoting the oxidation of S(IV) to S(VI). Accordingly, the expected lifetime of S(IV) compounds is greater indoors than outdoors [17]. As discussed earlier, not only the concentration of pollutants but also the air velocity determines the dry deposition velocity of corrosion stimulants. With decreased indoor air velocities follow significantly lower dry deposition velocities indoors than outdoors.

Consistent with the differences in outdoor and indoor characteristics, the corrosion rate of many metals is significantly lower indoors than outdoors. By examining the corrosion rates of copper, silver, nickel, cobalt, and iron in eight indoor locations it was found that all metals except silver exhibited much lower rates indoors than outdoors [102]. Within the UN/ECE exposure program a detailed study was made of the influence of sheltering nickel samples in a ventilated box, simulating exposure in unheated storage conditions. It was concluded that the deposition of SO_2 outside and inside the ventilated box differed by (approximately) a factor of 10, this difference being attributable to different airflow conditions, a factor of 2, and SO_2 concentrations, a factor of 5 [103].

As manifested by the ISO classification system, the outdoor corrosion behavior of structural metals can often be adequately predicted by only three parameters: SO_2 concentration, deposition of Cl^-, and time of wetness. With considerably less influence of these parameters indoors, it is reasonable to assume that the relative importance of other corrosion stimulants increases. Evidence for this can be exemplified in different ways. A classification system from the Instrument Society of America (ISA) for predicting corrosivity in indoor environments includes measurements of SO_2, NO_2, H_2S, and Cl_2 in addition to relative humidity and temperature [104]. Corrosion products formed on copper show much larger variations in chemical composition after indoor than after outdoor exposure [17]. Results from Fourier transform infrared reflection absorption spectroscopy analysis of corrosion products on copper, zinc, nickel, and iron formed in various benign corrosivity indoor environments exhibit large amounts of infrared bands from carboxylate ions, such as formate, acetate, and oxalate [105]. This may be an indication of a stronger influence of carboxylic acids or other organic species under benign conditions than in more aggressive environments.

The deposition of particles on corroding surfaces is of significant importance in indoor exposures [106,107]. This is clearly seen when a comparison is made between the main sources of deposited SO_4^{2-} and Cl^- on aluminum and zinc surfaces during outdoor and indoor exposure. Outdoors, the accumulated SO_4^{2-} on both metal surfaces mainly originates from gaseous SO_2 and from SO_4^{2-} in precipitation. Indoors, surface-accumulated SO_4^{2-} is derived mainly from particles. Similarly, surface-accumulated Cl^- has three approximately equal outdoor

Copyright © 2002 Marcel Dekker, Inc.

sources—reactive gases, precipitation, and particles—and two approximately equal indoor sources: reactive gases and particles [107,108]. It is evident that future descriptions of the mechanisms governing indoor atmospheric corrosion processes must involve deposition of particles as a major source of corrosion-stimulating pollutants [109,110].

Lower corrosion rates indoors than outdoors will require the development of more sensitive techniques for corrosivity evaluation of indoor environments and also an extended classification of indoor corrosivities [111].

DISPERSION OF METALS

So far this chapter has treated various aspects of the impact of the atmospheric environment on metals. The opposite situation, in which a corroding metal can have detrimental influences on the surrounding environment, is now an important issue because of the increased concern regarding the amount of heavy metals dispersed from roofs, facades, and other outdoor structures. Whereas long-term corrosion rates of metals, including copper and zinc, have been studied in many outdoor exposure programs, the dispersion of the same metals and their potential impact on the environment are less well understood. Risk assessments by, e.g., organizations and legislators have assumed that the runoff rate of a metal from a structure is equal to its corrosion rate. It has moreover been assumed that all metal dissolved and dispersed is bioavailable and therefore toxic to the environment. Both assumptions represent upper limits, and the risk assessments made therefrom are quite conservative. A realistic risk assessment of the corrosion-induced dispersion of metals in the environment needs answers to at least the following questions:

1. What is the ratio between the runoff rate of a metal and its corrosion rate?
2. How does the runoff rate vary with time?
3. How bioavailable is the metal?

Copper and zinc have become the most frequently studied metals from this perspective. The copper corrosion rate in unsheltered outdoor environments is always highest in the beginning and slowly decreases with exposure time. The reason is the gradual formation of more corrosion-resistant corrosion products, including Cu_2O (cuprite), $Cu_4SO_4(OH)_6 \cdot H_2O$ (posjnakite), and $Cu_4SO_4(OH)_6$ (brochantite). The time for this sequence to happen varies considerably between different environments but brochantite, the end product in most patina formation, is often found within 2 years of unsheltered exposure.

From the large changes in corrosion product composition during the first 2 years and the concomitant reductions in copper corrosion rate, one would suspect that the runoff rate undergoes similar changes as a function of exposure period. Results from measurements on new or naturally aged copper have shown, however, that the copper runoff rate is relatively constant during the investigated 2 year periods. Values in the range between 1.0 and 1.5 g/m^2 per year have been found in relatively benign urban environments such as Stockholm. These values increase with intensity and acidity of precipitation [112,113]. From a decreasing copper corrosion rate with time, measured as the total copper mass loss, and a

Copyright © 2002 Marcel Dekker, Inc.

relatively constant copper runoff rate follows that the quotient between copper runoff and copper mass loss initially is low and increases with time. Taking Stockholm as an example, the quotient was 7% after 1 month and 22% after 2 years [112].

As with copper, zinc runoff rates in atmospheric environments have turned out to remain relatively constant over exposure periods of a few years. Measured zinc runoff rates ranged from around 3 to 5 g/m^2 per year and could be correlated with the SO_2 concentration at sites with comparable annual amounts of precipitation [114]. For most sites the quotient between zinc runoff rate and zinc corrosion rate varied between 50 and 60% during the first 2 years of exposure.

In all, evidence has been provided for both copper and zinc that suggests that the runoff rate is determined more strongly by precipitation parameters (e.g., amount, intensity, and pH) than by corrosion product parameters (e.g., chemical composition, age, and morphology). This is in contrast to corrosion rates of the same metals, which are also determined by corrosion product properties. Runoff rates are in general significantly lower than corrosion rates. These values gradually get closer until the corrosion product eventually reaches a constant thickness, at which point the runoff rate equals the corrosion rate. This may take a few years or more on zinc and a few decades or so on copper.

The runoff rates found for copper and zinc show only the total release of metal from an outdoor construction without considering the chemical speciation of the metal or its bioavailable fraction, i.e., the part of the metal that can interact with living organisms and cause toxic effects. The most bioavailable, and therefore most toxic, form is usually the free, hydrated, cation. Hence, in the case of copper or zinc, $Cu(H_2O)_n^{2+}$ and $Zn(H_2O)_n^{2+}$ are among the most bioavailable species. Immediately after leaving the copper surface, the fraction of free, hydrated, cupric ion in the copper runoff is very high, in the range from 60 to 90% depending on the conditions of the actual precipitation event. During its way to the biosphere, copper will react with, e.g., organic matter and the fraction of bioavailable copper will become successively smaller. When copper eventually enters agricultural soil only about 2% is considered to be bioavailable and only 1% of all copper in natural water systems [115].

CONCLUDING REMARKS

Atmospheric corrosion of metals comprises a broad range of electrochemical, chemical, and other processes in the interfacial domain, ranging from the atmospheric region over the thin aqueous layer to the solid metal region. Of utmost importance is the thin aqueous layer, which forms the medium for electrochemical reactions and accommodates gaseous, particulate, or other pollutants from the atmospheric region. Anode rather than cathode reactions are normally rate limiting and may be facilitated by acidifying pollutants, such as SO_2. The subsequent reaction sequences in the aqueous layer are governed mainly by kinetic constraints, including the concept of dry deposition velocity of pollutants and the nucleation, spreading, and coalescence of corrosion products. Atmospheric corrosion rates are strongly influenced by the formation and properties of corrosion products, where the formation

Copyright © 2002 Marcel Dekker, Inc.

process can be described in a sequence of consecutive steps: dissolution–coordination-reprecipitation. The dissolution step is usually acid dependent; possible coordination steps can be predicted by the HSAB principle, and the reprecipitation depends on the activities of species involved.

Extensive outdoor exposure programs have provided evidence that corrosion rates can be interpreted in terms of deposition of primarily SO_2 and Cl^- and time of wetness. The history of indoor exposure programs is much shorter. Atmospheric corrosion indoors is, in general, influenced by more constant humidity conditions and lower levels of SO_2 and Cl^-, from which follows an increased relative importance of other corrosion stimulants including organic gaseous species and particulate pollutants.

Despite all progress made in understanding individual processes, there is a need to develop more comprehensive models in the study of atmospheric corrosion. The first computional model developed in atmospheric corrosion [116] considers six distinct regimes, namely the gas phase (G), the gas-liquid interface (I), the liquid phase (L), the deposition layer (D), the electrodic regime (E), and the solid phase (S), and is designated GILDES. Chemical reactions within the regimes can occur to change the constituents of the regimes. Transport of chemical species of interest between the regimes is also considered together with condensation and dissolution processes and deposition and transport through the reaction products. For the six regimes, mathematical formulations have been specified to describe the transitions and transformations that occur. The conceptual framework used in the GILDES formulation is truly multidisciplinary and requires the incorporation of many scientific fields: gas phase—atmospheric chemistry; interface layer—mass transport engineering and interface science; liquid phase—freshwater, marine, and brine chemistry; deposition layer—colloid chemistry, surface science, and mineralogy; electrodic regime—electrochemistry; and solid phase—solid-state chemistry. GILDES model studies have so far included the initial SO_2-induced atmospheric corrosion of copper [117] and of nickel [118]. Comparison with experimental data suggests that the model has been able to capture some of the most important processes.

Atmospheric corrosion involves a series of processes with periods of high corrosion rates interrupted by periods of negligible corrosion rate. For a deeper understanding of atmospheric corrosion, there is a need for more sophisticated techniques for measuring instant corrosion rates coupled with monitoring the deposition of the most important corrosion stimulants. Activities in these and other areas are presently being carried out, and it is anticipated that atmospheric corrosion will continue to develop into a multi-disciplinary scientific field.

ACKNOWLEDGMENTS

The author wishes to express his gratitude to Dr. J. Tidblad for compilation of environmental data and to Prof. E. Mattsson, Dr. I. Odnevall Wallinder, Dr. D. Persson, and Dr. J. Tidblad, all from the Royal Institute of Technology or Swedish Corrosion Institute in Stockholm, Sweden, for most valuable review comments. Mr. B. Edin, Stockholm, is acknowledged for linguistic examination of this chapter.

Copyright © 2002 Marcel Dekker, Inc.

REFERENCES

1. D. Fyfe, The atmosphere, *Corrosion*, 2nd ed. (L. L. Shreir, ed.), Newnes-Butterworths, Sevenoaks, Kent, England, 1976, p. 2.26.
2. K. Barton, *Protection against Atmospheric Corrosion*, Wiley, London, 1976.
3. U. R. Evans, *The Corrosion and Oxidation of Metals*, Edward Arnold, London, 1960, p. 482.
4. W. H. J. Vernon, Effect of sulphur dioxide on the atmospheric corrosion of copper, *Trans. Faraday Soc. 27*:35 (1933).
5. I. L. Rozenfeld, *Atmospheric Corrosion of Metals*, National Association of Corrosion Engineers, Houston, 1972.
6. V. Kucera and E. Mattsson, Atmospheric corrosion, *Corrosion Mechanisms* (F. Mansfeld, ed.), Marcel Dekker, New York, 1987.
7. C. Leygraf and T. Graedel, *Atmospheric Corrosion*, John Wiley & Sons, New York, 2000.
8. (a) *Atmospheric Factors Affecting the Corrosion of Engineering Metals*, ASTM STP 646 (K. Coburn, ed.), American Society for Testing and Materials, Philadelphia, 1978; (b) *Atmospheric Corrosion of Metals*, ASTM STP 767 (S. W. Dean and E. C. Rhea, eds.), American Society for Testing and Materials, Philadelphia, 1982.
9. (a) *Degradation of Metals in the Atmosphere*, ASTM STP 965 (S. W. Dean and T. S. Lee, eds.), American Society for Testing and Materials, Philadelphia, 1988; (b) *Atmospheric Corrosion*, ASTM STP 1239 (W. W. Kirk and H. H. Lawson, eds.), American Society for Testing and Materials, Philadelphia, 1995. (c) *Symposium on Outdoor and Indoor Atmospheric Corrosion*, ASTM STP 1421 (H.E. Townsend, ed.), American Society for Testing and Materials, Philadelphia, 2002
10. *Atmospheric Corrosion* (W. H. Ailor, ed.), Wiley, New York, 1982.
11. T. E. Graedel, D. T. Hawkins, and L. D. Claxton, *Atmospheric Chemical Compounds, Sources, Occurrence, and Bioassay*, Academic Press, Orlando, FL, 1986, p. 9.
12. T. E. Graedel, D. T. Hawkins, and L. D. Claxton, *Atmospheric Chemical Compounds, Sources, Occurrence, and Bioassay*, Academic Press, Orlando, FL, 1986, p. 543.
13. J. G. Calvert and W. R. Stockwell, Mechanisms and rates of the gas-phase oxidations of sulfur dioxide and nitrogen oxides in the atmosphere, *SO_2, NO, and NO_2 Oxidation Mechanisms: Atmospheric Considerations* (J. G. Calvert, ed.), Butterworth, Woburn, MA, 1984, p. 1.
14. L. R. Robbin, Kinetic studies of sulfite oxidation in aqueous solution, *SO_2, NO, and NO_2 Oxidation Mechanisms: Atmospheric Considerations* (J. G. Calvert, ed.), Butter-worth, Woburn, MA, 1984, p. 63.
15. T. E. Graedel, D. T. Hawkins, and L. D. Claxton, *Atmospheric Chemical Compounds, Sources, Occurrence, and Bioassay*, Academic Press, Orlando, FL, 1986, p. 68.
16. B. J. Finlayson-Pitts and J. N. Pitts, Jr., *Atmospheric Chemistry: Fundamentals and Experimental Techniques*, Wiley, New York, 1986, p. 29.
17. S. K. Chawla and J. H. Payer, Atmospheric corrosion: a comparison of indoor vs. outdoor, Proceedings 11th International Corrosion Congress, Florence, Italy, 1990, p. 2.17.
18. T. E. Graedel, Copper patinas formed in the atmosphere—II. A qualitative assessment of mechanisms, *Corros. Sci. 27*:721 (1987).
19. T. E. Graedel, Corrosion mechanisms for silver exposed to the atmosphere, *J. Electrochem. Soc. 139*:1963 (1992).
20. R. B. Comizzoli, R. P. Frankenthal, R. E. Lobnig, G. A. Peins, L. A. Psota-Kelty, J. D. Siconolfi, and J. D. Sinclair, Corrosion of electronic materials and devices by submicron atmospheric particles, *Eletrochem. Soc. Interface 2*:26 (1993).
21. P. A. Thiel and T. M. Madey, The interaction of water with solid surfaces: fundamental aspects, *Surf. Sci. Rep. 7*:211 (1987).

Copyright © 2002 Marcel Dekker, Inc.

22. M. A. Barteau and R. J. Madix, The surface reactivity of silver: oxidation reactions, *Chem. Phys. Solid Surf. Heretog. Catalysis*, Vol. 4 (D. A. King and D. P. Woodruff, eds.), Elsevier, Amsterdam, 1982, p. 95.
23. W. J. Lo, Y. W. Chung, and G. A. Somorjai, Electron spectroscopy studies of the chemisorption of oxygen, hydrogen and water on the titanium dioxide (100) surfaces with varied stoichiometry: evidence for the photogeneration of titanium (3+) and for its importance in chemisorption, *Surf. Sci. 71*:199 (1978).
24. C. Benndorf, C. Nöbl, and T. E. Madey, Water adsorption on oxygen-dosed nickel (110): formation and orientation of adsorbed hydroxyl, *Surf. Sci. 138*:292 (1984).
25. R. L. Kurtz and V. E. Henrich, Surface electronic structure and chemisorption on corundum transition-metal oxides: a-ferric oxide, *Phys. Rev. B 36*:3413 (1987).
26. D. J. Dwyer, S. R. Kelemen, and A. Kaldor, The water dissociation reaction on clean and oxidized iron (110), *J. Chem. Phys. 76*:1832 (1982).
27. (a) E. Mc Cafferty, V. Pravdic, and A. C. Zettlemoyer, Dielectric behaviour of adsorbed water films on the α-iron(III)oxide surface, *Trans. Faraday Soc. 66*:1720 (1970); (b) P. B. P. Phipps and D. W. Rice, The role of water in atmospheric corrosion, *Corrosion Chemistry*, ACS Symp. Ser. 89 (G.R. Brubaker and P.B.P. Phipps, eds.), American Chemical Society, Washington, DC, 1979, p. 235.
28. Y. R. Shen, A few selected applications of surface nonlinear optical spectroscopy, *Proc. Natl. Acad. Sci. USA*, *99*:12104 (1996).
29. Y. N. Mikhailovsky, Theoretical and engineering principles of atmospheric corrosion of metals, *Atmospheric Corrosion* (W. H. Ailor, ed.), Wiley, New York, 1982, p. 85.
30. B. D. Yan, S. L. Meilink, G. W. Warren, and P. Wynblatt, Water adsorption and surface conductivity measurements on a-alumina substrates, Proceedings 36th Electronic Components Conference, 1986, p. 95.
31. W. H. J. Vernon, A laboratory study of the atmospheric corrosion of metals, Part I, *Trans. Faraday Soc. 27*:255 (1931).
32. W. H. J. Vernon, A laboratory study of the atmospheric corrosion of metals. Part II and III, *Trans. Faraday Soc. 31*:1668 (1935).
33. H. Kaesche, Elektrochemische Merkmale der atmosphärischen Korrosion, *Werkst. Korros. 15*:379 (1964).
34. F. Mansfeld, Electrochemical methods for atmospheric corrosion studies, *Atmospheric Corrosion* (W. H. Ailor, ed.), Wiley, New York, 1982, p. 139.
35. C. Fiaud, Electrochemical behaviour of atmospheric pollutants in thin liquid layers related to atmospheric corrosion, *Atmospheric Corrosion* (W. H. Ailor, ed.), Wiley, New York, 1982, p. 161.
36. M. Stratmann, The atmospheric corrosion of iron-a discussion of the physico-chemical fundamentals of this omnipresent corrosion process, *Ber. Bunsenges. Phys. Chem. 94*:626(1990).
37. M. Stratmann, The investigation of the corrosion properties of metal surfaces covered by condensed or adsorbed electrolyte layers, *Proceedings*, *1st International Symposium on Corrosion of Electronic Materials and Devices* (J. D. Sinclair, ed.), The Electrochemical Society, Pennington, NJ, 1991, p. 1.
38. D. Persson and C. Leygraf, *J. Electrochem. Soc. 142*:1459 (1995).
39. W. Stumm, B. Sulzberger, and J. Sinniger, The coordination chemistry of the oxide-electrolyte interface; the dependence of surface reactivity on surface structure, *Croat. Chem. Acta 63*:277 (1990).
40. W. Stumm and G. Furrer, The dissolution of oxides and aluminum silicates; examples of surface-coordination-controlled kinetics, *Aquatic Surface Chemistry* (W. Stumm, ed.), Wiley, New York, 1987, p. 197.

Copyright © 2002 Marcel Dekker, Inc.

41. S. E. Schwartz, Gas-aqueous reactions of sulfur and nitrogen oxides in liquid-water clouds, *SO_2, NO, and NO_2 Oxidation Mechanisms: Atmospheric Considerations* (J. G. Calvert ed.), Butterworth, Woburn, MA, 1984, p. 173.
42. H. Rodhe, Luftföroreningars Sprinding (in Swedish), Compendium, University of Stockholm, Sweden, 1991.
43. G. A. Sehmel, Particle and gas dry deposition: a review, *Atmos. Environ. 14*:983 (1980).
44. P. J. Hanson and S. E. Lindberg, Dry deposition of reactive nitrogen compounds: a review of leaf, canopy and non-foliar measurements, *Atmos. Environ.* 25*A*:1615 (1991).
45. Effects of Acidic Deposition on Materials, State-of-Science/Technology Report 19, National Acid Precipitation Assessment Program, 1990.
46. P. S. Liss and P. G. Slater, Flux of gases across the air-sea interface, *Nature 247*:181 (1974).
47. F. W. Lipfert, Dry deposition velocity as an indicator for SO_2 damage to materials, *J. Air Pollut. Control Assoc. 39*:446 (1989).
48. L. Volpe, New studies using the tubular corrosion reactor, Proceedings 11th International Corrosion Congress, Florence, Italy, 1990, p. 2.25.
49. L. Volpe, Mass-transport limitations in atmospheric corrosion, *Proceedings 1st International Symposium on Corrosion of Electronic Materials and Devices* (J. D. Sinclair, ed.), The Electrochemical Society, Pennington, NJ, 1991, p. 22.
50. F. W. Lipfert and R. E. Wyzga, Application of theory to economic assessment of corrosion damage, *Proceedings Degradation of Materials due to Acid Rain* (R. Baboian, ed.), American Chemical Society, Washington, DC, 1986, p. 411.
51. E. Mattsson, The atmospheric corrosion properties of some common structural metals—a comparative study, *Mater. Perf. 21*:9 (1982).
52. M. Carballeira, A. Carballeira, and J. Y. Gal, Contribution to the study of corrosion phenomena in industrial atmosphere. Thermodynamic approach, Proceedings 14th International Conference on Electric Contacts, Société des Électroniciens, Paris, 1988, p. 239.
53. T. E. Graedel, K. Nassau, and J. P. Franey, Copper patinas formed in the atmosphere. I. Introduction, *Corros. Sci. 27*:639 (1987).
54. E. Matijevic, Preparation and characterization of model colloidal corrosion products, *Corrosion NACE 35*:264 (1979).
55. D. A. Vermilyea, Physics of corrosion, *Phys. Today 9*:23 (1976).
56. G. A. Somorjai, *Chemistry in Two Dimensions*, Cornell University Press, Ithaca, NY, 1981, p. 293.
57. N. Sato, Some concepts of corrosion fundamentals, *Corros. Sci. 27*:421 (1987).
58. R. G. Pearson, Hard and soft acids and bases, *J. Am. Chem. Soc. 85*:3533 (1963).
59. W. L. Jolly, *Modern Inorganic Chemistry*, 2nd ed., McGraw-Hill, New York, 1991, p. 238.
60. W. Feitknecht, Ordnungsvorgänge bei kolloiddispersen hydroxyden und hydroxysalzen, *Kolloid Z. 136*:52 (1954).
61. (a) D. Persson and C. Leygraf, Analysis of atmospheric corrosion products of field exposed nickel, *J. Electrochem. Soc. 139*:2243 (1992). (b) I. Odnevall and C. Leygraf, The atmospheric corrosion of nickel in a rural atmosphere, *J. Electrochem. Soc. 144*:3518 (1997).
62. T. E. Graedel, Corrosion mechanisms for zinc exposed to the atmosphere, *J. Electrochem. Soc. 136*:193C (1989).
63. T. E. Graedel, Corrosion mechanisms for aluminum exposed to the atmosphere, *J. Electrochem. Soc. 136*:204C (1989).
64. T. E. Graedel and R. P. Frankenthal, Corrosion mechanisms for iron and low alloy steels exposed to the atmosphere, *J. Electrochem. Soc. 137*:2385 (1990).

Copyright © 2002 Marcel Dekker, Inc.

65. I. Odnevall and C. Leygraf, Formation of $NaZn_4Cl(OH)_6SO_4 \cdot 6H_2O$ in a marine atmosphere, *Corros. Sci. 34*:1213 (1993).
66. I. Odnevall and C. Leygraf, *Reaction Sequences in Atmospheric Corrosion of Zinc*, ASTM STP 1239 (W. W. Kirk and H. H. Lawson, eds.), American Society for Testing and Materials, Philadelphia, 1995, p. 215.
67. A. Krätschmer, I. Odnevall Wallinder and C. Leygraf, The evolution of outdoor copper patina, *Corros. Sci. 44*:425 (2002).
68. L.-G. Johansson, SO_2-induced corrosion of carbon steel in various atmospheres and dew point corrosion in stack gases, thesis, Chalmers University of Technology and University of Gothenburg, Göteborg, Sweden, 1982.
69. G. Schikorr, Über den mechanismus des atmosphärischen rostens des eisens, *Werkst. Korros. 14*:69(1983).
70. J. Tidblad, C. Leygraf, and V. Kucera, Acid deposition effects on materials: evaluation of nickel and copper, *J. Electrochem. Soc. 138*:3592 (1991).
71. S. Zakipour and C. Leygraf, Evaluation of laboratory tests to simulate indoor corrosion of electrical contact materials, *J. Electrochem. Soc. 133*:21 (1986).
72. J. Tidblad, C. Leygraf, and V. Kucera, UN/ECE International Co-operative Programme on Effects on Materials. Report No. 8: Corrosion Attack on Electric Contact Materials. Evaluation after 1 and 2 Years of Exposure, Swedish Corrosion Institute, Stockholm, Sweden, 1991.
73. H. Guttman, Atmospheric and weather factors in corrosion testing, *Atmospheric Corrosion* (W. H. Ailor, ed.), Wiley, New York, 1982, p. 51.
74. S. K. Coburn, Corrosiveness of various atmospheric test sites as measured by specimens of steel and zinc, *Metal Corrosion in the Atmosphere*, ASTM STP 435 (S. W. Dean, Jr. and E. C. Rhea, eds.), American Society for Testing and Materials, Philadelphia, 1968, p. 360.
75. H. Guttman and P. J. Sereda, Measurement of atmospheric factors affecting the corrosion of metals, *Metal Corrosion in the Atmosphere*, ASTM STP 435 (S. W. Dean, Jr. and E. C. Rhea, eds.), American Society for Testing and Materials, Philadelphia, 1968, p. 326.
76. D. Knotkova, B. Bosek, and J. Vlckova, Corrosion aggressivity of model regions of Czechoslovakia, *Corrosion in Natural Environments*, ASTM STP 558, American Society for Testing and Materials, Philadelphia, 1974, p. 52.
77. O. B. Ellis, Effects of weather on the initial corrosion rate of sheet zinc, *ASTM Proc. Am. Soc. Test. Mater. 47*:152 (1947).
78. H. Guttman, Effects of atmospheric factors on the corrosion of rolled zinc, *Metal Corrosion in the Atmosphere*, ASTM STP 435 (S. W. Dean, Jr. and E. C. Rhea, eds.), American Society for Testing and Materials, Philadelphia, 1968, p. 223.
79. I. Odnevall and C. Leygraf, *Atmospheric Corrosion*, ASTM STP 1237 (W. W. Kirk and H. H. Lawson, eds.), American Society for Testing and Materials, Philadelphia (1994).
80. P. J. Sereda, Measurement of surface moisture, *ASTM Bull. 53*:228 (1958).
81. N. D. Tomashov, *Theory of Corrosion and Protection of Metals*, Macmillan, New York, 1966, p. 672.
82. V. Kucera and E. Mattsson, Electrochemical technique for determination of the instantaneous rate of atmospheric corrosion, *Corrosion in Natural Environments*, ASTM STP 558, American Society for Testing and Materials, Philadelphia, 1974, p. 239.
83. M. Forslund and C. Leygraf, Humidity sorption due to deposited aerosol particles studied in-situ outdoors on gold surfaces, *J. Electrochem. Soc. 144*:105 (1997).
84. M. Benarie and F. L. Lipfert, A general corrosion function in terms of atmospheric pollutant concentrations and rain pH, *Atmos. Environ. 20*:1947 (1986).
85. ISO 9223 Corrosion of metals and alloys. Classification of corrosivity of atmospheres, International Organization for Standardization, Geneva, Switzerland, 1991.

Copyright © 2002 Marcel Dekker, Inc.

86. ISO 9224 Corrosion of metals and alloys. Guiding values for the corrosivity categories of atmospheres, International Organization for Standardization, Geneva, Switzerland, 1991.
87. ISO 9225 Corrosion of metals and alloys. Corrosivity of atmospheres. Methods of measurement of pollution, International Organization for Standardization, Geneva, Switzerland, 1991.
88. ISO 9226 Corrosion of metals and alloys. Corrosivity of atmospheres. Methods of determination of corrosion rate of standard specimens for the evaluation of corrosivity, International Organization for Standardization, Geneva, Switzerland, 1991.
89. D. Knotkova and L. Vrobel, ISOCORRAG—The International Testing Program within ISO/TC 156/WG 4, Proceedings 11th International Corrosion Congress, Florence, Italy, 1990, p. 5.581.
90. S. W. Dean, Corrosion testing of metals under natural atmospheric conditions, *Corrosion Testing and Evaluation: Silver Anniversary Volume*, ASTM STP 1000 (R. Baboian and S. W. Dean, eds.), American Society for Testing of Materials, Philadelphia, 1990, p. 163.
91. R. B. Husar, *Acid Deposition: Long-Term Trends,* National Academy Press, Washington, DC, 1986, p. 48.
92. P. Eriksson, Effects of SO_2 and NO_2 on metal surfaces: atmospheric corrosion of copper and surface reactions on gold, thesis, Chalmers University of Technology and University of Gothenburg, Göteborg, Sweden, 1992.
93. S. Zakipour, C. Leygraf, and G. Portnoff, Studies of corrosion kinetics on electrical contact materials by means of quartz crystal microbalance and XPS, *J. Electrochem. Soc. 133*:873 (1986).
94. J. Henriksen, Corrosion Rates of Various Metals in SO_2/NO_2 Polluted Atmospheres, *Proceedings 10th Scandinavian Corrosion Congress*, Swedish Corrosion Institute, Stockholm, Sweden, 1986, p. 39.
95. J.-E. Svensson and L.-G. Johansson, A laboratory study of the effect of ozone, nitrogen dioxide and sulphur dioxide on the atmospheric corrosion of zinc, *J. Electrochem. Soc. 140*:2210 (1993).
96. V. Kucera, A. T. Coote, J. Henriksen, D. Knotkova, C. Leygraf, and U. Reinhardt, Effects of acidifying air pollutants on materials including historic and cultural monuments—an international exposure programme within UN ECE, Proceedings 11th International Corrosion Congress, Florence, Italy, 1990, p. 2.433.
97. J. Tidblad, V. Kucera and A. A. Mikhailov, UN/ECE international co-operative program on effects on materials including historic and cultural monuments, Reports no. 30, Statistical analysis of 8 year materials exposure and acceptable deterioration and pollutant levels, Swedish Corrosion Institute, Stockholm, Sweden (1998).
98. F. Mansfeld and R. Vijayakumar, Atmospheric corrosion behaviour in southern California, *Corros. Sci. 28*:939 (1988).
99. W. H. Abbott, Corrosion of electrical contacts: review of flowing mixed gas test developments, *Br. Corros. J. 24*:153 (1989).
100. D. W. Rice, R. J. Cappell, P. B. P. Phipps, and P. Peterson, Indoor atmospheric corrosion of copper, silver, nickel, cobalt and iron, *Atmospheric Corrosion* (W. H. Ailor, ed.), Wiley, New York, 1982, p. 651.
101. G. Frankel, Corrosion of microelectronic and magnetic storage devices, *Corrosion Mechanisms in Theory and Practice* (P. Marcus and J. Oudar, eds.), Marcel Dekker, New York, 1995, p. 547.
102. D. W. Rice, R. J. Cappell, W. Kinsolving, and J. J. Laskowski, Indoor corrosion of metals, *J. Electrochem. Soc. 127*:891 (1980).
103. J. Tidblad, C. Leygraf, and V. Kucera, Acid deposition effects on materials: evaluation of nickel after 4 years of exposure, *J. Electrochem. Soc. 140*:1912 (1993).

Copyright © 2002 Marcel Dekker, Inc.

104. ISA-s 71.04-1985 Standard: Environmental conditions for process measurements and control system: airborne contaminants. Instrument Society of America, Research Triangle Park, NC, 1985.
105. D. Persson and C. Leygraf, *J. Electrochem Soc. 142*:1468 (1995).
106. J. D. Sinclair, Corrosion of electronics: the role of ionic substances, *J. Electrochem. Soc. 135*:89C(1988).
107. J. D. Sinclair, L. A. Psota-Kelty, R. B. Comizzoli, R. P. Frankenthal, R. L. Opila, and G. R. Crane, Corrosion of electronics: the role of ionic substances, Proceedings 11th International Corrosion Congress, Florence, Italy, 1990, p. 2.95.
108. J. D. Sinclair, L. A. Psota-Kelty, and C. J. Weschler, Indoor/outdoor concentrations and indoor surface accumulations of ionic substances, *Atmos. Environ. 19*:315 (1985).
109. R. E. Lobnig, D. J. Siconolfi, L. Psota-Kelty, G. Grundmeier, R. P. Frankenthal, M. Stratmam, and J. D. Sinclair, Atmospheric corrosion of zinc in the presence of ammonium sulfate particles, *J. Electrochem. Soc. 143*:1539 (1996).
110. R. E. Lobnig and C. A. Jankoski, Atmospheric corrosion of copper in the presence of acid ammonium sulfate particles, *J. Electrochem. Soc. 145*:946 (1998).
111. E. Johansson, Corrosivity measurements in indoor atmospheric environments—a field study, licentiate thesis, ISBN 91-7170-267-9, Royal Institute of Technology, Stockholm, Sweden, 1998.
112. I. Odnevall Wallinder and C. Leygraf, A study of copper runoff in an urban atmosphere, *Corros. Sci. 39*:209 (1997).
113. W. He, I. Odnevall Wallinder, and C. Leygraf, A comparison between corrosion rates and runoff rates from new and aged copper and zinc as roofing material, *Water Air Soil Pollu., 1*:67 (2001).
114. I. Odnevall Wallinder, P. Verbiest, W. He, and C. Leygraf, The influence of patina age and pollutant levels on the runoff rate of zinc from roofing materials, *Corros. Sci. 40*:1977(1998).
115. Report No. 12/95. National Chemicals Inspectorate, Stockholm, Sweden (1995).
116. L. A. Farrow, T. E. Graedel, and C. Leygraf, GILDES model studies of aqueous chemistry. II. The corrosion of zinc in gaseous exposure chambers, *Corros. Sci. 38*:2181 (1996).
117. J. Tidblad and T. E. Graedel, GILDES model studies of aqueous chemistry III. Initial SO_2-induced atmospheric corrosion of copper, *Corros. Sci. 38*:2201 (1996).
118. J. Tidblad and T. E. Graedel, GILDES model studies of aqueous chemistry V. Initial SO_2-induced atmospheric corrosion of nickel, *J. Electrochem. Soc. 144*:2676 (1997).

Copyright © 2002 Marcel Dekker, Inc.

16

Microbially Influenced Corrosion

Dominique Thierry
Swedish Corrosion Institute, Stockholm, Sweden

Wolfgang Sand
Universität Hamburg, Hamburg, Germany

INTRODUCTION

Microbially influenced corrosion (MIC) is, by definition, corrosion associated with the action of microorganisms present in the system. Microbially influenced corrosion is therefore an interdisciplinary subject that embraces the fields of materials science, chemistry, microbiology, and biochemistry.

The first report of MIC on metals was published in 1891 by Garrett [43], who found that the corrosion of covered cables could be attributed to biogenic ammonia, nitrite, and nitrate. Almost two decades later, it was shown by Gaines [42] that sulfate-reducing, sulfur-oxidizing, and iron bacteria were responsible for part of the corrosion of iron in soils. These observations were associated with aerobic conditions. In 1934, Von Wolzogen Kühr and Van der Vlugt [130] presented the first evidence that microorganisms play a direct role in the corrosion of metals under anaerobic conditions. They postulated that sulfate-reducing bacteria were able to pick up adsorbed hydrogen from the metal surface. From 1934 up to now there has been an increasing number of reports of MIC on metallic and nonmetallic constructions and in various environments.

The cost of MIC is very significant. Several estimates have been made in the United States and in the United Kingdom. For instance, it has been reported by Iverson [58] that the annual cost of MIC of buried pipes in the United States was $500 million to $2000 million. In the United Kingdom, it was postulated that at least 50% of the corrosion occurring on buried metals was of microbial origin [8].

The main purpose of this chapter is to provide an overview of present knowledge of the mechanisms of microbially influenced corrosion on common constructional materials. This review includes both metallic and nonmetallic materials. The reason for including nonmetallic materials is that biodegradation occurs on these materials and that they are widely used for construction purposes. Because detailed knowledge in the fields of microbiology and biochemistry is necessary in order to understand the mechanisms of microbially influenced corrosion, considerable space has been devoted to a general description of microorganisms and to a

Copyright © 2002 Marcel Dekker, Inc.

description of natural cycles of matter in which microorganisms play an important role. A later section briefly presents the most commonly used countermeasures for avoiding or minimizing the influence of microorganisms on the degradation of materials.

MICROORGANISMS

The term microorganism covers a vast diversity of life forms. Bacteria, blue-green cyanobacteria, algae, lichens, and fungi together with protozoa are all classed as microorganisms. The main characteristic is the size of the individual organism. As a rule, it ranges between 0.5 and 10 μm, although organisms several meters in size are known (e.g., brown algae). Because of their small size, microorganisms have a large, catalytically active surface. A volume of $1cm^3$ can contain 10^{12} bacterial cells having a surface of approximately $1m^2$ (cell size 1 to 1 μm, length to width). Through this enormous surface area, agents may be excreted into the surrounding medium, causing detrimental effects on materials. The vast majority of microorganisms cannot be detected with the naked eye. Techniques such as light and/or electron microscopy (transmission and/or scanning) are required to magnify single cells so that they become visible [6]. The detection may be enhanced using dyes, which bind to cells and make them colored or fluorescent. Specific detection can be achieved using the polymerase chain reaction (PCR) technique with specific gene probes and/or immunolabeled antibodies binding to selected microorganisms. Thus, microorganisms with special characteristics may be detected in a mixed population.

Other indirect techniques measure the effect of the metabolism of microorganisms on the environment, such as acidification; alkalization; oxygen consumption; degradation of substrates, production of insoluble, dissolved, and/or gaseous intermediates and/or end products of catabolism; and heat production [107]. An indirect technique for visualization of "single" cells of microorganisms is transfer of a cell to a solidified nutrient solution and subsequent incubation at a given temperature, which enables the cell to grow and to multiply. After several multiplication cycles, a colony (consisting now of at least 10^7 daughter cells) becomes visible to the naked eye. The solidifying agent may be agar-agar, derived from algae, a polysaccharide forming a gel.

A powerful, recently developed tool is the PCR technique. The technique allows theoretically the detection of a single cell in 10^7 or more cells. A probe containing a counterpart of that piece traps a piece of genetic information, unique for a microorganism (a genetic fingerprint). Afterward, the double-stranded piece is multiplied by means of an enzyme, taq polymerase. After several multiplication cycles, the genetic information is sufficiently amplified to become detectable, e.g., by autoradiography (because of the use of radioactive components). However, so far only a few absolutely specific probes for detection exist.

Microorganisms exhibit a vast diversity with regard to their metabolism. Nevertheless, this diversity may be described by six main terms. Microorganisms obtaining their metabolic energy by use of light are called *phototrophs*. In constrast, those gaining energy through chemical reactions are known as *chemotrophs*. The source of reducing power is used for a further subdivision. In the case of inorganic hydrogen donators, the microorganisms are called *lithotrophs*, whereas those using

Copyright © 2002 Marcel Dekker, Inc.

organic compounds are called *organotrophs*. Finally, the source of cell carbon is important. If CO_2 is used, the organisms are called *autotrophs*. If carbon is derived from organic molecules, they are designated *heterotrophs*. By combing these six terms, bacteria can easily be described with regard to their nutritional requirements. For instance, if energy is derived from inorganic hydrogen donators and biomass is derived from organic molecules, they are called mixotrophs (= chemolithoorganotroph). *Escherichia coli*, for example, a bacterium occuring in the gut of animals, is a chemoorganoheterotroph because it grows by chemical oxidation of organic compounds such as glucose in the medium and derives cell carbon by assimilating part of the glucose. Another example is the chemolithotrophic bacterium *Acidithiobacillus thiooxidans*, which grows by the chemical oxidation of inorganic sulfur compounds using the energy of the oxidation for metabolism and deriving the cell carbon from CO_2 of the air.

Most microorganisms may be classified as chemoorganoheterotrophs. Exceptions are photosynthetic microorganisms (mainly a few bacterial genera), cyanobacteria, algae, and in part lichens because of the algal or cyanobacterial symbiont. Exclusively restricted to bacteria are chemolithotrophic life forms.

An important feature of microbial life is the possibility to degrade any naturally occuring compound. This is called microbial omnipotence. Exceptions to this rule are a few manmade compounds such as highly polymerized materials (resins, plastics, etc.) and halogenated compounds. These are called xenobiotica because they are strange to the living world and living organisms have had too little time to adopt to these compounds and develop degradative enzymes. Eventually, genetic engineering of microorganisms may help in the development of degradatively active ones.

Besides energy and carbon sources, microorganisms need nitrogen, phosphorus, and trace elements. Nitrogen compounds may be inorganic ammonium and/or nitrate (sometimes nitrite, too) as well as organically bound nitrogen (amino acids, nucleotides, etc). Some microorganisms (bacteria and cyanobacteria) are able to fix nitrogen from atmospheric nitrogen with the help of an enzyme called nitrogenase. The end product is ammonia, which is incorporated in cell constituents.

Phosphorous is usually taken up as inorganic phosphate or as (organically bound) phosphorylated compounds such as phosphorus-containing sugars and lipids. Phosphate in the form of adenosine triphosphate (ATP) serves as the main energy storage compound. Whenever a reaction takes place generating metabolically useful energy, ATP is produced to conserve at least a part of it.

Trace elements are needed for many metabolic purposes. They make up only a negligible amount of the total cell weight, but they support vital functions. Iron as Fe^{2+} or Fe^{3+} is necessary for the electron transport system. It functions as an oxidizable/reducible central atom in cytochromes or in nonheme iron-sulfur proteins. Magnesium plays this role in the chlorophyll molecule. Cobalt functions in the transfer of methyl groups from/to organic or inorganic molecules (vitamin B_{12}, cobalamine, is involved in the methylation of heavy metals such as Hg). Copper is an integral part of a cytochrome (aa_3), which at the terminal end of the electron transport system mediates the reduction of oxygen to water (cytochrome oxidase). Further examples exist for other metals.

Microbial growth is influenced and sometimes restricted by several chemical and physical factors. Life generally cannot exist without water. Hence, water is

Copyright © 2002 Marcel Dekker, Inc.

a prerequisite for microbial life and growth. Microorganisms differ considerably with regard to the amount of water needed. In particular, fungi are able to live under extremely dry conditions. Three types of water surrounding a solid material need to be distinguished: hygroscopic, pellicular, and gravitational water. Hygroscopic water, a film 3×10^2 μm thick, directly surrounds the solid particle. It is not available for life and does not freeze or move. Pellicular water and gravitational water are biologically available and, thus, may be used by microorganisms. The biologically available water is usually measured as the water activity a_w of a sample:

$$a_w = \frac{\text{vapor pressure of a solution}}{\text{vapor pressure of pure water}} \quad \text{(at the same temperature)}$$

Most bacteria are restricted to a_w values of more than 0.90 (equivalent to an osmotic pressure of –150 bar). Exceptions are bacteria living in salterns or salinas—halobacteria—that exhibit a_w values of 0.75 (equivalent to an osmotic pressure of –400 bar). The lowest known value for a (micro) organism has been found for the fungus *Xeromyces bisporus* [115]. The organism is able to grow at an a_w value of 0.61, equivalent to –681 bar. For comparison, egg powder has an a_w value of 0.40 (–1260 bar) and biscuits of 0.30 (–1660 bar). Lichens, because of the symbiosis of a photosynthetic partner (alga or cyanobacterium) with a fungus, may resemble fungi in their need for available water. All other microorganisms (and also higher organisms) are very sensitive to water stress. They barely tolerate water shortage. The tolerated a_w value is 0.99 (–15 bar). Physical factors may contribute to water shortage. In porous systems such as soil or sedimentary stone (sandstone), water activity is already reduced because of the capillary bonding in pores of low diameter (below 10 μm).

Another important factor is the hydrogen ion concentration. Microorganisms may be distinguished by their ability to grow under acidic, neutral, or alkaline conditions. Hence, they are called acidophiles, neutrophiles, or alkaliphiles. The bacterium *A. thiooxidans* has been detected in samples exhibiting a negative pH value, whereas in soda lakes life has been detected at pH values of 12 and above. Fungi are able to grow over a large range of pH values. Species of *Penicillium* have been found at pH 2 and up to pH 12. Most microorganisms, however, thrive in the neutral pH range from 6 to 8.

The redox potential is another factor determining microbial growth. If, under standard conditions, hydrogen is assumed to have a redox potential (E_h) of –420 mV and oxygen to have an E_h value of +820 mV, this gives the range in which metabolism can take place. The basic process of life is the reaction of hydrogen with oxygen to form water. Depending on oxidizing or reducing conditions, different types of metabolism are found. Under oxidizing conditions with E_h values of +500 mV and above, oxygen is usually used as terminal electron acceptor. E_h values of +400 mV favor the reduction of nitrate if oxygen is not available. If neither oxygen nor nitrate is available, Mn^{4+} may serve as an electron acceptor, being reduced to soluble Mn^{2+} species. At an E_h value of –180 mV, ferric iron starts to be used as terminal electron acceptor. At an even lower redox potential sulfate is reduced to sulfide (–220 mV). The lowest potential (–250 mV) is necessary for the reduction of carbon dioxide to methane.

Copyright © 2002 Marcel Dekker, Inc.

Closely linked to the redox potential is the available oxygen. Microbial life is possible under well-aerated as well as under totally oxygen-free conditions. The differences are used to characterize the oxygen needs of microorganisms. Aerobes are organisms living with the amount of oxygen contained in the air. They may tolerate shortage of up to 5 or 10% of the regular partial pressure of oxygen. Facultative aerobes are able to live with the oxygen partial pressure even under conditions of exhaustion. In this case, they convert their metabolism to the use of chemically bound oxygen (nitrate) or to fermentation. Anaerobes are organisms that perform their metabolism without any free oxygen. They are able to use only bound oxygen (sulfate, carbon dioxide) or to ferment organic compounds [73]. In the latter group there are a few species that are called strict anaerobes because oxygen is highly toxic to these organisms. The process of utilization of chemically bound oxygen is called anaerobic respiration. It is also used for the reduction of inorganic metal ion species such as Mn^{4+} or Fe^{3+}.

Last but not least, the temperature needs to be discussed. Microbial life is possible between –5°C and +114°C. Again, the temperature needs of microorganisms are used for their classification.

Psychrophiles are organisms living in the range of –5°C up to 20°C. *Psychotrophs* live between 5°C and 30°C. *Mesophiles* thrive in temperatures between 20°C and 45°C. At higher temperatures, *moderate thermophiles* find their habitat (40–55°C). The next group are the thermophiles, living in the range from 55°C to 85°C. The *extreme thermophiles* grow at temperatures up to about 120°C. Above that, living organisms have not so far been detected. Most organisms live in the mesophilic range corresponding to the usual temperature on the surface of the earth. Interestingly, only a special group of bacteria is able to grow at elevated temperatures (above 70°C). They are called archaebacteria and are distinguished from eubacteria by many chemical and physiological traits. Many of them seem to represent ancestors who are believed to have been active in the early history of this planet (high temperature, reducing atmosphere). Organisms are usually not restricted to grow at a certain temperature. Adaptation within a range of 20 to 30°C above or below their optimized growth temperature is possible. It is achieved by a modification of the fatty acid composition in the cytoplasmic membrane. At higher temperatures, unsaturated and/or branched fatty acids prevail, whereas at lower temperatures saturated, unbranched ones are found.

In summary, microbial life is influenced by many parameters. Adaptation to a change is possible [13,26]. This allows microorganisms to be present wherever a substrate is available for metabolism. A variation in the parameters previously mentioned may be used to control microbial growth. However, care must be taken to ensure that merely adaptation of the microorganisms present and not a change in the composition of the microbial biocoenosis takes place.

Microorganisms grow predominantly attached to surfaces. It is estimated that more than 90% of all microorganisms live sessile on the surface of a solid material (called the substratum, in contrast to the nutrient, which is called the substrate). Attachment of microorganisms is mediated by a complex series of events by excretion of linking exopolymers resulting in firmly substratum-bound cells.

The exopolymers consisting of lipopolysaccharides, lipoproteins, and sometimes nucleic acids [14] constitute the outer membrane of the cells and, because

Copyright © 2002 Marcel Dekker, Inc.

they are strain specific, may be used for identification purposes. Furthermore they may contain metal cations, some of which are known to be necessary for substrate degradation [47]. If several cells are growing together on a substratum, the exopolymers fill the voids. This is called a biofilm. If a biofilm grows and increases in thickness, it becomes stratified or patchy. The oxygen supply of cells buried deeply in a biofilm may become limiting. Thus, anaerobic zones or layers develop [70]. This may result in the appearance of closely associated zones with aerobic and anaerobic types of metabolism. Localized biofilm (microcolonies) may have serious detrimental effects on materials [55]. Because of the oxygen consumption by a microcolony or a biofilm, localized aeration elements exist, causing in the case of metals an enhanced dissolution by stimulation or electrochemical effects. Another effect may be reduced heat transfer in heat exchange systems [40]. Furthermore, biofilms protect the organisms living there because of reduced penetrability of poisons such as heavy metals, biocides, and natural enemies such as viruses (phages) and grazing protozoa [20,41]. In addition, a biofilm protects against dryness. The microorganisms growing in a biofilm have, thus, created a microenvironment of their own favorable for their survival and growth. Another aspect is that in dilute solutions, due to ionic interactions, (organic) molecules tend to adsorb to surfaces and thus becoming increasingly available for attached organisms.

MICROBIALLY INFLUENCED GEOCHEMICAL CYCLES

Most elements on earth are subject to cycling. During this process the oxidation status may be changed from fully oxidized to totally reduced. All cycles are influenced by microorganisms, and some are controlled by them [36]. Four examples, the carbon cycle, the nitrogen cycle, the sulfur cycle, and the iron cycle, are selected here to illustrate the importance of microorganisms.

Carbon Cycle

Carbon occurs in the biosphere either reduced (methane, fatty acid, carbohydrate) or oxidized (alcohol, aldehyde, carbonic acid, carbon dioxide). The valence state 0 is found only in coal (a compound of biological origin).

(Micro)organisms control the carbon cycle (see Fig. 1). By fixing CO_2 from the air, cell carbon is generated. Primary producers such as green plants, algae, cyanobacteria, and photosynthetic bacteria are responsible for this reaction. The enzyme mainly involved in this process is called ribulose-1,5-bisphosphate-carboxylase/oxygenase (RubisCO). It is the most abundant protein on earth. The resulting cell carbon is degraded by organisms, the end product being carbon dioxide, which may be fixed again. Another possibility is the incomplete degradation occurring in sediments, etc. This may give rise to accumulations of organic matter as observed in shallow marine areas, swamps, and marshes. Presumably, deposits of carbon such as oil, gas, and coal were formed in this way [2]. Another pathway is the fixation of CO_2 followed by its use in structural elements of organisms such as valves and bones. In this way, inorganic deposits such as limestone and shales are formed.

Copyright © 2002 Marcel Dekker, Inc.

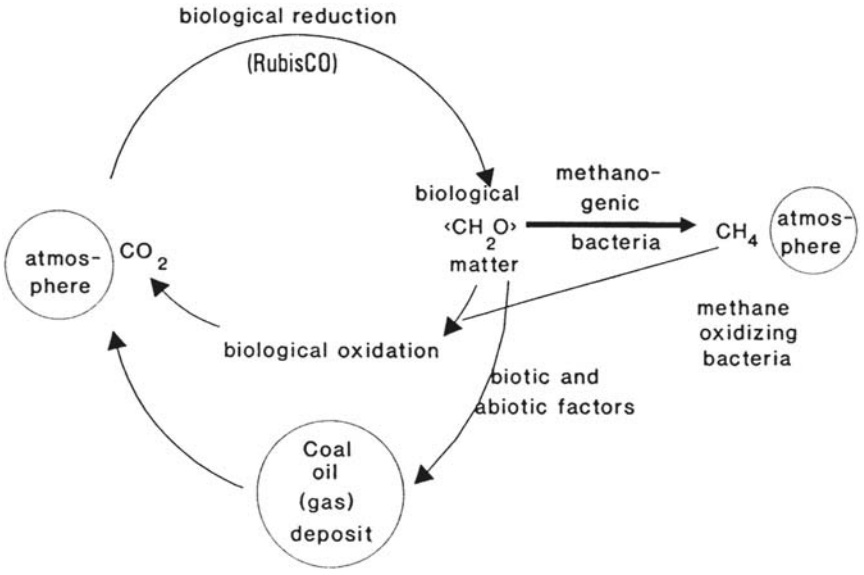


Figure 1 Carbon cycle.

Nitrogen Cycle

Nitrogen occurs in the biosphere either reduced (to ammonium) or oxidized (nitrite, nitrate), together with intermediates such as hydroxylamine (NH_2OH), nitrogen (N_2), and nitrogen oxides (N_2O, NO, NO_2). In addition, organically bound nitrogen is found in many compounds such as proteins, nucleic acids, amines, and urea. Microorganisms mediate all and control most of the reactions in this cycle (see Fig. 2). The cycle starts with an enzymatic reaction unique to bacteria and cyanobacteria. Atmospheric dinitrogen, N_2, is reduced and fixed by the action of the enzyme nitrogenase. The product NH_3 is incorporated in cell constituents, the amount of ammonia that becomes available for the biosphere being comparable to the amount produced in technical ammonia production. When cell constituents are degraded, ammonia is liberated and may be used for the synthesis of other nitrogenous compounds. Because nitrogen is usually a limiting factor for life, organisms take care not to lose it. However, upon the death of cells, ammonia may become available. Usually, a process called nitrification starts. Nitrifying bacteria oxidize ammonia via nitrites to nitrate. The nitrifying bacteria consist of two groups: the ammonia oxidizers, which are responsible for the oxidation of ammonia to nitrite, and the nitrite oxidizers, which are responsible for converting nitrite to nitrate. Hence, a cation is converted to an anion plus protons (acidification). The process has positive and negative consequences. Whereas ammonia may be adsorbed to clay particles and, thus, may become unavailable for plant growth, nitrate is a mobile ion, which can be washed out of soil by rainfall and enter into ground water. Because of this, nitrification is responsible for nitrogen loss from fertilizers and ground water pollution by nitrate. In the case of a large supply of organic matter, the availability of oxygen is often limiting for

Copyright © 2002 Marcel Dekker, Inc.

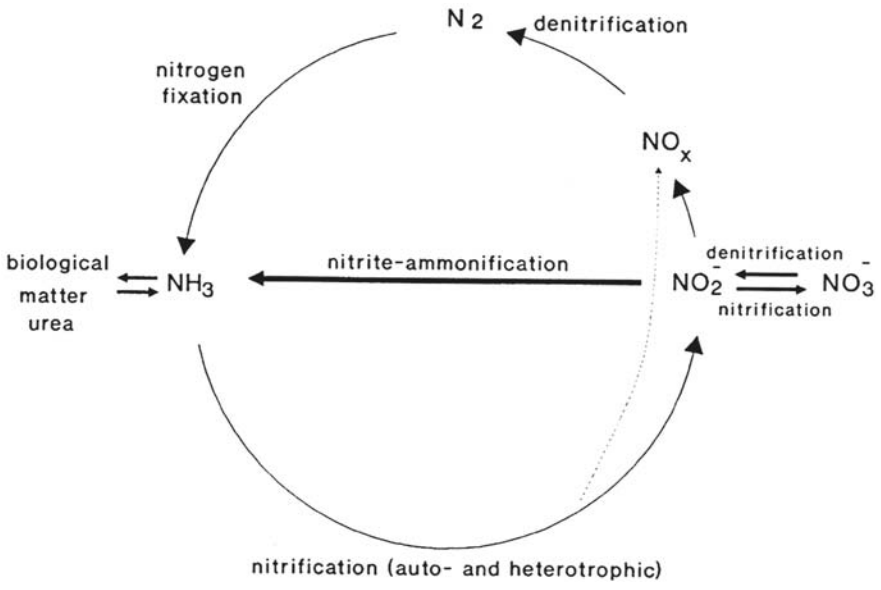


Figure 2 Nitrogen cycle.

degradation. Under these circumstances, a reductive process called denitrification or nitrate (nitrite) respiration gains importance.

Nitrate and other oxidized nitrogen compounds may serve as electron acceptors and be reduced to nitrite, NO, N_2O, and finally N_2 [4]. The oxygen is released as water. Thus, denitrifiers can get rid of hydrogen resulting from the oxidation of organic matter. By this mechanism a considerable amount of organic matter may be mineralized under anaerobic conditions. Growth yields with chemically bound oxygen are in the range of atmospheric oxygen usage (less than 10%). The reduction does not always proceed until dinitrogen is released. Often, NO or N_2O are the end products. These may either be reoxidized or be further reduced by microorganisms. In any case, the nitrogen cycle is closed by these microbiologically catalyzed reactions. It needs to be added that there is an enormous input of ammonia mainly from two processes: the degradation of manure from livestock breeding and loss of fertilizers from farmland. Compared with industrial processes such as the use of ammonia for flue gas desulfurization, these two processes dominate the ammonia emission. Nitrogen oxides are becoming increasingly important because of their influence on the global climate. In contrast to the emissions of dust particles and sulfur dioxide, the emission of nitrogen oxides is still increasing because of increasing use of combustion processes, e.g., for automobiles and heating systems. Microbiology will adapt to the increased supply of these compounds, which furthers the growth of ammonia-oxidizing and NO-oxidizing microorganisms.

Sulfur Cycle

Sulfur occurs in the biosphere in many compounds. It is essential for the formation of the sulfurylated amino acids methionine and cysteine/cystine. Other highly

Copyright © 2002 Marcel Dekker, Inc.

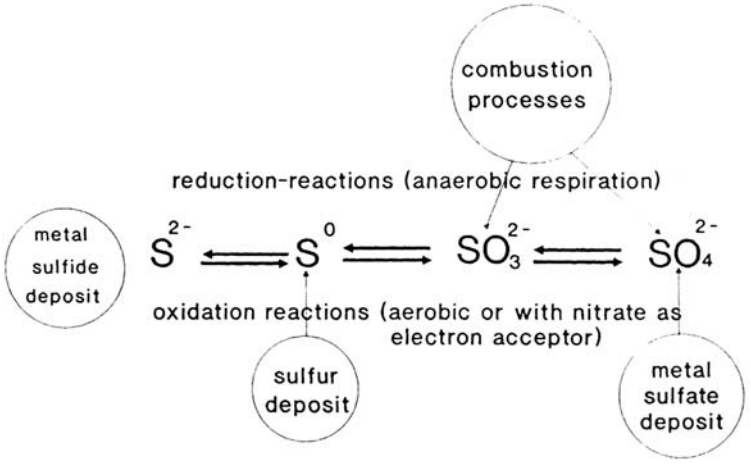


Figure 3 Sulfur cycle.

important compounds are those containing reactive thiol groups, such as coenzyme A or iron-sulfur redox centers involved in electron transfer reactions. The commercially most important sources are deposits of metal sulfides (production of valuable metals by mining) and sulfur (source of sulfur for sulfuric acid production). Metal sulfides can be attacked and degraded microbiologically by the action of highly specialized bacteria, which oxidize the metal sulfide to a metal sulfate [105]. This is accompanied by sulfuric acid production, which keeps the metal ions solubilized. The metals may be recovered by processes such as sedimentation, solvent extraction, or ion exchange and further purified for practical use. The oxidation of the sulfide moiety takes place in several steps including sulfur, polythionate, and sulfite (see Fig. 3). The energy liberated by this oxidation is recovered by ATP production. The microorganisms active in this process tolerate high heavy metal concentrations (up to several grams per liter) and low pH values (pH 1.5 and below). They may grow at temperatures from 4°C up to 90°C. Once sulfate has been produced, a process similar to denitrification may take place. If sufficient organic matter is available and anaerobic conditions prevail, sulfate may act as an electron acceptor for reduction equivalents, being reduced via sulfite and sulfur to sulfide [31]. The process is called sulfate reduction (sulfate respiration) and the bacteria are referred to as sulfate reducers or sulfate-reducing bacteria (SRB). This is a physiologically diverse group of microorganisms including photosynthetically active bacteria. Besides mesophilic eubacteria, very ancient life forms belong to this group. It contains archaebacteria, which are able to live at 110°C by sulfate reduction, conditions probably resembling early stages of life on this planet. If sulfide accumulates, two different pathways are selected depending on the oxygen availability. Under aerobic conditions, oxidation to sulfate occurs as described before. Under anaerobic conditions in the light another type of oxidation takes place. Photosynthetic microorganisms oxidize sulfide to sulfur and, at least some of them, to sulfate using the electrons liberated to fill up their photosynthetic system. Without light it has been discovered that sulfide oxidation coupled to nitrate reduction can take place. A small part of the sulfide is used for the

Copyright © 2002 Marcel Dekker, Inc.

production of sulfur-containing biomolecules. Thus, biology may oxidize and reduce sulfur and its compounds by many reactions. Deposits of sulfur compounds resulting from this activity may include elemental sulfur, metal sulfides, and sulfates like barites. The biological origin can be detected by measurement of the $^{32}S/^{34}S$ ratio. The enzymes involved in sulfur metabolism often prefer to handle the lighter isotope. In consequence, a biological deposit will be enriched with ^{32}S compared with sulfur from meteorites which has a strictly defined ratio of 22.22/1.

Iron Cycle

Iron is an essential element for life. Although it belongs to the trace elements, a shortage endangers many vital functions. Generally, it exists as Fe^{2+} or Fe^{3+} mediating redox reactions combined with electron transfer (see Fig. 4). For example, iron is the central atom of cytochromes (heme type) and is part of redox proteins having an iron-sulfur reaction center (nonheme). Ferrous iron may serve as energy source for many bacteria. Well known are the acidophilic lithoautotrophic bacteria *A. ferrooxidans* and *Leptospirillum ferrooxidans* living in sulfidic, aerobic habitats by oxidizing ferrous to ferric iron (besides sulfide oxidation to sulfuric acid with *A. ferrooxidans*). The energy of the reaction is used for metabolic purposes. Reaction products are usually ferric iron, sulfuric acid, and to a certain extent intermediary sulfur. Although these bacteria thrive best at a pH range of 1 to 3.5 [18], where ferrous iron is only slowly autoxidized by oxygen, organisms such as *Metallogenium* sp. (pH 3.5–6.5) and *Gallionella ferruginea* (pH 6–8) as well as *Leptothrix ochracea* (= *Sphaerotilus natans*, pH 6–8) are responsible for ferrous iron oxidation at higher pH values. As Fe^{2+} becomes increasingly autoxidizable at pH values above 3.5, these organisms must be adapted to live with low concentrations of ferrous iron and/or a reduced oxygen partial pressure (microaerophiles). Once ferric iron has entered the cycle, it will probably be precipitated in the form of ferric hydroxide, $Fe(OH)_3$, followed by several reactions resulting in formation of hematite, Fe_2O_3. Under conditions where organic compounds are available, e.g., in anaerobic sediments with decaying organisms, ferric iron may be used as an electron acceptor and be reduced to ferrous iron [73]. Thus, an immobile iron form is transformed into a mobile one. This process becomes even more important because coprecipitated heavy metals also become solubilized, consequently endangering the environment.

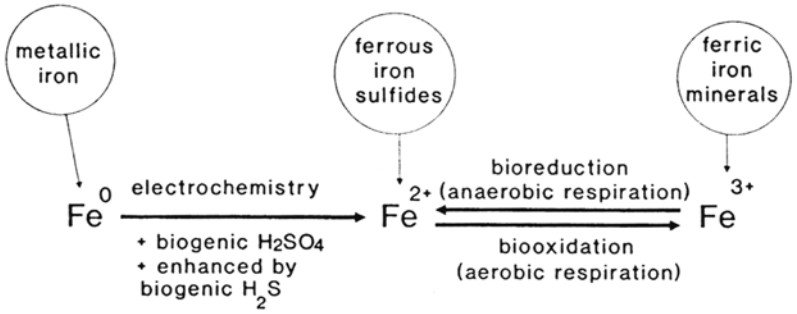


Figure 4 Iron cycle.

Copyright © 2002 Marcel Dekker, Inc.

Many microorganisms, bacteria and fungi, are able to use this reduction reaction. Even the ferrous iron–oxidizing bacteria may be able to perform this reaction in the event of oxygen shortage. The reactions are not restricted to mesophilic bacteria. Thermophilic bacteria are known to participate in these reactions (oxidatively as well as reductively).

As mentioned, sulfuric acid is produced concomitantly with the metal sulfide oxidation. Sulfuric acid may react with metallic iron, Fe^0, to give ferrous sulfate and hydrogen. Both compounds may be oxidized biologically. Furthermore, ferric iron may react with metallic iron to form ferrous iron, $Fe^0 + 2Fe^{3+} \rightarrow 3Fe^{2+}$, which may then be oxidized to ferric iron. Another reaction with iron results from the sulfur cycle and demonstrates the intimate connection between both cycles. Reduction of sulfate under anaerobic conditions, e.g., by SRB, results in the formation of hydrogen sulfide. This may react with ferrous iron to form a precipitate of ferrous sulfide and, if sulfide is in excess, finally pyrites (FeS_2).

In summary, it becomes obvious that most reactions of materials with the environment are influenced by microorganisms and are often even controlled by them [36]. Thus, in the case of microbially influenced corrosion, the participation of microorganisms needs to be anticipated [54,95]. Furthermore, cases are known in which excreted metabolic products, e.g., EPS free from microbial cells, cause corrosion.

MECHANISMS OF BIODETERIORATION

Despite the vast diversity of microorganisms participating in various natural cycles, the biological mechanisms contributing to or causing biodeterioration may be summarized in a few main categories [48]. It needs to be pointed out, however, that one microorganism may exert multiple detrimental effects. In addition, under natural conditions pure cultures do not exist. Thus, mixed cultures called biocoenoses are active by usually creating growth conditions for the corrosion-causing microorganisms. In most cases microorganisms cause an attack resulting from a chemical compound produced and excreted by metabolism. Thus, the basic action will be a chemical reaction.

Excretion of Acid

Specialized bacteria are able to produce and excrete strong mineral acids. Usually under aerobic conditions, thiobacilli oxidize inorganic sulfur compounds and sulfur to *sulfuric acid*. The energy of this oxidation is coupled via special enzymes to growth. Besides sulfur and sulfur compounds, the bacteria need only carbon dioxide (cell mass). The genus *Thiobacillus* consists of several species that are able to grow at moderately alkaline down to strongly acidic pH values. The species able to grow and proliferate on alkaline materials are pioneers for the species growing only under acidic conditions. After the buffer substance of, e.g., concrete (lime) has been exhausted, the pH value in the surface water declines and the acidophilic species start to proliferate. This finally causes severe biogenic sulfuric acid corrosion [6,7,80,89,96].

Copyright © 2002 Marcel Dekker, Inc.

The second group to be mentioned here is the nitrifying bacteria excreting *nitric acid*. The nitrifying bacteria consist of two groups. The ammonia oxidizers convert ammonia to nitrite, and the nitrite oxidizers subsequently form nitrate. Like sulfuric acid, nitric acid can react with alkaline materials forming highly soluble salts (in contrast, sulfates are much less soluble). Biogenic deterioration results [7,64,66,76]. Nitrifiers are also lithoautotrophs. The energy source is a nitrogen compound; cell carbon is derived from CO_2.

The third important acid is produced by all life forms. Carbon dioxide is excreted as the end product of metabolism. It reacts with water to *carbonic acid*, which may dissolve, e.g., to carbonates forming soluble bicarbonates. In this way the binding material of concrete, lime, may be dissolved.

The fourth group of microorganisms consists of those which during their metabolism excrete *organic acids* such as oxalic, citric, malic, lactic, or acetic acid, amino acids, uronic acids, etc. [25,34]. Usually, these acids are excreted because of an unbalanced metabolic state. However, they may thus be taken up again by the cells in later growth phases or be metabolized by other microorganisms present in the biotope. This means that organic acids are usually available only temporarily. Nevertheless, their presence may have caused transformations in the crystal lattice. Organic acids may be excreted by almost all bacteria, cyanobacteria, algae, lichens, and fungi. Sometimes the excretion is coupled to the uptake of limiting cations into the cell.

Chelatization

Besides acid attack on materials, organic acids are *chelating* cations. Because of the stability of the complexes, metals may be dissolved from a crystal lattice resulting in a weakening of the structure. The action is sometimes deliberate because it allows the cells to replenish limiting cation concentrations; e.g., pathogenic bacteria possess special iron chelators to replenish growth-limiting ferric iron at the expense of the host.

Organic Solvents

Many microorganisms are able to metabolize organic substances under anaerobic conditions. If an electron acceptor such as nitrate, Fe^{3+}, Mn^{4+}, or sulfate is not available, fermentation results [73]. This means that hydrogen (= redox equivalent) is transferred from one to another organic compound. By this transfer, growth may be possible because of a substrate phosphorylation. The result of a fermentation process is thus usually another organic compound, sometimes carbon dioxide. The organic compounds are in many cases organic acids, as mentioned before, or organic solvents such as ethanol, propanol, or butanol. These solvents may react with materials of natural and/or synthetic origin, causing swelling, partial or total dissolution, etc., which finally results in deterioration.

Other Metabolic Compounds

An important compound for MIC is *hydrogen sulfide*. It is produced under anaerobic conditions by the action of sulfate-reducing bacteria from sulfate, sulfite, and sometimes sulfur [88]. It has also been shown that thiosulfate can by used by SRB

Copyright © 2002 Marcel Dekker, Inc.

[75]. As mentioned before, the SRB use the not fully reduced sulfur compounds as electron acceptors in anaerobic respiration.

Hydrogen sulfide may act in several ways. Either it is reoxidized to sulfuric acid under aerobic conditions [101] or in the presence of compounds such as nitrate or it may react with cations to form metal sulfides that precipitate [50]. Further, H_2S may be oxidized anaerobically in the light by photosynthetic bacteria (mostly to sulfur, sometimes to sulfate). In the case of materials containing acid-reactive substances, the biogenic acid will become harmful. In the case of metals the presence of H_2S may cause MIC. Another source of H_2S is not restricted to anaerobiosis. Amino acids containing sulfur are degraded under aerobic conditions, giving rise to H_2S (cysteine and cystine).

Another important compound is *ammonia*. It may be generated as a result of amino acid or urea degradation by microorganisms. Furthermore, ammonia (or mainly ammonium salts such as sulfates or chlorides) is a major part of airborne gases (or dust particles). By dry or wet deposition ammonia/ammonium salts reach the surface of materials and, in the case of porous materials, enter the pore system and become biologically available. Nitrifying bacteria as already described may degrade ammonia/ammonium compounds. However, chemical reactions with materials may also be possible.

Nitrogen oxides, N_2O, NO, NO_2, resulting from biological activity (nitrogen cycle—oxidation of ammonia or nitrite reduction to N_2) as well as from processes such as the burning of fuels (heat and power generation, traffic), are a group of compounds that may react with materials. NO_2 is a water-soluble gas dissociating upon dissolution into nitric and nitrous acid. These acids may attack susceptible materials. NO is less reactive but may be oxidized to NO_2 by light. N_2O is not known to interfere with materials.

Biofilm

Microorganisms tend to adhere to surfaces [48,56,106,141]. It is believed that more than 90% of all microorganisms grow in this way [14]. Concomitantly, exopolymeric substances are excreted. This may result in a slimy superficial layer on materials and/or, in the case of porous materials, in total clogging of the free pore volume [60]. The exopolymers are usually hydrated and may contain ionic groups favoring water inclusion. Thus, one result may be an increase in water content in the case of porous materials (a consequence is freeze–thaw attack; see the following).

Furthermore, the biofilm may act as insulation, reducing heat transfer. In the case of heating systems, the efficiency may be considerably reduced [40]. Another effect is the reduction of the cruising speed of ships due to increased friction caused by the surfacial biofilm [5]. Finally, biofilm development may cause technical processes to become susceptible to trouble. In paper machines, the inclusion of exopolymers in the pulp may cause the paper web to break in the paper machine. The coating of cans with resins may also be affected. Cans for food are coated on the inside with a resin to protect the metal from corrosion by foodborne acids. If the metal is covered at a few spots with biofilm (microcolonies), the coating process will not be totally successful. Pores will remain in the resin at these spots, rendering the metal accessible to acids from the food. Corrosion from the inside combined with deterioration and spoilage of the contents will result.

Copyright © 2002 Marcel Dekker, Inc.

Salt Stress

The biogenic reactions that have been mentioned result in the generation and, generally, accumulation (except in an aquatic environment) of salts as reaction products. Because salts are hydrophilic they are usually hydrated, resulting in an increase in the water content of a porous material. This may increase the susceptibility to physical attack by freezing and thawing because of the volume change in water/ice crystals.

Furthermore, upon desiccation, salt crystals may develop, causing the surfacial removal of layers of material, e.g., deterioration destroying wall paintings on natural stone. The third detrimental effect of salts results from the formation of large crystals causing a swelling attack. A well-known example is the formation of ettringite from gypsum crystals destroying concrete and bricks.

Exoenzymes and Emulsifying Agents

Besides exopolymers of a lipopolysaccharidic nature, microorganisms excrete lipoproteins and proteins. The latter include *exoenzymes* for the degradation of high-molecular-weight compounds such as cellulose. Cellulases degrade the insoluble cellulose fibrils to soluble molecules such as cellobiose (dimer) and glucose, which may be taken up by the cells for metabolism. Similar exoenzymes exist for other materials, e.g., esters, amines, and waxes. Other molecules, although not as large as cellulose, may also be insoluble and, thus, only poorly degradable.

In some cases microorganisms excrete emulsifying agents to increase the solubility of hydrophobic substances [112]. In the case of elemental sulfur, which is highly insoluble due to its hydrophobic nature, the excretion of such emulsifying agents causes an increase in dispersibility from 5 to 20,000 μg/L [114]. This holds for other hydrophobic materials as well. Water-insoluble hydrocarbons become water soluble because of microbial production of emulsifying agents and consequently become degradable.

These microbial deterioration mechanisms represent the main categories of action. Several mechanisms are usually active jointly, and because these mechanisms may also influence other types of physical or chemical attack, the microbial share of the total attack can rarely be determined. Much too often, studies of deterioration mechanisms suffer from inadequate microbiological analysis (if it is done at all). If corrosion occurs in the range where life is possible, a microbial contribution needs to be taken into account and, hence, a microbiologist should be consulted [54,84].

MICROBIAL CORROSION OF CONSTRUCTIONAL MATERIALS

Metallic Materials

Metallic materials are an important group of construction materials. Microbially influenced corrosion may occur for these materials for many industrial applications, as listed in Table 1 [27]. Microbially induced corrosion of metallic materials does not involve any new form of corrosion. Thus it is necessary to discuss the electrochemical nature of corrosion briefly before continuing with the mechanisms of MIC for different construction metals.

Copyright © 2002 Marcel Dekker, Inc.

Table 1 Industrial Applications for Which Microbial Corrosion Has Been Reported

Industry	Problem areas
Chemical processing industries	Stainless steel tanks, pipelines, and flanged joints, particularly in welded areas after hydrotesting with natural river or well waters
Nuclear power generation	Carbon and stainless steel piping and tanks; copper-nickel, stainless, brass, and aluminum-bronze cooling water pipes and tubes, especially during construction, hydrotest, and outage periods
Onshore and offshore oil and gas industries	Mothballed and waterflood systems, oil and gas handling systems, particularly in environments sourced by sulfate-reducing bacteria (SRB)–produced sulfides
Underground pipeline industry	Water-saturated clay-type oils of near-neutral pH with decaying organic matter and a source of SRB
Water treatment industry	Heat exchangers and piping
Seawage handling and treatment industry	Concrete and reinforced concrete structures
Highway maintenance industry	Culvert piping
Aviation industry	Aluminum integral wing tanks and fuel storage tanks
Metalworking industry	Increased wear from breakdown of machining oils and emulsions

Source: Ref. 27.

The corrosion of metals in the presence of water is of an electrochemical nature. This includes corrosion in water-containing solutions, atmospheric corrosion due to the presence of a humidity film at the metal surface, and corrosion in soils due to the humidity of the soil. A detailed discussion of electrochemically induced corrosion is outside the scope of this chapter. For more details, a large number of good comprehensive reviews may be consulted (for instance, Ref. 63). Hence only some basics will be given here insofar as they may help in understanding MIC of metals.

The anodic reaction involves the oxidation of the metal into metal ions, whereas the cathodic reaction involves the reduction of some component in the corrosive environment:

$$\text{Anodic reaction:} \quad \text{Me} \rightarrow \text{Me}^{n+} + ne^- \tag{1}$$

Cathodic reactions may be summarized as follows:

$$O_2 + 2H_2O + 4e \rightarrow 4OH \quad \text{(acidic, neutral, or alkaline solutions)} \tag{2}$$

$$O_2 + 4H^+ + 4e \rightarrow 2H_2O \quad \text{(acidic solutions)} \tag{3}$$

$$2H^+ + 2e \rightarrow H_2 \quad \text{(acidic solutions)} \tag{4}$$

Copyright © 2002 Marcel Dekker, Inc.

$$2H_2O + 2e \rightarrow H_2 + 2OH \qquad \text{(neutral and alkaline solutions)} \qquad (5)$$

The rates of the anodic and cathodic reactions must be balanced in order to preserve electroneutrality.

The nature of the cathodic reaction depends on the pH of the solution and on the presence of dissolved oxygen or other oxidizers such as dissolved CO_2. For instance, in the pH range between 4 and 10, the diffusion of dissolved oxygen to the metal surface controls the rate of corrosion of iron. In this pH range and in the absence of oxygen, very low corrosion rates should therefore be expected.

The term "uniform corrosion" implies that the anodic and cathodic sites are virtually inseparable, whereas "localized corrosion" implies that macroscopic anodic and cathodic sites are physically separable.

As already stated, MIC of metallic materials does not involve any new form of corrosion. The mechanisms involved in the biodeterioration of materials have already been given in detail. The main ways in which microorganisms may enhance the rate of corrosion of metals and/or the susceptibility to localized corrosion in an aqueous environment are given below in relation to known corrosion mechanisms (for each case some examples are also given):

Formation of concentration cells at the metal surface and in particular oxygen concentration cells. This effect may occur when a biofilm or bacterial growth develops heterogeneously on the metal surface. Concentration cells are also associated with the tubercles formed by iron-oxidizing bacteria, such as *Gallionella*. Certain bacteria may also trap heavy metals such as copper and cadmium within their extracellular polymeric substance, resulting in the formation of ionic concentration cells.

Modification of corrosion inhibitors. To this group belong microorganisms that may destroy corrosion inhibitors such as bacteria that transform nitrite (corrosion inhibitor for iron and mild steel) to nitrate, or nitrate (corrosion inhibitor for aluminum and aluminum alloys) to nitrite and ammonia and N_2.

Production of corrosive metabolites. Bacteria may produce different metabolites, such as inorganic acids (e.g., *T.thiooxidans*), organic acids (almost all bacteria, algae, and fungi), sulfide (sulfate-reducing bacteria), and ammonia, that are corrosive to metallic materials.

Destruction of protective layers. Various microorganisms may attack organic coatings, and this may lead to corrosion of the underlying metal.

Stimulation of electrochemical reactions. An example of this type of action is the evolution of cathodic hydrogen from microbially produced hydrogen sulfide.

Hydrogen embrittlement. Microorganisms may influence hydrogen embrittlement on metals by acting as a source of hydrogen or/and through the production of hydrogen sulfide.

In summary, all known cases of microbial corrosion of metals can be attributed to known corrosion mechanisms. In the following sections, the mechanisms of microbially induced corrosion for different metals and alloys are discussed.

Copyright © 2002 Marcel Dekker, Inc.

Mechanisms of Microbially Induced Corrosion of Iron and Mild Steel

Corrosion Under Anaerobic Conditions Considering the electrochemical reactions discussed earlier, very low corrosion rates are expected for iron and steel in near-neutral conditions and in the absence of oxygen. However, a large number of case histories in the literature, particularly for buried pipes and marine structures, report that the corrosion may be very severe and can be several orders of magnitude higher than that experienced under normal aerobic conditions [47]. It is well accepted that this is due to sulfate-reducing bacteria and their ability to produce sulfide. However, despite the large body of literature available, the exact mechanism(s) responsible for the corrosion in such environments is still the subject of discussion. Several good review articles present this subject in more detail than is attempted here [50,123,124,128].

The first attempt to explain the anaerobic corrosion of iron was that by Von Wolgozen Kühr and van der Vulgt [130]. These authors proposed as early as 1934 that sulfate-reducing bacteria were responsible of the pitting corrosion they observed on buried cast-iron pipes through their ability to remove the hydrogen from the metal surface via their enzyme hydrogenase for the dissimilary reduction of sulfate according to the following reactions:

$$4Fe \rightarrow 4Fe^{2+} + 8e \quad \text{(anodic reaction)} \tag{6}$$

$$8H_2O \rightarrow 8H^+ + 8OH \quad \text{(dissociation of water)} \tag{7}$$

$$8H^+ + 8e \rightarrow 8H_{ad} \quad \text{(cathodic reaction)} \tag{8}$$

$$SO_4^{2} + 8H_{ad} \rightarrow S^{2} + 4H_2O \quad \text{(cathodic depolarization by sulfate-reducing bacteria)} \tag{9}$$

$$Fe^{2+} + S^{2} \rightarrow FeS \quad \text{(corrosion products)} \tag{10}$$

$$3Fe^{2+} + 6OH \rightarrow 3Fe(OH)_2 \quad \text{(corrosion products)} \tag{11}$$

$$4Fe + SO_4^{2} + 4H_2O \rightarrow 3Fe(OH)_2 + FeS + 2OH \quad \text{(overall reaction)} \tag{12}$$

Reaction (9) represents the ability of SRB to remove the adsorbed hydrogen from the metal surface through the enzyme hydrogenase. This reaction was referred to by the authors as "depolarization." This term was used only to underline that there was an undefined change in the electrochemical response of the system studied [33]. This is an alternative reaction path compared with the classical hydrogen evolution reaction:

$$H^+ + e^- \rightarrow H_{ad} \quad (13)$$

$$2H_{ad} \rightarrow H_2 \quad \text{(chemical desorption)} \tag{14}$$

$$H_{ad} + H^+ + e^- \rightarrow H_2 \quad \text{(electrochemical desorption)} \tag{15}$$

Copyright © 2002 Marcel Dekker, Inc.

Reactions (14) and (15) are the rate-determining steps (i.e., a higher activation energy is required for these reactions compared with the discharge of hydrogen ions) for many metals and alloys, including iron in deaerated aqueous solutions. The rate-determinating steps may, however, be different in the case of complex corrosion layers. Sulfate-reducing bacteria, by removing adsorbed hydrogen to form sulfide according to reaction (9), lower the activation energy for the desorption steps. As these steps are rate determinating, this may lead to higher corrosion rates if hydrogen evolution is thermodynamically possible (i.e., if the immunity potential is lower than the redox potential for H_2/H^+).

This theory, also referred to in the literature as the classical depolarization theory, suggests that only sulfate-reducing bacteria that are hydrogenase positive (i.e., bacteria in which the enzyme hydrogenase is present) are responsible for the anaerobic corrosion of iron. Even though there are data supporting this view [9,57], it has been shown in many other works that this is not the case and that a high corrosion rate may be obtained with hydrogenase-negative strains [10,81,92]. In addition, several other important factors are not taken into account in the classical depolarization theory: (a) the effects of sulfide, bisulfide, and hydrogen sulfide produced from the sulfate reduction on the anodic reaction; (b) the effect of hydrogen sulfide on the cathodic reaction; (c) the effect of elemental sulfur from the biotic or abiotic oxidation of sulfur; (d) fluctuations in the environmental conditions between anaerobic and aerobic conditions [47]; (e) the production of other corrosive metabolites [128].

It is therefore now widely accepted that, even if the so-called depolarization of the cathodic reaction by the enzyme hydrogenase occurs, it plays no more than a secondary role in the pitting corrosion of iron in anaerobic conditions. This theory is therefore reported here more for historical interest than as a potential mechanism for pitting corrosion of iron in presence of SRB.

More recent theories have been proposed in which the role of the biogenic sulfide, the formation of a galvanic cell between the metal and the iron sulfide film formed, the role of elemental sulfur, the role of iron phosphites, and the local acidification of anodes have been discussed. The alternative theories to the classical depolarization theory are presented briefly in Table 2.

It has also been shown that the nature of the iron sulfide film plays an important role in the initiation of pitting corrosion. Figure 5 shows the different biogenically and chemically formed iron sulfide films [93]. When protective films such as mackinawite and siderite are formed, the corrosion rate may be very low. However, with changes in the environmental conditions these films may be transformed to iron sulfides that are less protective, such as pyrrhotite, with the possible initiation of pits as a result. The importance of the environment for the initiation of localized corrosion by SRB as been mentioned by several authors [24,51]. Of particular importance is the ability of SRB to regulate pH, the ionic composition, the composition of Fe^{2+}, aerobic/anaerobic cycles, and the presence of other microorganisms, as they may lead to conditions resulting in passivation or uniform corrosion or localized corrosion. This is probably the main reason why the severe pitting corrosion experienced in the field is only seldom reproduced in the laboratory using growing cultures of SRB, where uniform corrosion is generally observed. Indeed, in practice SRB are not found in isolation but in consortia of microorganisms or biofilms in which many physicochemical parameters such as pH and dissolved oxygen

Copyright © 2002 Marcel Dekker, Inc.

Table 2 Alternative Mechanism to the Classical Depolarization Theory

Name referred to in the literature and references	Main mechanisms	Role of hydrogenase
Depolarization by iron sulfide [65]	Formation of an iron/iron sulfide galvanic cell, iron sulfide acting as the site for cathodic reduction of molecular hydrogen	Secondary through the regeneration of ferrous sulfide
Depolarization by hydrogen sulfide [19]	Cathodic reduction of microbially produced hydrogen sulfide: $H_2S + e \rightarrow HS + H_2$	Secondary through the production of hydrogen sulfide
Elemental sulfur [104]	Formation of a concentration cell with elemental sulfur acting as the reactant	Secondary through the production of elemental sulfur
Iverson's mechanism [59]	Production of a volatile and corrosive iron phophite metabolite	Not defined
Local acidification of anodes [24]	Localized acidification of anodes due to the formation of iron sulfide corrosion products $Fe^{2+} + HS \rightarrow FeS\downarrow + H^+$	None

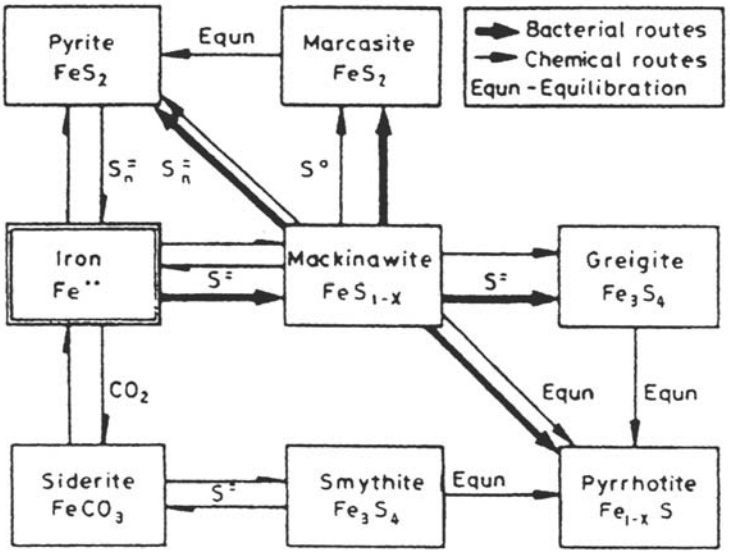


Figure 5 Chemical and biological interrelationships between iron sulfides [93].

Copyright © 2002 Marcel Dekker, Inc.

concentration change both with time and within the thickness of the biofilm. This dynamic picture of microbial corrosion is discussed in more detail later.

Corrosion Under Aerobic Conditions Corrosion may occur under aerobic conditions through the production of sulfuric acid by bacteria of the genus *Thiobacillus* [119]. The sulfuric acid is produced through the oxidation of various inorganic sulfur compounds, as illustrated in Table 3 [22]. Some of these bacteria can tolerate a concentration of sulfuric acid up to 10–12%. Under these conditions, iron and mild steel are heavily corroded.

Corrosion of iron and steel may also occur in aerobic conditions due to the colonization of bacteria at the metal surface and the formation of an uneven patchy biofilm. Nonuniform biofilms or bacterial colonization results in the formation of differential aeration cells in which the anodic areas are found under respiring colonies or in the thick part of the biofilm (zones depleted in oxygen) whereas the cathodic areas are found in noncolonized areas or in the areas where the biofilm is thin (regions rich in oxygen). This is schematically illustrated in Figure 6. The iron-oxidizing bacteria such as *Gallionella ferruginea*, *Crenothrix*, and *Leptothrix* are often associated in the literature with this form of corrosion, particularly in the internal surfaces of water pipes. These bacteria are aerobes and are believed to oxidize ferrous ions into ferric ions with the resulting formation of heavy deposits of ferric oxide or hydroxide, also referred to as tubercles. However, even if iron-oxidizing bacteria are the best-documented case, many other organisms may be involved in this kind of microbially influenced corrosion.

Finally, it should be mentioned that microorganisms may cause the degradation of corrosion inhibitors such as aliphatic amines, nitrite, and phosphate-based corrosion inhibitors used, for instance, for steel pipes in cooling water systems. This results in a higher demand for corrosion inhibitor and an increase in the bacterial population, which leads to high corrosion rates, if the system is not controlled [120,121].

Microbial Biofilms and the Interactions Between Aerobic and Anaerobic Populations In the preceding discussion, the mechanisms of microbial corrosion have been divided in the traditional way into anaerobic and aerobic mechanisms, which refer to the living conditions of the microorganisms involved in the

Table 3 Oxidation Reactions of Thiobacilli and Other Aerobic Sulfur-Oxidizing Bacteria

$S_2O_3^{2-}$	+	$2O_2$	+	H_2O	→	$2SO_4^{2-}$	+	$2H^+$		
2S	+	$3O_2$	+	$2H_2O$	→	$2SO_4^{2-}$	+	$4H^+$		
$4S_2O_3^{2-}$	+	O_2	+	$2H_2O$	→	$2S_4O_6^{2-}$	+	$4OH^-$		
$2S_4O_6^{2}$	+	$7O_2$	+	$6H_2O$	→	$8SO_4^{2-}$	+	$12H^+$		
2SCN	+	$4O_2$	+	$4H_2O$	→	$2SO_4^{2}-$	+	$2CO_2$	+	$2NH_4^+$
		H_2S	+	$2O_2$	→	SO_4^{2-}	+	$2H^+$		
		$2H_2S$	+	O_2	→	2S	+	$2H_2O$		
$2S_3O_6^{2}$	+	$4O_2$	+	$4H_{2_o}$	→	$6SO_4^{2}$	+	$8H^+$		
		$5H_2S$	+	$8NO_3$	→	$5SO_4^{2-}$	+	$4N_2$	+	$4H_2O$
5S	+	$6NO_3$	+	$2H_2O$	→	$5SO_4^{2-}$	+	$3N_2$	+	$4H^+$
$5S_2O_3^{2-}$	+	$8NO_3$	+	H_2O	→	$10SO_4^{2-}$	+	$4N_2$	+	$2H^+$

Source: Ref. 22.

Copyright © 2002 Marcel Dekker, Inc.

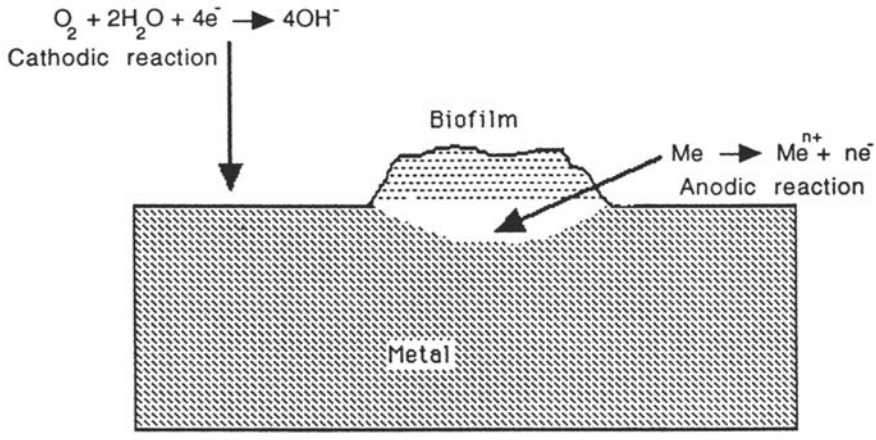


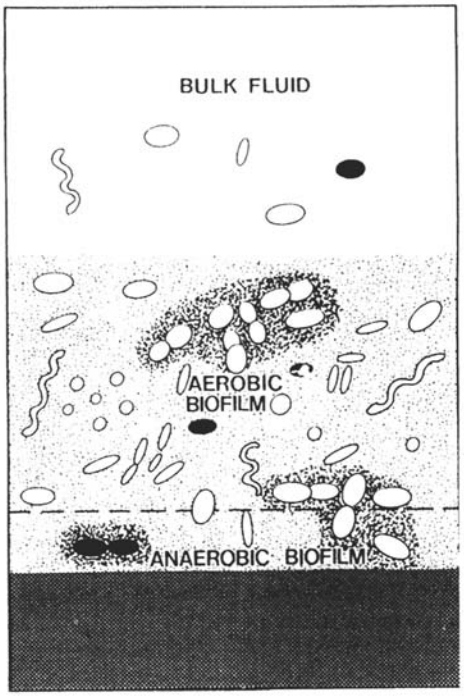
Figure 6 Schematic representation of the influence of the biofilm in the formation of differential aeration cells.

corrosion processes. However, it is now well known that bacteria are not found in isolation but rather in consortia or biofilms in which many bacterial communities coexist. A good illustration of this is given in Figure 7 [21]. As already mentioned, a biofilm is composed mainly of bacterial cells, extracellular polymers, inorganic ions, and water. It influences the mass transfer of different species and in particular dissolved oxygen from the solution to the metal, thereby creating a zone depleted in oxygen at the metal–biofilm interface (Fig. 7a). In this part of the biofilm, facultative and obligate anaerobic microorganisms such as sulfate-reducing bacteria may find suitable conditions of growth (anaerobic conditions and low redox potential). The result of this is the formation of microcolonies of SRB, which, through their production of metabolite products, may generate conditions favorable for other anaerobic bacteria to grow (Fig. 7b). This creates areas on the metal surface with local gradients in, for instance, hydrogen sulfide and hydrogen concentrations that may initialize localized corrosion on iron and steel (Fig. 7c). Many authors [44–46], have reported similar synergistic effects of bacterial consortia on the rate of corrosion of mild steel.

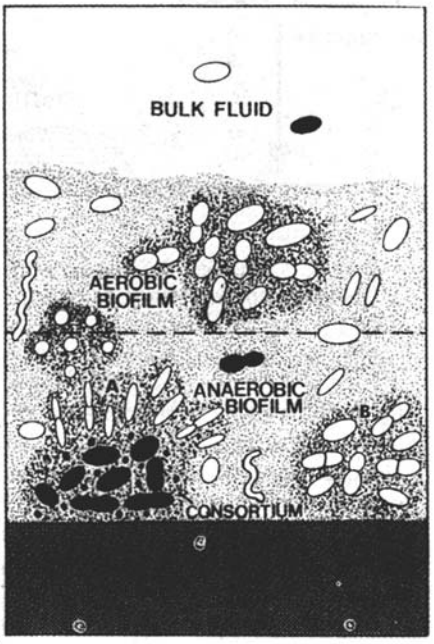
In addition to the ways already mentioned in which microorganisms influence the corrosion of iron and mild steel, there are numerous reports that microorganisms may cause hydrogen embrittlement, stress corrosion cracking, and corrosion fatigue [35,132,133]. It has been shown that in pure cultures of hydrogen-producing bacteria (hydrogen is produced as an end product of the fermentation process) hydrogen embrittlement is enhanced. In natural microbial biofilms, the situation may be described according to Figure 8 [133]. Consortia of hydrogen-producing and hydrogen-consuming bacteria are formed at the metal surface, creating, for instance, gradients of hydrogen [102,127]. Hence, depending on the primary colonizers (hydrogen producers or hydrogen consumers) and their distribution on the metal surface, hydrogen embrittlement may or may not occur.

It is also obvious that the production of H_2S from SRB may accelerate hydrogen embrittlement, stress corrosion cracking, and corrosion fatigue.

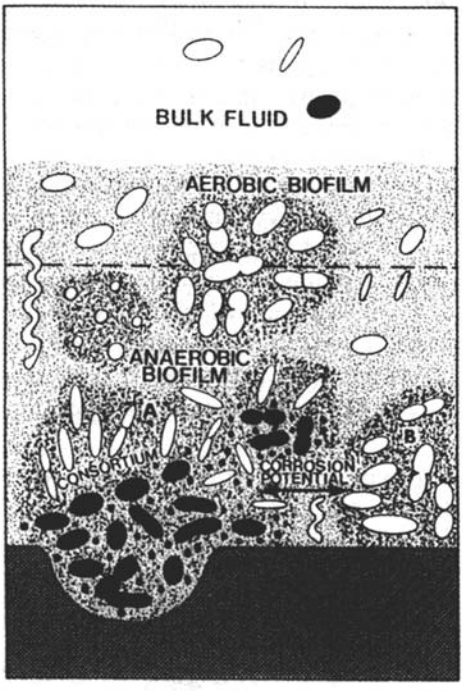
Copyright © 2002 Marcel Dekker, Inc.



(a)



(b)



(c)

Copyright © 2002 Marcel Dekker, Inc.

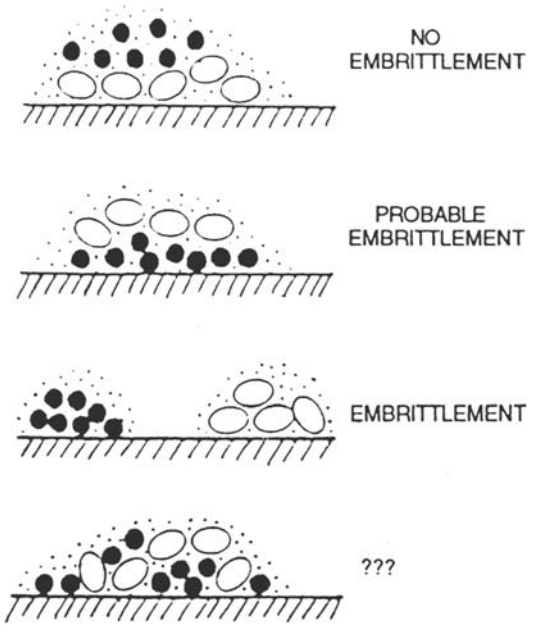


Figure 8 Diagrammatic representation of the effects of the spatial arrangement of hydrogen producers and consumers in a natural biofilm on the embrittlement of metals (black circles represent hydrogen producers, open ovals represent hydrogen consumers.) (From Ref. 133.)

From these studies it seems clear that, even if studies of microorganisms in isolation (i.e., in pure cultures) give valuable information concerning the mechanisms of MIC of a particular species in a given environment, more work should be done on the effect of mixed bacterial populations on the mechanisms of MIC.

Mechanisms of Microbially Induced Corrosion of Stainless Steels and Titanium

There are large numbers of reported case histories of MIC on stainless steel in water and aqueous waste systems. They are related to different industrial applications such as freshwater storage and circulation systems in nuclear power plants [103, 113,116,142] and cooling water systems in chemical process industries [117,118]. There are basically three cases: (a) crevice corrosion under unexpected deposits, (b) sensitivity of pitting and crevice corrosion to trace of H_2S, and (c) crevice corrosion in natural seawater. Most of these reports are not well documented concerning the microorganisms involved in the process. However, some general features are

Figure 7 Diagrammatic representation of the formation of microbial consortia and their influence on the corrosion processes. (a) When the film becomes sufficiently thick its inner part will be anaerobic with the possible development of SRB microcolonies (black cells). (b) The SRB attracts secondary colonizers by its metabolic products and forms a consortium with them. (c) The development of local areas with varying physicohemical parameters leads to pitting corrosion. (From Ref. 21.)

Copyright © 2002 Marcel Dekker, Inc.

common in almost all cases: (a) MIC is reported for the alloys with a relatively low content of molybdenum; (b) pitting or crevice corrosion generally occurs at or around welds (i.e., near the fusion line, or with sensitization in the heat-affected zones); (c) discrete localized deposits are often found in direct connection, with or close to the corrosion sites.

The higher sensitivity to MIC of welds compared with the unwelded metal may be explained by a difference in surface roughness or/and chemical composition that facilitates the colonization of the surface by microorganisms.

In some reports, a higher sensitivity to MIC of the delta-ferrite in duplex welds has been reported [12,67], and in others both the austenite and delta-ferrite phases have been shown to be sensitive to MIC [11]. There is also evidence that surface treatment of welds, such as solution annealing and pickling or polishing and grinding, may result in welds that are less susceptible to microbial corrosion [11,134].

The observation of localized deposits is often associated with the presence of slime-forming bacteria such as *Pseudomonas* and iron bacteria. These bacteria consume oxygen diffusing into the deposit and thus create a differential aeration cell that may initiate crevice corrosion. Under the deposit, the environment becomes anaerobic with the subsequent possibility of growing SRB in a scenario similar to that described for microbial biofilms. Besides the effect of concentration cells, the specific role of metal-concentration/oxidizing bacteria such as iron- and manganese-oxidizing bacteria in the initiation of localized corrosion is often mentioned [29]. By controlling the redox potential of Fe^{2+}/Fe^{3+} and/or Mn^{2+}/Mn^{4+}, these bacteria may polarize the metal surface at a potential at which Fe^{3+} and/or Mn^{4+} may exist. Together with the accumulation of chloride ion (due to the necessity of preserving electroneutrality), this leads to the formation of $FeCl_3$ and $MnCl_4$ solutions that are aggressive to stainless steels. It is well known that both situations facilitate the breakdown of the passive film with crevice corrosion and/or pitting corrosion as a result.

Sulfate-reducing bacteria have also been reported to be responsible for pitting corrosion on stainless steels in aqueous environments. The mechanisms proposed are mostly related to iron and steel. However, a different mechanism has been proposed in which the role of thiosulfate in the microbial pitting of stainless steel has been emphasized [137]. The same authors have also demonstrated clearly that SRB-induced pitting corrosion of stainless steel is unlikely to occur in a uniformly anaerobic SRB medium, whereas it will occur when the anaerobic sites are coupled to an oxygen cathode [136].

This discussion is related almost solely to alloys with a relatively low molybdenum content, but the high molybdenum alloy stainless steels may also be susceptible to MIC. 904L, AL-6X, and 254 SMO were attacked by bacteria in pure cultures of *Desulfovibrio desulfuricans* and *Hyphomicrobium indicum*. The corrosion attack seems to be localized at the grain boundaries [108]. However, MIC on highly alloyed stainless steels has never clearly been reported in natural environments.

Besides the reports of MIC described above that are mainly related to water with relatively low salt content such as fresh water, an increase in the corrosion potential has also been reported for stainless steels exposed to natural seawater. The ennoblement of the corrosion potential has been observed for various stainless steel compositions (i.e., austenitic, ferritic, duplex, and superaustenitic stainless steels) exposed in natural seawater with different salinities and at different temperatures

Copyright © 2002 Marcel Dekker, Inc.

[3,28,30,61,62,82]. It is well known that in a given steel/environment system, localized corrosion occurs on stainless steel when the corrosion potential becomes greater than the pitting potential. Hence, the result of the potential ennoblement is that there is a higher probability of localized corrosion of stainless steel in a natural environment than in artificial seawater. This effect has been connected with the presence of a biofilm on the metal surface as shown in Figure 9. The corrosion potential of 21Cr-3Mo steel increases as a function of time in natural seawater to a value of about 400 mV/ECS, whereas it remains unchanged in sterilized seawater. When a specific inhibitor of respiratory activity (sodium azide) is added to both natural and sterilized seawater, a rapid decrease in the corrosion potential is observed in the case of natural seawater but it remains unchanged in sterile seawater [109]. The increase of the corrosion potential on stainless steel has been correlated with an increase of the rate of the cathodic reaction, e.g., the reduction of oxygen. This is shown in Figure 10. During the development of the biofilm at the stainless steel surface, an important depolarization of the oxygen reduction reaction occurs. This will lead to a higher rate of propagation of localized corrosion on stainless steel. Hence the effect of the biofilm settlement on stainless steel may be summarized as follows:

1. The corrosion potential of stainless steel increases in the noble direction, which increase the probability of localized corrosion.
2. A higher corrosion propagation rate is observed once localized corrosion develops.
3. Higher galvanic currents between stainless steel coupled to less noble materials are measured.

The study of the mechanisms of the ennoblement of stainless steel is complex, as seawater constitutes an environment in which numerous parameters can act.

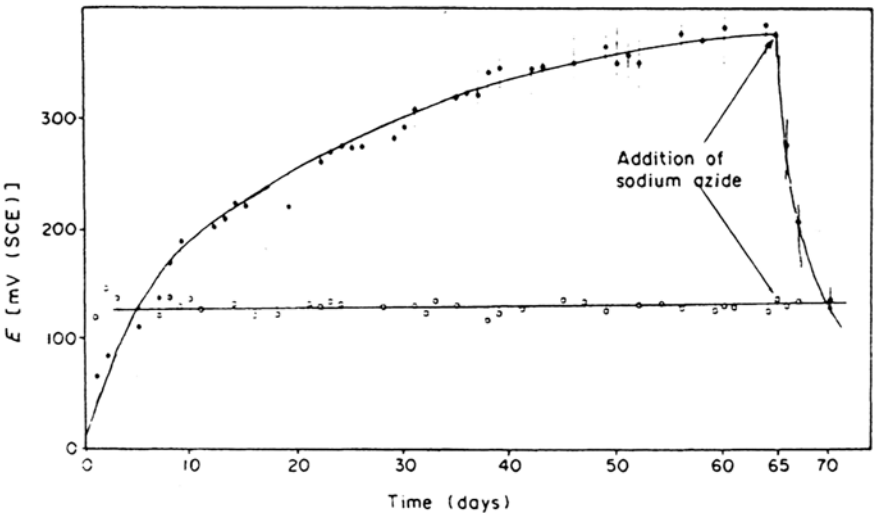


Figure 9 Corrosion potential as a function of exposure time for 21Cr-3Mo steel in natural seawater (black circles) and in artificial seawater (white squares). Time of addition of sodium azide is indicated by arrows. (From Ref. 109.)

Copyright © 2002 Marcel Dekker, Inc.

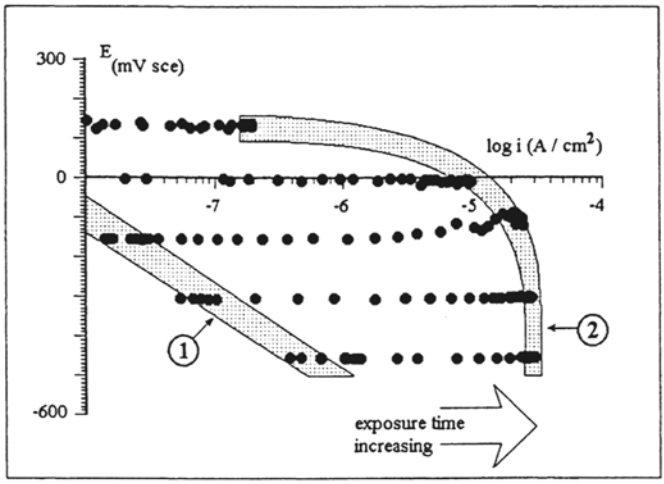


Figure 10 Oxygen reduction current density on stainless steel exposed to natural seawater and continuously polarized at fixed cathodic potentials. The envelopes of curves 1 and 2 correspond to the set of data on clean and already fouled stainless steel surfaces, respectively [83].

A literature review of the subject has been published [16]. It has been shown that the potential ennoblement in the presence of biofilms is probably due to an enhancement of the cathodic reduction of oxygen by (a) a decrease in pH at the metal-biofilm interface, (b) the formation of macrocyclic organometallic catalysts, such as porphyrins and phtalcyanins, (c) bacterially produced enzymatic catalysis, or (d) the production of hydrogen peroxide within the biofilm or ie. the catalyse of the oxygen reduction by manganese. More recent literature on the subject seems to confirm the role of enzymes in the depolarization of the oxygen reduction reaction on stainless steel [1,32]. A possible mechanism in which the potential ennoblement results from enzymatic competition between the production of hydrogen peroxide and acids by oxidases and the enzymatic consumption of these two chemicals has been proposed. This is schematically shown in Figure 11. Based on a large amount of biofilm growth on stainless steel at different European locations, it has been shown that enzymes entrapped in the EPS matrix of the biofilm could be responsible for the ennoblement of the corrosion potential on stainless steel [110]. Finally it should be noted that potential ennoblement of stainless steel has also been reported for stainless steel exposed to river water [49]. The mechanisms are, however, similar to that of seawater.

According to a literature review, there is no reported case of MIC on titanium [72].

Mechanisms of Microbially Induced Corrosion on Aluminum and Aluminum Alloys

Case histories of MIC on aluminum and aluminum alloys have been mainly reported for aircraft fuel storage tanks and heat exchanger tubes using water with different salinities. In all cases, pitting corrosion occurred.

Even though these cases are not as well documented as MIC on iron and steel, the possible mechanisms and microorganisms involved have been given for the

Copyright © 2002 Marcel Dekker, Inc.

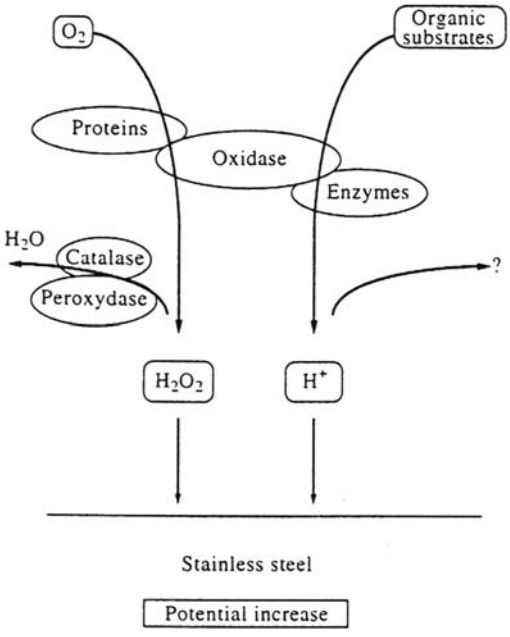


Figure 11 Hypothetical mechanism of the stainless steel ennoblement in natural seawater [32].

microbial contamination of aircraft aluminum fuel tanks [17,52]. Some of the most predominant bacteria and fungi are *Pseudomonas aeruginosa*, *Aerobacter aerogenes*, *Desulfovibrio*, and *Cladosporium* species. The corrosion occurs mainly in the water phase of the fuel-water mixture at the bottom of the tanks and at the fuel-water interface. The mechanisms involved are the same as those already given for iron and steel: (a) the production of corrosive metabolites by bacteria and fungi (organic acids and hydrogen sulfide), (b) the creation of differential aeration cells, (c) the transformation of nitrate (corrosion inhibitor for aluminum) to nitrite, and (d) extracellular activity resulting in the removal of major or minor metallic atoms from the basic structure of the alloy [92].

Mechanisms of Microbially Induced Corrosion on Copper and Copper Alloys

As in the case of aluminum and aluminum alloys, the MIC of copper and its alloys is not very well documented. This is probably due to the general belief that copper is toxic to microorganisms, which is not, however, the case for all microorganisms. As an example, bacteria of the genus *Thiobacillus* may tolerate copper concentrations up to 6%.

Case histories of MIC on copper and its alloys have been reported for piping systems and heat exchangers. Whereas heat transfer problems are observed with growing biofilms, the corrosion increases after the death of the microorganisms within the biofilm. This is believed to be due to the production of ammonia and carbon dioxide upon the death of cells that may result in pitting corrosion and/or stress corrosion cracking for copper and its alloys [72,92].

Copyright © 2002 Marcel Dekker, Inc.

The production of hydrogen sulfide by sulfate-reducing bacteria is also believed to lead to pitting corrosion and stress corrosion cracking on copper and copper alloys. In this case the corrosion is due to the formation of a thick nonadherent layer of chalcocite (Cu_2S) or covellite (CuS_{1-x}). Pitting corrosion may occur where the copper sulfide film has been removed, with the cathodic reaction taking place on the intact copper sulfide film [79].

Microbially induced pitting corrosion has also been observed in isolated locations in Europe, the United States, Australia, and New Zealand in potable water reticulation systems plumbed by copper [131,138]. This results in a contamination of the water such that the water is in breach of the maximum copper levels permitted by the U.S. EPA lead-copper rule (i.e., 1.3 ppm) [126]. Generally a biofilm is observed under a black deposit of copper (II) oxide and basic copper salts. Although the link between the pitting corrosion of copper and the microbial activity has been clearly established, the exact mechanism by which microorganisms increase the probability of initiation of pitting corrosion on copper is not known at the present time. However, it has been suggested that the role of the biofilm could be to oxidize copper (I) oxide to copper (II) oxide [15]. Finally it should be noted that an increase in the bicarbonate level of the water as well as a change in the cholride/sulfate ratio with increasing chloride content yielded a decrease in the initiation and propagation of pitting corrosion copper, respectively [131].

Other Construction Materials

Mineral Materials

Concrete is a mixture of a coarse-grained aggregate, hydraulic binding agents (cement, gypsum, lime, asphalt, sulfur, and resin), and water (except in the case of sulfur and resin, where water is not needed). For a limited period after preparation, the mixture can be molded into different shapes until hardening occurs as a result of chemical reactions between the components.

Ceramics are products made from fired clay–containing masses such as kaolin. The products are distinguished by the grain size of the clay and additives used and the firing temperature.

Glass is a transparent, sometimes colored, inorganic material, which is fragile and predominantly noncrystalline. It has no well-defined melting point, but with continuous heating it changes from being viscous to a soft and finally thin fluid state (i.e., an undercooled melt without cyrstallization).

Natural stone originates from rocks obtained from quarries in natural deposits. Rocks are defined as natural, solid formations of the earth's crust. They consist of a mixture of minerals or a single mineral and may contain organic residues.

Characteristics are the composition of primary (main), secondary, and auxiliary minerals, the structure, and the stratification. Three main groups need to be distinguished. Magmatic rocks are molten masses in the earth's crust (basalt, granite, etc.). Sedimentary rocks contain grains (often quartz) held together by a binding material (often calcareous or siliceous, such as gypsum, limestone, sandstone, schist). Metamorphic rocks are formed by transformation from magmatic or sedimentary types by heat and pressure (quartzite, marble, crystalline schist).

Copyright © 2002 Marcel Dekker, Inc.

All these materials are characterized as nonmetallic mineral materials. A biogenic attack can be caused by almost all microorganisms and by the mechanisms described above [7,25,34,68,71,80,85,86,90,91,97–100]. Only the action of exoenzymes, emulsifying agents, and organic solvents seems to be negligible for these materials. However, if mixtures of mineral materials with organic polymers are used to improve the properties, as in resin-modified mortars or in resin- or sulfur-bound concrete, the latter mechanisms may contribute to some extent.

Organic Polymers of Natural and Synthetic Origin

To the group of construction materials [54] belong, besides stone, those that have been used since humans began construction work. *Wood* is the oldest known construction material. Because of its unique characteristics, it is still in use today. The main components of wood are cellulose, polyoses (hemicelluloses), and lignin. The proportions are 40–50%, 15–35%, and 25–35%, respectively. Extractable compounds such as terpenes, waxes, or tannins may account for 1–3% and mineral compounds for 0.1–0.5%. The tensile strength of wood is determined by the cellulose cell structure. The cellulose molecule contains from 10,000 up to 14,000 β-(1,4)-glycosidically bound glucose units and represents the valuable part of wood for further products such as paper, cardboard, foils, films, and fibers.

Polyoses are also polysaccharides, but with lateral chains and ramifications. Between 50 and 200 saccharide molecules are polymerized. Galactoglucomannan or 4-*O*-methylglucuronoxylan is the main constituent. The polyoses connect the polysaccharides with the lignin in the cell wall. They determine the swelling and shrinkage of wood.

Lignin, either guaiacylpropane solely or combined with syringylpropane, is a complex molecule responsible for the pressure resistance of wood. The extractable substances such as terpenes provide the resistance against degrading microorganisms, e.g., bacteria and/or fungi. From these two groups and lichens, wood-degrading microorganisms originate. The main action is due to exoenzymes degrading the highly polymerized substances into water-soluble monomers or dimers. Similar mechanisms are involved in the degradation of wood-based materials such as laminated timber, blockboard, plywood, chipboard, and fiberboard. Plywood and chipboard may be especially endangered by biogenic attack because the binders used for these materials may increase their susceptibility. Binders may be urea-formaldehyde resins, phenol-formaldehyde resins, cresol-formaldehyde resins, isocyanates, etc., which may serve as a nitrogen source.

Besides wood, construction materials are made from *plastics*. These are materials consisting mainly of macromolecular organic compounds obtained synthetically or by modification of natural products. On application of heat and pressure, synthetics melt and become formable. Three main groups of synthetic polymers may be distinguished.

The term *polycondensates* covers phenolic, urea, thiourea, melamine, unsaturated polyester, alkydic, and allyl resins as well as silicones, polyimides, and polybenzimidazoles in the group of duroplasts. To the category of thermoplasts belong polyamides, polycarbonates, polyesters, polyphenylene oxides, polysulfones, and polyvinyl acetals.

Polymerizates are generally thermoplasts (polyethylenes, polypropylenes, poly-1-butenes, poly-4-methyl-1-penteneionomers, polyvinyl chlorides, polyvinylidene

Copyright © 2002 Marcel Dekker, Inc.

chlorides, polymethyl methacrylates, polyacrylonitriles, polystyrenes, polyacetals, fluorosynthetics, polyvinyl alcohols, polyvinyl acetates, and poly-*p*-xylylenes).

Polyadducts include duroplasts such as epoxidic resins and cross-linked polyurethanes as well as thermoplasts such as linear polyurethanes and chlorinated polyethers.

Although natural compounds are believed to be degradable by microorganisms in general—microbiological omnipotence—this does not always apply to synthetic polymers. These substances belong at least partially to the xenobiotica, which are known to be resistant to biological attack. For a few synthetic resins, experience of biodegradability has been available for nearly a century. Perspex has been demonstrated to be biologically not degradable. The same holds for nonflexible PVC. The main groups of resins may be characterized with regard to their biodegradability as follows. *Polyurethanes* with molecular weights of 10,000 and above are generally believed to be easily biodegradable. However, introducing substituents into the molecule may modify this. *Polyethylenes* with molecular weights of 1500 to 7000 range from resistant to easily biodegradable. *Polypropylenes* (MW 25,000 to 500,000) also vary from resistant to easily biodegradable. *Polymethyl methacrylates* (MW 500,000 to 1,000,000) and *polyamides* (MW 10,000 to 100,000) are comparable to those already mentioned. *Polystyrenes* (MW 200,000 to 300,000) are generally believed to be resistant to biological attack. The same holds for *polyvinyl chlorides* (MW 30,000 to 520,000) and *polytetrafluoroethylenes* (MW 500,000 to 5,000,000).

Besides the basic polymers, the final products often contain a variety of additives to adapt a resin to the intended purpose. This includes softeners (may make up to 60% of the final product), stabilizers, antioxidants (0.01–2%), antistatics, light-protecting agents (0.1–1%), optical brighteners, anti-ignition agents (up to 30%), microbicides (0.3–5%), lubricating agents, filling agents (up to 30%), accelerators, and pigments (0.02–5%).

It is not possible in the available space to mention all the compounds used. It is important that the majority of these additives are organic compounds, which are often easily biodegradable. As a consequence, a synthetic polymeric material may not be biodegradable with respect to the polymeric backbone, the synthetic polymer, but it becomes biodegradable because of the additives used. A result may be an embrittlement of the material (e.g., flexible PVC after being used several times). Even if a synthetic material is not attacked structurally, depending on the use, microbial growth may cause deterioration associated with, e.g. aesthetically intolerable color changes. A variety of microorganisms produce pigments (mainly black, some also blue or red) that may diffuse into the resin, causing a change in appearance.

Rubber, of either natural or synthetic origin, also contains because of its method of production many biodegradable compounds. It is used for purposes in which it needs to maintain its elasticity for a long time. Generally, synthetic rubbers are more stable than natural ones. In any case, rubbers may be attacked by microorganisms.

COUNTERMEASURES

A large number of approaches may be used to prevent or minimize the microbiological degradation of construction materials. The choice of the proper

Copyright © 2002 Marcel Dekker, Inc.

approach depends on many factors, such as the nature of the environment in which MIC occurred (e.g., soil, cooling water, seawater), the type of microorganisms involved, and the nature of the material. In practice, several approaches are often used in order to increase their efficiency. Many reviews on this subject are available in the literature [37,78,111,122,123]. Thus, the different approaches are discussed here only briefly. In any case, it is important to note that in the case of MIC the affected structure should not be cleaned prior to analysis in order to be able to trace the origin of the problem.

Changing or Modifying the Material

The choice of a material that is not susceptible or less susceptible to bacterial degradation may be one solution. However, this is often not possible for economic reasons.

Modifying the Environment or Process Parameters

The environment can be modified through, for instance, avoidance of anaerobic zones or modification of the pH in order to prevent acid accumulation. A good example of this is in the use of sand, gravel, or chalk as a nonaggressive backfill around buried steel pipes. This provides drainage and consequently better aeration of the soil. Chalk also provides an alkaline environment that may prevent acid accumulation. Similarly, stagnant conditions should be avoided in water systems. The process parameters may also be changed. For example, an increase in water velocity in heat exchanger tubes leads to partial detachment of biofilm. However, it is not always possible to change the process parameters. Besides, one must be careful not to induce other corrosion problems. For instance, a high water velocity may cause erosion-corrosion on some metals and alloys.

Organic Coatings

Organic coatings are widely used for the protection of steel in environments such as buried pipes, exteriors of buildings, and marine structures. However, all paint coatings are more or less biodegradable (see plastic materials). Besides, care must be taken with the surface preparation before painting and application of organic coatings in order to avoid voids or pores, where microorganisms may grow with highly localized corrosion as a result.

Cathodic Protection

Cathodic protection is widely used in the case of buried steel pipes and marine structures. As a rule, in order to control the anaerobic corrosion of iron by SRB, the potential of the structure is depressed to at least –1 V versus $Cu/CuSO_4$ instead of –0.85 V versus $Cu/CuSO_4$, which is usually recommended in the absence of SRB [125]. Cathodic protection is often used in combination with organic coatings because the presence of the organic coating diminishes the need for protection current by several decades compared with that of the unpainted metals. In addition, the cathodic protection will be efficient at defects in the organic coating.

Copyright © 2002 Marcel Dekker, Inc.

Biocides

Biocides are commonly used for many industrial applications such as industrial water systems. Biocides may be divided into two categories: (a) oxidizing agents such as chlorine, ozone, and chlorine dioxide and (b) nonoxidizing agents such as bisthiocyanate, isothiazolines, acrolein, dodecylguanidine hydrochloride, formaldehyde, glutaraldehyde, chlorophenols, and quaternary ammonium salts.

However, bacteria may adapt to biocides in different ways, such as the production of enzymes, changes in the internal structure of the cell, or changes in the composition of the cell wall. In order to minimize this problem, several biocides are generally used alternatively in practice. Furthermore, although all biocides are efficient on the planktonic population (i.e., microorganisms in the water phase), few are efficient in the case of microorganisms in a biofilm, so that an increase in the dosage up to 100 times is needed [129]. Besides, the use of biocides is more and more limited by environmental legislation due to their toxicity to higher organisms.

Microbiological Methods

As already mentioned, bacterial life depends on many factors. A variation in, for instance, pH, oxygen concentration, temperature, or light conditions may be used to control microbial growth. However, care must be taken to ensure that changes in these parameters do not induce changes in the bacterial population that result in the growth of other microorganisms that may cause MIC. Besides, a change in these parameters may increase the electrochemical corrosion of metals and alloys. A decrease or increase in pH, for instance, may cause corrosion on copper and aluminum alloys.

Physical Methods

Physical methods such as filtration of the water, mechanical removal of the biofilm, or the use of ultraviolet (UV) radiation can be used for some specific applications. For instance, UV light sterilization has been used in potable water systems and cooling water systems instead of chlorination, which is otherwise commonly used. However, in general, these methods are less efficient and more costly than the use of chemicals [120,121].

Simulation of the Biogenic Attack

Besides the previously mentioned countermeasures, a technique that has gained in importance reproduces the biogenic attack under conditions that are optimized for the deterioration-causing agents, the microorganisms. By simulation of the biogenic attack on materials, a quick-motion effect can be produced that allows materials to be tested for their suitability for given applications. The simulation may even be used for the development of resistant materials [97]. This has been shown in the case of biogenic sulfuric acid attack on cement-bound concrete, mortar, and bricks; on resin- or sulfur-bound concrete; on pipeline linings made of synthetics; and in the case of biogenic nitric acid attack on cement-bound concrete and natural stone. It must be emphasized that simulation of biogenic attack on materials requires profound

Copyright © 2002 Marcel Dekker, Inc.

knowledge of *all* the processes and participating microorganisms. If these are known, the situation may be remodeled under conditions optimized for the microorganisms resulting in a reduced time span for the corrosion to become detectable. The problem of biogenic sulfuric acid corrosion in sewage pipelines has been described extensively [6,7,38,80]. A countermeasure was a simulation that allowed remodeling of the microbially caused process within a period of 1 instead of 8 years. Corrosion is caused in this system by sulfuric acid–excreting thiobacilli, which thrive because of hydrogen sulfide emissions from the sewage. H_2S was increased if sewage became anaerobic and was stripped later on. Thiobacilli need water, grow optimally at 30°C (instead of 16°C in the Hamburg sewage system), and need oxygen. These conditions were created in a simulation apparatus constructed for materials testing. The results of the experiments confirmed that thiobacilli were the corrosion-causing agents [96]. However, differences were noted between the results of chemical testing (resistance of the same materials against pure sulfuric acid) and the results of these biotests. The chemical test was not able to detect significant differences in the resistance of the materials toward the acid attack (all materials corroded more or less similarly), whereas the biotest revealed severe differences. Some concretes were only slightly attacked (1 % loss of substance after 1 year of simulation) whereas others lost 10% of their substance [97]. This finding demonstrates that microbial interactions between material and microorganism are of the utmost importance in the determination of resistance to a biogenic attack. The biotest cannot be replaced by chemical and/or physical tests. Because of these test results, the simulation apparatus is now used (internationally) for the development of new materials with increased resistance to biogenic attack.

DIAGNOSTIC OF MIC

The diagnosis of MIC is a severe problem. In most cases, damage seems to be explainable by the well-known and from the practical work familiar mechanisms involving chemistry, physics, and materials sciences. This is a result of the fact that engineers and technicians were never introduced, while studying, to the possibility of microorganisms being a causative agent in corrosion. Thus, the often-observed sediments, deposits, slimy layers, etc. tend to be neglected, although they indicate at least the presence of microorganisms. Whereas it is well known that under natural conditions microorganisms are ubiquitous, this fact seems to be neglected in the case of technical environments.

However, life may also be possible in the latter case if several requirements are fulfilled. Microorganisms, like all living beings need water. However, they are more versatile than other organisms, because their growth limit is the water activity value of $a_w = 0.6$ (–680 bar osmotic pressure). Active microorganisms have been detected in the temperature range from –10°C to 114°C; in the pH range from 0 to 12; at pressures above 1000 bar (deap sea vents); with and without oxygen, hydrogen sulfide, carcinogenic and mutagenic compounds; and even under conditions of high radiation (storage basins of nuclear power plants). Thus, if these requirements are met, participation of microbes in cases of corrosion should be anticipated.

Especially when the following additional markers are found, MIC damage becomes likely:

Copyright © 2002 Marcel Dekker, Inc.

1. The occurrence of a slimy layer on the surface of a material. This can be tested with the finger. Besides, removal of some slime and burning with a lighter might cause the smell of burned hair = proteins.
2. The smell of mud or even rotten eggs (H_2S) indicates MIC.
3. Coloration or discoloration of a material is suspicious.
4. A high water content besides a soft nature of deposits is often indicative of MIC.
5. Finally, crevice or pitting corrosion is often the result of microbial activity.

In general, almost all materials are susceptible to MIC problems: metals such as mild and stainless steels, alloys, aluminum, copper; mineral materials such as concrete, stone, brick, marble, sandstone, ceramics, glass; natural organic materials such as wood, paper, leather, textiles, starch, polymers (lipids); synthetic organic materials such as plastics, paints, coatings, glues, polymers; and hydrocarbons such as mineral oils, waxes, tar, lubricants, cutting emulsions, fats, and greases. Only in the groups of plastics are there several compounds that are not biodegradable. Microorganisms do not have the enzymes necessary for a depolymerization. Besides, some nondegradable compounds resulting from chemical synthesis called xenobiotics exist (often pesticides, etc.).

Consequently, MIC may play an important role in many cases of (bio)deterioration/corrosion. For a thorough diagnosis it is crucial that the preceding points are checked and that experts are consulted. The site of corrosion should be left untouched and under the same conditions as before the detection of the failure. Cleaning should be avoided in any case. Good documentation is needed, meaning photographs, video, data from probes, materials, history, etc. If the diagnosis is not done properly, a good chance exists that there will soon be another failure at the same (or a neighboring) site.

CONCLUDING REMARKS

Microbially induced corrosion is a ubiquitous phenomenon, but the participation of microorganisms and their importance are not fully realized. This is often the result of a lack of knowledge, because courses of study in the technical disciplines do not impart this knowledge to students [53]. Another reason may be the fact that, in contrast to a case of corrosion in which no biological factors are involved, in a case of MIC only an interdisciplinary approach will give the knowledge necessary to understand the mechanisms, However, this is inevitable because the microbiology and the physicochemical processes causing MIC are usually too complicated to be solved by simple test methods [23,85,86,140]. Most processes involved belong to naturally occurring terrestrial cycles of matter. These cycles are the reason why life can persist. Thus, we shall only be able to modify and slow down these processes, never to inhibit them totally. Profound knowledge of all participating processes will make it possible to enhance the life span of materials considerably [135].

REFERENCES

1. H. Amaya and H. Miyuki, Development of accelerated evaluation method for microbially influenced corrosion resistance of stainless steel. *Corros. Eng. 44*:123–133 (1995).

Copyright © 2002 Marcel Dekker, Inc.

2. R. M. Atlas, Microbial degradation of petroleum hydrocarbons: an environmental perspective, *Microbiol. Rev. 45*:180–209 (1981).
3. J. P. Audouard, C. Compere, N. J. E. Dowling, D. Feron, A. Mollica, T. Rogne, V. Scotto, U. Steinsmo, C. Taxen, and D. Thierry, Effect of Marine Biofilms on Stainless Steel: Results from a European Exposure Program. EFC Publication No 19, The Institute of Materials, UK, 1996.
4. M. Baumgärtner, A. Remde, E. Bock, and K. Conrad, Release of nitric oxide from building stones into the atmosphere, *Atmos. Environ. 24B*:87–92 (1990).
5. S. G. Berk, R. Mitchell, R. J. Bobbie, J. S. Nickels, and D. C. White, Microfouling on metal surfaces exposed to seawater, *Int. Biodeterioration Bull. 17*:29–37 (1981).
6. E. Bock and W. Sand, Applied electron microscopy on the biogenic destruction of concrete and blocks—use of the transmission electron microscope for identification of mineral acid producing bacteria, *Proceedings of the Eighth International Conference on Cement Microscopy* (J. Bayles, G. R. Gouda, A. Nisperos, eds.), International Cement Microscopy Association, Duncanville, TX, 1986, pp. 285–302.
7. E. Bock and W. Sand, A review: the microbiology of masonry biodeterioration, *J. Appl. Bacteriol. 74*:503–514 (1993).
8. G. H. Booth, Bacterial corrosion, *Discovery 6*:524–527 (1964).
9. G. H. Booth and A. K. Tiller, Cathodic characteristics of mild steel by sulphate reducing bacteria—an alternative mechanism, *Corros. Sci. 8*:583–600 (1968).
10. G. H. Booth, L. Elford, and D. S. Wakerley, Corrosion of mild steel by sulphate reducing bacteria: an alternative mechanism, *Br. Corros. J. 3*:242–245 (1968).
11. S. W. Borenstein, Microbiologically influence corrosion of austenitic steel weldments, *Mater. Perform. 1*:52–54 (1991).
12. L. R. Brown and G. S. Pabst, *Proceedings 3rd International Symposium on Biodegradation* (J. M. Sharpley and A. M. Kaplan, eds.), Applied Science Pub., Barking, England, 1976, pp. 875–882.
13. J. P. Busalmen, S. R. de Sánchez, and D. J. Schiffrin, Ellipsometric measurement of bacterial films at metal-electrolyte interfaces. *Appl. Environ. Microbiol. 64*:3690–3697 (1998).
14. H. J. Busscher and A. H. Weerkamp, Specific and nonspecific interactions in bacterial adhesion to solid substrata, *FEMS Microbiol. Rev. 46*:165–173 (1987).
15. A. Chamberlain and P. Angell, Influences of microorganisms on pitting of copper tube, *Proceedings Microbially Influenced Corrosion and Biodeterioration* (N. J. Dowling, M. W. Mittleman, and J. C. Danko, eds), University of Tennessee, Knoxville, 1990, pp. 3/65–3/69.
16. P. Chandrasekaran and S. C. Dexter, Mechanism of potential ennoblement on passive metals by seawater biofilms, *CORROSION 93*, New Orleans, paper No. 493, NACE, 1993.
17. A. V. Churchill, Microbial fuel tank corrosion, *Mater. Protect. 6*:19–23 (1963).
18. A R. Colmer and M. E. Hinkle, The role of microorganisms in acid mine drainage; a preliminary report, *Science 106*:253 (1947).
19. J. A. Costello, Cathodic depolarizaiton by sulphate reducing bacteria, *S. Afr. J. Sci. 70*:202–204 (1974).
20. J. W. Costerton and E. S. Lashen, Influence of biofilm on efficacy of biocides on corrosion-causing bacteria, *Mater. Perform. 23*:34–37 (1984).
21. J. W. Costerton and G. G. Geesey, The microbial ecology of surface colonization and of consequent corrosion, *Proceedings Biologically Induced Corrosion* (S. C. Dexter, ed.), NACE-8, Houston, 1986, pp. 223–232.
22. G. Cragnolino and O. H. Tuovinen, The role of sulphate reducing and sulphur oxidizing bacteria in the localized corrosion of iron-base alloys—a review, *Int. Biodeterioration 20*:9–26 (1984).

Copyright © 2002 Marcel Dekker, Inc.

23. J. L. Crolet, From biology and corrosion to biocorrosion, *Oceanol. Acta 15*(1):87–94 (1992).
24. J. L. Crolet, S. Daumas, and M. Magot, pH regulation by sulphate-reducing bacteria, *CORROSION 93,* New Orleans, paper 303, NACE, 1993.
25. W. Dannecker and K. Selke, Simultanbestimmung organischer und anorganischer Anionen aus verwitterten Natursteinoberflächen mittels Gradienten-Ionen-Chromatographie, *Fresenius Z. Anal. Chem. 335*:966–970 (1989).
26. S. R. de Sánchez and D. J. Schiffrin, Bacterial chemo-attractant properties of metal ions from dissolving electrode surfaces, *J. Electroanal. Chem. 403*:39–45 (1996).
27. S. C. Dexter, Localized corrosion, *Metals Handbook*, 13, 9th ed., ASM International, 1987, 104–122.
28. S. C. Dexter and G. Y. Gao, Effect of seawater biofilms on corrosion potential and oxygen reduction of stainless steel, *Corrosion 44*:717–723 (1988).
29. W. H. Dickinson and Z. Lewandowski, Manganese biofouling and the corrosion behavior of stainless steel. *Biofouling 10*(1–3):79–93 (1996).
30. W. H. Dickinson and Z. Lewandowski, Electrochemical concepts and techniques in the study of stainless steel ennoblement. *Biodegradaiion 9*:11–21 (1998).
31. W. Dilling and H. Cypionka, Aerobic respiration in sulfate-reducing bacteria, *FEMS Microbiol. Lett. 71*:123–128 (1990).
32. I. Dupont, D. Feron, and G. Novel, Effect of glucose oxidase activity on corrosion potenital of stainless steels in seawater, *Int. Biodeterioration Biodegradation 41*:13–18 (1998).
33. D. J. Duquette and R. E. Ricker, Electrochemical aspects of microbiologically induced corrosion, *Proceedings Biologically Induced Corrosion* (S. C. Dexter, ed.), NACE-8, Houston, 1986, pp. 121–130.
34. F. E. W. Eckhardt, Solubilization, transport, and deposition of mineral cations by microorganisms—efficient rock weathering agents, *The Chemistry of Weathering* (J. I. Drever, ed.), Reidel, Dordrecht, The Netherlands, 1985, pp. 161–173.
35. R. J. G. Edyvean, C. J. Thomas, and I. M. Austen, The use of biologically active environments for testing corrosion fatigue of offshore structural steel, *Proceedings Biologically Induced Corrosion* (S. C. Dexter, ed.). NACE-8, Houston, 1986, pp. 254–267.
36. H. L. Ehrlich,. *Geomicrobiology,* Marcel Dekker, New York, 1990, pp. 1–646.
37. K. Eistrat and A. Thoren, Microbiological corrosion—a literature survey, Swedish Corrosion Institute Report 1980:9, 1–85.
38. T. Emmel, E. Brill, W., Sand, and E. Bock, Screening for biocides to inhibit biogenic sulphuric acid corrosion in sewage pipelines, *Proceedings Biodeterioration 7* (D. R. Houghton, R. N. Smith, and H. O. W. Eggins, eds.), Elsevier Applied Science, London, 1988, pp. 118–122.
39. W. Fisher, H. H. Paradies, I. Hanßel, and D. Wagner, Copper deterioration in a water distribution system of a county hospital in Germany caused by microbial induced corrosion, *Proceedings Microbially Induced Corrosion and Biodeterioration* (N. J. Dowling, M. W. Mittleman, and J. C. Danko, eds), University of Tennessee, Knoxville, 1990, pp. 8/47–8/48.
40. H.-C., Flemming and G. G. Geesey, eds. *Biofouling and Biocorrosion in Industrial Water Systems*, Springer, Berlin, 1991.
41. T. E. Ford, J. S. Maki, and R. Mitchell, The role of metalbinding bacterial exopolymers in corrosion processes, *CORROSION 87*, NACE, Washington, DC, 1987.
42. R. H. Gaines, *N. Eng. Ind. Chem. 2*:128 (1910).
43. J. H. Garrett, *The Action of Water on Lead*, H. K. Lewis, London, 1891.
44. C. C. Gaylarde and J. M. Johnston,. The effect of *Vibrio anquillarum* on the anaerobic corrosion of mild Steel by *Desulfovibrio vulgaris*, *Int. Biodeterioration 18*:111–116 (1982).

Copyright © 2002 Marcel Dekker, Inc.

45. C. C. Gaylarde and J. M. Johnston, Anaerobic metal corrosion in cultures of bacteria from estuarine sediments, *Proceedings Biologically Influenced Corrosion* (S. C. Dexter, ed.), NACE-8, Houston, 1986, pp. 137–143.
46. C. C. Gaylarde and H. A. Videla, Localized corrosion induced by a marine vibrio, *Int. Biodeterioration, 23*:91–104 (1987).
47. T. Gehrke, M. Drews, and W. Sand, Microbiological examinations of low-water corrosion on steel piling structures, *DECHEMA-Monographie 133, Biodeterioration* (W. Sand, ed.), VCH, Weinheim, 1996, pp. 101–106.
48. P. S. Guiamet, S. G. Gómez de Saravia, and H. A. Videla, An innovativ method for preventing biocorrosion through microbial adhesion inhibition. *Int. Biodeterioration Biodegradation 43*:31–35 (1999).
49. P. Gümpel and R. Kreikenbohm, Betrachtungen über den Zusammenhang zwischen bakteriellem Wachstum und der mikrobiell induzierten Potential verschiebung bei nichtrostenden Stählen. *Mater. Corros. 50*:219–226 (1999).
50. W. A. Hamilton, Sulphate-reducing bacteria and anaerobic corrosion, *Annu. Rev. Microbiol. 39*:195–217 (1985).
51. J. A. Hardy and J. L. Bown, The corrosion of mild steel by biogenic sulphide films exposed to air, *Corrosion 40*:650–654 (1984).
52. H. G. Hedrick, Microbiological corrosion of aluminum, *Mater. Protect, 1*:27–31 (1970).
53. E. Heitz, A. D. Mercer, W. Sand, and A. K. Tiller, *Microbiological Degradation of Material—and Methods of Protection,* European Federation of Corrosion Publications Number 9, The Institute of Materials, London, 1992, pp. 1–88.
54. E. Heitz, H.-C. Flemming, and W. Sand, *Microbially Influenced Corrosion of Materials*, Springer, Berlin, 1996.
55. E. C. Hill, J. L. Shennan, and R. J. Watkinson, eds., *Microbial Problems in the Offshore Oil Industry*, Institute of Petroleum. John Wiley, Chichester, Great Britain, 1987.
56. A. P. Hunt and J. D. Parry, The effect of substratum roughness and river flow rate on the development of a freshwater biofilm community, *Biofouling 12*:287–303 (1998).
57. W. P. Iverson, Direct evidence for the cathodic depolarization theory of bacterial corrosion, *Science 151*:986–988 (1966).
58. W. P. Iverson, Biological corrosion. *Advances in Corrosion Science and Technology* (M. G. Fontana and R. W. Staehle, eds.), Plenum, London, 1972, 2.
59. W. P. Iverson, Anaerobic corrosion mechanisms, *CORROSION 83*, Anaheim, CA, paper 243, NACE, 1983.
60. G. E. Jenneman, M. J. McInerney, and R. M. Knapp, Microbial penetration through nutrient saturated Berea sandstone, *Appl. Environ. Microbial. 50*:383–391 (1985).
61. R. Johnsen and E. Bardal, Cathodic properties of different stainless steels in natural sea water, *Corrosion 41*:296–301 (1985).
62. R. Johnsen and E. Bardal, The effect of microbiological slime layer on stainless steel in natural seawater, *CORROSION 86*, paper No 227, NACE, Houston, 1986.
63. D. A. Jones, *Principles and Prevention of Corrosion*, Macmillan, New York, 1991, pp. 1–568.
64. M. J. Kauffmann, Rôle des bacteries nitrifiantes dans l'alteration des pierres calcaires des monuments, *C. R. Acad. Sci. Paris. 234*:2395–2397 (1952).
65. R. A. King, J. D. A. Miller, and D. S. Wakerley, Corrosion of mild steel in cultures of sulphate reducing bacteria: effect of changing the soluble iron concentration during growth, *Br. Corros. J. 8*:89–93 (1973).
66. K.-O. Kirstein, W. Stiller, and E. Bock, Mikrobiologische Einfluße auf Betonkonstruktionen, *Beton-Stahlbetonbau 81*:202–204 (1986).
67. G. Kobrin, Corrosion by microbiological organisms in natural waters, *Mater. Performance 7*:38–43 (1976).

Copyright © 2002 Marcel Dekker, Inc.

68. W. E. Krumbein, Zur Frage der biologischen Verwitterung: Einfluβ der Mikroflora auf die Bausteinverwitterung und ihre Abhängigkeit von edaphischen Faktoren, *Z. All. Mikrobiol. 8*:107–117 (1968).
69. M. Kuehn, M. Hausner, H.-J. Bungartz, M. Wagner, P. A. Wilderer, and S. Wuertz, Automated confocal laser scanning microscopy and semiautomated image processing for analysis of biofilm. *Appl. Environ. Microbiol. 64*:4115–4127 (1998).
70. W. C. Lee and W. G. Characklis, Corrosion of mild steel under an anaerobic biofilm, *CORROSION 90,* Las Vegas, NV, NACE, 1990.
71. F. Lewis and E. May, Isolation and enumeration of autotrophic and heterotrophic bacteria from decayed stone, Proceedings Fifth International Congress on Deterioration and Conservation of Stone, Lausanne, Switzerland, 1985, pp. 633–642.
72. B. Little, M. McNeil, and F. Mansfeld, The impact of alloying elements on microbiologically influenced corrosion—a review, Proceedings 12th International Congress on Metal Corrosion, NACE, Houston, 1993, pp. 3680–3686.
73. D. R. Lovley, Dissimilatory Fe(III) and Mn(IV) reduction, *Microbiol. Rev. 55*:259–287 (1991).
74. D. R. Lovley, Microbial Fe (III) reduction in subsurface environments, *FEMS Microbiol. Rev. 20*:305–313 (1997).
75. M. Magot, L. Carreau, J. L. Cayol, B. Oliver, and J. L. Crolet, Sulphide-producing, not sulphate reducing anaerobic bacteria presumptively involved in bacterial corrosion, Proceedings 3rd European Workshop on Microbial Corrosion, Estoril, Portugal, 1994.
76. R. Mansch and E. Bock, Microbial deterioration of materials- simulation, case histories and countermeasures: testing of the resistance of ceremic materials, *Werkst. Korros. 45*:96–104 (1994).
77. F. Mansfeld, R. Tsai, B. Little, R. Ray, and P. Wagner, An electrochemical and surface analytical study of stainless steels and titanium exposed to natural seawater, *Corros. Sci 33*:445–456 (1990).
78. J. W. McCoy, *Microbiology of Cooling Waters*, Chemical Publishing Co., New York, 1980.
79. M. B. McNeil, J. M. Jones, and B. J. Little, Production of sulphide minerals by sulphate reducing bacteria during microbiologically influence corrosion of copper, *Corrosion 9*:674–677 (1991).
80. K. Milde, W. Sand, W. Wolff, and E. Bock, Thiobacilli of the corroded concrete walls of the Hamburg sewer system, *J. Gen. Microbiol. 129*:1327–1333 (1983).
81. J. D. A. Miller and R. A. King, Biodeterioration of metals, *Microbial Aspects of the Deterioration of Materials* (D. W. Lovelock and R. J. Gilbert, eds.), Academic Press, London, 1975, pp. 83–103.
82. A. Mollica and A. Trevis, Correlation between the formation of a primary film and the modification of the cathodic surface of stainless steel in seawater, Proceedings of 4th Int. Cong. Marine Corrosion and Fouling, Antibe, France, 1976, pp. 351–355.
83. A. Mollica, E. Traverso, and D. Thierry, On oxygen reduction depolarisation induced by biofilm growth on stainless steels in sea water, *Aspects of Microbially Induced Corrosion* (D. Thierry, ed.), University Press, Cambridge, UK, 1996.
84. L. H. G. Morton, ed. *Biodeterioration of Constructional Materials,* Biodeterioration Society Occastional Publiction No. 3, Publications Service, Lancashire Polytechnic, Great Britain, 1987, pp. 1–140.
85. N. N. Microorganisms in nuclear waste disposal. I. Multi-author review, *Experientia 46*:777–851 (1990).
86. N. N. Spécial corrosion, *Mater. Tech. 78*:1–76 (1990).
87. N. N. Microorganisms in nuclear waste disposal. II. Multi-author review, *Experientia 47*:507–640 (1991).

Copyright © 2002 Marcel Dekker, Inc.

88. I. P. Pankhania, A. N. Moosavi, and W. A. Hamilton, Utilization of cathodic hydrogen y *Desulfovibrio vulgaris* (Hildenborough), *J. Gen. Microbiol 132*:3357–3365 (1986).
89. C. D. Parker, The corrosion of concrete. I. The isolation of a species of bacterium associated with the corrosion of concrete exposed to atmospheres containing hydrogen sulphide, *Aust. J. Exp. Biol. Med. Sci. 23*:81–90 (1947).
90. K. Pedersen, Microbial life in deep granitic rock, *FEMS Microbiol. Rev. 20*:399–414 (1997).
91. J. Pochon, P. Tardieux, J. Kajudie, and M. Charpentier, Degradation des temples d'angkor et processus biologiques, *Ann. Inst. Pasteur. 98*:457–461 (1960).
92. D. H. Pope, D. J. Duquette, A. H. Johannes, and P. C. Wayner, Microbiologically influenced corrosion of industrial alloys, *Mater. Performance 4*:14–18 (1984).
93. D. T. Rickard, The microbiological formation of iron sulphides, Proceedings Contribution to Geology, Stockholm, Sweden, 1969, pp. 67–72.
94. F. L. Roe, Z. Lewandowski, and T. Funk, Simulating microbiologically influenced corrosion by depositing extracellular biopolymers on mild steel surfaces. *Corrosion 52*:744–752 (1996).
95. A. H. Rose, *Microbial Biodeterioration,* Academic Press, London, 1981, pp. 1–516.
96. W. Sand, Importance of hydrogen sulfide, thio-sulfate, and methylmercaptan for growth of thiobacilli during simulation of concrete corrosion, *Appl. Environ. Microbiol. 53*:1645–1648 (1987).
97. W. Sand, E. Bock, and D. C. White, Biotest system for rapid evaluation of concrete resistance to sulfur-oxidizing bacteria, *Mater. Performance 26*:14–17 (1987).
98. W. Sand, B. Ahlers, T. Krause-Kupsch, M. Meincke, E. Kreig, M. Diercks, F. Sameluck, and E. Bock, Mikroorganismen und ihre Bedeutung für die Zerstörung von mineralischen Baustoffen, *UWSF Z. Umweltchem. Ökotox. 3*:36–40 (1989).
99. W. Sand and E. Bock, Mikrobielle Zerstörung kerami-scher Werkstoffe, *Werkst. Korros. 41*:64–68 (1990).
100. W. Sand and E. Bock, Biodeterioration of ceramic materials by biogenic acids, *Int Biodeterior. 27*:175–183 (1991).
101. W. Sand Microbial mechanisms of deterioration—a general mechanistic overview, *Int. Biodeterioration Biodegradation 40*:183–190 (1998).
102. C. M. Santegoeds, T. G. Ferdelman, G. Muyzer, and D. de Beer, Sructural and functional dynamics of sulfate-reducing populations in bacterial biofilms. *Appl. Environ. Microbiol. 64*:3731–3739 (1998).
103. J. W. Santo Domingo, C. J. Berry, M. Summer, and C. B. Fliermans, Microbiology of spent nuclear fuel storage basins. *Curr. Microbiol. 37*:387–394 (1998).
104. E. Schaschl, Elemental sulphur as a corrodent in deaerated, neutral aqueous solutions, *Mater. Performance 7*:9–12 (1980).
105. A. Schippers, T. Rohwerder, and W. Sand, Intermediary sulfur compounds in pyrite oxidation: implications for bioleaching and biodepyritization of coal. *Appl. Microbiol. Biotechnol. 51* (in press).
106. G. Schmitt, Sophisticated electrochemical methods for MIC investigation and monitoring, *Mater. Corros. 48*:586–601 (1997).
107. A. W. Schröter and W. Sand,. Estimations on the degradability of ores and bacterial leaching activity using short-time microcalorimetric tests, *FEMS Microbiol. Rev. 11:* 79–86 (1993).
108. P. J. B. Scott, J. Goldie, and M. Davies, Ranking alloys for susceptibility to MIC-a preliminary report on high-Mo alloys, *Mater. Performance 1*:55–57 (1991).
109. V. Scotto, R. Di Cento, and R. Marcenaro, The influence of marine aerobic microbial films on stainless steel corrosion behaviour, *Corros. Sci. 25*:185–194 (1985).

Copyright © 2002 Marcel Dekker, Inc.

110. V. Scotto and M. E. Lai, The ennoblement of stainless steel in seawater: a likely explanation coming from the field. *Corros. Sci. 40*:1007–1018 (1998).
111. L. J. Seed, The significance of organisms in corrosion, *Corros. Rev. 9*:3–75 (1990).
112. J. M. Shively and A. A. Benson, Phospholipids of *Thiobacillus thiooxidans*, *J. Bact. 94*:1679–1683 (1967).
113. U. P. Sinha, J. H. Wolfram, and R. D. Rogers, (1990). Microbially influenced corrosion of stainless steels in nuclear power plants, *Proceedings Microbially Influenced Corrosion and Biodeterioration* (N. J. Dowling, M. W. Mittleman, and J. C. Danko, eds.), University of Tennessee, Knoxville, 1967, pp. 4/51–4/60.
114. R. Steudel and G. Holdt, Solubilization of elemental sulfur in water by cationic and anionic surfactants, *Angew. Chem. Int. Ed. Engl. 27*:1358–1359 (1988).
115. H. Stolp, *Microbial Ecology: Organisms, Habitats, Activities,* Cambridge University Press, Cambridge, Great Britain, 1988, pp. 1–308.
116. S. Stroes-Gascoyne and J. M. West, Microbial studies in the Canadian nuclear fuel waste management program. *FEMS Microbiol. Rev. 20*:573–590 (1997).
117. R. E. Tatnall, Case histories: bacterial induced corrosion, *Mater. Performance 8*:41–48 (1981).
118. R. E. Tatnall, Fundametals of bacterial induced corrosion, *Mater. Performance 9*:32–38 (1981).
119. J. Telegdi, Z. Keresztes, G. Pálinkás, E. Kalman, and W. Sand, Microbially influenced corrosion visualized by atomic force microscopy, *Appl. Phys. A66*:S639–S642 (1998).
120. D. Thierry, Microbial corrosion in a closed cooling water system: the role of *Nitrobacter,* Swedish Corrosion Institute, Stockholm. Internal report, 1987, pp. 1–4.
121. D. Thierry, Field observations of microbiologically induced corrosion in cooling water systems, *Mater. Performance 26*:35–41 (1987).
122. D. Thierry, Methods for combating microorganisms in cooling water systems—a literature review and market inventory, Swedish Corrosion Institute, Stockholm, report 1989:3, 1–23.
123. A. K. Tiller, Aspects of microbial corrosion, *Corrosion Processes* (R. N. Parkins, ed.), Applied Science, London, 1983, pp. 115–159.
124. A. K. Tiller, A review of the European research effort on microbial corrosion between 1950 and 1984, *Proceedings Biologically Induced Corrosion* (S. C. Dexter, ed.), NACE, Houston, 1986, pp. 8–29.
125. K. Tiller, Biocorrosion in civil engineering, *Proceedings Microbiology in Civil Engineering* (P. Howsam, ed.), Chapman & Hall, London, 1990, pp. 24–38.
126. United States Environmental Protection Agency, Control of lead and copper in drinking water, EPA/625/R-93/001, Office of research and development, Washington DC, 1983, p. 105.
127. F. P. van den Ende, J. Meier, and H. van Gemerden, Syntrophic growth of sulfate-reducing bacteria during oxygen limitation. *FEMS Microbiol. Ecol. 23*:65–80 (1997).
128. H. A. Videla, Sulphate reducing bacteria and anaerobic corrosion, *Corros. Rev. 9:* 103–141 (1990).
129. H. von Rège and W. Sand, Evaluation of biocide efficacy by microalorimetric determination of microbial activity in biofilms. *J. Microbiol. Methods 33*:227–235 (1998).
130. G. A. H. von Wolzogen Kühr and L. R. van der Vlugt, De graphiteering van gietijzer ais electrobiochemisch proces in anaerobe gronden, *Water 18*:147–165 (1934).
131. D. Wagner, M. Tietz, O. von Franqué, and W. R. Fischer, Remedial measures versus microbiologically influenced corrosion in copper potable water installations, *Proceedings 13th International Corrosion Congress,* Melbourne, paper 143, 1996.
132. M. Walsh and R. Mitchell, The role of microorganisms in the hydrogen embrittlement. *CORROSION 93,* New Orleans, paper 249, NACE, 1983.

Copyright © 2002 Marcel Dekker, Inc.

133. M. Walsh and R. Mitchell, Microbial influence on hydrogen uptake by metals, *Proceedings Biologically Induced Corrosion* (S. C. Dexter, ed.), NACE-8, Houston, 1986, pp. 201–208.
134. D. Walsh, J. Seagoe, and L. Williams, Microbiologically influenced corrosion of stainless steel weldments; attachment and film evolution, *CORROSION 92,* Nashville, paper 165, NACE, 1992.
135. O. Wanner, Modelling of biofilms. *Biofouling 10*(1–3):31–41 (1996).
136. B. J. Webster, R. J. Kelly, and R. C. Newman, The electrochemistry of SRB corrosion in austenitic stainless steel, *Proceedings Microbially Influenced Corrosion and Biodeterioration* (N. J. Dowling, M. W. Mittleman, and J. C. Danko, eds.), University of Tennessee, Knoxville, 1990, pp. 2/9–2/18.
137. B. J. Webster, R. J. Kelly, and R. C. Newman, SRB-induced localized corrosion of stainless steels, *CORROSION 91,* Cincinnati, OH, paper 106, NACE, 1991.
138. B. J. Webster, D. B. Wells, and P. J. Bremer, Potable water biofilms, copper corrosion and copper by-products release, *Proceedings 13th International Corrosion Congress, Melbourne,* 1996, paper 408.
139. D. C. White, A. A. Arrage, D. E. Nivens, R. J. Palmer, J. F. Rice, and G. S. Sayler, Biofilm ecology: on-line methods bring new insights into mic and microbias biofouling. *Biofouling 10*(1–3):3–16 (1996).
140. F. Widdel, Mikrobielle Korrosion, *Jahrbuch Biotechnologie,* Band 3 (P. Präve, M. Schlingmann, W. Crueger, K. Esser, R. Thauer, and F. Wagner, eds.), Carl Hanset, Munich, 1990, pp. 277–318.
141. K. M. Wiencek and M. Fletcher, Effects of substratum wettability and molecular topography on the initial adhesion of bacteria to chemically defined substrata. *Biofouling 11*(4):293–311 (1997).
142. J. H. Wolfram, R. D. Rogers, and B. J. Buescher, A summary of microbias influenced corrosion in nuclear power plants, Proceedings of the 1988 ASME Pressure Vessels and Piping Conference, Pittsburgh, 1988, pp. 99–23.

Copyright © 2002 Marcel Dekker, Inc.

17

Corrosion in Nuclear Systems: Environmentally Assisted Cracking in Light Water Reactors

F. P. Ford and Peter L. Andresen
General Electric Company, Schenectady, New York

INTRODUCTION

The phenomena of initiation and subcritical propagation of cracks in structural materials due to the conjoint actions of stress, material microstructure, and environment have been recognized for many years, and the mechanisms have been extensively investigated. This is especially the case for stressed alloys in environments containing high anionic concentrations of e.g., chlorides, phosphates, and hydroxides, either in the bulk environment (e.g., in the paper, chemical, petrochemical, and marine industries) or in localized environments where boiling or gradients in electrochemical potential, temperature etc. can concentrate species. However, it has been recognized that environmentally assisted cracking under static or cyclic loading (i.e., stress corrosion or corrosion fatigue) can occur in ultrahigh-purity water even when the concentration of non-OH^- anions is < l0 ppb. Although the cracking susceptibility is generally lower than in the concentrated environments, it is sufficient to cause concern when extended lives or high levels of plant availability are required, as in the power generation industry and especially for light water reactors (LWRs). The objective of this chapter is to discuss the development and use of mechanistically based models of environmentally assisted cracking of structural materials in highpurity water, with special emphasis on boiling water reactors (BWR) and occasional reference to pressurized water reactors (PWR).

THE PRACTICAL PROBLEM AND THE PROPOSED SOLUTION

There have been well-documented instances of environmentally assisted cracking in high-temperature water of austenitic stainless steels, nickel-base alloys, low-alloy and carbon steels, and their weld metals in various subcomponents of pressure vessels, pressurizers, steam generators, piping, deaerators, etc. Consequently, there is a strong driving force to derive design and life prediction codes which can account for

Copyright © 2002 Marcel Dekker, Inc.

the multitude of material, stress, and environmental combinations relevant to these systems. This requirement has posed a difficulty for the experimentalist, since it is not easy to control adequately the system conditions (e.g., water purity, loading) and to measure crack propagation rates with a sensitivity that is relevant to a typical 40-year design life. As a result, the current life prediction codes for environmentally assisted cracking of structural materials in high-temperature water usually represent upper bounds of the available data base and do not account for the wide range of material and environment conditions that are possible for the "nominal" system. This conservative "upper-bound" scenario can put unreasonable constraints on the continued operation of specific plants which are operating under far different system conditions than those represented by the design or life evaluation code. In other cases, life prediction codes do not exist either because of wide scatter in the data (e.g., stress corrosion of low-alloy pressure vessel steels) or because of lack of relevant data (e.g., irradiation-assisted cracking of stainless steel).

This unsatisfactory situation is offset, however, by the increase in mechanistic understanding of environmentally assisted cracking, which has accelerated in the last decade because of the availability of experimental and analytical procedures that allow quantification and validation of various cracking hypotheses. The ultimate validation of any such mechanistically based model is its ability to predict the extent of crack penetration as a function of the wide combination of the material, stress, and environment factors relevant to LWR operation (Fig. 1).

Since the precise shape of the crack depth–operational time curve in Figure 1 must be a function of the specific material, environment, and stressing conditions, it follows that if there is a range in the actual system conditions, there will be a predictable range in the observed data, with the distribution of the range in cracking mirroring the distribution of system conditions which affect the propagation process. This provides a bridge between deterministic and statistical or probabilistic life prediction methodologies [1,2].

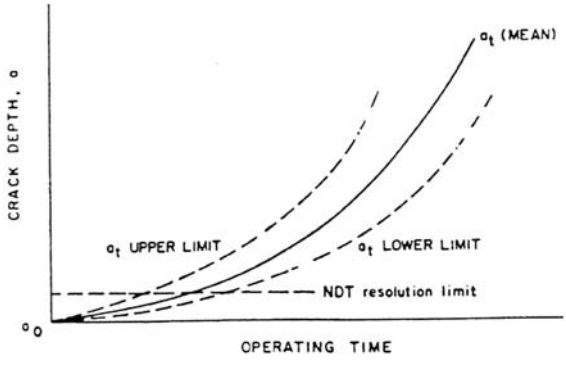


Figure 1 Schematic crack depth–time relationships for a range of relevant material, environment, and stress conditions.

Copyright © 2002 Marcel Dekker, Inc.

CANDIDATE CRACKING MECHANISMS

Historically, environmentally assisted cracking has been divided into the "initiation" and "propagation" periods. To a large extent this division is arbitrary, for in most investigations initiation is defined as the time at which a crack is detected, or when the load has relaxed a specific amount (in a strain-controlled test); in these cases such a definition of initiation corresponds to a crack depth of significant metallurgical dimensions (e.g., ≥2 mm). Thus, for the purpose of lifetime modeling it is assumed (Fig. 2) that, phenomenologically, initiation is associated with microscopic crack formation at localized corrosion or mechanical defect sites generally associated with pitting, intergranular attack, scratches, weld defects, or design notches. If it is further assumed that the probability of such initiation sites existing or developing relatively early in the life of the component is high, then the problem of life prediction devolves to understanding the growth of small cracks from these geometrically separated initiation sites and the coalescence of these small cracks to form a major crack, which may then accelerate or arrest depending on the specific material, environment, and stress conditions.

There has been relatively little fundamental work on the growth of such microscopically short cracks. For brevity, this will not be reviewed in detail, apart from mentioning that most work has been done under fatigue loading [3–7], with emphasis on the microstructural interactions required for microscopic crack arrest or propagation and modifications to linear elastic fracture mechanics analyses to account for the observed behavior in this crack size range. In the area of environmentally assisted cracking, the coalescence of microscopically small cracks has been investigated for carbon steels in carbonate-bicarbonate solutions [8,9] and stainless steels and nickel-base alloys [10] in high-temperature water. In these cases it is observed that the crack growth rate increases as the small cracks coalesce and approaches a

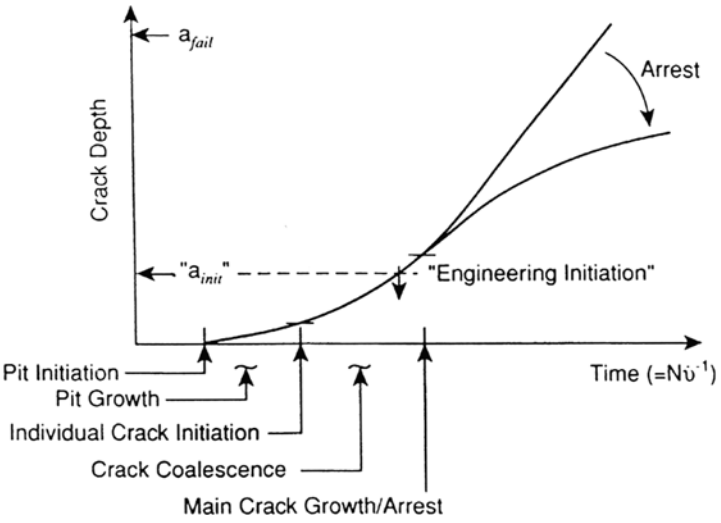


Figure 2 Proposed sequence of crack initiation, coalescence, and growth for steels undergoing subcritical cracking in aqueous environments.

Copyright © 2002 Marcel Dekker, Inc.

steady-state value when the mean crack depth is about 20 to 50 μm (Fig. 3); thereafter the crack propagation rate may be analyzed in terms of linear elastic fracture mechanics normally applicable to "deep" cracks. Thus, attention can be focused on current mechanistic knowledge of crack propagation rates for deep cracks (e.g., ≈1 grain diameter and greater), recognizing that the resultant life prediction may be conservative because the microscopic crack initiation and crack coalescence periods are not accounted for.

The basic premise for all of the proposed crack propagation mechanisms for ductile alloys in aqueous solutions is that the crack tip must propagate faster than the corrosion rate on the unstrained crack sides so that the crack does not degrade into a blunt notch [11,12]. Based on this criterion, the material-environment conditions for cracking can be defined based on the thermodynamic criteria for the existence of a protective oxide, salt, or compound film on the crack sides. For instance, cracking susceptibility of mild steel in hydroxide, carbonate-bicarbonate, nitrate, phosphate, and molybdate solutions can be predicted to occur in the specific potential-pH ranges where the protective film is thermodynamically stable [13]. Very similar thermodynamic arguments may be made for other systems, (e.g., brassammoniacal solutions [14]), and may be extended to kinetic arguments [15–17] which require that the electrochemical reaction rates (e.g., dissolution or oxidation) at the strained crack tip be significantly higher than those on the crack sides for an "electrochemical knife" [15] to propagate. Indeed, the suppression of stress corrosion and corrosion fatigue in many systems may be explained in terms of chemical blunting of cracks during the early propagation stage. The cracking of mild and low-alloy steels in aqueous environments offers ideal examples of this criterion. For instance, low-alloy steels will not exhibit stress corrosion in acidic or concentrated chloride solutions unless the general corrosion-blunting effect is counteracted with

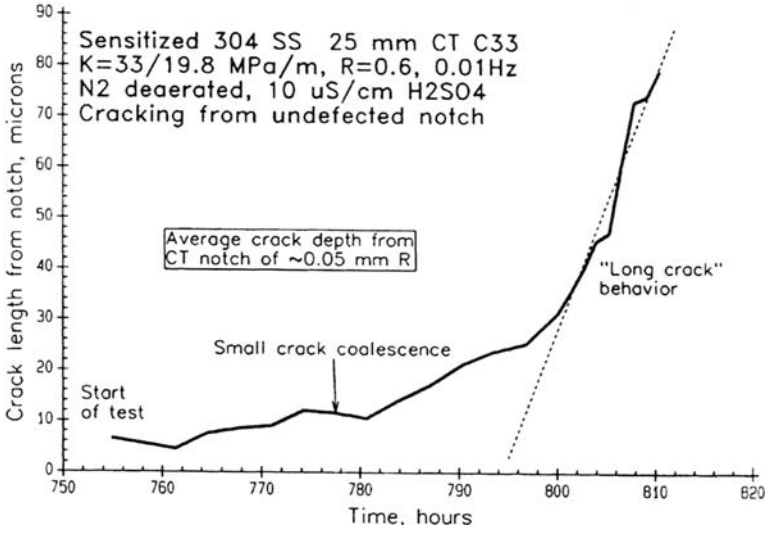


Figure 3 Crack depth–time relationship for intergranular cracks initiating, coalescing, and growing in a notched 1T CT specimen of sensitized stainless steel in 288°C water. (From Ref. 10.)

Copyright © 2002 Marcel Dekker, Inc.

chromium or nickel alloying additions [13,18]. Similarly, in high-purity water systems, carbon steel will not undergo stress corrosion cracking in low-temperature, oxygenated environments, since the embryo crack will be blunted by pitting; however, at temperatures >150°C, cracking is possible because of the protective nature of magnetite, Fe_3O_4 [19], which constitutes the inner film of the duplex surface oxide.

For systems in which chemical blunting is not an issue, numerous crack propagation mechanisms were proposed in the period 1965–1979 [20–31], ranging from preexisting active path mechanisms, to strain-assisted active path mechanisms, to mechanisms that depend on various adsorption-adsorption phenomena (e.g., hydrogen embrittlement mechanisms). There was considerable debate concerning the dominant mechanism in a given system, promulgated in part by the fact that up to 15 years ago there were few analytical techniques to test the various hypotheses quantitatively. Parkins [32] pointed out early on, however, that it was likely that there was a "stress corrosion spectrum" which logically graded the cracking systems between those that were mechanically dominated (e.g., hydrogen embrittlement of high-strength steels) to those that were environmentally dominated (e.g., preexisting active path attack in the carbon steel–nitrate system). Indeed, it was suggested that two mechanisms may operate in one alloy-environment system with a dominant mode being determined by relatively small changes in the material, environment, or stressing condition. This was followed by the suggestion (e.g., [1,11,32–34] that a similar spectrum of behavior occurs between constant load (stress corrosion), dynamic load (strain induced cracking), and cyclic load (corrosion fatigue) conditions.

With the advent in the last 15 years of more sensitive experimental and analytical capabilities, many of the earlier cracking hypotheses have been shown to be untenable, and the candidate mechanisms for environmentally assisted crack propagation (stress corrosion and corrosion fatigue) have largely been narrowed down to slip dissolution, film-induced cleavage, and hydrogen embrittlement. These mechanisms are briefly described below, followed by a discussion of the development of the slip dissolution model for life prediction for austenitic stainless steels in BWR coolant. Modifications to the basic model to explain changes in cracking susceptibility due to (a) irradiation for reactor core components, (b) material (e.g., nickel-base or low-alloy alloys), and (c) environment (e.g., BWR vs PWR) are then outlined.

Slip Dissolution Mechanism

Various crack advance theories have been proposed to relate crack propagation to oxidation rates and the stress-strain conditions at the crack tip, and these theories have been supported by a correlation between the average oxidation current density on a straining surface and the crack propagation rate for a number of systems [12,35]. There have been various hypotheses about the precise atom-atom rupture process at the crack tip—for example, the effect that the environment has on the ductile fracture process (e.g., the tensile ligament theory [36], the increase in the number of active sites for dissolution because of the strain concentration [37], the preferential dissolution of mobile dislocations because of the inherent chemical activity of the solute segregation in the dislocation core [38]).

Copyright © 2002 Marcel Dekker, Inc.

Experimentally validated elements of these earlier proposals have been incorporated in the current slip dissolution model, which relates the crack propagation to the oxidation that occurs when the protective film at the crack tip is ruptured [39–44]. Different types of protective films have been proposed, including oxides, mixed oxides, salts, or noble metals left on the surface after selective dissolution of a more active component in the alloy. As discussed below, quantitative predictions of the crack propagation rate via the slip dissolution mechanism are based on the faradaic relationship between the oxidation charge density on a surface and the amount of metal transformed from the metallic state to the oxidized state (e.g., MO or M^{+}_{aq}).

The change in oxidation charge density with time following the rupture of a protective film at the crack tip is shown schematically in Figure 4. Initially, the oxidation rate and, hence, crack advance rate will be rapid, typically controlled by activation or diffusion kinetics as the exposed metal dissolves, although availability of the balancing cathodic reduction current is also clearly necessary. However, in most LWR cracking systems, a protective oxide re-forms at the bared surface and the rate of total oxidation (and crack tip advance) decreases with time. Thus, crack advance can be maintained only if the film rupture process is repetitive. Therefore, for a given crack tip environment, corrosion potential, and material condition, the crack propagation rate will be controlled by the change in oxidation charge density with time and the frequency of film rupture at the strained crack tip. This latter parameter will be determined by the fracture strain of the film, ε_f, and the strain rate at the crack tip, $\dot{\varepsilon}_{ct}$. By invoking Faraday's law, the average environmentally

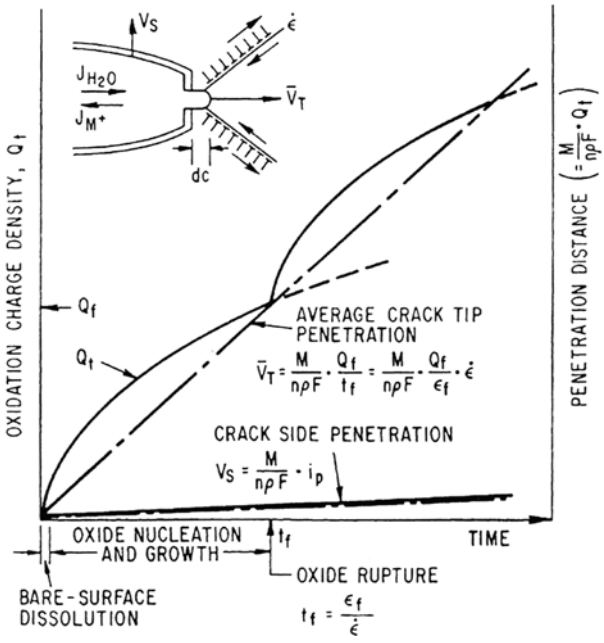


Figure 4 Schematic oxidation charge density–time relationship for a strained crack tip and unstrained crack sides. (From Ref. 11.)

Copyright © 2002 Marcel Dekker, Inc.

controlled crack propagation rate, $\bar{V}_t$, can be related to the oxidation charge density passed between film rupture events, Q_f, and the strain rate at the crack tip, $\dot{\varepsilon}_{ct}$:

$$\bar{V}_t = \frac{M}{z\rho F}\frac{Q_f}{\varepsilon_f}\dot{\varepsilon}_{ct} \tag{1}$$

where M, ρ = atomic weight and density of the crack tip metal
F = Faraday's constant
z = number of electrons involved in the overall oxidation of an atom of metal

Because the oxidation charge density on a bare surface varies with time at a rate that is dependent on the material and environment compositions that control the passivation rate at the crack tip, Eq. (1) can be adequately represented (and reformulated) in terms of a power law relationship:

$$\bar{V}_t = A(\dot{\varepsilon}_{ct})^n \tag{2}$$

where A and n are constants that depend on the material and environment compositions at the crack tip. These constants are related to the oxidation reaction rates, or current densities, in the specific crack tip material-environment system [45]. The current transients generally have an initially high bare surface dissolution current density, i_0 for a short time, t_0; thereafter, oxide formation or precipitation leads to a decay in the oxidation current density which often follows a general power law relationship:

$$i_t = i_0\left(\frac{t}{t_0}\right)^{-n} \tag{3}$$

If a *bare surface* condition is maintained at the crack tip (i.e., $\varepsilon_f / \dot{\varepsilon}_{ct} < t_0$), then integration of Eq. (3) leads to a predicted maximum crack propagation rate:

$$\bar{V}_{max} = \frac{M}{z\rho F} i_0 \tag{4}$$

This relationship is the quantitative basis for the early empirical observations discussed at the beginning of this section relating the oxidation current density on a straining surface and the crack propagation rate. However, these early correlations were obtained primarily for alloys in concentrated environments (boiling $MgCl_2$, 9 M NaOH solutions, etc.) under dynamic straining conditions. By comparison, in relatively dilute environments characteristic of LWRs it is expected that (a) the passivation rate will be high, and thus "n" [in Eq. (3)] will be high and t_0 will be short, and (b) under constant load or displacement conditions, the periodicity of oxide rupture, $\varepsilon_f / \dot{\varepsilon}_{ct}$, will be much greater than t_0. Under these circumstances a bare surface will not be maintained at the crack tip, and the crack propagation rate will be given by the integration of Eq. (3).

$$\bar{V}_t = \frac{M}{z\rho F}\frac{i_0 t_0^n}{(1-n)\varepsilon_f^n}\dot{\varepsilon}_{ct}^n \tag{5}$$

This is an expanded version of Eq. (2) and relates the parameters A and n to the specific oxidation rates [e.g., Eq. (3)] and the fracture strain of the oxide at the crack tip.

Copyright © 2002 Marcel Dekker, Inc.

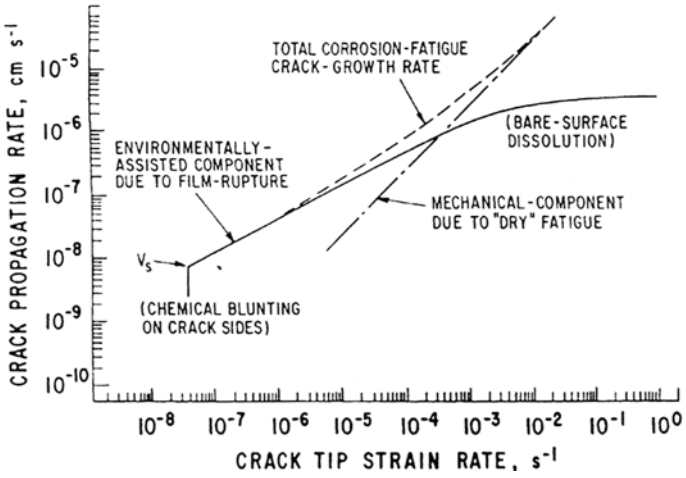


Figure 5 Illustration of the strain rate dependence of the crack propagation rate due to the slip dissolution model, and the additive properties of the mechanical and environmental components of crack advance during corrosion fatigue.

Under constant load or displacement conditions, the crack tip strain rate can be related, as discussed later, to the creep processes at a moving crack tip [1,45]. Under monotonically or cyclically changing bulk strain conditions, $\dot{\varepsilon}_{ct}$ can be related to an applied strain rate $\dot{\varepsilon}_{app}$. Thus, the slip dissolution mechanism may be applied to not only stress corrosion but also strain-induced cracking [46] and corrosion fatigue. Under cyclic loading conditions, however, the crack is also moving forward be irreversible cyclic plastic deformation, e.g., fatigue striation formation. Since this mechanical crack advance is occurring independently of the crack advance by oxidation processes, these two crack advance mechanisms (striation formation and oxidation) are considered additive, as shown by the dashed lines in Figure 5.

Film-Induced Cleavage Mechanism

In some incidences of transgranular cracking it has been observed [47] that the faradaic equivalent of the oxidation change density at a strained crack tip is insufficient to account for the observed crack advance. Moreover, the cleavage-like crystallographic features on the fracture surfaces are hard to rationalize convincingly in terms of a dissolution-oxidation model. Consequently, several authors [47–51] have proposed that transgranular environmentally controlled crack propagation may occur by a combination of oxidation and brittle fracture mechanisms. Specifically, the crack front is envisioned to move forward by an oxidation process that is controlled by the same rate-determining steps as those in the slip dissolution model but, when the film rupture event occurs, the crack in the film may rapidly penetrate a small amount, a^*, into the underlying ductile metal matrix (Fig. 6). Thus, Eq. (1) is modified as follows:

Copyright © 2002 Marcel Dekker, Inc.

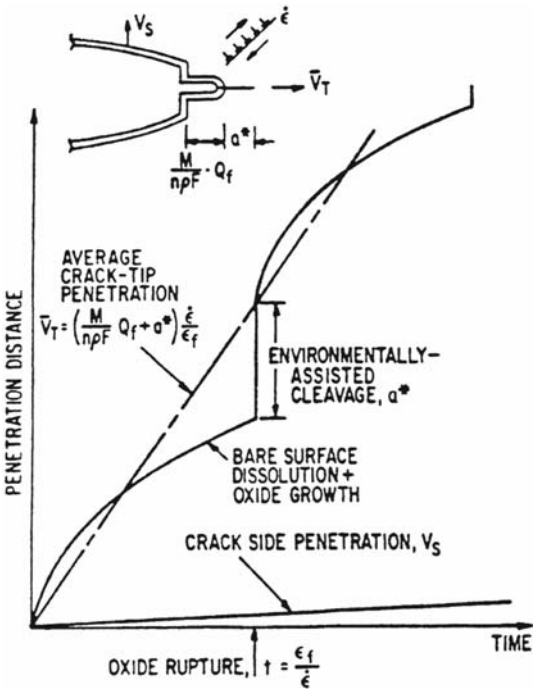


Figure 6 Schematic illustration of the elements of the film induced cleavage mechanism of crack propagation [1]. Note similarity to the slip dissolution model (Fig. 5) during initial stages of propagation cycle.

$$\bar{V}_t = \left(\frac{M}{z\rho F} Q_f + a^*\right)\frac{\dot{\varepsilon}_{ct}}{\varepsilon_f} \tag{6}$$

The extent of the additional film-induced cleavage component of crack advance, a^*, is governed [47] by the state of coherence between the surface film and matrix, the fracture toughness of the substrate, the film thickness, and the initial velocity of the cleavage crack emerging from the surface film. Although the surface film has been traditionally considered to be an oxide, more recent investigations [50,51] have shown that dealloyed surface films (e.g., copper-rich films in Cu-Zn or nickel-rich films in Fe-Cr-Ni alloys) can also form, exhibit "passive" behavior, and be very brittle. The extent of the cleavage propagation into the matrix is estimated to be of the order of 1 μm and to depend on the plasticity and microstructural factors mentioned above. Although there is evidence for this mechanism in copper-base alloys and austenitic nickel-base alloys and stainless steels in some low-temperature environments (i.e., <115°C), it has not been extensively tested for other alloy systems, including those relevant to LWRs. Its attractiveness is, however, that it provides a rational basis for explaining the interrelationships between the electrochemical parameters and the transgranular fractographic features in e.g., the carbon and low-alloy steel–high-temperature water systems peculiar to nuclear reactor pressure vessels and steam generator shells and quantitatively predicting the

Copyright © 2002 Marcel Dekker, Inc.

transitions between intergranular and transgranular cracking in stainless steels in high-temperature water [1].

Hydrogen Embrittlement Mechanisms

The general concepts and concerns behind the various hydrogen models have been reviewed by Thompson and Bernstein [52], Hirth [53], Nelson [54], and Birnbaum [55]. In brief, the subcritical crack propagation rate due to hydrogen embrittlement in aqueous environments depends on a sequence of events (Fig. 7) [56].

- Diffusion of a reducible hydrogen-containing species (e.g., H_3O^+) to the crack tip region
- Reduction of the hydrogen-containing ions to give adsorbed hydrogen atoms
- Absorption of the hydrogen adatoms followed by interstitial diffusion of these hydrogen atoms to a "process" zone at a distance, X, in front of the crack tip
- Once the hydrogen concentration in a "process" zone has reached a critical level, C_{crit}, over a critical volume, d_{crit}, localized crack initiation within this zone is followed by rapid propagation back to the main crack tip [57]

Setting aside the specifics of these localized fracture mechanisms in the process zone for the present, it is apparent that hydrogen embrittlement models predict discontinuous crack propagation at an average rate of

$$\bar{V}_t = \frac{X}{t_c} \tag{7}$$

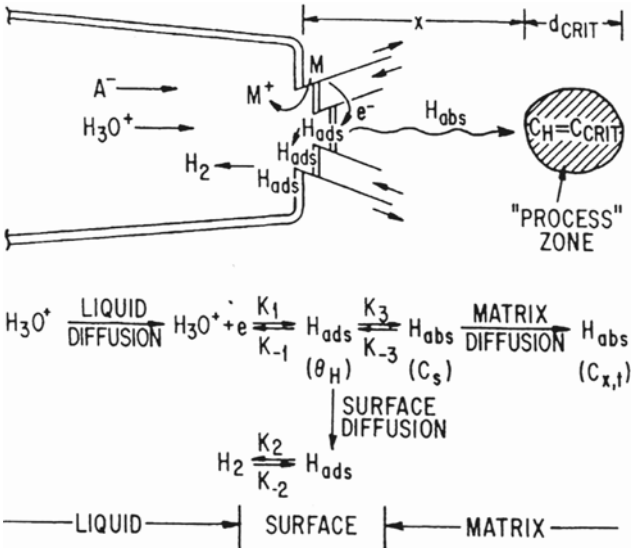


Figure 7 Schematic of various reactions at crack tip associated with hydrogen embrittlement mechanisms in aqueous environments. (From Ref. 45.)

Copyright © 2002 Marcel Dekker, Inc.

where X is the distance from the main crack tip to the process zone (which, in turn, is defined by the values of C_{crit} and d_{crit}) and t_c is the time for the concentration of absorbed hydrogen, $C_{x,t}$, to reach a critical value, C_{crit}, over the volume d_{crit}. To evaluate the validity of Eq. (7), quantitative data for X and T_c are needed. Unfortunately, these are difficult to predict from first principles [58] and rely mechanistically on the validity of the various atom-atom rupture hypotheses (e.g., decohesion [59,60], gas rupture [61,62], enhanced plasticity [63,64], hydride formation [65], and martensite formation [66]) that have been made.

Although traditionally such hydrogen embrittlement mechanisms have been applied qualitatively to high-strength alloys, Hanninen, Torronen, and co-workers [67,68] have suggested that a hydrogen embrittlement mechanism is operating in the relatively ductile pressure vessel steels in 288°C water. The prime experimental evidence for this hypothesis is the observation of the "brittle" cracks associated with elongated MnS stringers ahead of the main crack tip. The degree of environmental enhancement in fatigue crack growth rates is therefore directly correlated with the extent of these "brittle" fracture areas on the fracture surface. The following steps are hypothesized [68] to occur in these systems:

- Enhanced oxidation (dissolution and oxide reformation) at the strained crack tip.
- Hydrolysis of the cations with corresponding acidification of the crack environment.
- Dissolution of exposed MnS particles in this acidic environment, leading to the creation of H_2S and incorporation of sulfur into the reforming oxide.
- Creation of adsorbed hydrogen atoms due to the local hydrogen ion reduction reaction, followed by absorption. The kinetics of these reactions are believed to be accelerated both by the necessity to balance the enhanced oxidation reactions and by the presence of the sulfur species in the crack tip environment.
- Recombination of hydrogen atoms at MnS inclusions in front of the crack tip, leading to the formation of brittle cracks at the inclusion-matrix interface, which propagate under the action of hydrogen gas pressure and triaxial tensile stress.
- Linkage of these microcracks to give a discontinuous crack propagation over and above that due to "mechanical" fatigue failure.

PREDICTION METHODOLOGY FOR DUCTILE STRUCTURAL ALLOYS IN LWR SYSTEMS

Thermodynamic and kinetic criteria have been applied to determine which of the above candidate crack propagation mechanisms are valid for various alloy-environment systems [12,45]. However, it is comparatively rare that a candidate cracking mechanism can be categorically dismissed using this reasoning. Thus, qualitative predictions of cracking have centered around the observation that the rate-determining step in all of the cracking mechanisms is not necessarily the atom-atom rupture process itself but is one or a combination of (a) mass transport of species to and from the crack tip; (b) the oxidation or reduction reactions; and (c) the dynamic strain processes at the crack tip [11,12]. Thus, changes in cracking

Copyright © 2002 Marcel Dekker, Inc.

susceptibility for most ductile alloy–aqueous environment systems with, e.g., changes in temperature, electrode potential, stressing mode (dynamic or static stress, plane strain or plane stress, dislocation morphology, etc.), or environment composition can be explained [11,12] by movement over a reaction rate surface (Fig. 8) regardless of the specific atom-atom rupture mechanism at the crack tip.

Recognition of the fundamental importance of controlling mass transport, oxidation and reduction rates, and crack tip strain rates has proved invaluable in identifying the system changes that are likely to solve a particular environmentally controlled cracking problem. For instance, increasing the cracking resistance by increasing the passivation rate at the crack tip by controlling the corrosion potential, anionic activity, and material composition or by reducing the crack tip strain rate (for a given imposed stress history) by attention to dislocation morphology, etc., can be understood within this skeleton of fundamental logic [11,12]. Moreover, this knowledge can be used to predict limiting system conditions below which cracking will be minimal. An example is the evaluation of threshold stresses for cracking via their influence on a minimal crack tip strain rate and, thereby, crack propagation rate [69]. In recent years, as economic and technical pressures dictate longer design and operating lives, the emphasis has been on studying cracking in dilute environments where the relevant crack propagation rates are $< 10^{-7}$ mm/s, and on developing the quantitative prediction capability outlined in Figure 1. Thus, in the following section, the advances in quantifying the crack tip atom-atom rupture mechanisms and their rate-determining reactions are described.

To limit discussion, attention is focussed on the quantitative prediction of cracking in austenitic type 304/316 stainless steels in 288°C high-purity water (e.g.,

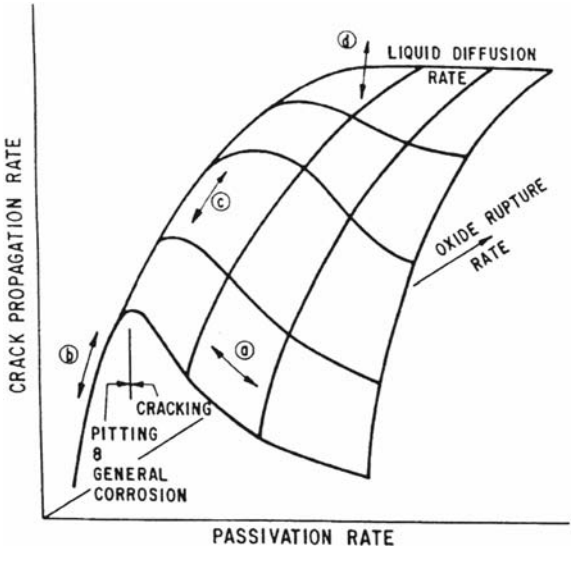


Figure 8 Reaction rate surface illustrating the variation in crack propagation rate with the rate controlling parameters in the slip dissolution, film-induced cleavage, and hydrogen embrittlement mechanisms for environmentally assisted cracking in ductile alloy—aqueous environment systems [11,12].

Copyright © 2002 Marcel Dekker, Inc.

BWR environments) in which it is assumed [1] that the slip dissolution model is a reasonable working hypothesis for the crack propagation mechanism. This baseline prediction methodology is then extended to treat the effects of irradiation on the cracking of stainless steel. Further extension to other alloys (e.g., nickel-base, low-alloy steels) and environments (PWR) is also outlined.

The starting point in this process is the theory and quantitative elements in Eq. (5). To develop this concept to a state of practical usefulness, it is necessary to redefine this fundamental equation in terms of measurable engineering or operational parameters. This involves (a) defining the crack tip alloy-environment composition in terms of, e.g., bulk alloy composition, anionic concentration or solution conductivity, dissolved oxygen content or corrosion potential, etc.; (b) measuring the reaction rates for the crack tip alloy-environment system that corresponds to the "engineering" system; and (c) defining the crack tip strain rate in terms of continuum parameters such as stress, stress intensity and loading frequency. Extensive work has been conducted in these areas, and the progress will be reviewed only briefly in this chapter before illustrating how these advances have been incorporated into verified, quantitative life prediction methodologies.

Definition of Crack Tip Alloy-Environment System

On the basis of direct measurements on stainless steel, alloy 600, and low-alloy steel-water systems at 288°C, it is known that the electrode potential and pH conditions at the tip of a crevice or crack can differ markedly from those at the exposed crevice or crack mouth [1,70–74]. These variations are understood and have been extensively reviewed [45,75–77] in terms of the thermodynamics of various metal oxidation and metal cation hydrolysis reactions and how they are influenced by the reduction processes of e.g., dissolved oxygen at the crack mouth. From a practical viewpoint, the corrosion potential which exists at the deaerated crack tip is controlled primarily by pH, but it can be defined [1] in terms of the measurable dissolved oxygen content in the external water environment (Fig. 9) (or preferably by the measurable corrosion potential of the external system) and the purity of the external water.

The transient and steady-state concentrations of anions in the crack have also been experimentally measured and analytically modeled [1,70,78]. The anion level present at the crack tip is directly dependent on the external anionic activity, the dissolvable metallurgical impurities (e.g., MnS) level, the corrosion potential difference between the crack mouth and tip, and convective influences. For example, the steady-state sulfur anion concentration at the crack tip in low-alloy steels can be defined by the MnS content, aspect ratio, and orientation; the solution flow rate; and the oxygen concentration in the water [1,79,80]. Under specific conditions the dissolved sulfur concentration can be of the order of 3 ppm versus <10 ppb in the bulk solution. For stainless steel exposed under normal BWR conditions, the potential drop down the crack length leads to a concentration of anions at the crack tip such that typical crack tip anion concentrations between 0.1 and 1.0 ppm are expected; under deaerated operating conditions, where no potential drop exists along the crack length, the (non-OH^-) anion content at the crack tip will approximate that in the bulk environment (e.g., ≈15ppb). To maintain electroneutrality in the crack enclave, it is necessary that there be a corresponding concentration of cations at the

Copyright © 2002 Marcel Dekker, Inc.

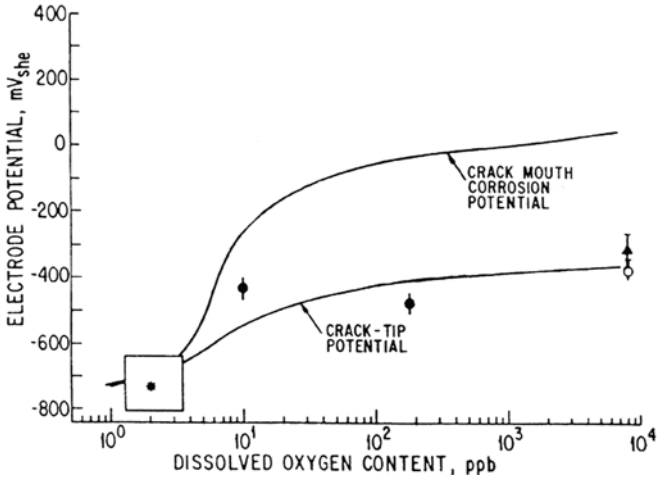


Figure 9 Crack tip potential variations as a function of dissolved oxygen content in water external to the crack. The observed data for crack tip conditions at 288°C are for carbon steel, A533B, and stainless steel [1,45,88].

crack tip. Because of the low solubilities of most transition metal cations, hydrolysis occurs and the pH decreases at the crack tip under most conditions. However, under water purity conditions relevant to BWRs, the concentration of (non-OH^-) anions is only sufficient to produce acidification of 1–2 pH units [70]. In the absence of non-OH^- anions, acidification cannot occur and generally a slight increase in pH is observed both in aerated [70] and deaerated [88] water.

Apart from the influence of MnS inclusions, the alloy composition at the tip of transgranular cracks is generally assumed to be that of the bulk alloy. However, the alloy composition at the tip of an integranular crack may be considerably different from the bulk composition if metal solute segregation or denudation at the grain boundary exists; such compositional heterogeneity will be controlled by, e.g., thermal diffusion and/or irradiation assisted damage. Discussion of these metallurgical aspects is outside the scope of this chapter, but adequate knowledge exists, including extensive analytical electron microscope studies, to permit definition of the grain boundary composition in terms of the bulk alloy composition and the thermal history during fabrication or irradiation history during reactor operation [81–86]. Thus, the crack tip alloy-environment system can be defined in terms of measurable or definable bulk system parameters.

Evaluation of Reaction Rates at Crack Tip

Various techniques have been used to create a macroscopic analogy to the crack tip bare surfaces on which the oxidation and reduction rates can be measured. These include mechanical methods to rupture the surface oxide that involve slowly [87–91] or rapidly [92,93] straining the alloy, complete fracturing of the specimen to create a bare fracture surface [94,95]; cyclic straining [88,96], scratching the alloy surface [97–102], and grinding [103]. Electrochemical methods have also been used to cathodically reduce the oxide [1,104–106] and then pulse to the potential of interest.

Copyright © 2002 Marcel Dekker, Inc.

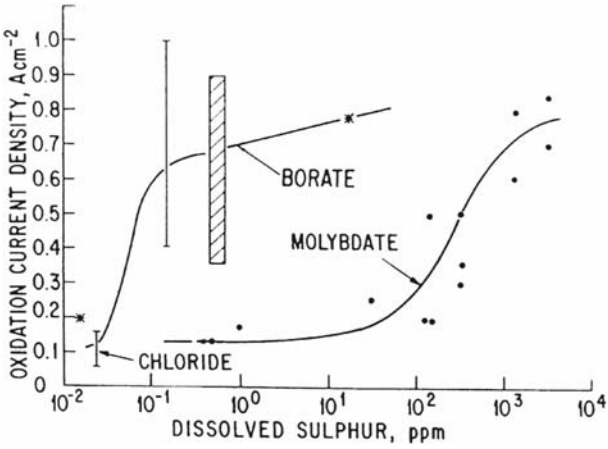


Figure 10 Relationship between the bare surface dissolution rate, i_0, on low-alloy steel at –620 mV_{she} and the dissolved sulfur activity [1,88,109].

Most of these techniques have been applied in the study of environmentally assisted cracking. The experimental difficulties with these techniques have been reviewed [45,107,108], along with the interpretations of the atomistics of the reaction rate [45] as a strained crack tip. These topics will not be covered further in this chapter.

The main conclusions with regard to dissolution and repassivation kinetics in structural materials in 288°C crack tip environments are that both the oxidation and reduction reaction rates are increased when the protective oxide is removed. The bare surface oxidation rate, i_0, is a function of the electrode potential and the dissolved anion content, as shown in Figure 10 for the effect of sulfur on the bare surface dissolution rate of low-alloy steels [1,88,109]. Explanations for this behavior range those by Ford, Andresen, and their colleagues [1,70], who argue that the rate-controlling process for bare surface dissolution is the diffusion of solvating water molecules to the oxidizing surface (and the influence of anionic activity and pH and on the solubility of impeding oxide precipitates), to those of Combrade [88], who argues that adsorbed sulfur on the surface impedes the incipient solid-state passivating oxide nucleation.

Oxide formation leads to a decrease in the overall oxidation rate, according to Eq. (3). The value of n in this equation [which is the same as in the crack propagation rate Eq. (5)] varies with the alloy chemistry [e.g., chromium content for a denuded grain boundary of type 304 stainless steel, or sulfur content for low-alloy steels (Fig. 11)], electrode potential, and anionic activity, and this can be related to e.g., solid-state oxide growth, dissolution-precipitation reactions, and oxide breakdown [1,11]. Thus, all of the parameters in Eq. (5), apart from $\dot{\varepsilon}_{ct}$, can be quantified for the crack tip system, which can, in turn, be related to definable or measurable bulk system conditions.

Definition of Crack Tip Strain Rate

It has been recognized for many years that the oxide rupture prerequisite for crack advance leads to a relationship between cracking susceptibility and slip morphology, since coarse slip at the crack tip will more readily rupture a brittle film of given

Copyright © 2002 Marcel Dekker, Inc.

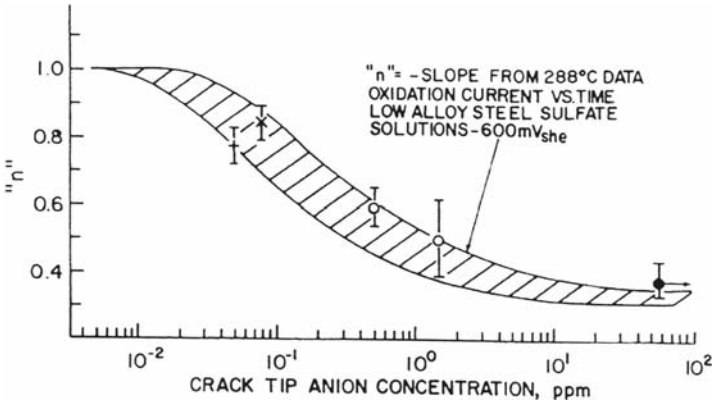


Figure 11 Relationship between the value n in Eq. (3) for the same system as in Figure 10. (From Ref. 1).

thickness [110] than fine slip. This relationship has been observed [52] for various alloys in both aqueous and gaseous environments, where the different dislocation morphologies are related to changes in stacking fault energy, short-range order, precipitate-matrix coherence, and precipitate distribution.

Despite these known effects of microscopic hetergeneity of plastic flow at a crack tip on the cracking susceptibility, the main emphasis in formulating expressions for the periodicity of film rupture has been on continuum parameters such as strain rate and oxide fracture strain. Reviews of the formulations for crack tip strain rate have been conducted by Parkins et al. [111], Lidbury [112], and Ford [45,113], among others. These reviews address the need for the crack tip strain rate formulations to account for various observed factors, including:

1. Can the strain rate formulations account for the limiting stress conditions for cracking, defined by σ_{th}, ΔK_o, or K_{Iscc}? This aspect has been covered by e.g., Parkins and co-workers [69] in assessing the criteria for maintaining a critical creep rate and how this might be achieved by various stressing conditions.
2. How will the crack tip strain rate vary with time-dependent stressing conditions and the degree of plastic constraint? A subsidiary aspect is the examination of the belief that σ_{th} and K_{Iscc} are system constants.
3. How does the fact that the crack is propagating affect the crack tip strain rate when dislocation movement is governed by an exhaustion theory of creep? Associated with this is the definition of the criteria that determine the onset of crack arrest.

Numerous formulation approaches have been suggested and reviewed [45,111–113] but currently these questions have not been completely answered. However, an earlier section reviewed the urgent practical importance of evolving usable life prediction algorithms, and preliminary crack tip strain rate algorithms have been developed for LWR systems in the following form:

$$\text{For constant load:} \qquad \dot{\varepsilon}_{ct} = A\dot{\varepsilon}_{creep} + B\left(\frac{\bar{V}_t}{x^*}\right) \tag{8}$$

Copyright © 2002 Marcel Dekker, Inc.

$$\text{For slow strain rate:} \qquad \dot{\varepsilon}_{ct} = C\dot{\varepsilon}_{appl} + D\left(\frac{\bar{V}_t}{x^*}\right) \tag{9}$$

$$\text{For cyclic load:} \qquad \dot{\varepsilon}_{ct} = \left(\frac{\delta\varepsilon}{\delta K}\right)\dot{K} + \left(\frac{\delta\varepsilon}{\delta a}\right)\bar{V}_t \tag{10}$$

In all of these equations, it is recognized that the crack tip strain rate is a function, not only of the applied stress, stress intensity, or strain rate, but also of the crack propagation rate, $\bar{V}_t$. In other words, the movement of the crack tip stress field into the underlying metal matrix by an amount, x^*, activates new dislocation sources in a given time period, thereby increasing the strain rate above that in a stationary crack.

Despite the simple yet sound logic inherent in the above formulations, they have proved to be remarkably difficult to quantify in terms of crack tip plasticity and to verify independently. For instance, uniaxial creep deformation laws at low homologous temperatures are not necessarily applicable to the multiaxial stress conditions in the surface region adjacent to the crack tip, and the use of linear elastic fracture mechanics has limitations in the region of high plastic deformation near the crack tip. These difficulties have been discussed in some detail [45,111–113] and will not be covered further. Despite these fundamental difficulties, empirical formulations between the crack tip strain rate and "engineering" parameters have evolved which have proved useful for a wide range of stressing conditions for structural alloys in 288°C water (Table 1) [1,45].

VERIFICATION AND USE OF CRACKING PREDICTIONS FOR LWR SYSTEMS

The methodology outlined above provides a specific framework for quantitatively predicting environmentally assisted cracking in structural alloy–water systems at 288°C. This is illustrated below for stainless steels under both unirradiated and irradiated conditions, where intergranular stress corrosion has been observed, e.g., in weldsensitized and thermally sensitized piping, and irradiated core components. The methodology is also illustrated for transgranular stress corrosion cracking of A533B and A508 low-alloy steels used for pressure vessel plates and forgings and forintergranular cracking of nickel-base alloys used for safe ends, weldments, etc. Remarks are then made about the extension of these capabilities to other, e.g., PWR, systems.

Table 1 Crack Tip Strain Rate (s^{-1}) Formulations for Unirradiated Steels in 288°C Water

	Type 304 stainless steel	A533B Low alloy steel
Constant load	$4.1 \times 10^{-14}\,K^4$	$3.3 \times 10^{-13}\,K^4$
Slow strain rate	$5\dot{\varepsilon}_{app}$	$10\dot{\varepsilon}_{app}$
Cyclic load	$68.3\dot{\nu}\,A_R\Delta K^4$	$547\dot{\nu}\,A_R\Delta K^4$

$K(\Delta K)$ = stress intensity (amplitude in MPa $\sqrt{m}$; $\dot{\varepsilon}_{app}$ = applied strain rate in s^{-1}; $\dot{\nu}$ = frequency of (symmetrical) load cycle in s^{-1}; A_R = constant in "dry" Paris Law = 2.44×10^{-11} (for $R \le 0.42$) = $-2.79 \times 10^{-11} + 1.115 \times 10^{-10}\,R + 5.5 \times 10^{-11}\,R^2$ (for $R > 0.42$); R = minimum load/maximum load.

Copyright © 2002 Marcel Dekker, Inc.

Sensitized or Irradiated Type 304 Stainless Steel/BWR System

Extensive investigations of the relevant fundamental reactions pertinent to crack tip systems have led to a quantification of the basic parameters in Eq. (5). For stainless steels, this equation may be simplified [1] to

$$\bar{V}_t = 7.8 \times 10^{-3} n^{3.6} (\dot{\varepsilon}_{ct})^n \tag{11}$$

As discussed previously, n is fundamentally related to the crack tip environment (pH, potential, anionic activity) and material (chromium denudation at grain boundaries) conditions. For practical use, n has been reformulated [1] in terms of measurable system parameters such as anionic activity (or solution conductivity, κ), corrosion potential (ϕ_c, which, in turn, is a function of the dissolved oxygen, hydrogen peroxide, and dissolved hydrogen concentrations), and the electrochemical potentiokinetic repassivation (EPR) parameter (which is related to the chromium denudation in the grain boundary). The formulation is of the form (Fig. 12)

$$n = \left(\frac{e^{f(\kappa)}}{e^{f(\kappa)} + e^{g(\phi_c)}} \right)^{h(\mathrm{EPR})} \tag{12}$$

The crack tip strain rate, $\dot{\varepsilon}_{ct}$, in Eq. (11) is related to the engineering stress (or stress intensity) parameters via the formulations in the Table 1.

The validity of the prediction methodology with respect to the strain rate sensitivity is indicated in Figure 13, which covers data obtained on sensitized type 304 stainless steel in 288°C water containing 8 ppm oxygen and stressed over a wide range of constant load, monotonically increasing load, and cyclic load conditions [1]. The solid line is the theoretical relationship and illustrates the applicability of the methodology to the whole stress corrosion–corrosion fatigue spectrum. The specific effects of changes in corrosion potential and solution conductivity on the propagation rate under constant load are shown in Figures 14 and 15. An example the effect of compositional changes is illustrated later in reference to irradiation-induced chromium denudation at the grain boundaries.

The comparison between the theoretical and observed crack growth rate-stress intensity relationships are shown for a sensitized stainless steel in a somewhat impure BWR environment (Fig. 16a) and a more modern "hydrogen water chemistry" BWR environment (Fig. 16b). The agreement between observation and theory is apparent, as is the inapplicability of a single life prediction law such as the "NRC disposition line" to a system which can exhibit a wide range of conditions within a nominal specification.

The broad agreement between observation and theory for propagation of environmentally assisted cracking in the stainless steel–water system at 288°C is shown in Figure 17. In this diagram, the data refer to a wide range of material, environment, and stressing conditions for the generic "stainless steel–water system at 288°C. Again, the agreement between observation and theory is apparent. Indeed, given the sensitivity of the crack propagation rate to relatively small changes in the system conditions (e.g., Figs. 14–16), it has been proposed [1] that the scatter in Figure 17 is due primarily to relatively small unmeasured changes in the system conditions. For instance, unmonitored changes in corrosion potential of ≈l00 mV in 200 ppb oxygen water–a range which is perfectly possible because of flow rate effects, etc.–would give

Copyright © 2002 Marcel Dekker, Inc.

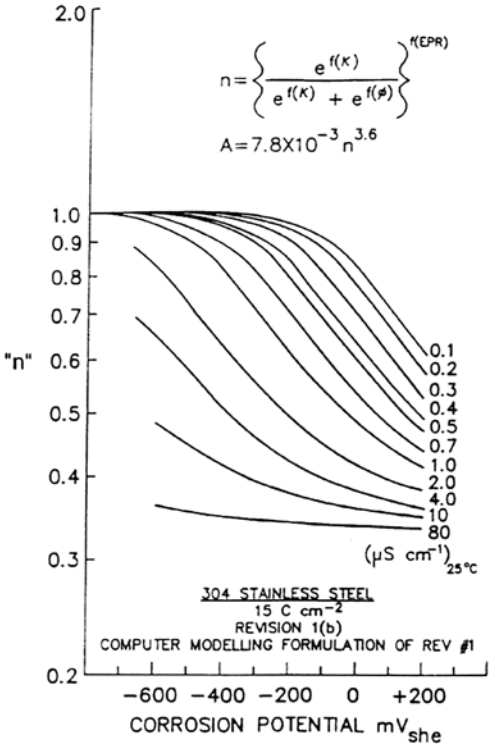


Figure 12 Relationships between n in Eqs. (2) and (5) and the corrosion potential and bulk solution conductivity for a sensitized (EPR = 15 C/cm^2) type 304 stainless steel in water at 288°C. (From Ref. 1).

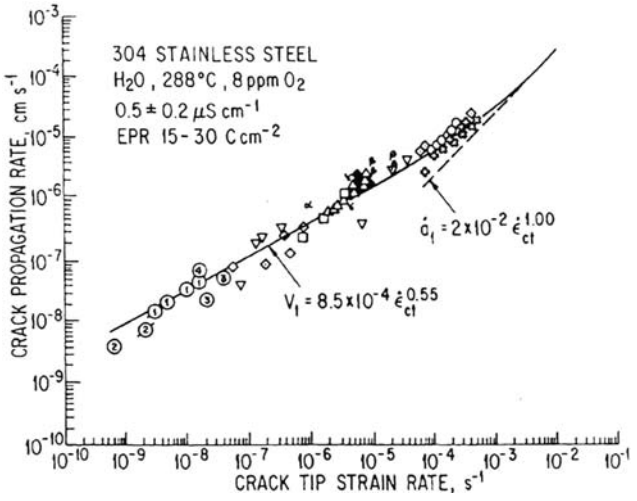


Figure 13 Observed and theoretical crack propagation rate–crack tip strain rate relationships for sensitized type 304 stainless steel in oxygenated water at 288°C. (From Ref. 1).

Copyright © 2002 Marcel Dekker, Inc.

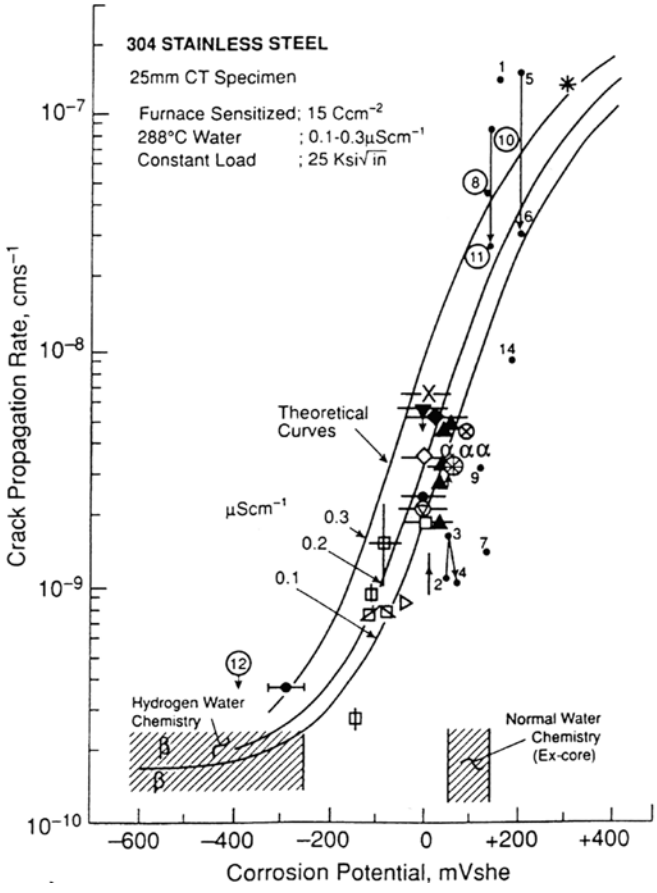


Figure 14 Observed and predicted relationships between the crack propagation rate and corrosion potential for sensitized type 304 stainless steel in water under constant load. Water conductivity in range 0.1 to 0.3 μS/cm. (From Ref. 1).

a predictable change in crack propagation rate of about a factor of 4. It follows, therefore, that the practical use of such a prediction methodology for life prediction, codification, etc. hinges on an adequate definition of the actual system via the use of system monitors for corrosion potential, solution conductivity, etc. [2].

Integration of the crack propagation rate algorithms leads to an appropriate crack depth—time ($a - t$) relationship, which, for a uniform tensile stress situation, is of the form

$$a_t = \left\{ a_i^{(1-2n)} + 7.8 \times 10^{-3} n^{3.6} (1-2n) \left[C\pi^2 (B\sigma)^4 \right]^n t \right\}^{1/(1-2n)} \tag{13}$$

This particular form applies in the simple case in which the stress intensity can be defined by

$$K = B\sigma\sqrt{\pi a} \tag{14}$$

Copyright © 2002 Marcel Dekker, Inc.

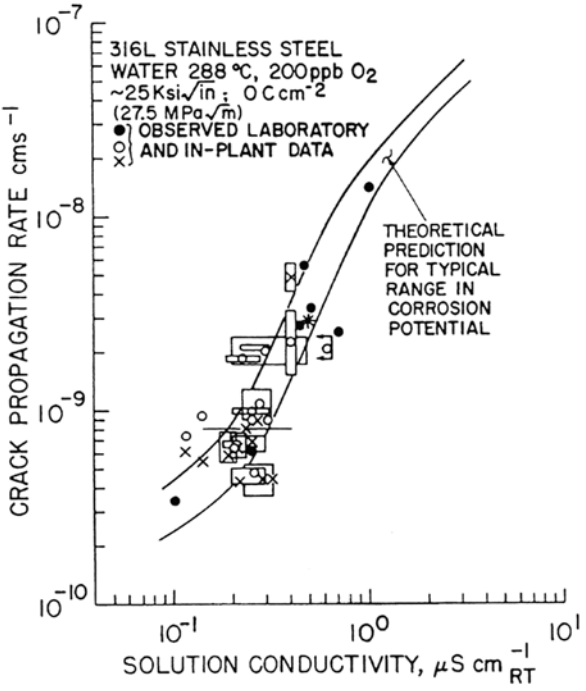


Figure 15 Observed and predicted relationships between the crack propagation rate and solution conductivity for type 316L stainless steel under constant load (25 ksi $\sqrt{\text{in}}$) in water containing 200 ppm oxygen. (From Ref. 1).

These formulations can become more complicated, e.g., for complex stress fields adjacent to welds. Examination of Eq. (13) indicates that, at time zero, there is an assumed intrinsic initiating defect, a_i; in the following analyses for "smooth" stainless steel components, a value of 50 μm has been used [2,10].

Equation (13), in conjunction with the variation in stress intensity as a crack grows through a residual stress field adjacent to a weld, provides a prediction of the effects of, e.g., (a) water purity on the crack depth–operating time for stainless steel piping and (b) a range in residual stress on the predicted range of crack depths in a piping system (Fig. 18). A range in actual system conditions inherently leads to a predicted range in cracking response, as illustrated in Figure 19 for the theoretical relationships between the coolant purity and the operating time required for a crack to penetrate 25% of the wall thickness in a welded type 304 stainless steel pipe. These theoretical relationships are shown for typical ranges in carbon contents (i.e., EPR values) and in residual stress profiles. Figure 19 shows that the observed data lie within the theoretical bounds. Thus, with this proven prediction capability, quantitative decisions can be made about the future behavior for proposed modifications in environment, material, or stress (Fig. 20).

Similar predictions can be made for the effect of irradiation on the intergranular cracking susceptibility of stainless steel components in the reactor core [114]. The prediction methodology developed for unirradiated conditions was modified to account for the effect of fast neutron and gamma irradiation on (a)

Copyright © 2002 Marcel Dekker, Inc.

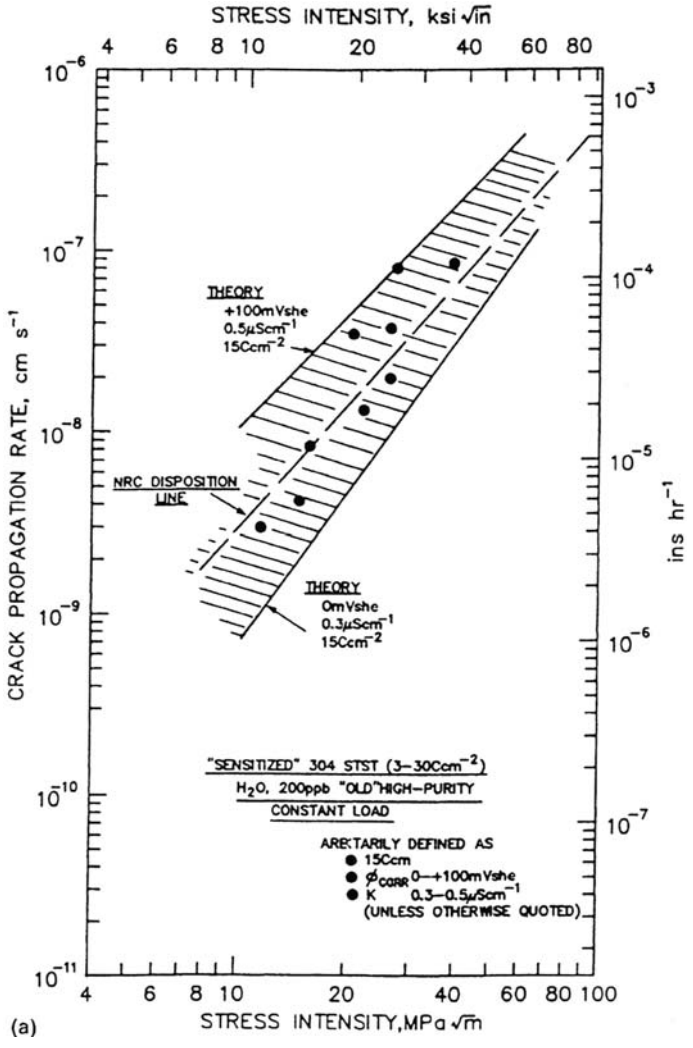


Figure 16 Comparison between observed and theoretical crack propagation rate–stress intensity relationships for sensitized type 304 stainless steel in water at 288°C; 200 ppb O_2; 0.2 to 0.5 μS/cm.

irradiation hardening and its effect on crack tip strain rates, (b) irradiation-induced relaxation of residual stresses, (c) irradiation-induced depletion or enrichment of compositional elements species at the grain boundary, and (d) the corrosion potential via the radiolysis of water.

Once these individual effects have been qualified and verified, it is relatively easy to extend the existing prediction methodology for IGSCC of unirradiated stainless steels to cover the effects of fast neutron fluence on the time to failure of stainless steels in oxygenated water (Fig. 21). Figure 22 shows the predicted variation of a "*threshold*" fluence (below which cracking is not observed in, e.g., 10 operating years) for different combinations of stress and

Copyright © 2002 Marcel Dekker, Inc.

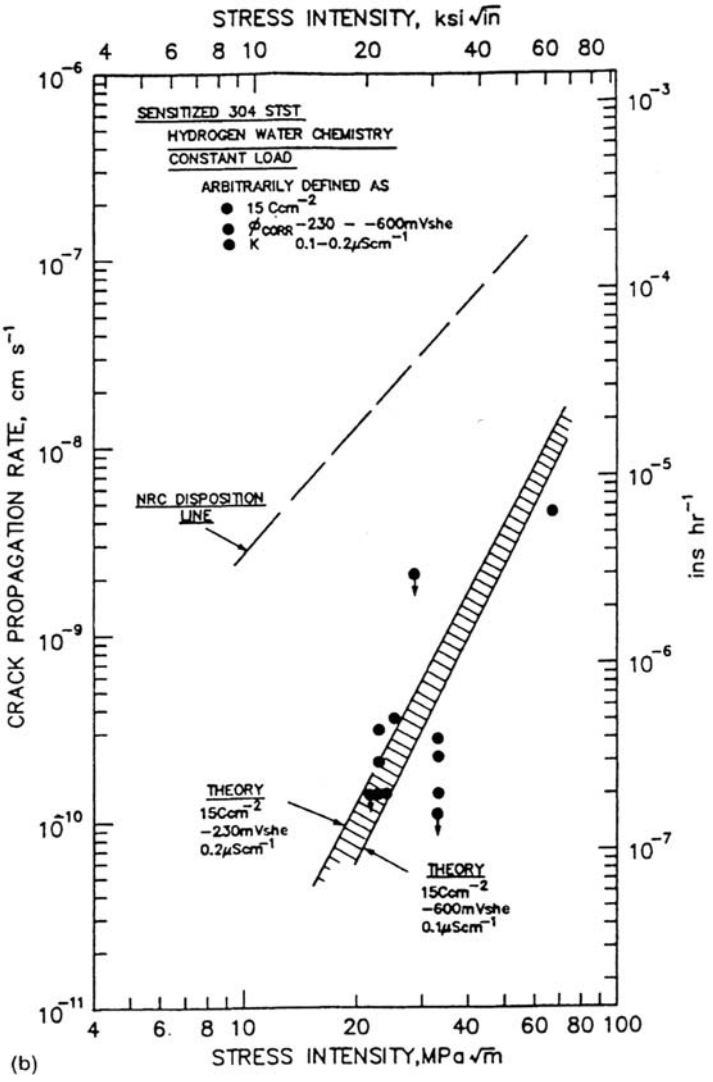


Figure 16 (Continued)

solution purity. Moreover, specific remedial actions can be defined to arrest cracking which is detected in a reactor component. For example, Figure 23 shows the changes in corrosion potential necessary to arrest a crack in a BWR core shroud.

Low-Alloy Steel/ BWR System

It is assumed that the slip dissolution model is applicable to transgranular environmentally assisted cracking in the A533B/A508 low-alloy steel–water system at 288°C [1]. It is recognized that this assumption may introduce a systematic error due

Copyright © 2002 Marcel Dekker, Inc.

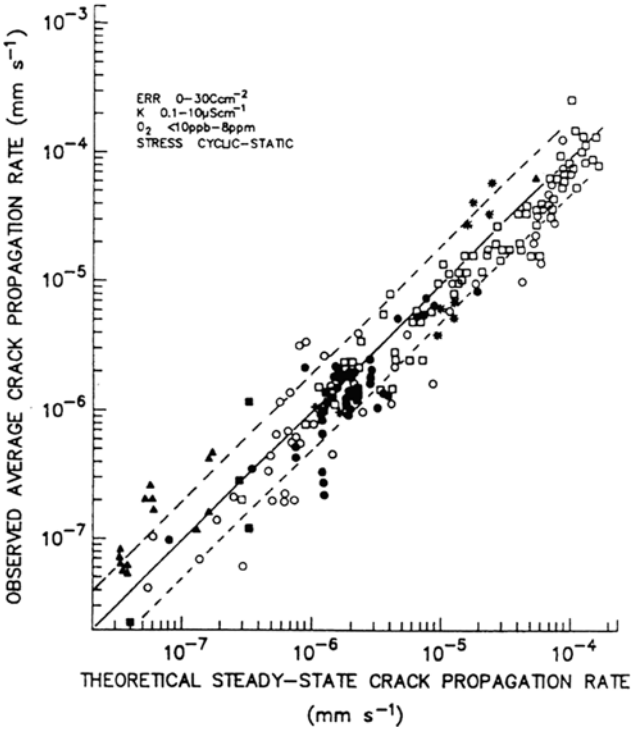


Figure 17 Relationship between the observed and theoretical steady-state propagation rates for stainless steel in water at 288°C for a wide combination of material, stress, and environment conditions. (From Ref. 1.)

to undefined components of crack advance associated with film-induced cleavage or hydrogen embrittlement, but this is regarded as a small error at this stage of the life prediction methodology development [1,113]. Thus, Eq. (5) is retained as the primary basis for prediction, and its quantification has been accomplished [1,79,113] in a similar manner to that described for stainless steel. A primary difference, however, has been the unique role played by the dissolution of MnS inclusions and the associated definition of the crack tip environment [1,79,80]. This is addressed in detail elsewhere [1,79,80,115–119], and it should merely be recognized that MnS inclusions do dissolve in high-temperature water. The dissolution rate is sufficiently rapid to increase the concentration of dissolved sulfur species in the crack and, thereby, to increase the crack growth rate significantly. Other influential factors, such as anion enhancement in the crack due to a gradient in potential down the crack and anion deletion due to flushing of the crack at high bulk solution flow rates, are also important, as in stainless steel.

The agreement between theory and observation of cracking under laboratory conditions is encouraging [1,79], as in the agreement between the observed and theoretical crack depth–operating time relationships for cracks in the limited number of incidences of cracking in A508 feedwater nozzles of BWR reactors (Fig. 24). In this latter case, cracks were observed to initiate on the surface due to thermal fatigue

Copyright © 2002 Marcel Dekker, Inc.

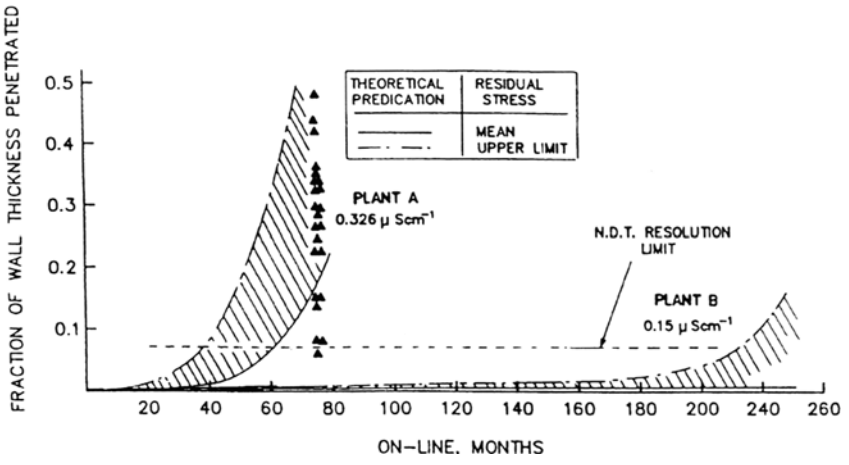


Figure 18 Theoretical and observed crack depth vs. operational time relationships for 28-inch-diameter schedule 80 type 304 stainless steel piping for two BWRs operating at different mean coolant conductivities. Note the bracketing of the maximum crack depth in the lower-purity plant by the predicted curve that is based on the maximum residual stress profile and the predicted absence of observable cracking in the higher-purity plant (in 240 operating months).

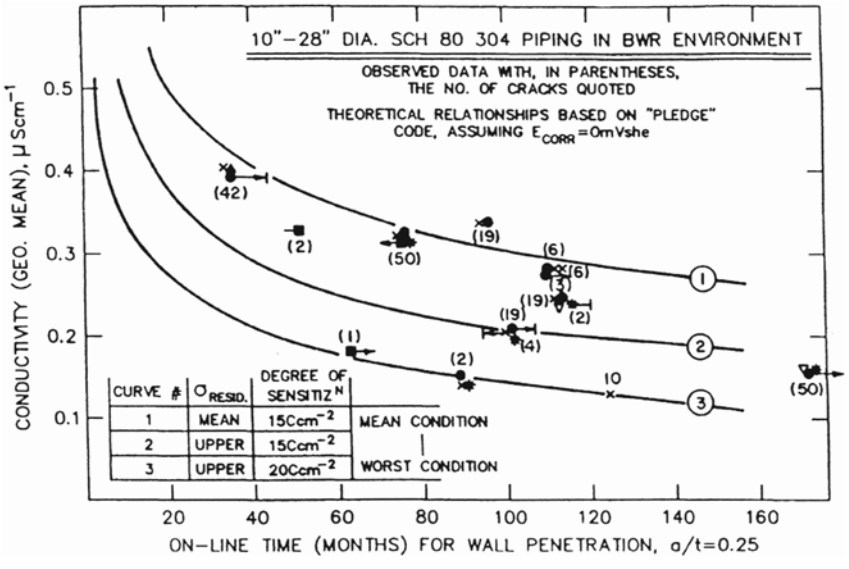


Figure 19 Observed and theoretical relationships between average BWR coolant conductivity and the operational time to achieve quarter wall penetration. Observed data from various operational BWRs are shown with the number of cracks detected shown in parentheses beside each data point. Theoretical curves are for the quoted combinations of stress and degree of sensitization at the HAZ.

Copyright © 2002 Marcel Dekker, Inc.

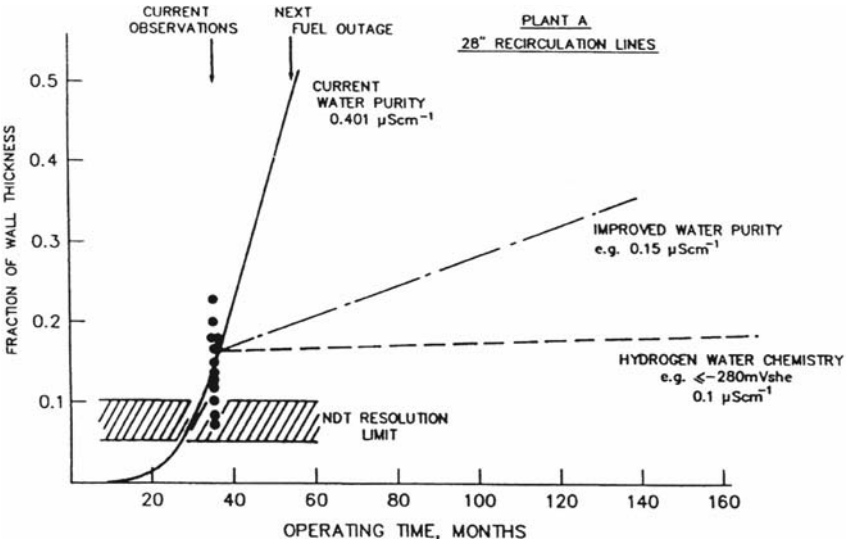


Figure 20 Predicted response of defected piping for defined changes in water chemistry in BWR plant.

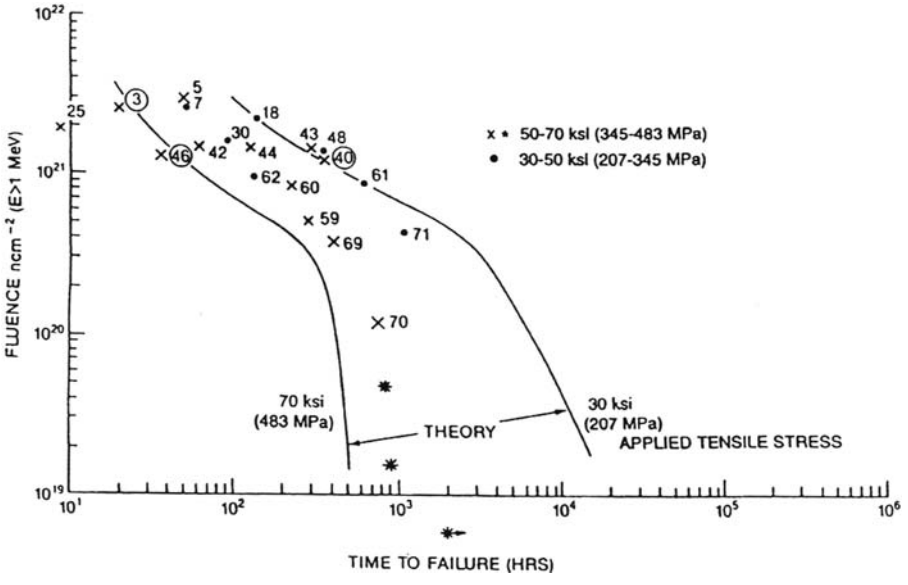


Figure 21 Comparison between observed and theoretical relationships for the effect of fast neutron fluence on the time to failure of irradiated type 304 stainless steel under constant load in 32 ppm oxygenated water at 288°C.

Copyright © 2002 Marcel Dekker, Inc.

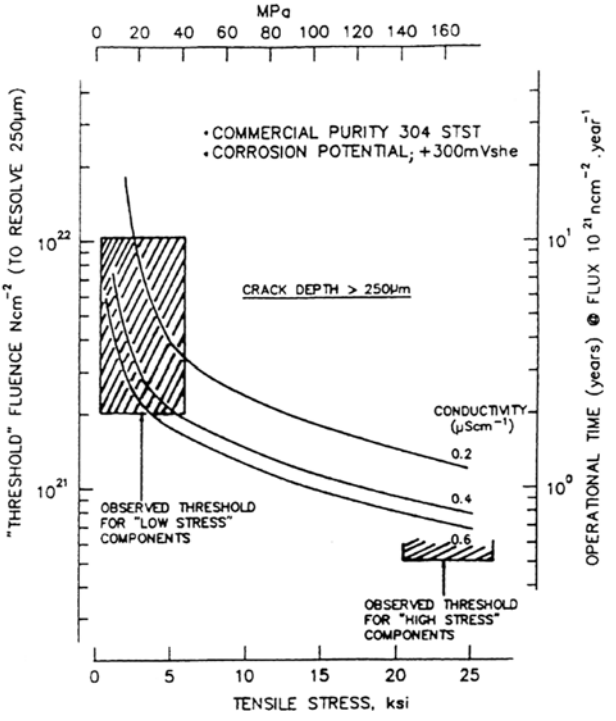


Figure 22 Predicted and observed variations between threshold fluence for observation of cracks in irradiated BWR components and the tensile stress and solution conductivity.

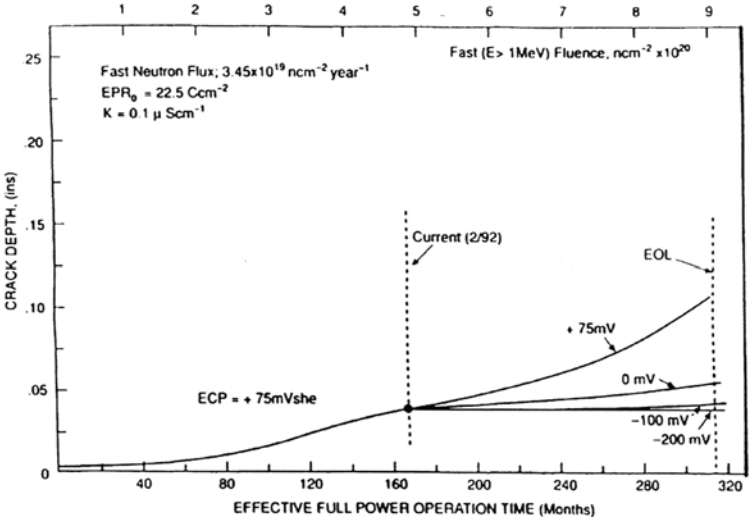


Figure 23 Predicted crack depth–time relationship for cracking in a hypothetical BWR core shroud and the defined changes in corrosion potential required to slow down and arrest the crack propagtion.

Copyright © 2002 Marcel Dekker, Inc.

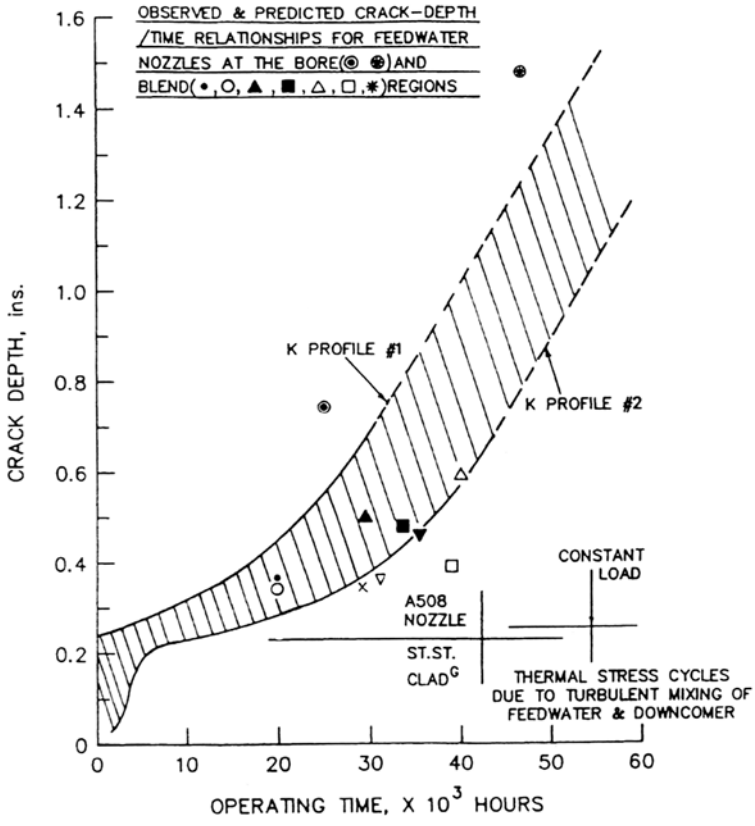


Figure 24 Predicted and observed crack depth–operating time relationships in BWR feedwater nozzles. (From Ref. 79.)

caused by mixing of hot water coolant and the cooler feedwater, and the theoretical analysis [79] addressed the subsequent propagation of these cracks due to stress corrosion from pressurization stresses alone.

As with stainless steels, the stress corrosion predictions can be logically expanded to cover corrosion fatigue. Corrosion fatigue of low-alloy steels in LWR environments and the impact on ASME XI life evaluation analyses have been exhaustively reported [115–117]. In summary, the current ASME XI code for corrosion fatigue crack propagation of low-alloy steels can be overly conservative under certain operating conditions; however, under specific conditions of low cyclic frequencies, high oxygen content environments, and high-sulfur steels, it is predicted and observed that $(da/dN)_{\Delta K}$ values greater than the ASME XI code curve are possible [118].

The validity of the current ASME III code for corrosion fatigue crack *initiation* in low-alloy and carbon steels in LWR environments is under current review [119]. Although the model development actions are still in a preliminary stage, it is apparent that the cycles to crack initiation (N_i) are predictable and that the conditions under which the ASME III design curve is nonconservative can be defined (Fig. 25).

Copyright © 2002 Marcel Dekker, Inc.

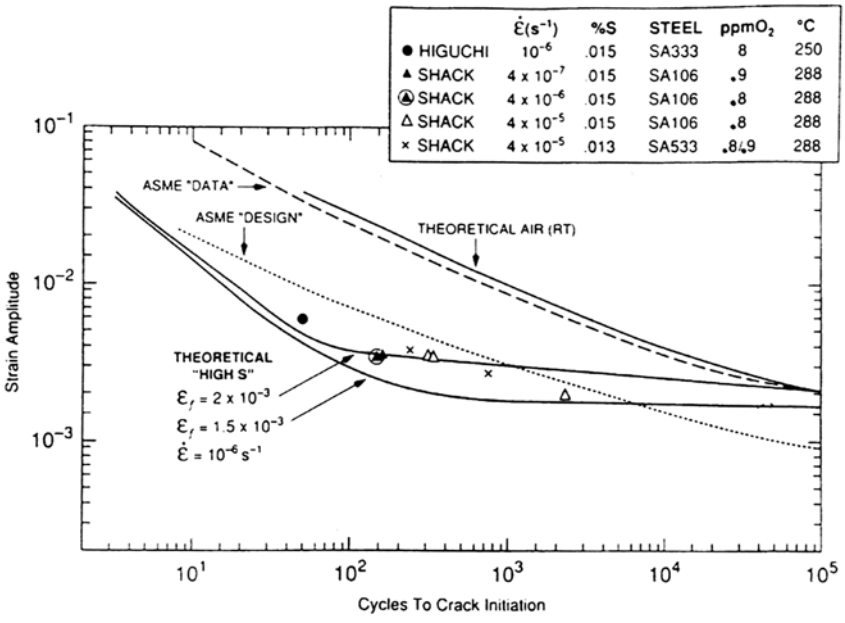


Figure 25 Predicted [119] and observed [121–123] strain amplitude vs. cycles to intiation relationships for (unnotched) carbon and low-alloy steels in high-temperature water, under the worst combination of material and environmental conditions. Note that carbon and low-alloy steels behave very similarly, with a $N_i/\Delta\epsilon_t$ response in high oxygen 250/288°C water which is dictated by the high sulfur content of the steel.

The laboratory and field experiences base for environmentally assisted cracking low-alloy steel is far smaller than for sensitized stainless steel, and more development and validation work is required before the prediction methodology can responsibly be reduced to practice.

Nickel-Base Alloys/BWR System

The development of prediction models for environmentally assisted cracking of nickel-base alloys in BWR systems is made difficult by the fact that the data base against which the prediction models can be validated exhibits extreme scatter (Fig. 26) and/or was obtained under conditions which are not directly applicable to BWR operation (e.g., high conductivity). Establishing a link between crack growth rates in stainless steels and ductile nickel-base alloys helps to resolve this problem, since it permits the much broader base of data and modeling for stainless steels to provide guidance on the expected response of nickel-base alloys in BWR systems [70,120]. This mechanistic link is reasonable for the following reasons:

- Intergranular cracking is the dominant failure mode and is associated with chromium depletion at the grain boundary in both types of alloys. For stainless steels, EPR is used to quantify sensitization, as described above. However, the EPR technique cannot be used without significant modification

Copyright © 2002 Marcel Dekker, Inc.

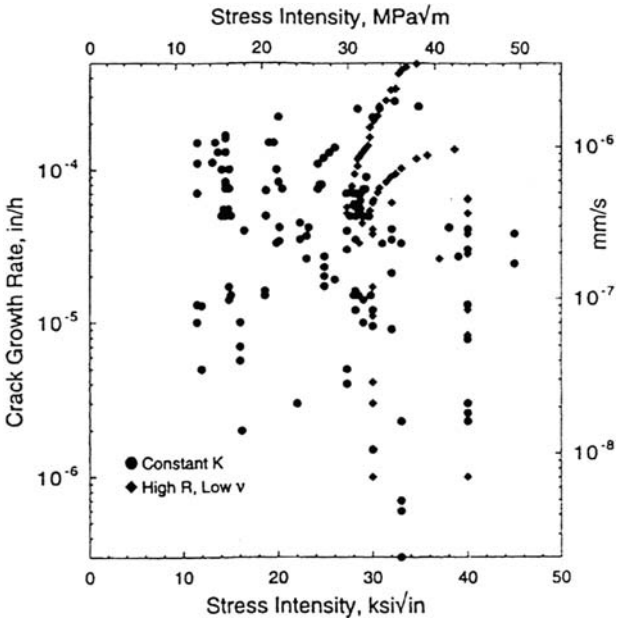


Figure 26 Crack growth rate vs. stress intensity in 288°C water for alloy 600 and alloy 182 weld metal. Data are from many sources, many of which provide only nominal water and material chemistry conditions. This inadequate definition results in orders of magnitude spread in crack growth rate that can mistakenly be interpreted, e.g., for a very high dependence on stress intensity.

on nickel alloys; thus, an "equivalent EPR" is used to represent equivalent chromium depletion profiles in nickel alloys.

For alloy 182 weld metal, an equivalent EPR in the range 10 to 20 C/cm^2 is used. For fully solutionized (or fully healed, i.e., no Cr depletion) alloy 600, an equivalent EPR of 0 to 5 C/cm^2 is appropriate, and for sensitized alloy 600 a value of 10 to 20 C/cm^2 is used. Alloy 82 is higher in chromium than alloys 600 or 182 and has less tendency to sensitize; thus an equivalent EPR of 0 to 5 C/cm^2 is justified for the as-welded condition, and 5 to 10 C/cm^2 is appropriate for the postweld heat-treated condition. Clearly, more work is needed to evolve a test to quantify the grain boundary compositional effects in nickel alloys.

- Both alloy systems involve ductile face-centered cubic (fcc) structures with similar mechanical properties. Thus, it is reasonable, in preliminary model derivations, to use the same crack tip strain rate algorithms for ductile nickel-base alloys as for stainless steels.
- The solubilities of the (NiCr) oxides and (FeCr) oxides are similar in BWR water at 288°C, and thus from an electrochemical viewpoint the rate-determining steps in the bare surface oxidation kinetics are likely to be comparable for the nickel-base and austenitic stainless steel systems. Thus, it is to be expected that the i_0, t_0 and n values in Eq. (5) will be similar in the

Copyright © 2002 Marcel Dekker, Inc.

two systems and, hence, the general propagation Eq. (11) can be used for nickel-base alloys.

- Studies show that the cracking responses of sensitized alloy 600/182 and sensitized stainless steel are very similar as a function of temperature [124] and water chemistry [125].

Despite these assumptions, the prediction capabilities are in remarkably good agreement with the observations of stress corrosion and corrosion fatigue in the nickel-base alloy/BWR systems. For instance, the observed crack propagation rate–stress intensity data for alloys 182 and 600 are in reasonable agreement with the theoretical predictions for a variety of conductivities in 288°C water containing 200 ppb oxygen (Fig. 27). Similarly, the dependence of the crack propagation rate on the BWR water conductivity is accurately predicted for 1TCT specimens of alloy 182 exposed to BWR recirculation water (Fig. 28). Finally, the incidence of cracking of alloy 600 shroud head bolts as a function of average plant conductivity is also predicted with reasonably accuracy (Fig. 29).

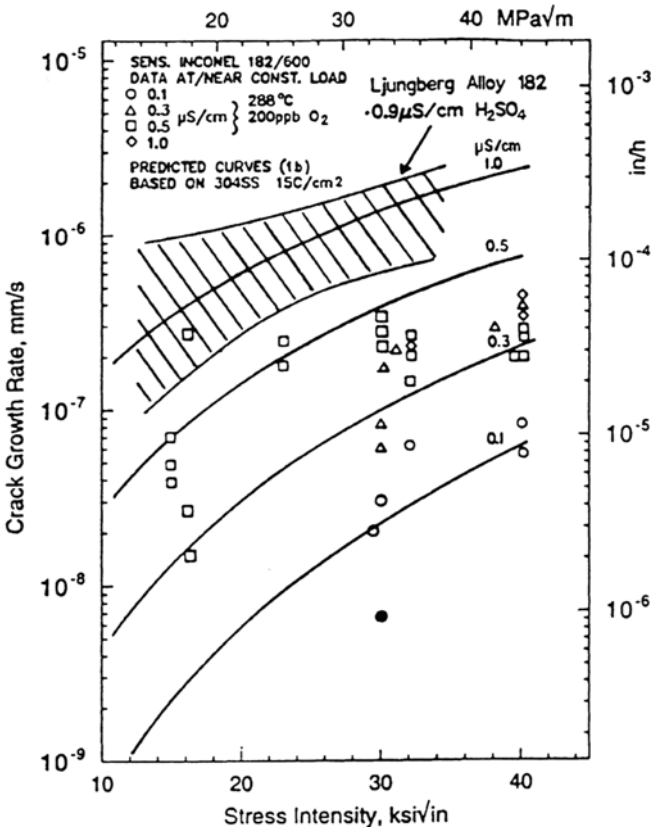


Figure 27 Plot of crack propagation rate vs. stress intensity showing a comparison of the predicted and observed crack growth rates for data on alloy 600 and alloy 182 weld metal tested at or near constant load in 288°C water containing 200 ppb oxygen.

Copyright © 2002 Marcel Dekker, Inc.

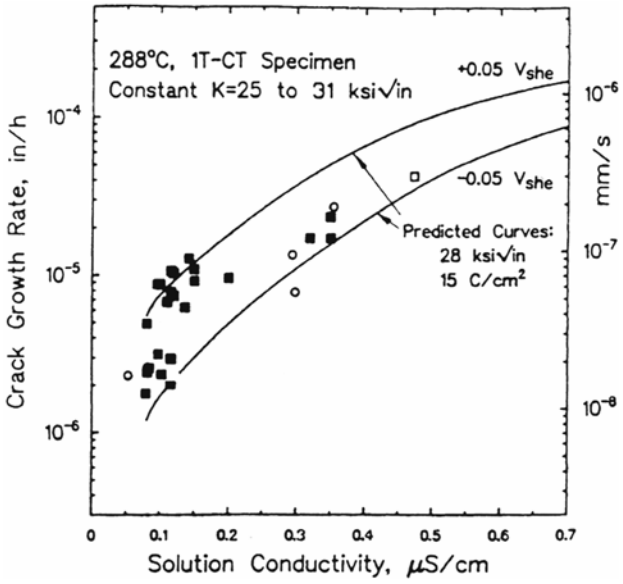


Figure 28 Comparison of the predicted and observed crack growth rates vs. solution conductivity for in-plant GE "CAVS" data on alloy 182 weld metal tested at constant load in BWR water of varying chemistry (corrosion potential).

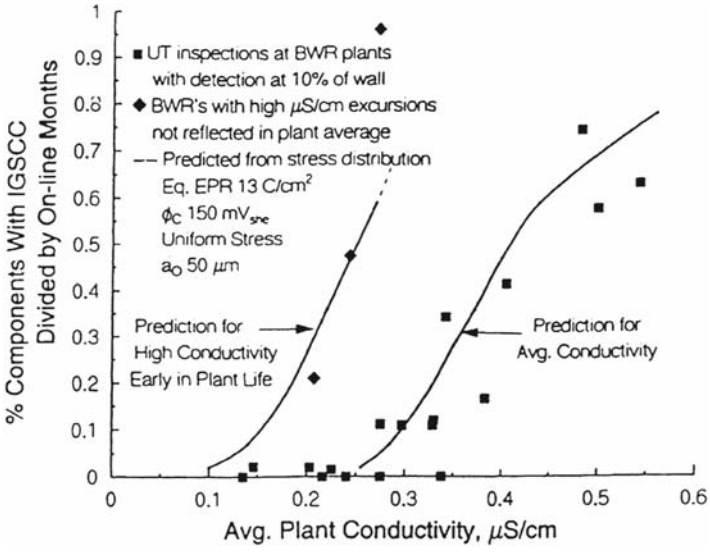


Figure 29 Predicted and observed effects of average plant water purity on crack incidence in field correlations of creviced alloy 600 shroud head bolts.

Copyright © 2002 Marcel Dekker, Inc.

Pressurized-Water Reactor Systems

A variety of factors distinguish most PWR systems from BWRs. On the primary side of commercial PWRs, additions of about 1000 ppm H_3BO_3, several ppm LiOH, and more than 1 atmosphere of hydrogen are commonly made. The H_3BO_3 and LiOH levels are shifted throughout the fuel cycle and provide an elevated, buffered pH. The higher pH coupled with the hydrogen addition (which suppresses radiolysis) yields low corrosion potentials (e.g., –700 to –950 mV_{she}) and dramatically reduces or eliminates the potential gradient in the crack which drives the anion concentration and pH-shifting mechanism in BWR environments. On the secondary side, allvolatile treatments (AVTs) are generally used, which also tend to produce low corrosion potentials. However, there is a possibility for elevated corrosion potentials from oxygen in-leakage and the presence of reducible copper ions. In addition, the presence of sludge piles and thermal gradients in the steam generator provides an opportunity for significant shifts in local chemistry on the secondary side.

Regardless of these chemistry differences, however, PWRs and BWRs do not represent fundamentally different systems in terms of the concepts or modeling of crack propagation. For example, the crack enclave in either case is fully deaerated. Also, the presence of crack enclave potential gradients does not play a necessary or fundamental role in environmentally assisted cracking, in that high crack propagation rates have been observed in fully deaerated water if it is sufficiently acidic or basic [70]. Metallurgical effects also follow a continuum, in that the minimal importance of grain boundary chromium depletion observed in PWR environments also applies to BWRs where the potential is lowered (e.g., due to hydrogen water chemistry) or the crack tip pH is maintained near neutral. In PWRs other depassivation mechanisms can come into play; e.g., at higher pH values the presence of sulfide (or other forms of sulfur that can reduce to sulfide) above ≈ 100 ppm inhibits repassivation.

Unfortunately, few crack propagation rate data have been generated in PWR systems; much more focus has been placed on various types of U-bend specimens. Preliminary efforts [126] indicate that the crack growth data in PWR environments are accurately predicted using the same modeling methodology. Given the similarity in alloys, temperature, (crack tip) environments, etc., this is not surprising, unless one insists that cracks propagate by fundamentally different mechanisms (e.g., slip dissolution in BWR and hydrogen embrittlement in PWR systems).

CONCLUSIONS

A summary was presented of the unique characteristics of environmentally assisted cracking of structural materials in high-temperature, dilute aqueous environment systems associated with LWR operation. Candidate mechanisms of environmental crack advance were discussed, and quantification and use of the slip dissolution model were presented. The predictive model was shown to be quantitatively accurate for the stainless steel–BWR water system. Extensions to address the special characteristics of irradiation, nickel-base alloys, low-alloy and carbon steels, and PWR environments were also presented. The advantage over existing, mechanics-based codes of quantitative, fundamental models of environmentally assisted crack propagation in addressing the design and life evaluation issues was also highlighted.

Copyright © 2002 Marcel Dekker, Inc.

REFERENCES

1. F. P. Ford, D. F. Taylor, P. L. Andresen, and R. G. Ballinger, Corrosion assisted cracking of stainless steel & low alloy steels in LWR environments, Report NP5064S, EPRI, Palo Alto, February 1987.
2. F. P. Ford, P. L. Andresen, M. G. Benz, and D. Weinstein, On-line BWR materials monitoring & plant component lifetime prediction, Proceedings, Nuclear Power Plant Life Extension, Snowbird, Utah, American Nuclear Society, June 1988, Vol. 1, pp. 355–366.
3. S. Suresh and R. Ritchie, The propagation of short fatigue cracks, Univ. of California Berkeley Report UCB/RP/83/1014, June 1983.
4. J. Lankford, *Fatigue Eng. Mater. Struct. 6*: 15 (1983).
5. S. Pearson, *Eng. Fracture Mech. 7*: 235 (1975).
6. W. L. Morris, O. Buck, and H. L. Marcus, *Metall. Trans. A 74*: 1161 (1976).
7. M. H. El Haddad, T. H. Topper, and B. Mukherjee, *J. Test Eval. 9*: 65 (1981).
8. R. N. Parkins, *Corrosion 43*: 130 (1987).
9. R. N. Parkins and P. M. Singh, *Corrosion 46*: 485–498 (1990).
10. P. L. Andersen, I. P. Vasatis, and F. P. Ford, Behavior of short cracks in stainless steel at 288C, Paper 495, NACE Conference, Las Vegas, April 1990.
11. F. P. Ford, Mechanisms of environmental cracking peculiar to the power generation industry, Report NP2589, EPRI, Palo Alto, September 1982.
12. F. P. Ford, Stress corrosion cracking, *Corrosion Processes* (R. N. Parkins, ed.), Applied Science, 1982.
13. R. N. Parkins, N. J. H. Holroyd, and R. R. Fessler, *Corrosion 34*: 253 (1978).
14. T. P. Hoar and G. P. Rothwell, *Electrochem. Acta 15*: 1037 (1976).
15. T. R. Beck, *Corrosion 30*: 408 (1974).
16. C. Manfred, I. Maier, and J. R. Galvale, *Corros. Sci. 27*: 887 (1987).
17. J. M. Sutcliff, R. R. Fessler, W. K. Boyd, and R. N. Parkins, *Corrosion 28*: 313 (1972).
18. B. Poulson and R. Robinson, *Corros. Sci. 20*: 707 (1980).
19. F. P. Ford, BWR environmental cracking margins in carbon steel piping, Final Report, Contract RP1248-1, EPRI, Palo Alto, 1981.
20. A. R. C. Westwood and N. S. Stoloff, eds., *Environmental Sensitive Mechanical Behavior,* Gordon & Branch, Baltimore, 1965.
21. R. W. Staehle, A. J. Forty, and D. VanRooyen, eds., *Fundamental Aspects of Stress Corrosion Cracking,* Ohio State Univ., NACE, Houston, 1967.
22. J. C. Scully, ed., *Theory of Stress Corrosion Cracking*, Ericera, Portugal, NATO, Brussels, 1971.
23. O. Devereaux, A. J. McEvily, and R. W. Staehle, ed., *Corrosion Fatigue Chemistry, Mechanics and Microstructure*, Univ. of Connecticut, Storrs, June 1971, NACE, Houston, 1972.
24. M. P. Bastein, ed., *L'Hydrogene dans les metaux*, Science et Industrie, Paris, 1972.
25. I. M. Bernstein and W. W. Thompson, eds., *Hydrogen in Metals*, ASM, Metals Park, OH, 1973.
26. R. W. Staehle, J. Hochmann, R. D. McCright, and J. E. Slater, eds., *Stress Corrosion Cracking and Hydrogen Embrittlement of Iron-Base Alloys*, Firminy, France, June 1973, NACE, Houston, 1977.
27. A. W. Thompson and I. M. Bernstein, eds., *Effect of Hydrogen on Behavior of Materials*, Jackson Lake, Wyoming, AIME, September 1975.
28. R. M. Latanision and J. T. Fourie, eds., *Surface Effects on Crystal Plasticity, Hohegeiss, Germany, September 1975*, Noordhof-Leyden, 1977.
29. P. R. Swann, F. P. Ford, and A. R. C. Westwood, eds., *Mechanisms of Environment Sensitive Cracking of Materials*, University of Surrey, UK, The Metals Society, April 1977.

Copyright © 2002 Marcel Dekker, Inc.

30. Corrosion fatigue, University of Newcastle, *Metal. Sci. 13*: (1979).
31. Proceedings of First International Conference on "Environment Induced Cracking of Metals," Kohler, Wisconsin, NACE, October 1988.
32. R. N. Parkins, *Br. Corros. J. 7*: 15 (1972).
33. R. N. Parkins and B. S. Greenwell, *Metal. Sci. 405*: (1977).
34. C. Laird and D. J. Duquette, *Surface Effects on Crystal Plasticity*, Hohegeiss, Germany, September 1975 (R. M. Latanision and J. T. Fourie, eds.), Noordhof, Leyden, 1977, p. 88.
35. R. N. Parkins, Environment sensitive fracture—controlling parameters, Proceedings of 3rd International Conference on Mechanical Behavior of Materials, Cambridge, August 20–24, 1979 (K. J. Miller and R. F. Smith, eds.), Pergamon, New York, 1980, Vol. 1, pp. 139–164.
36. J. M. Kraft and J. H. Mulherin, *Trans. ASM 62*: 64 (1969).
37. T. P. Hoar, *Corrosion 19*: 331 (1963).
38. P. R. Swann, *Corrosion 19*: 102 (1963).
39. T. R. Beck, *Corrosion 30*: 408 (1974).
40. H. L. Logan, *J. Natl. Bur. Stand. 48*: 99 (1952).
41. R. W. Staehle, *Theory of Stress Corrosion Cracking*, Ericera, Portugal (J. C. Scully, ed.), NATO, Brussels, 1971, p. 223.
42. J. C. Scully, *Corros. Sci. 8*: 771 (1968).
43. T. P. Hoar, *Theory of Stress Corrosion Cracking,* Ericera, Portugal (J. C. Scully, ed.), NATO, Brussels, 1971; p. 106.
44. D. A. Vermilyea, *J. Electrochem. Soc. 119*: 405 (1972).
45. F. P. Ford, The crack tip system and its relevance to the prediction of environmentally assisted cracking, Proceedings of First International Conference on "Environment Induced Cracking of Metals," Kohler, Wisconsin, NACE, October 1988, p. 139–166.
46. J. Hickling, Strain induced corrosion cracking; relationship to stress corrosion cracking/corrosion fatigue and importance for nuclear plant service life," 3rd IAEA Specialists Meeting on Subcritical Crack Growth, Moscow, May 1990.
47. K. Sieradzki and R. C. Newman, *Philos. Mag. A51*: 95–132 (1985).
48. C. Edeleanu and A. J. Forty, *Philos. Mag. 5*: 1029 (1960).
49. J. A. Beavers and E. N. Pugh, *Metall. Trans. 11A*: 809 (1980).
50. K. Sieradzki, Atomistic and micromechanical aspects of environment induced cracking of metals, Proceedings of First International Conference on "Environment Induced Cracking of Metals," Kohler, Wisconsin, NACE, October 1988, pp. 125–138.
51. R. C. Newman, Stress corrosion of austenitic steels, Proceedings of First International Conference on "Environment Induced Cracking of Metals," Kohler, Wisconsin, NACE, October 1988, pp. 489–510.
52. A. W. Thompson and I. M. Bernstein, The role of metallurgical variables in hydrogen assisted environmental fracture, Rockwell Science Center Report SCPP-75–63, 1975.
53. J. P. Hirth, *Metall. Trans. 11A*: 861–890 (1980).
54. H. G. Nelson, Hydr ogen embrittlement, *Treatise on Material Science and Technology*, Vol. 25 (C. L. Briant and S. K. Banerji, eds.), Academic Press, New York, 1983, pp. 275–359.
55. H. K. Birnbaum, Hydrogen embrittlement, Proceedings of First International Conference on "Environment Induced Cracking of Metals," Kohler, Wisconsin, NACE, October 1988, pp. 21–29.
56. F. P. Ford, *Metal Sci.,* July: 326–334 (1978).
57. R. Raj and V. K. Varadan, The kinetics of hydrogen assisted crack growth, *Mechanisms of Environment Sensitive Cracking of Materials*, Univ. of Surrey, UK (P. R. Swann, F. P. Ford, and A. R. C. Westwood, eds.), The Metals Society, April 1977, p. 426.

Copyright © 2002 Marcel Dekker, Inc.

58. R. A. Oriani, Hydrogen effects in high strength steels, Proceedings of First International Conference on "Environment Induced Cracking of Metals," Kohler, Wisconsin, NACE, October 1988, pp. 439–448.
59. R. A. Oriani, *Bert. Bunsenges Phys. Chem. 76*: 848 (1972).
60. W. W. Gerberich, Y. T. Chen, and C. St. John, *Metall. Trans. 6*: 1485 (1975).
61. F. de Kazinski, *J. Iron Steel Inst. 177*: 85 (1954).
62. C. A. Zapffe and C. E. Sims, *Trans. AIME 145*: 225 (1941).
63. C. D. Beachem, *Metall. Trans. 3*: 437 (1972).
64. S. P. Lynch, *Met. Forum 2*: 189 (1979).
65. R. A. Gilman, The role of surface hydrides in stress corrosion cracking, *Stress Corrosion Cracking and Hydrogen Embrittlement of Iron-Base Alloys*, Firminy, France, June 1973 (R. W. Staehle, J. Hochmann, R. D. McCright, and J. E. Salter, eds.), NACE, Houston, 1977, p. 326.
66. C. L. Briant, *Metall. Trans. 10A*: 181 (1979).
67. H. Hanninen, K. Torronen, M. Kempainen, and S. Salonen, *Corros. Sci. 23*: 663 (1983).
68. K. Torronen, M. Kemppainen, and H. Hannine, Fractographic evaluation of specimens of A533B pressure vessel steel, Final Report of EPRI Contract RP1325-7, Report NP 3483, May 1984.
69. W. R. Wearmouth, G. P. Dean and R. N. Parkins, *Corrosion 29*: 251 (1973).
70. P. L. Andresen, Modeling of water and material chemistry effects on crack tip chemistry and resulting crack growth kinetics, Proceedings 3rd International Conference on Environmental Degradation of Materials in Nuclear Power Systems—Water Reactors, Traverse City, AIME, 1987, pp. 301–314.
71. D. F. Taylor and C. A. Caramihas, High temperature aqueous crevice corrosion in alloy 600 and 304L stainless steel, Proceedings of "Embrittlement by Localized Crack Environment," AIME/ASM Symposium, Philadelphia, (R. Gangloff, ed.), October 1983, pp. 105–114.
72. D. F. Taylor and C. C. Foust, *Corrosion 44*: 204–208 (1988).
73. G. Gabetta and G. Buzzanaca, Measurement of corrosion potential inside and outside growing crack during environmental fatigue tests, Proceedings of 2nd International IAEA Specialists Meeting on Subcritical Crack Growth, NUREG CP0067, Vol. 2, Sendai, Japan, May 1985, pp. 219–230.
74. P. Combrade, M. Foucault, and G. Slama, About the crack tip environment chemistry in pressure vessel steel exposed to primary PWR coolant, Proceedings of 2nd International IAEA Specialists Meeting on Subcritical Crack Growth, NUREG CP0067, Vol. 2, Sendai, Japan, May 1985, pp. 201–218.
75. A. Turnbull, *Rev, Coatings Corros. 5*: 43–171 (1982).
76. A. Turnbull, *Corros. Sci. 23*: 833–870 (1983).
77. A. Turnbull, Progress in the understanding of the electrochemistry in cracks, as Ref. 71. pp. 3–31.
78. P. L. Andresen, Transition and delay time behavior of high temperature crack propagation rates resulting from water chemistry changes, Proceedings, Second International Symposium on Environmental Degradation of Materials in Nuclear Power Systems—Water Reactors, American Nuclear Society 1986, p. 84–92.
79. F. P. Ford and P. L. Andresen, Stress corrosion cracking of low alloy steels in 288°C water, Paper 498, Corrosion/89, NACE, 1989.
80. P. L. Andresen and L. M. Young, Crack tip chemistry measurements in low alloy steel in high temperature water, MnS Workshop, August 9, 1993, Babcock & Wilcox, Alliance, OH. Submitted to *Corros. J.*
81. S. M. Bruemmer, L. A. Charlot, and B. W. Arey, *Corrosion 44*: 328–333 (1988).
82. S. M. Bruemmer, L. A. Charlot, and D. G. Atteridge, *Corrosion 44*: 427–434 (1988).

Copyright © 2002 Marcel Dekker, Inc.

83. K. L. Luthra and C. L. Briant, *Metall. Trans. A. 19*: 1091–2108 (1988).
84. G. S. Was and V. B. Rajan, *Corrosion 43*: 576 (1987).
85. T. M. Devine, *Acta Metall. 36*: 1491 (1988).
86. Proceedings of Symposium on "Radiation Induced Sensitization of Stainless Steels," CEGB, Berkeley Nuclear Laboratories (D. I. R. Norris, ed.), September 1986.
87. T. P. Hoar and F. P. Ford, *J. Electrochem. Soc. 120*: 1013 (1973).
88. P. Combrade, Prediction of environmental crack growth on reactor pressure vessels, EPRI Contract RP2006-8, UNIREC Report 1667, February 1985.
89. D. Engseth and J. C. Scully, *Corros. Sci. 15*: 505 (1975).
90. T. Zakroczmski and R. N. Parkins, *Corros. Sci. 20*: 723 (1980).
91. Y. S. Park, J. R. Galvele, A. K. Agrawal, and R. W. Staehle, *Corrosion 34*: 413 (1978).
92. R. B. Diegle and D. A. Vermilyea, *J. Electrochem. Soc. 122*: 180 (1975).
93. F. P. Ford and M. Silverman, *Corrosion 36*: 558–565 (1980).
94. T. R. Beck, *Corrosion 30*: 408 (1974).
95. R. P. Wei and A. Alavi, *Scripta Met. 22*: 969–974 (1988).
96. C. Patel, *Corros. Sci. 21*: 145 (1981).
97. F. P. Ford, G. T. Burstein, and T. P. Hoar, *J. Electrochem. Soc. 127*: 6 (1980).
98. T. Hagyard and W. B. Earl, *J. Electrochem. Soc. 115*: 623 (1968).
99. J. Pagetti, D. Lees, F. P. Ford, and T. Hoar, *C. R. Acad. Sci. Paris 273*: 1121 (1971).
100. D. J. Lees and T. P. Hoar, *Corros. Sci. 20*: 723 (1980).
101. R. C. Newman and G. T. Burstein, *Corros. Sci. 21*: 119 (1981).
102. R. B. Diegle and D. M. Lineman, *J. Electrochem. Soc. 131*: 106 (1984).
103. J. R. Ambrose and J. Kruger, *Corrosion 28*: 30 (1972).
104. Z. Szklarski-Smialowska and W. Kozlowski, *J. Electrochem. Soc. 131*: 234 (1984).
105. B. McDougall, *J. Electrochem. Soc. 130*: 114 (1983).
106. G. M. Bulman and A. C. C. Tseung, *Corros. Sci. 12*: 415 (1972).
107. A. T. Cole and R. C. Newman, *Corros. Sci. 28*: 109–118 (1988).
108. M. Cid, M. Puiggali, H. Fatmaoui, and M. Petit, *Corros. Sci. 28*: 61–68 (1988).
109. P. Hurst (UKAEA Risley), private communication, Vasteras, Sweden, June 1988.
110. R. W. Staehle, J. J. Royuela, T. L. Raredon, E. Serrate, C. R. Morin, and R. V. Ferrar, *Corrosion 26*: 451 (1970).
111. R. N. Parkins, G. P. Marsh, and J. T. Evans, Strain rate effects in environment sensitive fracture, Proceedings of EPRI Conference on "Predictive Methods for Assessing Corrosion Damage to BWR Piping and PWR Steam Generators," Mt. Fuji, Japan, May/June 1978 (H. Okada and R. Staehle, eds.), NACE, Houston, 1982.
112. D. P. G. Lidbury, "The Estimation of Crack Tip Strain Rate Parameters Characterizing Environment Assisted Crack Data", Proceedings of "Embrittlement by Localized Crack Environment", AIME/ASM Symposium, Philadelphia, (Ed. R. Gangloff), pp. 149–172, October 1983.
113. F. P. Ford, *J. Pressure Vessel Technol. 1*: 113 (1988).
114. P. L. Andresen, F. P. Ford, S. M. Murphy, and J. M. Perks, State of knowledge of radiation effects on environmental cracking in light water reactor core material, Proceedings of 4th International Conference on "Environmental Degradation of Materials in Nuclear Power Systems—Water Reactors," Jekyll Island, NACE, Houston, 1990, pp. 1–83 to 1–121.
115. Proceedings of the First International Atomic Energy Agency Specialists Meeting on Subcritical Crack Growth, Vol. 1,2 Freiberg, Germany, NUREG CP-0044, May 13–15, 1981.
116. Proceedings of Second International Atomic Energy Agency Specialists Meeting on Subcritical Crack Growth, Vol. 1,2 Sendai, Japan, NUREG CP-0067, May 15–17, 1985.

Copyright © 2002 Marcel Dekker, Inc.

117. Proceedings of Third International Atomic Energy Agency Specialists Meeting on Subcritical Crack Growth, Moscow, USSR, NUREG/CP 0112, May 1990.
118. F. P. Ford and P. L. Andresen, Corrosion fatigue of pressure boundary materials, Manuscript 1571, 7th International Conference on Fracture, Houston (K. Salama et al., eds.), ISBN 0-08-034343-0, Vol. 2, March 1989, pp. 1571–1583.
119. F. P. Ford, Prediction of corrosion fatigue initiation in low alloy and carbon steel water systems at 288C, Proceedings of 6th International Conference for Environmental Degradation of Materials in Nuclear Power Systems—Water Reactors, San Diego, TMS, 1993.
120. P. L. Andresen, *Corrosion 44*: 376 (1988).
121. M. Higuchi and K. Iida, *Nucl. Eng. Des. 129*: 293–306 (1991).
122. W. Shack et al., Environmentally assisted cracking in LWR, NUREG/CR 4667, Vol. 14, Semiannual Report, October 1991–March 1992, pp. 4–13.
123. W. Shack, Presentation to ASME PVRC Meeting, New York, October 13, 1992.
124. P. L. Andresen, Effects of temperature on crack growth rates of stainless steel and alloy 600, *Corrosion 49*: 714–725 (1993).
125. P. L. Andresen, Fracture mechanics data & modeling of environmental cracking of nickel-base alloys in high temperature water, *Corrosion 47*: 917–938 (1991).
126. C. D. Thompson, N. Lewis, and H. Drasodomski, Analysis of A600 and X-750 SCC cracks, Alloy 600 Experts Meeting, Arlie, VA, EPRI, Palo Alto, April 6–9, 1993.

Copyright © 2002 Marcel Dekker, Inc.

18

Corrosion of Microelectronic and Magnetic Data-Storage Devices

Gerald S. Frankel
The Ohio State University, Columbus, Ohio

Jeffrey W. Braithwaite
Sandia National Laboratories, Albuquerque, New Mexico

INTRODUCTION

Technological advances in microelectronic and magnetic-storage devices continue at an incredible rate. For example, over the past 30 years, microprocessor power has doubled every 1 ½ to 2 years. Associated with this performance improvement is the miniaturization of integrated circuit (IC) packaging. The width and separation of conductor lines have been cut in half approximately every 5 years and are now less than 0.5 μm on some devices. Relative to data-storage media, the aerial bit density of thin magnetic films has doubled every 2 years and the separation distance (fly height) between heads and disks has been reduced to ~250 Å. These accomplishments have been coupled with increasingly long service life and more stringent reliability requirements.

Intuitively, because of their general use in relatively benign external environments, the vulnerability of electronic components to corrosion-induced failure could be considered to be less of an issue than that associated with other equipment and structures that are commonly exposed to severe environments (e.g., automobiles, bridges, airplanes, chemical processing, and oil production). However, there are several reasons why corrosion in electronics remains a major reliability concern. First and foremost, corrosion itself can directly cause failure of the device. This first-order result is in contrast to many other corrosion effects in which a material property is degraded and another subsequent process actually causes the failure (e.g., metal thinning that leads to mechanical overload or pitting that breaches housing hermeticity, thus permitting contamination of internal parts). Second, the two main factors needed for significant corrosion vulnerability can certainly exist: susceptible metallic materials and aggressive environments. Metals are selected primarily for their electrical or magnetic properties. Standard approaches to improving corrosion resistance, such as alloying with chromium, are often not possible because of deleterious effects on either these properties or indirectly on the properties of other

Copyright © 2002 Marcel Dekker, Inc.

nearby materials. Moisture and corrosion-enhancing contaminants (e.g., particulate, halogen compounds, oxidants) are almost always present around electronics. The electrical functioning of many devices, such as ICs, can also promote corrosion because metallic lines are often biased electrically relative to nearby lines. Given the dimensions and voltages involved, electric fields can reach in excess of 100,000 V/cm. Finally, the dimensions of the metal features are so small that the allowable loss of material to corrosion can be minuscule. Whereas a car can function with even pounds of metal lost to corrosion, an electronic device may fail after the loss of less than 1 picogram, a factor of 10^{15} smaller!

The ability to predict and control the effects of corrosion on the service life or reliability of electronic devices must be based on a physical understanding of the relevant corrosion processes and controlling mechanisms. The state of knowledge of this key area for microelectronic and magnetic-storage devices is reviewed in this chapter. The microelectronic discussions focus on the primary components of present concern: packaged ICs are component interconnect technologies (printed circuit boards, connectors, and contacts). Corrosion of the other major components of microelectronics—discrete devices (e.g., resistors, diodes, and capacitors) and semiconductor materials—has been observed under certain conditions but is currently not viewed as important. Similarly, the section on magnetic-storage media addresses the most significant reliability concern: high-density data storage.

The body of this chapter is divided into three main sections. Initially, to enable a better understanding of the application of corrosion science to this subject, a very brief description of the hardware technologies and physical structures of these devices is presented. In the subsequent section on microelectronic corrosion, important environmental factors and relevant corrosion mechanisms are discussed. This is followed by an account of the observed impact of these mechanisms on three specific types of microelectronic hardware; finally, the application of accelerated-aging techniques and their effectiveness in qualifying product acceptance and determining reliability are considered. The concluding section addresses corrosion of magnetic data-storage devices.

OVERVIEW OF HARDWARE TECHNOLOGIES

Microelectronic Devices

Integrated Circuits

Metals are used for several functions in integrated circuits. On-chip metal lines provide local interconnection to join a cluster of elements, connect circuit elements globally to far regions on a chip, and provide power and input/output (I/O) signals to the elements [1,2]. Because many of the prime conductor materials form deep levels in the band gap of Si, other metals are sometimes used as diffusion barriers to prevent unwanted doping of the Si. To form dense circuitry on a chip, also called a die, multiple layers of metal are commonly separated by insulating dielectrics layers (referred to as IDLs). Metals form the vias to connect the different layers and also act as thin adhesion layers. Connector lines can be as small as ½ μm wide (but typically are > 1 μm) and from 1 to 1 ½ μm thick. The top metallic layer on the die is protected by a passivation layer that is patterned to expose pads for wirebonding

Copyright © 2002 Marcel Dekker, Inc.

(~100 μm square). A schematic view of these general features and structures is shown in Figure 1.

The most common materials used for conductors are aluminum-based alloys, which typically contain small amounts of Si to reduce interdiffusion with the substrate and Cu to strengthen the metal and limit electromigration. Passivation layers are often sputter-deposited SiO_2, chemical-vapor-deposited (CVD) phosphosilicate glasses (that provide better coverage), and plasma-deposited silicon nitride. For corrosion engineers, this passivation layer should not be confused with the intrinsic oxide layer that protects many engineering alloys. Patterning of the Al lines is often achieved by subtractive techniques such as wet chemical etching or reactive ion etching (RIE). Metal selection is sometimes dictated by processing requirements. For example, tungsten metallization has been used because it can be deposited by a selective CVD process in which deposition occurs selectively on metal surfaces. Thus, high-aspect-ratio holes can be filled, an important consideration as the line widths continue to shrink. Refractory metals, such as tungsten, are also used as an underlying diffusion barrier. With the decreasing dimensions of very large scale integration (VLSI) devices, the on-chip interconnections account for an increasingly large fraction of the total circuit delay time. As a result, there has been a trend to more conductive metals and lower dielectric insulators. Recently, IBM pioneered the development and implementation of technology that permits the use of copper conductors in state-of-the art IC devices [3].

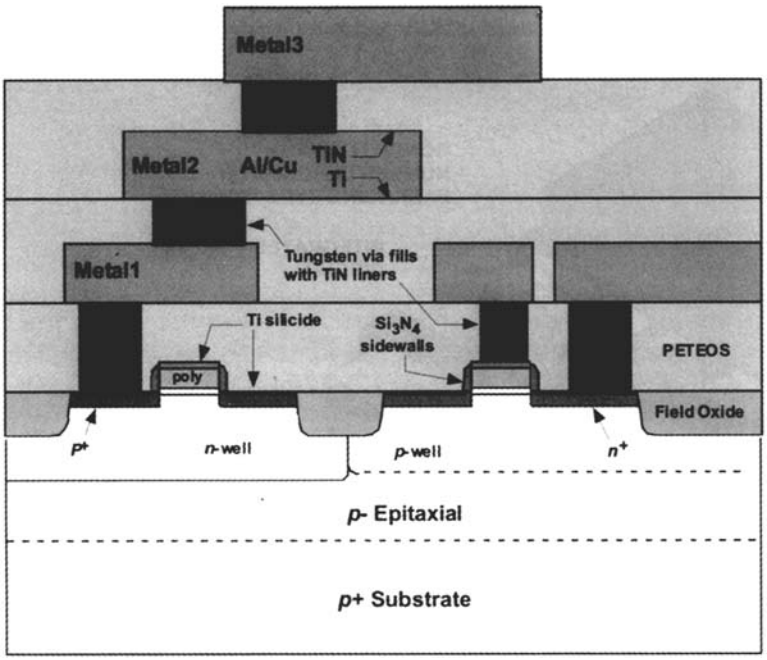


Figure 1 Interconnection structure of typical submicrometer integrated circuit technology that implements chemical-mechanical polished (CMP) planarized dielectric layers.

Copyright © 2002 Marcel Dekker, Inc.

IC Packaging

Electronic components (e.g., computer mainboard or motor controller) typically use a multiple-level packaging hierarchy to ensure proper power and signal distribution among the various discrete devices [1,4,5]. The core, or first level of packaging, is within the IC itself [6]. Besides permitting electrical communication to the outside, secondary packaging roles include providing robust mechanical support and environmental protection to the chip. Two general types of IC packaging technology exist: ceramic-hermetic package (CHP) and plastic-encapsulated microelectronics (PEM). As the terminology implies, CHP devices have ceramic bodies and the chip enclosure is hermetically sealed, normally by welding, brazing, or glassing on a metal or ceramic lid. Hence, the chip environment can be tightly controlled. This technology was dominant 25 years ago and is still preferred by many for high-reliability applications. With PEM technology, the chip is attached to a metal support/lead frame fixture and the entire assembly is encapsulated with a plastic molding compound (Fig. 2 [7]). The molding material is usually a water-permeable polymer such as epoxy or silicone that is filled with inorganic particles. The encapsulant material is normally injection molded but can also be cast as a liquid (glob). Initially, PEM devices were considered unreliable because of corrosion and encapsulant cracking/delamination issues [8]. However, substantial technological improvements have been made over the past 20+ years to the point that their reduced cost, size, and weight; improved reliability; and now high level of availability have pushed the PEM worldwide market share to over 97% [9]. An excellent detailed description of the PEM technology and its application is available [9].

The exposed pads on the chip top-level passivation windows are connected to fingers on the metallic lead frame with fine 25-μm Au or Al wire (Cu or Ag is

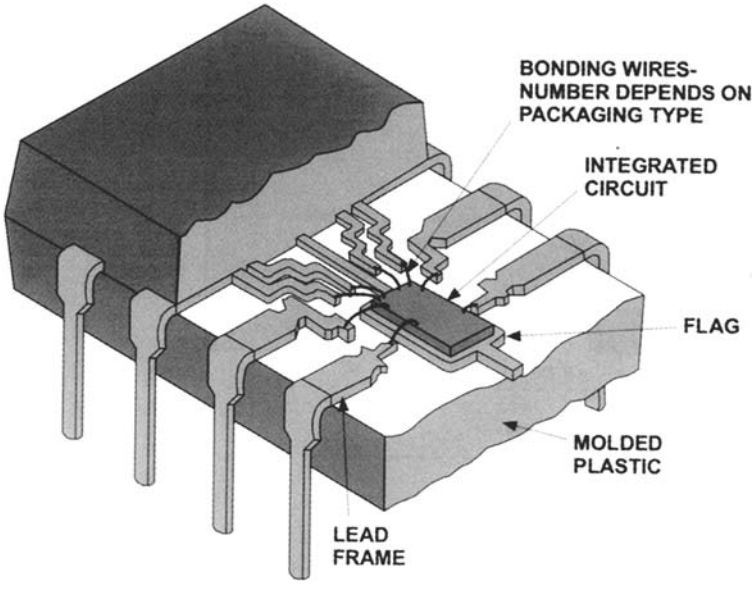


Figure 2 Sectioned schematic view of a typical plastic-encapsulated integrated circuit. (From Ref. 7 with permission from General Electric Co. Copyright 1984 by RCA.)

Copyright © 2002 Marcel Dekker, Inc.

sometimes also used) by a solid-state wirebonding process using thermocompression and/or ultrasonic welding [9,10]. The lead frame, which also forms the external, board-level interconnects, is usually made from an Ni-Fe alloy, Cu alloy, or Cu-clad stainless steel. As with discrete connectors, the bare frame is usually given an Ni or Ni-Co strike and then plated with Au, Ag, or Pd for improved corrosion resistance and reduced contact resistance [9].

Tape automated bonding (TAB) and controlled collapse chip connection (C4) are two other common first-level packaging technologies that allow increased I/O density compared with wirebonding in molded plastic packages. In TAB, chips are thermocompression bonded to the inside ends of radially patterned metal leads on polymer tape. The outside ends of the leads are then soldered to a second-level package and the chip is covered with an encapsulant, so the reliability concerns are similar to those of PEM devices. In C4 bonding, an array of solder bumps deposited on a chip is joined to a matching array of pads on the substrate. This technology, which allows maximum I/O density, has been used primarily in hermetic high-end applications but is now becoming popular in low-end, nonhermetic applications.

Macro Interconnects

Functional electrical circuits are formed by interconnecting packaged ICs with other devices using printed circuit boards (PCB). These boards can be viewed as second-level packaging. Individual devices are attached to the PCB using some form of automated or manual soldering process [9]. PbSn alloys are still the predominant choice for solder, although more environmentally compatible alternatives are emerging. The conducting lines on PCBs are normally made from copper and are protected with an Sn or SnPb plating, an organic coating, or an inorganic passivation layer. Often, a protective, organic-based conformal coating (e.g., acrylic, polyurethane, epoxy, or silicone based) is applied to the entire board to ensure cleanliness and reduce direct exposure to the external environment [9].

Low-force, low-voltage separable connectors and contacts also have wide use in electronic systems [11,12]. A variety of different configurations exist, but the substrate of most is made from copper, brass, bronze, or copper-beryllium. The use of copper alloys ensures some susceptibility to environmental degradation. To reduce interfacial resistance and corrosion, the substrate is plated with a nickel diffusion barrier and then with a precious metal (e.g., gold, palladium) [11,13]. However, a trade-off exists between plating cost (thickness) and reliability [14]. Hence, physical defects (pores and cracks) are usually present. In the past, connectors and contacts could not be coated because of interference with their function, although some new coating inhibition formulations have been developed for this purpose [11,12].

Magnetic-Storage Components

All computers, from mainframes to portables, use some form of technology for long-term data storage and retrieval. This chapter focuses on corrosion in high-performance magnetic disk storage because this technology is extensively used and has significant vulnerability to corrosion. The primary material components of a disk drive are the disk, which has a hard magnetic layer that stores the information, and a head, which uses a soft magnetic material to write and read the information to and

Copyright © 2002 Marcel Dekker, Inc.

from the disk. In obsolete hard drive technology and current low-end devices such as floppy drives, both heads and disks are made from ceramic materials such as ferrites and iron oxide, so corrosion is not a concern. In the past 25 years, however, technological advances in the field of magnetic recording that have driven the improvements in performance have also introduced metals to both disks and heads. As a result, the components in disk drives are now susceptible to failure by corrosion. An excellent review of magnetic-storage technology is contained in the book my Mee and Daniel [15].

State-of-the-art hard disk drives use thin-film metal disks as a storage medium. A typical thin-film disk structure is shown in Figure 3a. The magnetic layer is a Co-based alloy that is on the order of hundreds of angstroms thick and is underneath a very thin overcoat layer that is often sputtered carbon. This carbon overcoat (COC) layer as drawn in Figure 3a should be an effective barrier to corrosion because it physically separates the metallic layers from the environment. In practice, the COC and thus the disk is also covered with a thin layer of lubricant that can further reduce corrosion by repelling and/or displacing water. However, Figure 3a is idealistic in that the layers are not smooth and the carbon overcoat does not completely cover

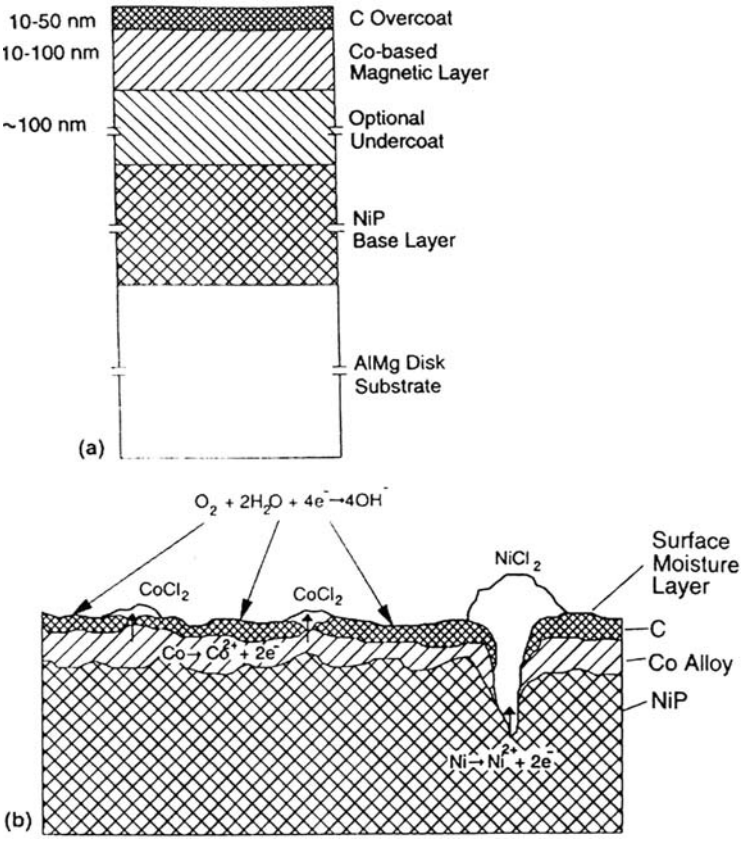


Figure 3 (a) Schematic representation of thin-film disk structure. (b) Schematic view of corrosion of roughened disk structure in a chloride-contaminated environment.

Copyright © 2002 Marcel Dekker, Inc.

the underlying metallic layers. A more realistic view is given in Figure 3b. The NiP base layer is intentionally roughened or "textured" to reduce sticking of the head to the disk when the drive is turned on. The magnitude of this texturing or roughness can be comparable to the thickness of the COC. As a result, the thin COC is often unable to cover completely and seal the underlying layers, thereby exposing susceptible metals to the environment. The corrosion that occurs can result in the formation of relatively large corrosion product deposits on the disk surface. The collision of heads with these corrosion deposits on the surfaces of spinning disks can cause head misalignment and disk failure. Such head "crashes" typically occur in practice long before the corrosion process causes a significant information error rate.

Several configurations of recording heads are used in disk drives. Thin-film inductive heads are standard components consisting of miniaturized horseshoe electromagnets manufactured by wafer-level fabrication techniques. These devices had been used for both reading and writing. Now they are used primarily as write elements that are combined with more sensitive sensors for reading data. The device is imbedded in an insulator, such as sputtered alumina. It is thus protected from the environment, except for the two ends of the pole piece (pole tips) and gold bondpads connected to the coil. The pole piece is often made from electroplated permalloy (Ni-20%Fe) and the exposed permalloy pole tips are a few μm^2 in area. As in microelectronics, loss of material from corrosion can have a large influence on such small structures.

The read elements in advanced magnetic heads make use of the magnetoresistance (MR) phenomenon in which the resistance of a material changes as a function of magnetic field. The various types of magnetoresistance that are currently used in magnetic storage devices or under development include, in order of increasing sensitivity, anisotropic magnetoresistance (AMR), giant magnetoresistance (GMR), and colossal magnetoresistance (CMR). At the time of this writing, AMR-based recording heads dominate the market. Enhanced sensitivity devices called spin valves that utilize GMR will be in full mass production by the year 2000. There are several designs for the various MR-type sensors that all contain a stack of numerous thin-film layers, such as Co, Cu, NiFe, and MnFe, each with thickness on the order of several nm [16]. Most MR sensors use antiferromagnetic layers to pin the domains of adjacent soft magnetic layers by exchange coupling, although many AMR devices use a hard magnetic layer instead. MnFe, containing about 50% of each element, is a commonly used antiferromagnetic layer and is extremely corrodible. To be used in a disk drive, a cross section of the thin films in the sensor must be exposed at the device surface. This is achieved by abrasive lapping in an aqueous environment. Lapping is potentially very aggressive because fresh metal area is continually exposed to the aqueous lapping environment. Like disks, MR heads are often covered with a thin carbon overcoat after lapping, and this COC provides corrosion protection once it is in place.

Magneto-optic (MO) recording is another type of data-storage technology that is not as widely used as magnetic storage but poses special corrosion concerns. MO disks are erasable and have very high bit density. Because the disks are removable and thus handled by users, they are exposed to an uncontrolled range of conditions. The active layer in some MO drives is composed of a rare earth–transition metal alloy such as Fe-25Tb and is several hundred angstroms thick. The high Tb content makes these alloys extremely reactive. The MO film is deposited onto glass substrates

Copyright © 2002 Marcel Dekker, Inc.

and then covered with a thin oxide layer and a thin metallic layer as such as Al. Two such substrates sealed back to back with epoxy constitute an MO disk. Moisture can penetrate through the permeable epoxy and cause corrosion of the Al layer or of the MO layer where it is exposed.

MICROELECTRONIC CORROSION

Because corrosion has been and continues to be one of the prime degradation modes observed in microelectronic devices, a significant number of in-depth corrosion studies have been performed during the past two decades and several noteworthy review articles have been written [7,17–23]. For reference and to be consistent with the terminology used in the electronics community, corrosion is defined as the degradation of metallic features resulting from interactions with environments containing water or moisture. An important consideration to remember when assessing some of the historical information that follows is that the microelectronic technology has improved substantially over the years. Many of the early concerns and problems are no longer relevant to modern microelectronics. Also, because microelectronic devices are exposed to atmospheric conditions only during use, much of our existing knowledge of atmospheric corrosion is applicable. This subject is addressed by Leygraf in Chapter 15 of this book. Leygraf and Graedel [24] have written a textbook on atmospheric corrosion. An additional reference is the comprehensive review of this subject was that was compiled by Ailor [25] and contains information on fundamental aspects, behavior of specific metal systems, and testing.

Environmental Factors

Regardless of the type of device or the offending corrosion mechanism, corrosion-induced degradation involves interactions with the environment. The critical factors that must always exist are a susceptible metallization, the presence of moisture, and some type of contaminating ionic species. This subsection describes some of the aspects of the latter two factors common to corrosion of all microelectronic devices.

Water Adsorption

Under noncondensing atmospheric conditions, water adsorbs on metal and metal-oxide surfaces and forms a thin layer. The thickness of the layer ranges from < 1 to tens of monolayers and depends primarily on the relative humidity (RH) and the substrate material [26,27]. At 20% RH, approximately one monolayer exists on average, whereas at 75% RH, the thickness increases to about five monolayers. Often the water layers cluster and so local thicknesses are probably greater. The corrosion rate for most metals is a function of the thickness of the adsorbed water layer and therefore the RH. Usually, the corrosion rate as a function of RH has a sigmoid-shaped response. The critical humidity level above which the corrosion rate significantly accelerates (lower inflection point in sigmoidal curve) ranges from 15 to 90% RH but is typically > 50% and is thought to be the RH at which at least three monolayers of water exist. In general, if the humidity is lower than the critical level, the corrosion rate is minimal and the reaction process is essentially dry (requiring a direct gas-metal ambient-temperature interaction). Above this critical level, the

Copyright © 2002 Marcel Dekker, Inc.

adsorbed water phase becomes "quasi-aqueous" and is thus capable of supporting faster electrochemical charge transfer reactions. The final important water-adsorption aspect is associated with the extremely small physical features found in microelectronics where capillary condensation can occur. Examples include under the lip of a wirebond, between connector surfaces, and in defects in the plastic encapsulant. This condensation phenomenon can produce very bulk-like localized aqueous conditions at humidity levels 100%. A more in-depth description of water adsorption is presented in the chapter on atmospheric corrosion.

The temperature of the device can have a dramatic effect on water adsorption. For a given absolute humidity level, higher surface temperatures result in desorption of water (localized decrease in relative humidity according to the psychrometric law). As noted in the previous paragraph, an associated decrease in the corrosion rate could be produced. For many ICs, these higher temperatures occur when their power is on because of internal ohmic heating. Besides surface desorption, water is also driven out of the package. Ajiki et al. [28] did a benchmark study in 1979 that is still relevant today. They showed that device reliability increases with increasing power dissipation and with an increasing ratio of time on to time off. This correlation is simply due to moisture effects and a related worst-case condition could then be long-term dormant storage [29].

Contamination

Introduction of corrosive contaminants that may result in long-term reliability concerns can occur during manufacturing and/or use. Many of the fabrication process steps involve exposure to aggressive species and can leave corrosive residues. For example, reactive-ion etching (RIE) of Al metallization is performed in plasmas containing combinations of gases such as Cl_2, CCl_4, $CHCl_3$, and BCl_3 [30–36]. If removed untreated from the etcher, patterned structures are covered with high levels of $AlCl_3$, which is hygroscopic and can later form HCl in the presence of moisture. The sidewalls of the patterned photoresist that is used to mask areas that are not to be etched can also retain large amounts of chloride contamination. Other typically benign process solutions, such as deionized (DI) water and organic solvent rinses, can become contaminated over time from process chemical residues [37,38].

In addition, airborne particles or particles that are too small to be filtered out by the best clean room facilities can be deposited on susceptible surfaces. Studies performed at AT&T Bell Laboratories have highlighted the potential role of airborne particles in the corrosion of electronic devices that are relevant to both manufacturing and actual use conditions [20,39,40]. Sinclair [20] has shown that there exist in the environment a large number of fine particles (with aerodynamic diameters of 0.05–2 μm) that are rich in ammonium acid sulfate, derived from anthropogenic sources, and difficult to remove by filtration. Ionic compounds, such as these, often deliquesce above a certain RH level [41,42]. Another significant contaminant that can be introduced during manufacturing is solder flux/residue that may not be completely removed or reacted during PCB soldering operations [43]. Some materials in the microelectronics themselves can be a source of undesired chemical species. For example, plastic epoxy encapsulants can contain a fire-retarding agent that includes an organic bromine compound. Phosphorus is a component in many of the passivation glasses. With time, interaction and leaching with

Copyright © 2002 Marcel Dekker, Inc.

adsorbed moisture can produce corrosive species such as bromide salts or phosphoric acid [10,17].

Leygraf, in the chapter on atmospheric corrosion, discusses the environmental differences between indoor and outdoor exposure conditions and why these differences are important to corrosion of electronics. Although the service environments for electronic devices are typically less severe than for many other types of equipment, industrial atmospheres do contain harmful oxidizing (e.g., Cl_2, SO_2, NO_x) and halide-containing (e.g., NaCl) species that can diffuse or migrate to microelectronic metallization, especially over an extended service life. Because of the importance of contamination control, techniques to quantify microscopic levels on have been developed [30,44].

Mechanisms

Because of the wide range of possible environments and the large number of metallic materials used in microelectronic devices, corrosion occurs by a number of different physical mechanisms that can be grouped into two general categories: those driven by the application of an applied potential (under electrical bias) and those occurring under static (open-circuit) conditions.

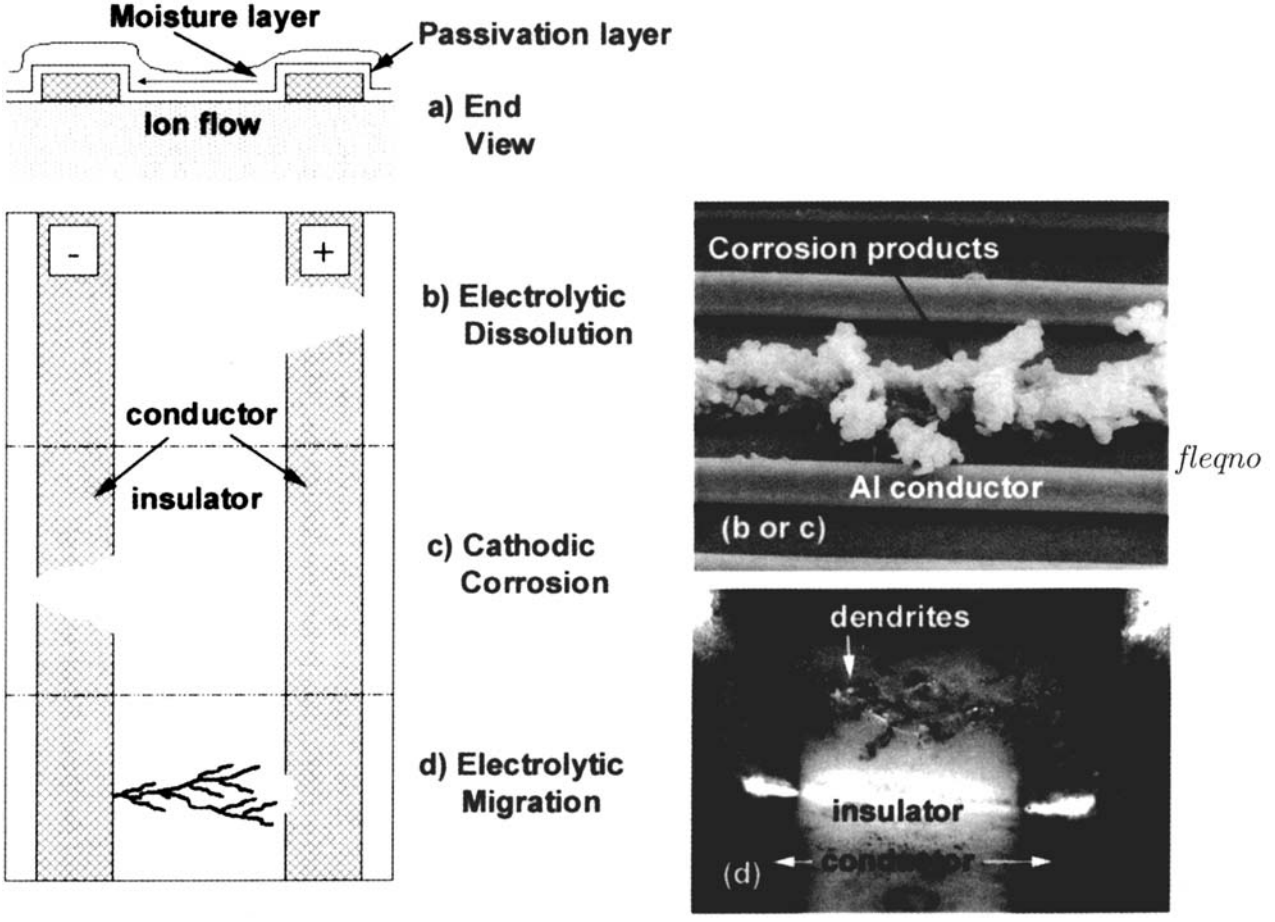
Under Electrical Bias

Although the potential that is applied to microelectronic devices is normally relatively limited (< 5V), very large electric fields can result because of the very small separation distances between conductors. When condensed water and ionic contamination are present between the lines (on the surface of separating insulators), these fields produce undesirable results by means of the three separate, but related mechanisms described next and shown schematically in Figure 4. For reference, these processes are often referred to as electrolytic. An extensive review of this subject was compiled by Steppan et al. [45]. The voltage driver is normally externally applied, but another source is the semiconductor junctions that exist within an IC [17]. Most environmentally induced failures in ICs that are observed in practice, and especially during accelerated aging, are caused by the applied electrical bias.

If an ionic path is present between two oppositely biased metal lines that are otherwise isolated and the path resistance is adequately low, then sufficient voltage will exist to enable an electrical current to flow between the lines (Fig. 4a). A portion of the applied voltage difference will exist at each metal-electrolyte interface, permitting electrochemical oxidation/reduction reactions to occur. The extent of the resulting corrosion depends on many factors, but the resistance of the ionic pathway is the most important. The influence of increasing moisture and contamination on decreasing the ohmic resistance of the ionic path is further explained by Osenbach [17] and has been phenomenologically modeled by Comizzoli [46]. Contamination has a further role because of its effect on the breakdown of the passive oxide on many metals.

Electrolytic Dissolution In this mechanism, the current leak results in electrochemical oxidation of the positive, anodic conductor. Eventually, the device can fail from an open circuit in the anodic line (Fig. 4b). Given the small dimensions and volume of the adsorbed electrolyte, severe concentration gradients exist and voluminous corrosion products can precipitate near the surface [e.g.,

Copyright © 2002 Marcel Dekker, Inc.



fleqno

Figure 4 Schematic diagram of the effect of the three primary corrosion mechanisms that occur in integrated circuits due to the presence of moisture and an applied electrical bias. The photograph in the upper right is a typical result of either electrolytic dissolution or cathodic corrosion (depends on location of defects in the passivation layer). The lower right photograph shows a short-producing electrolytic migration of solder that occurred in a ceramic capacitor in the presence of high humidity and a chloride-containing flux residue.

Copyright © 2002 Marcel Dekker, Inc.

$Al(OH)_3$]. Most of the metals used in microelectronics are susceptible to electrolytic dissolution.

Cathodic Alkalization (Cathodic Corrosion) This degradation mechanism is specific to active/passive, amphoteric metals such as aluminum. In the absence of chloride or other aggressive contamination, the leakage current through the conductive path causes anodization (oxide buildup) at the anode instead of localized dissolution. The potential drop across the oxide will consume part of the applied potential and tend to reduce the leakage current. However, while current is flowing, proton and water reduction reactions will take place at the cathodically biased line, causing an increase in local pH by the following reactions: $2H^+ + 2e^- \rightarrow H_2$ or $2H_2O + 2e^- \rightarrow 2OH^- + H_2$. Because the metal is amphoteric, the increase in pH results in dissolution of the protective oxide on the surface of the cathodic line. The metal can then dissolve rapidly, even with a net negative current at the surface. Analogous to the case of electrolytic dissolution at anodic lines, devices fail by an open circuit, except now on the cathodic line (Fig. 4c). Similarly, a corrosion product such as $Al(OH)_3$ will precipitate near the dissolution region.

Electrolytic Migration In this degradation mechanism, metallic ions dissolved from the anode (electrolytic dissolution) are transported through the surface electrolyte film and are electrolytically reduced at the cathode [45]. Metal dendrites grow from the cathode toward the anode and lead to failure via a short of the adjacent conductors (Fig. 4d). Important factors that affect dendritic growth include (1) properties of the metal (some metals such as Ag and solder readily electroplate with a dendritic morphology), (2) local current densities that, if high enough, deplete cations in the surface electrolyte film in the vicinity of the cathodic lines, and (3) mass transport–limited conditions that promote the stability and propagation of dendrites. Notably, metals such as aluminum that have a deposition potential that is outside the stability limit of water are not vulnerable to this mechanism. Steppan et al. [45] listed the order of susceptibility to electrolytic migration for many commonly used metals: Ag > Mo > Pb > solder > Cu > Zn > bronze. A small volume of metal dissolved from the anode can result in comparatively large dendrites, so the lines may short long before an open would have formed in the anodic line [45]. As dimensions of microelectronics shrink, this failure mechanism becomes more important. Warren, Wynblatt, and co-workers performed a series of studies on electrolytic migration of Cu [47–51]. Their work, which developed a good understanding of the phenomenon, showed that contamination greatly accelerates electrolytic migration. The phenomenon of electrolytic migration should be distinguished from another failure mechanism with a similar name, electromigration, which is not electrochemical in nature [45].

Open Circuit (without Electrical Bias)

Although deleterious environmental interactions normally occur in microelectronics under electrical bias, more traditional atmospheric corrosion mechanisms certainly do take place in unbiased regions during the powered-off state and/or during storage. As noted previously in this section, the power-off condition for ICs may actually be more aggressive in some circumstances because a greater amount of water may exist at the metal surface. Relevant mechanisms, with examples given in

Copyright © 2002 Marcel Dekker, Inc.

parentheses, include uniform attack (Cu contacts), pitting (Al lines and bondpads), crevice corrosion (Al under wirebonds and under passivation layers), and intergranular corrosion (Al bondpads). Under these unbiased conditions, chemical incompatibility is the primary driver. Given the wide variety of metals that are present in intimate contact with each other (e.g., Au/Al wirebonds), all of these mechanisms can be enhanced in specific configurations by galvanic interactions. To help characterize the potential galvanic effects, Griffin and co-workers [52] developed a galvanic series specifically for the common thin-film metallization and barrier layers used in microelectronic devices. The corrosion potential in 2000 ppm NH_4C1 solution decreased in the following order: Au-40%Pd, Au, Ag, Cu, Al-0.5%Cu-l%Si, CVD W, W-10%Ti, Al-2%Cu-l%Si, Al-2%Cu, Al-0.4%Pd-l%Si, Si, Al-l%Si on CVD W, Al on CVD W, Al on W-10%Ti, Al, Mg.

These traditional corrosion mechanisms are described in detail in standard corrosion textbooks [53] and elsewhere in this book. However, care must be exercised during the application of this conventional understanding to microelectronics because of their very small dimensions. This caution can be demonstrated by considering the atmospheric pitting of aluminum. A standard technique for characterizing the atmospheric corrosion susceptibility of Al involves a salt fog test (ASTM B117-90). An associated military specifications (mil-spec) (Mil-C-5541E) states that no more than five pits can exist on a panel and normal practice is not to count a pit that is less than 125 μm in diameter. As noted previously, many IC feature are < 1 μm. Clearly, even small metastable pits in the wrong place can be disastrous.

Device-Specific Corrosion Behavior and Concerns

Integrated Circuits

Aluminum Metallization Because of the predominant use of aluminum alloys in integrated circuits and their vulnerability to atmospheric corrosion, the majority of the environmentally induced problems that have historically occurred have involved aluminum. As introduced in the section on contamination, corrosion has been observed even during manufacture due to exposure to aggressive processing chemicals. During the early phases of the microelectronic industry, yield loss from in-process corrosion was a costly problem. Chemical and RIE processes have been the most damaging. The preferred use of Al-Cu alloys exacerbates the problem because Cu is enriched in the subsurface region during RIE due to the lower volatility of Cu chlorides compared with Al chlorides [36]. At the high etching temperatures, Al_2Cu θ-phase particles precipitate and accelerate the subsequent corrosion of the Al matrix. Several postetch process steps have been developed to reduce corrosion, including CF_4 plasma cleaning, O_2 plasma cleaning, DI water rinsing, wet etching, and heat treatments [30–36]. Brusic et al. [30] evaluated the efficacy of several of these cleaning steps. By simply rinsing in water before stripping the photoresist, the impurity level and associated corrosion rate were reduced by more than two orders of magnitude compared with parts cleaned only with an O_2 plasma. Elimination of $CHCl_3$ from the RIE gas in the last step resulted in still lower corrosion rates and, unlike those with etching in $CHCl_3$, the properties did not degrade during subsequent storage in air. Any in-process

Copyright © 2002 Marcel Dekker, Inc.

corrosion or staining that does take place on bondpads during manufacture can adversely affect long-term device reliability because the integrity of the subsequent wirebond can be reduced [54].

During service, biased Al metallization features most commonly fail at defects or breaks in the passivation layer (upper right photograph in Fig. 4). If chloride contamination is present, electrolytic dissolution occurs in the positive (or anodically) biased lines [55–57]. As implied in this photograph, the production of corrosion products causes more passivation layer defects and, in turn, more corrosion. As with pitting corrosion of aluminum, the presence of a halide is very important because it induces breakdown of the Al oxide film and permits rapid dissolution. Biased Al metallization that is not exposed to chloride-contaminated environments may still exhibit extensive corrosion and fail by cathodic corrosion [58–64]. This phenomenon is promoted for structures having a top passivation layer of phosphosilicate glass (PSG) with a high P content. The addition of P to SiO_2 improves coverage by lowering the stress in the oxide and reducing cracks. However, cracks along the sidewall and lack of coverage at steps and pinholes can still occur. When PSG containing more than about 5% P is exposed to moisture, phosphate dissolves to form a highly conductive surface layer. Cathodic corrosion is promoted because of the high surface conductivity and the absence of chloride ions. The anodic aluminum anodizes rather than dissolves. The activation energy for cathodic corrosion has been found to be similar to that for dissolution of Al in an NaOH solution [62]. Other ions besides phosphate can cause this form of corrosion, even those that do not form a strong base [62]. The effect of P in PSG was identified in the early 1980s and has been addressed by keeping the P content low or by using silicon nitride passivation, which has been found to be more protective [65–67].

Even in the absence of an applied bias, galvanic-induced electrochemical driving forces for corrosion can exist because unpassivated wirebonds often contain couples of Al and Au [57,68]. In the presence of moisture and chloride contamination, the galvanic driving force due to the Au can be sufficient to cause pitting and inergranular attack of Al and eventually produce device failure. Several researchers have studied the corrosion of Au/Al wirebonds [69,70]. Recent work at Sandia National Laboratories has focused on galvanic corrosion under dormant, unpowered storage conditions and has specifically been exploring the role of Al-Au intermetallic compounds that form during encapsulant curing operations. This study has shown that, under mildly accelerating conditions, unbiased Al bondpad corrosion occurs only in the presence of an Au wire and that it initiates under the wirebond and propagates along an Al/intermetallic interface (Fig. 5). Also, considerable variability exists in the distribution and structure of the intermetallic phases (Fig. 5). This latter finding suggests that the often-observed stochastic nature of corrosion may actually be the result of manufacturing process variability. If the galvanic influence of Au is not present, θ-phase particles in Al-Cu alloys can still initiate pitting or intergranular corrosion on an unbiased surface via local galvanic action [38,71,72]. Pits associated with θ phase may be limited in size but are large enough to cause failure of micrometer-sized features.

Gold Metallization Anodically biased gold metallization can fail in the absence of a contaminating salt by electrolytic dissolution if the ionic pathway contains an effective gold complexing agent. The dissolution is accompanied by

Copyright © 2002 Marcel Dekker, Inc.

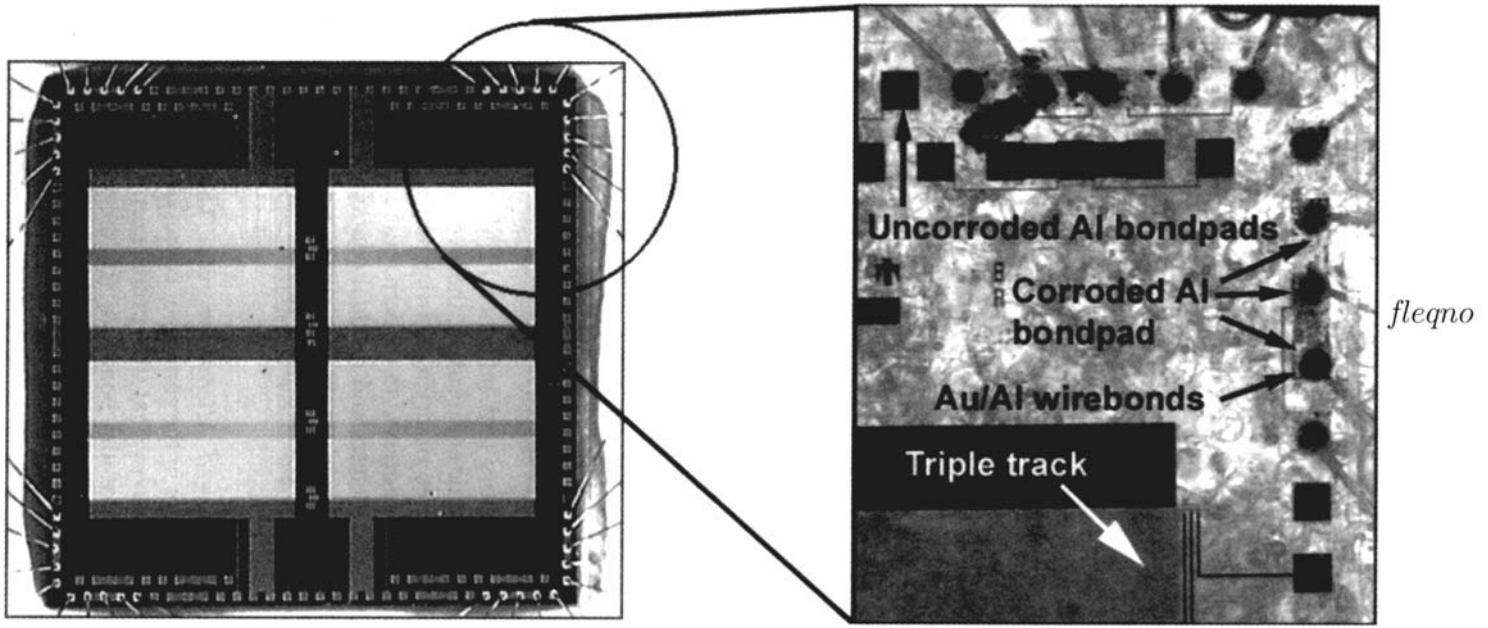


Figure 5 Corroded aluminum-bondpad metallization layer taken under back-lit conditions. A photograph of the entire test device prior to any corrosion is shown on the right. The photograph of the corroded structure shows the importance of galvanic interactions and the existence of crevice corrosion (under the passivation layer) and was taken after underlying silicon and glass insulation layer were etched away.

Copyright © 2002 Marcel Dekker, Inc.

the formation of a voluminous $Au(OH)_3$. However, examples of this type of failure have not been widely reported [73]. In the presence of a halide contaminant, failure can also result from electrolytic migration because gold metallization can form dendrites [73]. Der Marderosian [74] found a humidity threshold below which no migration of Au occurred. The threshold value was a function of the type and amount of purpose applied halide salt contamination but ranged from about 30 to 50% RH.

Plastic Encapsulated Microelectronics Because the plastic encapsulant materials are relatively permeable to water, chip metallization in PEM devices is vulnerable to corrosion when exposed to or operated in humid environments. Nguyen and colleagues [75–77] used an in situ capacitance monitor to study moisture permeation in plastic packages [5]. The uptake and transport of moisture in epoxy were Fickian in nature and exhibited a diffusivity of about 2×10^9 cm^2/s, meaning that water can penetrate a polymeric package and reach the metals on the die relatively quickly. Moisture can also migrate along defects in the lead frame–polymer interface and condense in undesirable voids near metallization surfaces. Because the bulk permeability of the plastic to typical external contaminants is very low, these lead frame defects appear to be a primary contaminant transport path. Historically, the plastic encapsulants themselves have been a source of significant contamination, with liquid/glob materials having higher corrosion-enhancing levels than the injection molded compounds. Once sufficient moisture and contamination reach the IC metallization and a void for adsorption/condensation exists, corrosion can occur and degradation may ensue by any of the mechanisms described previously, including electrolytic, pitting, galvanic, and crevice corrosion. It should be noted again that top-level conductor lines are normally under passivation layers that, if impermeable, would prevent corrosion [78,79]. Historically, defects such as cracks, pinholes, and inadequate edge coverage were commonly present [55]. During the past 10–l5years, processes and materials have improved to the point that passivation defects are no longer a primary concern. Now, the unpassivated bondpads themselves are the most susceptible.

In practice, the key factors that influence PEM corrosion vulnerability are probably the defects in the plastic encapsulant, the level of leachable contaminant in the encapsulant, and the degree of drying during power-on cycles. The first two factors have been adequately addressed in modern, best commercial practice devices to the point that passivation detects and residual contamination are essentially inconsequential. Pecht and co-workers [9,29] have now concluded that modern, properly fabricated PEM devices are very reliable under a variety of service conditions.

Ceramic Hermetic-Packaged Microelectronics The meaningful differences between CHP and PEM devices in the context of corrosion are the following: (a) Al wires are used instead of Au so that the prime corrosion vulnerability is the ultrafine 25-μm wire instead of the bondpad, (b) the internal environment can theoretically be controlled such that a benign environment will always exist, and (c) the cavity containing the die is unfilled so encapsulation defects are not needed as sites for water condensation. To achieve the environmental control advantage, three factors must be satisfied: (a) a hermetic seal, (b) a clean and dry assealed internal

Copyright © 2002 Marcel Dekker, Inc.

environment, and (c) control of outgassing from internal materials. If they are properly designed and manufactured, the reliability of CHP devices is not a concern. However, in practice, all three of these aspects have produced problems as evidenced by field-returned "hermetic" packages in which corrosion has occurred [80–82].

The specifications on hermetic seals are not always adequate to ensure total isolation from the environment for extended periods of time. For example, as noted by Pecht and Ko [83], hermeticity is defined by a maximum leak rate (e.g., 10^{-7} atm cc/s). If the device leaks at this particular maximum rate, the critical moisturecontent (three monolayers of water) can diffuse through the seal in as little as 2500 h. Supporting this finding is a study in which 20% of field failures of equipment sited in a tropical environment were due to corrosion of interconnects in packages that met the hermeticity specification [17]. Also, the seals and/or ceramic bodies can crack and create larger leaks during handling, soldering, or qualification thermal cycling, which permits both water and contamination to enter easily. If care is not exercised during fabrication, moisture adsorbed on the inside walls of the package can desorb during subsequent processing steps or during use. To address this possibility, mil-spec CHP parts are normally sealed in an atmosphere containing no more than 5000 ppm of water, ensuring that no liquid phase will exist at temperatures down to 0°C, where ice forms. The sealing glass used in some packages or a popular organic die-attach material can actually be sources of moisture. Devitrifying glass is one type of sealant with a high moisture content that is evolved during closure, whereas vitreous glass contains little moisture and can result in a ceramic package with less than 500 ppm moisture in the cavity [84]. Moisture trapped inside a sealed cavity can leach ions from the sealing glass or other sources to form a conductive electrolyte. Once an ionic path exists between conductors, corrosion and failure by any of the mechanisms described previously can ensue. Finally, one researcher found that residual stresses in Al-containing wirebonds could be an important factor in failure (e.g., by stress-induced corrosion) [85].

Macro Interconnects

Solder, copper conductors, and plated-copper connectors constitute the major metallic components of second-level packaging for functional electronic circuits. These metals are all susceptible to corrosion. Typically, interconnects are less protected and more exposed to ambient environments. However, their dimensions are much larger than those of chip metallization and more corrosion can therefore be tolerated before failure is produced.

Solder PbSn alloys, ranging from Pb-rich to Sn-rich compositions, are the most solder materials used in electronic applications. Pure Sn forms a protective oxide film, but Pb forms an oxide that is not stable and can easily react with chlorides, borates, and sulfates [86]. Frankenthal and Siconolfi [87,88] found that both Sn- and Pb-rich PbSn alloys form an Sn oxide, most likely SnO, during the initial exposure of oxide-free surfaces to oxygen. Lead is oxidized on the surface of PbSn and a mixed oxide results only after all the metallic Sn is totally depleted from the surface. Similarly, the corrosion product formed on Pb-50In solder during exposure to an aggressive gaseous environment was found to be rich in In [89]. Not surprisingly, the corrosion resistance of PbSn in various aqueous solutions and gaseous environments depends strongly on the alloy composition, improving greatly as the Sn content increases above 2wt% [86].

Copyright © 2002 Marcel Dekker, Inc.

In the presence of moisture and contamination, the most common degradation mechanism of solder is electrolytic migration (shown previously in lower right photograph in Fig. 4). Thus, the cleanliness of fabrication steps and the effective removal of flux residues are critical factors. Some IC package types (e.g., surface mount) are very hard to clean effectively. Manko [43] summarized the corrosion behavior of PbSn solders in various chlorides that are typically used as activators in fluxes and noted their deleterious effect in destroying the native passivating oxide layers. He also noted that corrosion related to flux use might result from flux or flux residue that is trapped in inaccessible locations or from fumes liberated during soldering and subsequent condensation in uncleaned regions. Specifically, water-white rosin flux has been found to leach Sn from the solder and therefore decrease its corrosion resistance [90]. Soldering traditionally uses nonaqueous fluxes that require cleaning with Freon-based solvents. In an effort to reduce chlorofluorocarbon usage, water-soluble fluxes have been substituted in some applications. Cleaning of water-soluble fluxes can normally be accomplished in deionized water. Sn-Pb-In solders corrode in water-soluble fluxes containing chloride-based activators but are not attacked in fluxes containing phosphate-based activators [91]. Finally, in-process corrosion can result in poor quality solder joints or decreased thermal fatigue life. This latter result is especially significant for C4 solder connections [90].

Copper Conductors Although precautions are taken to protect the copper conducting lines in printed wiring boards from environmental exposure, defects exist and corrosion does occur under many atmospheric conditions. For most environments that are encountered, copper is not thermodynamically stable. However, its native cuprous oxide surface film does offer some limited protection. Atmospheric corrosion of copper is briefly described in the chapter on atmospheric corrosion. Examples of typical industrial atmospheric pollutants that are harmful to copper include SO_2, H_2S, COS, NO_x, Cl_2, and CO_2.

Contamination of copper surfaces with atmospheric particulate matter can accelerate the corrosion process. For example, the corrosion of copper in 100°C air in the presence of submicrometer ammonium sulfate particles has been found to depend strongly on RH [40]. Below the critical RH, Cu_2O formed uniformly on the Cu surface. At the critical RH of 75%, $Cu_4(SO_4)(OH)_6$ formed in the region where the $(NH_4)_2SO_4$ particles had been deposited. At 85% RH, a thick corrosion product covered the entire surface. Particulate contamination such as this is typically believed to be an issue during manufacturing. However, it can also cause field failures in electronic installations, such as telecommunications centers [92].

The formation of conductive anodic filaments (CAFs) has been observed during accelerated aging testing to cause failure in epoxy-glass printed circuit boards containing copper conductors, a process clearly related to electrolytic dissolution [93]. Here, a conductive ionic path consisting of precipitated corrosion products presumably forms between the oppositely biased conductors. These fibres grow from the corrosion-producing anodic line to the cathodic line. The degradation was found to be most severe between two nearby through-holes. Because CAF has not been observed in field-returned parts, it may be only an artifact of the test conditions.

Au-Plated Connectors and Contacts As noted earlier, the subtrates of connectors and contacts are normally fabricated from copper or copper alloys and

Copyright © 2002 Marcel Dekker, Inc.

then plated with a noble metal. The presence of the thin plating that almost always contains some level of physical defects (e.g., cracks and pores) enhances the corrosion susceptibility of the substrate and enables other processes to take place. Slade [22] and Abbott [23] recently published a comprehensive review of connector/contact corrosion. One form of observed degradation occurs when corrosion products creep across a noble metal surface. When Au-plated Cu is exposed to a sulfide-containing atmosphere, a tarnish film composed of copper oxide and copper sulfide forms in the plating pores and cracks where the Cu layer is exposed [94,95]. With time, a predominately copper sulfide tarnish film migrates over the Au surface, resulting in increased contact resistance. This phenomenon, termed creep corrosion by Tierney [94], is becoming increasingly important as the thickness of the gold plating is reduced for economic reasons and as the edges of exposed Cu become closer to contact points as a result of miniaturization. A second relevant degradation mode is often referred to as pore corrosion and simply consists of accelerated corrosion of locally exposed regions of the substrate. Two important processes are probably responsible: (a) capillary condensation of water in cracks, pores, and between mated surfaces and (b) galvanic interactions with a potentially large cathode-to-anode area. Ming et al. [14] showed that contact force and electrical loading can also affect corrosion. For example, contact force can improve performance in stationary contacts and applied voltage can accelerate growth of surface films and decrease contact service life. Finally, in recent years, a few special contact lubricants have been developed that can also inhibit corrosion [23].

Product Qualification/Reliability Testing and Analysis

A significant effort has been made over the past quarter century to develop effective techniques to test and assess the effect of corrosion on the performance and life of electronic devices. Such techniques are desired for two specific uses: (a) as a means of rapidly characterizing product quality during manufacturing (acceptance testing) and (b) to provide customers and users with an accurate estimate of expected service life. In this context, corrosion degradation is primarily characterized in terms of reliability, which is the probability that a device will not perform its intended function (i.e., electrically fail). Such device-level studies are required because the direct measurement of corrosion is very difficult or even impossible in actual operating environments using standard corrosion characterization techniques (e.g., electrochemical and gravimetric). A device manufacturer wants to be certain that a product will have at least a certain functional lifetime in service with a minimum number of failures. A typical historical requirement is 100 failures in 10^9 device hours (100 FIT) or 0.01% failure in 1000 hours [96]. In modern practice, most electronic devices are expected to function reliably for at least 10 years [17], although obsolescence can certainly set in much sooner. Therefore, reliability engineers are forced to perform accelerated aging exposures on large numbers of parts. For general reference, Nelson [97] has published a comprehensive overview of accelerated aging, and Osenbach [17] describes factors and issues associated with accelerated aging of microelectronics. A clearly recognized deficiency of the reliability approach is that such tests do not permit a fundamental understanding of the corrosion mechanisms and processes to be easily identified. Truly predictive reliability

Copyright © 2002 Marcel Dekker, Inc.

assessments must have this type of physical basis. Nevetheless, accelerated reliability testing is of tremendous practical importance because susceptible materials, design flaws, and processing problems can be identified in a timely manner and a qualitative understanding of the degradation processes can be generated.

The underlying principle behind the use of accelerated aging is that the functional behavior of real devices or the response of test structures with similar materials and dimensions can be characterized using various combinations of environmental stress factors that include temperature, humidity, bias, and contamination. Each of these variables is typically used at levels more severe than actual operating conditions. Osenbach also notes that all of the accelerated aging strategies include two significant assumptions: (a) the parameters that characterize failure under high-stress conditions (where failure occurs in short time periods of days to months) can be extrapolated to actual use conditions where failure occurs after years of exposure, and (b) the test population is representative of the entire population. This section contains brief descriptions of (a) the aging techniques commonly being used, (b) resultant models of acceleration factors, and (c) the concerns and potential deficiencies associated with this subject.

Techniques

Microelectronics Peck and Zierdt [98] led the way for adopting elevated humidity and temperature as the primary stress factors. The most common accelerated test used over the past 25 years is referred to as THB (temperature, humidity, and bias). In this test, parts are exposed for extended periods (> 1000 h) at 85°C, 85% RH, wih the conductor lines biased at, or sometimes above, the operating voltage [68,99]. As PEM device reliability improved during the 1980s due primarily to a reduction in residual chloride contamination and molding compound cleanliness, exposure times under THB conditions required to generate failures started approaching 10,000 h. In order to formulate predictive relationships, failure during accelerated testing must be observed. The extremely long times needed in conventional THB tests led to the development of tests with more severe conditions to reduce needed test time. A pressure-cooker test at 100% RH and temperatures above 100°C has been used for this purpose [99–102]. Its efficiency can be demonstrated by the observation that for one specific device, results equivalent to those obtained in 1000 h at 85°C, 85% RH could be produced in 20 h at 140°C, 100% RH [99]. However, artifacts associated with condensation and difficulties in applying voltage in saturated atmospheres complicated widespread adoption of this procedure. Because of attractive equipment cost and availability, many manufacturers still use this type of testing and the standard conditions are 121°C, 100% RH and no bias. More recently, the highly accelerated stress test (HAST) has become the standard. HAST tests typically use temperatures up to 150°C and humidity levels less than 100% [63,103,104]. Several other variations of the standard THB aging techniques have been developed that involve additions of internal and external contamination and/or cyclic application of the environmental parameters to better simulate actual use [28,105–109]. Failure analysis techniques to supplement the reliability information have also been reported [110].

Although most accelerated aging studies are performed on actual functional devices and the time to failure is directly measured, some studies have used test

Copyright © 2002 Marcel Dekker, Inc.

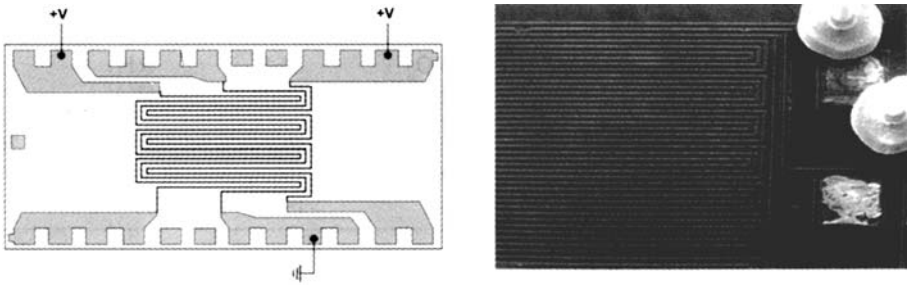


Figure 6 Schematic diagram (left) and an SEM photograph (right) of two triple-track test structures that are used to study electrolytic corrosion mechanisms along with the effectiveness of passivation layers. The structure shown on the right was encapsulated and then exposed to HAST conditions until failure. This particular structure is part of the integrated test device shown previously in Figure 5. These test devices contain eight triple-track sections (the left set with windows in the passivation layer) and exposed wirebond pads.

structures designed specifically to better address particular degradation modes. For corrosion under electrical bias, common configurations include two interdigitated combs, a triple track with three parallel but meandering lines, and combinations of tracks and bondpads/wirebonds [8,65,66,103,111,112]. Example of triple-track structures are shown in Figure 6 [8]. The two outer track conductors are normally biased positively and the center one is negative or grounded. The portion of the triple-track structure in Figure 6b is contained within the test device previously shown in Figure 5. To assess wirebond degradation, the design permits conventional four-point resistance measurements to be made. Such test devices can be tested bare or as packaged.

Macro Interconnects Because connectors and contacts are usually exposed without protection to the environment during operation, testing typically has been performed in the context of atmospheric corrosion [113]. Various forms of accelerated tests for indoor office environments have been developed for this purpose [26,114–117]. For example, procedures have been developed at IBM [the G1(T) test] [26,114,117], Battelle Institute (Flowing Mixed Gas Class II or FMG II) [23,115,116], and in Europe by the International Electrotechnical Commission (IEC Test 68-2-60) [118] for simulating an indoor office environment. These techniques vary slightly but involve exposure to an atmosphere containing a combination of dilute pollutants such as H_2S, SO_2, NO_2, and Cl_2 and humidity (Table 1) and are usually performed at near-ambient temperatures because of complications arising from reactions between the various components at higher temperatures. Acceleration factors from 10 to 1000 are possible depending on the chosen conditions [115]. These aging environments are now used to test and qualify many electronic parts other than connectors and contacts, including printed circuit boards. The reliability of PCBs is also routinely tested using THB testing as discussed in the previous paragraph.

Mathematical Relationships for PEM Aging

When plastic-encapsulated microelectronic devices are exposed to aggressive environments, there is often a bimodal distribution in the time to fail resulting from

Copyright © 2002 Marcel Dekker, Inc.

Table 1 Specifications for Three Standardized Atmospheric Corrosion Test Environments

ID	Cl_2 (ppb)	SO_2 (ppb)	NO_2 (ppb)	H_2S (ppb)	RH (%)	T (°C)
G1 (T)	3	350	610	40	70	30
FMG II	10	—	200	10	70	30
IEC	10	200	20	10	75	25

latent manufacturing defects and long-term wearout [119]. These two causative mechanisms are very different directly correlate to the two primary reasons for performing accelerated aging noted in the first paragraph of this section. The elapsed time to fail and cumulative failure percentile are often plotted using a lognormal distribution (Fig. 7). Two statistical measures result: the mean time to failure (MTTF, the time for 50% of the population to fail) and the population standard deviation (calculated from the slope) [8,119]. Because the goal of accelerated aging is to establish a relationship between the environmental parameters and service life under operating conditions, the MTTF metric can be used to calculate an important parameter known as the acceleration factor (AF). In terms of MTTF,

$$AF = MTTF_{field}/MTTF_{test} \tag{1}$$

The acceleration factors are experimentally measured as a function of the environmental stresses using the techniques described in the previous subsection.

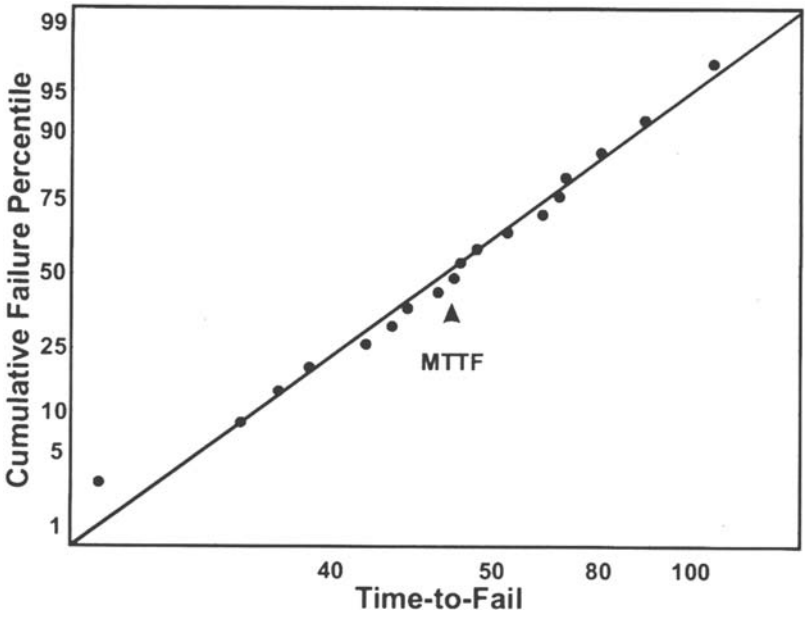


Figure 7 Example of a lognormal distribution of failure times and the definition of the mean-time-to-failure (MTTF) metric.

Copyright © 2002 Marcel Dekker, Inc.

Using triple-track test devices, the surface conductance, G, can be directly measured. This parameter is a more fundamental indicator of the susceptibility to electrolytic degradation mechanisms compared with MTTF because, as noted earlier, electrolytic corrosion will occur only if the ohmic resistance between lines does not consume the applied voltage difference and leakage current flows [111,120]. G is calculated by multiplying the leakage current by the area of insulator and dividing by the applied voltage. The resistance change of the lines can also be used as a measure of degradation (either electrolytic or open circuit). The important assumption inherent in these types of tests is that the specific metric being measured (e.g., surface conductance or wirebond resistance) is directly related (proportional or inversely proportional) to failure rate and thus to MTTF [66,111,120].

The cumulative values for MTTF determined by any of these techniques for a range of conditions permit the formulation of general relationships that describe the dependence of failure rate on the stressing parameters. The effect of temperature, T, on reaction or failure rate, R, can usually be described by an Arrhenius-type relationship:

$$R = A \exp(-E_a/kT) \tag{2}$$

where E_a is activation energy, k is Boltzmann's constant, and A is an empirical constant. A range of activation energies for failure of ICs has been reported, from 0.4 to 1.2 eV. The acceleration factor associated with temperature becomes

$$\mathrm{AF_T} = \exp[E_a/k(1/T_{\mathrm{field}} - 1/T_{\mathrm{test}})] \tag{3}$$

Because of the concern that higher voltage levels will increase the internal temperature (ohmic heating) and dry the device, most investigators use the normally applied operating voltage during testing. However, for the corrosion mechanisms that occur due to electrical bias, the corrosion rate is proportional to the current between the conductors and therefore scales with applied voltage. As such, the MTTF decreases as bias increases and an inverse relationship may exist [7,60,121,122]. For the limited cases in which a higher voltage level is used, Shirley [123] has proposed a general linear acceleration model where a and b are constants:

$$\mathrm{AF_V} = (a + bV_{\mathrm{test}})/(a + bV_{\mathrm{field}}) \tag{4}$$

Unfortunately, the influences of RH and impurities are most poorly established than the effects of temperature and bias. Many investigators have measured MTTF or G for actual devices or test structures in high-temperature and -humidity environments and developed empirical relationships by fitting the data to various equations. Several commonly referenced variants are presented in Table 2. Each expression in this table has a parameter A that represents a proportionality constant. These equations can be used to determine an acceleration factor by considering the ratio of field to test MTTF as was done in Eq. (3). Using this technique, the proportionality constants cancel. Then by using Eq. (1), the service life under operational conditions may be predicted after measuring lifetime under stress conditions. The first four expressions in Table 2 are "Eyring" models because the influences of T and RH are considered separately and then multiplied together to get a combined equation. The last expression does not assume that the

Copyright © 2002 Marcel Dekker, Inc.

Table 2 Empirically Derived Models Describing the Influence of Temperature, T, and Relative Humidity, RH, on Mean Time to Failure, $MTTF$

Expression for MTTF	Constants	Reference
$A \exp [B(T+\mathrm{RH})]$	$B = -0.06$ to -0.09	126
$A(\mathrm{RH})^n \exp(E_a/kT)$	$E_a = 0.77$–0.81 eV	99
	$n = -2.5$ to -3	
	$E_a = 0.9$ eV	127
	$n = -3$	
	$E_a = 0.8$ eV	123
	$n = -4.64$	
$A \exp [E_a/kT + B(\mathrm{RH})^2]$	$E_a = -0.7$–0.95 eV	112
	$B = -0.0004$	
$A \exp (E_a/kT + B/\mathrm{RH})$	$E_a = 0.65$ eV	68
	$B = 304$	
$A \exp [B/kT + C(\mathrm{RH})/kT + D(\mathrm{RH})]$	$B = 1.0$–1.1 eV	66
	$C = -.00444$ to $-.0077$	
	$D = 0.076$–0.13	

effects of temperature and humidity are independent and has an activation energy that is dependent on RH [124]. These models have been used in a number of investigations to fit experimental data, and different values for the constants have been determined for various systems and degradation modes [96,98,99,102–105,119,121,125]. An example of how such models are applied is shown in Figure 8, which is based on surface conductivity measurements that were made with an Al-Cu triple-track structure in a HAST chamber [103]. The temperature and humidity combinations were fit to various equations and those shown in Figure 8 are for the last expression in Table 2, which contains an RH-dependent activation energy. The correlation coefficient for this expression was found to be higher than those for other models [103].

As will be discussed in the next subsection, to be truly effective, predictive capabilities must be based on fundamental physical understanding. The models presented in Table 2 are simply empirical correlations. Limited progress has been made to date to improve this situation. Comizzoli [46] has provided a mechanistic explanation and associated mathematical expression for the exponential dependence of surface conductance (and MTTF) on relative humidity that is contained in some of the models listed above. Pecht and Ko [83] developed a comprehensive model for predicting absolute time to failure when microelectronic die metallization is corroded by an electrolytic process. Their phenomenological underpinning involves ion transfer based on Ohm's and Faraday's laws. The other key feature is their treatment of the critical process involving moisture ingress that permits this model to be useful for both PEM and CHP devices. A final reference that is relevant to this subject is the work being performed by Graedel and co-workers [128]. This team is developing and exercising a physically based atmospheric corrosion model referred to as GILDES that conceptually can include all microelectronic corrosion processes (e.g., gas transport, adsorbed water layer, corrosion product layer, electrochemistry).

Copyright © 2002 Marcel Dekker, Inc.

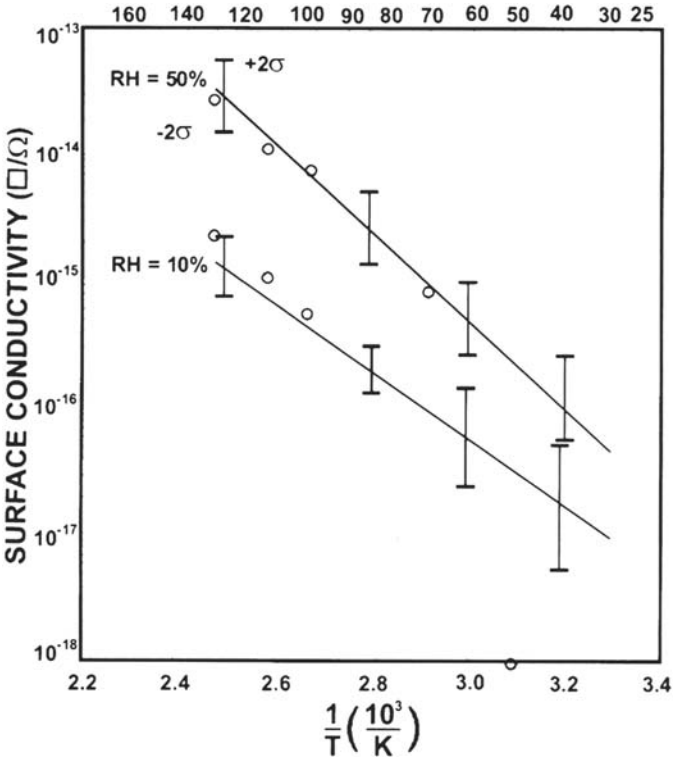


Figure 8 Surface conductivity as a function of temperature. RH is the relative humidity and the lines are fits of the last equation shown in Table 2. (From Ref. 103. Copyright 1980 by IEEE.)

Concerns and Limitations

In general, the reliability engineer cannot ignore failures observed during testing. The expense of accelerated testing and the often costly effort required to address the problems highlighted by such tests are rationalized by the assumption that failures have a finite probability of occurring during service if they are observed at all during testing. In other words, the accepted belief is that improved test yields correlate with longer service life. A device may actually be redesigned without any knowledge of whether the failure mechanism occurs under operating conditions at a rate that can be extrapolated from stress conditions or if it is just an artifact of the test. The prediction of device lifetime in the field by extrapolation of data obtained under high-stress conditions is extremely sensitive to the model chosen. The basic issue here goes back to the use of empirical equations—one cannot reliably extrapolate outside the range of testing conditions. Thus, the goal has to be to obtain data on the behavior in the mildest conditions possible [97]. The authors of this chapter do not know of a sole expert in this field who believes at this time that actual service life can be accurately predicted and, as such, in practice, accelerated aging is presently useful only for product qualification and identification of latent manufacturing defects and

Copyright © 2002 Marcel Dekker, Inc.

design deficiencies. The remainder of this subsection provides support for these statements.

Changing Failure Mechanisms as a Function of Environmental Stress This classical issue is relevant to all applications of accelerated aging [97]. The complexity inherent in microelectronic devices results in a multitude of coupled processes that must be properly identified and accounted for in accelerated aging models. Every process that affects a failure mechanism could have a different sensitivity to the environmental parameters. Lall [129] has documented some of the problems associated with the common use of temperature as a stress agent for microelectronics. The wide variability in activation energy mentioned before is indicative of different or changing mechanisms. Three relevant examples further illustrate the issue of changing mechanisms. The first involves the formation of conductive anodic filaments (CAFs) on PCBs described earlier. Work performed subsequent to the discovery of CAF formation found that a threshold in the temperature/humidity phase space may exist below which CAF growth does not take place [130]. This threshold is apparently not encountered in typical use environments and thus the phenomenon of CAF may be only an artifact of accelerated testing. The second example is from an investigation of conduction in printed circuit boards by Takahashi [130]. He studied the various conduction paths in boards using an AC impedance technique during humidified exposures without bias and identified both ohmic and diffusion-controlled processes. He then made the point that because multiple conduction paths and mechanisms exist at a single temperature and humidity condition, it is possible for conduction processes determined in stress tests to have no bearing on failure mechanisms under field conditions. The final example concerns the observation that the glass-transition temperature of the encapsulating plastic in PEM devices cannot be exceeded in testing because a large difference in water permeability results. Nevertheless, sometimes this requirement is satisfied. A few studies have shown that data obtained from THB and HAST/pressure cooker testing can be fit to a single mathematical relationship, indicating that the failure mechanisms may be the same [68,99,104].

Evolving and Improving Technology The continuing rapid evolution of microelectronic technology leads to several related difficulties. The first is that the dominant failure mechanisms change and thus long-term field failure information is not necessarily relevant to state-of-the art devices. Historically, during accelerated aging, two types of moisture-related phenomena have been observed: distributed Al track corrosion and Au wire/Al bondpad interfacial degradation. The root cause of track corrosion was probably moisture penetration through defects in the protective passivation layer and the presence of contamination. Modern best commercial practice has effectively eliminated passivation defects and thus track corrosion as a significant failure mechanism. Now, the exposed wirebonds are the prime susceptibility. Lall [129] documents another important factor: field failure information is becoming more limited because the reliability of state-of-the art devices has now improved to the point that it no longer limits useful system lifetime. The final factor is that posttest analyses of aged devices have often been limited to simply confirming a failure, not determining root cause. Thus, the ability to correlate the results with true service life or identify actual failure mechanisms has not been developed to any significant extent.

Copyright © 2002 Marcel Dekker, Inc.

Effect of Humidity and Device Type A specific disconcerting aspect of the existing T/H models that is easy to identify is their wild divergence at low RH values. Figure 9 shows humidity acceleration factors relative to 85% RH calculated for each of the expressions in Table 2. In these calculations, temperature was normalized out by setting its value to 25°C. There is relatively good correspondence of the models in the high-RH range where the experimental data exist. However, at low RH, the models differ by many orders of magnitude. One possible explanation is that none of the mathematical relationships proposed have a phenomenological basis. For example, water adsorption on the metallization may be the key process and, if so, the rate response should be sigmoidal (which none of these equations simulate). Osenbach [17] describes another physical basis that involves the observation that surface leakage current is minimal below about 50% RH and has an exponential dependence above this level. Few experimenters examine the RH range less than 50% because of the long times needed to obtain failure. Unfortunately, this RH range is where most operating conditions exist, especially considering the local heating associated with power dissipation. Furthermore, there is no reason to expect different systems to exhibit similar temperature or, for this topic, different humidity relationships. For instance, silicone-encapsulated devices fail at much lower rates in a given environment than devices encapsulated in epoxy [60,96,112]. This occurs despite the faster transport of moisture in silicones and could result from low impurity content and improved adhesion to the die surface [75,112]. Silicone-encapsulated parts may therefore display a different humidity acceleration factor than unencapsulated or epoxy-encapsulated parts [66].

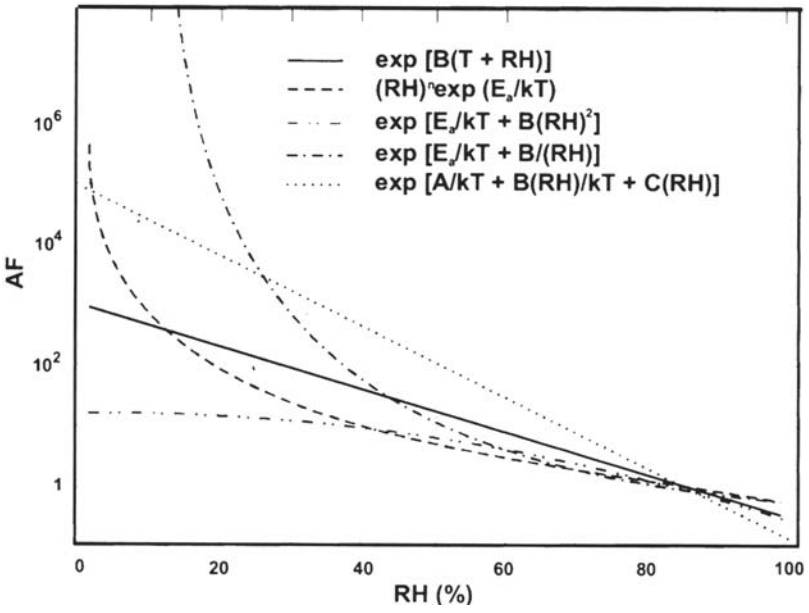


Figure 9 Humidity acceleration factor as a function of RH relative to 85% for the various models shown in Table 2.

Copyright © 2002 Marcel Dekker, Inc.

Effect of Contamination As discussed previously, contamination at metallization surfaces is a critical corrosion factor. For example, the level of contamination affects the ionic strength in the adsorbed water layer that, in turn, influences surface conductance. Contamination also affects the critical relative humidity, which, for some salts, can be quite low. Finally, the type of contamination often determines the corrosion mechanism (e.g., whether electrolytic anodic or cathodic corrosion of Al predominates). In many accelerated aging approaches, this dominant factor is uncontrolled and often uncharacterized. In fact, T/H testing may really be a measure of the cleanliness of the part prior to testing. This observation is an example of why Osenbach's second assumption noted earlier (testing of representative devices) is probably not, in general, valid. To address this problem, many investigators have either purposely contaminated the part prior to exposure or added controlled contamination to the stressing environment [42,65,74,106,107,122, 131–133]. These approaches are useful for making comparative assessments of various structures. However, it is a difficult task to generate a model that predicts behavior under conditions of lower contamination levels. Pitting potentials of various metals have been found to decrease linearly with a logarithmic increase in chloride concentration [134]. Predicting part lifetime for a given surface contamination concentration from such information, however, remains quite challenging.

CORROSION OF MAGNETIC DATA-STORAGE COMPONENTS

The critical metallic components of advanced magnetic and magneto-optic (MO) storage devices—thin-film metal disks, inductive or magnetoresistive heads, and MO layers—are all susceptible to corrosion and each has been a subject of considerable study. Several review articles covering corrosion of magnetic-storage media may be found in the literature [135,136].

Thin-Film Magnetic Disks

As described in the technology overview section, the carbon overcoat layer on thin-film disks typically does not fully cover the underlying layers as a result of intentional roughening of the disk. The lack of coverage has two implications for the corrosion behavior. First, the Co-based magnetic layer and perhaps even the NiP substrate are exposed at small regions and can corrode. Furthermore, the overcoat layer, which is often sputter-deposited carbon, can be somewhat conductive and quite noble in comparison with the exposed areas of magnetic alloy. The unfavorable anode-to-cathode area ratio can therefore result in aggressive galvanic corrosion.

Figure 10 shows potentiodynamic polarization curves measured in DI water [135,137]. The plated Co-8%P material was considered for use as the magnetic alloy in thin-film disks when they were first developed. Like pure Co, it is not very corrosion resistant and does not readily passivate. The corrosion potential of two different sputter-deposited carbon thin films is seen to be about 600 mV higher than that of plated CoP. Although the nature of C thin films can change drastically as a function of deposition conditions, the two C films sustain reasonably large cathodic

Copyright © 2002 Marcel Dekker, Inc.

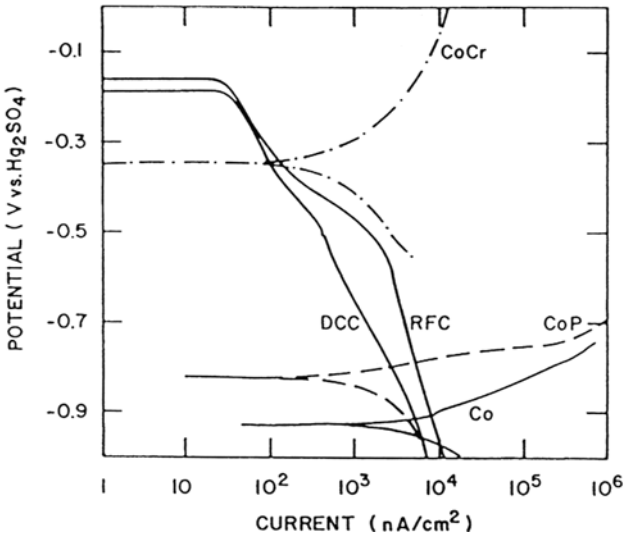


Figure 10 Potentiodynamic polarization curves of thin-film disk materials in a droplet of DI water. Parameter definitions: DCC DC sputtered C; RFC RF sputtered C; CoCr, Co + l7%Cr; CoP, CO + 8%P; Co, pure Co. (From Ref. 135.)

currents. In fact, galvanically induced corrosion of the small active areas of the magnetic alloy by the C overcoat is the primary mechanism of corrosion of thin-film disks. When an uncoated CoP film is exposed to an aggressive gaseous environment at 25°C containing 70% RH and 10 ppb Cl_2 gas, a 30-Å-thick uniform corrosion product forms [135,137]. However, a C-coated CoP sample forms a high density of localized corrosion product particles that are several μm in diameter. This dimension is 100 times larger than the head-disk separation in advanced disk files.

Corrosion can thus be minimized by decreasing the galvanic mismatch between the magnetic layer and the overcoat. As shown in Figure 10, a sputter-deposited Co-17%Cr film has a corrosion potential much closer to C and is spontaneously passive in the DI water droplet. In deaerated Na_2SO_4, the corrosion current was found to decrease and the corrosion potential increased as the Cr content in CoCr alloys increased from 0 to 20% [136,138]. Nonconducting overcoats can also reduce corrosion but do not eliminate it if they are not totally covering, a requirement that is quite difficult given the thickness limitations of the overcoat and the roughness of most disks.

The trend in magnetic recording is, of course, to continually higher densities. As with microelectronic devices, higher density is achieved by shrinking the dimensions, including the separation of the magnetic medium and the sensor in the head, which has implications relative to corrosion. In order to bring the head and disk closer, the head must fly closer to the disk, and the carbon overcoat thickness must decrease. The decrease in fly height means that less corrosion product accumulated on the disk surface will cause detrimental interactions with the head. A decrease in carbon thickness is also potentially deleterious to corrosion resistance

Copyright © 2002 Marcel Dekker, Inc.

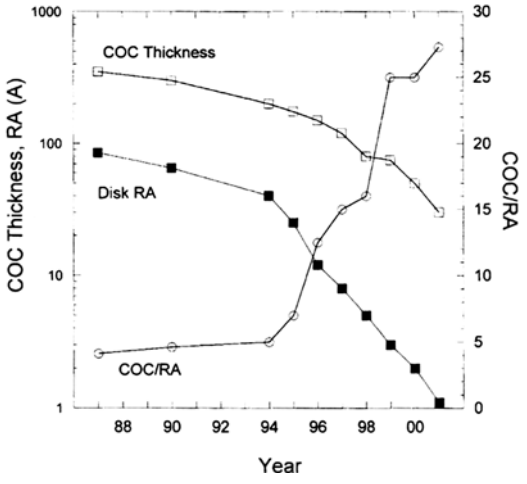


Figure 11 Trend of carbon overcoat (COC) thickness and disk texture or average roughness (RA) with time. Also shown, with right axis, is the ratio COC/RA. (Data from HMT Technology, Inc.)

because it is harder to cover the magnetic layer with a very thin carbon overcoat. On the other hand, in order to fly closer, the disk roughness must also decrease. The trend toward smoother disks is beneficial to corrosion resistance because the magnetic layer can then be more easily covered by the carbon overcoat. Figure 11 shows the time trends for carbon overcoat thickness and disk roughness average (RA), as well as the ratio of the two. The average roughness of magnetic disks has decreased faster than the carbon overcoat thickness. Therefore, the ratio of COC thickness to disk roughness increased significantly during the 1990s, indicating that the COC should now provide a better covering despite being much thinner. In essence, the disk structure now tends to be more like Figure 3a than 3b. As a result, disk corrosion should be less of a problem than in the past, and this trend will apparently continue for the next few years.

Figure 12 presents polarization behavior in a droplet of water for more recent disk materials and structures than those shown in Figure 10 [139]. The disk had low roughness and a thin carbon overcoat. First note the two curves from full disk structures. One is from a lubricated disk, the other from an unlubed disk. The lube decreases the current only slightly, perhaps as a result of water displacement. The anodic current flowing at a given potential from the unlubed disk is about 100 times less than that of the blanket magnetic layer on glass. It is clear that the magnetic layer is rather well covered by carbon. In the past, it was assumed that the anodic current measured from a disk originated largely from spots not covered by COC. However, for the disks studied here, the anodic signal is not coming only from the small amount of uncovered magnetic layer because a blanket layer of C (unlubed) on glass exhibits an electrochemical signal that is a large fraction (about half as large) of the signal measured on the unlubed disk. Carbon is not really an extremely noble material. More accurately, the oxidation of C is kinetically hindered. Carbon can, in fact, oxidize to form various species, such as carbonyl, carboxyl, phenol, quinone, or

Copyright © 2002 Marcel Dekker, Inc.

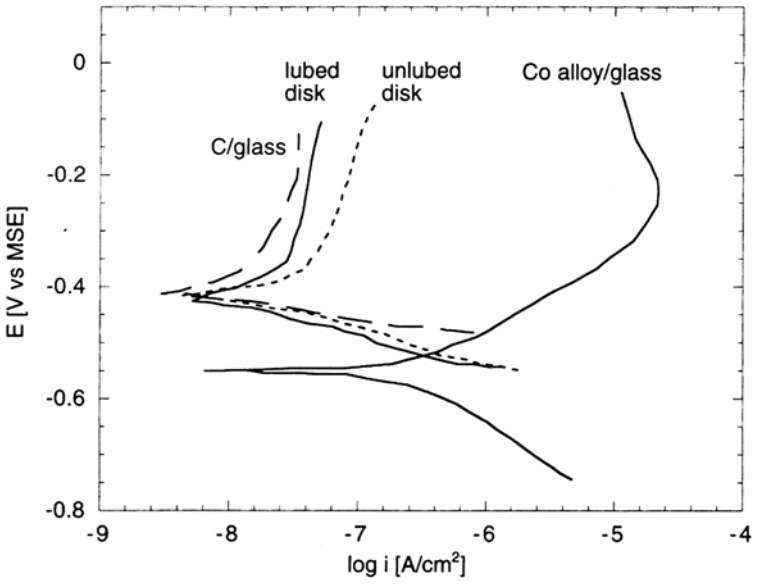


Figure 12 Polarization curves in a water droplet for a lubed and unlubed disk as well as a blanket magnetic layer and carbon layer on glass. (From Ref. 141.)

lactone [140]. The polarization curve for the carbon film is similar to that of a spontaneously passive metal. It supports a reasonable amount of cathodic current, which is the cause of galvanic corrosion. At anodic potentials, there is some steady-state oxidation current, which is probably associated with a low rate of C oxidation. From the polarization curves, it could be suggested that the difference in current between the unlubed disk and the C blanket is the corrosion current of the magnetic layer. The finding that carbon oxidation is now a significant fraction of the total current flowing to a thin-film disk is reasonable given the trend of the increasing ratio of carbon thickness to disk roughness. However, despite the good coverage, very small areas of magnetic layer are still exposed in the disk structure. Therefore, corrosion will still occur if the disks are exposed to aggressive environments (such as chloride) or if problems in disk texture control occur.

An electrochemical study of the protectiveness of carbon overcoats as thin as 5 nm has been reported [141]. Polarization resistance of disk structures in 0.5 M sulfuric acid was measured. Disks coated with hydrogen-containing ion beam deposited carbon were found to have much lower corrosion rates than those coated with standard sputtered C of equivalent thickness. The composition of the sputtered carbons was varied by changing the sputtering gas. The corrosion rate depended on the type of carbon: ion beam C-H < sputtered C-H, < sputtered C-N < sputtered C. The different corrosion rates may be a result of differences in both coverage and catalytic activity of the carbon layers.

Novotny and colleagues [136,142] have described methods for estimating lifetimes of disks in drives using accelerated T/H tests. In the first approach, the extent of corrosion of a disk following T/H exposure was determined by a measurement of the surface Co concentration on the disk surface using Auger electron spectroscopy

Copyright © 2002 Marcel Dekker, Inc.

[142]. The surface Co concentration is a measure of the extent of corrosion. An unexposed disk surface generates no measurable Co signal despite small pores in the C overcoat that expose the Co-based alloy to the environment. Following T/H exposure, a Co-containing corrosion product forms on top of the overcoat as a result of attack of the exposed areas (Fig. 3b). Using the data of Novotny et al., the Co surface concentration is found to vary with exp(RH/21) and $t^{1/2}$, with a thermal activation energy of 0.25 eV. In order to estimate disk lifetime with these data, one must assume that lifetime is inversely proportional to surface Co concentration. A later work describes an approach to lifetime estimation that uses a functional test, a head flying over a disk after T/H exposure [136]. If the head contains a magnetoresistive sensor, the number of asperities on the disk can be determined. This is a very relevant measurement because, as mentioned earlier, disk drives fail by head crashes long before they develop measurable increases in error rate from corrosion of magnetic material. In that work, the disk lifetime was found to vary with exp(-RH/13), with an activation energy of 0.27 eV. Another study determined activation energy by electrical resistance changes for sputter-deposited CoCr films exposed to T/H conditions [143]. Depending on composition and deposition conditions, values ranging from 0.08 to 0.3 eV were determined. The very low thermal activation energies reported in this study call into question the usefulness of performing stress tests at elevated temperatures for this system.

Thin-Film Inductive Head Materials

The structure of thin-film inductive recording heads results in the exposure to the environment of small areas of metal, often permalloy (Ni-20Fe), which is a relatively corrosion-resistant alloy. In fact, in-service corrosion of permalloy is not a problem and thin-film inductive heads have no history of corrosion-induced field failure. However, corrosion of permalloy can occur during manufacturing, leading to yield losses.

Exposure of freshly deposited permalloy films to the atmosphere or oxidation in pure O_2 up to 250°C results in surface segregation and preferential oxidation of Fe to Fe_2O_3 [144–146]. However, anodically formed films are enriched in Ni and consist of an inner layer of NiO and an outer layer of mixed nickel and iron hydroxides [147,148]. The more reactive element Fe oxidizes first and is enriched at the surface during atmospheric oxidation but dissolves into solution during anodic oxidation.

The method of deposition has been reported to have a large influence on the corrosion properties of permalloy [149–151]. In particular, plated permalloy films have been found to be more susceptible to corrosion than either bulk material or vacuum-deposited films of nominally the same composition. For instance, sputter-deposited permalloy was found to passivate in pH 2 solutions, but plated films did not [150]. Another study in neutral chloride solutions showed that plated permalloy had a lower pitting potential than bulk permalloy [151]. These reports suggested that plated films either have regions locally enriched in Fe or have a crystallographic orientation that is more susceptible to attack. However, little supporting evidence was provided.

An explanation for the enhanced corrosion susceptibility of plated permalloy films was offered in a study that examined the walls of pits in thin-film samples using Auger electron spectroscopy [149]. The pit walls showed a large enhancement of

Copyright © 2002 Marcel Dekker, Inc.

S compared with top surfaces at regions away from pits. C and N were also enriched at the pit walls. Analogous experiments with sputter-deposited permalloy films indicated that S was present in negligible amounts at both the pit wall and top surface, N was absent at both locations, and less C was present on the newer pit wall surface than on the top surface. The coincidental appearance of S, C, and N at pit walls in plated permalloy suggested that saccharin ($C_7H_5NO_3S$), a stress-relieving agent added to the plating bath, was responsible for the poor corrosion resistance. Apparently, a small amount of the surface-active molecule is incorporated in the alloy during plating, reduces corrosion resistance, and enriches at the pit surface during pit growth. Similar behavior has been described for the case of small S additions to Ni-25Fe single crystals [148].

As described before, current magnetic recording technology uses only inductive heads for writing. However, modern high-density disks with high magnetic coercivity require a write head fabricated from a material with a higher magnetic moment than permalloy. Many current production devices make use of a NiFe alloy having higher Fe than permalloy (45Ni-55Fe). The corrosion characteristics of high-Fe NiFe have not been reported, but it is certainly more susceptible to corrosion than permalloy given the higher Fe content. Co alloys have also been suggested for use as a high-moment soft magnetic material in write heads [152]. The corrosion behavior of electrodeposited CoNiFe alloys has been reported [153,154]. As with permalloy, sulfur incorporation into CoNiFe was shown to be detrimental to the corrosion behavior in 2.5% NaCl. The presence of 0.3 at % S resulted in a 400 mV lower pitting potential than for a similar alloy with < 0.1 at % S [153]. An alloy deposited with thiourea as an additive instead of saccharin and an extremely high S content (3.8 at %) exhibited only active dissolution in 2.5% NaCl with no evidence of passivity [154].

A corrosion protection scheme developed for Co and Co-based alloys may be useful for reducing corrosion during processing [155]. The concept takes advantage of the remarkable corrosion resistance imparted to Cu by benzotriazole (BTA). A Cu-BTA film is generated on the surface of a Co sample when it is immersed in a solution containing cupric ions and BTA. Due to its relative nobility, Cu tends to exchange with Co and plate on the surface. However, the two-step sequential reduction of cupric is stopped before metallic Cu is produced because cuprous ions react with the BTA to form a Cu(I)-BTA protective film. This film is robust in the sense that it provides protection even after the part is removed from the BTA-containing solution and is subsequently exposed to environments devoid of BTA. Such treatments have resulted in a 100-fold reduction of corrosion rate for Co samples in a DI water droplet.

Magnetoresistive (MR) Head Materials

A cross section of the nm-thick layers in MR heads is exposed during the lapping process. If all of the metals used in the device do not corrode slowly or spontaneously passivate in the potentially aggressive lapping environment, severe corrosion can result. In addition, given the variety of the metals used, their susceptibility to corrosion, and their intimate contact, galvanic corrosion can be a severe problem. Considerable work has been performed in recent years addressing this liability. In particular, the corrosion behavior of the antiferromagnetic layer has been extensively

Copyright © 2002 Marcel Dekker, Inc.

characterized because it is usually the most susceptible layer in the structure. MnFe, a commonly used antiferromagnetic layer, has been shown to be extremely corrodible; for instance, it exhibits only active dissolution 0.1 N Na_2SO_4 [139]. In a buffered borate solution of higher pH, it forms a protective passive film at high potentials after a rather large active peak, and the corrosion rate, peak current density, and passive current density all decrease with increasing pH. These results are interesting because the possibility exists that environment control may be an effective corrosion mitigant in certain process steps (e.g., lapping) that might otherwise be aggressive.

Given the corrosion susceptibility of MnFe, the suitability of using several alternative antiferromagnetic layers has been investigated, including MnIr [139,156–158], MnRh [158], MnNi [157–160], MnNiCr [159], MnPd [160], MnPdPt [160], and NiO [161]. The noble metal substitutions for Fe make the potential of these new alloys much more positive, which decreases galvanic interactions with other metals in the structure such as Cu. The corrosion rates of MnIr and MnRh are apparently only slightly lower than that of MnFe in many environments [139,157,158]. The pitting potentials in chloride for MnNi, MnPd, and MnPdPt have been reported to be significantly higher than that of MnFe [160]. Replacement of the most susceptible material in the structure with an oxide certainly is desirable from the corrosion standpoint. For example, spin valves made with NiO antiferromagnetic layers were shown to exhibit remarkable corrosion resistance [161].

Magneto-Optic (MO) Alloys

The alloys used as MO recording media are extremely reactive because of their high rare-earth (e.g., Tb) content. Given the free energy of formation of terbium oxide (–446 kcal/mol), there exist few metal oxides that are thermodynamically stable in the presence of Tb metal, even at room temperature [162]. Therefore, attempts to protect Tb by using an oxide overlayer result in oxidation of the Tb and reduction of the overlayer. The oxides that form on Fe-26Tb in air at 200°C have been studied by AES [163,164]. Upon exposure to air at room temperature, a 20-Å outer layer of iron oxide covered a 60-Å layer of terbium oxide with approximate compositions of Fe_2O_3 and Tb_2O_3, respectively. Oxidation at 200°C resulted in the formation of an internally oxidized zone consisting of terbium oxide and metallic FeTb that was enriched in Fe. This zone grew initially with parabolic kinetics, and then the growth rate accelerated. At that point, the two outer oxide layers started to thicken.

Exposure of MO films to aqueous solutions or high-humidity conditions results in localized attack [162,165]. Pits can form even during brief immersion in DI water or long-term storage in office ambient conditions. Analysis of pits in Fe-23Tb-12Co by scanning Auger microscopy found depletion of Fe and Co from the pitted region [162]. This apparently reflects the low solubility of Tb_2O_3, which nonetheless does not provide corrosion protection. Such pits formed in aqueous solutions are circular in shape. In contrast, the localized corrosion formed under atmospheric conditions is wormlike, similar in nature to filiform corrosion.

Many different alloying elements, when added to FeTbCo in the amount of about 5%, have been found to improve the corrosion resistance [135,165]. Both improved passivity and reduced pitting susceptibility have been achieved in this fashion. The primary protection of MO disks, however, derives from protective

Copyright © 2002 Marcel Dekker, Inc.

overlayers. The MO layer is typically covered by a dielectric layer for optical and thermal reasons. Some designs employ a metallic layer such as Al as a reflector, which covers the dielectric layer. Sputter-deposited Al binary alloys, which display for superior pitting resistance compared with pure Al, have also been used. The metallic reflective layer in MO disk is the first application of these remarkably corrosion-resistant alloys that have generated significant attention [166–171].

Corrosion Mitigation of Magnetic-Storage Components

The preceding subsections describe the corrosion concerns and liabilities of magnetic-storage components and devices, as well as efforts taken to reduce corrosion. As a summary, care must be taken in materials selection, in particular to minimize galvanic corrosion. Heads and disks are covered with carbon layers in service, so it is important to consider issues such as electrochemical reactivity of the carbon layers (which will vary with composition and details of the deposition method) and coverage (which depends on the thickness of the carbon layer and the roughness of the head or disk). Certain processes, such as lapping and rinsing, are amenable to environmental control, and it is critical to understand and control the response of all exposed metals to process fluids. On the disk drive level, sealing is a critical issue. It is possible to seal drives using gaskets in an attempt to excluse the external environment, although rubber gaskets are permeable to water to a certain extent. Also, breather holes are often incorporated into drives to allow pressure equilibration, which is important, for instance, in laptops used in airplanes. One can envision how a portable device might be transported between a cool air-conditioned environment and a hot and humid one. The relative rates of heat and humidity transport will control whether deleterious water condensation occurs under such conditions.

CONCLUDING REMARKS

Significant progress has been made during the past quarter century in reducing environmentally induced damage in microelectronic and magnetic data-storage devices. These improvements have been made even though metallization features continue to become more susceptible to corrosion. Important advancements responsible for this progress have involved such aspects as improved manufacturing control, elimination of contamination sources, use of improved materials, and development of less vulnerable designs. One remaining significant shortcoming is the lack of a capability to predict reliability and service life using accelerated-aging data. This situation primarily exists because we still have not developed an adequate physical understanding of the relevant corrosion processes. Several factors have contributed to this "corrosion science" inadequacy including (a) the existence of numerous coupled and complex phenomena, (b) a rapidly evolving technology (moving target), and (c) the success with eliminating actual corrosion issues. Challenges to satisfy this need along with new emerging engineering-level problems will certainly continue well into the future as dimensions continue to shrink, more susceptible materials such as copper are used, and higher service life and reliability are demanded.

Copyright © 2002 Marcel Dekker, Inc.

REFERENCES

1. H. B. Bakoglu, *Circuits, Interconnections, and Packaging for VLSI*, Addison-Wesley, Reading, MA, 1990.
2. M. B. Small and D. J. Pearson, *IBM J. Res. Dev. 34*:858 (1990).
3. P. C. Andricacos, *Interface 8*(1):32(1999).
4. D. P. Seraphim, R. Lasky, and C. Li, *Principles of Electronic Packaging*, McGraw-Hill, New York, 1989.
5. R. R. Tummala and E. J. Rymaszewski, *Microelectronics Packaging Handbook*, Van Nostrand Reinhold, New York, 1989.
6. K. R. Kinsman, *Electronic Packaging and Corrosion in Microelectronics* (M.E. Nicholson, ed.), ASM International, Metals Park, OH, 1987, p. 1.
7. L. Gallace and M. Rosenfield, *RCA Rev. 45*:249 (1984).
8. D. R. Johnson, D. W. Palmer, D. W. Peterson, D. S. Shen, J. N. Sweet, J. T. Hanlon, and K. A. Peterson, *Microelectronics Plastic Molded Packaging*, Sandia National Laboratories, Albuquerque, NM, 1997.
9. M. G. Pecht, L. T. Nguyen, and E. B. Hakim, *Plastic-Encapsulated Microelectronics*, John Wiley & Sons, New York, 1995.
10. G. G. Harman, *Wire Bonding in Microelectronics: Materials, Processes, Reliability, and Yield*, McGraw-Hill, New York, 1997.
11. P. G. Slade, ed. *Electrical Contacts: Principles and Applications*, Marcel Dekker, New York, 1999.
12. R. Holm, *Electric Contacts*, Springer-Verlag, New York, 1967.
13. F. Chen and A. J. Osteraas, *Electronic Packaging and Corrosion in Microelectronics* (M.E. Nicholson, ed.), ASM International, Metals Park, OH, 1987, p. 175.
14. S. Ming, M. Pecht, and M. Natishan, *Microelectron. J. 30*:217 (1999).
15. C. D. Mee and E. D. Daniel, *Magnetic Recording*, Vol. I, *Technology*, McGraw-Hill, New York, 1987.
16. J. A. Brug, T. C. Anthony, and J. H. Nickel, *MRS Bull. 21*:23 (1996).
17. J. W. Osenbach, *Semiconductor Sci. Tech. 11*:155 (1996).
18. R. B. Comizzili, R. P. Frankenthal, and K. J. Hanson, *Mater. Sci. Eng. A A198*:153 (1995).
19. R. P. Frankenthal, *Solid State Electron. 33*:69 (1990).
20. J. D. Sinclair, *J. Electrochem. Soc. 135*:89C (1988).
21. S. C. Kolesar, *Ann. Proc. Reliab. Phys. 12*:155 (1974).
22. P. G. Slade, *Electrical Contacts: Principles and Applications* (P.G. Slade, ed.)., Marcel Dekker, New York, 1999, p. 89.
23. W. H. Abbott, *Electrical Contacts: Principles and Applications* (P.G. Slade, ed.)., Marcel Dekker, New York, 1999, p. 113.
24. C. Leygraf and T. Graedel, *Atmospheric Corrosion*, John Wiley & Sons, New York, 1999.
25. W. H. Ailor, ed. *Atmospheric Corrosion*, Wiley Interscience, New York, 1982.
26. P. B. P. Phipps and D. W. Rice, *Corrosion Chemistry* (J.R. Brubaker and P.B.P. Phipps, eds.), American Chemical Society, Washington, DC, 1979, p. 235.
27. S. P. Sharma, *J. Vac. Sci. Technol. 15*:1557 (1979).
28. T. Ajiki, M. Sugimoto, H. Higuchi, and S. Kumada, *IEEE Ann. Proc. Reliab. Phys. 17*:118 (1979).
29. E. B. Hakim, J. Fink, S. M. Tam, P. McCluskey, and M. Pecht, *Circuit World 23*:26 (1997).
30. V. Brusic, G. S. Frankel, C.-K. Hu, M. M. Plechaty, and B. M. Rush, *Corrosion 47*:35 (1991).
31. C. Hoge, *IEEE Trans. Comp. Hybrids Manuf. Tech. CHMT-13*:1098 (1990).

Copyright © 2002 Marcel Dekker, Inc.

32. J. Maa, H. Gossenberger, and R. H. Paff, *J. Vac. Sci. Technol. B 8*:1052 (1990).
33. N. Parekh and J. Price, *J. Electrochem. Soc. 137*:2199 (1990).
34. S. Mayumi, Y. Hata, K. Hujiwara, and S. Ueda, *J. Electrochem. Soc*., *137*:2534 (1990).
35. J. M. Eldridge, *3rd Conference on Electronic Packaging, Materials, and Processing in Microelectronics* (M.E. Nicholson, ed.), ASM, Metals Park, OH, 1987, p. 283.
36. W.-Y. Lee, J.M. Eldridge, and G. C. Schwartz, *J. Appl. Phys. 52*:2994 (1981).
37. P. A. Totta, *J. Vac. Sci. Technol. 13*:26 (1976).
38. S. Thomas and H. M. Berg, *IEEE Trans. Comp. Hybrids Manuf. Tech. CHMT-10*:252 (1987).
39. J. D. Sinclair, L. A. Psota-Kelty, C. J. Weschler, and H. C. Shields, *J. Electrochem. Soc. 137*:1200 (1990).
40. R. P. Frankenthal, R. Lobnig, D. J. Siconolfi, and J. D. Sinclair, *J. Electrochem. Soc. 140*:1902(1993).
41. W. H. J. Vernon, *Trans. Faraday Soc. 31*:1668 (1935).
42. J. E. Anderson, V. Markovac, and P. R. Troyk, *IEEE Trans. Comp. Hybrids Manuf. Tech. CHMT-11*:152 (1988).
43. H. Manko, *Solders and Soldering*, McGraw-Hill, New York, 1979.
44. J. Brous, *Electronic Packaging and Corrosion in Microelectronics* (M.E. Nicholson, ed.), ASM International, Metals Park, OH, 1987, p. 161.
45. J. J. Steppan, J. A. Roth, L. C. Hall, D. A. Jeannotte, and S. P. Carbone, *J. Electrochem. Soc. 134*:175(1987).
46. R. B. Comizzoli, *Materials Developments in Microelectronic Packaging Conference Proceedings* (P.J. Singh, ed.), ASM, Materials Park, OH, 1991, p. 311.
47. B. D. Yan, G. W. Warren, and P. Wynblatt, *Corrosion*, *43*:118 (1987).
48. S. L. Meilink, M. Zamanzadeh, G. W. Warren, and P. Wynblatt, *Corrosion 44*:644 (1988).
49. M. Zamanzadeh, Y. S. Liu, P. Wynblatt, and G. W. Warren, *Corrosion 45*:643 (1989).
50. M. Zamanzadeh, S. L. Meilink, G. W. Warren, P. Wynblatt, and B. D. Yan, *Corrosion 46*:665 (1990).
51. G. W. Warren, P. Wynblatt, and M. Zamanzadeh, *J. Electron. Mater. 18*:339 (1989).
52. A. J. Griffin, S. E. Hernandez, F. R. Brotzen, and C. F. Dunn, *J. Electrochem. Soc. 141*:807 (1994).
53. D. A. Jones, *Principles and Prevention of Corrosion,* Prentice-Hall, Englewood Cliffs, NJ, 1992.
54. R. Brownson, K. Butler, S. Cadena, and M. Detar, *Microelectronic Manufacturing Yield, Reliability, and Failure Analysis II*, Int. Soc. Optical Eng, 1996, p. 95.
55. G. L. Schnable, R. B. Comizzoli, W. Kern, and L. K. White, *RCA Rev. 40*:416 (1979).
56. R. Padmanaghan, *IEEE Trans. Comp. Hybrids Manuf. Tech. CHMT-8*:435 (1985).
57. P. R. Engel, T. Corbett, and W. Baerg, *Elec. Comp. Conf. 33*:245 (1983).
58. R. B. Comizzoli, *RCA Rev. 37*:483 (1976).
59. W. M. Paulson and R. W. Kirk, *Ann. Proc. Reliab. Phys. 12*:172 (1974).
60. R. C. Olberg and J. L. Bozarth, *Microelectron. Reliab. 15*:601 (1976).
61. R. B. Comizzoli, *J. Electrochem. Soc. 123*:386 (1976).
62. E. P. G. T. v. d. Ven and H. Koelmans, *J. Electrochem. Soc. 123*:143 (1976).
63. T. Wada, H. Higuchi, and T. Ajiki, *Ann. Proc. Reliab. Phys. 23*:159 (1985).
64. V. Bhide and J. M. Eldridge, *Ann. Proc. Reliab. Phys. 21*:44 (1983).
65. M. Iannuzzi, *IEEE Trans. Comp. Hybrids Manuf. Tech. 6*:191 (1983).
66. N. L. Sbar and R. P. Kozackiewicz, *IEEE Trans. Electron. Dev. ED-26*:56 (1979).
67. R. K. Ulrich, D. Yi, W. D. Brown, and S. S. Ang, *Corros. Sci. 33*:403 (1992).
68. N. Lycoudes, *Solid State Tech.* October:53 (1978).
69. C. G. Shirley and M. S. DeGuzman, *IEEE/Ann. Proc. Reliab. Phys. 31*:217 (1993).

Copyright © 2002 Marcel Dekker, Inc.

70. V. Koeninger, H. H. Uchida, and E. Fromm, *IEEE Trans. Components Packaging Manufac. Tech. Part A 18*:835 (1995).
71. J. R. Scully, R. P. Frankenthal, K. J. Hanson, D. J. Siconolfi, and J. D. Sinclair, *J. Electrochem. Soc. 137*:1365 (1990).
72. J. R. Scully, D. E. Peebles, J. A. D. Romig, D. R. Frear, and C. R. Hills, *Metall. Trans. 23A*:2641 (1992).
73. R. P. Frankenthal and W. H. Becker, *J. Electrochem. Soc. 126*:1718 (1979).
74. A. D. Marderosian, *IEEE 15th Ann. Proc. Reliab. Phys. 15*:92 (1997).
75. L. T. Nguyen and C. A. Kovac, SAMPLE Electronics Materials and Processes Conference, 1987.
76. L. T. Nguyen, SPE 46th ANTEC, 1988.
77. J. J. Lietkus, L. T. Nguyen, and S. L. Buchwalter, SPE 46th ANTEC, 1988, p. 462.
78. T. Wada, M. Sugimoto, and T. Ajiki, *J. Electrochem. Soc. 136*:732 (1989).
79. J. S. Osenbach and J. L. Zell, *IEEE Trans. Comp. Hybrids Man Tech. 16*:350 (1993).
80. R. W. Thomas, *Proc. Elec. Comp. Conf. 26*:272 (1976).
81. W. E. Swartz, J. H. Linn, J. M. Ammons, M. kovac, and K. Wilson, *Ann. Proc. Reliab. Phys. 21*:52 (1983).
82. M. Pecht, *IEEE Trans. Comp. Hybrids Manuf. Tech. 13*:383 (1990).
83. M. Pecht and W. C. Ko, *Int. J. Hybrid Microelectron. 13*:41 (1990).
84. R. K. Lowry, C. J. V. Leeuwen, B. L. Kennimer, and L. A. Miller, *Ann. Proc. Reliab. Symp. 16*:207 (1978).
85. A. H. Rawics, *Microelectron. Reliability 34*:875 (1994).
86. V. Brusic, D. D. DiMilia, and R. MacInnes, *Corrosion 47*:509 (1991).
87. R. P. Frankenthal and D. J. Siconolfi, *J. Vac. Sci. Technol. 17*:1315 (1980).
88. R. P. Frankenthal and D. J. Siconolfi, *Corros. Sci. 21*:479 (1981).
89. K. J. Puttlitz, *IEEE Trans. Comp. Hybrids Manuf. Tech. CHMT-13*:188 (1990).
90. H. L. Yeh and H. Dalal, *Reliability of Semiconductor Devices and Interconnection and Multilevel, Metallization, Interconnection and Contact Technologies* (H.S. Rathore, G.C. Schwartz, and R. Susko, eds.), The Electrochemical Society, Pennington, NJ, 1989, p. 81.
91. J. R. White, D. D. Coolbaugh, and M. A. Chopra, *Corrosion of Electronic Materials and Devices* (J.D. Sinclair, ed.), The Electrochemical Society, Pennington, NJ, 1991, p. 319.
92. R. B. Comizzoli, J. P. Franey, G. W. Kammlott, A. E. Miller, A. J. Muller, G. A. Peins, L. A. Psota-Kelty, J. D. Sinclair, and R. C. Wetzel, *J. Electrochem. Soc. 139*:2058 (1992).
93. D. J. Lando, J. P. Mitchell, and T. L. Welsher, *Ann. Proc. Reliab. Phys. 71*:51 (1979).
94. V. Tierney, *J. Electrochem. Soc.128*:1321 (1981).
95. D. W. Noon, *3rd Conference on Electronic Packaging, Materials, and Processing in Microelectronics* (M.E. Nicholson, ed.), ASM, Metals Park, OH, 1987, p. 49.
96. K. M. Striny and A. W. Schelling, *Elec. Comp Conf. 313*:238 (1981).
97. W. Nelson, *Accelerated Testing—Statistical Models, Test Plans, and Data Analysis,* John Wiley & Sons, New York, 1990.
98. D. S. Peck and J. C. H. Zierdt, *Ann. Proc. Reliab. Phys. 11*:146 (1973).
99. D. S. Peck, *IEEE/Ann. Proc. Reliab. Phys. 24*:44 (1986).
100. P. W. Peterson, *IEEE Trans. Comp. Hybrids Manuf. Tech. CHMT-2*: 422 (1979).
101. R. P. Merrett, J. P. Bryant, and R. Studd, *Ann. Proc. Reliab. Phys. 21*:73 (1983).
102. C. F. Dunn and J. W. McPherson, *J. Electrochem. Soc. 135*:661 (1988).
103. W. W. Weick, *IEEE Trans. Reliab. R-29*:109 (1980).
104. J. E. Gunn, R. E. Camenga, and S. K. Malik, *Ann. Proc. Reliab. Phys. 21*:66 (1983).

Copyright © 2002 Marcel Dekker, Inc.

105. J. W. Osenbach and J. L. Zell, *Reliability of Semiconductor Devices and Interconnection and Multilevel, Metallization, Interconnection and Contact Technologies* (H.S. Rathore, G.C. Schwartz, and R. Susko, eds.), The Electrochemical Society, Pennington, NJ, 1989, p. 53.
106. D. R. Sparks, *Thin Solid Films 235*:108 (1993).
107. T. Yoshida and T. Takahashi, *IEEE Proc. IRPS* 268 (1982).
108. C. G. Shirley and C. E. C. Hong, *IEEE/Ann. Proc. Reliab. Phys. 29*:12 (1991).
109. K. D. Cluff and D. B. Barket, *J. Inst. Environ. Sci. Tech. Jul/Aug*:36 (1998).
110. L. C. Wagner, *Electronic Packaging and Corrosion in Microelectronics* (M.E. Nicholson, ed.), ASM, Metals Park OH; 1987, p. 275.
111. H. Koelmans, *Ann. Proc. Reliab. Phys. 12*:168 (1974).
112. S. P. Sim and R. W. Lawson, *IEEE 17th Ann. Proc. Reliab. Phys. 17*:103 (1979).
113. R. P. Frankenthal, *Properties of Electrodeposits: Their Measurement and Significance* (R. Sard, J. H. Leidheiser, and F. Ogburn, eds.), The Electrochemical Society, Pennington, NJ, 1975, p. 142.
114. D. W. Rice, P. B. P. Phipps, and R. Tremoureux, *J. Electrochem. Soc. 126*:1459 (1979).
115. W. H. Abbott, *IEEE Trans. Comp. Hybrids Manuf. Tech. CHMT-11*:22 (1988).
116. W. H. Abbott, *IEEE Trans. Comp. Hybrids Manuf. Tech. CHMT-I3*:40 (1990).
117. R. R. Gore, R. Witska, J. R. Kirby, and J. L. Chao, *IEEE Trans. Comp. Hybrids Manuf. Tech. CHMT-13*:27 (1990).
118. T. F. Reichert and K.-F. Ziegahn, *Corrosion and Reliability of Electronic Materials and Devices* (R.B. Comizzoli and J. D. Sinclair, eds.), The Electrochemical Society, Pennington, NJ, 1993, p. 364.
119. R. T. Howard, *IEEE Trans. Comp. Hybrids Manuf. Tech. CHMT-5*:454 (1982).
120. R. T. Howard, *IEEE Trans. Comp. Hybrids Manuf. Tech. CHMT-4*:520 (1981).
121. I. Lerner and J. M. Eldridge, *J. Electrochem. Soc. 129*:2270 (1982).
122. H. M. Berg and W. M. Paulson, *Microelectron. Reliab. 20*:247 (1990).
123. C. G. Shirley, *IEEE/Ann. Proc. Reliab. Phys. 32*:72 (1994).
124. J. W. McPherson, *Ann. Proc. Reliab. Phys. 24*:12 (1986).
125. D. Stroehle, *IEEE Trans. Comp. Hybrids Manuf. Tech. CHMT-6*:537 (1983).
126. B. Reich and E. B. Hakim, *Solid State Tech.* September:65 (1972).
127. O. Hallberg and D. S. Peck, *Quality and Reliability Engineering International 7*:169 (1991).
128. T. E. Graedel, *Corros. Sci. 38*:2153 (1996).
129. P. Lall, *IEEE Trans Reliability 45*:3 (1996).
130. K. M. Takahashi, *J. Electrochem. Soc. 138*:1587 (1991).
131. N. L. Sbar, *Proc. Elec. Comp. Conf. 26*:277 (1976).
132. W. M. Paulson and R. P. Lorigan, *IEEE Ann. Proc. Reliab. Phys. 14*:42 (1976).
133. S. K. Fan and J. W. McPherson, *Ann. Proc. Reliab. Phys. 26*:50 (1988).
134. Z. Szklarska-Smialowska, *Pitting Corrosion of Metals*, NACE, Houston, 1986.
135. V. Brusic, J. Horkans, and D. J. Barclay, *Electrochemistry in Transition* (O.J. Murphy, S. Srinivasan, and B.E. Conway, eds.), Plenum, New York, 1992, p. 547.
136. V. J. Novotny, *Adv. Info. Storage Syst. 4*:255 (1992).
137. V. Brusic, M. Russak, R. Schad, G. Frankel, A. Selius, D. DiMilia, and D. Edmonson, *J. Electrochem. Soc. 136*:42 (1989).
138. V. J. Novotny and N. Staud, *J. Electrochem. Soc. 135*:2931 (1988).
139. G. S. Frankel, *Electrochemical Synthesis and Modification of Materials* (S.G. Corcoran, *et al*., eds.)., Materials Research Society, Pittsburgh, 1997, p. 541.
140. K. Kinoshita, *Carbon, Electrochemical and Physiochemical Properties*, John Wiley & Sons, New York, 1988.
141. E. V. Anoikin, G. S. Ng, M. M. Yang, J. L. Chao, and J. R. Elings, *IEEE Trans. Magn. 34*:1717(1988).
142. V. Novotny, G. Itnyre, A. Homola, and L. Franco, *IEEE Trans. Magn. MAG-23*: 3645 (1987).

Copyright © 2002 Marcel Dekker, Inc.

143. K. Tagami and H. Hayashida, *IEEE Trans. Magn. MAG-23*:3648 (1987).
144. R. A. Pollak and C. H. Bajorek, *J. Appl. Phys. 46*:1382 (1975).
145. W.-Y. Lee and J. Eldridge, *J. Electrochem. Soc. 124*:1747 (1977).
146. W.-Y. Lee, G. Scherer, and C. R. Guarnieri, *J. Electrochem. Soc. 126*:1533 (1979).
147. G. Dagan, W.-M. Shen, and M. Tomkiewicz, *J. Electrochem. Soc. 139*:1855 (1992).
148. P. Marcus, A. Tessier, and J. Oudar, *Corros. Sci. 4*:259 (1984).
149. G. S. Frankel, V. Brusic, R. G. Schad, and J.-W. Chang, *Corros. Sci. 35*:63 (1993).
150. J. G. Bornstein, C. H. Lee, L. A. Capuano, and D. A. Stevenson, *J. Appl. Phys. 65*:2090 (1989).
151. C. H. Lee, D. A. Stevenson, L. C. Lee, R. D. Bunch, R. G. Walmsley, M. D. Juanitas, E. Murdock, and J. E. Opfer, *Corrosion of Electronic and Magnetic Materials (P. Peterson, ed.), AIME,* Philadelphia, 1991, p. 102.
152. J.-W. Chang, P. C. Andricacos, B. Petek, and L. T. Romankiw, *Magnetic Materials, Processes, and Devices* (L.T. Romankiw and D. A. Herman, eds.), The Electrochemical Society, Pennington, NJ, 1992, p. 275.
153. T. Osaka, M. Takai, K. Hayashi, K. Ohashi, M. Saito, and K. Yamada, *Nature 392*:796 (1998).
154. T. Osaka, M. Takai, Y. Sogawa, T. Momma, K. Ohashi, M. Saito, and K. Yamada, *J. Electrochem. Soc. 146*:2092 (1999).
155. V. Brusic, G. S. Frankel, A. G. Schrott, T. A. Petersen, and B. M. Rush, *J. Electrochem. Soc. 140*:2507 (1993).
156. H. N. Fuke, K. Saito, Y. Kamiguchi, H. Iwasaki, and M. Sahashi, *J. Appl. Phys. 81*:4004(1997).
157. A. J. Devasahayam, P. J. Sides, and M. H. Kryder, *J. Appl. Phys. 83*:7261 (1998).
158. A. Veloso, P. P. Freitas, N. J. Oliveira, J. Fernandes, and M. Ferreira, *IEEE Trans. Magn. 34*:2343 (1998).
159. T. Lin, D. Mauri, N. Staud, C. Hwang, and J. K. Howard, *Appl. Phys. Lett. 65*:1183 (1994).
160. H. Kishi, Y. Kitade, Y. Miyake, A. Tanaka, and K. Kobayashi, *IEEE Trans. Magn. 32*:3380 (1996).
161. S. L. Burkett, S. Kora, J. L. Bresowar, J. C. Lusth, B. H. Pirkle, and M. R. Parker, *J. Appl. Phys. 81*:4912 (1997).
162. M. M. Farrow and E. E. Marinero, *J. Electrochem. Soc. 137*:808 (1990).
163. R. B. v. Dover, E. M. Gyorgy, R. P. Frankenthal, M. Hong, and D. J. Siconolfi, *J. Appl. Phys. 59*:1291 (1986).
164. R. P. Frankenthal, D. J. Siconolfi, R. B. v. Dover, and S. Nakahara, *J. Electrochem. Soc. 134*:235(1987).
165. G. Kirino, N. Ogihara, and N. Ohta, *J. Electrochem. Soc.138*:2259 (1991).
166. G. S. Frankel, M. A. Russak, C. V. Jahnes, M. Mirzamaani, and V. A. Brusic, *J. Electrochem. Soc. 136*:1243 (1989).
167. W. C. Moshier, G. D. Davis, J. S. Ahearn, and H. F. Hough, *J. Electrochem. Soc. 133*:1063 (1986).
168. W. C. Moshier, G. D. Davis, J. S. Ahearn, and H. F. Hough, *J. Electrochem. Soc. 134*:2677 (1987).
169. W. C. Moshier, G. D. Davis, and G. O. Cote, *J. Electrochem. Soc. 136*:356 (1989).
170. G. D. Davis, W. C. Moshier, T. L. Fritz, and G. O. Cote, *J. Electrochem. Soc. 137*:422 (1990).
171. B. A. Shaw, T. L. Fritz, G. D. Davis, and W. C. Moshier, *J. Electrochem. Soc. 137*:1317 (1990).

Copyright © 2002 Marcel Dekker, Inc.

19

Organic Coatings

J. H. W. de Wit
Netherlands Institute for Metals Science, Delft University of Technology, Delft, and Corus Research and Development, Ijmuiden, The Netherlands

D. H. van der Weijde
Corus Research and Development, Ijmuiden, The Netherlands

G. Ferrari
TNO Industrie, Den Helder, The Netherlands

GENERAL INTRODUCTION

Construction metals are expected to have excellent mechanical properties and machinability at a low price, while at the same time they should be corrosion resistant. These properties can seldom be met in one and the same material. Separating the base metal with good mechanical properties from the corrosive surrounding by applying a surface layer can solve this problem. These layers can be:

1. Metallic layers
2. Nonmetallic inorganic layers such as conversion layers, anodized layers, some ceramic chemical vapor deposition (CVD) and physical vapor deposition (PVD) layers, and enamel layers
3. Organic layers such as paints, lacquers, and polymer sheets

In this chapter we will discuss organic layers. The use of organic coatings for the protection of metals against corrosion is widespread in building, construction, food packaging, automotive, and marine applications. For these applications, typical and mostly successful types are developed. The choice of coating also depends on the type of substrate—steel, galvanized steel, or aluminum—combined with specific surface treatments. Evaluation of coating quality on site on a ship, a building, a car, or structural steelworks normally takes place when visible deterioration or defects occur. Moreover, apart from cleaning schedules, coating maintenance is usually a matter of planned repainting or unexpected repair when the coating fails. The development of coatings is mainly based on years of experience and accelerated testing in salt fog and humidity chambers, Q-UV, Weather-O-meters, Kesternich, etc. The conditions in these tests are based on the physical or chemical load in practice that is assumed to be the most important, and moreover the load is

Copyright © 2002 Marcel Dekker, Inc.

increased in order to speed up coating aging or corrosion. In these tests that are also used for screening of existing coatings, a reference sample with well-known properties is included to allow estimation of the quality. Outdoor exposures have to be used for a final verification of the quality, often in parallel with the actual use of the newly developed coating product. Cyclic weathering tests have been developed. Examples are the Hoogovens Cyclic Test (HCT) [1], the Hoogovens Atmospheric Corrosion Test (ABC) and the Volvo Indoor Corrosion test. The conditions in these tests are much more representative of the actual situation of practical use of the coatings. Still results are to be validated with actual exposition under practical conditions. When evaluating the coating systems, the total system should be taken into account.

First of all, in order to achieve good protective action of the applied layers, it is important to obtain excellent adhesion of the coating to the base metal. For this reason the substrate surface must be cleaned very well before further surface treatment and application of the surface layer.

Cleaning is often performed in two stages. First, the organic impurities such as oil, grease, and paint are removed from the surface. Then solid inorganic material such as rust, mill scales, and other corrosion products can be removed. The organic impurities can be removed in various ways:

With organic solvents
With strongly alkaline solution
With emulsion baths
By steam cleaning

The solid inorganic material can be removed by:

Mechanical treatment including brushing, grinding, polishing, and sandblasting and shot peening with various kinds of shot, such as metallic particles, corundum, and glass beads
Heat treatment with flames or induction heating followed by fast cooling to obtain scaling
Chemical picking with strong acids

Pickling in acid will probably be used less intensively in the coming years because of environmental problems. In many cases, optimized mechanical treatment (e.g., micropeening, an optimized form of shot peening with glass beads) will then be the substitute [2].

In most cases, after cleaning a further surface pretreatment, which may involve metallic and/or nonmetallic layers, is necessary in order to obtain good adhesion and thus protective properties. Also, the quality of the application procedures determines the final protective properties [3–18]. Of course, the structure of the polymeric network, the chemical composition, flaws, and the ease with which the coating is damaged on mechanical impact are also relevant for the final effectiveness of the protection. In fact, we have to take into account the properties of the whole system.

THE COMPOSITION OF COATING SYSTEMS

Organic coatings consist of four basic constituents: binder, pigments and fillers, additives, and solvents. Therefore the properties depend strongly on the

Copyright © 2002 Marcel Dekker, Inc.

actual recipe and the procedures and precautions taken during application of the layer.

Organic coatings may protect metal structures against a specific otherwise corrosive environment in a relatively economical way. The efficiency with which protection is provided is determined by a number of properties of the total coated system, which consists of the paint film(s), the metal substrate, and its pretreatment.

The composition of the paint film itself has a major influence on the corrosion protection provided by the coatings. Therefore the major constituents of organic coating systems are given here in a very concise form. More elaborate information can be found in the literature [12,13].

Binder

The binder forms the matrix of the coating, the continuous polymeric phase in which all other components may be incorporated. Its density and composition largely determine the permeability, chemical resistance, and ultraviolet (UV) resistance of the coating.

A continuous film is formed out of a recently applied liquid coating through either physical curing, chemical curing, or a combination of these. An example of the physical curing process is the sintering of thermoplastic powder coatings. Before application, this type of paint consists of a large number of small binder particles. These particles are deposited on a metal surface using special application techniques. Subsequently, the paint is baked in an oven to form a continuous film by sintering.

Chemical curing involves film formation through chemical reactions. This may be oxidative curing, where oxygen from the atmosphere reacts with the binder monomers, thus causing polymerization. Another example is reactive curing, where a polymer network is formed through polycondensation or polyaddition reactions. This may be the case with multicomponent coatings, where the binder reacts with cross-linkers.

Most often, both physical and chemical curing take place, as is the case with the film formation of thermosetting powders. At elevated temperatures, physical sintering of the particles takes place, followed by chemical reactions between different components in the powder. Another example is film formation of solvent-based reactive coatings, such as the common house paints. In this case, the solvent (physically) evaporates from the curing film, causing the binder molecules to coalesce and start chemical polymerization reactions.

Pigments

Pigments may be added to a coating for two reasons. (a) They can provide color to the coating system, which is an important issue for aesthetic reasons. (b) Pigments may be used to improve the corrosion protection properties of a coating. This improvement may be obtained, for example, by incorporation of flake-shaped pigments parallel to the substrate surface. If a sufficiently large pigment volume concentration (PVC) is used, the flakes will hinder the permeation of corrosive species into the coating by elongating their diffusion pathways, resistance inhibition.

Furthermore, so-called anticorrosion pigments may provide active protection against corrosion phenomena. These pigments may dissolve slowly in the coating

Copyright © 2002 Marcel Dekker, Inc.

and may provide protection by covering corrosion-sensitive sites under the coating; by sacrificially corroding themselves, thus protecting the substrate metal; or by passivating the surface.

Blocking pigments may adsorb at the active metal surface. They reduce the active area for corrosion and form a transport barrier for ionic species to and from the substrate. An example of this type is a group of alkaline pigments (lead carbonate, lead sulfate, zinc oxide) that may form soaps through interaction with organic oils.

Galvanic pigments are metal particles that are non-noble relative to the substrata. On exposure, these particles (zinc dust on steel) corrode preferentially, while at the original metal surface only the cathodic reaction occurs.

Passivating pigments reconstruct and stabilize the oxide film on the exposed metal substrate. Commonly, chromates with limited water solubility are used as passivating pigments (zinc chromate, strontium chromate). In aqueous solutions they may cause anodic passivation of a metal surface with a very stable chromium- and oxygen-containing passive layer.

Fillers

The main function of fillers in organic coatings is to increase the volume of the coating through the incorporation of low-cost materials (e.g., chalk, wood dust). They may also be used to improve coating properties such as impact and abrasion resistance and water permeability.

Additives

The term additives refers to a large group of components with very specific properties, which typically are added to a paint in very small quantities. The functions of the different additives may be quite diverse. Examples are thickeners, antifungal agents, dispersing agents, antifoam agents, anticoalescence agents, UV absorbers, and fire-retarding agents.

Solvents

The solvent has the function of reducing the viscosity of the binder and other components and enabling their homogeneous mixing. Furthermore, the reduced viscosity makes it possible to apply the coating in a thin, smooth, continuous film on a specific surface. The roles of the solvent in a coating prior to and after application are quite contradictory. In the liquid state, prior to application, paint should form a solution or a stable dispersion or emulsion of binder, pigments, and additives in the solvent. In other words, all solid components should remain more or less homogeneously distributed in the liquid phase. This requires high compatibility between solvent and components and the presence of repulsive forces between components to avoid clustering. In contrast, after the paint has been applied, a major attractive force between the components is necessary for the formation of a continuous film. The interaction with the solvent should decrease to enable the solvent to evaporate from the curing film. In order to achieve optimum storage and application properties, a correct choice of additives is vital. Correct material

Copyright © 2002 Marcel Dekker, Inc.

selection for coating formulation is often a complicated operation, where elaborate practical experience is needed.

In some specific cases, organic paint may be mixed and applied without the presence of solvents. These paint systems are referred to as solvent free. Examples of this are low-viscosity two-component epoxies and powder coatings. The application and curing of the powder coating were mentioned earlier. The epoxy coatings may be mixed and applied without the use of a solvent, as the two components typically have low viscosity. Mixing and application of these coatings are often done at elevated temperatures to reduce the viscosity as much as possible.

For environmental reasons, waterborne coatings are being used increasingly. The binder may be either dispersed or dissolved in the water phase. Dispersion coatings show lower gloss and less good adherence than the dissolved types such as alkyds, ureum and melamine, phenol, and acrylic-type coatings.

Also, high-solids coatings are used to minimize the loss of organic solvent to the atmosphere. These coatings consist of a larger amount of solid particles than normal organic solvent–based coatings. In order to reach an acceptable viscosity despite the high content of solid particles, the molecular weight of the binder molecules is lowered. Of course, this will also influence other properties of the coating such as sagging.

COMPLEX COATING SYSTEMS

Pretreatment: Conversion Layers

The corrosion protection of metallic substrates by simple organic layers is often not good enough because of, e.g., poor adhesion. Conversion layers are then applied. For these layers the substrate metal provides ions that become part of the protective coating after (electro-) chemical reaction of the substrate with a reactive medium. Well-known conversion layers are phosphate layers on steel and zinc, chromate layers on zinc and aluminum, and anodized layers on aluminum, the latter mostly without an organic topcoat. Anodizing is electrochemical treatment of a metal (mainly aluminum) while the metal itself is the anode. In this way a reasonably thick oxide layer (passive layer) is formed, with the thickness ranging from 1 to 30 μm, depending on the process conditions. Anodizing is performed in sulfuric acid, chromic acid, boric acid, oxalic acid, and other organic acids. Most important are anodizing processes in sulfuric acid and in chromic acid.

Pretreatment layers are used for a variety of reasons:

To improve the adherence of the organic layer
To obtain electrically insulating barrier layers
To provide a uniform grease-free surface
To provide active corrosion inhibition by passivating the metallic substrate or by reducing the rate of the oxygen reduction reaction

For an overview of this extensive field we refer to the literature [19–21]. Two important examples will be treated here very briefly, and some recent developments will also be mentioned.

Copyright © 2002 Marcel Dekker, Inc.

Chromate coatings can be produced on aluminum and its alloys, magnesium, cadmium, and zinc. They offer good protection and improve the adhesion of the organic layer [22–26]. The corrosion resistance provided by chromate is based on the following three properties [27]:

1. Cr(III) oxide, which is formed by the reduction of Cr(VI) oxide, has poor solubility in aqueous media and thus provides a barrier layer.
2. Cr(VI) will be included in the conversion coating and will be reduced to Cr(III) to repassivate the surface when it is damaged, thereby preventing hydrogen gas from developing.
3. The rate of the cathodic oxygen reaction is strongly reduced.

Chromate baths always contain a source of hexavalent chromium ion (e.g., chromate, dichromate, or chromic acid) and an acid to produce a low pH. Typical pH levels range from zero to around 3. Most chromating baths also contain a source of fluoride ions, which effectively attack the original (natural) aluminum oxide film and thus expose the bare metal substrate to the bath solution. Fluoride also prevents the aluminum ions (which are released by the dissolution of the oxide layer) from precipitating by forming complex ions. The fluoride concentration is critical. A low concentration does not result in a conversion layer at all because of failure to attack the natural oxide layer, and a high concentration results in poor adherence of the coating due to reaction of the fluoride with the aluminum metal substrate.

During the reaction hexavalent chromium is partially reduced to trivalent chromium, forming a complex mixture consisting largely of hydrated (hydr) oxides of both chromium and aluminum:

$$6H^+ + H_2Cr_2O_7 + 6e \rightarrow 2Cr(OH)_3 + H_2O$$

The formation of the chromate layer according to this reaction preferentially occurs along grain boundaries and other heterogeneities at the aluminum substrate.

Chromate coatings are generally amorphous, nonporous, and gel-like when initially formed. If necessary, they can be readily dissolved in nitric acid at this stage. As the coating dries, it slowly hardens and becomes hydrophobic, less soluble, and more abrasion resistant. Up to 20% (Alodine 1200S) of unreacted hexavalent chromium is also included in the coating, which provides good corrosion resistance as described earlier.

Chromate conversion coatings are based on two types of processes: chromic acid processes and chromic acid–phosphoric acid processes. The reaction for the formation of a chromic acid–based conversion coating is given by the following overall equation:

$$6H_2Cr_2O_7 + 30HF + 12Al + 18HNO_3 \rightarrow 3Cr_2O_3 + Al_2O_3 + 10AlF_3 + 6Cr(NO_3)_3 + 30H_2O$$

The formed oxide, given as Cr_2O_3, is probably better described as amorphous chromium hydroxide, $Cr(OH)_3$. The color of the formed conversion coating is yellow to brown and typical coating weights range from 0.3 to 2.0 g/m^2. Those layers can be used as a primer for a paint layer or powder coating but can also be applied unpainted.

Copyright © 2002 Marcel Dekker, Inc.

A possible overall reaction for the formation of a phosphoric acid–processed coating is

$$2H_2Cr_2O_7 + 10H_3PO_4 + 12HF + 4Al \rightarrow CrPO_4 + 4AlF_3 + 3Cr(H_2PO_4)_3 + 14H_2O$$

The resulting greenish layer consists mainly of hydrated chromium phosphate with hydrated chromium oxide concentrated toward the metal. At the conversion coating–aluminum substrate interface, aluminum oxides and other aluminum salts are present. The thinner chromic acid–phosphoric acid conversion coatings ($1g/m^2$) are an excellent base for paint layers. Thicker coatings are often applied unpainted.

In most countries today extreme care is taken when applying chromate coatings due to toxicological and environmental hazards. It is possible that legislation will prevent the widespread use of these excellent layers in the future. A review of key literature that describes the toxicological and health effects of chromium, chromium (II), and chromium (VI) can be found elsewhere [28]. As a result of these constraints, new developments of nonchromate conversion layers have been taking place. However, it will be difficult to find a good substitute for the chromate layers. A more extensive review of new developments in corrosion prevention by nonchromate conversion coatings has been given by Hinton [29].

Treating the metal surface in a weak phosphoric acid solution of iron, zinc, or manganese phosphate produces phosphate layers. Phosphate layers offer only limited protection of their own but greatly improve the adhesion of the organic layers. A good example of a phosphate coating is the treatment generally used in the car industry. After degreasing the (galvanized) steel substrate in mild alkaline phosphate baths, the surface is phosphated by a mixed spray-dip process. A crystalline phosphate layer is formed with a total weight of about $2–5g/m^2$. The composition and structure of the layer depend on the substrate and the bath. Two common phosphate compounds are $Zn_3(PO_4)_2 \cdot 4H_2O$ and $Zn_2Fe(PO_4)_2 \cdot 4H_2O$. After phosphating, the material is given a standard chromate rinsing procedure.

During the cathodic electrodeposition of the primer layer the phosphated layer is attacked by the alkalis (pH of about 12 or higher) at the interface [30]. The phosphate is then treated at 200°C for 30min when the painted metal is baked. During this treatment the phosphate compounds lose two water molecules. When the total coating system is in service later, water from the environment permeates the paint film and reacts with the partially dehydrated phosphate, and it may dissolve partially or completely in the water phase depending on the pH of the penetrating water [31]. When anodic and cathodic reaction sites emerge during propagation of the undercoating corrosion process, the phosphate layer can even completely dissolve either in the acid anodic medium or in the basic cathodic medium, especially when NaCl is present [32].

Modification of the actual chromium-based pretreatments has been undertaken by using trivalent chromium, especially on aluminum substrates. By forming trivalent chromium compounds on aluminum it has been shown possible to oxidize part of the film to hexavalent chromium, attaining a corrosion-resistant film comparable to the normal Cr(VI)-based layer [33].

Copyright © 2002 Marcel Dekker, Inc.

Some no-rinse chromate-free formulations based on solutions of chromium trifluoride, phosphoric acid, and small quantities of polyacrylic acid give good coating adhesion [34].

Also, molybdates have been used as alternative passivity- and adhesion-enhancing oxidants, but with limited success [e.g., 35].

Cerium compounds have been found effective in reducing the corrosion rate of aluminum alloys by inhibition of the cathodic reaction. The cerium can be incorporated in the passive oxide film to provide a protective conversion coating [36,37].

Zirconium, titanium, and hafnium compounds have been used in combination with fluoride as alternatives to chromates with reasonable success but are never as good as the Cr(VI)-treated surfaces [38,39].

Recent developments to be mentioned are the application of lithium salts, permanganates, self-assembling monolayers, and finally silanes to promote adhesion of the organic layers [40–43].

Metallic Layers, Conversion Layers, and Organic Topcoats

The complete coating system in automotive materials is quite complicated. A schematic overview is given in Figure 1. From this picture it is clear that any description of corrosion mechanisms in such complicated systems should encompass the possibility of a variety of defects caused by impact or degradation. A selection has been made here to describe the initial processes, damage exposing the primer, damage exposing the zinc coating, and damage exposing the steel.

The environmental factors determining the degradation of car body panels are salt (from deicing salt and from the sea in marine environments), humidity, temperature, impact by pebbles, sand, and acid rain. Of course, the most direct cause of corrosion initiation is physical damage due to impact by any kind of material. The propagation of any corrosion process depends on the depth of the damage.

During exposure, water permeats an intact paint film and reaches the interface, as we have seen before. On its way in, the water dissolves organic and inorganic compounds, which are later deposited on the metal surface, because the whole system goes through wet and dry cycles and also through mostly anticyclic temperature cycles. The water displaces the polymer from the metal surface during the wet period, resulting in poor wet adhesion behavior. Adhesion is sometimes partially restored

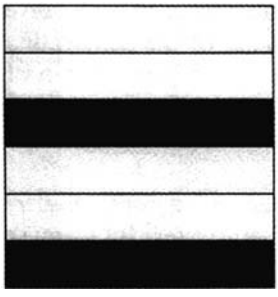


Figure 1 Schematic representation of the general buildup of the coated specimen.

Copyright © 2002 Marcel Dekker, Inc.

during dry periods. After many cycles, the area of metal surface where the coating has delaminated, while the water phase at the metal surface incorporates more impurities, will be considerable. The increasing concentration of dissolved species at the interface also stems from the huge variety of inorganic water-soluble species present in the galvanized layer. Oxygen will also diffuse to the zinc layer, which is a rather good catalyst for the oxygen reduction reaction. However, no real corrosion damage normally results because of the active corrosion inhibition of the Zn-containing layer.

After damage by impact, this picture changes considerably. In Figure 2, a schematic picture is given of a coated system after impact resulting only in damage in the topcoats. Aggressive species can directly reach the primer surface. When water and oxygen have reached the phosphate layer by diffusion, the cathodic delamination process can start. Different authors found that the diffusion rate of water in the typical primers used for car body coatings is high and above the rate for epoxy-polyamide resins [44–46]. The diffusion rate of oxygen being of similar magnitude, it must be concluded that the permeation rate through the primer is not rate determining for the corrosion process. Corrosion proceeds as discussed for the cathodic delamination process. The corrosion spots spread radially. The pH increases at the cathodic sites, and the phosphate layer dissolves. Eventually a blister will form and further damage to the system will result in the mechanism that takes place at an earlier stage when the coating is damaged to the galvanic layer, as given in Figure 3.

In that case the phosphate layer provides hardly any protection. The zinc layer is consumed locally by the anodic reaction, and the steel substrate is exposed. The corrosion products are not taken up in the paint film. The cathodic delamination takes place along the zinc-paint interface. The corrosion process continues where the damaged site reaches the steel substrate as shown in Figure 4. All contaminants reach the paint-phosphate-metal interface. Zinc dissolves anodically at the tip while oxygen reduction takes place at the exposed steel surface. At cathodic sites the pH

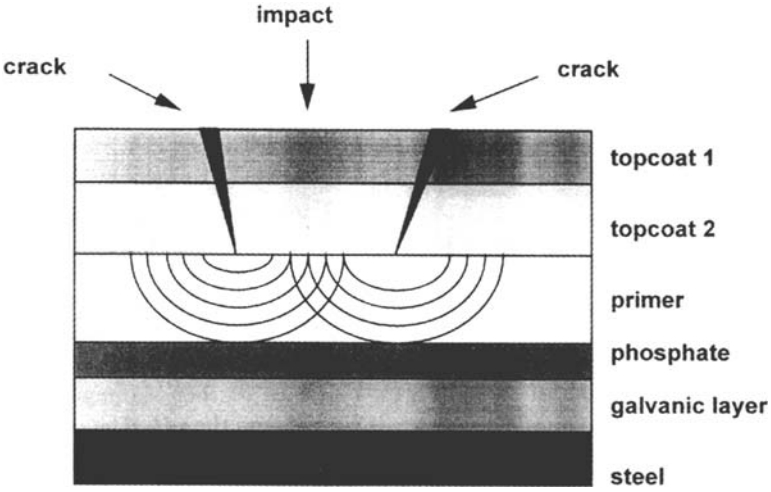


Figure 2 Schematic picture of the partially damaged coating system on a car body panel. Cracks after impact reach the primer. Diffusion of water and oxygen through the primer. (Picture drawn free after Granata [47].)

Copyright © 2002 Marcel Dekker, Inc.

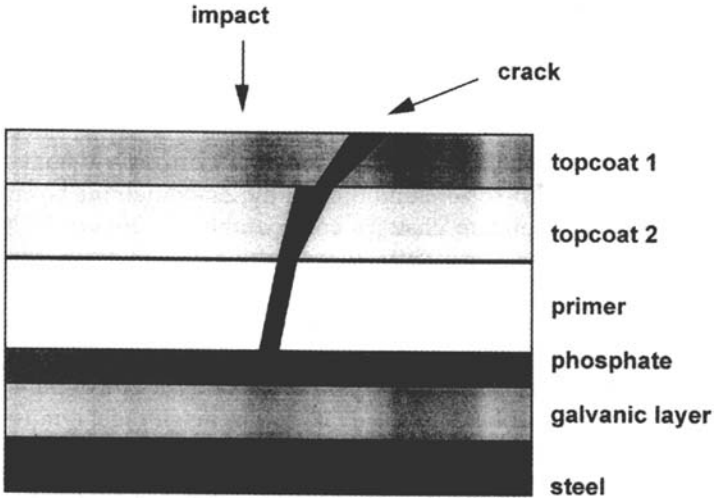


Figure 3 Schematic picture of the partially damaged coating system on a car body panel. Cracks after impact reach the phosphate and through porosity the zinc layer. (Picture drawn free after Granata [47].)

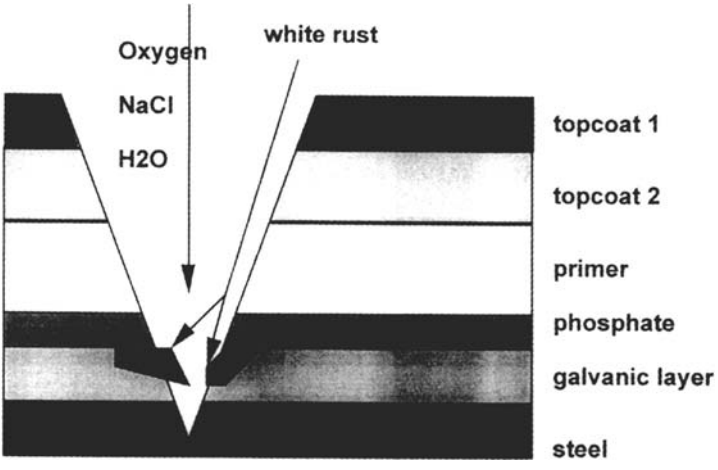


Figure 4 Schematic picture of the partially damaged coating system on a car body panel. Cracks after impact reach the steel substratum. (Picture drawn free after Granata [47].)

increases, leading to loss of adhesion. Also, chloride ions can now easily reach the corroding surface. The formation of zinc hydroxychloride further damages the interface by a wedging action. The anodic reaction of zinc lowers the pH. The primer is not very stable at low pH and is hydrolyzed. Phosphate also partially dissolves, thus further weakening the paint-phosphate-metal interfaces. It is clear from this short description that the overall reaction mechanism is very complicated and not yet unambiguously resolved. Opinions differ considerably and research is going on [47–48].

Copyright © 2002 Marcel Dekker, Inc.

APPLICATION TECHNIQUES

Organic coatings can be applied to surface by different methods. The application depends mainly on the

Purpose of application: protection or decorative
Type of coating, target layer thickness, number of layers
Size and geometry of the object to be coated
Site of application: in a conditioned room, confined space, or in the field

Moreover, environmental and health aspects have a large influence on the application techniques. A short overview of the different techniques with (dis-) advantages is given next.

Brushing

Application by brushing is labor intensive and consequently time consuming and expensive. The layers obtained by brushing depend on the painter and can vary greatly. Brushing is still indispensable for small areas, repair purposes, and for less accessible places for parts that are difficult to protect, such as edges, angular parts, and welds. An advantage of this technique is the very low wastage. Also, it is generally believed that brushing gives better penetration of paints into pores, cracks, and crevices [49]. In the case of a solvent-based paints, health risks have to be taken into account, in particular in confined spaces. However, the technique is suitable for waterborne and high-solid systems.

Brushing is less suitable for very fast drying products; brush marks remain visible and the paint film is not homogeneous. It is also difficult to apply more layers of some types of physically drying paints: the solvent of the last coat layer may soften the previous layer.

Rolling

Painting by roller is much faster than brushing. It is suitable for large flat surfaces. On the other hand, it is not suitable in corners, edges, and welds. Additional brushing is necessary in these cases. Further, the same restrictions apply for the type of paint as in the case of brushing.

Dip Coating

The object to be coated is dipped in the coating. This method is very simple, cheap, and can be quick. The quality depends on a number of factors: time of withdrawal, viscosity, the rate of solvent loss, and the mixing of the coating. The method can be automated to deal with a large quantity of objects to be coated.

Conventional (or Air) Spraying

The paint is forced from a container to the spray gun by pressurized air or by a pump. As the paint passes through the nozzle, it is mixed with air and atomized at pressures of about 2 to 4 bar. Spray guns can be equipped with fluid air supplied by a

Copyright © 2002 Marcel Dekker, Inc.

compressor with sufficient extra capacity to compensate for the drop in the long hoses. The air is freed from oil, moisture, and dust by means of an oil-water separator.

Air spraying is a much faster application technique than brushing or rolling; moreover, the layers obtained are more uniform in thickness. The disadvantage of this technique is the larger waste. Part of the paint is lost in the so-called overspray: missing the object to be coated. Another cause of paint loss is the rebound of the air containing paint spray from the surface of the object to be painted. Paint losses can be excessively high when spraying is done outdoors.

The directions for spraying distance, pressure, and nozzle type are rather critical and should always be followed. Distance from surface should normally be 45–60 cm. If the spray gun is held too far from the substrate, the paint droplets are already dry when they reach the surface and will not aggregate. This phenomenon, called dry spray, gives a discontinuous, porous film.

Dry spray may also be expected in the case of highly pigmented products (for example, zinc silicate) or paints containing very volatile solvents (for example, vinyl paints). This phenomenon may also be expected when the paint material is insufficiently thinned or spraying is done during hot or windy weather.

Airless Spraying

The paint is brought to a high pressure (75–300 bar) by means of a pump and forced though a narrow nozzle, which atomizes the paint. In contrast to air spraying, in this case the paint is not atomized by air and consequently the amounts of spray mist, overspray, and rebound are much less than in air spraying. Because the paint is not mixed with air, there is almost no risk of contamination with impurities such as oil or water. Further advantages are:

Significantly higher production rates: faster spraying.
Paint can be applied at a higher viscosity, resulting in higher dry film thickness.
Loss of solvents and thinner by evaporation is much lower than in air spraying.

The technique is also suitable for more volatile solvents.

Airless spraying is in particular appropriate for painting surfaces, such as buildings, ships, and offshore structures. It has the following disadvantages:

The worker has to work in a very fast and concentrated way because of the high rate of deposition.
It is unsuitable for spraying small objects.
To obtain thin layers, very narrow nozzles are requited. Consequently, they become warm (particularly with paints that contain hard pigments and extenders) and malfunction.
The paint jet has such a high velocity that it can injure workers.

Electrostatic Spraying

In this process atomized paint and the object to be painted are respectively negatively and positively charged. This results in a good adhesion and a uniform layer.

Further, it is an economical process because of the low waste, and application of water-based paints is possible. Disadvantages are the restriction to coat objects only on the outside and the occurrence of defects due to an incorrect viscosity/solvent balance.

Copyright © 2002 Marcel Dekker, Inc.

Powder Coating

Powder coating can be considered as a variation of the previous technique. A constant flow of powder, fluidized in an air stream, passes through a highly charged (40–150V) region of ionizing discharge. The charged paint particles are directed to the (grounded) substrate. Together with the electrostatic attraction, an enforced airflow increases the velocity of the particles to the substrate. After deposition, the layer is fused in an oven at 180° for 10 to 15 min, depending on the characteristics of the powder. Coated thicknesses of up to 500 μm are possible with these coatings without loss of flexibility; thickness between 300 and 450 μm are more common.

Electrodeposition

Charged paint particles in a solution of water-soluble resins are directed by a potential field between cathode and anode (respectively the object to be painted and bath tank or vice versa) to the surface of the object.

Advantages are that a uniform coating is obtained, penetration in narrow places (for example, seams) is possible, the process is fast, and there is no fire risk. The main disadvantage is the limitation of the thickness (due to the electrical resistance of the formed coating). The limit is 25 μm and only one coat is possible.

PROTECTIVE MECHANISMS

The corrosion protection provided by organic coatings results either from the barrier action of the layer, which may be supported by inert inorganic particles especially if these are arranged like tiles (e.g., aluminum flakes or iron phosphates), or from active corrosion inhibition provided by pigments in the coating. Ideally, a coating provides protection by forming a physical barrier between the metal substrate and the aqueous corrosive environment. In practice, however, these physical barrier properties are limited, as all organic coatings are permeable to water and oxygen to a certain extent. This, however, mostly does not influence the protective action of the coating as long as the coating adheres well. In fact, adhesion is the primary protection criterion. Permeation of the coating with water is not damaging as long as no condensation of water at the metal/coating interface takes place.

Corrosion under a coating can take place only after an electrochemical double layer has been established at the metal surface. For this to occur, the adhesion between the coating and the substrate must be broken, after which a separate thin water layer at the interface can be formed when the water permeates the coating.

Under normal, outdoors conditions an organic coating is saturated with water at least half its service life. For the remainder of the time it contains a quantity of water comparable in its behavior to an atmosphere of high humidity [50]. Furthermore, the average transmission rate of water through a coating is about 10 to 100 times larger than the water consumption rate of a freely corroding surface [13]. Because it has also been established that in most cases the diffusion of oxygen through the coating is large enough to facilitate unlimited corrosion, it is clear that the physical barrier properties alone may not account for the protective action of imperfectly adherent coatings.

Copyright © 2002 Marcel Dekker, Inc.

Resistance inhibition, which is also part of the barrier mechanism, may supply additional protection. Inhibiting the charge transport between cathodic and anodic sites retards the corrosion reaction. An increase in the electronic resistance and/or the ionic resistance in the corrosion cycle may reduce the reaction rate. The electronic resistance may, for example, be increased by the formation of an oxide film on the metal. This is the case for aluminum substrates. The application of organic coatings on a metal surface results in an increase of the ionic resistance.

One of the weak points of organic coatings in corrosion prevention is the fact that these coatings are relatively easily damaged under mechanical and thermal load. This may cause corrosion under the paint film at and near the damaged site. The otherwise adequate barrier properties of the coating will no longer give sufficient protection. Active pigments are then often incorporated in the polymer matrix of the first coating layer near the substrate: the primer. These pigments (passivating, blocking, or galvanic) provide protection through an active inhibitive mechanism immediately when water and some corrosive agent reach the metal surface.

Again, protection can result only if the adhesion of the coating is good. Also, the mechanical properties (e.g., the glass transition temperature) of the polymer reflect to some extent the quality of the coating, as these determine the formability of coated substrates (e.g., for coil-coated products) and their sensitivity to external damage.

Water Permeation

All organic coatings are to some extent permeable to water. The effective permeability is closely related to the polymer structure and composition. The permeability of a coating is often given in terms of the permeation coefficient P. This is defined as the product of the solubility of water in the coating (S, kg/m^3), the diffusion coefficient of water in the coating (D, m^2/s), and the specific mass of water ρ (kg/m^3). Different coatings can have the same permeation coefficient even though the solubility and the diffusion coefficient, both being material constants, are very different. Therefore the usefulness of the permeation coefficient is limited.

Water permeation occurs under the influence of various driving forces:

A concentration gradient. e.g., during immersion or during exposure to a humid atmosphere, resulting in true diffusion through the polymer

Osmosis due to impurities or corrosion products at the interface between the metal and the coating

Capillary forces in the coating due to poor curing, improper solvent evaporation, bad interaction between binder and additives, or entrapment of air during application

When a coated system is exposed to an aqueous solution or a humid atmosphere, water molecules eventually reach the coating substrate interface. Normally, a coating under immersion will be saturated after a relatively short time (of the order of 1 h), depending on the values for D and S and the thickness of the layer. Typically values for D and S are 10^{13} m^2 s^{-1} and 3% [7–9]. For atmospheric exposure the actual cyclic behavior of the temperature and the humidity determines largely the periods of saturation. In any case, situations will result in which water molecules reach the coating-metal interface, where they can interfere with the bonding between the two phases, eventually resulting in loss of adhesion and corrosion initiation if a

Copyright © 2002 Marcel Dekker, Inc.

Table 1 Permeability of Oxygen and Water Vapor in Several Resin and Coating Films: Results Obtained for Free Films That Were Cast on Glass

Polymer	Permeability[a]	
	Oxygen [cm^3 100 µm $(m^2$ d atm$)^{-1}$] at 23°C and 85% RH	Water vapor [g 10 µm $(m^2$ d$)^{-1}$] at 38°C and 95% RH
Resin films		
VC-VDC copolymer latex	22 ± 9	28 ± 10
Chloropolymer, solvent borne[b]	82 ± 19	100 ± 20
Epoxy/polyamide	130 ± 33	155 ± 20
Chlorinated rubber, plasticized	183 ± 7	95 ± 5
Styrene acrylic latex	1464 ± 54	2300
Coating films		
VC-VDC copolymer latex	12 ± 5	68 ± 12
Chlorinated rubber unmodified	30 ± 7	50 ± 8
Chloropolymer, solvent borne[b]	33 ± 2	65 ± 12
Aluminum epoxy mastic	110 ± 37	105 ± 15
Coal tar epoxy	213 ± 28	75 ± 3
Acrylic water-borne primer	500	1800 ± 92
TiO_2 pigmented alkyd	595 ± 49	645 ± 15
Red lead oil–based primer	734 ± 42	535 ± 8

[a]The permeability of oxygen is given as the number of cm^3 gas of 1 atm permeating through a coating of 100 µm thickness per m^2 per day.
[b]Product under development.
Source: Ref. 54.

cathodic reaction can take place. For a corrosion reaction to proceed, a constant supply of a cathodic species such as water or oxygen is required. Some authors suggest that the transport rate of oxygen through the coating is higher using the interconnected water phases in a saturated polymer [51,52], whereas other experiments lead to the conclusion that the oxygen permeation is independent of the presence of water [53].

Dickie [12] determined the quantities of water and oxygen consumed during corrosion of a freely corroding unpainted steel substrate. Both were of the same order of magnitude and also comparable to the average permeability of coatings for oxygen. An overview of some data is given in Table I. This leads to the conclusion that for some coatings with somewhat lower permeability for oxygen the transport of oxygen may be rate determining. Water permeation may also result in the buildup of high osmotic pressures, which are responsible for blistering and delamination.

CORROSION UNDERNEATH ORGANIC COATINGS

The causes of proceeding delamination underneath organic coatings can be roughly categorized in two types: delamination due to clustering of water at the interface and delamination caused by specific corrosion processes that produce either low or high

Copyright © 2002 Marcel Dekker, Inc.

pH values at the interface. In the case of blisters underneath an intact paint layer, the first mechanism will often be the starting point for the more "chemical" delamination caused by processes of the second category. Within the first category wet adhesion and osmotic blistering are the main mechanisms. The second category is mainly referred to as cathodic or anodic delamination.

Clustering of Water

Clustering of water at the metal-polymer interface and the subsequent formation of an electrochemical double layer can occur only if the adhesion between metal and coating is weaker than the bond between metal and water or polymer and water. For a proper evaluation, however, a distinction must be made between wet adhesion and osmotic blistering.

Wet adhesion is the complete deadherence of the coating without actual blistering. From a thermodynamic point of view this implies that the whole interface must have very weak binding energy. Therefore the bonds will be easily broken by water that can be transported through the coating at a sufficient rate. Fast temperature cycling of saturated coatings may, however, also lead to this type of delamination although the adherence under static conditions is sufficient.

Typical of wet adhesion is the absence of real blisters in the first stages. This is due to the fact that the water at the interface is relatively pure and as long as corrosion processes have not generated enough ions, osmotic mechanisms will not cause a further growth of the water layer. Therefore the adhesion may also be partly restored when coatings are completely dried after immersion. Only when ions are present due to contamination or are formed by corrosion processes may further blistering occur.

Osmotic blistering is caused by the presence of soluble species underneath the coating. Water that normally penetrates the coatings will dissolve these species at the interface and form a highly concentrated solution. Also, some acid fumes containing acetic on hydrochloric acid may penetrate through polymers and condense together with water in small voids or places with minor adhesion. Due to osmotic forces, more water will then be attracted to these solutions. This causes an internal pressure within the blisters, which has been calculated to be as high as 3 Pa [5,6]. These high internal pressures may even cause further delamination. Because corrosion processes within the blister tend to produce their own ions, the osmotic pressures may remain high for long times. In many cases these blisters will eventually burst or gradually develop into the electrochemical delamintation mechanisms described in the following.

Cathodic Delamination and Anodic Undermining

In the literature two mechanisms are proposed to describe the propagation of underfilm corrosion in case of intact and defective coatings. These mechanisms are:

Cathodic delamination
Anodic undermining

In cathodic delamination the adhesion of the coating fails and causes lateral blister growth as a result of a high pH at the delamination front [6,55,56]. The loss of

Copyright © 2002 Marcel Dekker, Inc.

adhesion in anodic undermining is caused by the dissolution of the metal or the metal oxide at the interface with the coating [6].

Both cathodic delamination and anodic undermining are the result of a specific type of electrochemical cell: the differential aeration cell. In this cell separation of anodic and cathodic reaction sites takes place, but for both mechanisms this happens in different ways depending on the path for oxygen transport to the metal interface. This transport is, of course, also determined by whether the coating is intact of defective. With intact coatings, oxygen is mainly supplied through the coating or through both coating and formed solid corrosion products as schematically shown in Figure 5. The length of the oxygen transport path to the interface at the edge of the blister is shorter than that at other places in the blister where oxygen also has to diffuse through the corrosion products. According to the differential aeration cell theory, the cathodic reaction will occur at the edge of the blister and the anodic reaction in the center of the blister as shown in Figure 5.

The separation of the anodic and cathodic reaction sites in Figure 5 can be promoted by the nature of the corrosion products. When corrosion products consist of species that can be further oxidized, oxygen may be reduced during the transport through the corrosion products. The amount of oxygen that will reach the metal will therefore collapse and in the center of the blister less oxygen will reach the metal surface. An example is the formed corrosion product of iron, which initially consists mainly of Fe(II). In the presence of oxygen, Fe(II) will be oxidized to Fe(III) and will therefore consume the oxygen [7,12]. Because the solubility product of Fe(III) (hydr)oxides is very low, a solid film is formed. The proceeding corrosion process leads to film growth at the center of the blister, which hinders further oxygen transport at the center effectively.

From the preceding discussions it is concluded that blisters under intact coatings grow due to cathodic delamination.

When defective coatings are considered, the situation is much more complex. Part of the substrate is now directly exposed to the corrosive solution. Corrosion will initiate at the defect and subsequently the formed corrosion products will block the pore. Corrosion propagation depends on the nature of the corrosion products in the pore. These stages are shown in Figure 6a and b.

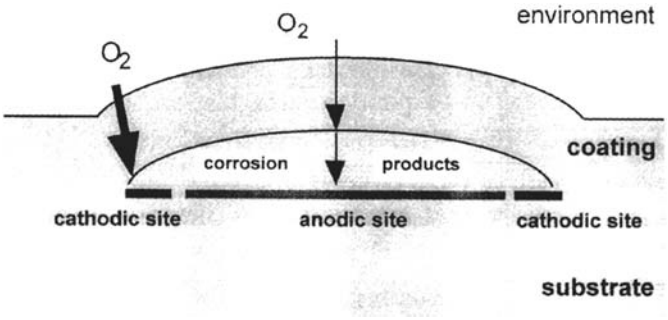


Figure 5 Oxygen transport paths in a blister in case of an intact coating. The resulting anodic and cathodic sites are shown. The transport paths for oxygen are shown.

Copyright © 2002 Marcel Dekker, Inc.

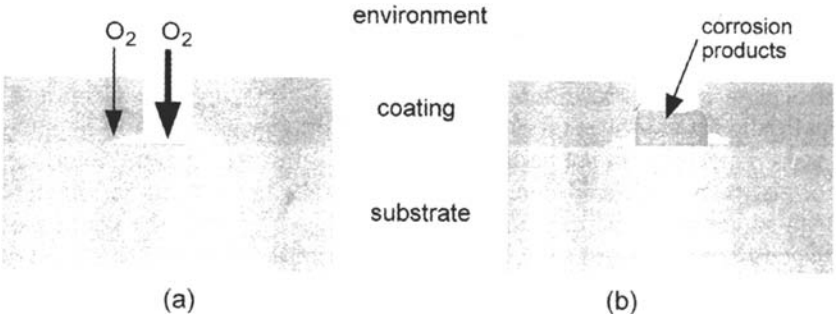


Figure 6 (a) Corrosion initiation at defective coatings. (b) Blocking of the pore. Initial loss of coating adhesion at the edges of the pinhole is shown.

Whether anodic undermining or cathodic delamination will develop at defective coatings depends on the ratio of the transport rates of oxygen through the coating and that through the formed corrosion products. When the rate of oxygen transport through the coating exceeds that through the corrosion products, the mechanism is cathodic delamination; the opposite leads to anodic undermining.

The Model as Presented in the Literature

In more detail, the model of cathodic delamination can be described and understood as follows [3,57]: the delamination starts with randomly distributed anodes and cathodes in a defect or at a dalaminated area. When iron is taken as an example, the dissolved Fe^{2+} at the anode is further oxidized to Fe^{3+} by oxygen and forms insoluble corrosion products in the defect that often adhere to the polymer (in the case of a blister) and at the edges of the defect (where oxygen enters the defect). In what way the defect is blocked and a cap of corrosion products is formed on the top of the blister; see Figure 7. In this cap oxygen is consumed through oxidation of Fe^2 (the cap is sometimes said to be impermeable to oxygen [7]). Because of this, the area underneath the cap will have a lower oxygen concentration than the regions at the edges where no cap is present and where oxygen "easily" penetrates the coating. This stimulates the separation of anodic and cathodic regions, which finally leads to large pH differences due to the different reactions that take place at anode and cathods ($\frac{1}{2}\ O_2 + H_2O + 2e^- \rightarrow 2OH^-$ at the cathode and $Fe \rightarrow Fe^{2+} + 2e^-$ followed by subsequent hydrolysis at the anode). This process is shown schematically in Figure 7 for a delaminated and a defective coating. In both cases the same end situation results.

Taking a closer look at this model, some questions arise that are not directly answered by the model as presented normally:

What is the mechanism of growth of these blisters?

How can these large pH differences that are reported in literature exist for prolonged periods of time in such a confined space (differences of 10 pH units over less than a few mm)?

Despite these remaining questions, the model could explain recent model experiments on test panels that were deliberately contaminated with sodium chloride. On most panels a large (set of) blister(s) was present at the contaminated site, but

Copyright © 2002 Marcel Dekker, Inc.

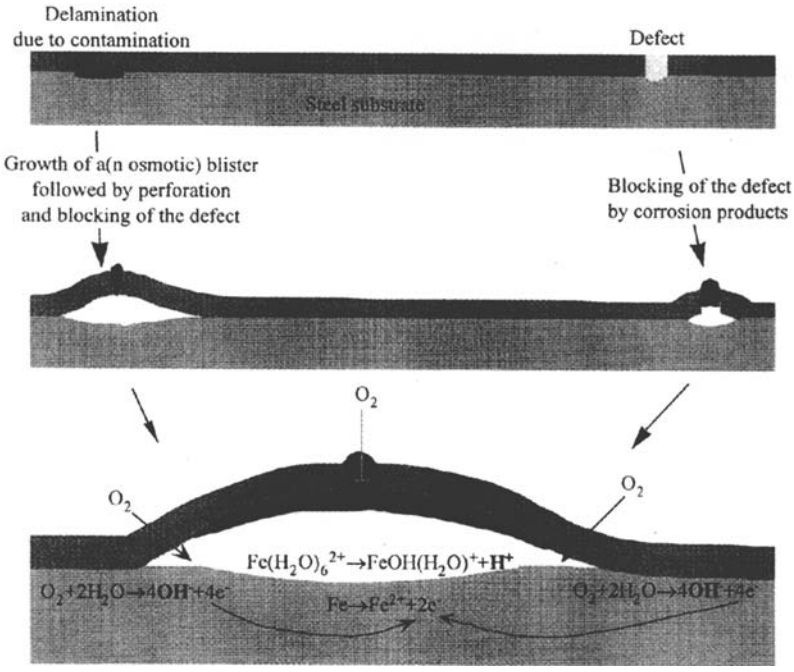


Figure 7 Schematic representation of the mechanism of cathodic delamination starting from a defect and from an osmotic blister.

also other, small blister were present at other places on the panel. In between these blisters, the polished metal underneath the transparent coating still has a mirror-like surface. Closer examination showed, however, that even on these apparently undamaged sites there was a thin layer of liquid present between coating and metal. When the completely deadhered coating was lifted off, the pH of this thin layer of liquid was "measured" with a pH indicator liquid. It was approximately 12.

Underneath the larger blisters the metal was etched as can be seen in Figure 8. This can only be the result of the attack by a quite acid solution. Below pH 3, however, hydrogen evolution may occur. Sometimes the presence of hydrogen bubbles on steel is reported in the literature [58], but in all cases the cathodic disbondment is caused by cathodic protection. As very little solutions be available within the center of the blister, it is extremely difficult to measure the pH in this area. Judging from the metal attack is should, however, be around pH 3.

Figure 8 also shows the undamaged cathodic areas around the blisters. These observations lead to the conclusion that the large pH differences do indeed exit.

Observations on smaller blisters give the answer to the question how these large pH differences can exist in such small areas. It appeared that in the case of very small blisters a closed sphere of corrosion products remained when the coating was removed. So there is not only a "cap" as presented in Figure 7 but also "walls" between anodic and cathodic sites. Together with the cap, the walls form a closed sphere of iron (hydr)oxides. This result can be observed only on very small blisters because larger ones are damaged when the coating is removed. A photograph of such

Copyright © 2002 Marcel Dekker, Inc.

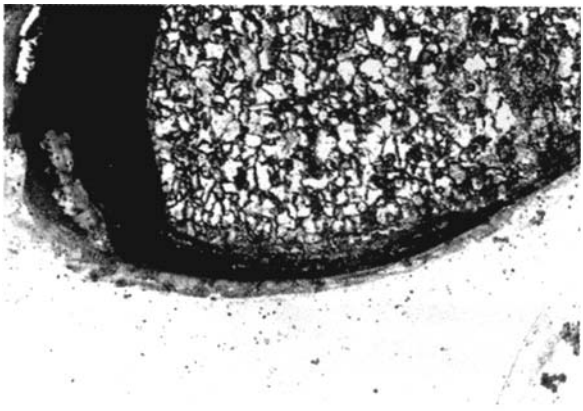


Figure 8 Photograph of a large blister after removal of the coating and the corrosion product (enlargement 20 times).



Figure 9 Photograph of a small blister. The top cap is visible at the top (enlargement 50 times).

a small blister is shown in Figure 9. In this picture one can also see the beginning of the etched surface that is also present in Figure 8. To look inside the blister, the top cap was in this case removed with a needle (it is still visible at the top of the picture). Around the blister again a fully reflective surface is visible; only some debris from the opening of the sphere of corrosion products is present.

The formation of the walls of the sphere can be understood considering the ions that are present in the system: at the cathode OH^- will be present in rather high concentrations. In the center, the anodic region, Fe ions are present in rather high

Copyright © 2002 Marcel Dekker, Inc.

concentrations. Low soluble iron (hydr)oxides will precipitate after interdiffusion of OH^- and Fe^{2+} at the boundary region [59]. These precipitates form a wall that is connected with the cap, thus forming a closed sphere.

Extended Model for Cathodic Delamination

From the preceding observations the model for cathodic delamination can be extended in the following way:

1. Initially, the normal model as presented by Funke [3,57] describes the delamination process.
2. After some time the anodic and cathodic areas become separated as a barrier of corrosion products is formed in between them. This wall stabilizes the pH differences that occur due to the separation of the anodic and cathodic reactions. Wall and cap together form the observed sphere
3. The wall slowly dissolves from the inside in the increasingly acid environment within the sphere. Fe ions diffuse through the wall, resulting in the formation of new $Fe(OH)_2$-like products on the outside. In this way the anodic area of the blister is able to grow. The high pH on the cathodic edges causes the delamination of the organic coating to proceed (as was already assumed in the existing model)

The mechanism of growth implies that the center of the anodic area has been exposed for a longer period to the acid corrosive environment than the edges of the anodic area. As a consequence of this a shallow "crater" must be formed under every blister. Figure 10 shows that this is indeed the case.

Another importance consequence of the introduction of the wall is that contaminating ions such as Na^+ and Cl^- are necessary in both the anodic and the cathodic region for cathodic delamination to occur: the Fe ions cannot compensate the charge of the OH^-; they would directly produce a solid product in the cathodic region. On the other hand, in the anodic areas the H^+ and Fe^{n+} should be compensated by a negative ion such as Cl^- (OH^- would, of course, react directly with H^+). So the positive and negative ions of the contaminating salt will be separated. This further implies that the final pH values are also determined by the amount of

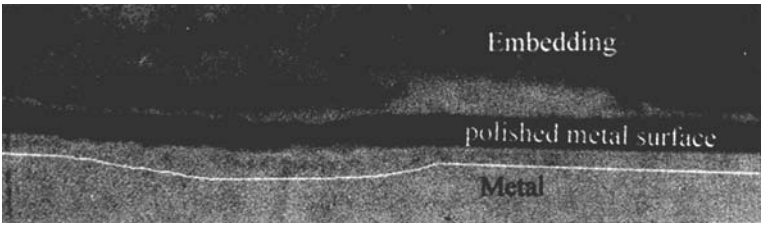


Figure 10 Cross section of a metal with a shallow "crater" due to cathodic delamination of a coating. The coating was pulled off before the sample was embedded and the cross section was made. The black areas are formed by a crevice between the metal and the embedding. The white line parallel to the metal surface indicates the (exaggerated) formation of a crater. The cross section was embedded as a metallographic specimen and photographed with an optical microscope.

Copyright © 2002 Marcel Dekker, Inc.

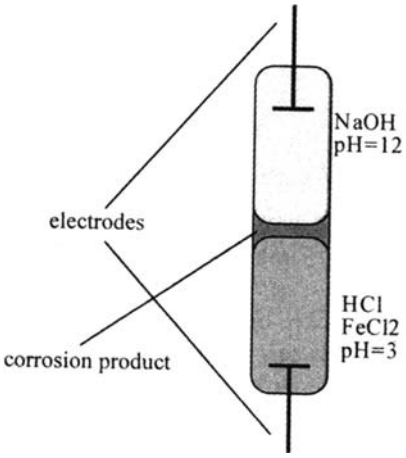


Figure 11 Schematic picture of the situation in a test tube.

contaminating ions. The importance of the contaminating ions for the delamination process is also known from literature in which the influence of cations of different sizes is described. It proved that the size (and therefore the diffusion coefficient) of the cations has a relation to the delamination rate [15,60–62].

Further proof of the existence of a membrane-like structure can be obtained through simple model experiments: it proved to be possible to produce a similar film in a test tube [63]. When such a tube is filled halfway with an NaOH solution of pH 12, an HCl solution of pH 3 containing Fe^{2+} ions can be injected underneath (the density of the acid is higher). When this is done, a film of $Fe(OH)_2$-like products is formed instantly and the geometry shown in Figure 11 is created.

This situation is stable for several weeks. Depending on the disturbance during the injection of the acid, the film can be thick (several millimeters) and colorful or very thin (hardly visible) and pale white. If the iron ions are omitted from the acid solution, the situation can also be created, but after 10 min the two solutions have completely mixed. So this Fe-containing film indeed has a stabilizing effect as was predicted from the observations on small blisters.

Further proof of the existence of the stabilizing film was also found in other tests: it was also possible to create it in a neutral NaCl solution by electrochemical dissolution of the central electrode in Figure 12. In this experiment a disk of carbon steel was placed in a sheet of carbon steel. The whole panel was embedded in epoxy and on the surface a container was glued. A 3% sodium chloride solution was put in the container and the central electrode was connected to a potentiostat and was made the anode, the rest of the panel being the cathode. One volt was applied, causing rapid dissolution of the disk (Fe to Fe^{2+}). On the cathode hydrogen gas was formed (and maybe also oxygen consumed). In that case the pH is increased at the outer ring, resulting in the formation of the sphere of corrosion products.

Anodic Undermining

The model for anodic undermining shows large similarities to cathodic delamination. The main difference is the fact that oxygen transport through an open defect or

Copyright © 2002 Marcel Dekker, Inc.

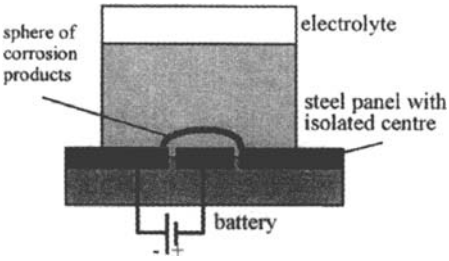


Figure 12 Production of the artificial sphere of corrosion products; 3% sodium chloride is poured into a container that is glued on the surface.

porous corrosion products is faster than through the coating. As a result of this, the location of cathodic and anodic sites underneath the deadhering coating is reversed. Delamination now proceeds through dissolution of the interface between coating and metal in the acidic anolyte. In some cases also the osmotic pressure that is caused by the formation of voluminous solid corrosion products may help the delamination process by "lifting" the coating.

Anodic undermining is mainly reported on aluminum, which forms only Al^{3+} ions and porous corrosion products. Especially in the presence of chlorides, the natural oxide is easily attacked. Similarly to cathodic delamination, in this case also the anions and cations are separated leading to the formation of an HCl solution at the delamination front.

Filiform Corrosion

A specific type of delamination that is also driven by a differential aeration cell is filiform corrosion [5,6,62,63]. In most cases it is related to anodic undermining, especially because it occurs mainly on aluminum alloys. Filiform corrosion is a specific type of delamination that occurs only under atmospheric condition with relative humidity between approximately 50 and 90%. Small threadlike delamination tracks are formed that in general follow irregularities on the surface (either rolling or grinding marks). New interest in this special form of corrosion was stimulated by many practical cases along the coastal areas in Europe. It may be expected that new mechanistic information will become available within the next 2 years.

Flash and Early Rust

Two special types of corrosion failure that occur exclusively with water-based coatings are flash and early rust. Both look similar and are often treated similarly in the literature. They are, however, caused by different mechanisms and although they occur under similar circumstances they should be treated differently.

Early Rusting

A measles-like rusty appearance may occur when a cold steel substrate is pained under high-moisture conditions with a latex paint [6,50,62] immediately when the coating is touch dry. This is called early rusting. This corrosion form occurs only when the following conditions are met:

Copyright © 2002 Marcel Dekker, Inc.

A thin (up to 40 μm) latex coating has been applied.
The substrate temperature is low.
The air humidity is high.

Early rusting is a result of the special curing mechanism of latex coatings. Water evaporates from the coating, while dispersed latex particles coalesce. Capillary forces and surface tension deform the particles and diffusion of the polymer chains among latex particles finally results in film hardening. It occurs under conditions in which water-soluble iron salts diffuse through the coating to the outer surface before the coating is completely hardened, which explains the conditions given before. After final evaporation of the moisture at the outer surface, the typical measles-like corrosion spots become visible.

To prevent early rust, inhibitors are often added to the paint formulation.

Flash Rusting

The appearance of brown rust stains on a blasted steel surface immediately after applying a water-based primer is called flash rusting [62]. The cause of this type of corrosion is the remaining contaminants after the blast cleaning. The grit on the surface provides crevices or local galvanic cells that activate the corrosion process as soon as the water-based primer wets the surface. This type of corrosion generally also occurs when coatings have remained wet for longer times due to lower temperature, high relative humidity, or extreme thickness of the layer.

Although inhibitors might provide a certain degree of protection, the most logical choice to prevent this type of corrosion is to prevent the presence of contaminants on the surface.

SPECIALTIES

Coatings for Marine Applications

Seawater and the atmosphere above seawater are extremely corrosive environments. Organic coatings are widely used to protect steel constructions in these cases, so the choice and buildup of the coating system are often illustrative of the possibilities of protection by organic coatings [64].

Protection of the underwater part of a ship's hull or offshore construction requires corrosion inhibition, water resistance, antifouling properties, and compatibility with cathodic protection. Cathodic protection is used to protect the steel in case the coating is damaged.

The corrosion inhibition and water resistance are obtained by paint systems formed by several anticorrosive coats based on epoxy, vinyl, chlorinated rubber, or bituminous coatings.

Coal-tar epoxy systems and vinyl tar coating have been used rather successfully from a technical point of view, but their use is now forbidden in some industrialized countries because of their effect on human health. In their place, high solid tar-free epoxy and glass flake–reinforced epoxies are used.

Aluminum flakes are usually added to bituminous coatings, but these flakes have also been added to epoxy systems to act as active anticorrosive agents [9].

Normally, the buildup of a protective system is as follows:

Copyright © 2002 Marcel Dekker, Inc.

Primer (indication 50 μm)
One or two layers of anticorrosive coating (indication 250 to 400 μm)
Tiecoat/sealer (indication 75 μm) to serve as intermediate between anticorrosive system and antifouling (for example, to improve adherence or to prevent bleeding of the tar)
Antifouling (indication 200 μm)

Coatings for Fouling Prevention

Some attention is given to a particular group of organic coatings, intended for the protection of ships and marine structures against plant and animal growth: the antifoulings.

In the sea and in estuaries, fouling chiefly consists of microorganisms, algae, barnacles, shellfish, tube worms, etc. Fouling develops most rapidly on stationary and slow-moving vessels (speed < 4 knots).

The disadvantages of fouling for vessels are evident in higher fuel consumption, reduction of maximum speed and maneuverability, corrosion, mechanical damage, and high maintenance costs [65]. Even with a limited amount of fouling (~ 1% of the underwater surface of the vessel), the friction is increased to such an extent that significantly more fuel must be consumed in order to maintain the same sailing speed. This can lead to substantial financial loss, depending upon fuel prices; e.g., during the 1970s oil crisis, a loss of $300,000 per ship, per year, was not uncommon [66,67]. Fouling on ships between 1850 and 35,000 tons causes an increase of 35–50% in fuel consumption after 6 months in temperate waters [68]. Even a thin biofilm results in higher resistance and thereby a fuel loss of up to 20% [69–71].

Fouling on seagoing vessels and pleasure craft is mostly treated by paints from which toxic components with an antifouling action are encouraged to leach [67–75]. The active ingredients are freed at the coating-water interface and any organisms that try to stick to the hull are killed.

Organotin-Based Antifoulings

Organotin-based antifouling have been technically the most successful product for years. They owe this success to a unique mechanism to prevent fouling. They combine the toxic properties of TBT (tributyltin) with a controlled-release mechanism, which guarantee constant activity up to 5 years (coating thickness is the limitation).

A controlled and slow chemical reaction with the seawater at the paint surface occurs and guarantees a constant but very low TBT release: The TBT binder, a copolymer of tributyltin methacrylate and methyl methacrylate, hydrolyzes in seawater at a constant linear rate. The binder becomes water soluble as soon as enough TBT has been hydrolyzed. Seawater flowing against the ship's hull polishes off the hydrolyzed remainder of the binder.

The major disadvantage of TBT and other biocide-containing antifouling coatings is the environmental problems that they cause [72], which have resulted in legal restrictions on their use. For vessels under 25 m in length TBT has already been prohibited in many countries, and a complete ban starting from 2003 is in preparation by the International Maritime Organisation.

Copyright © 2002 Marcel Dekker, Inc.

Consequently, a great deal of research is going on all over the world. However, so far alternatives technically and economically comparable to the TBT-based systems have not been developed. The best new systems, based on copper acrylate with some erodable properties, have a lifetime of only 3 years. Moreover, they contain a large amount of copper with addition of "antifouling" compounds from agriculture. In any case, it is clear that the environmental problem is not solved with these new systems.

However, some useful methods for certain classes of ships have now become available. These methods can serve in the future as an alternative to toxic paints for all ships, "can serve" because a gulf exists between scientific developments and practical use for shipping. Ship owners are understandably wary of completely new and untried products and will make the change only when the risk is minimal. This is, for example, currently the case with nonstick coatings.

Nonstick Coatings

Nonstick coatings, mostly based on silicon polymers, have, where fouling organisms are concerned, an unattractively low surface energy [66,76–80]. The free surface energy of the material determines whether an organism attaches or not. Only limited prevention of fouling is provided, but the adhesion between the fouling and the coating is weak; therefore, fouling can easily be removed or will fall off while sailing if the speed is high enough (5–10 knots). In theory, the lifetime is unlimited except when substances are used that have an additional antifouling effect through leaching, e.g., "sweating" silicon oil or paraffin.

Systems were introduced on the market and presented as wonder products with promised effective long-lasting protection, enduring for decades. However, reports about the effectiveness of nonstick coatings became very contradictory. The materials often showed insufficient antifouling properties, but fouling was easily removed. Weakness of the coatings and difficulties with their application are often reported. The best results were achieved with polysiloxanes (silicon elastomers). In recent years, with the exception of small improvements in mechanical strength and adhesion to subsurfaces, no decisive developments have occurred and attention is now focused on practical efficiency. Even though the antifouling effect is obviously improved, some major obstacles are difficult to overcome: price (estimates vary: 5–100 times higher than the classic antifouling paints), difficult application (special apparatus is needed; normal appliances are not suitable), mechanical frailty (with, as a result, damaged areas where fouling quickly occurs), bad adhesion, and the necessity to remove fouling if sailing is insufficient.

Pollution when using nonstick coatings is low in comparison with that of systems based on biocide leaching, but emissions as a result of damage, pieces of the coating chipping off, and possible leaching of coating ingredients must be taken into account. Rapidly biodegradable silicon products could possibly minimize pollution.

There are no products freely available on the market as yet. Practical application has been effected in other areas (especially cooling water systems). Recent or current sea trials with ships—e.g., in the United States, Australia, and France—confirm the potential suitability, but because of the previously mentioned obstacles, the step to commercial use will take several years at least, especially for larger vessels.

Copyright © 2002 Marcel Dekker, Inc.

MEASURING AND MONITORING METHODS

Introduction

An abundance of measuring techniques for characterizing or monitoring the performance or organic coatings is available. In the last few years, several "new" techniques were introduced to study the behavior of organic coatings at an almost microscopic level. The standard techniques include electrical or electrochemical techniques such as electrochemical impedance spectroscopy (EIS), dielectric measurements, corrosion potential measurements, or polarization resistance measurement. The new, local techniques are in general called "scanning probes" and include the Kelvin probe, scanning vibrating electrode (SVET), scanning reference electrode (SRET), and local EIS. Various techniques for developing a detailed understanding of the polymer properties, including FTIR, DSC, DMTA, TG, hardness measurements, and AFM, are also frequently used, and naturally also test methods for dry and wet adhesion are important tools [7,9]. It is important to combine the results of these various techniques in order to compose suitable models for the different chemical and physical phenomena in these very complex systems. In most cases, a specific method measures only one specific parameter of the coated system that has no direct relation to the subject of interest. The water diffusion coefficient (D), for instance, can easily be estimated with EIS [81]. The direct relation of D to underfilm corrosion, however, is questionable. Therefore the selection of a set of measuring techniques depends very much on the specific aim of the investigator, who may be interested in a variety of phenomena such as water uptake, curing, and underfilm corrosion that have a relation in a complete, complex systems. These techniques, with their specific possibilities and limitations for research and monitoring of organic coatings, could well be the subject of a complete monograph. Within the framework of this chapter, a limited choice had to be made.

Because impedance measurements in the form of dielectric sensors, also in situ, can in principle give a rather extensive package of information on all charge- and dielectric-related phenomena including charge transfer reactions, diffusion processes, and delamination, these will be described first. A second reason for this choice is the possibility offered by this technique to arrive at lifetime predictions based on short-term measurements [81–86]. After relatively short exposure times, an indication of long-term behavior may be obtained. A third and not unimportant reason is the fact that in the literature a rather extensive discussion is going on the possibilities and impossibilities of this technique.

Second, we will focus briefly on electrochemical techniques in general. This will be used as a starting point for a brief description of the more recently developed local techniques. In the part also the information on corrosion mechanisms as presented earlier in this chapter will be used to evaluate the different methods.

Besides these measuring techniques, various weathering tests are, of course, used. These may vary from the natural weathering, via the well-known and often discussed salt spray test, to more sophisticated cyclic weathering tests that are designed specially, for instance for atmospheric corrosion of buildings. The combination of the previously mentioned measuring techniques with these weathering tests is a subject that is discussed more and more. Finally, adhesion measurements are briefly addressed.

Copyright © 2002 Marcel Dekker, Inc.

Electrochemical Impedance Spectroscopy

Impedance spectroscopy offers the possibility to study various phenomena. Here we first focus on delamination. In the next section we discuss the study of corrosion initiation. The study of the curing of coatings and special monitoring techniques has been left out of the discussion [7,9,87–91].

Electrochemical impedance spectroscopy (EIS) has been described by several authors as a technique for measuring all kinds of properties of organic coatings. But corrosion processes underneath coatings also have their own response in an impedance measurement. If corrosion occurs underneath coatings, electrons are transferred between molecules and metals in the corroding system. This charge transfer can be studied with normal electronic entities such as the impedance. The impedance Z as the ratio between a small sinusoidal potential perturbation [$V = V_0 \sin(\omega t)$] and the current resulting from this perturbation [normally $I = I_0 \sin(\omega t + \varphi)$]:

$$Z = \frac{V_0 \sin(\omega t)}{I_0 \sin(\omega t + \varphi)} \tag{1a}$$

Often this equation is represented using complex numbers:

$$Z = \frac{V_0 \exp(j\omega t)}{I_0 \exp(j\omega t + \varphi)} \tag{1b}$$

This impedance Z is frequency dependent and is characteristic of the system that is measured. In case of measurements of electrochemical reactions (e.g., corrosion), Z is called the electrochemical impedance. Normally Z is measured for many frequencies to create an impedance spectrum.

If a system that contains an electrochemical reaction is characterized by electrochemical impedance spectroscopy, there are often also nonelectrochemical parameters contributing to the total impedance. These might be the resistance of the electrolyte but also the dielectric behavior of an intact coating. In fact, part of the literature describes only the dielectric behavior of coatings during water absorption in the absence of corrosion.

The evaluation of the measured impedance is normally performed using complex numbers. In that case Z is written as complex number [9]:

$$Z = \mathrm{Re}(Z) + j\mathrm{Im}(Z) \tag{2}$$

with Re(Z) as the real part and Im(Z) as the imaginary part of the impedance. Re(Z) and Im(Z) are normally used to represent the impedance results.

In the analysis and interpretation of EIS, two fundamentally different approaches are possible, one using a complete transfer function and another simplified approach using equivalent circuits based on an assumed simplified physical model.

If the reaction mechanism is known, a transfer function may be calculated using the kinetics of the reactions, the diffusion equations, and so on. This transfer function couples the input from a system to the output. It includes all possible variables and is directly fitted to the measurements. In this way direct information on reaction parameters is obtained from the impedance. If the reaction mechanism is known and the system is not too complex, this method is favorable [92].

Copyright © 2002 Marcel Dekker, Inc.

It is obvious that a drawback of this method is that the reaction should be almost fully understood in order to produce a reliable transfer function. Another drawback is the fact that for more complex reactions the number of variables is very high. For a reliable fit the less important processes have to be ignored or variables have to be fixed; in other words, the important parameters of the system have to be estimated prior to the fitting procedure. In many cases the interpretation of measurements on coatings will be extremely complex due to the unknown geometries and local variation in electrolyte concentrations.

In this approach, one has to start with at least some idea of a physical model of what is happening in the measured system. This physical model is then transformed into an equivalent electrical circuit using only electrical components such as resistors and capacitors and some special components representing transport phenomena. An objection to this method is the fact that often more than one circuit is possible and circuits might also be rewritten in a different configuration without changing the response. This makes the interpretation in terms of chemical and physical parameters difficult. Figure 13, for example, shows two different circuits that give exactly the same response if the right values for resistors and capacitors are used.

Despite these objections, it is often possible to configure reasonable circuits that can be fitted to the measured data. Especially for intact coatings, the dielectric behavior and deviations from ideal behavior may give valuable information. Due to the precision of the measurements, it is in many cases also possible to measure small changes in coating properties that result from changes due to weathering, aging, etc.

Three examples of the use of EIS will be given next: atmospheric water uptake, measurements during delamination of intact and perforated coatings, and measurement of reproducible laser defects.

Atmospheric Water Uptake

The water uptake of organic coating can easily be monitored using the strong dipole of the water molecule. Because of this dipole character, the dielectric constant of water is high compared with that of most polymers [93]. Therefore a small amount of water absorbed in an organic coating will give a strong change in the dielectric constant of the system coating plus water. Dielectric constants can be studied using impedance spectroscopy. In this situation the term "electrochemical impedance spectroscopy" is not quite correct because no electrochemical but only physical parameters are measured. It is, however, widely accepted to use the term EIS instead of IS and for simplicity this terminology will be followed here too.

It is also interesting to follow water uptake under atmospheric conditions. Because no bulk electrolyte is present in this situation, special arrangements have to

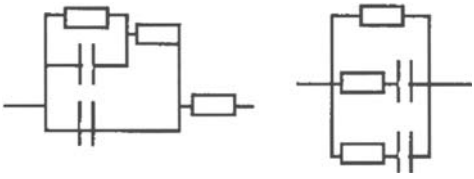


Figure 13 Two different equivalent circuits with the same impedance response. Rectangles represent resistors, parallel segments capacitors.

Copyright © 2002 Marcel Dekker, Inc.

be made in order to make impedance measurements possible. This can, however, easily be done with the setups presented next.

If grids of a conduction metal are applied by, for instance, PVD on top of the coatings, an EIS measurement can be performed using either the two combs of the grid as electrodes or the grid and the metal substrate as the electrodes. The grids may also be placed underneath a coating if the substrate is not conductive. In the case of multilayer coating systems they may be placed in between the different layers to ensure the properties of the individual layers. A possible configuration for a grid is given in Figure 14.

The geometry of the grids may of course differ from the one presented here. Normally, measurements are performed between the metal substrate and both arms of the grid. It is, however, also possible to measure between the two arms of the grid.

A disadvantage of this type of setup is the fact that an impermeable metal coating covers part of the surface. This changes the transport route for water. Grids arms should therefore be as thin as possible.

Grids can easily be produced on top of coatings by PVD. Often gold is used for this purpose. If coatings are applied to inert and nonconductive substrates (e.g., glass) the grid can be placed underneath the coating and the higher precision of lithographic techniques can be used produce finer grid lines.

Using these grids, a series of impedance measurements was performed on panels coated with a clear two-components epoxy. The panels were put for at least 3 days in a furnace at 40°C to dry completely and after this period they were exposed to an atmosphere with an RH of 20%. Starting from 20% RH, the humidity was increased stepwise after some days of exposure. This stepwise increase was repeated until in three steps an RH of 90% was obtained. Then the atmosphere was brought back again in the same steps to 20% RH. During these periods the impedance of the grids was measured continuously. The results of these measurements are shown in Figures 15 and 16. In these figures the capacity values as determined from impedance data are presented.

Both series of measurements in Figures 15 and 16 seem to give approximately the same picture. The differences that are visible between the two cycyles are caused by differences in exposure times in the different atmospheres. One big difference

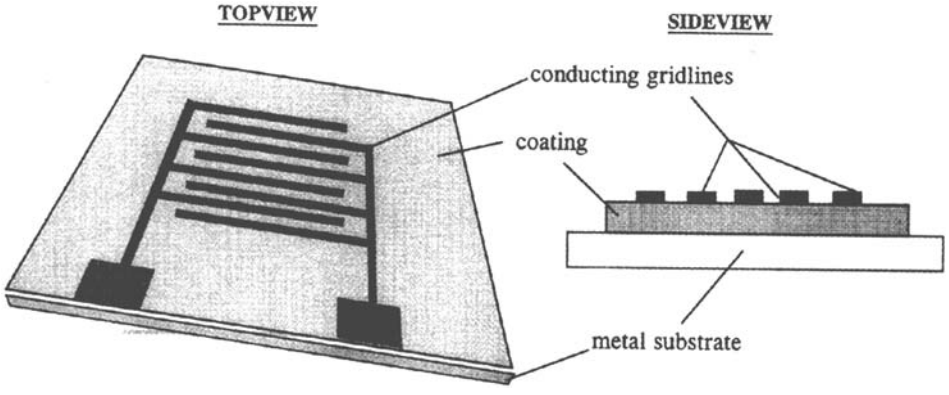
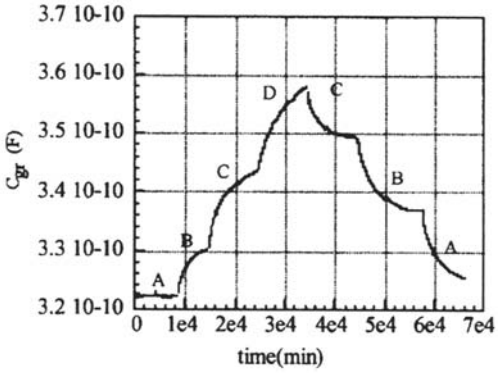
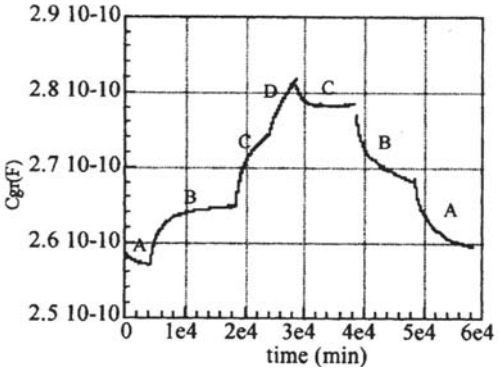


Figure 14 A possible configuration for a grid used to study atmospheric water uptake [63].

Copyright © 2002 Marcel Dekker, Inc.





Figures 15 and 16 Two examples of the capacitance (C_{gr}) as determined from impedance measurements performed on the grids as a function of time. A, B, C, and D refer to RH values of 20, 60, 80, and 90%, respectively. Thickness of the coatings was 92 μm (left) and 98 μm (right). The cycle in Fig. 15 took about 7 weeks, and in Fig. 16 about 6 weeks.

between the two series is, however, the absolute value of the capacitance. This is caused by the different surface area of the two grids.

For the transport of water the diffusion coefficient is also an important factor. The cyclic experiments can now be used to test whether D is independent of the amount of water absorbed in a coating. This is normally assumed in studies of water uptake by organic coatings. To describe the diffusion in a one-dimensional system, Fick's law is used:

$$J = -D\frac{\delta c}{\delta x} \tag{3}$$

Because all coatings in the cyclic experiments have a thickness (δx) of around 90 μm and within the cycles the thickness is assumed to be constant (no swelling occurs), a comparison of the diffusion coefficient of water in the cycles can be made. Because of the constant thickness δx can be set to unity. Furthermore, the flux J is equal to the increase in water content in time, which is approximately proportional to $\delta C/\delta t$ (C = capacitance), which is the derivative of the curves in Figures 15 and 16. Finally, δc is the change in relative humidity going from one atmosphere to another.

Copyright © 2002 Marcel Dekker, Inc.

Combining these assumptions, this leads to a comparative diffusion coefficient of water D^*, which can be calculated using:

$$D^* = \frac{\delta(\text{capacitance})}{\delta(\text{time})} \times (\text{RH2}(\%) - \text{RH1}(\%))^{-1} \quad (4)$$

In which RH1 and RH2 are the relative humidities of the atmospheres (of course, this D^* is not a real diffusion coefficient, but it can be used for comparison of the results). When this equation is used to calculate the D^* value of each step in the cycles of Figures 15 and 16, it gives the results presented in Table 2.

From these data, despite the rough method, it is clear that there are quite large variations in D^* as a function of the RH. The higher the concentration of water in the coating, the higher the D^*. This can be expected because of the plasticising effect of water on epoxies [94]. As expected, both grids do have comparable values for D^*.

Impedance Measurements and Delamination

EIS can also be used to measure and characterize defects in coating. This because a defect will also have a specific impedance response. Not very defect is, however, visible in measurements and care must therefore be taken in the interpretation of the data. To show this, two essentially identical panels were tested and will be referred to as cases A and B. On both panels a 100-µm-thick industrial coating was applied over a salt film that was present on the metal surface. As a result of this, both panels showed delamination and osmotic blistering as soon as they were exposed to an electrolyte.

Directly after immersion, case A showed a Nyquist and Bode plot that deviated from the expected plots for intact coatings. Representative measurements after 1 h and 10 days are given by Figure 17a and b.

Analysis of the data with equivalent circuits showed that at least four overlapping time constants were present. This implies that a rather complex equivalent circuit should be used to explain the data and that it is not sufficient for a fundamental study to monitor only one frequency or phase angle [95]. A complete analysis of these data is beyond the scope of this chapter, but an important conclusion is that the corrosion component in the equivalent circuit is in parallel with the coating component. This implies a real defect that penetrates through the coating. Prolonged exposure indeed showed corrosion products coming out of a small pore in the coating.

Table 2 Comparative Diffusion Coefficient for Two Cycles and Different Changes in Atmospheres as Calculated from the Results of Figures 15 and 16[a]

From RH to RH	δc	D^* cycle 1 (m^2/s)	D^* cycle 2 (m^2/s)
20 to 60%	40	2.76e-15	3.00e-15
60 to 80%	20	8.98e-15	7.7e-15
80 to 90%	10	1.64e-14	9.67e-15
90 to 80%	10	9.41e-15	6.56e-15
80 to 60%	20	7.95e-15	6.9e-15
60 to 20%	40	3.75e-15	2.99e-15

[a]Values can be used only for comparison within this table.

Copyright © 2002 Marcel Dekker, Inc.

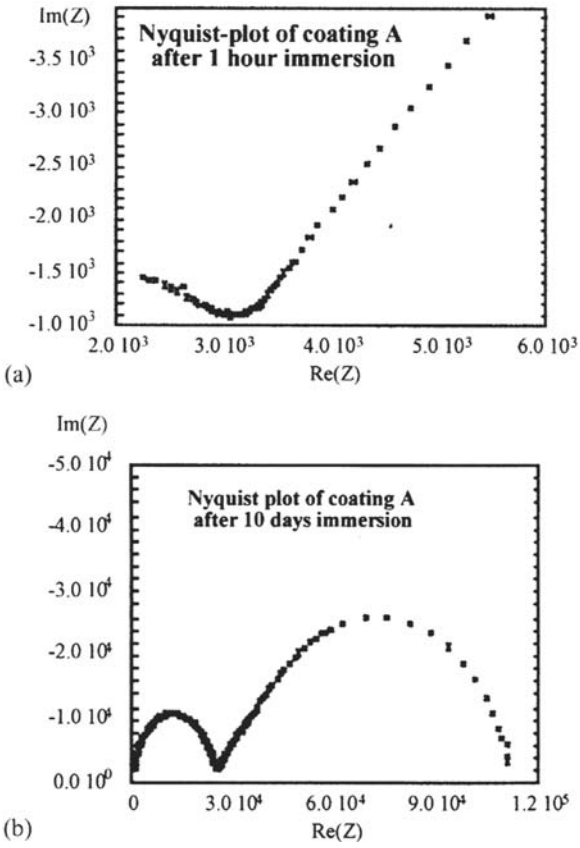


Figure 17 Two Nyquist plots of measurement on coating A: (a) after 1 h and (b) after 10 days of exposure to water (plots are not isotropic).

The almost identical panel B has a completely different start upon exposure. Here we see a normal, capacitive behavior after 1 h of immersion as can be seen in Figure 18a. After 2 days this still has not changed, as can be seen in Nyquist plot of Figure 18b. This behavior is observed for several days. However, after 2 days delamination is already clearly visible as a small blister above the contaminated area. So in this case it is clear that, although a defect is present, it is not (easily) visible in the EIS data.

The corrosion potential of panel B also appeared to be unstable. Several times the open-circuit potential drifted to –3000 mV versus SCE. Every time this happened it was polarized at a normal potential for steel in the electrolyte. This unstable behavior is due to the very high resistance of the coating, which in this case exceeds the input impedance of equipment used.

These observations support the conclusion that the coating is completely intact although partly delaminated due to the contamination underneath.

From the measurement of the water uptake in the first hours of immersion, some qualitative information on this delamination can be obtained. From the coating capacitance (C_{pf}) against time plot of Figure 19 it is clear that the coating does not show stable Fickian water uptake but shows deviations that are probably

Copyright © 2002 Marcel Dekker, Inc.

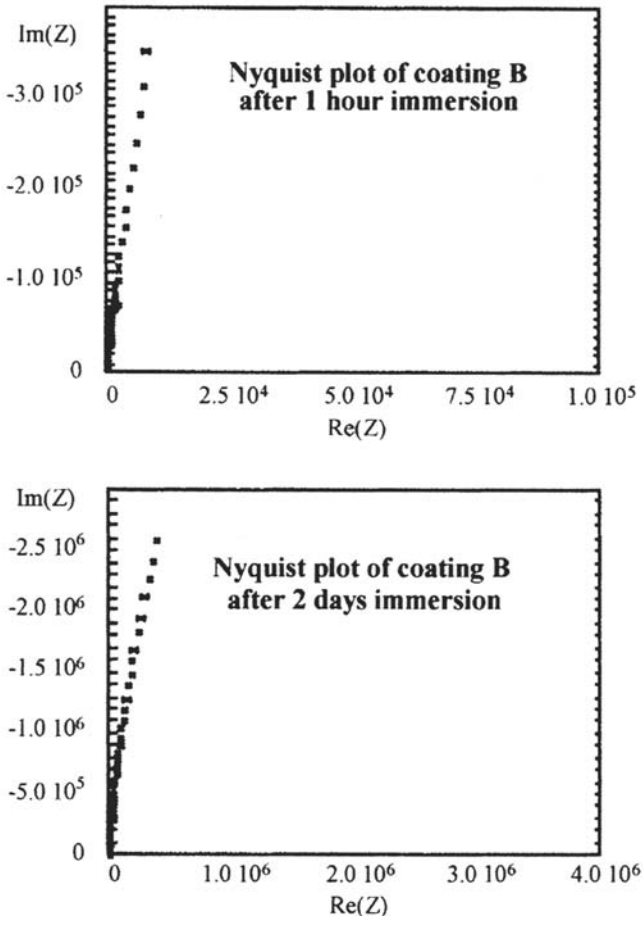


Figure 18 (a and b) Two Nyquist plots of measurement on coating B (plots are not isotropic).

caused by the delamination. Because the delamination is forced and is already starting when the coating is still taking up water, the water uptake and the deviation from normal saturation behavior are not visible separately.

To further prove the similarity between panels A and B, the blister on panel B was perforated deliberately with a needle. Directly after this the impedance spectrum of Figure 20a and b was measured, which is rather similar to the data measured on panel A. Because it is known that defect and delamination are in this case combined, an equivalent circuit with a corrosion component in parallel to the coating impedance must be used if further analysis is to be performed.

From the results of the measurements just described it is clear that quantitative measurements on delamination under an intact coating are not possible with impedance measurements as long as the impedance of the systems remains high, which is often the case for thicker heavy-duty systems. In terms of equivalent circuits that are used to explain impedance measurements, this implies that the corrosion

Copyright © 2002 Marcel Dekker, Inc.

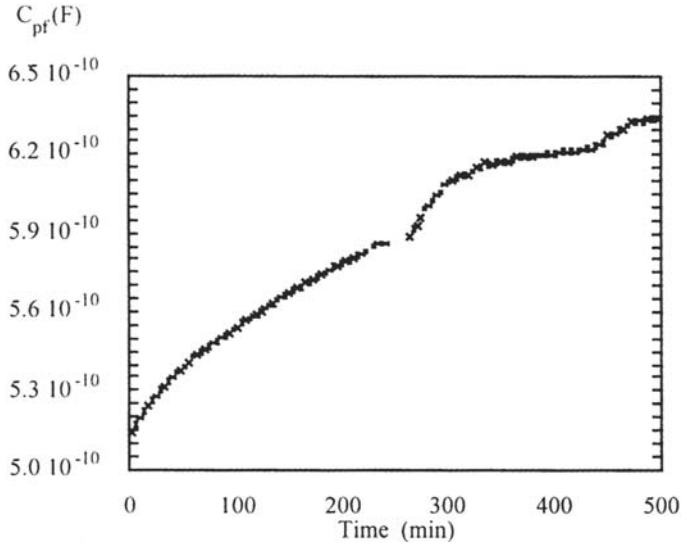


Figure 19 Coating capacitance as a function of time during water uptake of coating B.

component of the circuit has to be in series with the intact coating components. In the literature this corrosion component is often placed in series with a relatively low resistor, meaning that the properties of the coating have already changed considerably (e.g., porosity and other flaws have developed).

Impedance Measurements and Artificial Defects, Laser Ablation

Often organic coatings do not fail early even under severe laboratory conditions. Therefore it is necessary to make artificial defects in a coating system to study the corrosion initiation under a coating. Both standard testing by exposure of standard panels with or without mechanically induced scribes and laboratory research into the mechanisms of the reactions suffer from the rather uncontrolled application method for these artificial defects. The width and the height of the scribe largely determine the mechanisms. Sometimes, for complicated systems with more layers as in car body panels, one wants to make sure that a certain layer is still intact, and for mechanistic studies in the laboratory one wants to study the very early stages of the delamination. In both cases, artificial defects made with the laser ablation technique may provide the answer [96–98].

Defects in surface coatings are used to study the protective properties of these coatings. Defects made by ablation with excimer lasers have important advantages with respect to traditional techniques. A resolution of the geometry down to the micrometer scale with high precision and good edge definition is feasible, yielding little, if any, distortion of the remaining coating layer: no coloring, foaming, or melting. Moreover, the results show no ruptures and no delamination of the coating layer from the substrate material. Normally, subsequent laser pulses perform the etching of a defect until the underlying metal substrate is reached. The etching is automatically stopped at the metal surface, as the threshold for ablation of the metal higher than the threshold for organic materials. The laser beam will not change the remaining metal surface.

Copyright © 2002 Marcel Dekker, Inc.

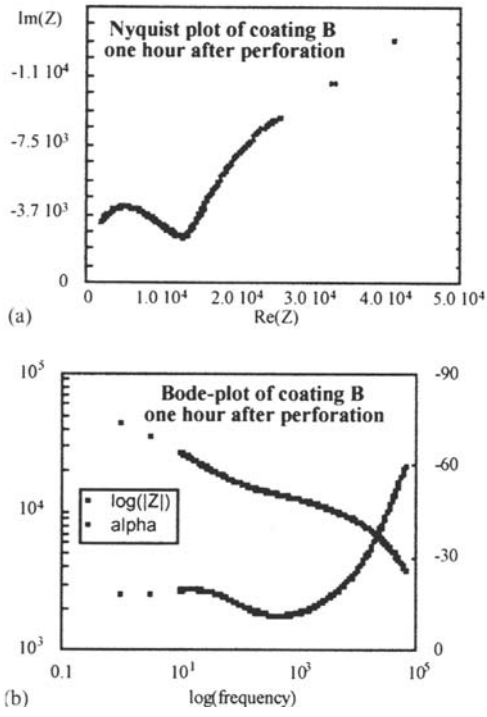


Figure 20 Nyquist and Bode plots measured on coating B directly after perforation. (b) Log *Z* is given on the left axis and alpha on the right axis.

The fine control over the ablation process makes another feature possible. If the etching is interrupted just before the metal is reached, a defect with a thin (several μm) residual layer on the bottom can be produced, as illustrated schematically in Figure 21. It is this defect that proved to have ideal characteristics for broad characterization of organic coatings, including electrochemical impedance spectroscopy.

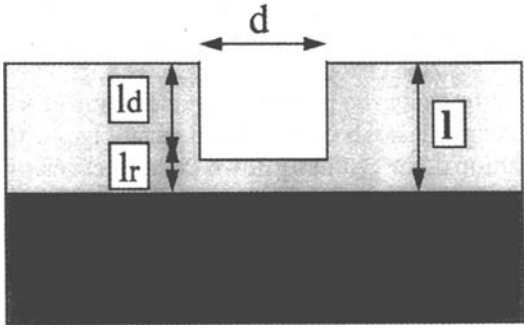


Figure 21 Typical geometry of an artificial laser defect in an organic coating. d = defect diameter, I_d = defect depth, and I_r = thickness of the residual coating layer in the defect.

Copyright © 2002 Marcel Dekker, Inc.

After impedance measurements have been performed, meaningful physical information on the system may be obtained only from a correct analysis and interpretation of the data as discussed before. Impedance analysis may be performed at different levels of complexity. The easiest form is a visual inspection of the measured impedance diagrams or changes in these diagrams with time. This may give first insight into the performance of a specific system. More detailed information on mechanisms and corrosion phenomena may be obtained from an elaborate analysis procedure. In Figure 22 the different stages that may be distinguished in the behavior of a coated system as a function of exposure time to water are illustrated schematically. At different exposure times the coated system, with laser defect, is shown with the typical shape of the impedance response and the corresponding general equivalent circuits. The following stages are distinguished:

A. Water permeation
B. Corrosion initiation
C. Quasi-stationary corrosion

It should be stressed that the very start of the corrosion process is visible in the changing appearance of the Nyquist plot as given in Figure 22, but no quantitative interpretation of the impedance data is possible because of the relatively fast changes of the system. When the quasi-stationary stage, C, has been reached, detailed quantitative analysis is again possible, leading to a more detailed equivalent circuit supported by a physical model. It must be stressed that data from different techniques are always needed when searching for a detailed physical model. Also, the changes in time during exposure of the various components of the equivalent circuit can be used to check the practical value of a proposed model.

Local Electrochemical Test Methods

The local electrochemical techniques that are used for coatings research are mainly used in the more fundamental studies of corrosion mechanisms. They can be divided into techniques in immersion (SVET end SRET) and in atmospheric conditions (Kelvin). All techniques are based on the observation that corrosion mechanisms underneath coatings are generally mechanisms in which anodic and cathodic processes take place on separated sites with a slightly different local "corrosion potential." The techniques are used to visualize these differences. SRET and SVET can also be used on polarized samples to detect pinholes.

SRET is a technique in which a reference electrode is scanned over a surface. A second reference electrode is used to monitor the overall corrosion potential. In this way, small differences in the potential can be visualized. An alternative type of SRET has a tip with two platinum needles that are both placed close to the surface. If local potential differences exist over the surface, a corrosion current will run through the solution. In that case a small potential drop will occur in the solution between the two platinum wires. Assuming an ohmic behavior for the solution resistance, this potential difference is proportional to the potential differences on the surface.

A drawback of the SRET is the fact that it has to measure very small differences in a direct current mode. It is therefore not very sensitive and in most cases the substrate has to be polarized to increase the current that is flowing through the

Copyright © 2002 Marcel Dekker, Inc.

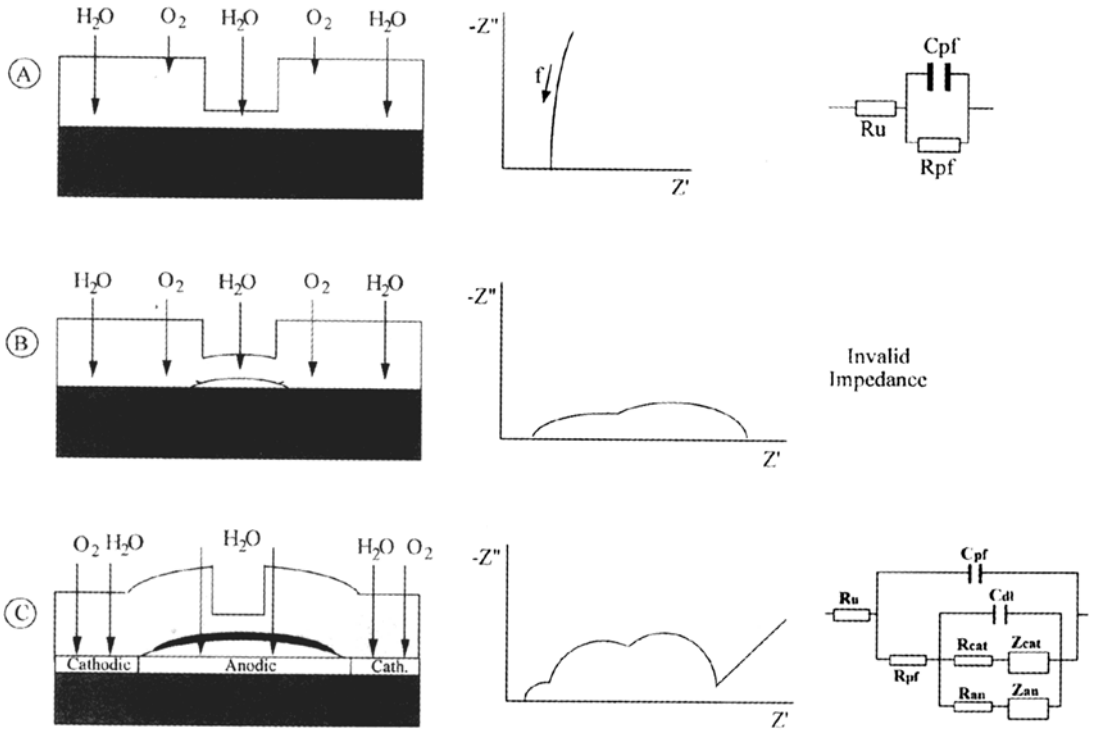


Figure 22 Different stages in behavior of a coated system with progressing exposure time to water. (Left to right) System, impedance response, and equivalent circuit Stages: (A) Water permeation; (B) corrosion initiation; (C) quasi-stationary corrosion. (*R* = resistance, *C* = capacitance, *Z* = diffusion impedance, pf = paint film, cat = cathodic, an = anodic, dl = double layer, u = electrolyte.)

Copyright © 2002 Marcel Dekker, Inc.

solution. In this mode it can be used only to show the location and size of defects in a coating.

A more sensitive technique is measuring the same *IR* drop in the solution by the SVET. In the SVET the potential of a small vibrating tip is measured. If this tip is vibrating in a potential gradient, the resulting potential vibration in the tip is easily detected (AC mode) with sensitive electronics. Although more accurate, this method is much slower than the SRET.

A drawback of both methods is that complex corrosion mechanisms underneath coatings including total delamination cannot be determined. Calculations with current distribution models [99] can easily show that in the case of underfilm corrosion almost no corrosion currents will be present in the outside electrolyte. Polarization of the substrate is therefore necessary to show the presence of defects. This will, however, at the same time influence the corrosion mechanisms.

The Kelvin probe is, unlike the other techniques, able to measure through an insulating coating layer. Lord Kelvin used the principle of the Kelvin probe to show that a Volta potential difference exists between metals. Apart from the obviously modern electronics, the principle of the Kelvin probe is still the same: if two metal plates are coupled through a wire and are brought close to each other, a potential difference that is equal to the Volta potential difference between the two metals exists over the narrow gap between the plates. As a result of this, the metal plates will have a capacitive charge. If one of the plates is now vibrated, the capacity between the plates is varied and as a result of this an AC current will flow through the external circuit with a magnitude of

$$I_{ac} = \Delta V \delta C/\delta t$$

in which ΔV is the Volta potential difference between the two metals and $\delta C/\delta t$ the variation of the capacitance in time due to the vibration. If in this circuit an external DC voltage source U is introduced, this equation changes to

$$I_{ac} = (\Delta V - U)\,\delta C/\delta t$$

From this equation it becomes clear that for the case in which the external DC voltage U is equal to ΔV, the AC current I_{ac} goes to zero, independent of $\delta C/\delta t$. This implies that with this measurement it is even possible to measure through vacuum, air, or an organic coating as this will influence only the term $\delta C/\delta t$.

Stratmann showed in several articles published around 1987 that for metals with a thin moisture layer the Volta potential difference was proportional to the corrosion potential of that system [100]. Using a calibration, it is therefore possible to measure the corrosion potential of a corroding system through an air gap and without making contact.

Although powerful, this technique is still under further development. Especially the interpretation of the measured results is still a matter of discussion. Without doubt it will in the future bring more and more results, especially on specific corrosion mechanisms underneath coatings and on atmospheric corrosion. Recent developments have shown that it is even possible to combine the extremely high resolution of the AFM with the measuring principle of the Kelvin probe. For special systems (uncoated), this may reveal even more details of corrosion mechanisms.

Copyright © 2002 Marcel Dekker, Inc.

Other Electrochemical Methods

Among the other electrochemical methods are the measurement of the corrosion potential and the determination of the polarization resistance (R_p). Both methods are relatively simple but may give relevant information.

The polarization resistance is determined as the slope of a polarization curve at the corrosion potential at the point where the external current is zero. In this way it is a linearization of the more complex polarization curve. The value of R_p/cm^2 is directly related to the reactivity of the exposed metal substrate through the Stern and Geary relation. For a coated system the total value of R_p is also determined by the amount of metal that is exposed. Both a higher reactivity and a larger exposed area lead to a lower R_p. If for a given system the R_p is rather constant in time, this technique can be used to predict the corrosion rate. In closed metal containers as used for beer and soft drinks only a minimum amount of oxygen in present in a normally rather acidic electrolyte. In that situation, no solid corrosion products are formed and the R_p is constant over time. In these drinks the amount of iron after a certain shelf life is an important quality check. Figure 23 shows the correlation between $1/R_p$ as measured after 2 weeks and the iron pickup of the drinks after 6 months. The R_p was measured over a 20-mV range around the corrosion potential of the system in the beverage itself (in this case cola, which has a pH of around 2.5).

In the case that no defect is present in the coating, an R_p measurement is measuring only the normally very high resistance of the polymer layer. In that case, the obtained value should be similar (if measurable) to the values obtained from fitting an impedance measurement.

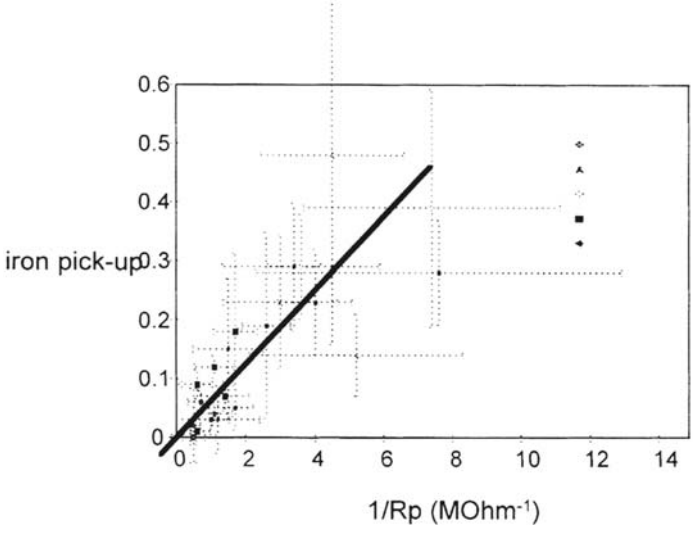


Figure 23 Iron content of the electrolyte after 6 months of exposure versus polarization resistance. Iron pickup in mg/L. Different points represent different series of filled cans corresponding to various closing conditions.

Copyright © 2002 Marcel Dekker, Inc.

The Value of Enhanced Weathering Tests

The recent developments of electrochemical testing procedures, of which we have discussed two, may result in better system lifetime prediction methods and monitoring techniques for coating systems than are now available. Many new coating systems are being developed as a result of the various environmental demands and legislation together with demands for high quality for improved lifetime.

The industrial need for fast testing methods is therefore enormous because testing by, e.g., atmospheric exposure of the systems takes too much time. Many fast testing procedures exist. One of the first enhanced weathering tests was the exposure of coated panels in Florida, where 3 years of exposure would be more or less similar to 10 years of exposure in Europe because of the high temperature and humidity in Florida. However, many new tests have been developed, and the exposure in Florida is now not regarded as a fast test. Shortening the test period means that various parameters determining the corrosion initiation and propagation processes are considerably changed compared with natural conditions. These include:

The temperature
The composition of the corrosive including NaCl, pH, SO_2, and additions such as copper
The relative humidity
UV radiation

For modern cyclic testing some of these parameters are changed in time at regular intervals, simulating more natural exposure conditions.

The aim of any testing procedure is to find a simple, perferably linear relation between natural exposure and enhanced testing results. However, according to many authors there is no such simple relation [101]. Some authors state that enhanced weathering just gives some indication of the relative quality of coating during testing, without any predictive value for the lifetime. Even standard tests (e.g., ASTM B117) emphasize the lacking relation between, e.g., the salt spray test and corrosion protection in different surroundings due to the enormous differences in the reaction mechanisms. It has been stated that coated galvanized steel always performs worse in a salt spray test than normal cold-rolled steel, whereas in reality it always performs better [102]. Cyclic testing improves the relation between test and practice [103].

It has been reported [104] that standard salt spray tests give reasonable results for coatings in use in surroundings with a high salt concentration (seawater, deicing salt) and high RH but not for other applications. The high salt concentration would be responsible for decreased action of the anticorrosive pigments, which perform well under natural low-salt conditions. Also, salt spray tests often give blistering, which is often not relevant except for marine applications. Cyclic testing again results in less blistering, which at least seems to indicate a better simulation of natural conditions.

A comparison of a cyclic test newly developed by Hoogovens for automotive panels with the salt spray test, the SCAB (simulated corrosive atmospheric breakdown) test, and the VDA (Verein der Deutschen Automobilindustrie) test showed that some differences can be observed in the test results for the ranking as far as undermining is concerned. A negative relation exists between the results of the new cyclic test and the salt spray test. The new cyclic test shows reasonable agreement in

Copyright © 2002 Marcel Dekker, Inc.

many cases with the SCAB test. Detailed research showed that the different test procedures indeed result in different corrosion mechanisms [1].

Therefore is must be concluded that enhanced weathering tests normally should be cyclic, simulating many practical parameters with their changes in time. Interpretation should be performed with extreme care. Improvements of fast testing procedures, e.g., by incorporating electrochemical and dielectric sensors, are of extreme importance in order to arrive at laboratory-based lifetime prediction.

Adhesion Tests

As mentioned before, adhesion is one of the major properties of a protective coating. Testing of adhesion seems therefore of prime importance for the characterization of organic coatings. In practice it is, however, rather difficult to measures the adhesion of organic coatings.

One group of simple and straightforward techniques can be categorized as "deformation techniques." Among these are T-bend, direct impact, and Erichsen cup tests. In all these tests the specimen of interest is subjected to a nonuniform deformation (mainly stretching). The amount of deformation at which the coating deadheres is in these cases a measure of the adhesion. Although important for many mainly practical applications, these methods cannot be used to gain more fundamental knowledge of adhesion. This is because the measured value is a combination of the mechanical properties of the coating and the adhesion. Besides that, these methods mainly look at shear stresses.

Another method that is often used is a "crosshatch cut." In this method a cross pattern is scratched into the coating. This operation also causes shear stresses on the coating-metal interface. As a result of this the smallest squares will completely deadhere. The minimum size of the squares that remains attached is in this case a measure of the adhesion.

Both these techniques (deformation and crosshatch) are generally used in combination with a sort of "tape test" to determine the exact degree of delamination. Any part of the coating that has higher adhesion to the tape that is glued on top is removed in this test. This means that it is a binary method and is not able to quantify the exact adhesive properties.

One method that is designed for these more quantitative adhesion measurements is a pull test. For this test a dolly is glued unto the coating surface. The coating around the dolly is scratched down to the bare metal to isolate the area underneath the dolly from the other parts. After complete curing of the glue, the dolly is pulled from the coating in normal tension tests. In the case that the coating-metal interface fails, an exact value is obtained for the adhesion in tensile mode. In the case that either the coating polymer itself or the glue fails, of course, only a minimum value is obtained. A disadvantage of this method is the fact that the dolly has to be glued on the surface. Apart from the chemical effects this may cause, it effectively screens the interface from, for instance, water. It is therefore difficult (although maybe not impossible) to measure under wet conditions.

A last technique that will be mentioned here is also a quantitative method but it can be used under wet conditions. It is testing under a relatively realistic load, which is a combination of tensile and shear stress. In this method a strip of the coating is scratched and at one side freed from the substrate. This lip is then pulled from the

Copyright © 2002 Marcel Dekker, Inc.

surface at a constant speed and a constant angle to the substrate. The force necessary to do this is a measure of the adhesion of the coating. This method also gives the possibility to determine the adhesion along a part of the substrate. For the region just in front of underfilm corrosion this was recently illustrated by Fuerbeth and Stratmann and also discussed in Ref. 62. The only disadvantage of this method is the fact that the tensile force is applied on the coating. This makes it suitable only for thicker coatings. Thin coatings (such as used in the canning industry) will in many cases break before delamination starts.

As a conclusion to this section on adhesion measurements, we can say that the despite the importance of this topic only a limited number of relevant techniques is available. When selecting a method it is important to use a method with a relevant force mode (shear, tensile, or a combination) and relevant conditions.

REFERENCES

1. F. Blekkenhorst and E. Nagel Soepenberg, Proceedings Corrosion '88, St. Louis, paper 354, 1988.
2. J. H. W. de Wit and C. B. M. Nagel, Micropeenbehandlung mit guten Resultaten, *Chem. Anlagen Verfahren* June:5 (1992); J. H. W. de Wit, Refinement of stainless steel surface through micropeening, Proceedings ACHEMA, Frankfurt, 1991, p. 16.
3. W. Funke, *Prog. Org. Coatings 9*:29 (1981).
4. K. R. Gowers and J. D. Scantlebury, *Corros. Sci. 23*:935 (1983).
5. W. Funke, *Ind. Eng. Chem. Prod. Res. Dev. 24*:343 (1985).
6. J. R. H. Leidheiser, Corrosion of painted metals—a review, *Corrosion 38*:374–383 (1982).
7. F. M. Geenen, Characterization of organic coatings with impedance measurements, Thesis, Delft University of Technology, Delft, 1991.
8. F. M. Geenen, Corrosion protection by organic coatings, Lecture notes (Dutch), Delft University of Technology, Delft, 1989.
9. E. van Westing, Determination of coating performance with impedance measurements, Thesis, Delft University of Technology, Delft, 1992, and a series of five papers in *Corrosion Science*: Part 1, *34*:1511 (1993); Part 2, *36*:957 (1994); Part 3, *36*:979 (1994); Part 4, *36*:1323 (1994); Part 5 to follow.
10. F. Geenen, E. van Westing, and J. de Wit, *Prog. Org. Coatings 18*:295 (1990).
11. F. Geenen and J. de Wit, Proceedings, 30th ACA Conference, Auckland, NZ, paper 59, 1990.
12. R. A. Dickie, *ACS Symp. Ser. 285*:773 (1985).
13. A. D. Wilson, J. W. Nicholson, and H. Y. Prosser eds., *Surface Coatings 1 and 2*, Vol. 1 1987, Vol. 2 1988, Elsevier Applied Science, Amsterdam.
14. H. Leidheiser, *Polymeric Materials for Corrosion Control* (R. A. Dickie and F. Louis Floyd, eds.), *ACS Symp. Ser.*, 1986, p. 124.
15. H. Leidheiser, W. Chang, and L. Ingetoft, *Prog. Org. Coatings 11*:19 (1983).
16. J. S. Thornton, J. F. Cartier, and R. W. Thomas, *Polymeric Materials for Corrosion Control* (R. A. Dickie and F. Louis Floyd, eds.), *ACS Symp. Ser.*, 1986, p. 169.
17. E. L. Koehler, *Localised Corrosion* (R. W. Staehle, B. F. Brown, J. Kruger, and A. Agarwal, eds.), NACE, Houston, 1974, p. 117.
18. G. M. Kogh, *Localised Corrosion* (R. W. Staehle, B. F. Brown, J. Kruger, and A. Agarwal, eds.), NACE, Houston, 1974, p. 134.

Copyright © 2002 Marcel Dekker, Inc.

19. W. Loven, Pretreatments for aluminium, Literature Review (Dutch), Division of Corrosion Technology, Delft University of Technology, 1992.
20. T. Van der Klis, *Vademecum—Surface Techniques for Metals*, 5th ed., Bilthoven, The Netherlands, 1989.
21. D. B. Freeman, *Phosphating and Metal Pretreatment*, Woodhead, Cambridge, 1986.
22. *Tool and Manufacturing Engineers Handbook*, Vol. 3, *Materials, Finishing and Coating*, 3rd ed. Society of Manufacturing Engineers, Dearborn, MI, 1985.
23. G. M. Brown, K. Shimizu, G. E. Kobayashi, et al., The growth of chromate conversion coatings on high purity aluminum, *Corros. Sci. 34*:1045–1054 (1993).
24. M. W. Kendig, A. J. Davenport, and H. S. Isaacs. The mechanism of corrosion inhibition by chromate conversion coatings from X-ray absorption near edge spectroscopy (XANES), *Corros. Sci. 34*:41–49 (1993).
25. A. H. Reed, For performance and economy: chromate coatings, *Prod. Finish. 51*:60–64 (1986).
26. M. Koudelkova, J. Augustynski, and H. Berthou, On the composition of the passivating films formed on aluminum in chromate solutions, *J. Electrochem. Soc. 124*:1165–1168 (1977).
27. H. Leidheiser, Mechanism of corrosion inhibition with special attention to inhibitors in organic coatings, *J. Coat. Technol. 53*:29 (1981).
28. 2262. Toxicological Profile for Chromium (Public Health Service Report ATSDR/TP-88/10), Agency for Toxic Substances, Atlanta, 1989.
29. B. R. W. Hinton, Corrosion prevention and chromates: the end of an era? Proceedings Asia Interfinish '90 (paper 30), Singapore, 1990.
30. D. G. Anderson, E. J. Murphy, and J. Tuccir, *J. Coat. Technol. 50*:38 (1978).
31. W. J. van Ooij, *Polym. Mater. Sci. Eng. 53*:698 (1985).
32. E. N. Soepenberg, H. G. Vreijberg, J. A. F. M. S. van Westrum, W. J. van Ooij, and O. T. de Vries, Corrosion/85, NACE, Houston, paper 388, 1991.
33. F. Delaunois, V. Paulaini, and J. P. Petjtjean, *Mater. Sci. Forum 142*:213 (1997).
34. R. Mady, C. Reis, and R. Morlock, Eur. Pat. Appl. 831126107, 1993.
35. B. A. Shaw, G. D. Davis, T. L. Friz, and K. A. Olver, *J. Electrochem. Soc. 137*:359 (1990).
36. B. Hinton, A. Hughes, R. Taylor, M. Anderson, K. Nelson, and L. Wilson, International Symposium on Aluminium Surface Science and Technology, Antwerp, Belgium, May 12–15, 1997, p. 165.
37. F. Mansfeld, Y. Wang, and H. Shih, *Electrochim. Acta 37*:2277 (1992).
38. L. Fedrizzi, F. Florian, and S. Rossi, International Symposium on Aluminium Surface Science and Technology, Antwerp, Belgium, May 12–15, 1997, p. 243.
39. M. J. Rijkhoff, R. Bleeker, and J. Bottema, International Symposium on Aluminium Surface Science and Technology, Antwerp, Belgium, May 12–15, 1997, p. 125.
40. C. M. Rangel and M. A. Travassos, *Corros. Sci. 33*:327 (1992).
41. J. W. Bibber, *Corros. Rev. 15*:303 (1997).
42. R. Feser and Th. Schmidt-hansberg, Eurocorr '97, Trondhiem. Norway, September 22–25, 1997, p. 291.
43. W. van Ooij, *Corrosion 54*:204–215 (1998).
44. W. J. van Ooij and T. J. Ossic, SAE International Congress and Exposition, paper 870647, 1987.
45. C. Barreau, D. Massinon, and D. Thierry, Proceedings, 5th Automotive Corrosion and Prevention Conference, SAE, paper 327, 1991.
46. D. Massinon and D. Thierry, Corrosion/91, NACE, Houston, paper 574, 1991.
47. R. D. Granata, Corrosion/91, NACE, Houston, paper 382, 1991.
48. J. H. W. de Wit, E. P. M. van Westing, and D. H. van der Weijde, *Mater. Sci. Forum 247*:69 (1997).

Copyright © 2002 Marcel Dekker, Inc.

49. *Marine Paint Manual*, Graham and Trotman Ltd., London, 1989.
50. J. E. O. Mayne, *Corrosion*, 2nd ed. (L. Shreier, ed.), Vol. 2,15, Newnes-Butterworth, London, 1976, p. 24.
51. F. Belluci, L. Nicodemo, and R. M. Latanision, *J. Mater. Sci. 25*:1097 (1990).
52. U. R. Evans, *The Corrosion and the Oxidation of Metals*, St. Martins Press, New York, 1960.
53. C. Haberer, C. M. Wolf, Y. P. Collin, Y. L. Leibenguth, and P. Schwing, *Electrochim. Acta 6*:755 (1981).
54. N. L. Thomas, *J. Prot. Coat. Linings 6*(12):63 (1989).
55. J. S. Hammond, J. W. Hobluka, and R. A. Dickie, *J. Coat. Technol. 51*:45 (1979).
56. J. E. Castle and J. F. Watts, Proceedings Corrosion Control by Organic Coatings, NACE, Houston, 1981, p. 78.
57. W. Funke, H. Haagen, Empirical or Scientific Approach to Evaluate the Corrosion Protective Performance of Organic Coatings, *Ind. Eng. Chem. 17*: (1978).
58. R. N. Parkins, A. J. Markworth, J. H. Holbrook, and R. R. Fessler, Corrosion '84, New Orleans, 1984.
59. CRC *Handbook of Chemistry and Physics*, 56th ed., Cleveland (Ohio), CRC Press, 1976.
60. W. S. Tait and K. A. Handrich, Corrosion, 50, 1994.
61. T. N. Nguyen and J. B. Hubbard, A Mathematical Model for the Cathodic Blistering of Organic Coatings on Steel Immersed in Electrolytes, *J. Coat. Technol. 63*(794):43–52 (1991).
62. W. Fuerbeth and M. Stratmann, *Corros. Sci.* 3 (1999).
63. D. H. van der Weijde, Impedance spectroscopy and organic barrier coatings. Thesis, TU-Delft, 1996.
64. *Marine Paint Manual*, Graham and Trotman Ltd., London, 1989.
65. P. R. Willemsen and G. M. Ferrari, A review of antifouling methods. TNO report CA/95.1026 (study carried out for the Netherlands Ministry of Housing, Physical Planning and Environment), 1995.
66. P. R. Willemsen and G. M. Ferrari, Possibilities and impossibilites of alternative antifouling techniques, An International One-Day Symposium on Antifouling Paints for Ocean-Going Vessels, The Hague, 21 February 21, 1996, pp. 60–67.
67. P. R. Willemsen and G. M. Ferrari, The removal of biofouling from ships' hulls: state of the art, TNO report CA/96.9906 (in Dutch) (study carried out for the Netherlands Ministry of Housing, Physical Planning and Environment), 1996.
68. E. C. Haderlie, A brief overview of the effects of macrofouling, Marine Biodeterioration: An Interdisciplinary Study, Proceedings of Symposium on Marine Biodeterioration (J. D. Costlow and R. C. Tipper, eds.), Univ. Health Sciences, April 20–23, 1981, pp. 163–166.
69. F. H. de la Court, Aangroeiwerende verven. *Chemische feitelijkheden—Aktuele chemische encyclopedie*, 1990, pp. 2–6.
70. G. I. Loeb, D. Laster, T. Gracik, and D. W. Taylor, The influence of microbial fouling films on hydrodynamic drag of rotating discs, Marine Biodeterioration: An Interdisciplinary Study. Proceedings of Symposium on Marine Biodeterioration (J. D. Costlow and R. C. Tipper, eds.), Univ. Health Sciences, April 20–23, 1981, pp. 88–94.
71. Fischer E. C., Castelli V. J., Rodgers S. D. & Bleile H. R. (1981). Technology for control of marine biofouling—a review, Marine Biodeterioration: An Interdisciplinary Study. Proceedings of Symposium on Marine Biodeterioration, Univ. Health Sciences, April 20–23, 1981, pp. 261–299.
72. J. D. Pidgeon, Critical review of current and future marine antifouling coatings, Lloyd's Register, Engineering Servic. Propulsion and Environmental Engineering Department, report 93/TIPEE/478719, 1993.
73. Anonymous, TBT copolymer antifouling paints: the facts, CEFIC Brochure (based on paper presented to MEPC in November 1990), 1992.

Copyright © 2002 Marcel Dekker, Inc.

74. C. C. ten Hallers-Tjabbes, TBT in the open sea: the case for a total ban on the use of TBT antifouling paint, *North Sea Monitor* September:12–14 (1994).
75. R. De Nys, P. D. Steinberg, P. R. Willemsen, S. A. Dworjanyn, C. L. Gabelish, and R. J. King, Broad spectrum effects of secondary metabolites from the red algae Delisea pulchra in antifouling assays, *Biofouling*, *8*:259–271 (1995).
76. A. S. Clare, D. J. Gerhart, and D. Rittschof, Development of nontoxic antifoulants based on natural product chemistry, Poster presented at the International Symposium on Marine Biofouling and Corrosion, Portsmouth, UK, June 13–16, 1993.
77. D. J. Gerhart, D. Rittschof, and S. W. Mayo, Chemical ecology and the search for marine antifoulants, *J. Chem. Ecol. 14*:1905–1917 (1988).
78. M. Fletcher and J. H. Pringle, The effect of surface free energy and medium surface tension on bacterial attachment to solid surfaces, *J. Colloid Interface Sci. 104*:5–14 (1985).
79. R. C. Wallis and K. R. Strudwick, Nontoxic marine fouling release coatings, *Surf. Coat. Austr*. March:14–17 (1989).
80. R. F. Brady and J. R. Griffith, Nontoxic alternatives to antifouling paints. *J. Coat. Technol. 59*:113–119 (1987).
81. J. H. W. de Wit and E. P. M. van Westing, paper at UK Corrosion, London, October 1993.
82. J. H. W. de Wit, Proceedings 12th International Corrosion Congress, Houston, paper 324, September 19–24, 1993.
83. E. P. M. van Westing, G. M. Ferrari, F. M. Geenen, and J. H. W. de Wit, *Prog. Org. Coatings 23*:85 (1993).
84. J. H. W. de Wit, Proceedings 10th European Corrosion Congress, Barcelona, July 1993.
85. D. H. van der Weijde, E. P. M. van Westing, and J. H. W. de Wit, *Corros. Sci. 36*:6935 (1994).
86. F. Deflorian, L. Fedrizzi, and P. L. Bowona, *Electrochim. Acta 38*:1609 (1993).
87. F. Geenen, E. P. M. van Westing, and J. H. W. de Wit, Study of the degradation mechanism of epoxy coatings on steel using impedance spectroscopy, Proceedings of the 11th International Corrosion Conference, Vol. 2, Florence, April 2–6, 1990, p. 231.
88. E. P. M. van Westing, F. M. Geenen, G. M. Ferrari, and J. H. W. de Wit, The influence of solvents on the water uptake and dielectrical and mechanical properties of epoxy coatings investigated using electrochemical impedance spectroscopy, Proceedings 16th International Conference in Organic Coating Science and Technology, Athens, July 1990.
89. F. M. Geenen, H. J. W. Lenderink, E. P. M. van Westing, and J. H. W. de Wit, A detailed impedance spectroscopy investigation into the performance of different coated systems in weathering tests, Proceedings XXth FATIPEC Congress, Nice, 1990.
90. Geenen, F. M., H. J. W. Lenderink, and J. H. W. de Wit, The structure of epoxy coatings studied with impedance measurements, Proceedings 5th International Conference on Electrochemical Methods for Corrosion Research, Helsinki, July 1991.
91. F. M. Geenen and J. H. W. de Wit, Revêtements sur l'aluminium, *Eurocoat 3*:101 (1992).
92. J. A. L. Dobbelaar, Ph.D. thesis, TU Delft, 1990.
93. J. B. Hasted, *Aqueous Dielectrics*, C&H, London (1973).
94. W. Bosch and W. Funke, Peasticization of organic coatings by water, *Farbe Lack 98*(8): 589–592 (1992).
95. R. Hirayama and S. Haruyama, *Corrosion 42*:952 (1991).
96. M. Dings, R. de Jonge, S. M. Peters, E. J. H. Koot, F. M. Geenen, E. P. M. van Westing, and J. H. W. de Wit, Un nouveau test pour characteriser les produits de revêtements à l'aide des défusts artificiels apportés au laser et de la spectroscopie

Copyright © 2002 Marcel Dekker, Inc.

d'impédance électrochimique, *Double Liaison*, *Chimie des Peintures*, no. 425–426, 1991, 61/13.
97. M. M. M. Dings, R. de Jonge, S. M. Peters, E. J. H. Koot, F. M. Geenen, E. P. M. van Westing, and J. H. W. de Wit, An novel characterisation test for organic coatings based on artificial laser defects and electrochemical impedance spectroscopy, Proceedings, XX FATIPEC Congress, Nice, 1990.
98. F. M. Geenen, M. M. M. Dings, E. J. H. Koot, R. de Jonge, S. Peters, and J. H. W. de Wit, Characterisation of organic coatings using artificial laser defects and impedance measurements, Proceedings, 5th International Conference on Electrochemical Methods for Corrosion Research, Helsinki, July 1990.
99. B. van den Bossche, L. Bortels, J. Deconinck, S. Vandeputte, and A. Hubin, *J. Electroanal. Chem. 411*:129 (1996).
100. W. Fuerbeth, M. Stratmann, *Corros. Sci.*, to be published.
101. J. Mazia, *Metal Fin. 75*:49 (1977).
102. G. D. Kent, K. J. Hacias, and N. A. Fotinos, Proceedings, 2nd Automotive Corrosion Prevention Conference, Michigan, 1983, p. 23.
103. J. B. Harrison and T. C. K. Tickle, *JOCCA 45*:571 (1962).
104. W. Funke, *Farbe Lack 84*:389 (1978).

Copyright © 2002 Marcel Dekker, Inc.